Proceedings of

International Conference on Physical Modeling of Transport and Dispersion

In conjunction with

The Garbis H. Keulegan Centennial Symposium

Editors: E. Eric Adams
and
George E. Hecker

held at

Massachusetts Institute of Technology
August 7–10, 1990

Background

This conference, the fourth in a series organized by the IAHR Section on Experimental Methods and Physical Modeling, explores the capabilities and limits of hydraulic models in scaling transport and mixing phenomena. Previous conferences in this series have evaluated scale effects in other areas of hydraulics, including hydraulic structures, sediment transport, and soil-water-structure interaction.

The 1990 conference is co-sponsored by the American Society of Civil Engineers with support from the U.S. Army Corps of Engineers' Waterways Experiment Station, Massachusetts Institute of Technology, Alden Research Laboratory, Inc, and the Boston Society of Civil Engineers Section/ASCE.

Organizing Committee

Eric Adams, Co-chairman
George Hecker, Co-chairman
Dominique Brocard
Jonathan French
Donald Harleman
Mahadevan Padmanabhan
Y. J. Tsai

International Technical Committee

Gerrit Abraham, The Netherlands
Torkild Carstens, Norway
Huiquan Chen, Beijing China
Vincent Chu, Canada
Jorg Imberger, Australia
Peter Larsen, FRG
Bruno Manoha, France
K. G. Ranga Raju, India
Oleg Vasiliev, USSR
Akira Wada, Japan
T. J. Weare, UK
C. M. Wu, Taipei China

Keulegan Symposium

The conference is held in conjunction with the Keulegan Centennial Symposium in honor of the late Garbis H. Keulegan. Special keynote and invited presentations describe the contributions of Dr. Keulegan and their relationship with present work in mixing processes, stratified flow, and other areas of fluid mechanics.

ASCE Task Committee on Keulegan Centennial

William McAnally, Chairman
Rex Elder
Donald Harleman
Jorg Imberger
Gerhard Jirka
Henry Simons
Todd Walton

Table of Contents

Session 4A Jets and Plumes

Session 4B Turbulence and Interfacial Effects

Session 5 Keulegan Centennial Symposium: Stratified Flow

Session 6A Estuarine Processes

Session 8B Physical Model Studies

Session 8C Particle Settling

Session 9A Internal Mixing Processes

Session 12A Density Currents

Session 12B Mixing in Channels

Session 12C Sediment Laden Flows

Session 13A Mixing in Ponds, Lakes, and Reservoirs

Session 13B Coastal and Ocean Mixing

Session 14A Mixing in Tanks and Channels

Session 14B Sediment Laden Flows

Session 1

Keulegan Centennial Symposium: Keynote

GARBIS H. KEULEGAN: A LONG LIFE IN HYDRAULICS

by John F. Kennedy
Iowa Institute of Hydraulic Research
Iowa City, IA 52242-1585 USA

Abstract

Garbis H. Keulegan (1890-1989) was one of the giants of Twentieth Century hydraulics and fluid mechanics. His long life (which began in Turkish occupied Armenia), education, involvement in the two World Wars, technical contributions, and career as a U.S. Government employee (the longest on record) are recounted. His research and engineering work produced major contributions in electricity and magnetism, properties of materials, elasticity and vibrations, instrumentation, fluid mechanics, oceanography, and hydraulics. He was equally gifted as an imaginative researcher, a resourceful mathematician, and an applications-oriented engineer.

Biographical Sketch

One who studies the history of any arena of human endeavor soon realizes that the life stories of the creative individuals who developed the subject are at least as interesting as the annals of the subject itself. In hydraulics, one would be hard pressed indeed to find a more fascinating, a more productive, or a longer career than that of the engineer and scientist we honor and celebrate at this symposium: G.H. Keulegan. Because of his very modest--indeed, shy and almost humble--personality and his small physical stature, it is perhaps difficult to think of him as a giant of our field, but he was precisely that, as this Symposium on the occasion of the centennial of his birth attests.

Garbis Hvannes Keuleyan was born on 12 July 1890 in the city of Sebastia-Sivas (the ancient Roman City of Sebastia, dating from the time of Trajan) in Turkish occupied Armenia Minor (now Sivas, Turkey), one of the major population centers on the Anatolian Plain. He was the first of six children born to Hvannes Gerabed Keuleyan, an Armenian engineer, and Emma Marguerite née Klein, a German. In 1910, at the age of only about twenty, he received his first engineering degree from Anatolia College in Marsovan, Armenia Minor (now Merzifon, Turkey), which is some 100 miles northwest of the city of his birth. After serving one year in the Turkish army and working another as an engineer, he departed his homeland (never to return, as it turned out) in early 1912 for the United States to continue his engineering education. While awaiting the start of the academic year, he visited cousins first in Syracuse, where he worked in an office-furniture factory and a printing establishment; and later in Detroit, while employed in Cadillac and Ford factories.

In the fall of 1912 he enrolled at Ohio State University (OSU) on a scholarship, first registering in the Civil Engineering Department. It was here, through a typographical error that he neglected to correct, that his name evolved from Keuleyan to Keulegan. Apparently he felt it was easier to change his name than to correct his records. At OSU he supported himself by working as a cataloguer and bookbinder in the university library. His special talent with mathematics soon was recognized by his engineering professors, one of whom suggested that he transfer to the School of Arts to specialize in physics and mathematics. He received an A.B. in Mathematics and Physics in 1914. His performance as an undergraduate at OSU was so outstanding that he was granted a University Fellowship, under which he served as a teaching assistant, for pursuit of his graduate studies. He completed the requirements for his Masters degree, including a thesis entitled "Modern Theories of Matter", within a year and was granted the degree in the spring of 1915.

Following his graduation he entered the Westinghouse Apprenticeship Course, and in 1917 was employed as a research engineer by Westinghouse Electric and Manufacturing Company, East Pittsburgh, PA. His early work at Westinghouse was concerned with electrical hysteresis losses and magnetism. On 31 May 1918, he enlisted in the army. In the course of his infantry training, at Camp Sherman, Ohio, his linguistic abilities were recognized (he was fluent in several languages, including Armenian, Turkish, German, French, and English; he could also read Latin and Greek), and he was assigned to the staff of General John J. Pershing as a translator. He was serving with General Pershing in France when the armistice was signed. For many years thereafter he attended periodic reunions of World War I veterans who served under Pershing, until "there weren't many left. Just me and Irving Berlin."

His original plan had been to return to his native Armenia after the war, to go into engineering practice in his father's business. However, his entire family, except one brother who was studying in Paris at the time, was killed in the 1915 deportation to Syria and Mesopotamia of some 1,750,000 Armenians living under Turkish rule, and the attendant massacre of 600,000 of them. Because of this, and the continued domination of his country by USSR, Turkey, and Iran, he had no desire to return to it, and decided to remain in the United States, which he had come to love. He had been granted United States citizenship in 1918, while serving in the army. Following his discharge from the military he returned to Westinghouse, where he resumed his work on hysteresis and magnetism until 1920. For about six months during 1920-21 he was employed by the Terrestial Magnetism Department of the Carneige Institution in Pittsburgh.

Keulegan applied for a job with the National Bureau of Standards (NBS) in 1921, attracted apparently by the greater liberty to pursue his own research interests, not to mention the prestige of a position in the "Nation's Laboratory." In his own modest words he recalled: "I applied for a low grade position, but they would not accept me. They told me I was qualified for a higher grade, which I accepted." Thus he began his employment as a physicist with NBS, a position he would hold until 1962. His early work at NBS was concerned principally with solid mechanics, and included theoretical and experimental studies of hysteresis in structural members subjected to cyclic loading; vibration of bars; development of various instruments and meters for use in aircraft; and, building on his Masters thesis, temperature coefficients and moduli of metals.

Shortly after joining the NBS staff, Keulegan started work toward his doctorate in physics by taking night courses at Johns Hopkins University, a pursuit which involved frequent commuting by train between Washington, D.C., and Baltimore. In 1928 he submitted a doctoral thesis to Johns Hopkins on a problem, which he had been investigating at NBS, "On the Vibration of U Bars." He was awarded his Ph.D. in the spring of that year, and that fall, on 15 September, married Nellie Virginia Moore, in Washington, D.C. Thus, at age 38 he had completed his formal schooling, married, and finally was prepared to settle down and pursue his career--although he had been far from idle previously. It is as though this "late start" anticipated his very long life and career.

Keulegan's early work at NBS, on strut (bar) vibration, development of a fabric-tension meter, and optimal liquid damping of aircraft instruments, was done for the National Advisory Committee for Aeronautics (NACA, the predecessor of NASA). It apparently was his work for NACA that stimulated his interest in the mechanics of solids and fluids. The latter subject was to occupy most of his professional attention from the early 1930's onward. Two other (not entirely unrelated) developments of that period were to provide him with ample outlet for these interests.

The first of these was the establishment of the National Hydraulic Laboratory (NHL) at NBS, at the instigation of John R. Freeman and Senator Joseph E. Ransdell of Louisiana. NHL finally was established under the Hydraulic Laboratory Act of 1930, signed by President Hoover on 14 May of that year. The first director of NHL was Herbert N. Eaton, who assembled a staff initially comprising Karl H. Beij, Lawrence L. DeFabritis, and Keulegan. Despite the grand plans and vision for NHL, little notable research was done there except that of Keulegan and his close collaborators (Rouse 1976). Moreover, practically none of this research required the large, and largely inflexible, equipment installed in the laboratory, principally as a result of Freeman's design which had been heavily influenced by his exposure to European laboratories.

A second impact on his work, which he was not to experience until some years later, resulted from the establishment of the Beach Erosion Board (BEB) of the Department of the Army. BEB was established by the 71st Congress as part (Section 2) of the River and Harbor Act, which was approved on 3 July 1930 (Quinn 1977). In the late spring of 1940 Freeman Scholar Martin A. Mason transferred to BEB from NHL. During the early war years he realized that BEB's knowledge of beaches and shore processes might be useful in the planning and execution of amphibious landings. In June 1942 a meeting was held to discuss BEB's potential role in providing beach intelligence to the military. A result of this conference was an order from the Chief of Engineers to BEB to carry out its first intelligence study, "Landing Area Report: Cherbourg to Dunkirk," in anticipation of the D-Day landings. The report so impressed the Joint Chiefs of Staff that they, along with their European-Allies counterparts, requested that BEB augment its military beach-intelligence program. Among those recruited to the program were Keulegan and William C. Krumbein, a geologist from the University of Chicago. Kingman, Mason, Keulegan, Krumbein, and Jay Hall constituted the core of BEB's staff until the end of the war.

Keulegan was seconded from NHL to BEB from 1942 until 1946. During this time he applied his extensive knowledge of waves, tides, and currents to a variety of military problems, working principally with Hall. Experiments were run almost continuously in BEB's 24-foot and 85-foot wave tanks. The mission of the beach-intelligence group was to provide military planners of military amphibious landings with information on beach slopes, sand characteristics, reef positions and sizes, and tide and surf conditions; intelligence that was essential to successful execution of these operations. Much of this had to be inferred from aerial photos of wave-diffraction patterns. The staff often had a month or less to prepare these data and present them, in forms understandable to and usable by military planners. Their first study for an actual landing, "Operation Torch," was of the North Africa coast between Casablanca and Tangiers. The report was completed in September 1942, and the landing took place two months later. Subsequent studies were concerned with landing sites on Sicily and southern Italy. After these, the European Allies assumed responsibility for future beach-intelligence studies in their theaters of operations, and the BEB group's attention then turned to the Pacific, starting with the north coast of New Guinea, followed by other beaches northward up the Pacific Island chains (the Solomons, Carolines, Phillipines, etc.). Other BEB activities on which Keulegan worked and consulted during the war years included the beaching and retraction characteristics of landing craft; development of towed breakwaters; and a feasibility study of a mid-Atlantic floating landing field for aircraft refueling.

In a letter dated 19 December 1945, the Chief of Engineers requested NBS to; "...investigate and establish the basic laws of similitude for models involving the density currents and the mixing of salt water and fresh water." The Corps' interest in this problem arose principally from salt-water intrusion problems that were being encountered at the mouths of the Sacramento and Mississippi Rivers, as well as at navigation locks between fresh- and salt-water bodies. These problems were complicated by water waves and, especially, tides. Density-current problems also were being encountered in the Corps of Engineers' and Bureau of Reclamation's reservoirs, in which it was being found that sediment-laden density currents could persist along the full lengths of reservoirs and up to the dams--distances amounting to hundreds of miles at some installations. Keulegan was, of course, the logical NHL staff member to head these efforts. In the organization chart presented in the 1946 proposed program for NHL, he was designated as head of Unit 3--Theoretical Hydraulics. His staff was to be comprised of an assistant head, four physicists, and three laboratory mechanics (National Bureau of Standards 1946).

The general course of Keulegan's technical activities for the next 16 years, until he retired from NBS in 1962, was pretty well set. By the end of 1946 he already had submitted to the Corps of Engineers two progress reports on his study of density-current model laws: "Model Laws for Density Currents; First Progress Report"; and, "The Problems of Salt Water Intrusion in Canal Locks and the Sufficient Conditions for Adequate Model Experiments." In addition, in the years following his return to NHL, he continued his theoretical work on water waves and completed his famous paper on damping of solitary waves. He commenced his series of studies on surges in small basins connected to the sea, and also found time to write Chapter 11, "Wave Motion" of Rouse's Engineering Hydraulics (Rouse 1950). Upon reaching the then-mandatory retirement age of 70, Keulegan received two one-year presidential extensions, to complete a beach-erosion study he was conducting at NHL for BEB. Much of Keulegan's published work from the early 1930's until his retirement from NBS in 1962 appeared in NBS or NHL reports submitted to clients, the National Bureau of Standards Journal of Research or Transactions of the American Geophysical Union. Topics on which he published during this period included: laminar-flow pressure losses in curved pipes (with K. Beij); oscillatory-water-wave theory (in a series of classical papers, most co-authored with G.W. Patterson); the stability of flow in steep channels (the roll-wave problem); interfacial stability and mixing in two-layer flows; resistance laws for open-channel flows; solitary waves; and the dynamics of density-stratified flows (for which he coined the term "density currents"). His NHL studies had been primarily theoretical in nature, although he made extensive use of the experimental results of others, and had an uncanny ability to recognize questionable data and spurious correlations. He did not participate extensively in the activities of professional societies, and only rarely attended technical conferences and symposia. A notable exception was the NBS Semicentennial Symposium on Gravity Waves, which was held at NBS on 18-20 June 1951. This speciality symposium was planned, organized, and conducted by Keulegan and his long-time NBS colleague, K.H. Beij. They also edited the symposium proceedings (National Bureau of Standards 1952).

Keulegan's work on density currents and salinity intrusion at NHL attracted the attention, and eventually financial sponsorship, of the Army Corps of Engineers Waterways Experiment Station (WES). During the later years of this work, as retirement age drew near, he wondered aloud on occasion to Henry Simmons (who was monitoring the WES studies at NHL) what he might do to remain professionally active following retirement. Simmons encouraged him to consider coming to WES, and brought this possibility to the attention of Eugene Fortson (then Chief of the WES Hydraulics Division) and Colonel Edmund Lang (then WES Director). They were enthusiastic about the prospect, and in March 1960 Lang wrote to Keulegan to explore it formally. Keulegan's conditions for employment at WES were straightforward: that he be given an office; that the office have a window, and that there be a tree outside the window. An extended period of correspondence and visits followed, during which Keulegan completed his BEB work at NHL, and an administrative avenue was sought to employ him at WES. He eventually was offered a half-time position as a Consultant and Special Assistant to the Chief, Hydraulics Laboratory. The initial appointment was for one year, and the Keulegans assumed that their relocation would be temporary. In January 1963, they rented out their Washington home, moved to Vicksburg, MS, and rented a house there. Keulegan rapidly became fully engaged in the beach-erosion study he was supervising at WES, but also found that he was being sought out by his WES colleagues to assist them with especially difficult problems involving hydraulics, fluid mechanics, or modelling. The Keulegan family soon found that they enjoyed living in Vicksburg, and Keulegan himself prized the opportunity to work on the most interesting aspects of a wide variety of problems. Thus, they decided to relocate permanently in Vicksburg, and within a year of arriving there bought a house. Their break with Washington, D.C. was made complete in 1984, when they sold their house there. Keulegan's work at WES continued to be concerned principally with waves and tides, and density currents and salinity intrusion. He also was invaluable in designing strategies for, and guiding the conduct of, particularly difficult model studies.

With the passage of time, his work day became shorter, and eventually he spent just his mornings in his office. His daily routine then consisted of coming to his office at about 7 am. There he would work on the problems of interest to him. He took special delight in helping others find new ways to approach technical problems that were troubling them. At about 11 am he would leave his office for lunch at home or a restaurant. Afternoons were spent in relaxation. Pencil and paper continued to be his principal research tools. He never even adopted the electronic desk-top calculators. Instead, he utilized progressively longer slide rules as his eyesight became weaker. Three bouts of surgery, including hip repair (following a fall on a WES model) and cataract removal, failed to stop his relentless research productivity.

He had several hobbies. He loved to read about American history, particularly that of the early West. He also liked western movies, especially those featuring Gene Autry or the Lone Ranger, and the family dinner hour was arranged so he could watch their televised programs. He was an avid gardener, and prized his roses and tomatoes. His morning delight was drinking his coffee while watching the birds around the birdhouses and bird-baths which he built and tended. At about age 95, as a gesture toward healthful living, he stopped smoking.

In 1989 the U.S. Office of Personnel Management recognized him as the oldest employee in Federal Service, and as the one who had served the most years. On this occasion, he received a letter from President Ronald Reagan and Mrs. Reagan. In 1981, when asked to what he attributed his longevity and ability to work for so many years, Keulegan explained: "I never had big ideas. I did not want to be a section chief, I did not want to be rich--I'm just interested in my work. I love people; I love working in the hydraulics laboratory. I enjoy my work immensely--it helps keep me alert."

In the course of his long and very distinguished career, Keulegan was accorded a full complement of professional recognitions. These included: the Commerce Department Gold Medal (1960); the National Medal of Science (1968); the Army Research and Development Award, and Honorary Membership in ASCE (1969); the Meritorious Civilian Service Award (1973); the Commander's Service Award for Civilian Service, and election to the National Academy of Engineering (1979); and selection for inclusion in the WES Gallery of Distinguished Civilian Employees (1986).

Time does not stand still even for the greatest of men, and in 1988 he wrote the following letter, in his own still steady hand, to Mr. Frank Herrmann, Jr. (Chief of the WES Hydraulics Laboratory):

215 Buena Vista Dr.
Vicksburg, MS 39180

Sept 17, 1988

Mr. Frank A. Herrmann
Chief Hydraulics Laboratory
U.S. Army Corp Eng., Waterways Experiment Station
P.O. Box 631, Vicksburg, MS 39180

Dear Frank,

Conditions are such that I will not be able to return and to resume my regular work at the laboratory. Thus, I am compelled to resign as of Sept. 26, 1988.

My association with you and with the other members of the laboratory staff has been a real source of pleasure. I hasten to express my deep appreciation of the all the kindness and favors shown.

Sincerely,

G.H. Keulegan

Garbis Keulegan died of multiple complications on 28 July 1989, at age 99, less than one year after retiring the second time. Services were held at St. Paul Catholic Church in Vicksburg, Mississippi. His remains are interred at nearby Green Acres Cemetery.

References

Keulegan, G.H., and Beji, K.H., 1952, "Gravity Waves," Proceedings of the NBS Semicentennial Symposium on Gravity Waves Held at NBS on June 18-20, 1951, Circular 521, U.S. Government Printing Office, Washington 25, D.C.

National Bureau of Standards, 1946, "Proposed Program for the National Hydraulics Laboratory," NBS, Washington, D.C.

Quinn, Mary Louise, 1977, "The History of the Beach Erosion Board, U.S. Army, Corps of Engineers, 1960-63," Miscellaneous Report No. 77-9, U.S. Army Corps of Engineers Coastal Engineering Research Center, Kingman Building, Fort Belvor, Virginia.

Rouse, Hunter, (ed), 1950, Engineering Hydraulics, Wiley and Sons, New York.

Rouse, Hunter, 1976, Hydraulics in the United States, 1776-1976, Institute of Hydraulic Research, The University of Iowa, Iowa City, Iowa.

Session 2A

Jets and Plumes

The Merging of Buoyant Jets in a Current

I.R. Wood and M.J. Davidson

Department of Civil Engineering
University of Canterbury
NEW ZEALAND

1.0 Abstract

The results of an experimental investigation into the merging of buoyant discharges in a current is presented. Trajectory data from the merging buoyant flows are reported. The investigation shows that the conditions at the point of merging have an important effect on the behavior of such flows.

2.0 Introduction

When a buoyant jet is released into coflowing fluid it may initially behave as an advected jet, then change to an advected plume and finally become an advected thermal. In the first two regions the velocity distribution in the flow is approximately gaussian and in the final region the flow is vortex like. This is illustrated in Figure 1.

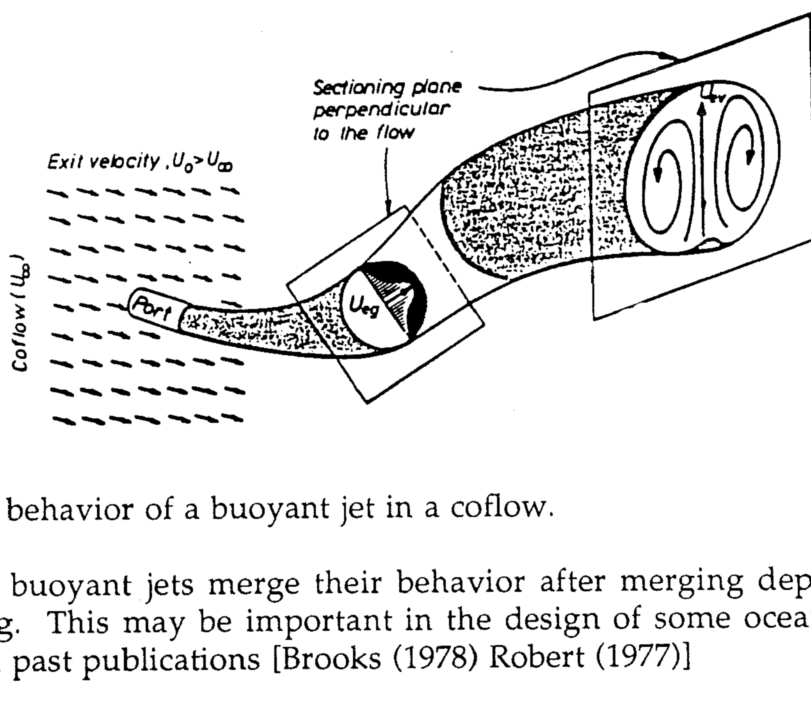

Fig. 1 The behavior of a buoyant jet in a coflow.

When the buoyant jets merge their behavior after merging depends on the conditions at merging. This may be important in the design of some ocean outfalls and has been ignored in past publications [Brooks (1978) Robert (1977)]

3.0 The Experiments

The investigation involved a series of experiments in which the trajectories of the merging buoyant flows in an ambient current were studied. A manifold (figure 2) was designed to enable the same discharge from each of up to 17 ports, with one or all of the ports being dyed. In figure 2 the discharge through the central port is independent of the others and is dyed. The ports were all 3.3mm in internal diameter (d_p). Port spacings (p_s) of 60mm and 90 mm were used. The manifold was mounted on a trolley and towed at a variety of speeds (ambient velocities (U_∞)) down a tank full of ambient fluid (fresh water). The manifold itself was not submerged and hence ambient turbulence was minimal. Density differences were created by discharging salt solutions (35 grams/litre) and the dye used was non-buoyant. The density differences were sufficiently small for the Boussinesq approximation to be appropriate and the flow could be interpreted as a lighter effluent rising. All results were recorded with a video camera.

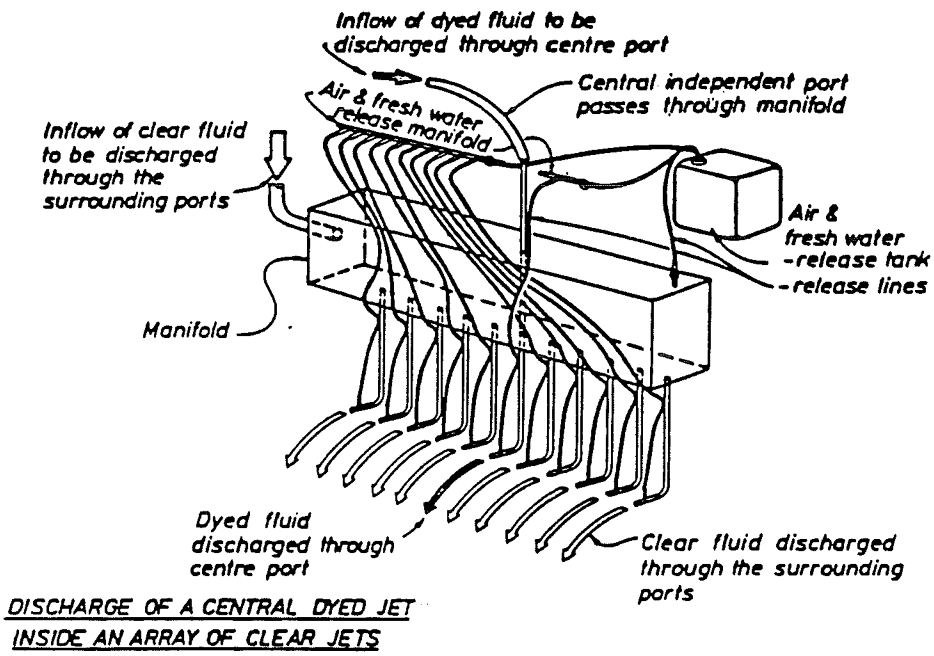

Fig 2. The manifold used in the experimental investigation (schematic)

Two sets of experiments were carried out. The first to examine the behavior of the central merging buoyant flow in a diffuser with a larger number of ports and the effect of reduced numbers of ports surrounding the central port. The second series examined the behavior of the edge buoyant flow under the same conditions. Comparisons could be made then between the behavior of the central and edge discharges. These experiments were then compared with the behavior of a single buoyant discharge under the same conditions. Each of the buoyant flows had the same discharge and density difference was towed at the same ambient velocity.

A computer program for a single buoyant jet in a coflow [Davidson 1988] was used to compute the transitions between the flow regions and it was assumed that the point of merging occurred when the calculated width [defined as the position where the velocity is [1/e] times the centreline velocity] was $0.3p_s$.

This was consistent with the observations.

4.0 Results

The data and tracings in this section are presented as if the flow was from an outfall and the effluent was rising to the ocean surface.

Figure 3 (a) shows a tracing of a single buoyant flow in an ambient current were the initial velocity ratio (U_r) is 0.5 and the Froude number (Fr_o) is 3.39. The initial velocity ratio is the ratio of the ambient velocity to the absolute velocity of the discharge. In Figure 3(b) a similar tracing of a central buoyant flow in an array of 17 ports is presented. In this case the central merging buoyant flows are behaving as advected thermals and there was in effect an infinite array of discharges. It is to be noted that the merging buoyant flow rises more slowly than the single buoyant flow and that the profiles are similar apart from minor variations in the outer edges of the dyed fluid where there is a slightly greater spread in the merged case. A brief study of merging buoyant discharges in a counterflowing ambient fluid revealed a similar behavior.

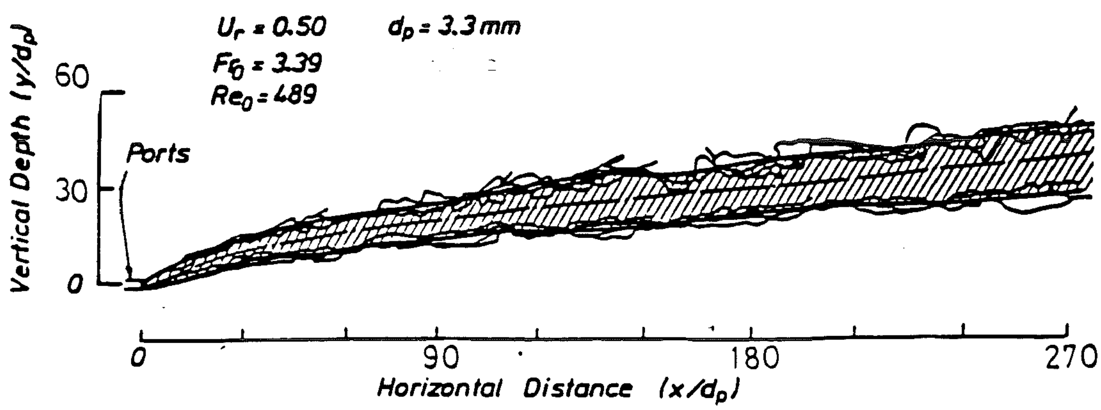

(a) A tracing of the rise of a single buoyant flow in a coflow.

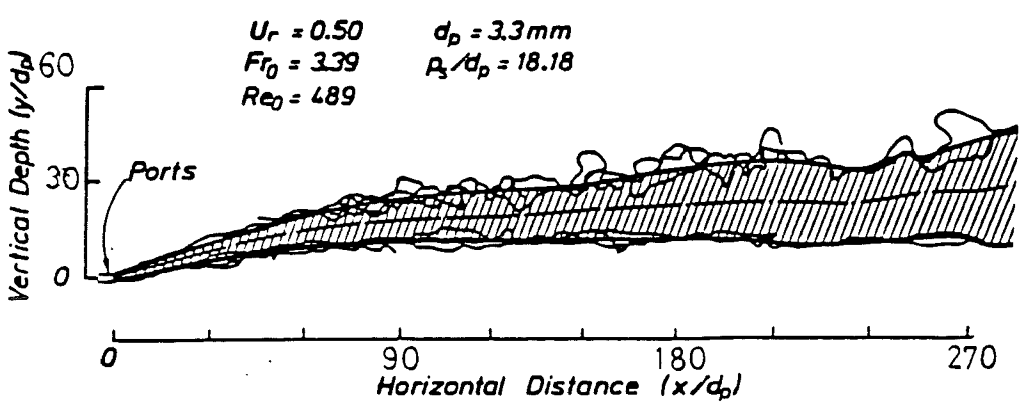

Fig. 3 (a) A tracing of the rise of merging buoyant flows in a coflow. The merging is in the advected thermal region.

Similar experiments were carried out when the merging was in the advected plume region and in the transition region between the plume and the thermal region. Apart from a marked discontinuity at the point of merging in the advected plume region the results were similar. In every case the trajectory of the centreline of the central buoyant jet of an array was less steep than that of a single buoyant jet with no surrounding buoyant jets.

The effects of the number of ports in the array was also investigated. Firstly the number of discharges in the array was increased from 1 to 17 ports. Where the merging was in the advected thermal region the entrainment into the flow was small and even with 17 ports in the centre of the tank the walls of the tank appeared to have a negligible effect. For the case of merging in the transition or advected plume regions the entraining flows were considerable and in order to overcome the wall effect for an array of ports greater than 11 one wall was treated as a centreline. For effective port numbers of twelve, fourteen and sixteen, six, seven an eight ports were used against the tank wall. This in effect doubled the tank width and in effect removed any influence of the wall. This data is presented in Figure 4. Only the cases of merging in the advected plume and the advected thermal regions are shown. It can be seen that in every case the merged trajectories are below those of a single buoyant flow in a coflowing ambient fluid. For merging in the advected thermal region, the central port of an array of 7 or more ports behaves as if it were in an infinite array of ports. For merging in the advected plume region 13 or more buoyant jets are required before the central port can be treated as if it were in an infinite array of ports.

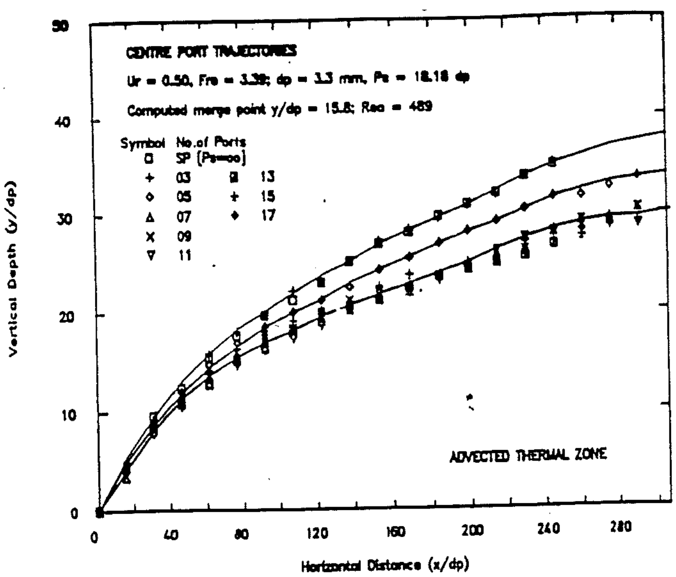

(a) The point of merging is in the advected thermal region

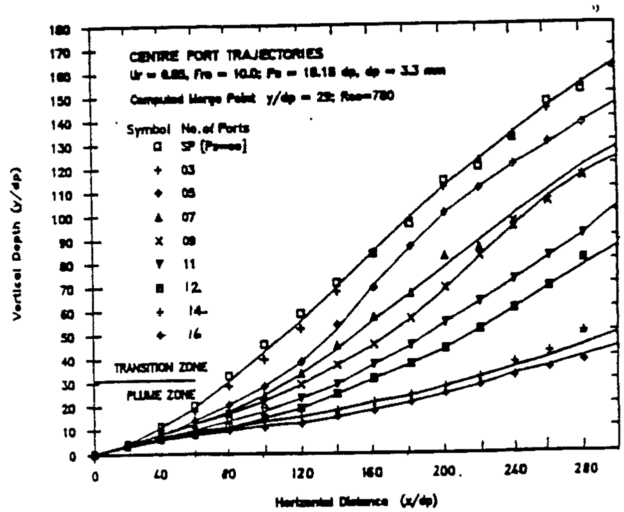

(b) The point of merging is in the advected plume region.

Figure 4. Trajectories of merging buoyant flows in a coflowing ambient current.

Finally, by studying the trajectories of the edge and central discharges in the array an idea of the buoyant clouds shape can be obtained. Figure 5 presents such data for 11 buoyant discharges which are initially advected thermals and hence they merge as advected thermals. It is notable that the trajectory of the buoyant jet on the edge of the cloud is above that of the central buoyant flow. This difference can be seen prior to point of merging. Where the merging is in the plume region the trajectory at the edge of the cloud is below that of the central trajectory, however, prior to merging the centre and edge trajectories coincide. This is illustrated in Figure 5b.

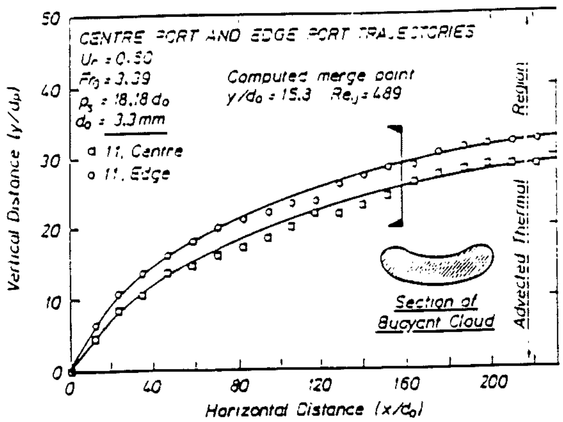

(a) Merging in the advected thermal region.

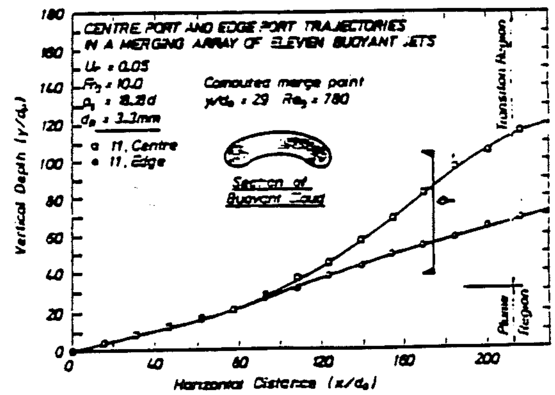

(b) Merging in the advected plume region.

Figure 5. A comparison of the trajectory of the central discharge and the edge discharge of an array of 11 buoyant flows in a coflowing ambient fluid.

A plausible explanation for the differences in the shapes of the merging buoyant discharges can be obtained for the case were the velocity at anytime is due to the vorticity in the advected thermals. The advected thermal region may be modelled as a line of two-dimensional vortex pairs. When, or soon after, merging occurs they will be approximately evenly spaced. This is illustrated for five vortex pairs with a vortex spacing of d in Figure 6.

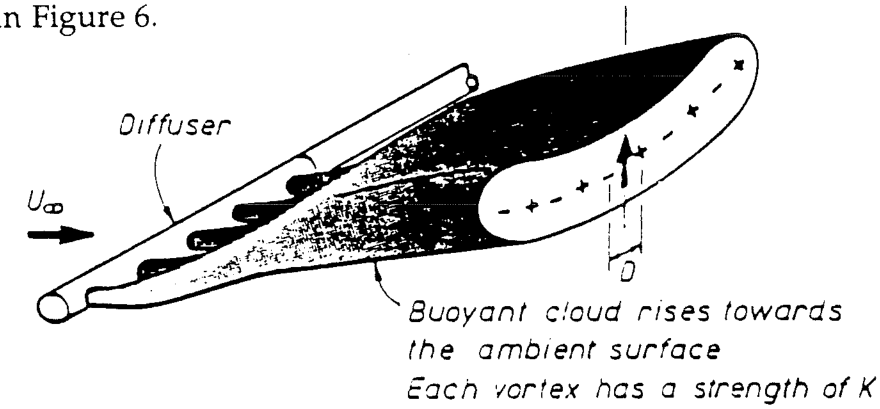

Figure 6. A merging array of advected thermals.

For either vortex of the central vortex pair the induced upward velocity v is $v = 0.2K/2\pi d$ (where K is the circulation and d is the vortex spacing)

For the edge vortices the induced upward velocity is $v = 0.75\ K/2\pi d$.

This implies that the merged advected thermal vortices move upwards more slowly than a single advected vortex which move with a velocity of $v = K/2\pi d$

In addition it implies that the outer vortices move upwards faster than the central vortex pair. This is consistent with the observations and is also consistent with the upward movement of the edge advected thermal relative the central advected thermal prior to the point of merging. The vortex type model also accounts qualitively for the difference in the movement of the edge and central plume prior to merging in the advected thermal case. After the point of merging the developed vorticity of the advected thermals will cross diffuse until the effective strength of each vortex pair becomes negligible. At this stage the merged flow becomes similar to that of merged plumes and the flow around the surface of the rising cloud causes the shape to change with the outer edge falling below the centre. It is presumed that in an indefinitely deep ocean the cloud will then eventually roll up into a single two dimensional advected thermal.

5.0 Conclusions

The above results have considerable practical implications. In an ambient flow each of the merged buoyant flows rise more slowly, to the surface, than a single buoyant flow with the same properties and the peak dilutions are of a similar magnitude. For a given total discharge increasing the number of ports will increase the dilution at the surface. If these discharges merge there is the added advantage of delaying the arrival of the effluent at the surface.

6.0 Acknowledgements

The authors would like to acknowledge the financial support of the National Water and Soil Conservation Authority (DSIR) and the University Grants Committee of New Zealand. This paper was prepared while the second author was at the D.A.M.T.P., University of Cambridge, United Kingdom, and the first author was the Mary Shepard B Upson visiting Professor at the Cornell University.

8.0 References

Brooks, N.H., [1979]. In Fischer, H.b., List, E.J., Koh, R.C. H., Imberger, J. and Brook, N.H.
Mixing in Inland and Coastal Waters. Academic Press, New York.

Davidson, M.J., [1980]
The Behavior of a Single, Horizontally Discharged, Buoyant Flow in a Non-Turbulent Coflowing Ambient Fluid. University of Canterbury Civil Engineering Dept. Report 89-3.

Roberts, Philip J.W. [1977] Line Plume and Ocean Outfall Dispersion. Journal of Hydraulic Division, A.S.C.E., Vol. 105, No. HY4, April, pp. 314-331.

Cheng, Chi-Wai, An Experimental Investigation of the Effects of Diffuser Width Upon Horizontally Discharged Merging Buoyant Flow in a Non-Turbulent Coflowing Ambient Fluid, ME thesis 1, Department of Civil Engineering, University of Canterbury [1989].

THREE COMPONENT VELOCITY MEASUREMENTS IN AN AXISYMMETRIC JET USING LDA

by

John M. Kuhlman and Robert W. Gross
West Virginia University
Mechanical and Aerospace Engineering Department
Morgantown, WV
26506

ABSTRACT

A commercial three-component laser doppler anemometer (LDA) has been used to acquire a detailed set of three-dimensional mean and fluctuating velocity measurements in a low-speed air jet entering a stagnant ambient, over the first 15 jet exit diameters along the jet trajectory. These data are consistent with previous measurements in axisymmetric, turbulent jets. Mean velocity and Reynolds stress data approach a self-preserving behavior by $x/D \cong 15$. However, the RMS turbulence fluctuations were not self-preserving at this axial location, as expected based upon previous experimental studies. These data confirm the ability to obtain reliable three-dimensional velocity data using the present 3-D LDA system.

INTRODUCTION

The laser doppler anemometer has become a widely-used tool for non-intrusive measurement in turbulent flows. Recently, several types of three-component systems have been developed, to enable simultaneous measurement of three fluctuating velocity components. As discussed by Meyers (ref. 1), many of these three-component systems suffer from a significantly compromised accuracy of one of the velocity components (along the optical axis).

In the present study, velocity measurements have been made in a nonbuoyant, axisymmetric air jet entering a stagnant ambient, as a means of assessing the reliability of three-component data obtained from a commercial 3-D LDA system. The axisymmetric jet is a relatively simple turbulent free shear flow which has previously been widely studied (for example, refs. 2-9) and which becomes self-preserving away from the jet exit. The flow field is axisymmetric, allowing a check between velocity measurements made with different channels of the LDA system. Mean velocity profiles become self-preserving within 10-20 exit diameters (refs. 2-7), while the turbulence field becomes self-preserving beyond 60-80 exit diameters (refs. 2, 8, 9). The data for the present study have been presented in dimensional form in ref. 10.

DESCRIPTION OF EXPERIMENTAL FACILITY AND PROCEDURE

The present LDA system is a commercial five beam DANTEC fringe-type LDA system with the general layout described by Buchave (ref. 11). The system has been described in some detail in ref. 10. Other types of 3-D LDA systems have been described in ref. 1. The jet facility consists of an air compressor which supplies air through a pressure regulator, oil separator, filters, control valve, and rotameter to a 120:1 area ratio contraction which exits to a 0.415 inch (10.54mm) diameter jet exit pipe which is nominally 45 jet diameters in length. For the present nominal exit Reynolds number of 23,000 based on jet exit diameter, it is expected that exit velocity profiles should correspond to fully developed turbulent pipe flow. The jet enters near the centerline of a 18" x 20" (.46x.51m) cross section low speed wind tunnel. The jet enters the tunnel test section transverse to the tunnel axis. For the present study, no crossflow has been used; the tunnel has been used simply to contain the jet flow seed particles. The tunnel is fitted with a vertical glass side, to allow optical access for the LDA system.

The jet flow has been seeded with 0.5-4 μm diameter glass microbeads from a cylindrical fluidized bed feeder which is fitted with an electric shaker, to ensure a uniform seed rate. In an effort to achieve a uniform seed particle number density throughout the flow field, the jet facility was run with the particle feeder on for 18-24 hours before any data taking was begun. The maximum particle diameter of 4 μm is estimated to be capable of following the flow up to frequencies of 2-3 kHz, based upon the work of Hjelmfelt and Mockros (ref. 12). Overall validated data rates yield calculated data densities on the order of 0.3, based on the computed Taylor micro time scale (ref. 13). Data files obtained in the current study at each location consist of 2816 measurements of each of the three velocity components, plus the sample interval time since the last validated coincident set of three velocity component measurements. For this study, coincidence between measured velocity components has been defined to occur when all three laser velocimeter channels send a validated velocity measurement to the buffer within 300 μs of one another. This is approximately twice the length of a typical burst on any of the three channels.

Data has been reduced using techniques discussed in refs. 13-17. The "tails" of frequency histograms are deleted for each channel, in an effort to eliminate spurious data. Approximately one percent of data for each channel is eliminated this way. Also, to investigate the need for velocity bias corrections, both sample interval time weighting as well as statistical averaging has been used to calculate average velocities, RMS values, and velocity cross-correlation distributions. Data presented herein has been calculated using statistical averaging. There was very little difference between these two averaging methods.

RESULTS

Data consist of a series of radial traverses across the jet axis in the horizontal or vertical directions at five locations along the jet axis and a traverse along the jet centerline. At each point the reduced data consist of the calculated mean and RMS velocity components, and the calculated velocity cross-correlations. Results for the lateral surveys across the jet radius are presented in Figs. 1-5, while the jet centerline traverse results are presented in Figs. 6-8. Note that all of these results are essentially three-dimensional measurements in what is basically a two-dimensional (x,r) mean flow field. As a check of the self-preserving behavior of the flow, radial profiles have been plotted versus (r/b) where b is the jet radius where U is is one half the centerline value, while for the axial traverse results, x has been normalized by the jet exit diameter, D. Velocities have been nondimensionalized by the local centerline axial mean velocity.

Mean axial velocity results (Fig. 1) appear self-similar, especially for the three traverses farthest from the jet exit. Mean velocities have been normalized by the local centerline axial mean velocity. Mean radial velocity data (Fig. 2) show considerable scatter, but display the correct magnitude (a maximum of about 5% of the axial velocity) and spatial variation (V changes sign across the jet centerline). Data have been presented from both sides of the jet centerline, with the absolute value of radial velocity shown in Fig. 2. Generally, as x increases, non-dimensional V increases somewhat.

Radial profiles of measured axial, and radial RMS velocities are presented in Figs. 3 and 4. RMS velocities have also been normalized by the centerline value of mean axial velocity. Circumferential RMS velocity is similar to the radial RMS values. The axial RMS velocity is consistently larger than the other two components. This behavior is expected on physical grounds (ref. 18), and has been observed in earlier studies (refs. 8, 9). All three RMS velocity profiles display a peak at $r/b \cong 0.7$ nearer to the jet exit, which disappears at larger x values. At the largest x value for the present study ($x/D \cong 15$), centerline values of the three RMS velocities have risen to approximately 25%, 15%, and 18% of the local centerline velocity. These values are somewhat lower than measured in refs. 8 and 9 beyond $x/D \cong 60$ to 80, where self-preservation of the turbulence field was observed. In refs. 8 and 9, once the turbulence field became self-preserving, the axial RMS velocity was measured to be about 28% of the centerline velocity, while both the radial and circumferential RMS velocities were found to reach about 23% of the centerline velocity.

Radial profiles of the $-\overline{u'v'}$ correlation (Fig. 5) show some scatter, but agree well with results in refs. 8 and 9. Other measured correlations were small (ref. 10). Reynolds stress is a maximum at $r/b \cong 1$; this maximum value increases with increasing x.

The variation of mean axial velocity on the jet centerline (Fig. 6) shows the expected development of an inverse variation with x. Jet width data extracted graphically from the lateral profiles of mean axial velocity (Fig. 7) also display the expected linear width growth. Axial variation of the three RMS velocities on the jet centerline (Fig. 8) confirm that the turbulence field has not yet become self-preserving at $x/D \cong 15$, as expected.

Finally, the scatter in measured circumferential and radial velocities of approximately ±0.5 m/s is believed to be representative of the typical measurement uncertainty order of magnitude for mean velocity in the present study. This corresponds to errors of between 1.5 and 3% in the mean axial velocity (Fig. 1). However, percent uncertainty is considerably larger for mean radial velocity (Fig. 2), since it is smaller in magnitude.

CONCLUSION

A set of three-component LDA data has been obtained in a low speed, turbulent, axisymmetric air jet entering a stagnant ambient. Mean and turbulent velocity results are consistent with other published results for turbulent, circular jets. The present data demonstrate the utility of the system to make accurate 3-D velocity measurements.

ACKNOWLEDGEMENTS

Partial support for this effort was provided by the NASA Langley Research Center under Grant NAG1-748, Mr. John W. Paulson, Jr., technical monitor. Mr. Edward Johnson was extremely helpful in learning to use the 3-D LDA system.

REFERENCES

1. Meyers, J. F., "The Elusive Third Component", Proceedings of Int'l. Symposium on Laser Anemometry, ASME FED-Vol. 33, A. Dybbs & P. A. Pfund, editors, 1985, pp. 247-254.
2. Rajaratham, N., Turbulent Jets, Vol. 5, Developments in Water Science, Elsevier Publishing Co., NY, 1976, pp. 27-49.
3. Corrsin, S., "Investigation of Flow in an Axially Symmetric Heated Jet of Air", NACA Wartime Report W-94, 1943.
4. Hinze, J. O. and Zijnen, B. G. Van der Hegge, "Transfer of Heat and Matter in the Turbulent Mixing Zone of an Axially Symmetrical Jet", J. Appl. Sci. Res., Vol. A1, 1950, pp. 435-461.
5. Albertson, M. L., Dai, Y. B., Jensen, R. A., and Rouse, H., "Diffusion of Submerged Jets", Trans. ASCE, Vol. 115, 1950, Paper 2409, pp. 639-697.
6. Ricou, F. P. and Spalding, D. B., "Measurements of Entrainment by Axisymmetrical Turbulent Jets", J. Fluid Mechanics, Vol. 11, 1961, pp. 21-31.
7. Sami, S., Carmody, T., and Rouse, H., "Jet Diffusion in the Region of Flow Establishment", J. Fluid Mechanics, Vol. 27, Part 2, 1967, pp. 231-252.
8. Wygnanski, I. and Fiedler, H., "Some Measurements in the Self-Preserving Jet", J. Fluid Mechanics, Vol. 38, Part 3, 1969, pp. 577-612.
9. Hussein, H. J., George, W. K., and Capp, S. P., "Comparison Between Hot-Wire and Burst-Mode LDA Velocity Measurements in a Fully-Developed Turbulent Jet", Paper AIAA-88-0424, presented at AIAA 26th Aerospace Sciences Meeting, Reno, NV, Jan. 11-14, 1988.
10. Kuhlman, J. M. and Gross, R. W., "Three Component Laser Doppler Measurements in an Axisymmetric Jet", NASA CR-181908, October 1989.
11. Buchave, P., "Three-component LDA Measurements", DISA Information No. 29, Jan. 1984, pp. 3-9.
12. Hjelmfelt, A. T., Jr. and Mockros, L. F., "Motion of Discrete Particles in a Turbulent Fluid", Applied Science Research, Vol. 16, 1966, pp. 149-161.
13. Edwards, R. V., editor, "Report of the Special Panel on Statistical Particle Bias Problems in Laser Anemometry", ASME J. Fluids Engineering, Vol. 109, June 1987, pp. 89-93.
14. Yanta, W. J. and Smith, R. A., "Measurements of Turbulence-Transport Properties with a Laser Doppler Velocimeter", Paper AIAA-73-169, presented at AIAA 11th Aerospace Sciences Meeting, Washington, D.C., Jan. 10-12, 1973.
15. Bendat, J. S., and Piersal, A. G., Measurement and Analysis of Random Data, Wiley, 1966.
16. Meyers, J. F., "Laser Velocimeter Data Acquisition and Real Time Processing Using a Microcomputer", presented at 4th Int'l. Symposium on Applications of Laser Anemometry to Fluid Mechanics, Lisbon, Portugal, July 11-14, 1988.
17. Gould, R. D., Stevenson, W. H., and Thompson, H. D., "Parametric Study of Statistical Bias in Laser Doppler Velocimetry". AIAA Journal, Vol. 27, No. 8, Aug. 1989, pp. 1140-1142.
18. Tennekes, H. and Lumley, J. L., A First Course in Turbulence, MIT Press, Cambridge, MA, 1972, pp. 74-75.

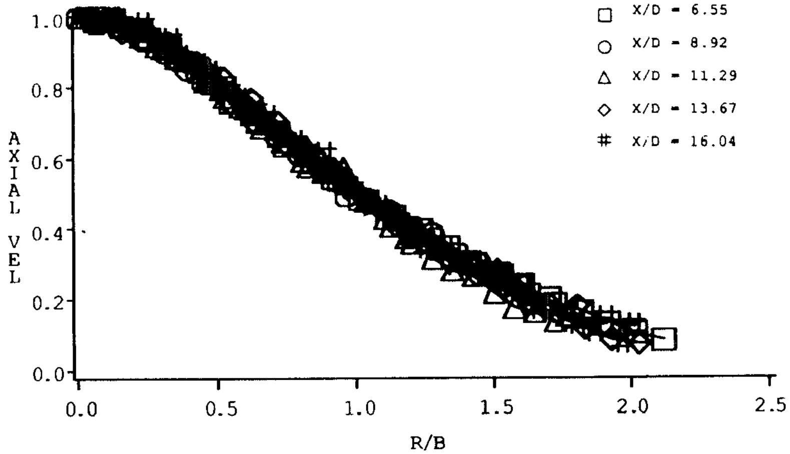

Fig. 1 Nondimensional mean axial velocity versus r/b

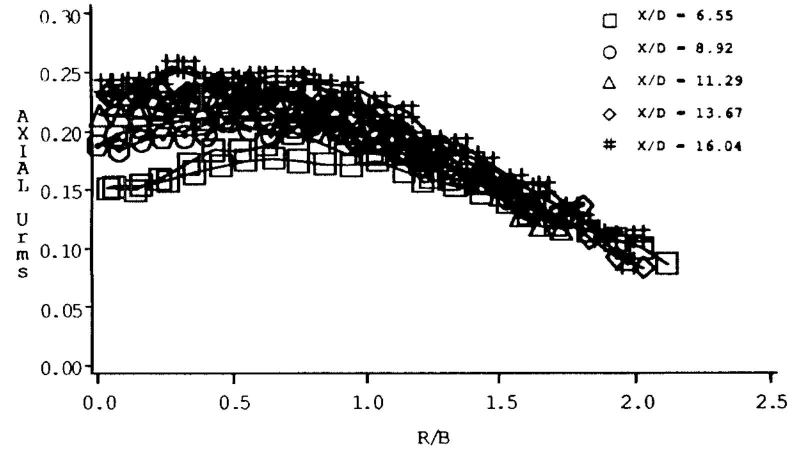

Fig. 3 Nondimensional RMS axial velocity versus r/b

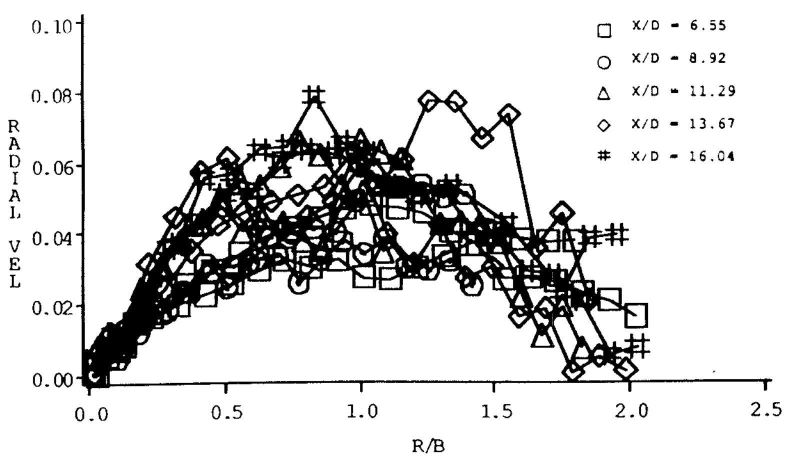

Fig. 2 Nondimensional mean radial velocity versus r/b

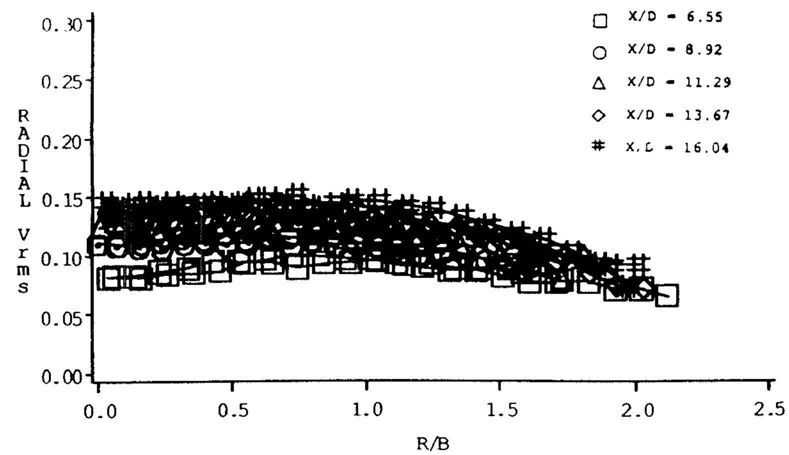

Fig. 4 Nondimensional RMS radial velocity versus r/b

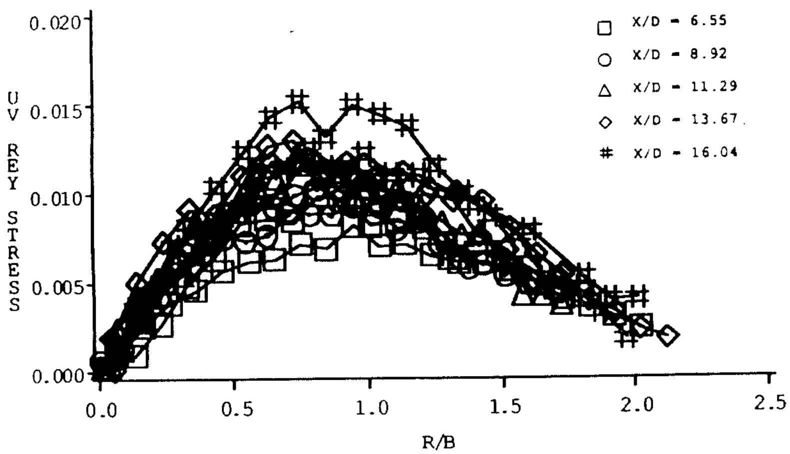

Fig. 5 Nondimensional Reynolds stress versus r/b

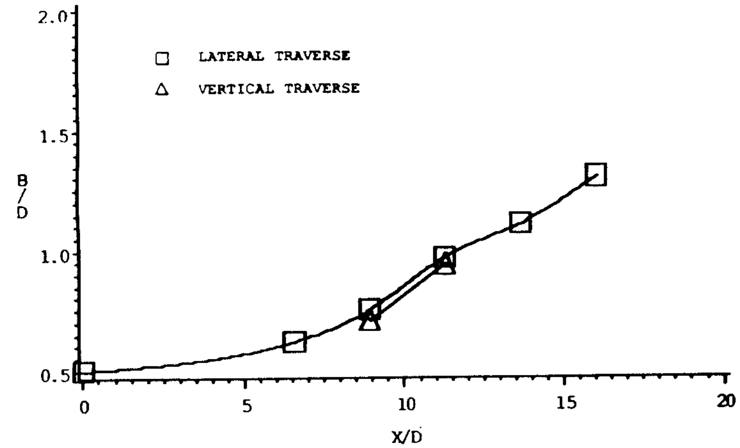

Fig. 7 Jet width versus x/D

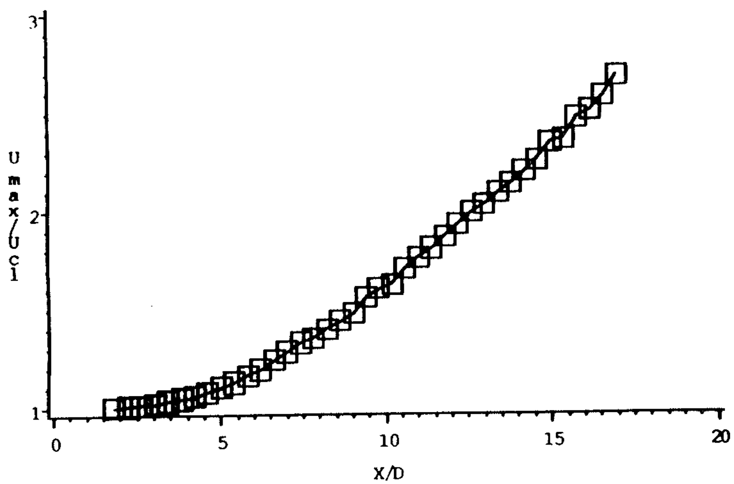

Fig. 6 Axial profile of inverse of centerline velocity

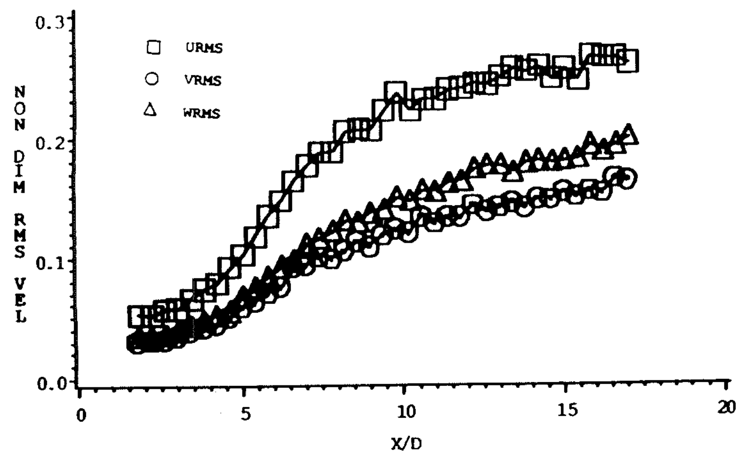

Fig. 8 Axial profiles of nondimensional centerline RMS velocities

TURBULENCE STRUCTURE OF THE HORIZONTAL BUOYANT JET

by

Professor N.E. Kotsovinos and Lecturer A. Pantokratoras
Democritus University of Thrace
671 00 XANTHI - GREECE

Abstract

The basic objective of this paper is to report the experimental results of a set of well organized experiments in a hot, horizontal buoyant jet where the turbulence structure of temperature fluctuations was studied as a function of the initial densimetric Froude number.

Introduction

In spite of the fact that the turbulence structure of horizontal buoyant jets is an interesting problem, both from a theoretical and from a practical point of view (e.g dilution of sewage from a submarine outfall), measurements of the turbulence are completely non-existent in the literature. The existing measurements in horizontal turbulent buoyant jets concern laboratory studies of the trajectories and time averaged measurements of concentration profiles; see for example Rawn and Palmer (1930), Bosanquet et al (1961), Caderwall (1963), Anwar (1969, 1972), Ryskiewich et al (1975) and Sobey et al (1988).

Assuming that to the first approximation the dilution, trajectory and turbulence structure of the turbulent buoyant jet is independent of the Reynolds number, we find that the physical model of a buoyant jet is based on the densimetric Froude number, which, is defined as

$$F_o = \bar{u}_o / \left(\frac{\rho_a - \rho_o}{\rho_o} gD \right)^{1/2}$$

where ρ_a is the density of the ambient fluid, $\bar{u}_o$ and ρ_o are respectively the velocity and density of the buoyant jet at the exit; D is the exit diameter and g the gravitational constant.

Previous studies of the turbulence structure of vertical buoyant jets indicated that the turbulence structure of a buoyant jet is not self - preserved, and that is in a transition process, from the turbulent structure of a jet to that of a plume. The important dimensionless length which describes this transition process (see List 1982, Kotsovinos 1985) is given by the parameter ξ.

$$\xi = \frac{S\, \beta_o^{1/2}}{m_o^{1/2}} = \left(\frac{\pi}{4} \right)^{-1/4} \left(\frac{S}{D} \right) \frac{1}{F_o}$$

where S is the distance along the buoyant jet axis; β_o and m_o are respectively the kinematic fluxes of buoyancy and momentum at the exit, which are defined as:

$$\beta_o = \pi \frac{D^2}{4} \bar{u}_o \frac{\rho_a - \rho_o}{\rho_o} g \qquad \text{and} \qquad m_o = \pi \frac{D^2}{4} \bar{u}_o^2$$

Experimental apparatus and procedure

The experiments were conducted in a transparent glass walled tank 450 cm long, 270 cm wide and 200 cm deep. The horizontal round buoyant jet was produced by discharging hot water from an orifice of diameter 1 cm into the tank. Measurements were taken by means of 10 calibrated thermistors, positioned to measure temperature distributions across the buoyant jet. Specifically, all measurements were taken in the vertical plane which included the vector of the exit velocity. The array of the 10 thermistors was always in this vertical plane and either along a vertical (VV') or an horizontal (HH') line (see Figure 1).

The bead diameter of the thermistors was 0.125 mm and the thermistor time constant for a 63 % response was 7 milliseconds. The thermistor response to temperature was measured with a bridge circuit, using precision metal film resistors. The absolute accuracy of the temperature measurements was less than 0.01 ^oC. The analog outputs corresponding to temperature measurements were fed into an analog to digital data acquisition system interfaced to HP 9845B microcomputer. The data sampling rate was 55 Hz and the sampling time for each thermistor 120 seconds. The structure of the turbulent temperature fluctuations were determined numerically on the HP 9845B microcomputer using the digitized records of the calibrated temperature fluctuations.

Presentation and discussion of results

The profile of the mean temperature $\bar{T}(x,y)$ along the vertical line VV' (see Fig. 1) is plotted in Figure 2 against non-dimensional distance from the buoyant jet axis. The mean temperatures $\bar{T}(x,y)$ are normalized using the local mean temperature $\bar{T}_M(s)$ on the jet axis (defined as the maximum mean temperature of the profile), and the distance using the temperature half width b_T. The profile of the turbulence intensity $\overline{T'^2}(x,y)$ along a vertical line, normalized by the local mean temperature $\bar{T}_M(s)$, is plotted versus the non-dimensional distance y/b_T from the jet axis in Figure 3, for $\xi = 0.93$ (jet-like flow) and $\xi = 14.44$, (plume - like flow).

The normalized turbulence intensity along the jet axis is plotted in Figure 4 versus the dimensionless length scale ξ. It can be observed that the normalized turbulence intensity increases with ξ and that for $\xi > 10$, the normalized turbulence intensity reaches a value $\sqrt{\overline{T'^2_M}} \,/\, \bar{T}_M \cong 0.52$, which is higher than the value of 0.44 which has been found for a vertical round plume, see Kotsovinos (1985) or by Papanikolaou and List (1987).

The centerline normalized turbulence intensity for the same ξ is plotted in Figure 5 as function of the curvature R of the buoyant jet axis. This plot indicates that the curvature of streamlines increases the turbulent intensity of the horizontal buoyant jet. The spectral density $E_{TT}(f)$ of the turbulent temperature fluctuations is plotted in Figure 6 as a function of the frequency f (in Hz). It is observed that there is a range of low frequency wave-numbers, next to the "-5/3" slope of the inertial subrange, where the spectral slope is "-3". This spectral slope was observed also by Kotsovinos (1986), in a vertical round plume. The "-3" spectral slope indicates that the efficiency of the transformation of the potential energy to kinetic energy increases with increasing the eddy size (or decreasing the wavenumber).

References

1. Anwar M.L. (1969), Behaviour of buoyant jet in calm fluid. J. Hyd. Div., ASCE, Vol.95, pp. 1239-1303.

2. Anwar M. L.(1972), Measurments on horizontal buoyant jet inin calm ambient fluid, with theory based on variable coefficient of entrainment determined experimentally. La Houille Blance, No.4, pp.311-319.

3. Bosanquet C.H., Horn G. and Thring M.W. (1961), The effect of density differences on the path of jets. Proc. Roy.Soc. London, No. 1314, pp. 340-352.

4. Cederwall K. (1963). The initial mixing on jet disposal into a recipient (in Swedish). Chalmers Inst. of Tech., Div. of Hyd., Publication No. 14.

5. Kotsovinos N.E. (1985). Temperature measurements in a turbulent round plume, Int. J. Heat Mass Transfer, Vol. 28, pp. 771-777.

6. Kotsovinos N.E. (1986). Low frequency power spectra in buoyant flows, International Symposium on Buoyant Flows, Ahens, Greece,(ed. G. Noutsopoulos)

7. List E.J. (1982). Turbulent jets and plumes. Ann. Rev. Fluid Mech., Vol. 14, pp. 189-212.

8. Papanicolaou, P.N.and List, E.J. (1987). Statistical properties of tracer concentration in round buoyant jets. Int. J.Heat Mass Transfer, Vol. 30, pp. 2059-1071.

9. Rawn A.M. and Palmer H.K.(1930), Predetermining the extend of a sewage field in sea water. Trans.ASCE, Vol. 94, pp. 1036-1060.

10. Ryskiewich B.S. and Hafetz L.(1975).An experimental study of the ree surface effect on a buoyant jet. General Dynamics Report No. U440-74-103.

11. Sobey J.R, Johnston J.A and Keane D.R (1988). Horizontal round buoyant jet in shallow water, J. Hyd. Div., ASCE, Vol. 114, pp. 910-929.

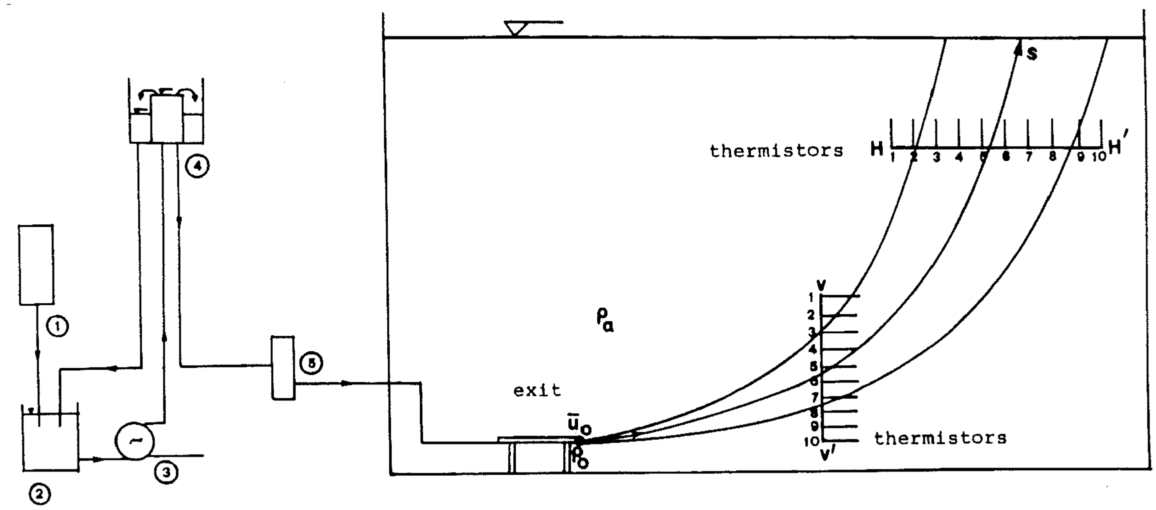

Figure 1. Experimental set-up. (1) Heater; (2) tank; (3) pump; (4) constant head tank; (5) flowmeter.

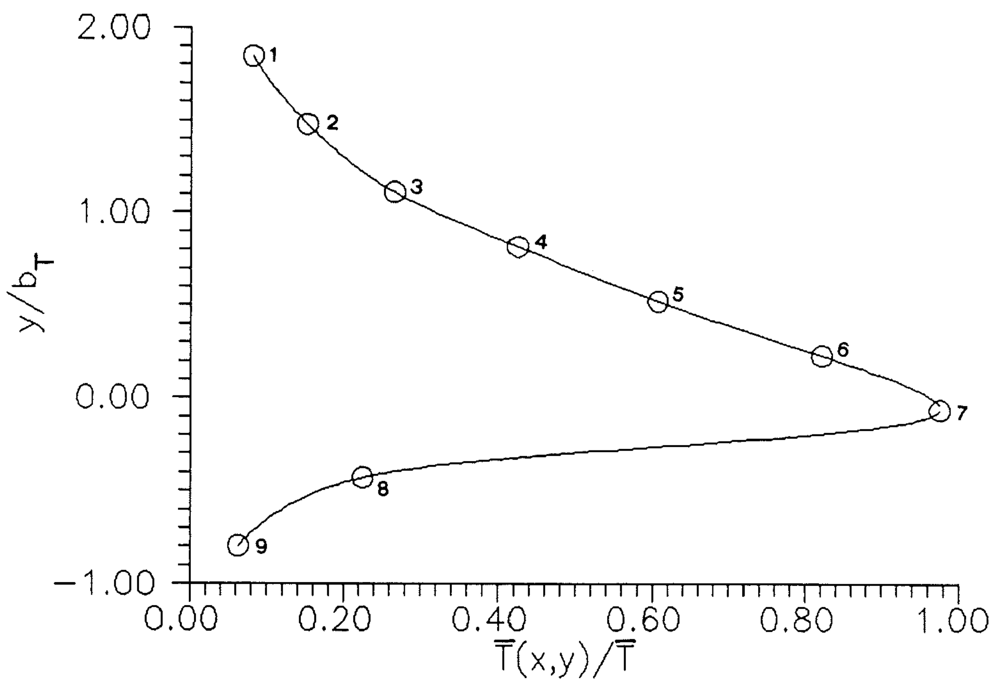

Figure 2. Non-dimensional profile of the mean temperature $\bar{T}(x,y)$ along the vertical line VV'(see Figure 1). o, measurements; ——, curve fitting. The numbers indicate the position of thermistor in the line VV'.

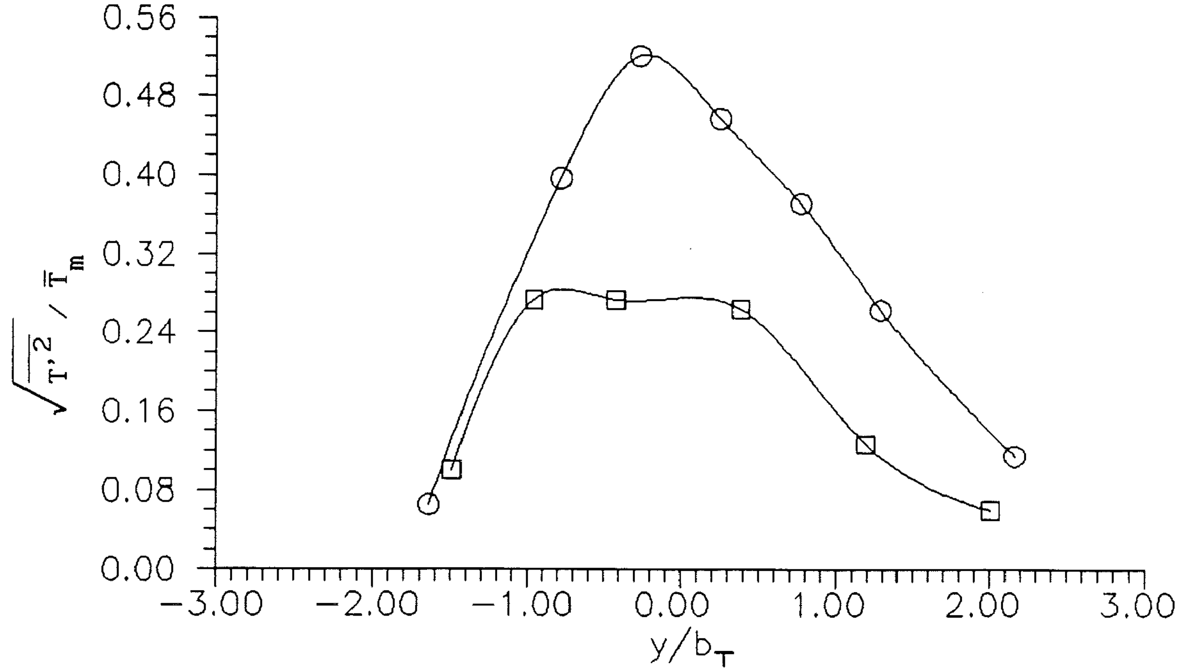

Figure 3. Profile of the non-dimensional turbulence intensity $\sqrt{\overline{T'^2}}\ /\ \bar{T}_m$ versus the non-dimensional distance y/b_T. □, ξ = 0.93; o, ξ = 14.44 ; ——, curve fitting.

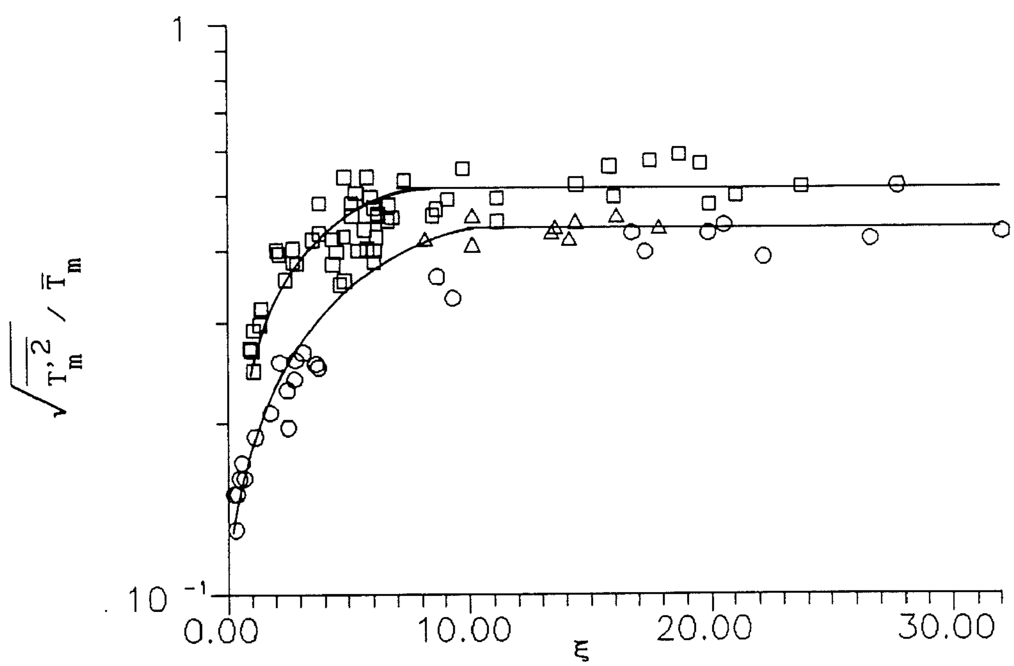

Figure 4. Non-dimensional turbulence intensity along the jet axis. □, horizontal buoyant jet (this work); △, Kotsovinos 1985, vertical buoyant jet; o, Papanicolaou and List 1987, vertical buoyant jet.

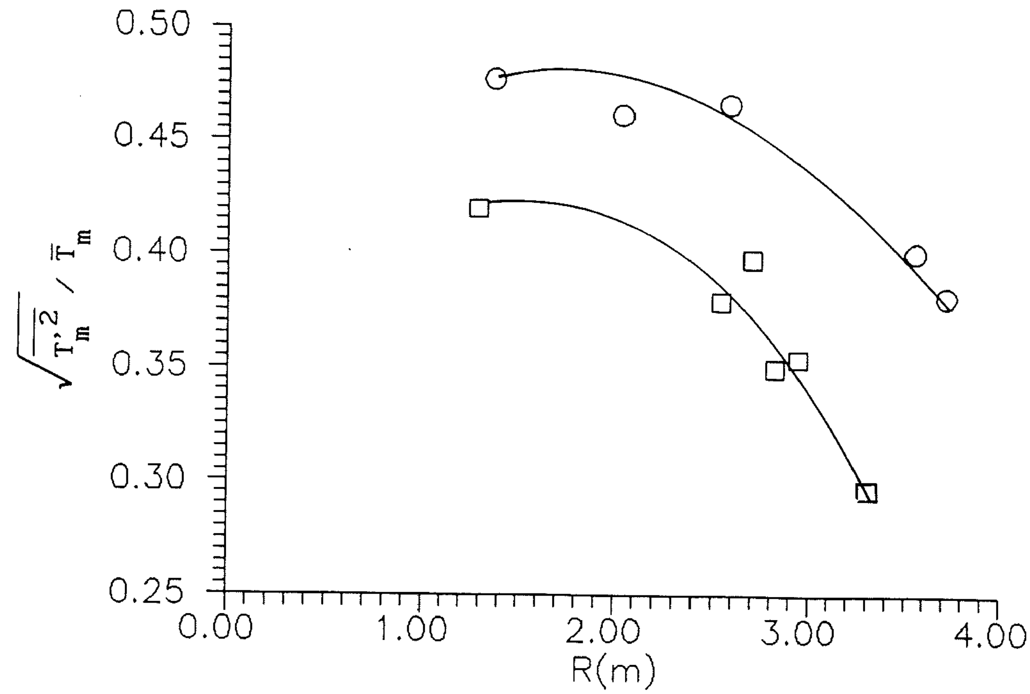

Figure 5. Non-dimensional turbulence intensity as a function of the curvature R(m) of the buoyant jet axis. □, ξ = 4.5; o, ξ = 6.

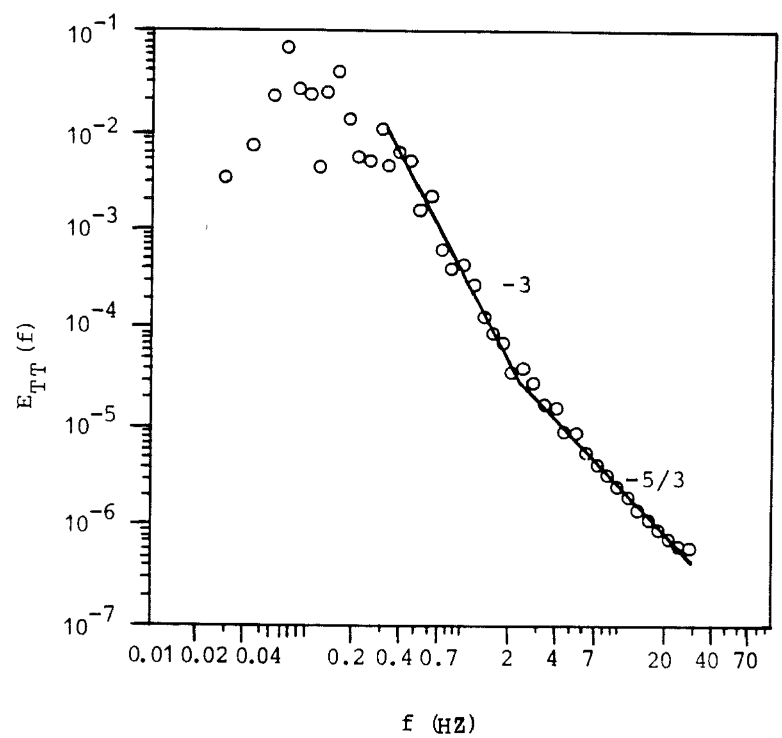

Figure 6. Spectral density $E_{TT}(f)$ of temperature fluctuations as a function of the frequency f(Hz). o, experimental data; ——, curve fitting; ξ = 2.75.

EXPERIMENTAL STUDY OF SUBMERGED PLANE TURBULENT JETS IN REVERSING CROSSFLOW

Daoyi Chen*, Changzhao Yu and Zhenhuan Xia
Department of Hydraulic Engineering
Tsinghua University, Beijing, China

Abstract:

In order to simulate sewage discharging into a tidal river, a submerged plane turbulent jet in a reversing channel crossflow was produced and measured in an experimental set-up with a 30 m long flume and a two-dimensional LDV.

Phase distribution of short-time averaged velocity showed time-dependent patterns of the unsteady flow field. The effect of unsteadiness on jet flows was studied experimentally by comparing between steady and unsteady flows the critical condition of flow pattern and the height of the circulation zone underneath the bending jet. The reversing period in tidal flow was found to be long enough to neglect the effect of unsteadiness on the jet flow.

Introduction:

Considering the "thermal pollution" caused by heated water discharging from power stations, Brocard[1] (1985) has experimentally studied a buoyant surface jet into a reversing crossflow.

Many coastal cities usually dispose of their sewage by discharging it into an estuary or a tidal river as a submerged plane jet for the purpose of diluting the pollutant. For example, a large sewage discharging system will be built in a tidal section of Yangzhe River near Shanghai City[3]. At this location, a "cloud" with high concentration of the pollutant will be formed in the oscillating ambient water near the jet outlet. Because of the complexities created by unsteady flow, the mixing characteristics of such a discharge are still a open question. This is the background for this study.

Experimental apparatus:

The reversing channel flow was produced by a mechanical device controlled by an Intel 86/330 computer. Its Rmx86 operating system is advantageous in real-time controlling. The plane jet was discharged from the bottom of the flume with a 2mm width slot, the water depth was about 15cm, and width of the flume was 60 cm.

Firstly, the interrupt control function of the computer was developed. Then, at each time given by the computer clock, the current job on computer CPU was automatically interrupted and turned to run a water level controlling subroutine which took water level data from a capacitive sensor, calculated an adjustment

*Presently at DeFree Hydraulics Laboratory, Cornell University, Ithaca, NY-14853, USA amount by the PID (proportion, integration and differential) algorithm, sent a control signal to the mechanical device, and finally returned to the current job. The LDV measurement could start at any expected time by means of the computer terminal, and usually continued for at least two reversing cycles.

In order to measure unsteady flow, usually, a time scale T_s must be very carefully determined such that $T_u \gg T_s \gg T_t$, where T_U is the reversing cycle period, T_T the largest turbulent time scale and T_S the time scale for time averaging. In many cases, this condition is not easy to meet.

One feature of this experiment is the combination of phase-averaging and time-averaging to overcome the difficulty of unsteady flow measurement. Measurement of velocity was carried out to get 8-16 points in each reversing cycle by the LDV.

For each particular flow field, the LDV was moved to various locations to get at least 200 points of velocity and water level data which were put into a large computer ELXSI 6400. Water level was used as a basis of a time sequence for determining the phase of the flow, and phase-averaging was applied to those short-time averaged velocities again. The velocity vector flow pattern was then reconstructed to show the development of flow field in reversing cycles.

Because water flows in tidal rivers are mainly subject to gravity and unsteadiness, Froude and Strouhal similarity laws were employed to evaluate what the cycle period in the experiment.

The water depth in Yangzhe River is about 25 m, the sewage discharge velocity 2 -2.5 m/s and the cycle period 12 hours. According to St and Fr laws, water depth of the channel flow was chosen to be 14 - 18 cm, plane jet velocity 0.15 - 0.18 m/s and tidal velocity from -0.031 to 0.046 m/s in the experiment. By similarity, the cycle period is about one hour. Thus it was too long to make efficient measurement. The cycle period in experiments was reduced to 6.4 minutes, 3.2 minutes and 1.6 minutes to create stronger unsteadiness than in tidal rivers for basic research purpose. Otherwise, the buoyant effect was not to be concerned.

Results and analysis:

Experiments indicate that flow patterns will change corresponding to the main current reversing channel flow[2]. Several brief schemes of these flow patterns in time sequence are shown in Fig.1. An example of a reconstructed flow pattern by the computer is shown in Fig.2 only for those data in a reversing cycle. When the tidal flow is in the downstream direction in case (1), the jet is bent by the main flow and a recirculation zone is generated under the jet. And then, the tidal flow velocity u decreases, the jet rises and the recirculation zone becomes larger and higher in case(2). When u is quite small, another recirculation zone appears at the surface of the upstream side. When u approaches zero, the jet impinges on the water surface and two large recirculation zones are formed at both the upstream and downstream sides of the jet.

After that point, the flow patterns reverse and finally only one recirculation zone exists at the upstream side. Obviously, there is a critical condition at which flow patterns switch from one recirculation zone to two circulation zones, or vice versa. Because the flow pattern is controlled by the momentum ratio of the jet to the tidal flow, a parameter was defined as

$$R = \left(\frac{V_j}{u}\right)^2 \frac{B}{H_0}$$

The critical condition of flow patterns switching was determined by experiment as about $R_c = 1.0$.

In shallow channel flow, the height and the length of these recirculation zones, as well as this critical condition of the flow pattern, will be the main characteristics of the reversing flow with a vertical jet. Because the ratio of the height to the length of the recirculation zone is about 0.2 for most of the flow situations, we are only concerned with its height, which is defined in Fig.2.

1). Critical condition of the flow pattern variation: This critical parameter is useful in studying the effects of unsteadiness. For the 6.4 minute cycle experiment, the variation of R and $\frac{H}{H_0}$ with time in a reversing cycle is given in Fig.3 and indicates these results match well with the critical condition derived for steady flow. This means that the unsteadiness may be too small to tell the difference between steady and unsteady cases for the T=6.4min condition.

For the T=3.2min case, the flow pattern does not follow the critical condition promptly. When R reaches its peak value which is larger than 1.0, the flow pattern still contains only one recirculation zone. Only after a time lag, it switches to two recirculation zones. This is the effect of unsteadiness which is controlled by inertia.

2) The height of the circulation zone: Taking advantage of the LDV, the height of the recirculation zone may easily be measured more precisely than with other techniques. The results shown in Fig.4 are the relative height obtained for T=6.4min. It appear that $\frac{H}{H_0}$ monotonically increases with R and these experimental data match well with one curve which was obtained from the steady flow. Considering that the critical flow pattern condition for T=6.4min is about the same as for a steady flow in section 1, one may conclude that the effect of unsteadiness for

T=6.4min may be neglected.

For T=3.2min and 1.6min in Fig.5 and Fig.6, respectively, the experimental data are quite scattered around the curve, caused by the lag of flow pattern variation. When the tidal current velocity u near zero, the acceleration attains its maximum value, and the effect of the unsteadiness may be the strongest in the whole cycle period. Those experimental data marked by "o" are obtained at the period with strong acceleration.

3) Discussion of the unsteadiness: The degree of unsteadiness of the flow may described by the St (Strouhal number). As we have discussed, Strouhal and Froude laws dominate the simulation of natural flows by experiments. A 12 Hour tidal cycle period corresponds to about 1 hour in the model. Its St number is about 0.5×10^{-3}.

The experimental results of T=6.4min have confirmed that the effects of unsteadiness may be neglected. And, the longer the cycle time, the weaker is the unsteadiness. Therefore, the effect of unsteadiness on discharge mixing also does not need to be considered in a tidal river like the Yangzhe.

Starting from this point, the accumulation of pollutant in a tidal river may be easily simulated by a quasi-steady numerical model. The authors have built a numerical k-ϵ model to solve this problem. Of course, that numerical model is capable of dealing with unsteady flow. But a quasi-steady assumption results in more efficient and economic calculations.

For shorter cycle times, the effect of unsteadiness gradually became obvious as the cycle was decreased from T=3.2min to T=1.6 min. One may conclude that unsteadiness becomes important when T < 3.2min corresponds to

$$St = \frac{H_0}{T\Delta u} > 0.8\times10^{-2}$$

where Δu is the velocity difference $u_{max} - u_{min}$ in tidal flow.

Otherwise, a monotonic relation was obtained between $(\frac{V_j}{u})^2\frac{B}{H_0}$ and $\frac{H}{H_0}$. When discharging effluent in a river with fixed water depth H_0 and current flow velocity u, it is found that the height of the circulation depends only on the jet velocity at exit

$$\frac{H}{H_0} \sim V_j$$

This is result valid for steady or unsteady flow. It should be helpful for engineering design.

Conclusion:

1) The slot jet experimental set-up with a LDV is advantageous for measuring velocity and turbulent quantities in unsteady flow. Of course, it is somewhat time-consuming due to unsteadiness.

2) The effect of unsteadiness exhibits a lag in the flow pattern change which is controlled by inertia. The height of the recirculation zone monotonically depends on the momentum ratio of the vertical jet to the horizontal current flow. At a critical condition of $(\frac{V_j}{u})^2 \frac{B}{H_0} \approx 1.0$, the flow pattern switches from one type with one recirculation zone to another type with two recirculation zones.

3). For some long term reversing cycle flows like those in tidal rivers, the effect of unsteadiness may be neglected. Then a quasi-steady assumption is valid for the Strouhal condition

$$St = \frac{H_0}{T\Delta u} < 0.5\text{x}10^{-2}.$$

Reference:

1). Brocard, D.N. (1985), J. of Hydraulic Engineering, V.111, No.5, pp 793-809.

2). Chen, Daoyi (1988), "The study of a turbulent jet in unsteady flow environment", Ph.D thesis, Tsinghua University

3). Zhao, Z, et.al (1987), The China Environmental Science, V.7, pp 5-10

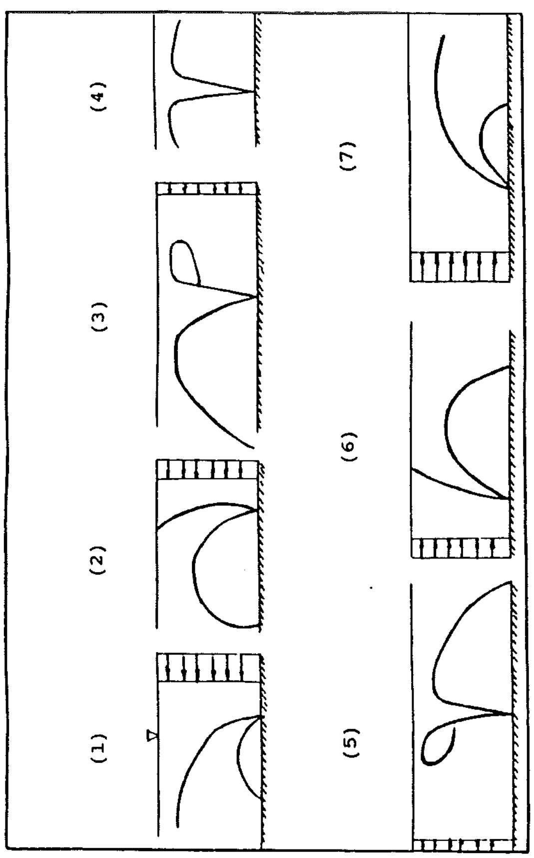

Fig.1 Scheme of flow patterns in time sequence

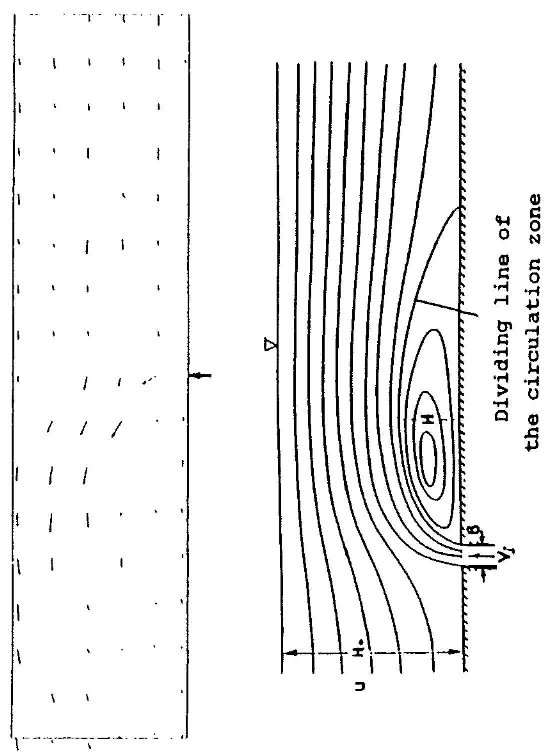

Fig.2 A example of reconstructed flow patterns and definition of parameters

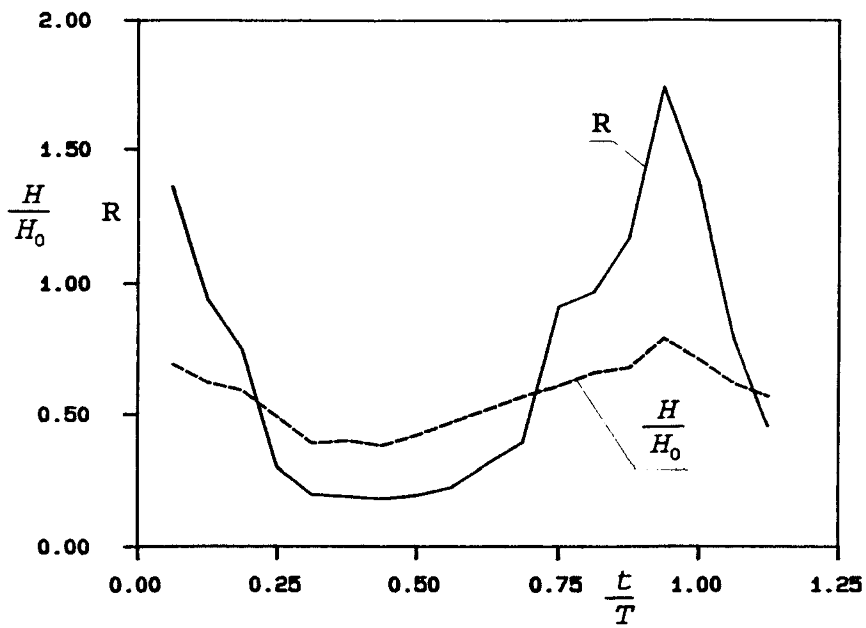

Fig.3 R and $\frac{H}{H_0}$ in a 6.4 minutes reversing cycle

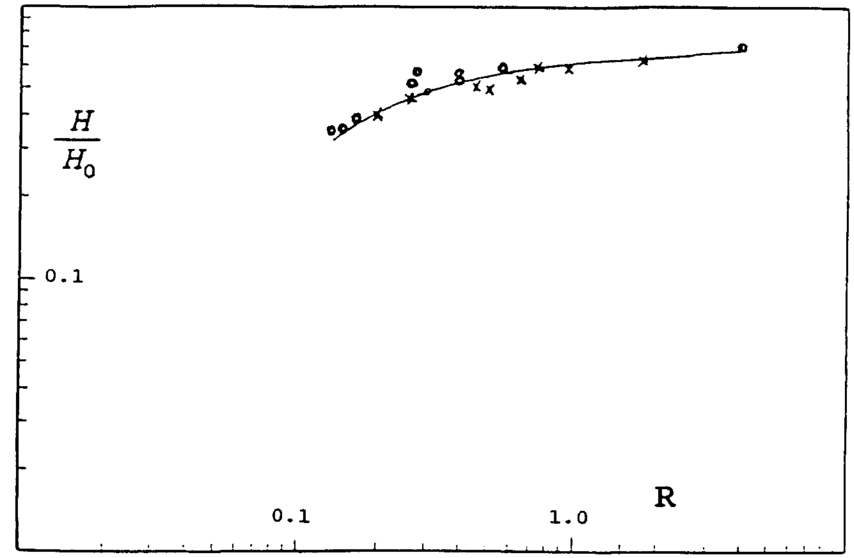

Fig.5 The relation of R and $\frac{H}{H_0}$ for T = 3.2 minutes

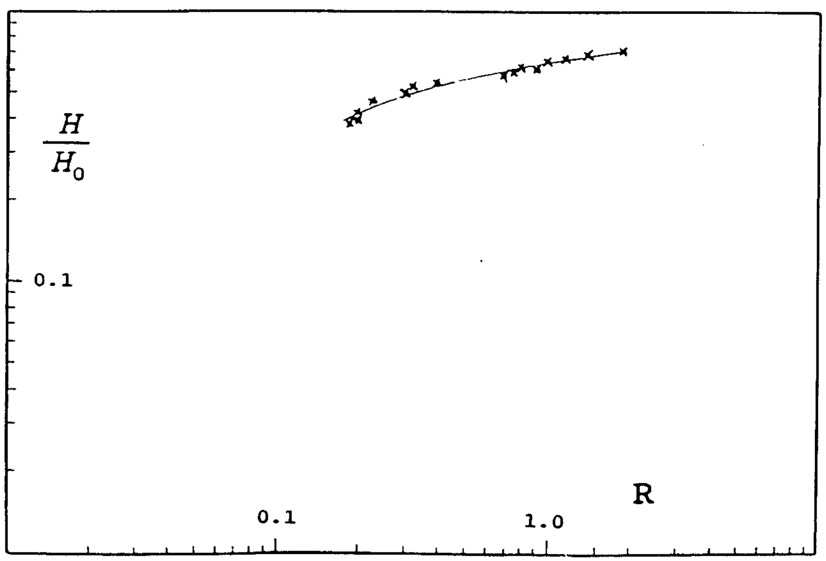

Fig.4 The relation of R and $\frac{H}{H_0}$ for T = 6.4 minutes

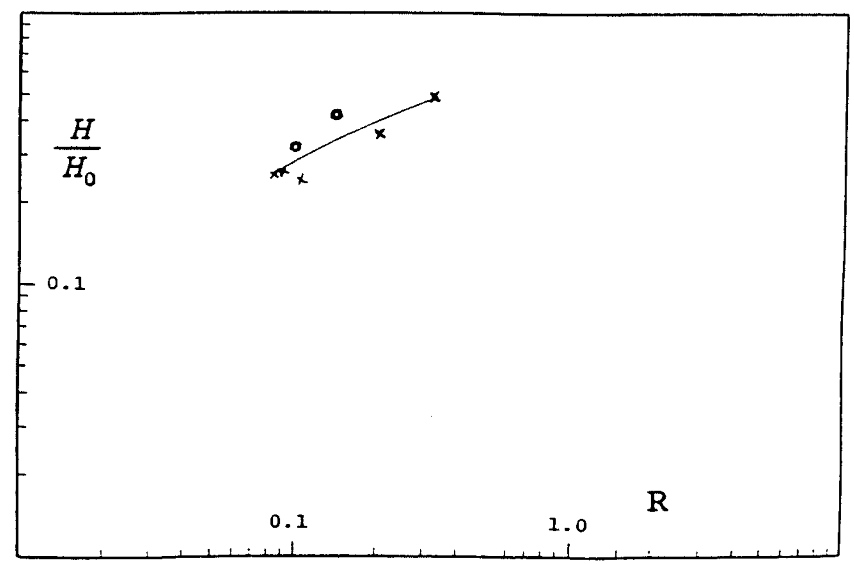

Fig.6 The relation of R and $\frac{H}{H_0}$ for T = 1.6 minutes

EMPIRICAL ENERGY TRANSFER FUNCTION FOR DYNAMICALLY COLLAPSING PLUMES

W.E. Frick[1], C.A. Bodeen[1], D.J. Baumgartner[2], and C.G. Fox[1]

Abstract

Dynamic collapse is recognized as one of several processes that determine far-field plume behavior, therefore, models that use the round plume assumption become invalid there. To overcome this limitation, a conservation of energy approach is used to model collapsing plumes in stratified ambient flows. A common time scale governing rise and collapse is found that further proves the importance of collapse.

Introduction

The near-field plume region is defined as the rising phase, generally about one half Brunt-Vaisala wavelength. However, the far-field is of interest to oceanographers studying hydrothermal plumes and to environmentalists concerned with the health of coastal waters, particularly as reliance on diffusers for wastewater disposal increases.

One reason many models apply only to rise is the round plume assumption. Far-field plume cross-sections frequently deform through dynamic collapse, in contradiction of the round cross-section hypothesis. Other processes (asymmetric entrainment, internal reflection, and center-of-mass effects) also contribute (Frick, Baumgartner, and Fox 1990).

Unfortunately, models for far-field plumes generally do not stand independently but depend on near-field model output for initial conditions. Consequently, they are sometimes joined. For example, Brandsma, Sauer, and Ayers (1983) fit a far-field collapse model to a round plume initial dilution model. Obviously, collapse is precluded until maximum rise is reached, an example of the compromises that result from patching together disparate models. While collapse may not affect rise and dilution significantly in the near-field, it does contribute to the determination of initial conditions (e.g. collapse kinetic energy) for the far-field model. Collapse is an inertial process with a characteristic time scale and delaying its onset invites tampering with the model structure to remedy the delayed collapse.

The concepts of this paper are being used to construct a unified model which will minimize the number of tuned coefficients and avoid difficulties associated with patching together different models. This three-dimensional Lagrangian plume model substantially generalizes the EPA plume model UMERGE (Muellenhoff et al., 1985). The model predicts identically to integral flux models using the same assumptions (Frick, Baumgartner, and Fox, 1990) but recasts the problem, providing new ways of identifying theoretical deficiencies. Because the basic model uses only one empirical coefficient while maintaining a level of performance competitive with multi-coefficient models, there is optimism that more empirical hypotheses may be used without overtuning to data.

An included theory of collapse, based on conservation of energy results in some interesting conclusions: a) when scaled by rise, collapse is not affected by the degree of stratification, b) observed behavior can be reasonably predicted using an empirical partitioning hypothesis and a second tuned coefficient, and c) a time parameter based on the Brunt-Vaisala frequency characterizes both rise and collapse temporally.

[1] Hatfield Marine Science Center, Newport, OR 97365

[2] Environmental Research Lab., Univ. of Arizona, Tucson, AZ 85706-6985

Physics of Collapse

Plumes are often analyzed using a control volume on which mass, energy, and momentum balances are performed. With Lagrangian models the relevant volume is an element -- a wedge shaped disc defined by the plume boundary and two faces perpendicular to its center-of-mass axis (Frick, Baumgartner, and Fox, 1990). A buoyant force due to the difference between the average element density and the corresponding ambient density accelerates the element's center-of-mass vertically. Perturbations on the average density differences produce the forces of collapse. Alternatively, the process can be viewed as a conversion of potential to kinetic energy.

The element is mixed by turbulence that tends to make its density uniform. Consequently, a density stratified ambient fluid will produce density differences that are functions of height within the element, causing different parts to accelerate at different rates, i.e. to deform the element. Subtracting the average density difference from the total density at any point leaves a density difference and associated potential energy, P, that governs the deformation. The inclination of the element also affects the magnitude of P.

As there are no constraints, P converts spontaneously into the kinetic energy, K -- embodied in an organized drift that spreads the plume horizontally as density differences drive mass towards the level of the center-of-mass. The potential energy depends only on the actual mass distribution (assumed to be elliptical, cf. Amen and Maxworthy, 1979) while the kinetic energy depends additionally on a characteristic velocity and on energy losses to the ambient fluid.

The derivation of the energies using elliptic integrals is avoided by noting that every point in an ellipse with semi-major and semi-minor axes a and b can be represented as a mapping of another point on an reference circle. This basic idea makes it easier to find K and P by integrating over the geometrically simpler circle.

Referring to point Q in Figure 1, $x = r \cos \alpha$ and $z = r(b/a) \sin \alpha$. Comparable expressions for x and z can be found when a and b change to become a + da and b + db. The speed of Q is $|\underline{v}| = (dx^2 + dy^2)^{1/2} / dt$, where $\underline{v}$ is the velocity vector of Q (relative to the element) and dt is the time increment during which Q moves to the new location. The relative position of the point Q (defined by r and α) in the reference circle remains unchanged.

The kinetic energy of an infinitesimal mass, $dm = \rho \;\; h \; r \cos \Phi \; d\alpha \; dr$ is expressed as

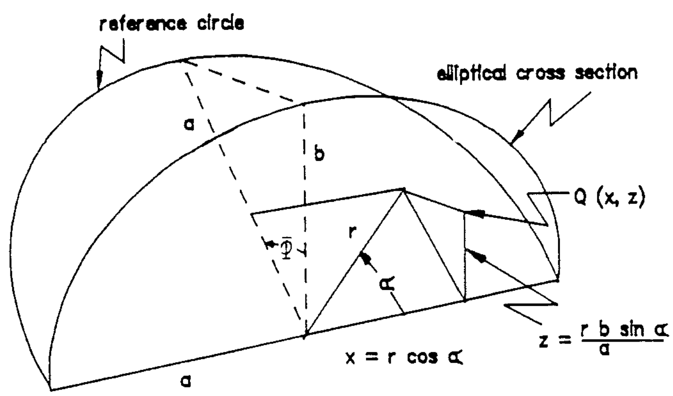

Figure 1. Geometric variables affecting the derivation of K and P.

$$1)\quad K = 1/2 \int_0^a \int_0^{2\pi} |\underline{v}|^2 \rho \; h \; r \cos \Phi \; d\alpha \; dr$$

where h is the thickness of the volume element and ρ is the average element density. The factor $\cos \Phi = b/a$ maps the ellipse onto the circle. Integrating Eqn. 1 yields Bell and Dugan's (1974) expression.

$$2)\quad K = (m/8)\,(db/dt)^2\,[\,1 + (a/b)^2\,]$$

Similarly,

$$3)\quad P = (mg/4)\,(b \cos \Theta)^2\,(d\rho_a/dz)/\rho_a$$

where g is the acceleration of gravity, Θ is the plume trajectory elevation angle, and $d\rho_a/dz$ is the ambient stratification. The value of P is twice that of Bell and Dugan (1974).

The total energy K + P will not be conserved due to losses from wave generation, initiation of motion in the ambient fluid, and viscous action between the plume and the ambient fluid. An empirical partitioning hypothesis is advanced to govern energy conversion:

$$4)\quad dK = -\,k_p\,dP$$

where dK and dP are the changes in K and P respectively and k_p is an empirical partitioning coefficient. The value of the coefficient is expected to be somewhat less than 0.5 because about half the energy is lost to the ambient fluid and because the element is only partially mixed. As collapse becomes pronounced, viscous forces may reduce further the apparent magnitude of the coefficient.

<u>Verification of Basic Concepts Using a Wake Model</u>

Wakes are round, horizontal, cylindrical volumes of well mixed fluid established, for our purposes, without net buoyancy in stratified ambient fluid. Wake experiments are useful for verifying basic collapse models because all dimensions of interest are reported (unlike most plume experiments) and there is no entrainment.

Figure 2 shows the predicted collapse of the wake region with time, as measured by the ratio of the semi-minor to the semi-major axes. Many cases are represented corresponding to different ambient stratifications, element diameters, and partitioning coefficients. A time parameter $tN(k_p)^{1/2}$ serves as the dimenionless independent variable where t is time and N is the Brunt-Vaisala frequency: $[(g/\rho)(d\rho_a/dz)]^{1/2}$.

The uniform dependence on the time parameter is not unexpected. Middleton and Thomson (1986) show that buoyancy dominated plumes rise in π Brunt-Vaisala periods (confirmed by the Lagrangian model, see Table 1). Collapse and rise are governed by the same time parameter, implying that collapse is normally significant in distal plumes in stratified ambient fluid. Thus, although collapse may proceed more slowly as stratification weakens, rise time increases correspondingly.

The effect of decreasing k_p is to retard collapse by transmitting more of the converted potential energy to the ambient. Inertial in its

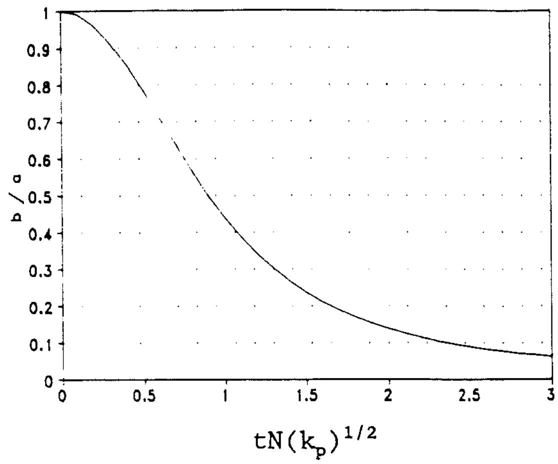

Figure 2. The temporal collapse response of wakes.

response, the ratio b/a changes slowly at first. However, given the same k_p it responds more rapidly than predicted by Bell and Dugan (1974). With $k_p = 0.5$ the model agrees with Equation 4 of Bell and Dugan (1974).

Entrainment and Collapse in Plumes

Entrainment, when coupled with collapse, complicates plume models considerably. First, it is not known how the element grows. We assume that entrainment varies smoothly around the plume perimeter such that $db/da = a/b$. This is consistent with the Taylor entrainment hypothesis, since entrainment should be stronger at the semi-minor axis than at the semi-major axis due to its proximity to the center of energetic motion. One result is that the plume will again tend to become round if it bursts through a stratified layer and re-enters an unstratified layer.

Second, K may be an explicit function of entrainment. If entrainment is a uniform process that separates all portions of the plume from each other like an expanding universe then there might be energy associated with this organized process. However, it is assumed that K is not so affected. Nor is P an explicit function of entrainment since the entrained fluid has identically the same density as the ambient fluid at the same level and hence no potential energy with respect to it. Internal conversion of turbulent kinetic energy is the sole source of P.

Third, collapsing wakes transmit energy into the ambient field, plumes undoubtedly do the same. However, plumes may recover some of the lost energy through entrainment.

The partitioning hypothesis parameterizes these unknown processes.

Verification

Eleven plumes in stratified, quiescent ambient are modelled using $k_p = 0.2$ and a Taylor entrainment coefficient of 0.116. They correspond to plumes described by Fan (1967) and are summarized in Table 1. The dimensionless collapse and rise times are given by t_cN and t_rN, where N is the Brunt-Vaisala frequency. The reflection parameter measures element facial overlap (Frick, Baumgartner, and Fox, 1990)--a value greater than 2.0 indicating upstream anvil formation, cf. Jet 16 in Figure 3. Suspected impending anvil formation is indicated by "imp".

TABLE 1. Plume predictions for cases given by Fan (1967).

Case	----horizontal discharges----						--45 degree discharges--				
	12	16	30	31	32	33	1	2	11	15	18
t_cN	3.13	3.58	3.96	3.35	2.88	2.77	3.20	2.86	3.01	3.00	2.88
t_rN	3.11	3.18	3.32	3.16	3.16	3.16	2.42	1.94	2.20	2.26	1.97
t_r/t_c	0.99	0.89	0.84	0.94	1.10	1.14	0.76	0.68	0.73	0.75	0.69
reflection	1.06	2.22	3.12	1.61	0.65	0.43	2.27	1.11	1.41	1.22	1.14
anvil	no	yes	yes	imp.	no	no	imp.	no	no	no	no

As theorized (Middleton and Thomson,1986), rise times are related to πN^{-1}. Furthermore, t_r/t_c is also approximately constant given a constant elevation angle, suggesting that the rise and collapse time scales are closely related. This is an important finding because it shows that in stratified fluid collapse is generally important in the distal plume. Variations are attributed to plume orientation since a vertically rising plume experiences no collapse while a horizontally discharged jet is subject to collapse. Also, the ratio of momentum to buoyancy length scales is likely to affect the degree of turbulent mixing and, indirectly, the values of Table 1.

Figure 3 depicts selected cases graphically. For comparison both round and collapsing plume predictions are given, the former showing the largest vertical widths. The relatively minor differences between the two predictions during rise support the use of the round plume assumption when interest is confined to that region. However, in the distal plume the differences become pronounced and considerable deformation is indicated. The residence time of large particles falling through the plume and other processes will be greatly affected.

Also shown in dotted outline are plume predictions when collapse is delayed until maximum rise is reached. In principle, the decision to delay collapse could wrongly influence tuned entrainment coefficients.

As indicated earlier, other mechanisms of deformation are omitted for pedagogical reasons. Similarily, the vertical velocity has been arbitrarily set to zero after maximum rise (Frick, Baumgartner, and Fox (1990) omit collapse but otherwise give a more realistic treatment). It is difficult to refine the value of k_p or justify additional empirical hypotheses without more complete experimental data. Indeed, the number of tuned coefficients should be inversely proportional to the uncertainty of the experimental data.

More basic experiments to define simple plumes in three-dimensional space are badly needed. With the limited verification data available (which usually do not provide simultaneous vertical and horizontal plume dimensional measurements) it cannot be asserted with confidence that all the observed collapse is due to energy conversion because a reduction in entrainment would cause a similar effect. However, the vertical dimension would never decrease.

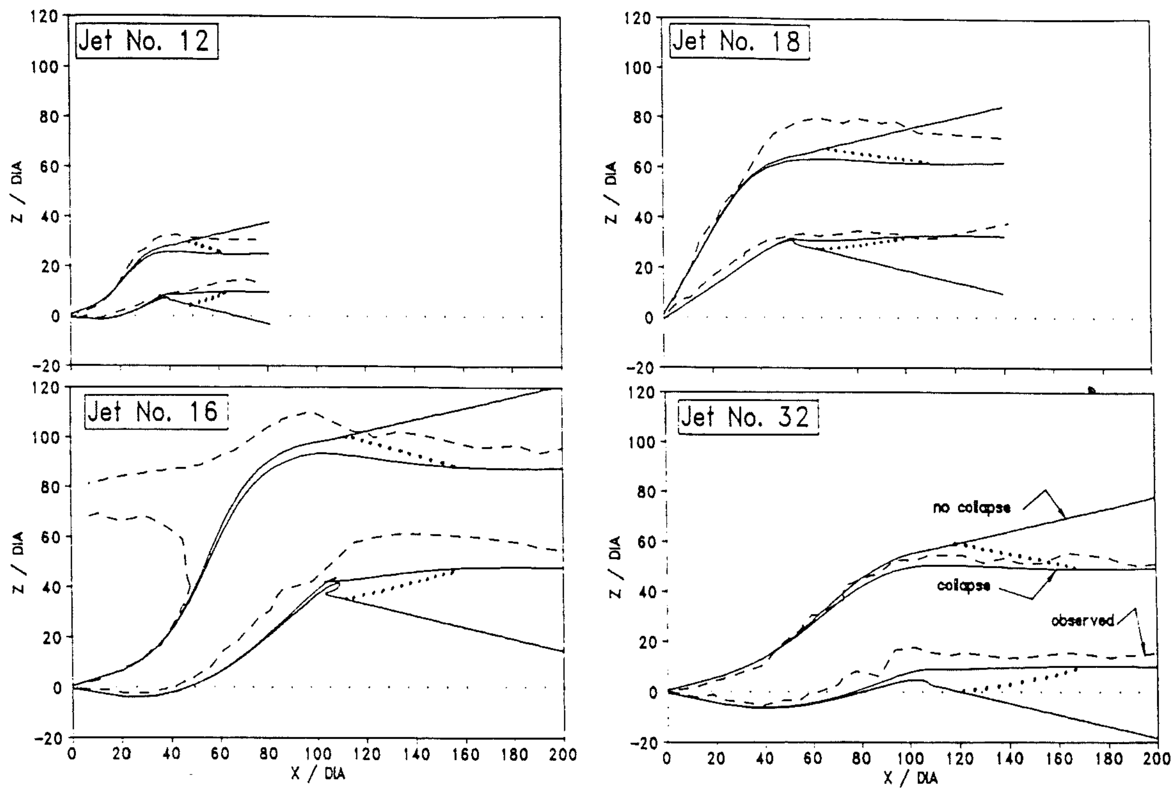

Figure 3. Model predictions compared to Fan (1967)

Acknowledgement

This is contribution number N-125 of the US EPA, Environmental Research Laboratory, Narragansett, RI.

References

Amen, R. and T. Maxworthy, 1979. The gravitational collapse of a mixed region into a linearly stratified fluid. J. Fluid Mech., 96.

Bell, T.H. Jr. and J.P. Dugan, 1974. Model for mixed region collapse in a stratified fluid. J. of Engrg Math., 8, No 3, 65-80.

Brandsma, M.G., T.C. Sauer Jr., and R.C. Ayers Jr., 1983. Mud discharge model; report and user's guide. Exxon Production Research Co.

Fan, L.N., 1967. Turbulent buoyant jets into stratified or flowing ambient fluids. Report KH-R-15, W.M. Keck Lab of Hydraulics and Water Resources, Cal Tech.

Frick, W.E., D.J. Baumgartner, and C.G. Fox, 1990. Deficiencies of the round plume assumption. In prep.

Middleton, J.H. and R.E. Thomson, 1986. Modelling the rise of hydrothermal plumes. Canadian Tech. Report of Hydrography and Ocean Sciences, 69, Dept of Fisheries and Oceans, Sidney, B.C. V8L 4B2.

Muellenhoff, W.P., A.M. Soldate, Jr., D.J. Baumgartner, M.D. Schuldt, L.R. Davis, and W.E. Frick, 1985. Initial mixing characteristics of municipal ocean discharges. EPA-600/3-85-073a & b. USEPA, Newport, OR.

THE STUDY ON THE DILUTION OF PURE JET IN THE RIVER

by Xu Liang
School of Environmental Engineering
Tongji University
Shanghai 200092 P.R.C.

Abstract

Experimental studies are reported for the pure jet in the river for which the factors which influence the dilution have been qualitativly analysed. The test results show that, for the case studied,the dilution increases obviously with the increasing jet angle and diameter. But the dilution weakly depends on jet velocity. The results are useful for designing the outfall in the river.

Introduction

In recent years,the natural purification process following the discharge through outfall has been called the 'marine treatment'.The way is used more and more widely and has been proved a good way to solve coastal city water pollution problem. Due to economic consideration this method is especially hopeful in China.The Yangtze River and other big rivers in China have huge dilution capacity.To discharge wastewater to the rivers by using river outfalls may be a feasible measure of solving the water pollution for the city along the big river. However the formula and experience about the river outfall or pure jet in the crossflow are lacking.

According to the similarity criteria the model was built up and modelling was conducted to study the factors which influence the dilution of pure jet,such as, jet angle,jet diameter, jet velocity and ambicent conditions (depth and current velocity) in the flume.

This paper is divided into three sections. The first is a description of the hydraulic modelling tests including a review of modeling, laws, apparatus and contents. The second is a prescentation of the model test results and physical interpretation ,and final secton contains a summary and conclusions.

1.Hydraulics Modelling Tests

1).Hydraulics Modelling Laws

Because there is no buoyancy, the jet is controlled by initial momentum flux, mass flux and crossflow.The process of jet is mainly controlled by gravity and viscosity. So the model is done by hydraulic similarity (gravity crirteria of similarity and resistance criteria of similarity) which requires that both the Froude number and Reynold number in the model and in the prototype keep unchanged.Generally,the prototype effluent jet is fully turbulent.If the model jet is kept fully turbulent the Reynold number stands at its auto similar range and Reynold number can be ignored, from the viewpoint of Robert , such a treatment is satisfactory. So the hydraulic model is designed by controlling Froude number, which requires the ratio of Froude number in the model and prototype to be unity. This result in.

$$Fr=\frac{Vr}{\sqrt{GrLr}}$$

in which Lr=length ratio (prototype:model) Vr=velocity ratio Gr=gravitalional ratio =1

By choosing the geometric scale ratio (i.e., Lr the length ratio), the velocity ratio, is determined.

In this model Lr=100 Gr=1

using the law of gravity criteria of similarity,

Fr=1
thus Vr=10

2).Modelling Apparatus and Contents

All tests were performeel in a flume which is 8m long, 0.8m wide, 0.6m deep(fig.1).There are three water lever meters to measure the water level at the two sides and at the centre of the flume. The flume is equiped with a movable carriage which is mounted with conductivity probes and can be moved easily to measure the concentration of simulated pollutant,e.g.,salt.

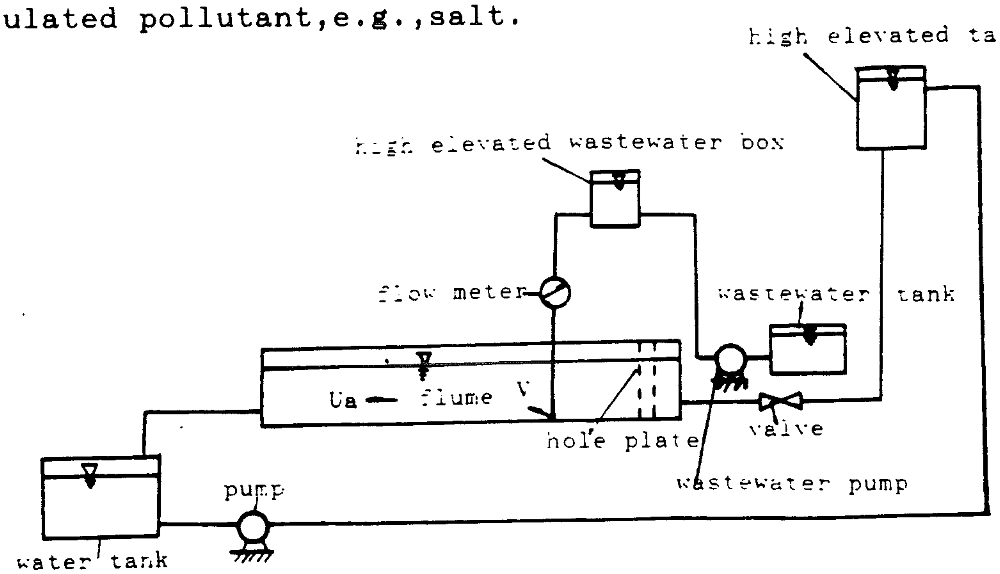

Fig.1 Schematic of Test Flume

The relation between conductivity and concentration was conducted and has been determined. The conductivity signal is translated into digital signal, which is printed on the paper by a computer program developed for this modelling test.

For all kinds of the outfall design, the appropriate choosing and determining parameters of outfall play a very important role.Therefore emphasis is focused on the study of how the jet diameter,jet angle,and jet velocity are influencing the dilution of the jet, of course,the influence of water depth and ambient current are also tested.

2.Flume Test Results

After the jet is injected through the outlet, due to its initial momentum the trajectory is almost a straight line near the port. because of the action of current and the increasing of horizontal momentum, The trajectory of the jet is gradually curved with the distance from the outlet . Finally ,the jet goes with the current and disappears little by little.

1).With the same jet velocity, port diameter and ambient condition, different jet angle.

The results of the tests in this condition are given in fig.2 . The results show that the dilution increases with the increasing the jet angle.The reason for this phenomena is very obvious .As soon as the jet is injected into ambient, the dilution depends on mometum entrainment produced by initial momentum and dynamic force entrainment produced by the action between the jet and ambient curret. From the theory study, We know that the momentum entrainment is controlled by the mode of vector of difference between jet velocity and ambient current.

For certain distance from the port, the larger the jet angle, the larger the mode, which makes the jet entrain more non-polluted water.From the experimental obervation. this phenomena is found that the jet with the larger jet angle induces more water and be full of whole section in height more quickly than the jet with less jet angle.

2).With the same jet angle, port diameter and ambient condition, different jet velocity.

The results are given in fig.3,they show that the influence of jet velocity on dilution is not obvious.which is somewhat contrary to the expectation.In fact, the increasig of the jet velocity causes the increasing of the entrainment and discharge of simulated pollutants, in some cases, the former increases more than the latter, while in other cases, the latter increases more than the former, So that the above phenomena takes place. Maybe there is a point which have the maximum dilution.Therefore the research on this problem will be continued.

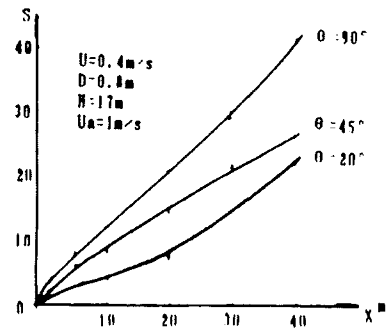

Fig.2 Comparison of Jet Angle

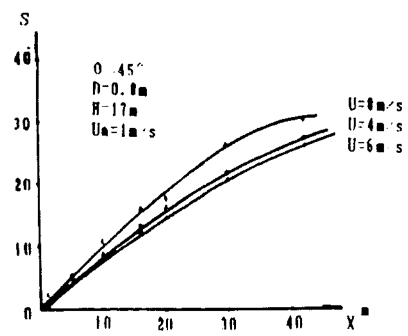

Fig.3 Comparison of Jet Velocity

3).with the same jet angle, jet velocity and ambient condition, different port diameter.

The results which are given in fig.4 show that the dilution increases with the decreasing of port diameter, which is consistant with the expectation.Due to the decreasing of port diameter, the discharge of a simulated pollutant contained in the jet also decreases,however, the other conditions are not changed,thereby,dilution increases.

For certain outfall project, the decreasing of port diameter is conditional. The economic factor must be considered. Therefore, there should be a decision referring to the degree of dilution and cost.

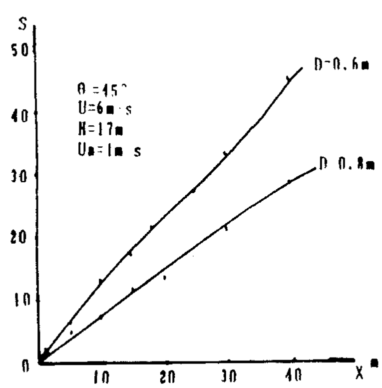

Fig.4 Comparison of Port Diameter

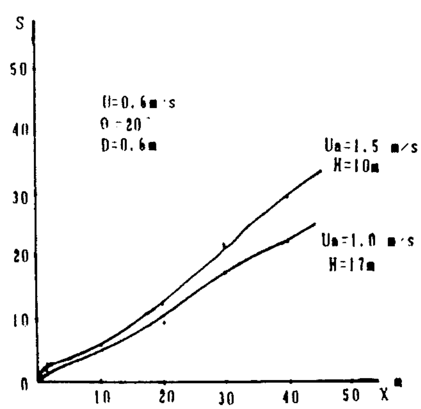

Fig.5 Comparison of Ambient Condition

3.Summary and Conclutions

Among the factors influencing dilution. i.e. jet angle, jet velocity and port diameter, the jet angle is the most sensitive one, the jet velocity is not obvious, and the port diameter plays some role,but its influence is conditional.

The influence of the ambient conditions on dilution are very obvious.The dilution increases with increasing of water depth and current velocity(fig.5).Comparing the influence of these two factors the influence of the current velocity is greater than that of water depth. Therefore,the prerequsite of designing outfall is to choose the position where the current velocity is higher,while for certain water depth the maximum dilution can be obtained by adjusting jet angle.This doesn't mean that the water depth can be neglected. It should be the case while considering the velocity, the water depth is also taken into account.

Acknowledgments:

The writer would like to express his appreciation to Prof.Wei Heping and Prof.Mao Sanpai of Tongji University for their valuable guide and assistance from bigining to end.

Reference:

1).Fischer,H.B.,et al.,"Mixing in Inland and Coastal Waters",Academic Press,New York,N.Y.,1979
2).Roberts,P.J.W.,"Ocean Outfall Dilution Effects of Currents,"Journal of the Hydraulics Division,ASCE,Vol.106, No.HY5,May 1980
3).Morton S.Isaacson,Robert C.Y.Koh,"Plume Dilution for Diffusers with Multiport Risers",Journal of Hydraulics Division,ASCE,Vol.109,No.HY2,Feb.1983
4).List,E.J.,and Imberger,J."Turbulent Entrainment in Buoyant Jets and Plumes,"Journal of the Hydraulics Division,ASCE, Vol.99,No.HY9,Sept.1972

Notation:

The following symbols are used in this paper:
V- jet velocity m/s
Ua-current velocity m/s
θ -jet angle
α_1-entrainment coefficient
λ -coefficient of concentration profile
D -diameter m
F -Froude number
G -gravitational acceleration
C -concentration of pollutant
C_∞-concentration of pollutant in a current

Subscript:
r-modelling ratio (prototype:model)

Session 2B

Coastal and Ocean Mixing

PREDICTION OF SEAWATER EXCHANGE RATIOS IN AND OUTSIDE THE BAY BY HYDRAULIC MODEL

by Takayuki Hattori, Researcher
Civil Engineering Laboratory, Chubu Electric Power Co., Inc.
and
Akira Wada, Professor
School of Marine Science and Technology, Tokai University

1. Introduction

In closed sea areas like bay where some fear is raised about water pollution caused by industrial or household effluents, a measure to preserve the quality of water has become an important problem. The authors have paid attention to the exchange of water mass inside the bay with water in the open sea, or the so-called seawater exchange phenomenon. As a method for this phenomenon, study by box model, 3D mathematical model, hydraulic model, etc. have been considered. Particularly, with respect to the hydraulic model, research has been conducted on the law of similarity so that the actual phenomenon can be maintained similar on the distortion model in relation to the problem of thermal diffusion prediction.

In this study, the authors conducted hydraulic test by simultaneously generating tidal current and constant current having two different types of periods within the distortion model, with Shimizu Port which has a complicated seabed topography and flow taken as a study area. The applicability of a hydraulic model using a distortion model to the prediction of seawater exchange phenomena was studied while comparing the results of field observations on flow with those of simulation analysis using a 3D mathematical model.

2. Flow characteristics of the sea area concerned

Shimizu Port faces Suruga Bay as shown in Fig. 1. The following phenomena can be observed according to the auto-correlation coefficients, energy spectra and harmonic analyses of flow which were calculated based on the results of continuous observations conducted on current in and outside the bay through all seasons. In Fig. 2, tidal-current ellipses and constant-current components (15-day mean current during the observation period) are shown.

(1) Inside the bay, the velocity component of semi-diurnal period can be recognized, though the velocity is small. The constant current is a northeast current flowing out of the innermost part of the bay, but the velocity is small (less than 5 cm/s).
(2) Outside the bay, the velocity component with diurnal period can be recognized, and the velocity is 5 to 20 cm/s. The constant current flows southward along the coastal line through all seasons. In the offing of Shimizu Port, the velocity is 4 to 10 cm/s, and 4 to 23 cm/s in the sea area in front of Miho, indicating a rapid flow and conspicuous constant flow. Outside the bay, therefore, the flow is the combination of a

constant-current component and a diurnal-tidal component.

3. Hydraulic model test

The hydraulic model test was conducted in the meteorological and oceanographic simulation building located in the Power Engineering Laboratory of Chubu Electric Power Co., Inc.

3-1 Model scale and test equipment

The model having a horizontal scale of 1/600 and vertical scale of 1/60 was used in the test. Froude's law was used as the law of similarity to maintain the similarity of flow phenomena between the prototype and the model. The semi-diurnal current inside the bay was generated using the tide generator (plunger type) installed in the offing of the water tank. On the other hand, the diurnal tidal current and constant current outside the bay were generated using the tidal current and constant current pipes installed at both ends within the tank (see Fig. 1).

3-2 Reproduction of flow patterns

The depth of water inside the bay is 5 to 20 m; outside the bay, the water becomes suddenly deep, i.e., 30 to 500 m, and there are rapid topographical changes in the sea bottom. In the sea areas having such a complicated seabed topography, the tidal current and constant current having two different types of periods mentioned above were reproduced simultaneously. A typical example of reproduced results is shown in Fig. 3. As is clear from the figure, the reproducibility of current ellipses and constant-current components was relatively good except for a point where the flow is weak. Meanwhile, the electromagnetic current meter was used to measure the velocity of flow.

3-3 Definition of seawater exchange ratio

A broken line was set to divide the bay between inside and outside (see Fig. 4). The seawater exchange ratio was defined so as to determine to what extent the unit water mass at any point (mark x for example) inside the bay is replaced with the water outside the bay after the lapse of a certain period of time. In the hydraulic model test, magnesium was used as tracer, and the ion concentration of magnesium was measured with an atomic spectro-photometer to determine the seawater exchange ratio at each point.

3-4 Hydraulic test method and cases

Seawater exchange test was conducted by installing a gate at the bay mouth and throwing magnesium chloride into the sea in such a way that the concentration of magnesium ion inside the bay would become about 3 to 3.3 ppm higher than that outside the bay. Then, the water inside the bay was kept stationary, and the gate was opened. At the same time, considering the tidal phase difference, the tide of semi-diurnal period was generated in the ebb direction and the tidal current with diurnal period was generated in the northern direction. The change of concentration at each point inside the bay owing to subsequent tidal development was followed.

The concentration at each point was represented by middle-layer water. Tests were conducted on two cases, and subsequent comparison was made of respective cases. Test on Case 1 was conducted to determine the seawater exchange ratio inside the bay under the present condition. Test on Case 2 was conducted to determine what kind of effect the intake and discharge of cooling water for a steam power station would have on the exchange of seawater inside the bay when the power station is installed inside the bay. Cooling water was withdrawn from a deep layer on the eastern side of the power station site and released into a surface layer in front of the site. The flow rate of cooling water is 94 m^3/s, and the temperature rise of discharged warm water is $7^{o}C$. The outlet has a width of 90 m, and the depth of water at the outlet is 3.5 m. Warm water was discharged at mean velocity of 30 cm/s.

3-5 Hydraulic test results

The seawater exchange ratios obtained at typical points inside the bay are shown in Fig. 5. This figure shows the mean seawater exchange ratios at each point per period (semi-diurnal period) calculated from the diagram showing the change of seawater exchange ratios with the lapse of time as illustrated in Fig. 6. It is evident from the figure that the seawater exchange ratios in the innermost part of the bay will be improved from 2% under the present condition to 9-11% in the future (when the power station is installed); from the center of the bay over to the bay mouth, 8-10% under the present condition to 11-15% in the future. Particularly, in the opening part on the Okitsu side, the flow of current toward the outside of the bay occurred owing to the effect of discharge current in the upper layer, and the flow of current toward the inside of the bay occurred in the lower layer. It can, therefore, be considered that these constant currents greatly contribute to improvement in the seawater exchange ratios inside the bay due to installation of the power station.

4. Numerical simulation

4-1 Basic equations of the mathematical model

The constant currents such as density current, discharge current and wind blowing current have a tendency to be reversed usually between the upper layer and the lower layer, thereby greatly contributing to the exchange of seawater in the bay. In this study, therefore, the model which can reproduce 3D phenomena was used. Navier-Stokes equations as well as equations of continuity and diffusion were used as basic equations in the model.

Among particles of number N which were thrown into each point (st. A-J) inside the bay, those of M pieces flowed out of the bay, and the seawater exchange ratio of this unit water mass was defined as M/N. The particles moved owing to flow and turbulence. The turbulence was assumed to follow the primary Markov process.

4-2 Results of numerical simulation

Diurnal-period current, semi-diurnal-period current, constant current and discharge current considering the effect of density current, river current, etc. were reproduced in the model.

The authors conducted study on the effect of difference in diffusion coefficients which are difficult to determine experimentally on the exchange of seawater, the effect of discharged warm water and river water on the exchange of seawater, and so on, obtaining the following information:

(a) In the closed inner bay, the inflow of fresh water such as river water has a large effect on flow patterns in the sea, even though its quantity is small.

(b) The release of thermal effluent from the power station greatly contributes to the exchange of seawater in the closed inner bay. In Fig. 6, seawater exchange ratios inside the bay in the same case as the hydraulic test are shown.

5. Conclusion

To examine the applicability of the hydraulic test method using a distortion model to the prediction of seawater exchange phenomena, comparative study was made with the results of field observations and numerical simulation with respect to the reproduction of flow in the model. As a result, the following points were clarified:

(1) The tidal current and constant current having two different types of periods can be reproduced with a high accuracy in the distortion model.

(2) For determination of seawater exchange ratio by hydraulic test, the authors could not make comparison and verification with field investigation results, but found that the test could be conducted with a certain level of accuracy on the whole by the use of a distortion model though there are some problems in test methods. Moreover, as a result of this study, the authors could obtain a conclusion that when the steam power station is installed inside the closed bay, the exchange of seawater makes considerable progress owing to intake and discharge of its cooling water inside the bay thereby producing a large water-purifying effect.

Acknowledgment

The authors would like to acknowledge the advice and assistance of Dr. Naoaki Katano and Chief Researcher Masafumi Mizutori of Central Research Institute of Electric Power Industry and Manager Kinya Adachi and Researcher Michiko Ohishi of Mistubishi Research Institute, Inc.

References

1) A. Wada and M. Kadoyu: Numerical Simulation of Water-Particle Motion in the Inland Sea of Japan, 20th Hydraulic Symposium Report, pp. 191-196, 1976.

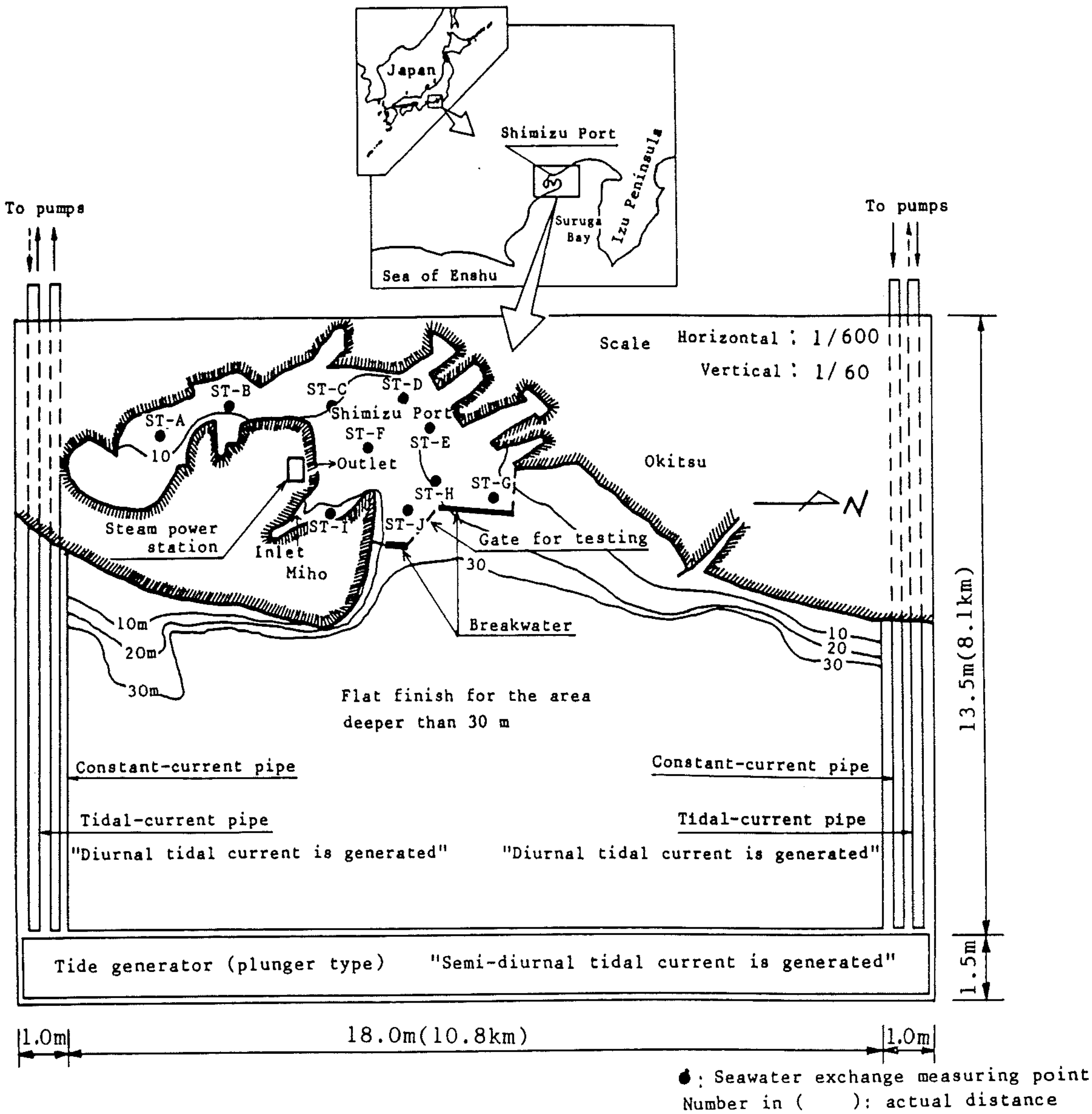

Fig.1 Hydraulic model and Seawater exchange measuring points

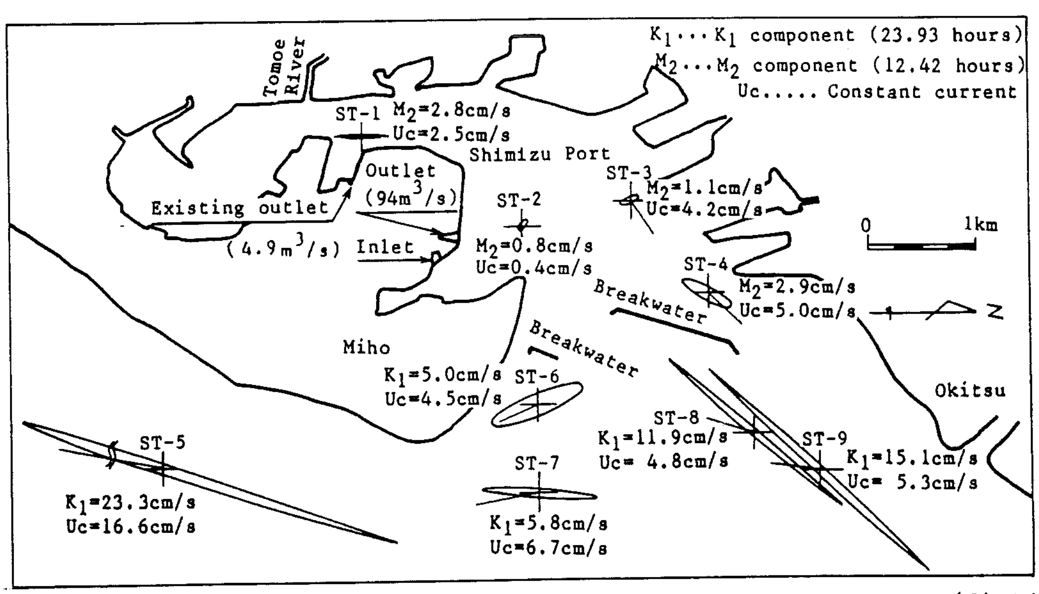

Fig. 2 Tidal-current plume and constant-current component (field observation values, winter, surface layer)

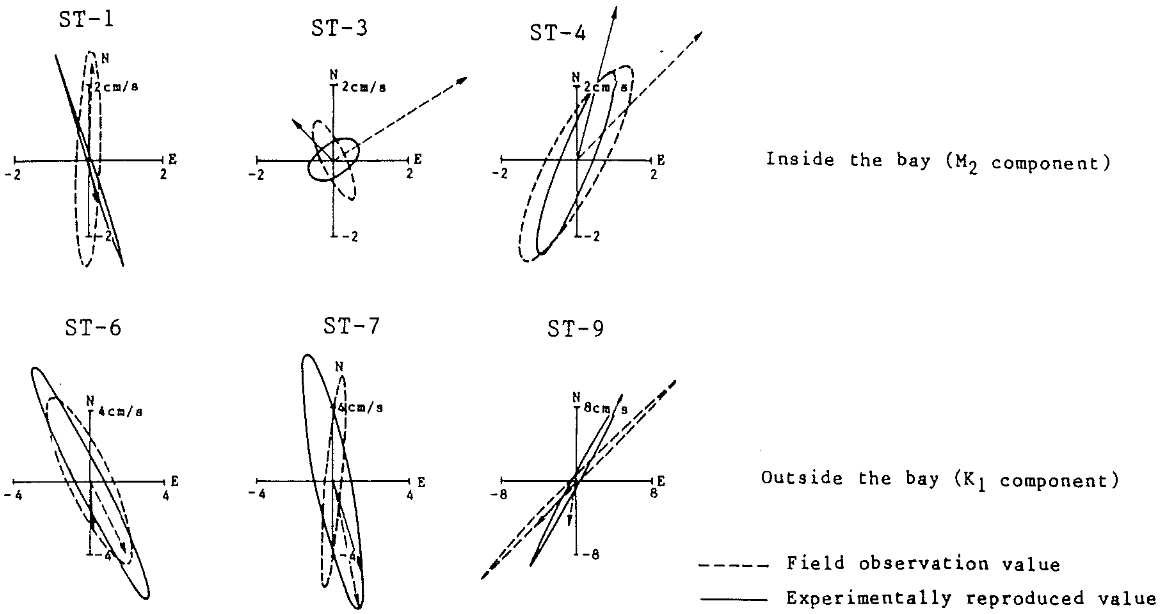

Fig. 3 Comparison of tidal-current plume and tidal current (upper layer)

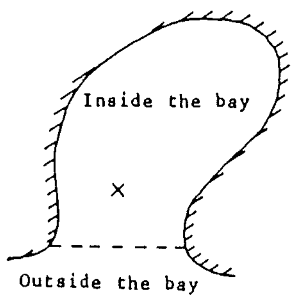

Fig.4 Definition of Seawater exchange

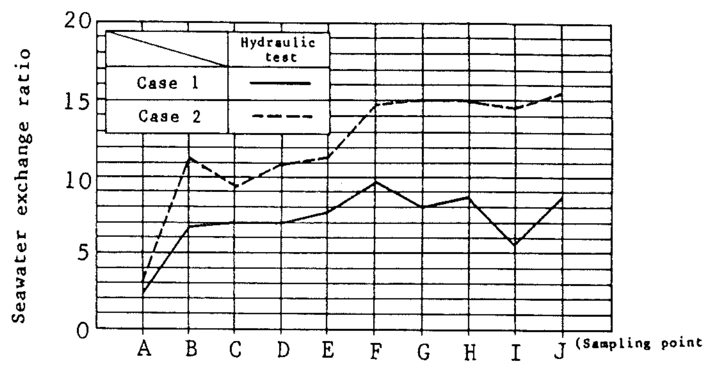

Fig. 5 Seawater exchange ratio per period inside the bay (12 hours)

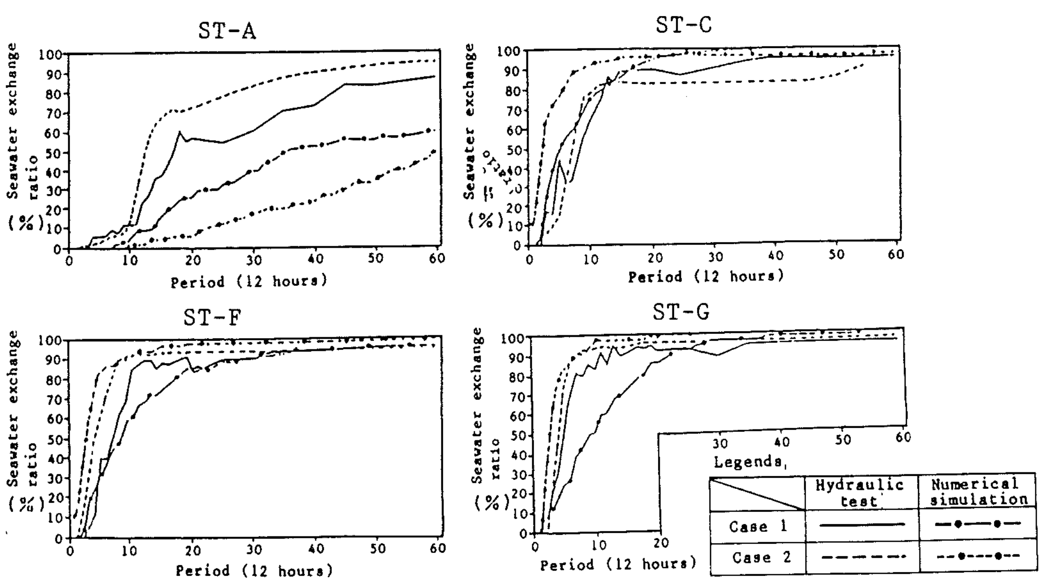

Fig. 6 Seawater exchange ratios inside the bay (hydraulic test, numerical simulation)

WATER EXCHANGE BEHIND THE INLET WEIR OF A SEMI-ENCLOSED LAGOON

by Soon-Keat Tan
School of Civil & Structural Engineering
Nanyang Technological Institute, Singapore.

Abstract

A submerged weir (with culverts at lower level) at the inlet of a lagoon was constructed to ensure a minimum depth of water at all times. This approach resulted in intense mixing of water behind the weir as the tide rises. The mixing or water renewal is restricted to areas near the inlet. A series of laboratory experiments were carried out to determine the volume of the paraboloid of water where mixing is intense. The results obtained could be used to apply to situations where there is an inlet channel behind a submerged weir.

Introduction

Coastal lagoons, be it natural or man-made, are popular locations for recreational activities. As such, good water quality in a lagoon always tops the list of the requirements. A second but of no less important requirement is the provision of a sufficient depth of water in a lagoon at all times (during both rising and receding tides). Some managers of lagoons have invested in water retaining structures such as submerged weirs, with lower culverts in some cases, to ensure that a minimum depth of water is maintained. The swimming and canoeing lagoon at Sentosa Island (located south of the Singapore Island) were constructed in this manner, Fig. 1. In so doing however, the effectiveness of natural tidal renewal of water in the lagoon could not be estimated using the tidal prism method.

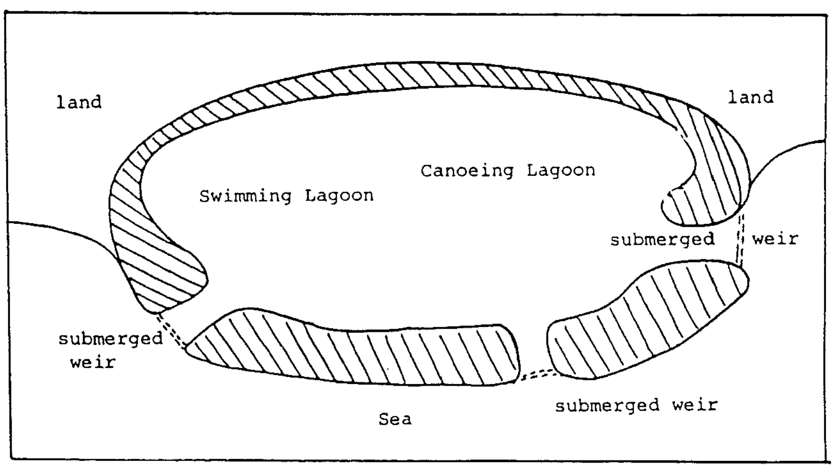

Figure 1. A sketch of Sentosa Lagoons

In order to assess the effectiveness of tidal flushing, one needs to have a detail understanding of the hydraulics due to the submerged weir at the inlet. Of paramount importance is the mixing volume as the tide rises and falls. Where there is a submerge inlet weir of crest level at an elevation between the low and high water, the hydraulics of flow over the weir changes from one of plunging over a vertical drop structure to flow over an obstruction as the tide rises. As the tide recedes, a reversal of flow characteristics takes place. However, the main bulk of water exchange is in the turbulent mixing zone at the inlet where the flow plunges over the weir, into the receiving body of water and reattached to the surface further downstream. The problem then is to estimate the paraboloid of water where mixing of sea and lagoon water takes place during the flood tides.

This paper describes the author's attempt to determine the extent of mixing caused by flow over a vertical drop structure into a reservoir of water below it. This is the first step towards the quantitative estimation of water exchange at the inlets.

Review

When water flow over a vertical drop structure into a body of water below it, intense mixing of the incoming water with the reservoir of water in the stilling basin takes place. This phenomenon has been used widely in water treatment work where a mixing process is called for. The hydraulics of the flow is only understood qualitatively. The design of the drop structure, shape and size of the stilling basin is generally based on empirical rules.

Vertical drop structures are also utilized as flow control structures in irrigation canals. However, the major concerns there are the design of appropriate weirs and stilling basins, for example, Christodoulou et. al. (1984) and Naib (1984). Noutsopoulos (1984) looked into the hydraulic characteristics in a straight drop structure of trapezoidal cross section. However, the author only dealt with shallow downstream flow, in which case, the problem was essentially one of impact of a sheet of water jet onto a solid surface.

While there are many publications on 'internal' jet flows (for example Sawyer (1963) and Johnson & Halliwell (1986), there are relatively few publications on impinging jet into a body of (deep) water. The few publications that the author is aware of are Mikis & Ting (1983) and Sene et. al. (1989). Of these two, the latter presented some results which are of direct relevance to the current study.

Approach of the study

The actual flow over the weir in the lagoon is a three dimensional phenomenon. However, in the case of the Sentosa lagoons, the inlets are actually narrow channels of about the same width as the weir. A first approach is to treat the problem as a two dimensional problem as shown in Fig. 2 which shows the schematic sketch of a two dimensional flow pattern in a channel when the tide rises to a level above the crest of the weir while the water level in the reservoir downstream is below the weir crest. The jet plunges into the receiving water, and reattached to the surface a certain distance downstream. Here, the body of water enclosed by the path of the jet is continuously being displaced further downstream as surface flow. The body of water below the path of the jet is put in circular motion also. However, replacement of water is slow.

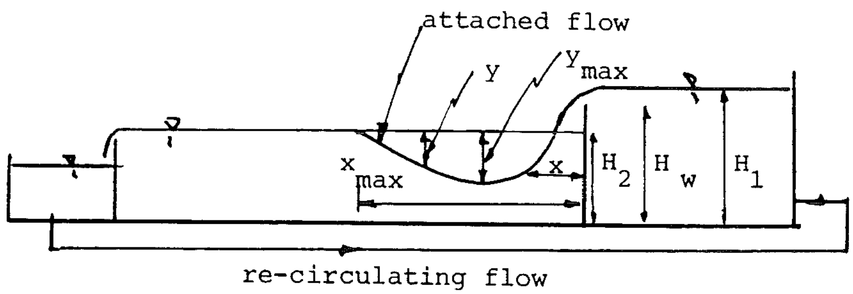

Figure 2 The experiment set up

Since the flow pattern due to the impinging jet is established within a few minutes while the change in water level in the rising tide and that in a reasonably large lagoon is relatively small during that few minutes, one can adopt a simpler approach of modeling the whole tidal cycle through a number of discrete steps of pseudo-stationary tidal levels. In fact, to model increasing tidal level one only needs to increase the incoming flow rate and raise the tail gate level according to the rate of filing of the lagoon. This approach has the advantage of establishing stationary flow patterns where the desired flow characteristics could be measured with ease.

A series of laboratory experiments was carried out to determine the shape and size of the paraboloid of water.

Experiment set-up and results

The experiment setup in a flume is as shown in Fig. 2. Two open channel flumes were used at various stages of the study. Altogether eight sets of experiments were carried out. Flow visualization techniques and video taping were employed in analyzing the overall flow pattern. Point velocities (horizontal and vertical component) were measured using cross-fibre constant temperature probes. The path of the jet was determined from the point of inflexion of the vertical velocity profiles at various locations along the flume.

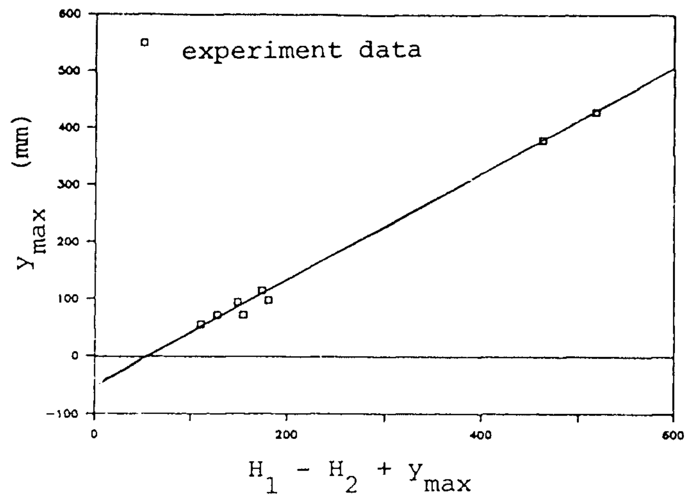

Figure 3a Maximum depth of plunge.

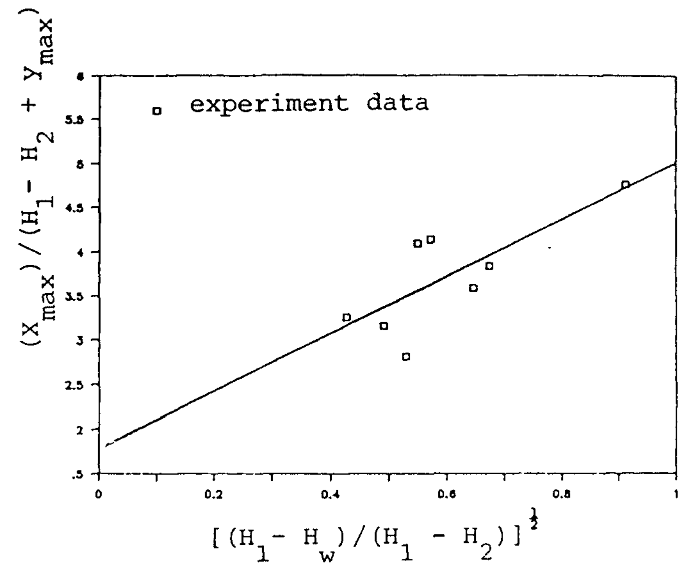

Figure 3b Maximum extent of attached flow.

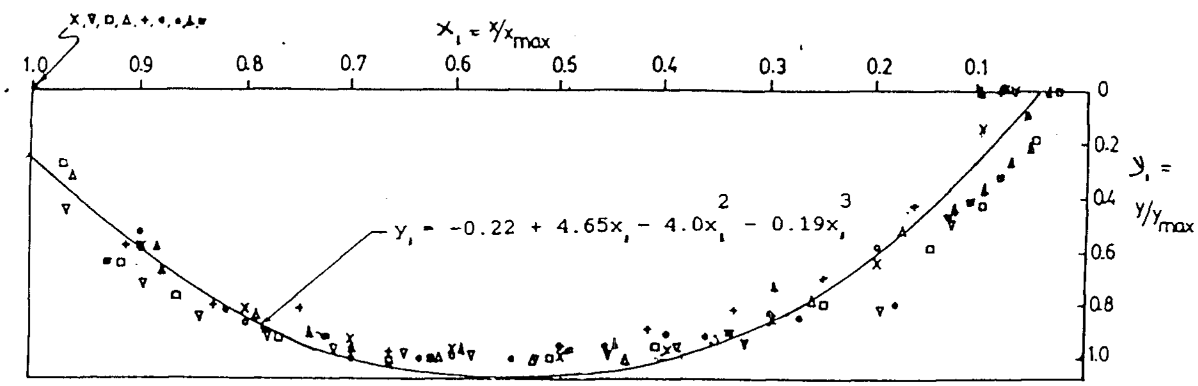

Figure 4 The locus of the impinged jet in the receiving water.

It was found that the path of the jet in the receiving water is well defined and when presented in terms of x/x_{max} and y/y_{max}, (the symbols are as defined in Fig. 2), the results from the eight sets of experiment fall into a well defined curve, Fig. 3.

Figure 4a shows the plot of the maximum depth of plunge of jet as a function of the potential difference. The function is well defined. Figure 4b shows the plot of dimensionless length of reattachment of jet as a function of dimensionless brink height above the weir. The goodness of fit of the data is not as good as that of Fig. 4a. Bearing in mind the nature of the experiment and the result was very good indeed.

Application of the results

Figures 4a and b can be used to estimate the maximum depth of plunge, y_{max} and the length of reattachment, x_{max}, since the other parameters are known constants. Then Fig. 3 can be used to obtain the path of the jet in the receiving water, hence the volume of water being renewed during each tidal cycle.

The average tidal range in Singapore water is approximately 2 m (approximately 0.25 m ACD to 2.25 m ACD). The maximum is slightly over 3 m (approximately 0.1 m ACD to 3.1 m ACD). The weir-crests of the lagoons are at 1.8 m ACD on the average and the lower culverts is at 1.5 m. However, because of the rise of the water level in the lagoons during the rising tide, the phenomenon of plunging jet over the weir normally does not last more than half an hour and the drop is seldom more than 0.5 m.

A computer program is currently being developed to simulate the tidal variation in the sea, change in water level in the lagoon as it is being filled, and the corresponding path of the plunging jet at various discrete time intervals.

Concluding remarks

The results of a series of experiments on the characteristics of a plunging jet from a vertical structure into a receiving body of water below it was presented. Due to the nature of the phenomenon, the laboratory model is actually a prototype in its own right. There is no clear cut scaling laws that can be used. However, when the results are analyzed and presented through combinations of various parameters, there emerges a way of extrapolating or interpolating the experimental results to apply to combination of conditions not tested in the laboratory experiment. Though the approach needs to be verified, the author believed that the results obtained are quite valid, at least for the case of two dimensional flow in a rectangular channel.

There will be some doubt whether the approach proposed is valid for the case of irregular channel boundary and when the flow concerned is three dimensional in nature. However, the approach will be useful to obtain a first solution.

References

Christodoulou, G C, Noutsopoulos G C and Andreou S A (1984) "Factors Affecting Brink Depth In Rectangular Overfalls". Proceedings of the 1st International Conference on Hydraulic Design in Water Resources Engineering: Channels & Channel Control Structures, University of Southampton, April 1984. pp I-3 - I-17.

Johnston, A J and Halliwell, A R (1986) "Jet Behaviour in Shallow Water" Proc Instn Civil Engrs (part 2) No 81. pp 549 -568

Miksis, M J and Ting L (1983) "Surface Waves Induced By An Impinging Jet" Phys. Fluids. 26. pp 2378-2384

Naib, S K A (1984) "Hydraulic Research On Irrigation Canal Falls". Proceedings of the 1st International Conference on Hydraulic Design in Water Resources Engineering: Channels & Channel Control Structures, University of Southampton, April 1984. pp I-59 - I-73.

Noutsopoulos G C (1984) "Hydraulic Characteristics in A Straight Drop Structure of Trapezoidal Cross Section". Proceedings of the 1st International Conference on Hydraulic Design in Water Resources Engineering: Channels & Channel Control Structures, University of Southampton, April 1984. pp I-167 - I-181.

Sene K J, Thomas N H, Goldring B T (1989) " Planar Plunge-zone Flow Patterns And Entrained Bubble Transport" Journal Of Hydraulic Research 27, 1989 No 3. pp 363-383.

FLOW AND MASS TRANSPORT OFFSHORE FROM TIDAL INLETS

by Rodger B. Tomlinson
University of New South Wales
Water Research Laboratory
Manly Vale NSW 2093 Australia

Abstract

Physical model studies of the structure of the flow emerging from a tidal inlet are reported for the case of an idealised sinusoidally varying discharge. The characteristic structure of the ebb tidal flow was similar to that of a starting jet and the flood tidal flow was similar to a potential sink. The spatial structure of the discharge can be normalised with respect to a length scale $l = [m_o T^2 / \rho]^{1/3}$. Only a small fraction of water discharged from the inlet on the ebb tide was found to return on the following flood tide. Comparison of experimental results with prototype flow observations suggests that the model flow behaviour and the derived characteristic length scales describe the mass transport in unsteady flow features such as those generated by tidal forcing at inlets and straits.

Introduction

Studies by Özsoy (1977), Mehta and Zeh (1980) and others have examined the nearshore hydrodynamics of the flow issuing from a tidal inlet. These studies have considered the ebb discharge to be a quasi-steady turbulent jet and give a good estimate of the velocity distribution, sediment movement and induced flow near the entrance.

Wilkinson (1978) and Tomlinson (1986) have examined the gross features of the offshore flow structure (shown schematically in Figure 1) in an idealised two-dimensional physical model in which a sinusoidally reversing flow was discharged from an open channel into a stagnant basin. During each period of ebb flow, a vortex pair was observed to form and ultimately become the dominant feature of the flow. Initially the vortex pair rolled up until its strength was sufficient to move away from the inlet. During the remainder of the ebb phase the flow was like a starting jet with the motion of the vortex pair cap being controlled by the advection of mass, momentum and vorticity from the jet "tail", the entrainment of ambient fluid into the cap, and the bottom frictional resistance to the flow. During the flood phase, the flow back into the inlet approximated a potential radial sink flow. The influence of this flow reversal on the behaviour of the ebb discharge flow structure depended on the extent of the flood withdrawal. As the vortex pair cap moved further away from the inlet its motion became less dependent on the dynamics of the jet tail, with the dominant force acting on the cap being bottom friction. This, combined with a diffusion of vorticity, caused the flow to slow down and grow in size.

It can be shown for a turbulent periodic jet that a characteristic length scale exists, which depends on the momentum flux per unit depth, m_o, the density, ρ, and the period, T and which is given by:

$$l = \left[\frac{1}{\rho} m_o T^2 \right]^{1/3}$$

Physically, this length scales the size of a large Reynolds number jet after one period from the commencement of the ebb flow. The inlet channel width, b_o, is also used as a scale and the time, t, can be non-dimensionalised with respect to the period, T. These length and time scales can thus be used to derive parameters which characterise the flow based on the inlet source conditions.

Tomlinson (1986) has carried out extensive modelling of the flow structure and a brief outline of these experimental results is presented here. The features observed suggest a different fate for water discharged on the ebb tide and in particular, any pollutant load carried by it, than would be predicted by the quasi-steady formulations.

Experimental Techniques and Idealised Flow Behaviour

The laboratory experiments were conducted in a 5 m square tank with a false floor (3 m square) representing the bottom boundary. The sinusoidally varying discharge entered the basin from an inlet channel which could be varied in width (0–200 mm) and in depth (0–100 mm). Uniform offshore bed slope was possible by raising the inlet end of the false floor. The period of the flow used was 60 seconds in most cases. Experiments were run with periods up to 250 seconds. The capacity of the experimental apparatus was such that characteristic lengths, l, up to 5 m were achieved, although the majority of tests were conducted with l approximately 1 m.

For all but a few tests with small l/b_o values, the vortex pair was not influenced by the flow reversal to the inlet. In most cases the vortex pair remained stable for at least one cycle and data were obtained for this period. The experimental technique was to take time exposure photographs of the flow development. Dye and surface particles were used as tracers. From the photographic record the following were obtained:- the unsteady velocity distribution, centre of rotation of the vortices, translation velocity of the cap, lateral spread of the cap, entrainment velocities.

Typical results for the idealised uniform depth flows are shown in Figures 2 and 3. Also shown on these figures are the predictions obtained using a semi-empirical mathematical model utilising integral equations of mass and momentum for the general case of a two-dimensional shallow water unsteady jet. The self-preservation of flow in and around the vortex pair cap which is nearly circular in shape enabled empirical relationships to be derived for the conservation of cap mass and momentum.

The growth rate in the early stages of flow development (Figure 2) is primarily dependent on the rate of increase of the mass flux which scales as $(l/b_o)^{1/2}$. As the rate of supply of mass from the jet decreases with time, the growth rate asymptotes to that for an isolated vortex pair. Typical results for the rate of seaward translation of the periodic jet are shown in Figure 3. The influence of bottom friction is also evident, particularly after the vortex pair has decoupled from the jet. In general, in the early stages of the flow the translation of the cap is a function of the inlet width ratio for values of l/b_o up to around 50, with a weak dependence on the depth ratio, l/h_o. For times greater than $t = 0.5T$ the cap translation is approximately independent of the inlet width ratio for l/b_o values greater than 20. This suggests that approximate depth independent solutions (such as Van Senden, 1985) are possible for the early flow stage when the source mass flux in increasing nearly linearly with time.

The influence of flow depth and hence bottom frictional resistance has not adequately determined due to the limitations of the experimental facilities. The numerical predictions however suggest a reduction in the growth rate with increasing values of the ratio of the characteristic length to the inlet depth, l/h_o.

In a basin with a linearly increasing offshore depth, the periodic jet growth rate and seaward migration were suppressed with increasing bed slope.

The clearly defined vortex pair structure is reorganised by a cross-flow. For uniform cross-flows with low velocity relative to the jet exit velocity, the vortex pair was deflected downstream and migrated away from the inlet and the boundary. For larger values of cross-flow the vorticity associated with the upstream vortex was dispersed by the cross-flow shear and the downstream vortex was spun up near the boundary. This vortex then migrated away from the inlet along the boundary under the influence of the cross-flow and the self-induced motion of the image vortex across the boundary.

From the experimental results it is taken that the downstream vortex will attach to the boundary for a dimensionless cross-flow velocity, $v_c/(l/T)$ greater than about 0.6. Once attached to the boundary the vortex appears to translate at a constant speed regardless of the initial flow conditions. A similar vortex-like structure develops in the lee of a steady jet, but in that case it remains stationary downstream of the jet.

Mass Transport

An important finding of the experimental study was that for all but flows with small l/b_o values, the bulk of the water discharged on an ebb cycle would not return to the inlet on the following flood flow reversal. If as an approximation, the ebb vortex pair is taken to move away from the inlet at an average velocity equal to $C(l/T)$, where C is a function of l/b_o only, then the limiting condition for the vortex pair cap to be outside the radius of withdrawal of the next flood tide was found to be that l/b_o be greater than about 13.

Dye concentration measurements were taken to quantify this tidal exchange. The fraction of ebb discharge returning on the subsequent flood tide was obtained by means of conductivity probes located at the inlet channel which detected the concentration of electrolyte labelled fluid in the flood flow. The total fraction of fluid re-entering the inlet shown in Figure 4 was calculated by integrating the product of the fraction returning and the total inflow over the flood phase of the cycle. The considerable scatter in the data for experiments with similar l/b_o values has masked any l/h_o dependence.

Model Case Study – Nerang River Entrance

A detailed description will now be given of an attempt to realistically model an ebb tidal discharge, outlining the scaling difficulties encountered. The inlet studied was the Nerang River entrance in Queensland (Wilkinson et al., 1979) where an ebb-staged sewage disposal scheme was planned. This river discharges into a large intra-coastal waterway which is connected to the ocean by a short channel. The average river discharge is less than 2% of the total discharge through the channel and was ignored.

The flow characteristics at a tidal entrance can be expressed in terms of the characteristic scales and parameters defined earlier. In terms of the tidal prism, P_T, the mean cross-sectional area of the channel, A_C, and the mean depth of flow in the channel, h_o, the characteristic length scale, l, is given by:

$$l = \left[\frac{\pi^2 P_T^2}{A_C h_o} \right]^{1/3}$$

Typical values of this length scale for tidal inlets range from 7 km – 19 km (US data, Per Bruun [1978]). The corresponding inlet depth ratio, l/h_o, ranges from 10^3 to 6×10^3, and the inlet width ratio, l/b_o, from 8 to 77. The characteristic length scale and inlet parameters for the Nerang entrance were estimated as:

$$\begin{aligned} l &= 7960\,\mathrm{m} \\ l/b_o &= 33.7 \\ l/h_o &= 1090 \end{aligned}$$

An undistorted scale model should ideally be used to correctly scale the lateral mixing of the jet. However, due to unavoidably low Reynolds numbers in a model, the requirement to correctly scale bottom shear necessitates distortion of the vertical model scale. A compromise between these two requirements was adopted in which water depths everywhere were increased by a fixed amount while bottom slopes were undistorted and were the same as in the prototype. This meant that momentum and lateral mixing were correctly scaled but that friction effects would only be correctly scaled at one particular depth contour. The flow at the inlet channel was considered two-dimensional.

Similarity of frictional and inertial forces between model and prototype can be achieved if $(l/h_o)_r = 1/f_r$, where f is a friction factor. In the model the bed was formed of fibrous cement sheeting. Reynolds numbers based on the flow depth were in the range of 2 000 to 800 in the area of interest. A mean friction factor of f = 0.04 was adopted for the smooth turbulent flow. In the prototype, the median diameter of bottom sediments is approximately 0.25 mm for a distance of 3 km offshore from the Nerang entrance channel. Taking the mean ripple height in such material to be approximately 20 mm, a mean depth of 25 m, and a typical velocity of 0.3 ms^{-1} in the jet, the relative roughness of the sea bed is 800 and the Reynolds number of the order 10^6 to 10^7. Under these conditions the bottom would be hydraulically rough and the friction factor would have a value of 0.014. The approximate depth scaling for the model was then given by $(l/h_o)_r = 2.87$. The horizontal length scale and time scales were fixed by the experimental facilities. The offshore slope was modelled in two linear stages.

The predicted and modelled behaviour of the periodic jet are shown in Figure 5. Verification of the results with field data has not been possible, however. In general the flow pattern observed was similar to that described earlier for the general experiments. However, frictional effects dominated this flow (the inlet depth ratio being much higher than previously modelled) and would also dominate most coastal flow situations, leading to instability of the vortex pair structure.

The mixing that would occur in the prototype was only partially reproduced in the model due to the very much lower Reynolds numbers which exist in the model. Concentration levels were continuously monitored during tests to determine the exchange efficiency and it was found that the strength of the offshore current had negligible effect on the fraction of fluid returning to the inlet on the flood tide. Figure 6 shows the fraction of returning fluid passing the entrance on the flood tide. The return fraction drops rapidly to a concentration of about 0.20 one hour after the flow reversal and then steadily reduces to zero by the end of the flood cycle. The total return fraction was found to be 0.14 with no offshore current, 0.14 for the 50% exceedance current and 0.17 for the 10% exceedance current.

Discussion

Despite the lack of direct field verification of the flow structure, sufficient evidence exists to suggest that the general features of the flow generated off tidal inlets and straits can be modelled in the manner described here. For example, LANDSAT remotely sensed imagery and physical model studies (Onishi, 1986) have been combined to confirm general features of the flow through narrow straits which are similar to those predicted off tidal inlets. Sheres & Kenyon (1989) have recently reported a vortex pair-like flow structure at the entrance to the Santa Barbara Channel. Finley & Baumgardner (1980) observed tidal inlet flows at Aransas Pass, Texas using LANDSAT imagery, which demonstrated the characteristic transient downstream circulation evident in the present cross-flow model studies. Van Senden (1985) monitored non-buoyant discharges from a tidal river and was able to describe the observed starting jet flow with a simple time dependent similarity model. Data measured by Mehta & Zeh (1980) and Tomlinson & Foster (1986) have shown enhanced entrainment into the nearfield of a tidal jet which is likely to be a result of the circulation around a vortex pair cap.

It has been seen from the experiments that ambient turbulence can greatly reduce the coherent duration of a vortex pair. In a real flow situation (particularly at a coastal inlet) wave activity, wind shear, and longshore drift are present at varying magnitudes throughout the flow cycle and would influence the spin-up of vorticity. However, the combined evidence presented in the studies referred to above, and that obtained recently by the author, suggests that the long term fate of the ebb discharge at a tidal inlet can be physically modelled to adequately account for the effects of bottom friction, offshore bed slope and longshore currents (outside the littoral zone). The results of the experiments have been used to predict the exchange of polluted waters discharged on the ebb tide for a number of proposed, and in the case of the Nerang, implemented sewage disposal schemes along the eastern seaboard of Australia (Tomlinson & Webb, 1989).

The characteristic length scales and parameters have been shown to be good indicators of the experimental flow behaviour with the characteristic length, l, approximating the seaward migration during one tidal period of a typical tidal inlet ebb discharge.

In conclusion, the physical model studies have demonstrated that tidally induced flows cannot be adequately described as quasi-steady flows. The vortices generated primarily due to flow separation at the end of the inlet channel, are seen to be the dominant feature of the exchange processes at the inlet and their existence explains a number of natural flow features, particularly in the presence of a longshore current.

References

Finley R J & Baumgardner R W, 1980. "Interpretation of surface water circulation Aransas Pass, Texas using LANDSAT imagery" *Rem Sens Envir*, 10, 3-22.

Mehta A J & Zeh T A, 1980. "Influence of a small inlet in a large bay" *Coastal Eng*, 4, 157-176.

Onishi S, 1986. "Roles of large scale eddies in mass exchange between coastal and oceanic zones" in *Physics of Shallow Estuaries and Bays*, Ed. J van de Kreeke; Springer-Verlag.

Özsoy E, 1977. "Flow and mass transport in the vicinity of tidal inlets", *Univ of Florida, Tech Rept* UFL/COEL/TR-036.

Per Bruun, 1978. *Stability of Tidal Inlets*, Elsevier

Sheres D & Kenyon K E, 1989. "A double vortex along the California coast", *J Geophys Res*, 94, C4, 4989-4997.

Tomlinson R B, 1986. "Periodic starting flows", *Univ of NSW, Water Research Lab Res Rept*, 168.

Tomlinson R B & Foster D N, 1986. "Sand bypassing at the Tweed River Entrance", *Univ of NSW, Water Research Lab Res Rept*, 167.

Tomlinson R B & Webb A T, 1989. "Effluent disposal in estuarine entrance channels", *9th Aust Conf Coastal & Ocean Eng, Adelaide, I E Aust Nat Pub* No 89/20, 42-46.

Van Senden D C, 1985. "Structure of tidal jets under variable source conditions", *Proc 21st IAHR Congress, Melbourne*, 86-93.

Wilkinson D L, 1978. "Periodic flows from tidal inlets", *Proc 16th Coastal Eng Conf*, Hamburg, 1336-1346.

Wilkinson D L, Tomlinson R B, Willoughby M A & Foster D N, 1979. "Gold Coast sewerage outfall study, Vol 1", *Univ of NSW, Water Res Lab Tech Rept* 79/05.

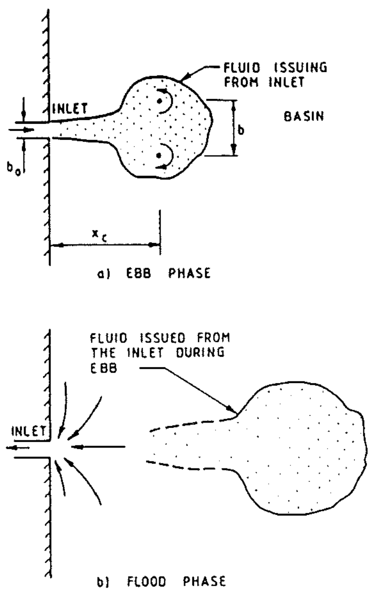

Fig 1 Idealised Flow Behaviour

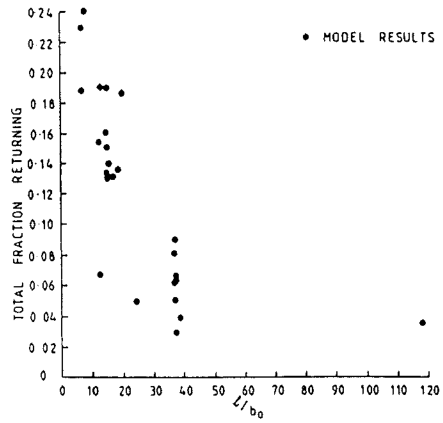

Fig 4 Tidal Exchange

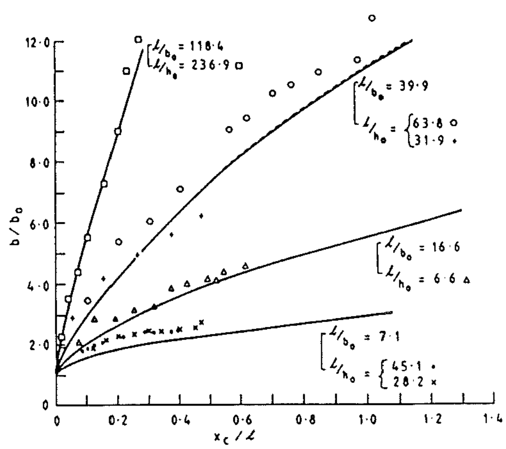

Fig 2 Ebb Jet Growth Rate

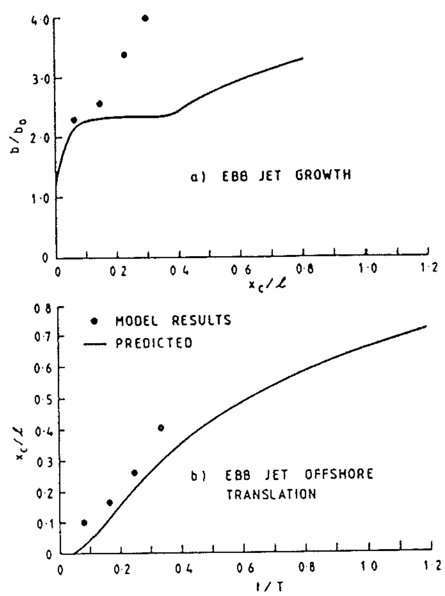

Fig 5 Case Study Nerang River Entrance Flow Behaviour

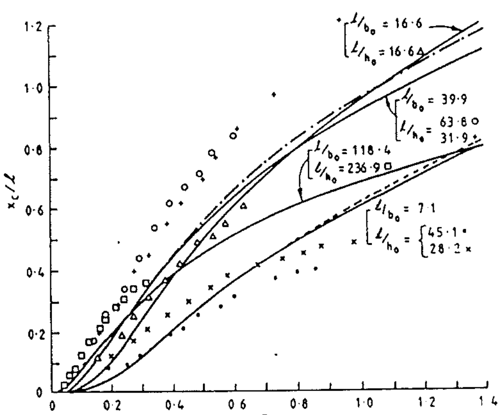

Fig 3 Ebb Jet Offshore Translation

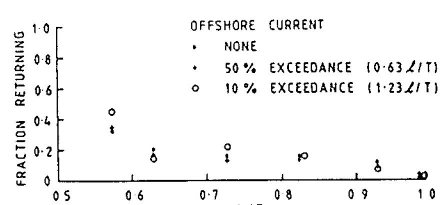

Fig 6 Case Study Nerang River Entrance Tidal Exchange

UNSTEADY FLOW AND EXCHANGE OF MATTER IN THE ENTRANCE OF A TIDAL HARBOR

by E.J.Langendoen and C.Kranenburg

Department of Civil Engineering, Delft University of Technology, P.O.Box 5048, 2600 GA Delft, the Netherlands

Abstract

Measurements of velocity and temperature distributions were made in a physical model of the entrance of a tidal harbor. The geometry of the entrance was varied, the flow varied sinusoidally with time, the water level was constant and density differences were absent. The formation and decay of gyres in the harbor is shown to correspond with variations in advective and turbulent transports of matter through the harbor entrance.

Introduction

Removal and disposal of sediments deposited in harbor basins usually involve high cost. The siltation of a harbor results from a net transport of sediments into the harbor that is caused by the often quite complicated flow patterns in the harbor entrance. Three main mechanisms of exchange of water through the entrance can be distinguished:

- exchange caused by gyres driven by the flow in the adjacent water body (e.g., a river or estuary),
- net flux caused by withdrawal of water from the harbor or by variations in water level,
- gravity currents driven by differences in density (generally related to differences in salinity) between the harbor and the estuary.

These mechanisms may act simultaneously, or one of them may be dominant during a certain phase of the tide. The third mechanism is an inherently unsteady process, whereas the first two may be either (quasi-) steady or unsteady.

Circulation patterns in harbor entrances driven by steady river flows have been extensively examined in the laboratory (Rohr, 1934; Vollmers, 1963; Dursthoff, 1970; Westrich & Clad, 1979). Most of these studies concentrated on the assessment of bulk exchange parameters. Booij (1986, 1989) reported detailed measurements of the flow patterns in several model harbors. Such measurements not only increase our insight into the flow phenomena (e.g., mixing layer at the transition from river to harbor, secondary currents, number and size of gyres, residence times, effect of a net flow through the entrance), but also serve the purpose of testing and improving computer models. These models can be used to design harbor entrances so as to minimize the cost of maintenance dredging.

Time-varying flows, caused by tidal motions, for example, further complicate the circulations in harbor entrances. Detailed measurements of velocity distributions seem to be scarce. Overall exchange properties of tidal harbors and the influence of their geometries were examined by Westrich (1977), Nece (1984), and Jiang & Falconer (1985) for the case where density differences were absent.

In this paper some results are presented of an ongoing research programme on the influence of the shape of the entrance of a tidal harbor on the resulting velocity fields. These results are concerned with laboratory experiments in three model harbors in which the velocity distributions and the exchange of (heated) water owing to an oscillatory (tidal) river flow were measured. The influences of variations in water level and density currents, and those of other geometries, will be dealt with elsewhere.

Physical model

The model consists of a basin in which harbor entrances of various geometries can be built, and an adjacent straight flume, width 1 m, representing a river in which a uniform time-varying (tidal) current is generated. The bottom of the model is horizontal and the sidewalls are vertical. The flow in the flume is generated by a water supply and an adjustable sharp-crested weir at each end of the flume. In the present experiments the flow rate varied sinusoidally in time, and no vertical tide was generated. The water depth was 0.11 m. Three geometries of the harbor were considered, see Fig. 1.

If the models are supposed to represent a harbor of width 200 m and depth 20 m, the length and depth scales are of the order 200. Recognizing that modeling of free-surface deformations is not essential here, the Froude number criterion can be dropped, and a velocity scale of 2.5 was assumed. Assuming a maximum water velocity in the field of 1 m/s, the related maximum Reynolds number in the model harbors is about 15000. A Reynolds number this large is needed to maintain turbulent flow. The amplitude of the flow rate in the flume was 42 ℓ/s.The period, T, of the oscillating flow in the model river was determined from a Strouhal number, $\hat{u}T/L$, where $\hat{u}$ is the amplitude of the velocity in the river and L the width of the harbor entrance. For a diurnal tide and the values of $\hat{u}$ and L mentioned above this number, which is related to the Keulegan-Carpenter number for oscillating flow around rigid bodies, becomes about 224. Since for the model L=1 m and $\hat{u}$=0.38 m/s, the model period would become 590 s. To speed up the experiments a little, a period of 500 s was selected.

Depth averaged velocities were measured using floats that drew about 10.5 cm. The movements of the floats were recorded on video. Images were digitized on a micro-computer each 0.25 s, and the positions of the floats were determined. Velocities were obtained by time-differencing. Mean horizontal flow components were also measured at some tens of locations (at 1.5, 4, 6 and 8 cm above the bottom) using electro-magnetic velocity meters, diameter 33 mm. The instantaneous velocities were averaged using a triangular filter with a width of 20 s. The accuracy of the velocity measurements is ± 1 %.

The exchange of mass between harbor and river is caused by advection due to the mean flow and turbulence. To examine the combined effect of advection and turbulence, the water in the harbor was heated by 1 or 2 degrees centigrade by mixing with hot water when the current in the river was near maximum. This water was sprayed into the water inside the harbor so as to obtain a horizontally and vertically uniform temperature distribution while disturbing the flow as little as possible. The hot water was dyed so that the degree of mixing could be observed by eye. Subsequent time histories of temperature were measured using thermistors (response time 0.8 s) at 24, 36 and 24 locations in harbors (1), (2) and (3), respectively.

Results

The results presented concentrate on the square harbor (1). Results for harbors (2) and (3) will be discussed in so far as they differ substantially from those for harbor (1).

Depth averaged flow patterns

Depth averaged flow patterns in harbor (1) at four time levels are shown in Fig. 2. The flow patterns were found to reproduce well from one cycle to another. The patterns shown in Fig. 2 have been composed of several recordings. Around maximum current (t=125 s and 375 s) a single, quasi-steady gyre exists in the harbor (Fig. 2a). When the velocity in the river decreases to that in the harbor, the gyre starts to increase in size and its center moves towards the river (Fig. 2b, slack water). After slack water the direction of the flow reverses, and the flow in the river is guided into the harbor by the rotating gyre while water is flowing out of the harbor at its downstream side (Fig. 2c). A new gyre starts to develop at the upstream corner of the entrance, and the old gyre is squeezed and breaks up in two parts. One part is advected with the river flow, and the other part is pushed to the back of the harbor while decaying (Fig. 2d). The new gyre grows, moves towards the downstream corner, and after some time occupies the complete harbor. A flow pattern then arises that is the reverse of that shown in Fig. 2a.

In harbor (2) a second, counter rotating gyre exists at the back of the harbor around maximum current. This gyre spans the width of the harbor, and its breadth gradually increases from about .25 m to .5 m. The flow near the entrance at slack water resembles that in harbor (1), but the old gyre decays much slower while transporting a patch of new water in the direction of the second gyre. This second gyre disappears, and a new one rotating in opposite direction comes into existence, before the next maximum current phase.

In harbor (3) a single gyre as observed in harbor (1) exists around maximum current. However, the water velocities are less by 30 to 50 per cent. The flow in the harbor decelerates more rapidly when slack water is approached, and at slack water the gyre remains completely within the harbor. The new gyre initially grows mainly in a direction parallel to the river, and the old gyre is more long-lived than that in harbor (1). Around the next maximum current the old water reaches the entrance as a result of the circulation induced by the new gyre.

Depth dependence of flow patterns

Fig. 3 shows flow patterns at four levels in harbor (1) at t=375 s. Two notable processes can be observed. Firstly, as is to be expected, a secondary current with the velocities directed towards the center of the gyre at 1.5 cm above the bottom, and a flow in opposite direction near the free surface occurs. This secondary current extends up to the bottom, since small particles moving along the bottom were found to spiral towards the center of the gyre. Secondly, the near-bottom velocities close to the downstream sidewall normal to the river are clearly larger than those higher in the water column. Near the bed high-momentum fluid from the mixing layer between harbor and river appears to be transported into the harbor. These two processes may be related to each other. Harbors (2) and (3) showed a similar behavior.

Temperature measurements

Estimates of heat losses at the boundaries and the free surface indicate that these effects are negligible. The total rate of heat transport Q_θ through the entrance therefore can be determined from

$$Q_\theta(t) = - c_p \frac{d}{dt} \int_V \theta \, dV = -c_p V \frac{d\bar{\theta}}{dt} \tag{1}$$

where t is time, c_p the specific heat of water, θ the excess temperature with respect to the river water, $\bar{\theta}$ is the mean excess temperature of the harbor, and V the volume of the harbor. A normalized rate of exchange, λ, can be defined according to

$$\lambda(t) = - \frac{Q_\theta(t)}{c_p A \hat{u} \bar{\theta}(t)} \tag{2}$$

where A is the area of cross-section of the harbor entrance. The integral in (1) was approximated using the thermistor measurements to obtain $\bar{\theta}(t)$. This signal was low-pass filtered and numerically differentiated with respect to time. Fig. 4 shows the resulting time histories of $\lambda(t)$ for harbors (1), (2) and (3). For harbor (1) the large peaks around slack water evidently result from the pronounced advective exchange which then occurs (Fig. 2, t=260 s). The second peak is lower than the first, since water that is less easily exchanged remains in the harbor after the first slack water. The dip in λ after slack water seems to result from the fact that the new gyre has not yet developed. The subsequent rise is caused by the arrival of old water, which is advected by the new gyre, at the entrance. The gradual decrease in λ during the quasi-steady phase may possibly be attributed to the time lag between the decelerating flow in the river and the flow in the gyre, which results in a decreasing velocity difference. The first peak for harbor (2) in Fig. 4 is lower than that for harbor (1), since the second gyre does not contribute to the exchange process. However, the second peak is relatively high because more old water is present near the entrance. The sudden increase around maximum current is caused by the arrival of the remnants of the old primary gyre at the entrance. The peaks at slack water in the case of harbor (3) are low, since the gyre does not move into the river. However, λ is quite large between the slack periods. The time averaged values of λ are 0.019, 0.022 and 0.023 for harbors (1), (2) and (3), respectively. These values are remarkably close to each other, although the flow conditions are rather different. The value of λ in steady-flow conditions ($\hat{u}$ now being the constant water velocity in the river) is about 0.032 (Booij, 1989), which is also about the value near maximum current in the present experiments. Turbulent exchange is dominant during this phase of the tide.

References

Booij (1986), Report nr. 9-86, Delft University of Technology.

Booij (1989), Proc. 23rd IAHR Congress, Ottawa, Technical session D pp. D69-D74.

Dursthoff (1970), Mitteilungen des Franzius-Instituts für Grund- und Wasserbau der Technischen Universität Hannover, heft 34, pp. 194-368.

Jiang & Falconer (1985), Int. Conf. on Numerical and Hydraulic Modelling of Ports and Harbours, Birmingham, England, pp. 65-74, BHRA.

Nece (1984), Journal of Waterway, Port, Coastal and Ocean Engineering, ASCE, vol. 110, nr. 2, pp. 251-269.
Rohr (1934), Untersuchungen aus dem Flußbaulaboratorium der Technischen Hochschule zu Karlsruhe, Verlag von R. Oldenburg, München und Berlin 1934.
Vollmers (1963), Dissertation, Universität Karlsruhe.
Westrich (1977), Proc. 17th IAHR Congress, Baden Baden, vol. 2, paper A 133, pp. 461-468.
Westrich & Clad (1979), Proc. 18th IAHR Congress, Cagliari, vol. 3, paper B.B.11, pp. 269-276.

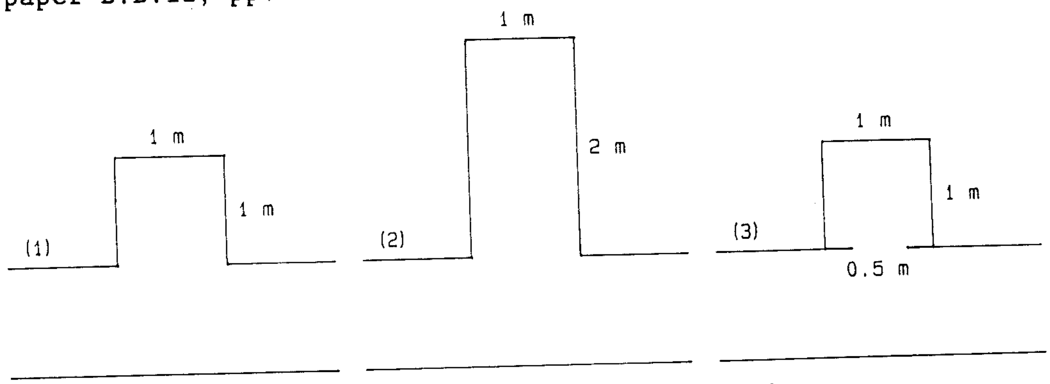

Fig. 1 Top views of model harbors

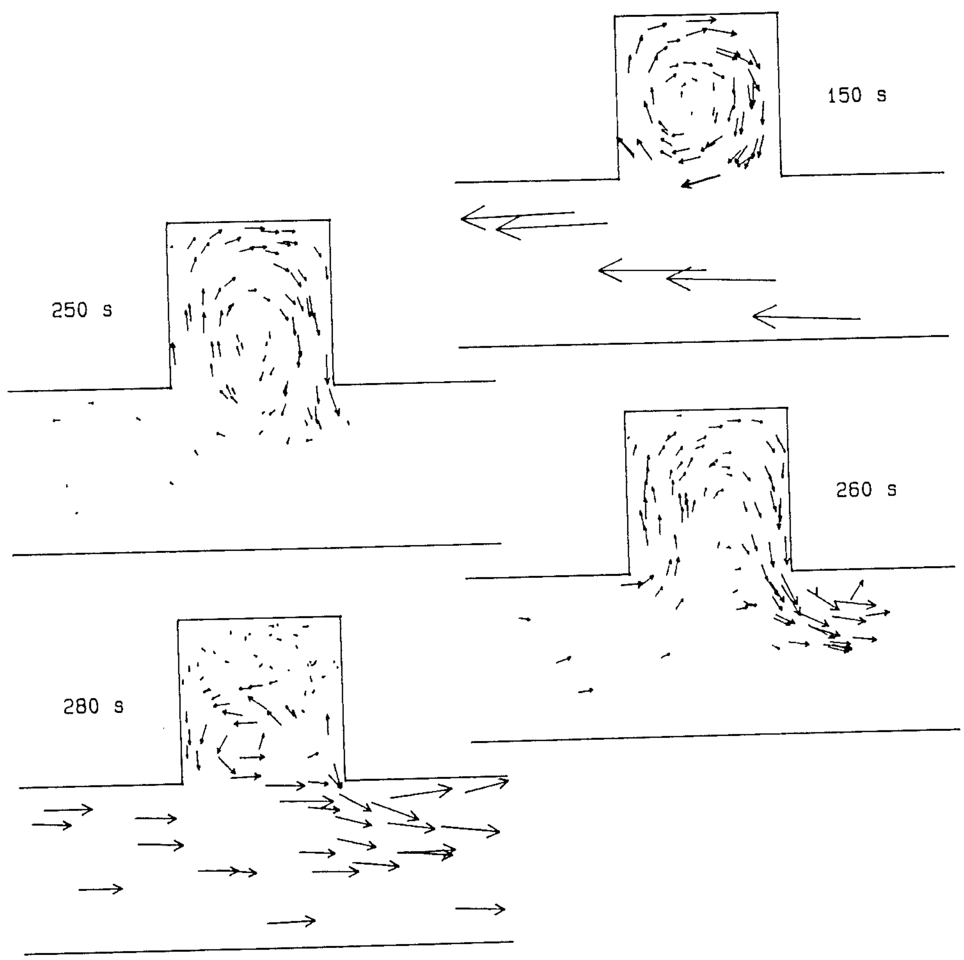

Fig. 2 Depth averaged flow patterns in harbor (1)

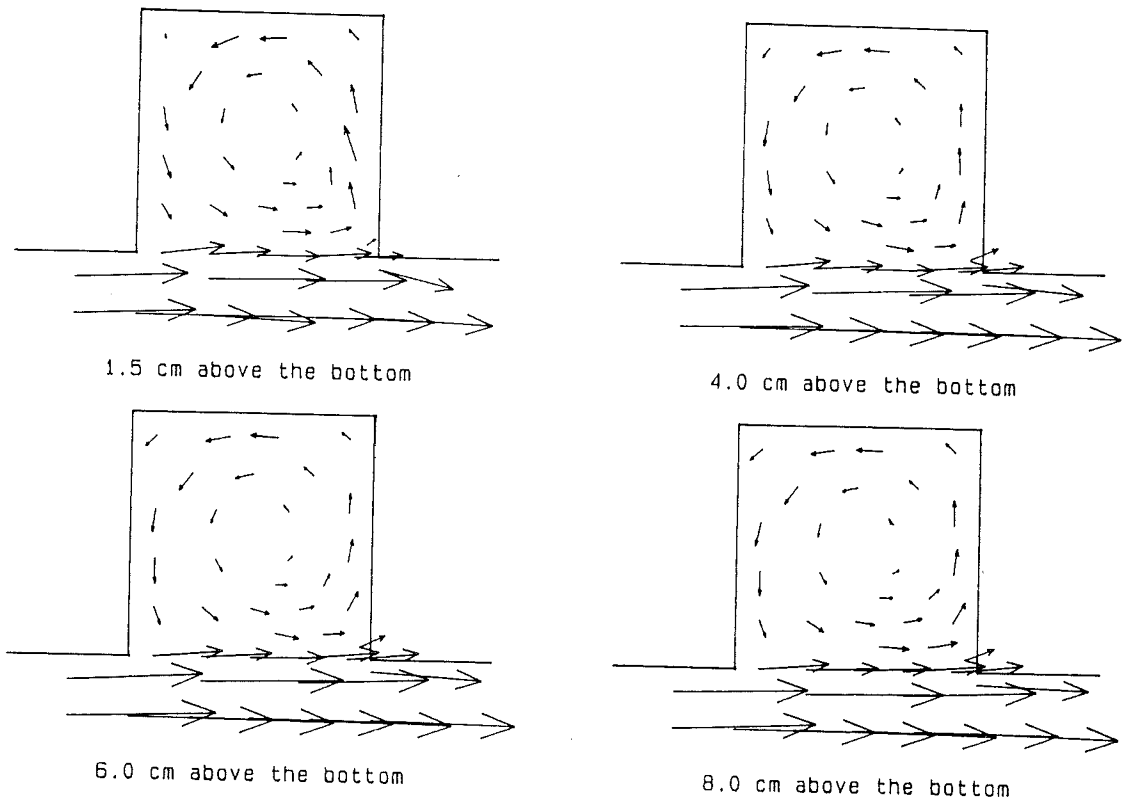

Fig. 3 Flow patterns at four levels in harbor (1) at t=375 s.

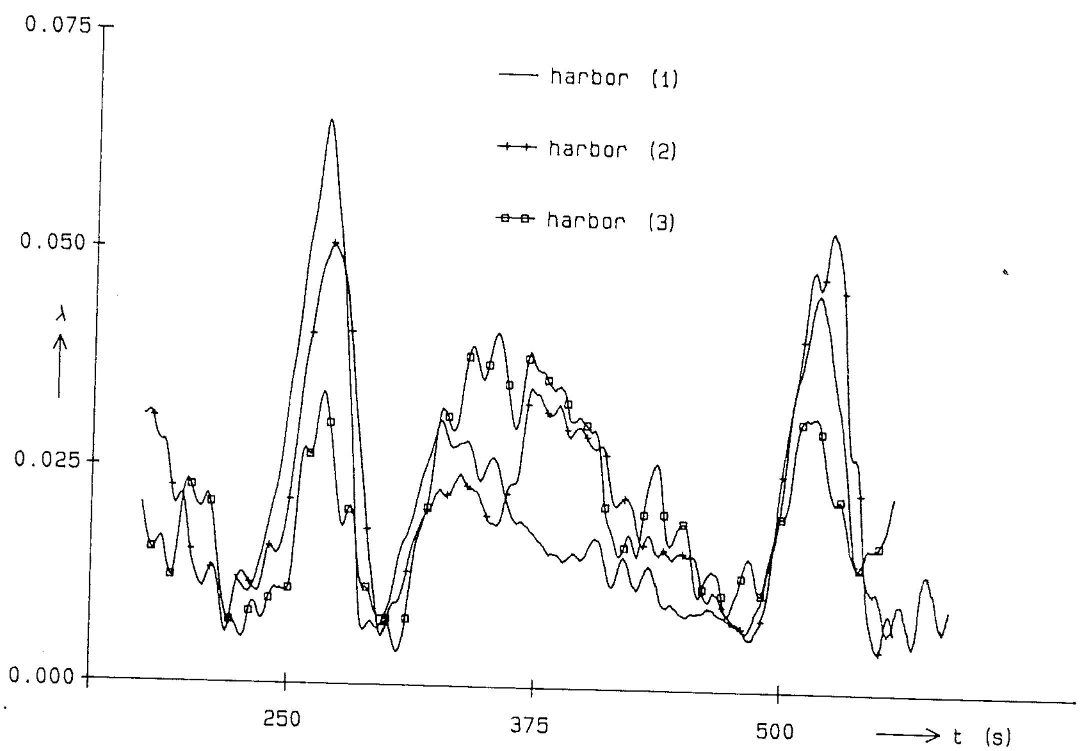

Fig. 4 Rates of exchange as functions of time

Session 3

Keulegan Centennial Symposium: Mixing Processes

Contributions of Garbis H. Keulegan to
An Understanding of Mixing Processes in
Estuaries and other Stratified Water Bodies

Donald W. Pritchard
Professor Emeritus, SUNY at Stony Brook
401 Laurel Drive
Severna Park, MD 21146

ABSTRACT

Included among the large bibliography of Garbis Keulegan are some 30 published papers and reports, spanning a period of 49 years, which have contributed to our understanding of motion and mixing in estuaries and other stratified water bodies. An understanding of motion and mixing in stratified estuaries must start with an understanding of motion and mixing in vertically homogeneous open channels. Thus I consider Keulegan's 1938 paper, "Laws of Turbulent flow in Open Channels", to mark the start of this nearly half century long period. Keulegan's last paper dealing with this subject area, co-authored with W. H. McAnally and titled "Salinity Intrusion Predictions by Analytical Methods", was published in 1987.

The characteristics of mixing in open channel flow depend in large part on the degree of vertical stratification. Keulegan's 1938 paper as well as his 1942 paper, "Equation of Motion for the steady mean flow of water in Open Channels" treated one extreme of the range of possible characteristics of such flows, that of zero vertical stratification,. His 1944 paper, "Laminar Flow at the Interface of two Liquids", treats the other extreme end of this range, that is, a flow in which motion and mixing are dominated by molecular diffusion and viscous stress.

In 1946 a paper by Keulegan entitled "Model Laws for Density Currents; First Progress Report" was issued by the USACE Waterways Experiment Station. This was the first of 14 such reports, each one detailing Keulegan's progress in a study sponsored by WES and extending over a period of some 14 years. The major results of this studied are contained in three published papers. The first, "Interfacial Stability and Mixing in Stratified Flows" was published in 1949 in the National Bureau of Standards, Journal of Research. The second, "The Mechanism of an Arrested Saline Wedge", and the third, "Model Laws for Coastal and Estuarine Models" were published in 1966 as Chapter XI and Chapter XVII of <u>Estuarine and Coastline Hydrodynamics</u>.

These papers were very important in influencing younger scientists and engineers in their studies of estuarine kinematics and dynamics. Of perhaps equal importance in the advancement of knowledge of this subject was Keulegan's personal interaction with others. Keulegan certainly strongly influenced this author in the early days of my studies of estuaries, starting in 1949. This aspect of Keulegan's contribution was particularly important during his 27 years of tenure at the Waterways Experiment Station. This tenure began in 1962, when Dr. Keulegan was 72 years old, having completed a career of over 40 years at the National Bureau of Standards. He never failed to give his time to provide advice and encouragement to the young staff at WES, and to suggest solutions to the problems they brought to him.

DISCHARGES INTO THE WATER ENVIRONMENT:
FROM EXPERIMENTS TO EXPERT SYSTEMS

by Gerhard H. Jirka
DeFrees Hydraulics Laboratory
School of Civil and Environmental Engineering
Cornell University, Ithaca, New York 14853, USA

Introduction

Over the past several decades, increasing public concern about the deteriorating quality of natural water bodies that receive polluting effluents from municipal, industrial and agricultural sources has spurred a flurry of research activities for understanding and predicting the associated mixing processes. Indeed, substantial advances have been made in our ability to analyze complex mixing processes arising from the interplay of discharge dynamics and ambient receiving water conditions.

From the viewpoint of engineering practice, however, effluent mixing analysis is plagued by significant problems, stemming primarily from the sheer number of discharge situations that require analysis and from their great hydrodynamic diversity. For example, even though exact figures are not available, it can be safely estimated that several hundred thousand point-source discharges exist in the United States. Annually, thousands of new or re-designed installations need to be analyzed, placing a burden on discharger and regulator, alike.

The hydrodynamic diversity is enormous: the site and flow characteristics of receiving water bodies vary widely; they may be small streams, large rivers, lakes, reservoirs, estuaries and coastal waters; they may be deep or shallow, stagnant or flowing; and may exhibit ambient density stratification of various degrees. Also, discharge type and configuration may vary greatly; the flow rate may range from small treatment plants to large cooling water flows; the exit velocity may be high or low; the effluent may be lighter or denser than the ambient; and it may exhibit various geometric detail ranging from single port submerged discharges to multiport submerged diffusers to surface shoreline discharges. As a consequence, the mixing process may entail a wealth of distinct hydrodynamic phenomena, including buoyant jet mixing, internal trapping in stratified ambient, dynamic bottom interactions (e.g. Coanda effects), vertical instabilities in limited water depth, buoyant spreading along the surface or bottom, large-scale induced circulations in shallow water, shoreline attachment, far-field passive diffusion, and other phenomena.

Efficient and reliable predictive technologies are needed in this context. Specialized "models" that are limited to a particular phenomenon carry the inherent danger of application outside their range of applicability. Examples of model misuse abound.

An expert system (CORMIX: Cornell Mixing Zone Expert System) has been developed for the analysis and prediction of effluent discharges under a variety of geometric and hydrodynamic conditions. CORMIX contains two key elements: a robust classification procedure that classifies any given discharge/ambient situation as to its hydrodynamic features, and a predictive element that gives detailed quantitative predictions of mixing patterns for each of the sub-processes for the given discharge/ambient situation.

The Experimental Base

All that is presently known about turbulent mixing phenomena in the water environment has been derived from experimental observations. Of particular interest for discharge classification are the so-called near-field mixing phenomena, i.e. those resulting from the influx of momentum and buoyancy into the receiving environment (of arbitrary depth, velocity and stratification).

A brief historical account will be given: Experimental work in the first half of the century by Prandtl and co-workers led to the concept of self-similarity, and the application of the mixing length hypothesis, for pure jets and pure plumes, respectively. Integral analyses, with the associated entrainment hypothesis, were pioneered in the fifties (Morton, Taylor and Turner; Priestley and Ball) leading to a global prediction of jet-plume transitions (buoyant jets). Length scale estimates, to determine the region of influence of specific dynamic phenomena based on dimensional analysis, also were developed in the late fifties (Scorer, Csanady), primarily for the atmospheric environment. Since the sixties, all of these techniques have been systematically applied to the water environment, and additional phenomena, singularly or in combination, have been studied experimentally: the effect of stratification, stratified crossflow, submerged multiport diffusers, surface buoyant jets, buoyant jets in shallow water layers, diffuser induced circulations, etc. Even though some additional work remains to be done, a solid experimental observational base has been established to guide the implementation of a comprehensive predictive scheme, e.g. in the form of an expert system.

CORMIX

Three subsystems have been developed: CORMIX1: submerged single port discharges; CORMIX2: submerged multiport diffusers; and CORMIX3: surface discharges. Each system is applicable to an ambient water body of constant depth, unsheared ambient velocity (including stagnant), and different types of ambient stratification (see Fig. 1, including uniform density). The discharge flow may be positively, neutrally, or negatively buoyant.

In each subsystem, the hydrodynamic flow *classification* is performed through a rigorous, systematic application of length scale analysis. That is, the multiple dynamic length scales (e.g. jet/plume transition scales), geometric length scales (e.g. water depth), and other geometric features (e.g. discharge angle) are compared with each other (i.e. forming non-dimensional groups). If this is done in a systematic fashion, different generic flow classes can be distinguished. As an example, Fig. 2 shows the different flow classes for a positively buoyant single port discharge into a uniform density water layer. In that case, flow classes range from submerged jets with weak surface interaction to vertically mixed discharges. In total, all three subsystems of CORMIX distinguish among some one hundred generic flow classes with distinct hydrodynamic features. Comparison with available experimental data allows validation of many of these flow classes and establishment of the numerical coefficients needed for the length scale analysis.

The detailed *hydrodynamic prediction* in CORMIX is carried out by a series of *flow modules* that are executed according to a *protocol* that pertains to each distinct flow class as determined by the classification scheme. The spatial extent of each flow module is governed by *transition* *rules*. Thus, each flow module applies to a specific hydrodynamic sub-process (e.g. a weakly deflected jet in crossflow, lateral buoyant spreading along the water surface in the far-field). CORMIX contains a total of about fifty modules for sub-processes; most of these models are simple perturbation solutions, describing the mixing due to a primary flow parameter with the perturbing influence of one or more parameters superimposed. A virtual source matching is used to provide a hydrodynamically conservative, smooth transition from one module to the next. Again, the existing experimental base is used to both choose appropriate coefficients for the predictive elements and to validate the entire system under a great variety of discharge/ambient situations. A few selected comparisons are given in Figs. 3, 4 and 5, for a variety of discharge/ambient conditions.

Research supported by U.S. Environmental Protection Agency, Environmental Research Laboratory, Athens, Georgia.

References

Doneker, R.L. and G.H. Jirka (1989), "CORMIX1: An Expert System for Mixing Zone Analysis of Conventional and Toxic Single Port Discharges," Tech. Rept., DeFrees Hydraulics Laboratory, Cornell University, Ithaca, NY. (Also published by U.S. Environmental Protection Agency, Tech. Rept. EPA/600-3-90/012, 1990.)

Akar, P.J. and G.H. Jirka (1990), "CORMIX2: An Expert System for Mixing Zone Analysis of Conventional and Toxic Submerged Multiport Diffuser Discharges," Tech. Rept., DeFrees Hydraulics Laboratory, Cornell University, Ithaca, NY.

Jones, G.R. and G.H. Jirka (1990), "CORMIX3: An Expert System for the Analysis and Prediction of Buoyant Surface Discharges into the Water Environment," Tech. Rept., DeFrees Hydraulics Laboratory, Cornell University, Ithaca, NY.

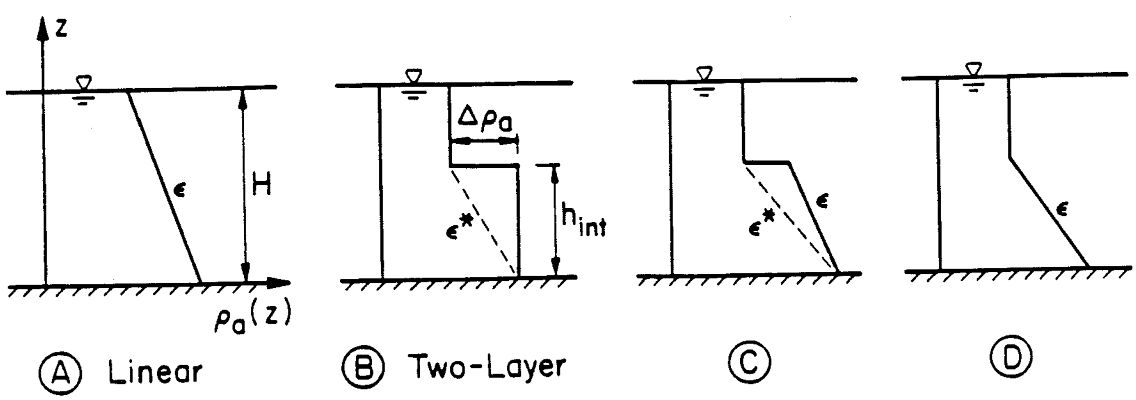

Fig. 1: Four Types of Stable Ambient Density Profiles Considered in CORMIX.

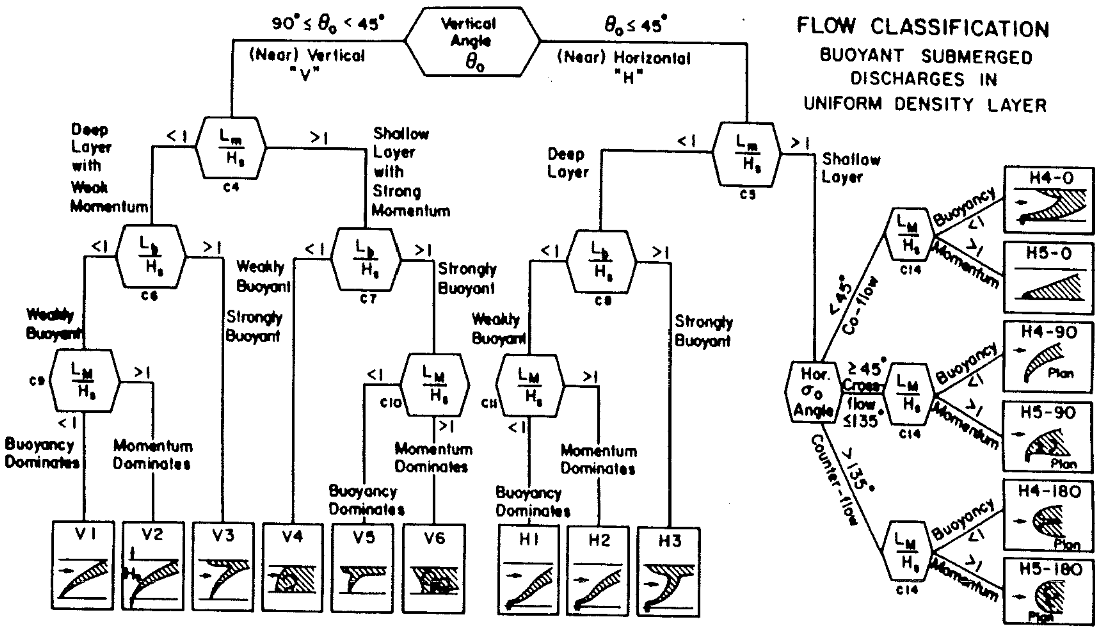

Fig. 2: Example of a Sub-Classification of CORMIX1: The Behavior of Positively Buoyant Submerged Discharges into a Uniform Density Ambient Water Layer.

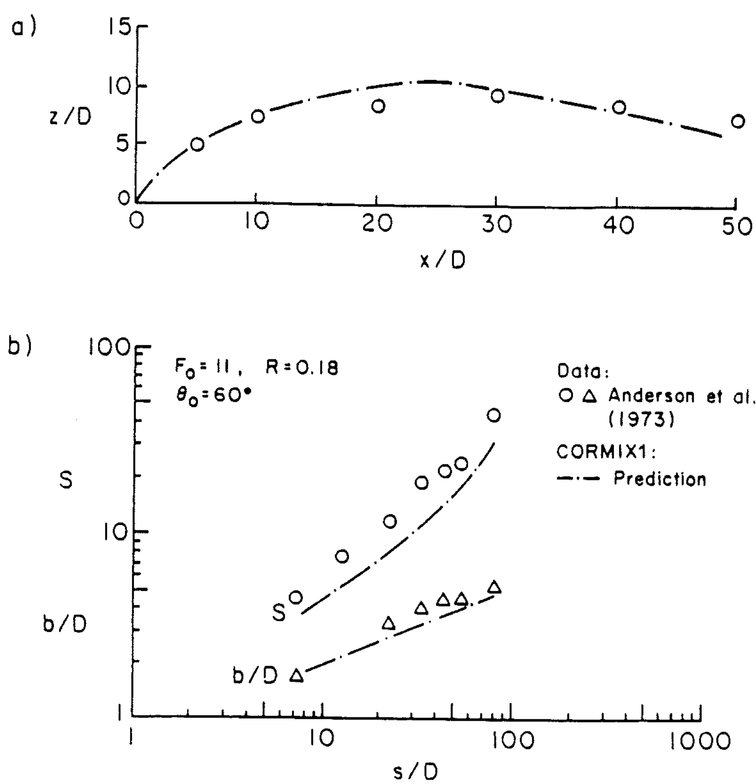

Fig. 3: Example of CORMIX1 Prediction: Trajectory, Width and Dilution of Negatively Buoyant Jet (Near-Field) Discharging Upward at 60° in Deep Flowing Receiving Water Without Boundary Interaction.

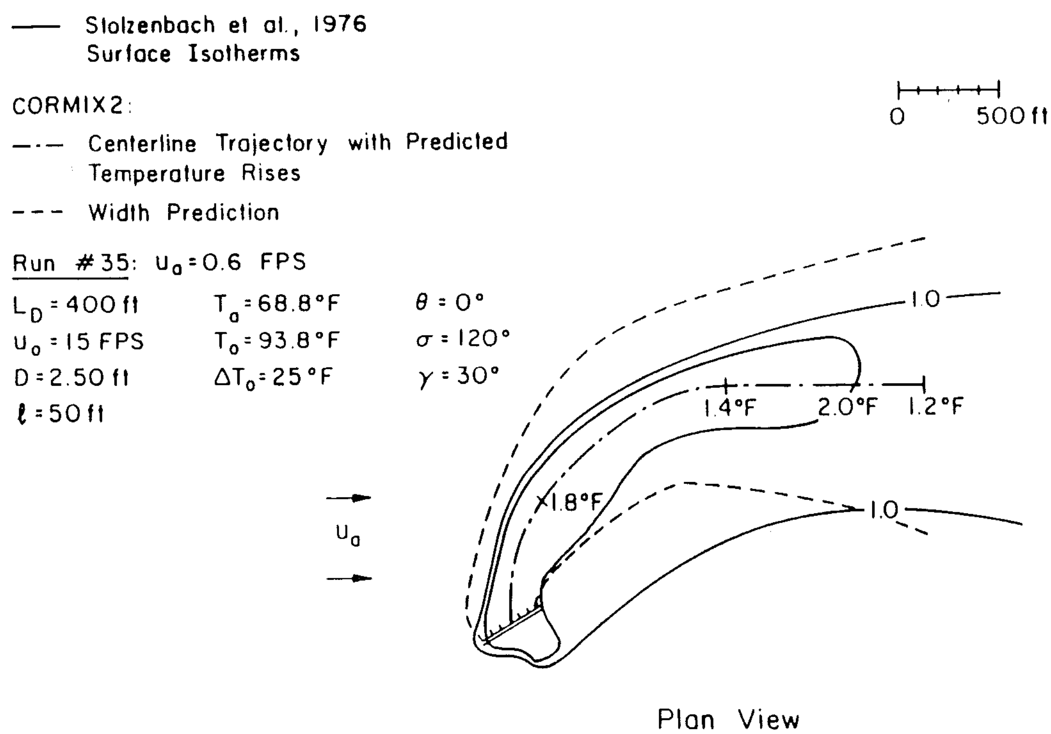

Fig. 4: Example of CORMIX2 Prediction: Trajectory, Width and Excess Temperatures for a Multiport Diffuser Plume (Vertically Mixed) in Shallow Receiving Water With a Crossflow.

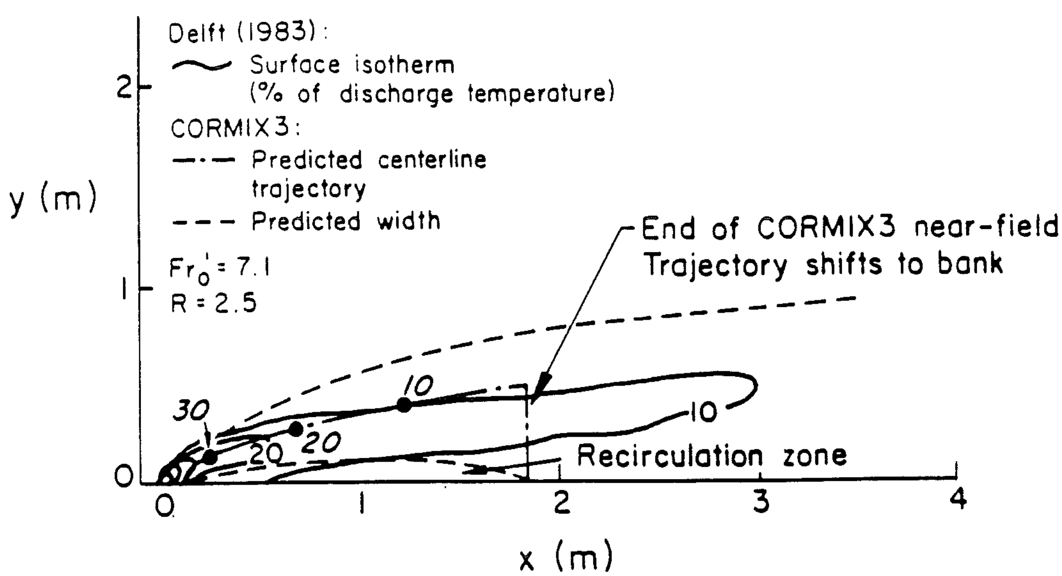

Fig. 5: Example of CORMIX3 Prediction: Trajectory, Width and Normalized ExcessTemperatures for a Buoyant Surface Jet Attaching to the Shoreline in a Strong Crossflow.

A Study of the Influence of Langmuir Cells on Low-Frequency Turbulence and Secondary Flows under Wind Waves

Stephen G. Monismith , Assoc. Member ASCE, Environmental Fluid Mechanics Laboratory, Dept of Civil Engineering, Stanford University, Stanford, CA. 94305-4020

1. Introduction

Two major themes of Garbis Keulegan's research, mixing in stratified flows and surface waves, were brought together in his pioneering laboratory study of wind mixing described in the 1960 NBS report, "Fourteenth progress report on model laws for density currents: mixing effects of wind-induced waves" (with Victor Brame). In this study, Keulegan sought to find out how wind-generated waves affected rates of mixed-layer deepening in a stratified fluid. While he was unable to directly establish the link between mixing rates and wind waves, his experiments clearly showed that upwelling is an important component of mixed layer processes in lakes. Recent theory and experiment indicate that this connection does exist and is potentially of enormous significance from the standpoints of mixed-layer physics and biology. This linkage does not appear to be one that directly involves turbulence; instead, the relationship between mixing and waves is one involving Langmuir cells, secondary flows that may develop through the interaction of the surface waves with the wind-drift current.

Langmuir cells (hereinafter LCs) are streamwise vortices that form in the surface layers of the oceans, estuaries, and lakes when the wind blows (Langmuir 1938). As evidenced by current measurements (Weller and Price 1988) and by observations of various tracers including air bubbles (Thorpe and Hall 1982), and heat (Weller and Price 1988), LCs consist of alternating zones of upwelling and downwelling in which significant quasi-steady vertical velocities are observed. Field observations show that LCs may possess a continuum of spanwise length-scales (Smith *et al.* 1987). The role of LCs in mixed-layer dynamics is thought by some to be important (Leibovich 1983), while others (Gargett 1989) argue that LCs can be thought of as particular eddies whose effects are already parametrized by existing models of mixed-layer physics. Experimental studies of simpler boundary-layer flows with organized streamwise vorticity (Peerhossaini and Wesfried1988) consistently reveal enhanced vertical mixing of momentum and heat.

While many explanations of how LCs are generated have been put forward, Faller was the first to establish (through physical experiment!) the importance of surface waves. The connection between Langmuir cells and waves has been given a strong theoretical foundation by Leibovich, Craik, their colleagues and students (see Leibovich 1983). The Craik-Leibovich (CL) theory shows that surface waves influence the mean velocity field through the interaction of their Stokes drift of the waves with the mean flow. While, the CL theory of Langmuir cell generation is supported by the series of laboratory experiments carried out by Faller and his students (Faller and Auer 1988), there are still many questions concerning whether or not waves generate LCs in the way predicted by the CL theory.

This report describes one set of measurements collected in our wind wave flume using our three-component LDA in combination with flow visualization. Our measurements show large strong, intermittent secondary flows which lead us to conclude the possibility that LCs may exist in our facility. Indeed, according to the CL theory, all the necessary ingredients for LCs, waves and current shear, are present. The purpose of presenting these measurements is that they show that streamwise vortices appear and, by inference, enhance mixing. However, the low-frequency unsteadiness we see in our velocity measurements, which we believe is a real feature of LCs, means that their effect on mixing can be hard to determine clearly both in the laboratory and in the field.

2. EXPERIMENTAL PROCEDURES

The measurements were made in the SWWWF which is 1.83 m deep, 915 mm wide and 35 m long. It is described in detail in Cheung and Street (1988). We worked with conditions for which Cheung and Street report two-dimensional LDA measurements. Using their data, we present a summary of various relevant parameters describing this flow in Table 1.

TABLE 1: EXPERIMENTAL CONDITIONS
Wind speed, U_a = 6.7 m s^{-1}
Water: boundary layer thickness, $\delta \approx 300$ mm / shear velocity, $u_* = 12$ mm s^{-1}
Average rms velocity fluctuations (low pass filtered)
x direction u = 18 mm s^{-1}
y direction v = 17 mm s^{-1}
z direction w = 12 mm s^{-1}
Surface drift velocity U_s = 137 mm s^{-1} (Eulerian)
= 189 mm s^{-1} (Lagrangian)
Turbulence time-scale, $T_\delta \sim \delta / u_* = 25$s
Rms wave height, $\eta' = 6$ mm, wave frequency, $f_d = 3.2$ hz

The three-component LDA used in this study consists of a two-component system that makes an angle of 105 degrees with respect to the channel axis and and a one-component system rotated 30 degrees from the two component one. The LDA is operated in side scatter mode. The analog outputs of the three frequency trackers were low-pass filtered at 0.5 Hz, sampled at 1 Hz for approximately 1000 s, and stored for later analysis, including projecting Tthe three measured velocities onto a Cartesian coordinate system aligned with the channel axis. We shall refer to U as the streamwise velocity (x direction); V as the spanwise velocity (y direction), and W as the vertical velocity (z direction). To visualize streamwise vortices, we illuminated a narrow slice of fluid oriented across the channel that spanned the entire width of the channel to a depth of about 500 mm. We injected fluorescent dye upstream of the slit in an horizontal sheet at a depth of approximately 200 mm. When the dye reached the slit and was illuminated, it fluoresced, with the intensity of fluorescence being approximately proportional to dye concentration. We placed our video camera downstream of the light slit so that an oblique view of fluorescing dye could be obtained. The processing technique is described in Monismith et al (1990); it suffices to provide crude maps of 16s averages of dye concentration.

3. RESULTS

Within the bounds of experimental error and the inherent long-term variability of the flow, spot measurements of the horizontal and vertical velocities on the channel centerline are comparable with those measured by Cheung and Street (1988). We made a detailed cross-channel profile of (U ,V,W) at 25 mm depth ($z/\delta \approx 0.08$); it covered, in increments of 20 mm, a region starting at the centerline and extending 300 mm towards the wall closest to the LDA. This set of profiles showed a trend towards larger mean streamwise velocities near the wall (by about 25%) than in the center of the channel. There also were clear trends in both the vertical and spanwise velocity components, indicating that the higher velocities seen near the wall were probably due to downwards advection of high momentum fluid from above. It is not clear that these profiles indicate the presence of Langmuir cells. Moreover, given that the apparent spanwise variations in the V and W are within the long-term temporal variability one might expect to find at a single-point in the channel, the spanwise variation in U may also not be attributable to a stationary pattern of secondary flows.

The variability of individual velocity records is more interesting than the means discussed above. Figure 1a and 1b present two such records, taken at y =100 and 180 mm respectively; these were subjected to a 100s moving average to smooth out high frequency fluctuations. In this plot, velocities are scaled by u_* and time by the natural mixing timescale $T_\delta = \delta/u_* \approx 25$ s. We use this scaling so that the natural variability of our flow might be related to flow variability in the ocean mixed layer, where T_δ might typically of the order of 10^4 s. We have also resolved the flow into its horizontal and vertical components (not shown) and have calculated the angle, θ_{xy}, made by the velocity vector with respect to the centerline of the channel . The low frequency variability shown in these two figures 6 and 7 typify time histories of flows measured in this experiment. These records show low-frequency flow variations for which θ_{xy} reaches quite large values, 40 and -55 degrees respectively, for periods of time than are 4 or 5 T_δ.

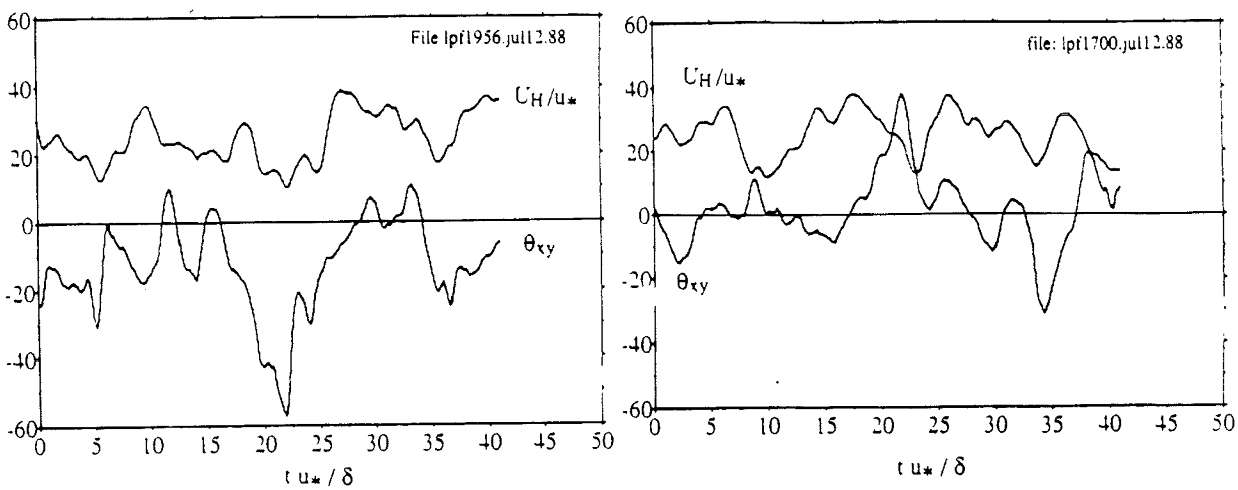

Figure 1: Low-pass filtered velocity U_h = the vector sum of U and V, divided by u_* (and multiplied by 10 to facilitate plotting) and θ_{xy}, the angle made by the velocity vector with respect to the channel axis, both measured at (a) a distance of 350 mm and (b) 270 mm from the channel wall .

To assess whether or not the low frequency variations shown above are typical of a turbulent boundary layer we computed an average spectrum from a set of 7 measured spectra and scaled the result using the outer flow scaling discussed by Perry et al. (1985):

$$\phi_{uu} \, (U/2\pi \, \delta \, u_*^2) = f\,(\kappa\delta),$$

where the wavenumber κ was related to frequency through the use of Taylor's hypothesis

$$\kappa = 2\pi f/U.$$

Since the frequencies of interest are much less than the wave frequency, this transformation is reasonably accurate (Lumley and Teray 1983). Our spectra, along with spectra measured by Perry et al. in a flat-plate turbulent boundary layer are given in figure 2. The error bars on the Perry et al. spectra represent the range of values measured for different values of z/δ. For $\kappa\delta > 6$, ϕ_{uu} and ϕ_{ww} are approximately equal and compare remarkably well with spectra reported by Perry et al.. This agrees with similar comparisons made by Jones (1985) of field and laboratory wind-drift layer spectra with flat-plate boundary-layer spectra. On the other hand, ϕ_{ww} rolls off at dimensionless wavenumbers < 2, indicating that low-frequency vertical motions are suppressed by the presence of the free surface, whereas ϕ_{uu} peaks at a somewhat smaller wavenumber, $\kappa\delta \approx 0.2$. In this low-frequency range, our values of ϕ_{uu} are as much as a 100% larger than those reported for a flat-plate boundary layer. This behavior is typical of flows with enhanced streamwise vorticity (Barlow and Johnston 1988). At small wavenumbers, there appears to be two-dimensional isotropy in that $\phi_{vv} \approx \phi_{uu}$. In fact, for all of the velocity records taken during this experiment u and v were roughly equal and were typically 50% larger than w.

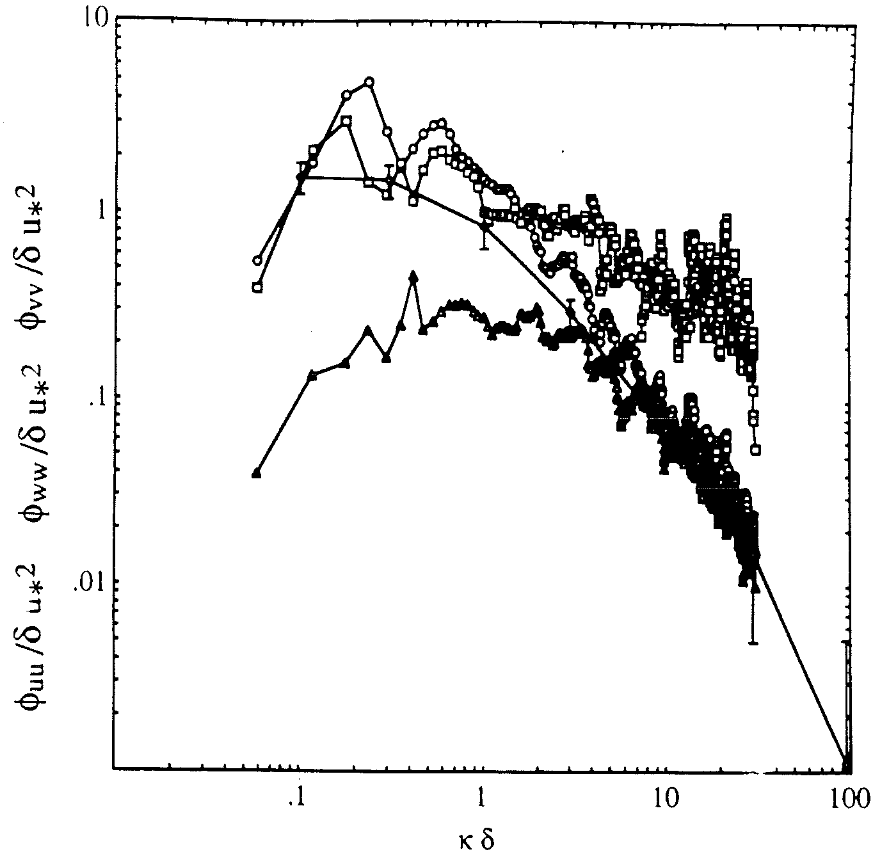

Figure 2: Averaged spectra of (o) u', (□) v', and (Δ) w'. For the sake of comparison these spectra have been scaled using the scaling described by Ligrani (1989) and compared to similar spectra measured by Perry et al. (1985) in a flat-plate boundary layer (±).

We obtained approximately 30 minutes of video of fluorescence images. These give some evidence that strong streamwise vortices do, at least intermittently, form and decay in the SWWWF. The clearest image we obtained showing evidence of Langmuir cells/ streamwise vortices is shown in figure 3. White corresponds to high dye concentration and black to little or no dye. The image shows the presence of three upwelling regions, one at the center and at one at each edge of the channel. Agreeing with the structure implied by a <v'w'> profile (not shown) derived from the cross-channel LDA section, we can infer that this image showed 2 pairs of Langmuir cells, or 4 streamwise vortices. However,this image was one of the best at showing streamwise vortices that we obtained. Other images (not given here) showed different patterns including a single weak roll with upwelling on the right side of the channel, larger numbers of smaller cells, or no cells . Thus, "organized" streamwise vortices appear to be only sporadically present in our flow.

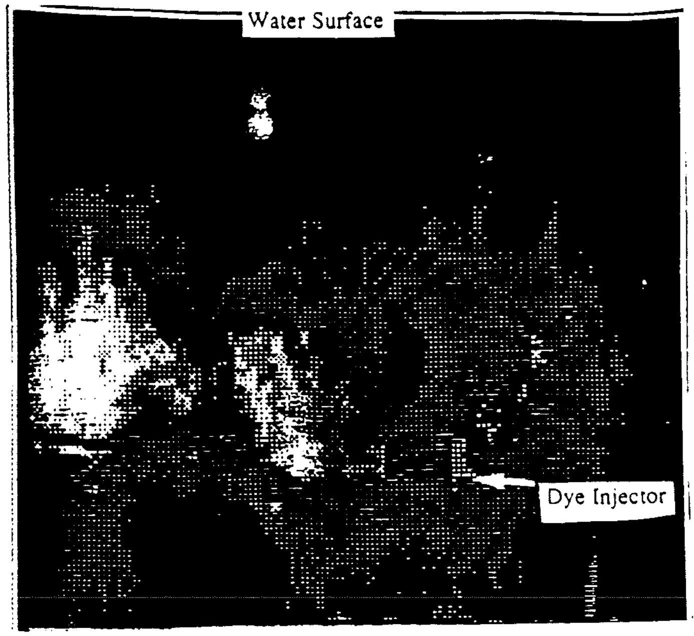

Figure 3: Grey-scale coded Intensity (dye concentration) field showing large-scale streamwise vortices.

5. Discussion and Conclusions

While it makes it difficult to positively identify and characterize Langmuir cells in our facility, the low-frequency unsteadiness we observe has been found to occur in virtually all boundary-layer flows in which streamwise vortices form naturally. For example, Ligrani and Niver (1988) show that Görtler vortices in a curved boundary layer can meander and undergo pairing. Prasad and Koseff (1989) also found evidence for meandering in a cavity flow where the streamwise vortex system slowly moved back and forth inside the cavity. Barlow and Johnston (1988) found that the locations of streamwise vortices changed throughout their experiments and were sensitive to details of the inlet conditions. In any event, this evidence from other centrifugally unstable flows suggests that we can hypothesize that if Langmuir cells exist, they should behave like other, similar sets of streamwise vortices, and thus, vary in time and space as the result of various possible instabilities. Is this variability observed in nature? As seen in several studies (Thorpe and Hall 1982, Smith *et al.* 1987), the answer appears to be yes. Most notably, Smith et al.'s power spectra of the spanwise shear in the ocean mixed layer exhibit clear variations throughout a two-day measurement period for which they give spectra. Based on our measurements we might suggest that the natural evolution time-scale is that of the largest eddies in the mixed layer, i.e., T_δ. Thus the variations with period $5T_\delta$ we observe, might correspond to 10 hour flow variations in the field.

On the basis of our LDA and flow visualization measurements, we conclude that unsteady (i.e., unstable) streamwise vortices are present in our flow. We can speculate that these unsteady vortices are the root cause of the observed low-frequency variability of the velocity field. The composite spectra we present suggest that while the main "energy bearing" eddies are similar to their counterparts in ordinary turbulent boundary layers, there is extra energy in our flow at low frequencies. In any event, whether or not the structures we observe in our flume are, in fact, Langmuir cells is not clear. We have argued that these measurements indicate that our facility does give streamwise vortices that behave similarly to those seen in other laboratory flows known to contain streamwise vortices and to those observed in the field which are thought to be Langmuir cells. Still, we can, at present, only hypothesize that the variability we observe in our facility is symptomatic of Langmuir cells. However, as seen in our flow visualization images, these extra low-frequency structures can clearly alter vertical scalar transport. Thus, possibly through the mechanism described by the CL theory, waves do appear to alter the transport properties of the surface mixed layer.

Acknowledgements

The author thanks Jeff Koseff, Jonathan Harris and Robert Street for their assistance with this work which was partially supported by ONR contract N00014-84-K-0242. SGM gratefully acknowledges support from NSF through grant CTS 8958314 and from the Charles Lee Powell Foundation.

REFERENCES

Barlow, R.S. and Johnston, J.P. (1988), "Structure of a turbulent boundary layer on a concave surface," *J. Fluid Mech., 191*, pp. 137-176.

Cheung and Street (1988), "The turbulent layer in the water at an air-water interface," *J. Fluid Mech., 194*, pp. 133-154.

Faller, A.J. and Auer, S.J. (1988), "The roles of Langmuir circulations in the dispersion of surface tracers," *J. Phys. Ocean., 18*, pp. 1108-1123.

Gargett, A. E. (1989), "Ocean turbulence," *Ann. Rev. Fluid Mech., 21*, pp. 419-452.

Jones, I. S. F. (1985), "Turbulence below wind waves," in: *The Ocean Surface*, ed. Y. Toba and H. Mitsuyasu, D. Reidel Publishing Co., pp. 437-442.

Langmuir, I., (1938), "Surface motion of water induced by wind," *Science, 87*, pp. 119-123.

Ligrani, P.M. and Niver, R.D. (1988), "Flow visualization of Dean vortices in a curved channel with a 40 to 1 aspect ratio," *Phys Fluids , 31*, pp. 3605-3617.

Leibovich, S. (1983), "The form and dynamics of Langmuir circulations," *Ann. Rev. Fluid Mech., 15*, pp. 391-427.

Lumley, J. L. and Teray, E. A., (1983), "Kinematics of turbulence convected by a random wave field," *J. Phys. Ocean., 13*, pp 2000-2007.

Monismith, S.G., Koseff, J.R., Thompson, J.K., O'Riordan, C.A., and Nepf, H.M. (1990), "A study of model bivalve siphon currents," Limnology and Oceanography. (in press).

Prasad, A.K. and Koseff, J.R. (1989), "Reynolds number and end-wall effects on a lid-driven cavity flow," *Phys Fluids A, 1*, pp. 208-218.

Perry, A.E. and others (1985), "A spectral analysis of smooth flat-plate boundary layers," *Proc. Fifth Symp. on Turbulent Shear Flows*, Ithaca, N.Y. Aug 7-9, 1985.

Peerhossaini, H. and Wesfried. J. (1988)" On the inner structure of Görtler rolls," *Int J. Heat and Fluid Flow, 9*, pp 12-18.

Smith, J., Pinkel, R. and Weller, R.A. (1987), "Velocity structure in the mixed layer during MILDEX," *J. Phys. Ocean., 17*, pp 425-439.

Thorpe, S.A. and Hall, A.J. (1982), "Observations of the thermal structure of Langmuir circulation," *J. Fluid Mech., 114*, pp. 237-250.

Weller, R. A., and Price, J.F. (1988), "Langmuir circulations within the oceanic mixed layer," *Deep Sea Res.*, 35, pp. 711-747.

Session 4A

Jets and Plumes

Laboratory Study of Dispersion of Buoyant Surface Plumes

by

Ole Petersen and Torben Larsen
Dept. of Civil Engineering
University of Aalborg
Sohngaardsholmsvej 57, DK-9000 Aalborg

Abstract

A laboratory study on surface dispersion of buoyant plumes in open channel turbulence is made, where the buoyancy is due to both salinity and heat. The measured parameters are the downstream derivative of a plume width and height, which are integral-characteristics of the distributions of density-differences. Other methods as infra-red sensing are used for visualizing purposes. The results are used to calibrate an integral model of the dispersion. Conclusions are that the dispersion of a bouyant surface plume can be treated as the superposition of a bouyancy induced stretching and turbulent diffusion, reduced in the vertical direction by the density gradient. The result implies a simplification of the description of near-field dilution.

1. Introduction

Dispersion and dilution of discharges of buoyant effluents is a problem of practical and theoretical interest, as for example in studies of sea outfalls for disposal of sewage. In the present work we use a laboratory model to study how the dispersion of buoyant surface plumes in channel shear flows depends on ambient turbulence and density difference.

The significance of buoyancy to dispersion of surface plumes was first pointed out by Larsen and Sørensen, 1968, who realized that the dilution was the result of a lateral stretching due to density differences and vertical diffusion by ambient turbulence, which is reduced by the presence of a stable density gradient. Their theoretical considerations were later confirmed from experiments on heated water plumes by Weill and Fischer, 1979. The reduction in vertical dispersion of a heated surface layer in open channel flow, where the turbulence is generated by shear near the bottom, has been studied by Schiller and Sayre, 1975.

Fig. 1. Thermal image of water surface plume. 1.1°C *between contours.* $U_o = 10\ cm/s$, *rough bed.* $\Delta T_o = 20°C$.

In the present experiments the plumes are formed by heated water discharged into a fresh or saline stream providing a wide range of density differences. The primary data are the downstream change of integral parameters as plume height or plume width, derived from measured distributions of density differences. These data enable us to obtain a consistent calibration of an integral model which combines the effects of turbulence and buoyancy.

The outline of the paper is as follows: First is a brief presentation of the theoretical background for plume dispersion, followed by a description of the laboratory model. Next is presented the results of the experiments which are used to calibrate the model and finally are given some conclusions on plume dispersion.

2. Theory

Buoyancy induced fronts

A lens of light water of weight $\rho + \Delta\rho$, confined to a volume of height h and width b, will rapidly be stretched into a thin layer, due to buoyancy induced pressure gradients.

Taking the pressure distribution as hydrostatic, the celerity of the front, V, can be found using Bernoulli's equation as

$$V = \sqrt{2g \cdot \frac{\Delta\rho}{\rho} \cdot h} \qquad (1)$$

The disturbance propagates in a direction perpendicular to the front. For a continuous discharge, which is conveyed downstream with velocity U_o, and assuming that $V << U_o$, geometrical considerations yields

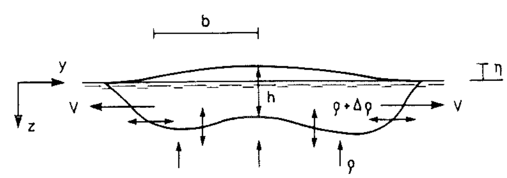

Fig. 2. Sketch of definitions.

$$\frac{db}{dx} = \frac{V}{U_o} \qquad (2)$$

and in the absence of mixing, conservation of mass requires that $h \cdot b = const$ thus

$$\frac{dh}{dx} = -\frac{h}{b}\frac{db}{dx} \qquad (3)$$

Turbulent diffusion

Taking for simplicity one dimensional diffusion, Fick's law postulates that the variance grows linear in time according to

$$\frac{db^2}{dt} = 2K \qquad (4)$$

where the plume width b, is defined as the standard deviation of the distribution of the diffusing substance and K is the Fickian diffusion coefficient. For the surface plume we obtain, inserting $dt = U_o \cdot dx$, and assuming a plane of symmetry at the water surface

$$\frac{db^2}{dx} = 2\frac{K_y}{U_o} \quad (5a) \qquad\qquad \frac{dh^2}{dx} = 2\frac{K_z}{U_o} \quad (5b)$$

Conservation of mass gives $h \cdot b \cdot \bar{c} = const.$

3. Experiments

Characterization of plumes

Assuming that a common set of local scales as a height, width and mean density difference applies to both diffusion and dispersion, is a simple consistent set of parameters derived from the moments of the distribution of density differences. The density difference is used because this is the parameter of dynamic significance. We define a plume width and height as

$$b^2 = \frac{\int_{\infty}^{\infty}\int_0^d \Delta\rho y^2\, dz\, dz}{\int_{\infty}^{\infty}\int_0^d \Delta\rho dz\, dy} \quad (6a) \qquad h^2 = \frac{\int_{\infty}^{\infty}\int_0^d \Delta\rho z^2 dz\, dy}{\int_{\infty}^{\infty}\int_0^d \Delta\rho dz\, dy} \quad (6b)$$

The excess mass per downstream distance, M, is the denominator in the two expressions. A mean density difference is defined assuming that the excess mass of the plume is contained in an area within two standard deviations from the centre of mass

$$\bar{\rho} = \frac{M}{2h4b} \quad (7)$$

As discussed in the next section, the instrumentation of the experiment is designed to allow a direct evaluation of these three parameters from a numerical integration of the measured density profiles.

Experimental facility

The experiments were made in a recirculating hydraulic flume, modified to use both saline and fresh water, as shown in Fig. 3. Salinity was introduced by adding common salt to the water. Artificial roughness of the bottom was supplied using triangular wooden list, 1 *cm* high placed with 5 *cm* spacing across the flume.

Fresh water was supplied by gravity from a 180 *l* insulated, constant head tank through a rotameter and a deaeration device. The water was discharged onto the surface through three circular nozzles ø70 mm, parallel to the main flow direction with the same velocity in the discharge and in the ambient water. In the experiments with fresh water in the flume, heated water was used to obtain the density difference, while cold water was used for the experiments with saline water; temperature here acting simply as a tracer.

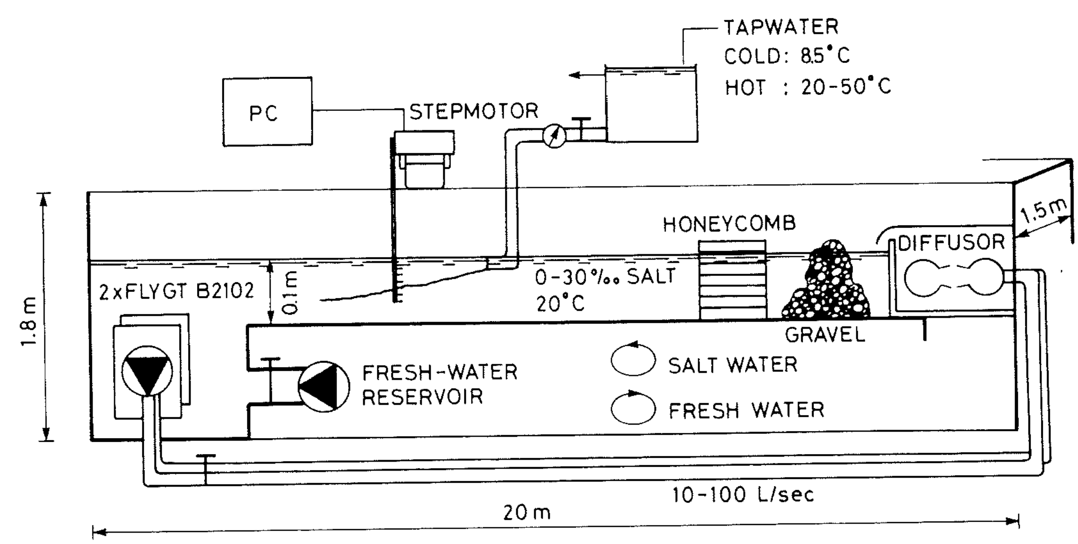

Fig. 3. Combined salt and fresh water flume.

Instrumentation

Temperature was measured using a column of Copper-Constantan, 0.5 *mm* thermocouples, connected to a PC with an A/D-converter. The transverse position of the thermocouples was also controlled from the PC by means of a step motor. Sensitivity of the temperature measurement was 0.01°C and 90% raise-time of the thermocouples was 0.04 *sec*.

As a tracer were used Rodamine-B. Concentration was measured using an Navitronic Q-200 in-situ fluorometer either directly or using a glass cuvette. Water was withdrawn to 250 *ml* samples using a column of 12 1 *mm* siphons. Salinity was measured by weighing a 25 *ml* pyknometer. An AGEMA Thermovision infra-red sensing system combined with digital image processing was used to measure surface temperatures in the plume. The instrumentation is described in details in Petersen et al., 1988.

Experimental procedure

In the experiment the plume is transversed by the column of thermocouples, measuring the mean density difference in 15-20 transverse positions, equally distributed across the plume. The instantaneous temperature is in each point converted to a density difference using an equation of state, relating density to temperature and salinity. From this a time average density difference is calculated. Dependency on temperature was found from a standard table, while dependency on salinity was calibrated by weighing. After the traverse the density profile is reduced to a plume width, height and a mean density difference. The mean and RMS temperature was also measured, allowing for calculation of the energy flux as a conserved quantity. The whole procedure is fully automated.

Experimental conditions

The range of conditions used was outlet excess temperature from $-12°$ to $35°C$, flow velocity $5-20$ cm/sec, Darcy bottom friction 0.006 to 0.017 for smooth and rough bed, water depth $10-25$ cm and density of ambient water $1000-1030$ kg/m^3.

4. Results

The undisturbed flow

Transverse dispersion was measured by recording the path of small wooden spheres. Positions were found using a videocamera and digital image analysis. Defining an effective dispersion coefficient by

$$K_y = \frac{U_o}{2}\frac{db^2}{dx} \tag{8}$$

K_y is found using (8) and measured transverse distributions. The results can be given as $K_y = a \cdot u_f \cdot d$ where $a = 0.12$. Fischer, 1979; Engelund, 1969.

The vertical dispersion coefficient, which is an integral property of the flow, is assumed to depend on the plume height. This is here described using a simple correlation of the form

$$K_{z_o} = \gamma\, u_f\, h \left(\frac{1}{\sqrt{3}} - \frac{h}{d}\right) \tag{9}$$

Using (9) and measured vertical distributions of tracer γ is found to 0.7.

5. Buoyant plumes

In Fig. 4 is shown shapes of average iso-density contours. Notice the distinct noses with relatively low mixing in the case with high buoyancy, Fig. 4a, a pattern characteristic of density fronts. Dye injections showed that the mixing in the central parts had character of vertical jets penetrating the plume causing a intermittent pattern of temperature fluctuations. With very high levels of buoyancy the plume is almost split into two parts. When turbulence is dominating the contours are more bellshaped, Fig. 4b. and the mixing irregular as it appears on the thermal image shown in Fig. 1.

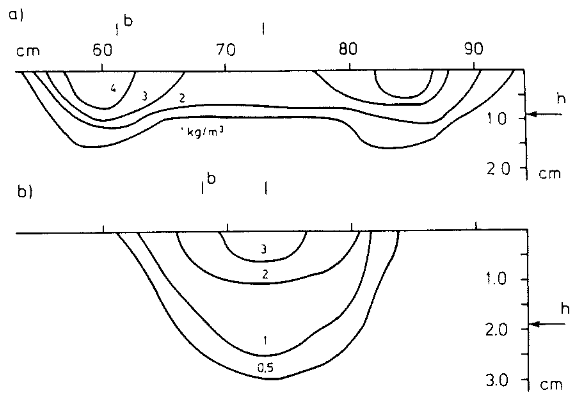

Fig. 4. Isodensity contours.
a) $U_o = 10$ cm/s rough bed
b) $U_o = 20$ cm/s rough bed

Plume dispersion

We assume that the total effect of buoyant and turbulent dispersion is linear in these two processes. Assuming changes in mean density difference to be linear, combining (2) and (5a) for the width and (3), (5b) for the height, yields

$$\frac{db}{dx} = \alpha \frac{V}{U_o} + \frac{K_y}{U_o b} \quad (10) \qquad \frac{dh}{dx} = -\alpha \frac{h}{b}\frac{V}{U_o} + \frac{K_z}{U_o h} \quad (11) \qquad h\, b\, \overline{\Delta\rho} = const. \quad (12)$$

where α has been introduced as an empirical factor.

It is not the aim here to resolve the complex mechanisms that results in the reduction of the vertical diffusion in the presences of vertical density gradients, so a simple form which relates the dispersion coefficient to a Richardson number is used. The reduction of the vertical dispersion coefficient is given as

$$\frac{K_z}{K_{z_o}} = \frac{1}{1 + \beta \mathbf{R}_{io}} \qquad \text{where} \qquad \mathbf{R}_{io} = \frac{g\, h\, \Delta\rho}{\rho u_f^2} \tag{13}$$

is a plume Richardson number, β is another empirical constant and K_{zo} is the dispersion coefficient, (9).

Calibration

The two empirical constants are estimated from the experimental results, employing an inverse technique. Using the measured values from one plume-section as initial conditions, the model is advanced forward and the outcome compared with measured values in the downstream section. Repeating this for all experiments one obtains a squared error sum as

$$E = \sum_{i=1}^{n} \overline{\Delta\rho} \left[\left(\frac{h_* - h}{h} \right)^2 + \left(\frac{b_* - b}{b} \right)^2 \right] \tag{14}$$

where index $_*$ refers to calculated values. This particular form expresses the deviation in dilution between experiment and model. The value of the two constants which minimizes this error is estimated to $\alpha = 1.2$ and $\beta = 3.5$.

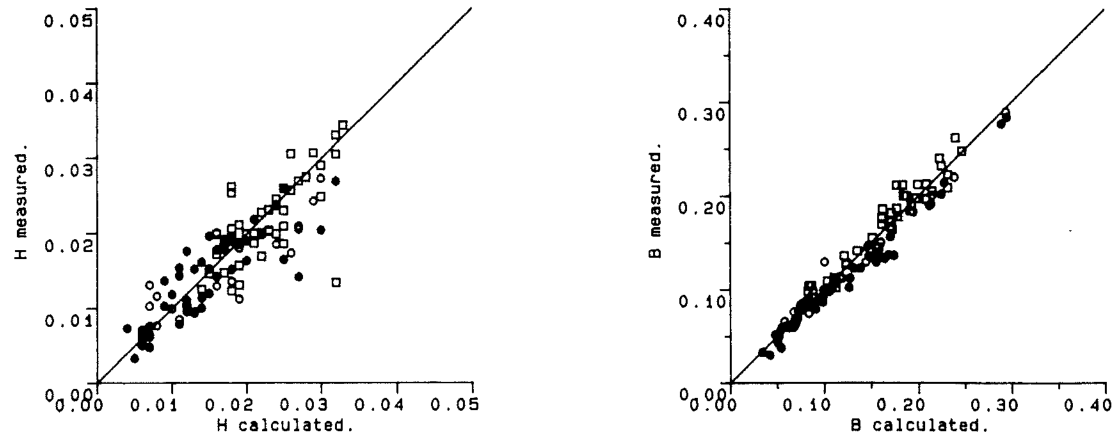

Fig. 5. Comparison between measured and predicted parameters
□ salt ○ fresh smooth bed ■● rough bed

Fig. 5 compares predicted and measured values of h and b, the full line being perfect agreement. Although there are some scatter in predictions of the height, there is good agreement between measured and estimated data.

6. Discussion and conclusions

Although direct comparison with other measurements are difficult due to differences in the choice of scales, there are at least a qualitative agreement on the value of α, Weill and Fischer, 1978. Benjamin, 1968. The reduction of turbulence in prescence of density gradients are well-established, Turner 1973, although quantitative predictions are still relatively uncertain.

The conclusions that emerges from this laboratory study are that the dispersion of a buoyant surface plume in channel shear flow can be treated as the superposition of a buoyancy induced stretching and reduced turbulent diffusion. The use of scales derived from moments of the density profile is valuable as a single set of measurable scales applies to both buoyant and turbulent dispersion.

Literature

Larsen, I. and Sørensen, T. 1968. *Buoyancy spread of waste water in coastal regions.* Proceedings of the Coastal Engineering Conf., p 1367, London.

Taylor, G.I. 1920. *Diffusion by continuous movements.* Proc. Roy. Soc. A, pp 196-212. London.

Weill, J. and Fischer, H.B. 1974. *Effect of stream Turbulence on Heated Water Plumes.* J. Hyd. Div. ASCE vol. 100 No. HY7, pp 951-970.

Schiller, E.J. and Sayre, W.W. 1975. *Vertical Temperature Profiles in Open Channel Flow.* J. Hyd. Div. ASCE vol 101, No. HY6, pp 749-761.

Fischer, H.B. et al. 1979. *Mixing in Inland and Coastal Waters.* Academic Press.

Benjamin, T.B. 1968. *Gravity currents and related phenomenae.* J. Fluid. Mech. vol 31, part 2, pp 209-248.

Petersen, Ole and Larsen, Torben 1988. *Infrared Sensing of Buoyant Surface Plumes.* Proc. of. Third Int. Symp. on Refined Flow Modelling and Turbulence Measurements, pp 701-707. IAHR. Tokyo.

Engelund, F.A. 1969. *Dispersion of floating particles in uniform channel flow.* J. Hyd. Div. ASCE vol. 95 No. HY4.

Turner, J.S. 1973. *Buoyancy effects in fluids* Cambridge University Press.

DILUTION HYDRAULIC MODEL STUDY FOR THE BOSTON WASTEWATER OUTFALL

by

Philip J. W. Roberts
School of Civil Engineering
Georgia Institute of Technology
Atlanta, GA 30332, USA

ABSTRACT

An extensive hydraulic model study was conducted to determine the dilution characteristics of various riser configurations for a tunneled outfall. It was found that the number of risers could be reduced significantly from that originally proposed, with a considerable cost savings. Various other hydrodynamic mixing phenomena were also investigated.

INTRODUCTION

As part of the Boston Harbor clean-up process, a new offshore outfall of unprecedented size is being designed to discharge the treated wastewater. The outfall will involve a deep rock tunnel approximately 9 miles (14 km) long with a diameter on the order of 24 feet (7.3 m). The tunnel terminates in a diffuser which consists of many risers extending to the sea floor capped with multiport outlets. The wastewater may contain stormwater runoff up to a peak design flow of 1270 mgd (56 m^3/s). The preliminary diffuser design had 80 risers spaced 83.5 ft (25 m) apart for a total diffuser length of 6600 feet (2012 m). Because of the high cost of the risers (on the order of $3 million each), a considerable cost savings would be achieved if the number of risers could be reduced without impairing the dilution capability of the diffuser.

Although multiport risers have been used on several outfalls throughout the world there are no reliable design guidelines. The plumes from each riser may merge to form a rising ring, behavior which the present generation of mathematical models cannot reliably predict. Because of these considerations, a hydraulic model study of a section of the diffuser was performed in a density-stratified towing tank. The objectives of the model study were to determine the minimum number of risers consistent with the dilution requirements and to establish the characteristics of the wastefield formed for typical oceanic conditions.

EXPERIMENTS

The hydraulic model is based on similarity of the jet densimetric Froude number and is undistorted. The jet densimetric Froude number is defined as:

$$F_j = \frac{u_j}{\left[g \frac{\Delta \rho}{\rho} d\right]^{1/2}} \qquad (1)$$

where u_j is the jet velocity, g the acceleration due to gravity, $\Delta\rho$ the density difference between the effluent and receiving water, ρ the effluent density, and d the nozzle diameter. As the acceleration due to gravity is the same in model and prototype, equality of the jet Froude number results in:

$$u_{jr} = \left[\left(\frac{\Delta\rho}{\rho}\right)_r d_r\right]^{1/2} \tag{2}$$

where the subscript r refers to the ratio of prototype to model. All linear dimension ratios are equal to d_r and the current speed ratio u_r is equal to u_{jr}, where u is the ambient current speed. Density differences over the water column are scaled in proportion to $(\Delta\rho/\rho)_r$. Thus, choice of the length scale ratio, d_r, and the density difference ratio $(\Delta\rho/\rho)_r$ automatically specifies all other ratios.

The tests were conducted in a density stratified towing tank of the U.S. Environmental Protection Agency Fluid Modeling Facility in Research Triangle Park, North Carolina. The towing tank is 4 feet deep, 8 feet wide and 83 feet long and can be filled with saltwater to an arbitrary stable stratification. An effluent more dense than the receiving water was discharged from the model diffuser near to the water surface and falls downward; the current was simulated by towing the diffuser at a constant speed. Blue dye is added to the effluent for dilution measurements and flow visualization. Dilution was measured by drawing water samples by vacuum through a sampling array towed behind the diffuser. The sampling array was in the shape of a 10 x 10 rectangular matrix for a total of 100 sampling probes.

In order to maintain a reasonable jet Reynolds number, only a portion of the diffuser was modeled. The number of risers modeled in the tank ranged from 2 to 7. Three different model scales were used, they were 52:1, 61:1, and 87:1 and the density differences in the models were increased compared to the prototype to augment the jet Reynolds numbers. The density difference ratios $(\Delta\rho/\rho)_r$ were 1/2, 1/3, and 1/4. The total port area was maintained constant and the total diffuser length was maintained constant at a nominal value of 6600 ft. The diffusers were tested for a variety of environmental conditions which were chosen based on oceanographic observations. Three density stratification profiles were modeled, as shown in Figure 1. These profiles are a late summer profile, an early summer profile, and unstratified, which could occur during winter. Currents of various speeds flowing perpendicular and parallel to the diffuser were tested. Almost 100 experiments were run; for a complete summary see Roberts (1989).

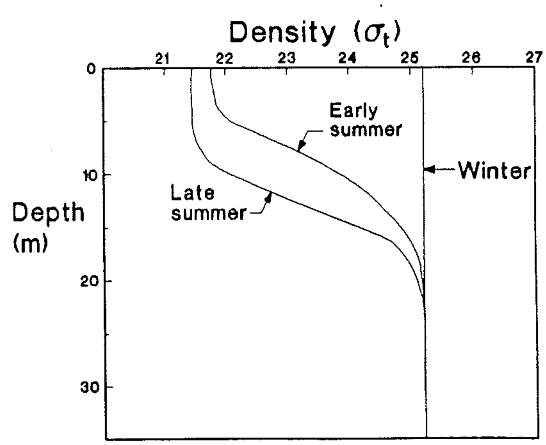

Figure 1. Density Profiles Modeled.

RESULTS: PHASE I TESTS

The primary objective of the Phase I tests was to determine the number of risers for the final design. A photograph of a typical experiment in a stagnant current is shown in Figure 2.

Figure 2. Photograph of Flow with 80 Risers, 620 mgd.

A typical density profile and the depth variation of concentration for each rake of probes are shown in Figure 3. The general characteristics of the flows are that the

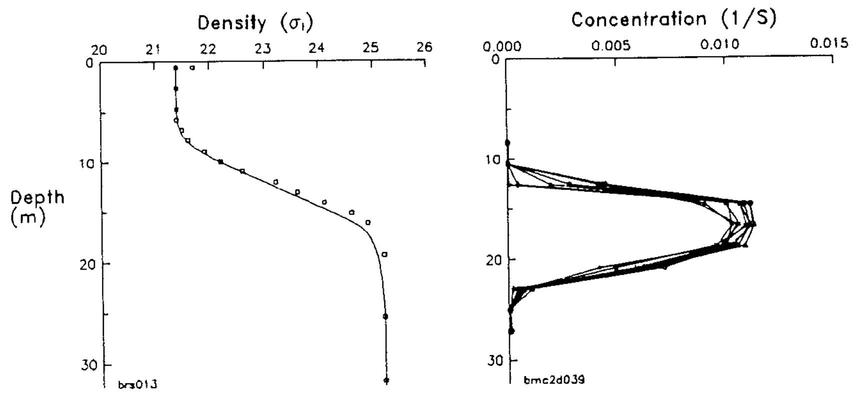

Figure 3. Density and Concentration Profiles of Typical Experiment.

plumes rise, reach a terminal rise height, collapse, and spread horizontally and mix to form a thick layer. As can be seen in the three-dimensional representation of the concentration profiles in Figure 4, this mixing causes the wastefield to be laterally quite uniform even when the risers are very widely spaced. At low flowrates and with wide riser spacings (see for example Figure 2) there is no plume merging prior to the plumes entering the horizontally spreading layer. At higher flows and narrower spacings, however, the plumes from the adjacent risers may directly impinge on each other.

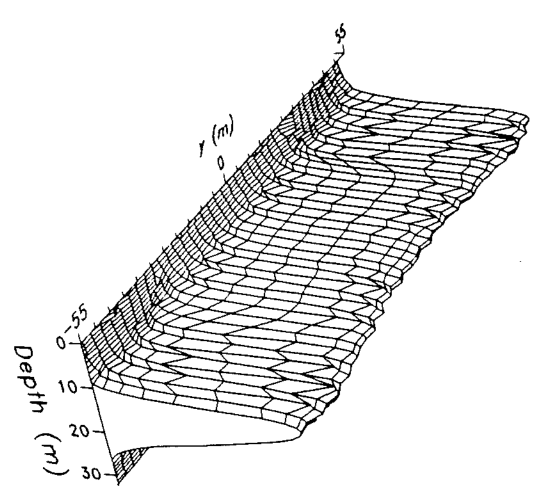

Figure 4. Concentration Profile.

The minimum dilution was calculated for each experiment. The effect of varying the number of risers is shown in Figure 5. Dilution generally increases as the number of risers, and hence ports, increases. As the flow rate decreases, the dilution increases. As the risers become very widely spaced, the discharges behave like individual plumes. The dilution for a fixed rise height then decreases in proportion to $Q_j^{2/3}$, where Q_j is the flow per nozzle. For a fixed number of ports per riser, the dilution would then increase with the number of risers, n_r, in proportion to $n_r^{2/3}$. As n_r increases further the plumes ultimately merge to a line source and the dilution approaches a limiting value independent of the number of risers.

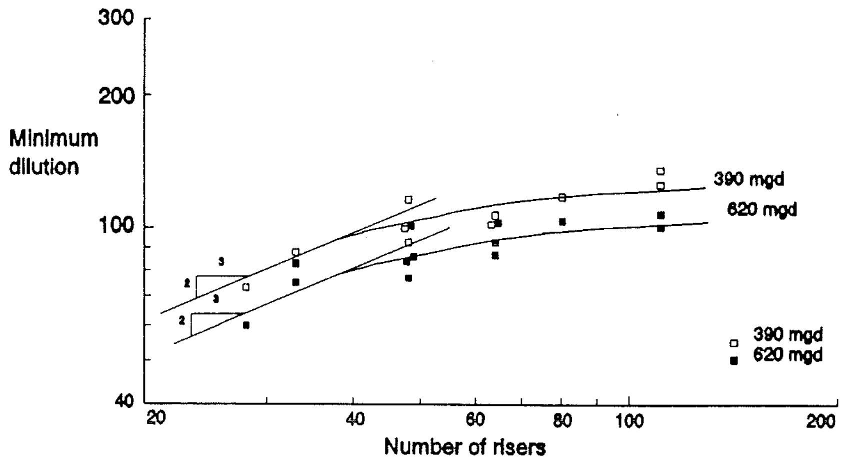

Figure 5. Effect of Number of Risers on Minimum Dilution, Stagnant Current.

Although there is too much scatter and also insufficient data to confirm this analysis the results do seem to follow these trends. Below about 50 risers the dilution drops off rapidly as the number of risers is decreased, whereas if the number of risers is increased above about 50 the gradual transition to a line plume causes the dilution to climb only slowly. Based on these results, a final diffuser configuration consisting of 55 risers was chosen. The spacing between the risers is 122 feet for a total diffuser length of 6,588 feet.

PHASE II TESTS: These tests were run for this riser configuration. The objectives were to choose the number of ports per riser, to investigate the nature of the established wastefield in stagnant currents, and to test a range of oceanic conditions to allow an environmental assessment of the final design configuration.

Dilutions with 8 and 12 ports per riser were compared. It was found that 8 ports gave higher dilutions than 12, but the difference between them decreases as the flowrate increases. In order to understand this unexpected result the experiments were repeated, videotaped, and photographed. It was found that with 12 ports the plumes form a ring around the riser preventing entrained water from getting to the core of the flow. The plumes then contract in and collapse, forming a single rising column. With 8 ports there is sufficient space between the individual plumes to allow the entrance of ambient water into the core and prevent this collapse.

Whether or not the flow collapses to a single rising column depends on the number of ports, the momentum flux, and the rise height.

Experiments were also done to investigate the stability and temporal variation of the flowfield in a stagnant current. The diffuser was placed in the center of the tank and the experiment continued until the spreading layer reached the tank ends. The long tank length allowed considerably longer times to be investigated than have been previously studied. It was found that the established wastefield changed only very slowly. A slight thickening of the layer with time was evident. After the front arrives at the sampling location the dilution decreases very slowly with time and the flowfield was always stable. The longest prototype time studied was greater than two hours, and it is unlikely that the ocean would actually be stationary for this long.

Another issue of great importance is the definition of initial dilution. The U.S. EPA defines dilution as a flux-averaged value, S_{fa}. S_{fa} cannot usually be computed, however, as details of the depth variation of velocity are not commonly available. Experiments were done to measure the flux-average dilution directly. This was done by photographing and videotaping the deformation of dye streaks dropped into the tank. A strong horizontal flow in the established wastefield was found with the velocity decreasing away from the centerline; an entrained counterflow moved towards the diffuser near the bottom. The results implied that the flux-average dilution may only be 10-20% higher than the minimum; that is, the ratio of flux-average to minimum dilution is probably in the range 1.1 to 1.2.

SUMMARY OF WASTEFIELD BEHAVIOR

Based on these results a final design configuration consisting of 55 risers, each with 8 ports was chosen. Tests were then run with the final diffuser configuration for a variety of oceanographic conditions to bracket the expected results. A selected summary of the results is given in Table 1. Based on the experiments discussed above, the flux-average dilution was calculated by assuming that $S_{fa} = 1.15 \times S_m$. The wastefield characteristics depend on flowrate, stratification, current speed and direction. Dilutions range from 64 with a flowrate of 1270 mgd, late summer stratification, zero current to 645 at 390 mgd, no stratification, and a 25 cm/s current flowing perpendicular to the diffuser. With the early and late summer density profiles, the wastefield was always submerged. Wastefield thicknesses ranged from 7.5 to 22.5 m.

Comparisons are also shown of results predicted by the mathematical model ULINE. ULINE is an EPA model which assumes the discharge to be a line source of buoyancy flux only, i.e. a line plume. The predicted dilutions are within 30% of the measured values, but are usually much closer. The predicted dilutions are generally conservative, especially at the higher flowrates. The reason for this is that ULINE neglects the effect of momentum flux, which can be quite important at the higher flowrates. The predicted rise heights always underestimate the measured values. A problem with comparing predicted and measured dilutions is uncertainty of the ratio of flux-average to minimum dilution. ULINE assumes that $S_{fa}/S_m = \sqrt{2}$, which is the ratio for a line plume in an unstratified environment, compared to the value of 1.1 to 1.2 measured here. If minimum dilutions are predicted from ULINE by dividing the average by $\sqrt{2}$, they would considerably underestimate the measured values.

Table 1. Summary of Wastefield Characteristics and ULINE Predictions.

Ambient current		Density stratification	Flowrate, mgd	Average dilution, S_{fa}		Rise height, m	
Speed, cm/s	Direction			Measured	Predicted	Measured	Predicted
0	-	Late summer	390	93	84	16.3	14.3
12	Parallel	Late summer	390	95	96	17.3	14.1
25	Perp.	Late summer	390	256	277	16.3	11.3
25	Parallel	Late summer	390	125	116	19.3	13.8
0	-	Late summer	620	81	63	17.8	14.6
0	-	Late summer	1270	64	42	17.8	15.5
25	Parallel	Late summer	1270	72	51	21.3	15.0
0	-	Early summer	390	129	91	20.3	15.5
12	Parallel	Early summer	390	121	102	20.3	15.0
25	Parallel	Early summer	390	153	121	20.3	14.4
0	-	Unstratified	390	207	185	31.3	31.3
12	Perp.	Unstratified	390	313	372	31.3	31.3
12	Parallel	Unstratified	390	242	212	31.3	31.3
25	Perp.	Unstratified	390	645	763	31.3	31.3
25	Parallel	Unstratified	390	253	263	31.3	31.3
0	-	Unstratified	1270	130	84	31.3	31.3
25	Parallel	Unstratified	1270	128	107	31.3	31.3

CONCLUSIONS

The model study demonstrated that dilution is insensitive to the number of risers over a quite wide range. Although ULINE is a useful and conservative model for predicting average dilution, it cannot predict the required number of risers as it assumes the discharge to be a line source. Other phenomena which could not be predicted by the present generation of mathematical models is the collapse of the rising ring of plumes to a single column, with the accompanying reduction in dilution, the thickness of the wastefield, and the relationship between average and minimum dilution. As a result of this model study, the number of risers was reduced from 80 to 55, with a cost savings of about $75 million.

ACKNOWLEDGEMENTS

This study was performed for the Massachusetts Water Resources Authority. It was sponsored by Metcalf & Eddy and I appreciate the support and expert help provided by Dr. Dominique Brocard and also the advice of Dr. Norman Brooks of the California Institute of Technology. The author is very appreciative of the assistance provided by the staff at the Fluid Modeling Facility. I would particularly like to thank the Director, Dr. William Snyder, and Len Marsh, Paul Bookman, Bob Lawson, Mike Shipman, Mike Stroud, and Brad Manning.

REFERENCE

Roberts, P. J. W. (1989). "Dilution Hydraulic Model Study of the Boston Wastewater Outfall," Report Number SCEGIT 89-101, School of Civil Engineering, Georgia Institute of Technology.

MIXING OF BUOYANT PLUMES IN A TIDAL CURRENT

by

Joseph H.W.Lee and Valiant Cheung
Department of Civil & Structural Engineering
University of Hong Kong, HONG KONG

Abstract

The mixing of a buoyancy-dominated vertical heated jet in a crossflow has been studied in laboratory experiments. Point concentration measurements and flow visualization show that the jet width, length of jet trajectory, and dilution increase substantially even in a weak current, with dimensionless depths (y/l_b) well below unity. The still water dilution is applicable only for y/l_b less than about 0.1. The experimental results are interpreted against field data of initial dilution at the Hastings outfall.

Introduction

The turbulent mixing of a submerged round buoyant jet in a current (Fig.1) is of special interest in the design of sea outfalls in many shallow coastal waters. Outfall design is often based on the calculation of a stillwater dilution [2,3]. Since in coastal waters a tidal current is present for the greater part of the time, attention has been directed in recent years towards developing more reliable predictions of initial dilution in moving water [1]. In particular, it has been demonstrated [5] that field dilution data of a buoyant sewage plume in an unstratified tidal current can be interpreted by a length scale analysis. The degree of mixing achieved at a given elevation, y, above the buoyant discharge is chiefly governed by $y/l_b = y\,u_a^3/B$, where l_b is a buoyancy length scale, u_a= ambient current, and B = discharge specific buoyancy flux. Simple equations for the prediction of minimum dilution in an ambient current were derived for both the buoyancy-dominated near field (bdnf) and buoyancy-dominated far field (bdff).

In a very weak current, $y/l_b \ll 1$, mixing behaviour is similar to a plume in stagnant water. However, the dilution constant derived from field data in the plume-dominated regime is often two to three times greater than the stillwater value [1,5,8]. Although an explanation for this apparent paradox has been offered [6], this point is best resolved by comprehensive experiments. Results of an experimental study of a vertical heated jet discharged at a low densimetric Froude number (F < 4) into a crossflow are reported herein. Special emphasis is placed on the near-far field transition. Characteristic dilution measurements are compared with field data of initial dilution at the Hastings outfall. Other important flow features are also summarized.

Experiments

A series of 48 experiments were performed with a buoyancy-dominated jet (F = 2-4) in a steady crossflow (u_a= 0.2-7 cm/s) in a 10m x 0.45m by

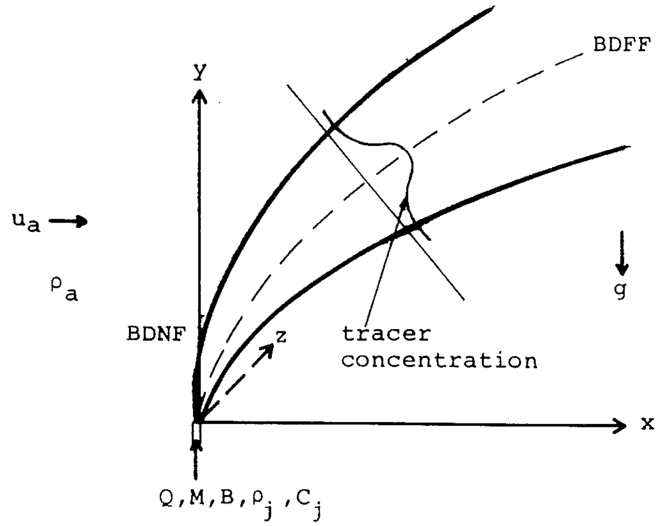

Fig. 1 A vertical round buoyancy-dominated jet in a crossflow

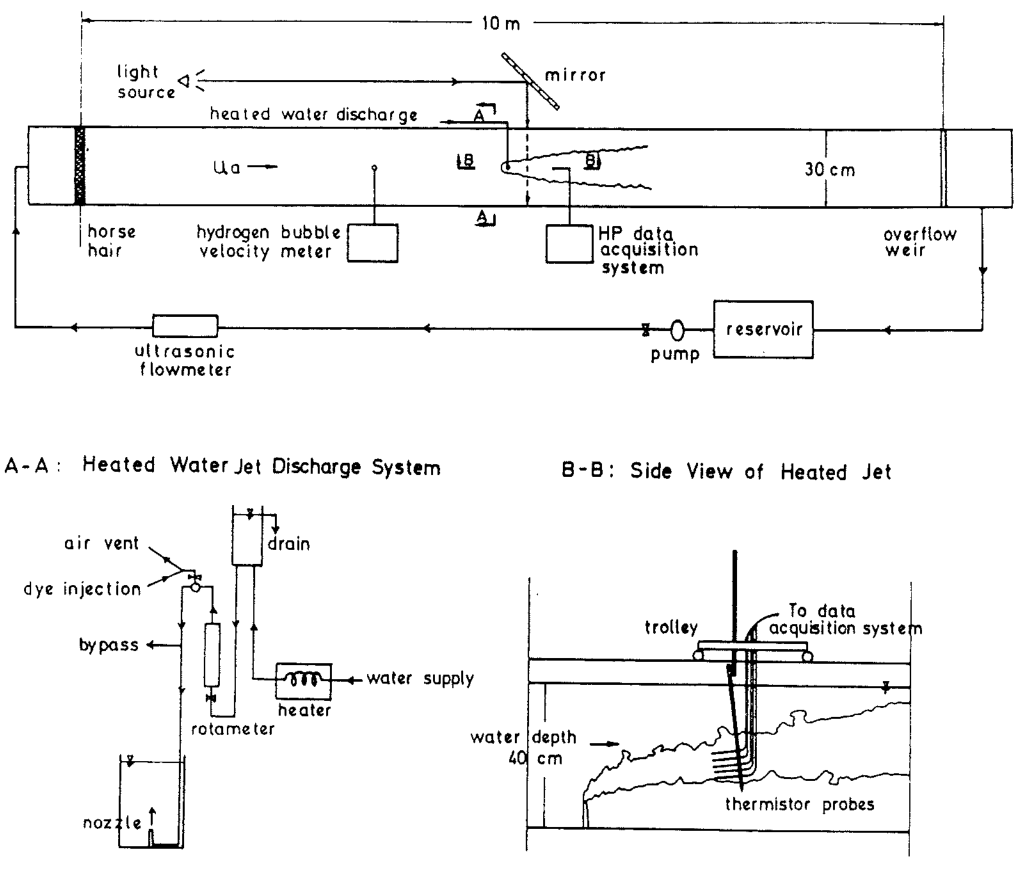

Fig. 2 Schematic Diagram of Experimental Setup

0.3m wide flume. The variation of characteristic dilution with y/l_b was studied over a wide range of y/l_b. The experimental set up is shown schematically in Fig.2. A tapered jet nozzle (D=0.75 cm) was located at the centre of the flume, with a clearance of about 10D from the bottom. The jet discharges at a temperature excess of 30-40^o C above the ambient. At various depths, the maximum temperature in the centre plane of symmetry was measured with a system of Fenwall fast response thermistor probes (time constant 0.5 sec). Based on a study of concentration contours generated by numerical models, the measurement resolution was kept within 2-5 jet diameters. In addition, transverse temperature transects and complete cross-section measurements were made in selected experiments. At each point the time-mean concentration represents a three-minute average of readings sampled at 3 second intervals. The positioning of the probes was greatly facilitated by a shadowgraph of the heated jet illuminated by a strong light beam. Ambient velocities were either directly measured (by miniature propeller or hydrogen bubble velocity meter), or taken as the cross-section average velocity.

Results and Discussion

By dimensional reasoning, the characteristic dilution S_m(defined as the ratio of discharge temperature excess to that at given elevation) in the bdnf, y/l_b<< 1, and the bdff, y/l_b>> 1, is given respectively by :

$$\text{bdnf:} \qquad \frac{S_m Q}{B^{1/3}\, y^{5/3}} = C_1 \qquad \text{or} \qquad \frac{S_m Q}{u_a l_b^{\,2}} = C_1\left(\frac{y}{l_b}\right)^{5/3} \tag{1}$$

and

$$\text{bdff:} \qquad \frac{S_m Q}{B^{1/3}\, y^{5/3}} = C_2\left(\frac{y}{l_b}\right)^{1/3} \qquad \text{or} \qquad \frac{S_m Q}{u_a l_b^{\,2}} = C_2\left(\frac{y}{l_b}\right)^{2} \tag{2}$$

where Q = discharge volume flux. Fig.3 shows the dimensionless dilution constant C_1 plotted against y/l_b. It can be seen that for y/l_b << 1, less than about 0.01, C_1 approaches an asymptotic value of 0.1, which is somewhat greater than the value of 0.091 reported by Rouse [7]. If the nonlinear density-temperature effect is accounted for (i.e. buoyancy flux not exactly conserved), it can be shown that our value is consistent with that obtained by George [4] , 0.11. The dilution diverges from the still water value at $y/l_b \cong 0.1$, and thereafter increases much more rapidly to greater than 0.3 for $y/l_b \cong 1.0$. The data taken within a distance affected by the initial jet momentum characterized by $y/l_M < 4$, where $l_M = M^{3/4}/B^{1/2}$, appears to contribute some scatter to the dilution data in the bdnf. Additional insight into the jet mixing characteristics is provided by the normal and transverse temperature profiles, which can be fitted by Gaussian distributions, with half-widths $b=b_N=\varepsilon_N y$ (and $b=b_T=\varepsilon_T y$) respectively. Our results (not shown) can be summarized as follows : i) In the bdnf, $y/l_b \lesssim 0.01$, the normal and transverse concentration variations are similar, with the

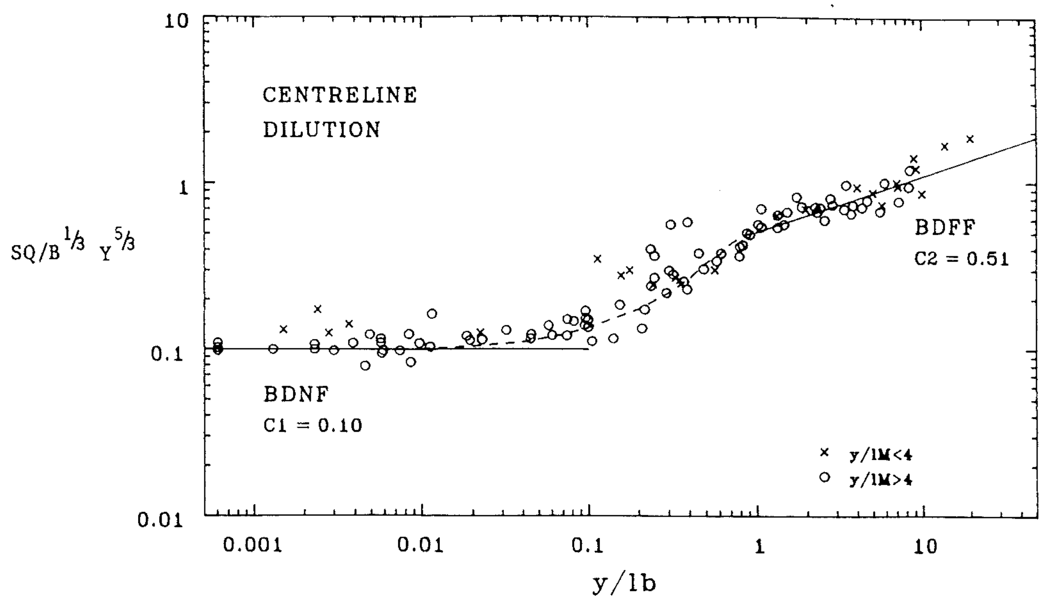

Fig. 3 Dimensionless centreline minimum dilution of a buoyancy-dominated jet in a crossflow as a function of dimensionless depth y/l_b

measured plume width $(\varepsilon_N, \varepsilon_T)$ = (0,12,0.13) , similar to a pure plume [3]. ii) As y/l_b increases to about 0.06, although the normal width is unchanged, the transverse plume spread is substantially greater (ε_T=0.16). In general, the transvere plume spread is significantly affected even in a weak current. iii) Within the bdnf-bdff transition, $y/l_b \cong$ 0.1 - 0.25, both the normal and transverse widths increase respectively to about ε = 0.2. iv) in the bdff, as y/l_b further increases, both normal and transverse profiles are substantially flatter, and half-widths increase to about 0.4-0.5y, indicating almost complete mixing over the height of rise. The sharp increase in measured dilution in the bdnf is primarily related to the increase in jet width, regardless of whether jet bifurcation occurs. In the jet cross-section, a double temperature maxima was not always observed in our measurements on a 1 cm grid. The dilution data in the far field gives an average value of C_2= 0.51.

The laboratory and field dilution data are plotted side by side in Fig.4, in a form that convincingly demonstrates the validity of Eq.1 & 2. The near field data at the Hastings outfall, characterized by 0.1 < y/l_b < 1 , lies in the bdnf-bdff transition as suggested by the laboratory experiments. Despite the greater scatter, the field data is seen to be comparable to the experimental data. In the far field, numerical model calculations show that the plume reaches the free surface when the jet centreline is at around y =0.75 H, where H = water depth above discharge. To account for the surface layer, the surface dilution should hence be calculated at this elevation. If H is used in the correlation of surface dilution data, our laboratory results would translate to a C_2 of 0.51 x $(0.75)^2$= 0.29. This compares with a bdff dilution constant of 0.32 obtained from the field data.

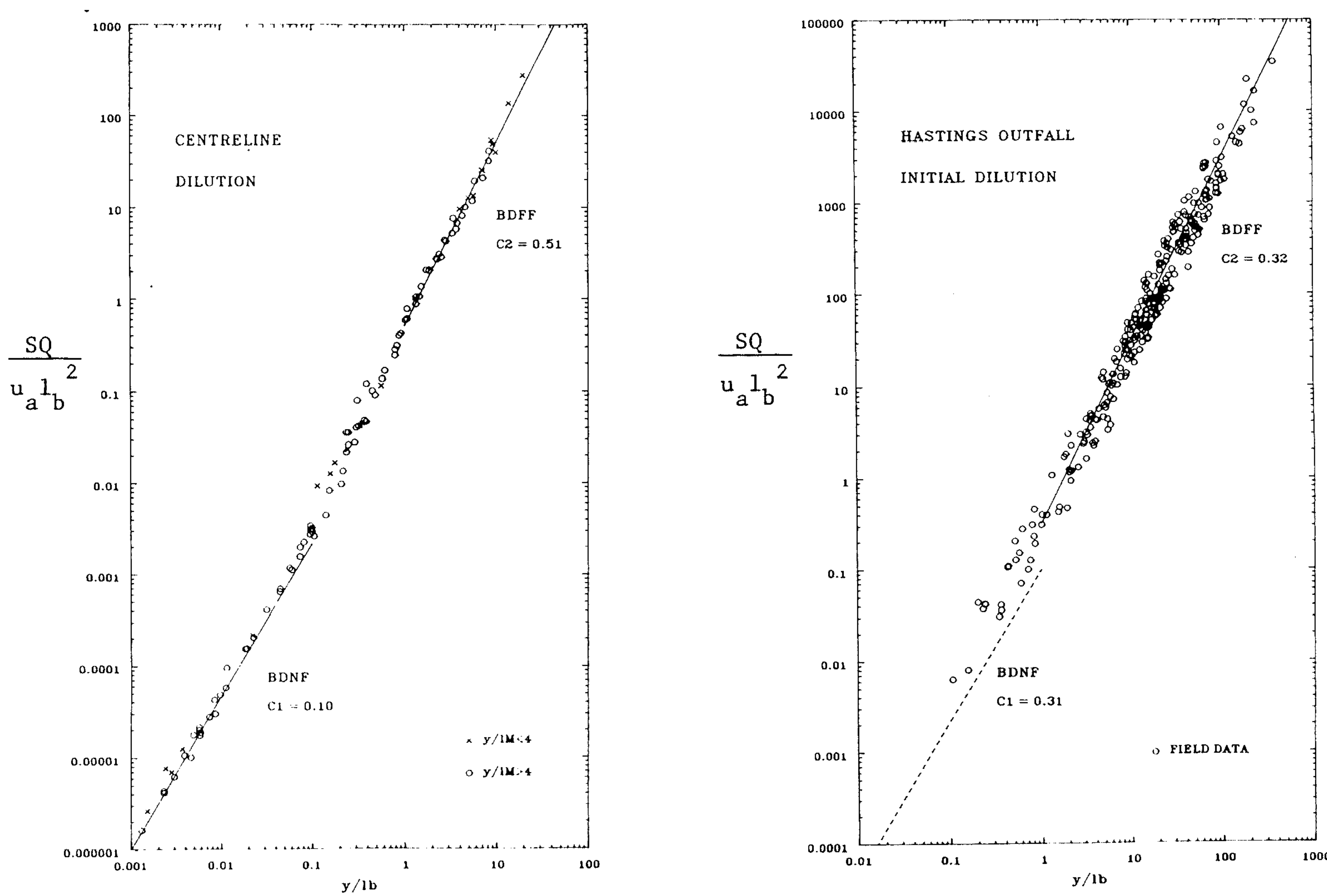

Fig. 4 Comparison of laboratory dilution data (left) and field dilution data at the Hastings outfall (right) as a function of y/l_b

Conclusion

Laboratory experiments of jet mixing are shown to correlate well with field measurements of initial dilution at a sea outfall. Consistent with field observations, the experiments show that substantial increases in dilution above the stillwater value can be expected in the near-far field transition (which may correspond to a u_a near the measurement threshold). The bdff dilution is consistent with the field data if a surface layer of 0.25 H is accounted for.

Acknowledgement : This work was supported by a Strategic Research Grant from the University of Hong Kong.

References

1) Bennett,N.J., "Initial dilution : a practical study on the Hastings long sea outfall", Proc. Inst. of Civil Engr., Part 1, Vol.70, 1981, pp.113-122.
2) Cedarwall,K., "Hydraulics of marine waste disposal", Report 42, Hydraulics Div., Chalmers Institute of Technology, Gotebörg, 1968.
3) Fischer,H.B. et al, Mixing in Inland and Coastal Waters, Academic Press, 1979.
4) George,W.K., Alpert,R.L., and Tamanini,F., "Turbulence measurements in an axisymmetric buoyant plume", Int.J.Heat & Mass Transfer, Vol.20, 1977, pp.1145-1154.
5) Lee, J.H.W., and Neville-Jones,P., "Initial dilution of horizontal jet in crossflow", J. of Hydraulic Engr., ASCE, Vol.113, May 1987, pp.615-629.
6) Lee,J.H.W., and Neville-Jones,P., "Sea outfall design - prediction of initial dilution", Proc. Inst. of Civil Engr., Part 1, Vol.82, Oct.1987, pp.981-994.
7) Rouse,H., Yih,C.S., and Humphreys,H.W., "Gravitational convection from a boundary source", Tellus, Vol.4, 1952, pp.201-210.
8) Toms,G., and Botes.W., "Dye studies of initial dilution and the applicability of the stagnant water dilution", Water Science & Tech., Vol.18, No.11, 1986, pp.189-197.

FLOW CLASSIFICATION AND GEOMETRY OF A VERTICAL JET
IN A TWO LAYER AMBIENT

by

George Noutsopoulos Kathrin Nanou
Professor Tech. & Res. Assistant
Applied Hydraulics Lab., Civil Eng. Dept.
National Technical University of Athens-Greece

Abstract

Experiments have been performed for a round vertical liquid jet of density ρ_o, discharging upwards in a two layer ambient, the lower layer of a depth h_1 and density ρ_1 and the upper layer of a depth h_2 and density ρ_2, where $\rho_1 > \rho_2 \geqslant \rho_o$. A model for the classification of possible flow configurations is proposed and well supported by the experiments as well as by published data for the plane jet. The main geometric features of the flow field have been measured and the experimental data are well correlated and properly presented in dimensionless forms.

Introduction

The problem of a round liquid jet, of density ρ_o, discharging vertically upwards in a two layer stratified ambient, the lower layer of density ρ_1 and depth h_1 and the upper one of density ρ_2 and depth h_2, with densities conforming to the inequalities $\rho_1 > \rho_2 \geqslant \rho_o$, has been examined thoroughly experimentally by the authors. The flow configurations which may develop are shown schematically in Fig. 1.

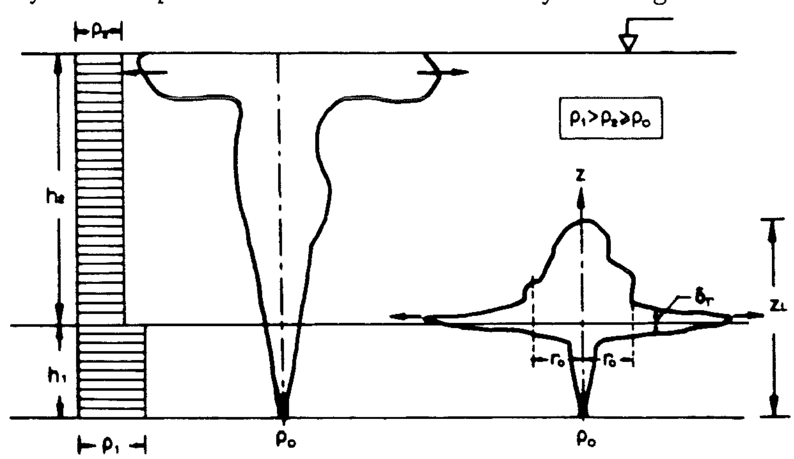

Case (a), Full penetration, Case (b), Entrapped field

Fig. 1. Flow configurations

The flow cases (a) and (b) may be observed for the round as well as for the plane jets.

In case (a) the jet flow fully penetrates both layers and spreads on the free surface in a way similar to the case of a positive buoyant jet in a uniform ambient.

In case (b) the jet flow after the interface is entrapped in the upper layer reaching a ceiling level z_L, reverses itself forming a bell like configuration and spreads horizontally as a discrete layer around the interface.

The experiments

The experiments for the round jet have been performed in a glass wall tank, of plan dimensions 1.00m x 1.00m, and a depth of 0.80m, and all the required accessories for flow regulation and measurements and colouring the jet flow at predetermined instances after flow initiation for each run. Common salt (NaCl) water solutions were used as ambient liquids and jet liquid. Special care has been given to the tank filling process in order to obtain a descrete interface. The tank filling process lasted more than 8 hours.

Two kinds of tests have been performed:

a) for flow geometry and centerline axial velocities
b) for concentration measurements.

a) For each run, after the filling process has been accomplished the jet flow was initiated. A 8mm movie camera placed in front of the tank was set in operation. After a time t_1 has passed from flow initiation for the jet flow to reach the maximum penetration height the jet flow was coloured. The whole operation lasted a few minutes. After film editing the flow configuration was studied frame by frame in a film editing apparatus. The instantaneous outer boundaries of coloured flow were traced on transparent paper placed on the screen of the apparatus at discrete intervals of time after the first coloured front appeared at the jet exit section. On the basis of the mapping of outer boundaries a diagram was formed of z_m (centerline position of the marked front) versus the time t (zero time the appearance of colour at the exit section). From the time history graphs of z_m vs t, the penetration height z_L was determined. The recorded value of z_L was an average value over a long time period. The centerline axial velocity at different levels z could be computed on the basis of the approximate formula:

$$w_m \Big|_{z_m} = \frac{dz_m}{dt} \Big|_{z_m} = \frac{(z_m+\Delta z)-(z_m-\Delta z)}{\Delta t^+ + \Delta t^-}$$

Axial velocities were thus computed at different selected levels z. A total of 31 runs were carried out and analyzed.

b) For concentration measurements the conductivity probe technique was used. Four conductivity probes, with one point electrode and a circular one, frequently calibrated, were used in the proper arrangement for simulationeous signal recording. Concentration measurements were made along the vertical jet axis, as well as at predetermined verticals along the horizontally spread discrete layer in the case of the entrapped field. Twelve runs were performed.

Flow classification

The following theoretical considerations were made to establish criteria for flow classification and to correlate experimental results. The flow behaviour in the whole extend of the lower layer is assumed to be the same with such of a positive buoyant jet in a uniform ambient of infinite extend and density ρ_1. Accordingly all flow characteristics in the lower layer should depend solely on the initial kinematic fluxes of volume Q_o, momentum M_o, and buoyancy B_o and the vertical distance from the exit z. The volume and momentum fluxes Q and M increase with distance z, while the buoyancy flux B remains equal to the initial value B_o up to just below the interface. Sufficient experimental data and theoretical work have been published for the positive buoyant jet, such as by Chen & Rodi (1980) and Noutsopoulos & Yannopoulos (1987), so that the values of volume and momentum fluxes at the interface ($z = h_1$) Q_i and M_i may be well estimated with a good degree of accuracy. Immediately above the interface the buoyancy flux suffers a nominal abrupt reduction, due to the change of ambient density from ρ_1 to ρ_2 ($\rho_1 > \rho_2$).

The nominal buoyancy flux B_i immediately above the interace defined as:

$$B_i = \frac{1}{\rho_o} \int_A g\,(\rho_2 - \rho) w\, dA$$

after introducing a relative stratification parameter, $\varepsilon = \dfrac{\rho_1 - \rho_2}{\rho_1 - \rho_o}$, may be expressed as:

$$B_i = B_o \left[1 - \varepsilon \frac{Q_i}{Q_o} \right]$$

The behaviour of the jet flow in the upper layer may now be examined and interpreted in terms of the buoyancy flux B_i just above the interface.

Case (a). For $B_i > 0$, the total buoyancy flux above the interface is positive (TPB) and the flow in the upper layer will be similar to that of a positive buoyant jet in a uniform ambient and will reach the free surface, spreading on it irrespectively of the magnitude of the upper layer depth h_2. Thus the criterion for full penetration of the jet flow in both layers is established as:

$$\frac{1}{\varepsilon} > \frac{Q_i}{Q_o}$$

Case (b). For $B_i < 0$, or $(1/\varepsilon) < (Q_i/Q_o)$ the total buoyancy flux above the interface becomes negative (TNB). If the depth h_2 of the upper layer is sufficient the jet flow is generally entrapped in the upper layer, reverses itself and spreads as a distinct layer around the interface.

The two sets of kinematic fluxes Q_o, M_o, B_o and Q_i, M_i, $|B_i|$ define the conventional two sets of length scales l_{Q_o}, l_{M_o} and l_{Q_i}, l_{M_i} and the corresponding Richardson numbers R_{io} and R_{ii} (see Fischer et al 1979 for definitions). For the lower layer the first set is used to correlate experimental results, while for the upper layer the second set.

The experimental results obtained by the authors for the round jet prove the validity of the theoretical considerations made above and the established classification criteria.

Centerline axial velocities w_m and concentrations c_m in dimensionless forms are plotted versus z/l_{M_o} for the lower layer in Figures 2 and 3 with the solid lines presenting the semiempirical expressions defined by Noutsopoulos and Yannopoulos (1987) for the round positive buoyant jet in a uniform ambient. The experimental data verify excellently the assumption that the flow behaviour in the whole extend of the lower layer is similar to that of the positive buoyant jet in a uniform ambient. The criteria for flow classification have been also very well verified by the 31 runs performed as has been well discussed in detail in a previous paper by the authors (1986).

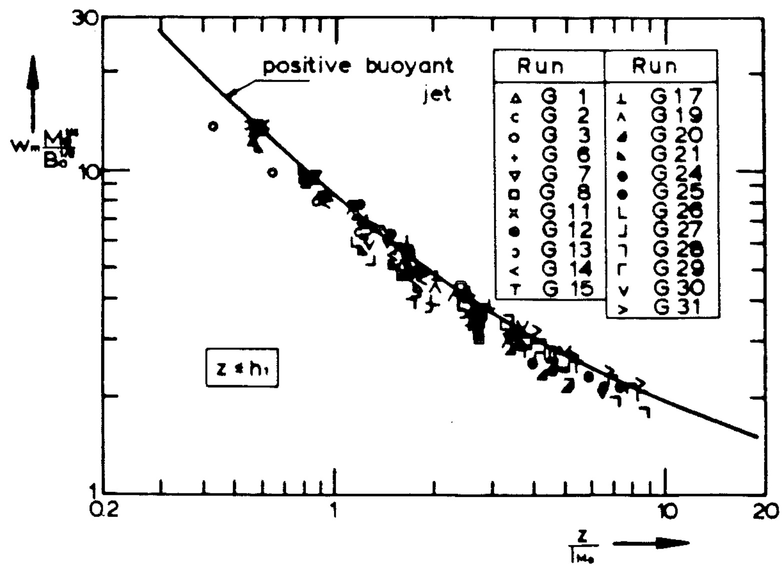

Fig. 2. Centerline axial velocities

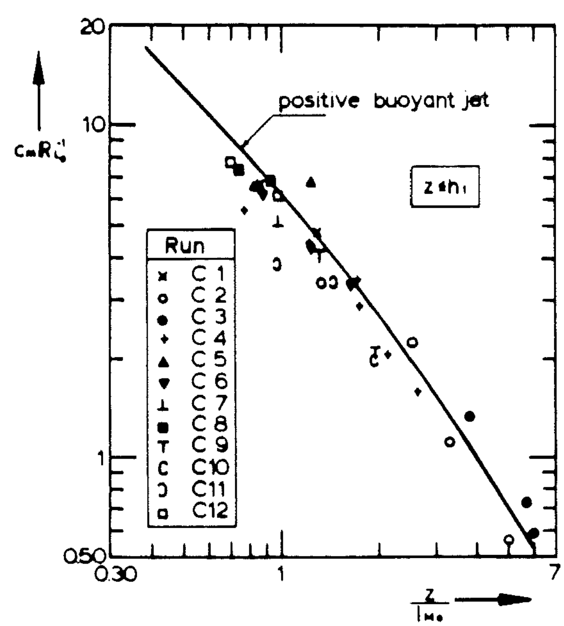

Fig. 3. Centerline concentrations

The flow classification criteria established have been also very well verified for the case of a two dimensional jet on the basis of experiments performed and published by Wallace and Sheff (1987).

Flow geometry

The penetration height z_L

The penetration height in the dimensionless form $(z_L{}^2 - h_1{}^2)/l_{Qi}{}^2$ has been found to be well correlated with the Richardson number at the interface R_{ii}. All experimental data from the observed cases of entrapped field have been plotted in the above form, in a log-log diagram and are presented in Fig. 4. A strong linear relationship is indicated, which by the least square method of best fit is written as:

$$\frac{z_L{}^2 - h_1{}^2}{l_{Q_i}{}^2} = 16\ \mathbb{R}_{ii}{}^{-5/3}$$

Experimental data for the plane jet published by Wallace & Sheff (1987) have been also analyzed using Kotsovinos (1975) and Chen & Rodi (1980) suggestions and are presented in Fig. 4 (closed symbols). They conform very well with the above found empirical formula extending its validity to higher R_{ii} values.

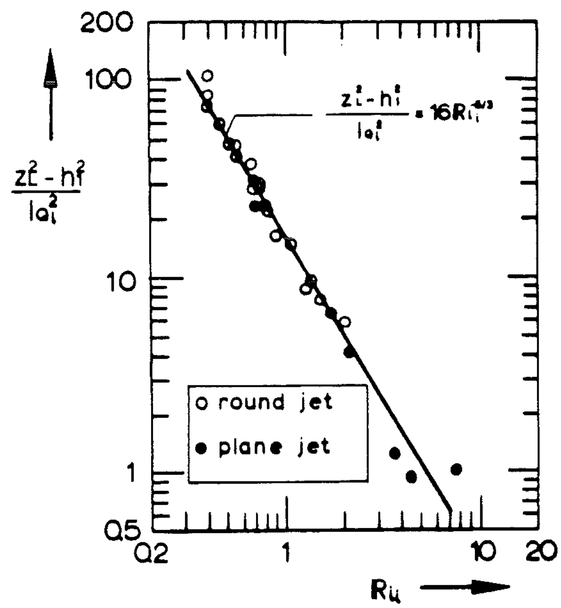

Fig. 4. The penetration height z_L

The radial width r_o of the reversed flow

The radial width r_o at the interface of the reversed flow, which separates the vertical flow from the horizontally spreading layer, has been also determined from the mappings of outer coloured boundaries for all cases of entrapped field. All data are presented in a log-log diagram in Fig. 5 in the dimensionless form of r_o/l_{M_i} vs $\mathbb{R}_{ii}$. A linear relationship is indicated which using the least square method of best fit is expressed as:

$$r_o/l_{M_i} = 1.05\ \mathbb{R}_{ii}{}^{1/5}$$

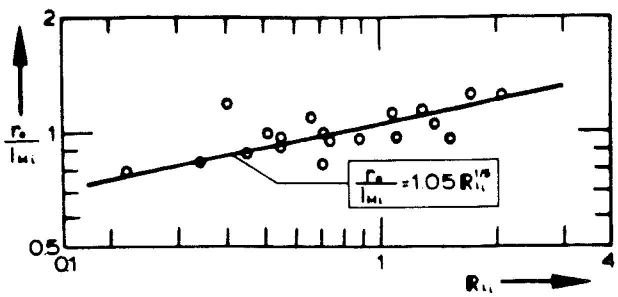

Fig. 5. The radial width r_o of the reversed flow.

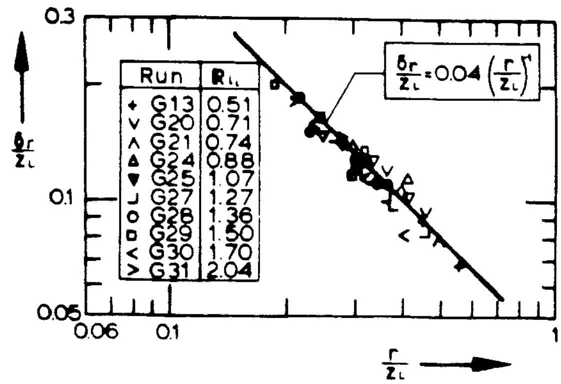

Fig. 6. The thickness δ_r of the horizontal layer.

The thickness δ_r of the horizontal layer

The thickness δ_r of the horizontal layer at three radial distances larger than r_o in the near field has been also determined from the mappings of the coloured fronts. From the time history graphs of δ_r versus time t, at each position, the ultimate quasi steady state value of δ_r before wall interference started was determined for each run. The ultimate values of δ_r in the dimensionless form of δ_r/z_L were plotted in a log-log diagram versus the dimensionless distance r/z_L and are presented in Fig. 6. A linear relationship is indicated which is expressed as:

$$\frac{\delta_r}{z_L} = 0.04 \left(\frac{r}{z_L}\right)^{-1}$$

Thus the thickness of the horizontal layer in the near field is inversely proportional to the radial distance.

Conclusions

Flow classification criteria for a vertical jet in a two layer stratified ambient have been established and are well verified by experimental evidence for the round and the plane jets. Geometric features of the entrapped flow field have been measured and are well presented by empirical formulae.

References

1. Chen, C.J. and Rodi, W., 1980, "Vertical Turbulent Buoyant Jets: A Review of Experimental Data", H.M.T. Series 4, Pergamon Press, Oxford.
2. Fischer, H.B., List, E.J., Koh, R.C.Y., Imberger, J. and Brooks, N.H., 1979, "Mixing in Inland and Coastal Waters", Academic Press, N.Y.
3. Kotsovinos, N.E., 1976, "A Study of the Entrainment and Turbulence in Plane, Buoyant Jet", Rep. No.KH-R-32, W.M. Keck Lab. of Hydraulics and Water Resources, California Inst. of Technology, Pasadena, California.
4. Noutsopoulos, G. and Nanou, K., 1986, "The Round Jet in a Two-Layer Stratified Ambient", Proc. of Intern. Symp. on Buoyant Flows, National Technical University of Athens, Greece.
5. Noutsopoulos, G. and Yannopoulos, P.,1987, "The Round Vertical Turbulent Buoyant Jet", J. Hydr. Res., vol. 25, No.4, pp. 481-502.
6. Wallace, R.B. and Sheff, B.B., 1987, "Two Dimensional Buoyant Jets in Two-Layer Ambient Fluid", J. Hydr. Eng., ASCE, Vol.113, No.8, pp. 992-1005.

SCALE-MODEL INVESTIGATION OF CIRCULATION AND MIXING IN PUMPED-STORAGE RESERVOIRS

by

Kamil H. M. Ali
Civil Engineering Department
University of Liverpool, U.K.

Reza Jaefar-Zadeh
Civil Engineering Department
University of Mashhad, Iran.

Abstract

The paper describes an experimental investigation of the circulation and mixing in homogeneous and stratified water-supply reservoirs. Various types of inlets and outlets were used and several measuring techniques were applied. The effects of jet momentum, the reservoir's aspect ratio and water density gradients were investigated.

Introduction

The factors affecting circulation in water-supply reservoirs include the shape and depth of the reservoir, wind action, water-density differences and inflow/outflow arrangements.

Wind and density effects cannot be controlled and various remedial measures have been developed to minimise the water-quality problem posed by stratification and stagnation.

Improvement of the inlet and outlet arrangements offer considerable potential as a preventive technique aimed at including conditions less favourable to the formation of stratification and stagnation.

Experimental investigation of jet-forced circulation, both in tanks and reservoirs, has been studied by many researchers, mostly using scale model tests (See Ref. 2).

Analytical work concerning the effects of the wind and the earth's rotation has been carried out and is well-documented[2].

However, the analysis of jet forced circulation has attracted relatively few researchers. Sobey and Savage[6] developed a two-dimensional theoretical solution for a tangential jet discharging into a circular reservoir.

Falconer[5] produced a two-dimensional mathematical model describing the jet forced circulation in reservoirs having very large inlets and outlets. Ali and Whittington[3] applied the well-known behaviour of two-dimensional turbulent jets to the problem of the circulation in reservoirs.

Extensive experiments were conducted by the authors to study the effects, on the circulation, of jet momentum, position and size of inlets, the geometry and aspect ratio of the reservoir, and density and temperature differences between inflow and reservoir's water.

Theoretical Considerations

Sobey and Savage[6] obtained theoretically, for a stationary circular reservoir, the following relationship:

$$\overline{Q}_c/(\sqrt{K_j}\ L) = \psi_1\left[\ (L/h),\ (k_s/h)\ \right] \qquad (1)$$

where $\overline{Q}_c$ = mean circulating discharge, K_j = kinematic momentum flux (= $Q_j V_j$), V_j = jet velocity, Q_j = jet discharge, L = diameter of reservoir, h = reservoir water depth and k_s = bed roughness.

Using Sobey and Savage's theoretical curves, the present authors obtained

$$\overline{Q}_c/(\sqrt{k_j}\ L) = \left[\ 5.527 - 9.226\ (k_s/h)^{0.238}\ \right]\ (L/h)^{-1} \qquad (2)$$

Experimental Arrangements and Models

Some of the models used are described below:

(i) A smooth circular reservoir having a radius of 1.5m together with a tangential jet (having a height b_o = 20mm and a width d_o = 2mm) and a central outlet. The circular reservoir mentioned in (i) was later run with four radial jets at right-angles to each other, and connected to the same inlet. These jets were positioned at the centre of the reservoir. All four jets were of height of 50mm and width 2mm. Using the same basic model, two further runs were made, one with two radial jets, at the centre, positioned directly opposite and one run with one radial jet at the centre of the reservoir.

(ii) Another circular reservoir of 1.22m radius was used to investigate the effect of the jet momentum and area on the reservoir circulation. The jet discharge was kept constant and the momentum was changed by altering the jet area. The values of b_o x d_o used were 20 x 2, 8 x 30, 8x 60, 8 x 90 and 8mm, 130mm. In all these experiments two outlets were used, one on either sie of the radial jet inlet.

(iii) A Lucite" cylindrical reservoir, 0.92m diameter was used to study stratification. It had a central outlet which was made of a 30mm diameter pipe,0.22cm long. A tangential jet 10mm high and 2mm wide was positioned so that its top was 15mm below the water surface. To maintain steady flow in the model, a constant head arrangement was used[4]. The method of preparing a stratified reservoir, using a saline solution, is also described in Ref. 4.

(iv) Another circular reservoir was also used to study thermal stratification. It had a diameter of 2m and a height of 0.5m. The perimeter wall was made of clear plastic. A tangential surface jet was used together with 12 outlets positioned uniformly along the wall. A large heated storage tank was used to feed the surface jet. Nine 50kw Halogen lamps were used to heat up the surface layer of the reservoir.

Measuring Techniques

Different methods were used to study the circulation and mixing in the model reservoirs. Dye photography was used to define the movement of dye injected through the inlets. Large velocities were measured using a miniature current-meter. Small velocities were obtained using illuminated floats of various types using time-laps photography.

The hydrogen bubble technique was used in some experiments, to determine the vertical distribution of small peripheral velocities. The conductivity method was used to measure densities in the reservoirs. Reservoir temperatures were measured using 6 temperature probes.

The method of preparation of the stratified reservoirs is described in Ref. 4.

Experimental Results

The experimental results for the 3m smooth circular reservoir were obtained using a tangential jet with d_o = 2mm, b_o = 20mm, Q_j = 11.2 - 73.5 ℓ/s, h = 0.02 - 0.20m. The following empirical relationship was fitted to the results of these experiments.

$$\overline{Q}_c/\left[\sqrt{K_j}\ L\right] = 1.36(L/h)^{-1}\left\{1.702 + \left[123.89(L/h)^{2.5}\right]/\left[\sqrt{K_j}/\nu\right]^{2.5}\right\} \qquad (3)$$

Equation (3) shows that the dimensionless average circulating discharge for this smooth reservoir is a function of the jet's Reynolds number and the reservoir's aspect ratio.

Effect of Jet Momentum on Reservoir Circulation (Radial Jet)

A series of experiments was conducted in a 2.44m diameter circualr reservoir, to study the effect of jet momentum on the circulation. Jet discharge and water-depth were kept at 0.192 x 10^{-3} m^3/s and 46mm respectively. The inflow momentum was altered by changing the area of the jet. Areas 0.4cm^2, 2.4cm^2, 4.8cm^2, 7.2cm^2 and 10.4cm^2 were used. The outlet was 0.4m wide and located opposite to the inlet.

Figure 1 shows measured velocity-distribution for the various jet areas. This figure demonstrates clearly the increase in reservoir velocities resulting from the increase in jet momentum.

Circulating discharges were calculated using the experimental velocity-distributions. The average experimental values of $\overline{Q}_c/Q_j$ for jet areas of 10.4cm^2 and 0.4cm^2 wide outlet, for these two jet areas, is 33% and 7% of the circulating discharge. These percentages explain why the outlet will have a much bigger effect on the circulation in the case of the large nozzle than in the case of the small one (for steady conditions).

The following relationship was fitted to the experimental results:

$$\overline{Q}_c/Q_j = 0.0292\ \sqrt{R} + 1 \qquad \text{where } R = hV_j/\nu \qquad (4)$$

Circulation Generated by Radial Jets at Centre of Reservoir

Figures 2-4 show velocity-distribution obtained using four, two and a single radial jet at the centre of a reservoir. These figures show that the number of gyres generated by the jets is twice the number of jets used. For example, the use of 4 jets (Fig. 2) resulted in eight gyres which in practice will help in reducing the zones of stagnation in the reservoir.

Using the velocity-distributions given in Figs. 2-4, average circulating discharges were calculated. For number of inlet jets of (1), (2), and (4), the total jet momentum flux per density was 3.534 x 10^{-4}, 0.845 x 10^{-4}, and 0.656 x 10^{-4} m^4/s^2 respectively. The resulting values of $\overline{Q}_c/Q_j$ were 7.57, 5.65, and 3.89. Clearly, circulation increases with the icnrease in jet momentum flux (K_j).

Figure 5 shows time-lapse photographs for homogeneous and stratified reservoirs (L = 0.92m). The depth of the top layer in the stratified reservoir was equal to the total water-depth in the homogeneous one. Clearly, the lengths of the tracks, and hence the peripheral velocities, are bigger in the stratified reservoir.

Figure 6 shows the spread of dye in stratified and homogeneous reservoirs for the same jet discharge and epth of the top layer. Again, mixing is markedly better in the stratified reservoir.

Figures 7 and 8 show the variation of reservoir water-density with elevation above the bed for various times using a surface jet. The plots show that the increase in jet discharge results in improved mixing in the stratified reservoir.

Figure 9 shows the effect of using an aerator, at the centre of the 2m reservoir, on the temperature sdtructure within it. Very small air-discharge resulted in considerable changes in temperature, and hence in improved mixing.

Conclusions

1. When mixing is produced by a momentum jet, the circulation patterns depend mainly on the number of the jets, the aspect-ratio and relative-roughness of the reservoir. The Reynolds number becomes important in the case of very small-scale models.

2. Dimensionless peripheral velocity-distributions, resulting from a tangential or a radial jet inlet, are similar and are quite close to those for a wall jet for large reservoir diameters and jet Reynolds numbers.

3. Experiments with $(L/d_o) > 50$ show that outlets have little influence on the circulation in reservoirs. Due to considerable entrainment; the circulating discharge is usually much bigger than the discharge of the inlet.

4. An implication of conclusion 1, that the aspect-ratio is of great importance, was verified in detailed experiments on scale-models of water-supply reservoirs. It follows that the common practice of exaggerating the vertical scale is not automatically valid.

5. The use of multiple jets improves the circulation and mixing and reduces the stagnation zones in reservoirs. Here, jet momentum is of primary importance.

6. In the present experiments, interfacial shear stress is smaller than boundary shear stress.

7. Surface jets and aerators, positioned near the bed, are efficient in mixing a stratified reservoir.

References

1. Ali, K. H. M. et al, "A scale model investigation of the circulation in reservoirs", Proc. Instn. Civ. Engrs., Part 2, 1978, 65, Mar., 129-161.
2. Ali, K. H. M. and Pateman, D., "Prediction of the circulation in reservoirs", Proc. Instn. Civ. Engrs., Part 2, 1981, 71, June, 427-461.
3. Ali, K. H. M. and Whittington, R. B., "Liquid-liquid mixing in tanks and reservoirs", Proc. Brit. Hydromech. Res./ Assn. 3rd Eur. Conf. Mixing, York, 1979, 37-60.
4. Ali, K. H. M. and Jaefar-Zadeh, M. R., "Circulation and mixing in a stratified reservoir", Journal of Hyd. Res. Vol. 27, 1989, No. 5, pp 683-697.
5. Falconer, R., A., "Mathematical modelling of jet-forced circulation in reservoirs and harbours", Ph.D. thesis, Imperial College, 1976.
6. Sobey, R. J. and Savage, S. B., "Jet-forced circulation in water-supply reservoirs", J. Hydraul. Div. Am. Soc. Civ. Engrs., 1974, f100, HY12, Dec., 1809-1828.

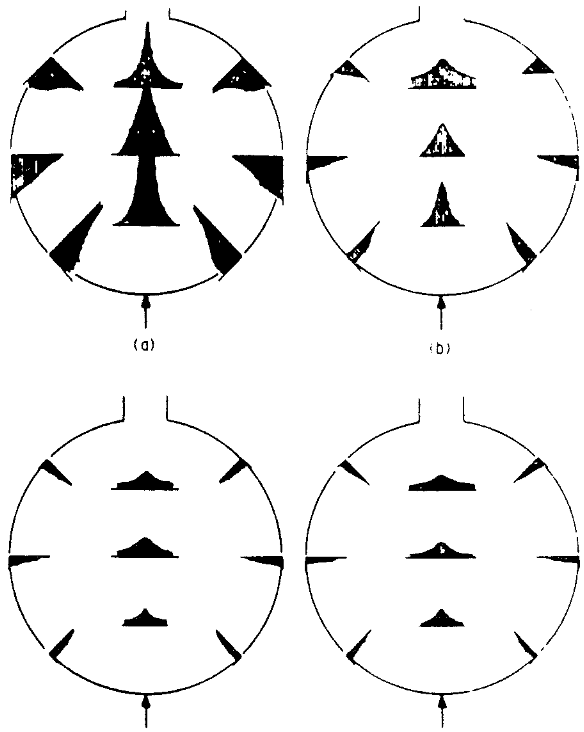

Fig. 1
Velocity-distribution for radial jets of various areas (a) A_j = 40 mm^2 (b) A_j = 240 mm^2 (c) A_j = 480 mm^2 (d) A_j = 1040 mm^2

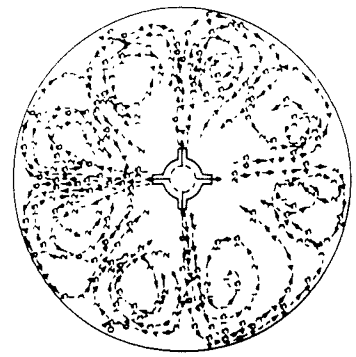

Q_j = 162cm³/sec b_0 = 5·0cm
h = 7·0cm d_0 = 0·2cm

Fig 2 Experimental Velocity Distributions

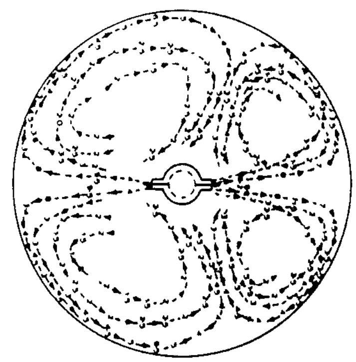

Q_j = 130cm³/sec b_0 = 5·0cm
h = 7·0cm d_0 = 0·2cm

Fig 3 Experimental Velocity Distributions.

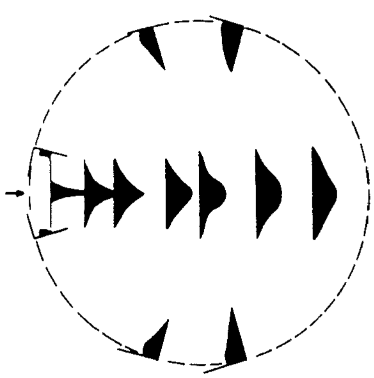

Q_j = 188cm³/sec   a = 150cm
h = 7·0cm   b = 150cm

Fig 4 Experimental Velocity Distributions

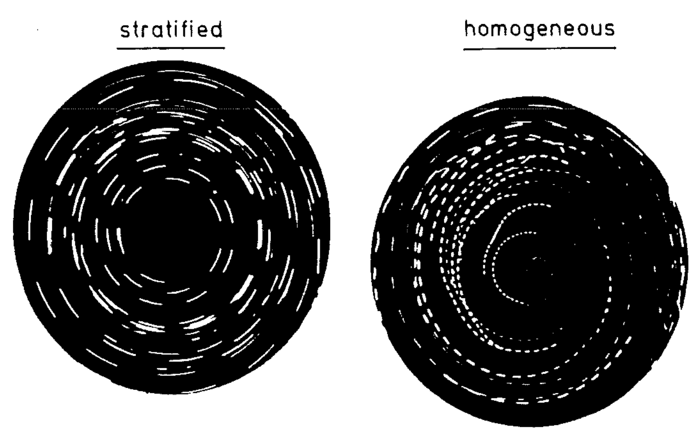

Fig. 5 Circulation patterns obtained using illuminated floats (Q_j = 5·75 cc/sec, h_1 = 4·7cm, $\Delta\rho/\rho$ = 9·1%, time lapse of 5 secs)

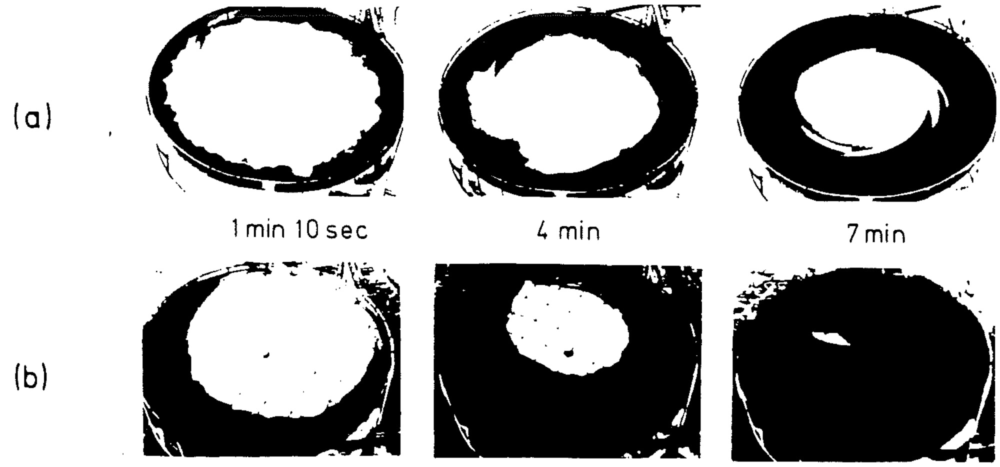

Figure 6 Circulation produced by a surface jet
(a) stratified reservoir and (b) homogeneous reservoir (h_1 = 4·7cm)

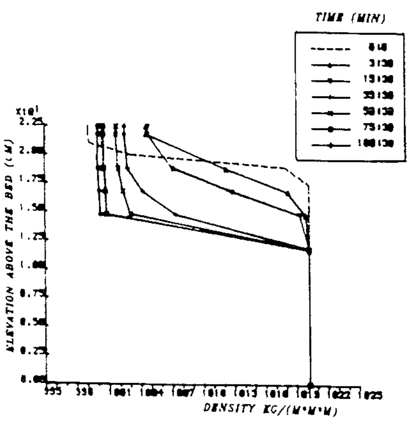

Fig. 7 Variation of density with elevation above the bed for station number 1, experiment number 4, Q_0 = 19.06 cc/sec, ε = 2.1%, h_1 = 2.5 cm).

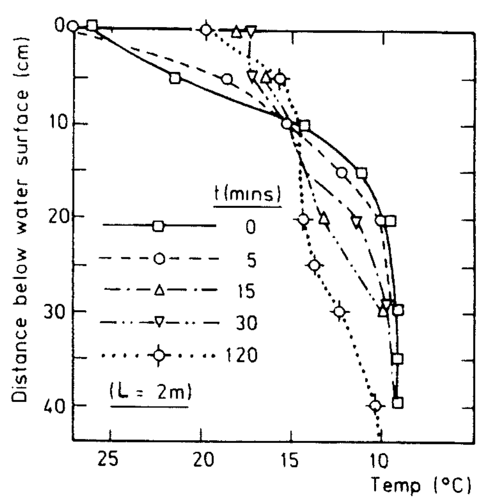

FIGURE 9. TEMPERATURE PROFILES OBTAINED USING AN AERATOR

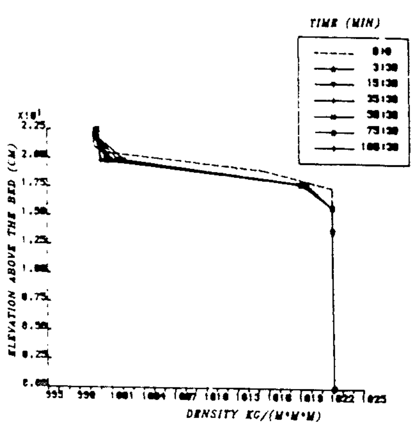

Fig. 8 Variation of density with elevation above the bed for station number 1, experiment number 10, Q_0 = 5.75 cc/sec, ε = 2.3%, h_1 = 2.5 cm).

ON THE INTERNAL STRUCTURE OF THERMALS AND MOMENTUM PUFFS

D. Papantoniou, J. Bühler and T. Dracos
Institute for Hydromechanics and Water Resources Management
ETH Hönggerberg, 8093 Zürich, Switzerland

1 Introduction

A thermal is an isolated mass of buoyant fluid, which moves under the influence of its own buoyancy force. It can be initiated by the sudden release of an amount of buoyant fluid from a flow source. A momentum puff, on the other hand, is an isolated mass of nonbuoyant fluid to which momentum is imparted during its release from the source. If the Reynolds number of the resulting motion is sufficiently high, thermals and puffs become turbulent.

Both types of motion are related to the corresponding vortex ring motion. In our view, what distinguishes puffs and thermals from vortex ring motion is that on buoyant and non-buoyant vortex rings ambient fluid stays present on the ring axis. The circulation, measured on a closed circuit passing through the axis, stays constant according to Kelvin's theorem. For self similar thermals the circulation also stays constant as predicted by dimensional considerations, but vorticity is generated by buoyancy along the axis and is destructed by the mixing of vorticity of opposite signs across the center line at the rear regions. An increase of the initial circulation relative to the total buoyancy can be shown to result to a smaller angle of spread and hence less mixing with the environment [1].

Previous measurements of the motions inside and around a thermal [2], were based on measurements of the trajectories of small sinking particles suspended in the ambient fluid. We are not aware of analogous measurements in the momentum puff. Since these flows are of fundamental interest, our experiments atempt to assess some of their dynamical and structural characteristics.

2 Experiments

The experiments were carried out in a water tank, 100 by 40 cm and 50 cm high. A 38 by 38 cm vessel, 30 cm deep was installed (inverted) at the top and was filled with water by suction, bringing the total depth of the facility to about 80 cm. Thermals and puffs were generated by releasing a measured amount of fluid through a 6 mm diameter orifice at the top of the apparatus. An electrically operated valve was used to start and stop the flow. The initial density difference for the thermals was 10%. For puffs, the temperature of the injected fluid was matched to that of the ambient to within 0.5 C to avoid the effects of negative buoyancy. Laser induced fluorescence (LIF), using Fluorescein dye as a tracer and the blue line of an argon-ion laser for illumination, was used to visualize the structure of flow interior and to record its advance as a function of time. The method relies on the measurement of the intesity of fluoresence of the tracer dye molecules, which is proportional to the local illuminating (blue) light intenstity and the local dye concentration [3]. For these measurements the axial flow plane was illuminated by a 1 mm thick laser light sheet, which entered the facility through the bottom glass wall. During each experiment, the flow evolution after the release was imaged by a CCD video camera and recorded on U-matic videotape. The observation region covered an area of 35.4 cm in the vertical (flow) direction by 23.8 cm in the horizontal direction, centered at the flow axis. The spatial resolution, determined from imaging a fixed grid placed at the image plane, was 692μ in the axial and 466μ in the radial direction. The top of the observation area was located at 27.1 cm from the nozzle exit. A synchronization circuit started and shut the valve, and maintained an electronic binary video frame counter, which was encoded onto each video frame prior its recording. The counter was zeroed at the moment the valve was opened. The camera framing interval is fixed at 40 ms. The illumination was shuttered by use of a Bragg-cell, driven synchronously with the vertical video sync. The total duration of each light pulse determines the effective sensor integration time, and it was kept between 20–40ms. Use of the shorter pulse duration increases the temporal resolution at the expense of decreasing the available signal. Due to the great dilution capability of the flow, it is very difficult to maintain a uniform dynamic range during the measurement since the fluid dilutes by more than a factor of 2 during its advance through the observation area.

The image sequences were digitized automatically by a suitably equipped PC/AT station and transferred via Ethernet on a Sun workstation for processing and analysis.

3 Results and Discussion

Observation of the flow image sequences reveals a few quite striking features of the motion. A typical picture of a thermal, presented in Figure 1, was obtained after 5.6 s had lapsed since the initiation of the release of 17 cc of buoyant fluid. (The release was completed within 750 ms). A large amount of undyed fluid can be observed in the interior, making the flow very intermittent. This is consistent with previous measurements of strongly heated buoyant thermals[4]. A large part in the central and back region of the thermal is hollow, a feature observed long ago by Scorer [5] and Woodward [2]. High concentration values occur (consistently) at the front off-center regions. This indicates that entrainment and mixing proceed mainly from the side and back regions.

The digital sequences were used to measure the speed of advancement of the thermal front. At each frame, the location of furthest downstream edge was computed by an edge-detecting procedure. Its instantaneous convection velocity was then computed by correlation with the next time frame. A patch of the imaged area, measuring 1.04 cm by 1.16 cm in the axial and radial directions respectively and centered at the front location was used for the correlation. The displacements were computed with an adaptive least squares correlation code (ALSC)[6]. This code has been developed, tested and used by photogrammetrists and its accuracy is superb (error less than 1% of a pixel between stereo views of rigid objects or aerial scenes). The diplacement estimation accuracy depends on the gray level distribution (features) in the patch. The front position is a rather weak feature, usually including a sharp boundary mainly in one direction. This slightly deteriorates the displacement estimate, but only in the radial direction (along the edge). The estimated precision in the measurement of the axial displacement is within 5% of the absolute instantaneous value.

The speed of advancement of the front is shown in Figure 2 in non-dimensional form. The observed fluctuation in the instantaneous front velocity arises mainly from the fact that the velocity estimation can be at different positions on the flow front. Also, at large values of x where the signal becomes weak due to dilution, the front position may be mislocated by the edge-detector by up to 2mm inside the thermal. Despite the fluctuation, the front velocity obeys (over the observation length) the power law which is predicted on dimensional grounds by assuming that the only quantity on which the speed can depend is the total buoyancy B and the distance form the source x, i.e.,

$$\frac{B^{1/2}}{U} = C_t x$$

where C_t is a dimensionless constant and x is measured from a virtual origin. This representation allows an estimation of this dynamical virtual origin of the flow, which is about 13 cm from the nozzle exit. The geometrical growth of the same thermal is obtained by measuring at each instant the front position and the radial distance between the two radially outermost edges (these edges are not necessarilly located at the same axial position). This is shown in Figure 3, from which the geometrical virtual origin and the growth angle can be estimated. In fact, the geometrical origin is also located at about 13 cm from the nozzle exit, indicating that the mean motion is self similar within the region of observation.

The instantaneous velocity field inside the thermal was computed by applying the correlation technique to a large number of points in the thermal interior. Points of interest were selected according to the orientation and intensity of local edges (variations of the local instantaneous concentration). The correlation code was applied with a patch size of 0.9 by 0.6 mm in the axial and radial directions respectively. The accuracy of the displacement estimation was very high, with a mean correlation coefficient of 0.96. The resulting velocity field, corresponding to the image in Figure 1, is shown in Figure 4. It is of interest to note that there appear to be at least 4 rotation centers in the dyed region. At the front the motions suggest the presence of a vortex ring. The highest velocities are observed behind the front, in agreement with Woodwards measurements [2].

A similar analysis was applied to the momentum puff. A typical concentration distribution is shown in Figure 5, an image obtained 6.4 s after the release of 25 cc were initiated (release time was 500 ms). The flow images of puffs and thermals bear certain similarities. The puffs are also very intermittent and, as in the thermals, the highest concentration values are observed at the front. However, the puffs decelerate much faster than thermals and obey a different scaling with x. On dimensional grounds, the only appropriate quantities available to form a local velocity scale are

M, the total momentum, and x, the distance from the source. The front velocity is thus expected to scale as

$$\frac{M^{1/2}}{U} = C_p x$$

where C_p is a dimensionless constant. The speed of advance of the front position of a puff was computed and presented in Figure 6 and its geometrical growth rate in Figure 7. It may be observed that, apart from the fluctuations which are present for the same reason as in the thermal, the puff flow is consistent the with above scaling. The position of the dynamic virtual origin is estimated to be 5cm from the nozzle exit.

In the puff flow the Reynolds number is diminishing with axial distance. The original kinetic energy of the large structure is continuously dissipating and hence turbulence is decaying with time; there is no generating mechanism to maintain it. After a sufficiently long distance from the source the large eddies lose enough energy and with it their ability to overturn and entrain so the motion can be expected to subside. The flow image in Figure 5 and the corresponding velocity vector field shown in Figure 7 indicate that the puff is still turbulen and at a quite disorganized state. The region of highest velocity is, as in the thermal, also behind the front. However, in comparison to the thermal, there is much less activity near the marked fluid boundaries at the side and back regions. This should reflect a dimished entrainment capability compared to the buoyancy driven flow. It is also of interest that the velocity field appears smoother in the puff than in the thermal, with smaller spatial variations of the velocity vectors.

The authors express their appreciation to their photogrammetrist colleagues M. Baltsavias and Prof. Gruen who developed the ALSC method and introduced us to its application.

4 References

1. J.S. Turner, 1986, JFM **173**, p. 431.
2. B. Woodward, 1959, Quart. J.Royal Meteor. Soc., **85**, p. 144.
3. D. Papantoniou and E.J. List, 1989, JFM **209**, p. 151.
4. S-C Lin, L. Tsang and C.P. Wang, 1972, Phys. of Fluids**157**,12, p.165.
5. R.S. Scorer, 1957, JFM **2**, p.583.
6. A. Gruen, E.P. Baltsavias, 1985, Adaptive Least Squares Correlation with geometrical constraints. Proc. SPIE, Vol. 595, Cannes-France, pp. 72-82.

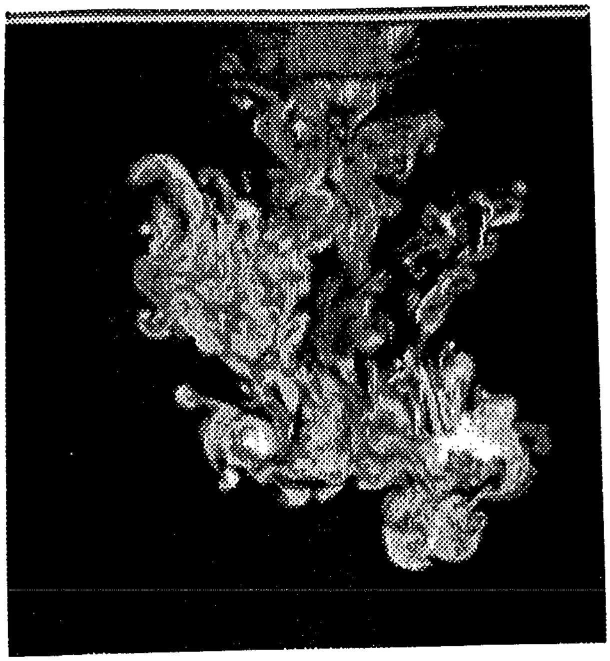

Figure 1. Instantaneous concentration distribution in a thermal.

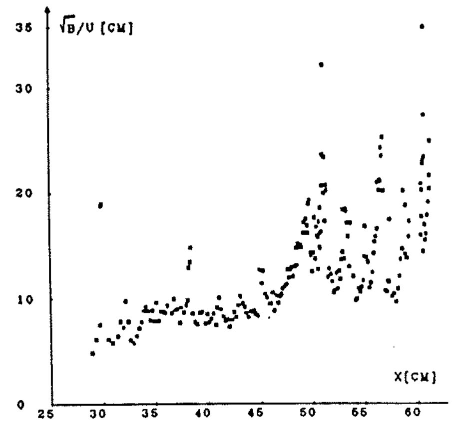

Figure 2. Axial speed of propagation of thermal front versus instantaneous front position from the nozzle exit.

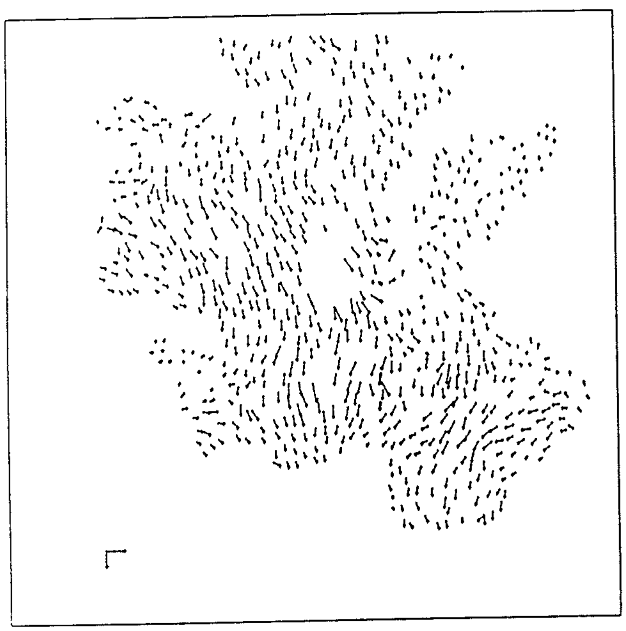

Figure 4. Velocity field in thermal corresponding to the flow image in Fig. 1. A 20 cm by 20 cm area is outlined. The bottom left arrows indicate velocity of 10 cm/s.

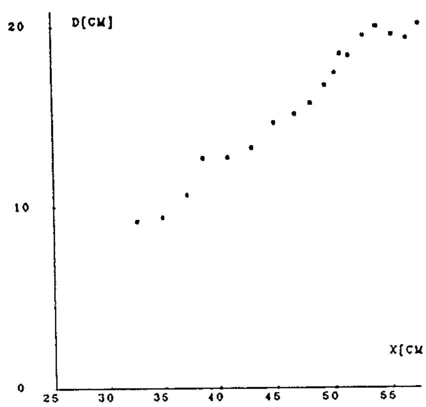

Figure 3. Lateral extent of thermal versus front position.

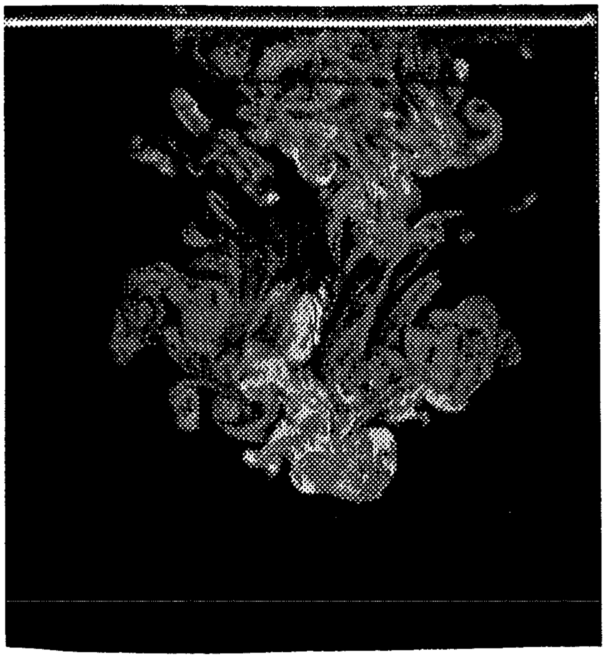

Figure 5. Instantaneous concentration distribution in the momentum puff.

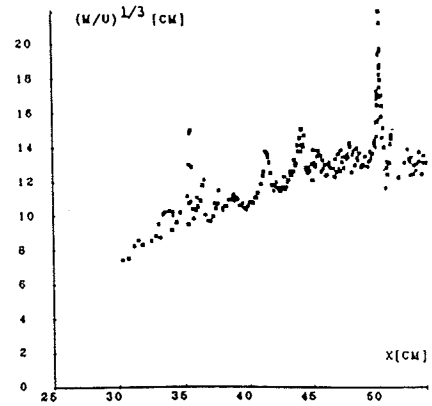

Figure 6. Axial speed of propagation of puff front versus instantaneous front position from the nozzle exit.

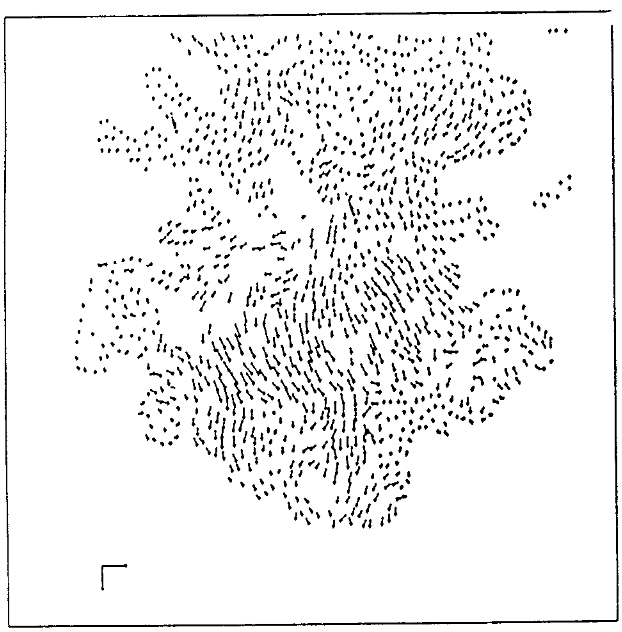

Figure 8. Velocity field in the puff corresponding to the flow image in Fig. 5. A 20cm by 20cm area is outlined. The bottom left arrows indicate velocity of 10cm/s.

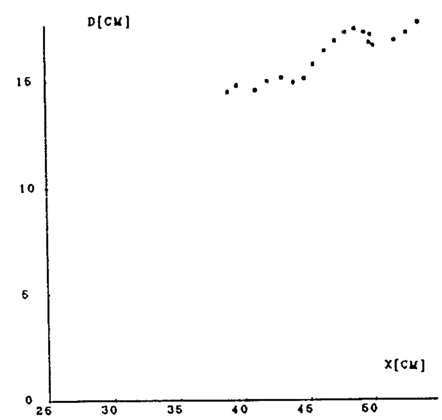

Figure 7. Lateral extent of puff versus front position.

Session 4B

Turbulence and Interfacial Effects

SCALING EFFECTS IN LABORATORY WIND-MIXING EXPERIMENTS

by Joseph F. Atkinson
Department of Civil Engineering
State University of New York at Buffalo
Buffalo, NY 14260 USA

Abstract

Laboratory wind-mixing studies are reviewed in the context of mixed-layer deepening, (entrainment) models. Variations in apparatus are noted, particularly with respect to fetch length. It is shown that, for given wind speed, entrainment generally increases with longer fetch and that the presence of end walls reduces mixing effectiveness. Extrapolation of laboratory results to field studies is discussed.

Introduction

The mixed-layer approach to modeling surface mixing in stratified water bodies is now fairly common. In natural systems wind provides a major driving force for mixing and it is important to be able to predict the mixed layer depth, h. Laboratory studies have been used to gain understanding of the physical processes controlling entrainment, which is characterized by a transfer of turbulent kinetic energy into potential energy as denser fluid is lifted across an interface and stirred into the mixed layer.

Unfortunately, results from different wind-mixing experiments have not provided sufficiently consistent data, needed to develop a generally accepted entrainment relationship. This may be due to variations in experimental conditions and parameter ranges considered. An important consideration in this respect is differences in fetch length. In general, for a given wind speed the mixing rates are higher for greater fetch. Variations in wind tunnel depths (above the water layer) also imply different air-water boundary layer development and significant variations in friction velocity, u_*, which is used in many studies to characterize wind-induced entrainment. These observations raise questions concerning scaling effects in laboratory wind-mixing studies, particularly when extrapolating results to much longer fetch conditions in the field.

One of the concerns in describing entrainment is the proper choice for scaling velocity, which should characterize the mixing energy available. For more idealized conditions, using oscillating grids or simple shear flow, the appropriate scale is more apparent than with wind studies, where there are several potential choices. The entrainment model should be able to account for these various velocity scales, since each represents a source of mixing energy.

Background

A number of laboratory studies have examined the interaction between wind and the water column, usually using some form of wind/water tunnel. Basic turbulence measurements provide some needed information for entrainment modeling, but the present paper will concentrate on studies concerned specifically with mixed-layer deepening.

From dimensional analysis it can be shown that the entrainment rate should be a function of a bulk Richardson number, Ri. Reported relationships usually take the form

$$E = u_e/u_s = C\, Ri^{-n} , \qquad Ri = g'h / u_s^2 , \qquad (1)$$

where E is the non-dimensional entrainment rate, $u_e = dh/dt$ is the rate of mixed-layer deepening, u_s is the scaling velocity, g' is reduced gravity and C and n are empirical constants. Molecular diffusive effects may also be important, especially at very high Ri. In this case E would depend on a Peclet number also. However, this effect is not considered in the present discussion, since it is not believed to be of importance in the experiments reviewed here.

To understand the mixing mechanisms, the simplest assumption is that a constant proportion of energy transferred from the wind to the water column is used for entrainment. The remaining fraction then serves to maintain the well-mixed condition of the layer. It was recognized some time ago that this assumption results in a value of n = 1. A number of studies have in fact found that this value provided a good correlation with experimental data. Other results have suggested that C may be a function of Ri, or have presented different arguments for the mixing mechanisms, to derive an exponent different from -1. Fig. 1 shows results from a number of wind-mixing studies, using u_* for u_s. Each curve represents the approximate range of experimental results reported. Table 1 summarizes the experimental conditions for each of these tests.

Discussion

It is difficult to draw firm conclusions when faced with the variability of results seen in Fig. 1. However, it is also clear from Table 1 that there are significant differences in experimental conditions. In particular, fetch length, L, varies considerably. It is well known that surface waves and drift current are fetch-dependent (for small L). For example, Fig. 2 shows surface drift values measured in a wind/water tunnel with a length of 25 m. Bulkheads were installed to artificially reduce the fetch, creating test sections 3.5 m or 7.0 m long. It is clear that the presence of end walls reduces drift. An important result of this (and

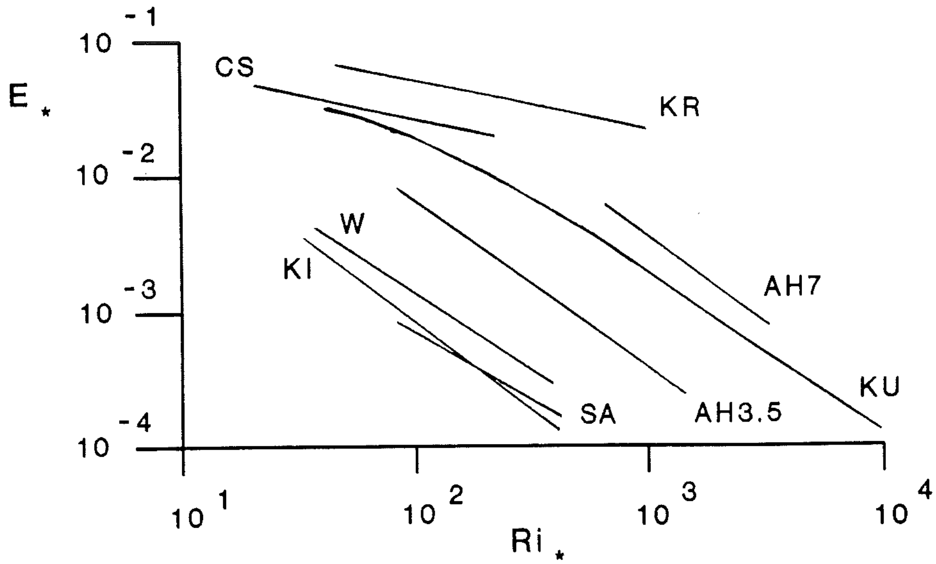

Figure 1. Comparison of results from wind-mixing studies (also see Table 1); E_* and Ri_* use u_* for u_s.

Table 1
Experimental conditions for studies shown in Fig. 1.

Reference (1)	Tank Dimensions (m) L (2)	D (3)	D_w (4)	W (5)	Result (6)
WU (Wu, 1973)	2.32	.28	.095	.205	$E = .234\ Ri^{-1}$
KU (Kullenburg, 1977)	(field observations)				$E\ \ Ri^{-1}$
KI (Kit et al., 1980)	5.00	.35	.15	.15	$E = 1.5\ Ri^{-1.5}$
SA (Shelkovnikov and Alyavdin, 1982)	7.10	.60	.115	.375	$E = .24\ Ri^{-1.2}$
KR (Kranenburg, 1984)	32.5	.405	.30	.80	$E\ \ Ri^{-.5}$
CS (Caussade and Souyri, 1986)	20.0	1.0	1.0	1.2	$E = .28\ Ri^{-.5}$
AH (Atkinson and Harleman, 1987)	3.50	.60	.26	.76	$E\ \ Ri^{-1}$
AH	7.00	.60	.26	.76	$E\ \ Ri^{-1}$

note: L = length, D = water depth, D_w = wind tunnel depth, W = width
Ri and E defined with $u_s = u_*$

also because of smaller roughness due to less wave build-up) is a reduction in u_*, as seen in Fig. 3.

Most studies have presented data in the form of Fig. 1, using u_* for scaling. This is a reasonable choice since u_* should characterize energy transfer at the air/water

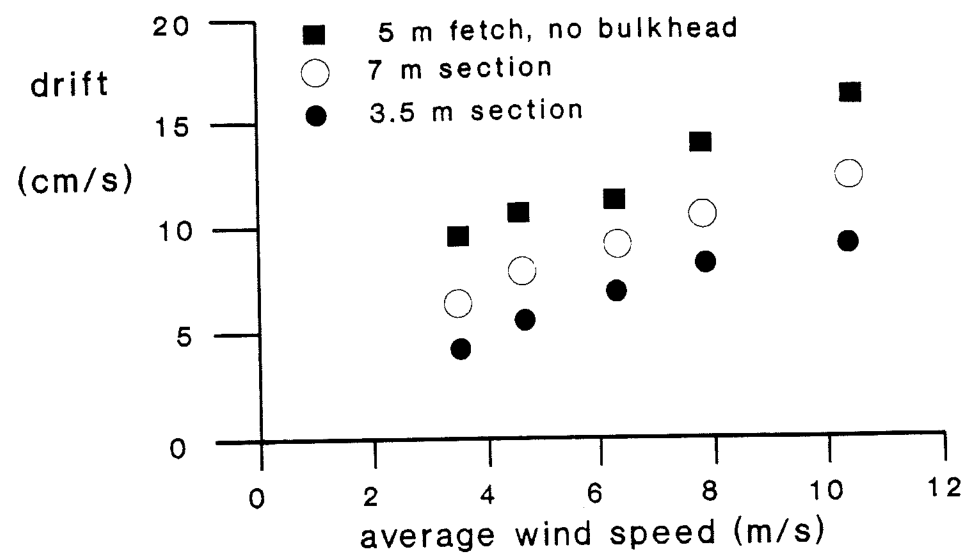

Figure 2. Surface drift velocities in 25 m wind/water tunnel (adapted from Atkinson et al., 1984).

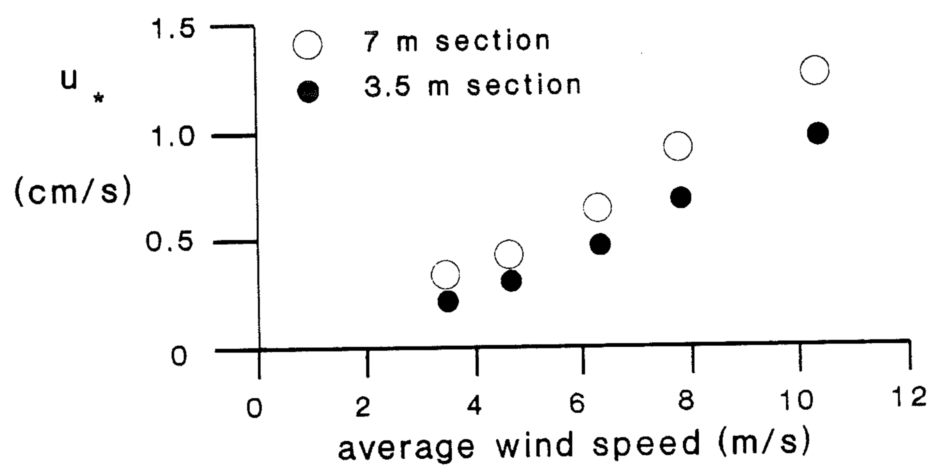

Figure 3. Average friction velocities in 3.5 m and 7.0 m test sections (adapted from Atkinson et al., 1984).

interface and also because the value of u_* should adjust to the specific experimental conditions used. That is, u_* will depend on wind tunnel characteristics and on water surface roughness, which in turn depends on fetch. Unfortunately, given the large variations in results, it appears that u_* is not the only variable of concern.

KI argued that the presence of end walls produced a more complicated flow pattern than would be expected in a true two-dimensional wind-driven flow. In particular, there is a flow reversal at the downstream wall and a return current is established along the interface. Furthermore, they argued that there is greater dissipation with end walls present, so that less energy is available for entrainment. Thus, experiments with longer fetch will have greater entrainment rates. (This relationship is also well known in field studies.) Fig. 4 shows variations in E_* with L for the studies listed in Table 1, at two different values of Ri_*. Although a well-defined relationship is difficult to determine, a general increase in E_* with greater L is observed, as expected.

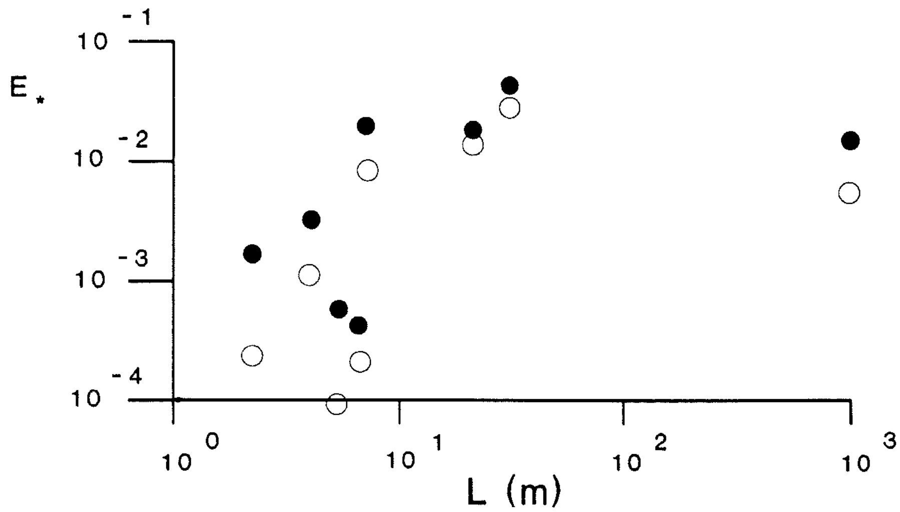

Figure 4. Fetch effect on E_*, for $Ri_* = 200$ (solid points) and $Ri_* = 500$ (open points); L = 1000 m was arbitrarily assigned for KU study and some data are extrapolated.

It is tempting to regard the field data (KU) as being "correct" since there is no fetch effect. However, it is difficult to maintain controlled conditions with respect to wind speed and direction. Also, most mixing will probably take place in extreme events (storms). AH observed minimal mixing for wind speeds less than about 3.5 m/s, but very noticeable mixing for winds greater than about 8 or 9 m/s. It is also worth noting that, of the studies listed above, KR and CS used the longest fetches and they both attempted to reduce end effects by allowing water to recirculate in their test sections. These studies seem better at reproducing field conditions.

As shown above, the use of u_* does not provide a good collapse of data from different experimental setups, and there is also apparently no simple dependence on L to correct for end effects. An alternative approach is to redefine u_s in terms of the actual velocities produced with each particular test. For example, KI initially suggested using the return flow velocity along the interface, u_r, implying that it was more important than u_* in driving entrainment. AH defined u_s as a function of both u_* and u_r and obtained a good collapse of data from their two test sections. This function was of the form

$$u_s = (u_*^3 + k^3 u_r^3)^{1/3} \quad , \qquad (2)$$

where k is a constant. Also, Atkinson and Wolcott (1990) have recently demonstrated the use of a similar procedure in combining velocity scales from an experiment in which mixing was driven by both a mean shear and an oscillating grid.

The variation of exponent values for the entrainment relationships in Table 1 is not of great concern, since a constant value is not expected to be applicable over the entire range of field conditions. Christodoulou (1986) reviewed a number of entrainment experiments with mean shear and showed that n changed with Ri. Although he did not consider wind-mixing specifically, the same general result should hold here.

Conclusions

It is difficult to come to a definite conclusion regarding the exact entrainment relationship for wind-induced mixing, given the wide range of experimental results reported. This makes it especially hard to extrapolate laboratory results to field conditions, since physical limitations imposed by the experimental apparatus appear to strongly influence the mixing rates. However, longer fetches (at least 7 m) appear to give results that approximate field measurements, at least for low to moderate Ri. At higher Ri there is still some uncertainty in E values. Considering Fig. 1, it is felt that results from CS, KR, AH7 and KU provide a reasonably consistent set of experimental results, though it is unfortunate that CS and KR did not examine higher Ri.

Due to the physical limitations imposed in a laboratory setting, it is important to determine details of the velocity distribution in the mixed layer. With some care in defining u_s it should be possible to correlate results for different fetches, but the use of longer fetches is strongly suggested for more direct extrapolation to field studies.

References

- Atkinson, J. et al. (1984), Tech. Rep. 300, MIT.
- Atkinson, J. and D. Harleman (1987), Solar Energy 38, 389-403.
- Atkinson J. and S. Wolcott (1990), J. Hyd. Eng. 116, 397-413.
- Caussade, B. and A. Souyri (1986), Advances Aerodyn., Fluid Mech., Hyd., ASCE Spec. Conf. 728-735.
- Christodoulou, G. (1986), J. Hydr. Res. 24, 77-92.
- Kit, E. et al. (1980), J. Hyd. Res. 18, 35-58.
- Kranenburg, C. (1984), J. Fluid Mech. 145, 253-273.
- Kullenberg, G. (1977), Estuarine and Coastal Mar. Sci. 5, 329-338.
- Shelkovnikov, N. and G. Alyavdin (1982), Oceanology 22, 140-144.
- Wu, J. (1973), J. Fluid Mech. 61, 275-287.

ON THE INTERFACE PHENOMENA IN TWO-LAYER STRATIFIED FLOW

by Borislav V. Georgiev
Institute of Water Problems
Bulgarian Academy of Sciences
Sofia 1113, Bulgaria

Abstract

Some results of experimental studies and analyses on the distribution of velocity, density and turbulent velocity fluctuations in interface of uniform two-layer stratified flow are reported. The relation of interfacial shear stress and friction factor from Reynolds and densimetric Froude numbers is discussed.

Introduction

The considerable interest in stratified flows in recent years has been prompted by their increasing importance in water resources management and environmental protection. The proper understanding of stratified flow mechanism and the possibility of its control in many practical cases would contribute to limiting the harmful effects of substances transported by it and the negative impact on water environment or to achieving certain engineering advantages.

Velocity and density distribution

Ippen and Harleman [7] have suggested an analytical solution for velocity distribution in laminar flow. A dimensionless form of this distribution is:

$$\frac{u}{u_m} = 1 + 2\frac{z}{h_2} - \frac{1}{2J}\left(\frac{z}{h_2}\right)^2 + \frac{1}{3}\frac{z}{h_2} - \frac{1}{12} \qquad (1)$$

where u is the local velocity, u_m is the mean velocity, z is the distance to the point of local velocity, h_2 is the layer depth, $J = Fr/Re\ I$ is a factor taking into acount the densimetric Froude number, Reynolds number and the botton slope.

In the case of turbulent density flow the following equations for velocity and density distributions are obtained [5] using Laplace integral transformation:

$$\frac{u_o - u}{u_o - u_1} = \mathbf{erfc}\ \phi \qquad \text{and} \qquad (2)$$

$$\frac{\rho_2 - \rho}{\rho_2 - \rho_1} = \frac{1}{2}\left(1 - \mathbf{erfc}\ \phi\right) \qquad (3)$$

where u_o, u_1 and u are the maximum, interfacial and local velocities, ρ_2, ρ_1 and ρ are the densities in upper and lower layer and local point and **erfc** is the complimentary error function, which has been tabulated.

A series of flume experiments [3,4], covering the range of **Re** from 300 to 14000, has been used to verify above mentioned equations. The experiments have been caried out in a laboratory flume eigth meters long, 0.29 meter width and about 0.35 meters total depth of two layers. The depth of moving lower layer varies from 9 to 16 centimetres. The experimental results allow the distinguishing of three various types of velocity distributions with respect of Re: for laminar flow (Re $\leq$ 780), corresponding to equation (1); for turbulent flow (Re $\geq$ 1700), corresponding to eq. (2); and velocity distributions for the transition region.

Distribution of turbulent velocity fluctuations

A lack of analytical methods for determination of the turbulent intensity makes the experimental results a single source of information for such important flow characteristics. In present experiments an impulse light photo technique has used to visualize and to register the instantaneous turbulent velocities. Standard statistical method has applied to obtain time average velocities and intensities of turbulence in interfacial region as well as for entire flowing layer (Fig. 1). The generalized results of these experiments show a similar distribution of longitudinal and vertical intensities ($\sqrt{u'^2}/u_o$ and $\sqrt{w'^2}/u_o$). The covariance $u'w'$ has its extremes in the regions of high velocity gradients (at the interface and near the bottom).

The limited range of experiments has involved some doubts on the representativeness of results obtained and their applicability in the field conditions. After first reporting of these data [4] the author's attempts for more information about the magnitude of these parameters were with a little success. Some single results of LDA measurements in two-layered stratified exchange flow [1], processed here in the same manner as author's data show a considerable differences. The intensity of turbulence ($\sqrt{u'^2}/u_o$ and $\sqrt{w'^2}/u_o$) obtained in our experiments is obout ten times higher than this reported in [1]. On the other hand the relations between vertical and longitudinal turbulent intensities $(\{\sqrt{w'^2}/u_o\}/\{\sqrt{u'^2}/u_o\})$ in the interface are about 0.8 in our results and 0.4 in [1]. The data for a turbulent covariance $(u'w'/u_o^2)$ demonstrate the same discrepancy.

Resistance in the interface

The interfacial shear stresses can be described in the most general form as

$$\tau_i = -\rho u'w' + \mu(du/dz)_i \qquad (4)$$

where $u'w'$ is the covariance of the longitudinal and vertical turbulent components of velocity in an interface, and $(du/dz)_i$ is the gradient of time average velocity in the interface. The $u'w'$ values in interface , obtained by processing the instantaneous turbulent velocity components, are used to determine the interface friction factor for each experiment.

The shear stress in interfacecould be expressed by the friction factor in analogy to the rigid boundary at homogenious flows:

$$\tau_i = \frac{f_i \rho (\Delta v)^2}{8} \qquad (5)$$

where Δv is the relative velocity between two layers and in the present case is equal to u_2.

If data on the interfacial friction factor (f_i) from a number of sources have been ploted against the appropriate Reynolds number, a

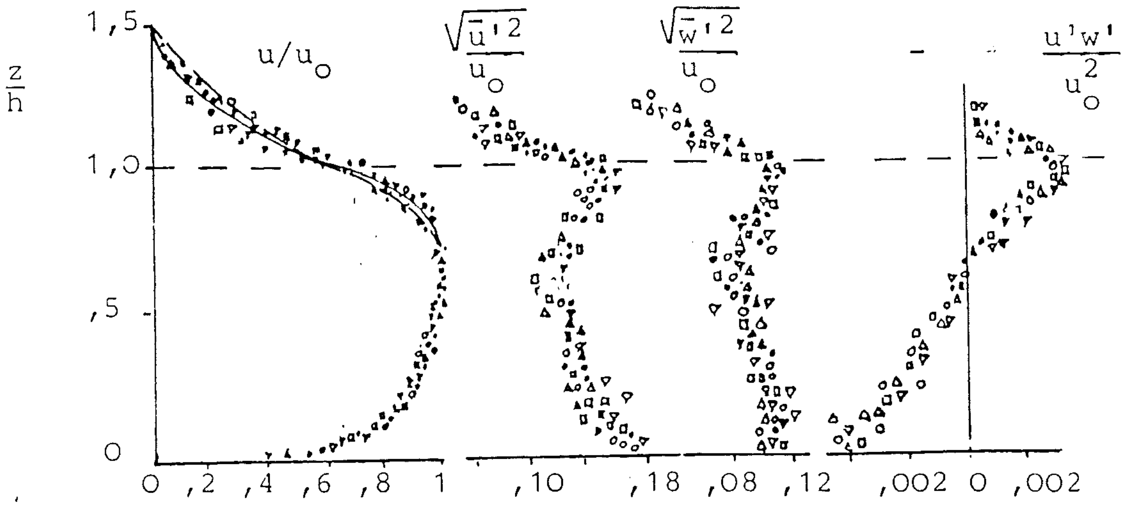

Fig. 1 Velocity parameters of turbulent density flow, obtained from 16 experiments (3380<Re<13260)

large scatter could be seen. Where is the cause for this situation?

Harleman and Ippen[7] have suggested to use a simple relation between f_i and f_b in the case of bottom density flow. According their analysis for a laminar density flow under a stagnant lighter fluid, $f_i = 0.64\ f_b$, where $f_b = 16/Re$ and Re is the lower layer Reynolds number based on the hydraulic radius. Hence from these relations we can estimate $f_i = 10.24/Re$. But in the case of a moving upper layer, there is not possible to use such relation between interfacial and botton friction factors. It is evident that a relation between interfacial and bottom friction factors is not applicable in all cases of two-layered stratified flows and one other type of relation could be found.

The analysis of governing factors on interfacial phenomena allows to seek the combined effect of viscous forces (expressed by Re) and inertial forces effected the interface stability(expressed by Fr').

In the early 1970's on the basis of limited own experiments and some data from other sources Georgiev[6] made an attempt to plot a graphical relation

$$f_i = \phi(Re,\ Fr') \qquad (6)$$

where: $Re = u_2 R/\nu$ and $Fr' = u_2^2/\{g(\Delta\rho/\rho)R\}$

The following reasons were in the basis of a search for such relation. From qualitative discussions [3, 8] it seems that fi should depend on the velocity profile (or type of flow: bottom density current, arrested wedge, exchange flow), on the Reynolds number, and on the stability characteristics in interface (expressed by densimetric Froude number or overall Richardson number, Ri_i). Harleman and Ippen [7], assuming a plane interface and no mixing, have obtained for a laminar flow - $f_i = 11.3\ /\ Re$. Therefore the shear stress depends on the second term of equation (4) only.

The instability of internal waves in the initial stages of turbulent flow causes an exchange of momentum between the upper layer and the lower layer. The interfacial shear also varies with the stage of development of the intermediate layer. In the present experiments the

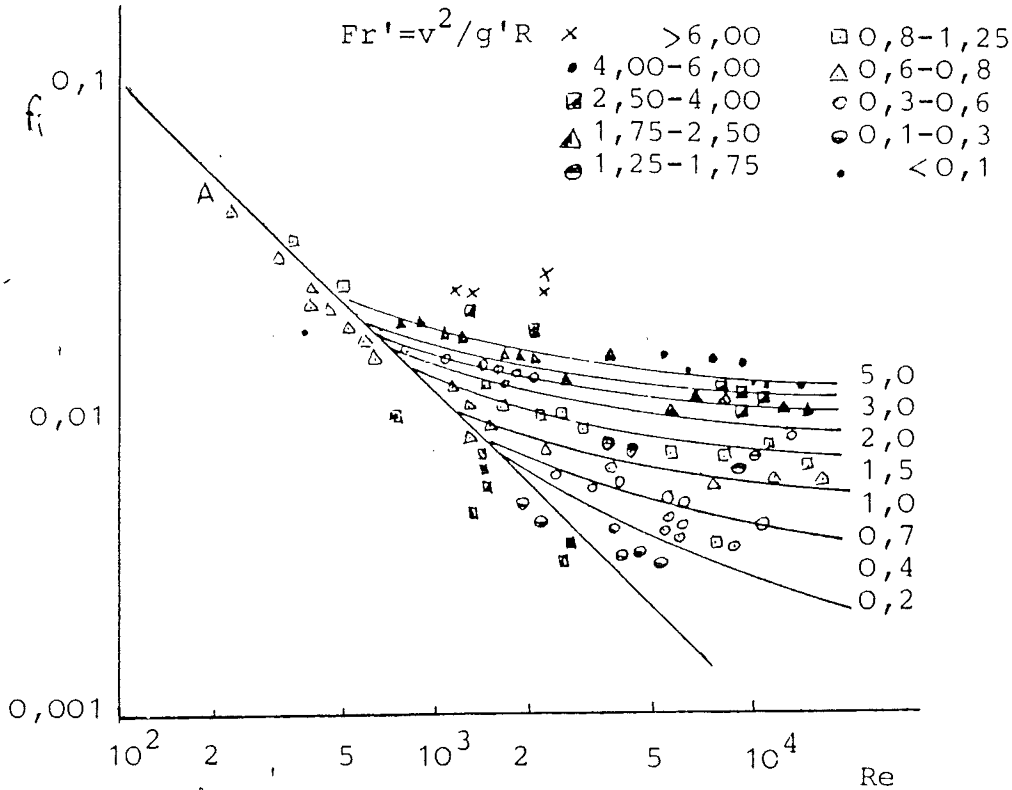

Fig. 2 Variation of the interfacial friction as a function of Re and Fr'; A is a linear equation.

intermediate layer has continuously swept and the sharp interface has maintained so that for the major part of the interfacee the interfacial shear is primarily due to turbulent momentum exchange. On the basis of such analysis of the turbulent density flow a new parameter reflecting the process of interfacial instability and turbulent mixing is necessary to be added. A number of other investigators have reached to the same conclusion [8, 9, 10], that the interfacial friction factor could be influenced by the densimetric Froude number which expresses the stability phenomena in interface. Thereby one important fact could be established: if the interface friction in a laminar density flow depents on Re only, the densimetric Froude number would influence the interfacial friction in turbulent density flow. So the greater the value of Fr', the higher interface resistance. Using the author's experimantal results and some data from other sources available in this time [6], processed in the sense of the above considerations, a graphical relation $f_i = \phi(Re, Fr')$ was plotted (Fig. 2). The experimental values of fi for laminar flow follow the linear equation given in [7]. The experimental data begin to deviate from the line at Re> 600. The magnitude of these deviations seems to be proportional to Fr'.

An important problem arises when the experimental data have processed. In many cases for typical range of Re and bottom roughness in laboratory flumes [5, 8 etc] the relation between interfacial and wall friction varies from 0.5 to 1.0. This fact indicates that the influences of fluid and rigid boundaries of density flow have the same order. So if the hydraulic radius has used for estimation of Re and Fr', the wet perimeter has to include not only the bottom and flume walls but also the interface. This approach of calculation has been used for an estimation of the hydraulic radius.

Values of friction factor in interface for turbulent flows are obtained from laboratory and field data by fitting known solutions of the stratified flow equation to data using various approaches. Many of the turbulent laboratory experiments were carried out near the transition from laminar to turbulent flow and this may account for the large scatter and wide discrepancy between the results of the various experimenters.

Intersting results are reported [9] from field measurements and empirical relation of the interfacial friction coefficient from Re and Fr'. This relation confirms in field conditions the considerations given above. The interface of the density current in these field measurements seems to be hydraulically rough because of high Froude number.

Conclusion

The present discussion is a simple attempt to shed more light on the problems of interface phenomena in two-layer stratified flow. The overall conditions at the interface and especially the interfacial shear are influenced by instability of internal waves and turbulence generated at the interface. The considerations given here can be useful in further studies in large scale flume experiments and field measurements at higher Reynolds numbers. The efforts in such study are needed to enlarge our entire knowledge on the interfacial phenomena at stratified flows.

REFERENCES

1. Anonimus, Hydrodelft, 74, 1986, p. 15.
2. Abraham G., M. Karelse and A. G. van Os, On the magnitude of interfacial shear of subcritical stratified flows in relation with interfacial stability, Delft Hydralics Laboratory publication No 225, 1980.
3. Georgiev B., Some results of researches on the dynamic characteristics of density flows, Reports of the Institute of Water Problems, BAS, vol. 12, 1970, (in bulgarian).
4. Georgiev B., Some Experimental Investigation on Turbulent Characteristics of stratified Flow, International Symposium on Stratified Flows, IAHR, Novosibirsk, 1972.
5. Georgiev B., Dynamic characteristics of two-layer density flows, Thesis for PhD, Institute of Water Problems, 1974, (in bulg.).
6. Georgiev B. On the interfacial resistance coefficient in two-layer density flow, Technical Ideas, BAS, No 2, 1974, (in bulg.).
7. Harleman D. R. F., Stratified Flow, in Hand Book of Fluid Dynamics, McGraw-Hill Book Co, NY, 1961.
8. Lofquist K., Flow and stress near an interface between stratified liquids, The Physics of fluids, vol. 3, No 2, 1960.
9. Ookubo K. and Y. Maramoto, Density current induced by the surface cooling in Lake Biwa, XXII Congress of IAHR, Lausanne, 1987.
10. Orlob G. T. (Ed.), Mathematical Modeling of Water Quality: Streams, Lakes and Reseroirs, John Wiley & Sons, 1983.

SHEAR STRESS AT THE INTERFACE OF A TWO-LAYERED DENSITY STRATIFIED OPEN CHANNEL FLOW

R. Friedrich and E.J. Plate

Sonderforschungsbereich 210
Universität Karlsruhe
Karlsruhe FRG

Abstract

Internal shear stress at the interface of fluid layers with different densities controls the thickness, the velocities, and the stability of the layers. Quantification is needed for a reliable calculation of the flow of layers with large horizontal dimensions as given in salt water wedges in estuaries, warm and cold water layers in slowly flowing rivers as well as in several oceanographical or limnological processes.

Experiments with fluid layers consisting of fresh and salt water were carried out in a rectangular open channel with smooth and rough bottom. The flow rate, the layer depth and the densities were changed. Thus, different flow situations occurred with interfaces varying from smooth to wavy and finally to mixing. The interfacial shear stress was calculated by momentum balance. The selected parameters in the shear stress diagrams take into account the relative velocities of the two layers. Both the effect of mixing on the shear stress and a stabilty criterion are also shown.

Introduction

Interfacial shear stress acting over long distances at the interface between two layers of fluid with different densities has an decisive effect on the flow conditions. The resulting layer depths, velocity distributions etc. depend on the adopted magnitude of the internal friction coefficient. In spite of the importance of the friction coefficient and the numerous investigations in that field, reliable information is not available as yet. The reports of the Delft Waterloopkundig Laboratorium (R 880, 1974 and R 880-2, 1977) show:

- the data scatter tremendously over several decades,
- Reynolds numbers >1000: there neither exists any clear dependency of the friction coefficient on the Reynolds number nor on the so-called Keulegan stability parameter,
- Reynolds numbers < 1000: there seems to exist some dependency on the inverse Reynolds number.

Bo Petersen (1980 and 1986) selected data of several publications concerned with dense bottom current, plane buoyant jet, lock exchange flow, arrested salt wedge and oil film on water under wind shear. He recommends these data for comparison purposes. Eq. 1, given by Bo Petersen, describes the dependency in the turbulent flow region:

$$(2/f_z)^{1/2} = 2.45 \cdot [(\ln (Re_{iz} \cdot (f_z/2)^{1/2}) - 1.3] \quad . \tag{1}$$

The function and the selected data are shown in Fig. 2. In Eq.1 the friction coefficient is defined by

$$f_z/2 = (\tau_z/\rho) \; / \; (u_m - u_z)^2 \quad , \tag{2}$$

with $Re_{iz} = (u_m - u_z) \cdot (y - h_2) \; / \; \nu$, τ_z, ρ, and u_z as shear stress, density, and velocity at the interface, h_2 as depth of the lower layer and $y - h_2$ as distance between the coordinates of the maximum velocity u_m and the interface. The details of the above publications are not repeated here. However, we extend the diagram by Bo Petersen, especially in the region Re < 1000.

Co-current two-layer flow experiments

Experiments with two-layer co-current fresh and salt water flow over smooth and rough bottom were performed in a rectangular tiltable laboratory flume in the Theodor Rehbock Flußbaulaboratorium of the University of Karlsruhe. The flume is 9 m long and 20 cm wide. The experimental device and its instrumentation are described by Friedrich (1979). In each category of experiments the given volume flow in the lower layer Q_2, the total depth h_g, and the reduced gravity g' were constant, whereas the flow in the upper layer was systematically increased, changing the interface from smooth to wavy and to strong mixing. The experimental program included the following variations: h_g = 6.5; 9.2; 10,8 cm, Q_2 = 0.1; 0.25; 0.4; 0.6 l/s, $g' = 981 \cdot (\rho_2 - \rho_1)/\rho_2$ cm/s^2 = 4.8; 6.9; 10 cm/s^2. The bottom slope was 0.001677 (rough bottom) and 0.001557 (smooth bottom).

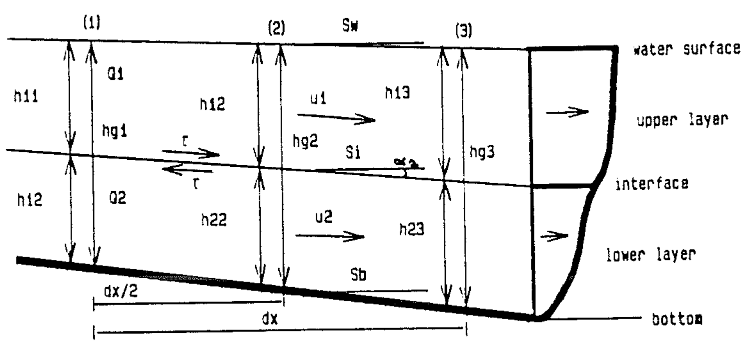

Fig. 1: Definition sketch of two-layer open channel flow

Manning's n of the flume depends (see below) slightly on a bulk Reynolds number Re_g which is based on the total flow and the total hydraulic radius R_g. $R_g^{1/6}/(n \cdot g^{1/2}) = a \cdot Re_g^{\,s}$, with a = 0.36; 2.56 and s = 0.4; 0.2 in the rough and smooth case, respectively. Using the measured data the shear stress τ_z at the interface (Fig. 1) is determined by the equation of momentum (Plate, 1974):

$$- \rho_1 \cdot Q_1 \cdot u_{11} + \rho_1 \cdot Q_1 \cdot u_{13} - 0.5 \cdot \rho_1 \cdot g \cdot b \cdot h_{11}^2 + 0.5 \cdot \rho_1 \cdot g \cdot b \cdot h_{13}^2 +$$

$$+ \rho_1 \cdot g \cdot [(h_{11} + h_{13})/2] \cdot \cos(90° - \alpha_2) \cdot dx \cdot b + 2 \cdot \tau_w \cdot [(h_{11} + h_{13})/2] \cdot dx +$$

$$+ \tau_z \cdot \cos(\alpha_2) \cdot b \cdot dx = 0 \quad , \tag{3}$$

where Q is the volume flow, u the mean velocity, g the gravity acceleration, b the width of the channel, h the layer depth, α_2 the inclination of the interface, τ_w the wall shear stress, dx/2 the cross-section distance, the first index the layer number, and the second index the cross-section number. The wall shear stress (often neglected) is given by:

$$\tau_w = 1/8 \cdot \rho \cdot \lambda_w \cdot [(u_{11} + u_{13})/2]^2 \quad . \tag{4}$$

The shear stress coefficient for a smooth surface is given by the Prandtl - Colebrook equation:

$$\lambda_w = 0.309 \cdot \log(Re_{12} \cdot f_m /7)^2 \quad . \tag{5}$$

The Reynolds number, based on the hydraulic radius, is defined by:

$$Re_{12} = \frac{u_{11} + u_{13}}{2} \cdot \frac{4 \cdot b \cdot (h_{11} + h_{13})/2}{b+2 \cdot (h_{11} + h_{13})/2} / \nu \quad , \tag{6}$$

and the Marchi coefficient (Loy, 1990):

$$f_m = 1.0433 \cdot (h_{12} /b)^{0.1772} \quad . \tag{7}$$

The application of the above mentioned equations to the flow situation in a laboratory flume causes problems. In order to avoid total mixing, flow velocities are slow, and the inclination of the free water surface is extremely small. Since, for the present situation the contributions of the first two terms in Eq. 3 are negligible, the force balance is mainly based on the layer depths at the inflow and out-flow cross-sections of the control volume. The slope of the channel bottom and the very small slope of the free surface determine the result.

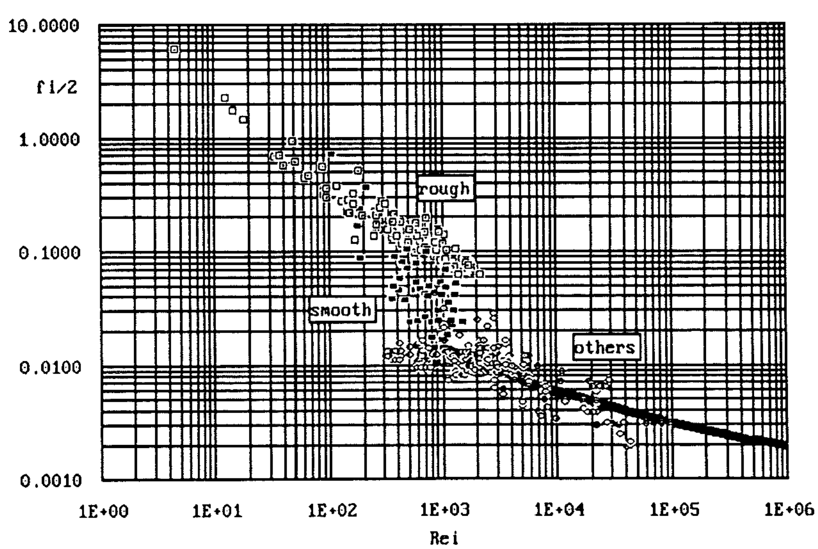

Fig. 2: The friction coefficient as function of the Re number (Note differences in definitions, Eqs. 2, 8 and text)

In order to improve the reliability of the measurements of the surface slope, the flow can be treated as a homogeneous non-uniform open channel flow. The total energy loss in the Bernoulli equation between the cross-sections 1 and 3 consists of a part caused by friction and another one by the changes in kinetic energy due to the changes of the cross-section areas. The latter part as well as the total energy loss can be obtained from experimental data. Their difference divided by the length of the control volume results in the energy slope, and thus in a Manning's coefficient for each experiment. There exists a slight dependency of Manning's n on a bulk Reynolds number. From this function the water level slope of each experiment is recalculated. The result can be controlled by the energy losses.

In Fig. 2 all data of the open channel flow experiments with rough and smooth bottom are plotted together with the selected data of Bo Petersen and the curve of Eq. 1. Comparison of all data is not easily possible, since the relative velocity in the Reynolds number and the friction coefficient of the open channel flow data are based on the difference between the mean velocity of the upper layer u_1 and the velocity of the interface u_z. The mean velocity is obtained from the measured volume flow and the depth of the upper layer and the velocity u_z from:

$$u_z = u_2 + (u_1 - u_2)\cdot a\cdot h_2/(h_1 + a\ h_2) \quad . \qquad (8)$$

This equation is derived from simple geometrical considerations. Velocity profile measurements and measurement of floating particles at the interface have shown, that in the special flow situation of Fig. 1, Eq.8 is applicable using a = 1 (Friedrich, 1979).

In Figs. 3 and 4 the ratio of the flow quantities of both layers are plotted against the (dimensional) shear stress and the ratio of the lower layer and the total depth, respectively. In comparison with the smooth case a larger interfacial shear stress is observed in the case of rough bottom as well as a bigger lower layer. Both effects contribute to the increase of the friction cofficient as shown in Fig 2.

Classification of data of the rough channel flow with respect to the reduced gravity g' (Fig. 5) or the total depth (Fig. 6) results in almost the same dependency. It is given by:

$$f_i = m\cdot Re_i^{\ n} \qquad (9)$$

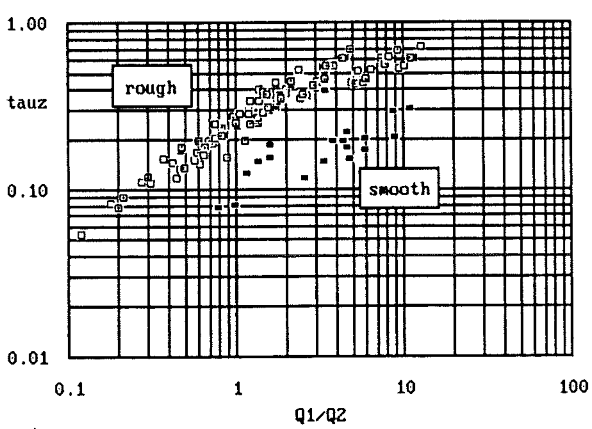

Fig. 3: The shear stress τ [g/(cm s^2)] as function of Q_1/Q_2

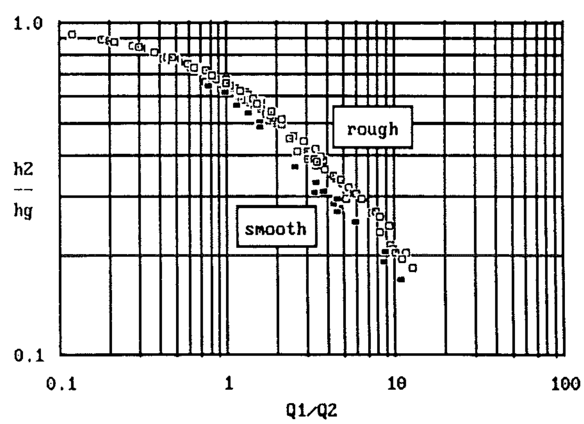

Fig. 4: The relative lower layer depth as function of Q_1/Q_2

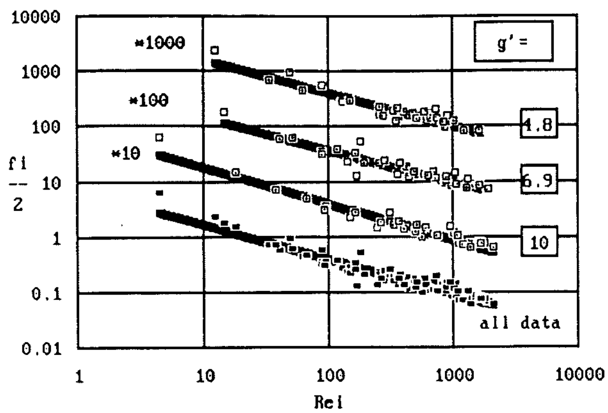

Fig. 5: The friction coefficient as function of the Re number and the reduced gravity g'[cm/s^2]

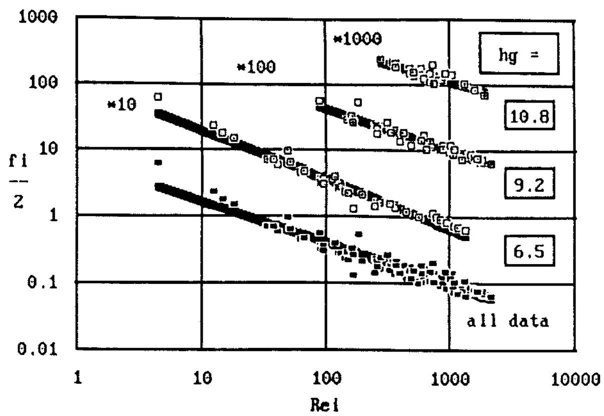

Fig. 6: The friction coefficient as function of the Reynolds number and the total depth h_g [cm]

with m = 6.9 and n = - 0.622, as global values. Refined analysis of the data of Fig. 6, however, shows some dependency on the total water depth, expressed in shape of an aspect ratio h_g/b:

$$f_i = 26.0 \cdot (0.75 - h_g/b) \cdot Re_i^{-(1 - 0.81 \cdot h_g/b)} \quad . \tag{10}$$

Eq. 10 implies that with decreasing aspect ratio (broad channels) the parameter m in Eq. 9 finally changes to 19.5 and n to - 1.0, well known from laminar flow.

Mixing and interfacial shear

A vibrating grid was used to produce a mixed layer between the fresh and the salt water layer in the above-mentioned channel (with smooth bottom). The flow depth (h_g = 8.8 cm) and the salt water flow Q_2 = 0.25 l/s) were kept constant. The fresh water flow was increased from about 0.3 to 0.85 l/s in order to change the interlayer from smooth to strong mixing. The data of a sharp interface is compared with a 1 cm and a 2 cm thick interlayer in Fig. 7 : the mixing layer causes an increase of the lower layer depth (measured from bottom to the center of the mixed layer). It can be concluded, that the interfacial shear is reduced by a mixed interlayer. This may be caused by damping the interfacial "roughness".

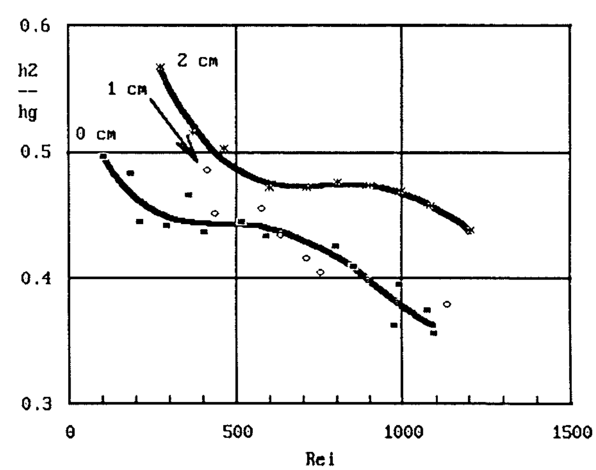

Fig. 7: The effect of a mixed interlayer (thickness= 0, 1 and 2 cm) on the lower layer depth (Q_2 = 0.25l/s, h_g = 8.9 cm in all experiments)

Stability of the interface

The following considerations demonstrate the influence of the internal shear stress on the stability of the interface. The analysis is confined to experiments with rough bottom; in future, it will be extended to smooth channel flow. The condition of the interface of the experiments in Fig. 6 (rough bottom) changed from smooth to wavy and mixing. A wave probe with two vertical wires was used to measure the ε_{rms} - values of the vertical movement of the internal waves and turbulent deformations of the interface. In spite of the fact that the wave record is somehow affected by mixed water particles, the obtained ε_{rms} values develop in the same way as the observed state of the interface. The product

$$E = \varepsilon_{rms} \cdot g'^{0.5} \tag{11}$$

represents the energy of the vertical movements of the interface and characterizes the different conditions from smooth to wavy. Applying the below outlined procedure a non-dimensional velocity gradient at the interface was determined:

$$Ri_{h2} = g'/[h_2 \cdot (du/dy)^2] \tag{12}$$

and plotted against the lower layer depth in relation to the total depth (Fig. 8). In this diagram three regression lines represent the data with $E < 0.38$ (smooth - wavy), $0.38 < E < 0.4$ (wavy - mixing), and $0.4 < E$ (strong wavy - strong mixing). The scatter of the data is caused by the above mentioned uncertainty when determining E. The regrés-sion line 'wavy - mixing' is described by:

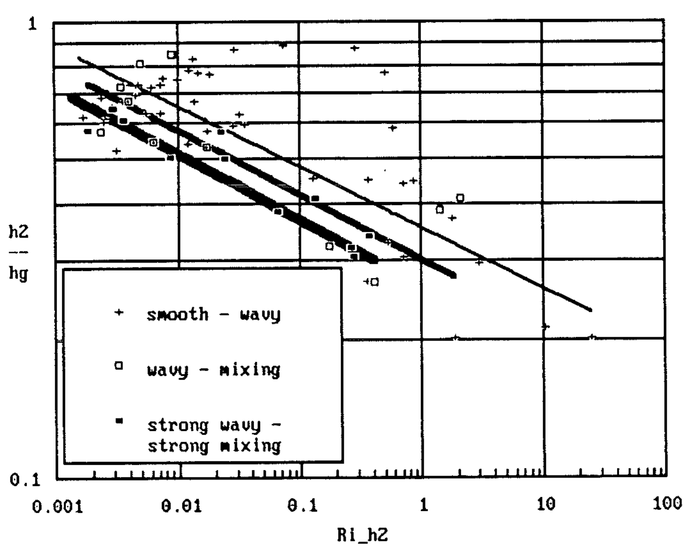

Fig. 8: The stability of the interface

$$h_2/h_g = 0.3 \cdot [Ri_{h2}]^{-1/7} \tag{13}$$

If ε_{rms} is chosen as the characteristic length scale instead of h_2 in the modified Richardson number (Eq. 12), the resulting plot is similar to Fig. 8. However, Eqs. 12 and 13 are based on basic parameters only: the layer depths, the densities, the volume flow, and the interfacial shear stress.

The velocity gradient at the interface

Assuming a linear distribution of the shear stress between the water level and the bottom, the vertical velocity distribution results from $\tau = \mu \cdot du/dy$ if the momentum exchange coefficient μ is known. The following equations include applicable vertical distributions of μ:

$$\left[\mu_l + \mu_z \frac{h_1 - y}{h_1} + k(h_1 - y)y\right] \frac{du}{dy} = \tau_z - \tau_z \frac{y}{h_1} \tag{14}$$

for the upper layer and

$$\left[\mu_l + \mu_z \frac{h_2 + y}{h2} + kb(y + h2)(-y)\right] \frac{du}{dy} = \tau_z - (\tau_b - \tau_z) \frac{y}{h_2} \tag{15}$$

for the lower layer (origin of the vertical coordinate y is the interface). τ_b stands for the bottom shear stress, μ_l for the laminar viscosity, μ_z for the momentum exchange coefficient at the interface, decreasing in a linear manner to the water level in Eq. 14, or to the bottom in Eq. 15. k and k_b are form parameters analogous to the assumptions that lead to the logarithmic velocity profile. From the conditions

$$u\ (y) = u_z \quad \text{for } y = 0 \text{ and} \qquad u_2 = (1/h_2) \int_{-h_2}^{0} u(y)dy \tag{16}$$

the parameters k_b and μ_z are calculated. Parameter k is obtained if μ_z is inserted in Eq. 14, and conditions similar to Eq. 16 are observed. Thus, du/dy and the whole velocity profile are known. Details are given by Friedrich in Larsen et al.(1990).

Acknowledgements

The study on which the paper is based is supported by the German Research Association in the frame of the Schwerpunktsprogamm "Physik abgelöster Strömungen" and the Sonderforschungsbereich 210.

References

Friedrich, R., 1979: "Stabilität der Zwischenfläche in einer zweischichtigen Gerinneströmung", Mitteilungen, Heft 13, Institut Wasserbau III, University of Karlsruhe

Larsen, P., Plate, E., Friedrich, R., Kertzscher, U., 1990: "Ablösungen an Sohlschwellen in geschichteten Strömungen", Arbeitsbericht des Instituts für Wasserbau und Kulturtechnik und des Instituts für Hydrologie und Wasserwirtschaft, University of Karlsruhe

Loy, T., 1990: "Turbulente abgelöste Überströmung von Grundschwellen und einer senkrechten Wand in einem offenen Gerinne", (not yet published) Institut für Hydrologie und Wasserwirtschaft, University of Karlsruhe

Pedersen, B., 1980: "Turbulent Entrainment and Friction in Two-Layer Stratified Flow", Monograph of the Institute of Hydrodynamics and Hydraulic Engineering, Technical University of Denmark, Series Paper No. 25

Pedersen, B., 1986: "Environmental Hydraulics: Stratified Flows" VIII, Vol. 18, Lecture Notes on Coastal and Estuarine Studies, Springer-Verlag

Plate, E., 1974: "Hydraulik zweidimensionaler Dichteströmungen", Mitteilungen Heft 3, Institut Wasserbau III, University of Karlsruhe

STRATIFIED FLOW DYNAMICS CONTROLLED BY WIND-INDUCED SURFACE TURBULENCE

G. Mocke*, A. Liné**, L. Masbernat**

* DEMAST (CSIR) PO Box 320 Stellenbosch 7600 South Africa
** Institut de Mécanique des Fluides - UA CNRS
Avenue Professeur C. Soula - 31400 - Toulouse. France

Abstract

The dynamics of the mixed layer is investigated by means of a two-equation (k,ε) model of turbulence. Special attention is devoted to the parametrization of the input of turbulent kinetic energy (TKE) at the surface, stemming from interactions between the mean, wave and turbulent fields. The turbulence model proved to be particularly effective for simulating experimental conditions when the density interface is situated in this upper layer. In an investigation into existing entrainment laws the representational nature of these two scales is demonstrated.

INTRODUCTION

An important feature of the ocean or other natural aquatic systems is the development of an upper mixed layer due to wind stress and buoyancy flux at the air-liquid interface. In the description of upper layer dynamics subject to wind action one is confronted with two fundamental classes of problems: -the quantification of energy transfer from the wind to the liquid which manifests itself in the form of currents, turbulence and wave motion ; -the behaviour of layers of variable density in response to these perturbations. The mixed layer is usually defined such that within this zone a sufficiently active state of turbulence exists. This asumption is the basis for a number of so-called bulk models first formulated by Kraus and Turner [1967] whereby the equation for turbuelnt kinetic energy (TKE) is integrated across the mixed layer. These models vary greatly in sophistication (cf. Sherman et al [1978] and Imberger and Hamblin [1982] for reviews) and usually include empirical relations for the evaluation of TKE production at the boundaries and the density interface, the dissipation rate of TKE and the buoyancy flux. A somewhat contentious approximation is that the dissipation term is estimated to be a certain empirical function of the production term. The situation is aggravated when one considers that the surface production of TKE is commonly assumed to be proportional to the third power of the wind friction velocity (u_*). Such a parametrization which adjusts the proportionality constant only as a function of the wind velocity is seemingly a gross simplification of a complex upper region dominated by mean, wave and turbulent field interactions.

Indeed, recent experience (cf. Kitaigorodskii et al [1983], Terray [1985]) has indicated that over depths seemingly related to statistical sizes of the surface waves, levels of turbulence which greatly exceeds that predicted for wall bounded shear flows ($\equiv u_*$) prevails. The interaction mechanisms for the generation of this turbulence is still not completely understood, although it is generally recognized that the situation is more complex than the immediately physically recognizable phenomenom of large scale surface wave breaking. Recent experimental studies carried out by Cheung and Street [1988] have recorded one such interaction mechanism whereby the wave field changes the slope of the mean flow hence leading to an increase in the turbulence which draws its energy from this flow.

The interaction of turbulence located within a mixed layer of instantaneous depth h and a density interface results in the entrainment of fluid from the lower layer at a rate We = dh/dt. In investigating this situation experimentally a number of studies (cf. Nokes [1988] and Christodoulou [1987] for partial review) have proposed entrainment laws relating this rate to a dimensionless Richardson number Ri representing the relative importance of buoyancy to inertial forces.

No general consensus has been reached in terms of a universal relationship relating the entrainment velocity and the Richardson number. At least to some extent this is probably due to the great variability in experimental conditions employed. Categorization may be made according to the mechanism of turbulent generation employed: a surface shear (Kantha et al [1971]), an oscillating or falling grid (Turner [1968], Hopfinger & Toly, E & Hopfinger [1986] and Hannoun & List [1988]), or by surface wind stress (Kranenburg [1984], Wu [1972], Kit et al [1980]). The physically most meaningfull case would seem to be with a wind stress, however as for surface shear experiments, constraints related to canal geometries often intrude. Not only as oscillating grid experiments avoid extraneous side effects, but also previous studies carried out for unstratified conditions (Hopfinger & Toly [1976]) have provided analytical expressions describing the essential properties of the turbulence throughout the flow.In relating Ri and the entrainment coefficient E,this approach has essentially presented two confligting hypotheses, both with theoretical support. In terms of a power law $E = KRi^{-n}$, n was adopted to be either 1.75 (Fernando & Long [1983] or 1.5 (E & Hopfinger [1984]). In a review of a great number of different experimental observations, Christodoulou [1986] was able to regroup most experimental data points through the definition of a velocity parameter charasteristic of the mean flow in the mixed layer. The only exceptions were the wind stress experiments of Wu [1973] and Kit et al. [1980] which eluded such a parametrization, seemingly correspondant with the complicated nature of this surface generated turbulence.Although computationally more cumbersome than the above mentioned integral models, 1D-vertical model avoid the a priori assumptions necessary for integrating over the extent of the mixed layer. In applying a buoyancy extended version of a classical two-equation (k,ε) turbulence model with boundary conditions initialized according to laboratory and field observations a more realistic representation of the turbulence and conservative properties in the upper mixed layer is desired. In addition the previously proposed entrainment laws are investigated with particular attention to the wind induced turbulence.

TURBULENCE k-ε MODEL

Introducing classical concepts for a unidimensional situation the time-averaged non-convective turbulence equations may be written in the form :

$$\frac{\partial k}{\partial t} = \frac{\partial}{\partial z}\left(D_k \frac{\partial k}{\partial z}\right) + \nu_t \left(\frac{\partial U}{\partial z}\right)^2 + Ri\, \nu_t \frac{\partial \Phi}{\partial z} - \varepsilon$$

$$\frac{\partial \varepsilon}{\partial t} = \frac{\partial}{\partial z}\left(D_\varepsilon \frac{\partial \varepsilon}{\partial z}\right) + C_{2\varepsilon} C_\mu k \left(\frac{\partial U}{\partial z}\right)^2 + C_{3\varepsilon} Ri \frac{C_\mu}{\sigma_t} k \frac{\partial \Phi}{\partial z} - C_{2\varepsilon} \frac{\varepsilon^2}{k}$$

$$\frac{\partial \Phi}{\partial t} = \frac{\partial}{\partial z}\left(D_{\Phi} \frac{\partial \Phi}{\partial z} \right)$$

where the variables have been non-dimensionalised. This gives rise to a reference Richardson number of the flow Ri in the buoyancy term.The values for the empirical constants are well represented for classical non-buyant flows (Launder and Spalding, [1974]) with the buoyancy extension stratification effects are felt through σ_t and the empirical constant $\sigma_{3\varepsilon}$ of the ε equation. With reference made to the work of Gibson and Launder [1976] and to Svenson [1980] for a similar flow situation these parameters are adjusted according to the degree of stratification. A further adjustment was deemed necessary with respect to the classical value of $C\mu = 0.09$ which has been evaluated from experiments carried out in flows characterized by local equilibrium between production P and dissipation ε of TKE. There are zones which deviate substantially from this ratio $P/\varepsilon = 1$ and hence reference is made to the relation proposed by Gibson and Launder [1976].

The wall boundaries represent the classical situation where the universal law of the wall is applicable. A free surface subject to wind stress presents a considerably more complex situation. Lacking explicit theoretical relations, we refer to laboratory and field measurements for the evaluation of this contribution. The field measurements refered to are those carried out by Donelan on Lake Ontario as reported by Kitaigorodskii et al [1983]. Using a laser-Doppler-anemometer (LDA) system Prodhomme [1988] made turbulence and mean-flow measurements in the 1 m deep x 15 m long wind wave flume of the Toulouse Fluid Mechanics Institute (IMFT). In a like manner to that of Howe et al [1982] and Kitaigorodskii et al [1983], wave and turbulent motions were separated by considering a linear deterministic coherence between the surface displacements and the purely wave induced fluctuations. Observations indicated that turbulent and wave induced motions were roughly of the same order of magnitude in an upper zone. This upper layer was bounded below by a zone correspondant with the classical motion of local mean shear production and dissipation of the TKE.

For the three experimental wind velocities considered 4, 8 and 11 m/s evaluation of the interfacial turbulence scales k_I and l_I is descriptive of the turbulence levels immediately below. In a like manner, effective turbulent scales were extracted from the exponential depth dependances proposed by Kitaigorodskii et al. [1983] for wind speeds of 6.1, 10.7 and 11.2 m/s in Lake Ontario.

For the parametrization of k_I, if wave-turbulence interactions are initially ignored this parameter may be related to the wind friction velocity in terms of a constant flux surface layer. In proposing a fetch parameter (ω the peak wave frequency and Hrms the R.M.S. wave height) similar to that of Kitaigorodskii et al [1983] a possible fit for the two sets of data would be following relation

$$\frac{k_I^{0.5}}{u_*} = 0.175 \, \frac{\omega \, \mathrm{Hrms}}{u_*} + 2.6$$

Care should be taken in interpreting such a relation not only due to the paucity of data values but also due to certain disparities in the mechanisms for wave generation between laboratory facilities and natural conditions as evoked by Wu [1972] and Harris [1976]. With wave growth even over the typically large fetch of the natural environment rather slow, the three data points at the limited and constant fetch of the laboratory are probably best representedd by a single point.

For the representation of the other important turbulent parameter, the interfacial length scale l_I, the subjectivity inherent in determining this value, especially at weak laboratory wind velocities where the upper layer is very limited, preduced a similar approach as for k_I. However, in comparing estimations with the wave statistics this parameter was found to scale fairly well on the length scale for wave motion decay with depth: $l_I = \lambda / 4\Pi$.

The governing equations are discretized using a finite difference approach. An implicite numerical scheme is employed for the resolution whereby a Thomas algorithm is applied to the triangular matrix.

MODEL SIMULATIONS

Intransient, homogeneous conditions

The validity of the interfacial turbulence scales are initially investigated in comparing experimental measurements with simulations. Although the interest of this study is primarily the upper layer, by means of a purely numerical exercise the parametrization of the mean shear production term P was investigated. A comprehensive representation of the flow regime in the flume, including observed secondary Langmuir type circulations, would considerably complicate our systems of numerical equations.Likewise a computation of two production terms at the canal axis, from the mean longitudinal velocity gradient and a secondary flow contribution, compared well

$$P = \frac{u_*^3 \, l_I^{1.5}}{\kappa \, z^{2.5}}$$

It should be noted that this term was not maintained in the upper zone.

Transient, stratified flow

In a series of tests carried out in the same IMFT wind wave flume, Souyri [1986] measured entrainment rates with an initial temperature interface at a mid-depth of the flume. This effectively placed the density interface below the upper layer and physically astute adjustments in the production term were required for simulating the measured rates. One such adjustment was the consideration of production due to secondary Langmuir type circulations blocked above the interface and having intensities inversely proportional to the depth of the mixed layer.

In fact, most previous wind wave flume entrainment experiments were carried out over significantly shallower water depths and such is the case with salinity gradient experiments of Kit et al [1980]. Although the overall dimensions of this canal were somewhat smaller overall scales is not deemed to be very important. Transposing turbulence scales for IMFT conditions the density interface is found to be well within the upper layer. In the interest of reducing ambiguity the production term which should have some dependance on the geometrics of the flume, is made negligeable.

Entrainment relations

In the like manner to that of Kit et al [1980], and most previous experimental investigations, the entrainment coefficient E and Richardson number Ri parameters were evaluated at a constant depth of the interface. This depth D which is defined to be within the upper layer is used along with the wind friction velocity for the definition of the Richardson number : $Ri_* = g\ \Delta\rho/\rho\ \ D/U_*^2$. Considering the relation $E_* = 1.5\ Ri_*^{-3/2}$ as obtained by Kit et al [1980], it would appear that the flume simulations compare well with experimental observations, at least when evaluated at the designated depth. Concerning the universality of the above relation however, the immense gap between laboratory and field data points seemingly indicates the inappropriateness of the flow parameters chosen.

Mixed layer deepening

The upper mixed layer deepens with time. From the data points a power law of the form $D = t^{-2/11}$ is fairly representational. Such an exponent compares well with the value of n = 1/4 as observed by Kit et al [1980]. It is interesting to note that for grid induced turbulence E and Hopfinger [1986] found n = 1/5 for two layer stratification and Fernando and Long n = 2/11.

Discussion and conclusions

In investigating the dynamics of the upper mixed layer subject to surface wind action this study has devoted particular attention to the upper zone The turbulence seemingly emanates from a complex interaction of the mean, wave and turbulent fields immediately below the free surface and remains rather poorly understood despite recent advances (Cheung and Street 1988). Disposing of a limited number of experimental and field turbulence observations, empirical relations for the parametrization of the interfacial scales of the turbulence k_I and l_I were explored. It was clearly demonstrated that without an effective scaling that includes the statistical wave field, in addition to a wind velocity scale, a common parametrization of both field and experimental observations is impossible. The proposed relations are far from ironclast, with cause not only the lack of observations for more contrasting wind and wave conditions, but also that in comparing fetch limited canal measurements and field observations we are dealing with two different wave development regimes.

The particular usefulness of these interfacial scales k_I and l_I is apparent in the analytical expressions describing turbulence throughout the upper layer and which have previously been verified for homogeneous conditions. Initializing a turbulence two-equations k-ε model by these interfacial scales allows the prediction of measured values throughout the upper diffusive layer. Below this upper layer the contribution of local mean shear production is explored numerically. In extending the model to buoyancy conditions, although the model does not give information on, nor explicitely take into account: billowing, bursting or turbulence collapse ; mean flow parameters such as the density gradient are well represented. The importance of adopting the correct flow parameters for representation of the entrainment rate at both laboratories and field scales is demonstrated. This is particularly true when the density interface is located within the upper layer .In the presence of an active sea state this zone can extend a significant depth and may in some cases be responsible for the relatively shallow summer thermocline.

In any event for the representation of intermittent events, such as wind bursting, or other circumstances on a diurnal or even hourly scale, the model is capable of predicting shallow density of microstructures important for interfacial transfer and biological blooming events. In conclusion although there rests room for improvement of the turbulence model extended for buoyancy effects, it would seem to respond well to global characteristics of the flow and has proved extremely useful in highlighting the importance of areas that demand further study.

REFERENCES

CHEUNG T.K. & STREET R.L. (1988) "The turbulent layer in the water at an air-water interface." J. Fluid Mech.,194,133-151

CHRISTODOULOU G.G. (1986) "Interfacial mixing in stratified flows." J. Hyd. Res.,24,77-92

E J. & HOPFINGER E.J. (1986) "On mixing acrossa an interface in stably stratified fluid." J. Fluid Mech.,166,227-244

FERNANDO H.J.S. & LONG R.R. (1985) "On the nature of the entrainment interface of a two-layer fluid subjected to zero mean-shear turbulence." J. Fluid Mech.,151,21-53

GIBSON M.M. & LAUNDER B.E. (1978) "Ground effects on pressure fluctuations in the atmospheric boundary layer" J. Heat Trans.

HANNOUN I., FERNANDO H. & LIST O.J. (1988) "Turbulence structure near a sharp density interface." J. Fluid Mech.,189,189-209

HARRISD.L. (1976) "Wind-generated waves for laboratory studies" Tecnical paper,76-12,U.S. Army,Corps of Engineers,Coastal Engineering Research Center,Fort Belvoir,Va Aug 1976

HOPFINGER E.J. & TOLY J.A. (1976) "Spatially decaying turbulencee and its relation to mixing across density interface." J. Fluid Mech.,78,155-175

HOWE B.M., CHAMBERS A.J., KLOTZ SS.P., CHEUNG T.K. & STREET R.L. (1982) "Comparison of profiles and fluxes of heat and momentum above and below an air-water interface." J. Heat Trans.,104,157-173

IMBERGER J. & HAMBLIN P.F. (1982) "Dynamics of lakes, reservoirs and cooling ponds." Ann. Rev. Fluid Mech.,14,153-187

KANTHA L.H. (1980) "Laboratory experiments on internal waves by turbulence in the mixed layer." Second International Symposium on Stratified Flows.

KIT E., BERENT E. & VAJDA M. (1980) "Mélange vertical induit par le vent ou par un ruban mouvant sur la surface d'un fluide stratifié dans un canal." J. Hyd. Res.,18,1

KITAIGORODSKII S.A.& LUMLEY J.L. (1983) "Wave-turbulence interactions in the upper ocean.Part I." J. Phys. Ocean.,13,1988-1999

KITAIGORODSKII S.A., DONELAN M.A., LUMLEY J.L. & TERRAY E.A. (1983) "Wave-turbulence interactions in the upper ocean.Part II." J. Phys. Ocean.,13,1988-1999

KRANENBURG G. (1984) "Wind-induced entrainment in a stably stratified fluid." J. Fluid Mech.,145,253-273

KRAUS B.E. & TURNER J.S. (1967) "A one-dimensional model of the seasonal thermocline, II.The general theory and its consequences" Tellus,19,98-106

LAUNDER B.E. & SPALDING DD.B. (1972) "Mathematical model of turbulence." Academic Press,London

NOKES R.I. (1988) "On the entrainment rate across a density interface" J. Fluid Mech.,188,185-204

PRODHOMME M.-T. (1988) "Turbulence sous les vagues de vent." Thèse de Doctorat de l'I.N.P.,Toulouse,France

SOUYRI A. (1986) "Turbulence sous les vagues de vent en écoulement isotherme ou stratifié thermiquement." Thèse de Doctorat de l'I.N.P.,Toulouse,France

SHERMAN F.S., IMBERGER J.& CORCOS G.M. (1978) "Turbulence and mixing in stably stratified waters"." Ann. Rev. Fluid Mech.,10,267-288

SVENSON U. (1980) "On the numerical prediction of vertical turbulent exchange in stratified flows." Second Inter. Symposium on Stratified Flows. Trondheim. Norway

TERRAY E.A. & BLIVEN I.F. (1985) "The vertical structure of turbulence beneath gently breaking waves." The Ocean Surface,395-400,Y. Toba & H. Mitsuyaso Eds

TURNER J.S. (1968) "The influence of molecular diffusivity on turbulent entrainment across a density interface." J. Fluid Mech.,33,639-656

WU J. (1973) "Wind-induced turbulent entrainment across a stable density interface." J. Fluid Mech.,61,275-287

Modelling of an Integral Length Scale for Temperature Fluctuation in Stratified Flows

By S.USHIJIMA

Abiko Research Laboratory, Central Research Institute of Electric Power Industry (CRIEPI)
1646 Abiko, Abiko-shi, Chiba-ken, 270-11, JAPAN

ABSTRACT

In a fully developed stratified shear flow, an integral length scale for temperature fluctuation can be defined as an integrated value of the vertical distribution of the cross-correlation coefficient. A second-order closure transport equation was derived for the integral scale and its algebraic expression was also proposed in this paper. The validity of the model was shown through the comparison with the results obtained by turbulence measurements in stratified flows.

INTRODUCTION

An integral length scale for temperature fluctuation (L_θ) is one of the basic variables that have close relation to the turbulence structure in stratified flows. Thus, to propose the modelled expression for the integral scale has an important meaning in deriving various relationships for turbulent mixing processes and other features.

Rotta [1] made an investigation on an integral scale for velocity fluctuation (L) and derived its modelled transport equation. It was used as one of the equations that constitute a turbulence model by such as Rodi [2]. In this paper, the second-order closure transport equation for L_θ is derived in a similar way to Rotta. In a fully developed stratified flow, this equation can be described as a simple algebraic expression, including two model constants. The values of the constants and the validity of the algebraic model are discussed with the results of turbulence measurements.

《NOMENCLATURE》

- t =time
- x =coordinate in streamwise direction
- y =coordinate in vertical direction
- z =coordinate in transverse direction
- $\overline{U}$ =mean velocity in x direction
- $\overline{V}$ =mean velocity in y direction
- $\overline{\Theta}$ =mean temperature
- u_k =k component of fluctuating velocity
- u, v, w =x, y, z components of fluctuating velocity
- θ =fluctuating temperature
- k =turbulence energy
- ε =dissipation rate of k
- T_1 =temperature of upper layer
- T_2 =temperature of lower layer
- U_1 =mean velocity of upper layer
- U_2 =mean velocity of lower layer
- H =total depth of stratified flow

TRANSPORT EQUATION FOR L_θ

In a fully developed stratified shear flow, the variables change mainly in the vertical direction. As a result, the integral scale L_θ is defined with one-dimensional vertical integration as follows:

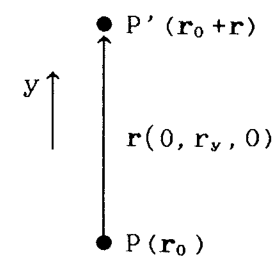

Fig. 1 P and P'

$$L_\theta(\mathbf{r}_0, t)=\frac{1}{\overline{\theta^2}(\mathbf{r}_0, t)}\int_{-\infty}^{\infty} R(\mathbf{r}, \mathbf{r}_0, t)dr_y \quad ---(1)$$

where $R(\mathbf{r}, \mathbf{r}_0, t)$ is given by

$$R(\mathbf{r}, \mathbf{r}_0, t)=\overline{\theta(\mathbf{r}_0, t)\,\theta(\mathbf{r}_0+\mathbf{r}, t)} \quad ---(2)$$

and it means cross-correlation function between two points separated vertically by r_y; P and P' shown in Fig. 1. The overbar defines ensemble or time averaging and the components of the vectors are $\mathbf{r}_0(x_0, y_0, z_0)$ and $\mathbf{r}(0, r_y, 0)$. From Eq. (1), we can obtain the transport equation for L_θ by integrating each term of the transport equation for $R(\mathbf{r}, \mathbf{r}_0, t)$. Consequently the following equation for L_θ is obtained:

$$\underbrace{\frac{\partial}{\partial t}\{L_\theta(\mathbf{r}_0,t)\,\overline{\theta^2}(\mathbf{r}_0,t)\}}_{C}+\underbrace{\overline{U}(\mathbf{r}_0,t)\frac{\partial}{\partial x}\{L_\theta(\mathbf{r}_0,t)\,\overline{\theta^2}(\mathbf{r}_0,t)\}}_{C}$$

$$+\underbrace{\overline{V}(\mathbf{r}_0,t)\frac{\partial}{\partial y}\{L_\theta(\mathbf{r}_0,t)\,\overline{\theta^2}(\mathbf{r}_0,t)\}}_{C}+\underbrace{\int_{-\infty}^{\infty}\{\overline{V}(\mathbf{r}_0+\mathbf{r},t)-\overline{V}(\mathbf{r}_0,t)\}\frac{\partial}{\partial r_y}R(\mathbf{r},\mathbf{r}_0,t)dr_y}_{C}$$

$$\underbrace{+\frac{\partial}{\partial y}\overline{\Theta}(\mathbf{r}_0,t)\int_{-\infty}^{\infty}R_{TV}\,dr_y+\int_{-\infty}^{\infty}R_{VT}\frac{\partial}{\partial y}\overline{\Theta}(\mathbf{r}_0+\mathbf{r},t)dr_y}_{P}$$

$$\underbrace{+\int_{-\infty}^{\infty}\frac{\partial}{\partial y}\overline{v(\mathbf{r}_0,t)R'(\mathbf{r},\mathbf{r}_0,t)}dr_y-\alpha\frac{\partial^2}{\partial y^2}\{L_\theta(\mathbf{r}_0,t)\,\overline{\theta^2}(\mathbf{r}_0,t)\}}_{D}\underbrace{-2\alpha\int_{-\infty}^{\infty}\frac{\partial^2}{\partial r_k^2}R(\mathbf{r},\mathbf{r}_0,t)dr_y}_{E}$$

$$\underbrace{+\int_{-\infty}^{\infty}\frac{\partial}{\partial r_k}\{\overline{u_k(\mathbf{r}_0+\mathbf{r},t)R'(\mathbf{r},\mathbf{r}_0,t)}-\overline{u_k(\mathbf{r}_0,t)R'(\mathbf{r},\mathbf{r}_0,t)}\}dr_y=0}_{E} \quad ---(3)$$

where R', R_{TV} and R_{VT} are given by $\overline{\theta(\mathbf{r}_0, t)\,\theta(\mathbf{r}_0+\mathbf{r}, t)}$, $\overline{v(\mathbf{r}_0, t)\,\theta(\mathbf{r}_0+\mathbf{r}, t)}$ and $\overline{v(\mathbf{r}_0+\mathbf{r}, t)\,\theta(\mathbf{r}_0, t)}$, respectively. The terms in Eq. (3) are labelled in the following way: C≡convection, P≡production, D≡diffusion and E≡dissipation. The terms except dissipation terms (E) can be modelled in the similar way to Rotta [1] and they are written as follows:

$$C=\frac{\partial}{\partial t}(L_\theta\,\overline{\theta^2})+\frac{\partial}{\partial x}(\overline{U}L_\theta\,\overline{\theta^2})+\overline{V}\frac{\partial}{\partial y}(L_\theta\,\overline{\theta^2}) \quad ---(4\text{-a})$$

$$P=C_{L1}L_\theta\,\overline{v\theta}\,\frac{\partial\overline{\Theta}}{\partial y} \quad ---(4\text{-b})$$

$$D = -C_{LD}\frac{\partial}{\partial y}\left(k^{1/2}L_\theta\overline{\theta^2}\frac{\partial L_\theta}{\partial y}\right) - \alpha\frac{\partial^2}{\partial y^2}\left(L_\theta\overline{\theta^2}\right) \qquad \text{---(4-c)}$$

The dissipation terms might be modelled with relationships established in an isotropic turbulence field. The dissipation rate of temperature fluctuation (ε_θ) is given by the following relationship on the basis of the results derived by Hinze [3] :

$$\varepsilon_\theta = c_1\frac{\overline{\theta^2}}{L_\theta^{2/3}}\varepsilon^{1/3} \qquad \text{---(5)}$$

On the other hand, the relationship for dissipation rate of turbulence energy (ε) was indicated by Rotta [1] as follows:

$$\varepsilon = c\frac{k^{3/2}}{L} \qquad \text{---(6)}$$

With Eqs. (5) and (6), $\varepsilon_\theta L_\theta$ is given by

$$\varepsilon_\theta L_\theta = c_1 c^{1/3}\lambda^{-1/3}k^{1/2}\overline{\theta^2} \qquad \text{---(7)}$$

where λ means L_θ/L. In Eqs. (5), (6) and (7), c_1, c and λ are assumed to be almost constant in a fully turbulent field. We can derive a modelled form for dissipation terms (E) using $\varepsilon_\theta L_\theta$, following that Rotta [1] described the dissipation terms in the transport equation for L as εL. From Eq. (7), we obtain

$$E = C_{LE}k^{1/2}\overline{\theta^2} \qquad \text{---(8)}$$

where C_{LE} is a model constant. Finally the second-order closure transport equation for the length scale L_θ is derived as follows:

$$\frac{\partial}{\partial t}(L_\theta\overline{\theta^2}) + \frac{\partial}{\partial x}(\overline{U}L_\theta\overline{\theta^2}) + \overline{V}\frac{\partial}{\partial y}(L_\theta\overline{\theta^2}) + C_{L1}L_\theta\overline{v\theta}\frac{\partial\overline{\Theta}}{\partial y}$$

$$-C_{LD}\frac{\partial}{\partial y}\left(k^{1/2}L_\theta\overline{\theta^2}\frac{\partial L_\theta}{\partial y}\right) - \alpha\frac{\partial^2}{\partial y^2}(L_\theta\overline{\theta^2}) + C_{LE}k^{1/2}\overline{\theta^2} = 0 \qquad \text{---(9)}$$

The Eq. (9) includes three model constants: C_{L1}, C_{LD} and C_{LE}.

ALGEBRAIC MODEL FOR L_θ

Sreenivasan [4] carried out an experimental investigation on temperature fluctuations and the associated length scale in an isotropic field. The turbulence field was formed with a heated grid in a tunnel. The transport model given by Eq. (9) reduces to a notably simple form, when it is applied to the same field. Thus,

$$\overline{U}\frac{d}{dx}(L_\theta\overline{\theta^2}) + C_{LE}k^{1/2}\overline{\theta^2} = 0 \qquad \text{---(10)}$$

The model constant C_{LE} can be estimated by substituting Sreenivasan's typical experimental values into Eq. (10). Consequently C_{LE} is given by

$$C_{LE} \cong 0.46 \qquad \text{---(11)}$$

In a fully developed stratified flow, the algebraic expression is derived from Eq. (9) as shown by Launder [5] . It can be assumed that the production and the dissipation terms are dominant in Eq. (9):

$$L_\theta = -\frac{C_{LE}}{C_{L1}}\frac{k^{1/2}\overline{\theta^2}}{\overline{v\theta}(\partial\overline{\Theta}/\partial y)} \qquad \text{---(12)}$$

In Eq. (12), only C_{L1} remains unknown and its value will be estimated with the experimental results as described in the next section.

TURBULENCE MEASUREMENTS IN STRATIFIED FLOWS

Turbulence measurements in stratified flows were made to determine the value of C_{L1} and to discuss the validity of the algebraic model indicated in Eq. (12).

The stably and unstably stratified shear flows were formed in the experimental flume shown in Fig. 2. The turbulence measurements were made by LDV and thermocouples [6]. The coordinate system and the general view of the flow are shown in Fig. 3. The experimental conditions are listed in Table 1.

Table 1 Experimental Conditions

Run-No.	H	T_1	T_2	U_1	U_2
	(m)	(k)	(k)	(m/s)	(m/s)
Run-C	0.28	298.0	292.5	0.053	0.12
Run-S1	0.28	290.3	287.5	0.067	0.12
Run-S2	0.28	293.0	287.3	0.051	0.11
Run-U1	0.28	290.6	291.8	0.070	0.11

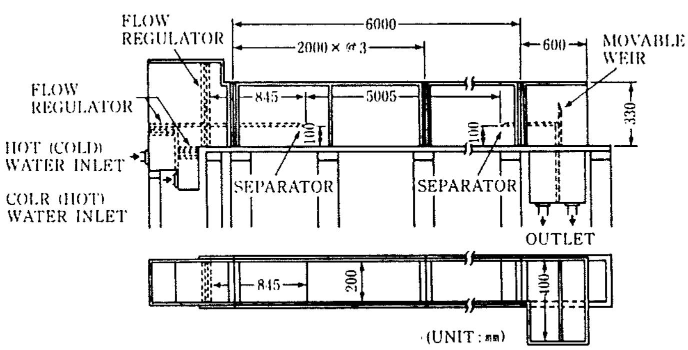

Fig. 2 Experimental Flume

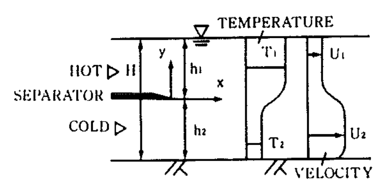

Fig. 3 Coordinate System

The value of C_{L1} was estimated with the experimental results obtained in Run-C. Fig. 4 shows vertical distributions of the normalized mean temperature T^* and cross-correlation function R^* indicated as follows:

$$T^* = (\overline{\Theta} - T_2)/(T_1 - T_2) \qquad \text{---(13-a)}$$

$$R^* = \overline{\theta(y_0/H)\,\theta(y/H)} \,/\, \overline{\theta^2(y_0/H)} \qquad \text{---(13-b)}$$

where the standard point y_0 is 0 in the present experiments. With Eq. (1), the integrated value of R^* shown in Fig. 4 equals L_θ/H and the calculated value is 0.114. It corresponds to the value of the left hand side of Eq. (12). The turbulence quantities, shown in Figs. 5 and 6, were measured in Run-C and by substituting these results into the right hand side of Eq. (12), we can estimate C_{L1} as follows:

$C_{L1} \cong 1.28$ ---(14)

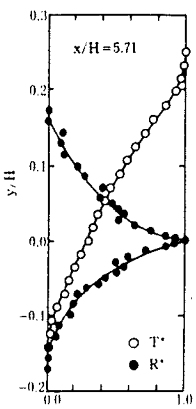

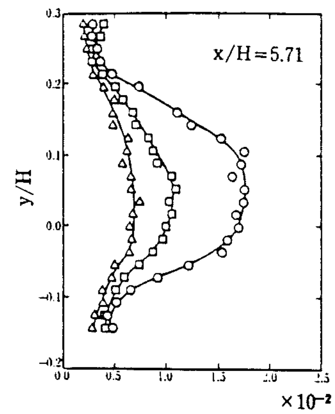

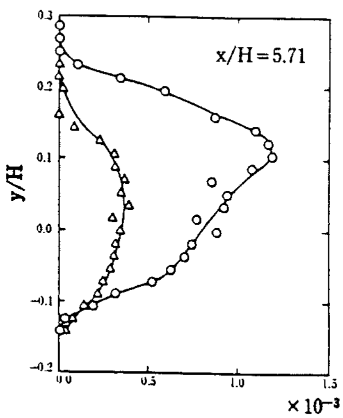

($\bigcirc\ \overline{u^2}/(U_2-U_1)^2$; $\Delta\ \overline{v^2}/(U_2-U_1)^2$; $\square\ \overline{w^2}/(U_2-U_1)^2$)

($\bigcirc\ -\overline{u\theta}/(U_2-U_1)(T_1-T_2)$; $\Delta\ -\overline{v\theta}/(U_2-U_1)(T_1-T_2)$)

Fig. 4 T^* and R^* Fig. 5 Velocity Fluctuation Fig. 6 Heat Flux

VALIDITY OF THE ALGEBRAIC MODEL

The validity of the algebraic model, constructed by Eqs. (11), (12) and (14), was examined with the experimental results obtained in Run-S1, S2 and U1. From Eq. (1), the integral scale based on the definition is given by

$$L_\theta/H = \frac{1}{\overline{\theta^2}(y_0/H)} \int_{-\infty}^{\infty} \overline{\theta(y_0/H)\,\theta(y/H)}\, dy/H \qquad \text{---(15)}$$

On the other hand, with the proposed algebraic model, the integral scale is calculated by

$$L_{\theta c}/H = \frac{C_{LE}}{C_{L1}} \frac{k^{1/2}\overline{\theta^2}}{\overline{v\theta}(\partial\Theta/\partial y)} \frac{1}{H} \Bigg|_{y=y_0} \qquad \text{---(16)}$$

The comparison between L_θ/H and $L_{\theta c}/H$ was made by substituting the experimental values into the right hand sides in Eqs. (15) and (16). The results are shown in Fig. 7. The integral scales increase with an increase in x/H as shown in Fig. 7. It could be concluded that L_θ/H and $L_{\theta c}/H$ show suitable agreement.

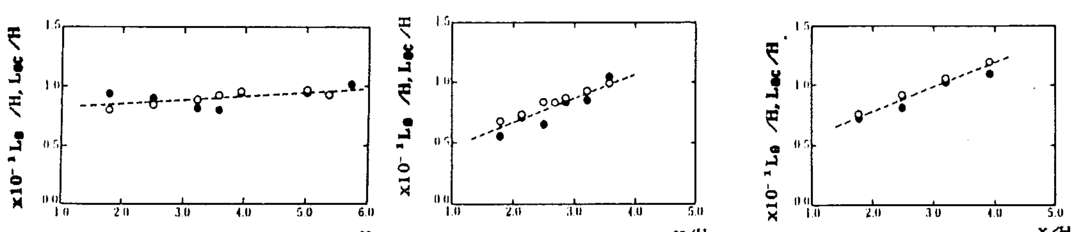

(a) RUN-S1 (b) RUN-S2 (c) RUN-U1

Fig. 7 Comparison between L_θ/H and $L_{\theta c}/H$
($\bigcirc$: L_θ/H , $\bullet$: $L_{\theta c}/H$)

CONCLUSION

A second-order closure transport equation and its algebraic expression were derived for an integral length scale for temperature fluctuation in stratified flows. The algebraic model includes two model constants and their values were estimated in this paper. The validity of the model was shown through the comparison with the experimental results obtained in stably and unstably stratified flows. The algebraic model might be useful to describe relationships on the turbulence structure in fully developed stratified flows.

On the other hand, the derived transport equation is expected to be applicable to more complicated flows and its unknown constant (C_{LD}) could be estimated through the computational optimization etc.

《REFERENCES》

[1] Rotta, J. C. : Turbulente Strömungen, B. G. Teubner, Stuttgart, 1972.

[2] Rodi, W and Spalding, D. B. : A Two-Parameter Model of Turbulence, and its Application to Free Jets, Wärme- und Stoffübertragung Bd 3, 1970.

[3] Hinze, J. O. : Turbulence, 2nd Edition, MCGRAW-HILL BOOK COMPANY, 1975.

[4] Sreenivasan, K. R., Tavoularis, S., Henry, R. and Corrsin, S. : Temperature Fluctuation and Scales in Grid-Generated Turbulence, J. Fluid Mech., vol. 100, 1980.

[5] Launder, B. E. : On the Effects of a Gravitational Field on the Turbulent Transport of Heat and Momentum, J. Fluid Mech., vol. 67, 1975.

[6] Ushijima, S., Moriya, S. and Iritani, Y. : Development of a Refined k-ε Model, and its Application to Stratified Sodium Flows, 4th Int. Conf. on Liquid Metal Engineering and Technology, 1988.

Session 5

Keulegan Centennial Symposium: Stratified Flow

Garbis H. Keulegan Centennial Symposium
In conjunction with
International Conference on Physical Modeling of Transport and Dispersion
August 7–10, 1990
Massachusetts Institute of Technology
Cambridge, Massachusetts

Abstract for Session C: Stratified Flow
Keynote paper by Donald R. F. Harleman
Ford Professor of Engineering
Massachusetts Institute of Technology

Title: THE KEULEGAN LEGACY: STRATIFIED FLOW

More than half of the sixty publications by Keulegan deal with the subject of stratified flow. His seminal research on this subject was done in the 1940–1960 period at the National Bureau of Standards under sponsorship of the COE Waterways Experiment Station. In this pre–computer era, progress in understanding the complex interactions of fresh and salt water were necessarily carried out by physical model studies.

Keulegan was an excellent experimentalist and his background in mathematics and theoretical physics proved invaluable in the analysis and development of theory based on experiment. Keulegan developed the non–dimensional parameters and model laws characterizing stratified flows. He dealt with salinity intrusions in canal locks, in river mouths as two–layer stratified systems and with mixing processes induced by interfacial shears.

One of the innovative topics he looked into, long before it was considered to be an important phenomenon, was the exchange of fresh and salt water in porous media.

Keulegan's last technical report, published a few months after he died at age 99, consisted of an insightful analyses of estuarine mixing processes. No one has had a more profound effect on the understanding of stratified flow processes.

ON THE NATURE OF TURBULENCE IN A STRATIFIED FLUID: THE IMPORTANCE OF THE COX NUMBER

by J. Imberger, G. Ivey and D. Luketina*
Centre for Water Research, University of Western Australia, Nedlands, Western Australia 6009, Australia
* Commonwealth Scientific and Industrial Research Organisation (Australia) Postdoctoral Awardee

Abstract

A procedure is presented, based on a simple energy and temperature fluctuation balance, which allows estimation of the flux Richardson number from a knowledge of the turbulent kinetic energy dissipation ε, the density fluctuations ρ', the displacement scale L_C and the Cox number C_T. Laboratory and field data are used to verify this relationship.

Introduction

Mixing in a stratified lake is energised by external forcing: momentum and energy transfers at the surface, inflows due to rivers and outflows at off-take points (Imberger and Patterson, 1990). The mixing and transport resulting from these disturbances is intermittent and spatially patchy with the probability of a particular mixing event taking place being determined not only by the strength of the disturbance but also by the degree of stratification in the lake as a whole, the shape of the lake basin, the bottom roughness and the location of the event within the lake (Imberger and Patterson, 1990).

The net vertical transport in a lake resulting from a particular mixing event is thus the combination of diapycnal mixing followed by gravitational adjustment along isopycnals. It is not widely realised that the instantaneous diapycnal transport is a function of the instantaneous state of the turbulent kinetic energy balance, characterized by the values of the turbulence Froude number, Fr_t, and Reynolds number, Re_t, (Ivey and Imberger, 1990); mixing events occur at random with a highly variable intensity and spatial distribution but the instantaneous transport is determined by the instantaneous values of Fr_t and Re_t.

Diapycnal transport

Consider first the diapycnal transport resulting from a mixing event in any part of a stratified lake. If we divide the velocity field (u_i) into a mean ($\overline{u}_i$) and fluctuating (u'_i) component and similarly partition the density field ρ into $\overline{\rho}$ and ρ' then the simplified turbulent kinetic energy equation becomes (Tennekes and Lumley, 1972):

$$-\overline{u}_j\left(\frac{\overline{u_i' u_i'}}{2}\right)_{,j} - \overline{u_i' u_j'}\,\overline{u}_{i,j} = \frac{g}{\rho_0}\overline{u_3'\rho'} + \varepsilon \ , \qquad (1)$$

where ε is the dissipation of turbulent kinetic energy.

Now if we define the flux Richardson number by

$$R_f = \frac{\dfrac{g}{\rho_0}\overline{u_3'\rho'}}{-\overline{u}_j\left(\dfrac{\overline{u_i' u_i}}{2}\right)_{,j} - \overline{u_i'u_j'}\,\overline{u}_{i,j}} \ , \qquad (2)$$

then by (1)

$$R_f = \frac{1}{1 + \dfrac{\varepsilon}{\dfrac{g}{\rho_0}\overline{u'_3 \rho'}}} , \qquad (3)$$

which is a generalization of the flux Richardson number normally used (Turner, 1973); here we account for all energy sources likely to contribute to the buoyancy flux, not just the local production of turbulent kinetic energy. Luketina and Imberger (1989) introduced the correlation coefficient,

$$R_{w\rho} = \frac{\overline{u'_3 \rho'}}{\tilde{w}\,\tilde{\rho}} , \qquad (4)$$

where $\tilde{w}$ and $\tilde{\rho}$ are the RMS values of u'_3 and ρ'. With this definition, (3) becomes:

$$R_f = \frac{1}{1 + \dfrac{\varepsilon}{\dfrac{g}{\rho_0}\tilde{\rho}\,\tilde{w}} \dfrac{1}{R_{w\rho}}} . \qquad (5)$$

Now Ivey and Imberger (1990) showed that,

$$\tilde{w} \sim (\varepsilon L_C)^{1/3} , \qquad (6)$$

where L_C is the centred displacement scale (Imberger and Boashash 1987) and if we introduce the Froude number Fr_t for the turbulent motion (Imberger 1990),

$$Fr_t = \frac{\tilde{w}}{(g' L_C)^{1/2}} \sim \frac{\varepsilon^{1/3}}{g'^{1/2} L_C{}^{1/6}} , \qquad (7)$$

where

$$g' = \frac{\tilde{\rho}\, g}{\rho_0} , \qquad (8)$$

then (5) becomes

$$R_f = \frac{1}{1 + \dfrac{Fr_t^2}{R_{w\rho}}} . \qquad (9)$$

It is important to stress that this expression is exact and not based on any simplifying assumptions other than that the turbulence is stationary. As shown in Ivey and Imberger (1990), $R_{w\rho}$ does depend on the Prandtl Number $Pr = \nu/D$ but (9) is equally valid in salt water ($Pr = 700$) or in heat stratified air ($Pr = 0.7$).

For large Fr_t the turbulence is independent of buoyancy and so it is reasonable to expect $R_{w\rho}$ to become constant. By contrast, when the turbulence becomes suppressed and internal waves dominate, then $R_{w\rho} \to 0$ and the density fluctuations become 90° out of phase with the vertical velocity fluctuations. This must occur when the strain rate, γ, due to the turbulent motion, becomes less than the buoyancy adjustment time $(g' L_C^{-1})^{1/2}$. Ivey and Imberger (1990) showed that this is given by:

$$Fr_\gamma = \frac{\gamma}{(g' / L_C)^{1/2}} = \left(\frac{\varepsilon\, L_C}{\nu\ g'}\right)^{1/2} < 3.9 \quad . \tag{10}$$

The flux Richardson number R_f therefore tends to zero both as $Fr_t \to \infty$ and when $Fr_\gamma = 3.9$, and reaches a maximum value at an intermediate value of the Froude number. Ivey and Imberger (1990) utilized the data from the water tunnel and wind tunnel experiments of Van Atta and his colleagues to verify (9). These results showed that for $Fr_t < 1$, R_f also depended on the Reynolds number Re_t of the turbulent motions where,

$$Re_t = \frac{\tilde{w} L_C}{\nu} \sim \frac{\varepsilon^{1/3}\, L_C^{4/3}}{\nu} \tag{11}$$

A complete specification of the vertical flux is thus available from the curves of R_f in figure 1 and measurements of Fr_t and Re_t through the relationship :

$$\frac{g}{\rho_0}\, \overline{u_3'\, \rho'} = \frac{\varepsilon\, R_f}{1 - R_f} \tag{12}$$

For undirectionally shear flow (2) further implies

$$\overline{u_3'\, u_1'} = \frac{\varepsilon}{(R_f - 1)}\, \bar{u}_{1,3} \tag{13}$$

<u>Flux Richardson number values from temperature microstructure</u>

The diapycnal mass flux in a lake can thus be determined from the values of L_C, g' and ε which, along with viscosity ν, completely specify Fr_t, Re_t and hence R_f. As shown by Imberger (1990), temperature microstructure measurements may be used to directly measure these quantities and so R_f may be determined from such measurements and the isoefficiency curves depicted in figure 1.

Temperature microstructure measurements may, however, also be used to independently verify the above methodology. Once again, consider a water body, stratified by temperature, then the temperature variance equation (see Tennekes and Lumley, 1972) reads:

$$\overline{u_i}\left(\overline{\theta'^2}\right)_{,i} + 2\, \overline{\theta' u_i'}\, \overline{\theta}_{,i} + \overline{u_i'\left(\theta'^2\right)_{,i}} = 2D\left(\overline{\theta'^2}\right)_{,ii} - 2D\overline{\left(\theta'_{,i}\right)^2} \tag{14}$$

where θ' is the temperature fluctuation and D the molecular diffusivity.

If we neglect transport by the mean velocity and the velocity fluctuations and if we assume that the molecular transport is small then (14) becomes:

$$\overline{\theta' u_3'}\, \overline{\theta}_{,3} = - D\overline{\left(\theta'_{,i}\right)^2} \ , \tag{15}$$

where we have further assumed that there is only a vertical mean gradient. Introducing the equation of state:

$$\theta' = \frac{1}{\rho_0 \alpha}\, \rho' \ , \tag{16}$$

where α is the coefficient of thermal expansion, and making the assumption that the length scale L_C is given by L_t (Luketina and Imberger, 1989) where

$$L_t = \frac{\rho'}{\bar{\rho}_{,3}}, \tag{17}$$

then (15) becomes

$$R_{w\rho} = \frac{D}{\nu}\frac{C_T}{Re_t}, \tag{18}$$

where

$$C_T = \frac{\overline{\left(\theta'_{,i}\right)\left(\theta'_{,i}\right)}}{\left(\bar{\theta}_{,3}\right)^2}, \tag{19}$$

with a sum on the i subscript.

The importance of (18) must be stressed; it allows a direct measurement of $R_{w\rho}$ (and thus R_f from (9)) from only a knowledge of the temperature (density) microstructure. Equation (15), however, specifies a balance production of temperature fluctuations near the Kolmogorov scale (Lienhard and van Atta, 1990) and so the estimate of C_T should not include the internal wave contributions to the temperature fluctuation variance. Therefore, for low Froude numbers, the raw estimate of the temperature gradient variance should not be used.

This is best seen by considering the shape of the temperature gradient signal, a typical example of which is shown in Fig. 2. The shape of various portions of the (dissipation) spectral curve may be derived from dimensional analysis :

I Low wave numbers (Internal wave straining):

$$S_\theta^{I} = f_I\left(\bar{\theta}_{,3}, k\right) = C_1\left(\bar{\theta}_{,3}\right)^2 k^{-1} \tag{20}$$

II Intermediate wave numbers (Inertial convective subrange):

$$S_\theta^{II} = f_{II}\left(\chi_\theta, \varepsilon, k\right) = C_2\,\chi_\theta\, k^{1/3}\,\varepsilon^{-1/3} \tag{21}$$

III High wave numbers (Batchelor spectrum) (Gibson and Schwartz, 1963):

$$S_\theta^{III} = f_{III}\left(\chi_\theta, D, k_B\right) = \frac{C_3\,\chi_\theta}{k_B D} f_{III}\left(\frac{k}{k_B}\right) \tag{22}$$

where $\chi_\theta = 2D\overline{(\theta'_{,i})^2}$ is the dissipation of temperature variance, k is the wavenumber and

$k_B = \left(\frac{\varepsilon}{\nu D^2}\right)^{1/4}$ is the Batchelor wavenumber.

The transition between these regimes may be obtained by equating the above forms. We note that

$$f_{III}\left(\frac{k}{k_B}\right) \approx \frac{k}{k_B} \tag{23}$$

for small values of $\frac{k}{k_B}$. The transition wave numbers are therefore

$$\frac{k_\theta}{k_C}=\left(\frac{C_1}{2C_2}\right)^{3/4}\left(\frac{Pr\,Re_t}{C_T}\right)^{3/4}=\left(\frac{C_1}{2C_2}\right)^{3/4}R_{w\rho}^{-3/4} \tag{24}$$

$$\frac{k_\beta}{k_C}=\left(\frac{C_1}{2C_3}\right)^{1/2}\frac{Pr^{1/2}\,Re_t^{3/4}}{C_T^{1/2}}=\left(\frac{C_1}{2C_3}\right)^{1/2}\frac{C_T^{1/4}}{Pr^{1/4}}R_{w\rho}^{-3/4} \tag{25}$$

$$\frac{k_k}{k_C}=\left(\frac{C_2}{C_3}\right)^{3/2}Re_t^{3/4}=\left(\frac{C_2}{C_3}\right)^{3/2}\frac{C_T^{3/4}}{Pr^{3/4}}R_{w\rho}^{-3/4} \tag{26}$$

where $k_C = L_C^{-1}$ and k_θ, k_β and k_k are the transition wave numbers as shown in Fig. 2.

These relationship reveal the interplay between C_T and $R_{w\rho}$. For a flow with $Fr_t > 1$, $R_{w\rho}$ is constant and thus $k_\theta \sim k_C$ which implies that the turbulent motions occupy the range of scales from k_β^{-1} to k_C^{-1} the overturn scale. By contrast as we approach the boundary $Fr_\gamma = 3.9$ (Fig. 1) internal waves predominate, the phase shift between ρ' and w' approaches 90°, $R_{w\rho}$ tends to zero and C_T must go to zero. From (24), we can see that $k_\theta >> k_C$ as $R_{w\rho}$ tends to zero; therefore the flow consists of turbulence embedded in (non-turbulent) overturns of much larger scales. Under such a scheme the turbulent eddies become smaller and less energetic but can be evenly distributed amongst the overturn structures in the flow.

The above suggest that in estimating C_T we should only include the area above S_θ^{I}, shaded in Fig. 2. The results obtained using a range of microstructure records are shown in Fig. 3 where the results are also compared to the laboratory measurements of van Atta and his colleagues (from Ivey and Imberger, 1990). Comparison is good indicating that (15) is valid in most field situations.

It is interesting to note that by fitting S_θ^{III} to the experimental data in order to obtain the dissipation ε and by using only the shaded area in Fig. 2 to compute C_T we automatically truncate our time series at a length k_θ^{-1} which, in most instances, will be less than the (statistically) stationary segment length (Imberger, 1990). The procedure thus ensures some averaging over adjacent identical events; this is an added advantage of this procedure.

Conclusion

Examination of the scales of turbulent motions in a stratified fluid has revealed the importance of the Cox number C_T, the Froude number Fr_t and the Reynolds number Re_t. The values of these numbers determines, by (17), the correlation coefficient $R_{w\rho}$ which then may be used in (9) to determine the flux Richardson number R_f. The value of this may in turn be substituted into (12) to evaluate the mass flux $\overline{u'_3\,\rho'}$ and into (13) to determine the momentum flux, $\overline{u'_3\,u'_1}$. Therefore, for most flows, closure is obtained once the values of L_C, g', ε and C_T are known.

References

Gibson, C. H., and Schwartz, W. H. (1963). *J. Fluid Mech.*, 16, 365-384.

Imberger, J. (1990) *J. Phys. Oceanogr.* (in press)

Imberger, J., and Patterson, J. C. (1990). *Advances in Applied Mechanics*, Academic Press, Cambridge, 303-475.

Ivey, G. N., and Imberger, J. (1990). *J. Phys. Oceanogr.* (in press).

Luketina, D. A., and Imberger, J. (1989). *J. Geophys. Res.*, 94, 12,619-12,636.

Turner, J. S., (1973) *Buoyancy Effects in Fluids.* Cambridge University Press, 365 pp.

Tennekes, H., and Lumley, J. L. (1972). "*A First Course in Turbulence.*" Massachusetts Institute of Technology Press.

Figure 1.

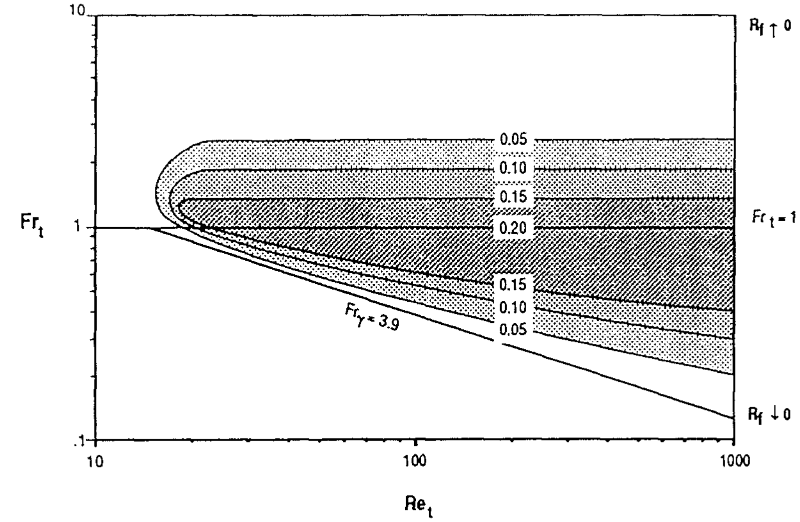

Figure 2.

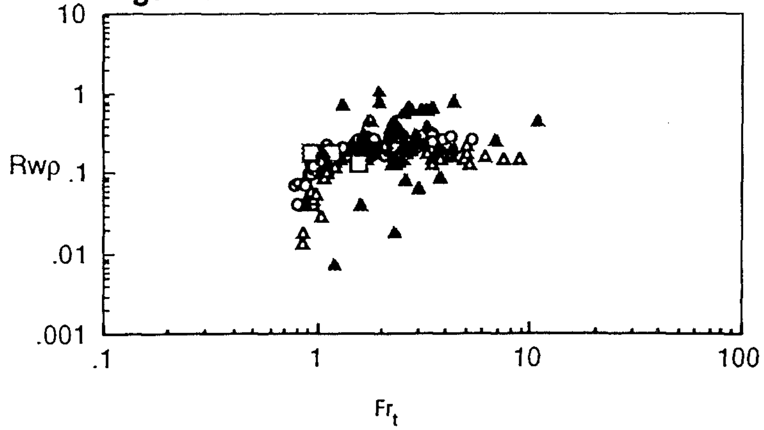

Figure 3.

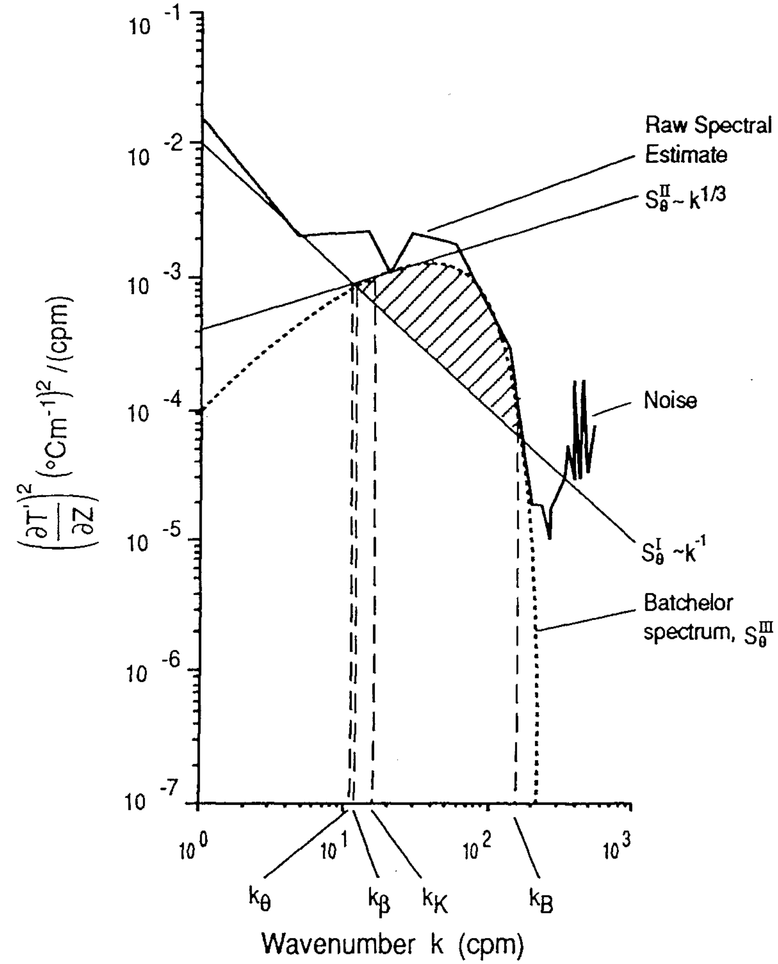

FIG. 1. Isoefficiency curves derived from the laboratory data summarized in Ivey and Imberger (1990) for salt stratification.

FIG. 2. Typical temperature gradient spectrum showing the internal wave, viscous-convective and the thermal equilibrium ranges.

FIG. 3. Correlation coefficient between the vertical velocity and the density fluctuation: ○ and △ (data of van Atta and co-workers as presented in Ivey and Imberger, 1990), □ direct field measurements (Ivey and Imberger, 1990), ▲ estimated from equation (18) using field data.

NUMERICAL MODELING OF SALINITY INTRUSION IN THE LOWER MISSISSIPPI RIVER

by

Billy H. Johnson,[1] Member, ASCE

EXTENDED ABSTRACT

Introduction

A two-dimensional (2-D) laterally averaged numerical model called LAEM (Laterally Averaged Estuary Model) has been applied to address the impact on salinity intrusion of deepening the navigation channel in the Lower Mississippi River. The numerical model has also been applied to address the impact upon salinity intrusion of constructing an underwater barrier in the river from natural sediments dredged nearby. Initial model verification relied primarily upon demonstrating that the numerical model was able to reproduce observed intrusion lengths for a historical low flow event in 1980-81. In addition, an arrested wedge analysis in which characteristics of the wedge computed by LAEM for a steady river flow of 150,000 cfs were compared to those observed by Keulegan (1949) in a laboratory flume served to strengthen the model verification.

During the 1988 drought on the Lower Mississippi River, the numerical model was applied to aid in assessing the performance of a sill that was constructed to protect water supplies to New Orleans. Although model results were of great benefit, the model computed a wedge of less strength than observed; thus, results were continually adjusted to reflect this discrepancy. During the period of July-December 1988, a large amount of salinity data were collected quantifying the initial intrusion of the saline wedge as well as the performance of the sill. These data are being used in a reverification of the model.

---

[1]Research Hydraulic Engineer, Hydraulics Laboratory, US Army Engineer Waterways Experiment Station, 3909 Halls Ferry Road, Vicksburg, MS 39180-6199

Numerical Model

Under the Environmental and Water Quality Operation Study (EWQOS) program of the US Army Corps of Engineers, a two-dimensional (2-D) laterally averaged, free-surface, variable-density, and heat-conducting model was developed for use in simulating flows in thermally stratified reservoirs. This effort, which extended earlier work funded by the US Army Engineer Division, Ohio River (Edinger and Buchak 1979), resulted in a numerically efficient model known as LARM. Under a contract with the US Army Engineer District, Savannah, LARM was modified for use in computing stratified flows in estuaries as a result of both salinity and thermal effects. This model is known as LAEM (Edinger and Buchak 1981), and was the basic model modified for application in the present study.

The basic set of equations that are solved in LAEM are statements of the conservation of mass and momentum of the flow field plus the conservation of the heat and salt content of the water body. The governing equations are developed by first performing a temporal averaging of the three-dimensional equations for laminar flow. Boussinesq's eddy coefficient concept is then employed to account for the effect of turbulence in the flow field. Next, the time-averaged equations are averaged over the estuary width and finally over an individual vertical layer to yield the equations that are solved in LAEM.

Basic assumptions in addition to the reduced dimensionalilty are that the Boussinesq approximation (ρ is constant except where multiplied by the acceleration of gravity) is applicable and that vertical accelerations are negligible so that the pressure can be considered hydrostatic. In addition, the concept of eddy coefficients is used to represent the effect of both time and spatial averaging. The horizontal dispersion coefficients are assumed to be constant, whereas the vertical dispersion coefficients are dependent upon the stratification of the water column.

Finite difference techniques are employed to solve the governing equations. The particular scheme employed is structured such that the water-surface elevations are computed implicitly. Using the new water-surface elevations, the x-component of the flow velocity is then explicitly computed from the longitudinal momentum equation. As in other hydrostatic models, the vertical component of the velocity is computed from the continuity equation which is reduced to the incompressibility condition as a result of the Boussinesq approximation. The solution begins at the bottom and progresses up the column of layers. With the flow field computed, the water temperature and salt concentration are then computed from their respective transport equations in an implicit fashion. A detailed discussion of the solution scheme can be found in the report by Edinger and Buchak (1979).

System Description

Figure 1 is a map showing the schematization of the Mississippi River from Baton Rouge at mile 228.4 above Head of Passes (AHP) to the Gulf of Mexico. This is the segment of the Mississippi River that would be deepened and/or widened where necessary to provide a 750-ft-wide by 45-, 50- or 55-ft-deep navigation channel (with overdepth dredging). At the Gulf where flow exits through three major distributaries (Southwest Pass, South Pass, and Pass a Loutre) and several smaller ones, it was assumed that the system could be satisfactorily reproduced by treating Southwest Pass as the dominant distributary and representing outflow through the other distributaries as lateral outflows at the appropriate locations. This assumption also implies that wedge intrusion into the system is dominated by saline water moving up Southwest Pass.

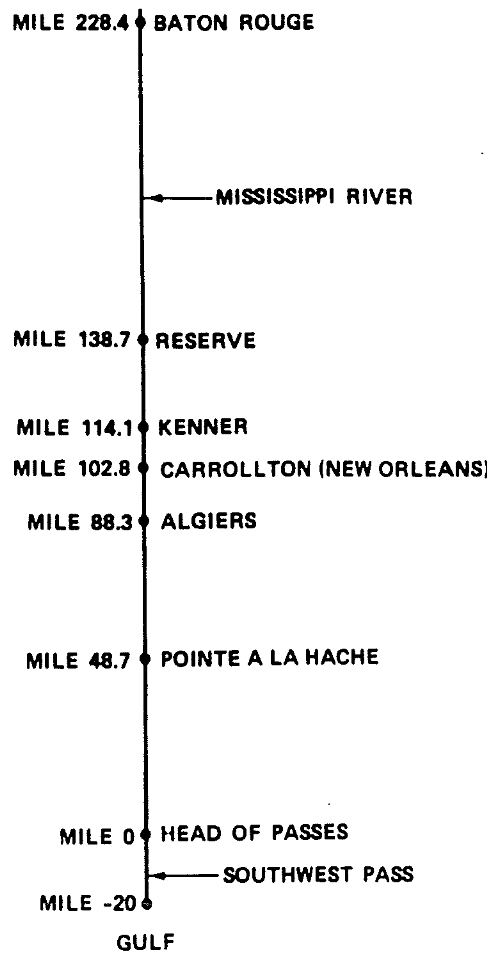

Figure 1. Schematic of Lower Mississippi River

Model Verification

Initial verification of the model relied upon a limited set of data collected during a relatively low flow period in 1981. This set of data consisted of the time-history of the tip of the wedge as well as vertical profiles of the salinity behind the tip of the wedge in January 1981. Results on wedge movement are shown in Figure 2. Computed and observed vertical salinity profiles are plotted in Figure 3. The field data plotted are from measurements on 28 January 1981 at a location 5 miles behind the tip of the wedge, which was located at about mile 59. The computed profile presented is on the same day, i.e., 28 January 1981, but at a distance of 8 miles behind the wedge tip. The computed interface is not as sharp as the field data imply; however, the computed and recorded concentrations of approximately 1.0 ppt that occur at a depth of about 50 ft below the water surface compare well.

Arrested Wedge Analysis

Results from computations made with a constant riverflow of 150,000 cfs have been used to analyze the characteristics of the

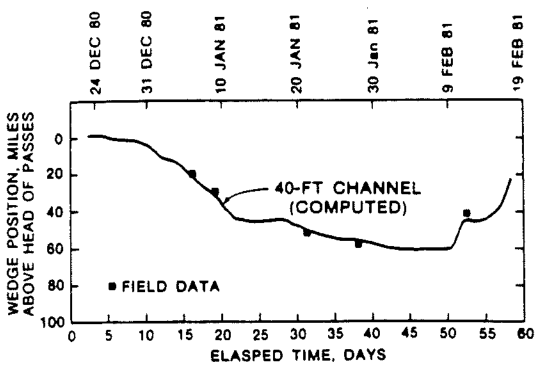

Figure 2. Model Computation of Wedge Position

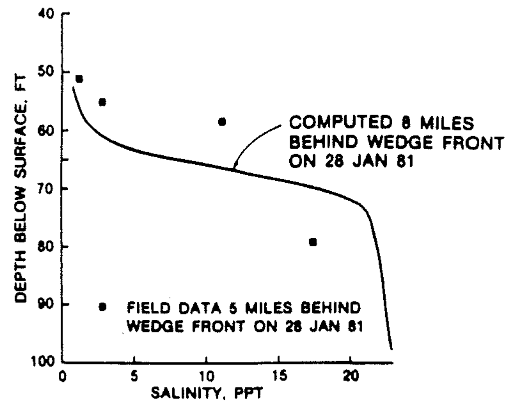

Figure 3. Vertical Structure of Salt Wedge

arrested saline wedge formed. These were then compared with experimental results obtained by Keulegan (1949) in laboratory studies. Factors considered included the vertical distribution of salinity and the longitudinal component of the velocity.

Based upon the computation of an effective interface layer thickness, Keulegan's experiments imply that the numerical results at the interface are too diffuse. However, the same interface thickness computed from the limited field data available agreed relatively well with the numerical results. The numerical results did agree quite well with functions determined by Keulegan for the vertical distribution of a dimensionless representation of the salinity and the vertical distribution of the normalized longitudinal velocity.

For the case of a constant 150,000-cfs flow, the computed freshwater depth was 10.39 ft and $\Delta\rho/\rho$ was 0.024 . Therefore the average freshwater velocity at the river mouth should be 2.83 fps since it is generally agreed that the river mouth is a critical flow section with the densimetric Froude number being equal to unity for the case of highly stratified salt wedges in estuaries. The numerical results yield an average velocity of 2.53 fps which results in a densimetric Froude number of 0.89.

In general, the numerical results compare quite well with Keulegan's experiments and known theoretical results and serve to increase the credibility of the unsteady results obtained from LAEM.

Impact of Channel Deepening with an Underwater Sill

To demonstrate the impact of channel deepening as well as channel deepening with an underwater barrier or sill constructed, the model was run with the 1953-54 discharge hydrograph as the river inflow. The 1953-54 hydrograph presented in Figure 4 resembles the 1980-81 hydrograph but with a lower flow that is maintained for a much longer period of time. As illustrated in Figure 5, deepening the navigation channel from 40 to 55 ft will significantly increase the duration of salinity intrusion. However, construction of an underwater barrier at mile 63 significantly reduces the duration, although the wedge still ultimately moves to Kenner Crossing located at mile 116 AHP.

Figure 4. 1953-54 Discharge Input at Baton Rouge

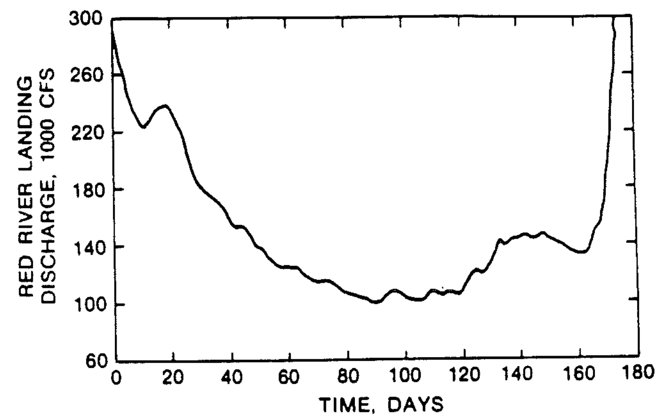

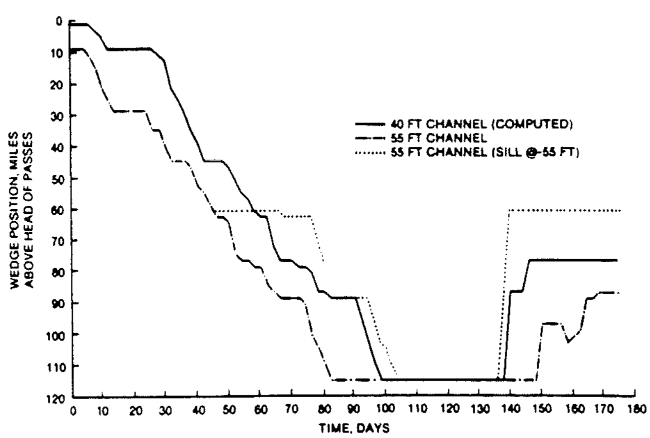

Figure 5. Effect of Sill at Mile 63.4 on Salt Wedge Intrusion in the 55-ft Channel for 1953-54 Hydrograph

Conclusions

In general, it is concluded that the numerical model, LAEM, provides a very useful tool for assessing the impact of major changes in channel geometry on the intrusion of salinity. Verification of LAEM for the Lower Mississippi River produced a model whose computed results were in good agreement with the limited field data available and responded well to the various boundary data imposed. Man-induced alterations to create greater heights at river crosssings, i.e., to create a sill in the river, appear to be an effective means of limiting wedge intrusion during critically low flow periods. For 1953-54 flow conditions and a 55-ft channel, a sill at mile 63 with a top elevation of -55 ft would result in salinity conditions at New Orleans similar to those that occur with a 40-ft channel.

Acknowledgements

The tests described and the resulting data presented herein, unless otherwise noted, were obtained from research conducted for the US Army Engineer District, New Orleans by the US Army Engineer Waterways Experiment Station. Permission to publish this paper was granted by the Chief of Engineers.

Appendix I. Conversion Factors, from US Customary to SI Units

Non-SI units of measurement used in this report can be converted to SI (metric) units as follows:

Multiply	By	To Obtain
cubic foot	0.02831685	cubic metre
foot	0.3048	metre
mile (US statute)	1.609344	kilometre

Appendix II. References

Edinger, J. E., and Buchak, E. M. (1979). "A hydrodynamic two-dimensional reservoir model: development and test application to sutton reservoir, Elk River, West Virginia." Prepared for US Army Engineer Division, Ohio River, Cincinnati, Ohio.

__________. (1981). "Estuarine laterally averaged numerical dynamics; the development and testing of estuarine boundary conditions in the LARM code." Miscellaneous Paper EL-81-9, US Army Engineer Waterways Experiment Station, Vicksburg, Miss.

Keulegan, G. H. (1949). "Fourth progress report on model laws for density currents for Chief of Engineers, U. S. Army." National Bureau of Standards, Hydraulic Laboratory, Washington, D. C.

Session 6A

Estuarine Processes

EXPERIMENTAL STUDY ON THE VELOCITY FIELD AND SALINITY TRANSPORT OF THE TIDAL RIVER FLOW

by Hajime Kato and Nobuo Mimura
Department of Civil Engineering, Ibaraki University
4-12-1 Nakanarusawa, Hitachi, Ibaraki, 316 Japan

Abstract

Experiments of tidal river flows were carried out using a small scale flume, focusing on the well and partially mixed types of the flows. Both temporal and spatial variations of salinity and current velocity were measured systematically. Through the experiments, the possibility of reproducing the well mixed type flow in a small scale flume, and effective parameters for classifying the mixing types were examined. The components of salinity transport were evaluated using the data of measured salinity and current velocity, then the relative magnitude of each component was determined for each mixing types.

Introduction

The tidal river flow is usually classified into three types: well, partially and weakly mixed (salt wedge). The state of mixing influences greatly on the salinity intrusion into the river and dispersive behavior of pollutants. Understanding the characteristics of velocity and salinity fields is essential for assessing these phenomena. They, however, are still little known for the well and partially mixed tidal flows.

The well and partially mixed type river flows have mainly been studied using field observation data. Experimental studies for these flows have been carried out only by using large scale tidal flumes more than 100 m long (e.g. Ippen and Harleman, 1961; Rigter, 1973; Perrels and Karelse, 1981). In the present study, an attempt was made to generate the well and partially mixed tidal river flows as well as weakly ones by using a small scale tidal flume. After examining whether or not the well and partially mixed type of flows were reproduced, the structure of salinity transport was investigated on the basis of precise measurement of velocity and salinity fields.

Experimental apparatus and procedure

The experimental apparatus consists of a river flume, 15 cm wide, 30 cm deep and about 6.7 m long, connected to a 2m x 2m tide basin, a tide-generating system and an overflow weir. The sinusoidal tide was generated by supplying or discharging salt water into or from the tide basin through perforated pipelines set on the bottom of the basin. For producing tides of the target wave profiles, the discharge of the pipelines and the elevation of the overflow weir were controlled synchronously by a personal computer. Figure 1 shows an example of the generated tide level.

In the experiments, all types of tidal river flows were intended to reproduce by changing experimental conditions. These conditions are the amplitude a, and period T, of the tide, fresh water discharge Qf, relative density difference between salt and fresh water ε, and bottom roughness of the river flume. The experiments carried out are divided into series I and II: in series I, longer tidal periods of 5 and 8 minutes were taken, while, in series II, a shorter one of 2 minutes was employed in order to increase the ratio of the flume length to the wavelength of the tide, and to promote the tidal mixing. The roughness elements are square pillars with 0.8 x 0.8 cm^2 and 0.5 x 0.5 cm^2 cross sections. The experimental conditions are summarized in Table 1. R and S attached to the case No. indicate rough and smooth bottom conditions, respectively.

The quantities measured in the experiments are salt concentration and current velocity. These were measured by conductivity probes, and hydrogen bubble method and a hot-film anemometer, respectively. Measurement was conducted at several sections along the flume over a different cycle of the tide for each position. By superposing the data measured in this way, temporal and spatial distributions of salinity and current velocity were obtained. Since this method requires measurements for several tidal cycles, it was certified that almost the same tidal phenomena repeated themselves.

The present study dealt with the longitudinal vertical plane, i.e. the transverse variation of phenomena was ignored. Then the x-axis was taken pointing upstream from the river mouth and z-axis upward from the flume bottom.

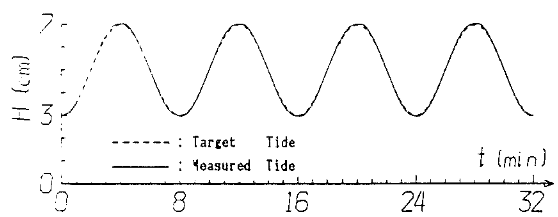

Fig.1 An example of the generated tide level.

Table 1 Experimental conditions, components of salinity flux ($x10^2$gr/s), and mixing types (cf. Fig.4).

Ser.	Case No.	H (cm)	T (min)	a (cm)	Q (cm^3/s)	bottom	ε	R (x=40)	F_1	F_2	F_3	F_{31}	F_{32}	F_{33}	M-type
I	RI-1	5	5	2.0	50	rough	.0020	0.105	-6.47	8.32	2.31	-0.03	1.97	0.37	◆
	RI-2	5	8	2.0	50	rough	.0020	0.359	-9.96	7.41	2.44	0.44	2.07	-0.03	⬘
	SI-1	5	8	2.0	50	smooth	.0020	0.485	-6.07	6.29	2.48	0.28	2.25	0.05	◈
	SI-2	5	8	1.0	50	smooth	.0020	3.19	-9.91	2.19	5.50	3.54	1.36	0.59	⟠
	SI-3	5	8	0.5	50	smooth	.0020	31.8	-9.03	1.05	5.59	5.01	0.45	0.13	◇
II	RII-1	4	2	.75	25	rough	.0020	.0263	-3.06	6.38	1.19	0.36	1.13	-0.30	◍
	RII-2	4	2	.75	50	rough	.0020	.0869	-9.82	10.68	0.88	0.50	1.07	-0.68	●
	RII-3	4	2	.75	50	rough	.0050	.136	-30.2	20.12	6.66	3.32	4.11	-0.77	◒
	SII-1	4	2	.75	25	smooth	.0020	.0216	-4.90	5.46	2.59	0.98	1.75	-0.14	⊕
	SII-2	4	2	.75	50	smooth	.0020	.0569	-7.75	11.54	1.59	0.63	1.36	-0.40	●
	SII-3	4	2	.30	25	smooth	.0020	.462	-3.79	1.26	3.17	2.60	0.53	0.05	⊖
	SII-4	4	2	.30	50	smooth	.0020	.706	-5.90	3.49	3.52	3.65	-0.31	0.17	⊖
	SII-5	4	2	.30	50	smooth	.0050	1.64	-23.70	1.11	20.22	18.71	1.42	0.10	○
	SII-6	4	2	.30	75	smooth	.010	6.13	-62.37	7.10	50.59	43.79	5.25	1.36	○

Velocity and salinity distributions

The velocity and salinity distributions measured in the present experiments showed typical characteristics for each type of the tidal river flow. The velocity profiles in a vertical cross section (x=40cm) over a tidal period are shown in Fig.2 for cases RI-2, SI-1 and SI-3. The dotted lines in Fig.2 denote the elevation where the salinity is a half of that at the bottom. This elevation is taken as an indicator for the position of interface between salt and fresh water.

The velocity profiles in the cases of well and partially mixed types (RI-2, SI-1) have a tendency to become vertically uniform except near the bottom. And the water of the whole depth oscillates back and forth, with the surface and bottom layers being almost in phase. For these cases, the salinity profile shows the same tendency, which can be seen in Fig.2 as the abrupt rise of interface to near the water surface in the flood tide phase. Moreover, longitudinal distributions of cross-sectional average salinity are shown in Fig.3. The spatial and temporal variation shown in Fig.3 is similar to the results obtained in fields and large scale physical models. This figure together with above-mentioned results indicates that well mixed type flows were reproduced in a rather small experimental facility in the present study.

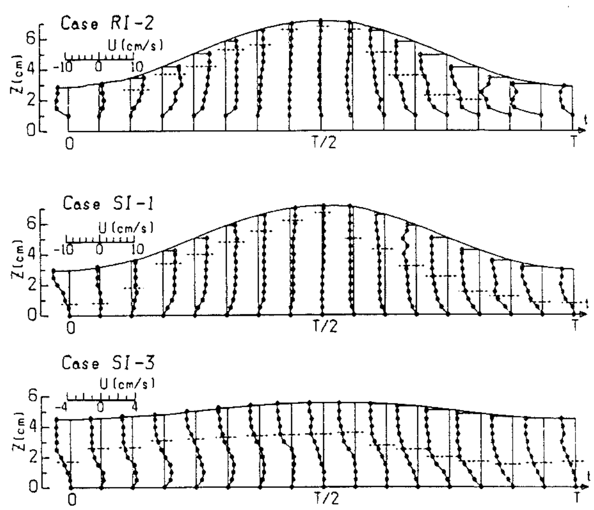

Fig.2 Velocity profiles in a vertical cross-section (x=40cm) over a tidal period.

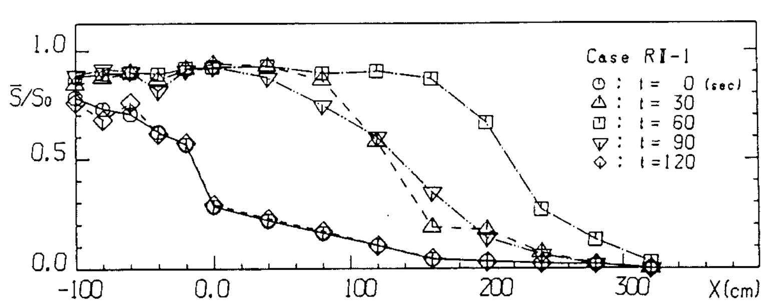

Fig.3 Longitudinal distributions of cross-sectional average salinity.

Classification of tidal river flows

Various parameters have been suggested for classifying the types of tidal river flows. Among them, Fischer(1972) introduced the "Estuarine Richardson Number", R:

$$R = (\Delta\rho/\rho)gQ_f/WU_t^3 = (1/F_{ri}^2)\cdot(U_f/U_t)^3 \qquad (1)$$

where ρ and $\Delta\rho$ are density of fresh water and density difference, Q_f the fresh water discharge, W width of the river flume, U_f river velocity, U_t rms tidal velocity, and $F_{ri}=U_f/((\Delta\rho/\rho)gh)^{1/2}$ densimetric Froude number. As shown in Eq.(1), R can be reduced to a function of the relative intensity of tidal current (U_t/U_f) and the densimetric Froude number (F_{ri}). U_t/U_f is similar to the ratio of tidal prism to the river discharge. Since these parameters represent the power generating mixing by tide and the buoyancy effect stabilizing the flow, respectively, R can be considered to represent the relative magnitude of the two conflicting effects.

U_t/U_f, F_{ri} and R were evaluated for each experimental case. Mixing types observed in the experiments are plotted on a F_{ri}^2 - $(U_f/U_t)^3$ plane as shown in Fig.4. It can be seen that the mixing are promoted as U_t/U_f increases and/or F_{ri} increases. From observations for real estuaries, Fischer(1979) suggested that the transition from a well mixed to a strongly stratified estuary occurs roughly in the range $0.08< R <0.8$. For the present experiments, the range is $0.15< R <0.8$ as seen in Fig.4, which is considerably consistent with the results from field data. Exceptionally, case SII-1 was classified into the partially mixed type though $R <0.15$. This indicates that the mixing power was insufficient for this case because of the smooth bottom condition and relatively low Reynolds number. On the contrary, the rough bottom cases tended to become the well mixed type, which is attributed to stronger turbulence generation by the roughness. In order to take into account the turbulence generation on the bottom a modified estuarine Richardson number, in which U_t is replaced by the friction velocity, may be more relevant.

Structure of salinity transport

In order to identify the relative magnitude of the salt transport mechanisms, the measured velocity and salinity data were divided into four components after Fischer (1979).

$$u(x,z,t)=u_0(x)+u_1(x,t)+u_s(x,z)+u'(x,z,t) \qquad (2)$$

$$C(x,z,t)=C_0(x)+C_1(x,t)+C_s(x,z)+C'(x,z,t) \qquad (3)$$

Since the water level variation can not be neglected in the present experiments, cross sectional area A was divided as follows:

$$A(x,t)=A_0(x)+A_1(x,t) \qquad (4)$$

Using an overbar ($\bar{\ }$) to denote a vertical average, and $\langle\ \rangle$ a tidal cycle average, $u_0=\langle\bar{u}\rangle$, $C_0=\langle\bar{C}\rangle$, and $A_0=\langle A\rangle$. Further,

$$u_1=\bar{u}-u_0, \quad C_1=\bar{C}-C_0, \quad A_1=A-A_0 \qquad (5)$$

$$u_s=\langle u\rangle-u_0, \quad C_s=\langle C\rangle-C_0 \qquad (6)$$

and u' and C' are the remainders. In the Eq.(6), $\langle u\rangle$ and $\langle C\rangle$ for the position above the low water level were evaluated during the period when the position was in water.

The total salinity flux F is decomposed as follows:

$$F=\langle A\cdot\overline{uC}\rangle=F_1+F_2+F_3, \qquad F_3=F_{31}+F_{32}+F_{33} \tag{7}$$

where

$$\begin{aligned}
F_1&=C_0A_0u_0+C_0\langle A_1u_1\rangle\\
F_2&=A_0\langle u_1C_1\rangle+\langle A_1u_1C_1\rangle+u_0\langle A_1C_1\rangle\\
F_{31}&=A_0\langle\overline{u_sC_s}\rangle+\langle A_1\cdot\overline{u_sC_s}\rangle\\
F_{32}&=A_0\langle\overline{u'C'}\rangle+\langle A_1\cdot\overline{u'C'}\rangle\\
F_{33}&=A_0(\langle\overline{u_sC'}\rangle+\langle\overline{u'C_s}\rangle)+\langle A_1\cdot\overline{u_sC'}\rangle+\langle A_1\cdot\overline{u'C_s}\rangle
\end{aligned} \tag{8}$$

F_1 is the flux due to the river discharge. F_2 is the tidal cycle

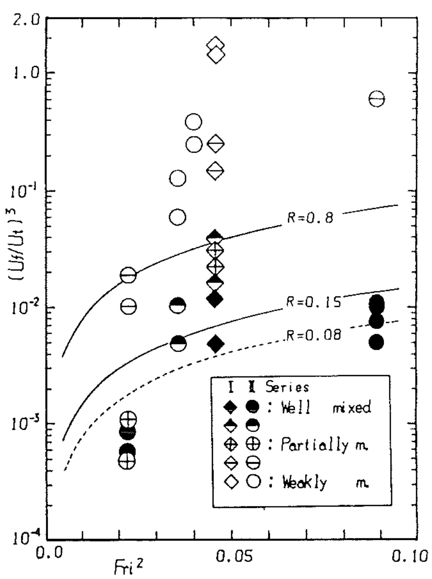

Fig.4 Classification of mixing type.

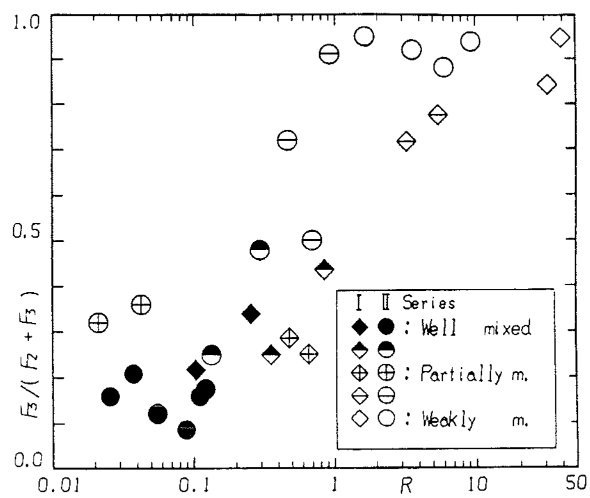

Fig.5 Relative magnitude of flux components F_2 and F_3.

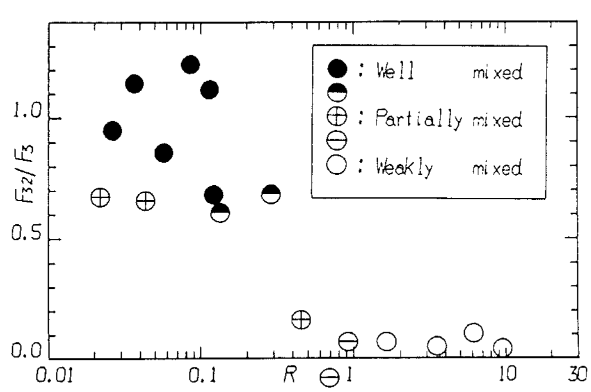

Fig.6 Relative magnitude of F_{32} in the component F_3.

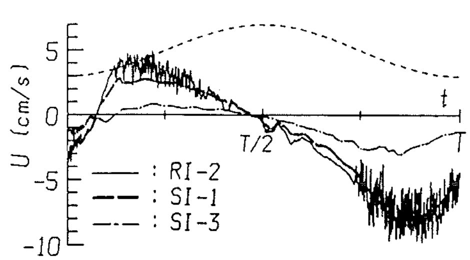

Fig.7 Variations of the measured velocity over a tidal period (x=40cm, z=2cm).

correlation of the cross-sectional averages. F_{31} is the component due to the residual circulation, and F_{32} is the one representing the effect of shear and turbulent diffusion.

These components were evaluated at two cross sections, x=0.4m and x=1.2m, by using the obtained data for each case, and were compared with each other. The results are shown in Table 1 and Figs.5 and 6. Figure 5 indicates the contribution of F_3 compared with F_2, and Fig.6 indicates the relative magnitude of F_{32} in the component F_3.

The significant characteristics for the well mixed type are that F_2 is relatively large compared with F_3, and that F_{32} is predominant in the F_3 component. Since F_2 is a tidal cycle correlation of velocity, salinity and water surface elevation, F_2 would be large if the temporal profiles of those quantities are distorted from the sinusoidal curve. The profile of salinity was observed to be deformed in the well mixed flows, and to change with the position along the flume. Large F_2 is caused by the asymmetry of the salinity between the flood and ebb phases.

As mentioned above, F_{32} is the component due to the dispersion and turbulent diffusion. Large F_{32} in well mixed case is considered to correspond to the stronger turbulence generation. Figure 7 shows the variations of the measured velocity over a tidal period for three cases in series I. It can be seen that large fluctuations of velocity appear as the mixing type changes toward the well mixed one.

Conclusion

Tidal river flows of well and partially mixed types have been studied mainly by field observations or large scale laboratory experiments. In the present study, it was shown that such flows can be reproduced even in a small scale flume if the experimental conditions are controlled properly. It was also certified that the estuarine Richardson number suggested by Fischer is effective to classify the mixing types even for the small scale models.

An advantage of the small scale flume is that dense and precise measurement is possible. For the first step of taking this advantage, the structure of salinity transport in the well and partially mixed type flows as well as the weakly mixed ones were determined in relation to the characteristics of the velocity and salinity fields.

The authors express their thanks to T.Manaka, T.Onuki, D.Sakuma, H.Tosaka and K.Saito for assistance in conducting the experiments and making figures.

References

Fischer, H.B. 1972. J. Fluid Mech., 53, pp.671-687.

Fischer, H.B. 1979. "Mixing in Inland and Coastal Waters", Academic Press, pp.229-278.

Ippen, A.T. & Harleman, D.R.F. 1961. U.S.Army Waterways Experiment Station Vicksburg, Miss. Tech. Bull. no.5.

Perrels, P.A.J. & Karelse, M. 1981. "Transport Models for Inland and Coastal Waters", Academic Press, pp.483-535.

Rigter, B.P. 1973. J. Hydraul. Div., Proc. ASCE, 99, pp.1475-96.

PHYSICAL MODELING OF SALINITY INTRUSION INTO ROTTERDAM WATERWAY ESTUARY

by Peter de Jong and Gerrit Abraham
DELFT HYDRAULICS, P.O.Box 177
2600 MH Delft, The Netherlands

Abstract

Reproducing vertical mixing due to bed-shear generated turbulence is a critical issue in physical salinity intrusion modeling for partly mixed estuaries. It involves the selection of a type of added resistance, which acts properly at a mixing device. Within this context, the paper summarizes experimental evidence, obtained in the Rotterdam Waterway salinity intrusion model, which shows that (1) to some extent the vertical salinity distribution can be influenced by the type of added resistance, and (2) using the type of resistance selected for this model, salinity is properly reproduced for a range of conditions.

1. Introduction

In the 1976 volume of Annual Review of Fluid Mechanics, Fischer (1976) concludes that hydraulic scale models, so long as their restrictions are borne in mind, are useful tools for problems of salinity intrusion, involving three-dimensionality, complex boundaries or stratification, for which hardly any other tools are available. With respect to the reproduction of the vertical salinity distribution in partly mixed models, he notes that vertical resistance strips play an empirically important role, but their role is by no means clear. Harleman (1971) gives scaling relationships for these models, elaborating upon the role of the strips as an empirical factor. Simmons and Bobb (1965) report an excellent reproduction of salinity distribution by means of the strips for the Hudson River model ($n = 10$).

Within this context the paper gives a short description of the processes, which influence the salinity intrusion into the partly mixed Rotterdam Waterway Estuary. It shows that reproduction of the large-scale processes is straightforward, while vertical small-scale mixing is insufficient unless compensated by added resistance acting as a mixing device. It presents experiments on the effect of the type of added resistance on the salinity distribution, and describes the type of added resistance used in the Rotterdam Waterway salinity intrusion model. It summarizes model-prototype comparisons, which show this type of added resistance to reproduce the salinity intrusion properly over a range of tidal conditions and fresh water discharges.

2. Rotterdam Waterway Estuary

The Rotterdam Waterway Estuary (Fig. 1), is formed by the New Meuse, the Old Meuse and the New Waterway. Fresh water, which flows into the estuary through the New Meuse and the Old Meuse, issues into the North Sea through the New Waterway.

On a large scale, salinity intrusion into the partly mixed estuary depends on tidal action and fresh water discharge. Gravitational circulation is a driving mechanism. Large-scale mixing is induced by phase differences between the tidal velocities in the New Meuse and the Old Meuse. It further is due to density induced exchange flows between the main estuary channels and harbor basins located along the estuary (Abraham et al, 1986). These large-scale processes act by advection.

Small-scale turbulent processes influence the stratification and thereby the strength of the gravitational circulation. They are due to bed-shear generated turbulence and turbulence generated by side walls and the groynes at the banks of the New Waterway.

3. Rotterdam Waterway salinity intrusion model

The salinity intrusion in the Rotterdam Waterway has been studied in a physical model (vertical length scale 1/64, horizontal length scale 1/640, distortion 10). In 1965 the model was built for a navigability study. The first task of the model was to provide information on the three-dimensional flow field near the entrance of the Rotterdam Waterway and the effect of coastal and density currents thereon. A model-prototype comparison showed this flow field to be properly reproduced (Breusers and van Os, 1981). In a later stage, emphasis shifted gradually to determining the effect of changes in the geometry of the estuary on salinity intrusion. At present the model is no longer in use. It is being replaced by a three-dimensional mathematical model. This development is supported by a flume study and field experiments, such as the observation of internal wave activity in the Rotterdam Waterway Estuary by acoustic images (Pietrzak et al, 1989). To account for the damping of turbulence by density stratification, the conversion of turbulent energy into internal wave energy, and vice versa, will eventually be incorporated in the mathematical model (Uittenbogaard and Baron, 1989).

4. Scaling requirements

The model follows the Froude scaling law, $u_r^2 = h_r$, with $\rho_r = 1$ and therefore $S_r = 1$, where subscript r is the ratio of model-to-prototype quantity, u is a longitudinal velocity, h is a vertical length, ρ is the density and S is the salinity. The model reproduces the above large scale processes correctly, once it is adjusted for tidal propagation.

Distortion implies $I_r = h_r/L_r = n$, where I is the slope of the water surface, L is a horizontal length and n is the distortion. The effect of the bottom shear stress, τ_b, on the surface slope is given by $\tau_b/\rho h$, that of the sidewall shear stress, τ_w, by $\tau_w/\rho b$, where h and b are the depth and width of the channel. Therefore, reproduction of tidal propagation requires

$$(\tau_b)_r = n\ h_r \qquad\qquad (\tau_w)_r = h_r \tag{1}$$

In accordance with Eq. 1, the required frictional resistance of the bed increases with the distortion and that of the side walls does not. Therefore, in a distorted model bottom roughness must be added, addition of side wall roughness is not needed and groynes and other protrusions from the side walls must be reproduced geometrically similarly. The distortion is not significant for this geometrically similar reproduction as the flow separates from the protrusion in nature.

Conservation of salinity implies that the vertical gradient of the vertical transport of salinity, F_z, must scale as the horizontal gradient of the longitudinal advective transport, uS. The turbulent energy balance requires the production of turbulent energy, P, to scale as F_z. Hence, since $S_r = 1$, proper reproduction of stratification requires

$$(F_z)_r = n\ h_r^{½} \qquad\qquad P_r = n\ h_r^{½} \tag{2}$$

In accordance with Eq. 2, the required mixing increases with the distortion. Therefore, after adjusting a distorted model for tidal propagation, the salinity distribution must be verified.

For side wall generated turbulence, eddy viscosity and eddy diffusivity are propositional to $(\tau_w/\rho)^{1/2}b$. This implies that the requirements of Eqs. 1 and 2 are compatible. Mixing due to side wall roughness generated turbulence is correctly reproduced in a distorted model, once its effect on tidal propagation is properly reproduced. The same holds for mixing due to groynes and other protrusions from the side walls, the shape of which is reproduced geometrically similar.

For bed-shear generated turbulence eddy viscosity and eddy diffusivity are proportional to $(\tau_b/\rho)^{1/2}h$. Assuming that after adjustment for tidal propagation this also holds for a distorted model, the production of turbulent energy is too much concentrated at the bottom, the vertical mixing is $n^{1/2}$ times too small, and the horizontal exchange is $n^{3/2}$ times too strong. This means that the additional frictional resistance must be provided by resistance elements, which act properly as a vertical mixing device. The strips mentioned in the introduction, which distribute the generation of turbulence over the depth and induce vertical currents along their faces, are introduced as such. While reinforcing the vertical mixing, the resistance elements are likely to reinforce the horizontal exchange as well.

5. Effect of type of resistance on salinity

Additional resistance elements - all with the same effective resistance - were compared with respect to their effect on salinity distribution: cubes ($5 \times 5 \times 5$ cm^3) placed on the bottom, vertical bars (horizontal cross-section $\frac{1}{2} \times \frac{1}{2}$ cm^2) over the whole depth, and elements with a cross-shaped horizontal cross-section (two vanes, 3×3 cm^2 each) (Fig. 2). The experiments were made in a flume, schematizing the Rotterdam Waterway Estuary as a single straight channel with constant rectangular cross-section without harbor basins along it at the same scale as the Rotterdam Waterway salinity intrusion model. The flume width-to-depth ratio was 3. It was about equal to that of the New Waterway section of the distorted model. The corresponding prototype value is ten times larger as a result of the model distortion.

Fig. 3 gives results of the experiments. For the flume experiments, the total resistance (of bottom and side walls combined) corresponded to that of the Rotterdam Waterway at model scales. For some of the flume experiments, the contribution of the side walls was about 10% (Fig. 3a), for other flume experiments (Fig. 3b) it was about 30% as for the Rotterdam Waterway salinity intrusion model (Fig. 3c) because of the groynes. Fig. 3 shows the effect of the type of additional resistance to decrease with increasing side wall resistance. From this perspective, relatively wide estuaries are more difficult to be modeled than relatively narrow estuaries.

Because of the large-scale mixing processes and the side-wall effects, the type of additional resistance was not deemed critical for Rotterdam Waterway conditions. The cross-shaped elements were finally selected for practical modeling reasons: They allowed easy cleaning of the model. Their resistance did not vary significantly with the direction of flow in the horizontal plane. They would cause little accumulation of bed material, simulating sediment transport.

6. Model-prototype comparisons

After the model was adjusted for tidal propogation, using the cross-shaped elements, model-prototype comparisons were made for verification of the velocity and salinity distribution. Table 1 gives the conditions involved for the comparisons given in this paper, in addition to those given by Breusers and van Os (1981). It lists: the fresh water discharge of the New Waterway (Q), the tidal range at the mouth of the estuary (Δh) and the estuary number, E_D, a measure of the stratification (Thatcher and Harleman, 1981), defined as

$$E_D = \frac{P_t}{Q\ T} \frac{u_o^2}{\frac{\Delta\rho}{\rho} g\ h_0} \qquad (3)$$

where $\Delta\rho$ is the difference in density between river and sea water, P_t is the volume of sea water entering the estuary on the flood tide, T the duration of the tidal cycle, u_o is the maximum profile averaged flood velocity at the mouth of the estuary, h_o is the time averaged depth at the mouth of the estuary and g is the gravitational acceleration.

For the 1979 measurements listed in Table 1, velocity and density distributions were obtained from field measurements made from vessels at the centre line of the channels. For the 1976 period field data were obtained from a limited number of continuous density registrations from the banks. Wind influence was insignificant for the 1979 measurements. The E_D values listed in Table 1 refer to partly mixed conditions. They cover the range of stratifications of interest.

Fig. 4 gives the model-prototype comparisons for the 1979 periods, for $E_D = 2.2$ and $E_D = 0.62$. Fig. 4 is representative for the model-prototype agreement found. For September 17, 1979 with a neap-tide ($E_D = 0.37$) and wind set-up at sea noticeable deviations were found (Van der Heyden et al, 1984).

Fig. 5 gives the model-prototype comparison for August 1976, when river discharge was low, E_D ranging from 0.56 to 3.2. Fig. 5a gives the tidal conditions at the mouth of the estuary. Fig. 5b illustrates that in the vicinity of critical intakes, a proper reproduction of the duration of the periods with salinities above that of river water was found. As the measurements involved were made from the banks, differences in salinities were to be expected.

Summarizing, the Rotterdam Waterway Estuary being relatively narrow (Section 5), satisfactory model-prototype agreement was found for the range of stratifications of interest ($0.6 < E_D < 3.2$).

Table 1 Conditions for model-prototype comparisons

date	Q m^3/s	Δh m	E_D
21 May 1979	1690	1.63	0.62
10 Sept. 1979	880	2.00	2.2
20 Aug. 1976	784	1.22	0.56
27 Aug. 1976	736	2.14	3.2

References
- Abraham, G, de Jong, P, and van Kruiningen F.E., "Large-scale mixing processes in a partly mixed estuary", Physics of shallow estuaries and bays, van de Kreeke, J. ed., Springer Berlin, 1986, pp 6-21
- Breusers, H.N.C., and Van Os, A.G. "Physical modeling of Rotterdamse Waterway estuary", Journal of the Hydraulics Division, ASCE, Vol. 107, No. HY11, Nov. 1981, pp 1351-1370
- Fischer, H.B., "Mixing and dispersion in estuaries", Annual Review of Fluid Mechanics, Vol. 8, 1976, pp 107-133
- Harleman, D.R.F., "Physical hydraulic models", Estuarine modeling: an assessment, Ward, G. and Espey, W., eds., Environmental Protection Agency, Report 16070 DZV 02/71, Washington DC, Government Printing Office, 1971, pp. 215-263
- Pietrzak, J.D., Abraham, G., and Kranenburg, C., "Field observations of internal waves in the Rotterdam Waterway", Report Z162-60, Parts 1 and 2, DELFT HYDRAULICS, 1989
- Simmons, H.B. and Bobb, W.H., "Hudson River channel, New York and New Jersey plans to reduce shoaling in Hudson River channels and adjacent pier slips, Technical report 2-694, U.S. Army Engineer Waterways Experiment Station, 1965
- Thatcher, M.L. and Harleman, D.R.F., "Long-term salinity calculation in Delaware Estuary", Journal of the Environmental Engineering Division, ASCE, Vol. 107, No. EE1, Febr. 1981, pp. 11-27
- Uittenbogaard, R.E. and Baron, F., "A proposal: Extension of the q^2-ε model for stably stratified flows with transport of internal wave energy", Proceedings of Seventh Symposium on Turbulent Shear Flows, Stanford, Vol. 2, 1989, pp. 18.4.1-18.4.6
- Van der Heijden, H.N.C.M., de Jong, P., Kuijper, C. and Roelfzema, A., "Calibration and adjustment procedures for the Rhine-Meuse estuary scale model", Proceedings of the Nineteenth International Conference on Coastal Engineering, Houston, Vol. 3, 1984, pp 3180-3196.

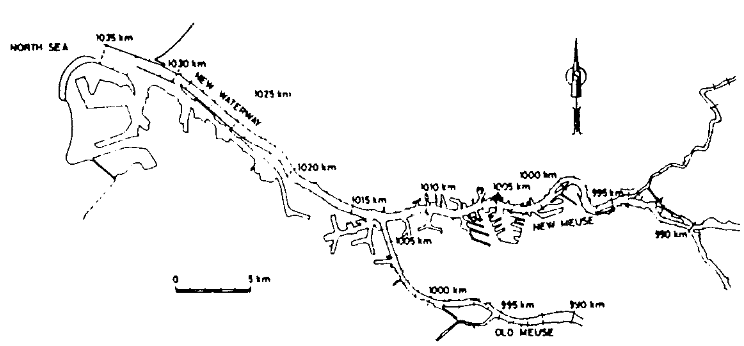

FIG 1. ROTTERDAM WATERWAY ESTUARY

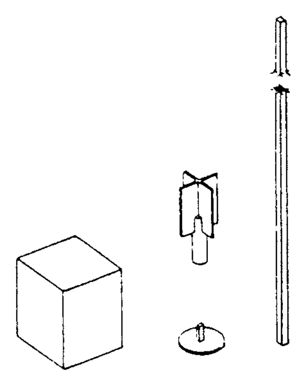

FIG 2. RESISTANCE ELEMENTS

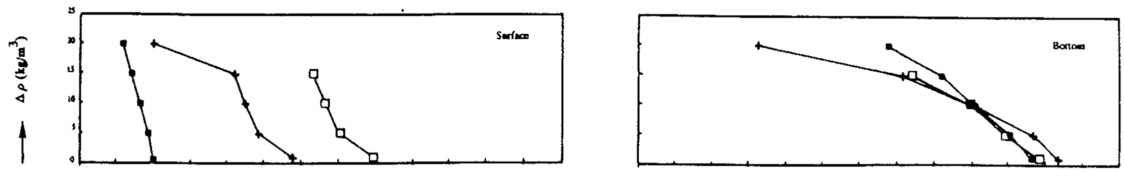

Fig3[a]. Tidal flume without side wall roughness ■T 3 (bars) +T 31 (cross shaped el.) □T 644 (cubes)

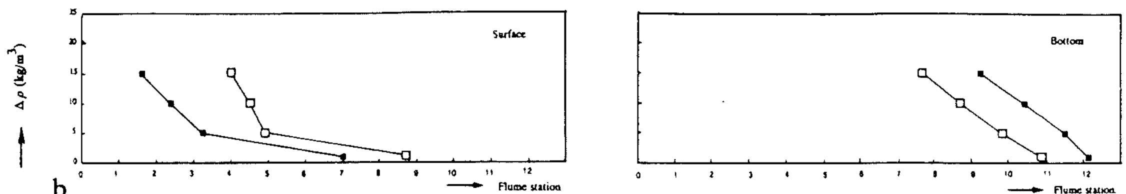

Fig 3[b]. Tidal flume with side wall roughness ■T 643 (bars) □T 640 (cubes)

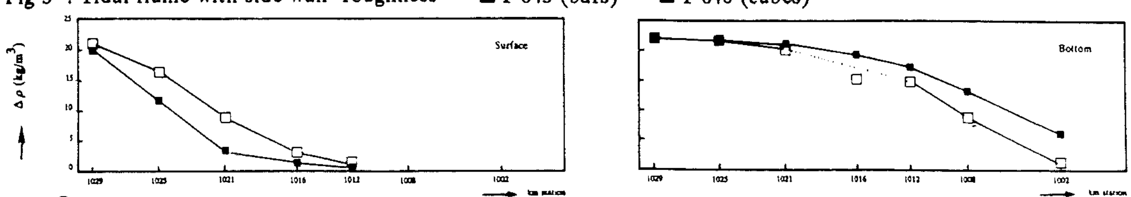

Fig 3[c]. Rotterdam Waterway Salt Intrusion Model ■T 41 (bars) □T 31 (cubes)

FIG 3. LONGITUDINAL DENSITY DISTRIBUTION AT HWS EFFECT OF TYPE OF RESISTANCE

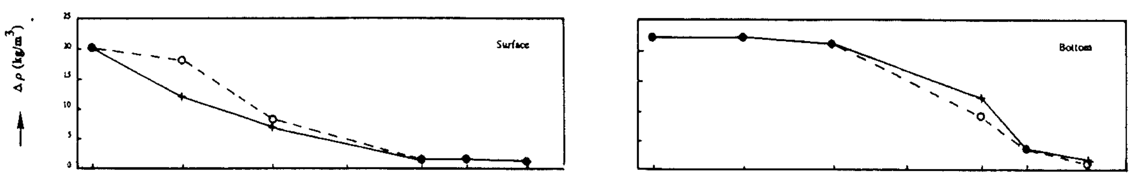

Fig 4[a]. 10 September 1979

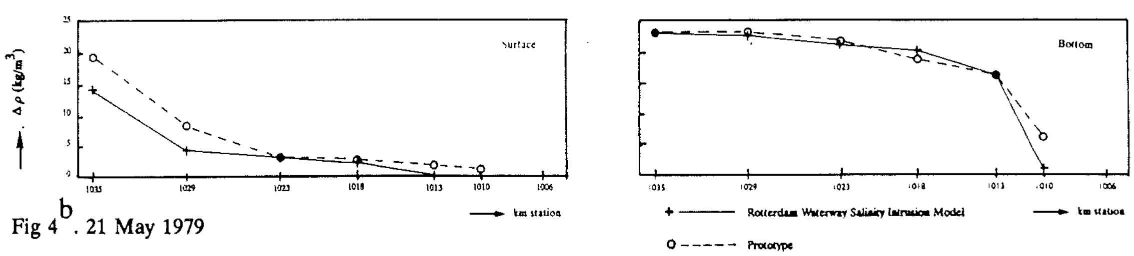

Fig 4[b]. 21 May 1979

FIG 4. LONGITUDINAL DENSITY DISTRIBUTION AT HWS MODEL-PROTOTYPE COMPARISON

Fig 5[a].
Tidal elevation
km station 1029

Fig 5[b].
Density response
Old Meuse
station 1003
1.0 m-MSL

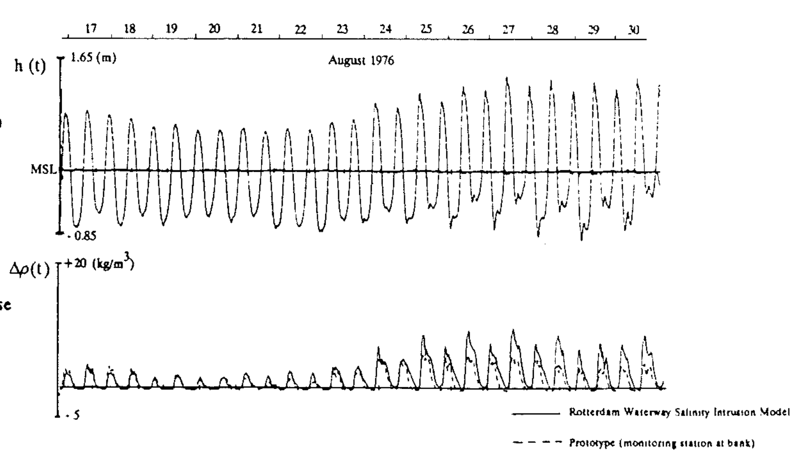

FIG 5. TIME SERIES MODEL-PROTOTYPE COMPARISON AUGUST 1976

EXPERIMENTAL STUDIES ON DYNAMIC CONTROL OF SALINITY INTRUSION

by

Gerhard H. Jirka and Paul Akar
DeFrees Hydraulics Laboratory
School of Civil and Environmental Engineering
Cornell University, Ithaca, New York, 14853

Some river and coastal waterways experience salinity intrusion over long distances in form of a salt wedge, a two-layer stratified system in which a bottom salt layer is overflown by the freshwater flow. Recent experimental and theoretical work at Cornell University (Jirka and Arita, JFM, 1987) has demonstrated that small local perturbations of the boundary layer (velocity distribution) of the ambient river flow can be used to locally arrest the salinity intrusion in the form of a stationary density current with a head wave and to eliminate thereby the long distance salt wedge intrusion. The dimensions of the control device (e.g. a small barrier or a suction device) are small relative to the ambient depth and the device indeed relies on a dynamic control effect (as opposed to a static control as would be exercised by a large physical barrier). The results of additional experiments on dynamic control will be presented in which alternate device geometries (e.g. bars, vanes or fences) and synergistic effects (e.g. combination with suction flow) have been examined.

Work supported by Waterways Experiment Station, U.S. Army Corps of Engineers.

ON KEULEGAN's "LAW OF MIXING IN THE SEA"

by T.A. McClimans,
Norwegian Hydrotechnical Laboratory
Norwegian Institute of Technology
N-7034 Trondheim, Norway

Abstract

In one of his many remarkable reports from the former National Bureau of Standards, Keulegan (1955) showed that mixing of seawater to the river plume in his experimental apparatus consistently gave a salinity increase to 34 % that of the seawater. He called this constant the "law of mixing in the sea". In a subsequent paper, McClimans (1979) showed that this constant could be used to calibrate a theory of frontal mixing in river plumes that matched a series of laboratory data for several different geometries.

Temperature-salinity analysis of field measurements in river plumes confirm the basic principles of the theory. Several examples from field observational programs give results which are consistent with the extension of Keulegan's "law" when the geometrical constraints are taken into account, showing the lasting value of his careful observation and documentation.

Introduction

Mixing of seawater to river plumes is an important process for the dilution of polluted waters and, in arctic and sub-arctic regions, also important for inhibiting ice formation during the coldest months of winter. It is therefore useful to have a law of mixing which is robust and applicable to many situations. Such a law was suggested by Keulegan (1955) as a spinoff of his study on mixing in salt wedges in a river channel. The present work, based largely on McClimans (1979), demonstrates the strength and limitation of Keulegan's result.

Frontal mixing

McClimans (1979) proposed a model for river plume entrainment of seawater which was based on the mixing processes associated with the energetic billows near the front of the spreading, densimetric flow. The motivation for the theory was the recognition that the potential energy flux of the river plume is important for the mixing mechanism and that the global aspects of this could therefore be modelled in the laboratory even with vertical distortion as long as two frontal regions do not merge. This requires further that the interfacial mixing beneath the centerline of the expanding plume makes only a minor contribution to the total entrainment.

Figure 1 shows a lateral cross section of an expanding river plume with useful nomenclature. The theory, which was developed for river flow to a fjord basin with finite width W, and therefore containing a two-layer hydrography, applies also to an open ocean ($W = \infty$) for which the salinity is constant with depth $S(z) = S_2$.

The justification of the frontal mixing model gained support from a field investigation of the Steinkjer river plume polynya in the ice-covered Beitstadfjord near Trondheim during the winter of 1978.

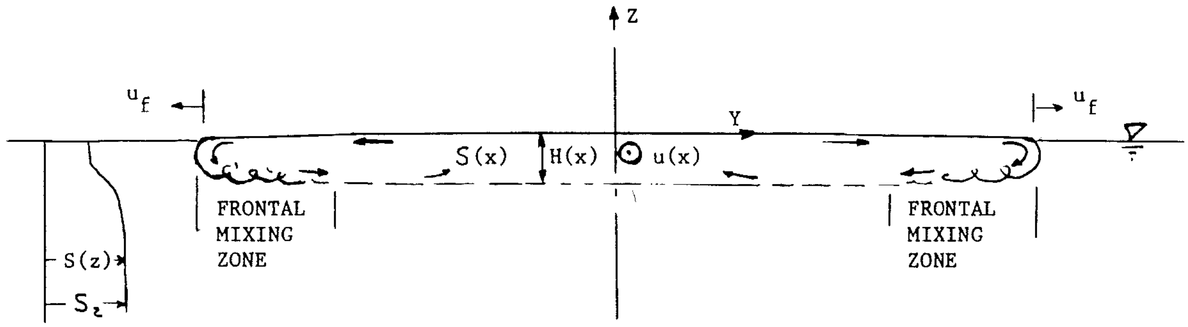

Figure 1. A lateral cross section through an expanding river plume: u(x) = longitudinal plume velocity, H(x) = plume thickness, S(x) = plume salinity and u_f = lateral velocity along the expanding front. The lateral secondary flow components which transport entrained sea water to the center of the plume are shown by arrows.

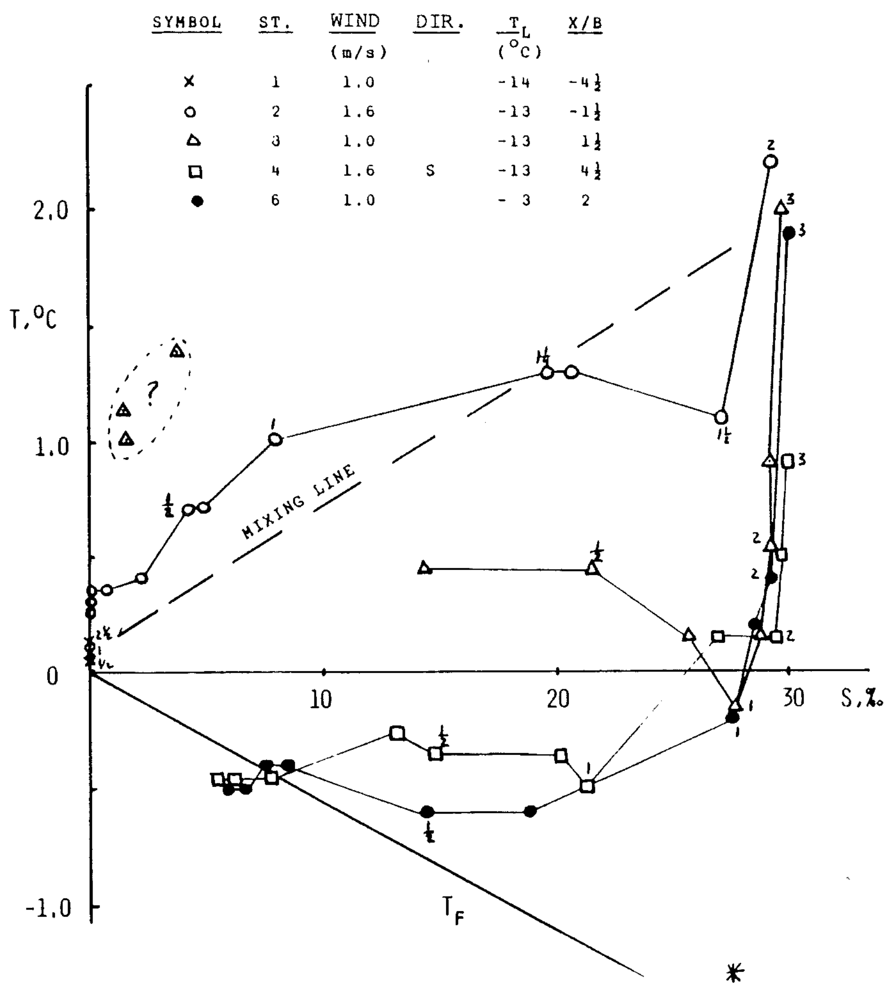

Figure 2. Vertical temperature-salinity profiles along the Steinkjer river plume, Feb 1978. Numbers give depths in meters. (The group of data with a question mark is believed to be from a local heated fresh water plume near the mouth of the river.) T_F is the freezing temperature.
(McClimans et al., 1978)

The temperature-salinity diagram of Figure 2 shows the essential features of the salinity increase seaward of the river mouth, $x/B > 0$, where B is the width of the river. The plume becomes colder as surface water from under the ice (noted by a star on Figure 2) gets advected to the central portion of the plume in the lateral secondary flow sketched in Figure 1. Vertical entrainment would produce the hydrography represented by the mixing line noted in Figure 2.

Assuming that the local frontal entrainment is proportional to the local river buoyancy flux, decaying exponentially in x, and integrating it over H(x) to large x, where $S(x) = S_1$, say, the following expression was obtained:

$$\frac{9}{4}\left(\frac{S_2}{S_2-S_1}\right)(B/W)^{4/3} - 3(B/W)^{2/3} + \frac{S_2-S_1}{S_2} - \frac{S_1}{S_2}\left[K_1+K_2(H_0/B)\right]^{-1} = 0$$

Here $H_0 = H(0)$ is the thickness of the river plume at the river mouth, and K_1 and K_2 are empirical constants of the theory.

Laboratory confirmation

The two empirical constants K_1 and K_2 were determined by the laboratory data of McClimans and Sægrov (1982) to be $K_1 = K_2 = 1.31$. The results are plotted in Figure 3 where Keulegan's "law of mixing in the sea" appears to be compatable with the frontal mixing model. In retrospect, the fact that $K_1 = K_2$ implies that a theory could be developed for only one unknown constant, in which case Keulegan's "law of mixing in the sea" would have satisfied the needs. This shows

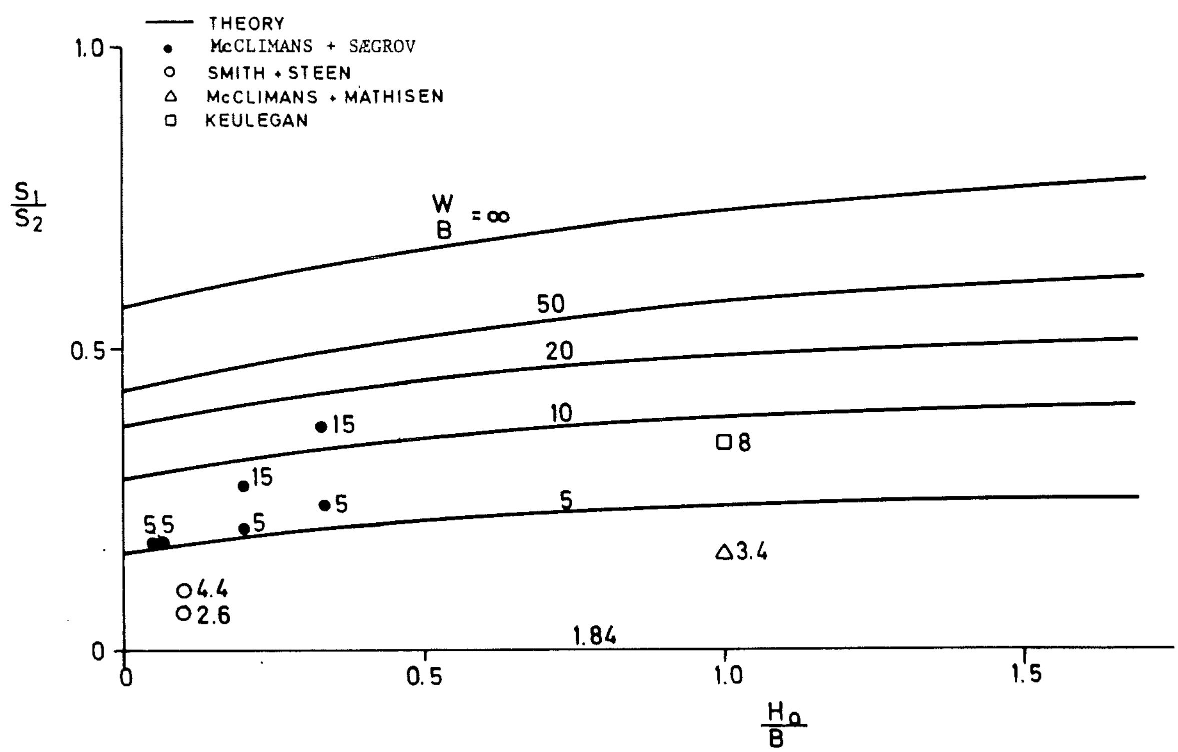

Figure 3. Comparison of laboratory data with the theory of frontal mixing of river plumes. Numbers refer to W/B (McClimans, 1979).

the lasting value of well-documented, careful laboratory observations even when they are spinoffs from other dedicated studies.

Applications

The situation of greatest interest is a river plume ($H_0/B << 1$) in an open ocean ($W/B \to \infty$) for which the law of mixing in the sea should be $S_1/S_2 = 0.57$. This means that the total entrainment of seawater to the active, potential energy driven frontal turbulence is about 4/3 times the river discharge. The laboratory results showed further that this total entrainment was accomplished within a plume distance $x \approx 7B$ from the river mouth. The laboratory results imply that the star in Figure 2 should have been placed near $S_1 = 17$ o/oo.

There are some well documented river plume studies which may be compared to this present result. Luketina and Imberger (1987) have commented some of these and have further presented a study of frontal entrainment with a time-varying outflow from an estuary to an open ocean. Unfortunately, there is no way to isolate the total river plume driven entrainment from other natural sources of mixing energy. For example, Garvine (1974) concluded that entrainment is away from the plume (downward) which is true for the far field where the level of ambient turbulence exceeds the contribution of energy from the river plume. The near fields of these studies, however, give rates of entrainment which are congruent with the river plume data mentioned above.

The weak gradient $\partial(S_1/S_2)/\partial(H_0/B)$ for $H_0/B \approx 0$ (Figure 3) implies that river plume entrainment is not very sensitive to the aspect ratio of a river mouth. This implies that the energetics of river plume mixing can be simulated in distorted laboratory models without regard to the detailed nature of the frontal vortices, provided they exist. Thus, the usual critical values of Keulegan number, etc must be maintained for dynamic similitude of flow instabilities that provide the overall mechanisms for conversion of potential energy flux to entrainment (McClimans and Sægrov, 1982).

Acknowledgement

This work was supported by Konsesjonsavgiftsfondet (The Fund of license fees).

References

Garvine, R.W. (1974): Dynamics of small-scale oceanic fronts. J. Phys. Ocean. 4:557-569.

Keulegan, G. (1955): Seventh progress report on model laws for density currents. Interface mixing in arrested saline wedges. NBS Report 4142.

Luketina, D.A. and Imberger, J. (1987): Characteristics of a surface buoyant jet. J. Geophys. Res. 92:5435-5447.

McClimans, T.A. (1979): On the energetics of river plume entrainment. Geophys. Astrophys. Fluid Dyn. 13:67-81.

McClimans, T.A., Mathisen, J.-P. and Gjerp, S.A. (1978): Is i fjorder. Delrapport 2. VHL rapport STF60 A78084. (In Norwegian).

McClimans, T.A. and Sægrov, S. (1982): River plume studies in distorted Froude models. J.Hyd. Res. 20:15-27.

HYDRAULIC MODELING OF BENTHIC SUSPENSION FEEDING BIVALVES IN SHALLOW ESTUARIES

Catherine A. O'Riordan, Jeffrey R. Koseff, and Stephen G. Monismith
Environmental Fluid Mechanics Laboratory
Department of Civil Engineering
Stanford University, Stanford, CA 94305-4020 USA

Abstract

We carried out experiments studying the hydrodynamics of bivalve siphonal currents in a laboratory flume. Rather than use living animals, we devised a simple model siphon pair connected to a pump. Fluorescence-based flow visualization was used to characterize siphon-jet flows for several geometric configurations and flow speeds. These measurements show that the boundary-layer velocity profile, siphon height, siphon pair orientation, and the size of siphon structure all affect the vertical distribution of the excurrent flow downstream of the siphon pair and the fraction of excurrent that is re-filtered. Due to the vorticity inherent to the velocity shear in the boundary layer, trajectories of excurrent flows are flatter than theoretical predictions of trajectories of a jet in a crossflow.

Introduction

Through recent studies it has become apparent that benthic bivalves can regulate phytoplankton biomass in shallow marine systems such as estuaries (Dame et al. 1980, Cloern 1982). To demonstrate this relationship between the water column and the benthos in unstratified systems, the usual approach (e.g. Cloern 1982) has been to estimate the time that benthic grazing by the bivalve population would require to consume the available phytoplankton biomass and then to compare this estimate with the time scales of other processes that affect phytoplankton biomass, e.g. zooplankton grazing and primary production. To estimate the time scale of benthic grazing, the average depth of the estuary or embayment is divided by the community filtration rate, expressed in terms of depth of water column filtered per day. This means of calculating the rate of phytoplankon removal from the water column by benthic bivalves assumes that hydrodynamics do not constrain particle transport from the water column to the benthos.

However, it is known that benthic bivalves feed from a zone of strong vertical gradients of flow velocity and particle concentration (Nowell and Jumars, 1984). As a result, the bivalves filter fluid that does not have the freestream (depth averaged) concentration of phytoplankton biomass; consequently, the simple method of estimating benthic grazing effects outlined above may fail in some cases. To predict when hydrodynamic processes will have an effect on phytoplankton removal by benthic bivalves, knowledge of a the vertical distribution of phytoplankton removal, or 'sink' distribution, may be crucial to correctly modeling the effects of mixing and advection on the efficiency of bivalve feeding, and thus the link between the benthic consumption and algae produced in the water column.

As a first step towards understanding the mechanics of phytoplankton removal by filter-feeding benthic bivalves, we have performed a study focussing on the hydrodynamic characteristics of feeding currents of a siphonate bivalve. In order to establish a number of the fundamental features of the siphonal currents, a single pair of model siphons was used with various geometric and flow configurations. The reason for doing so is because the flow associated with feeding by a single animal is clearly a fundamental component of the larger-scale process of feeding by an entire population of bivalves.

Experimental methods

For our study of a single siphon pair in a turbulent boundary layer, we installed a model siphon pair in a laboratory flume (Fig. 1). The flume is 12 m long and 0.31 m wide. To control the boundary-layer characteristics in the experiments, we constructed a false-floor test section 200 mm above the bed of the flume that starts 5 m from the inlet and extends for 1.22 m. The boundary layer was "tripped" near the upstream edge of the test section to ensure the existence of a turbulent boundary layer at the siphon pair. For all of the experiments reported below, the boundary-layer thickness (defined as the height at which $U = 0.99\ U_\infty$), was approximately 75 mm.

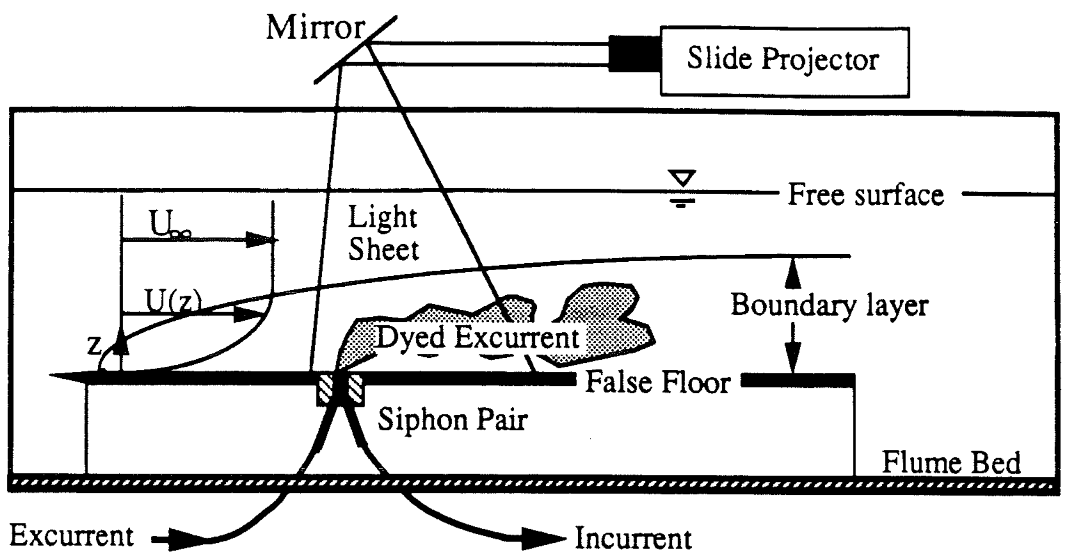

Figure 1: Sketch of experimental setup.

The scale of our model "bivalve" (physical size and pumping rate) corresponds to a large clam such as *Tapes japonica,* which is a common benthic bivalve in estuaries along the Pacific coast of the United States. The ratio of approximately 2:1 for incurrent to excurrent diameters used in our model is common in siphonate bivalves (Ansell 1961). The siphon heights (0-10 mm) were chosen to cover the range, starting with siphons fully buried (h_s = 0), observed for *T. japonica* in recent laboratory flume experiments reported in Cole et al. (unpublished).

To visualize the flow behavior of the siphon pair, we mixed a concentrated solution of Rhodamine WT (typically 10 cc) into the excurrent fluid. Because of the high velocities at the outlet, the dye was effectively neutrally buoyant (cf. List 1982). For the purposes of extrapolating our results to natural systems, dyed fluid represents phytoplankton-depleted water. We used a slit light source to illuminate the dye as it was ejected from the outlet hole in the form of a small jet. We obtained images of the fluorescing excurrent jet by photographing it with a monochrome CCD camera (8 bits, 512 x 496 pixels) connected to a super-VHS video recorder. Thus, the relative intensity of any part of a dye-plume image provides a measure of the relative dye concentration. To extract the information required for concentration-field mapping, the video tape was later played through our image processor. Average images were formed by averaging 256 ($\approx$ 16 s) alternate video frames. Mean trajectories were determined from these images by locating the highest intensity pixel in the plume at locations downstream of the jet.

Results

Examination of individual frames of the "raw" video recording showed that the major mechanism mixing the siphon excurrent with the overlying flow was large-scale entrainment of clear boundary-layer fluid into the jet by the ubiquitous coherent structures present in turbulent boundary layers (see Cantwell 1981). The general appearance was that of a shearing instability on the edge of the plume.

Mean trajectories determined from processed images are given in Figure 2, a plot of the nondimensional x and z coordinates of the plume axis (line of maximum relative concentration). The measured x and z coordinates are nondimensionalized using the jet-in-crossflow length scale z_m given in List (1982), viz:

$$z_m = d_j U_j / U_\infty, \qquad (1)$$

where d_j and U_j are the jet diameter and velocity.

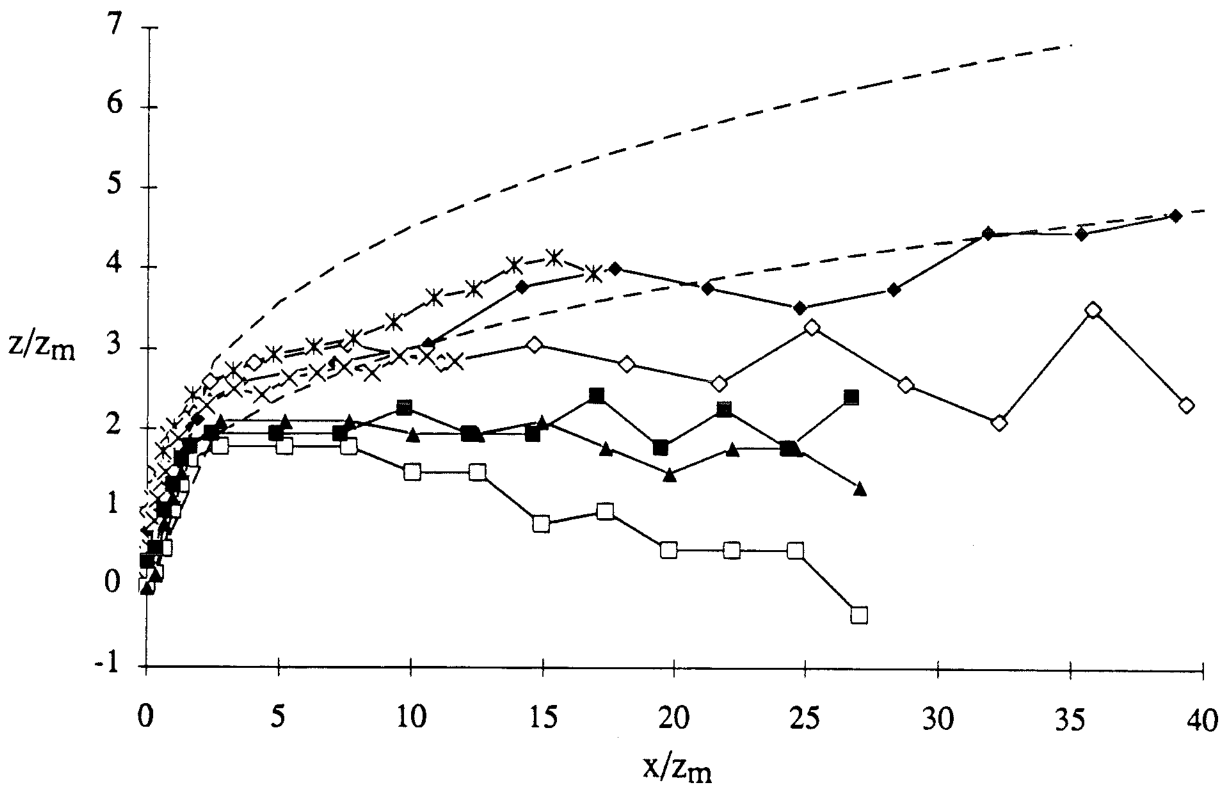

Figure 2: Excurrent jet trajectories: (●) excurrent siphon downstream, $h_s = 0$, $U_\infty = 280$ mm s^{-1}; (O) excurrent siphon upstream, $h_s = 0$, $U_\infty = 280$ mm s^{-1}; (■) excurrent siphon downstream, $h_s = 10$ mm, $U_\infty = 280$ mm s^{-1}; (□) excurrent siphon upstream, $h_s = 10$ mm, $U_\infty = 280$ mm s^{-1}; (▲) excurrent siphon upstream, incurrent siphon off, $h_s = 10$ mm, $U_\infty = 120$ mm s^{-1}; (✳) excurrent siphon upstream, $h_s = 0$, $U_\infty = 120$ mm s^{-1}; (✕) excurrent siphon upstream, $h_s = 10$ mm, $U_\infty = 120$ mm s^{-1}. The dashed lines represent the range of trajectories for a jet in a uniform crossflow (see text).

It is clear from these trajectories that siphon height, siphon orientation, crossflow velocity, and jet velocity all effect the shape of the trajectory. When the jet origin is at the bed, the jet experiences a weaker cross-flow than when it is elevated; as a consequence, the jet is less severely bent over by the overlying flow. The effect of siphon current strength is also illustrated by the flatter trajectory observed when $U_\infty = 280$ mm s^{-1} than when $U_\infty = 120$ mm s^{-1} indicating that the trajectory shape is a function of the ratio of jet speed to crossflow velocity, U_j/U_∞.

The effect of orientation is significant when the siphons are flush with the bed as well as when they are elevated (see Fig.2). When the excurrent siphon is downstream, the jet assumes the appearance of a "normal" jet in a cross-flow (see below) The attachment of the excurrent plume to the bed in the lee of the siphons for the outlet-upstream, $h_s = 10$ mm configuration was caused not only by the low pressure at the outlet, but also by the general flow around the siphon structure itself. When the siphon is not operating, the plume dips down behind the siphons, albiet less severely than when the inlet is operating .

Discussion

As reported by Ertman and Jumars (1988), the behavior of bivalve siphonal currents is similar to that observed for jets in cross-flows (e.g. Andreopoulos and Rodi 1984). The jet appears to be a "solid object" to the oncoming flow; as a consequence, it has a measurable effect on the overlying flow, modifying both mean-flow and turbulence properties near the bed (Monismith et.al. 1990). At the same time, the jet itself is bent over by the cross-flow, and any material it transports is mixed vertically downstream of the jet

There are several important differences between the siphon jet flows we have studied here and jets in uniform crossflows. Firstly, in the latter case, a single ratio, U_j/U_∞, expressing the relative importance of jet to crossflow momentum can be formed. In the present case, because the jet is immersed in the boundary layer, it experiences a range of velocities through its trajectory. For a jet in a uniform crossflow, List (1982) gives the following trajectory equation:

$$z(x)/z_m = C_2 \, (x/z_m)^{1/3} \tag{2}$$

where C_2 is a constant which has a value in the range of 1.4 - 2.1. The range of values for (2) are plotted as dashed lines in figure 2. Only two of the trajectories in this study fall into this range. Both of these trajectories are for the configuration of h_s=0 mm. Closer inspection reveals that the shape of the trajectories for h_s=10 mm cannot be represented by this equation.

To represent the trajectories in a boundary layer flow, we can derive a relationship similar to (2) for $U \sim (z/\delta)^{1/7}$ (an approximation to the actual log distribution). When the siphons are flush with the bed (h_s=0) the trajectory can be described by:

$$\left(\frac{z}{z_m}\right) = 1.03\, C_2^{\frac{21}{23}} \left(\frac{\delta}{z_m}\right)^{\frac{2}{23}} \left(\frac{x}{z_m}\right)^{\frac{7}{23}} \tag{3}$$

Because the velocity is less than U_0 near the bed, (3) always gives larger values of $z(x)/z_m$ than does (2) for a given value of C_2. Note, however, that the functional dependence on x/z_m is very close to that of uniform flow (1/3) and still does not describe the flattening.

Trajectories calculated using this power law relation with the range of values for C_2 given by List continue to rise rather than flatten out as observed. Therefore, using this modified power-law relation does not improve our prediction of trajectories found in this study.

The flattening of these trajectories can be explained by the effect of the vortex system which forms around the excurrent jet (Fric and Roshko 1989). The siphon-pair flow effectively slows down the cross-flow in a region just above it. Thus, momentum transfer in the boundary layer is locally different from that normally found. The reason for this difference is the "blocking" effect of the siphon jet due to its lack of horizontal momentum at its point of injection. In effect, stagnant fluid (in terms of horizontal momentum) is ejected vertically from the excurrent siphon into the boundary layer. Filaments of boundary-layer vorticity are twisted around the siphon jet, leading to the formation of a horseshoe vortex oriented with its open facing downstream. This vortex induces a down-flow along the center-line of the object which tends to draw down the excurrent jet.

Another factor that must be considered is the amount of fluid refiltered by the inlet siphon when it is downstream of the excurrent siphon. Significant amounts of exurrent fluid are refiltered, i.e. drawn into the incurrent siphon have been found to occur when the bivalve is in this configuration (Monismith et.al. 1990). The effect of refiltration on changing the shape of the trajectory may be an additional factor behind the lack of agreement of our measurements with theoretical predictions.

In terms of the effect of an individual bivalve on the concentration of suspended material in the overlying flow, the effective sink distribution is difficult to specify exactly. Nonetheless, we can specify its most important generic feature: the incurrent is primarily fluid drawn at the level of the inlet siphon, whereas the excurrent is distributed at a level above the excurrent siphon that is determined by the dynamics of the siphon jets. Most importantly, although fluid is withdrawn at the level of the inlet, the concentration of phytoplankton-biomass in the remaining fluid flowing at that level is unchanged. The fluid that passes through the bivalve population and is filtered, "reappears" with a concentration deficit as the excurrent plume. In effect, there is a conduit in the fluid that moves fluid from the intake level to the excurrent level, while also decreasing the amount of phytoplankton carried by the extracted fluid.

We can use this information to modify the steady-state phytoplankton mass balance equation given by Frechette et al. (1988) (their Eq. 5) through the addition of an appropriate term representing the effective sink created by the combined incurrent-excurrent flow-field. In terms of the concentration of phytoplankton biomass, F(x,z), which is a function of the mean velocity U(z), and the eddy diffusion coefficient K(z), we suggest the inclusion of the loss function given on the right-hand side below:

$$U\frac{\partial F}{\partial x} - \frac{\partial}{\partial z}\left(K\frac{\partial F}{\partial Z}\right) = -\frac{\alpha F_i}{\sigma}\phi\left(\frac{z - z_{out}}{\sigma}\right). \tag{4}$$

The sink term appearing on the r.h.s. of Eq. 4 is written in terms of the filtration velocity α, which is equal to the average flow per unit of area passing through the bivalve community, F_i, a flux-weighted average inlet concentration (which presumably is an average of the concentration very near the entrance to the inlet siphon), sink width and centroid elevation length scales σ and z_{out}, and a dimensionless function ϕ that mainly represents the shape of the vertical distribution of the excurrent plume.

Thus, in our model, (αF_i), the total loss of phytoplankton biomass (per unit of bed area), is determined by the inlet dynamics, whereas, the shape function ϕ, and the plume-width and centroid-elevation length scales σ and z_{out}, are determined by the excurrent dynamics. In other words, the total phytoplankton loss associated with bivalve filter feeding is set by the inlet siphon flow, whereas the elevation and distribution of its effect are set by the excurrent siphon flow. In this model, individual siphon heights and orientations may significantly influence the total rate of phytoplankton biomass removal by a bivalve population.

Conclusion

Our experiments show that the hydrodynamic characteristics of the siphon-jet flows in the near-bed region of a turbulent boundary layer can have a significant effect on the vertical distributions of phytoplankton-depleted fluid near the bed. Trajectories of excurrent siphon flows cannot be represented by theoretical predictions for a jet in a uniform crossflow. The effect of individual siphon jets on the overlying flow is determined by the effective sink distribution operating at the bed. In order to accurately predict this sink distribution, the terminal height of rise of the jet and the jet trajectory must be determined accurately. Thus, the hydrodynamic characteristics of feeding currents may affect both the effective clearance rate of an entire population of siphonate bivalves as well as the efficiency of feeding (i.e. the likelihood of re-filtration) of any individual.

Acknowledgements

Our research is supported by the USGS and by NSF grants OCE 8816931 and CTS 8958314 and by a gift from the Charles Lee Powell Foundation.

References

Andreopoulos, J., and W. Rodi. 1984. Experimental investigation of jets in a crossflow. J.Fluid Mech. **138**: 93-127.

Ansell, A. D. 1961. The functional morphology of the British species of Veneracea (Eulamellibranchia). J. Mar. Biol. Assoc. U. K. **41**: 489-515.

Cantwell, B. J. 1981. Organized motion in turbulent flow. Ann. Rev. Fluid Mech. **13**: 457-515.

Cloern, J. E. 1982. Does the benthos controls the phytoplankton biomass in South San Francisco Bay? Mar. Ecol. Prog. Ser. **9**: 191-202.

Dame, R., R. Zingmark, H. Stevenson, and D. Nelson. 1980. Filter feeder coupling between the water column and benthic subsystemsm, p. 512-526. *In* V. S. Kennedy [ed.], Estuarine perspectives. Academic Press

Ertman, S.C., and P.A. Jumars. 1988. Effects of bivalve siphon currents on the settlement of inert particles and larvae. J. Mar. Res. **46**: 797-813.

Frechette, M., C. A. Butman, and W. R. Geyer. 1989. The importance of boundary-layer flows in supplying phytoplankton to the benthic suspension feeder, *Mytilus edulis* L. Limnol. Oceanogr. **34**: 19-36.

Fric, T., and A. Roshko. 1989. Structure in the near-field of transverse jet, p. 6.4.1 to 6.4.6. In Proc. 7th Symp. Turbulent Shear Flows, Stanford Univ.

List, E.J. 1982. Turbulent jets and plumes. Annu. Rev. Fluid Mech. **14**: 189-212.

Monismith, S.J., J.R. Koseff, J.K. Thompson, C.A. O'Riordan, and H.M. Nepf. 1990. A study of model bivalve siphonal currents. Limnol. Oceanogr. In press.

Nowell, A.R.M., and P.A. Jumars. 1984. Flow environments of aquatic benthos. Ann. Rev. Ecol. Syst. **15**: 303-328.

Session 6B

Coastal and Ocean Mixing

KEULEGAN'S CONTRIBUTIONS TO ENVIRONMENTAL FLUID DYNAMICS

by

Jin Wu

Air-Sea Interaction Laboratory
College of Marine Studies, University of Delaware
Lewes, Delaware 19958

Microscale air-sea interaction has been an intensive research area for the past two decades, as the fluxes of momentum, heat and mass across the air-sea interface link the atmosphere and ocean systems. There is an added urgency lately, as we are moving to attack the problem of global variations, and to enter the age of satellite meteorology and oceanography. Dr. Keulegan led the way for this kind of research almost half a century ago; the following examples illustrate more specifically his contributions.

Sea-Surface Roughness: The sea surface features ripples riding the top of long waves. These ripples are the so-called surface roughness, which is the lowest boundary of dynamic structures of the atmosphere. In the meantime, the wind stress, closely associated with the roughness, drives oceanic flows. More recently, the remote sensing of oceanic parameters has been developed with the ripples serving as the primary tracers. Studies on the sea-surface roughness was initiated by Dr. Keulegan with a very creative approach, by separating ripples from long waves with the addition of detergent to the water. The physical insight deduced from his study has provided the basis of subsequent investigations even until today. In addition, his experimental technique has been followed by others in the past decade, as the sea surface over most areas is realized to be covered by natural films.

Near-Surface Flows: The air and aqueous flows, above and below, respectively, the air-sea interface, are obviously coupled and should be investigated simultaneously. This very concept was advanced by Dr. Keulegan, along with well-planned experiments. It, however, was not diligently followed in more modern studies, with the understanding on the air side progressing much further than those on the water side. Structures of near-surface aqueous flows, governing heat and mass fluxes across the air-sea interface, are urgently needed, as we start to deal with the ever-pressing problem of environmental variations, including the global warming.

There are, of course, many other examples in my own research, on environmental fluid dynamics, influenced heavily by Dr. Keulegan's work. There is an interesting problem in hydraulics, on which I also had memorable personal exchanges with him. It is the central problem in hydraulics: the open-channel flow. We had discussed wind effects on the open-channel flow. Nowadays, in addition to the depth and discharge of streams, the hydraulic engineers must also be concernied with the water quality. The latter is governed by processes of turbulent diffusion and longitudinal dispersion; both processes are significantly modified by the wind.

DILUTION AND MARKED FLUID PARTICLE ANALYSIS

P.C. Chatwin
Department of Mathematics and Statistics
Brunel University,
Uxbridge, UB8 3PH, England

P.J. Sullivan
Department of Applied Mathematics
University of Western Ontario
London, Canada, N6A 5B9

H. Yip
Department of National Defence
Operational Research & Analysis Estbl.
Ottawa, Canada, K1A OK2

Abstract

A new proposal to relate dilution of contaminant concentration, which only occurs through molecular diffusivity, to the mean concentration value, which can be derived from a marked fluid particle analysis that is independent of molecular diffusivity, is presented. Experimental evidence, although quite limited, shows support for this simple and basic approach.

Introduction

The rate of chemical reactions including flammability as well as the reduction of contaminant concentration values to safe toxicity levels depends on the instantaneous value of concentration $\Gamma(\underset{\sim}{x},t)$ at the position located by vector $\underset{\sim}{x}$ at time t. The complete mixing between a host and contaminant fluid can only take place by molecular diffusion. The probability density function (p.d.f.)

$$p(\theta;\ \underset{\sim}{x},t)\,d\theta = \text{prob}\left\{\ \theta \le \Gamma(\underset{\sim}{x},t) < \theta + d\theta\ \right\}\ , \qquad (1)$$

is a direct measure of a change in instantaneous concentration values and is substantially changed in shape exclusively through the agency of molecular diffusivity κ.

Significant experimental difficulties arise in measuring pertinent statistics of the contaminant concentration field. For example, the statistics of a contaminant cloud are intrinsically both inhomogeneous and non-stationary. Spatial and temporal experimental resolution problems arise due to the fact that mixing in the complex interaction between molecular diffusion and instantaneous gradients in the turbulent convective velocity field occurs over the conduction cut-off length scale which is of the order of 10^{-3} - 10^{-4} m. in most flows. This fine scale resolution is required irrespective of whether one is investigating a laboratory phenomenon with turbulence scales of the order of meters or environmental flows where turbulence scales can be of the order of tens of kilometers.

The most reliably measured and credibly predicted concentration statistic is the ensemble average value,

$$C(\underset{\sim}{x},t) = \int_0^\infty \theta p(\theta;\ \underset{\sim}{x},t)\ d\theta \quad . \tag{2}$$

$C(\underset{\sim}{x},t)$ is virtually unaffected by molecular diffusivity and relatively insensitive to the effects of time and space averaging. This mean value is predicted from a fluid particle analysis and essentially describes the extent in space over which contaminant is spread. Higher moments,

$$\overline{c^n\ (\underset{\sim}{x},t)} = \int_0^\infty \Big(\ \theta - C(\underset{\sim}{x},t)\Big)^n\ p(\theta;\ \underset{\sim}{x},t)d\theta \tag{3}$$

are dissipated by κ and are very sensitive to time and space averaging. The moments given in (2) and (3) are of course the same as the values arrived at with the regular Reynolds decomposition and virtually all of the comments made herein apply whether one uses an inertial or relative frame of reference.

Direct measurement of the p.d.f. in the laboratory is fraught with difficulties[1] especially as one approaches the periphery of the contaminant field. Laboratory difficulties are immensely compounded in environmental flows where one is inclined to achieve alternative statistics that are more reliably measured and contain equivalent information[2]. The objective herein is to provide a robust measure of the likely range $R(\underset{\sim}{x},t)$ of values of concentration encountered in terms of the spread of the p.d.f. over concentration values. That is,

$$R(\underset{\sim}{x},t) = C(\underset{\sim}{x},t) + N\Big(\ \overline{c^2}(\underset{\sim}{x},t)\Big)^{1/2}, \tag{4}$$

where N is an order one constant. The key issue is to relate $\overline{c^2}(\underset{\sim}{x},t)$ that is only taken out of the system by κ to $C(\underset{\sim}{x},t)$ which is insensitive to κ. This is done through an extension of some recent and quite general results for diffusion in self-similar flows[3] and the outcome is shown to have support from the limited field and laboratory measurements that are presently available.

<u>Relationship Between Fluctuations and the Mean</u>

It was shown[3] that in self-similar contaminant fields as found in turbulent wakes, jets, smooth and rough boundary layers and plumes in grid turbulence,

$$\overline{c^n}(\eta) = \frac{\beta^n}{\alpha}\ C_o{}^n \left\{C'(\alpha-C')^n + (-1)^n(\alpha-C')C'^n\ \right\}, \tag{5}$$

where $C'(\eta) = C(\eta)/C_o$, η is the cross-stream distance from the location of the maximum value of mean concentration $C_o = C(0)$ divided by the half-width i.e. $C'(1) = 1/2$. Equation (5) expresses all of the moments, and hence in principle the p.d.f., as a function of the mean concentration distribution in terms of the two constants (for a given flow and source configuration) α and β. The range $1 < \alpha \leq 3$ and $0.3 \leq \beta < 1$ were observed over a wide range of self-similar flows. Experimental values of β are expected to be sensitive to spatial resolution and recent measurements[4] showed a dramatic (almost 50%) increase in the centre-line mean-square concentration values of a jet over established results when a sample volume of approximately 2.4 x 10^{-12} m^3 was used. These results confirmed the behaviour of β with improved spatial resolution predicted in [5].

Of specific interest here is the second moment,

$$\overline{c^2}(\eta) = \beta^2 C(\eta)\left(\alpha C_o - C(\eta)\right) \quad . \tag{6}$$

For $\kappa=0$, an exact result can be written for (5) without unknown constants for general flow conditions including buoyancy effects and unsteadiness. In essence the result given in (5) derives from a disparity in the time scales required for the effects of molecular diffusivity and those for the effects of turbulent convective motions. This disparity is likely to prevail in a very large class of turbulent diffusion problems. That is, the result (6) should be recovered with suitable changes made to account for the lack of self-similarity in the flows under consideration. By allowing α and β to become functions of downstream distance (and/or time from release as appropriate) (5) becomes,

$$\overline{c^2}(\eta) = \beta(x)^2 C(\eta)\left(\alpha(x)\ C_o - C(\eta)\right) \ . \tag{7}$$

Near the source, when $x \to 0$ and $\kappa \simeq 0$, the asymptotic behaviour of (7) is,

$$\overline{c^2}(\underset{\sim}{x},t) = C(\underset{\sim}{x},t)(\theta_o - C(\underset{\sim}{x},t)) \ , \tag{8}$$

where θ_o is a uniform source concentration[3] such that $\alpha(0) = \beta(0) = 1$ and, comparing (8) with (7),

$$\alpha(x) \sim \frac{\theta_o}{C_o(x)} \quad . \tag{9}$$

There is also the restriction that $\alpha(x) \geq 1$ and $\beta(x) \leq 1$. It is evident from (7) that the distribution of $\overline{c^2}(\eta)$ is bimodal when $\alpha(x) \geq 2$. Thus in all flows the distribution of $\overline{c^2}(\eta)$ will initially be bimodal and (except for the presence of molecular diffusivity) would become unimodal as α exceeded 2 according to (9). Depending on the relative vigor of turbulent convective motions to molecular scale mixing the distribution of $\overline{c^2}(\eta)$ could remain unimodal for all x or pass from an initially bimodal distribution to one that is unimodal and ultimately return to the bimodal form (see figure 1). For contaminant fields that develop into self-similar form the large distance (or time from release) asymptotic $x \to \infty$ behaviour is $\alpha(x) \to \alpha$, $\beta(x) \to \beta$ which are constant and the distribution of $\overline{c^2}(\eta)$ could be either unimodal or bimodal.

In general the p.d.f. undergoes a significant change in shape in passing from the $\eta = 0$ location to the periphery where the p.d.f. is very skewed towards high values of concentration. The process consists of the export of fluid with large values of concentration from the central to the peripheral regions. Thus it is appropriate to use the $\eta = 0$ range value to provide an envelope of largest values of concentration to be encountered at any η. The $\eta=0$ range value, for each downstream location x, in a steady flow for example

$$R(x) = C_o(x)\left(1+N\ \beta(x)\ \sqrt{\alpha(x)-1}\ \right) \ , \tag{10}$$

contains the relevant information on the likely size of concentration values to be encountered there.

Three questions must be addressed experimentally. The first is whether or not (7) adequately describes observation. The second is whether or not the size and variability of $\alpha(x)$ and $\beta(x)$ remain small. The third is whether or not the value of N in (10) is reasonably universal.

Experimental Evidence

In the developing contaminant concentration field resulting from an elevated, continuous point source within a rough boundary layer in a wind tunnel[6] the form of (7) was reasonably well confirmed with a unimodal distribution of $\overline{c^2}(\eta)$ and $\alpha(x) \simeq 2$ throughout the developing region. Further downstream when the contaminant field became self-similar the result (6) was very well confirmed with a bimodal distribution[3]. In figure 2 a typical distribution of $\overline{c^2}(\eta)$ is shown across a plume in the surface layer of Lake Huron when a relative reference frame is used. A description of these experiments is found elsewhere[8], however, the results all appear to be consistent with (7) with both unimodal and bimodal distributions of $\overline{c^2}(\eta)$ in evidence. The values of $\alpha(x)$ are shown in figure 1 (the values of $\beta(x)$ although not inconsistent are not considered to be adequately resolved). In figure 3 a typical distribution of $\overline{c^2}(\eta)$ across a plume in a homogeneous shear flow[9] is presented. The distributions of $\overline{c^2}(\eta)$ in this flow are initially bimodal, become unimodal and return to a bimodal distribution as one proceeds downstream (see figure 4). The distributions of $\overline{c^2}(\eta)$ are everywhere consistent with (7), however, with the anomaly remarked upon by the investigators that the lack of symmetry in $\overline{c^2}(\eta)$ being due to buoyancy effects in the heated plume. The 'surprising' transition of modality with downstream distance that was reported in that paper appears to be explained in the context of the present work.

It is interesting to observe that in two experiments in the self-similar contaminant plumes in grid turbulence - one in a wind tunnel[10] and one in a water tunnel[11] - the former was found to exhibit bimodal while the latter unimodal distributions of $\overline{c^2}(\eta)$. This discrepancy is explained in the context of the present work when one considers the 10^5 larger value of κ in gases (leading to the bimodal distribution) over those of liquids (where the unimodal distribution was observed).

In full-scale field experiments with the continuous release of contaminant within the atmospheric boundary layer and extending over a kilometer downstream[12] the centre-line form of (6) was confirmed to prevail and the mean plus three standard deviations was found to provide an envelope that included all peak values of concentration recorded. That is a value of N=4 in (4). In all of the self-similar experiments reviewed in [3] a value of N=4 would certainly be adequate to encompass the largest value of θ shown on the p.d.f.s.

The conclusions at this time must remain tentative, in that there is a limited amount of experimental data available, however, promising in that the available data is not inconsistent with the simple explanation provided herein.

Acknowledgements

The authors have received financial support for this work from the National Science and Engineering Research Council of Canada, NATO (Research Grant No. R.G.115.81) and from the U.K. Ministry of Defense.

References

1. Derksen, R.W. and Sullivan, P.J., 1990, "Moment approximations for probability density functions", Combustion and Flame (in press).
2. Chatwin, P.C. and Sullivan, P.J., 1990, "Cloud average concentration statistics", Mathematics and Computers in Simulation, v. 32 (in press).
3. Chatwin, P.C. and Sullivan, P.J., 1990, "A simple and unifying physical interpretation of scalar fluctuation measurements from many turbulent shear flows", J. Fluid Mechs, v. 212 (in press).
4. Sakai, Y.; Nakamura, I.; Tsunoda H. and Shengion, L.; 1989, "On the influence of disturbances generated by obstacles on point source plume diffusion in grid turbulence. Characteristics of concentration fluctuations and conditional statistics", manuscript in preparation. (Material presented at Euromech 253, Brunel Univ. 30 August - 1 September, 1989)
5. Chatwin, P.C. and Sullivan, P.J., 1987, "Perceived statistical properties of scalars in turbulent shear flows", Proc. 6th Symp. on Turbulent Shear Flows, Toulouse, France, pp 9.1.1 - 9.1.6.
6. Fackrell, J.F. and Robins, A.G., 1982, "Concentration fluctuations and fluxes in plumes from point sources in a turbulent boundary layer", J. Fluid Mech., 117, 1-26.
7. Yip, H., 1988 "Predicting contaminant concentration values in environmental flows" PhD Thesis, University of Western Ontario.
8. Chatwin, P.C. and Sullivan, P.J., 1979, "Measurements of concentration fluctuations in relative turbulent diffusion", J. Fluid Mech. 94, 83.
9. Karnik, V. and Tavoularis, S., 1989, "Measurements of heat diffusion from a continuous line source in a uniformly sheared turbulent flow", J. Fluid Mech. 20, 233-261.
10. Gad-El-Hak, M. and Morton, J.B., 1979, "Experiments on the diffusion of smoke in isotropic turbulent flow", AIAA J. 17, 558-562.
11. Nakamura, I., Sakai, Y. and Miyata, M., 1987, "Diffusion of matter by a non-buoyant plume in grid-generated turbulence", J. Fluid Mech. 178, 379-403.
12. Mason, P., Mylne, K., "Experimental measurements of concentration fluctuations at a range of up to 1 km", manuscript in preparation. (Material presented at Euromech. 253, Brunel University, 30 August - 1 September, 1989.)

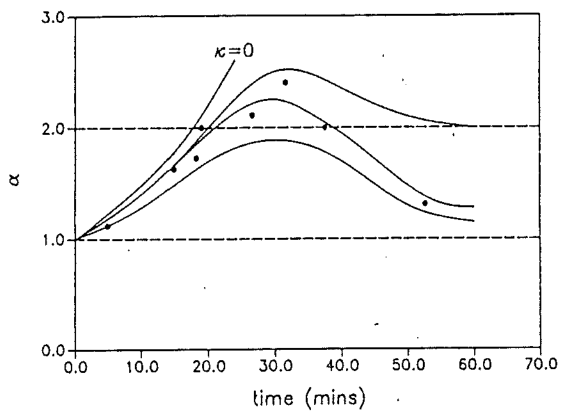

Figure 1. α values from Lake Huron data and schematic representation of α behaviour with convective time (or distance) downstream.

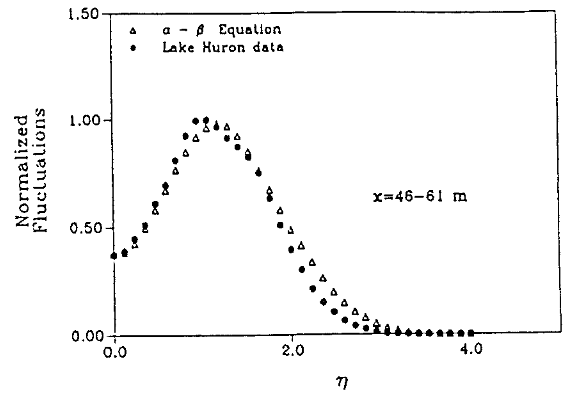

Figure 2. A comparison of (7) with Lake Huron data[8] at Exp. 5 Sec. 1.

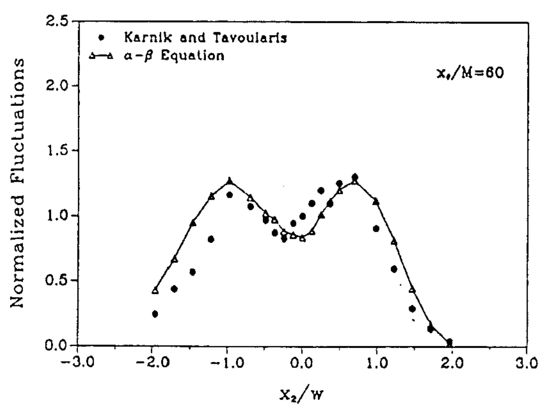

Figure 3. A comparison of (7) with homogeneous shear flow data[9] at x/M = 60.

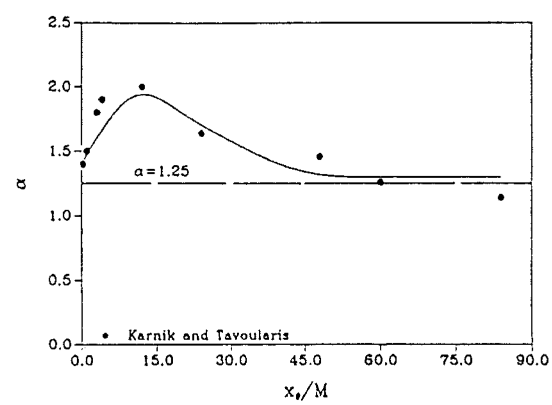

Figure 4. α values from homogeneous shear flow data.

TURBULENCE BARRIERS IN DISPERSION AND DIFFUSION PROCESSES

by Jan M. Jordaan
Departement of Water Affairs
Pretoria 0001 R.S.A.

Synopsis

In turbulent diffusion and convection processes both dispersion processes (diffusion and convection) when operating separately drive the dispersant away from the source. When operating together, however, their effects are not summative as turbulent diffusion annihilates the gradients responsible for gravitational convection and dispersion. This effect has become known as the turbulence barrier.

In three experiment series these interrelationships have been studied and are presented in this paper. The first experiment done at MIT, deals with the unsteady state diffusion of two fluids of different density in an ambient field of turbulence. There exists a turbulence level at which the dispersion is a mimimum. With lower turbulence levels the convective dispersion predominates and at higher turbulence levels turbulent diffusion predominates.

In the second experiment a steady state problem was analysed, also at MIT, in which the turbulent diffusion of a denser fluid into a steady counter-current was studied when it was introduced at a constant rate. The steady state concentration profile obtained showed that if the turbulence level in the approaching current was increased less convective dispersion in the upstream direction results. If the gravitational convection, on the other hand, is reduced to zero, by having no difference in specific gravity between the introduced and the receiving fluid, the turbulent diffusion alone will cause the dispersion into the steady current to moderately increase with turbulence level.

In the third experiment, conducted in a wind-wave flume at CSIR Pretoria, a statistically selected array of variables was tested for 25 test conditions to assess their influence on the dispersion of effluent away from coastline discharge point. Again it was found that intense turbulence, such as that due to breaker action, to a great extent counteracts the offshore dispersion of the effluent which otherwise would have resulted from wind-induced offshore drift or from circulation or gravitational convection due to density differences. These tests were extended to wave basin and shoreline experiments with significant conlusions arrived at.

In summary, it was explained from theoretical considerations why turbulent diffusion, instead of simply aiding dispersion, in the presence of convection actually retards it, by forming the so-called turbulence barrier which annihilates the density gradients. The rest of the paper will deal with the experimental methods employed.

Note on physical modeling test methods utilized

One objective of this paper and presentation is to indicate how the process of turbulent mixing with dispersion under gratívational convection was studied in three experiments. Firstly, in a turbulence flume with dye, and with neutrally byoyant particles (under zero density gradient) as well as with two values of density differential between diffusing and receiving fluid, both time-dependent and steady state counter-current diffusion/dispersion was simulated.

Next, a wind-wave flume study was carried out where turbulent mixing due to breaking wave action on a beach was simulated with the two-dimensional dispersion due to gravity,tide and wind action normal to the coastline. Finally a number of three-dimensional dispersion tests were carried out both in an outdoor wave basin and in the ocean.

M I T tests in turbulence flume

The aim was to simulate tests on tidal mixing done elsewhere in an artifically roughened bidirectional flow flume, by testing in a uniformly turbulent laboratory channel. Turbulence would be generated by oscillating screens, their energy input would be measured by a load cell, and the diffusion and dispersion by conductivity probes or by sampling. The diffusant was to be a traceable substance such as saline water, rhodamine B dye or polystyrene spherules. To effect neutrally buoyant conditions the saline diffusant or the spherules was received in an equally dense body of sugared water. Tracing of the dye concentration was by spectrophotometric comparison of samples taken to standard dilutions; of the spherules by filtration and weighing of off-syphoned samples; and of the saline concentration by immersed conductivity probing; all calibrated against known dilutions.

Unsteady-state tests

The load cell output and displacement gauge (strain gauge bridge and linear variable differential transformer respectively) yield records, via cardiac type oscillograph on heat-sensitive waxed graph paper, which were analysed in terms of force x velocity-vectors against time and integrated to give power. Elastic components in the force measurements were self-cancelling and only dissipative (rho.v^2) components derived. The work input and hence turbulent dissipation rate was thus measurable as a function of amplitude and angular frequency of the vibrating screen system. The rate of turbulent diffusion was related through an eddy-diffusion coefficient to the observed concentration-change history at various points. By plotting the distributions against a pre-calculated family of curves, each for a different value of turbulent diffusion coefficient, the diffusivity could be read off and thus could be related to energy input and the other parameters such as density differential.

Steady-state tests

For the steady-state tests a known rate of diffusant supply was balanced against a known counter-current and the steady-state distribution sampled. The analogy with the tidal-mixing flume results was that whereas here the mixing zone was stationary, in the tidal flume it traveled forward and back with the outgoing and incoming tide and became distended on the outgoing tide and compressed on the incoming

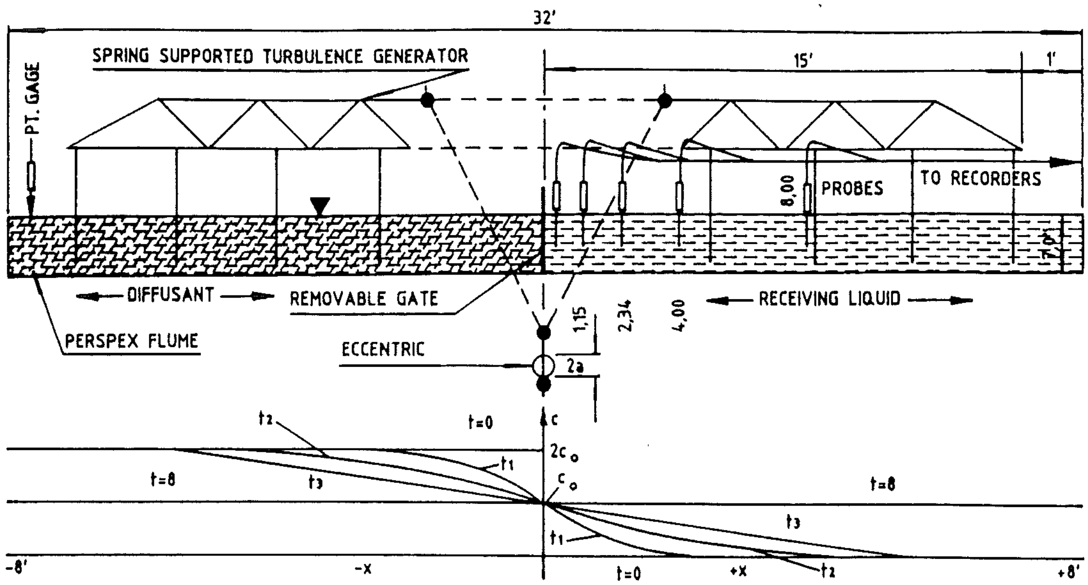

FIG. 1 SCHEMATIC DIAGRAM OF EXPERIMENTAL SET-UP FOR TYPICAL TIME-DEPENDENT DIFFUSION TEST SERIES.

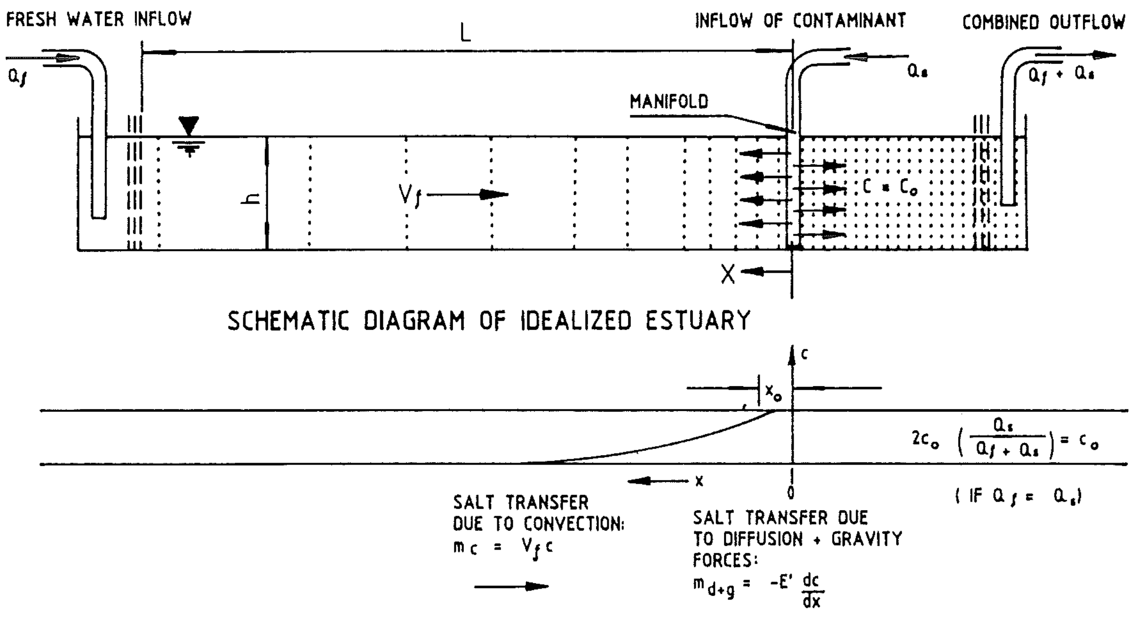

FIG. 2 DEFINITION SKETCH FOR TYPICAL STEADY-STATE DIFFUSION TEST.

FIGURES :

1. UNSTEADY STATE DIFFUSION EXPERIMENT , MIT
2. STEADY STATE DIFFUSION/CONVECTION EXPERIMENT , MIT
3. DIFFUSION COEFFICIENT VS. TURBULENCE PARAMETER (ABOVE CASE)
4. GRAECO-LATIN SQUARE TEST PLAN , CSIR FLUME DIFFUSION TESTS.

tide due to continuity effects.

C.S.I.R. tests in wind-wave flume

In the wind-wave flume tests, a perspex channel was set up in a 12 ft diameter open-jet wind-tunnel capable of wind speeds up to 36 ft/sec. Waves were created by the direct flow of wind over the water surface but were augmented by bellows-generated waves in the channel such that no obstruction was given to the wind passage over their crests. Tidal effects were almost statically created i.e. high, low, mid, rising and falling. Fluorescein dye introduced in a constant head device at the low water line served as a diffusant tracer and was sampled by syringe and pipette at equal intervals in the seaward direction. Analysis of concentration was by spectrophotometer. In order to cover a wide range of variables: 5 each of wave period, tidal state, wind strength and density differential, a group of 25 experiments was designed, combining the independent variables by a random choice method known as a Graeco-Latin square. The dependent variable, diffusion coefficient, was determined from the sampled concentration fields by standard statistical methods involving the mean square displacement of the diffusant, and subjecting it to significance tests. In the end meaningful relationships wre obtained between diffusion coefficient (mean square displacement / time) and wave, wind, tidal-state and density parameters. Breaking-wave turbulence opposed spreading due to wind, density and tide, thus confirming the turbulence barrier concept.

Wave basin tests

The two-dimensional results were extended to an experimental three-dimensional beach model in a wave tank equipped with tidal and current generating mechanisms. The same diffusant (fluorescein solution weighted with salt or lightened with ethyl alcohol) was used in a constant head feeding device. Both slug and continuous feeding was employed, as theory for both conditions was available. The peak decay with slug dosing was proportional to the square root of the time raised to the power equal to the number of diffusing dimensions. With continuous dosing a dilution ratio was obtained that gradually increased with time and distance. Because of the more complex three-dimensional mixing process, a compact Graeco-Latin square test plan could not be utilized and the model tests only showed the patterns likely to occur in practice in a qualitative way. These were, steady longshore current generated by oblique wave action, uniform parallel-to-shore current, and rip current generated by waves parallel to shore encountering irregularities such as headlands. The model enabled such situations to be identified on a prototype straight beach. Wind tests were not controllable in the outdoor model tank. The results clearly indicated the confinement of the mixed products in the inshore zone between the shore and the line of breakers, except for rip-current conditions which occurred with waves parallel to shore, and confirmed the flume tests.

Beach test - full scale

a Number of slug-dosing tests with fluorescein-dye solutions in canisters were undertaken for various wave and wind situations, injecting the dye in the breaker zone and following the patch with skiboats.

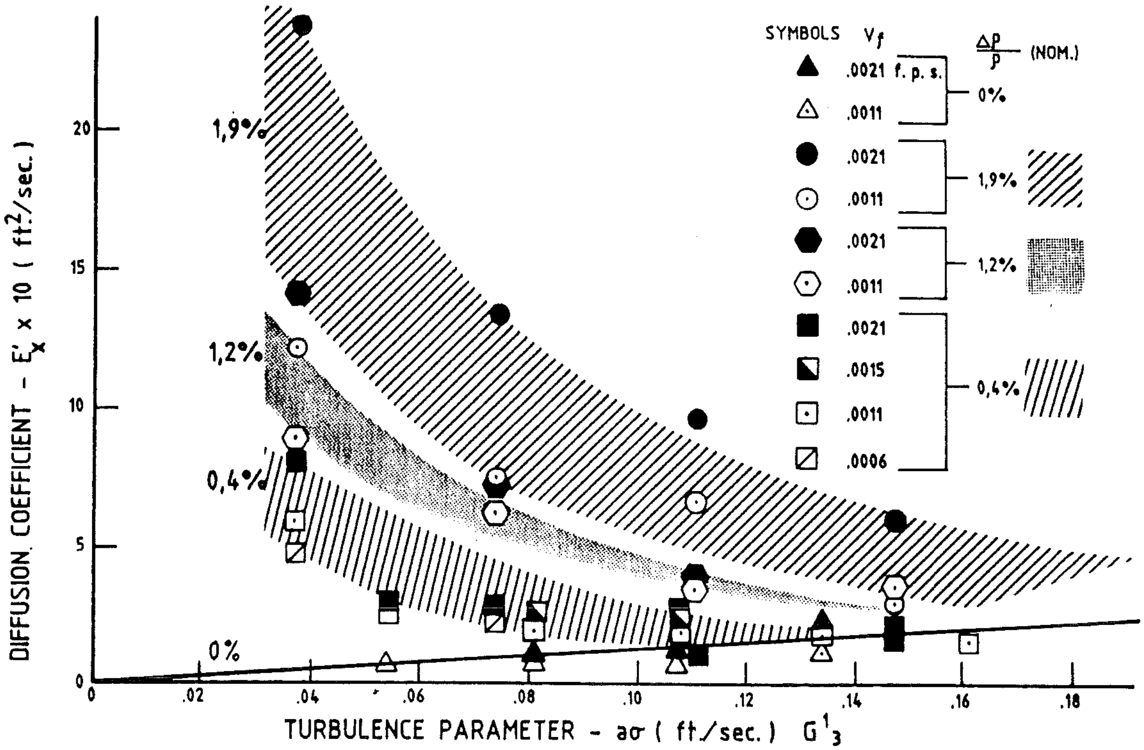

FIG. 3 DIFFUSION COEFFICIENT VS. TURBULENCE PARAMETER (FIG. 2 TESTS.)

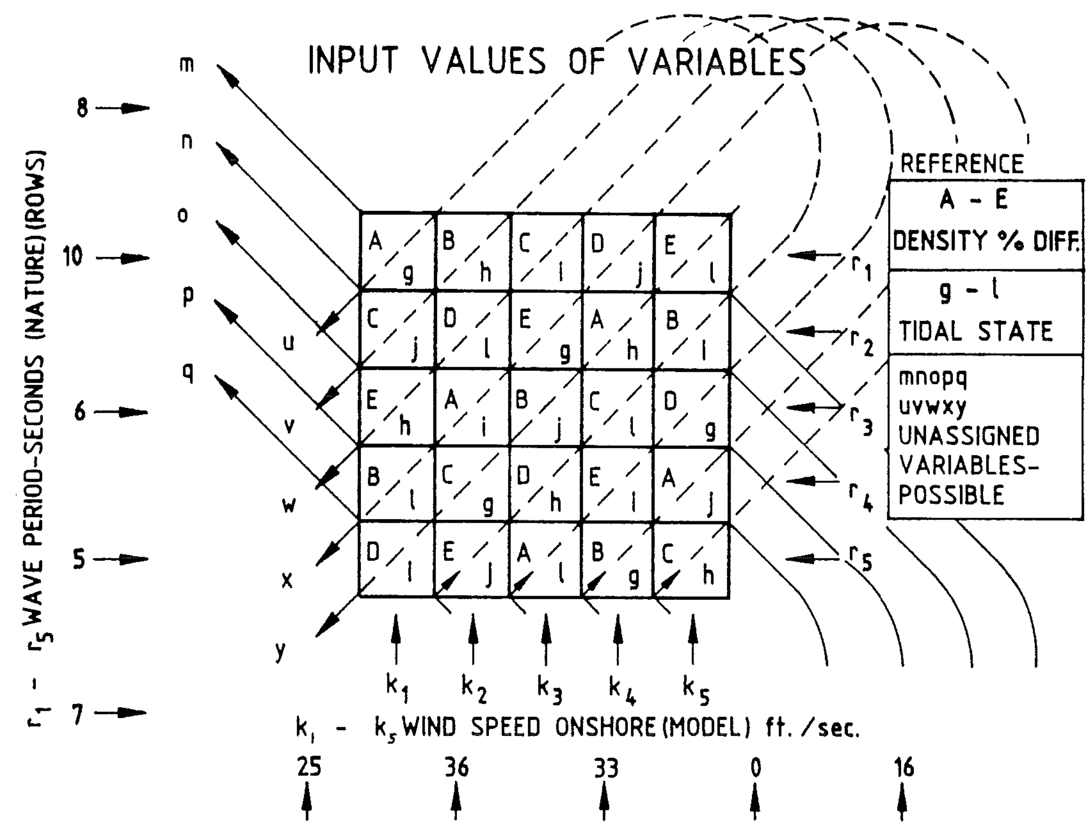

FIG. 4 TEST PLAN AND INPUT VALUES IN A STATISTICALLY DESIGNED SET OF EXPERIMENTS TO ESTABLISH SIGNIFICANT TRENDS[3].

The patch dimensions could be tracked over several km for a couple of hours. Concentration samples were taken. The results enabled a correlation between wave energy and diffusion coefficient to be found and led to the following conclusions:-

Surf discharge, although conductive to violent initial mixing and dilution, causes the field to remain inshore by turbulent mixing. The turbulence barrier thus prevents outward spreading and dilution.

Off-shore discharge is conducive to ultimate dispersal, but not to initial mixing and dilution, unless recourse is made to pressure jetting.

In off-shore disposal the dilution field upon re-entering the surf zone from off-shore is diluted further and the turbulence barrier protects the nearshore region from excessive pollution.

Summary

These series of experiments, demonstrate the value of physical modeling in effluent disposal problems. The understanding of the process involved was born out of the initial turbulent-tank experiments, followed by the wind-wave flume and wave basin tests. Methods of experimental design could readily be followed in the controlled laboratory environment, but less so in nature with a greater number of uncontrollable variables. Without the laboratory and model-scale groundwork the order and interpretation of field tests would not have been apparent.

References

J.M. Jordaan, Mass Transfer Rates in a Turbulent Fluid Body, Sc.D. thesis, Department of Civil Engineering MIT., 1958.
D.R.F. Harleman, J.M. Jordaan and J.D. Lin, MIT Hydrodynamics Laboratory Report, T.R. No 31, 1959.
J.M. Jordaan, Mechanics of dispersion of Pollutants in Coastal Environment, IWRA Convention, Chicago, "Water for the Future" 1973.

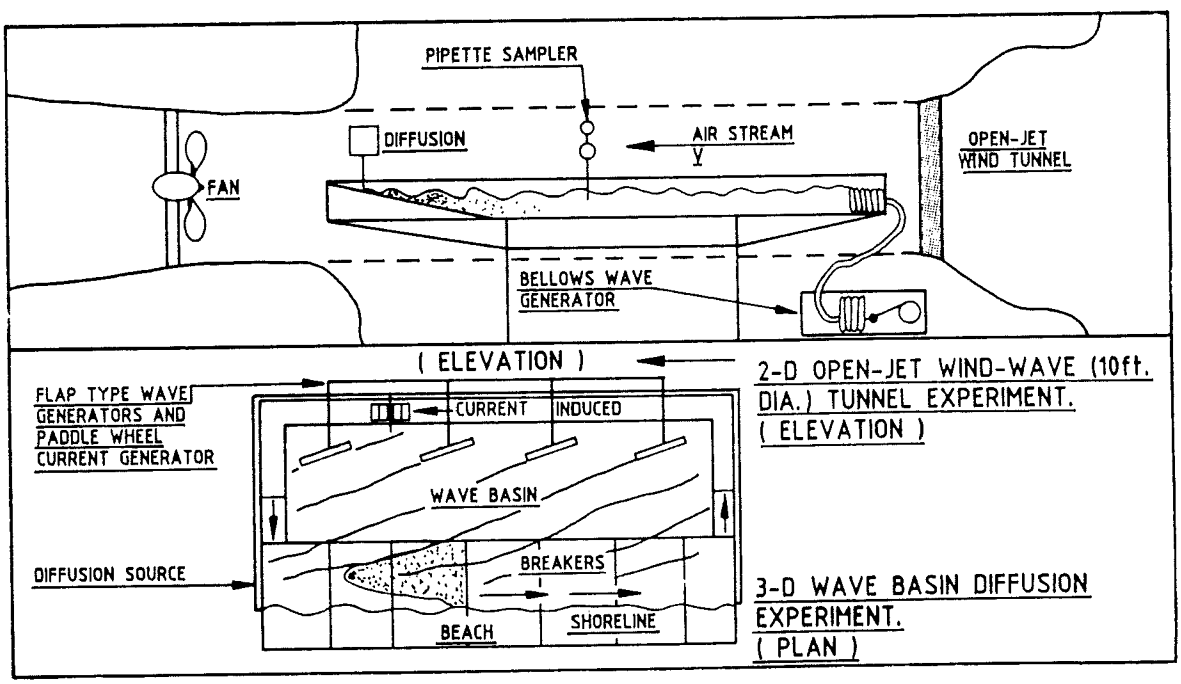

2-D OPEN-JET WIND-WAVE (10ft. DIA.) TUNNEL EXPERIMENT.
(ELEVATION)

3-D WAVE BASIN DIFFUSION EXPERIMENT.
(PLAN)

ACKNOWLEDGEMENT The permission of the Director General of Water Affairs to publish this material is acknowledged.

The Similarity of Horizontal Diffusivity in the Tidal Hydraulic Model

by

Norio Hayakawa
Nagaoka University of Technology

Abstract

The purpose of this study is to find a means to achieve the similarity of the horizontal turbulent diffusivity in the tidal hydraulic model. The first part of this paper is concerned with the horizontal diffusivity in the tidal waters based on the field data and concludes the validity of the Richardson-Ozmidov law. The second part concerns itself with the flume study to obtain the formula for the horizontal diffusivity under the presence of roughness bars. The derived formula is to be used to attain similarity in the hydraulic model.

Introduction

Large hydraulic models have been built throughout the world for past several decades. They have, in increasing number of cases,been used to study dispersion of pollutants in the water basin to be modeled. These hydraulic models are built with a small scale ratio, often one in the model to 1000 or 2000 in the prototype. This small scale ratio and necessary distortion, i.e. use of larger scale ratio in the vertical direction so as to maintain turbulent flow in the model, has cast a serious doubt as to the model's ability of reproducing turbulent mixing and diffusion of the prototype.

Thus it has been argued that attaining similarity of horizontal diffusivity in the model is impossible(1). The ground for this argument is the assumption of the logarithmic profile of turbulent shear flow and Reynolds' analogy with the conclusion that the model overdisperses horizontally whereas underdisperses vertically.

On the other hand, some people argue that the similarity of horizontal turbulent diffusivity is indeed possible under the premise that both the model and the prototype obey the Richardson -Ozmidov law of diffusion(2).

At present this dilemma remains unsolved. The problem is more complicated in practice, moreover,because, more often than not, roughness strips or bars are planted on the model surface to attain the flow similarity. These exaggerated roughness elements are believed to enhance turbulent diffusion in the model. Quantitative assessment of such roughness elements with regard to the horizontal diffusion, however, has not been studied extensively. Only study reported so far is that of Fischer and Hanamura(3), which relies unfortunately on extremely simplified analysis and limited experimental conditions.

It seems that the problem stems from the fact that the law of turbulent diffusion in both the field and the model is not fully understood. This paper first studies the law of horizontal diffusion in the field based on the field experiments. Secondly a flume study is reported to obtain the velocity defect law and the horizontal diffusivity under the presence of roughness bars. The horizontal diffusivity law is then derived using the Prandtl's concept of mixing length and the Reynolds'analogy.

Horizontal Diffusivity in the Field

The field under consideration in this study is either encroached bay or wide estuary. Typically, horizontal expanse is 10 to 50 km and average depth 20 to 50 m. Also influx of fresh water is imangined to be small and tidal motion is thought to be dominant. Under this situation, the logarithmic law of turbulent shear flow is not expected to be observed. Therefore, the horizontal diffusivity in such a basin is analyzed on the basis of the field data of slug dye release experiments,

Fig. 1 shows dye cloud area, S, against the lapsed time, t, since release of dye. In these experiments dye solution is dumped overboard on the water surface and the expanding dye cloud is photographed aerially. Sites of experiments are collectively called the Seto Inland Sea of Japan which is in reality a chain of bays whose names appear in the figure. From these data,horizontal diffusivity, ε, is estimated by discretizing the following formula,

$$\varepsilon = \frac{1}{4}\frac{dS}{dt} \qquad (1)$$

Fig. 2 shows the plotting of ε versus length scale of the cloud $l=(s/2\pi)^{1/2}$ and shows that the Richardson-Ozmidov law

$$\varepsilon \propto l^{4/3} \qquad (2)$$

reasonably represents the correlation and ε ranges from 10^3 to 10^5 cm^2/s for corresponding length scale of 10 m to 1 km. It should also be noted that the observed horizontal diffusivity is much larger than the value obtained invoking the law of the logarithmic shear flow given as

$$\varepsilon = \alpha h u_* \qquad (3)$$

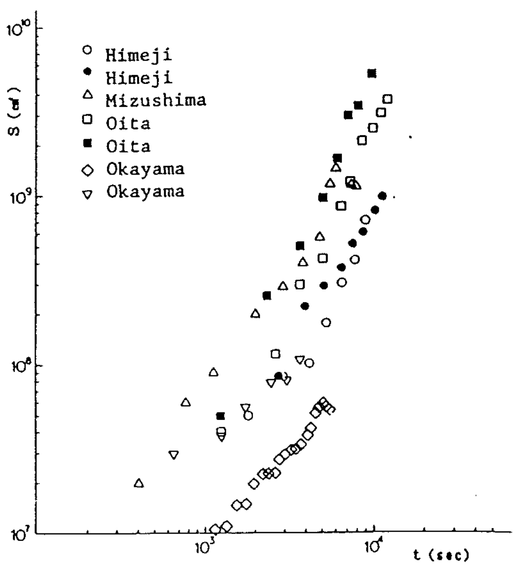

Fig.1 Dye Cloud Area vs. Time

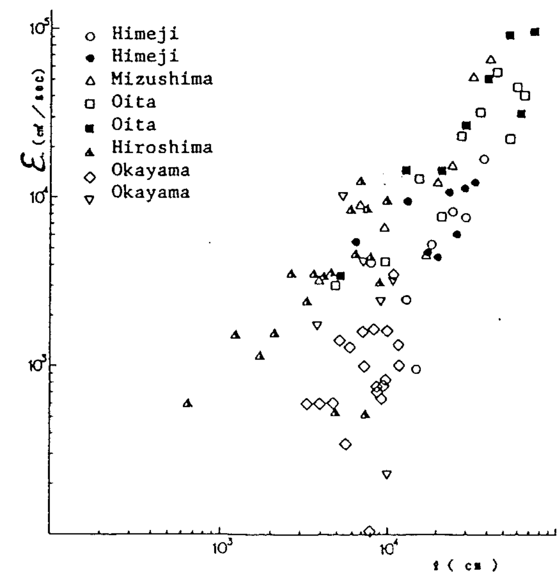

Fig.2 Horizontal Diffusivity vs. Length Scale

where h is flow depth, u* is friction velocity and the numerical constant α is given as 0.15, since depth is 20 m and the friction velocity is estimated to be about 2 cm/s for the maximum flow velocity of 50 to 60 cm/s.

Experiment

The experimental apparatus consisted of a tilting flume with length of 9 m and width of 40 cm. For roughness elements vinyl pipes with diameters of 2.4 cm and 1.8 cm are used. They are planted on the flume floor in a staggered fashion. In Table 1 is given the list of experimental conditions for all runs. It was found from the preliminary runs that the Manning's n for flume without roughness bars was 0.010. In all runs roughness bars are long enough so that they protruded the water surface. Velocity profiles were measured with a propellar-type current meter with a propellar diameter of 3 mm. Dye(methylene blue) was injected at midsection and dye concentration in the cross section was measured at distance L downstream as shown in Table 1, where dye is observed to be sufficiently mixed in the cross section.

From the measured distribution of dye concentration horizontal variance is calculated and the horizontal diffusivity ε is obtained by the formula

$$\varepsilon = 0.5\ \sigma^2\ U/L \quad (4)$$

where σ^2 is the variance and U is the cross-sectionally averaged flow velocity. The result is given in Table 1 also.

Table 1 Experimental Condition and Diffusivity

Run No.	h (cm)	u* (cm/s)	U (cm/s)	λ (cm)	ω/λ	d (cm)	L (cm)	ε (cm^2/s)	$\varepsilon/hu*$	$\varepsilon/\lambda U$
1	4.5	0.671	10.8	26.66	1	2.4	61	2.37	0.79	0.0081
2	8.5	0.854	14.7	26.66	1	1.8	61	2.50	0.34	0.0062
3	8.5	1.208	21.0	26.66	1	1.8	61	3.31	0.32	0.0058
4	4.5	0.671	9.5	13.33	1	2.4	67	3.51	1.16	0.0274
5	8.5	0.854	12.6	13.33	1	1.8	67	2.83	1.74	0.0169
6	8.5	1.208	19.0	13.33	1	1.8	67	4.57	0.45	0.0182
7	4.5	0.671	9.0	20	1	2.4	64	2.47	0.91	0.0152
8	8.5	0.854	12.3	20	1	1.8	64	2.35	0.32	0.0096
9	8.5	1.208	19.0	20	1	1.8	64	3.11	0.30	0.0082
10	4.5	0.671	9.6	13.33	1.5	2.4	64	3.02	1.00	0.0236
11	8.5	0.854	13.1	13.33	1.5	1.8	64	2.93	0.40	0.0168
12	8.5	1.208	19.7	13.33	1.5	1.8	64	4.41	0.43	0.0168
13	4.5	0.671	7.6	13.33	0.75	2.4	59	2.68	0.89	0.0265
14	8.5	0.854	11.6	13.33	0.75	1.8	59	2.99	0.41	0.0193

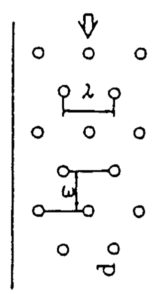

Diffusivity with Bar Roughness

It is necessary at first to obtain the velocity defect law under the presence of roughness bars in order to establish the calculation method of the horizontal diffusivity under a given experimental condition. In analyzing such a complicated flow a semi-empirical approach is resorted to using a set of measured data of the velocity profile. It is expected the velocity defect law under the presence of roughness bars in a staggered mesh is a result of superposition of velocity defect laws behind a single row of bars. A preliminary study of such a flow is carried out using the same tilting flume with a single row of bars and the velocity defect law is obtained. The velocity profile under the presence of roughness bars planted in a staggered fashion is derived under the following assumptions : [1] the velocity profile at any cross-section is governed by a row of roughness bars right upstream of the cross-section being considered and another row further upstream and [2] it is expressible by superposition of wake flow profiles pertaining to these two rows of roughness bars. The resulting velocity profile is written as follows

$$\frac{u}{U} = 1-0.235[[\frac{x-d/2}{\lambda}]^{-2/3}+[\frac{x+\omega-d/2}{\lambda}]^{-2/3}] +0.35[[\frac{x-d/2}{\lambda}]^{-1/2}$$
$$\times[1-\exp[-\frac{(y/\lambda)^2((x-d/2)/\lambda)^{-2/3}}{0.21*0.39^2}] +[\frac{x+\omega-d/2}{\lambda}]^{-1/2}$$
$$\times[1-\exp[-\frac{(5-y/\lambda)^2((x+\omega-d/2)/\lambda)^{-2/3}}{0.21*0.39^2}]] \qquad (5)$$

in which the meaning of symbols and the range this functional expression covers is shown in Fig.3. Fig.4 is an example of comparison of experimental data and Eq.(5). Comparison of Eq.(5) with all data of velocity profile measurement listed in Table 1 shows a good correspondence indicating the validity of Eq.(5) for the experimental condition studied in this paper,i.e. range of the Froude number between 0.21 and 0.39 and the Reynolds number between 5×10^3 and 2.9×10^4.

The horizontal diffusivity under the presence of roughness bars is calculated invoking the Prandtl's concept of mixing length and the Reynolds' analogy. The formula to that effect is given as

$$\varepsilon = \kappa(u_{max} - u_{min})w \quad (6)$$

in which u_{max} and u_{min} are, respectively, maximum and minimum velocities in the cross section, w is the width of mixing region and κ is a numerical constant. With the staggered disposition of roughness bars, however, the diffusivity is governed by wake flows behind two roughness bars as shown in Fig.5. Therefore the horizontal diffusivity in this case is calculated by averaging values related to these two wake flows. They are given as follows

$$\varepsilon = \kappa\{\frac{(u_{max} - u_{min1})w_1{}^2 + (u_{max} - u_{min2})w_2{}^2}{w_1 + w_2}\} \quad (7)$$

As the horizontal diffusivity given by Eq.(7) is a function of x, the value at $x = 0.5\ \omega$ is used as representative of the distribution.

Calculating the right-hand-side of Eq.(7) using the velocity profile Eq.(5) met the difficulty of being unable to fit all the experimental data of measured diffusivity ε whatever the value for κ was used. This is because κ does not remain constant in this case as the wake flow region close to the bars is concerned. Instead, κ is thought to be a function of d/λ and ω/λ from dimensional consideration and fitting κ values calculated from Eq.(7) with these two dimensionless parameters gives the following

$$\kappa = 4.0(d/\lambda)^{1.5}(\omega/\lambda)^{0.75} \quad (8)$$

Fig.6 gives the comparison between experimental data and calculation results from Eq.(7) together with Eq.(8). Good correspondence is obtained as expected. Still, it should be noted that the correspondence is obtained with respect to both d/λ and ω/λ, suggesting worthwhileness of the obtained relationship.

In Fig.6 is also shown a relationship given by Fischer and Hanamura (3) which reads as

$$\varepsilon = 0.075dU\lambda/\omega \quad (9)$$

It is apparent from Fig.6 that Eq.(9) does not represent experimental data as d/λ is increased.

Fig.7 gives the obtained relationship for a practical range of d/λ and ω/λ. It shows that $\varepsilon/\lambda U$ is only weakly dependent on ω/λ. For practical purpose, curves in Fig.7 are represented by a following equation.

$$\varepsilon/(\lambda U)=(0.0612+0.474d/\lambda)d/\lambda-0.000754, \quad 0.5<\omega/\lambda<1.5 \quad (10)$$

Conclusion

Horizontal diffusivity in the tidal waters is studied on the basis of experimental data of dye dispersion and is found to follow the Richardson-Ozmidov law.

The effect of roughness bars in the tidal hydraulic model on the horizontal diffusivity is studied using a tilting flume. From velocity measurement the similarity profile is obtained. The calculation method of the horizontal diffusivity is proposed on the basis of the Prandtl's mixing length concept and the Reynolds' analogy. The obtained relationship gives the horizontal diffusivity for given flow and size and disposition of roughness bars.

References

1. Fischer, H. B.,Annual Review of Fluid Mech.,Vol.8,pp.107-134,1976
2. Higuchi, H. and Iwagaki, Y.,Coastal Engineering in Japan,Vol.12,pp. 129-138,1969
3. Fischer, H. B. and Hanamura, T.,Water Resources Research,Vol.11,No.2 ,pp.362-364,1975

Acknowledgements

Experimental study reported in this paper was carried out by Mr. Masayoshi Shirayama, former graduate student, now with Construction Research Laboratory, Tokyo.

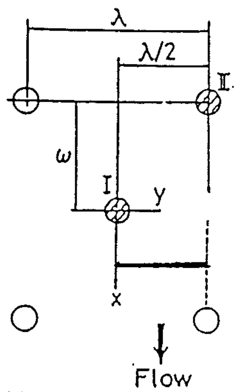

Fig.3 Definition Sketch for staggered Roughness Bars (Boldfaced line represent the region Eq.(5) is to be applied.)

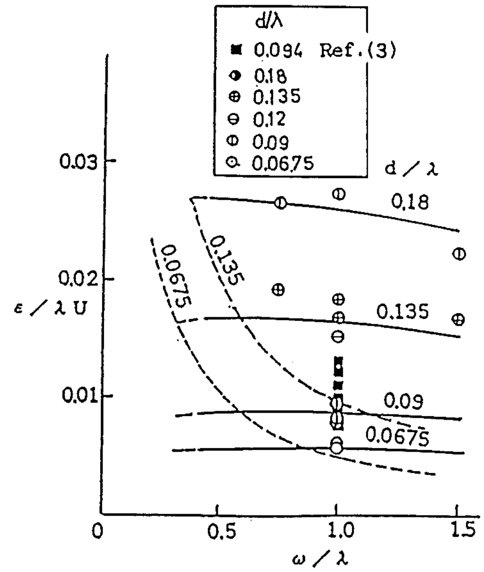

Fig.6 Relationship between κ and d/λ

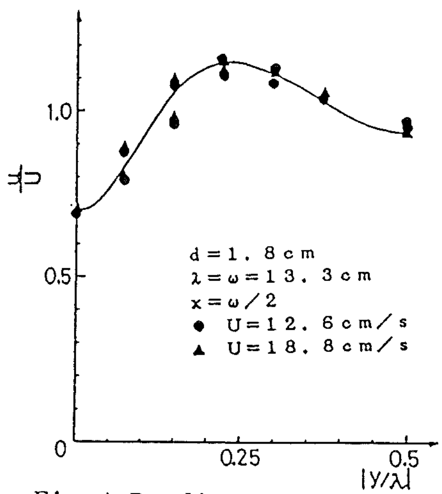

Fig.4 Predicted Velocity Profile and Experimental Data

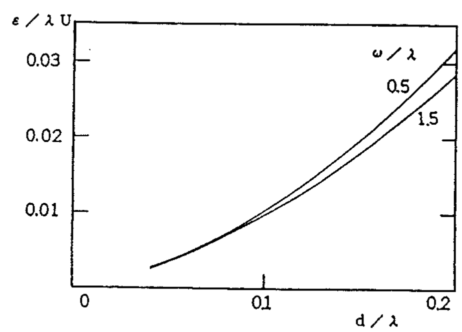

Fig.7 Horizontal Diffusivity with Roughness Bars

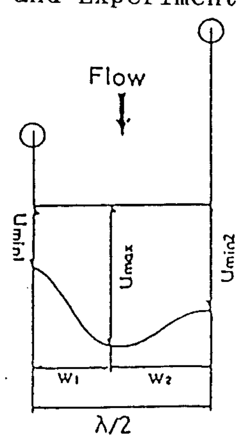

Fig.5 Definition Sketch of Wake Flow behind Staggered Roughness Bars

THE ABSENCE OF MIXING AT THE SEAWARD EDGE OF THE SURF ZONE

Cyril Galvin, Coastal Engineer
Box 623, Springfield, Virginia 22150

Abstract. Most longshore currents do not cause significant mixing between the surf zone and the nearshore water. Available hypotheses for such mixing can be interpreted as curve-fitting schemes with empirical coefficients, based on the work of McDougal and Hudspeth (1986). There are significant laboratory and field data that suggest relatively little mixing occurs on the time scale of the period of the waves causing the longshore current. Measurements of cross-shore velocity profiles of longshore currents by fixed gages smear out the velocity profile, implying more mixing than occurs.

Background. Longshore currents are wave-driven flows in the surf zone that move parallel to the shoreline. The surf zone extends from land out to the breaker line. The breaker line is where shoaling waves first break. The breaker line separates the surf zone from the nearshore.

Because longshore currents flow in the surf zone, and are essentially absent from the nearshore, the transition between the water bodies is assumed to undergo shear which brings about mixing. Several mechanisms of mixing between the longshore currents and the nearshore waters have been postulated. The interest in this mixing is because of its fluid mechanics and also because longshore currents may distribute pollutants. The less the mixing with the nearshore, the greater the longshore transport of the pollutants.

The equation of motion for longshore current velocity includes a mixing term related to the cross-shore gradient in longshore velocity (Longuet-Higgins, 1970). Such a term is used to smooth the discontinuity in the longshore current that otherwise exists in the theory at the seaward edge of the surf zone.

Comparison of Mixing Hypotheses. McDougal and Hudspeth (1986) extracted from the literature seven hypotheses for the mechanism of lateral mixing (see for example Longuet-Higgins, 1970; Battjes, 1975; Visser, 1982; and many others). Using a general equation of motion and a concave up (one-half power) profile, they develop solutions for the seven hypotheses. Their numerical solutions indicate that the cross-shore longshore current profile is rather insensitive to the form of the mixing hypothesis.

Plotted solutions all show that maximum velocity occurs at the shoreline (McDougal and Hudspeth, 1986, Figures 2 and 3). This shoreline ($X = 0$) is the intersection of the setup level and the beach, which is landward of the still-water shoreline usually used as the starting point on laboratory work.

Even with an experimental qualification explained below, a velocity maximum at the X = 0 shoreline is not in agreement with laboratory data. There are 194 cross-shore profiles in Table A7 of Galvin and Eagleson (1965), of which 100 include a measurement slightly landward of the still-water shoreline. Only 1 of these 100 velocity profiles locate the maximum velocity landward of the still-water shoreline.

The qualification is as follows. The velocity measurements of Galvin and Eagleson (1965) were made with a miniature propeller meter whose housing was 1.5 cm in diameter and whose propeller was about 1.0 cm in diameter. The measured setup at the still-water shoreline was typically on the order of 0.5 to 1.0 cm (Table A6 of Galvin and Eagleson, 1965) which suggests that local wave heights near the still water shoreline were about 1 to 2 cm. Thus, the propeller meter was only partially submerged during part of the wave cycle.

However, all things considered, it seems that the longshore has a current maximum somewhat seaward of the base of the runup, and inshore of the breaker point. (The breaker point in these experiments were defined as the point where some segment of the front face of the wave first became vertical.)

The general insensitivity of the results to the hypothesis in Figures 2 and 3 of McDougal and Hudspeth (1986), the monotonic velocity increase to the maximum at the X = 0 shoreline, and the fact that the dimensionless maximum velocity had a value of 0.5 or slightly below 0.5 all suggest that each of the mixing hypotheses is a form of curve fitting with coefficients.

Experimental Data. Few systematic laboratory observations of mixing across the breaker line have been published. The usual approach has been to take laboratory measurements of the cross-shore variation in longshore current velocity and deduce from them what might be plausible mixing mechanisms, using friction factor and turbulence concepts from steady, uniform flow.

For example, one of the few experimental studies to directly address lateral mixing (Kim, et al., 1987) contains estimates of the diffusion coefficient from dye measurements, as well as three-dimensional mean velocity measurements and observations of wave directions. However, the end results on mixing depend on the assumed mechanism of mixing and the fitting of data to the assumption through coefficients.

Even the careful experiments of Visser (1982) do not report direct observations of mixing, except to the extent that these observations were designed to produce uniform longshore currents. If I understand correctly, Visser's (1982) experiments were deemed "proper" when such mixing was minimized.

In my early experiments (Galvin and Eagleson, 1965), an attempt was made to observe physically the exchange of water between the surf zone and the offshore side of the breaker line. A primary conclusion of that study was "Observation and measurement show that most of the fluid in the surf zone stays there" (Galvin and Eagleson, 1965, p. 1), and again 'the fluid in the surf zone appears to remain there" (p. 35).

Field Data. Many studies have reported active mixing between the surf zone and the offshore, including especially studies of rip currents and related currents in southern California and the slow mixing of less well defined current systems along the shores of the Gulf of Mexico. See Bowman et al. (1988) for recent work on this subject in the Mediterranean. Moreover, there are anecdotal stories of severe rip currents discharging at high rates across the breaker line.

On the other hand, Inman et al (1971) showed field results that could be interpreted as indicating a lower degree of mixing between the surf zone and the nearshore. There are also many anecdotal descriptions of muddy water discharge from creeks and rivers being confined to the surf zone for great distances alongshore, an indication of limited mixing.

Perhaps the most extensive field study bearing on this mixing question was a biological investigation conducted to explain unusual variation in the concentration of an algae in the surf zone, as described in the next section.

Biological Evidence. The surf diatom, Anaulus birostratus, a microscopic algae, functions as a nearly neutrally buoyant tracer, at least in daylight hours. Concentrations of A. birostratus were observed to increase markedly during daylight hours in the surf zone along 48 km of Sundays River Beach, Algoa Bay, South Africa (Talbot and Bate, 1988a, 1988b, and preceding papers). Initially, Talbot and Bate (1988a) attributed the change in concentration to advection across the breaker line, but they were led by the data to conclude that diatoms reside in the sandy bottom of the surf zone during night (Talbot and Bate, 1988b).

After an unusually extensive series of field observations, using helicopters and large numbers of personnel, the authors concluded that there is a "general impermeability of the breaker line to surfzone A. birostratus during the day time" and that "the breaker line clearly forms a physical barrier to surfzone cells during the day, preventing their loss to the nearshore." The authors go on to point out that, in one of their earlier studies at the same site under similar conditions, they found "the breaker line to be an equally efficient barrier to surface drogues released within the surf zone."

The confinement of the surf diatom to the surf zone is not absolute. Changes in wind and wave conditions can cause exchange of water across the breaker line, and at least some of the daytime impermeability is due to the surf diatom collecting at the water surface (Talbot and Bate, 1988a). The authors suggest that surface water is less easily exchanged across the breaker line than water at lower depth in the surf zone.

A Non-Mixing Hypothesis. Longshore current velocities are typically quite low. For example, a histogram of 5591 observations from the Pacific coast of California showed that about 82 percent of the observations had velocities less than 30 cm/sec (Shore Protection Manual, 1977 ed., p. 4-47). The ocean surf zone is on the order of 100 m wide, and its depth is on the order of 1 or 2 meters. Given this wide, shallow channel and such low velocities, the magnitude of the shear between the surf zone and the nearshore water must be intrinsically low. The shear could be accommodated in a short distance, and not much mixing is required.

Point measurements of longshore current velocity are used to determine the cross-shore velocity profile of the longshore shore current. The instruments which make these measurements are fixed in space while the wave translates back and forth. The longshore current is advected with the wave-induced orbital velocity in the wave. Thus, the instruments are averaging longshore flows from a strip of the surf zone having a width on the order of a few wave heights (the breaker travel distance). Such a distance could accommodate the shear.

For those rarer currents with unusual longshore velocities (say 1 or 2 m/sec), there appears to be a wave-like shear instability between the surf zone and the nearshore (Bowen and Holman, 1989; Oltman-Shay, Hurd, and Birkemeier, 1989). Such an instability provides further means of smearing out the velocity sensed at fixed instruments without necessitating mixing.

Conclusion. The conclusion of this brief note is as follows: significant mixing between the surf zone and the nearshore water is usually not required by the data. Cross-shore velocity profiles of the longshore current have been measured in such a way as to smear out the velocity profile, exaggerating the apparent mixing. It appears probable that not much mixing occurs on the time scale of the wave period.

REFERENCES

Battjes, J.A., 1975, Modeling of turbulence in the surf zone, Symposium on Modeling Techniques, American Society of Civil Engineers, v II, pp. 1050-1061.

Bowen, A.J., and Holman, R.A., 1989, Shear instabilities of the longshore current: 1. Theory, J. of Geophysical Research, v. 94, n. C12, pp. 18,023-18,030.

Bowman, D., Rosen, D.S., Kit, E., Arad, D., and Slavicz, A., 1988, Flow characteristics at the rip current neck under low energy conditions, Marine Geology, v. 79, pp. 41-54.

Galvin, C.J., and Eagleson, P.S., 1965, Experimental study of longshore currents on a plane beach, U.S. Army Coastal Engineering Research Center Technical Memorandum 10, 80 pp.

Inman, D.L., Tait, R.J., and Nordstrum, C.E., 1971, mixing in the surf zone, J. of Geophysical Research, v. 76, pp. 3493-3514.

Kim, K.H., Sawaragi, T., and Ichiro, D., 1987, Lateral mixing and wave direction in the wave-current interaction region, Proceedings of the 20th Coastal Engineering Conference (Taipei), American Society of Civil Engineers, v. I, pp. 366-380.

Longuet-Higgins, 1970a, Longshore current generated by obliquely incident sea waves, 1, J. of Geophysical Research, v. 75, n. 33, pp. 6778-6789.

McDougal, W.G., and Hudspeth, R.T., 1986, Influence of lateral mixing on longshore currents, Ocean Engineering, v. 13, n. 5, pp. 419-433.

Oltman-Shay, J., Hurd, P.A., and Birkemeier, W.A., 1989, Shear instabilities of the mean longshore current: 2. Field observations, J. of Geophysical Research, v. 94, n. C12, pp. 18031,18042.

Talbot, M.M.B., and Bate, G.C., 1988a, Distribution patterns of the surf diatom Anaulus birostratus in an exposed surf zone, Estuarine, Coastal and Shelf Science, v. 26, pp. 137-153.

Talbot, M.M.B., and Bate, G.C., 1988b, The use of false buoyancies by the surf diatom Anaulus birostratus in the formation and decay of cell patches, Estuarine, Coastal and Shelf Science, v. 26, pp. 155-167.

Visser, P.J., 1982, The proper longshore current in a wave basin, Communications on Hydraulics, Report No. 82-1, Delft University of Technology, 86 pp.

Session 7

Keulegan Centennial Symposium: Waves and Tides

G.H. KEULEGAN CENTENNIAL SYMPOSIUM

THE SIGNIFICANCE OF THE KEULEGAN-CARPENTER PARAMETER

by

ROBERT T. HUDSPETH
OCEAN ENGINEERING PROGRAM
DEPT. CIVIL ENGINEERING
OREGON STATE UNIVERSITY
CORVALLIS, OR 97331 USA
MEMBER IAHR

ABSTRACT

At the beginning of the decade of the 1950's, DEAN M. P. O'Brien and his colleagues (1950 & 1952) introduced a formula consisting of two force components for estimating the wave-induced pressure force on small vertical cylinders given by

$$dF_x(t) = dF_m(t) + dF_d(t)$$
$$= C_m \rho \frac{du(t)}{dt} dV + \frac{1}{2} C_d \rho u(t)|u(t)| dA$$

The inertial force component $dF_m(t)$ and the drag force component $dF_d(t)$ required two empirical force coefficients C_m & C_d, respectively. This formula and its many variations would later become known as the "Morison equation". For simple harmonic kinematics they found that the maximum value of the force could be estimated from

$$|dF_x|_{max} = \left\{ \begin{array}{lll} |dF_m| & ; & \theta_{max} = \frac{\pi}{2} \\ |dF_d|[1+(2W)^{-2}] & ; & \theta_{max} = \text{ARCSIN}\left(\frac{1}{2}\frac{|dF_m|}{|dF_d|}\right) \end{array} \right\}$$

where the dimensionless O'Brien force ratio is $W = |dF_d|/|dF_m|$. The dimensionless O'Brien parameter W introduced at the beginning of the decade of the 1950's would appear repeatedly in analyses

throughout the next four decades along with another dimensionless parameter that would be introduced towards the end of the same decade; viz, the "Keulegan-Carpenter" parameter $K = U_m T/D$.

In 1958, G. H. Keulegan and L. H. Carpenter published a report for the National Bureau of Standards on the wave-induced pressure forces on cylinders and plates. This report was destined to become a classic treatise and a must on the reading list for anyone about to enter the laboratory or to initiate a field experiment on this topic. Keulegan and Carpenter initiated the era of correlating the two empirical force coefficients C_m & C_d "with any appropriate parameter". Only the following two objectives were stated for their seminal treatise:

1) to introduce a Fourier residual function ΔR that would provide a truer representation of the wave-induced force estimated by the Morison equation when considering constant values for the empirical force coefficients C_m & C_d; and

2) to correlate the average values of the two force coefficients C_m & C_d with the "period" parameter $K = U_m T/D$ that would later become known as the "Keulegan-Carpenter" parameter.

In fact, they did much more! They laid the foundation for all future efforts directed toward analyzing the wave-induced pressure forces on small bodies. Motivated, in part, by the exploration for petroleum reserves offshore, several decades of intense research on wave-induced pressure forces on small bodies would find the path illuminated by G. H. Keulegan. Because of the complete and thorough treatment of the topic and because of the meticulous attention to detail given in the description of the experiments (particularly the calibration methods), this treatise became a true classic and the standard by which all subsequent treatises on the topic of wave-induced pressure forces on small bodies would be measured.

The main contributions from each of the ten sections of this classic treatise are briefly summarized. These contributions would be elaborated during the next three decades; and although the significance of the Keulegan-Carpenter parameter $K = U_m T / D$ has permeated many areas of physics and engineering during the past three decades, only the following four areas are discussed in detail:

1) the scaling of the momentum transport theorem where K provides a measure of the ratio between the convective fluid acceleration (or drag force component) and the local fluid acceleration (or inertial force component) (Dean and Harleman (1966) and Wilson (1984), inter alios);

2) the connection between the critical values of K in the interval $11.40 < K < 13.16$ and the condition of the data when the inertia and drag force components in the Morison Equation are equal (Dean, 1976 and Hudspeth and Nath, 1990);

3) the publication of additional experimental data further confirming the stability of the transverse lift force near the critical values of K between $11.40 < K < 13.16$ when the ratio of eddy shedding period T_S to wave period T is exactly equal to 2.0 for values of the Stouhal parameter $.18 < S < .20$ (Hayashi and Takenouchi (1979) and Maull and Milliner (1979)); and

4) the correlation of a relative amplitude parameter that is proportional to K with wake effects as an explanation for the elevation of the drag coefficient C_d in the supercritical region for $R > 10^6$ (Garrison, 1980).

The need to continue to explore the sensitive region around the critical values between $11.40 < K < 13.16$ with corresponding values of the Reynolds parameter $R > 10^6$ is made relevant by considering the design specification for a typical jacket-type offshore structure.

Over three decades ago, G. H. Keulegan identified the area around values of $11.40 < K < 13.16$ as being a critical condition where "obviously, the process of eddy shedding has a very significant bearing on the variations of the so-called coefficients of mass and drag, and account needs to be taken of this in the theoretical formulation of the basic process". After three decades of research, there are still no data available for verifying our theoretical models between the critical values of $11.40 < K < 13.16$ for values of the Reynolds parameter $R > 10^6$.

ACKNOWLEDGEMENTS

Financial support has been provided by the Office of Naval Research under the University Research Initiative (ONR-URI) Contract No. N00014-86-K-0687 and by the Direccion General de Investigacion Cientifica y Tecnica (DGICYT), Madrid, Spain.

REFERENCES

Dean, R.G., (1976), BOSS '76

Dean, R.G. & Harleman, D.R.F.,(1966),Est. & Coast. Hyd., Ch. 8.

Garrison, C.J., (1980), Proc.12th OTC, V. II

Hayashi, K. & Takenouchi, T., (1979), Japan Conf.Coast. Engr

Hudspeth, R.T., et. al. (1988), JWPCOE, ASCE, V. 114(1)

Hudspeth, R.T. & Nath, J.H., (1990), JOMAE, (OMAE)

Keulegan, G.H. & Carpenter, L.H., (1958), J Res, NBS, V. 60(5)

Morison, J.R., et. al., (1950), Petr. Trans, AIMME, V. 189

O'Brien, M.P. & Morison, J.R. (1952), Trans., AGU, V. 33(1)

Wilson, J.F., (1984), Dyn. Offshore Structures, Ed.

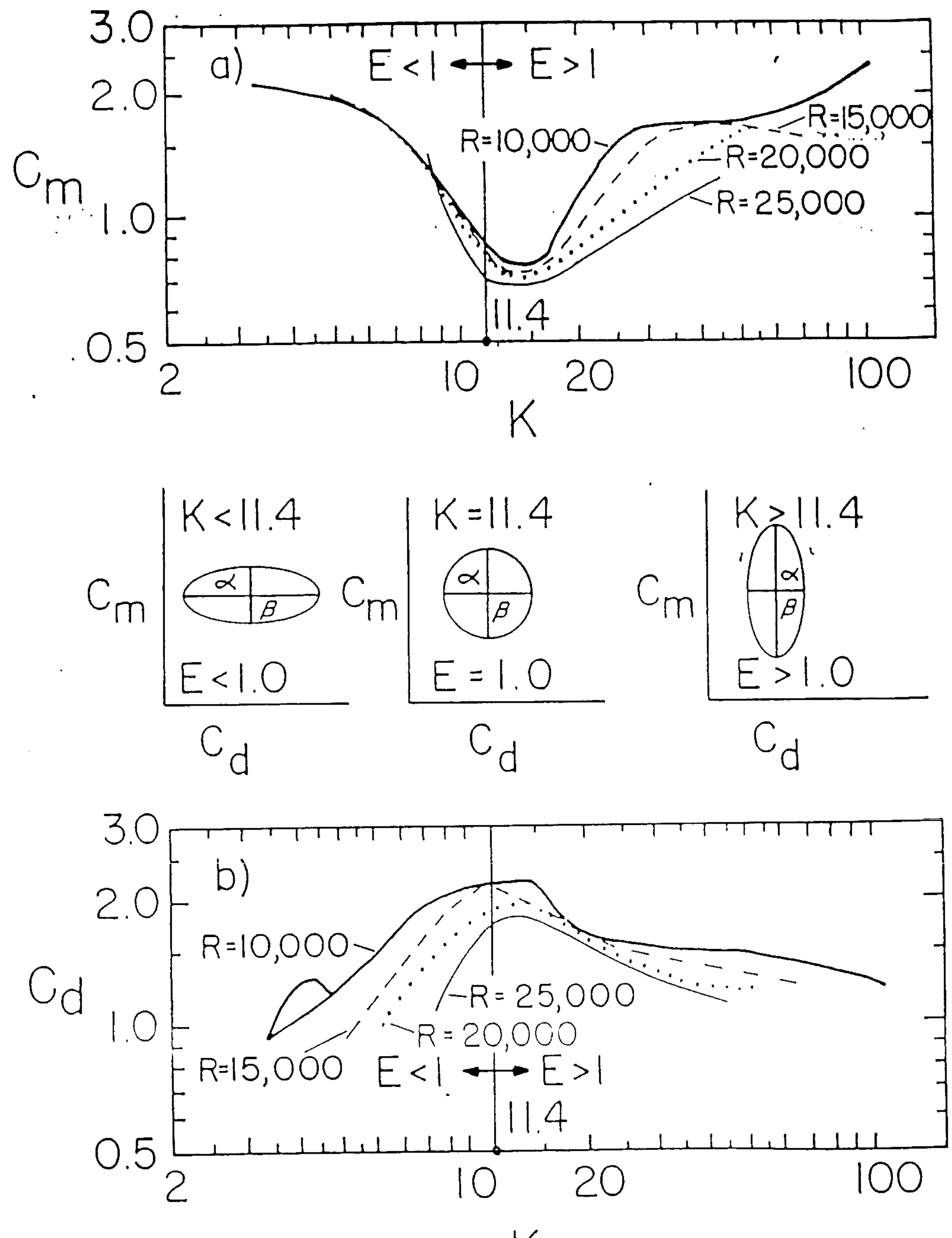

Fig. 1 Keulegan-Carpenter Data & Dean Error Ellipses

Dispersive Gravity Waves in Variable Depth: Comparison of Some Approximate Theories

Robert O. Reid
Department of Oceanography
Texas A&M University
College Station, Texas 77843

Summary

A long-standing problem in the theory of inviscid surface gravity waves is that of replacing the classical 3–D boundary value problem (an elliptic governing equation, having a predictive free surface condition) with an approximate 2–D hyperbolic wave equation, by stipulating a rational vertical structure of the dependent variables. Boussinesq's 1872 pioneering model of this nature, while restricted to weakly dispersive long waves in uniform depth, has proven to be a powerful one in the study of solitary and cnoidal waves (*e.g.*, Keulegan and Patterson, 1940). Extensions of the Boussinesq type model to *variable* depth were made by Peregrine in 1967 and more recently by Kim, Reid and Whitaker (hereafter KRW) in 1988. The generalization to waves of any relative wave length in variable depth requires the restriction to time-periodic (or slowly modulated) waves; the 1984 development of Kirby is a good example. An alternative generalization is given in the present paper, in which it is recognized that over variable depth two mathematically distinct classes of solutions must co-exist. Class I are governed by a hyperbolic wave equation, whose free solutions can propagate energy; while class II are governed by an elliptic equation forced by the class I mode acting on the sloping sea bed. As such, the class II mode can exist only in the presence of class I and represents a parasitic, bottom-trapped effect whose strength depends on the bottom slope.

One of the contributions of the present paper is the recognition that the problem of seeking an optimum 2–D hyperbolic wave equation is equivalent to that of performing a *Galerkin integral transform* of the classical wave equations, employing only the class I vertical structure functions (those commonly encountered in the classical constant depth theory). If this is done properly, the error incurred by neglecting the bottom-trapped class II mode will be of order proportional to the

bottom slope squared. An equivalent procedure is to employ the Luke variational principle (using only the class I structure) as was done by Kirby in his 1984 paper; however special care must be taken in dealing with the terms containing the bottom slope. In any event, the quantification of the error incurred by neglecting the class II contribution requires a separate analysis, and indicates that the optimum hyperbolic wave equation is justified for bottom slopes as large as $\frac{1}{4}$, even for long waves. This is important, since it implies that wave *reflection* as well as refraction and diffraction can be addressed within the context of the optimum hyperbolic equation.

The existing wave models of Peregrine, KRW, and Kirby are compared with the present model in the context of linearized, *monochromatic* waves of constant frequency (ω), in the absence of mean ambient flow and Earth rotation effect. The comparison is facilitated by converting all models to a common hyperbolic form, governing the (class I approximation of) water level anomaly (η):

$$\Gamma^{-m}\nabla\cdot\left(C^2\Gamma^{m-l}\nabla\left(\Gamma^l\eta\right)\right)+\omega^2\eta=0, \tag{1}$$

where ∇ is the horizontal gradient operator, C is the phase speed for given ω and local depth (h), while Γ is the ratio of group speed to phase speed (dependent on the relative depth $\omega^2 h/g$). Nominally the models have common C and Γ for given ω and h, within the range of relative depth for which they are intended; they are distinguished primarily by the values of the exponents l and m as follows:

Model	l	m	$l+m$	$l-m$
Peregrine, 1967	$\frac{1}{2}$	0	$\frac{1}{2}$	$-\frac{1}{2}$
KRW, 1988	1	0	1	-1
Kirby, 1984	0	1	1	1
Present paper	$\frac{1}{2}$	$\frac{1}{2}$	1	0

In the limit of very long waves ($\omega^2 h/g \ll 1$), Γ approaches unity, C approaches $(gh)^{\frac{1}{2}}$ and Eq (1) reduces to the shallow water Helmholtz equation

$$\nabla\cdot(gh\nabla\eta)+\omega^2\eta=0 \tag{2}$$

for all four models. Moreover, for constant depth, all models are consistent for common $C(\omega,h)$. For general ω and variable depth, under conditions of small diffraction, the waves are refracted by Snell's law with phase speed C, regardless of the parameters l and m. The two primary properties which are dependent on the model parameters l and m are the speed (C_e) at which energy propagates and the wave *admittance* (C_r) which governs reflection for the model concerned. It can be shown from the generic governing relation (1) that:

$$
\begin{aligned}
C_e &= C\,\Gamma^{m+l} \\
C_r &= C\,\Gamma^{m-l}
\end{aligned}
\tag{3}
$$

where Γ in general lies in the range $\frac{1}{2}$ to 1. For all but the Peregrine model, $C_e = C\,\Gamma$ which is the group speed, as expected. The Peregrine model is probably anomalous in this regard because it employs a mixture of class I and II structure for vertical velocity.

All the models have different wave admittance C_r for general ω and h. Only in the long wave limit ($\omega^2 h/g \ll 1$) does C_r (as well as C_e) approach a common value, namely $(gh)^{\frac{1}{2}}$. This fundamental difference among the models has not been recognized previously because no critical studies comparing their reflective properties seems to have been made, except in the long wave limit (where no difference is to be expected). The question of whether reflection is governed by phase speed (present model), group speed (Kirby model), or neither (Peregrine and KRW models) remains an important issue; it is an issue which could be resolved via critical laboratory experiments. However, based on an analysis of the expected error introduced in each model by neglecting the full effect of the class II mode, it is found that all but the present model have errors proportional to $\mid \nabla h \mid$. In contrast, the present model has an error proportional to $\mid \nabla h \mid^2$, as anticipated for the optimal version of Eq (1).

In order to resolve the difference between the Kirby model and the present model, a re-examination of his 1984 derivation using the Luke variational principle discloses a very subtle error concerning terms involving the bottom slope. When this is corrected, the result becomes identical to that of the present model. In the case of the Peregrine and KRW models, both can be derived from the Hamiltonian variational principle; however they require an extra constraint (not needed in the Luke principle). One source of error in these Boussinesq type models is in the adopted constraint; another source of error is in the adopted approximation for the vertical structure of velocity. Corrected linearized versions of these Boussinesq type models are derived by inference from the present model.

Thus from the standpoint of the mathematical theory, all the models with suitable corrections are made compatible in their linear representation. Nevertheless, it remains to confirm the prediction stemming from the present model that wave reflection is governed by phase speed for general $\omega^2 h/g$, at least in the limit of small amplitude waves. It will require an experimentalist with the care and inovativeness of the late Garbis Keulegan to provide the necessary laboratory data to confirm or refute the present theoretical findings.

References

Boussinesq, J.V., 1872. *J. Pure and Applied Math.*, **17**.

Keulegan, G.H. and G.W. Patterson, 1940. *J. Res. Nat. Bur. Standards*, **24**, 47–101.

Kim, K.Y., R.O. Reid and R.E. Whitaker, 1988. *J. Computational Physics*, **76** 327–348.

Kirby, J.T., 1984. *J. Geophys. Res., Oceans*, **89**, 745–747.

Luke, J.C., 1967. *J. Fluid Mechanics*, **27**, 395–397.

Peregrine, D.H., 1967: . *J. Fluid Mechanics*, **27**, 815–827.

Session 8A

Selective Withdrawal and Two-Layer Phenomena

SIMULTANEOUS, MULTIPLE-LEVEL SELECTIVE WITHDRAWAL WITH A SINGLE FLOW-CONTROL POINT

by Stacy E. Howington and Jeffery P. Holland
USAE Waterways Experiment Station
Vicksburg, MS 39180-6199 USA

Abstract

Simultaneous, multiple-level selective withdrawal from thermally stratified reservoirs is common in the management of in-reservoir and reservoir-release water quality. This type of withdrawal poses a problem when employed with a single point of flow control such as a hydroturbine at a power-producing dam. Density stratification influences the flow distribution among the uncontrolled open ports, thereby influencing the release water quality characteristics. To describe the influences of density, a simple algorithm has been developed that, when coupled with a description of selective withdrawal, can predict the composite release water quality.

The flow distribution algorithm was used with an existing one-dimensional, steady-flow selective withdrawal model. Comparisons were made with laboratory and field information. These comparisons included three diverse prototype reservoir intake structures and four intake structure physical models of various scale. Comparisons are favorable over most of the range tested. Significant differences between the algorithm predictions and the model and prototype observations are confined to an unlikely range of intake structure operations. Therefore, although the algorithm represents a simplification of the physical processes, it acceptably approximates the effects of density stratification on the flow distribution among the ports. This capability will permit the effective operation of multi-level, single-flow-control intake structures in a density-stratified environment.

Introduction

Aside from flow constraints, reservoir releases are often subject to water quality constraints on such parameters as temperature, dissolved oxygen, iron, and manganese. Operating a reservoir intake structure to satisfy these requirements and to maintain acceptable in-pool conditions is not a trivial exercise. During the stratification season, the water column in the reservoir may contain a wide assortment of water qualities. These different qualities may be accessed by selectively withdrawing water from different elevations. Often one level of withdrawal is not sufficient to satisfy the system's quality or quantity constraints and multiple levels of withdrawal are needed. So long as individual controls are maintained at each of the withdrawal locations, it is a relatively straightforward task to approximate the release quality through each location and calculate the necessary flow distribution to approximately achieve the release objective. However, when one attempts to withdraw water from multiple elevations in a stratified water body with a single control device, the density stratification can significantly affect the distribution of flow among these withdrawal locations and, thereby, affect release water quality.

Simultaneous multiple-level selective withdrawal with a single flow control device is increasingly common in reservoir operation for two primary reasons: (a.) Hydroturbines are being added to existing dams, often causing the intake structure's point of flow control to be relocated from the service gates to the hydroturbine. And, (b.) single- rather than dual-wet-well intake structures are being built to reduce construction costs. Trial-and-error operation of these structures is normally unacceptable because of the stress incurred by the downstream environment. Therefore, the reservoir operator must be able to predict the release characteristics of a proposed operational strategy prior to its implementation. If the operator can predict the flows through each intake location, existing selective withdrawal technology can be used to reasonably approximate the release quality.

Exactly predicting the near-field flow distribution among multiple intake ports is a geometry-dependent, three-dimensional, turbulent, stratified, external/internal flow problem that can only be performed by careful site-specific scaled physical modeling. At present, numerical methods are inadequate to characterize the flow and, if available, would probably not offer significant cost savings over physical models. Thus, the objective of this work was not to predict the exact flow patterns in or near hydraulic structures either through numerical or physical modeling, but rather to produce an accurate, general, easy-to-use, portable technique of approximating the effects of density on the flow distribution among the ports. An algorithm to suit these criteria for reservoir release quality management was proposed by Howington (1990).

Algorithm Development

The technique presented by Howington (1990) has been named the stratified flow distribution, or SFD algorithm. The equations used are based on the Euler equation and can be given, in general form, by

$$QT = \sum_{i=1}^{n} \sqrt{\frac{2gA_i^2}{k_i}(BH_i + \Delta H)} \tag{1}$$

$$BH_i = BH_{i-1} + \frac{1}{\rho_i}\int_{i-1}^{i} (\rho(z) - \rho_w)\, dz \tag{2}$$

where QT = total structure discharge, m^3/sec,
i = port index beginning with the uppermost port,
n = number of open ports,
g = gravitational acceleration, m/sec^2,
A_i = area of port *i* , m^2,
k_i = dimensionless (Darcy-Weisbach) loss coefficient for port *i* ,
BH_i = *buoyancy head* for port *i* (calculated as in Eq. 2), m,

ρ_i = water density entering port i , kg/m^3,
ΔH = water surface differential between the pool and wet well, m,
$\rho(z)$ = water density variation with depth in the reservoir, kg/m^3,
ρ_W = water density in wet well between ports i and $i-1$, kg/m^3.

Each of the radicals in the summation in Equation 1 represents an intake port flow. In essence, the SFD algorithm defines the smallest water surface differential that will produce the desired total discharge, subject to a potential energy contribution by the density. Buoyancy head in Equation 2 is computed beginning with the uppermost port for structures such as that in Figure 1, where the wet well outlet is located at or beneath the lowest intake port. Working toward the wet-well outlet permits estimation of ρ_w by summing the contributions from each port. Above the uppermost port ($i = 1$) there is assumed to be no density difference between the pool and the wet well. Therefore, buoyancy head for the uppermost port is 0.0. Between $i=1$ and $i=2$, ρ_w is simply the average density of the water entering the top port. In the figure, the unprimed numbers are associated with port centerlines and the primed numbers, with streamlines through the average densities entering each port.

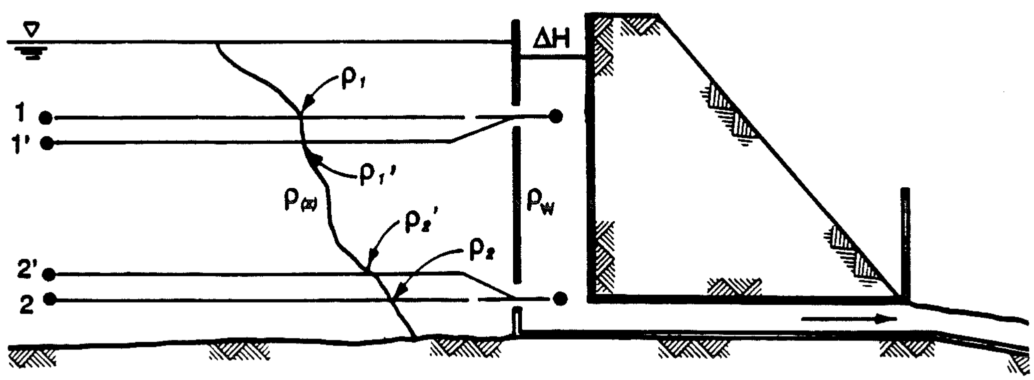

Figure 1. Example of a two-ported, single wet-well intake structure in an arbitrarily stratified reservoir.

For non-zero values of buoyancy head, there exists a threshold head loss (equal to the buoyancy head) at which the upper port flow goes to zero. For smaller discharges the algorithm is invalid. The discharge associated with this head loss is termed *critical discharge*. For smaller discharges, the restricted port (the upper port in Fig. 1) will contribute no flow to the total discharge and no water surface differential will exist between the pool and the wet well. This condition is referred to as *buoyancy blockage*. The given form of the equations requires the assumptions that (a.) friction losses within the wet well between port elevations are negligible, and (b.) water in the wet well between the port elevations is homogeneous.

As the flow rate increases beyond critical discharge, some contribution from the upper port is realized. However, the potential energy associated with the buoyancy head can still dramatically affect the flow distribution among the intake ports, thus affecting the release quality from the pool. It is not until the port entrance losses become large that the constant buoyancy head potential becomes negligible compared to the head loss terms. The algorithm may be applied whether the wet well outlet is located above, below, or among the intake ports, as long as the calculation of ρ_w is made properly. Solution of the SFD algorithm is based on iteration of ΔH using a Newton-Raphsen scheme.

Coupling with a Selective Withdrawal Model

The SFD algorithm has been coupled with SELECT (Davis et al 1987), a one-dimensional, steady-state model of selective withdrawal from a density-stratified impoundment. This model already had the capability to predict, assuming individual flow controls, the intake structure operations required to achieve a release objective. The modified version can now predict these operations with a single flow control device.

Since the amount of flow into each of the intake ports is needed to make a selective withdrawal calculation for temperature (and density) entering each port, and the temperature entering each port is needed to compute the port flows, the solution is necessarily iterative. The first pass through the SFD algorithm calculates intake port flows with no density effects. These flows are applied to the selective withdrawal calculations to predict the temperature (and density) entering each of the ports. The SFD algorithm then uses these densities to recompute the flows. These flows are then used in a selective withdrawal calculation. A final pass is then made through both the SFD and selective withdrawal components of the model.

Results of Comparison to Observed Data

SFD algorithm predictions have been compared to observations from three prototype structures and four scale physical models. Only a few of the physical model comparisons are presented herein. Additional comparisons can be found in Howington (1990). From experience, we know that, in a Froude-scaled physical model, the in-pool selective withdrawal aspects of the flow can be reasonably well produced, even at 1:50 or 1:100 scale for typical intake structure flow ranges. Also based upon experience, we felt that by maintaining turbulent flow in the model, (Reynolds numbers above 4000), we could adequately reproduce the internal mixing aspects at such small scales.

Figure 2 gives a comparison of SFD algorithm predictions (represented by the solid line) and 1:50 scale physical model test observations (represented by the filled circles). Figure 3 provides similar information with the same conventions for a 1:20 scale model test. Although representing only a small portion of the data from each of these structures the results indicate that a good, but not great, agreement exists. Similar results were obtained from other comparisons. In these figures, QU is the upper port flow, QH is the upper port flow that would occur with the same operating conditions in a homogeneous density pool, QT is the total structure discharge, and QC is the critical discharge. The shape of the curves reveals much about the response of the flow distribution to density stratification and discharge. For QT/QC less than 1.0, buoyancy blockage exists and no flow is predicted through the upper port. For large values of *QT/QC*, the flow through the upper port approaches that for homogeneous pool density. Obviously, for weak density stratifications, *QC* is small and *QT/QC* is large; the converse is true of strong stratifications. Although not readily demonstrated by these limited examples, differences between the predictions and observations were most common and extreme between *QT/QC* values of about 0.5 and 1.5.

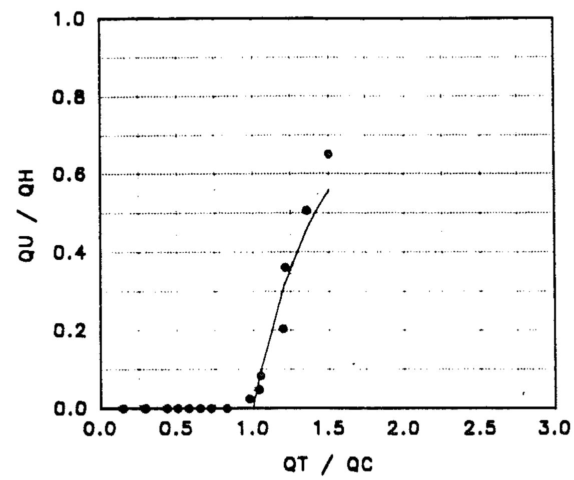

Figure 2. A 1:50 scale model.

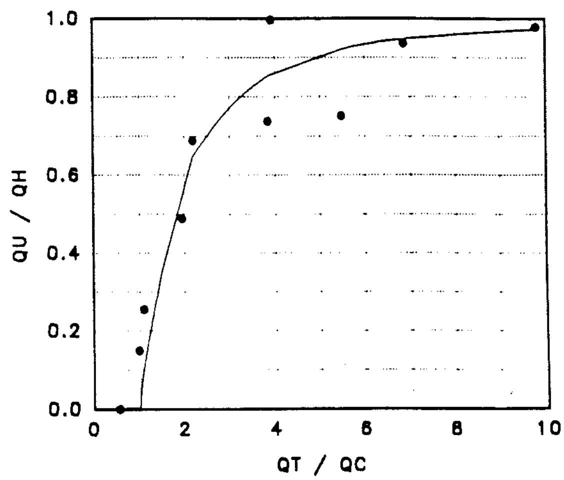

Figure 3. A 1:20 scale model.

Summary and Conclusions

An algorithm is proposed to approximate the effects of density stratification on an intake manifold such as a multi-level reservoir intake structure with a single flow control device. This algorithm predicts the resulting flows through each of the intake ports, inclusive of density effects. From this, existing selective withdrawal technology can estimate the ensuing release water quality characteristics. This algorithm does not aspire to predict the intricacies of the 3-D, geometry-dependent, turbulent flow. For reservoir intake structure design and operations, however, it is a useful tool.

The algorithm was compared to several physical models and prototypes of reservoir intake structures. These structures varied from small structures with relatively small flows to large structures with much larger flow capacities. The physical models tested varied in scale from 1:20 to 1:80. Some discrepancies between the algorithm predictions were identified. The most significant of these discrepancies occurs within an unlikely range of operating conditions. Operation very near critical discharge is unlikely in practice since very little flow is being contributed by the restricted intake port.

Potential sources of the discrepancies between the algorithm predictions and the model and prototype observations include the assumptions that a single, empirical equation and coefficient (such as a Darcy-Weisbach *k*) can approximate the head loss for various velocities (and corresponding flow rates) and that the loss coefficient is constant regardless of flow in the wet well. As demonstrated by Miller (1978), flow into an intake manifold in an unstratified environment requires an iterative solution since a relationship exists between the intake port loss coefficient (k_{1-3} in Figure 4) and the flow-by within the manifold. These subtleties are ignored in the proposed algorithm. However, if it becomes necessary to include these variations in k, the existing iteration procedure would readily accommodate an additional parameter.

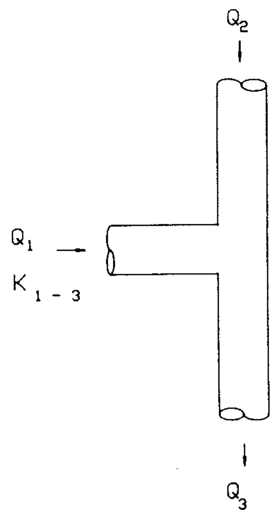

Figure 4. Combining flow in a tee.

Another potential source of error arises from neglecting the submerged jet entering the ports. The algorithm assumes that the density within the wet well is homogeneous between port centerline elevations. Deflection of the jet against the back wall of the wet well and vertical spreading detracts from the validity of this assumption. We cannot ascribe any specific error to the physical modeling process as similar errors (in direction and magnitude) were observed in prototype comparisons.

Issues of generality, portability, and ease-of-use suggested that we accept these discrepancies and tolerate the errors in prediction. Otherwise, we would be required to evaluate the effects of the geometry on the results and include the geometric description of each structure in any predictive analyses.

The purpose of the study, to reasonably well approximate, a priori, the release quality into the downstream environs, was achieved. This success was due partly to the forgiving nature of the problem concerned which masked some of the inadequacies in the description of the physical problem.

Acknowledgements

This study was conducted at the USAE Waterways Experiment Station, Vicksburg, MS, with funding from the Water Quality Research Program, sponsored by Headquarters, Army Corps of Engineers (HQUSACE). Permission was granted by HQUSACE to publish this information.

References

Davis, J. E., Holland, J. P., Schneider, M. L., and Wilhelms, S. C. 1987. "SELECT: A Numerical, One-Dimensional Model for Selective Withdrawal," Instruction Report E-87-2, US Army Engineer Waterways Experiment Station, Vicksburg, MS.

Howington, S. E. 1990. "Simultaneous Multiple-Level Withdrawal From a Density Stratified Reservoir," Technical Report in publication, US Army Engineer Waterways Experiment Station, Vicksburg, MS.

Miller, D. S. 1978. Internal Flow Systems. British Hydro-mechanics Research Association Fluid Engineering Series, Vol 5.

HYDRAULIC MODEL STUDIES FOR SELECTIVE WITHDRAWAL THROUGH HOOD INLET

by

V.V. Vaze P.P. Vaidyaraman Z.S. Tarapore

Central Water and Power Research Station
Pune, India

SYNOPSIS

Though a number of criteria are available for the design of selective withdrawal mechanisms such as skimmer wall, experience has shown that these are useful in the preliminary design but the final design would need to be based on physical model studies. This is explained in the paper based on the studies carried out at the Central Water and Power Research Station, Pune (India). The performance of a hood type of inlet structure which was satisfactory in the beginning was found to be influenced by the siltation taking place infront of the intake. periodical dredging of the area was required to restore the satisfactory performance of the hood inlet.

INTRODUCTION

Several alternative methods could be considered to ensure guaranteed supply of cold water for condensor cooling of the power stations. When the intake and outfall structures cannot be separated sufficiently apart, the use of 'Selective withdrawal' technique is quiute advantageous.

PROBLEM STUDIED

A Thermal Power Station exists at Trombay, Bombay (Fig.1) having an installed capacity of 4 units of 337.5 MW. In connection with the addition of the 5th unit of 500 MW, studies are carried out at the Central Water and Power Research Station, Pune (India) in regard to the design of the intake for drawing cold water for condensor cooling. The cooling water for the existing station is drawn from the Thane creek through a caisson with its bottom opening at -5.55 m (referred to chart datum). A similar intake was proposed for the 5th unit consisting of 4 pump chambers having a skimmer wall with 3 slit openings each 3.9 m wide and 1.3 m high (Fig 2) with the lip elevation at -0.01 m. With the operation of units 1 to 4 the thickness of warm water layer was observed to be between 1.5 and 2 m near the intake.

The design of the proposed skimmer wall opening was verified using the criteria indicated by Harleman (1), Debler (2), Wada (3), Silvester (4) and Jirka (5). Table 1 would indicate the findings. It would be apparent from Table 1 that the proposal is found effective according to Harleman, Silvester and Jirka, only at HHWL.

Table 1

Water Level	Effectiveness according to: Harleman & Elder	Debler	Wada	Silvester	Jirka
MLWL	NE	NE	NE	NE	NE
MSL	NE	NE	NE	NE	PE
MHWL	NE	NE	NE	NE	PE
HHWL	E	NE	PE	E	E

NE = Not effective PE = Partially effective E = effective

The following modifications were considered :

i) Instead of 3 openings of 1.3 m, a single opening of 3 m height, with lip elevation at -0.01 m.
ii) The width of skimmer wall opening be increased to 4.2 m or 5.0 m.

The effectiveness of these modifications are given in Table 2.

Table 2

Effectiveness of skimmer wall:size (A)4.2m x 3m,(B) 5.0m x 3m

Water Level	Effectiveness according to: Harleman & Elder		Debler		Wada		Silvester		Jirka	
	A	B	A	B	A	B	A	B	A	B
MLWL	NE	NE	NE	NE	NE	NE	NE	NE	NE	NE
MSL	NE	NE	NE	NE	NE	NE	NE	PE	PE	PE
MHWL	NE	E	NE	NE	E	E	E	E	PE	PE
HHWL	E	E	NE	E	E	E	E	E	E	E

The above modifications indicated only a marginal improvement. Experimental studies were further carried out.

DENSITY FLUME STUDIES

The studies for the performance of the skimmer wall were carried out in a density flume made of perspex having cross section 20.5 cm x 20.5 cm and length 4.75 m (Fig.3). The denser cold layer was reproduced by saline water and the warm water layer was reproduced by coloured fresh water using Rhodamine B as the colouring agent. Experiments for hot water recirculation had indicated that the temperature rise at the intake due to flow from outfall of the unit 5 would be of the order of 3 degrees C and accordingly, the density difference between two layers was reproduced. The salinity was measured continuously with the help of laboratory salinometer. A water level monitor was used to control the water level during each test. The discharge through skimmer wall opening was controlled by a valve and it was measured by passing the flow over a 45 degree V notch. The results of the model studies (scales 1:100 and 1:50) are summarised in Table 3.

Table 3

Percentage of hot water entrainment observed on density flume

Water Level	Size of skimmer wall opening			
	3.9mx3 slits of 1.3 m (original design) lip elevation -0.01m	3.9m x 3m -1.89m	4.2 m x 3m -1.89 m	5.0m x3m -1.89m
MLWL	100	66	50	33
MSL	80	50	35	20
MHWL	50	33	15	5

The results were not found to be fully satisfactory. Due to the restraints at site, it was not possible to have an opening greater than 5 m. In order to prevent the occurrence of swirls and vortices at low water level, it was not possible to provide the slit opening beyond 3 m. As such, the possibility of providing a hood over the inlet to prevent recirculation was considered.

SKIMMER WALL WITH HOOD

The exact length of the hood would be dependent on (i) rate of drawal Q (ii) the distance between the bed and bottom level of skimmer wall opening (iii) the water cover above the lip of skimmer wall.

The effectivenss of different lengths of hood was examined based on Senshu's criterion and is shown in Table 4 (for MLWL only), since at higher water elevations, the situation would be better.

Though Table 4 indicates a hood length of 2 m with an opening of 3.9 x 3 m to be satisfactory, experiments indicated that it is not the case. The coefficient C adopted by Senshu has been evolved based on the velocity distribution of the

Table 4
Effect of hood lengths

Size of opening	Lip elevation	Length of hood			
		0 m	1 m	2 m	3 m
3.9m x 3.9m	-0.01 m	NE	NE	NE	NE
3.9m x 3m	-1.89 m	NE	PE	E	E
4.2m x 3m	-1.89 m	NE	PE	E	E
5.0m x 3m	-1.89 m	PE	E	E	E

approach flow for a rectangular opening with a width to height ratio (n) of 4:1. Further it has been indicated that withdrawal characteristics (C) is not dominant for a range of n between 2 and 4 and with higher values of n, the value of C reduces slowly. In the case of intake for Trombay, the ratio n is 1.7:1 which is much smaller than the value mentioned above. Similarly other site specific parameters such as approach of the flow, the surrounding bathymetry, the effect of adjacent structures etc. need to be considered. In the light of the above, physical model studies are necessary.

DENSITY FLUME STUDIES

Studies were carried out in the density flume for hood lengths of 1m, 1.5m and 3m for different size of skimmer wall openings. The skimmer wall size of 3.9m x 3m with lip elevation at -0.01 m was not found to be effective. The results for skimmer wall opening size of 4.2m x 3m with lip elevation at -1.89m are given in Table 5.

Table 5

Percentage recirculation observed for different hood length with skimmer wall 4.2 m x 3 m with lip elevation -1.89 m

Water Level	Hood length		
	1 m	1.5 m	3 m
MLWL	50	30	5
MSL	20	20	0
MHWL	5	5	0

Based on the experimental results, skimmer wall opening of 4.2 m x 3 m, with a minimum hood length of 3m was recommended.

FIELD EXPERIENCE

The proposal was further implemented at site and the power station came into operation in 1984. Since then till 1987, almost for 2.5 years, the intake structure was found to be working satisfactorily. During the month of August 1987, warm water recirculation was experienced only during the low water stage. The temperatures were observed along the centre line of the plume, and also infront of the intake. The temperature profile did not show any radical change from that predicted. However, the bathymetry infront of the intake showed considerable change. The measurements taken just infront of the intake chambers are shown in fig. 4. It was observed that over a period of time, sedimentation infront of the intake opening had taken place which reduced the effective area of opening to the extent of 10 to 50 %, as a result of which, the velocity of drawal has increased considerably. During the high water stage, water cover being 5.75 m, there was no draw down of warm water layer. However, at low water as the water cover was reduced to about 3.2 m, the increase in the velocity of drawal has resulted in the draw down of the warm water layer causing recirculation.

The project authorities were advised to remove the accumulated silt from the area infront of the intake caissons. After the dredging was carried out, there has been no report of hot water recirculation for more than 2 years.

CONCLUSIONS

1. The various criteria available in literature are helpful only for a preliminary design of the skimmer wall opening. However, the final design would need to be based on physical model tests, in a density flume, since conditions vary considerably from site to site.

2. It is apparent that the change in bathymetry infront of the intake would affect the performance of intake. As such, it is essential to maintain the depths infront of intake by periodical maintenance dredging.

REFERENCES

1. Harleman and Elder, "Withdrawal from two-layer stratified flow", Proceedings of ASCE, Journal of Hydraulics Division, July 1965.
2. Handbook of fluid dynamics by V.L. Streeter, Chapter 26.
3. Jirka, G.H. "Supercritical withdrawal from two-layered fluid system, Part I" Two-dimensional skimmer wall", Journal of Hydraulic Research, No.1, Vol. 17, 1979.
4. Silvester, "Coastal Engineering" Vol.II, pp.266-269, Elsevier Scientific Publishing Company, New York, 1974.
5. Senshu S., "Some considerations on hydraulic design of bottom water intake", pp.1442-1452, Proc. 11th Conf. of Coastal Engineering, Vol.2, 1968.

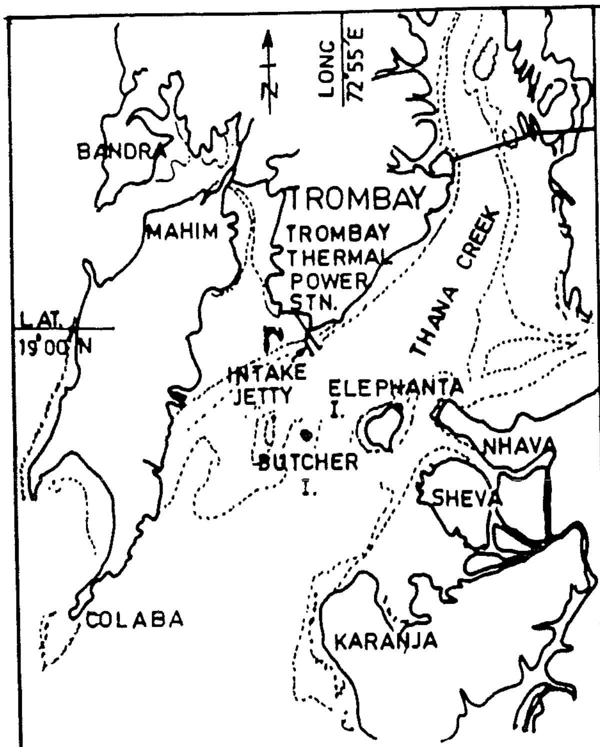

FIG.1 LOCATION PLAN

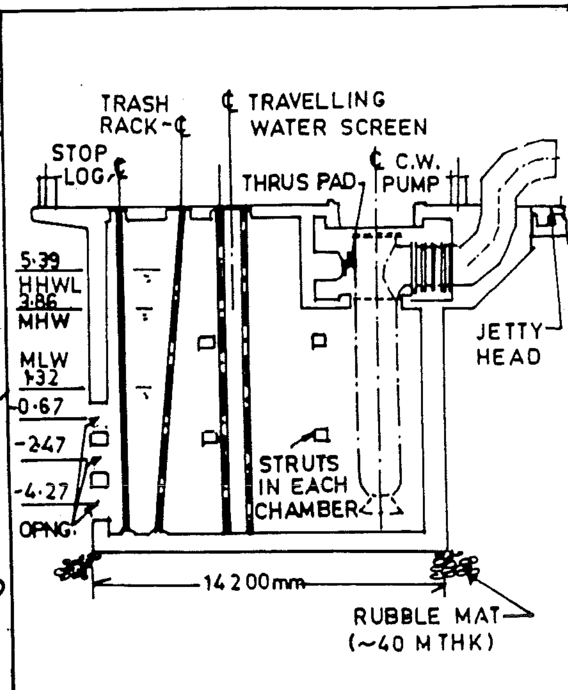

FIG.2 CROSS SECTION OF PROPOSED INTAKE (ORIGINAL)

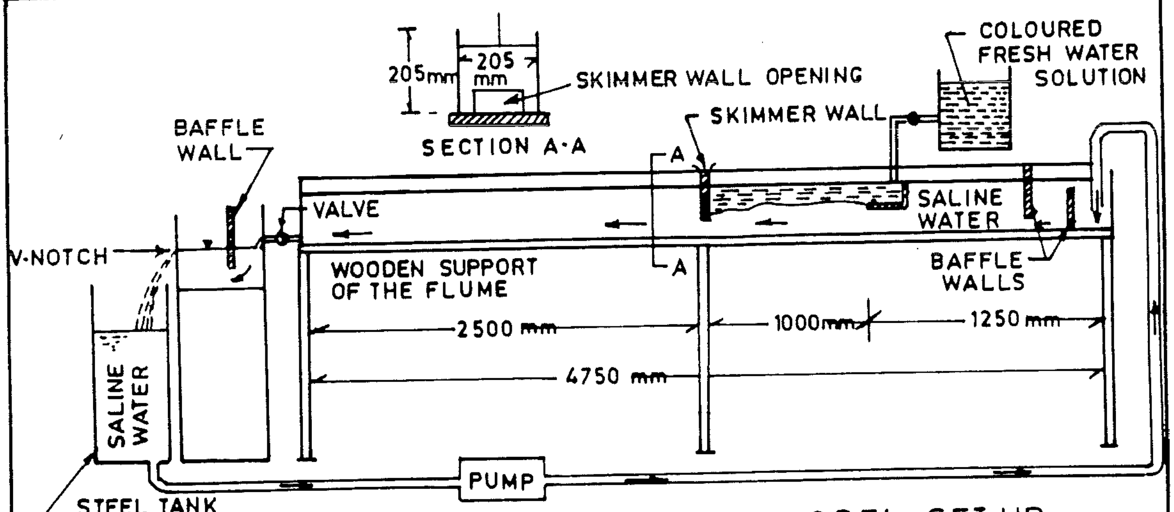

FIG.3 DENSITY FLUME MODEL SET-UP

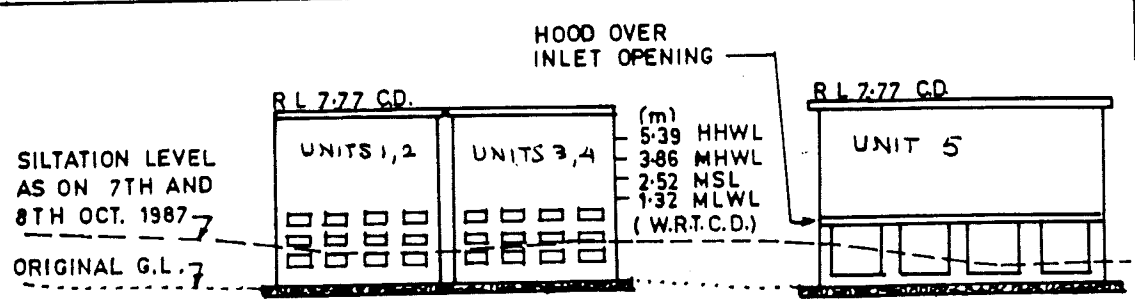

FIG.4 SILTATION INFRONT OF INTAKE CAISSON

INTERNAL HYDRAULICS, INTERFACIAL STABILITY AND MIXING IN EXCHANGE FLOW THROUGH A CONTRACTION

Gregory A. Lawrence and Emily A. Cheung

Department of Civil Engineering
University of British Columbia
Vancouver, B.C. V6T1W5
CANADA

The gravitational exchange of fluid through a convergent-divergent contraction connecting two reservoirs of slightly different density is investigated both theoretically and experimentally. The importance of the velocity shear between the layers is reflected in the value of the stability Froude number, defined as the ratio of the square of the velocity shear to the product of the reduced gravitational acceleration and the depth of flow. Frictionless internal hydraulic theory reveals that the stability Froude number may attain values greater than unity. This is a significant result since, if the stability Froude number is greater than unity, then the theory predicts imaginary phase speeds for long internal waves corresponding to the instability of these waves and the breakdown of the theory.

Internal hydraulic theory has to be extended to recognize that a crucial feature of the flow is the growth of short wave (Kelvin-Helmholtz) instabilities on the interface. The Kelvin-Helmholtz instabilities are of great practical significance since they lead to considerable interfacial mixing. This mixing affects the water quality in the reservoirs on either side of the contraction. The presence of interfacial mixing stabilises the flow with respect to long wave instabilities. The amount of mixing at the interface increases with increasing stability Froude number, but the rate of increase is constrained by the presence of the bed of the channel and the free surface.

The effect of friction is to reduce the magnitude of the flow velocities, and therefore the stability Froude number and the amount of mixing.

The modified theory has been validated in a 3.7 m x 1.1 m x 0.3 m tank, divided into two reservoirs with a narrow contraction connecting them. The flow has been visualised by dissolving a fluorescent dye into one layer and illuminating it with a thin sheet of light. Flow velocities have been determined by tracking neutrally buoyant beads. The results are applied to the exchange flow between Hamilton Harbour and Lake Ontario.

Visualization of two-layered flow over 2-D obstacles

by Lai, Chan Ji
Fan, Shiu Lun
Dept. Ocean & Hyd. Engng. Cheng-Kung Univ.,
Tainan, Taiwan, ROC.

ABSTRACT

This paper presents flow fields of two layered flow system in a two dimensional channel obtained by flow visualization and image processing techniques. Flow patterns of the homogeneous and layered flows over rectangular block and half circles are compared. Velocity profiles and interfical stress of nearly horizontal two layered flows are also obtained.

For all the experiments, the Reynolds number for the bottom layer are kept between 2000-4800. the interfical Froude number are between 0.881 - 1.753. Non-dimensional velocity profiles of two layer flows for these experiments are shown to have similar pattern for all experiments. The interfical shear stress obtained from these profiles have the same trend to those of Lofquist (1959). This study suggests that automatic measure should be used in image processing procedure to achieve more efficient produces.

Introduction

A two layered flow system is a system in which a interface exists between two fluids of different densities. In many practical cases, barriers may be built in some part of channel in which two layered flow presents. An understanding of flow structure near the barrier is needed for the purpose of flow control.

In this study, it is intended to directly distinguish flow patterns for homogeneous and two layer fluids as they passing through obstacles, the flow visualization technique is employed. Since hydrogen bubble technique have been used to observe two layer flows, e.g., Hino, (1980), thus it is adopted in this study. In addition, the image processing method is applied to the flow image recorded to test the possibility of quantifying velocity profile from the image. The approach methods and comparisons for flow patterns are shown in the following sections.

Equipment and methods of analysis

1. Equipment.

Two sets of equipment are used in the study. One is the two layer flow channel and the second is the flow visualization and image processing system. The two layered flow channel is supplied with cool water from bottom of the channel by a circulating pump system. The warm water is supplied from top of the channel from a head tank in which the water temperature is controlled by automatic heating system. An overflow weir at the entrance and a control gate at the end of the channel are used to keep a constant cool water flow rate thus an underflow two layer flow can be maintained.

The flow visualization system is composed of a hydrogen bubble generator, a TV camera, a 500 W light and a PC based image grabber. The image grabber is capable of capturing flow image at a speed of 1/30 per frame and the digitized image can be stored in computer storage for further analysis.

2. Method of image processing.

As shown in Fig. 1, by overlapping two flow images, which were taken at a very short time interval, e.g., 6/30 secs apart, the successive hydrogen bubble lines are used to estimate velocities. At one location the distance between the bubble lines has a distance of Δx which satisfies that,

$$\Delta x(x,z) = u(x,z)\ \Delta t\ \ M \qquad (1)$$

Since each frame is composed of 512 x 512 pixels, the horizontal and vertical distances can be obtained by counting the locations of the pixel where the bubble located. The horizontal velocity thus can be estimated.

The interfical friction factor, f_i, can also be estimated using the velocity profiles. It is assumed that f_i can be represented as

$$f_i = \bar{\nu}\,(\partial U/\partial z)_{max} / \bar{U}^2 \qquad (2)$$

These interfical friction factor can further be correlated with Reynolds and densimetric Froude numbers which are defined as:

$$R = (\bar{U}\ h)/\bar{\nu} \quad ; \quad F = U/\sqrt{(g\rho' h)} \qquad (3)$$

For comparison of flow patterns of homogeneous and layered flow, the flow images are captured and stored in separated files. These image files are combined and processed by a software to transfer them into vectorized files. They are further analyzed by other software, such as

AutoCAD, to correct the uneven scaling in the image. Fig. 1 is one of the typical example output.

Results and discussion

The experiments conducted in this study and their test conditions are listed in Table 1, which includes experiments of (a) parallel two layered flows, and (b) flow over circles and block.

Figs. 2, 3 show the non-dimensional velocity profiles and interfical friction factors for the 6 parallel flow cases. It can be observed that the velocity profiles for cases II to VI are very close. The deviation of the profile case I is probably because it is in a smaller Reynolds number range. The interfical friction factor, f_i, in Fig. 3 is found to be higher, although similar trend is found in the variations, than those obtained from Lofquist's experiments at the same RF^2. This might be due to the different fluids used in experiments. In Lofquist's tests, the salty water was used at the lower layer with a density difference between 1% - 8%. While in the present study, the warm water is used in the still upper layer with a density difference of 0.2% - 0.3%.

Figs. 4 - 7 show the comparisons of flow over obstacles for both of the homogeneous and two layer fluids. The experimental conditions are also given in Table.1. In each diagram, graphs (a) and (b) are for the homogeneous and two layer flow respectively. The interfaces are indicated in graphs (b) by the symbol " I ". For some diagrams, e.g., Fig. 5(b), paths of tracers are also shown by " X " . The time interval between each point "X" is 1/6 sec. It can be observed that the two layer flows tend to be unstable when they passing through the obstacles. Large

Table 1. Experimental conditions

(a) Parallel two layered flows

Case No.	I	II	III	IV	V	VI
Re. No.	2198	4440	4359	4816	2550	3956

(b) flow over circles and block.

Fig.No.	4a	4b	5a	5b	6a	6b	7a	7b
Re. No.	3305	2966	3186	3344	3331	3471	3266	3329

scale vortices are found to occur along the interfaces downstream of the obstacles, and then mixing process occurs. The internal Froude numbers for the four cases are between 1.28 - 1.75. It is also observed that the lengths of reattachment for all the (b) cases are much shorter than those of (a)s'and with a value of around twice the height of the obstacles.

Conclusion

Two layered flow passing over obstacles are shown to be unstable and may be accompanied with downstream mixing process. The length of reattachment is shorter than those in homogeneous fluid flows and is twice of the height of the obstacle. The flow visualization and image processing technique used are proved to be capable of quantifying velocity fields and is recommended for similar applications.

References

1. Hino, M., Hung, N.S., Nakamura, K.,(1980) " Entrainment and friction at the interface of salt wadge", Int. Sympo. Stratified flows., p763.

2. Lofquist, K., (1959), "Flow and stress near an interface between stratified liquids", Physics. of Fluids, v.3., no.2, p158.

Notations

$u(x,z)$: Lagrangian velocity at position (x,z)
Δt : Time interval of bubble bursts.
M : Image magnifying factor.
f_i : Interfical friction factor.
: Averaged kinematic viscosity at interface.
$\bar{U}$: Mean velocity of the low layer.
h : Depth of the lower layer.
g : Acceleration of gravity.
ρ : Density of lower layer
$\Delta\rho$: Density difference between the lower and upper layers.
R : Reynolds number of the lower layer.
F : Internal Froude number.

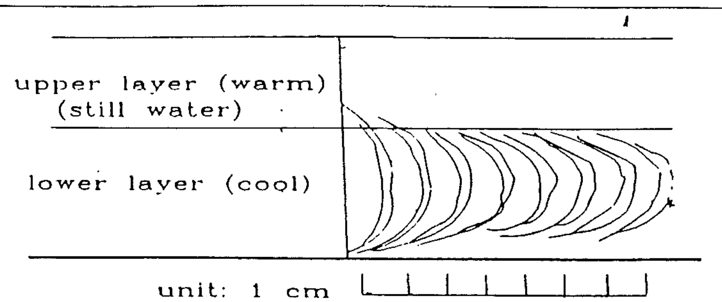

Fig. 1. Overlapping images of parallel two layer flows

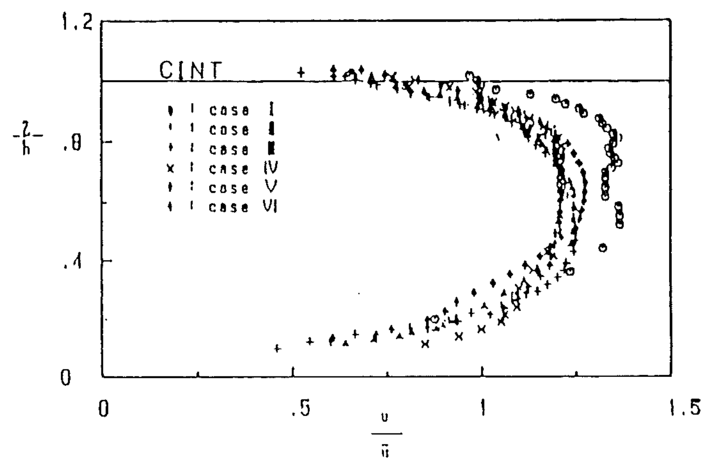

Fig. 2. Non-dimen. velocity profiles

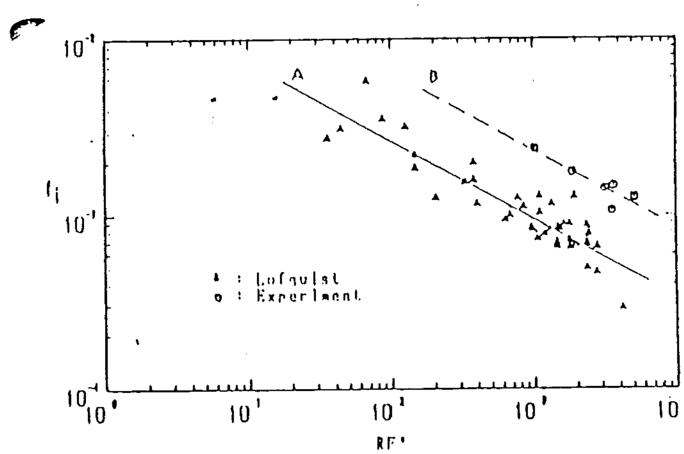

Fig. 3. Interfical friction factors.

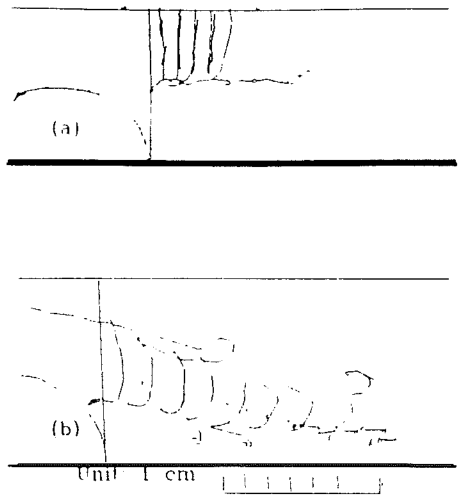

Fig 4. Flows over one half circle

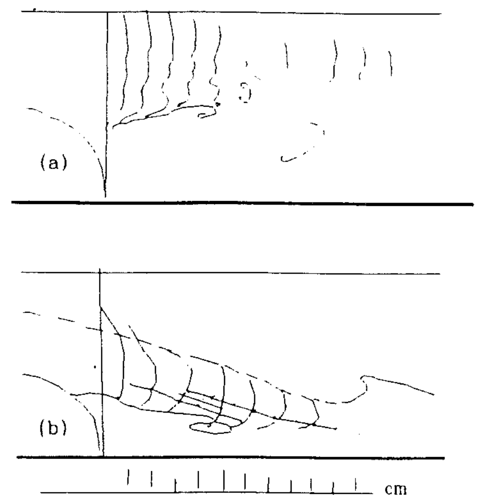

Fig. 5. Flows over two adjointed circles

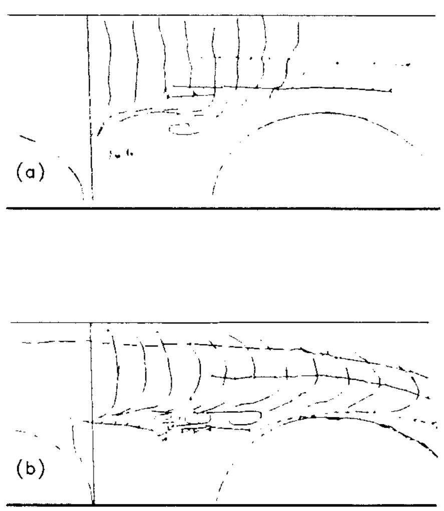

Fig. 6 Flows over two seperated circles

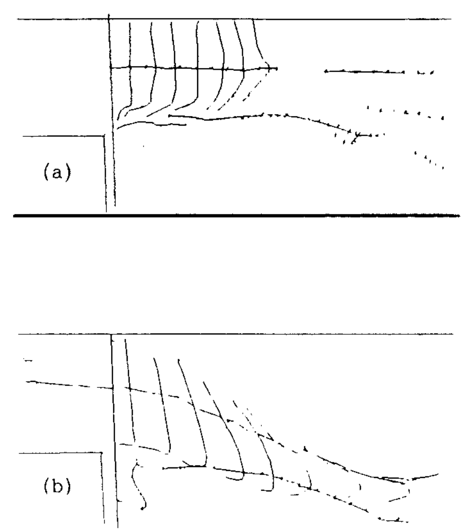

Fig. 7 Flows over rectangular block

Session 8B

Physical Model Studies

Physical Modeling of Heated Effluent Transport

——A State of Art of Thermo–Hydraulic Modeling Practice in China

Chen Huiquan

Institute of Water Conservancy and Hydroelectric Power Research (IWHR), Beijing, China

Abstract

The paper is a summary of the theory and practice of physical modeling of heated water circulation in China. Emphasis is put on the following aspects: (1) classification of thermo–hydraulic models and their similarity criteria; (2) some recent explorations in modeling; and (3) comparisons between model and prototype observations.

It is recommended to establish the idea that the true sense of physical modeling technique depends largely on the correct choice of governing parameters of the physical phenomena to be simulated and on the proper balancing between the feasibility of modeling and the necessary relaxation of the similarity criteria required.

Introduction

The electric power industry of China has kept a steady development. Up to 1989, the total installed generation capacity amounts to 1.1×10^5MW in which 3 / 4 attributed to thermal power. Extensive studies of pollutant transport due to cooling water have been carried out. Early in 1958, model law taking into consideration the simulation of cooling process above free water surface and heat balance of a confined aquatic surrounding was established, and since then, about 150 thermo–hydraulic models designed accordingly have been performed. Basic research on modeling additional physical phenomena and study of scale effect of geometric distortion etc have been conducted. A general resume of the work done in this respect and some ways followed for years in dealing with modeling are presented herewith.

Classification of Thermo–Hydraulic Models

It is a common practice to classify the thermo–hydraulic models in two categories: undistorted model for near field of the heat effluent receiving water region and distorted model for far field. The actual situation, however, is not so simple for the classification of water region and thereby the classification of models to be made definite due to the fact: (1) the intake and outlet of the cooling water system are usually studied as a whole and modelled in the same model; (2) the far and near fields are inseparated and corelated with, the thermo–hydraulic data of the one field forms some boundary conditions of the other; (3) the concept of "far" and "near" is but a fuzzy one, and it seems impossible to model the in–between water region where similarity requirements of both fields should be satisfied.

The classification which in great extent makes clear the adequate choice of the similarity criteria should be determined therefore in a more broad sense. It should be in close relevance to the main objective to be studied in the model, the accuracy of modeling required and the provisions lab provided etc. The classification recommended is tabulated in Table 1. The length and depth scales of the models conducted in this country signified with the said classification are illustrated in Fig.1. Figures beside the dot indicates the number of models using the same scale.

Table 1 The Classification & Similarity Criteria of Modeling of Cooling Water Circulation

Model Type	Main Objectives to be Studied	Lab Condition	Similitude Criteria: Necessary Requirement	Similitude Criteria: Requirement could be Relaxed
(A) GD T–Hy Model	1.T–Hy features of flow pattern in water region 2.optim of I&O 3.cooling capacity 4.envir assessment	large lab space available	$F_r = 1, (\frac{\Delta\rho}{\rho})_r = 1$ $h_m > h_{min} \backsimeq 5cm$ $n_r = \frac{L_r^{1/2}}{Z_r^{1/3}}$. $Q_m > Q_{cr}$ $Z_r \backsimeq K_r^{2/3} L_r^{2/3}$.	$\frac{L_r}{Z_r} < 3—5$ outfall pattern near O. similar to GuD Model
(B) GuD T–Hy Model	1. T–Hy features & optim of I&O locally 2. Hy optim of I&O with near envir flow well modeled 3. Hy optim of I&O with heat dissipation neglected 4. 1–D thermo–density flow	no large lab space required; complicated topography near O; sensible for GD Model envir flow pattern easy to be simulated	$\frac{L_r}{Z_r} = 1–2$, $(F_\Delta)_r = 1$, $Re_0 > Re_{cr} \backsimeq 1000$, $h_m > h_{min} \backsimeq 5cm$	$(\frac{\Delta\rho}{\rho})_r = 1$ $n_r = L_r^{1/6}$ or $L_r^{1/2} / Z_r^{1/3}$ Model water region possibly large
(C) pilot T–Hy Model	same as (A): 1, 2, 3, 4.	limited lab space; large water region to be simulated; no high accuracy required; short test period	$(F_\Delta)_r = 1$, $Q_m > Q_{cr}$, $h_m > h_{min}$,	$(\frac{\Delta\rho}{\rho})_r = 1$, $n_r = L_r^{1/2} / Z_r^{1/3}$
(D) HuD Hy Model	1. optim of I&O for intensive upstream flow 2. I& O optim for shallow non– stratified water region 3. sand prevent for I.	lab with large water supply	$F_r = 1$, $Re_m > Re_{cr}$ $h_m > h_{min}$, $n_r = L_r^{1/6}$	model inclu. I, sand dia. φ, $\varphi_r = Z_r (\Delta\rho')_r^{-1}$ $\Delta\rho' = \rho_s - \rho_w$
(E) GD T–Hy–Sal Model	same as (A): 1, 2, 3, 4, with sal intrusion	sufficient lab space with sal circulating & measuring equip	$F_r = 1, (\frac{\Delta\rho}{\rho})_r = 1$. $(\frac{\rho_s - \rho}{\rho_r}) = (\frac{\Delta\rho''}{\rho})_r = 1$ $Q_m > Q_{cr}$, $h_m > h_{min}$	$Z_r \backsimeq K_r^{2/3} L_r^{2/3}$ $\frac{L_r}{Z_r} < 3–5$
(F) GD T–Hy–Ftr Model	1. T_2 varied with tidal flow when project optim taken 2. comparison of Hy project 3. water envir varied along with tidal flow	lab with sufficient length	as (A), $\frac{L_r}{Z_r}$ larger than (A) is acceptable	cooperate with GuD Model
(G) GD T–Hy–Sal –Ftr Model	Same as (F): 1, 2, 3 with sal intrusion	same as in (E) and (F).	as (F), $(\frac{\Delta\rho}{\rho})_r = 1$ $(\frac{\Delta\rho''}{\rho})_r = 1$	$\frac{L_r}{Z_r} < 5 - 7$ cooperate with GuD Model

Abbreviation:

GD— geometric distorted; GuD— geometric undistorted; HY— hydraulic; T–Hy— thermo–hydraulic; Ftr— full tidal range; Sal—saline; I—intake; O—outlet; I&O—intake and outlet; optim—optimization planning; envir—enviroment; M— model.

Modeling of Surface Cooling

The similarity criterion of the cooling process through free surface is

$$Q_r = K_r L_r^2 \tag{1}$$

where K is the coefficient of heat dissipation at water surface, defined as

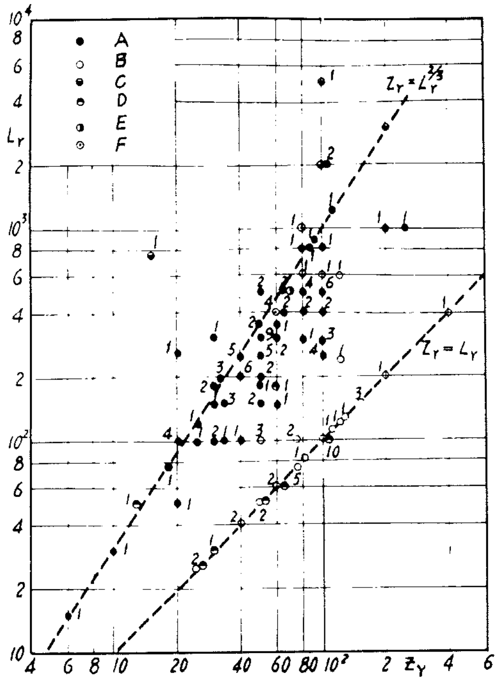

Fig.1 Scale Ratios in Thermal Models in China, 1958—1990

$$K = \alpha_1 + k\alpha_2 + \alpha_3 \tag{2}$$

Q is the effluent discharge, α_1 ,$k\alpha_2$, $\alpha_3$are coefficients of convection loss, evaporation loss and radiation loss respectively and $k = \frac{\partial e_0}{\partial T}$ is the slope of temperature T and saturated vapor pressure e_0 curve.

Since α_1 is linearly correlated with α_2 throgh Bowen ratio B; α_3 shares not the major part of K and can be obtained with reasonable accuracy by calculation, the adequate determination of K and thereupon the determination of K_r and Q_r relies highly on the reliability and accuracy of α_2.

On the basis of systematic study on evaporation of heated water body in a temperature– moisture controlled wind tunnel, a formula has been suggested as[1]:

$$\alpha_2 = 10[19.6 + 1.6(\Delta T_v) + 12.5w^2]^{1/2} \quad (w \cdot m^{-2} kpa^{-1}) \tag{3}$$

where W= wind velocity at 2m above water surface.

$\Delta T_v = (T_s)_v - (T_0)_v$ = virtual surface water temp.–virtual air temp.

The formula, simple in form, taking care of mechanism of free and forced convection in a single expression, reflect more closely the real picture of mass and heat transfer at air–water interface and has been well verified by many field measurements.

from Eq. (2),
$$K = (k + b)\alpha_2 + 4\varepsilon\sigma(T_s + 273)^3 \tag{4}$$

where σ = Stefan–Bolzman Constant, $b = B / (\Delta T / \Delta e)$, ε = coeff. of emission.

K_r and Q_r can be obtained from Eq. (3) (4), and (1) with an improved accuracy.

Modeling of Icing

Simplified similarity criteria has been presented for modeling icing phenomena in cooling pond. Model should be operated under the similar negative air temperature condition as in the prototype, a condition which is usually difficult to realize.

In predicting the possibility of preserving non–icing water region by inducing in the heated effluent, some similarity approach with more relexation has been used in feasibility study for turning Yingkou Bay into a non–icing port in cold winter by using the cooling water from a power plant situated near the port.[2] The model was designed just as for an ordinary thermo–hydraulic distorted model but with strict observance to the similarity criterion;[3]

$$(T_e - T_0)_r = 1 \tag{5}$$

T_e , T_0 are the ambient water and air temperature respectively.

Temperature obtained from model T_m is transfered to prototype temperature T_p by

$$(T - T_e)_r = 1 \tag{6}$$

water region with negative T_p value thus obtained is recognized as the icy zone. If the icy zone is so large to effect the general flow pattem of the relevant water region, it could be modeled as land, and the new restricted model made is operated with corrected boundary as before. Test measures run on repeatedly until no negative temperature is predicted in the model. The final land margin so reached is expected to be the assumed true icy boundary.

Modeling of Wind Drift

Wind impact to cooling water circulation involves in two folds, enhancing heat and mass exchange at water surface and inducing wind drift with relevant secondary flow. The former could be assessed by some well–verified formulas.The latter effect, however, could be simulated directly in the model. A low velocity wind tunnel has been specially designed for this purpose with dimensicn of $18 \times 9 \times 1.2$m as shown in Fig 2. Model with large length scale is set in the test section and is run after densimetric Froude Law. Wind velocity in the model is controlled by [4]

$$u'_r = V_r = (\Delta\rho / \rho)_r^{1/2} z_r^{1/2} \tag{7}$$

with wind velocity above the water surface $u' = \text{const} \cdot V$.

The wind tunnel has been used for predicting wind impact to cooling water circulation for several engineering projects with good results. Take Zhangze cooling reservoir as an example [5]; under the unfavorable wind and the original outlet condition,the intake temp access $\Delta T_2$was 3.6℃ with outfall $Q = 3.6\text{m}^3/\text{s}$; however when the suggested outlet scheme was taken and Q increased to $36\text{m}^3/\text{s}$, 10 times of the original discharge, ΔT_2 was not increased thereupon but reduced to 2.8℃ under the same unfavorable wind condition. See Fig.3.

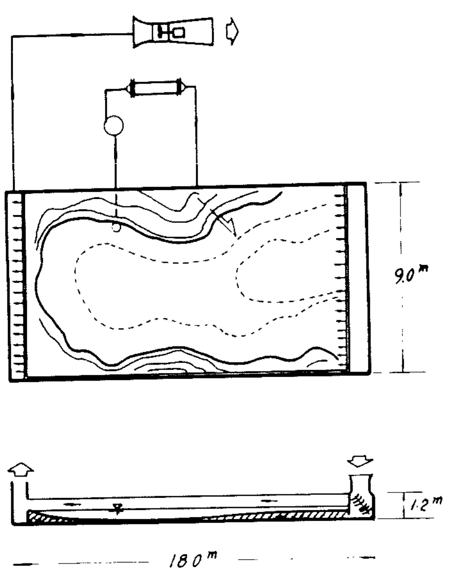

Fig.2 Wind Tunnel with Enclose T–H Model

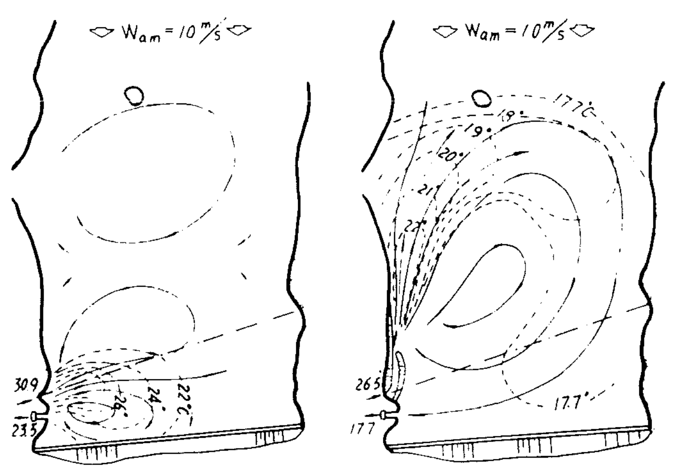

(a). original scheme (b). suggested scheme

Fig.3 Wind Impact to Thermal Flow in Zhangze Reservoir Model

Verification of Similarity

The prototype–model comparison for more than 10 projects have been conducted.A common conclusion is that the overall flow pattern can be well predicted; but the thermal diffusion is somewhat larger horizontally and thinner vertically in models than those in field data. Two of these are illustrated herein:

1) The overall flow pattern in an enclosed water region: [6]

The area of Taiyuan cooling reservoir is about 5 km^2 with average water depth of 4m, $Q=4.2m^3/s$. There was no wind during field measurement. The flow patterns of both the upper and the bottom layers of a model with $L_r=250$, $Z_r=40$ were carefully investigated and compared with the field data. The model–prototype comparison shown in Fig.4 reveals their pronounced agreement.

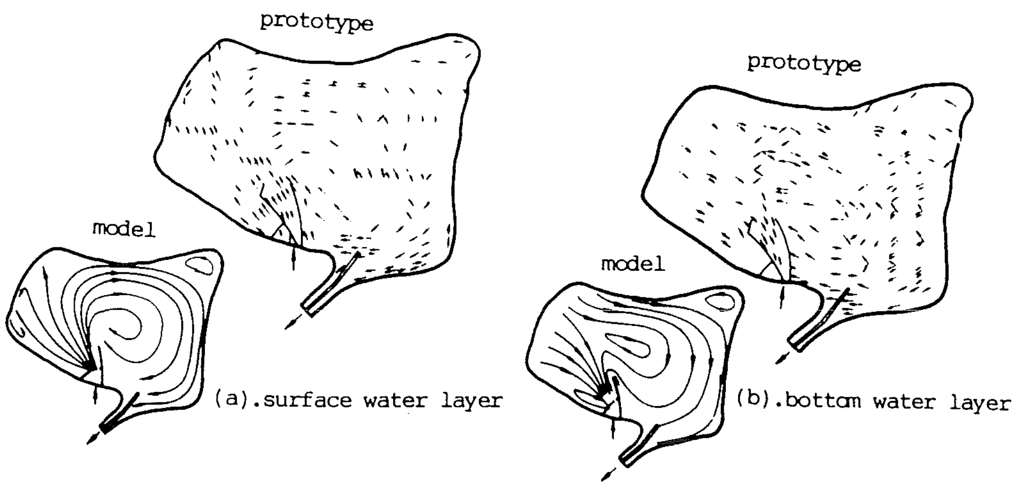

Fig.4 Comparison of Flow Pattern in Model and Prototype of Taiyuan Reservoir

2) The longitudinal temp field in river: [7]

Huainan plant discharges its thermal surface outfall into Huai River and draws the cooling water back from the river through 2 submerged intakes. A model with, $L_r=500$, $Z_r=100$ have been carried out. Temperature distributions along the longitudinal river cross section were surveyed both in the model and in the prototype. Their comparison shown in Fig.5 leads to the conclusion that the overall thermal patterns can be predicted with certain degree of accuracy throngh thermo–hydraulis modeling.

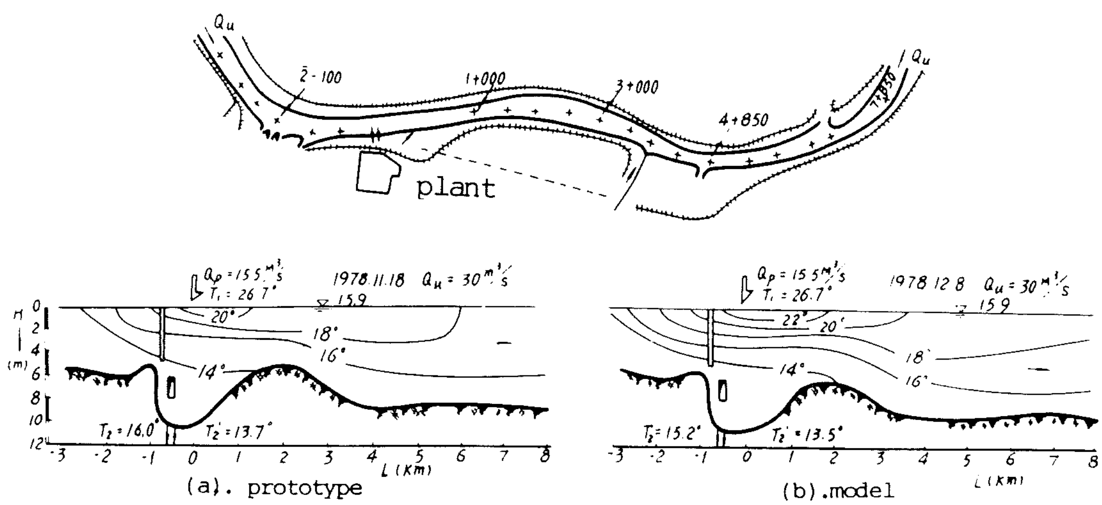

Fig.5 Comparison of Longitudinal Temp Pattern in Model and Prototype of Huai River

Conclusions and Discussion

1) A feature of thermo–hydraulic models is the entering of the temperature variable. Correct modeling is made difficult by the presence of anisotropy of the fluid and the heat exchange at water surface. In order to render the modeling feasible, some compromising similarity criteria are presented with various simplifications and assumptions. Strictly speaking, no thermo–hydraulic model is an undistorted one without inavoidable scale effects. The degree of similarity of the model required depends on both the realizability and accuracy of the original data the model based on and the accuracy of the experimental results actually expected.

2) Different types of thermo–hydraulic models possess respective characteristics. The quality of model investigation does not lie on whether the model is large or small, distorted or undistorted, but on its adaptability to what the model simulated; a simple physical model built on some resonable assumptions with field material whose precision is conformable to that required by the current design stage is always in a real sense better than models built on false assumption without verification. It is in this context that a pilot model with large geometric distortion is also preferable at certain condition, while a large sophisticated model with simulation of tidal and wind effect is extremely necessary at other condition.

3) Based on more than 30 years' experience on thermo–hydraulic modeling, all the experimental studies finished and engineering projects constructed accordingly have not encountered the contradictory examples concerning operation results and test predictions. The overall prototype investigations have proved the realizability of their going through model studies. With the rapid development of numerical simulation, physical modeling still shows its own usefulness and vitality.

References

[1] Chen Huiquan, Mao Shimin et al., Experimental Study of Mass and Heat Exchange at Air–Water Interface of Water Body. Proceeding of 22th Congress, IAHR, 1989.

[2] Ni Haoquing et al., Experimental Study on Utilizing Thermal Flow from Power Plant to Alleviate the Icing in Yengkou Port, Research Report of IWHR,1988.(in Chinese)

[3] Chen Hriquan, Similarity Criteria of Icing of Cooling Water Circulation under Non–negative Ambient Temp.Research Report of IWHR, 1988. (in Chinese)

[4] Chen Huiquan, Study of Simulation of Cooling Water Circulation with Consideration of Wind Impact.Research Report of IWHR, 1983. (in Chinese).

[5] Chen Lintao, Zhu Qiumei, Model Study on the Wind Impact to Cooling Water Circulation in Zhangze Reservoir. Research Report of IWHR, 1988.(in Chinese).

[6] Chen Huiquan, Yue Juntang et al., Experimental Study on Taiyuan Cooling Reservoir. Research Reporrt of IWHR, 1960. (in Chinese)

[7] Mao Shimin, The Comparison of Prototype and Model Study on Hydro–Thermo Characteristics of Thermal Flow in Huai River. Research Report of Auhui Water Resources Research Institute, 1988. (in Chinese)

PHYSICAL MODELING OF SURFACE BUOYANT PLUME - A METHOD TO CORRECT SURFACE TEMPERATURE MEASUREMENTS FROM DISTORTION DUE TO ATMOSPHERIC HEAT EXCHANGE

by

D. Fritsch (1), M. Darras (1), B. Manoha (1), Xu Zhengmei (2), Su Weidong (2)

(1) Laboratoire National d'Hydraulique - Electricité de France - 78400 Chatou - France

(2) Guangdong Nuclear Power Joint Venture Company - China

Abstract

Experimental studies of thermal impact in the near field have been realized in a physical model of surface buoyant plume for a chinese nuclear power plant [1]. Atmospheric heat exchange in the model was strictly investigated and distortion between model and prototype, due to the lack of control of the heat exchange speed scale, was applied to surface temperature measurements after validation on a 3D numerical model.

Introduction

In a small-scale physical model, the similitude laws cannot be respected alltogether. For free-surface models, the most important non-dimensional number is the densimetric Froude number which represents the ratio of inertia to buoyant propagation forces. The respect of this number implies distortion relatively to other phenomena such as turbulence (Reynolds number) or atmospheric heat exchange.

The paper presents a method to correct temperature measurements from distortion due to the impossibility to control the atmospheric heat exchange in a small-scale physical model. The proposed method is based on experimental measurement of atmospheric exchange made in a small tank near the physical model. In parallel to the tests of temperature recirculation in the physical model of surface buoyant plume, the value of the model atmospheric exchange coefficient can then be recorded. This value, given at prototype scale, A_m, is compared to the actual value of the atmospheric exchange coefficient on prototype, A_p ; the difference between those two values is introduced in an exponential corrective factor which is applied to the time-derivative of the surface temperatures measured in the model.

1. Presentation of the physical model

The physical model of thermal impact in the near field was built in a tank of 50 m x 30 m at a length scale of 1:100. Figure 1 presents the instrumentation set used in the model: at three limits of the tank, variable flow pumps enable to reproduce constant or tidal currents ; surface currents and plume spreading were measured by means of black-and-white or colour cameras ; temperatures were recorded at fixed points or by means of a travelling bridge. Atmospheric heat exchange for the model was recorded in a small tank of 2.5 m x 1.7 m in the vicinity of the basin.

2. Laboratory values of the heat exchange coefficient

Analysis of the temperature time evolution in the small tank, under heat exchange influence only, yields :

(1) $$T = T_o\, e^{\frac{-t}{\tau}}$$

with a time constant $\tau = \dfrac{\rho Ch}{A}$

where :

- ρ = density of water (kg/m^3),
- C = 4 185 J/kg/°C ; specific heat of water,
- h = thickness of the plume (m),
- A = Atmospheric heat exchange coefficient ($W/m^2.°C$).

Figure 2 presents an experimental determination of the A coefficient for a twelve hours test duration. Results for different tests are all around 20 $W/m^2.°C$, the biggest one being 21.6 W/m^2 and the lowest one 15.2 $W/m^2.°C$, for equivalent ambient conditions in the laboratory (mean air temperature from 19.2°C to 24.0°C, no wind).

The time scale for heat exchange is fixed by the Froude similitude ; as the density and the specific heat are the same for the model and the nature, the scale for the heat exchange coefficient should be 1/10. This is not feasible because on the model the heat exchange coefficient is similar to the heat exchange in nature ; an observed value of 20 $W/m^2.°C$ in the model is equivalent to 200 $W/m^2.°C$ at prototype scale which corresponds to irrealistic natural conditions. Therefore, in order to compensate the distortion between the nature and the model, a correction on the plume observation is needed.

3. Principle of the correction

This correction has been determined taking into account the evolution of the temperature at a fixed location in the plume. First, the temperature increases rapidly when the plume front reaches the given location. Further increase of temperature elevation is much slower and after some time can reach a steady state value in a permanent current context ; during this period, the increase is due to the mixing of the jet in a water already heated by the previous releases. The time of transfer, t, since the beginning of the test indicates the "age" of the hot water body, i.e. the time during which atmospheric heat exchange has been effective. Therefore, a corrective factor following a time exponential law, deduced from the one presented above, is applied to each elementary time evolution of the temperature elevation ; thus, the correction is efficient only in case of temperature evolution, and a permanent temperature state is not corrected.

Then, at a given point, if T represents the temperature elevation measured in the modeled plume above the ambient water temperature, the correction is done on the time derivative $\frac{\partial T}{\partial t}$ and the corrected temperature at the considered point is :

$$T_c(t) = \int_{t=0}^{t} \frac{\partial T}{\partial t} e^{-t/\tau_c} \, dt \tag{2}$$

with : $\tau_c = \frac{\rho C h}{A_p - A_{m'}}$

The difference between the atmospheric heat exchange coefficient as observed in nature, A_p, and the coefficient issued from model and given at prototype scale, $A_{m'}$, is introduced in the correction through the time constant τ_c.

4. Validation by means of numerical tests

To get a global approach of the thermal impact, a far field thermal study was previously achieved on a larger area by means of a 3D numerical model of current and temperature [2]. This model was run for different values of the atmospheric heat exchange coefficient, which was introduced in the boundary conditions at the free water surface level. The idea was then to take two time dependent computed data sets of temperature for two different values of this atmospheric heat exchange coefficient and to apply the above correction to one of this data set in order to get the other one back.

In practice, two numerical data sets were available for $A_1 = 45$ W/m^2.°C and $A_2 = 20$ W/m^2.°C and we intended to correct the first one to obtain something similar to the second one. The above corrective formula was used in a cumulative way, time step after time step, and we wrote :

(3) $$\Delta T_c(t) = \Delta T(t) \, . \, e^{\frac{-(A_2 - A_1)\,t}{\rho C h}}$$

The plume thickness in the far field was evaluated to h = 1.0 m.

Figure 3 shows surface temperature fields at high tide for A_2 (above) and A_1 before and after correction (below) : the corrected one obtained from A_1 is quite similar to the first one got with A_2. This is confirmed by the time dependent temperature curves at points P_2 and P_3 (figure 4). Those good comparisons fully justify our corrective approach.

5. Application to model temperature measurements and limits of the method

In the physical model we got $A_m = 20$ W/m².°C which corresponds at prototype scale to $A_{m'} = A_1 = 200$ W/m².°C, when we would have liked a prototype value of $A_2 = 45$ W/m².°C. The above correction has then been systematically applied to surface temperature measurements at fixed points. An average value of the plume thickness for this near field study was deduced from vertical measurements and fixed to h = 1.5 m. As information, with those figures, the time corrective factor after ten hours is $e^{-t/\tau_c} = 2.43$.

Because of the increasing of the corrective factor with time, this kind of correction is limited by the accuracy of the measurements : thus, in our model, after t = 15 hrs, an error of 0.1°C in temperature recording would induce an error of about 0.4°C for the corrected value.

6. References

[1] Guangdong Nuclear Project - Report n° 23 - The near field thermal study on physical model - EDF/LNH HE/42-87.33, April 88.

[2] Guangdong Nuclear Project - Report n° 15 - The far field thermal study - EDF/LNH - HE/42-87.02, March 87.

PHYSICAL MODEL

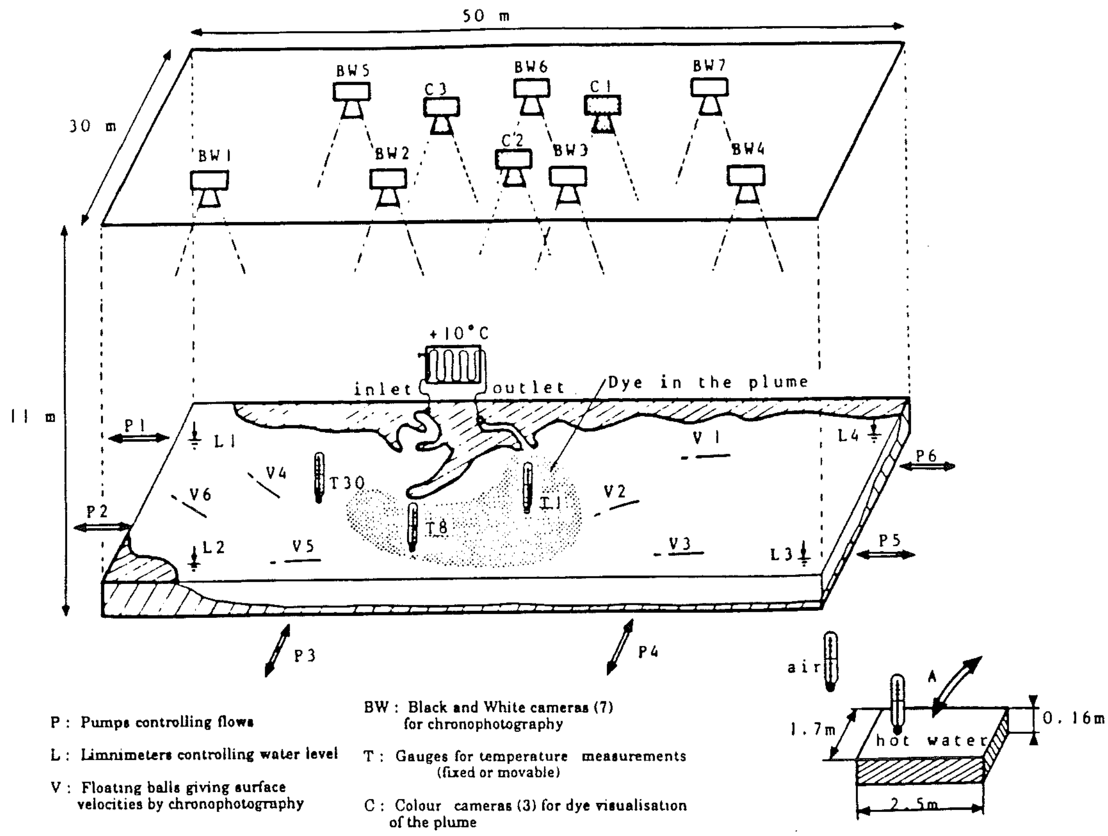

SMALL TANK

(for atmospheric exchange measurements A)

Fig 1 - Panoramic view of instrumentation

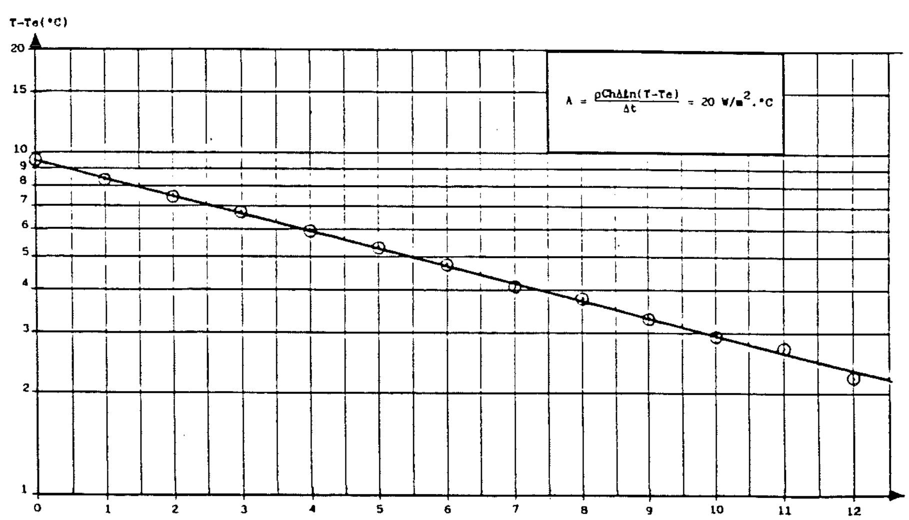

Fig 2 - Exponential decreasing of temperature in the small tank

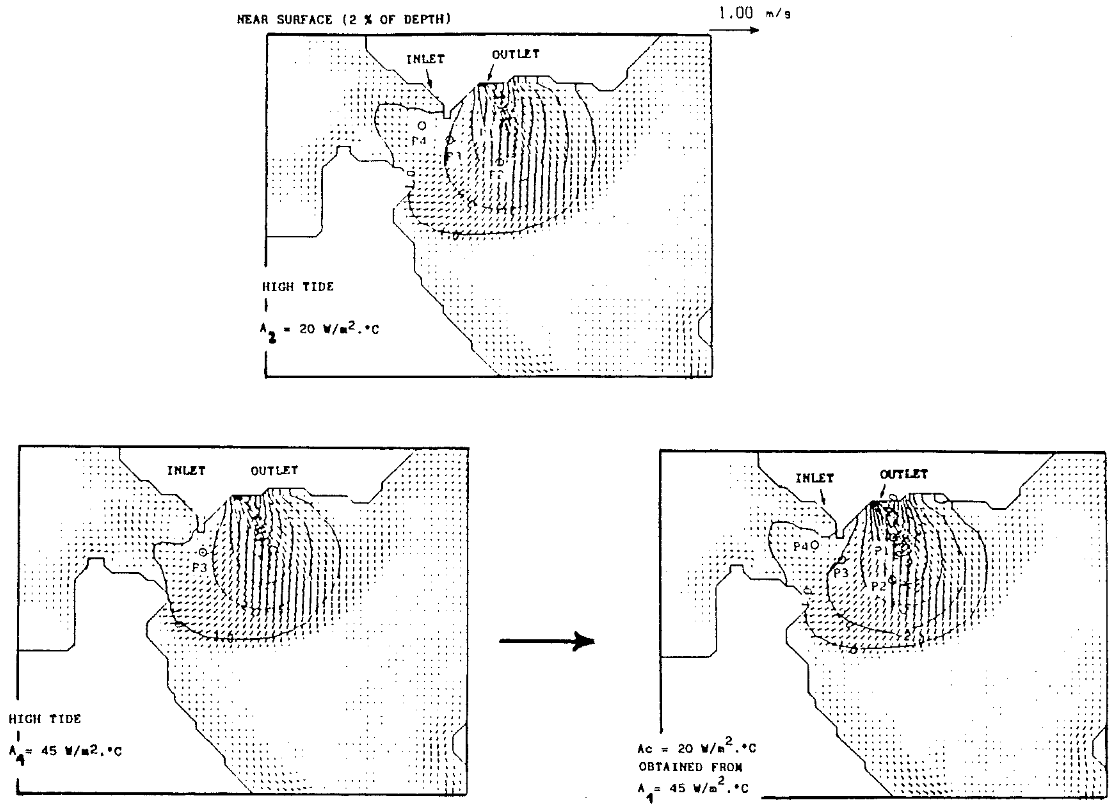

Fig 3 - Surface temperature fields for A_2, A_1 and A_1 corrected

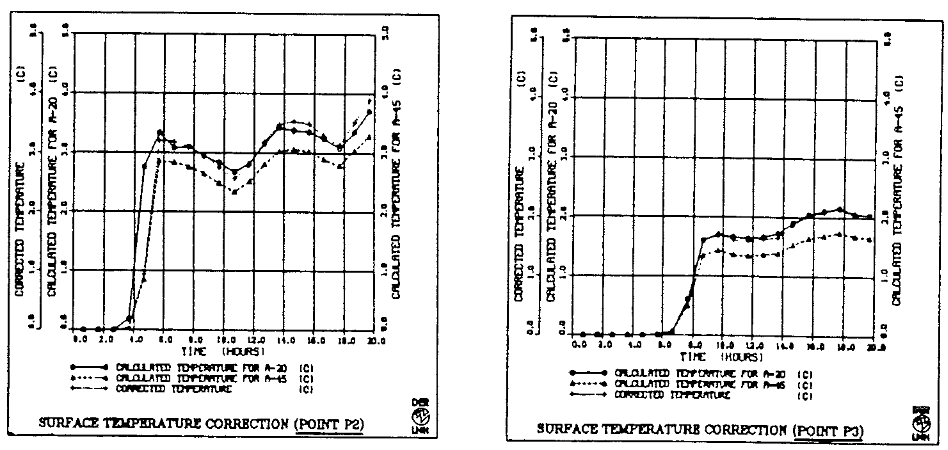

Fig 4 - Time temperature evolutions at points P_2 and P_3 (see fig 3)

FIELD VERIFICATION OF A PHYSICAL MODEL OF A THERMAL DISCHARGE

by P. J. Ryan (1) and S. W. Tu (2)

The cooling water outfall for the Diablo Canyon Nuclear Plant has been extensively tested, both in the field and in a 1:75 scale physical model. Overall, over fifty field tests and more than 100 model tests have been performed, resulting in an unprecedented comparison of model and field data.

From 1984 - 1986, during the power ascension tests for the Diablo Canyon Power Plant, an extensive series of field tests was performed to collect data on the temperature structure in the vicinity of the cooling water outfall. Horizontal and vertical temperature profiles and surface temperature isotherms were obtained for a wide range of plant load and receiving water conditions, including extreme low to high tides, calm seas to strong wind and high wave conditions, and stagnant to strong upcoast and downcoast current conditions. In addition to the temperature profiles, data were also collected on currents, waves, wind, tide and plant discharge and temperature. These data were used to calibrate and verify a 1:75 scale hydraulic model of the discharge structure and vicinity. QA procedures were developed for the model operation to ensure that the model data were collected, analyzed and stored in a consistent, reliable manner. Statistical procedures were developed to compare model and field data to ensure an objective approach to model calibration and verification.

Comparison of model and field data indicates that a number of parameters, which receive little or no attention in typical outfall models, can have a considerable impact on the near-field temperature distribution. These parameters include wave height, period and direction, details of the bottom topography, and bottom roughness. An overview of the model testing program will be given, and the significance of the above parameters will be discussed.

(1) Chief Hydrologic Engineer, Bechtel Corporation, San Francisco, CA
(2) Research Engineer, Pacific Gas and Electric Co., San Ramon, CA

A Model-Prototype Comparison of Cooling Water Circulation in Tidal Bay

Chen Kaiqi

Institute of Water Conservancy and Hydroelectric Power Research

Abstract

The paper presents a case study which gives a vivid comparison of results obtained from physical modelling, numerical simulation and field observations.

Liaodong Bay is used as heat receiving water body with large amount of waste thermal energy effluented from the 1,400 MW Ying-kou Power Plant. Extensive field observations of the water region near the plant were conducted and both mathematical and physical modelling of the heated effluent circulation in the bay were performed. In numerical simulation, method of fractional step with L_∞-stability was applied with due consideration of the local topographic characteristics in boundary treatment. A model with $L_r = 300$ and $z_r = 6$ was then operated in conformity with the boundary tidal conditions given by field tests. The very good agreement of the comparisons indicates the adaptability of the distorted model with even rather high geometric distortion ratio provided the model is carefully designed and well calibrated.

Introduction

Since 1970s', much of the work carried out by hydraulic laboratories has been directed to the development of mathematical models which apparently need not suffer scale effects. However, experience of years' practice in this field has also shown the significant deviation of the results predicted by the numerical simulation in certain cases due to the over simplification in deriving the governing equations, the inadequate treatment of the boundary conditions or the inadequate choice of the parameters used. It is therefore commonly reconized that hydraulic modelling is sometimes indispensible yet especially for the near field, and the verification of results either from physical or numerical model seems to be ever more important for complicated physical phenomena.

The paper gives a typical case study of Ying-kou cooling water project for which both the mathematical and physical modelling were made.

Ying-kou Power Plant, situated adjacent to the Ying-kou Port, is planned to have a total installed generation capacity of 1,400MW. The cooling water of $Q = 47\ m^3/s$ in Summer is drawn from Liaodong Bay and discharged back to the Bay with an temp. increment $\Delta T = 9°C$. The Bay is subjected to irregular tides with an average tidal range $\Delta H = 3.34m$ for high tide and $\Delta H = 1.70m$ for low tide. Fig.1 and Fig.2 show the location of the plant site and the water region near the site being simulated and studied in the models. Average water depth of the region is about 6-7m. The intake and outlet of the cooling water were also sketched in the figure.

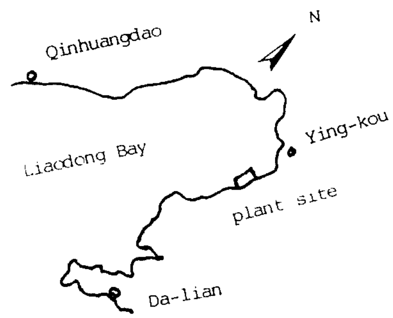

Fig. 1 Plant Site

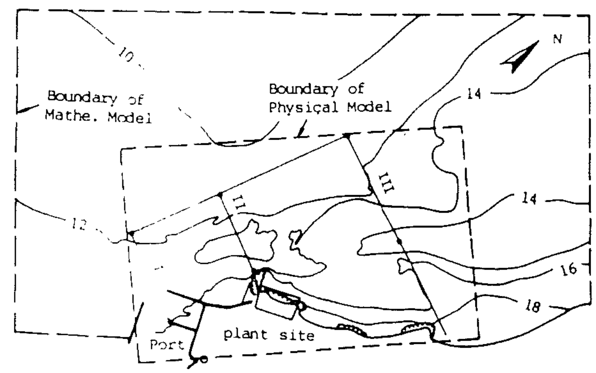

Fig.2 Boundaries of Models

Physical Modelling

A scale model was undertaken with the objective of (1) studying the thermo-hydraulic behavior of the water region and optimizing thereupon the general layout of intake and outlet works; and (2) collecting quantitive data for undertaking direct comparisons with those from mathematical model investigations and field measurement. The model scales were so selected so as to meet the requirements of both the similarity criteria for simulating the main physical phenomena to be studied and the limitation of laboratory facilities. As the flow directions of the tidal current some distance away from the shore have proved to be nearly in a 180° difference in tide and ebb, the current boundary could be correctly simulated by a solid model boundary. Fig. 3 illustrates the general planning of the model with scale ratios:

Length scale	$L_r = 300$
Depth scale	$z_r = 60$
Density-diff scale	$(\Delta\rho/\rho)_r = 1$
Velocity scale	$v_r = (z_r)^{\frac{1}{2}} = 7.07$
Time scale	$t_r = L_r/z_r^{\frac{1}{2}} = 42.4$
Temperature scale T_r	

after $(T_1 - T_\infty)_r = (T - T_\infty)_r$

where T_1 = effluent temp at outlet
T_∞ = ambient temp.

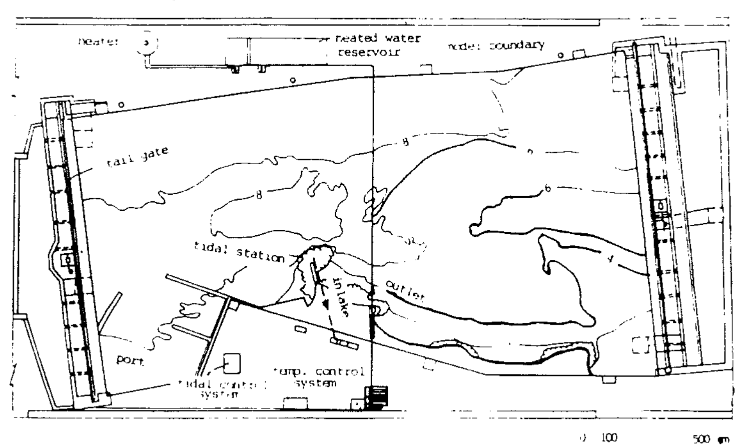

Fig 3 General layout of model

Heated water was furnished by an electric heater system with the prescribed feeding water temperature. The sliding gates at the two ends of the model were controled by a computer to simulate the given time variation of water level at the relevant stations. The model was calibrated with bed roughness and verified finally by the velocity distribution obtained from field observations. The good agreement of data from model with those from field are demostrated in Fig. 4.

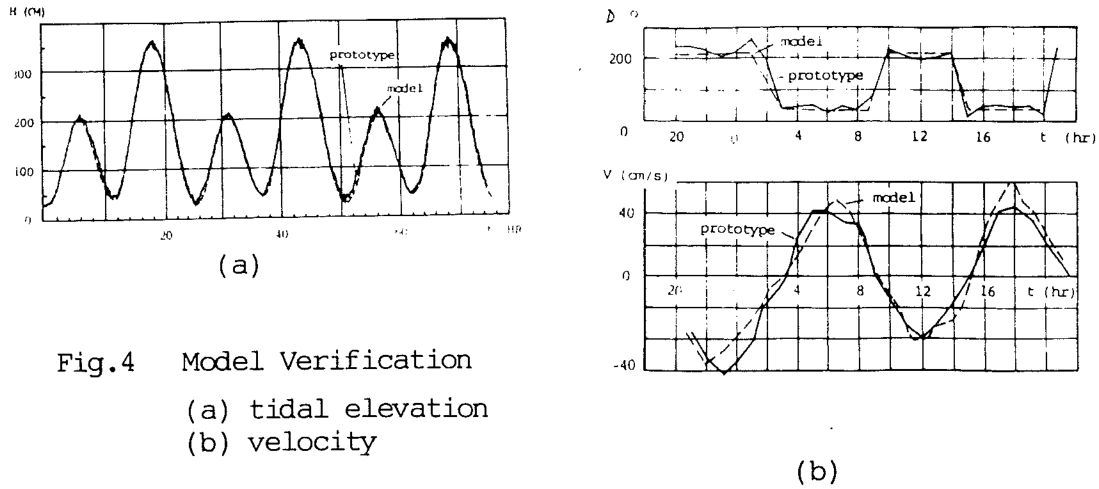

Fig.4 Model Verification

(a) tidal elevation
(b) velocity

A total of 265 temperature probes were mounted on 5 monitoring frames which were set up and down synchronizelly with the tidal variation. The temperature at water surface and at the intake and outlet were measured at definite time interval and all the data were collected and analyzed by a data logger sustem with an accuracy of $0.1^{\circ}C$ [1].

Mathematical Modelling

An hybrid method of fractional steps with L_∞-stability for numerical modelling of tide-generated circulation and thermal/nuclear pollution have been developed and used successfully in temperature prediction of the tidal water region in Lionin Province[2]. The method proves to be superior to previous in: (1)neither linearization nor interpolation is introduced for treatment of hyperbolic terms, so the numerical damping is minimized, and (2)numerical solutions from parasitic oscillations can be prevented and stability and convergence can be guaranted. In the numerical modelling of cooling water circulation of Ying-kou power plant where the water region interested is just a small part of much large Liaodong Bay, the conditions at the open and moving boundary were treated theoretically. Moreover, due to the complexity of the local topographic condition near the plant site, special treatment of the said boundary condition with the consideration of the local topographic characteristics was taken [3]. The domain simulated is shown in Fig.5. The model was well calibrated with the field data in low tide and verified with the relevant field data at the high tide [3].

Comparisons between the Physical-Mathematical Modelling

A typical comparison of these modellings at different tidal stage is shown in Fig.6 with the same engineering layout under the same hydro-

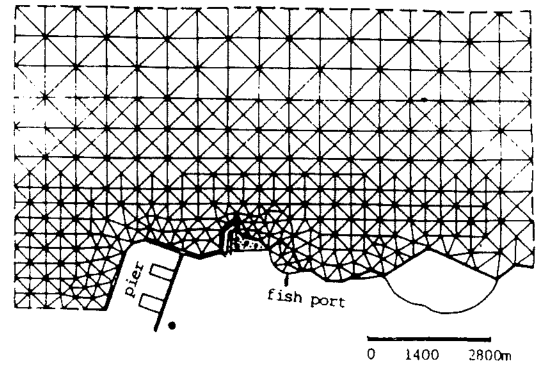

Fig.5 The Boundary and Finite Elements Grid used in the Simulation

-logical and operational conditions[3]. The agreement seems satisfactory.

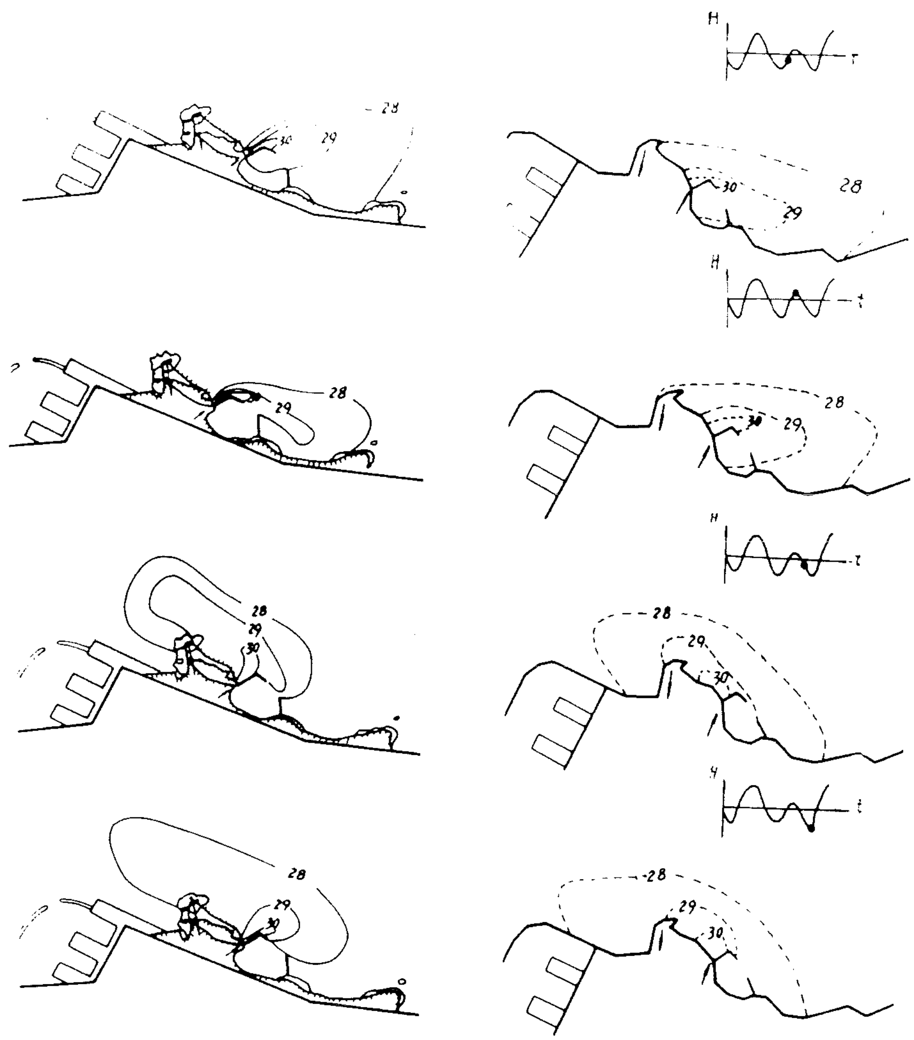

Physical Model Numerical Simulation

Fig.6 Comparison of Surface Temperature Distribution

The predicted intake temperature T_2 of the cooling water also well checked with the results obtained from the numerical simulation as shown in the following table.

Case	T_2 (°C)	
	Physical Modelling	Mathematical Modelling
1	28.7	28.9
2	29.0	29.0
3	28.4	28.3
4	28.6	28.4

A lot of simplications and assumptions have been introduced in physical and mathematical modelling. The relaxation thus made will more or less leads to the deviation of the results from the real case. The excellent agreement between the two kinds of modelling is by no means in a sense of indicating the true accuracy of the modelling, however, the agreement does prove the adequacy of using such models to solve the problem.

Comparisons of Model Calculation with Field Measurement

The plant is being under construction and no operation data could be offered yet to compare with those predicted in the model. However, the field data measured under tidal action with no heated effluent have been carefully analyzed and compared with the relevant data obtained from mathematical modelling. The comparison is illustrated in Fig.7 and Fig.8. Very good agreement is demonstrated. The fact in turn verifies the agreement of the results from the physical modelling with the prototype investigations.

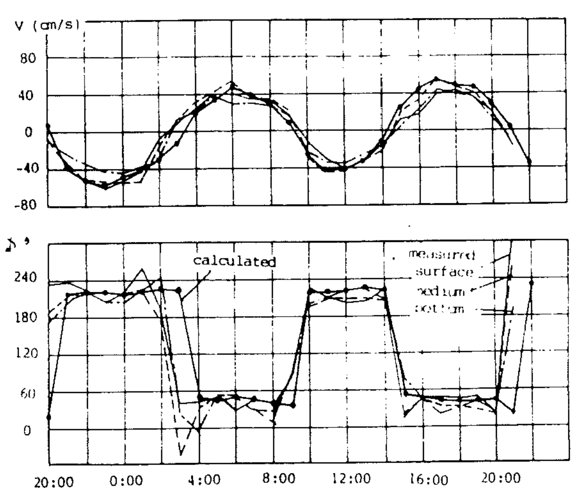

Fig.7 Comparisons of Velocity (magnitude & direction) measured verus calculated 1985.5.25-1985.5.26

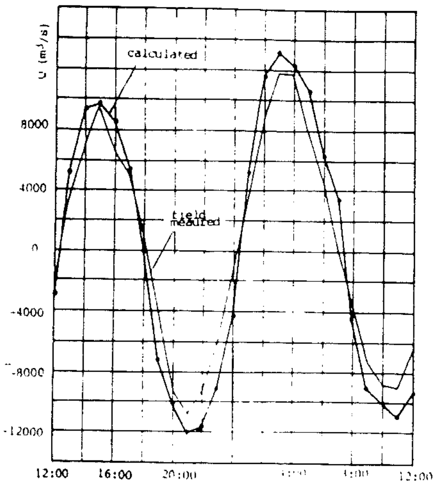

Fig.8 Comparison of Tidal Discharge through Crosssection III measured versus calculated

Conclusion

Either physical modelling or numerical simulation has its own merits and limitations. Mutual complement and hybrid integration of the two means is necessary for many cases and emphasis should be laid on the calibration and verification of the models. A physical model with delibrate consideration for choosing L_r and z_r as well as some other important scale ratios can solve a lot of rather complicated problems with acceptable accuracy. The comparisons of physical-mathematical modelling -field data of the case study of Ying-kou Project does show the reliability of the physical modelling. Not only the theoretical analysis but also the engineering and laboratory experiences are important, however, in correctly simulating from prototype and predicting back to prototype the physical phenomena interested.

References

[1] Ni Haoquing et al.,"Experimental Study of Cooling Water Circulation of Ying-kou Power Plant" Research Report of IWHR (1986)

[2] Wu Jianghang, Chen Kaiqi, "A Hybrid Method of Fractional Steps with L_∞- Stability for Numerical Modelling of Harbours and Bays", Proceedings of International Conference of Mathematical Modelling of Ports and Harbours, Birmingham, England (1985)

[3] Chen Kaiqi, "Simulation of Cooling Water Circulation due to Effluent discharged from Ying-kou Power Plant", Selected Papers of IWHR, (1986)

PRACTICE IN HYDRAULIC MODELING AND PROTOTYPE OBSERVATION

by Liu Daming, Ding Zhuoyi
Yangtze River Scientific Research Institute
Wuhan, Hubei 430010 China

ABSTRACT

On the basis of plenty of data in model test and prototype observation for many hydro-projects, this paper discusses two subjects:

(1) The influence of Reynolds number on flow capacity and the condition of its similarity between model and prototype when hydraulic models for outlet works are designed according to Froude criterion of similitude;

(2) Simulation and discrimination method of cavitation flow in hydraulic structures.

As the results in this paper are based on the comparison between model and prototype, they are valuable for hydraulic model experiment in solving engineering problems.

1. INTRODUCTION

The hydraulics division of Yangtze River Scientific Research Institute (YRSRI) is wellknown among the nation's hydraulic research agencies both in scope and in equipments. Since 1951, it has conducted hydraulic investigation for 52 projects including Gezhouba and Three Gorge project on the main stream of Yangtze River. Thousands of field observation instruments were fitted on constructing or completed projects to make prototype observations or sustained monitoring, plenty of valuable data from field tests had been obtained, on the basis of which, a monography named "Field Hydraulic Investigation Practice" was published in cooperation with another institute[1].

Using part of data from some engineering cases, this paper only discusses the modeling of flow capacity passing through several outlet works and cavitation flow occured on some hydraulic structures.

2. INFLUENCE OF REYNOLDS NUMBER ON FLOW CAPACITY THROUGH OUTLET WORKS

2.1 Flow Capacity Over Spillway

In general, discharge coefficient is used to express flow capacity. The discharge coefficient for spillway is defined as:

$$m = Q/b\sqrt{2g}\, h^{1.5} \qquad (1)$$

where m—discharge coefficient; Q—discharge; h—head above spillway crest; b—spillway width; g—gravity acceleration.

Here m shown in Eq. (1) is a function of many factors. According to Bernouilli equation, the following expression can be derived.

$$m = \psi k \varepsilon \sqrt{1-\zeta}\,(1+\frac{\alpha_o V_o^2}{2gh}) \tag{2}$$

where ψ—velocity coefficient; k, ε—flow contraction coefficient in vertical and horizontal direction, respectively; ζ—proportional factor of pressure head at spillway face to h; $\alpha_o V_o^2/2g$—approaching velocity. It can be seen from Eq.2 that besides ψ which is influenced by Reynolds number, all other factors are mainly related to head h. That is why the discharge coefficient m in some experience formula was usually expressed as the function of relative head h/p (p is spillway height)[2]. From our model tests with different scale and prototype observations on some spillways, it is obtained that gravity is the main factor for modeling of spillway discharge and the effect of Reynolds number on it is relatively small. Generally, when model Reynolds number corresponding to design discharge $(R_e)_m=(vh/\nu)_m \geqslant 1.5\times10^5 (v=Q/bh)$, the discharge coefficient, m measured from models can be used as that of prototype.

The relation of m and h/h_d measured from three models with scale of 1/57, 1/110 and 1/120 and from field observation (1 : 1) for Dangjiangkou spillway is plotted in Fig.1 [3]. It can be seen from Fig.1 that m from prototype is in agreement with that from models of 1/57 and 1/110. But on model 1/120, m is smaller than that of others. As the $(R_e)_m$ of 1/110 model equals 1.5×10^5, it is suggested that the discharge coefficient, m measured from model tests under the condition of $(R_e)_m \geqslant 1.5\times10^5$ will be satisfactory in accuracy to estimate that in prototype.

2.2 Flow Capacity Through Discharge Gallery of Ship Lock

As the tainter gate in the discharge gallery is opened continuously during filling or emptying of ship lock, the discharge through gallery is usually expressed by:

$$Q = \mu A \sqrt{2g(H - \frac{Ln}{gA}\frac{dQ}{dt})} \tag{3}$$

where Q—discharge; μ—discharge coefficient; A—area of flow section; H—water head; Ln—computed length of gallery; (Ln/gA)dQ/dt—inertia head.

Owing to considerable length and complex configuration of gallery, the accurate similitude of resistance for every part of model gallery is of significant importance for flow capacity experiment. On models of 1 : 40 and 1 : 25 and in prototype, the flow capacity through the galleries of ship locks NO.1, NO.2 and NO.3 of Gezhouba project have been studied. The results indicate that the difference of μ between models and prototype is negligible at small gate opening n, but increases obviously with increasing of n.

Fig.2 gives the relation of discharge coefficient μ and gate opening n measured from 1/25 model and in prototype of Gezhouba ship lock NO. 3 under filling process[4]. It can be seen from Fig.2 that the difference of μ ($\Delta\mu$) between model and prototype is small when $n<0.6$, then, $\Delta\mu$ increases with increasing of n, and finally $\Delta\mu = 15.8\%$ when $n=1$. The reason can be explained by the variation of total resistance. During small gate opening, the form drag is dominant, which has little differerce between model and prototype. But with the increase of n, the frictional drag becomes superior in magnitude, which is dissimilar to prototype at small model scale. If it is difficult to make the model scale still larger than 1/25, it is the only way to manage to reduce the friction of model boundary.

2.3 Flow Capacity Through Short Pressure Conduit

On nine types of bottom outlet model for Three Gorge and Geheyan projects, their flow capacity were studied[5]. Three of the relation curves of discharge coeffiecient, μ and Reynolds number in model, $(R_e)_m$ are plotted in Fig.3. μ is expressed by:

$$\mu = Q/BD\sqrt{2gh} \qquad (4)$$

where Q—discharge; B—width of sluiceway; other symbols are shown in Fig. 3; $(R_e)_m = (VD/\nu)_m$; $v = Q/BD$. It can be seen from Fig.3 that μ for three types varies with $(R_e)_m$ and trends toward constant, respectively. Let $(R_e)_k$ be Reynolds number corresponding to constant value of μ. It shows that μ from model cnn be used as that of prototype only under the condition of $(R_e)_m \geqslant (R_e)_k$, i.e. model scale must satisfy certain requirement. According to Froud criterion, the relation of Renolds number of model, $(R_e)_m$ and prototype, $(R_e)_p$ and length scale $L_r = L_p/L_m$ is

$$(R_e)_p/(R_e)_m = L_r^{1.5} \qquad (5)$$

Because of $(R_e)_m \geqslant (R_e)_k$, L_r have to be

$$L_r \leqslant [(R_e)p/(R_e)_m]^{2/3} \qquad (6)$$

The studied results for nine types of short pressure conduit indicate that $(R_e)_k \approx 7\times10^5 \sim 10^6$.

Fig. 4 gives the relation of μ and R_e of Dangjiangkou bottom outlet, including data from 1/36 model and prototype[6]. it can be seen from Fig.4 that model μ varies with R_e and trends to a constant 0.934, when $R_e \approx 6.7\times10^5$, i.e $(R_e)_k \approx 6.7\times10^5$. μ from prototype is approximately constant because of $R_e>10^8$ having mean value of 0.936, very close to that from the model. Meanwhile, the results in Fig.4 is also an important certification of the idea in Fig.3.

3.SIMULATION AND DISCRIMINATION OF CAVITATION FLOW

In Hydraulics division of YRSRI,there is a vacuum tank of 16m long,3.5m high and 0.8m wide with necessary instrument for studing cavitation flow.

Cavitation problems for some projects, such as Lushui, Dangjiangkou, Gezhouba, Geheyan, and Wan'an etc, had been tested in the vacuum tank and in-situ. For model experiment in vacuum tank, atmospheric pressure in it should be reduced by scale except that based on Froude criterion. The identity of cavitation number in model and prototype gives necessary ambient pressure in vacuum tank as follows:

$$p_o = p_v + (P_o - P_v)/L_r \quad (7)$$

where p_o—the necessary ambient pressure in vacuum tank; p_v, P_v—saturated vapour pressure of water in model and prototype, respectively; P_o—atmospheric pressure at dam site; $L_r = L_p/L_m$—model length scale.

Acoustic sounding method is used to detect flow cavitation in model or in-situ. Hydrophones are set near cavitation noise source. Magnetic tape recorder and FFT analysis system are used, herefrom the noise-spectral distribution is obtained.

There are various discriminating criteria to determine whether cavitation occurs in flow by acoustic characteristics. In this paper, only the variation of noise pressure level in noise-spectral distribution curves is adopted. It is considered that the noise pressure level rises (10～20) dB at the very moment when cavitation occured. Our experience shows that this criterion is more accurate than others and has a better reproducibility.

Fig.5, Fig.6 shows the spectral distribution curve of cavitation noise measured from model and prototype at gate region of Gezhouba ship lock gallery, respectively[7][8]. It can be seen from Fig.5 that the noise pressure level rises evidently from background noise when head $H=27$m, 23m, 17m and gate opening $n=0.3$, 0.4. But, there is none when $H=8$m. Although the testing conditions in Fig.6 are not fully corresponding with that in Fig.5, the noise pressure level in Fig.6 also rises evidently when $H=23$m, 17m, 14m and $n=0.2$, 0.4 but none when $H=9$m. All these show that the result in model is in agreement with that in prototype. Besides, the cavitation sound could be heard in prototype during lock operating at $H>14$m and cavitation damage had discovered on gate skin and at gallery top when it was dewatered for inspection[9].

In addition, resemble researches were made with baffle piers in stilling basin of Lushui project which were damaged by cavitation at first, then it was tested in vaccum tank. After seeking out the cause and working out suitable remedying scheme, the stilling basin was reconstructed and had been operated for years without any trouble [10].

CONCLUSIONS

(1) Reynolds number in model under which the discharge coefficient measured from model can be used as that in prototype is $(R_e)_m = (vh/\nu)_m \geqslant 1.5\times10^5$ for spillway, and $(Re)_m = (vD/\nu)_m \geqslant 7\times10^5 \sim 10^6$ for short pressure conduits.

(2) In general, owing to the total resistance in model for discharge gallery of ship lock is not similar to that in prototype, the discharge coefficient measured from prototype is usually greater than that from model. Try to reduce the friction of model boundary is a way to alleviate the scale effect in flow capacity.

(3) Conducting model test in vacuum tank is an effective way to detect cavitation behavior in solving engineering problems.

REFFERENCES

[1] Yangtze River Scientific Research Institute and Research Institute of Songliao Water conservancy committee, Field Hydraulic Investigation Practice, Water Resources and Electric Power Press, 1988.8.

[2] Chengdu University of Science and Technology, Hydraulics, Education Press, 1979.

[3] Xiao Xingbing, Model Tests and Prototype Operation for Spillway of Dangjiangkou Project, YRSRI, 1980.

[4] Deng Tingze, Hydraulic Tests in-Situ for Ship Lock of Gezhouba Project, YRSRI, 1989.9.

[5] Ding Zhuoyi, Scale Effect on Flow Capacity Passing Through Short Pressure Sluiceway, YRSRI, 1989.9.

[6] Xiao Xingbing, Prototype Observation and Model Verifications for Dangjiangkou Project, Journal of High Velocity Flow, NO.1, 1984.

[7] Liu Keihuang, Detection and Discrimination for Cavitation Noise, YRSRI, 1988.8.

[8] Liu Keihuang, Jing Feng, Problems of Cavitation at Tainter Gate Region of Gallery of Ship Lock NO.3 of Gezhouba Project, YRSRI, 1987.

[9] Fu Tongxian, Liu Keihuang, Report on Prototype Observation for Cavitation Noise in Gezhouba ship Lock NO.3, YRSRI and 701 Istitute, 1985.

[10] Chen Jisheng, Yu Jianmin, Studies on Cavitation Problems in Stilling Basin with Baffle Piers. Journal of Yangtze River, NO.3, 1979.

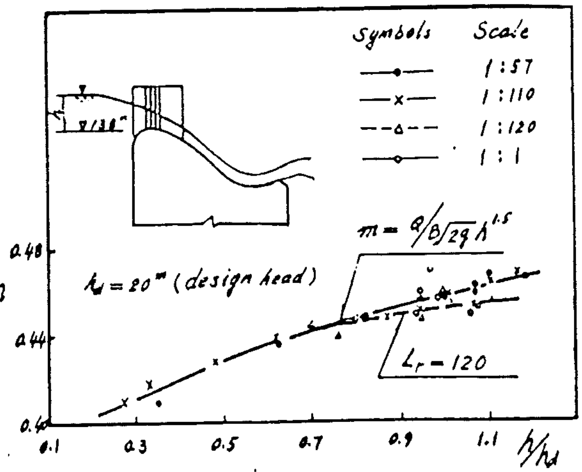

Fig.1 The relation of m and h/h$_d$ [3]

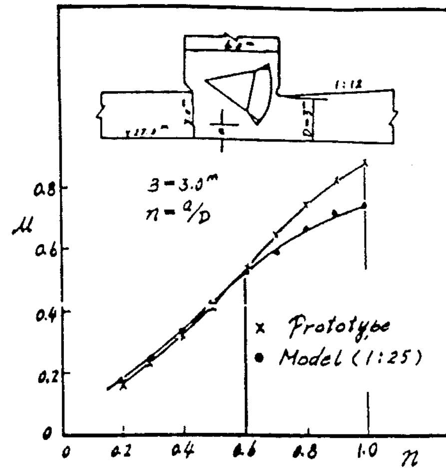

Fig.2 The relation of μ and n [4]

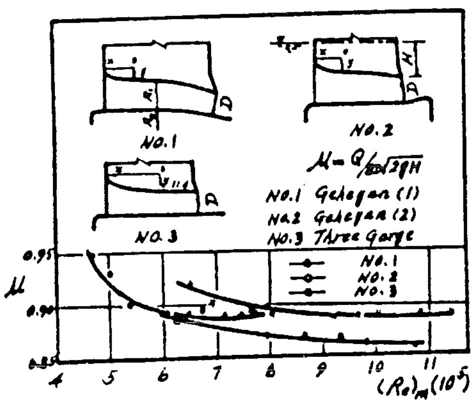

Fig.3 The relation of μ and (Re)$_m$ [5]

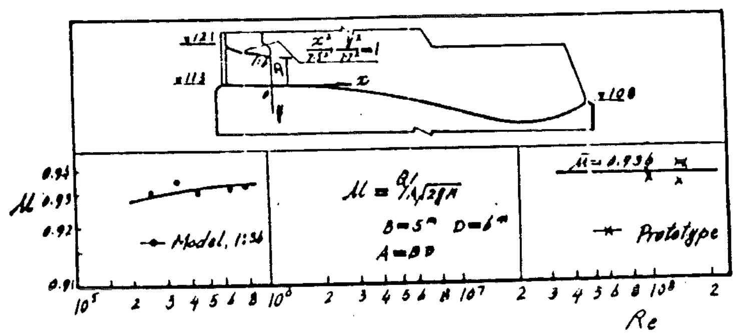

Fig.4 The relation of μ and Re [6]

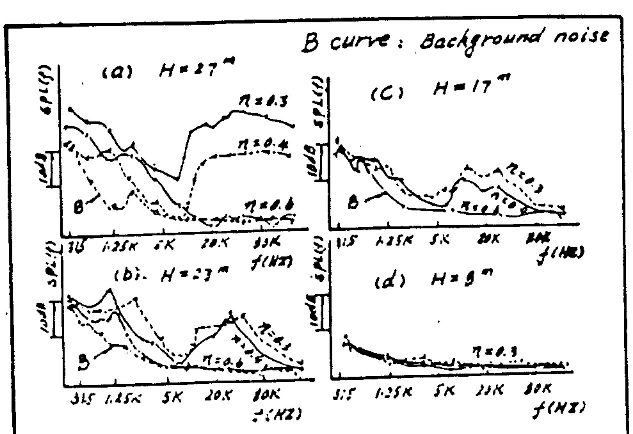

Fig.5 Noise spectrum from model [7]

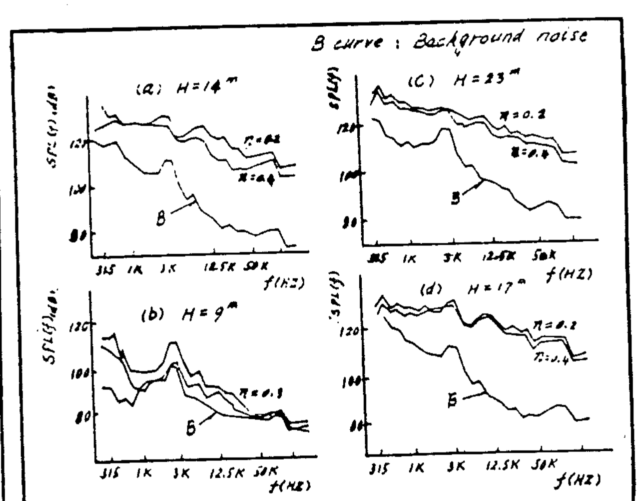

Fig.6 Noise spectrum from prototype [8]

Session 8C

Particle Settling

DYNAMIC BEHAVIOURS OF SAND CLOUD IN WATER

by K. Nakatsuji, M. Tamai and A. Murota
Department of Civil Engineering, Osaka University
Suita City, Osaka 565, Japan

Abstract

The behaviour of sand cloud in water released from bottom-dump barges and the resultant deposition pattern are examined experimentally. The sand cloud is found to be like heavy thermals produced in a fluid by buoyancy force according to the particle size and volume of sand. The experimental results are discussed on the basis of the thermal theory and the governing equation of the falling motion of discrete particles suspended in water.

Introduction

In Japan, large-scale land-fill operations and plans have recently increased in urban coastal areas. It is proved by experience in the reclamation such as Kobe Port Island and New Kansai International Airport to be true that the bottom-dump barges capable of loading 7500 m^3 and more are economically salutary for transporting a large amount of sand and soil.

There are, however, various technological and environmental problems relevant to such reclamation projects. The preliminary problem to be solved is the dynamic behaviours of sand cloud released from the barges in water. Its dynamics may be intimately related with deposition patterns and impulse pressure on the sea bed, and dispersion of fine sediments and turbidity. Similar phenomena were reported on the convection of isolated masses of buoyant fluid in a water tank by Scorer(1957) et al.. Measurements of Mutoh et al.(1974) have shown the interesting fact that the deposition pattern of sand released from the bottom-dump barge model changes from a triangle to a double-peaked shape, and to a trapozoid with an increase in water depth.

The purpose of this research is to show how ideas may be used to investigate the dynamics of sand cloud in water, and in particular to explain the mechanism which produces the difference in deposition pattern on the sea bed. Buoyancy is understood to be its fundamental effect.

Experiment I - Falling Behaviour

For simplicity in the experiment, glass beads were stored into a bottom-dump barge model placed at the top of a 130cm high, 90cm wide and 15cm deep tank of water. The lid of a 5cm wide and 15cm deep barge model was quickly inverted by hand, allowing the glass beads to drop down from rest through the water. Their growth was observed photographically. The mean diameter of glass beads, d_{50}, was 0.8, 1.3, 3.0 and 5.0 mm; and the corresponding Reynolds number were 90, 180, 1040 and 2320 respectively. The Reynolds number can be from the falling velocity U_d and the particle diameter d_{50}. The volume at release is so sufficiently small compared with its subsequent volume that the subsequent growth is expected to be independent of the initial configuration of

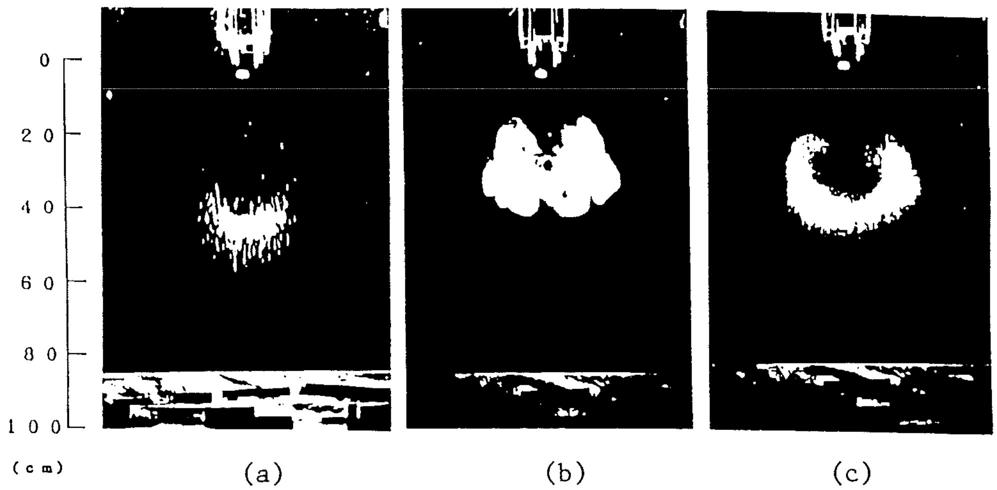

(a) (b) (c)

Fig. 1 Typical pattern of falling motion of bead cloud taken a photograph at 1.2 second after release. Exposure time is 1/125 second. (a) settling of discrete particles (d_{50}=5mm, Q_o=75cm^3); (b) thermal with buoyancy force (d_{50}=1.3mm, Q_o=300cm^3); and (c) intermediate motion (d_{50}=3.0mm, Q_o=300cm^3).

glass beads. The volume Q_o was set to be 75, 150 and 300 cm^3.

Figure 1 shows a typical pattern of falling motion of glass beads released in water. Figure 1(a) is a case of a small quantity of relatively larger size of glass beads. Their behaviours seem to be dominated by the falling motion of discrete particles. The glass beads independently settle while spreading the width of bead cloud with small irregular motion. No mutual interference between them can be recognized. The larger the size of particle is, the faster the particle drops down. Hence, the separation of glass beads takes place in the falling process.

Figure 1(b) is a case of a large quantity of smaller size of glass beads. It shows a mashroom cloud of isolated mass. A pair of circulation occurs inside the isolated cloud to produce the entrainment of an exterior fluid at the rear and mixing with the fluid takes place. As a result, the isolated cloud makes up a solid-fluid two-phase lump. It continuously grows with a downward distance while keeping similar in shape. Such a behaviour is similar to turbulent thermal, which can be observed in a warm air rising in the atmosphere or a heavier fluid descending in coastal waters. Following the resemblance, the growing cloud in Fig. 1(b) is called 'thermal-like motion' herein.

The third pattern as shown in Fig. 1(c) is a transitionary state from thermal-like motion to settling motion of discrete glass beads. Just after release symmetrical circulations distinctly appear so as to allow the isolated cloud to grow in the lateral and vertical directions. As a downward distance increases, the gravitation has direct effects upon each constituent of the cloud, namely a glass bead.

Figure 2 shows the variation of falling velocity of the bead cloud normalized by the settling velocity of its constituent as a function of a distance from the release point normalized by the volume flux per unit depth, $\sqrt{q_o}$. In case of relatively larger sizes of d_{50} = 5.0mm, the falling velocity of the cloud is almost the same as the settling velocity, U_d. On the other hand, the case of d_{50} = 0.8mm indicates the peculiar transition that just after release the fluid accerelates to the maximum velocity at $x/\sqrt{q_o} \cong 5$ and deceleration begins. It is worthy

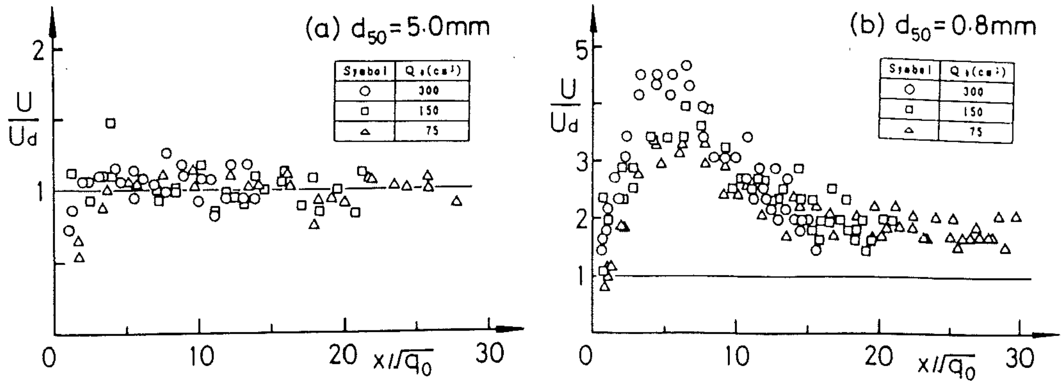

Fig. 2 Variation of falling velocity of cloud normalized by settling velocity of its constituent against downward distance: (a) settling; and (b) thermal corresponding to Fig. 1.

noting that the maximum falling velocity attains to three to five times as much as the settling velocity. It suggests that the falling motion of smaller particles as demonstrated in Fig. 1(b) could be dominated by the quite different physical mechanism from the settling motion of discrete beads.

Application of Thermal Theory to Falling Behaviour

Assuming that the suspended solid particle functions as an increase of density in the fluid, the vertical momentum of released mass is expected to so steadily increase through action of buoyancy force that a heavy thermal appers. Bains and Hopfinger(1984) has already extended a two-dimensional thermal theory for the heavy thermal with large density difference. The outline is as follows:

For simplicity it is assumed that the thermal is an ellipse of its width and height, W and H. The rates of change of mass and momentum via entrainment are given by

$$\frac{dm}{dt}=\alpha M\left(\frac{\rho_a}{m}\right)^{1/2} \tag{1}$$

$$\frac{d}{dt}(M+M_v)=\beta WH\Delta\rho g \tag{2}$$

where $m = \rho\beta WH$, $M = \rho\beta WHU$ and $M_v = k_v\rho_a/\rho\ M$ represent the mass of the thermal, the momentum of the fluid of the thermal and the momentum of the fluid comprising the added mass of the thermal, ρ and ρ_a are the interior and exterior densities, α is an entrainment coefficient, $\beta = \pi/4$ is a shape factor, and $K = W/H$.

After conversion of the variable of integration from time to distance from release point using $U = dx/dt$, the integrated form of Eq.(1) is as follows.

$$W=\frac{2\alpha}{\sqrt{\pi}}\sqrt{K}\left(1-\frac{\pi}{4\alpha^2}\frac{\Delta\rho_0}{\rho_a}\frac{W_0^2}{x_*^2}\right)x_* \tag{3}$$

where $x_* = x + (\pi/2\alpha)\cdot(\rho/\rho_a)^{1/2}W_o$, $\Delta\rho = \rho - \rho_a$ and the suffix 'o' indicates the origin: x = 0.

The above equation shows that the thermal grows linearly in shape with a downward distance. This is consistent with the experimantal result shown in Fig. 1(b).

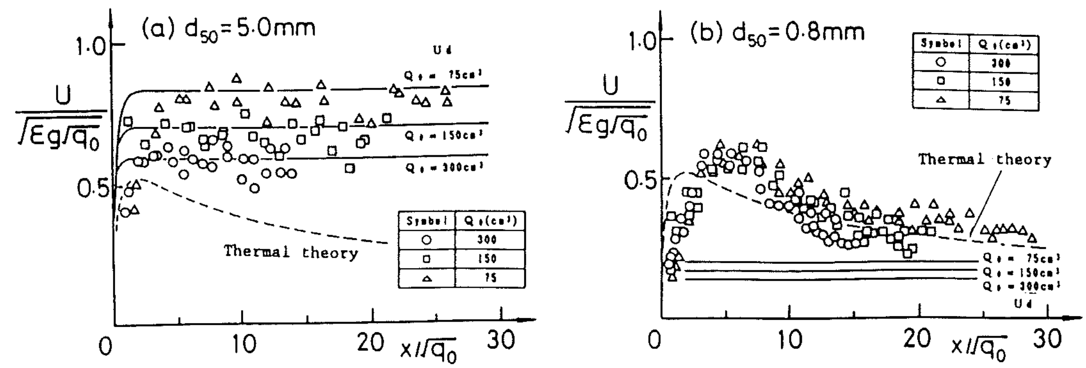

Fig. 3 Variation of falling velocity of cloud normalized by characteristic velocity scale against downward distance: (a) settling; and (b) thermal corresponding to Figs. 1 and 2.

In the similar way, the thermal velocity can be derived from Eq.(2) where $U_o = 0$ at $x_* = 0$.

$$U^2 = \frac{2B}{3}\left\{x_* \frac{x_*^2 - 3A}{(x_* - A)^2} - x_0 \frac{x_0^2 - 3A}{(x_*^2 - A)^2}\right\} \tag{4}$$

where

$$A = \frac{k_v}{(1+k_v)\alpha^2 K}\left(\frac{\Delta\rho_0}{\rho_a}\right)Q_0, \qquad B = \frac{g}{(1+k_v)\alpha^2 K}\left(\frac{\rho_0}{\rho_a}\right)Q_0$$

Figure 3 presents the comparison of the thermal theory with the measurements for the falling velocity of released cloud corresponding to Figs. 1 and 2. In this figure the falling velocity is normalized by the characteristic velocity scale based on buoyancy flux $\sqrt{\varepsilon g\sqrt{q_o}} = \sqrt{\Delta\rho/\rho \cdot g\sqrt{q_o}}$. The dotted line indicates the thermal theory obtained using $\alpha = 0.4$, $K = 1.3$ and $k_v = 1.0$, whose values are determined based on experimental data. The solid lines indicate the settling velocity of glass bead for each experiment, U_d. As is evident from the figure, the falling velocity in the case of d_{50} = 0.8mm agrees precisely with that obtained by the thermal theory. That is, the released cloud tends to initially accerelate through action of buoyancy force but after travelling to $x/\sqrt{q_o} = 6$ to decrease to the settling velocity, U_d. Such a tendency and the consistency with the thermal theory are also recognized in the case of d_{50} = 1.3mm. In the case of d_{50} = 5mm, however, the experimental data show to be larger than the thermal velocity and almost equal to the settling velocity.

Judging from these results, the falling pattern of the cloud depends on whether the thermal velocity accounting for the buoyancy flux exceeds the settling velocity of each bead particle or not.

Experiment II - Deposition Pattern

Another experiments were performed using sand to determine the falling motion and the resultant deposition pattern on the bed. Since a horizontal flow along the bed becomes predominant after impinging, in particular, in transporting fine sediments, it is necessary to use a broad flume. Hence, sand was released in a flume of 50cm high, 600cm wide and 15cm deep in the similar manner as Experiment I. The mean diameter of sand was 3.4mm and the Reynolds number was 895. In this series, the volume flux of sand released, Q_o varied from 75 - 300 cm^3. and the height of released point from the bed, D from 5 - 30 cm.

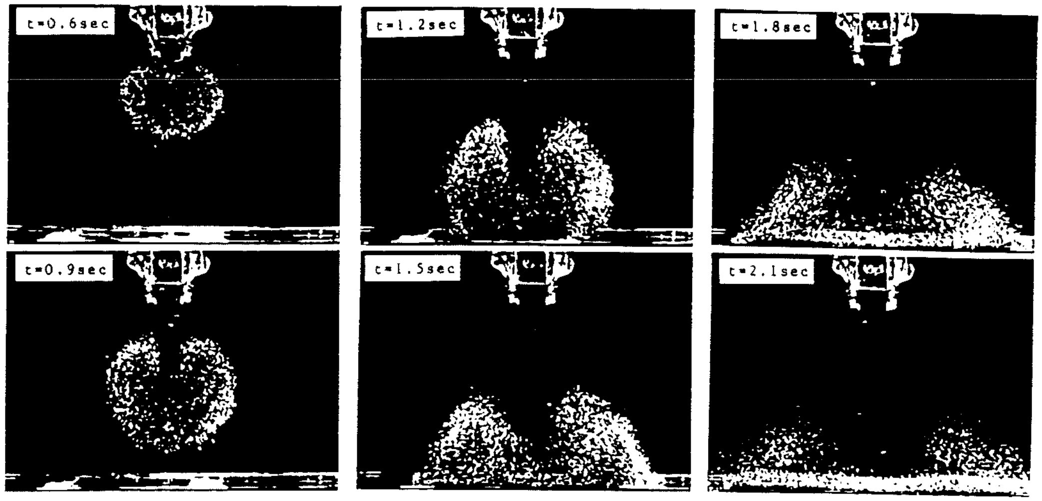

Fig. 4 Series of pictures illustrating growth of sand cloud in water flume and resultant deposition pattern in case of d_{50} = 3.38mm, Q_o = 300cm^3 and released height from bed, D = 30cm.

Figure 4 demonstrates an example of series of pictures taken from a cine-film every 0.3 second showing the growth of sand cloud in water. It is a case of a relatively large volume of sand. The sand cloud drops with accelerating just after release. The width and height of cloud increase with a downward distance. At 0.9 second after release, a pair of counter-rotating circulation manifests itself inside the sand cloud. It can be seen that the cloud entrains an exterior fluid at the rear. When impinging on the bed, the sand cloud is torn away to two symmetrical parts. The induced flow causes fine sediments contained in the sand to sweep along the bed and to form a double-peaked deposition pattern. Such a thermal-like motion does not always occur in all the experiments.

Figure 5 shows the deposition pattern as a function of the volume flux, Q_o and the height of released point, D. It can be easily divided into two catagories. In cases of large volume of Q_o = 300cm^3, a double-peaked pattern appears prominently except for that of D = 5cm. In cases of Q_o = 150cm^3 the deposition pattern changes from a double-peaked shape to a trapozoid with an increase in D. And, in cases of Q_o = 75cm^3 all the patterns show to be a trapozoid. These are in agreement with the

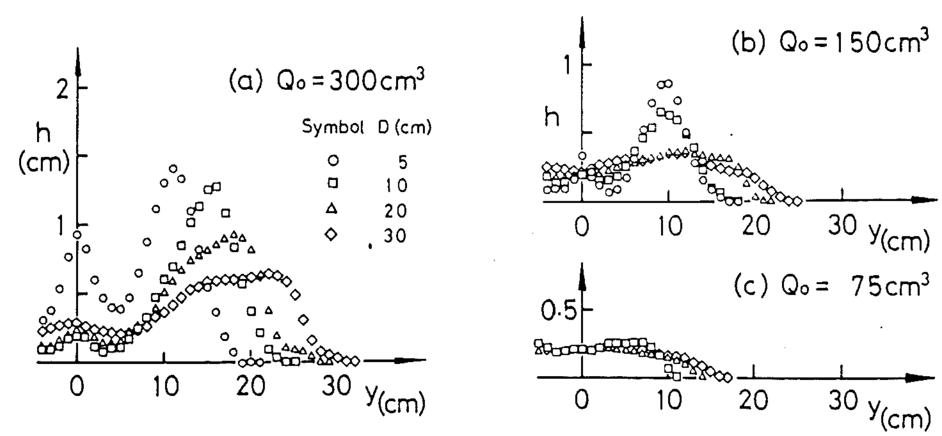

Fig. 5 Deposition pattern of sand cloud as a function of Q_o and D.

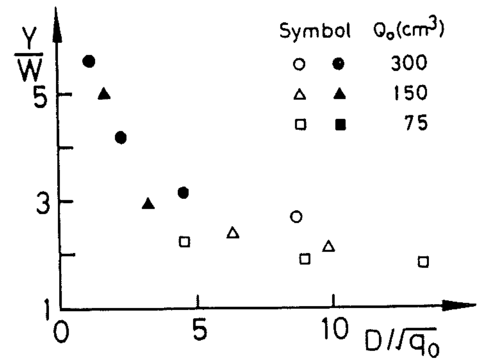

Fig. 6 Variation of ratio of deposition width to sand cloud width against height.

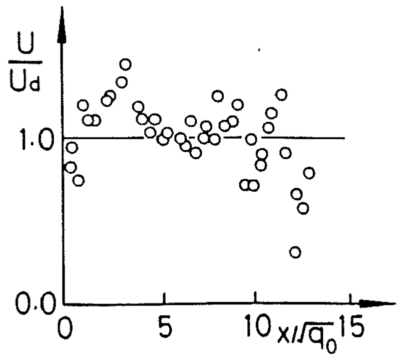

Fig. 7 Variation of falling velocity of sand cloud normalized by settling velocity against distance.

experiment of Mutoh et al.(1974).

Then, the ratio of the width of deposition pattern to the width of the sand cloud in falling motion at the height equivalent to D, Y/W, is plotted against the normalized height of released point from the bed, $D/\sqrt{q_0}$ in Fig. 6. The cloud width, W was measured using sand of d_{50} = 3.38mm and the water tank of Experiment I in the same manner as Experiment I. Open and closed symbols indicate a trapozoid and a double-peaked pattern, respectively. The discrimination of the deposition pattern is judged depending on whether the ratio of height at the peak to that at the mass centerline exceeds 3.0 or not. It is clear from the figure that the ratio of Y/W decreases with increasing D and with decreasing Q_0 and that its ratio drastically changes at $D/\sqrt{q_0}$ = 4.5.

As is obvious from Fig. 7 showing the variation of the falling velocity of sand cloud normalized by the settling velocity, the falling behaviour of sand cloud changes from thermal-like motion to settling motion of discrete particls at $x/\sqrt{q_0} \fallingdotseq 4.5$ as above mentioned. It indicates that the effects of falling motion of sand cloud appears clearly on the deposition pattern on the bed.

Conclusion

The behaviour of sand cloud released from bottom-dump barges is examined experimentally in relation to land reclamation works. The sand cloud is found to be described by the hydrodynamically same equation of thermal phenomena according to the particle size and volume of sand released. The knowledge of thermals enable us to reasonably understand the hitherto indicated difference in deposition pattern of sand on the bed.

References

Bains, W.D. and Hopfinger, E.J.(1984): Thermal with large density difference, Atmosphere Environment, Vol.18, No.6, pp.1051-1057.

Mutoh, S., Yoshii, S. and Ishida, T.(1974): Sand heap undulation on the sea bed by the bottom-dump barge for large-scale land reclamation, Tecnol. Rept., Mitsubishi Heavy Industry, Vol.11, No.1, pp.92-104.

Scorer, R.S.(1957): Experiments on convection of isolated masses of buoyant fluid, J. Fluid Mech., Vol.2, pp.583-594.

SOLIDS SUSPENSION IN SIDE ENTERING MIXING TANK - EXPERIMENTAL RESULTS

by Hanna Gladki, PH.D., IAHR, AICHE Member
ITT Flygt Corporation, Norwalk, CT USA

Abstract

The side entering three-blade propeller mixer was considered to agitate solid-liquid mixture in limited circular tank conditions. Experimental data are provided for solids in complete suspension and critical hydraulic conditions were established.

Introduction

Solids suspension studies were run by many authors, mainly for top entering mixers. Generally, side entering mixers have not been investigated as solid liquid agitators. In this case, actual jet velocity from propeller is transferring hydrodynamic power to confined water volume, and imposing circular horizontal flow in tank. Our goal is to answer the question of how much specific energy is needed for complete suspension of tested slurry, with different concentrations. The tested slurry has been solid particles in water up to 6% volume. Following particle fluid properties were considered: particle liquid density difference, fluid viscosity, particle size, and still fluid terminal velocity and concentration. Tank geometry has been described by its hydraulic radius.

Power provided to induce a motion in the tank can be expressed as:

$$P \propto T v_j$$

the product of thrust and jet velocity. When the thrust is:

$$T = \tau_o S_p \quad \text{and} \quad v_j = ND$$

Hence, specific energy can be express as:

$$\varepsilon = \frac{P}{\rho V} = \frac{\tau_o}{\rho} \frac{S_p}{V} ND$$

then:

$$\varepsilon = \frac{\tau_o}{\rho} \frac{D}{R} N \qquad (1)$$

Complete suspension exists when all particles are in motion and no particle remains on tank bottom for more than two seconds. To achieve this condition, minimum shear stress τ_o and specific energy ε is required.

A particle lifted from the bottom of the vessel has a tendency to return there due to excess of gravity over buoyancy, or so-called downward drag forces:

$$D_r = 1/2\, \rho\, C_D A\, v_t^2$$

which cause a particle to fall. To offset the downward particle drag force in mixing tank, one has to incur relative forces created by turbulence, which can be expressed in two-dimensional flow as local sheer stress τ

$$\tau = \rho \overline{v'u'}$$

To balance the drag forces and keep particles in suspension, one can employ τ, hence:

$$\tfrac{1}{2} \rho C_D A v_t^2 \propto g C_T \tau A$$

assuming that local $\tau = \tau_o$ and

when $$\tau_o / \rho = v_*^2$$

then $$v_t / v_x \propto \sqrt{g \frac{C_T}{C_D}} \qquad (2)$$

The turbulence coeeficient C_T has been unknown as well as the ratio C_T/C_D, but after Simons, et al it is known that v_x/v_t, as the Reynolds number function for dynamic velocity shows a critical relationship between motion and no movement conditions. Laursen used v_x/v_t as the parameter responsible for mean concentraction in the channel cross section. According to Graf, it "expresses the effectiveness of the mixing action of the turbulence". Fundamental work for channel flow has been done by Rouse and Vanoni and later by others, and shows the increasing vertical distribution of the relative concentration when v_t/v_x is decreasing to zero. In the mixing tank, v_t/v_x is the critical ratio for complete suspension and is related to the slurry properties as:

$$v_t, \; \rho, \; \Delta\rho_s, \; d_p, \; \mu, \; C_W$$

or dynamic forces in the tank described by the Kolmogoroff scale λ_K, and the tank geometry described by its hydraulic radius, R. Using the Buckingham theorem, a relationship can be written in π terms in general form:

$$F\left(\frac{v_*}{v_t}, \frac{\mu}{v_t d_p \rho}, \frac{\lambda_K}{d_p}, \frac{\Delta\rho_s}{\rho}, C_W, \frac{R}{d_p} \right)$$

The test has been allowed to find relation between dimensionless numbers.

Experimental

Experiments were carried out in cylindrical glass vessels with flat bottoms. The depth of fluid to diameter ratio during experiment varies from 0.41 to 1.

Agitation was provided by 3 blades side entering propeller driven by 0.3KW motor with variable speed control within range 50 to 3000 RPM. The power input to the impeller was determined by measured torque.

Complete off-bottom suspension, so called "one-second-criterion" was based on the visual observation in a well-illuminated transparent tank. At complete suspension there was a decrease in concentration with tank height but a clear liquid zone was not observed at the top.

Water and glass beads and plastic beads were used as slurry in the test.

To estimate free settling velocity in the still fluid, McCabe and Smith method was used. They have proposed a convenient criterion for the estimation of the terminal velocity in the still fluid .

Results and Discussion

In the present study 18 runs were done for three different particle diameters and for two different densities. The highest concentration per weight C_w for presented test is 5.7%.

Kolmogoroff microscale of turbulence λ_K does not vary very much for test for the same density solids and is from 0.019 to 0.030mm for solids of specific gravity 1.5. Value λ_K is higher and ranges from 0.037 to 0.051mm for particles of specific gravity 0.03. The results show that λ_K is related to the density and diameter of beads as well as to slurry concentration. Fig. 1 shows three relations between v_t / v_* and d_p/λ_K for three different particle diameters. One inclined line shows this relation for one diameter and one specific gravity but for different concentrations. The higher the concentration the smaller v_t/v_* value. The general equation of lines in Fig. 1 in terms of d_p/λ_K and v_t/v_* can be written as:

$$v_t/v_* = a\left(d_p/\lambda_K\right)^b$$

The slope of the inclined lines can be determined graphically as tangent of an angle, hence $b = -1.3$. Defined factor a is shown in Fig. 1 above each line.

Factor a was plotted against dimensionless hydraulic radius (Fig. 2). The points in Fig. 2 indicate the influence of relative radius on the microscale of turbulence for complete suspension.

The tested slurry regarding its diameters , settling velocity as well as concentration belong to the coarse solids with Reynolds number in the transition zone. The increase of concentration requires larger energy which should contain turbulence scale λ_K that is responsible for keeping the particles in suspension. In this case critical energy necessary in the vessel is expressed as shear velocity v_* .

Terminal velocity to shear velocity ratio v_t/v_* was plotted against concentration by weight in Fig. 3. From the presented results it may be concluded that velocity ratio v_t/v_* decreases when concentration increases. The results indicate Reynolds number for settling velocity impacts on the velocity ratio v_t/v_*. This ratio is complex function of particle properties and the intensity of fluid energy in the tank. If the terminal velocity v_t is expressed in general as:

$$v_t \propto \left(g\, d_p \frac{\Delta\rho_s}{\rho\, C_D}\right)^{1/2} \qquad \text{and} \qquad v_* \propto \left(\frac{\tau_o}{\rho}\right)^{1/2}$$

then

$$v_t/v_* \propto \left(g\, d_p\, \Delta\rho_s/\tau_o C_D\right)^{1/2} \tag{3}$$

Relation (3) explains behaviour of the suspended particles in Fig. 3. The smaller the drag coefficient C_D and the higher the Reynolds number then the higher is the v_t/v_* ratio. Upper relation in Fig. 3 has higher Reynolds number than the lower. In the relation (when the drag coefficient is excluded) expression $g\, d_p \Delta\rho_s/\tau_o$ is so-called Shields parameter for incipient motion. For the tested range with concentration less than 10% and for Reynolds number Re_{v_t} in intermediate zone, Shields parameter is in close relation with concentration (Fig. 4). Hence, it can be concluded that critical Shields parameter can describe complete off-bottom suspension in the vessel in the most general way.

The test results prove the critical value of the velocity ratio v_t/v_{*CR} for complete suspension is related in general form to:

$$v_t/v_{*CR} = B\left(d_p/\lambda_K\right)^x \left(Re_{v_t}\right)^y \left(C_W\right)^z \left(R/d_p\right)^w \left(\Delta\rho_s/\rho\right)^u \tag{4}$$

The term of the shear velocity represents a measure of intensity of turbulent fluctuation and can be easily related to the shear stress. The shear stress expressed in dimensionless way was reported by Shields (1936) as criterion for incipient motion and is an excellent criterion for complete suspension for tested range for experimental data.

NOTATION

A	- Surface area of falling particle;
C_D	- Drag force coefficient;
C_T	- Turbulence coefficient;
C_W	- Weight concentration of solid phase;
D	- Mixed diameter;
d_p	- Diameter of particle;
N	- Speed of mixer;
R_{evt}	- Reynolds number for settling velocity;
S_p	- Wetted surface area of the tank;
T	- Thrust force;
V	- Tank volume;
vj_1	- Jet velocity from mixer;
v_t	- Terminal settling velocity;
v_x	- Dynamic (shear) velocity.

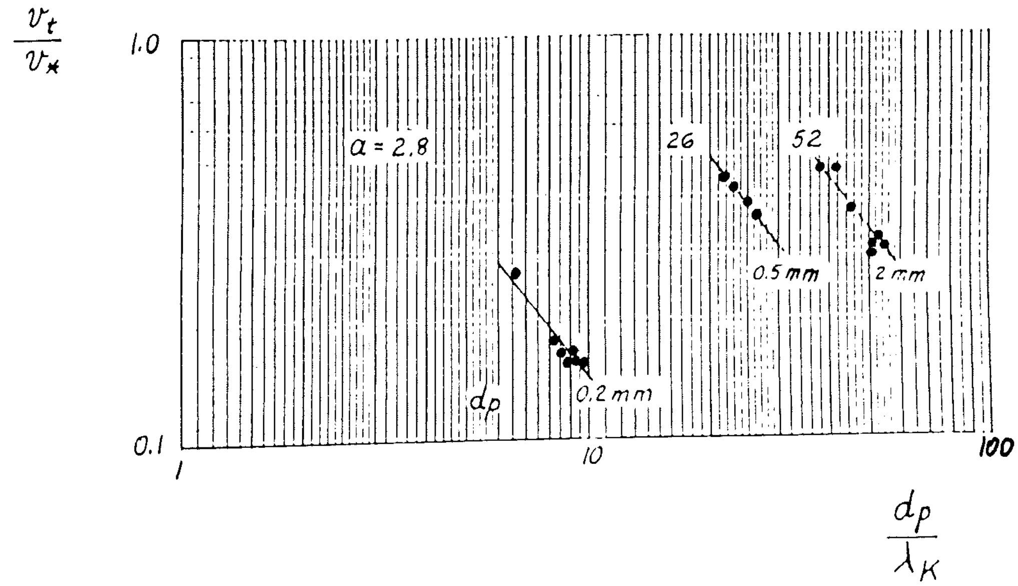

Fig. 1 Tested Relationship between Velocity Ratio v_t/v_* and Solids Diameter Ratio to Kolmogoroff Microscale d_p/λ_K

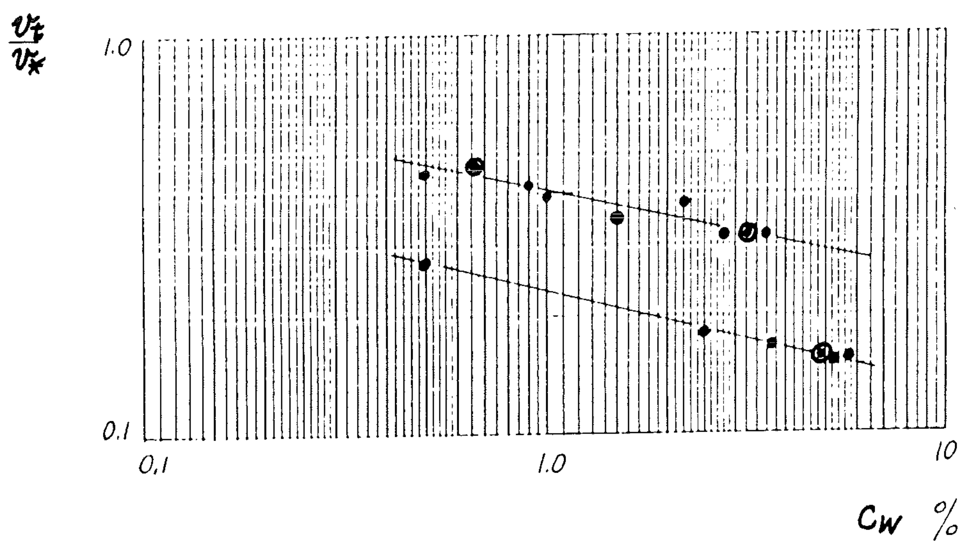

Fig. 3 Relationship between Velocity Ratio and Concentration c_w for Two Different Reynolds Numbers for Settling Velocity.

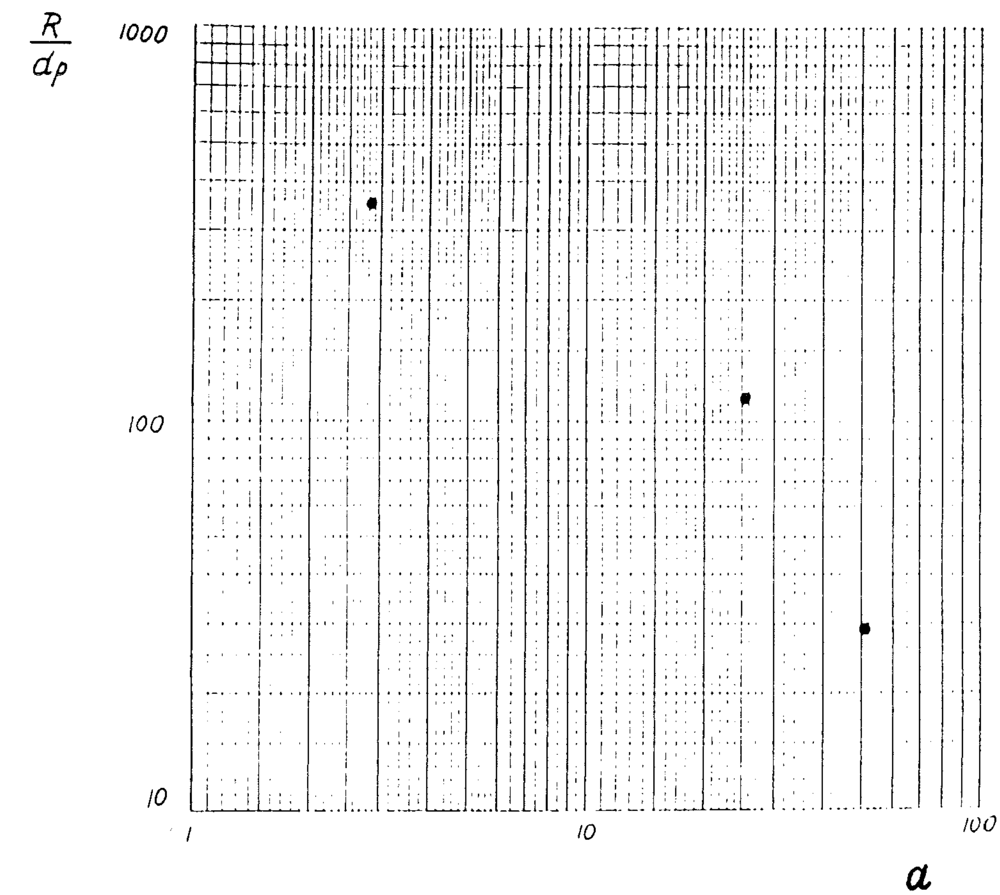

Fig. 2 Effect of Relative Hydraulic Radius on Factor a.

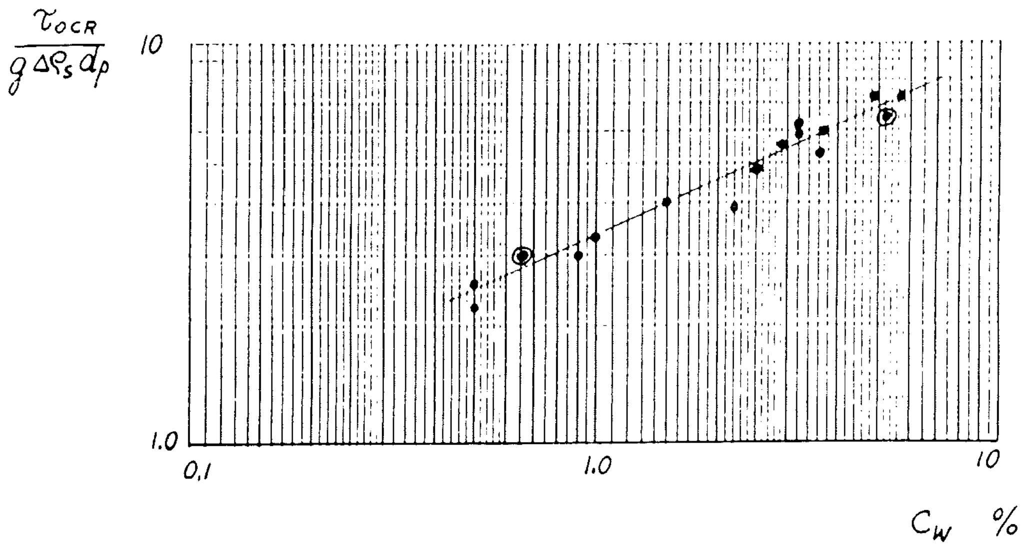

Fig. 4 Shields Parameter as a Function of Concentration by Weight for Complete Suspension.

PHYSICAL AND MATHEMATICAL MODEL COMPARISONS FOR WINDERMERE BASIN

by

I.K. Tsanis[1], M. Blaisdell[1], Y. Krestenitis[3], V.H. Chu[2] and P. Engel[4]

[1] Department of Civil Engineering, McMaster University, Hamilton, Ontario, Canada
[2] Department of Civil Engineering, McGill University, Montreal, Quebec, Canada
[3] Department of Civil Engineering, Aristotle University, Thessaloniki, Greece
[4] National Water Research Institute, Burlington, Ontario, Canada

Abstract

A two-dimensional depth-averaged model is used to simulate the hydraulic circulation in a distorted model of Windermere basin. The results from this model are compared with the experimental results. In the distorted model the bed friction influence is underestimated with respect to the convective influence resulting in overprediction of the size of the recirculation regions.

Introduction

The Windermere basin lies at the south east corner of Hamilton Harbour, Ontario, Canada. The inflow consists primarily of runoff from the Red Hill Creek watershed and outflow from the Hamilton sewage plant. Mean daily flows are about 3.5 m^3/s and the 100 year average storm flow is about 64 m^3/s. The flows from the basin pass into Hamilton Harbour through a constriction spanned by a small railway bridge. A cleanup of the Windermere Basin is to be undertaken, accompanied by dredging a portion of the basin, The dredged material, containing toxic substances, will be stored in a confined area behind impermeable berms, within the perimeter of the present basin, effectively creating a new but smaller basin. A physical model study was conducted to study the flow patterns of the proposed basin design, and a mathematical model was used for verification.

Physical Basin Model

The physical model was designed as a fixed bed model. Available floor space and accuracy of measuring water depths, dictated a horizontal scale ratio of 1:60 and a vertical scale ratio of 1:15 resulting in a model with a 4:1 distortion. As a result the model was restricted to simulating prototype flows greater than about 17 m^3/s in order to ensure that viscous scale effects were minimized.

The model was constructed inside a water tight enclosure consisting of concrete blocks built on the laboratory floor. Standard procedures, using plywood templates, sand and mortar, were used to construct the model bed.

The surface was then spray-painted with a light blue latex paint to provide a good background for overhead photographs and video tape recordings. A 1m x 1m black grid was painted on the model bed to facilitate the determination of flow velocities and rates of change of flow patterns. The berms were built of wood framing covered with sheet metal which was then covered with coarse sand or gravel to simulate the design rip rap. The railway bridge at the basin outlet was built from plywood, with particular attention being paid to the proportioning of the piers and abutments to ensure proper development of local flow patterns.

The depth in the model was 175 mm with a central trap of 350 mm. According to Froudian similitude, the flow rate was 11.4 l/s representing a prototype flow of 40 m^3/s. The discharge was measured to an accuracy of about 2% with a 90^o V notch weir in a headbox upstream of the model basin. All water levels were measured using stilling wells fitted with Mitutoyo point gauges, having a resolution of 0.05 mm. The gauges were set to a common reference level, equivalent to the prototype project datum of 74.0 m chart datum. Flow patterns were visualized by using Potassium Permangenate. In addition to the dye, 22 weighted ping-pong balls were released at the entrance of the basin at various times as an additional aid to visualize flow paths and to calculate the surface velocities in the model basin. The model is given in Figure 1, where the vectors drawn indicate the magnitude in cm/s and direction of the velocities in different locations in the basin.

Mathematical Basin Model

A two-dimensional horizontal (large width to depth ratio) flow model is used to simulate the hydraulic circulation in the Windermere Basin Model. The equations of motion in the x and y directions and mass continuity are simplified under the assumptions (a) the water is incompressible and homogeneous, (b) Coriolis forces are negligible for the size of the Model Basin (c) the flow is quasi-hydrostatic. The resulting equations are given as

$$\frac{\partial U}{\partial t} + U\frac{\partial U}{\partial x} + V\frac{\partial U}{\partial y} = - g\frac{\partial \zeta}{\partial x} - \frac{C_b}{H} U\sqrt{U^2+V^2} \qquad (1)$$

$$\frac{\partial V}{\partial t} + U\frac{\partial V}{\partial x} + V\frac{\partial V}{\partial y} = - g\frac{\partial \zeta}{\partial y} - \frac{C_b}{H} V\sqrt{U^2+V^2} \qquad (2)$$

$$\frac{\partial}{\partial x}(UH) + \frac{\partial}{\partial y}(VH) + \frac{\partial \zeta}{\partial t} = q \qquad (3)$$

where U and V are the depth-averaged velocities, g is the acceleration due to gravity, ζ is the free surface elevation relative to the still water level h, H is the total water depth, q(x,y,t) ($[q]=L^3/L^2/T$) is the specific discharge of a source or a sink and C_b is a dimensionless bed friction coefficient defined as

$$C_b = \frac{n^2 g}{H^{1/3}} \qquad (4)$$

where n is the Manning's coefficient. A smoothing factor t_h in the form

$$t_h = 1 - 4 \frac{\nu_h \Delta t}{(\Delta x)^2} \tag{5}$$

is used in the calculation of the time derivative of the velocities U and V in a horizontal rectangular grid with mesh size Δx (Krestenitis, 1988) where Δt is the time step of the calculation and ν_h is the numerical horizontal eddy viscosity. The system of equations (1) to (3) are solved numerically using an explicit finite difference scheme (Koutitas, 1988).

Using an inflow $Q = 0.0114\ m^3/s$ and a Manning's coefficient n=0.011 in the distorted model of Windermere basin, equations (1) to (5) are solved for a space step of Δx=0.20 m, a time step of Δt=0.04 sec and a value of smoothing factor t_h=0.995 (ν_h=0.00125 m^2/s). The resulting hydraulic circulation of the above simulation is shown in Fig. 2. The magnitude and the direction of the velocity vectors and the size of the recirculation zones are similar to those determined experimentally.

Discussion

Froudian models have been used for some years to study the dispersion of waste by Lagrangian techniques. Laboratory space limitations dictate the use of vertically distorted physical models that alter the characteristics of turbulent mixing and advection of pollutants. This results in model behavior which varies from the prototype behavior depending on the distortion used. For example failure to maintain the jet characteristics, i.e., Reynolds number ($R_j=U_j h/\nu$, U_j is the jet velocity), while retaining the same jet Froude number ($Fr_j=U_j/\sqrt{g\,h}$) leads to a different hydrodynamic pattern in the basin. The resulting velocity pattern in the basin based on the 1:1 undistorted model given in Fig. 3 is different than the one of Fig. 2. The advection of the distorted model is larger, resulting in smaller spreading of the inflow jet, which is consistent with the results of Roberts and Street, 1982. Table 1 shows the different parameters for the three numerical model applications and their corresponding Peclet numbers ($Pe_j=U_j\Delta x/\nu_h$). By equating the horizontal turbulent Peclet number in the 1:1 model and the prototype the mathematical model was able to predict the circulation in the prototype basin. Comparison between the velocity patterns in the prototype basin (shown in Fig. 4) and the 1:1 model reveal good agreement. The validity of this assumption will be tested by field studies in the prototype after construction of the Windermere basin is complete.

Conclusions

A distorted physical model was used to study the circulation and flow patterns of the Windermere basin and compared with results from a two-dimensional horizontal flow model. The mathematical model was successfully used to predict the hydrodynamic pattern of a distorted model of the Windermere basin. The distorted model overpredicts the size of the recirculation regions by reducing the spreading of the inflow jet due to imbalance of bed friction influence versus convective influence.

References

Koutitas, C. 1988. Mathematical Models in Coastal Engineering, Pentech Press, London.

Krestenitis, Y.N., 1988. Numerical Study of the Wind-induced circulation and examination of the open-sea boundary conditions. Case study of Thermaikos Gulf. Tech. Chron. - A, Greece, Vol. 8, No. 4.

B.R. Roberts and R.L. Street. 1982. Mixing in Surface Jets Under Distorted Conditions, Proceedings of the Conference Applying Research to Hydraulic Practice, ASCE, pp. 206-215.

TABLE 1

	4:1	**1:1**	**Prototype**
Inflow Q (m^3/s)	0.011400	0.001425	39.7368
Inlet Depth h (m)	0.1750	0.04375	2.6250
Inlet Velocity U_j (m/s)	0.0814	0.0407	0.3154
Manning's n	0.0115	0.0045	0.0090
Length Scale L (m)	10	10	600
Time Scale $\tau = L/U_j$ (sec)	123	246	1902
Space Step Δx (m)	0.20	0.20	12.00
Time Step Δt (sec)	0.04	0.04	0.3097
Smoothing Factor t_h	0.995	0.995	0.995
Eddy Viscosity ν_h (m^2/s)	0.00125	0.00125	0.5812
Inlet Froude Number Fr_j	6.21×10^{-2}	6.21×10^{-2}	6.21×10^{-2}
Inlet Reynolds Number R_j	1.415×10^4	1.768×10^3	8.222×10^5
Inlet Peclet Number Pe_j	13.024	6.512	6.512

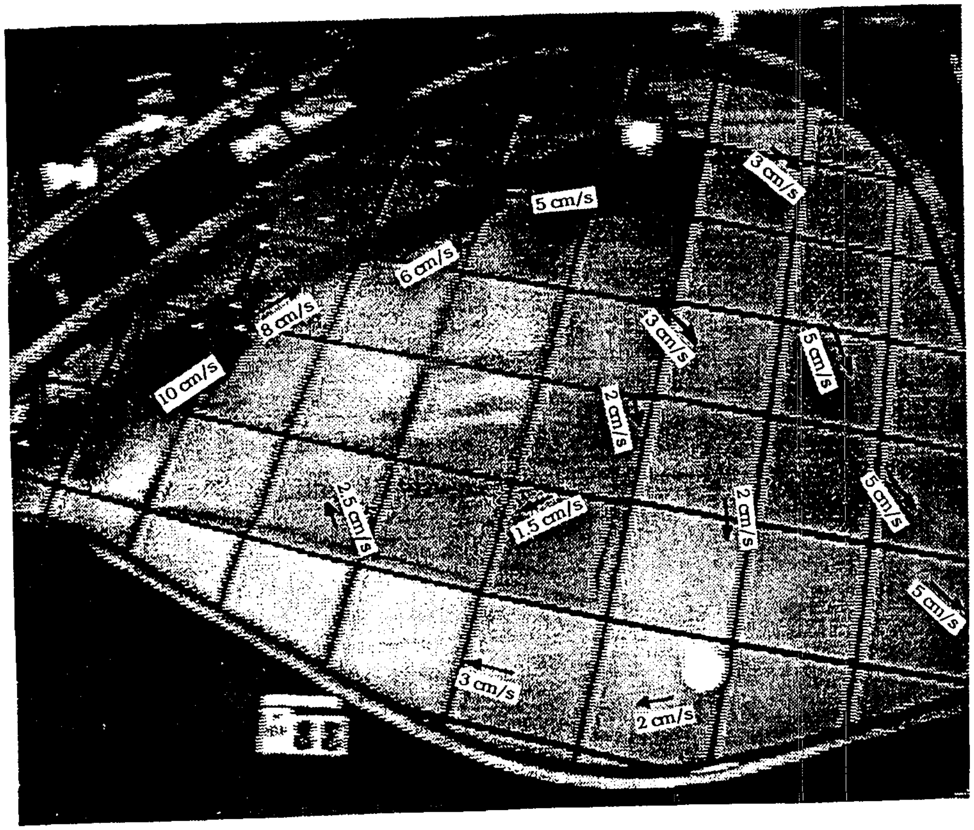

Figure 1

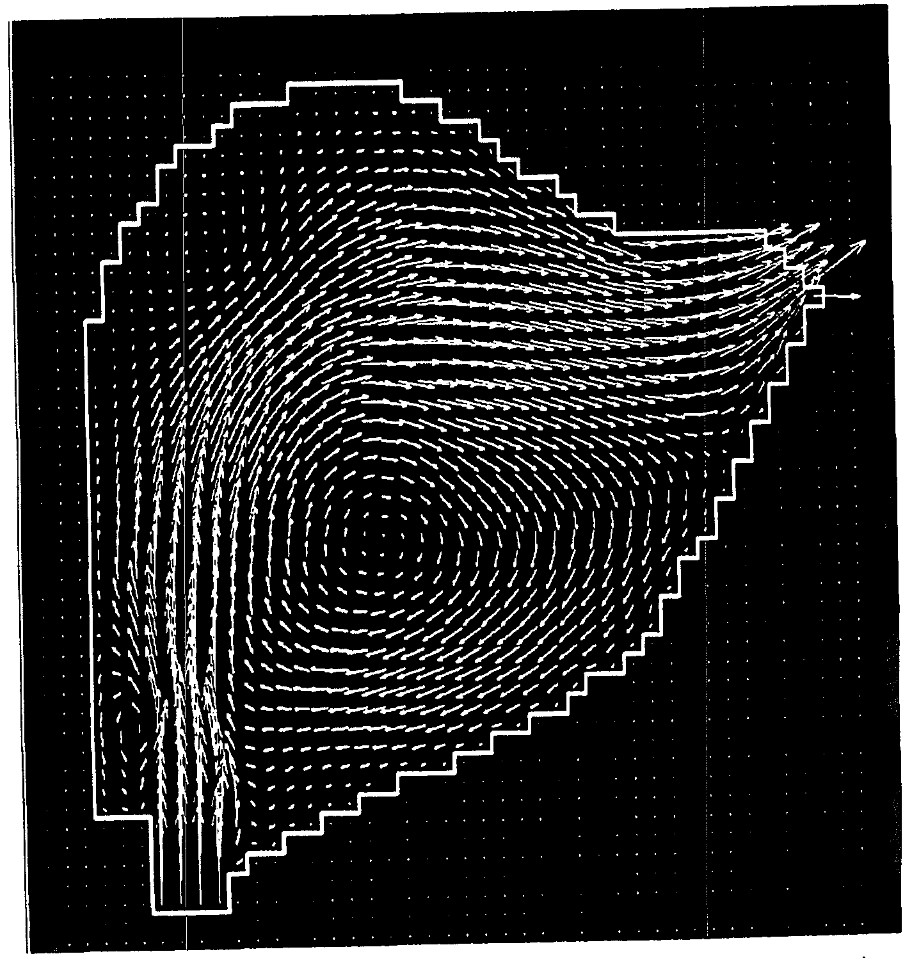

Vector equal to one grid distance represents a velocity of 1.6 cm/s

Figure 2

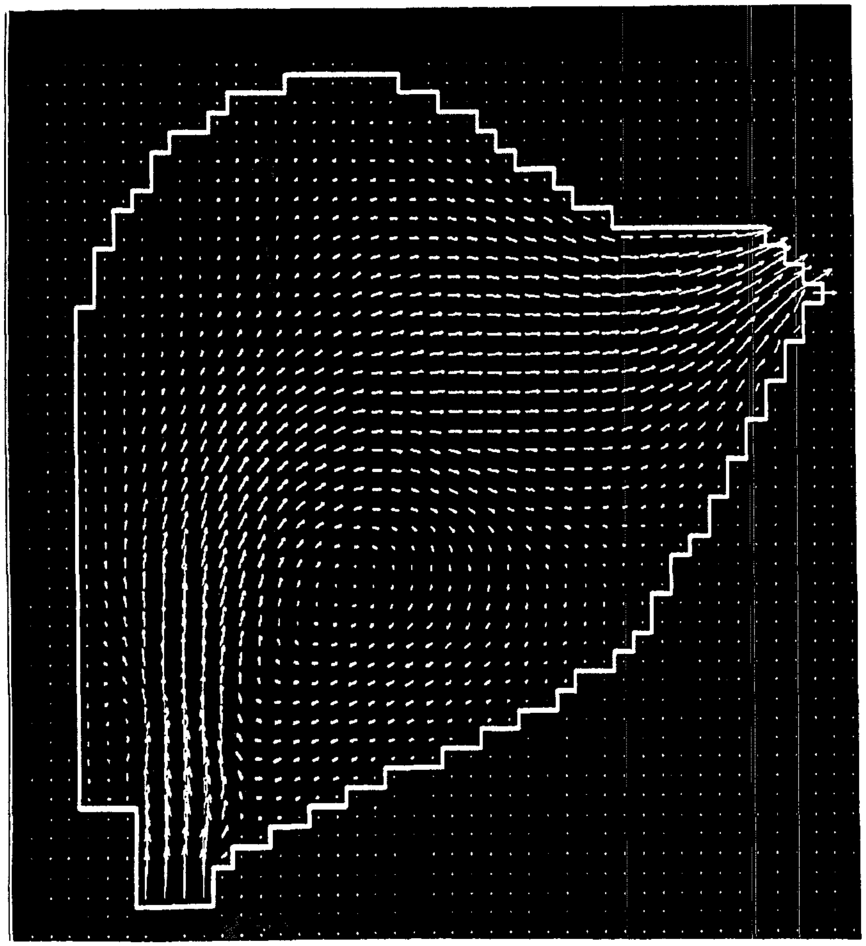

Vector equal to one grid distance represents a velocity of 1.6 cm/s

Figure 3

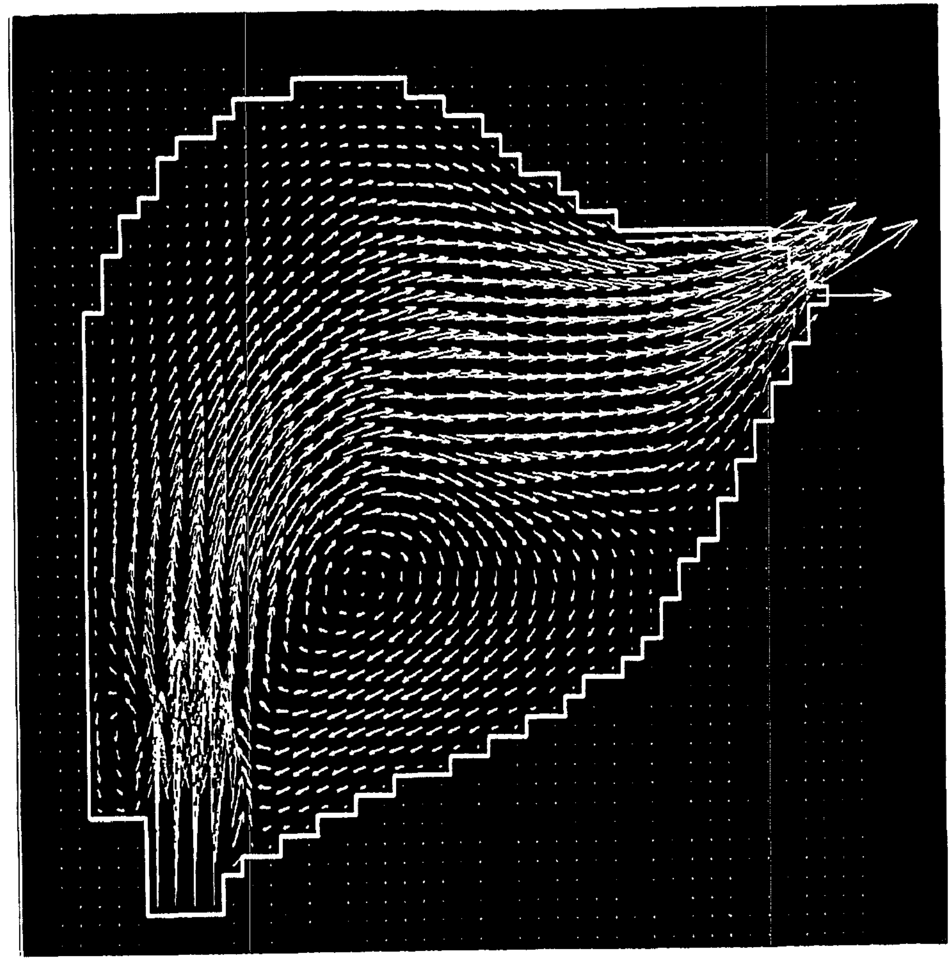

Vector equal to one grid distance represents a velocity of 4.5 cm/s

Figure 4

Model and Prototype Studies for Reservoir Desiltation

by Chian Min Wu
Water Resources Planning Commission
Taipei, Taiwan, ROC

Abstract

Experience on hydraulic flushing of sediment deposits through low-level sluices to clear reservoir sedimentation in Taiwan is described for studies conducted both in models and in prototypes. It is found that the transport behavior of fine and coarse sediments which are flushed through the reservoirs are quite different. In this regard, two groups of equations , one each representing fine and coarse sediment desilting capacity are formulated using the hydraulic model data and supplemented with the prototype data.

Introduction

Reservoir sedimentation creates major problems in the planning ,design and operation of water resources systems. The conventional design of a dam and reservoir usually only takes into account the retention of sediment-laden inflow. One solution to this problem, which in the last three decades has been successfully applied in Taiwan, is the hydraulic flushing of sediment deposits through low-level sluices. Unfortunately ,no equation describing sediment desilting capacity has so far been established. Laboratory and prototype studies found that the hydraulic properties of the sediment flushing behave quite differently for reservoirs with fine and coarse sediments. Hence two groups of equation representing sediment desilting capacity are formulated .

Sediment Flushing Technique

Towards the end of the water supply season or before the beginning of the high flow season, a reservoir normally retains some water; this can be used to desilt the sediment deposits from the previous years. When the desilting sluices are opened (Fig.1), the water level in the reservoir begins to fall, and flow towards the sluices is generated . The reservoir can be flushed by either pressurized condition or free flow condition. Both prototype and model operations showed that flushing under free flow is capable of transporting a much greater sediment load than when flushing occurs under pressurized conditions. Tests showed that the desilting flows for fine sediment usually behave differently as compared to the coarse one .For fine sediment, the flows sometime behave as a hyper-concentrated flow, whereas for coarse sediment particles, usually perform as a fluvial flow. In the following ,the results of these two sets of studies are given.

Reservoir Desilting with Fine Sediments

In the southern part of Taiwan there are many watersheds which are characterized by their easily erodable mudstone formation where the sediments are fine in size, uniform in gradation and are easily eroded after saturation. Gen-Shan-pei reservoir is one of the reservoirs located within this area. Completed in 1938, it is an earth dam 30.0 meters high and 256 meters long with an initial storage capacity of 6.98 x 10^6 m^3 .However since its initial impounding it has suffered from severe sedimentation problems.In 1951, the owner,the Taiwan Sugar Company conducted a careful observation of the sediment movement near the sediment deposited intake area, and found there might be a possibility of desilting the sediment through a newly constructed sluice tunnel.Prior to the construction of the desilting tunnel, a 1:50 scale non-distorted model of the main pocket area was constructed and the most effective means of desilting the reservoir sediments was studied. Froude law was adopted to determine the model scale, and coal powders were used as movable materials.The movable material was scaled down using the particle fall velocity.It was found that the qualitative behavior of sediment movement near the existing intake area was in good agreement with the prototype.After the proposed desilting sluice was installed in the model different alternatives were compared and it was concluded that sediment withdrawal is the greatest under an empty reservoir conditions. As a results of the model studies the desilting tunnel was designed to be 203 meters in length and 1.5 m in diameter and has a maximum flow capacity of 9.82 cms.

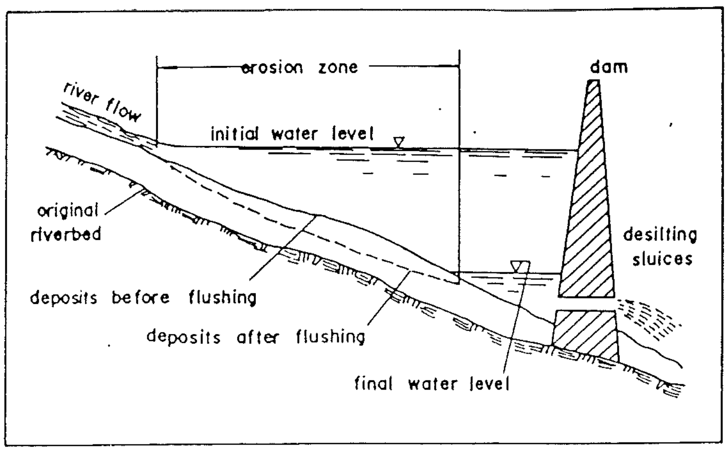

Fig.1. Hydraulic flushing of reservoir sediment

Model-Prototype Conformity

From the model data a rating curve for the desilting capacity of the sluicing tunnel was obtained.The flow duration curve and the sediment rating curve were combined to obtain an annual desilting capacity of 616,700 m^3 of sediment .However,past 33 years of prototype operation showed the average annual sediment withdrawal is 329,000 m^3 .The discrepancy between the estimated and the historical average is mainly due to the actual desilting period available in the prototype operation.However ,in order to provide design data a series of prototype experiment was performed and it was found that the efficiency of the sluicing operation is primarily determined by (1) the desilting capacity of the sluice tunnel, and (2) by the resuspension, headcut and transport potential of the deposited materials in the reservoir.

(1) Desilting Capacity of Sluice Tunnel

Numerous sediment transport equations have been proposed for the prediction of sediment load or concentration in rivers. Using the prototype desilting data, the applicability of different sediment transport parameters was studied. Among them two parameters , Vs/w and V^3/gdw were proven to be significant. For operation of the desilting tunnel under pressurized conditions, they can be described by

$$C_w = 64.9(V^3/gdw)^{-0.45} \quad r = -0.34 \qquad (1)$$

or

$$C_w = 51.4(Vs/w)^{-0.64} \quad r = -0.43 \qquad (2)$$

where C_w = the sediment concentration, in kg/m^3
V = the flow velocity in the tunnel, in m/sec
s = the energy gradient of flow in the tunnel
d = the depth of flow in the tunnel, in m
w = the falling velocity of the particles, in m/sec
r = the correlation coefficient.

Under free flow conditions, the relationship is

$$C_w = 847.1\ (V^3/gdw)^{-0.49} \quad r = -0.82 \qquad (3)$$

or

$$C_w = 369.3(Vs/w)^{-0.69} \quad r = -0.93 \qquad (4)$$

In both series of equations, the parameter Vs/w gives a better correlation. The correlation coefficients for other parameters such as the tractive force, shear velocity, flow velocity, flow discharge and slope are minimal.

(2) Resuspension Capacity of Reservoir

As the reservoir bed was so muddy that it was impossible to approach the sampling site ;thus prototype measurements of headcut scour and resuspension were impossible. Hence, the prototype sediments were tested in the laboratory flume to obtain the empirical equation for the resuspension capacity of the reservoir during the desilting process. The generalized equation was

$$C_w = 0.02\ (V^3/gdw)^{1.73} \qquad (5)$$

or

$$C_w = 147.4\ (Vs/w)^{1.65} \qquad (6)$$

(3) Properties of Desilting Flow

Capillary viscosimeter studies of the deposited materials (Fig.2) showed the desilting fluid is in a hyper-concentrated state. As were found by Naik and Roberson (1984), the flow property of a sediment laden fluid is a dependent of the flow condition . As flow velocity increases the fluid will transition from that of Bingham plastic into that of Newtonian. The transition occurs at

$$\S = 1/2\ \sigma_m V^2/\tau_\beta \geq 1{,}000 \qquad (7)$$

where § is a dimensionless number, σ_m is the density of the silty water , and τ_β is the Bingham shear stress. It can be seen from the sediment-carrying capacity curve(Fig.3), that the turning point is corresponding to the transition stage of the flow regime change .

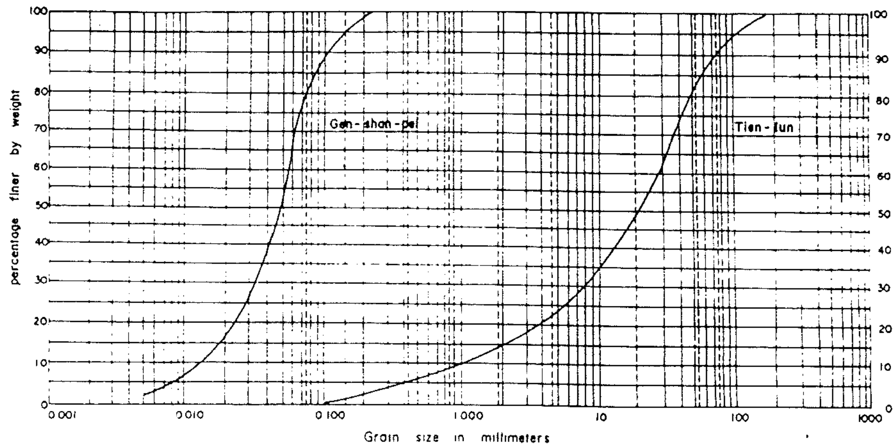

Fig. 2. Cumulative Size

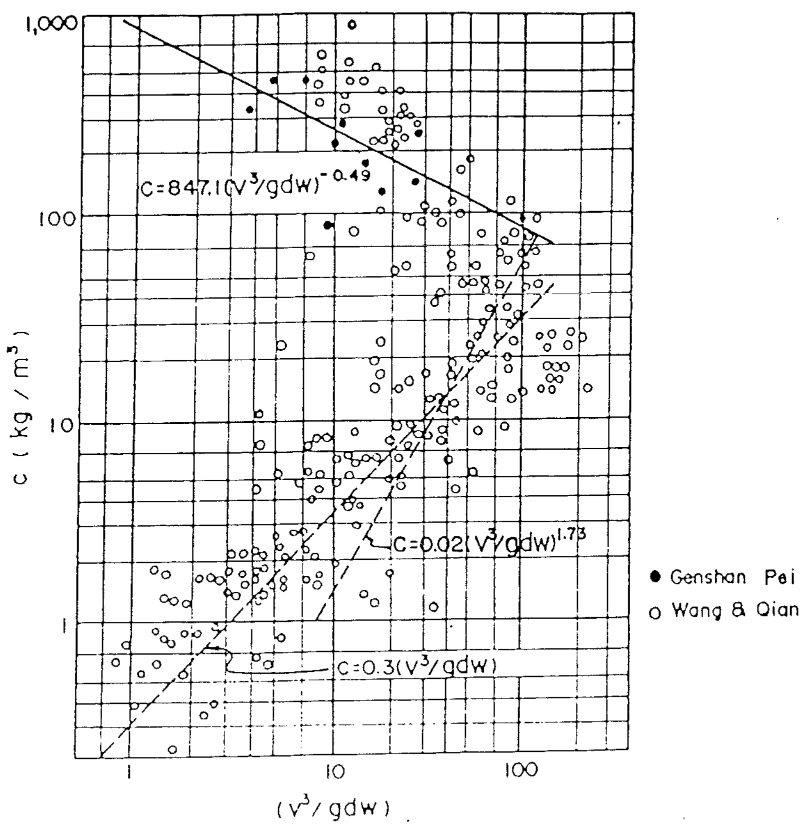

Fig. 3. Transport Capacity

Reservoir Desilting with Coarse Sediments

In the central part of Taiwan there are many rivers characterized by another extreme composition of coarse sediments ranging from gravel to cobble. Tachia river is one of the typical examples,where a series of dams ,from upstream to downstream,Te-chi, Chin-shan, Kukuan and Tien-lun were built. In this series of dams and reservoirs, hydraulic flushing through low-level sluices was applied at Kukuan and Tien-lun Dam.The problems related to their operation are uncertainty of desilting capacity of the sluices, blockage of the gates by sediments and abrasion/erosion of concrete structures.In order to solve these problems ,since their operation,two hydraulic models were built at different stages for Kukuan, and three for Tien-lun Dam. Common to these models are the adoption of Froude law to determine the model scales, and a linear scaling of the prototype sediments. A 1:40 scale non-distorted model of the main pocket area was constructed .Experiments were conducated for sluices with different shapes and sizes to determine their desilting capacity and optimal layouts.

(1) Desilting Capacity of Sluices

From the model data the desilting capacity of the sluice may be expressed in the form of

$$C_w = 0.024 \; (V3 \; /gdw \;)^{2.66} \qquad (8)$$

or

$$C_w = 181.4 \; (Vs \; / \; w \;)^{2.54} \qquad (9)$$

In addition to being a function of the sluice geometry, the desilting capacity of a sluice also depends upon the flushing discharge and the scour length of the sediment deposits.The following empirical formula is developed to include these parameters.

$$C_w = 1170 \frac{B^{2/5} L^{2/5}}{Q^{2/5}} (0.56 s_b{}^{3/2} - 0.0003) \qquad (10)$$

where C_w = the desilting sediment concentration in kg/m
B = width of desilting flow, in m
L = length of desilting reach, in m
s_b = $\Delta H/L$ = slope between the location where desilting begins and the sill of the bottom outlet,see Fig.4.

The gorge under studied are relatively narrow and flow is relatively two-dimensional,hence, the sediments are deposited in a concentrated form and can be flushed relatively effectively.

(2) Shape of Sluices

As the sediment concentration is high in the sluice, hydraulic structures are usually subjected to the abrasion/erosion of the sediment laden flow. Hence , the shape of sluices, especially the energy dissipator, is critical in the hydraulic design of the structure. For example,the downstream part of the Tien-lun sluice was Ogee shaped.However,operation of the original sluice induced tremendous trouble in maintaining the sluice invert in shape. As a results of' the 1:40 scale model, the Ogee shape was changed into a superelevated chute type structure with a side wall whose height decreases gradually from the upstream to the downstream end so that some flow can fall from the side of the chute.Flow in the sluice acted as a spatially varied flow decreasing its momentum from upstream to downstream,thus reducing the impact forces at the downstream end of the spillway apron where tremendous erosion had been recorded in the original layout.

Conclusions

The desilting experience in prototype and model reservoirs indicates that hydraulic flushing is an efficient technique for the removal of sediment deposits,however, the desilting capacity formula is different for fine and coarse sediment. The suggested desilting capacity equations can provide means for preliminary estimates.In the final design, hydraulic model tests are recommended .

Reference

Jim S. O'Brien and Pierre Y. Juline (1988), "Laboratory Analysis of Mudflow Properties", Jour. of Hyd. Engrg., Vol. 114, No. 8, ASCE.

Naik, B., and Roberson, J. A(1984), "Mechanics of Mudflows", Proc. ASCE, water for Resource Development, pp.158-162.

Wang, Shang Yi (1984), "The Principle and Application of Sediment Effective Power", Jour. of Hyd. Div., ASCE, Vol. 110, No. 2 ASCE.

Wu, Chain Min (1986), "Reservoir Sedimentation and Desilting in Taiwan", Water Forum '86, Vol. 1 ASCE.

Yang, C.T. (1972), "Unit Stream Power and Sediment Transport", Jour. of Hyd. Div., ASCE Vol. 18, No. HY 10, pp.1805-1826.

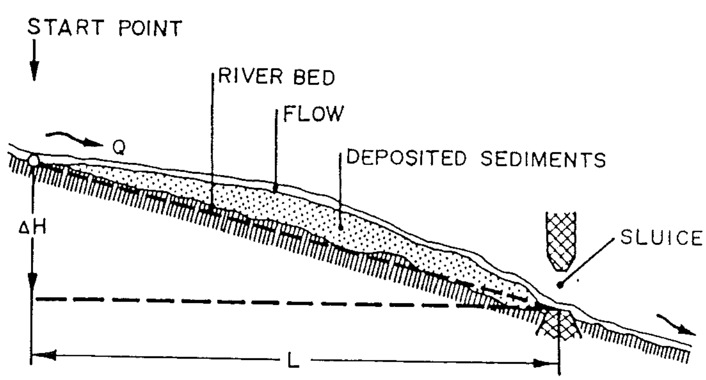

Fig. 4. Definition Sketch of Desilting

LABORATORY STUDY OF THE SETTLING OF WASTEWATER PARTICLES IN AN OUTFALL PLUME IN SEAWATER

by Theresa R. F. Wang†, Robert C. Y. Koh, and Norman H. Brooks

Environmental Quality Laboratory
California Institute of Technology
Pasadena, California 91125 USA

Abstract

A holographic camera system was applied to study the settling characteristics of sewage and sludge particles in seawater after they were coagulated inside a laboratory reactor, which was designed to approximately simulate the mixing conditions inside a discharge plume. Experimental results show that the sludge and effluent particles have very similar settling characteristics (velocity versus size), and that particle coagulation is small under the simulated plume mixing conditions. The median fall velocity is 0.0004 cm/sec for the digested primary sludge and less than 0.0001 cm/sec for the effluent. In general, the holographic technique indicates slower settling velocities than all the previous investigations by other procedures.

Introduction

Ocean discharge of treated sewage and digested sludge has been a common practice for the disposal of municipal and industrial wastewaters for years. Since particles in the discharge are one of the main causes of adverse effects on the marine environment (Jackson, 1982), the transport processes and the final destinations of particles and the associated pollutants must be studied in order to evaluate the environmental impact and the feasibility of the disposal processes. The settling velocity of sewage and sludge particles is among the most important factors in controlling the transport and deposition pattern of particles (Koh, 1982). The settling velocity of wastewater particles may be altered by particle coagulation in the discharging plume.

Experimental Design

The purpose of this research was to make direct measurements of the fall velocity of wastewater particles in seawater by means of holography, with controlled pre-coagulation. The conventional settling column has been found deficient because coagulation is uncontrolled and changes the test results (Wang, Koh, and Brooks, 1990). For our tests, the coagulation/dilution time history was simulated to be like that which occurs in a typical wastewater plume.

The mixing and coagulation of sewage particles in a buoyant jet in the ocean are difficult to simulate properly in the laboratory. In our study, we controlled the most important parameters—duration of mixing, rate of dilution, and energy dissipation rate—in the laboratory simulation of coagulation. A laboratory scale plume cannot be used in this case because the mixing time is much shorter. Instead, a continuous-flow-stirrer-tank reactor (CFSTR) was designed to approximate the mixing conditions inside a buoyant plume by varying the particle concentration by progressive dilution with artificial seawater (Riley and Skirrow, 1965) and the turbulent shear rate by means of variable speed paddle, according to predetermined

† Present Address: Environmental & Ocean Technology, 150 N. Santa Anita Ave., Suite 885, Arcadia, CA 91006

scenarios based on plume dynamics (Fischer *et al.*, 1979). As the coagulating experiment progressed, samples were withdrawn from the reactor at different times and diluted immediately with filtered artificial seawater to suppress further coagulation. The settling velocities and the size distributions of particles were then measured for these diluted samples (concentration $\leq 2\ mg/l$) using an in-line holographic camera system. Since sewage particles have very small settling velocities (of the order of 10^{-4} to $10^{-2}\ cm/sec$), a special settling cell was designed to eliminate the influence of convection currents during measurements.

Four sets of experiments were conducted using digested sludge and effluent. Detailed experimental procedures and results are found in the Ph.D. Thesis by Wang (1988). Our discussion here will focus on the physical modeling of the settling behavior and the possible coagulation of wastewater particles in seawater.

Experimental Apparatus

(1) The coagulating reactor: To simulate the coagulation inside a rising plume, the time history of the dilution and the energy dissipation rate were calculated first based on the plume mixing theory and averaging across the plume. A CFSTR with a two-blade paddle was designed to generate the desired dilution and mixing history (Fig. 1). The dimensions of the reactor and the impeller are $T{=}H{=}3D{=}6\ in$ (15.24 cm), where T is the diameter of the tank, H the water depth inside the tank, and D the diameter of the paddle. The dilution ratio or the particle concentration inside the reactor was controlled by adjusting the flow rate of the dilution water into and out of the reactor. Clean seawater entered the reactor from the bottom through a diffuser to minimize disturbance and to ensure a uniform inflow. After mixing with the sewage suspension inside the reactor, the excess mixture left the container over the circular weir around the top of the reactor.

(2) The settling cell: The settling cell consists of two parts: a rectangular lucite box ($6.35\ cm \times 7.62\ cm \times 10.16\ cm$ high, 492 ml) with two parallel windows made of high quality optical glass, and a funnel on the top. For suppression of convection, ambient density stratification was established by carefully feeding solutions with different densities ranging from 1.021 to 1.028 g/cm^3 into the cell. The density-stratified cell was left undisturbed to stablize for at least 8 hours, resulting in a density gradient of about 0.07 m^{-1} in the vertical direction. Caution was exercised when introducing sludge samples into the funnel, *i.e.*, samples were transferred onto a floating plate instead of into the water directly. The temperature of the samples was raised by about 2^oC to compensate for the density difference and to prevent convective overturning in the funnel. Settling measurements using this settling cell were calibrated with standard PSL particles of known density ($\rho = 1.05\ g/cm^3$) and size (10, 20, 50, and 100 μm). Our calibration results indicated that the convection current was effectively eliminated and settling velocities in the range from 1×10^{-4} to $1 \times 10^{-2}\ cm/sec$ can be obtained with accuracy within $\pm 6\%$. For recording a size distribution using a single hologram, the suspension was poured directly into the cell and photographed immediately.

(3) The holographic camera system: The settling velocities of individual particles in a sample and the size distribution of the whole sample were measured separately with the holographic camera system (Fig. 2). Holography, a two-step

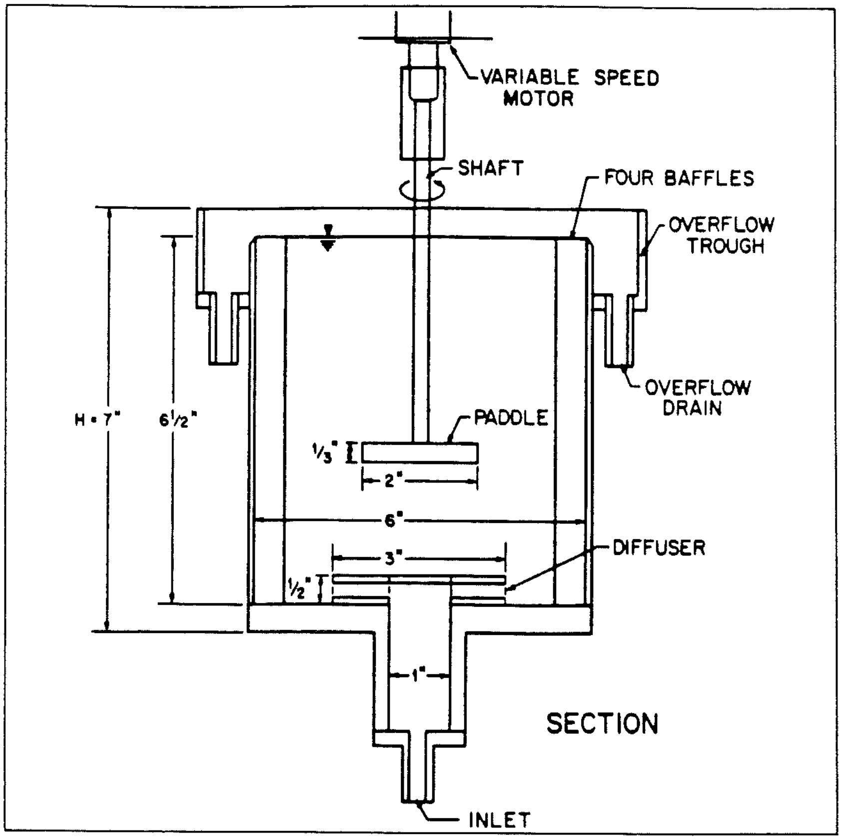

Figure 1 Schematic diagram of the cylindrical coagulation reactor

photographic process, includes the recording and reconstruction of holograms (e.g. Collier *et al.*, 1971). A 5 mW He-Ne laser was used as a coherent light source to record the three-dimensional (3D) sampling volume inside the settling cell on holograms. Later, the same laser beam was used to reconstruct the 3D images of the sampling volume from recorded holograms for data analysis. The size distributions were obtained from singly-exposed holograms by measuring the sizes of particles within a certain volume. The settling velocities were measured from doubly-exposured holograms by measuring the distance between pairs of images of the same particle at two time instances. A video camera and a three-dimensional translating stage were used to focus and project the reconstructed images onto a television screen for image analysis. To facilitate the data analysis and to provide better accuracy, a PC-based image processing system was developed for digitizing, storing, and processing the focused images to automatically calculate the size and velocity of particles.

Experimental Procedure

(1) Sample preparation: At this stage, raw sewage samples taken from the treatment plant were prepared for the coagulation experiment. The suspended solids concentration and particle size distribution were measured using filtration and the holographic technique to record the initial condition before mixing with seawater.

(2) The coagulation experiment: At the start of the coagulation experiment, the coagulating reactor was filled with filtered artificial seawater. A small amount

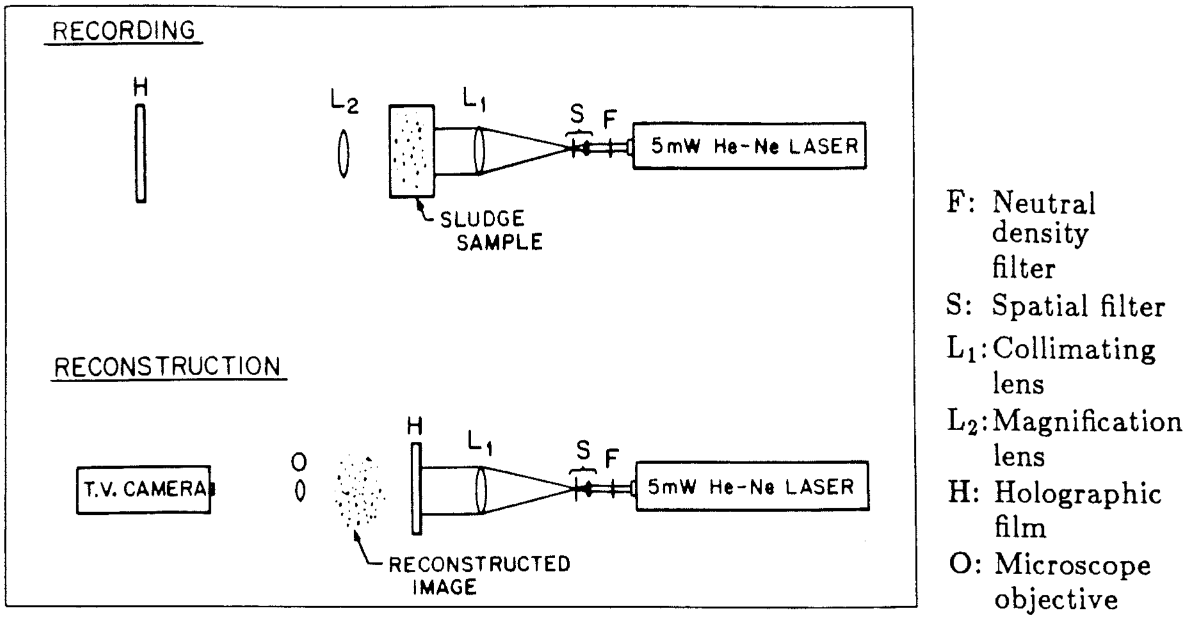

Figure 2 Schematic diagram of the optical arrangement to record and reconstruct holograms

of a pre-processed sludge sample or of a raw effluent sample was then injected into the reactor from the bottom to create a small vertical buoyant jet. This jet entrained and mixed with the surrounding seawater when rising up to the surface. Stirring by the paddle generated the turbulence needed for mixing and coagulation. Dilution water came in according to the predesigned flowrate. As the experiment progressed, samples were withdrawn from the center of the reactor and were diluted immediately to a concentration less than 2 mg/l to suppress further coagulation.

(3) The settling experiment: The experimental procedure for obtaining the fall velocity distribution for individual samples consisted of four steps: filtration, size distribution measurement, settling velocity measurement, and image analysis. A sludge sample of 20 ml (concentration $\sim$ 2 mg/l), or an effluent sample of 40 ml (concentration $\sim$ 0.5 mg/l), was introduced at the top of the density-stratified cell. A timer was started after feeding of the samples to monitor the elapsed time. Hologram recording began three minutes after the sample was introduced. Doubly-exposed holograms were recorded according to a pre-calculated schedule to cover the velocity range from 1×10^{-4} to 0.05 cm/sec. A long elapsed time of up to 48 hours was needed to allow the particles of varying velocity to fall from the top of the funnel down to the observing area. Velocity measurements were obtained by examining the reconstructed images of particles from doubly-exposed holograms.

Sample Results

In presenting the experimental data, the equivalent diameter, $d_{equ} = \sqrt{\frac{4}{\pi} A_p}$ (calculated based on the projected area A_p), was used to classify particles and to correlate particle size with settling velocity. Results from the settling measurements are presented in two ways: the w–d graphs, which show the relations between the particle sizes and the settling velocities, and the distribution curves (probability density functions and cumulative distributions). For w–d plots, d_{equ} is used as the abscissa. In addition, several lines calculated from the Stokes' law,

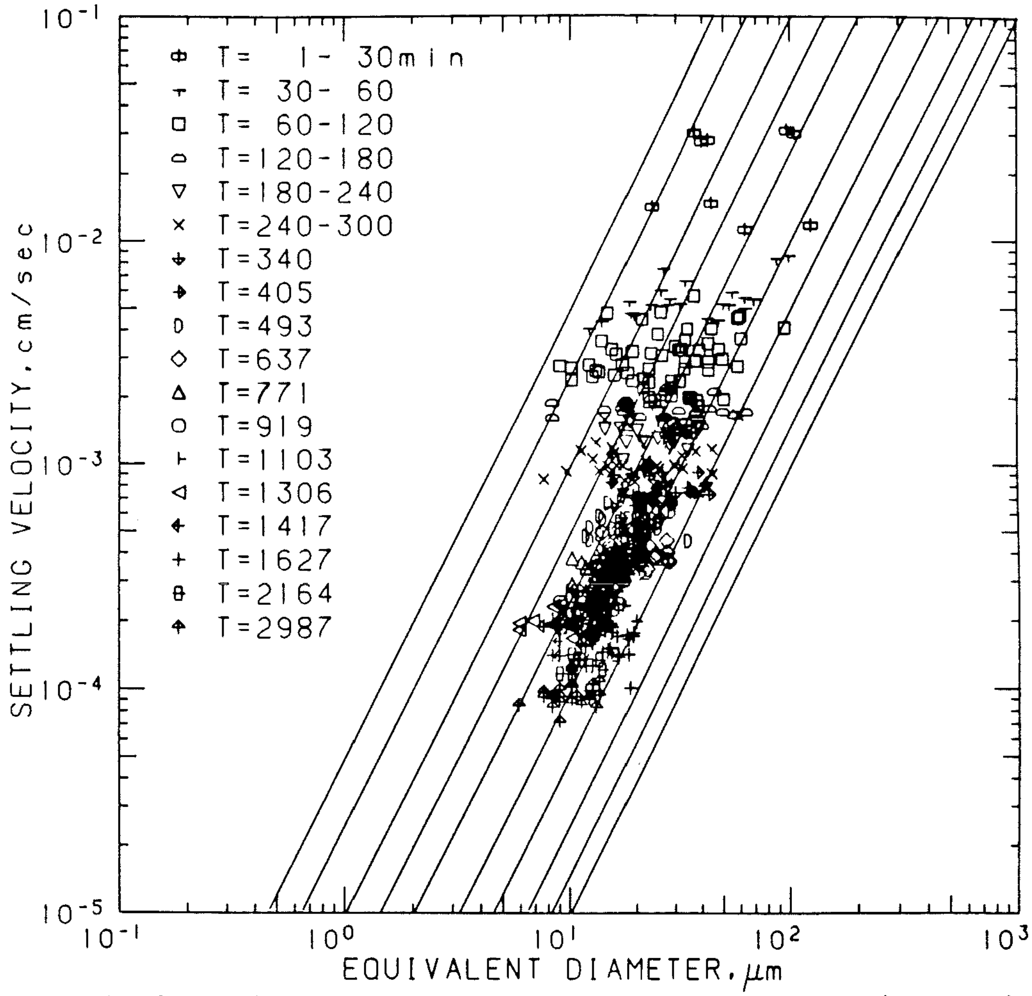

Figure 3 Settling velocity versus equivalent diameter for D.P.S. (CSDOC) measured in seawater after plume mixing for 5′40″

$w = A\frac{g}{18\mu}\Delta\rho d_{equ}^2$, with different values of $A\Delta\rho$ are depicted in the same graphs, in which A is the shape factor of particles (A=1 for sphere), g the gravitational acceleration constant, μ the dynamic viscosity of fluid, and $\Delta\rho$ density differences between the particles and fluid.

Figures 3 and 4 show the results from the experiment with digested primary sludge (D.P.S.) from the County Sanitation Districts of Orange County (CSDOC) at $t = 5'40''$. Figure 3 shows the w–d relationship, which is very similar to that observed at $t = 0$, *i.e.* very little coagulation had time to occur in the reactor. The cumulative velocity distribution (by volume) is depicted in Figure 4, which shows that the 50-percentile velocity is about 4×10^{-4} cm/sec. The results have been adjusted for the residual fraction of particles settling slower than 10^{-4} cm/sec (approximately 10 μm in size).

Main Conclusions

1. The holographic system permits the fall velocity to be measured directly without errors due to coagulation during the test.

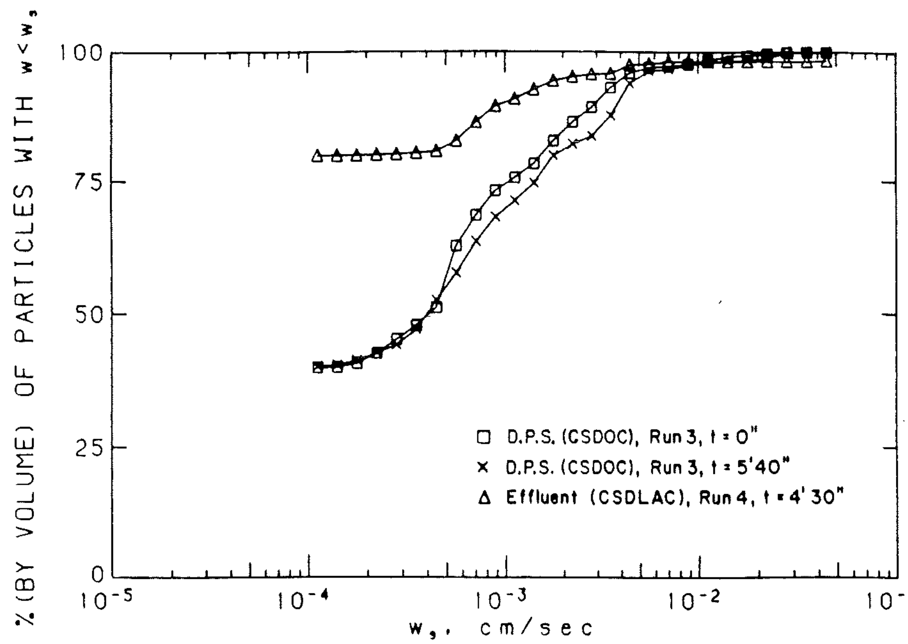

Figure 4 Settling velocity distributions based on the holographic measurements and the filtration analysis

2. Digested sludge and effluent particles have similar settling characteristics in artificial seawater.
3. Coagulation was small under the simulated plume conditions, and had little effect on the fall velocity distribution.
4. The fraction of the particles (by mass) in digested sludge (CSDOC) having fall velocities greater than 0.01 *cm/sec* was found to be only 2.5% by the holographic method, but 14 – 43% by the conventional settling column.

Acknowledgement

The authors acknowledge support from the Andrew W. Mellon Foundation, the William and Flora Hewlett Foundation, NOAA, and the County Sanitation Districts of Orange and Los Angeles Countries.

References

Collier, R.J., C.B. Burckhardt, and L.H. Lin. "Optical Holography," Academic Press: New York, New York, 1971.

Fischer, H.B., E.J. List, R.C.Y. Koh, J. Imberger, N.H. Brooks. "Mixing in Inland and Coastal Waters," Academic Press: New York, 1979.

Jackson, G.A. *Environ. Sci. & Technol.* **1982**, *16*, 746–757.

Koh, R.C.Y. *Environ. Sci. & Technol.* **1982**, *16*, 757–763.

Riley, J.P. and G. Skirrow. "Chemical Oceanography," Academic Press, New York. 1965.

Stumm, W. and J.J. Morgan. "Aquatic Chemistry. 2nd Ed.," Wiley-interscience, New York, 1981.

Wang, R.T., R.C.Y. Koh, and N.H. Brooks. "Interpretation of settling column measurements of sludge," in *Physical & Chemical Processes: Transport and Transformation of Oecanic Processes in Marine Pollution,* Krieger Publ. Co., Melbourne, FL, 1990.

Wang, R.T. Ph.D. Thesis, California Institute of Technology, Pasadena, CA, 1988 (avaliable as Environmental Quality Laboratory Report No. 27, 265 pp).

Study of deposition patterns obtained after injection of sand particles at flow surface

by

J.M. Tanguy(1), R. Frenette(2), A. Blouin(2), M. Frenette(2), G. Dhatt(3)

(1) Service Technique des Ports Maritimes et des Voies Navigables 60200 Compiègne - France
(2) Laval University Quebec - Canada

Abstract

A set of physical experiments is conducted in a laboratory flume to analyse the two different deposition patterns obtained after injection of fine sand particles at flow surface: an oblong one and a horseshoe-shaped, depending on the ratio solid discharge vs celerity of the flow. Through 31 experimental runs the transition zone is delimited. In fact, it represents the limit of the convection-diffusion theory, only valid for the oblong patterns.

1- Dumping materials into sea or rivers.

For many years, engineers have taken a great interest in Sediment Transport by the flow. Coastal and fluvial modifications due to sediment transferts often cause irreversible and injurious consequences on natural sites or on their planning. The equipment of a site consists, most of the time, in building construction works, which modify their precarious equilibrium. On erodible bottoms, made of fine sand or silt particles, these works imply pick up and dumping of material.

The purpose of this laboratory flume modelling study is to analyse the deposition process through sand injection at the surface of flow, in terms of time and spatial transport and deposition.

2- The set of experiments.

This set of experiments follows the one conducted by A. Blouin at the Hydraulic Laboratory of Laval University in Quebec, which were essentially qualitative ones. These experiments are similar with those conducted by Sayre [1], except that for A. Blouin's, the flume was wide, so that the transverse diffusion of material inside the flow is not visible. Among 26 runs, two different types of deposition pattern appeared, depending on hydraulic conditions and sedimentation parameters. The first deposition pattern presents an oblong shape, and the second presents a horseshoe-shape.

With this new set of experiments we are now able to explain the qualitative observations and to determine the appearance conditions of each pattern. In the following, we describe the experimental setting and the results obtained after 31 runs, conducted with a unique sand of homogeneous granulometry.

3- Description of the settling.

3.1- The physical model.

The laboratory flume (fig. 1) is 15m long and 2.49m wide. The flow discharge, evaluated by means of a triangular weir, is maintained constant for each run. Downstream, a 0.19m height fixed outlet controls the water level.

The sand distribution is made up of a supply funnel with a vibrator and two cascade gutters. The lower gutter contracts the sand flow diameter to 1.5cm. Its lowest point is located at 32cm from the bottom, so at a distance varying from 1.9 to 5.3cm from the surface level, depending on the run.

3.2- The experiments.

Hydraulic data consist of water discharge and two water levels, one upstream (X_1=-2.14m) and the other downstream (X_2=3.90m). Measurements of sand thicknesses are limited inside a domain of 4m long and the canal width. They are made by means of a pin-carrier, movable in a 3 dimensions. Sand thicknesses are read at the end of each run, after stopping water discharge and slowly lowering the water level, to avoid sand entrainment. The expected precision is the operator's one: it is evaluated about 2mm. The limits of our experiments are:

$$0.05\text{m/s} < V < 0.188\text{m/s}$$
$$0.235\text{m} < H < 0.301\text{ m}$$
$$0.09\text{ g/s} < Qs < 46\text{ g/s}$$

where V,H and Qs are the flow velocity, the water height and the sand discharge.

4- Observations.

4.1- Qualitative aspect.

Whatever the run, borders of deposition areas appear a few minutes after the start and change very little with time. All the patterns are symetrical about the central axe.

- The fist type of pattern presents an oblong elongated shape, close to the central axe of the canal. A beginning of narrowing appears for the majority of this pattern, before the extremity of the canal. This type of pattern is characterized by a small ratio of solid discharge vs flow celerity (fig. 5,6,7).
- The second type of pattern is horseshoe-shaped, widens quickly downstream and presents two symetrical horns. The maximum deposition area is located in the upsteam part of it. A sandless area, just downsteam from the main deposition one is the main characteristic of this pattern. The ratio solid-discharge vs flow celerity (fig. 2,3,4) is high. External and internal borders are a little bit hazy and difficult to precise.

To display water circulation, colouring is poured into water at the injection point. It appears that:

- In the case of oblong shape, the colouring cloud is all in one block, increasing its volume by diffusion. At the opposite, in the case of horseshoe-shaped pattern,the colouring is divided in two symetrical clouds, diverging from the central axe. It clearly appears that this process starts at the injection point.

Explanation:

For the first type of pattern, particles entering the flow are immediatly entrained by the currents. The rather small solid discharge is well mixed and homogeneized by the turbulence. The concentration of particles remains quite small during the entire process. For the second type of pattern, the high solid discharges entering the flow induce a vertical dragging effect on water particules. This phenomenon generates two helicoidal currents, symetrical about the central axe, starting from the injection point and propagating separately downsteam (fig. 8).

4.2- Quantitative aspect.

The 31 runs can be shared in two sets:

- A set of 12 runs (1 to 12), well instrumented and whose deposition thicknesses are measured. The purpose of this set is to provide quantitative and precise information on this patterns. Transverse diffusion coefficients can also be evaluated.
- A set of 19 runs, more succinct, whose purpose is to precise the type of pattern, correlated with hydrodynamic parameters and solid discharge. They contribute to define the border between the two different patterns.

5- Exploitation of the results.

* On the graphic (fig 9), all the runs have been reported, as a function of the solid discharge vs the celerity of the flow, with the identification of the type of deposition pattern: oblong or horseshoe-shaped. A sharp transition area appears.
* The measurements of sand thicknesses show small concentration in the two horns. The main deposition volume is located near the injection point, which signifies that the sand injected with high discharge is not very sensitive to the transport capacity of the flow.
* The nearer the transition border is, the less the action of the sand is dominant and the more it is submitted to the transport capacity of the flow.
* In the case of the oblong profile (fig. 5,6,7), the action of the sand is negligible. Particles are transported inside the flow by convection and dispersion.
* Fig. 10 illustrates the evolution and the extend of deposition, for a given flow velocity. The increasing solid discharge tends to open the deposition patterns and to concentrate them upstream.
* Fig. 11 shows the evolution and the extend of deposition for a given solid discharge. The increasing flow velocities make the pattern elongated from a horseshoe-shaped towards an oblong one.

Conclusion.

This set of physical experiments has permitted the analysis of the deposition pattern after sand injection at the surface of flow. It has shown that the appearance of each type of pattern is mainly a function of the ratio between sediment discharge and sand velocity.

In the fluvial or maritime sites, consequences of material dumping into the flow can be analysed through different processes: the fall stage -time and spatially concentrated- and the transport stage -conditionned by waves and currents, which transport materials on long distances, for a long time-.

The sand process has been studied for a long time and mathematics models, based on convection-diffusion equation, can reproduce rather well the transport mechanism, but for low concentrations only. However, at high dumping rates, helicoidal currents appear and the classical approach can't reproduce these complex interactions between fluid and sediment. In general, we are interested in evaluating the consequences of material dumping into the sea or rivers, in terms of time and spatial transport and deposition. This study shows that we can make great mistakes in such evaluations, depending on the type of process which is used.

BIBLIOGRAPHY

[1] W.W. SAYRE - "Dispersion of Silt Particles in Open channel Flow" Journal of the Hydraulics Division, Vol. 95, N° HY3, May 1969, p. 1009, 1038

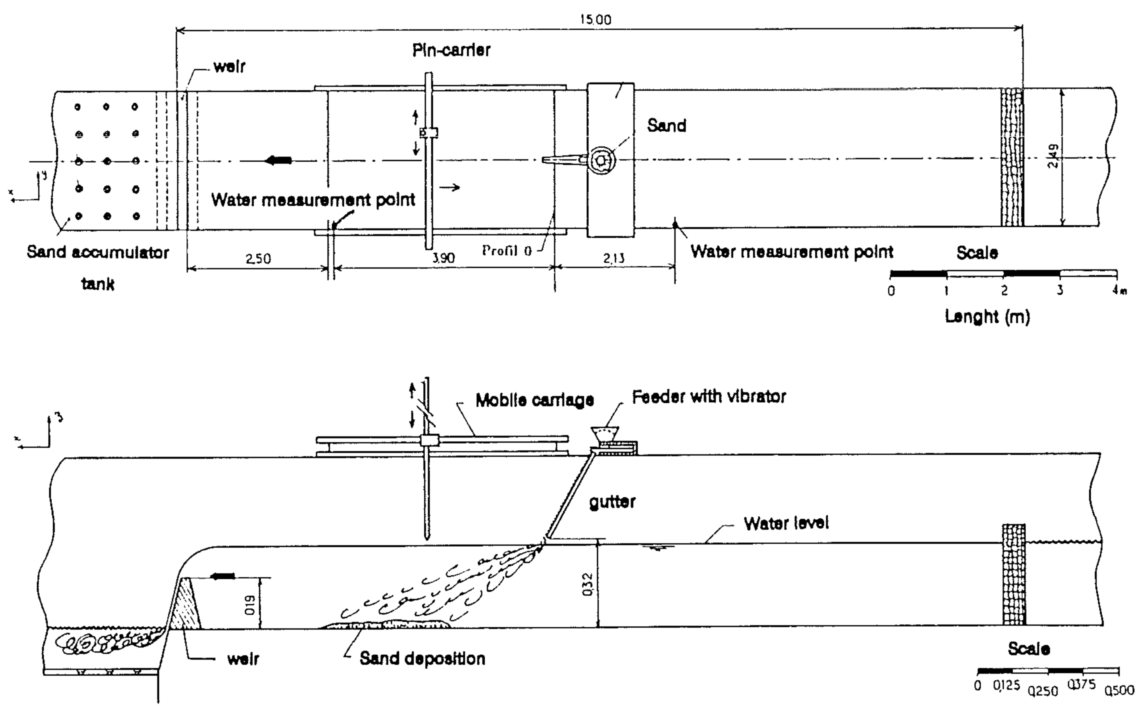

Fig. 1 : physical model

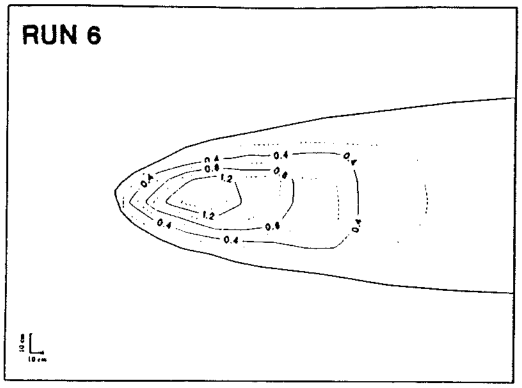

Fig. 2

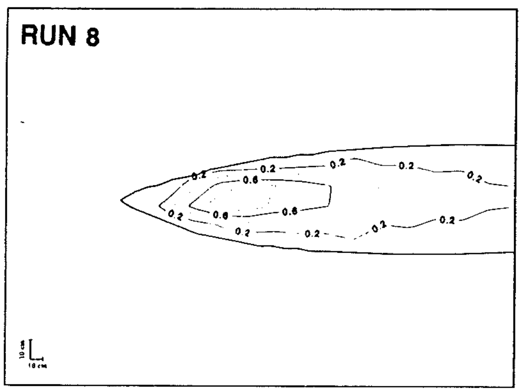

Fig. 3

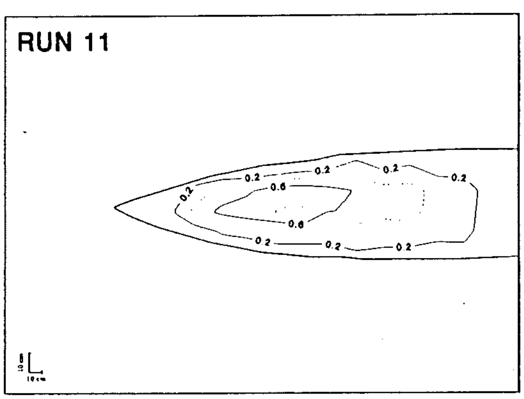

Fig. 4

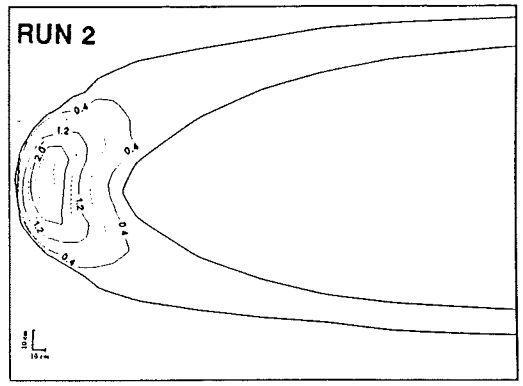

Fig. 5

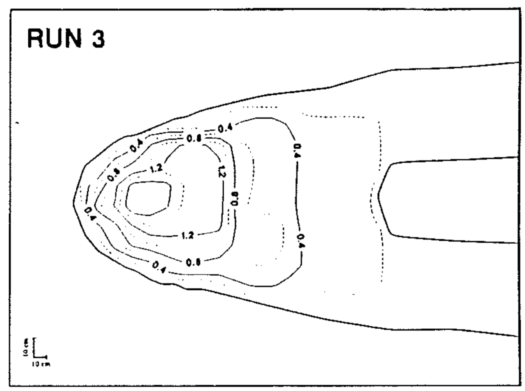

Fig. 6

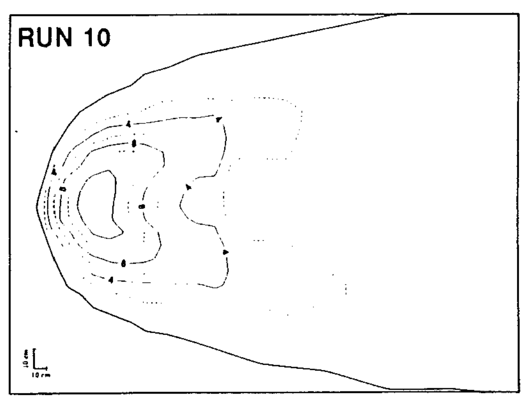

Fig. 7

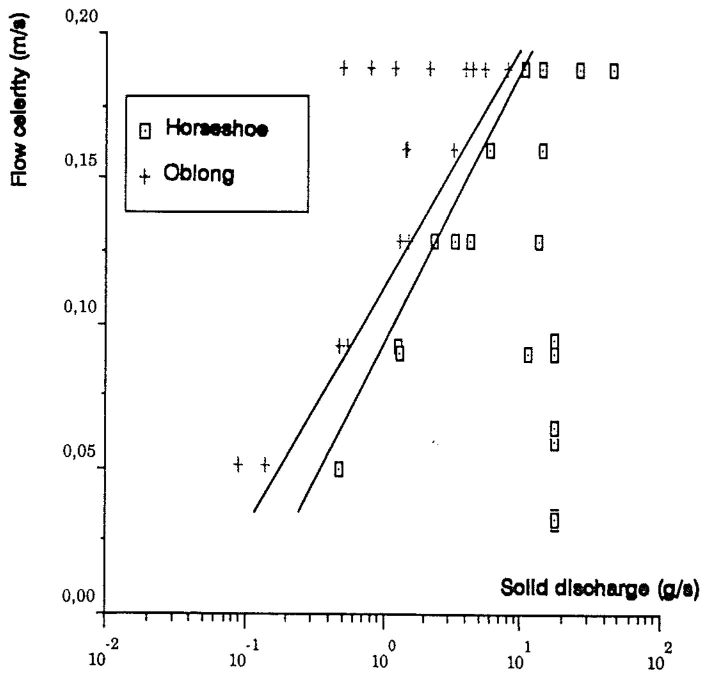

Fig. 9

Fig. 8

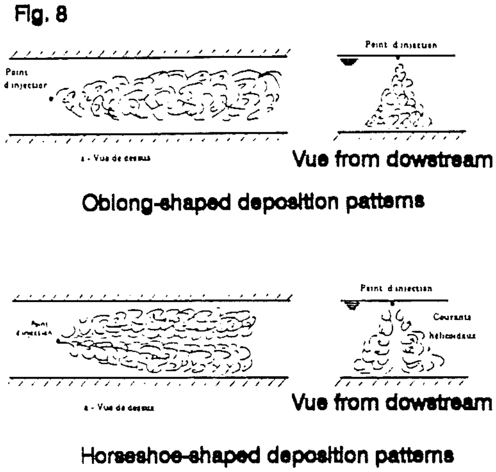

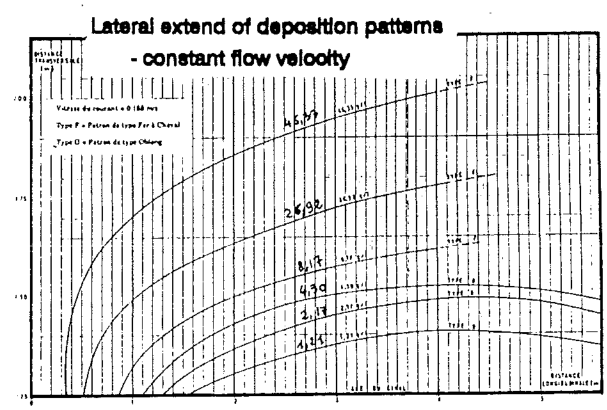

Fig. 10

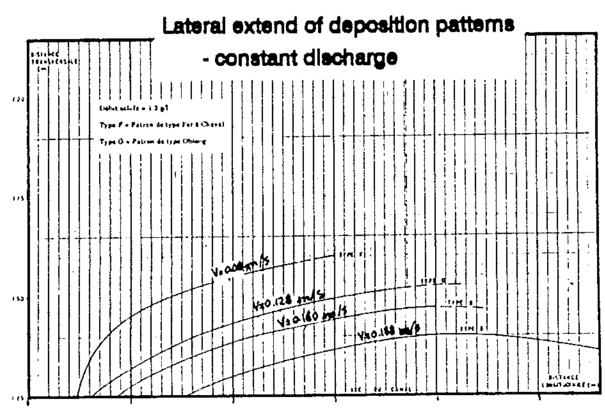

Fig. 11

Session 9A

Internal Mixing Processes

Double Diffusion in Two-Layered Shear Flows

by

Norikazu NAKASHIKI and Masafumi MIZUTORI

Hydraulics Department, Abiko Research Laboratory,
Central Research Institute of Electric Power Industry (CRIEPI),
1646 Abiko, Abiko-city, Chiba, 270-11 JAPAN

Abstract

Mixing processes in shear flows with temperature and salinity gradients are studied both experimentally and numerically. The experiments are carried out on two types of double diffusive flows (diffusive and finger types). In each type of diffusion, the eddy viscosity and the eddy diffusivities of heat and salt are estimated in relation with Richardson number. A two-dimensional numerical model is applied to simulate the double diffusive shear flows. The performance of the simulation model is evaluated by comparison of numerical results with experimental measurements.

Introduction

A diffusion process of dissolved substances with different molecular diffusivities is very complicated, and it is important in hydraulic engineering to study double diffusion in shear flows. For example, in a coastal area where river water flows in, warm water discharged from a power plant is affected by fresh river water, and the diffusion of warm water is suppressed by river water. The investigation of the mixing of hot salty discharge and cold fresh river water is important to predict a dispersion of warm water discharge.

The purposes of this study are to reveal the mixing process of hot salty water and cold fresh water in stratified shear flow, and to present a numerical simulation model.

Mixing of warm water discharge and fresh river water was measured by M. Mizutori and N. Katano (1988), in which observed velocity, temperature and salinity distributions were reported. They broadly classified the mixing pattern of warm water and river water into two types. One is the type of cold fresh water underneath warm salty water, and the other is the opposite type of warm salty water underneath cold fresh water. In both types, density distributions are stable.

Firstly, the mixing was studied experimentally in two-layered shear flows. The series of experiments were carried out on the above-mentioned two types. The longitudinal and the vertical components of velocity, temperature and salinity were measured simultaneously. The eddy viscosity and the eddy diffusivities of heat and salt in the vertical direction were estimated in relation with Richardson number. Secondly, a two-dimensional numerical model is applied to simulate the double diffusive shear flows. The mixing at the interface was presented as a function of Richardson number. The performance of the two-dimensional model was evaluated by comparison of numerical results with experimental measurements.

Experimental Study

It is generally known that mixing of warm water discharge and river water is a complicated and three-dimensional phenomenon. The vertical mixing is principally induced by a breaking of a internal wave and double diffusion at the interface. A front between two waters is formed in the horizontal direction, at which temperature and salinity change abruptly. It is difficult to experimentally represent these three-dimensional mixing. In this paper, the vertical mixing at the interface was studied in a two-dimensional open channel, which was essentially important to estimate warm water dispersion.

The series of experiment were carried out by using a flume, which was 1.8m wide, 1m depth and 20m long. The bottom and the side wall were made of stainless steel and plexiglass plate, respectively. The test section which was 11.8cm wide and 8m long was divided by the wall in the flume, avoiding the effect of the drain. Warm salty water and cold fresh water were made separately, and their temperature were controlled automatically. The outlet was vertically separated into two layers, by which two kinds of water were discharged simultaneously onto stagnant ambient fluid. First, the mixing process of warm salty water and cold fresh water was visually investigated. The fluorescent dye contained in lower discharge was visualized by a laser light sheet. The velocities in the vertical and the horizontal directions were measured with a fiber-optic laser velocimeter which reduced a optical error due to a density stratification. The salinity and temperature were measured by using a coductivity meter and a thermistor, respectively. The data were recorded after passing a low-pass filter with 1/200sec time interval, and the number of data per a measured point was 8,192. The experimental conditions are shown in Table.1, Figs.2 and 3, which were determined on the bases of the measurements of salinity and temperature distributions in

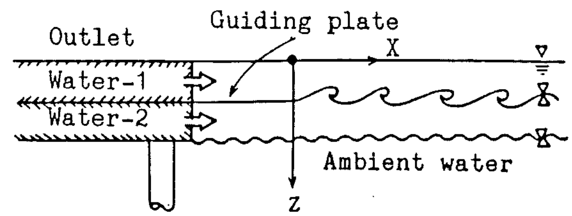

Fig.1 Schematic diagram of the experiment

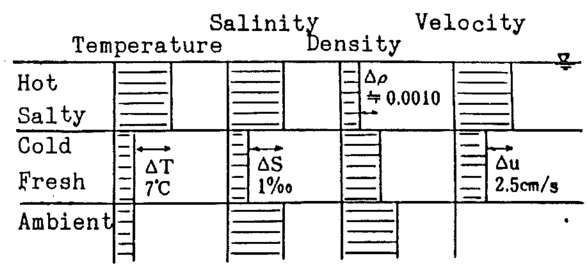

Fig.2 Definition of type (type-1)

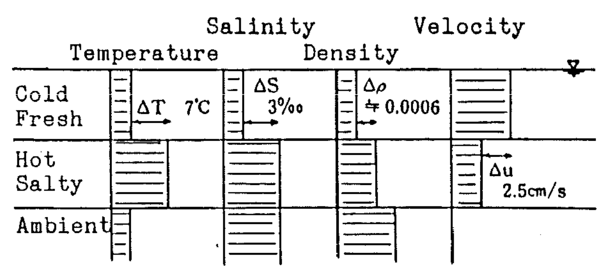

Fig.3 Definition of type (type-2)

Table.1 Experimental conditions

Case	Type	Upper T (℃)	Upper S (‰)	Upper U (cm/s)	Lower T (℃)	Lower S (‰)	Lower U (cm/s)	Density difference (g/cm³)	X*) (m)
1	1	28.3	10.2	2.5	21.4	8.9	5	0.001032	100
2		28.3	10.2	2.5	21.3	8.9	5	0.001056	50
3		26.8	10.2	5	18.8	8.9	2.5	0.001056	20
4		30.4	10.2	5	24.0	8.9	2.5	0.001039	20, 50
5	2	21.4	6.7	5	28.3	10.2	2.5	0.000628	100
6		19.0	6.7	5	26.5	10.2	2.5	0.000627	50
7		24.4	6.7	5	30.7	10.2	2.5	0.000620	20
8		24.4	6.7	5	30.7	10.2	2.5	0.000620	50

*) distance from the edge of the guiding plate

the coastal area.

The observed mixing processes are shown in Figs.4 and 5. In the type-2, the mixing was mainly caused by the breaking of K-H waves induced by the shear stress between upper and lower layers. Although type-1 is more stable on density stratification than type-2, the mixing at the interface in type-1 was clearly different from that in type-2, which primary depended on the double diffusion induced by the difference between the molecular diffusivities of heat and salt. Salt finger(for example, Turner (1973)) occurred due to the instability at the interface, increased the mixing.

The characteristics of the mixing process were investigated quantitatively. On the bases of the boussinesq's assumption, the eddy viscosity, eddy diffusivities of heat and salt in the vertical direction are defined as follows.

Eddy viscosity (A_v):

$$-\overline{u'w'} = A_v \frac{\partial u}{\partial z} \qquad (1)$$

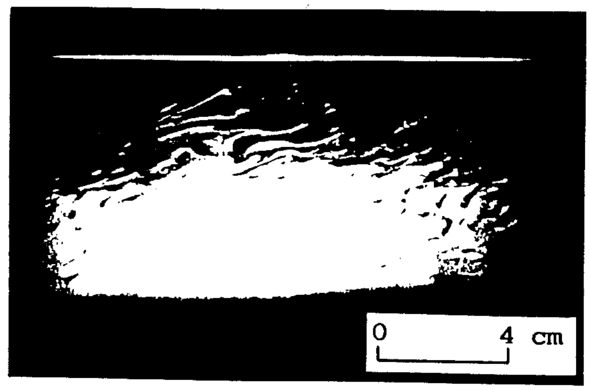

Fig.4 Mixing at the interface (type-1)

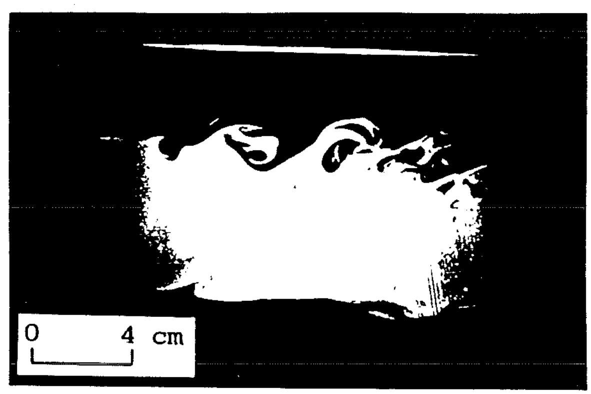

Fig.5 Mixing at the interface (type-2)

Eddy diffusivities ($K_{T,V}$, $K_{S,V}$):

$$-\overline{T'w'} = K_{T,v} \frac{\partial T}{\partial z} \quad \text{(heat)} \qquad -\overline{s'w'} = K_{s,v} \frac{\partial s}{\partial z} \quad \text{(salt)} \qquad (2)$$

Local Richardson number(R_i), turbulent Plandtl number(P_r) and turbulent Shimidt(S_c) number are written as follows.

$$R_i = -\frac{g(\partial\rho/\partial z)}{\rho_0(\partial u/\partial z)^2} \qquad P_t = \frac{A_v}{K_{T,v}} \qquad S_c = \frac{A_v}{K_{s,v}} \qquad (3)$$

It is expected that the thickness of the mixing layer(d) and the velocity difference between the upper and the lower layers(U) are essentially important on the mixing at the interface. The turbulent diffusion near a interface is suppressed (for example, Rodi (1980)), and expressed by a function of R_i. The non-dimensional eddy viscosity was written as follows.

$$Av/U \cdot d = f\ (Ri) \qquad (4)$$

The visualization denoted that the mixing processes were different between type-1 and 2. The eddy viscosities in two types were shown in Figs.6 and 7, respectively.

$$A_v/U \cdot d = 0.01(1+10 \cdot Ri)^{-1} \qquad \text{(type-1)}$$

$$A_v/U \cdot d = 0.01(1+25 \cdot Ri)^{-1} \qquad \text{(type-2)} \qquad (5)$$

In the same way, the eddy diffusivities of heat and salt are expected to be a function of R_i at a interface. Remarkable difference between the eddy diffusivities of heat and salt was not shown in the range of experiments. P_r and S_c were shown in Figs.8 and 9.

$$1/Pr = 1/Sc$$

$$= (1+2.5\,Ri)^{-1} \qquad (6)$$

These results qualitatively agree with the values using by Rodi(1980), Bloss(1988) and Ushijima(1988).

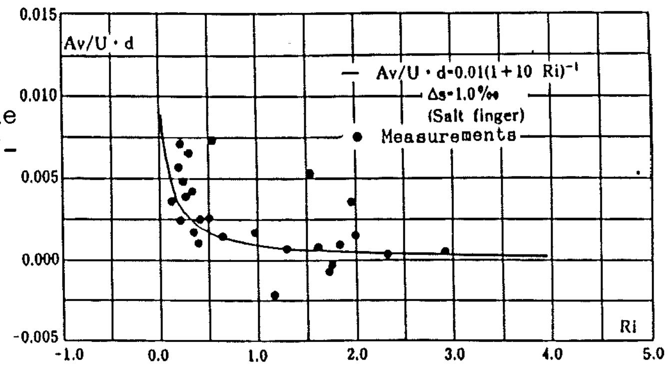

Fig.6 A_v vs. R_i (type-1)

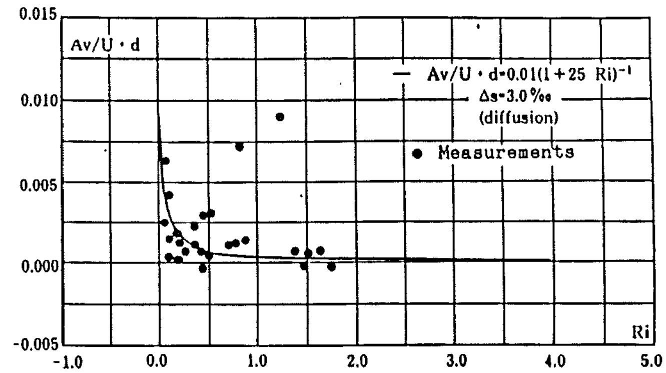

Fig.7 A_v vs. R_i (type-2)

Numerical Simulation

The investigation with a two-dimensional model which contains the empirical formulas for the eddy viscosity and the eddy diffusivities of heat and salt in the vertical direction, were carried out to study the mixing process of the double diffusive shear flows. Employing the Boussinesq approximation that density variation is account for only in the gravitational term, the governing equations for velocity, temperature and salinity are

Mass:

$$\frac{\partial u}{\partial x} + \frac{\partial w}{\partial z} = 0 \qquad (7)$$

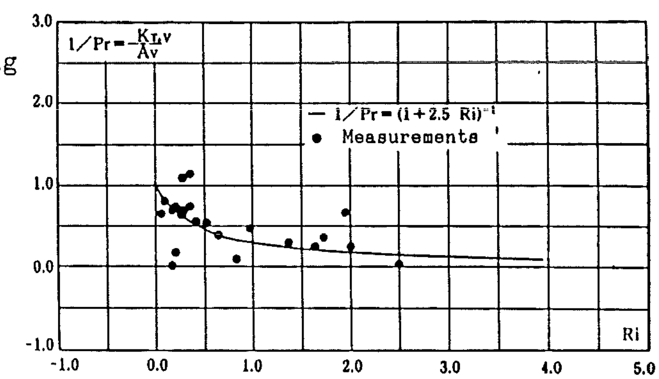

Fig.8 $1/P_r$ vs. R_i

Momentum:

$$\frac{\partial u}{\partial t} + u\frac{\partial u}{\partial x} + w\frac{\partial u}{\partial z}$$

$$= -\frac{1}{\rho}\frac{\partial P}{\partial x} + \nu\left(\frac{\partial^2 u}{\partial x^2} + \frac{\partial^2 u}{\partial z^2}\right)$$

$$+ A_h\frac{\partial^2 u}{\partial x^2} + A_v\frac{\partial^2 u}{\partial z^2} \qquad (8)$$

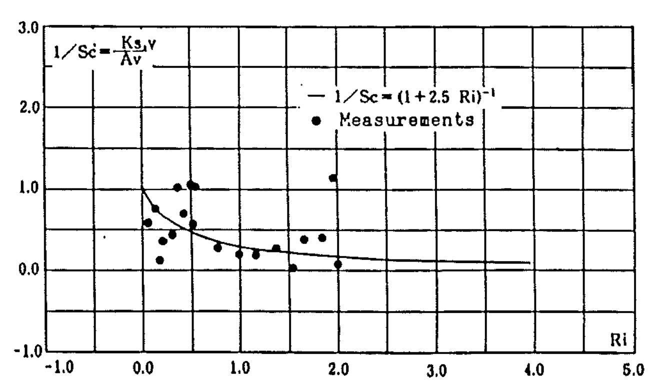

Fig.9 $1/S_c$ vs. R_i

$$\frac{\partial w}{\partial t}+u\frac{\partial w}{\partial x}+w\frac{\partial w}{\partial z}=-\frac{\Delta\rho}{\rho}g-\frac{1}{\rho}\frac{\partial P}{\partial z}+\nu\left(\frac{\partial^2 w}{\partial x^2}+\frac{\partial^2 w}{\partial z^2}\right)$$

$$+A_h\frac{\partial^2 w}{\partial x^2}+A_v\frac{\partial^2 w}{\partial z^2}$$

Temperature:

$$\frac{\partial T}{\partial t}+u\frac{\partial T}{\partial x}+w\frac{\partial T}{\partial z}=k_T\left(\frac{\partial^2 T}{\partial x^2}+\frac{\partial^2 T}{\partial z^2}\right)+K_{T,h}\frac{\partial^2 T}{\partial x^2}+K_{T,v}\frac{\partial^2 T}{\partial z^2} \quad (9)$$

Salinity:

$$\frac{\partial s}{\partial t}+u\frac{\partial s}{\partial x}+w\frac{\partial s}{\partial z}=k_s\left(\frac{\partial^2 s}{\partial x^2}+\frac{\partial^2 s}{\partial z^2}\right)+K_{s,h}\frac{\partial^2 s}{\partial x^2}+K_{s,v}\frac{\partial^2 s}{\partial z^2} \quad (10)$$

where ν, k_s and k_T denote the molecular viscosity and diffusivities, the subscripts h and v indicate the components in the horizontal and the vertical directions, respectively. The density of water was computed by using Knudsen's formula. The computational domain which represented the hydraulic experiment, and boundary conditions are schematically shown in Fig.10. The equations were discretized onto a grid using up-wind differencing for advection and central differencing for diffusion on a non-uniform mesh. The eddy viscosity and the eddy diffusivities are constant(10cm^2/s) in the horizontal direction, and are estimated by using Eqs. (5), (6) in the vertical direction. The mixing layer was defined by using the computed temperature or salinity distribution at one time-step before, in which gradient was over 20 percent of the maximum value.

The computed results were shown in Figs.11 and 12. The close agreement was obtained between calculated distributions of velocities, temperature and salinity, and experimental measurements. The difference at the 5cm depth was primary due to the representation of the guiding plate near the outlet in computations. Although measured turbulent intensities of velocities, temperature and salinity were scattered, the computational results were qualitatively in agreement with the measurements.

Conclusion

The mixing process in the double diffusive shear flow were studied both experimentally and numerically. In the case of cold fresh water

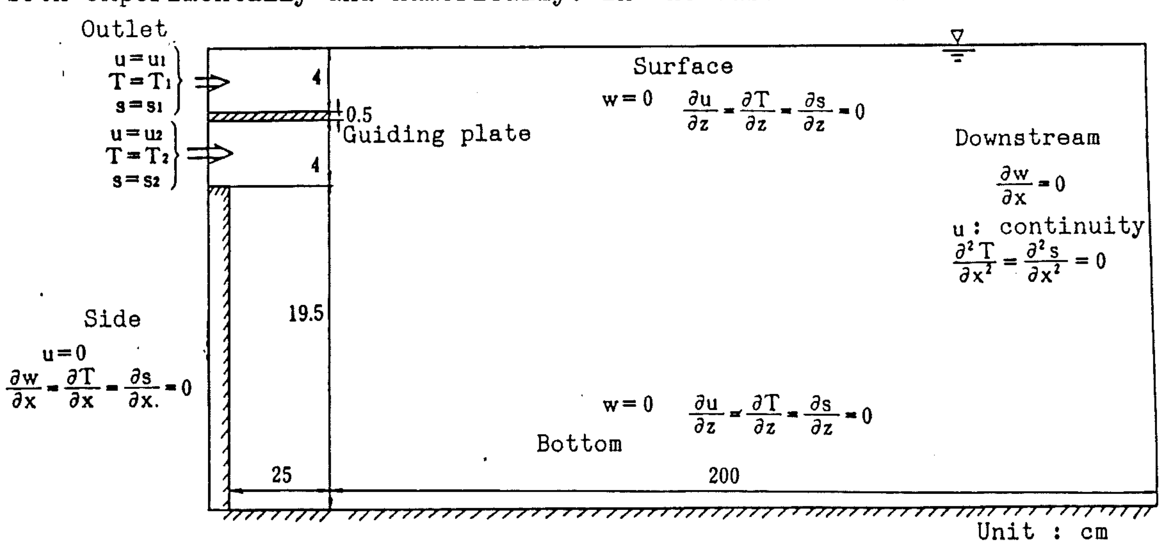

Fig.10 Computational domain and boundary conditions

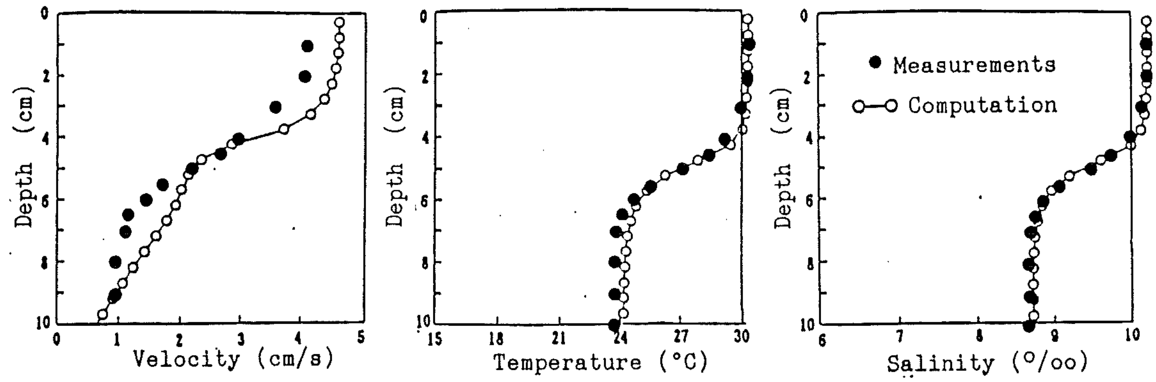

Fig.11 Comparison of computational results and measurements (type-1, case-4)

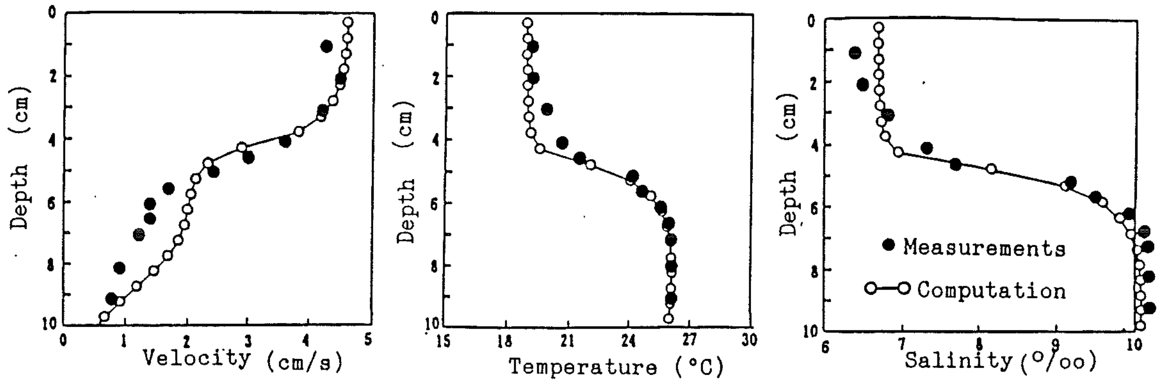

Fig.12 Comparison of computational results and measurements (type-2, case-6)

underneath warm salty water, the double diffusion occurred and increased the mixing at the interface. The opposite case, the mixing at the interface was mainly induced by the breaking of internal waves. The eddy viscosity and the eddy diffusivities of heat and salt in the vertical direction were investigated, and were presented as the functions of R_i. A two-dimensional numerical model was proposed, in which the mixing at the interface was estimated by using Eqs. (5), (6). The good agreement was obtained between experimental measurements and computational results.

The authors would like to thank Dr. Katano for giving much helpful advice, and the staffs of Japan Oceanographic Science Co., Ltd. and Denryoku Computer Center for Technical help.

Reference

1.Mizutori,M. and Katano,N.(1988),"Diffusion Processes of Warm Water Discharged in Stratified Environment", Proc. of Hydr. Eng. JSCE,pp239-244
2.Turner,J.S.(1973),"Buoyancy Effect in Fluid",Cambridge Univ. Press
3.Rodi,W.(1980),"Turbulence Models and Their Application in Hydraulics - A State of The Art review",IAHR
4.Bloss,S.,Lehfeldt,R. and Patterson,J.C.(1988),"Modeling Turbulent Transport in Stratified Estuary",J. Hydr. Eng.,Vol.114,No.9,ASCE,pp1115-1133
5.Ushijima,S. and Moriya, S.(1988),"Turbulence Measurements and Calculation of Stratified Shear Flow",CRIEPI report, U87070

THERMOHALINE INTRUSIONS IN A TWO COMPONENT DENSITY STRATIFIED SYSTEM

Ellen Thomas, S. Geoffrey Schladow, Jeffrey R. Koseff
Environmental Fluid Mechanics Laboratory
Stanford University
Stanford, CA 94305-4020

Abstract

Experiments were performed for a linearly stratified heat-salt system, uniformly heated at one endwall. The initial stratification was in the diffusive sense. Intrusions formed at the heated endwall and propagated out into the interior fluid. Three regimes of flow were identified, based upon the gravitational stability ratio, R_ρ, and a lateral stability parameter, R_l. In all regimes, a region of salt fingering developed due to gradient reversal at the heated endwall. Two very distinct merging processes were observed depending on the specific flow regime. The first process occurred under conditions of high gravitational and lateral stability, and appeared to be controlled by horizontal motions induced by the intrusions. The second process was observed under less stable conditions and was a result of vertical motions at the heated endwall within the intrusions themselves.

Introduction

Double diffusive convection typically occurs in vertically stratified thermohaline systems, where large differences in the diffusivities of temperature and salinity (NaCl) can lead to convective instabilities in what were initially gravitationally stable, diffusing systems. When the stabilizing gradient is provided by the component of lower diffusivity (salinity), the ensuing convection is termed the 'diffusive' mode. When the opposite is true, it is referred to as the 'finger' mode. In this paper we consider initial stratifications that conform to the 'diffusive' mode. When horizontal gradients of the components exist, a far greater variety of motions have been observed (see for example Turner, 1985). They generally, however, take the form of distinct intrusions propagating away from the region of maximum horizontal gradient.

While previous studies of the effects of lateral gradients have provided useful insight into the behaviour of these flows, most work has focused on the onset of instability, the thickness of the intrusions produced, and a qualitative description of the motions within the intrusions. With the exception of Turner and Chen (1974), these studies have also been limited to singly stratified systems. In this paper we focus on two issues related to the behavior of intrusions in a *two component* stratification. These are: 1) the internal structure of the intusions as a function of initial stratification and endwall heating rates and 2) the mechanisms governing the merging of the initial convective cells into larger intrusions.

System Description-Physical Apparatus

The system we consider comprises negative, linear gradients of both temperature and species in the vertical. The working fluid is water, and the species gradient is provided by common salt (NaCl). The net density gradient in the vertical is such that the system is initially gravitationally stable. Vertical fluxes of temperature and salinity at the top and bottom boundaries are assumed to maintain the linear gradients. At time t=0, a constant heat flux is applied to the initially quiescent system, and at some time thereafter intrusions begin developing at the boundary.

The experimental facility consists of a 4.0m long, 0.8m wide and 0.5m deep tank as shown in Figure 1. The walls are of composite construction, the inner pane being 6.25mm thick glass separated by a 6.25mm air gap from an outer plexiglas pane of similar thickness. Additional insulation is provided by external cladding on the bottom and sides of the tank made from 25 mm, high-density styrofoam sheeting. A constant heat flux at the lateral boundary is provided by radiant heating. At present a maximum flux of approximately 100W m^{-2} is produced at the inside surface of the wall.

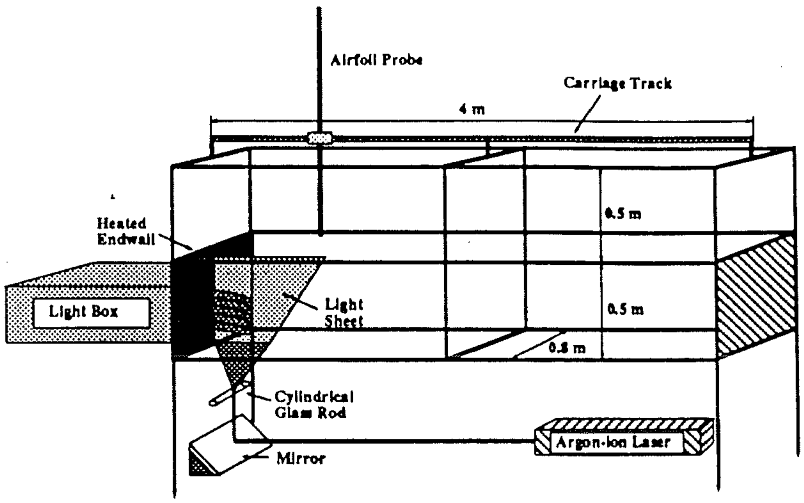

Figure 1: Schematic of experimental facility.

Fast-response thermistor (Thermometrics FP07) and conductivity (Precision Measurement Engineering 4-electrode) probes are used to obtain vertical temperature and salinity profiles. A thermistor / conductivity probe pair is mounted at the end of a chrome-alloy plated airfoil section which is driven vertically by a small DC motor. To measure a profile, the airfoil is driven down through the water column at approximately 10 cm s^{-1} and the output of each probe is sampled at 100hz. The raw conductivity and temperature data is low-pass filtered at 30 hz prior to computing the salinity.

Considerable use is made of video recording the flows as a means of reviewing experiments at a later time. Flow visualization is accomplished by using Rhodamine-B and Fluorescein dye illuminated by a laser light sheet. This is shown schematically in Figure 1. The camera views the experiment through a small port cut in the side insulation. Experiments are recorded at 30 frames per second by a monochrome CCD camera with 512 x 512 pixel resolution. Additional details of the physical apparatus, instruments and techniques are provided in Thomas et al. (1989).

Results

The general evolution of the intrusions is common to all experiments. Initially small roll cells develop along the heated wall. In time these become more elongated and take the form of a series of fully or partially mixed layers separated by sharp density interfaces. At a later time they thicken by merging with neighbouring intrusions. Between each layer, strong shear is created along the interfaces by flow moving away from the wall in the upper region and back towards the wall in the lower region. The shear velocities are O(1mm s^{-1}) whereas the propagation speed of the intrusion fronts are O(10) times smaller. Motions near the endwall are also generally common to all experiments. A parcel of fluid very close to the endwall appears to rise until the salinity retained by that parcel inhibits any further upward motion. The parcel is then forced out away from the wall, cools, becomes denser than the surrounding fluid, and as a consequence tends to fall. This produces the characteristic downward slope of the intrusions adjacent to the wall. Eventually the fluid is entrained by the counterflow that comprises the bottom of each intrusion. This process continues as the initial convective cells combine to form larger intrusions.

Internal structure of the intrusions

The specific flow behaviour and structure of the intrusions vary significantly depending on the stability of the system. To classify the experiments, we use two dimensionless quantities, $R_\rho = (\beta\partial S/\partial y)/(\alpha\partial T/\partial y)$ and $R_l = -(\alpha(q/k))/(-\alpha\partial T/\partial y + \beta\partial S/\partial y)_i$. Here α and β are the coefficients of thermal and saline expansion, respectively, q is the lateral heat flux, k is the thermal conductivity of the fluid, and T and S are the local tempature and salinity, respectively. The subscript i indicates initial conditions. Physically R_l may be interpreted as the ratio between the density gradient at the heated boundary to the initial, net vertical density gradient. Generally, a large value of R_l indicates strong lateral forcing and weak vertical stability, while a large value of R_ρ indicates weak double diffusive effects and large gravitational stability.

Three regimes of intrusions have been defined, based upon the initial values of R_ρ and R_l in each experiment. The intrusions are distinguished by their characteristic dimension (h), propagation velocity (u_p), temperature (T) and salinity (S) fields, as well as their ability to continue propagating after the heat flux is removed. The characteristics of the intrusions are summarized in Table 1. Sample profiles for Regimes I and II are shown in Figure 2. Since they are very similar to Regime II, profiles are not shown for Regime III. The step-like nature of the profiles indicates the presence of the horizontal intrusions or convecting layers.

Regime I flows, which evolve under conditions of relatively high gravitational and lateral stability, are more quiescent than flows in Regimes II and III. Overall the motions develop on a smaller scale and are characterized by lower velocities and less mixing. They are similar to the intrusions previously observed in single component stratifications. As can be seen in Figure 2a, a relatively strong stable temperature stratification develops within the intrusions, accompanied by a well mixed or sometimes slightly unstable salinity distribution.

Regime	Final h (mm)	u_p (cm/hr)	T	S	Self-Propagating?
I	<10	5-10	stably-stratified	well-mixed	no
II	10-40	10-30	stably-stratified	well-mixed	no
III	30-50	>25	well-mixed	well-mixed	yes

Table 1: Summary of characteristics in three flow regimes.

Motions in Regime II are seemingly more dynamic than those in Regime I. As in Regime I, the intrusions stop propagating when the applied heat flux is removed, and the layered structure eventually diffuses back to a continuous stratification. Overall, much more active convection is observed visually in this regime due to the lower stability and stronger shear. The depthwise profiles in Figure 2b indicate that within each intrusion the salinity is generally well mixed or slightly unstable, whereas the temperature develops a discernible stable stratification.

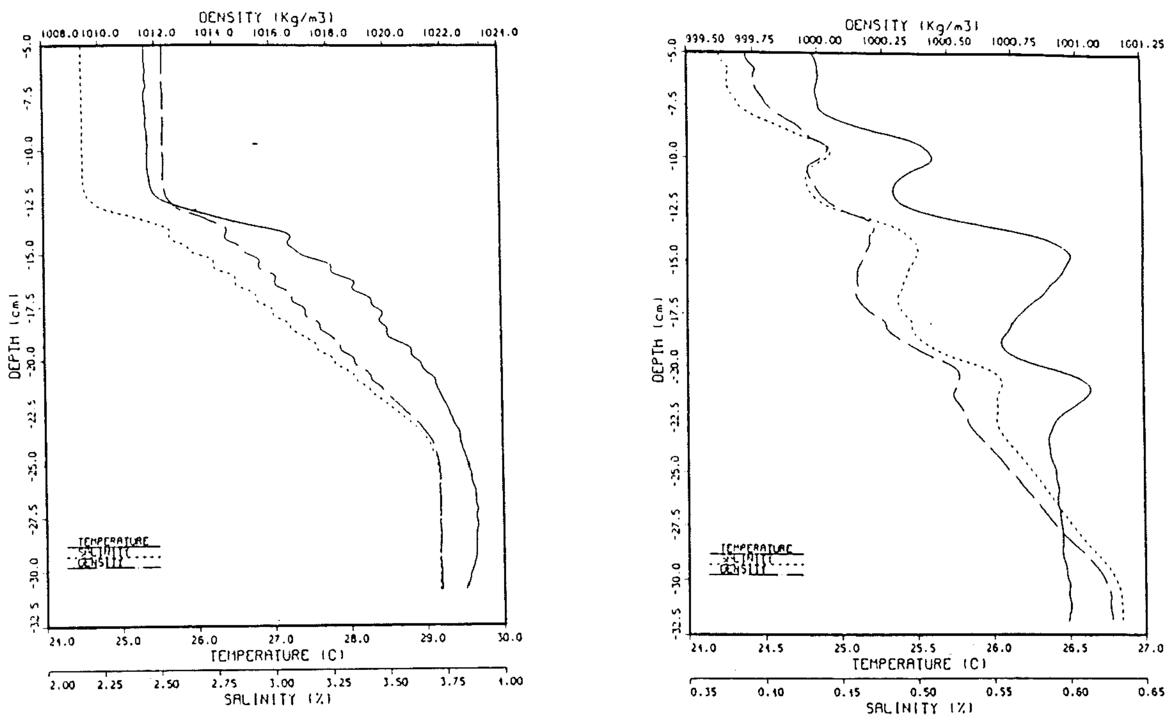

Figure 2: Vertical T, S, and ρ profiles, a) Regime I and b) Regime II.

Motions in Regime III are the most dynamic of the three regimes, and occur under conditions of relatively low gravitational and lateral stability. Within the developed intrusions, mixing of both properties occurs relatively rapidly, yielding uniform profiles of temperature and salinity over layer depths of 30-50 mm. As noted in Table 1, the distinguishing characteristic of Regime III flows is that the intrusions are *self-propagating*. That is, they continue to propagate out away from the endwall after the applied heat flux has been removed.

Merging

A sequence of images showing Regime I intrusions at times after initiation of heating is shown in Figure 3. Initially R_ρ was 8.3 and R_l was 0.9. Intrusions first appear after 10-15 minutes. At 21 minutes, the third intrusion from the top has begun to recede, and after 30 minutes has receded almost to the endwall where it becomes fully entrained by the adjacent overlying intrusion. After 41 minutes, the intrusion at the top of the region shown has merged with the intrusion above it, as has the partially shown intrusion at the bottom of the image. Thus the original set of seven intrusions has been reduced to four.

This sequence illustrates a case where the merging process is controlled by motions external to the intrusions themselves. It has been frequently observed that shear waves propagate ahead of the advancing intrusions. A vertical dye streak placed ahead of the intrusions would, for example, distort into a sinusoidal pattern reflecting the horizontal flows and counterflows of the intrusions. Flows ahead of the upper half of the intrusions move away from the wall, and are balanced by counterflows in the lower half. The middle intrusion of Figure 3 (the first to merge), initially behaves this way, but eventually the larger flow (and counterflow) of its neighbours literally overwhelms it, gradually forcing it back towards the wall.

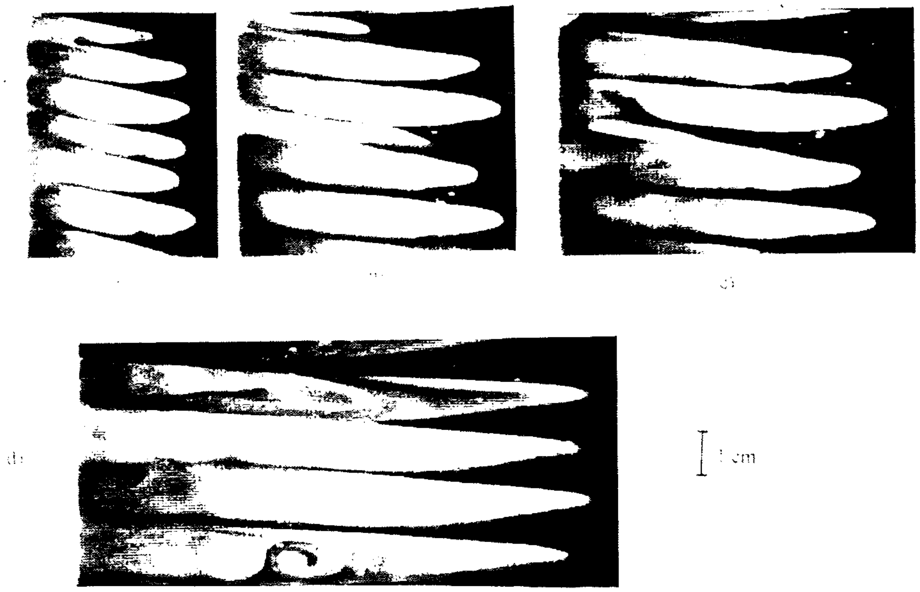

Figure 3: Regime I merging sequence, a) t=17.5 min, b) t=24 min, c) t=28 min, d) t=41 min

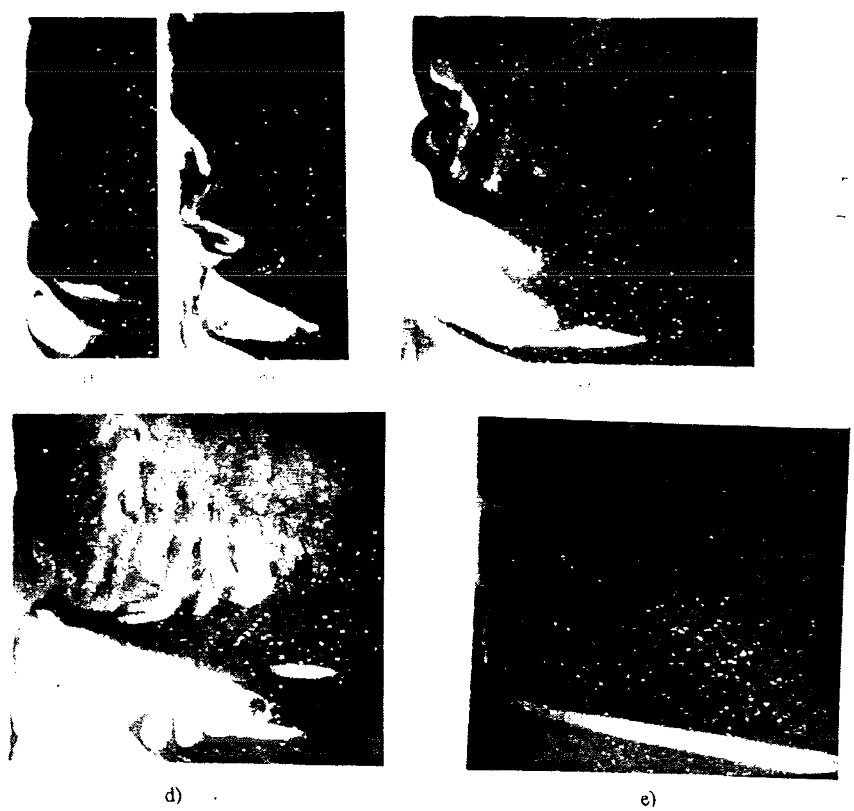

Figure 4: Regime II merging sequence, a) t=3.5 min, b) t=9.5 min, c) t=17 min, d) t=22 min, e) t=51 min.

The second type of merging process observed suggests that motions within the intrusions themselves may have a role in the merging process. A sequence of images for a Regime II flow is shown in Figure 4. Initial values of R_ρ and R_l were 3.2 and 10.8 respectively. In this case, intrusions began to form ~1-2 minutes after initiation of heating. Although only one intrusion can be seen at early times in Figure 4 due to the absence of dye, intrusions are present throughout the entire depth of the image. At later times dye has been entrained from the lower intrusion, as well as the overlying mixed layer, so that motions could be visualized over the whole depth.

The initial formation takes place much more rapidly and is followed by a merging process dominated by strong vertical motions near the heated endwall. After 10 minutes the intrusion marked by dye in Figure 4 is already beginning to merge with the intrusions above it. In contrast to Regime I, the merging appears to be caused by penetration of the vertical motions near the endwall into the adjacent layers. This penetration leads to interface breakdown, in the vicinity of the wall only, and subsequent merging of the adjacent layers. After about 19 minutes, the intrusions have reached their final thickness. By this time fingering motions are clearly visible in the upper layer due to the process described earlier in which warm, salty water is inserted above colder, fresher water as a result of the lateral heating.

Conclusions

Experiments to date indicate that the presence of the destabilizing component (temperature) in the vertical density gradient leads to processes not observable with only single component stratifications. Using two dimensionless parameters to classify stability, three regimes of intrusions have been distinguished . The internal structure of the intrusions, as characterized by vertical profiles of temperature and salinity, intrusion thickness, propagation speed, and self-propagation varies significantly depending on the specific flow regime. A region of salt fingering occurs within the intrusions for all flow regimes, as a result of gradient reversal in the vicinity of the heated endwall.

The merging process was also found to differ between regimes. Two types of merging have been described. The first, observable in Regime I flows, appears to be controlled by the motions induced by the intrusions. The second, observable in Regime II, is the result of motions at the heated sidewall within the intrusions themselves. These motions allow the interface between two adjacent intrusions to be eroded, resulting in a merging process that advances out from the endwall. In no case was merging found to be caused by shear instability or by an equalization of density across the length of an intrusion interface.

Acknowledgements

This work is supported by the Department of Energy under grant DE-FG03-87ER13757.

References

Thomas, E., Schladow, S.G. and Koseff, J.R. (1989), "The Formation of Lateral Intrusions in a Thermohaline Stratification", Proc. Seventh Symposium on Energy Engineering Sciences, Argonne National Laboratory, June 19-21, pp. 137-144.

Turner, J.S. and Chen, C.F. (1974), "Two-Dimensional Effects in Double Diffusive Convection", J. Fluid Mech., **63**, pp. 577-592.

Turner, J.S. (1985), "Multi-component Convection", Ann. Review of Fluid Mech., **17**, pp. 11-44.

The Double-Diffusive, Convective Behavior of

a Sharp, Vertical, Sediment-Concentration Gradient

T. Green and E.S. Mogahed
Department of Civil and Environmental Engineering
University of Wisconsin-Madison

1. INTRODUCTION

The settling of small particles in water is fundamental to sedimentation. There are almost countless studies of particles moving downward through a fluid, under the influence of gravity. Sometimes, however, the water itself plays an active role in the process. When the particles are very small, they tend to move with the water. When they are also very numerous, the sediment-water suspension often can be considered a continuum, and be described by the equations of continuum mechanics. "Convective" motions are those driven by variations in the density of the suspension itself, in conjunction with the force of gravity. Such motions can transport particles very efficiently, and are of great interest in industrial processes. They have also been mentioned in sedimentology, but may well merit much more attention.

A complication arises when the suspension density is also changed by changes in temperature or by changes in the concentration of a dissolved substance. This occurs often in lakes and coastal regions. For example, rivers can carry a substantial amount of sediment to the ocean (Burton, 1988). This muddy water will sink to its own density level in the receiving water, which is usually stably stratified by temperature (or salt content). That is, one often finds a layer of warm, sediment-laden water overlying colder, clearer, but denser water. Such situations have been documented by Whitney (1937), Bryson and Suomi (1951), Drake (1971), Pharo and Carmak (1979), and others, and have figured prominently in several nearshore deposition models (Pierce, 1976).

Houk and Green (1973) pointed out the rather obvious relation between these situations and the well-studied "double-diffusive" situation in which warm, salty water overlies colder, fresher, and denser water, and conducted some simple experiments to verify the analogy. Similar but more qualitative experiments were conducted by Bradley (1965), whose work came before the ideas of double diffusion were well known. This situation is gravitationally stable, but dynamically unstable. Sediment diffuses by Brownian motion, and much more slowly than either heat or salt. Then the gradient of the stabilizing contributor to the vertical density gradient (heat or salt) is removed quickly, leaving the unstable sediment gradient. Fingers form, which carry sediment downward very efficiently.

Green (1987) compared the results of experiments of Houk and Green (1973) with similar heat-salt results by Green and Kirk (1971), and then used flux laws found by several other workers in heat-salt double diffusion to suggest a criterion for when "sediment fingering" would occur, and dominate Stokes settling at an originally sharp horizontal interface separating warm, muddy water from lower, colder, clear, and denser water. This suggestion was based on rather crude arguments. For example, the interaction between Stokes settling and convection of the suspension was neglected. However, it did suggest that double-diffusive fingering could be quite important in nature.

2. THE EXPERIMENTS

The experiments were conducted in a small tank having two identical compartments, side-by-side. Each compartment is 8 cm square in the horizontal, and has upper and lower parts which are separated by a thin, horizontal plate. The upper part is 7 cm high, the lower part 20 cm high. This arrangement allowed two different experiments to be run simultaneously, and compared. A commercial Talc powder (specific gravity 2.72 g/cm^3) was used as the sediment. The density of the lower, clear, deionized water was adjusted by adding sucrose. The initial density differences between the upper suspension and the more dense, lower, clear water were fixed at 0.5 g/l ($\pm$ .01). To avoid coagulation, 5 g/l of Calgon was used in both the suspension and the clear water. All experiments were run at room temperature (20$\circ$C). Great care was taken to avoid heating by the lighting, which tended to induce secondary motions. The sediment size ranges were obtained using free settling in a long cylinder. Densities of the suspension and clear (sugar-) water were measured with a Mettler-Paar DMA 46 density meter, to an accuracy of .01 g/l. The lower part of each compartment was filled with clear distilled water containing a known amount of dissolved sucrose, covered by the horizontal plate and sealed with grease. The less-dense suspension was then poured slowly into the upper part, to a depth of 5 cm. After both suspension and clear water had come to rest, the experiments began by gently sliding back both plates. The flow patterns were made visible by the sediment, and were photographed every few seconds. Observations were also made from all possible vantage points and recorded, with sketches. (These notes and sketches proved to be important: many very fine scale flow features did not appear clearly in the pictures.)

3. GENERAL OBSERVATIONS

The somewhat random nature of the observed convective motions together with the two-dimensional character of the data (i.e., the pictures) made accurate quantitative information difficult to obtain. The results given below are based primarily on the pictures, but also rest heavily on the visual observations in cases where the more subtle and/or finer scale motions did not appear clearly in the pictures. However, the general behavior noted (and the somewhat fragmentary numerical estimates) seem to be quite typical of at least the well formed flow structures.

Two downward-moving features were seen, in addition to Stokes settling:

(a) FINGERS: distinct columnar structures with clearly defined mushroom-shaped heads. These heads usually evolve into vortex rings, which then become unstable and break up, producing yet more fingers. The rings are quite likely associated with a shear instability, due to the strength of the fingering motion, and have been discussed in a qualitative fashion by Bradley (1965), Shirtcliffe (1972), and Green and Schettle (1986). Such rings do not seem to be typical of salt fingers. Following past terminology, fingers observed in our experiments will be called "sediment fingers."

(b) CLOUDS: globular, bulk downward motions of the suspension, apparently moving as an entity. This phenomenon will be referred to as "settling convection," following Kuenen (1968), although it should be noted that his experiments had no dissolved-substance gradient. These clouds descended as a single plume, for large sediment concentration C, which had a periodic behavior (like water dripping from a faucet). After perhaps five such "drips", fingers occurred at the (still fairly sharp) interface. The fingers also occurred in pulses, which will be described in more detail later. For smaller C, several clouds appeared at once, more-or-less evenly spaced horizontally across the interface. Also, the fingers appeared sooner (say, after the third cloud pulse). These clouds soon merged with each other, became quite convoluted, and were thus very hard to describe. In all cases, they descended much faster than any individual particle. Side-wall effects were clearly important, especially for large C, in which cases the fluid rose only around the outer edges of the apparatus. It should be pointed out here that such clouds may in fact be many tiny fingers, which were obscured by their small size, and the graininess of the film. This will be discussed below.

4. THE PERIODIC NATURE OF THE FINGERS

For a wide range of particle diameter d, direct visual observations together with the successive photographs showed that the generation of fingers was periodic. That is, the fingers are produced in pulses. The descent velocity of succeeding pulses diminished, and the horizontal spatial frequency of the fingers decreased. Fingers appeared at the same sites along the interface from one pulse to the next, but some sites became inactive with each succeeding pulse. This seems in accord with intuition, since each succeeding pulse grew from a less concentrated upper layer. Up to four pulses were seen in an experiment. The phenomenon is similar to that reported by Sparrow et al (1970) for the instability of a thermal boundary layer just above a heated plate. It should be noted that such pulses were always seen (for a wide d range), although a very strong first pulse then could almost totally obscure the following pulses.

Sparrow et al (1970) successfully explained their observations by using a theory due to Howard (1964). It seems that we can do the same, but perhaps more qualitatively and with some modifications. According to the model of Howard (modified to suit our case), fingers were produced by a periodic process, each period of which consists of a local concentrating phase followed by a break-off and mixing phase. At the beginning of the concentrating phase, the suspension adjacent to the sharp interface is envisioned as having a uniform concentration which may be different from that of the rest of the top layer. As a result of vertical diffusion (from below) and settling (from above), the thickness and concentration of the boundary layer surrounding the originally sharp interface is such that the corresponding local Rayleigh number **R** exceeds a critical value. This locally unstable boundary layer becomes unstable and breaks up, thereby producing a pulse of fingers. The mixing and agitation associated with the break-up of that boundary layer, together with the continuing settling and diffusion, restore the fluid adjacent to the interface to a uniform, stable regime, and the entire process begins again, with period t_p.

Howard's model thus offers a method to predict the duration of the concentrating phase, based on the postulate that the duration of the break-off phase is much shorter than that of the concentrating phase, t_*. The Rayleigh number of the sediment suspension (here, the unstable substance) in the boundary layer is estimated from

$$\mathbf{R} = \frac{\alpha g \delta^3 C}{\kappa \nu}$$

where g is gravity, ν kinematic viscosity, and α the coefficient of expansion. The diffusivity κ is calculated assuming Brownian motion (see, eg, Friedlander, 1977), and using the median grain diameter. The boundary layer thickness δ is taken to be the distance below the interface at which the sediment concentration is calculated to differ from that in the fluid for above the interface by only 5%. (Thus, both δ and **R** increase with time.) Then, the boundary layer becomes unstable when $\mathbf{R} \sim 10^3$, according to linear stability theory for a uniform vertical gradient over a thin layer. The time at which this occurs is t_*.

The observed pulse periods t_p are shown for several typical experiments in Table 1. These pulse periods were used to calculate δ (which assumes that $t_* \sim t_p$), and thus **R**. Note that the calculated **R** values are all on the order of 10^3. However, **R** generally decreases with increasing d and C. Thus, settling seems to make the boundary layer more unstable. The finger width is about the same size as δ. This is also in accord with the uniform-gradient theory. The statements above relating frequencies to C and d are also borne out by the results in Table 1. See Mogahed (1988) for an expanded discussion of these calculations.

$d(\mu)$	C(g/l)	t_p(sec)	k (finger/cm)	δ	**R**
<10	9.8	18	2.4	3.8	1600
<20	2.0	29	2.2	4.8	3300
<22	4.2	20	2.0	3.8	1900
<25	4.9	16	2.0	3.6	1350
<40	9.8	12	1.0	3.1	900

Table 1. Observed pulse periods (t_p), spatial finger frequencies (k), estimated boundary layer thickness (δ) and local Rayleigh numbers (**R**) for some typical experiments.

5. DISCUSSION

Settling seems to make the originally sharp interface less stable, as noted above. This appears physically reasonable, and is in accord with the results of some instability calculations made by using a Galerkin technique, along the lines of those made by Green (1990) for a porous medium. However, a quantitative measure of this tendency is not yet available.

The sediment-finger phenomenon could conceivably also be important to the vertical motions and distribution of plankton, which are also known to exhibit layering (see, e.g., Derenbach et al., 1979). In this case, the particle density is very close to that of water

(Reynolds, 1989), and the reasoning of Green (1987) gives the criterion for the vertical convective flux to exist and be much greater than that due to settling:

$$C^{1/3}\ \delta\rho^{-2/3}\ d^{-2} >> 10^5 \tag{1}$$

Here, cgs units are used, and $\delta\rho$ is the (small) density difference between the particles and water. This criterion may be satisfied when C has a large value typical of a bloom. For example, for $C = 10^{-5}$, $\delta\rho^{-2}$, and $d = 10^{-4}$ cm ($1\ \mu$), the left side of (1) is 10^9. Thus, the possibility would seem to deserve checking.

The relation between settling convection and fingering is still unclear. However, close scrutiny of the pictures suggests that settling convection may actually be fingering with a very high spatial frequency, k. It was very hard to pick out individual fingers with k > 5 fingers/mm (i.e., a finger width of 100μ). Such fingers would still be large enough so that the suspension may behave as a continuum (at least for small d). Thus, the first pulse may appear to the naked eye (and camera) to be a continuous descending cloud. Succeeding pulses would be more clearly seen, as the number of fingers (and k) diminishes with increasing time.

A related complication is that individual fingers, especially after some vortex ring activity, tend to become less well defined, and to merge. This may prove to give a natural limit to finger length, and to be loosely related to the ideas of Stern (1960) and others, which focus on the instability of well-developed heat-salt fingers. The vortex rings may also lead to a layering phenomenon such as is often seen in situations where double-diffusive activity exists, so that a layer thickness may be related to the distance below the interface at which vortex rings appear. Similar experiments in a much larger tank may resolve such matters.

A final point regards coagulation, and its relation to the double-diffusive phenomenon discussed in this paper. Green (1987) considered this relation in some detail, for an originally sharp interface and concluded that coagulation, because of the larger time scales involved, would have little effect in a situation such as that envisioned above. However, the interaction in other, more natural situations requires study, along with the relation of double-diffusive phenomena to "marine snow".

REFERENCES

Bradley, W.H. 1965. Vertical density currents. Science, 150, pp. 1423-1428.

Bryson, R.A. and Suomi, V.E., 1951. Midsummer Renewal of Oxygen within the Hypolimnion. J. Marine Research, 10, pp. 263-269.

Burton, J.D. 1988. River Inputs to Ocean Systems. UNESCO technical papers in marine science #55, 25 pp.

Derenbach, J.B., Astheimer, H., Hansen, H.P., and Leach, H. 1979. Vertical Microscale Distribution of Phytoplankton in Relation to the thermocline. Marine Ecology Progress Series, 1, pp. 187-193.

Drake, D.E., 1971. Suspended sediment and thermal stratification in Santa Barbara Channel, California. Deep-Sea Research, 18, pp. 763-769.

Green, T. and Kirk, R.G., 1971. Descent Rates of Salt Fingers. Nature: Physical Science, 232, Aug. 9, 1971.

Green, T., and Schettle, J.W. 1986. Vortex rings associated with strong double-diffusive fingering. Physics of Fluids, 27, pp. 2109-2112.
Green, T., 1987. The importance of double diffusion to the settling of suspended material. Sedimentology, 34, pp. 319-331.

Green, T., 1990. The Momentary Instability of a Saturated Porous Layer with a Time-Dependent Temperature Distribution. Water Resources Research (in press).

Houk, D., and Green, T. 1973. Descent rates of suspension fingers. Deep-Sea Research, Vol. 20, pp. 757-761.

Howard, L.N. 1964. Convection at high Rayleigh number. Proc. 11th Int. Cong. Appl. Mech. (Ed. H. Gortler.), Spring-Verlag, Berlin, pp. 1109-1115.

Kuenen, Ph. H. 1968. Settling Convection and Grain-Size Analysis. J. Sedimentary Petrology, 38, pp. 817-831.

Mogahed, E.A. 1988. Theoretical and Experimental Investigation of Double-Diffusive Instability at a Sharp Interface. Ph.D. Thesis, Dept. of Civil and Environmental Engineering, University of Wisconsin-Madison, 141 pp.

Pharo, C.H. and Carmak, E.C. 1979. Sedimentation processes in a short residence-time intermontane lake, Kamloops Lake, British Columbia. Sedimentology, 26, pp. 523-541.

Reynolds, C.S. 1989. The Ecology of Freshwater Phytoplankton. Cambridge University Press, NY.

Schettle, J.W., 1978. A study of surface plumes with suspension fingering. University of Wisconsin M.S. Thesis, 55 pp.

Sparrow, E.M. and Husar, R.B. and Goldstein, R.J., 1970. Observation and Other Characteristics of Thermals, J. Fluid Mech., 41, pp 793-800.

Stern, M.E., 1960. The salt fountain and thermohaline convection. Tellus, 12, pp. 172-175.

Whitney, L.V., 1937. Microstratification of the waters of inland lakes in summer, Science, 85, pp. 224-225.

FORMATION OF WAVES IN THERMAL STRATIFIED FLOW

W. HÄFNER, Battelle-Institut e.V.
Am Römerhof 35, 6000 Frankfurt, FRG
and
J. H. SPURK, Technische Hochschule Darmstadt
Petersenstr. 30, 6100 Darmstadt, FRG

Abstract

Based on experimental research at the large scale HDR test facility, an analytical investigation has been conducted in order to understand the instabilities at the transition layer between the cold and the hot fluid in a thermal stratified flow in horizontal pipelines. A similarity solution is given for the velocity and temperature distribution in the transition layer. The observed waves are identified as Kelvin–Helmholtz instabilities; the stability is determined by the gradient Richardson number. The theoretical results are in excellent agreement with the experimental data.

Introduction

In recent years a particular form of crack formation has been observed in a number of pressurized water reactor (PWR) as well as in boiling water reactors (BWR) on the internal surface of horizontal feedwater piping. The appearance suggested a fatigue crack, even though the reason for the corresponding necessary stress cycles was at first not apparent. It has subsequently been shown that these cracks were caused by thermal stratified flows, which may occur under certain operating transients associated with reduced feedwater mass flow. Under such conditions a rather thin transition layer forms with large temperature gradients between the cold water at the bottom and the hot water in the upper part of the pipe. Despite the strong stability of the overall stratification, instabilities at the interface have been observed under certain flow conditions. These oscillations result in fluctuating thermal loads to the pipe inside surface. An experimental test program has been conducted at the large scale HDR facility in Karlstein (FRG) to obtain detailed and consistent sets of experimental data.

HDR Stratification Experiments TEMR

To investigate the thermal stratified flows and to analyse the formation of waves at the transition layer, the TEMR test series has been performed at the HDR test facility. Figure 1 shows the horizontal test section, consisting of an approx. 6 m long pipe with 400 mm diameter. The cold water is supplied through the vertical inlet pipe. Along the horizontal pipe several measurement sections have been inserted; tube I is fitted with extensive instrumentation (shown in fig. 2). Overall test conditions were:

system pressure:	p	=	1 – 40 bar
initial hot water temperature:	ϑ_h	=	100 – 250 °C
injected cold water mass flow:	m_c	=	3 – 46 t/h

The cold water inlet temperature ϑ_c was always kept at 30 °C. Further details about facility and experiments are provided in the design report [1] and in the data report [2].

Experimental Results

The strong global stability of the stratification even over long flow paths, is a characteristic feature of the investigated flow. The small thickness of the transition layer between the cold water at the bottom and the hot water at the top of the pipe is of particular significance for the development of thermal stress. Figure 3 shows a measured temperature profile for an experiment without wave formations. This small transient layer and the associated large temperature gradients are the result of laminar flow, where the heat transport transverse to the flow direction is due to conduction. Wave formation has been observed only at four TEMR experiments. The conditions of these tests are characterized by high injection mass flow rates. The measured temperature profile shown in fig. 4 is obtained from an experiment with wavy transition layer. This is recognized from the apparent broadening of the layer caused by viewing the oscillatory motion of the interphase by temperature sensors at fixed positions.

A characteristic feature of these waves is the extended start up time due to intermittent perturbations, which appear as irregularities. An example for a completely developed wave motion is shown in fig. 5.

Evaluation of Experimental Data

For the load functions of the pipe wall, typical frequencies and amplitudes of the temperature fluctuations are needed. The amplitudes were counted by means of the rainflow analysis. Characteristic frequencies have been determined from spectral analysis, and the dominating frequencies at quasi steady state conditions is in the range of 0.4 to 0.7 Hz. Figure 6 shows a typical result of a Fourier analysis, where the frequency spectra of all transducer signals in the transition layer has been superimposed. This summation process results in:

- suppression of unimportant frequencies,
- enhancement of significant frequencies,
- display of the frequency shift during initiation process.

Analytical Estimate of the Local Instability

Oscillatory sequences of movements under steady state boundary conditions are expressions of hydrodynamic instabilities. These are conditions under which small perturbations to the motion of the flow can grow. For thermally stratified flows, Benjamin [3] distinguishes three different types of instability:

- Tollmien-Schlichting waves close to solid walls cased by friction.
- Surface waves produced by shear stress influences on the surface (wind-sea).
- Kelvin-Helmholtz waves arising due to an imbalance of inertia over the stabilizing effect of buoyancy.

The agreement between characteristic features of the experiment and the analytical assessment confirms the assumption of Kelvin-Helmholtz waves occurring in TEMR. The mechanism of this instability is practically independent of viscosity, being governed by the vertical distribution of temperature and velocity. The velocity profile, however, is determined by friction. Hazel [4] has shown that the stability characteristics for such inviscid two-dimensional shear flows are determined by the Richardson number

$$\mathrm{Ri} = -\frac{g}{\varrho}\,\frac{\partial\varrho/\partial y}{\left[\partial u/\partial y\right]^2}\,, \qquad (1)$$

where y is the coordinate normal to the axial direction. The density ϱ and the velocity u are assumed to be independent of the axial position x.

Because the flow is laminar, the velocity and temperature profiles can be found from a similarity solution of the laminar mixing layer [5]. Introducing the stream functions ψ defined as $u = \partial\psi / \partial y$; $v = -\partial\psi / \partial x$ and the similarity variable η:

$$\eta = y \sqrt{\frac{U_\infty}{\nu \ x}} \quad , \tag{2}$$

where ν is the kinematic viscosity and U_∞ the undisturbed velocity outside the transition layer, the dimensionless streamfunction ϕ is found as:

$$\phi(\eta) = \frac{\psi}{\sqrt{\nu \ U_\infty \ x}} \quad . \tag{3}$$

Since the pressure is constant, the Blasius equation

$$2\phi''' + \phi \, \phi'' = 0 \, , \tag{4}$$

is obtained while the energy equation with the boundary layer assumption results in

$$u \frac{\partial\vartheta}{\partial x} + v \frac{\partial\vartheta}{\partial y} = \frac{\nu}{Pr} \frac{\partial^2\vartheta}{\partial y^2} \quad , \tag{5}$$

where $Pr = c_p \, \mu / \lambda$ is the Prandtl number. With the viscosity μ, the stream function ϕ, and the dimensionless differential temperature

$$\Theta(\eta) = \frac{\vartheta - \vartheta_c}{\vartheta_h - \vartheta_c} \quad , \tag{6}$$

the second order differential equation

$$\Theta'' + \frac{1}{2} Pr \, \phi \, \Theta' = 0 \quad , \tag{7}$$

for the temperature is obtained. Particular attention has been paid to the temperature dependency of the flow properties. The best agreement with the experimental data was obtained using constant values for the entire transition layer based on average temperature. The results, however, differ insignificantly from those using piecewise constant flow properties which lead to two different Ri numbers at the point of discontinuity.

The solution for the dimensionless velocity and temperature distribution satisfying the boundary conditions:

$$\begin{aligned} \phi'(\infty)_c &= 1. & \qquad \theta(\infty)_c &= 0. \\ \phi'(\infty)_h &= 0. & \qquad \theta(\infty)_h &= 1. \\ \phi \ (0) &= 0. & & \end{aligned} \tag{8}$$

is shown in figs. 7 and 8. From these solution we obtain with

$$u = U_\infty \phi' , \qquad (9)$$

(2) and (6) the velocity and temperature distributions for every axial position x along the flow path. Figure 9 shows a comparison of the measured temperature distribution with the analytic profile for experiment T33.19. In despite of the simplifying assumption leading to the similarity solutions, the analytical results are in excellent agreement with the experimental data. The calculated temperature profile is expectedly slightly steeper than the measured one.

Again, with (2) and (6) the gradient Richardson number (1) is

$$Ri = \frac{g\ \beta\ (\vartheta_h - \vartheta_c)}{U_\infty^2} \frac{\Theta'(\eta)}{\phi''(\eta)^2} \sqrt{\frac{\nu\ x}{U_\infty}} , \qquad (10)$$

where the expansion coefficient β has been used to express the density gradient through the temperature gradient. The stability analysis is performed using θ' and ϕ'' at $\eta = 0$ (the largest gradients occur in the middle of the transition layer). Figure 10 shows the calculated Richardson number for T33.19 as a function of the axial position x. Over the entire flow length of 5 m the curve is within the unstable range $Ri < 0.25$. The summary of the stability analysis in fig. 11 shows unstable conditions for the experiments T33.15, T33.16, T33.19 and T33.25. Stable conditions are predicted for the 13 other experiments. These results agree with the experimental observations.

Above the stability limit, the most unstable wave has the wavelength λ which does not depend strongly on the shapes of the velocity and temperature profiles but rather, and primarily, on the thickness of the transition layer [4]; for smooth profiles, $\lambda = 6.3$ h.

The stability depends on the ratio of velocity to temperature profile as shown by Hazel. Figure 12 shows the dependence of the most unstable wave number $\alpha = kh/2$ as function of thickness ratio $r = \delta_u / \delta_t$. By defining the layer thickness at 99% of the undisturbed values for both, the temperature and the velocity profile, the most unstable frequency is calculated from

$$f_c = \frac{U_\infty}{h} \frac{\varrho_c}{\varrho_c + \varrho_h} \frac{\alpha}{2\ \pi} . \qquad (11)$$

The computed frequencies for T33.19, at position x = 4 m, are about 1 Hz. Compared to the value of .68 Hz determined by the Fourier analysis, the agreement is satisfactory.

From the results we conclude that the present analytical method allows one to asses flow stability and thus avoid operating conditions, that lead to damage of horizontal feedwater pipes.

Literatur

[1] Schygulla, U.; Wolf, L. : PHDR working report No 3.495/86, (1986).
[2] Wenzel, H.; Grimm, R; Löhr, L. : PHDR working report No 3.497/86, (1986).
[3] Benjamin, T.B. : J. Fluid Mech. 16, 436–50, (1963).
[4] Hazel, P. : J. Fluid Mech. 51, 39–61, (1972).
[5] Lock,R.C. : Quat. Journal Mech. and Applied Math., vol IV, (1951).

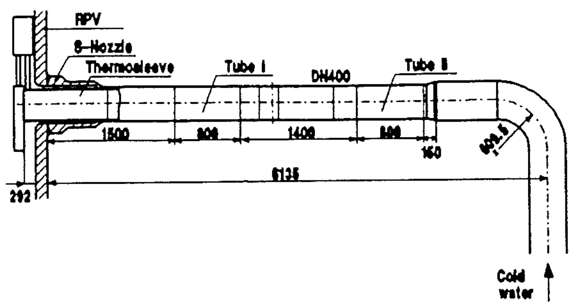

Fig.1: HDR-TEMR test section

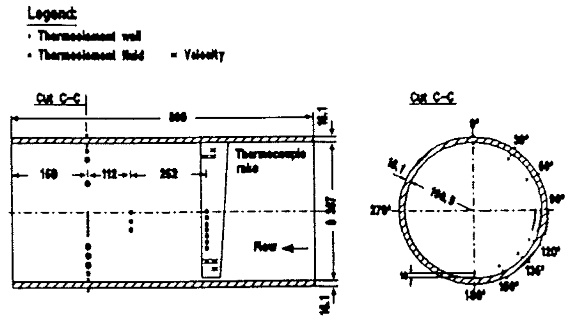

Fig.2: Axial and radial cross section tube I

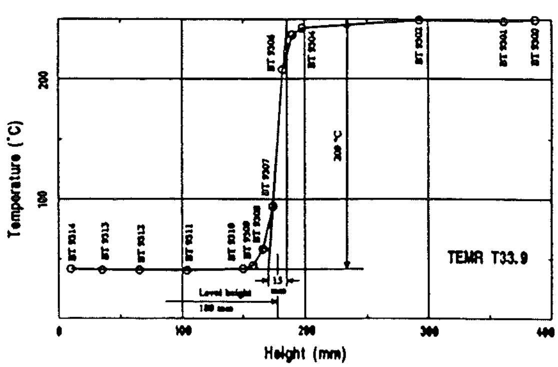

Fig.3: Measured temperature profile (smooth interface)

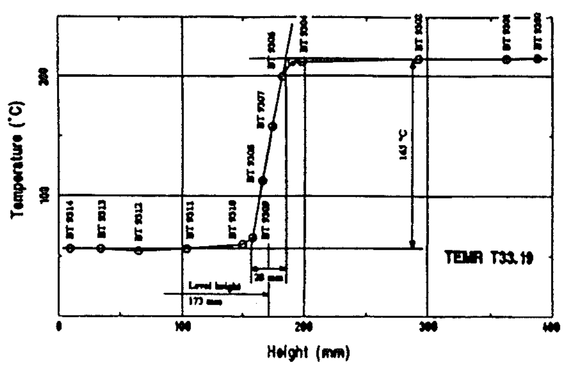

Fig.4: Measured temperature profile (wavy interface)

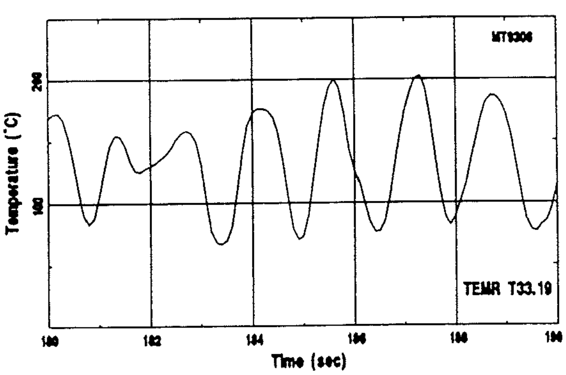

Fig.5: Temperature history (completely developed wave motion)

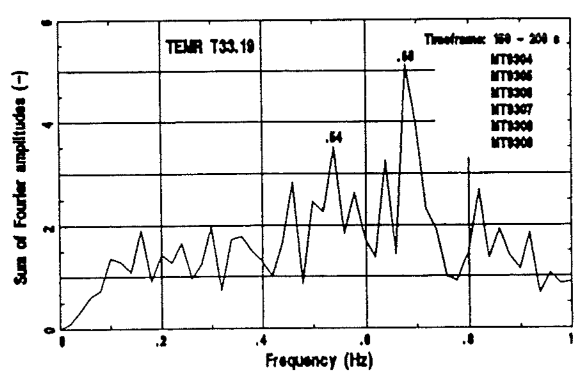

Fig.6: Fourier analysis of fluid temperature measurements

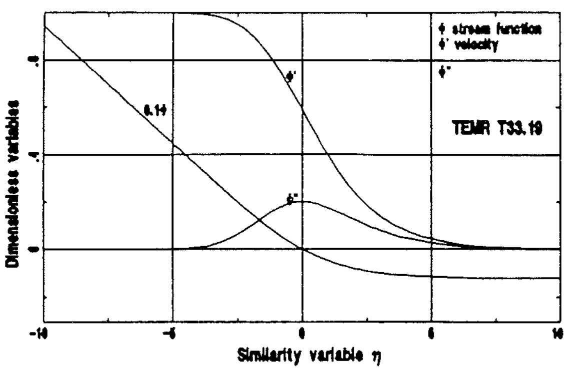

Fig.7: Solution of the Blasius equation

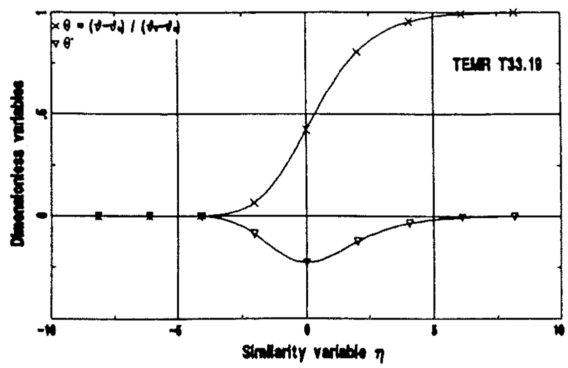

Fig.8: Solution of energy equation

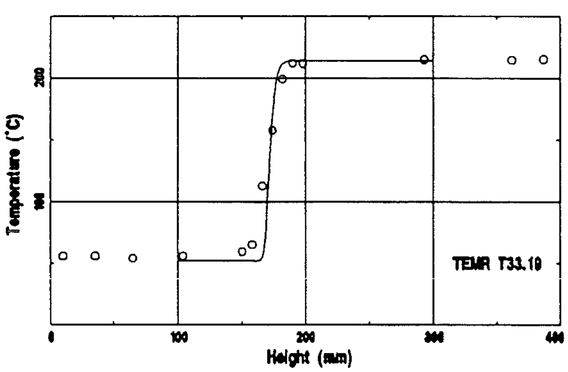

Fig.9: Comparison: Analytical temperature profile with measurement

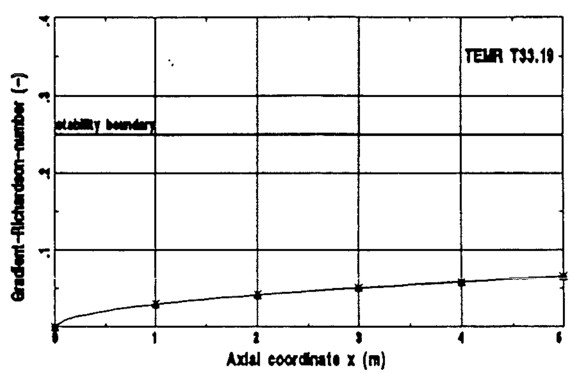

Fig.10: Result of stability analysis T33.19

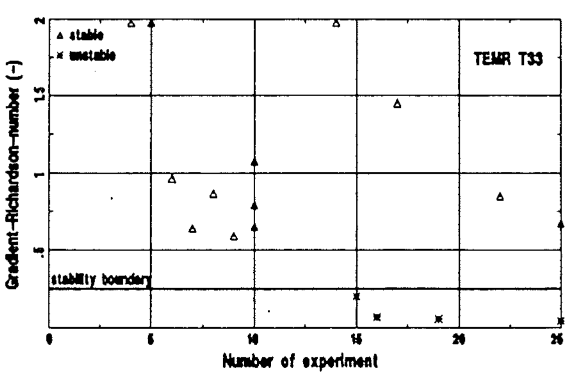

Fig.11: Summary of stability analysis (17 experiments)

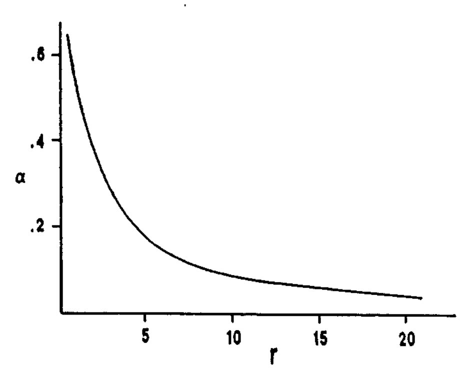

Fig.12: Most unstable wave number vs. thickness ratio

SEDIMENT INDUCED DENSITY CURRENTS IN RECTANGULAR SETTLING BASINS

Alexandre K. Guetter[1] and Subhash C. Jain
Iowa Institute of Hydraulic Research
The University of Iowa
Iowa City, IA 52242-1585

Abstract

An analytical model to predict density-driven currents in settling basins is presented. The analytical results are used to develop scaling laws for physical modeling of flows through settling basins. The hydraulic simulation requires that the dimensionless parameter J (defined later), which is a measure of the ratio of the densimetric velocity to the particle fall velocity, be the same in model and prototype.

Introduction

Field data on flow velocity in settling tanks presented by Larsen (1977) show that the vêlocities of density-driven currents near the upstream region of settling tanks are one order magnitude larger than the average through-flow velocities in the tanks. In spite of this verity, most scaling laws for modeling flows in settling basins neglect the effect of density currents, and are based on Froude and Hazen criteria; i.e., $\lambda_{Fr} = 1$ and $\lambda_{Ha} = 1$, where Froude number, $F_r = Q^2/gD^5$; Hazen number, $H_a = Q/wLB$; λ = model to prototype ratio for the variable denoted by the subscript; Q = discharge; g = gravitational acceleration; D = flow depth; L = basin length; B = basin width; and w = particle fall velocity. According to these criteria, $\lambda_v = \lambda_D^{1/2}$ and and $\lambda_V = \lambda_W$, where V = flow velocity. Scaling laws for modeling density-driven currents are not fully established.

This paper presents an analytical model to describe the density-induced current in rectangular settling basins with negligible through flow. The results of the analytical model are used to derive the scaling laws for modeling density currents and flows in settling basins.

Analytical Model

Figure 1 schematically depicts the basic flow pattern along the longitudinal direction of a basin. The flow field consists of three reaches: the entrance reach; the established-flow reach, and the closed-end reach. The flow in the established-flow reach is a two-layer system in which the flow in upper and lower layers moves in opposite directions. Due to continuous settlement of solids at the bottom of the established-flow reach, a negative longitudinal pressure gradient is developed, which generates a current in the lower layer. A reverse current occur in the upper layer to satisfy the continuity equation.

In the entrance reach rapid changes in velocities, concentrations and depth of the interface between inflow and outflow currents may occur. The governing forces are inertia and buoyancy. The entrance reach is short in length and is not important in terms of sediment settlement. The flow established reach is the zone that succeeds the entrance reach and is the main reach where most of the sediment is deposited on the bottom. Viscous and buoyant force are the main governing forces in this reach. As sediment

---

[1] Currently Department of Civil Engineering, Stanford University, Stanford, California 94305-4020.

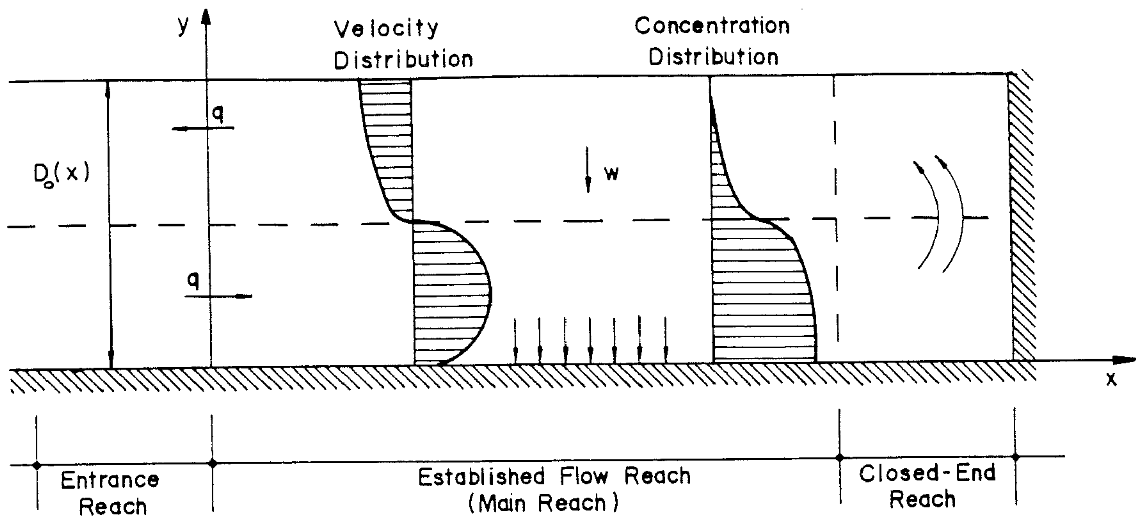

Fig. 1. General characteristics of the flow field.

settling reduces concentration along the x-direction, the rate of settling gradually decreases, which in turn reduces density gradients. Consequently, inflow and outflow velocities are also reduced. Stratification is clearly stable since the denser fluid remains in the lower layer. Application of boundary-layer approximations to the equations of motion is valid for the main reach because the vertical velocities are small in comparison to horizontal velocities. Additionally, diffusive momentum and concentration gradients in the underflow are much stronger vertically than horizontally. If the basin length is sufficiently long, both the concentration and the velocity at a certain distance L_e from the beginning of the main reach will be zero, and the length beyond this section will not be effective in settling suspended solids. The length L_e is hereinafter referred to as the equilibrium length. Basins of lengths $L>L_e$ and $L<L_e$ are hereinafter referred to as "long" and "short" basins, respectively. For a "short" basin the flow in the lower layer near the closed end is non-zero.

The analysis is concerned with the flow established region of rectangular basins, with horizontal bottom, and with large length (L) to depth (D) ratio, L>>D. The governing equations based on both boundary-layer and Boussinesq's approximations are

$$\frac{\partial u}{\partial x} + \frac{\partial v}{\partial y} = 0 \quad \text{(continuity)} \tag{1}$$

$$u\frac{\partial u}{\partial x} + v\frac{\partial u}{\partial y} = -\frac{1}{\rho_n}\frac{\partial p}{\partial x} + \frac{1}{\rho_n}\frac{\partial \tau_{xy}}{\partial y} \quad \text{(x-momentum)} \tag{2}$$

$$0 = -\frac{\partial p}{\partial y} - \rho g \quad \text{(y-momentum)} \tag{3}$$

$$u\frac{\partial C}{\partial x} + v\frac{\partial C}{\partial y} = \frac{\partial}{\partial y}\left(\varepsilon_y \frac{\partial C}{\partial y}\right) + w\frac{\partial C}{\partial y} \quad \text{(sediment concentration)} \tag{4}$$

$$\rho = \rho_w + (\rho_s - \rho_w)\, C \quad \text{(state)} \tag{5}$$

in which u and v are the velocities components in the x- and y-directions respectively,p is the pressure, w is the settling velocity of sediment particles, C is the local concentration defined in terms of volume, ρ_n is the reference density of the mixture (density of the mixture at the dead-end of the basin), ρ is the local density of the mixture, ρ_w is the density of the fluid phase, ρ_s is the density of the sediment, and τ_{xy} is the shear stress component applied to the face perpendicular to y-direction, and ε_y is turbulent diffusion coefficient. Turbulence is implicitly taken into account in the term τ_{xy}, and in the coefficient ε_y. The boundary conditions are: zero velocity at the bottom, no re-entrainment of settled sediments into the flow, no sediment flux across the free surface, and known vertical concentration distribution at x=0. The boundary conditions at the free surface contain an additional unknown D(x). To resolve the problem of closure and additional equation, mechanical energy, is required. The mechanical energy equation is obtained by multiplying the x- and y-momentum equations by u and v, respectively, and adding the results,

$$u^2 \frac{\partial u}{\partial x} + uv \frac{\partial u}{\partial y} = -\frac{1}{\rho_n}\left(u \frac{\partial p}{\partial x} + v \frac{\partial p}{\partial y} + v \rho g \right) + \frac{u}{\rho_n} \frac{\partial \tau_{xy}}{\partial y} \tag{6}$$

The governing equations were reduced to normalized ordinary differential equations by integrating them over flow depth and invoking the assumptions that vertical velocity, concentration and shear-stress distributions are self similar. The detailed derivations are given elsewhere (Guetter 1988). The normalized ordinary differential equations are:

$$\left[c_1 \theta + \frac{1}{2\sigma C_{B0}} \right] \frac{d\delta^2}{\delta \xi} + c_1 \delta^2 \frac{d\theta}{d\xi} + F\phi^2 = 0 \tag{7}$$

$$\delta \frac{d}{d\xi}(\phi\theta) + (\phi\theta)\frac{d\delta}{d\xi} + \left(\frac{1}{c_4 R}\right)(\theta + \theta_n) = 0 \tag{8}$$

$$\theta \left(c_2 + \frac{c_3}{2} \right) \frac{d\delta^2}{d\xi} + c_2\, \delta^2 \frac{d\theta}{d\xi} + c_5 F \phi^2 = 0 \tag{9}$$

where $\phi = \dfrac{u_s}{\sqrt{\sigma g C_{B0} D_0}}$, $\theta = \dfrac{C_B - C_n}{C_{B0}}$, $\theta_n = \dfrac{C_n}{C_{B0}}$, $\delta = \dfrac{D}{D_0}$, $\xi = \dfrac{x}{D_0}$,

$$\sigma = \frac{\rho_s - \rho_w}{\rho_n}, \quad F = \frac{u_{*B}^2}{u_s^2}, \quad R = \frac{\sqrt{g\sigma C_{B0} D_0}}{w},$$

$C_{B0} = C_B$ at x = 0; u_{*B} = shear velocity at the bottom; and c_1 thru c_5 = constants which depend on assumed self-similar velocity concentration, and shear-stress profiles. The inertia term in both momentum and mechanical energy equation was shown to be negligible in comparison to the density term (Guetter 1988) and are neglected in Eq. (7) and (9). The problem is now defined by a system of three ordinary non-linear differential equations (7), (8) and (9) in which the dependent variables are ϕ (normalized velocity), θ (normalized concentration), and δ (normalized depth), whereas the independent variable is ξ (normalized longitudinal length). An expression for $(d\delta^2/d\xi)$ may be found by eliminating $(d\theta/d\xi)$ between Eqs. (7) and (9) and suitably manipulating the system of equations. As indicated by experimental evidence, the magnitude of δ is very nearly 1. Thus, the expression for the variation of depth $(d\delta^2/d\xi)$ is uncoupled from the remainder equations. This assumption leads to system of two nonlinear ordinary differential equations in ϕ and θ which, upon application of order of magnitude analysis are reduced to

$$\left(\frac{d\theta}{d\xi}\right) + \left(\frac{c_5 F}{c_2}\right)\phi^2 = 0 \tag{10}$$

$$\theta\frac{d\phi}{d\xi} + \phi\frac{d\theta}{d\xi} + \left(\frac{1}{c_4 R}\right)(\theta + \theta_n) = 0 \tag{11}$$

The solution (Guetter 1988) of Eqs. (10) and (11) in terms of the original variables is

$$\frac{u_s D_o}{wL_e} = \frac{1}{4c_4}\left[\left(1 + \frac{C_n}{3C_{B0}}\right)^{1/3} - \frac{x}{L_e}\right] \tag{12}$$

$$\frac{C_B}{C_{B0}} = \left[\left(1 + \frac{C_n}{3C_{B0}}\right)^{1/3} - \frac{x}{L_e}\right]^3 - \frac{4C_n}{3C_{B0}} \tag{13}$$

where

$$\frac{L_e}{D_0} = \left(\frac{48c_2c_4^2}{c_5}\right)^{1/3}(J)^{1/3}; \; J = \frac{R^2}{F} \tag{14}$$

The layer velocity decreases linearly along the length, whereas the longitudinal concentration decay is cubic. Both velocity and concentrations are function of the parameter J which is a measure of the ratio of the velocity of density current to the particle fall velocity. It should be pointed out that the bed-friction parameter, F, is proportional to the Darcy-Weisbach friction factor, f.

The analytical results are compared with the field data for Qing Shan Canal (Fan et al. 1980) and settling tanks (Larsen 1977; Nemerow 1978) in Figs. 2 and 3.

Scaling Laws

The model must be undistorted which requires

$$\lambda_L = \lambda_D \tag{15}$$

where λ represents model to prototype ratio for the variable denoted by the subscript. For the simulation of the density-driven currents

$$\lambda_J = 1 \tag{16}$$

Equation (16) can be written as

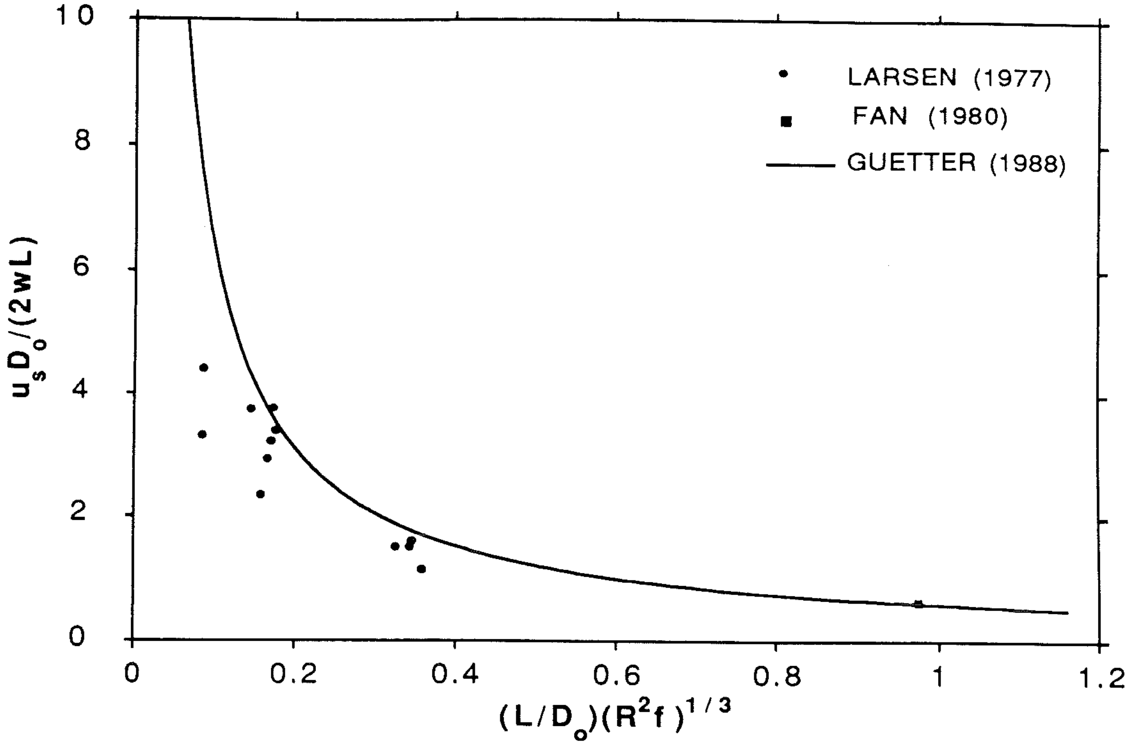

Fig. 2 - Outflow velocity

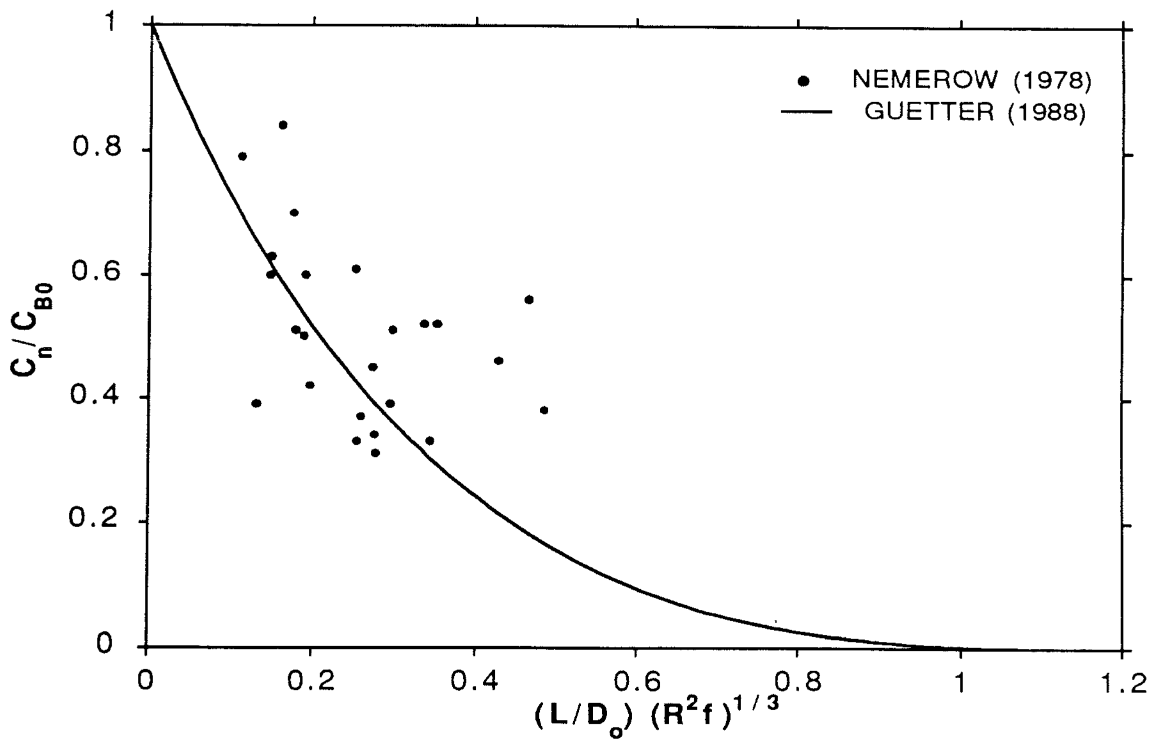

Fig. 3 - Residual sediment concentration

$$\lambda_f \lambda_w^2 = \lambda_\sigma \lambda_{C_{B0}} \lambda_D \quad (17)$$

Furthermore, the scales for the through-flow velocity, V, and density-driven velocity must be the same; hence from Eq. (12)

$$\lambda_V = \lambda_{u_s} = \lambda_w \quad (18)$$

Equation (18) is the same as given by the Hazen criterion. The particle fall velocity is given by

$$w^2 = \frac{g\sigma d}{C_d} \quad (19)$$

where C_d = drag coefficient; and d = sediment particle size. The scaling relation for the fall velocity from Eq. (19) is

$$\lambda^2{}_w = \lambda_\sigma \lambda_d \lambda_{C_d}^{-1} \quad (20)$$

Substitution for λ_w from Eq. (20) into Eq. (17) yields

$$\lambda_d = \lambda_{C_{B0}} \lambda_D \lambda_{C_d} \lambda_f^{-1} \quad (21)$$

For most models, $\lambda_{C_d}>1$ and $\lambda_f>1$; allowing $\lambda_{C_{B0}}>1$ produces more flexibility in selecting the model particle size.

Conclusions

The density-driven currents in a settling tank depend on a dimensionless parameter J which represent the ratio of densimetric velocity to particle fall velocity. Scaling laws for settling basins are given by Eqs. (18) and (21).

References

Fan, J., Wu, D., Shen, S., and Jiang, N. 1980. "Experimental Studies on Turbidity Density Currents and Their Applications," Proc. Intl. Sym. on River Sedimentation, Vol. 2.

Guetter, A., 1988. "An Analytical Solution for Stratified Flows Induced by Settling Solids," thesis presented to the University of Iowa, at Iowa City, IA, in partial fulfillment of the requirements for the degree of Master of Science.

Larsen, P. 1977. "On the Hydraulics of Rectangular Settling Basins - Experimental and Theoretical Studies," Report No. 1001, Department of Water Resources Engineering, Lund Institute of Technology/University of Lund.

Nemerow, N.L. 1978. "Industrial Water Pollution - Origins Characteristics and Treatment," Addison-Wesley Publ. Co., Reading, Mass.:" 118-119.

Session 9B

Physical Model Studies

GENERALITY AND POWER OF DIMENSIONLESS PRESENTATIONS

by Walter O. Wunderlich
Consulting Engineer
Knoxville, TN 37918 USA

Abstract

The combined use of conceptual and physical models, supported by selective field verification is a means of reliably predicting hydraulic prototype performance. This approach is especially useful when conceptual models alone cannot solve the problem on hand and when physical models are seriously distorted by lack of dynamic similarity. While the use of nondimensional relationships is a prerequisite for sound transfer of physical model data into prototype dimensions, errors may be caused by the use of inadequate similarity parameters. Two examples are discussed.

Introduction

The overall satisfactory performance of hydraulic engineering works over the past half century is undoubtedly attributable to a large extent to designs that were developed and tested by scale models. But physical model testing is still an art as much as a science. There are pitfalls which must be avoided when physically modelling complex problems, as it is usually impossible to meet all scaling requirement for perfect dynamic similarity. The resulting distortions demand attention in model setup, test conduction and result interpretation, if valid answers are to be obtained.

The recommended approach to transfering physical model results to prototype dimensions is to present the test results (dependent variables) in dimensionless form as functions of dimensionless (independent) variables. The nondimensionalized equations of fluid movement provide guidance for the choice of these parameters. All dimensionless parameters that appear in these equations must be the same in model and prototype, if dynamic similarity of the model is to be achieved. This requirement is usually not met and only the equality of the dominant parameters is satisfied. The consequence is uncertainty about the validity of the physical model and the scaling of the results obtained from it. The combined use of mathematical and physical models and field verification is a way to increase confidence in model results.

Interfacial Instability and Entrainment

When a lighter fluid moves on top of a heavier fluid or when a heavier fluid moves under a lighter fluid, the interface is smooth as long as the relative velocity of one fluid against the other is small. With increasing velocity, it becomes increasingly wavy. Finally the waves break and a mixed zone is established as interface between the two fluids. Examples are wind over water and density overflows and underflows. Keulegan (1949) studied interfacial instability and mixing for water (ρ_1 = 1 g/cm³) moving over a denser sugar solution (ρ_2 = 1.01 to 1.3 g/cm³). He theoretically derived the stability parameter

$$\theta = (n_2 \; g \; D\rho/\rho_1)^{1/3}/U \qquad (1)$$

with n_2 the kinematic viscosity of the heavier liquid, in this case non-moving liquid, g the acceleration due to gravity; D ρ the density difference between the light and the heavier liquid, ρ_1 the density of the moving lighter liquid and U the velocity of the moving lighter liquid.

In order to generalize the test results, Keulegan considered a Reynolds number defined as $Re_c = U_c \; hr/n_1$, with U_c being a critical velocity above which mixing by breaking waves occurs, h_r is the hydraulic radius and n_1 the viscosity of the moving lighter liquid. In analogy with similar phenomena involving laminar convective movements in the presence of (positive or negative) buoyancy, the stability parameter θ itself can be expanded into a combination of a Grashof and a Reynolds number,

$$\theta = (Gr^{1/3}/Re) \; (n_2/n_1) \; (h/l_r) \qquad (2)$$

with $Gr = (g \; D\rho/\rho_1 \; l_r^3)/n_2^2$, the Grashof number, and $Re = U \; h/n_1$ the Reynolds number, n_2/n_1 the ratio of viscosities of upper and lower fluids, h is the depth of the current and l_r is a vertical distance over which the density change occurs, $l_r = |D\rho \,/(d\rho/dz)|$, according to Lofquist (1960).

The change from the laminar to the turbulent smooth flow regime is typically characterized by a change in the exponent of the Reynolds number. For example, the exponent 1/4 in Blasius formula for laminar pipe flow changes to 1/2 in Prandtl's formula for turbulent smooth wall flow (Schlichting, 1965). Likewise, the combination Gr/Re for turbulent flow changes to Gr/Re^2 which corresponds to the bulk Richardson number

$$Ri_b = (g \; l_r \; D\rho/\rho_1)/U^2 \; (n_1/n_2)^2 \; (l_r/h)^2 \qquad (3)$$

If l_r in the first term of Eq. 3 is exchanged for h, then Ri_b can be expressed by the densimetric Froude number of the current, Fr:

$$Ri_b = (n_1/n_2)^2 \; (l_r/h)^3/Fr^2 \qquad (4)$$

with $Fr = U/\sqrt{(g \; h \; D\rho/ \rho_1)}$. Lofquist (1960) presented his entrainment data as function of Fr^2 using the hydraulic radius h_r instead of the depth h as a length. He also demonstrated that the velocity distribution in the interface was reasonably uniform over the channel width. His data (table 1 of the reference) show that l_r/h is remarkably stable with $0.019 \le l_r/h \le 0.038$ and mean 0.029, so that the first two terms in Eq. 4 collapse into a coefficient. It is known that flow separation can only exist if $Fr \le 0.32$, theoretically, or about 0.25 empirically (Yih, 1965). Lofquist's entrainment velocity ratios, U_e/U, calculated from data obtained for a saltwater underflow, (with index 1 identifying the moving liquid) against Fr (instead of Fr^2) are given in Fig. 1. They essentially do not exceed this critical Froude number. Some entrainment ratios calculated for self-generated underflows in two reservoirs (Elder and Wunderlich, 1973) line up around Fr = 0.25. Also a sample of Keulegan's (1949) data used by Lofquist (1960, Fig. 9) fall into this same area. Thus, by proper selection of the length parameter, the data from such different sources (overflows and underflows) obtained at very different scales (small models and sizable rivers), despite certain similarity problems and technical problems (field measurement difficulties), albeit of limited quantity, can be arranged to exhibit a remarkable degree of conformance with theory.

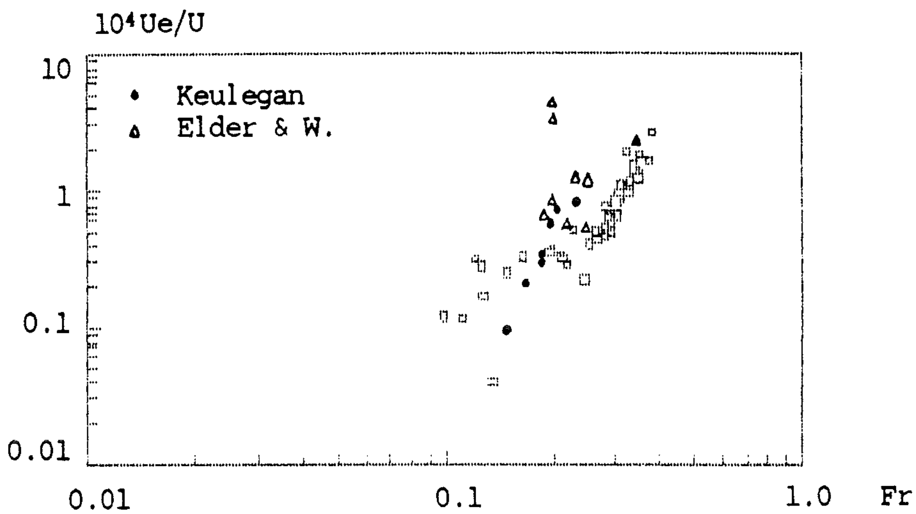

Fig. 1 Entrainment by a Density Curent as Function of Froude Number.

Air Entrainment by a Plunging Jet

The second example to be discussed here is air entrainment by a jet exiting from a nozzle and plunging vertically down into a pool. Of interest is the maximum depth to which air bubbles are entrained in order to protect sensitive parts of a facility from the disruptive effects of captured air. As the jet enters into the water, it entrains air along its periphery. But the drag of the jet decreases as it expands in the water. Finally the downward drag on the bubbles is exceeded by their buoyancy and they escape back to the surface.

As a mathematical base for this problem the round laminar free jet model is used (Schlichting, 1965). For the steady state, the time derivatives are dropped. The transition to the turbulent free jet model is accomplished by introducing a turbulent viscosity, $\epsilon = k\, b\, U$, with k being an empirical coefficient, b the jet width and U the center line velocity. If b is assumed to be proportional to the distance z, measured from the origin of the jet (water surface) downward, then $b = \beta z$. If U is assumed to be inversely proportional to z, $U = \alpha/z$. These asssumptions produce $\epsilon = k\, \alpha\, \beta$ = constant. Therefore, the kinematic solution of the laminar problem can be used as the solution for the turbulent problem. We assume further that the entrainment velocity is the velocity in the zone of maximum shear, i.e., where the velocity gradient is strongest. The entrainment velocity at depth z is then

$$U_z = a' \ (d\ U_o)^2/(\epsilon\ z) \tag{5}$$

where a' is a numerical factor, d and U_o are jet diameter and velocity at the water surface. At the maximum bubble penetration depth, zmx, the buoyancy of the bubble is equal to the downpull by the jet, which is expressed by

$$\rho_w\ c_D\ (U_z{}^2/2)\ \pi\ d_b{}^2/4 = (\pi\ d_b{}^3/6)\ g\ (\rho_w - \rho_a) \tag{6}$$

with c_D a drag coefficient of the bubble, d_b the bubble diameter, g the acceleration due to gravity and $\rho_w - \rho_a$ the density difference between water and air. Since ρ_w is about 1000 times bigger than ρ_a, the difference between the two is practically equal to ρ_w. Solving Eq. 6 for U_z and substituting it into Eq. 5, produces

$$zmx/d = a\ (U_o\ d/\epsilon)\ U_o/U_b \tag{7}$$

with zmx the maximum penetration depth of a jet with initial diameter d at z = 0, the water surface; a is a coefficient; $Pe = U_o\ d/\epsilon$ is a Peclet number; $De = U_o/U_b$ is the 'degasification number', the ratio of the initial jet velocity, U_o, and the upward directed air bubble rise velocity, U_b.

The steady state air bubble rise velocity also follows from Eq. 6 by exchanging U_z for U_b which marks the terminal velocity as a result of the equilibrium between flow resistance and bubble buoyancy. This yields

$$U_b = k_b\ (g\ d_b)^{1/2} \tag{8}$$

with $k_b = ((4/(3\ c_D))\ (\rho_w - \rho_a)/\rho_w)^{1/2}$. For air in water, at 20 C, $(\rho_w - \rho_a)/\rho_w = (998.2-1.2)/998.2 = 0.9988$. The resistance coefficient for a sphere is $c_D = 0.5$. Hence, $k_b = 1.63$, a number that should be verified by tests.

No interference of air bubbles is included in the model derivations above. These simplifications in the mathematical model make a verification by a physical model necessary. Data for testing Eq. 7 are due to Vigander (1984). Fig. 2 shows zmx/d versus U_o/U_b, with U_b = 0.755 ft/s (assumed constant here). Based on these data, the average bubble penetration depth can be represented by

$$zmx/d = a\ U_o/U_b = a\ De \tag{9}$$

with a = 1.47 (with standard deviation 0.039). This fit, though simplified, seems to bear out the validity of the mathematical model used here.

As is the case in other air/water mixture problems, it is conceivable that the data representation is chosen as

$$zmx/d = b\ Fr \tag{9a}$$

with $Fr = U_o/\sqrt{(gd)}$, the Froude number of the jet. The nozzle diameter d ranged from 7 to 40 mm. The data plot is very similar to Fig. 2, only with De replaced by Fr and b = 2.06 (with standard deviation 0.066). This fit is slightly worse than by Eq. 9 but seems acceptable.

The important point here is that Eq. 9a suggests Froudian similarity which may actually not exist. To illustrate this point we scale the results of both Eq. 9 and 9a into prototype dimensions. With indices m and p indicating model and prototype, one can express the modeling scales of all involved quantities as ratios of prototype to model quantities

$$(zmx_p/zmx_m)/(d_p/d_m) = (a_p/a_m)(U_{op}/U_{om})/(U_{bp}/U_{bm})$$

and

$$(zmx_p/zmx_m)/(d_p/d_m) = (b_p/b_m)(Fr_p/Fr_m)$$

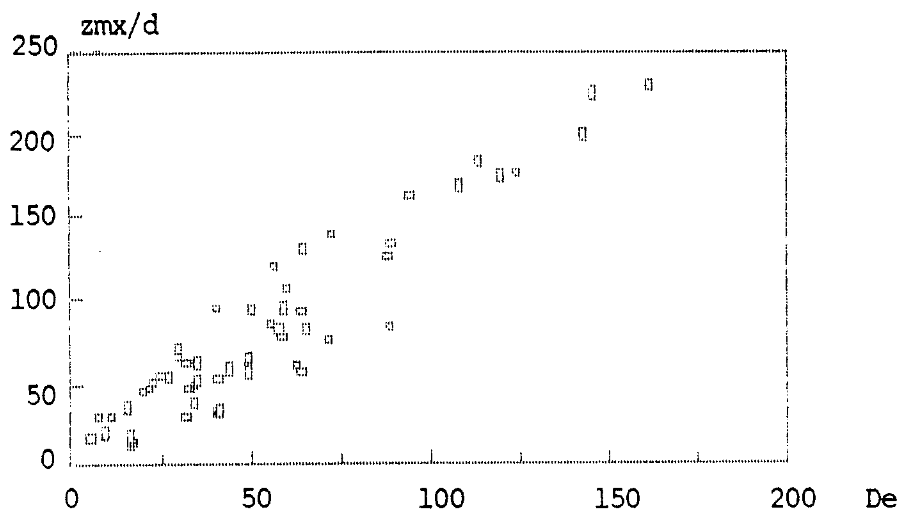

Fig. 2 Jet Penetration Depth as Function of Degasification Number De

For Froudian similarity, the time scale is the square root of the length scale which makes the Froude numbers the same in model and prototype. Assume the length scale is s (for example, s = 6 for a model 1:6), and also $a_p/a_m = b_p/b_m = 1$, then the two models yield

$$s_r = s * s^{1/2}/s_b \tag{10}$$

and

$$s_r = s \tag{10a}$$

For distinction we denote the transfer scale for the model result, zmx, with $s_r = zmx_p/zmx_m$. For Froudian similarity it should be equal to s, as is the case for Eq. 10a. In Eq. 10, s_b is the bubble rise velocity scale, assumed to be an unknown instead of the Froudian velocity scale $s^{1/2}$, which may or may not apply. So unless we learn more about s_b, the transfer scale for zmx_m is $s_r = s^{1.5}/s_b$. As a limiting case, assume the bubble velocity does not scale at all, that it is the same in model and prototype, or $s_b = U_{bp}/U_{bm} = 1$. Then, the Froudian model, Eq. 10a, suggests a bubble penetration depth in the prototype 6 times the one measured in the model, while according to Eq. 10 it is actually $6^{1.5}$ = 15 times the one measured in the model. In other words, because of the relatively fast rise of the bubbles in the model, the penetration depth measured in the model would be too small for protoype conditions when just scaled by s. The true penetration depth may lie somewhere in between. To resolve this question, additional testing would have to be done to develop information on bubble rise velocity and bubble diameter as they can be expected to exist in the prototype environment. Equation 7 should then be used with the 'true' bubble velocity to calculate zmx.

Conclusion

The examples discussed here demonstrate dimensionless presentation of data as a powerful and necessary tool in model/prototype analysis. But it is not sufficient for transfering model results from scale models to prototype. Unless the correct dimensionless combinations are used for the presentation of model results, wrong transfer scales may result. Data transfer problems also result with dynamically distorted models, because certain dimensionless parameters are not the same in model and prototype. A companion conceptual model can help to pinpoint such problems and make the user aware of pitfalls inherent in the choice of similarity parameters for model-prototype transfer of test results.

References

Elder, R. A. and W. O. Wunderlich, "Inflow Density Currents in TVA Reservoirs," Internat. Symp. on Stratif. Flows, ASCE, N.Y. 1973.

Keulegan, G. H., "Interfacial Instability and Mixing in Stratified Flow," U.S. Nat. Bureau of Standards, RP 2040, vol. 43, Nov. 1949.

Lofquist, K., "Flow and Stress near an Interface between Stratified Liquids," Physics of Fluids, 3:3, March-April, 1960.

Schlichting, H., Grenzschicht Theorie, G. Braun, Karlsruhe, 1965.

Vigander, S., "Bubbles, Drops and Friction on the Judgement Scale," Rept. WR28-1-900-124, TVA, Eng. Lab., Norris, TN 37828, March 1984.

Yih, C.S., Dynamics of Non-Homogeneous Fluids," MacMillan, N. Y.,1965.

A PHYSICAL THEORY OF SIMILARITY

by Shragga Irmay*
Technion-Israel Institute of Technology
Haifa, 32000 Israel

Abstract

Most model studies are based on dimensional numbers Pi obtained by dimensional analysis and the Vaschy-Buckingham theorem. They are products of a medium property, e.g. density, and of powers of undefined 'characteristic' parameters, e.g. length, velocity, pressure or temperature differentials. Dimensionless parameters, e.g. relative concentrations, cannot be considered. The Pi's are often interpreted heuristically as force ratios, e.g. a Froude number *Fr* as ratio of inertial to gravity forces, though they are vectors of different directions. As natural phenomena are always accompanied by an energy exchange, it seems simpler to redefine the Pi's as ratios of scalar additive energies. The characteristic parameters are replaced by well-defined ones. Thus in *Fr* the length can be shown to be a dynamic parameter, not a geometric one. The Weber number is shown to include the relative concentration of dispersed droplets or bubbles. This physical method can easily be extended to thermodynamics, electromagnetism, chemistry or quantum mechanics. It is applicable also to inequalities, e.g. the entropy inequality.

Dimensional Analysis

Most model studies are based on dimensional and sometimes on inspectional analysis [Vaschy, 1896; Buckingham, 1915; Bridgman, 1931; Birkhoff, 1950]. Dimensional analysis is the determination of physical laws on the basis of dimensions only. It is an algebraic theory, used by engineers under the name of *Pi-theorem*, which states that any physical equation can be expressed in terms of dimensionless monomials Pi, products of powers of positive variables. This results from the fact that any set or relations valid under all units is equivalent to a set of Pi's. These Pi's are expressed in terms of medium properties, local physical variables and global parameters representing the boundaries in space and time. The results are often trivial, they include unspecified 'characteristic' parameters whose choice requires considerable skill, common sense and experience. The advantage of the method is that it may be used even when the exact laws are not known.

Similarity

We compare two physical systems: *prototype (p)* and *model (m)* using the same units. They are similar with respect to a scalar property Q when there exists at all corresponding points a constant ratio or scale $Q_r = Q_m/Q_p = Q'_m/Q'_p = Q''_m/Q''_p$. As $Q_m = Q_r Q_p$, the ratio of the Q's at two corresponding points should be the same in both systems: $Q'_m/Q''_m = Q'_p/Q''_p$. In mechanics we distinguish three types of similarity; geometrical, kinematical and dynamic similarity.

Geometrical Similarity

In *isotropic* models this requires that at all corresponding points and times there exists a single constant length scale $L_r = dL_m/dL_p$ for the corresponding length elements

----

**Professor Emeritus, Faculty of Civil Engineering.*

dL of all displacements, streamlines, boundaries and vectors with a linear length dimension.

In *distorted* or *anisotropic* models there may exist 3 (or 2 in the plane) different length scales $x_r = dx_m/dx_p$, $y_r = dy_m/dy_p$, $z_r = dz_m/dz_p$ in 3 mutually orthogonal principal directions x,y,z. It can be shown [Irmay, 1964] that for an oblique direction R_m and its correpsonding R_p the square of the scale $R_r = R_m/R_p$ is a symmetric second rank tensor with its principal directions along the x,y,z axes. The polar diagram of R_r is a lemniscate.

Kinematic Similarity

In *isotropic* models this requires geometrical similarity, a constant time scale $t_r = dt_m/dt_p$ for all corresponding time elements dt, and a constant scale of all velocities $V_r = V_m/V_p = L_r/t_r$, and for the fluxes at the boundary $q_r = q_m/q_p = V_r$, as $V = dL/dt$. Often V_r is the primary scale, then $t_r = L_r/V_r$.

In *distorted* models the requirements are: geometrical similarity with 3 length scales x_r, y_r, z_r in 3 principal directions, a constant time scale t_r, and consequently 3 constant scales of all velocity components (u, v, w), namely $u_r = u_m/u_p$, $v_r = v_m/v_p$, $w_r = w_m/w_p$ of the 3 flux components at the boundary with $t_r = x_r/u_r = y_r/v_r = z_r/w_r$ as deduced from $dt = dx/u = dy/v = dz/w$. In distorted models similarity of vorticity, circulation or velocity potential is impossible.

Dynamic Similarity

This requires kinematic similarity and a constant mass scale $m_r = m_m/m_p$ for all corresponding masses m, and an adequate constant scale $\tau_r = \tau_m/\tau_p$ for all corresponding stresses τ_{ik} at the boundary. Hydraulic engineers often replace m_r by a constant force scale $F_r = F_m/F_p$; m_r canot be used in inertialess processes. This applies also to F_r which is limited to parallel forces. In general dynamic similarity is inapplicable to distorted models.

Inspectional Analysis

This method [Ruark, 1935; Irmay, 1964, 1965] consists of testing for invariance under linear homogeneous transformations of every equation on which a given theory is based. As an example consider the Navier-Stokes equation of motion of a constant-density ρ fluid of kinematic viscosity ν and dynamic viscosity $\mu = \rho\nu$ in the gravity field g at an elevation Z and pressure p, giving the acceleration component a_1 :

$$a_1 = u_t + uu_x + vu_y + wu_z = -gZ_x - p_x/\rho + \nu(u_{xx}+u_{yy}+u_{zz}) \qquad (1)$$

Introducing a characteristic length L_o, velocity V_o , pressure P_o, and dimensionless (or numerical) local variables:

$$d\bar{x}=dx/L_o,\quad d\bar{y}=dy/L_o,\quad d\bar{z}=dz/L_o,\quad \bar{Z}=Z/L_o,\quad \bar{t}=tV_o/L_o,$$
$$\bar{u}=u/V_o,\quad \bar{v}=v/V_o,\quad \bar{w}=w/V_o,\quad \bar{a}_1=a_1L_o/V_o^2,\quad d\bar{p}=dp/P_o,$$

Eq.(1) becomes:

$$\bar{a}_1 = \bar{u}_{\bar{t}} + \bar{u}\,\bar{u}_{\bar{x}} + \bar{v}\,\bar{u}_{\bar{y}} + \bar{w}\,\bar{u}_{\bar{z}} = -(1/Fr)\bar{Z}_{\bar{x}} - (1/Eu)\bar{p}_{\bar{x}} + (1/Re)(\bar{u}_{\bar{x}\bar{x}} + \bar{u}_{\bar{y}\bar{y}} + \bar{u}_{\bar{z}\bar{z}}) \qquad (2)$$

We get 3 dimensionless Pi's: Froude number $Fr = V_o^2/gL_o$ Euler number $Eu = \rho V_o^2/P_o$ and Reynolds number $Re = V_oL_o/\nu$. If the viscosity effect is negligible, *Re* is large and the corresponding term may be omitted. If the pressure effect is small the *Eu* term may be omitted. If gravity effect is small, we may omit the Fr term. Inspectional analysis can be used whenever the mathematical law is known. The use of unspecified characteristic parameters introduces new unknowns.

This can partially be remedied by a modified method [Irmay, 1965]. Let us apply it to a distorted model of a laminar boundary layer obeying Blasius' equation in two-dimensional flow:

$$a_1 = u_t + uu_x + vu_y = \nu u_{yy} \tag{3}$$

both in m and p, then:

$$a_{1r} = a_{1m}/a_{1p} = (u_t + uu_x + vu_y)_m/(u_t + uu_x + vu_y)_p = (\nu u_{yy})_m/(\nu u_{yy})_p = (\nu_r u_r/y_r^2) =$$

$$= [(u_r/t_r)(u_t)_p + (u_r^2/x_r)(uu_x)_p + (u_r v_r/y_r)(vu_y)_p]/(u_t + uu_x + vu_y)_p$$

or: $$(u_r/t_r - \nu_r u_r/y_r^2)(u_t)_p + (u_r^2/x_r - \nu_r u_r/y_r)(uu_x)_p + (u_r v_r/y_r - \nu_r u_r/y_r^2)(\nu u_{yy})_p \equiv 0.$$

This is an identity for all the variables in p, so their coefficients must vanish and:

$$a_{1r} = u_r/t_r = u_r^2/x_r = u_r v_r/y_r = \nu_r u_r/y_r^2$$

Hence: $$t_r = x_r/u_r = y_r/v_r; \quad v_r y_r/\nu_r = 1; \quad y_r^2 = \nu_r t_r$$

Replacing $(r) = (m)/(p)$, we get:

$$(vy/\nu)_m = (vy/\nu)_p \quad (4.1); \qquad (y/\sqrt{\nu t})_m = (y/\sqrt{\nu t})_p \quad (4.2)$$

Eq. (4.1) shows that the significant Re is not the *longitudinal* $Re_{11} = ux/\nu$, nor the *mixed* $Re_{12} = uy/\nu$, but the transversal $Re_{22} = vy/\nu$.

The exact solution of (3) [Schlichting, 1968] at the end of the laminar boundary layer of thickness δ, is $v\delta/\nu = 1.48$ for the displacement thickness or 0.49 for the momentum thickness, on the average $v\delta/\nu = 0.99 \sim 1$. This may serve as a new definition for the thickness of the boundary layer $\delta = \nu/v$. For as $v/u = y/x \sim 1/Re_{11}^{1/2}$, $Re_{22} \sim 1$. The transition from laminar to turbulent flow occurs at $Re_{11} \sim 10^6$; $Re_{12} \sim 10^3$; $Re_{22} = 1$ as befits a critical number. This explains why for pipe flow of mean longitudinal velocity U and radius r the critical $Re_{12} = Ur/\nu \sim 1000$. The importance of Re_{22} is in the fact that the transition to turbulence is due to transverse disturbances at the entrance. In isotropic models it does not matter which Re is used. Eq. (4.2) defines the dimensionless transverse development number $De = y/\sqrt{\nu t}$ to be used in a developing boundary layer of parabolic growth.

Physical Similarity

The author suggests to redefine the major Pi 's as ratios of energy components. Dynamic similarity requires replacing m_r and F_r by constant scales of all energy components: $(E_i)_r = (E_i)_m/(E_i)_p$. The advantages are:

(i) Energy is an additive scalar function, independent of direction.

(ii) Energy is involved in all physical, chemical, or quantum-mechanical processes which are accompanied by energy interconversion.

(iii) Energy components are more easily assessed, even when the laws are not exactly known.

(iv) Negligible energy components may be omitted, thus increasing the number of degrees of freedom.

The total energy E in m and p is: $E_m = \Sigma E_{im}$; $E_p = \Sigma E_{ip}$

By similarity of m and p :

$$E_r = E_m/E_p = \Sigma E_{im}/\Sigma E_{ip} = \Sigma(E_{ir}E_{ip})/\Sigma E_{ip} \qquad \text{or:} \qquad \Sigma E_{ip}(E_r - E_{ir}) \equiv 0$$

This identity, valid for arbitrary values of E_{ip}, requires that all coefficients vanish, so that the scales of all energy components are the same:

$$E_{ir} = E_{1r} = E_{2r} = ... = E_r$$
$$E_{im}/E_{ip} = E_{1m}/E_{1p} = E_{2m}/E_{2p} = ... = E_m/E_p$$
$$E_{1m}/E_{2m} = E_{1p}/E_{2p} = \text{const} \equiv P_{12}$$

Hence the important *theorem of dynamical similarity* : Similarity with respect to two energy compenents E_1 and E_2 requires that the ratio be the same in m and p, thus defining a dimensionless Pi of the Pi-theorem. A few examples follow:

Froude Similarity

When there is interconversion of kinetic energy $E_1 = mV^2/2$ and gravity free energy $E_2 = mg\Delta Z$, the corresponding Pi is the *Froude number* $Fr = E_1/E_2 = V^2/g\Delta Z$. Dimensional analysis gives only V_o^2/gL_o with L_o an unspecified length. ΔZ is a potential drop, not a geometric length. Thus we may choose different scales L_r and Z_r, which gives an additional degree of liberty. In hydraulic literature $V/\sqrt{gL_c}$ is used.

Euler Similarity

In fluid flow from a tank under a pressure differential Δp, there is interconversion of kinetic energy and Gibbs free energy of pressure $E_2 = \Delta p.m/\rho$. The corresponding Pi is the Euler number $Eu = E_1/E_2 = \rho V^2/\Delta p$. In hydraulic literature $V/\sqrt{\Delta p/\rho}$ is used. In compressible barotropic flows of $p(\rho)$, the sound velocity $c = [dp/d\rho]^{1/2}$, hence:

$$\Delta p = \Delta\rho.dp/d\rho = c^2\Delta\rho \ ; \quad Eu = (\Delta\rho/\rho) \cdot c^2/V^2$$

The ratio $Ma = c^2/V^2$ is the Mach number.

When there are both gravity and pressure effects:

$$E_2 = mg\,\Delta Z + \Delta p.m/\rho = mg\Delta h$$

where $h = Z + p/g\rho$ is the piezometric head, Irmay [1964] defines a piezometric number:

$$Pz = E_2/E_1 = g\Delta h/V^2 = 1/Fr + 1/Eu$$

Weber Similarity

A suspension of liquid droplets (radius r , specific surface M, number of droplets N, volume concentration c) in a dispersive medium (mass m, density ρ, volume $U = m/\rho$), with $cU = N \cdot 4\pi r^3/3$. With surface tension σ, the surface energy is $E_2 = \sigma N 4\pi r^2$. The corresponding Pi is the ratio of E_1 to E_2, or Weber No. $We = E_1/E_2 = \rho V^2/c\sigma M$. The usual definition is $V/\sqrt{\sigma/\rho L_0}$. Here we replace L_0 by c/M.

Reynolds Similarity

Reynolds number may be defined as ratio of kinetic energy E_1 to the dissipated energy E_2. In Couette flow along a flat plate of area $A = BL$ moving at speed V at a distance H from a stationary flat plate, the shearing stress is $\tau = \mu V/H$, the resistance is $F = \tau A$ and the energy dissipated in time $t = L/V$ is: $E_2 = \mu VBL^2/H$. Then $Re = E_1/E_2 = (VH/\nu)(H/L)$. In *isotropic* models where $H_r = L_r$ we get the usual form VH/ν. In *anisotropic* models $V/L = v/H$, $V \rightarrow u$, $u/L_r = v/H_r$, and we get eq. (4.1):

$$Re_{22} = vH/\nu .$$

The Asymptotic Law

Esnault- Pelterie [1946] proved that any dimensionless coefficient, function of the Pi's in their usual form with V in the numerator (e.g. $Fr = V/\sqrt{gL}$, $Eu = V/\sqrt{\Delta p/\rho}$, $Re = VH/\nu$, $We = V/\sqrt{\sigma/\rho L}$), tends to infinity for large Pi. An example is the friction coefficient f(Re) in pipe flow in the Stanton-Moody diagram which has a horizontal asymptote. This result is trivial, for when viscosity is negligible, $Re \rightarrow \infty$, and the graph is a horizontal aysmptote. It is preferable to choose the inverse of each Pi as the new Pi.

Similarity in Chemistry and Physics

When molecules are activated we may define an *activation number*, ratio of the activation energy E_2 to their mean kinetic energy $E_1 = kT$ (k-Boltzmann constant, T-absolute temperature): $Ac = E_2/E_1 = E_2/kT$.

In quantum mechanics we may define a *quantum energy number*, ratio of the photon energy $E_2 = hf$ (h - Planck's constant, f - frequency) to $E_1 = kT$: $Qn = E_2/E_1 = hf/kT$, a parameter appearing in Einstein's formula for the specific heat of solids.

Similarity in Heat Transfer

By Fourier's law of conductivity, the amount of heat crossing an area A in time t under a temperature gradient $\Delta T/L$, is $Q_F = ktA\,\Delta T/L$ (k-thermal conductivity of the medium, k_f in fluids, k_s in solids). By Newton's law of cooling, the amount of heat transferred from a fluid to a wall (or conversely) through an area A in time *t* under a differential ΔT is $Q_N = hAt\Delta T$ (*h* - heat transfer coefficient).

In forced or natural heat conduction in fluids we may choose as Pi the *Nusselt number* $Nu = Q_N/Q_{Ff} = hL/k_f$. Similarly in solids we define the *Biot Number* $Bi = hL/k_s$.

The amount of heat stored in a body of mass $m = AL$ and specific heat c at constant pressure under a temperature rise ΔT is $Q_s = c\rho AL\Delta T$. In forced convection we define the *Stanton number* by $Sta = Q_N/Q_s = h/\rho cV$ with $L/t = V$.

The *Eckart number* is the ratio of kinetic energy $E_1 = mV^2/2$ to Q_s: $Ec = E_1/Q_s = V^2/c\Delta T$.

The above definitions assume equality of ΔT in all cases. A more physical definition would be:

$Nu^* = (hL/k_f)(\Delta T_f/\Delta T_N)$; $Bi^* = (hL/k_{.}/(\Delta T_s/\Delta T_N)$;$Sta^* = (h/\rho cV)\Delta T_N/\Delta T_s)$

Similarity of Inequalities

There are laws based on inequalities, e.g. the second law of thermodynamics. Consider such a law in m and p:

$$E'_m + E''_m > E_m; \quad E'_p + E''_p > E_p$$

We can prove that $E'_r = E''_r \gg E_r$ (6)

Proof

$$E'_r E'_p + E''_r E''_p > E_r E_p \rightarrow E'_p > (E_r E_p - E''_r E''_p)/E'_r$$

$$E'_p + E''_p - E_p > E_p\,(E_r/E'_r - 1) + E''_p(1 - E''_r/E'_r)$$

In order to have $E'_p + E''_p - E_p > 0$ even for large E''_p, E_p, we should have

$$E_r \lesssim E'_r \qquad \text{and} \qquad E''_r \gtrsim E'_r\ . \tag{7}$$

Similarly:

$$E'_p + E''_p - E_p > E_p\,(E_r/E''_r - 1) + E'_p(1 - E'_r/E''_r)$$

In order to have $E'_p + E''_p - E_p > 0$ for large E'_p, E , we should have: $E_r \lesssim E''_r$ and $E''_r \lesssim E'_r$. Comparing this with eq. (7) we obtain eq. (6).

References

Birkhoff, G. Hydrodynamics - a study in logic, fact and similitude. Princeton Univ. Press, 1950.

Bridgman, P.W. Dimensional analysis. Yale Univ. Press, 1931.

Buckingham, E. On physically similar systems. Phys. Review, vol. 4, 1914.

Esnault-Pelterie, R. L'analyse dimensionelle. Lausanne, F. Rouge et Cie, 1946.

Irmay, S. Stress velocities and numbers and their use in hydrodynamic distorted and undistorted models. Israel J. of Technol., vol 3(3), 1965, p.203-208.

Irmay, S. La similitude hydrodynamique des modèles distordus. Hommage Campus, Liège, 1964, p. 175-180.

Ruark, A.E. Inspectional analysis: a method which supplements dimensional analysis. J. Elisha Mitchell Sci. Soc., vol. 51, 1935, p. 127-133.

Vaschy: Théorie de l'électricité. Baudry, Paris, 1896.

THE MODLE STUDY ON OUTFALL FOR SHANGHAI COMBINED SEWERAGE PROJECT CONSTRUCTION

Wei Heping
Tongji University
(Shanghai,China)

Abstract:

The principal purpose of the outfall modelling study is to provide necessary design prameter for The First Stage Shanghai Sewerage Project.The small flume was used primarily to determine the difusser characteristics such as numbers of nozzles,space of risers and jet angle.The large flume was used test the near field dispersion pattern of a complete outfall system which is based on the results obtained from small flume tests.

The general configuration of the outfall as presently planned in consistent with the results of this modelling study.

I Forward

The first stage project of Shanghai Sewerage Project settles mainly the problem of water pollution of Suzhou Creak, the project intercepts and drains the sewage from the catchment area along the Suzhou Creak, after a simple treatment,Sewage is discharged into Yangtze Rivers at Zhuyan(Fig.1),the area served is 70.6km,the population served is 2,550,000,the average DWF is 19.8cms, the maximum DWF is 32cms,and maximum WWF is 44.5cms.

The planned river outfall system consists of two tunnels,each approximately 1400 meter long. The outfall tunnels will be extended under the river to the edge of the south main channel and sewage is discharged at an average depth of about 13 meters.Current Velocity at the edge of the Channel is generally high , reaching a maximum about 2.5m/s, and slack water periods are short.

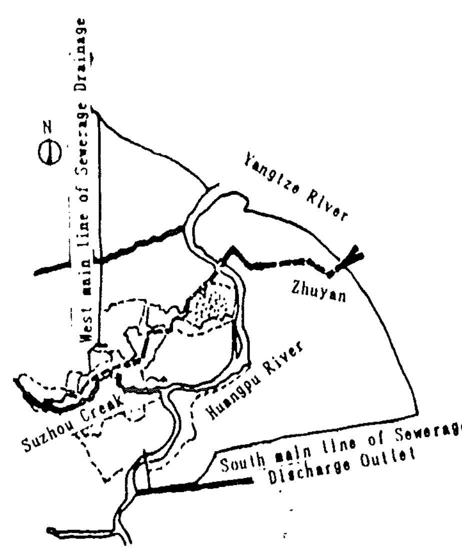

The principal purpose of outfall modelling study is to provide necessary base and parameters for designing diffuser at Zhuyan outlet.

This report covers the near-field hydraulic model studies conducted at Tongji University as a part of diffuser design study.

II Hydraulic Modelling Tests

The model test have been carried out in two flumes. Froude law was used to design the model and undistorted model should be adoped. Taking the length scale $L_r=100$, then Velocity scale is $U_r=\sqrt{L_r}=10$ and discharge scale $Q_r=100,000$. Combining prototype project. In small flume (fig.2), part of diffuser is to be modelled for partical model test, one diffuser section and two diffuser sections wirh different jet velocity, spacing of risers, jet angle, were used, and the concentration in near mfield and mixing zone were measured respectively, the dilution effects were analysed and compared, so as to determine the suitable spacing of risers, the number of nozzles and jet angle. In big flume the whole diffuser model test was done with the test parameters provided by the test in small flume, and the results were analysed, in order to determine the length of diffuser.

III Small Flume Model Test

The small flume is 8m long, 1.6m wide and 0.6m deep.

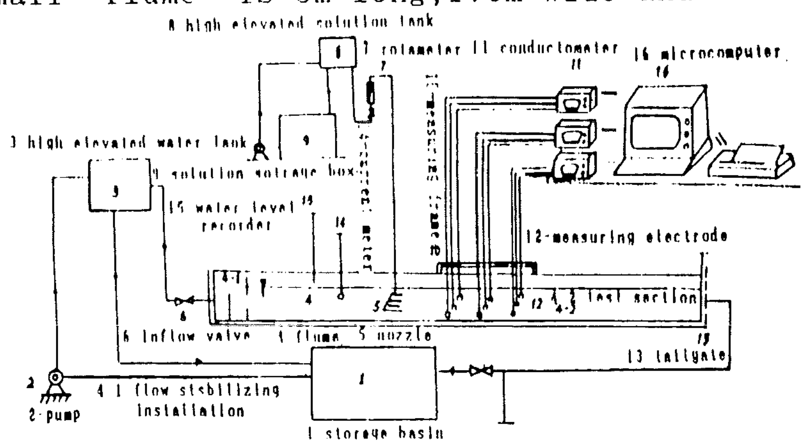

Fig.2 Scheme showing small fluse test equipment and installation

Partical model has the same scale with the whole model, the length of model diffuser section is 1.2m. At first, we fix the spacing of risers, and make different combination of number of nozzle, jet angle etc. The water depth above nozzle is 14m, ambient velocities are 0.1m/s, 0.5m/s, jet velocities are 2m/s, 2.55m/s and 3.55m/s. Under those above hydraulic condition, we do equal density concentration field dilution and diffusion tests. the test working conditions are as follows:

1. Number of nozzles

Initial dilution rises with decreasing of port ridiam when discharge of diffuser of unit length and sum of area of ports do not change. For jet angle 45°, the dilution of one riser having 2 nozzles 4 nozzles, 6 nozzles, 8 nozzles, 10 nozzles respectively (Satisfying $\Sigma a_i^{(4)} = \Sigma a_i^{(a)} = \Sigma a_i^{(b)} = \Sigma$

$ai^{(8)} = \sum ai^{(10)}$, $a^{(2)}, a^{(4)}, a^{(6)}, a^{(8)}, a^{(10)}$ are respectively nozzle areas of 2 nozzles, 4 nozzles , 6 nozzles, 8 nozzles ,10 nozzles),have been tested under different hydraulic Condition,the test results are shown in Fig.3.From Fig.3 one can see that the dilution of riser with 10 nozzles increases more slowly than that with 8 nozzles.

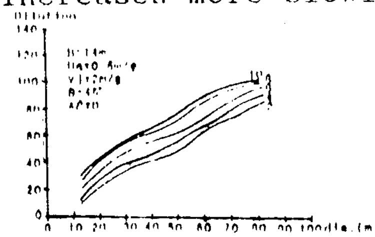

Fig.3 Comparison of nozzle number

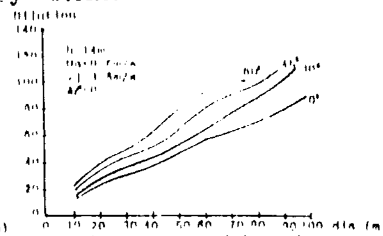

Fig.4 Comparison of jet angle

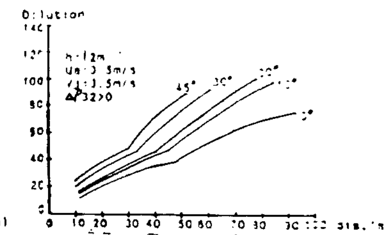

Fig.5 Comparison of jet angle

2. Jet angle

With four nozzles of a riser,the dilution of different jet angle e.i. 0°,10° ,20°,30°,45° were tested.For $\Delta\rho = 0$, the inital momentum of jet is the dominant factors to make the jet pollution cloud situated in what layer of receiving water body .It can be seen the greater the jet angle, the higher the slope of the s-x curves(see Fig.4). When $\theta = 0°$ or very small angle,the pollutunt cloud conceintrates at near the river bottom,where the river current velocity is small.the convection and diffusion of sewage in water is weakened: on the other hand ,the angle with cross current also small,so the dilution is weak.

The density difference is an important factor which affects appropriate jet angle.The outfall is situated at Yangtze estuary which is a salt tidal estuary.The superficial salinity variation range at Yangtze estuary(31 N,122 E)are in general 5-10% in summer ,15-20% in winter, and so at the site of proposed outfall ,the density difference is smaller than at the ocean.During test , we added suittable quantity of alcohol in the 'sewage' to make $\Delta\rho > 0$. The test results are shown in figure 5,from which, we see the dilution with 10° and 20° jet angle is better than that with 0° and 45°.

3. Spacing of Riser

Take two diffuser section for partial model test,each of length 1.20m, the spacing of riser are respectively 20cm,30cm,40cm,50cm. The risers of two diffuser sections arestaggered. We set up three salmping cross sections,each with distance along the flow of 40cm,60cm,80cm from the second diffuser section;at each cross section,we take 5 vertical. From the test, we know that the multiport jets are travelling a

table 1

Ua (cm/s)	Uj (cm/s)	θ	ρ_a	ρ_0	s (cm)	Nozzle diameter	Cross section minimum dilution 40 cm	60 cm	80 cm
5	35.5	30°	0.9985	0.9985	20	3.2	28	31	50
5	35.5	30°	0.9990	0.9990	30	3.8	27	31	52
5	35.5	30°	0.9985	0.9985	40	4.5	29	33	54
5	35.5	30°	0.9980	0.9980	50	5.5	30	33	55
5	35.5	30°	0.9985	0.9985	20	3.2	29	33	51
5	35.5	30°	0.9990	0.9980	30	3.8	29	34	51
5	35.5	30°	0.9985	0.9975	40	4.5	31	34	54
5	35.5	30°	0.9980	0.9980	50	5.5	32	35	53
1	35.5	30°	0.9985	0.9982	20	3.2	29	30	45
1	35.5	30°	0.9975	0.9975	30	3.8	28	31	47
1	35.5	30°	0.9982	0.9982	40	4.5	32	31	53
1	35.5	30°	0.9975	0.9975	50	5.5	34	33	52
1	35.5	30°	0.9982	0.9982	20	3.2	35	33	49
1	35.5	30°	0.9975	0.9975	30	3.8	33	31	51
1	35.5	30°	0.9982	0.9982	40	4.5	29	33	53
1	35.5	30°	0.9975	0.9975	50	5.5	30	33	51

certain distances, the neighboring jets mingle with each other, and the mingled jets undergo mixing and entraining. The entrained "sewage" will evidently lower the dilution effect, when the vertical component of the momentum does not become zero.Generally speaking ,the larger the spacing,the more favourable for dilution ,when hydraulic conditions of discharge,velocity, depth are fixed, we do tests for diffuser sections with riser spacing of 10cm,20cm,30cm, 40cm,50cm respectively ,the results shown for 10,20,30 spacing,the neighboring jets mingle very quickly. We suggest the spacing to be adopted is w=40cm or 50cm, in prototype the spacing is w=40m or 50m.

The Effect of riser spacing on effluent dilution were showen in table 2.

IV Big Flume Model Test

The big flume is 25m long,7m wide,0.7m deep,at two ends of flume,there are energy dissipating and flow stabilizing installations, and tailgates for controlling the flume water level and flow velocity .Ahead the flume is the control buliding.

Tn big flume we do the nine working conditions for test. At downstream of diffuser 100cm,200cm,300cm,500cm,four fixed cross sections were set up,each cross sections set 8 verticals,each vertical with five sampling points because the concentrations of pollutant clouds evidenlly pulsating,for every one sampling point,we take 500 samples per minute,and take the average,maximum and minimum values as output.The testing results are shown from figure 6 to figure 8. From those,we see that the longer the diffuser,the better the dilution effect. Only viewing on the point of dilution,one may take the diffuser length of 480m is fine .But the longer the diffuser ,the higher the constraction cost,the difficulty in construction also increases,furthermore the diffuser is situated at Zhu Yuan,to prolong the diffuser length would possibly impede navigation.

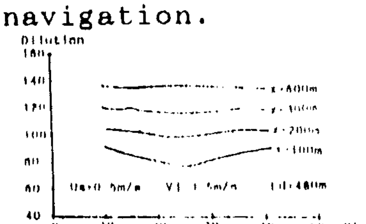

Fig.6 lateral distrib. of dilution

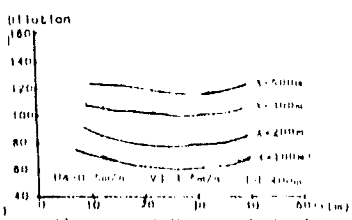

Fig.7 lateral distrib. of dilution

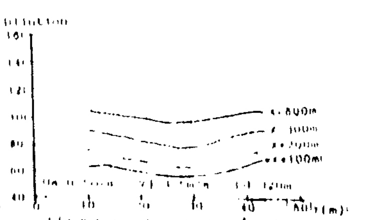
Fig.8 lateral distrib. of dilution

VI Conclusion and Suggestion

From our modelling study experiment,the multi-nozzles for one riser is favorable.The ambient flow has very big influence upon the dilution of effluent jet, even for very small surrounding river flow,its dilution effect is significant.The length of diffuser is of vital importance to dilution,jet angle and velocity,spacing of riser ,water depth also have effects on initial dilution. After the laborious test and comprehensive analysis of test data,we suggest the following parameters for diffusor project at Zhuyuan:

1. Numbers of nozzles:

Multiple nozzles are actually devised in all direction around the riser, it means that the the effluent will be distributed much more uniformly in the waste field along diffuser .That could be helpful in the dilution process,on the other hand clustered several nozzles per riser decreases the number of expensive risers needed.

The port number than 8 shows no obvious benefit,and therefore which is not recommended.

2. Jet angle

The greater the port angle from horizontal, the higher the slope of the curves.It seems that for more upward incline port ,the same dilution could be gained at shorter distance from the outlet.On the other hand,the plum might rise rather rapidly to reach the water surface if the jet angle is bigger and water depth isshallow. Based on test results,we suggest the jet angle be about 15°.

3. Spacing of rises

The mergence of the adjacent plume is given by the model test.It is generally within 20 meters, when the vertical component of velocity of plumes became zero.So,our suggestions is the spacing of the adjacent risers is 40m,and these two diffuser,their riser are staggered.

4. Length of diffuser

The determination of the length of diffusor is a comprehensive analysis among the environmental,economical and social benefits,for the outfall at Zhuyuan,because its location is very near the navigation channel of Yangtze River,too much extension of length of diffuser is not good choice.For length of 400 meters, under common hydraulic condition,at downtream 500 meters of outlet,the dilution can attain a value 100,only when the ambiend velocity Ua=0.2m/s,the dilution will below 100. while Ld=480m,the dilution is better,even for Ua=0.2m/s the dilution will be 100.

After analysing the hydraulogic data at Gaoqiao (near Zhuyuan),the maximum ambient current velocity is over 2m/s,and the lowect current velocity of 50% occurrence is

1.0-1.1m/s,and even the lowest velocity of 80% occurrence is 0.47-0.50m/s.Considering the possible overlapping of pollution cloud and conbining those three aspects of benefit.We suggest the length of diffuser is of 400 meters.

Above all the judgement has been on a sense of relativity. It was hard to say how precise or reliable the results predicted by the model test could be.But the relative comparison might be reasonable,

Achnowledgments

This study was supported by Shanghai Sewerage Project Construction Company,I am indebted to Professor Gao Tingyao Professor Gu Guowei,Professor Cai Butai,Professor Zhou Shansheng for pointing out to me some of the beneficial arguments.The writer would like to thank Mr. Xu liang ,Wang Zongtang,Chen Jinxia,and Chen Huixing for their many helpful comments.

Appendix I-Reference

1. Mixing in inland coastal water,
   Hugob.Fischer E.John List
2. Line plume and ocean outfall dispersion,
   Phliip J.W Roberts A.M. ASCE
3. Fluid mechanics of waste-water disposal in the ocean,
   Robert C.Y.Koh and N.H.Brooks
4. Two-dimensional flow field of multiport diffuser,
   Philip J.W.Roberts, A.M.ASCE
5. Spreading layer of two-dimensional buoyant jet,
   Roger B.Wallace and Steven J.Wright

Appendix II-Notation

The following symbols are used in this paper:

H -water depth of river at point of discharge m
Ua-ambient current velocity m/s
Vj-inicial jet velocity m/s
θ -angle of jet center line with horizontal
ρ_a -ambient density m/t
ρ_o -sewage density m/t
$\Delta\rho$ -difference in density between the ambient fluid and sewage in a jet m/t

EXPERIMENTAL EVALUATION OF THE EFFECT OF DISTORTION IN THERMAL PLUME MODELS

by

Bommanna G. Krishnappan
National Water Research Institute
Canada Centre for Inland Waters
Burlington, Ontario Canada

C.K. Jonys
Ontario Hydro
Toronto, Ontario Canada

Abstract

The effect of distortion in thermal plume models was studied in the Hydraulics Laboratory of Ontario Hydro, Toronto, Canada using a thermal plume model built to simulate the surface discharge of once-through cooling water of a nuclear power plant near Lake Ontario. The model was first operated as an undistorted model and then converted into a distorted model with a distortion of two. The results from the study show that the distortion tested did not have significant effect on the temperature distributions in the "near-field" zone. But, in the far-field zone, there was a large difference between the results of the two models. The difference in the far-field zone has been attributed to the lack of similarity of the Stanton Number which is a measure of the heat transfer rate at the air-water interface and the rate of heat input into the thermal plume.

Introduction

Distortion in thermal plume-models could have two opposing effects. In the near-field region where the spreading of the warm water discharge is dominated by the entrainment process, the distortion could produce a negative effect as the entrainment process depends on the characteristics of flow geometry and the topography of the receiving waterbody and hence requires the fulfilment of the geometric similarity. In the far-field region, on the other hand, the distortion can have positive effect because it enhances the turbulent mixing due to the vertical exaggeration and compensates the reduction of turbulence as necessiated by the Froude Number similarity. It also improves the ratio of the heat transfer rate at the air-water interface and the rate of heat input into the plume between the model and prototype and facilitates the adherence of Stanton Number similarity. These two processes are the dominating mechanisms for the spreading of warm water discharge in the far-field region. To quantify the effects of distortion, an experimental study was undertaken during the model testing of surface discharge of once-through cooling water from a nuclear power plant in the vicinity of Lake Ontario. The details of this study are presented in this paper.

Description of the Thermal Plume Model

The plan view of the modelled area and the discharge channel configurations tested are shown in Fig. 1.

GROIN LENGTH	GROIN SPACING SECTION A–A IN METERS	*Aspect Ratio	Flow Area m^2	Discharge Velocity m/s	Densimetric Froude No
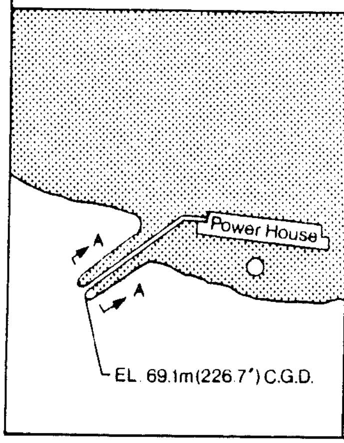	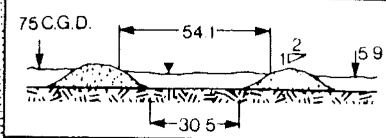	0.118	249.5	0.78	1.9
	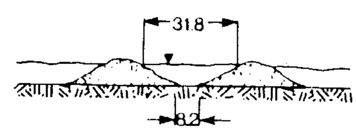	0.295	118.0	1.64	4.0
	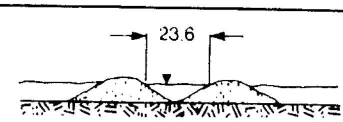	0.500	69.62	2.79	8.09

*corresponds to prototype

Fig.1. Summary of model data

This figure also contains the relevant parameters such as the aspect ratio, flow area and the discharge velocity of the warm water discharge. The values quoted correspond to prototype dimensions. The geometric scales used for the model study are as follows:

$\lambda_x = \lambda_y = 1/125$ for undistorted model

$\lambda_x = 1/250$ and $\lambda_y = 1/125$ for distorted model

where the symbol λ stands for the ratio of model value to prototype value. The scale relationships for the exit velocity u_o and the discharge rate, Q, of the warm water discharge were derived using the densimetric Fronde Number similarity as:

$$\left.\begin{aligned} \lambda_{u_o} &= \lambda y^{1/2} \\ \lambda_Q &= \lambda_x \lambda_y^{3/2} \end{aligned}\right\} \qquad (1)$$

The ambient flow was modelled according to the Froude Number similarity.

First, the model was operated as an undistorted model. Three different exit velocities were tested for the same discharge of 195 m^3/s and for the same initial temperature difference of 11°C. The discharge channel configurations were adjusted as shown schematically in Fig. 1. to achieve a densimetric Froude Number range of 8.09 to 1.90. The temperature distributions were measured using thermocouples mounted at a horizontal plane of 0.75 m from the free surface and the measured temperature distributions were plotted as isotherms in solid lines in Fig 2. Then, the model scales were changed and the model was operated as a distorted model with a geometric distortion of two. The same three exit velocities were tested. The flowrate of the warm water discharge was recalculated according to equation (1). The measured temperature distributions were also plotted in Fig 2 as dotted lines to the prototype-scale so that a direct comparison of the two model results could be made.

Results and Discussion

From Fig 2 it can be seen that as the degree of isotherm increases the agreement between the distorted and undistorted model results improves and for the degree isotherm which is nearly confined within the "nearfield" zone as calculated by the method fo Stolzenbach and Harleman (1971) and shown as circular arcs in Fig 2, the agreement is very good for all three exit velocities tested. The agreement deteriorates for lower degree isotherms which are in the "farfield" region. Again, as the densimetric Froude Number becomes small, the deterioration in agreement between the two model results becomes worse. From this result, one can conclude that the entrainment process responsible for mixing in the nearfield region is not effected by the distortion that was tested in the study.

The distortion seems to have larger impact in the "farfield" region where the heat transfer at the air water interface and the turbulent mixing due to ambient flow are the major governing mechanisms for the spreading of warm water discharge. Since distortion was achieved by changing the horizontal scale, the ambient flow field had not been changed and the turbulent mixing is the same in both models. Therefore, the differences in the results of the two models are mainly due to the difference in the values of the Stanton Number. Indeed, in the undistorted model, the actual size of the plume in the model is larger as the discharge rate is higher the whereas the distorted model, plume is smaller plume because of the reduced flow rate as required by the modelling criteria, i.e. eqn. (1).

A correction for the temperature distributions can be made by forcing the Stanton Number of the distorted model to be equal to that of the undistorted model (see Hindley & Miner, 1972, 1973). Since the Stanton Number is expressed as

$$S_t = \frac{\phi b_0}{\rho_a C_p . u_o h_0 \Delta T_0}. \qquad (2)$$

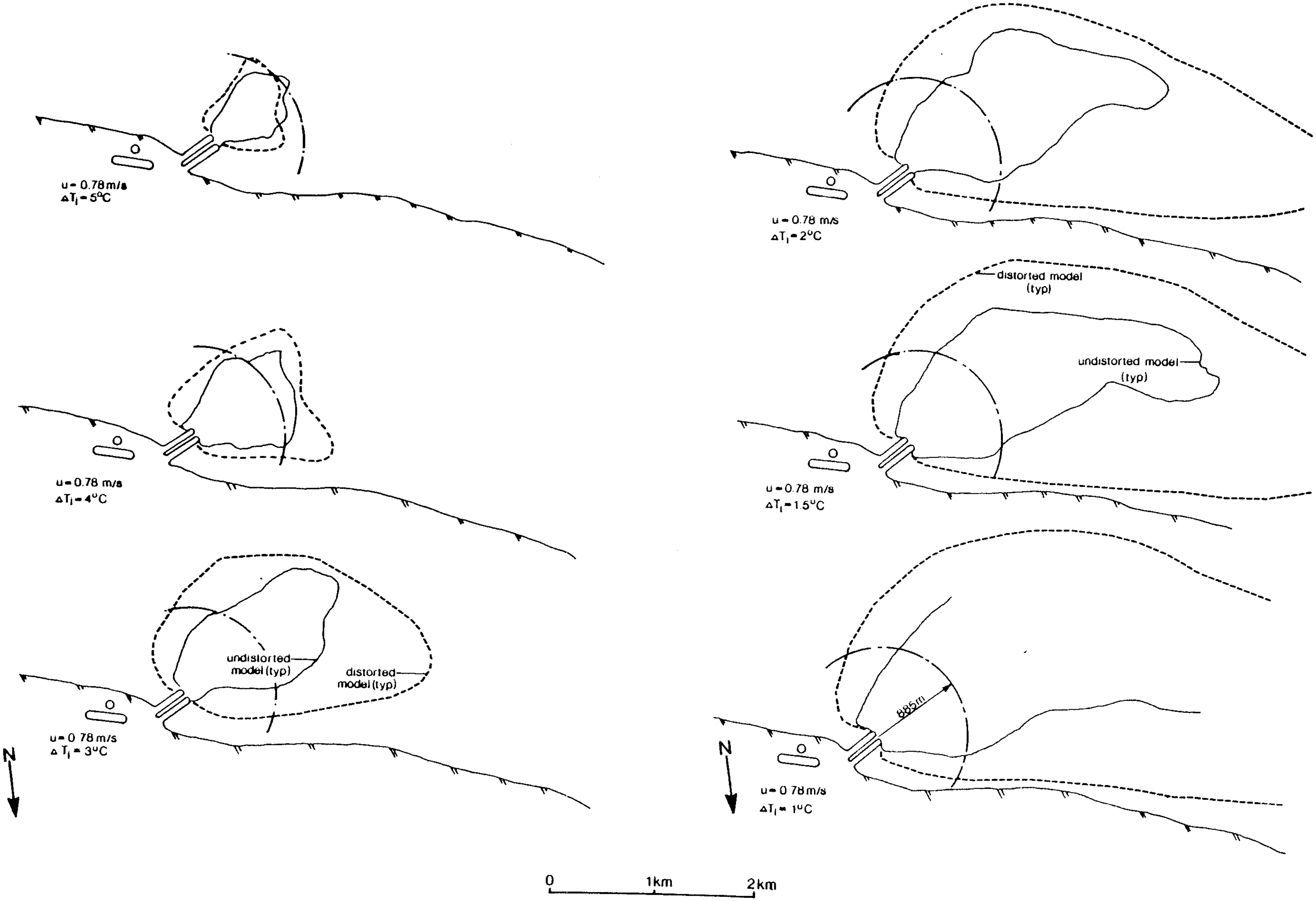

Fig.2. Comparison of temperature distributions for run no.1

where ϕ is the heat transfer rate at the airwater interface per unit area, b_0 is the width of the warm-water discharge, ρ_a is the density of the receiving body of water, C_p is the specific heat of water and the other symbols are as defined before, it is easy to show that the temperature correction that has to be made to compare the two distributions is equal to the value of distortion. In otherwords, if the undistorted model is considered as a "hypothetical prototype', the scale relationship for the temperature in the distorted model can be calculated as:

$$\lambda_{(T-T_a)} = n. \tag{3}$$

This means that a 2°C isotherm in a distorted model is equivalent to a 1°C isotherm in the undistorted model. In Figs 5 and 6, the areas enclosed by the different isotherms before and after performing the

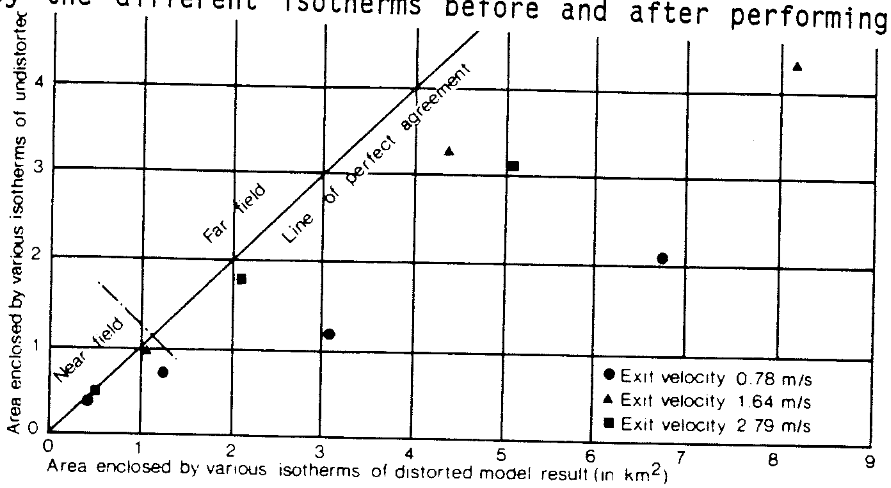

Fig. 5. Area enclosed by various isotherms of distorted and undistorted models

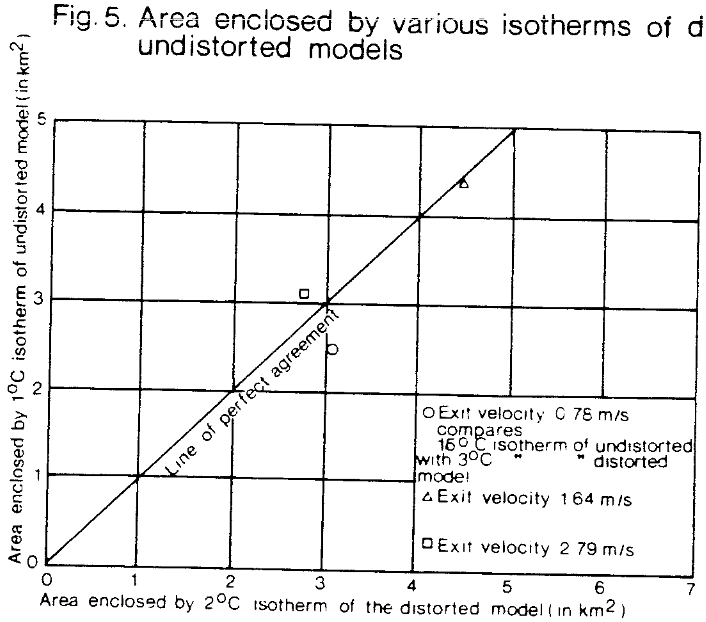

Fig.6. Area enclosed by 1°C isotherm of undistorted vs. 2°C isotherm of distorted model

above correction are plotted. It can be seen from Fig. 6 that the correction to the temperature distributions has resulted in a good agreement between the two model results.

Conclusions

From this study, the following conclusions can be drawn.

a) Distorting a thermal plume model by a factor of two did not produce significant effects to the entrainment process in the "near-field" zone.

b) The heat transfer rate at the air-water interface is significant in his far-field zone and should be taken into account in terms of the Stanton Number similarity.

References

1. P.D. Hindley and R.M. Miner, 1972. "Evaluating Water Surface Heat Exchange Coefficients", Journal of the Hydraulics Division, Proc. ASCE, vol. 98, No. 498.

2. P.D. Hindley and R.M. Miner. 1973. "Evaluating Water Surface Heat Exchange Coefficients", closure, Journal of the Hydraulic Division, Proc. ASCE, vol. 99, No. HYRO.

3. K.D. Stolzenbach and D.F. Harleman, 1971. "An Analytical and Experimental Investigation of Surface Discharges of Heated Water", R.M. Parsons Laboratory for Water Resources and Hydrodynamics, Dept. of Civil Engineering, MIT Technical Report No. 135.

Scale Effect of Geometric Distortion of Cooling Water Circulation Models

Chen Huiquan   Chen Yanru

Institute of Water Conservancy and Hydroelectric Power Research (IWHR), Beijing, China

Abstract

The paper presents some theoretical analysis and experimental study on the scale effect of model's geometric distortion. Contradiction and incompatibility of various simulation requirements are discussed. The flume investigations were carried out in a flume of $21 \times 2 \times 0.6$m. Simple configurations of receiving water body and intake–outlet structures were simulated with geometric distortion ratio ranging from 1 to 10. It is found the scale effect is connected with the effluent densimetric Froude No. and the crossflow ratio. Comparisons of experimental results obtained from models with different distortion ratios are illustrated. It is verified that model's distortion trends to exaggerate the horizontal diffusion and alleviate the vertical diffusion, a conclusion made by the writers decades ago.

Analysis of the Influence of Geometric Distortion

The influence of geometric distortion in modeling has been investigated early in 1970's by Chen[1], Abraham[2], Häggström[3]et al.. People used to simulate cooling water circulation in undistorted model for near field and in distorted model for far field. However, due to the coexistance of the two fields in the same model and their interaction, the problem is far more complicated in determining whether a geometric distorted model should be used and which distortion ratio is preferable. The complexion arises mainly from:

1) Contradiction of similarity requirement in diffusion

Let x, y, u, v, D_x, D_y are length, velocity, coefficient of diffusion in 2 perpendicular direction of $x-y$ plane, L, V, D_l the relevant value in any direction of the $x-y$ plane; z, w, D_z the relevant value in the water depth direction;

for distored model, $x_r = y_r = L_r \neq z_r,\ u_r = v_r = V_r \neq w_r,$

where subscript r denotes the ratio of prototype to model.

Similarity criteria from continuity, and energy equation:

$$(D_x)_r = (D_y)_r = (D_l)_r = u_r L_r = V_r L_r \tag{1}$$

$$(D_z)_r = w_r z_r = u_r z_r^2 / L_r = V_r z_r^2 / L_r \tag{2}$$

Similarity criteria from kinematic equation:

$$V_r = \Delta\rho_r^{1/2} z_r^{1/2} \quad (3) \qquad \text{and} \qquad V_r = z_r^{1/2} \quad (4)$$

when $\Delta\rho_r \neq 1$, keep (3) only. $\Delta\rho$ is the density diff. due to temp diff.

The similarity criteria for diffusion term is thereupon:

$$(D_l)_r = \Delta\rho_r^{1/2} z_r^{1/2} L_r \tag{5}$$

$$(D_z)_r = \Delta\rho_r^{1/2} z_r^{5/2} L_r^{-1} \tag{6}$$

Assume $D \sim U^a L^b$ (7), where U and L are the characteristic velocity and length of the water region.

Let $$\psi = \frac{\text{real value of } D_r}{D_r \text{ similarity criteria required}}$$

then for horizontal diffusion, $$\psi = \frac{U_r^a L_r^b}{\Delta\rho_r^{1/2} z_r^{1/2} L_r} \tag{8}$$

for vertical diffusion, $$\psi = \frac{U_r^a L_r^b}{\Delta\rho_r^{1/2} z_r^{5/2} L_r^{-1}} \tag{9}$$

For $a=b=1$, $U=V$ or $V^* = \sqrt{\dfrac{\tau_0}{\rho}}$, $L=l$ or h, value of ψ is shown in the following table in which ε is the distortion ratio, $\varepsilon = L_r / z_r$.

Characteristic of D	ψ	
	Horizontal Diffusion	Vertical Diffusion
$D \sim V^* h$	$\Delta\rho_r^{-\frac{1}{2}}\varepsilon^{-\frac{3}{2}}$	$\Delta\rho_r^{-\frac{1}{2}}\varepsilon^{\frac{1}{2}}$
$D \sim Vh$	$\Delta\rho_r^{-\frac{1}{2}}\varepsilon^{-1}$	$\Delta\rho_r^{-\frac{1}{2}}\varepsilon$
$D \sim Vl$	$\Delta\rho_r^{-\frac{1}{2}}$	$\Delta\rho_r^{-\frac{1}{2}}\varepsilon^{2}$
$D \sim V^* l$	$\Delta\rho_r^{-\frac{1}{2}}\varepsilon^{-\frac{1}{2}}$	$\Delta\rho_r^{-\frac{1}{2}}\varepsilon^{\frac{3}{2}}$

The table indicates a larger horizontal diffusion and a smaller vertical diffusion will present in the distorted model with $\varepsilon > 1$. The discrepancy depends upon the characteristics of diffusion which is closely related to the nature of the turbulence dominating the water region concerned.

2) Contradiction of similarity requirement in heat exchange

From similarity criterion of heat loss at free surface

$$\left(\frac{\text{heat flux through water}-\text{air interface}}{\text{total heat flux increment}}\right)_r = 1$$

$$(\rho C Q)_r = K_r A_r \qquad \text{or } V_r = K_r L_r / z_r$$

with Eq. (3), $Kr = \Delta\rho_r^{1/2} L_r^{1/2}$ (10), where K is the coefficient of heat dissipation and Q is the effluent discharge. Eq. (10) is difficult to realize. In fact, $K_r \ll \Delta\rho_r^{1/2} L_r^{1/2}$, i.e. $(K_m)_{\text{act}} \gg (K_m)_{\text{req'd}}$; the intensity of surface cooling in the undistorted model is exaggerated.

3) Contradiction of similarity requirement in ambient flow condition

The water region simulated in an undistorted model is usually much limited than that in a distorted model. Too small the water region involved in the model results in discrepancy in boundary flow condition, both hydraulically and thermally. Such scale effect in undistorted model is especially pronounced in the case of tidal flow.

The influence of geometric distortion to a certain physical phenomena is actually the combined scale effects induced by the above factors. Take intake temperature of cooling water T_2 as an example.

due to (1), T_2(distorted model) $<$ T_2(undistorted model)

due to (2), T_2(distorted model) $>$ T_2(undistorted model)

due to (3), T_2(distorted model) $>$ T_2(undistorted model)

Whether T_2 obtained from distorted model is less than T_2 from undistorted model is different from case to case.

Flume Investigation[4]

Through a lot of simplification, $\Delta T / \Delta T_0$ can be expressed as:

$$\frac{\Delta T}{\Delta T_0} = \varphi(\varepsilon, F_\Delta, \alpha^*) \tag{11}$$

where, ΔT is the temp. diff. of the water surface temp T and the ambient water temp T_∞ at any point in heated effluent receiving water region; ΔT_0, the temp diff of the outfall temp T_0 and T_∞, $F_\Delta$is densimetric froude number and α^* is ratio of the crossflow and outfall velocity.

In accordance with Eq. (11), scale effect of distortion were investigated through comparison of the $\Delta T / \Delta T_0$ distribution with ε under various combination of F_Δ and α^*. For all the test runs, the horizontal dimensions remain constant with water depth changed to form the different ε. Discharge Q is changed accordingly.

The experiments were carried out in the flume with dimension of $21 \times 2 \times 0.6$m as shown in Fig. 1. The ranges of the experimental parameters are: $\varepsilon = 1-10$; $\alpha^* = 0-1.05$; and $F_\Delta = 1.9-4.9$.

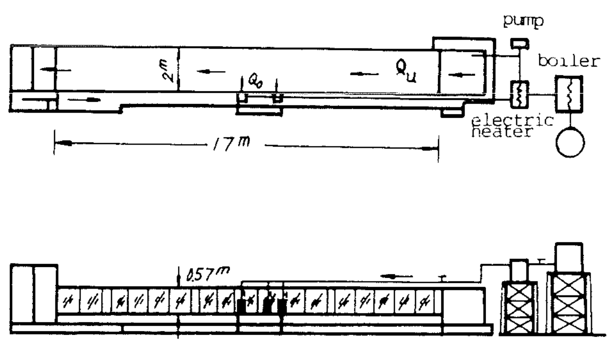

Fig. 1 Test Flume

With the variation of α^*, three types of flow with somewhat different thermo-hydraulic characteristics for modelling could be classified:

$\alpha^* > 0.3$, intensive crossflow type;

$\alpha^* = 0.08-0.3$, weak crossflow type;

$\alpha^* < 0.08$, reservoir or pond type.

Over 100 test sets have been run and some typical comparisons are illustrated in Fig. 2,3,4. It is obviously shown that the intensity of thermal stratification increases with geometric distortion. The results of flume tests also disclose the fact that the modification due to the geometric distortion affects on flow pattern and temperature distribution with the change of ε is in a continuous way and no abrupt change could be definitely found. The limited value of ε therefore

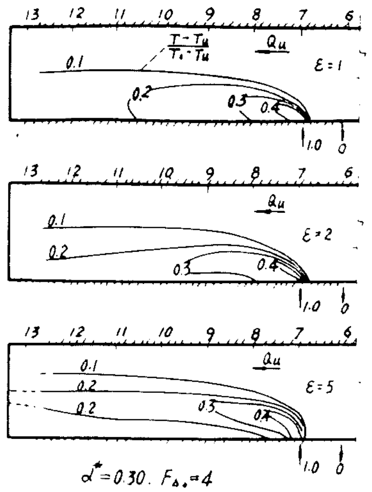

Fig.2 Surface Temp Pattern under Different Distorted Scale

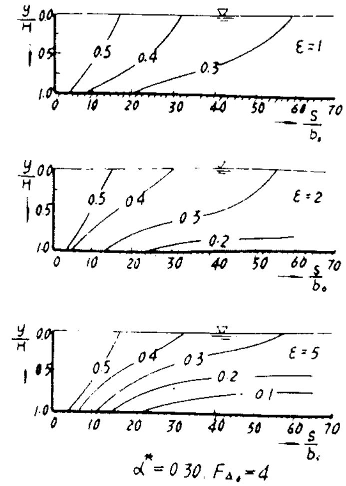

Fig.3 Vertical Temp Pattern along Jet Axis under Different Distorted Scale

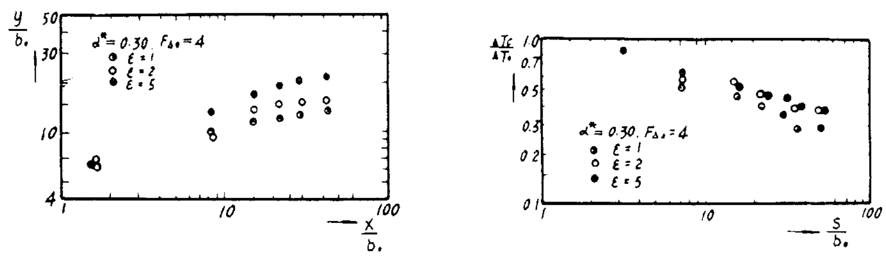

Fig.4 $\frac{y}{b_0} \sim \frac{x}{b_0}$ *and* $\frac{\Delta T_c}{\Delta T_0} \sim \frac{S}{b_0}$

seems to be a some fuzzy number determined with some personal judgement. It can be concluded:

(1) Geometric distortion trends to exaggerate the horizontal diffusion and the vertical stratification.

(2) The distortion effect is closely connected with the F_Δ and α^*, smaller the F_Δ and α^*, more significant the scale effect.

(3) Scale effect due to geometric distortion is in general not pronounced with $\varepsilon < 2-3$, and in some cases, model with distortion ratio $\varepsilon = 5-6$ or even more is acceptable.

Case Studies

About 20 cases of physical simulation with thermo–hydraulic models of 2 different distortion ratio for the same engineering project have been conducted in China. Here 2 typical examples are introduced to illustrate their comparisons of experimental results for the same water region obtained from models of dfferent ε.

1) Sunan Nuclear Power Plant: $Q = 210\text{m}^3/\text{s}$. A distorted model with $L_r = 800$, $z_r = 80$ was used to investigate the overall behavior of the relevant course of the Yangtze River and an undistorted model with $L_r = z_r = 100$ was used to study the thermo–hydraulic features of the local water region near outlet. [5]The temperature patterns obtained from two models are shown in Fig.5. Their comparison indicates that the geometric distortion is accompanied with larger the thermal diffusion, thinner the upper thermal layer and higher the surface temp, the same conclusion drawn from both the theoretical analysis and flume tests.

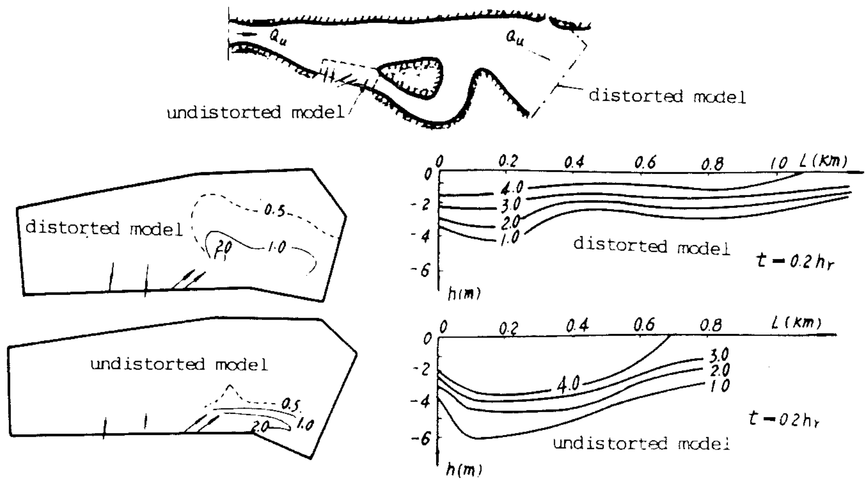

(a). Surface Temp Pattern (b). Vertical Temp Pattern along Jet Center Line

Fig.5 Distorted and Undistorted Model of Sunan Power Plant

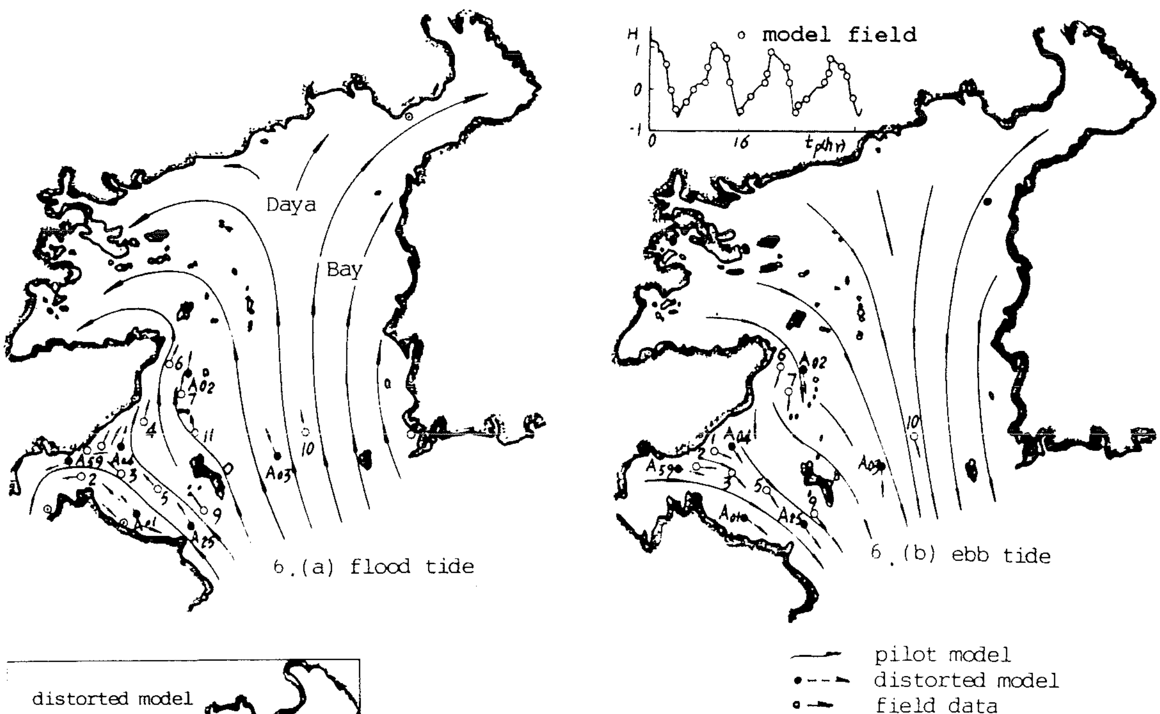

Fig.6 Comparison of Tidal Flow Pattern in Daya Bay Models

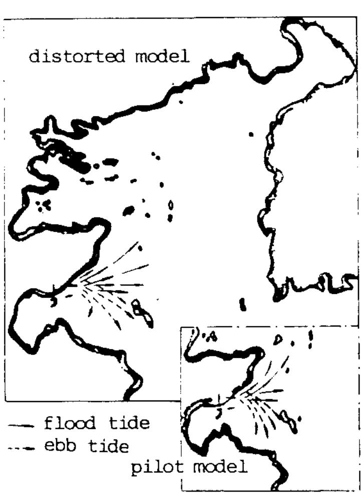

Fig.7 Comparison of Thermal Flow Prediction of Daya Bay Models

2) Daya Bay Nuclear Power Plant: $Q=98\ m^3/s$, two models simulating the same water region were performed:[6] a pilot model with $L_r=5000$, $z_r=100$ and a distorted model with $L_r=800$, $z_r=100$. Fig.6 is the tidal flow patterns from these model with some prototype data also presented. Fig. 7 is their thermal flow predictions.

All the comparisons show a good conformity between the models. It also reveals that a model with ε up to 50 could still be used effectively as an available means for feasibility study if it is properly designed.

Concluding Remarks

It is usually a complex and annoying problem to reach a decision whether a geometric distorted model should be used in thermo–hydraulic modeling and which distortion ratio is prefer able. The complexity arises from the fact that not only the scale effect due to geometric distortion are related to many factors, including hydrological, topographical conditions of the effluent receiving water region, the engineering aspect of the intake and outlet and their performances, but also a correct assessment should be made for the relative weight of the geometric distorted scale effect to the total scale effect induced by non–fulfillment of other similarity criteria. The following three points should be noted in the selection of model scale ratios:

1) In a strict sense, no thermo–hydraulic model can be designed to fulfill all the similarity requirements and no thermo–hydraulic models are undistorted. It is appropriate to examine beforehand the priority and the relative ratio of the scale effect due to geometric distortion to those from other distortions.

2) Due to the conflicting requirments in the different similarity criteria, the model deformity due to geometric distortion may cause positive effect in simulating other physical phenomena.

3) The scale effect of geometric distortion is different for different physical feature to be simulated and studied in the model.

Therefore, the limitation of distortion ratio could not be determined straightway. The correct choice of model scales is in fact a balancing of many mutual conflicting necessities, a trade off with advantages and disadvantages of geometric distortion, and a harmony of (1) the main objective of the model studies, (2) the accuracy of the model investigation pursuited, and (3) the space and facility the lab provided.

It is an overall estimation and judgement to make the thermo–hydraulic test possible in the given time and lab space in the one hand and to have the similarity requirements satisfied to the full possible extent on the other hand. It should be treated not only as a science but an art as well, and it is in this context that the problem of geometric distortion deserves further exploration.

References

[1] Chen Huiquan, On the Theory and Practice of Simulation of Cooling Water Flows. Research Report of IWHR, 1974. (in Chinese).

[2] Abraham G.,Hydraulic Near–field Modeling and Far–field Modeling, Heat Disposal from Power Generation in the Water Environment, Chapter 10, A, B. 1975.

[3] Häggström S., Surface Discharge of Cooling Water, Effects of Distortion in Model Investigations. Report Series A:3, Dept. of Hydr, Univ. of Technology, 1978.

[4] Chen Huiquan, Chen Yanru, Zhang Yukong, Kang Zhanshang, Study on the Scale Effect of Geometric Distortion of Cooling Water Circulation Models. Research Report of IWHR, 1988. (in Chinese).

[5] Li Ruisheng, Chai Fangkun, Distorted and Undistorted Model Studies on Cooling Water for Power Plants. Journal of Hydraulic Engineering, No. 5, 1989. (in Chinese).

[6] Yue Juntang, Model Study on Cooling Water Circulation in Daya Bay. Rsearch Report of IWHR, 1985. (in Chinese).

Session 10A

Jets and Plumes

PHYSICAL MODELLING OF THERMAL DISCHARGES IN SURF ZONE

By N. M. Ismail[(1)] A.M. ASCE, R.L. Wiegel[(2)] F.ASCE. P.J. Ryan[(3)], M. ASCE and S.W. Tu[(4)],M.ASCE

ABSTRACT: The mixing of thermal jets being discharged from Diablo Canyon power plant into a semi-enclosed embayment, and heading directly into surface gravity waves coming from offshore, was modelled in the laboratory. A series of sensitivity tests was conducted to verify the 1:75 scale undistored hydraulic model. The results showed that correct modelling of offshore incident wave field, wave breaking, wave reflection and nearshore bathymetry is significant for accurate prediction of plume trajectory and temperature distributions. Although, with the modelling limitations of wind-waves and offshore bounderies, the model proved to be a valid predictive tool over the total range of plant operating and oceanographic parameters.

INTRODUCTION

During 1985 and 1986 an extensive series of model tests were performed to verify the physical model of the Diablo Canyon Power Plant thermal discharge, as required by the findings of the 1975 NRC Environmental Hearings. The plant layout and an overall plan view of the physial model are shown in Fig.1 The physical model is located at the hydraulic laboratory (RFS) of University of California, Berkeley. The basic approach of model verification consisted of running the model for the plant discharge and ambient current, the tide and wave conditions that existed during the Unit 1 and Unit 2 Power Ascension Tests (P.A.T.), and comparing prototype and model temperature distributions in the vicinity of the discharge, both within and outside Diablo Discharge Cove.

---

1 Asst. Prof. of Environmental Engrg., Dept. of Civ. Engrg., Jordan Univ. of Sci. & Tech. Jordan; formerly, Sr. Engr.,Bechtel Petroleum,Inc., San Francisco, Calif.
2 Prof. of Civ. Engrg., Univ. of Calif., Berkeley, Calif.
3 Chief Engr., Hydraulics/Hydrology Group, Bechtel Civil Inc., San Francisco, California.
4 Research Engr., Dept. of Engr. Research, Pacific Gas and Electric Company, San Ramon, Calif.

PHYSICAL MODEL OF DIABLO CANYON

The model is an undistorted densimetric Froude model with a scale of 1:75. The model basin is 85ft by 64ft by 2.5ft deep (26m x 19.6m x 0.76m). Model bathymetry was based on prototype hydrographic studies plus aerial photography. Coastal currents parallel to the coast were generated using a pump/manifold system. Dynamic tides were simulated using a computer controlled system. A piston-type wave maker was used to generate monochromatic waves of the deep-water significant height and period. Temperature measurements were taken using a 45 sensor array, spaced at 50 ft (15.2m) (prototype) centers in the horizontal and 4 ft (1.2 m) in the vertical. The entire array could be moved in 3 directions, allowing the 3-dimensional plume field to be measured. Ranges of plant and field ambient conditions are 2000-4000 cfs for flow discharge, 17-20°F for temperature rise, 0-7ft for tide level, up to 300fpm for current speed and 3-8ft for waves significant height.

Experimental Procedures - Detailed model operating and instruments calibration procedures for the model were developed and strictly adhered to. Water level, currents, waves, discharge flow and its temperature were established (Ref.2) to simulate field conditions. The system was allowed to come to quasi-steady state prior to taking any wave, temperature and velocity measurements.

SENSITIVITY LABORATORY TESTS

During this stage it was observed as the modelled wave height increased, the difficulty of simulating temperature field conditions in the model was increased significantly. It was observed that wave-induced currents due to breaking of waves in the south part of the west entrance and wave reflection at the entrance sides, had a significant impact on temperature profiles in Diablo Cove. In addition the model offshore boundaries had a pronounced effect on the current profile in the far-field and a uniform offshore profile could not be maintained. Thus it was found that modelling of wave transformamtion and boundaries have an important effect, both on plume trajectory and mixing in the model. Wave reflection and breaking effects were reached in the model by installing wave absorbing materials and small rocks in key areas due to the lack of bathymetric data in these areas. This approach was followed until the observed effects in the field on plume trajectory and temperature profiles were obtained in the model. Fig.2 shows a photo of dye visualization of the cold water ingress and circulation in the discharge cove due to wave breaking on the plateau near the west entrance. (Ref.1).

LABORATORY RESULTS

The overall model results indicated that the model satisfactorily simulated the behavior of the prototype over a wide rage of Unit 1 and Unit 2 operating levels and ambient conditions. Based on the model/ prototype comparisons the following results can be drawn :-

- o For near surface temperatures the agreement between model and prototype was generally excellent as illustrated in Fig. 3
- o The model/prototype agreement was good in terms of both isothermal surface area and plume configuration. Fig.4 shows a comparsion of isothermal surface area.
- o For low water levels the agreement of vertical temperature profiles was generally good for all depths and all lines. For high water levels, the model tended to understimate the depth of the plume on the offshore lines as shown in Fig. 5

CONCLUSIONS

The physical model has been verified over a wide range of plant and ambient oceanographic conditions. Although of the limitations of exact modelling wind-waves mixing effects and lateral boundaries in the far field, it can be said that the physical model was a reliable predictive tool over a wide range of ambient conditions, as long as it is operated in a way which minimizes the effects of the model boundaries. However, some types of ambient conditions, e.g. weak or upcoast current conditions, or rapidly changing current conditions, cannot be simulated in the model, at least in terms of the configuration of the offshore plume.

APPENDIX 1. REFERENCES

1. Ismail , N.M., Ryan , P.J. and Tu, S.W. "Role of Wave Transformation on Mixing of Buoyant Jets", ASCE Speciality Conf. on Nearshore Hydrodynamics, Delaware, June 29-July 1, 1987.
2. Ryan, P.J. , Ismail , N.M., Lou R. Tu, S.W. and Wiegel, R.L., "Hydraulic Model Verification Tests for Units 1 and 2 Diablo Canyon Power Plant", Report No. 420-DC-87.15, Dept. of Engrg. Research, Pacific Gas and Electric Co., Calif., March 1987.

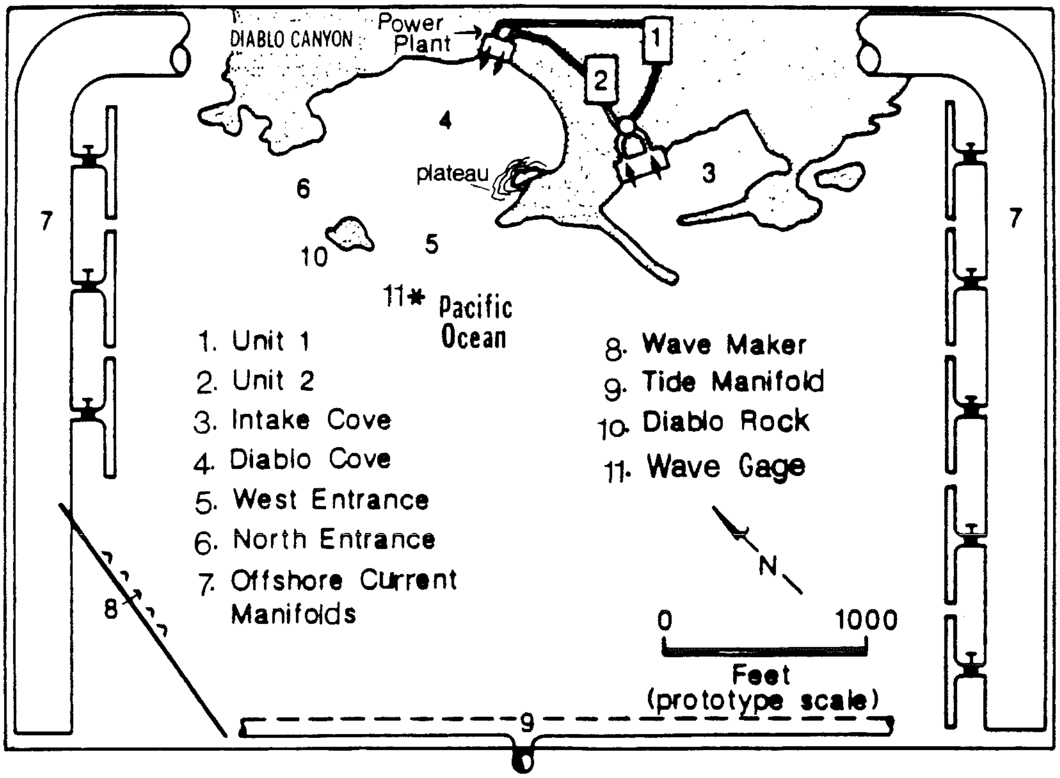

FIG.1 Layout of Physical Model

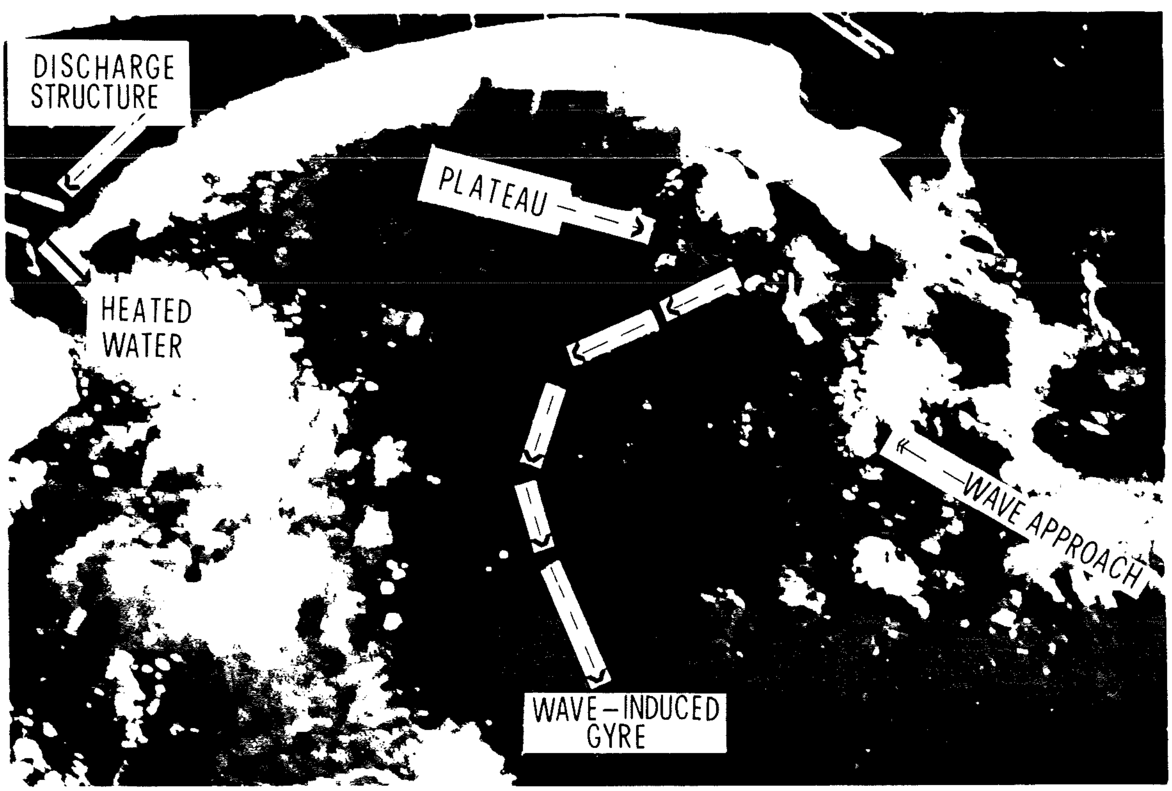

FIG.2 Dye-Visualization of Induced Currents & Circulation in Diablo Cove

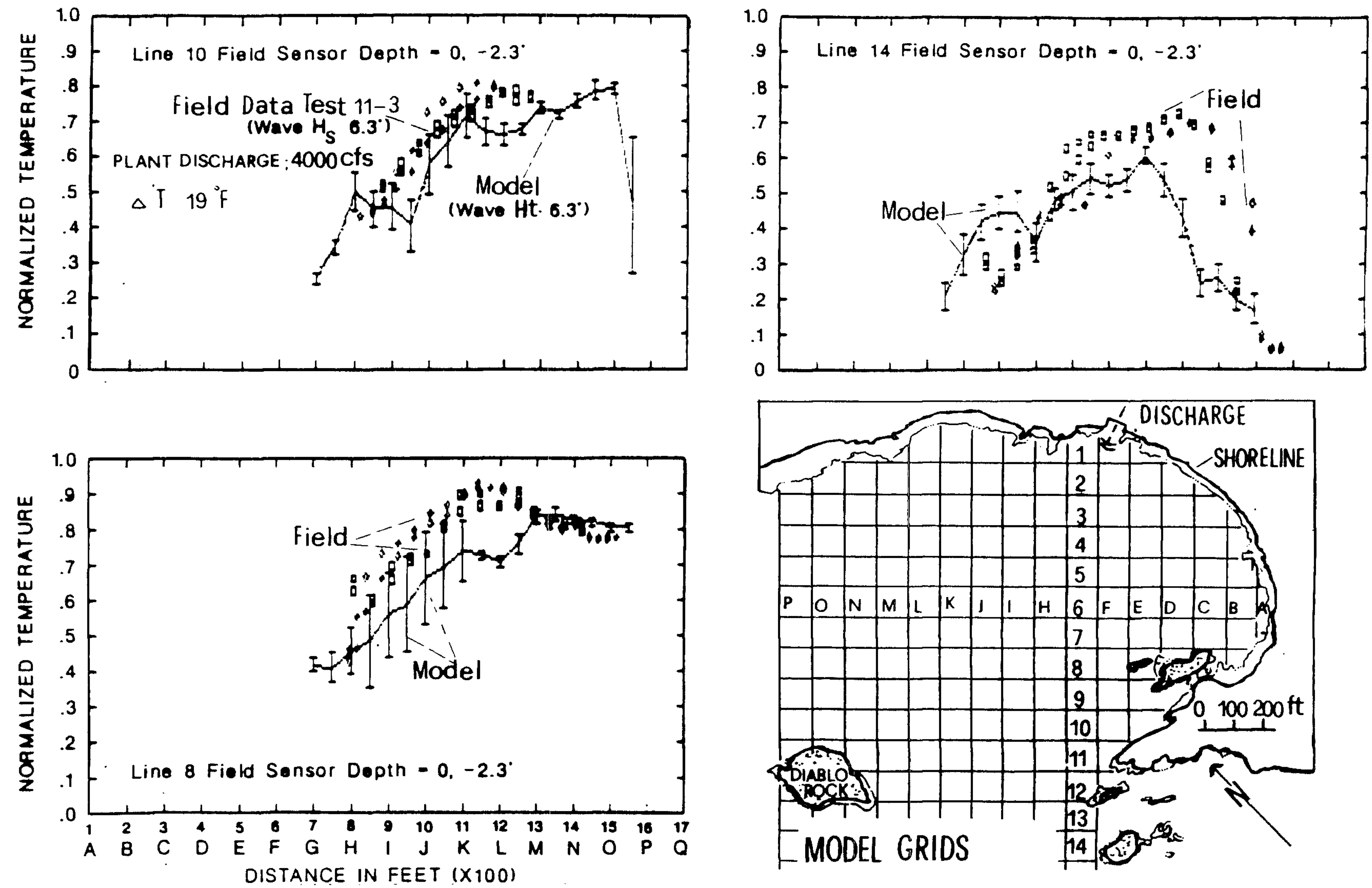

FIG. 3 Comparison of Model and Field Horizontal Temperature Profiles; Low Tide

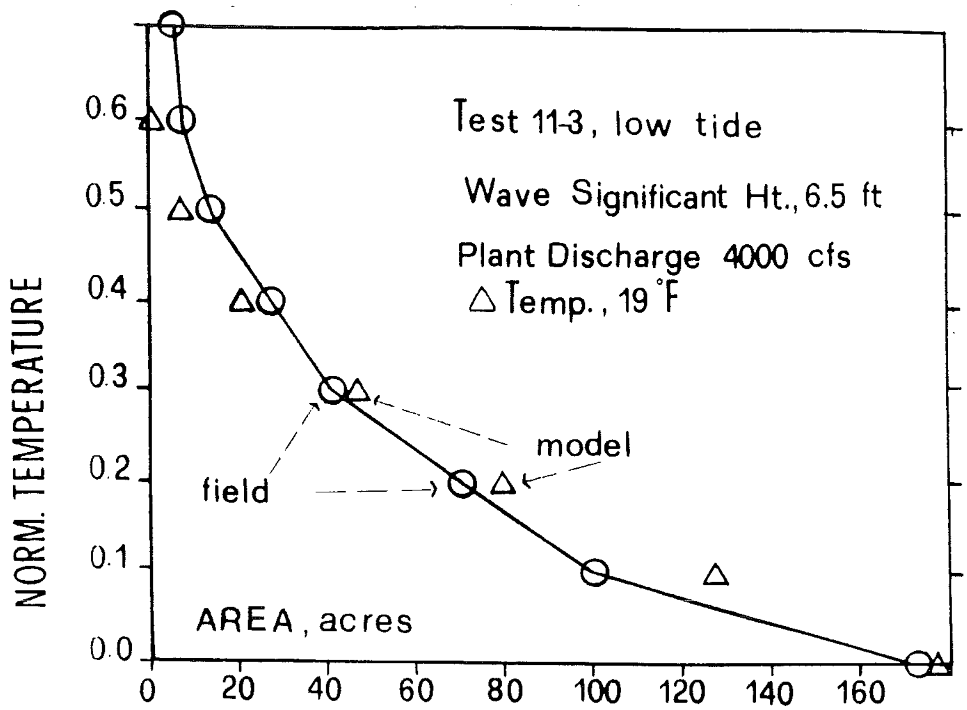

FIG.4 Comparison of Model and Field Isotherm Areas

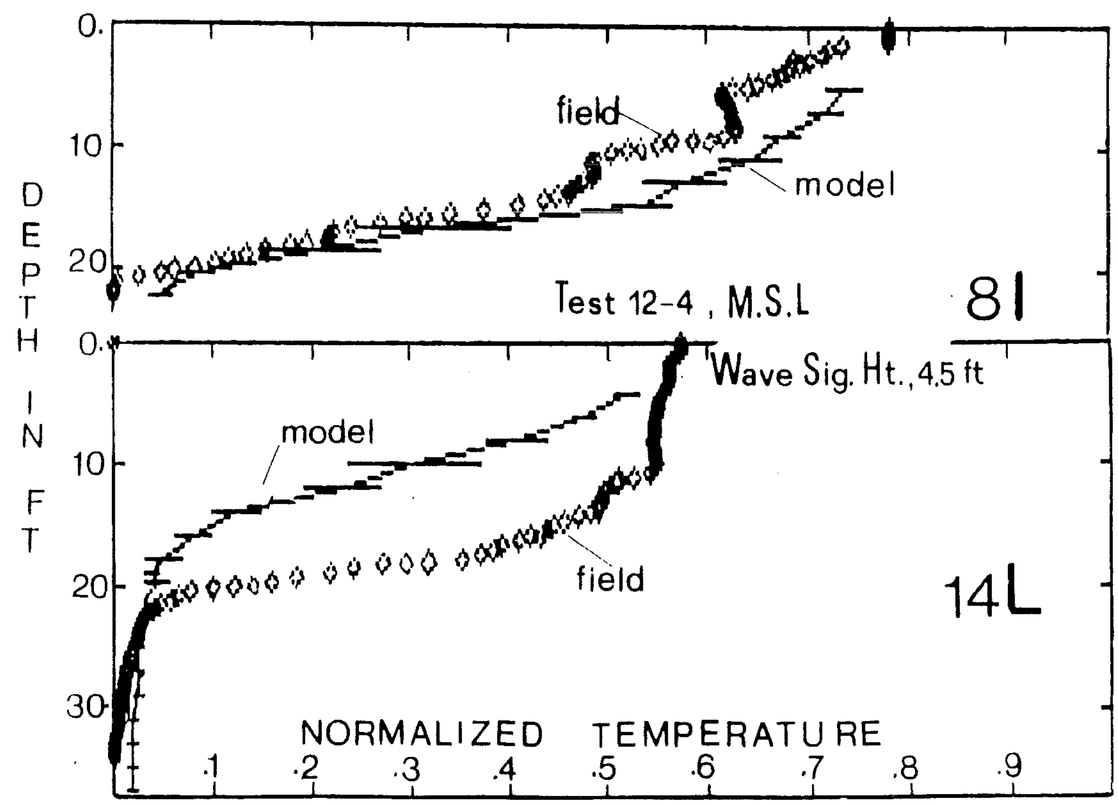

FIG.5 Comparison of Model and Field Vertical Temperature Profiles at Grids 8 I & 14 L (FIG.3)

REYNOLDS NUMBER EFFECTS ON TURBULENT JET DILUTION

by George E. Hecker
Alden Research Laboratory, Inc.
Holden, MA 01520 USA

ABSTRACT

Experimental studies are reported for horizontal, round buoyant jets for which the densimetric Froude number was maintained constant while the Reynolds number was varied from 2×10^3 to 4×10^4. Results show that dilution is a function of Reynolds number in the tested range, and that entrainment is somewhat higher at the lower Reynolds numbers. Presented data are useful in the interpretation of hydrothermal model studies.

INTRODUCTION

Physical hydraulic models based on Froude similitude are frequently used to study the dilution of effluents and to predict prototype concentrations. The Reynolds number of the discharge is orders of magnitude smaller in the model, and practical constraints typically result in model jets with Reynolds numbers between 10^3 and 10^4. The influence of the reduced Reynolds number on scaling jet dilution is assumed to be small for jets turbulent from their origin. Little data are available, however, which indicate if dilution changes with Reynolds numbers in the fully turbulent range. This paper reports on experiments to determine whether or not model tests are "conservative" (have less dilution) due to this scale effect, as frequently assumed.

PREVIOUS WORK

It is generally accepted that a jet is fully turbulent from its origin for $R=VD/\nu>2.5\times10^3$, Pearce (1966); Anwar (1972). An early investigation on the affect of Reynolds number on fully turbulent jet characteristics was conducted by Baines (1948), who determined that the length of the potential core, L, was a minimum at about $R=10^4$, as seen in Figure 1. Since other jet flow parameters can be related to changes in the potential core, Baines concluded that the Reynolds number should be considered when studying fully turbulent jets.

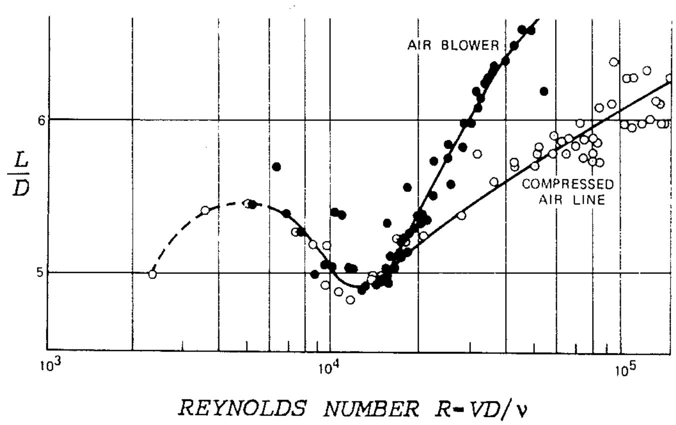

FIGURE 1 VARIATION IN LENGTH OF POTENTIAL CORE FOR AIR JETS (BAINES, 1948)

Ricou and Spalding (1961) published the results of a study based on a novel experimental technique to measure jet dilution. Basically, the technique consisted of surrounding an air jet with a porous container, and of supplying an accurately measured quantity of air through the porous wall until the longitudinal pressure gradient was zero, thereby simulating a free jet. This method allowed direct measurement of the total entrainment to a given distance from the jet origin and avoided the problem of integrating the asymptotic lateral velocity profile. At Reynolds numbers greater than 2.5×10^4, measured entrainment coefficients agreed with other published values. Figure 2 indicates that as the Reynolds number was decreased, the dilution, S, increased to a maximum value at about $R = 3 \times 10^3$, and then decreased with continued decreases in Reynolds number as the jet origin became laminar.

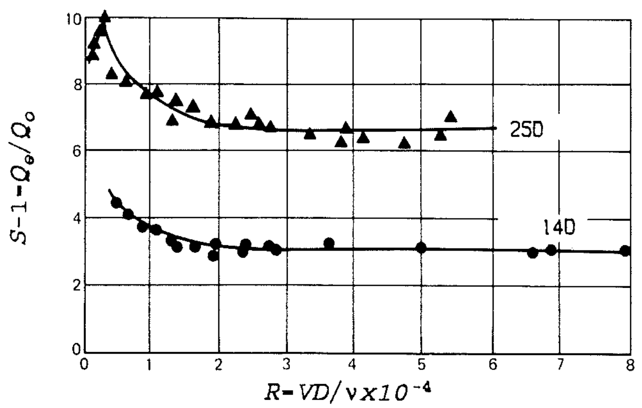

FIGURE 2 DILUTION VERSUS REYNOLDS NUMBER (RICOU AND SPALDING, 1961)

Ungate (1974) measured concentration profiles in a vertical buoyant jet specifically to determine Reynolds number effects on dilution. Clear decreases in dilution were noted as the jet origin became laminar, for $R < 2.5 \times 10^3$, see Figure 3. No apparent effects of Reynolds number on dilution were said to occur beyond $R > 1.2 \times 10^3$, although some increase in dilution is evident for increasing Reynolds number. Since Reynolds numbers greater than 5×10^3 were not tested, any decrease in dilution at higher turbulent Reynolds numbers was not apparent.

Numerous studies have demonstrated that the larger scale turbulence in jets is not random, but exhibits some coherence. Crow and Champagne (1971) showed that there is a concentration of the large scale turbulence at a characteristic Strouhal number of 0.30, based on the frequency of a fluctuating parameter, the exit velocity, and the initial jet diameter. Such coherence appears limited to the potential core, according to Hussain and Zaman (1981), whose data indicate that details of the coherent structure depends on the jet Reynolds number, and that Reynolds number similarity would not be achieved even at $R = 10^5$.

Available information thus indicates that a jet is fully turbulent from the point of discharge at $R > 2.5 \times 10^3$, but that variations in the jet potential core length, entrainment, and turbulence structure occur even for jets with Reynolds numbers higher than this transitional value. This experimental study of fully turbulent jets was conducted to determine what Reynolds number would be necessary to achieve similarity of

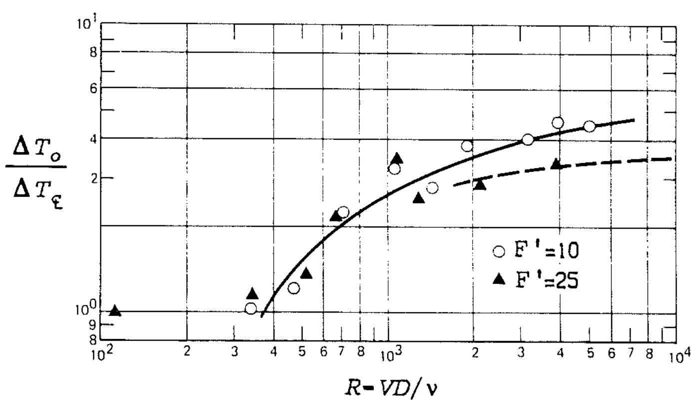

FIGURE 3 CENTERLINE DILUTION VERSUS REYNOLDS NUMBER FOR BUOYANT JETS AT x/D = 15 (UNGATE, 1974)

jet entrainment. Since entrainment is also a function of the densimetric Froude number, a procedure was devised which allowed the Reynolds number to be varied at a constant densimetric Froude number.

EXPERIMENTAL PROCEDURE

The main series of tests reported on herein was conducted at a fixed jet densimetric Froude number of 35. This value was chosen as typical for buoyant jets, and was held constant within ±3% to eliminate the Froude number as a variable. A single horizontal, buoyant jet was sampled at three distances along its trajectory from the origin, 20D, 40D and 60D, where D = the initial jet diameter. In addition, the maximum surface concentration approximately 95D from the jet origin was also measured to obtain integral dilutions in comparison to centerline dilutions evaluated from the jet profile data. In all cases, the initially horizontal jet was submerged 40D and had a clearance of 20D to the tank bottom. To obtain the desired range of Reynolds number, two jet diameters were used, 0.25 inch (6.3mm) and 0.75 inch (19mm). For each jet, the initial velocity and discharge temperature were varied such that the densimetric Froude number was held constant while varying the Reynolds number. Jet discharge was measured by calibrated flow meters. Effects of residual swirl, turbulence, and boundary layer thickness of the approach pipe flow were minimized by inserting baffling upstream from elliptical contractions which formed the jet. Velocity traverses for each jet using commercial LDA equipment verified the desired flat discharge velocity profile over the range of Reynolds number tested.

Due to the relatively large tank size used, time was available to obtain steady state measurements, particularly below the heated surface layer. Care was taken to let all currents in the tank dissipate prior to initiating the jet discharge, such that the jet was not deflected nor its dilution affected by ambient currents or turbulence.

The heated jet was sampled one cross-section at a time by the thermocouple grid shown in Figure 4. For each position along the trajectory, the vertical section was fixed at right angles to the centerline trajectory, calculated according to Fan and Brooks (1969). Each sensor was attached to the support such that the measuring tip, which had a time constant of approximately 0.3 seconds, was located sufficiently upstream to obtain undisturbed temperatures. During measurements of maximum surface temperature, this probe array was removed and a separate probe array was mounted with the sensors just below the water surface.

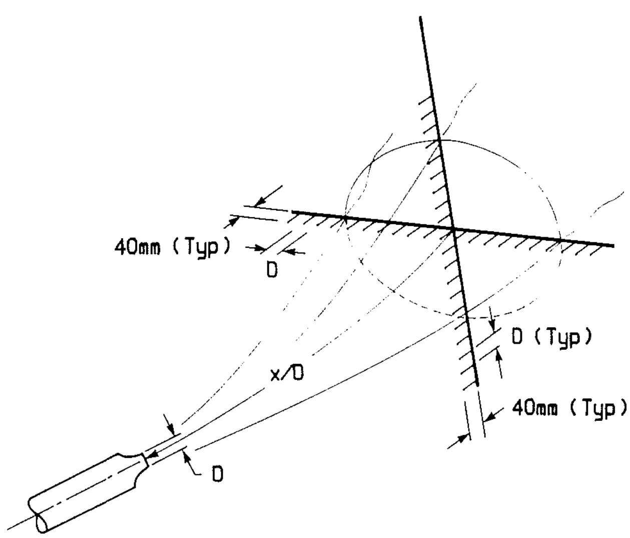

FIGURE 4 ARRANGEMENT OF SENSOR GRID FOR CROSS-SECTIONAL MEASUREMENTS

Scanning of probes, including those measuring the ambient and initial jet discharge temperatures, was controlled by a small computer. Approximately 60 scans were obtained for each position of the sensor array, and these data were reduced by computer such that 40 scans representing steady state conditions could be selected. For each sensor, the mean temperature rise and the standard deviation from the mean were calculated, and a plot of the mean temperature rise versus probe position allowed evaluation of jet profile shape and position of the maximum concentration relative to the center of the probe array. The maximum surface concentrations were determined by selecting two sensors having the maximum temperatures. Any probe reading for which the standard deviation was greater than the mean concentration was discarded, which was the case for some probes near the jet boundary.

A second stage of data reduction determined a least square fit of the data for the horizontal and vertical traverse segments, and provided extrapolated centerline concentrations after an axis shift to locate the actual jet center. The curve fitted data were also used to find the relative spread, $\lambda^2 b^2/D^2$, from

$$\Delta T/\Delta T_{℄} = e^{-r^2/\lambda^2 b^2}$$

where ΔT = temperature rise at a measured point, $\Delta T_{℄}$ = maximum centerline temperature rise, r = radial distance from jet center to the measuring point, λ = a factor relating temperature to velocity profiles, and b = the characteristic jet width.

A plot of $\ln \Delta T$ versus r^2 for each segment of the probe array allowed determination of $\Delta T_{℄}$ and $(-\lambda^2 b^2)^{-1}$. The value of r used in the plots was in jet diameters, after translation of coordinates. Translation of coordinates was performed based on a search grid until a minimum difference in extrapolated centerline concentration was achieved between the four segments of the probe array. The left and right sides of the horizontal probes produced symmetrical profiles, while the vertical profiles were not expected to be symmetrical due to buoyant forces. Centerline concentrations from each of the four segment extrapolations are plotted versus Reynolds number. It should be noted that the curve fitting, axis shifting, and centerline extrapolation techniques produced only small changes in centerline positions and maximum concentrations from those measured directly.

TEST RESULTS AND EVALUATION

Centerline concentrations were plotted versus jet Reynolds number for the various distances from the jet origin. For a distance of 40D, Figures 5 and 6 show the change in centerline concentration and jet width, respectively, with Reynolds number. In general, these plots illustrate a gradually increasing concentration and decreasing jet width with increasing Reynolds number. The increase in concentration over the tested range of Reynolds number was from approximately 0.10 to 0.13, representing a decrease in dilution of from approximately 10 to 7.7. From these data, it seems that model tests with jets should be conducted with as high a Reynolds number as practicable. Alternately, some correction for the decrease in concentration at low Reynolds numbers may be made.

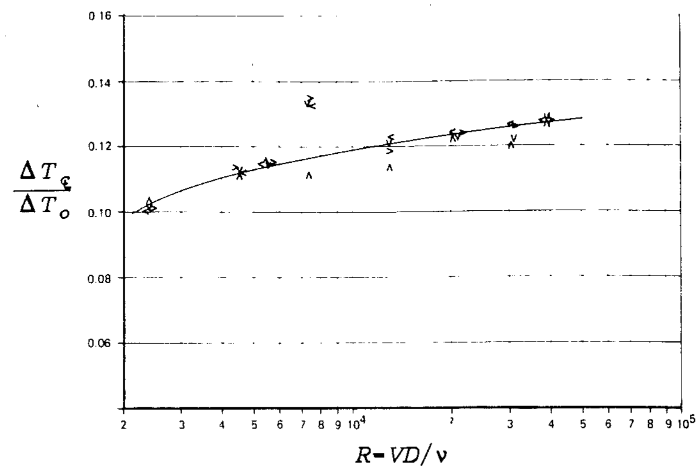

Although the data show a tendency for the characteristic jet width to decrease with increasing Reynolds number, consistent with the data on concentration, it may be concluded that the variation in jet width (or spread angle) is not a sensitive indicator of jet dilution for turbulent jets.

FIGURE 5 CENTERLINE CONCENTRATION AT 40D VERSUS REYNOLDS NUMBER (F'=35)

Since the surface layer of a buoyant jet consists of a more representative sample of the total jet flow, the maximum surface concentration was also measured and plotted versus Reynolds number. Figure 7 shows less tendency for the surface concentrations to increase with increasing Reynolds number compared to the case for centerline concentrations, indicating a model Reynolds number of 10^4 may be adequate.

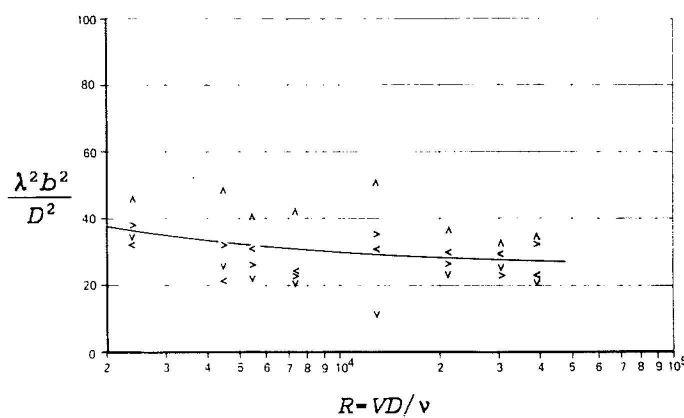

FIGURE 6 JET WIDTH VERSUS REYNOLDS NUMBER (F'=35)

These results from tests on a single horizontal buoyant jet should not be used directly for multi-jet discharges since other factors, notably total water depth, jet interference, and restrictions in the available path of entrained water may dominate diffuser induced dilution and overshadow the secondary effects of Reynolds number. However, it may be concluded that model tests are not "conservative" (produce higher concentration) due to low jet Reynolds numbers.

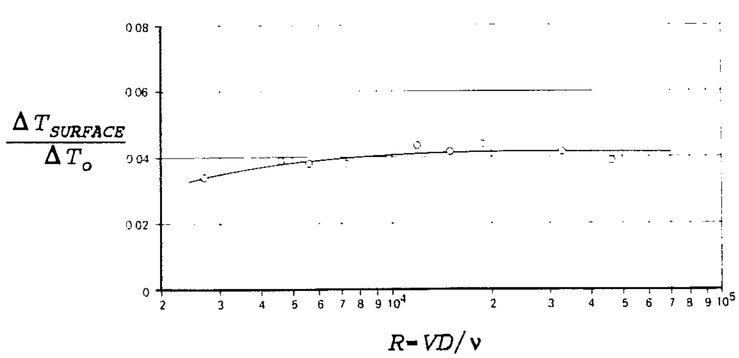

FIGURE 7 SURFACE CONCENTRATIONS AT 90D (F'=35)

REFERENCES

Anwar, Habib, O., "Appearance of Unstable Buoyant Jet", Journal of the Hydraulics Division, ASCE, Vol. 98, HY7, July 1972, p. 1143.

Baines, W.D., "Investigations in the Diffusion of Submerged Jets", M.S. Thesis, Department of Mechanics and Hydraulics, State University of Iowa, 1948.

Crow, S.C. and Champagne, F.H., "Orderly Structure In Jet Turbulence", Journal of Fluid Mechanics, Vol. 48, 1971, Part 3, pp. 547-591.

Fan, Loh-Nien, and Brooks, N.H., "Numerical Solutions of Turbulent Buoyant Jet Problems", Report No. KH-R-18, W.M. Keck Laboratory of Hydraulics and Water Resources, California Institute of Technology, January 1969.

Hussain, A.K.M.F., and Zaman, K.B.M.Q., "The 'Preferred Mode' Of The Axisymmetric Jet", Journal of Fluid Mechanics, Vol. 110, 1981, pp. 39-71.

Pearce, A.F., "Critical Reynolds Number for Fully-Developed Turbulence in Circular Submerged Water Jets", National Mechanical Engineering Research Institute, Council for Scientific and Industrial Research, South Africa, CSIR Report MEG 475, 1966.

Ricou, F.P., and Spalding, D.B., "Measurements of Entrainment by Axisymmetrical Turbulent Jets", Journal of Fluid Mechanics, Vol. 11, Part 1, 1961, pp. 21-32.

Ungate, C.D., "Temperature Reduction in a Submerged Vertical Jet in the Laminar Turbulent Transition", M.S. Thesis, Department of Civil Engineering, MIT, 1974.

LIST OF SYMBOLS

b = characteristic jet width

D = initial jet diameter

F' = densimetric Froude number = $V/\sqrt{g \frac{\Delta\rho}{\rho} D}$

g = gravitational constant

L = length of potential core

Q_o = initial jet discharge

Q_e = entrained flow

r = radial distance from center of jet cross-section

R = jet Reynolds number = VD/ν

S = dilution = Q_e/Q_o+1

V = initial jet velocity

ν = kinematic viscosity

ρ = water density

$\Delta\rho$ = change in water density

ΔT_o = initial jet temperature rise

$\Delta T_{\mathbb{C}}$ = temperature rise at centerline of jet

$\Delta T_{surface}$ = temperature rise at free surface

λ = ratio of mass to momentum flux

FLOW FIELD OF AN OFFSET JET

by

Ali A. Salehi-Neyshaboury
Tarbiat Modarres University
Faculty of Engineering, Tehran

Kamil H. M. Ali
Civil Engineering Department
Unviersity of Liverpool, UK

Abstract

An experimental study is presented which details the mean flow characteristics of a two-dimensional offset jet.

One single offset ratio was used with three different discharges. The ratio of the height of the nozzle above the solid wall to the nozzle height was 26.2.

Velocities were measured, in the horizontal and vertical directions, in the pre-attachment jet region using a propeller meter.

The experimental results of the present writers' were compared with previously-published data.

Introduction

The flow field of an offset jet is shown in Fig. 1. A plane, incompressible, turbulent water jet is discharged into quiescent ambient surroundings in the vicinity of a plate offset from and parallel to the axis of the jet. When the jet enters the tailwater, its action is similar to that of a turbulent free jet, in that it entrains fluid from the surrounding tailwater. However, when the jet efflux is close to a solid boundary there is only a finite volume of fluid which is available to be entrained between the jet and the bed boundary. Therefore, the surrounding fluid being entrained must be replenished by a back flow near the plate. This will set up vortices in the surrounding fluid. Because of the back flow and the vortices set up in the region, the pressure below the jet will be considerably lower than that above the jet, and consequently the jet deflects towards the boundary and eventually attaches to it.

By attaching to the boundary, the jet encloses a region of eddying motion known as the recirculation region (Fig. 1). The jet region extending from the nozzle's exit to the point of attachment is commonly referred to as the pre-attachment region.

Experimental Facilities and Procedures

In the experiments described herein, the behaviour of a two-dimensional offset jet impinging on a rigid bed was investigated. The experiments consisted of velocity measurements in both of the horizontal and vertical directions. These velocities were measured at various sections along the centreline of the jet.

The experimental set up is shown in Fig. 2. A glass open channel was 3.4m long, 0.6m wide and 1.0m deep. A vertical sluice gate was constructed from a 25mm thick perspex cut to the width of the channel. The gate was supported by a metal frame and could be lifted using a gear box. The sluice gate opening was measured by using two dial gauges located on top of the gate and having an accuracy of 0.01mm. A bottom vertical weir was fixed to the channel wall and had a height of 0.3m. To ensure uniform and two-dimensional flow, two pieces of half-rounded perspex pipes were used to form a well-designed sluice entrance (Fig. 2).

A centrifugal pump was connected between the storage tank and the header tank and was used to produce the required discharge. The flow rate was adjusted using a valve. The incoming flow was efficiently streamlined by the header tank and its gradually convergent sections (Fig. 2).

Downstream of the end weir, water was guided and collected in the storage tanks, thus completing the flow circulation.

The flow-rate was calculated by measuring the average incoming velocity at the sluice entrance using a propeller meter. Depth gauges were used to measure the water levels upstream and downstream of the sluice gate. These depths were used to calculate the theoretical discharge.

Velocity Measurement

All velocities were measured using a streamflow miniature current meter manufactured by Nixon Instrumentation Ltd. (Ref. 6).

The velocity measurements were taken over a grid of location in both the horizontal and vertical planes. To do so, two types of probes were used, one straight probe to measure the horizontal velocities, and a bend probe to measure the vertical velocities. The streamflow probes were held in a perspex block which was attached to a depth gauge. This assembly was fixed to a carriage which could be positioned at any desired point in the experimental area.

At various horizontal distances, x, two components of velocity at various vertical distances, y, above the bed were measured. In this study, the "floor velocity" was measured at y = 0.8cm (equal to half the diameter of the streamflo rotor) above the bed. Since the probe only recorded positive velocities, negative velocities were noted when the rotor reversed its direction of turn.

A single jet height and nozzle thickness were used. However, experiments were done using four different flow rates (Experiments No. 1 to No. 4).

Experimental Results

In order to obtain information about the flow field, detailed time-averaged velocity profiles were obtained at several downstream locations. The horizontal components of velocity, U, are shown in Fig. 3 with the magnitude of the velocity represented by displacement of the profile.

The vertical components of velocity, V, are shown in Fig. 4, with the magnitude of the velocity represented by displacement of the profile in the x-direction (a downward V velocity is represented by a negative x displacement). Again, the traverse location indicator in each figure represents the zero velocity position for a particular profile.

The resultant velocity vectors for this flow are shown in Fig. 5 with the length of each vector corresponding to the velocity magnitude in the indicated direction. The point represented is located at the "tail" of the velocity vector. It can be observed in Fig.5, that between the lower portion of the jet, the bed and the wall containing the sluice, a clockwise vortex or eddy has been formed by the entraining effect of the jet.

As can be seen from Fig. 5, the primary jet flow curves slowly towards the bed, through the first half of the recirculation region and then turns sharply downward as the jet impinges on the offset channel floor. This trend has been observed in previous studies of this geometry and also in backward-facing step flows. The division between the forward and reversed jet flow along the offset channel is observed to occur in the vicinity of $x/b_o = 40$. Downstream of this point the flow approaches that of a wall jet.

Figure 6 shows the maximum horizontal velocity of the flow near the bed. This figure shows that for all of the jet flows, the "floor" velocity initially increases with x/b_o reaching a maximum then decreasing with further increase in distance from the jet. Also, the floor velocities for the maximum jet discharge are considerably higher than those for the other flows.

Attachment Length

The exact location of the intersection of the dividing streamline with the offset channel, i.e. the attachment length, x_A, was obtained by considering detailed mean velocity measurements in the x direction, in the jet impingement region. Based upon these results, the average attachment length was determined within $0.1b_o$ to be $x_A = 40.3b_o$.

In Fig. 7 the present attachment length data are plotted along with other investigators' results. The present results for the offset ratio agree well with the experimental results presented in previous studies, where different measurement techniques were used to obtain the attachment length.

Locus of Maximum Velocity

To define a trajectory for the offset jet is very useful in any theoretical work. The locus of the position of the maximum velocity was chosen as the reference streamline, s, and the cross-stream co-ordinate, n, is normal to s.

A least square curve fit was applied to the locus of maximum velocity (Fig. 8) resulting in the following expression

$$y_m/h = C_o + C_1(x/x_A) + C_2(x/x_A)^2 + C_3(x/x_A)^3 + C_4(x/x_A)^4 + C_5(x/x_A)^5 \quad (1)$$

where $C_o = 1$, $C_1 = 0.581$, $C_2 = -4.452$, $C_3 = 10.708$, $C_4 = -12.31$ and $C_5 = 4.85$.

The resulting curve is shown in Fig. 8.

Velocity Decay

The maximum total velocity, V_{max}, was determined as a function of distance along s. A plot for the decay of the non-dimensional maximum velocity (V_{max},$/U_1$), in the downstream direction, s, was next produced for the results of the present experiments (Fig. 9). Due to turbulent diffusion, V_{max}, in general, decreases with s. The present results indicate that for $s/b_o > 32$, decay of the maximum velocity, in the pre-attachment region, is different from that of the free jet flow shown in the same figure.

Jet Spread

To determine the upper jet spread, linear interpolation of the velocity components was used along the line perpendicular to the s axis, to find the value of n where the jet velocity is equal to one-half the maximum velocity. A plot of the upper jet spread, b_u, (value of n where $U = 0.5\ V_{max}$), is given in Fig. 10. Also given is the line for the spread of a two-dimensional free jet whose equation is (Rajaratnam, 1976): ($b_u = 0.11s$).

Figure 10 shows that the variation of b_u/b_o with s/b_o is almost linear for $s/b_o < 27$, where the effect of curvature is negligible. However, for bigger values of s/b_o, the flow is curving sharply towards the bed and it results in a considerable increase in b_u/b_o.

Conclusions

The characteristics of the turbulent plane offset jet flow, with a single offset ratio but with different discharges were examined.

Comparison of the attachment length with the experimental results of previous investigations showed good agreement.

Detailed mean horizontal and vertical velocity components were measured in the pre-attachment region. Using these components, a plot of velocity vectors was made which provided a clear visualisation of offset jet flow and in particular the recirculation region and the jet's curvature. The jet is observed to curve slowly through the first half of the recirculation region and then turn sharply downward to the attachment point.

References

1. Ali, K. H. M. and Salehi-Neyshaboury, A. A., "Application of the strip integral method to turbulent offset jets", XXIII Congress of IAHR, August 1989, Ottawa, Canada, pp A-339-A-346.
2. Bourque, C. and Newman, B. G., "Reattachment of a Two-Dimensional Incompressible Jet to an Adjacent Flat Plate", Aeron. Quar., VII, Aug. 1960, pp 201-232.
3. Hoch, J., "Two-dimensional jet-boundary interaction for submerged thermal discharges", Doctoral Dissertation, The City Univ. of New York, 1979.
4. Hoch, J. and Jiji, L. M., "Two-Dimensional Turbulent Offset Jet-Boundary Interaction", ASME J. of Fluids Engerrr., V103, Mar. 1981, pp 154-161.
5. Rajaratnam, N. and Subramanya, N., "Plane Turbulent Reattached wall Jets", ASCE J. of Hydraulics Div., V94, HY1, 1968, pp 95-112.
6. Salehi-Neyshaboury, A. A., "Impingement of offset jets on rigid and movable beds", Ph.D thesis, University of Liverpool, 1988.
7. Sawyer, R. A., "The flow due to a two-dimensional jet issuing parallel to a flat plate", J. of Fluid Mech. Vol. 9, 1960, pp 543-560.

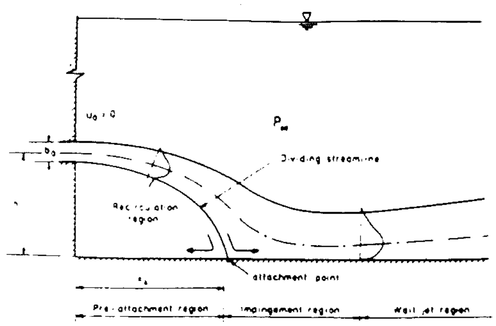

FIG 1 DEFINITION SKETCH FOR AN OFFSET JET

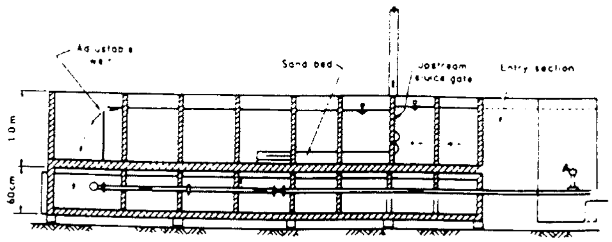

FIG 2 SKETCH OF LABORATORY LAYOUT

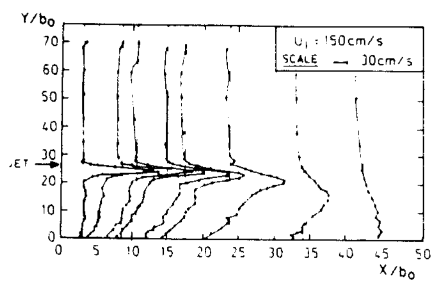

FIGURE 3 HORIZONTAL VELOCITY DISTRIBUTION OF OFFSET JET No 4

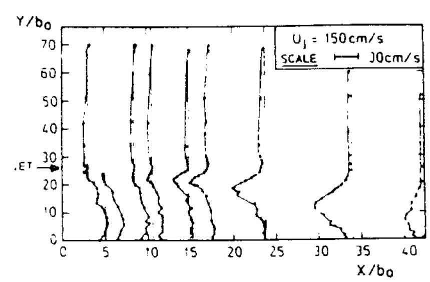

FIGURE 4 VERTICAL VELOCITY DISTRIBUTION OF OFFSET JET No 4

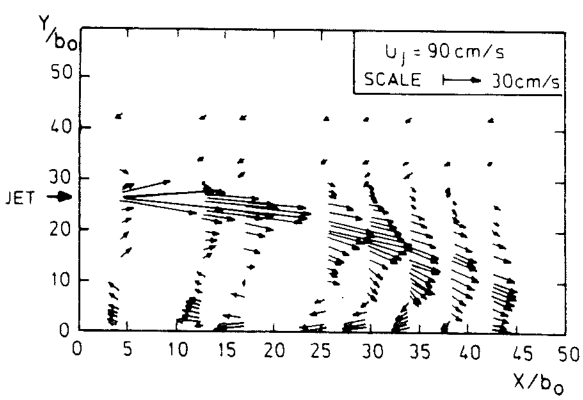

FIGURE 5 VELOCITY VECTOR FOR OFFSET JET (No 3)

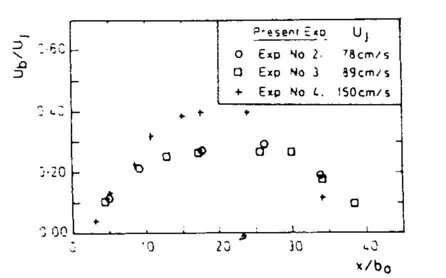

FIGURE 6 DISTRIBUTION OF MAXIMUM VELOCITY OF NEAR-BED FLOW FOR OFF-SET JET

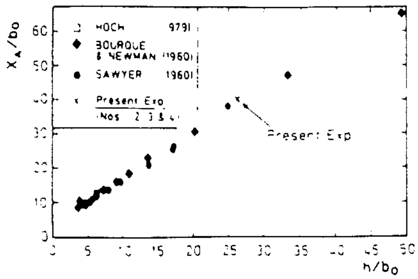

FIGURE 7 ATTACHMENT LENGTH vs OFFSET RATIO

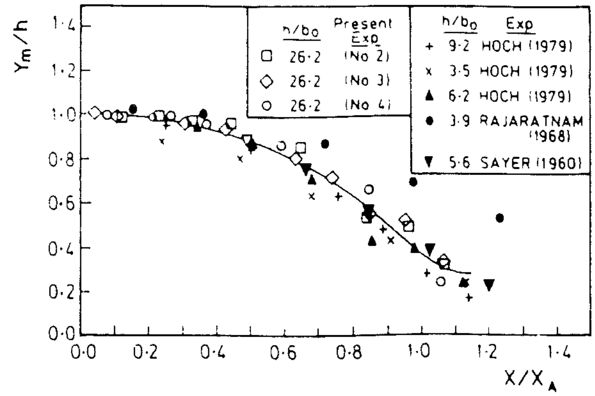

FIGURE 8 LOCUS OF MAXIMUM VELOCITY

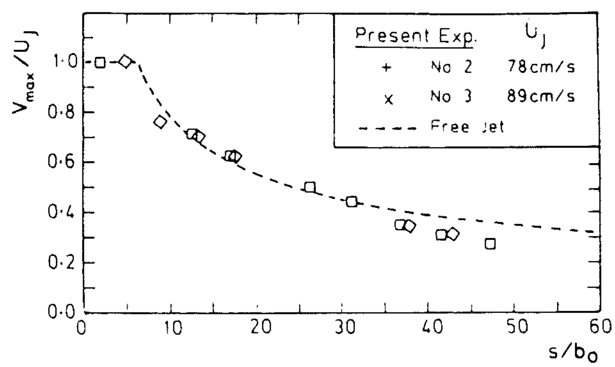

FIGURE 9 STREAMWISE DECAY OF MAXIMUM VELOCITY OF OFFSET JET

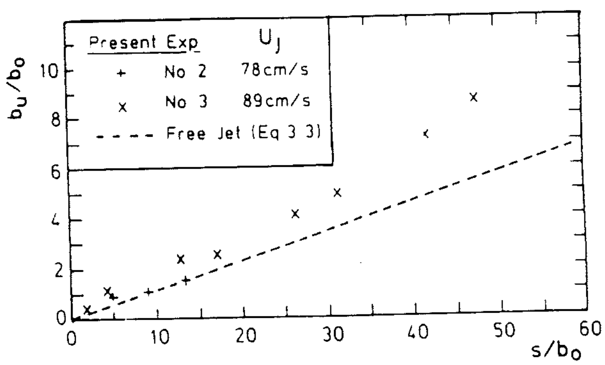

FIGURE 10 STREAMWISE DEVELOPEMENT OF HALF-WIDTH OF UPPER JET

THE VORTEX STRUCTURES OF ROUND JETS IN WATER WAVES

BY Hwung H. Hwung

Tainan Hydraulic Laboratory, National Cheng Kung Univ.
Tainan, Taiwan, R.O.C.

Jih M. Chyan

Department of Environment Eng., National Cheng Kung Univ.
Tainan, Taiwan, R.O.C.

Abstract

The purposes of this paper is to investigate the flow structures of vertical round jet in water waves. Flow visualization and LDV combined with LIF measurements are employed to detect the velocity and concentration respectively. The comparisons of flow structures, velocities, concentrations and turbulent intensities between pure round jet and jet in water waves are made in this paper.

Introduction

Most submerged outfalls are located in the intermediate water depth of ocean. The effluents discharged from diffuser ports are transported continuously by jet momentum, currents and wave motion. In general, jet momentum, buoyancy, crossflow and the structures of ambient fluid are considered in the processes of outfall disposal, however, the effect due to wave motion is always ignored. According to Ismail-Awadalla(1980) and Hwung et al.(1981), They had proved that the characteristics of jet flow in fully developed region will be influenced by wave moton in coastal water area. Although the mean flow of plane jet interacting with opposite wave were obtained by above-mentioned researches from experiments and theoretical analysis, respectively, but the variations of vortex and turbulent structures of jet flow in water waves are still not fully understood. Accordingly, in this paper, the LDV and LIF measurements are employed to discuss the flow structures and concentration distributions of round jet in water waves.

Experiments

The experiments were carried out in a 9.5m*0.7m*0.3m wave flume. Two side walls of the flume are made of glass, that it is convenient for LDV and LIF measurements. A round pipe of 2.3 mm diameter was fixed vertically on the bottom to simulate the round jet in water waves. In order to understand characteristics of submerged round jet due to wave motion, flow visualization and LDV with LIF measurements are employed in the experiments. According to the experience, water quality control is certainly important for the fluid dynamic experiments by LDV. In

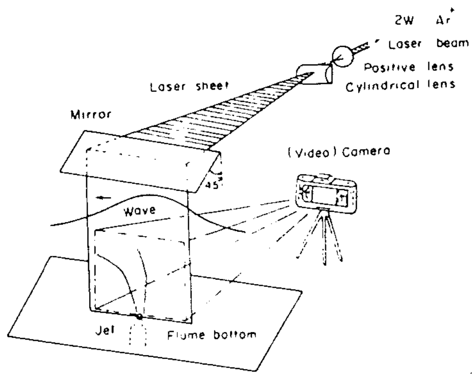

Fig.1 The setup of flow visualization

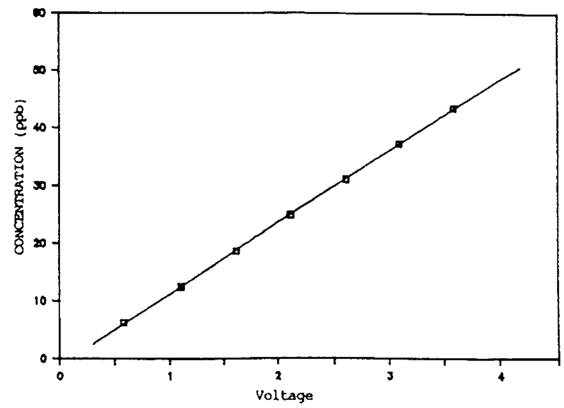

Fig.2 Calibration relationship between output voltages from photo-detector and dye (Rhodamine 6G) concentration.

this paper two sets of 5μ m filter screen are used to remove the natural particles suspended in water before the fresh water discharges into wave flume .After that, the signal drop-out would be reduced and the experimental quality would keep in good condition.

Rhodamine 6G is chosen as the tracer to observe the vortex structures from flow visualization,and to detect the concentration by LDV with LIF measurement simultaneously. The installation of flow visualization is sketched in Fig.1. It is valuable to notice that the calibration of concentration measurement by LIF is of importance in the experiments. Since the fluorescent intensity is the function of temperature, the samples should be disturbed continuously in the calibration process . In this situation , a linearly stable relationships between concentration and voltage output from photo-detector would be obtained and one of the results is shown in Fig.2.

The water surface elevation and the corresponding velocities with concentration were detected by wave gauge and LDV with LIF simultaneously. All the sampling interval and rate were set on 60 sec. and 100 Hz respectively. The experimental results were decomposed into wave and turbulent fluctuation components by inverse FFT method.

Results and Discussion

To understand the differences between vertical round jet in stagnant environment and in water waves, the flow visualization was used initially in this paper.Photo 1 through photo 3 are the results of wave passing by,on the phase of wave trough,mean water level and crest respectively.Photo 4 is the results of vertical round jet discharging into still water. From the above photos, it is obviously to see that the wavy phenomena close to potential core take place more earlier under wave action.It is also shown from these photos that the length of potential core in water waves are shorter than that in pure jet. Further,the jet flows in water wave swing back and forth periodically, the area of tracing material scatters far and wide in fully developed flow region. It is also found that the vortex stretching exists apparently in the back side of jet flow which is similar to the results proposed by Andreopoulos(1985).

Photo 1.Jet-wave interaction at a phase near wave trough

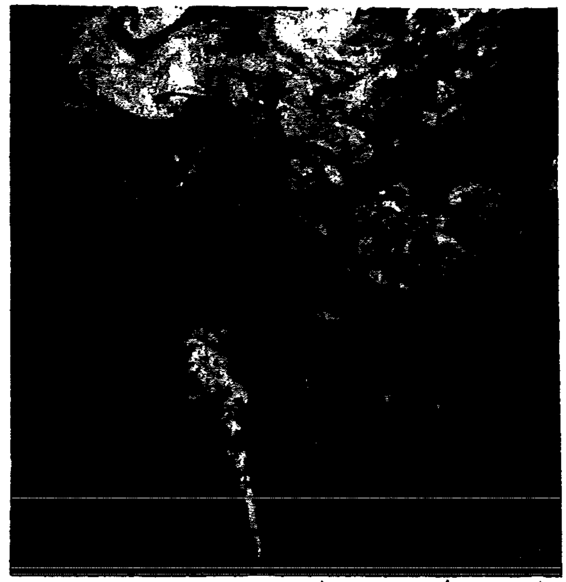

Photo 2.Jet-wave interaction at mean water level

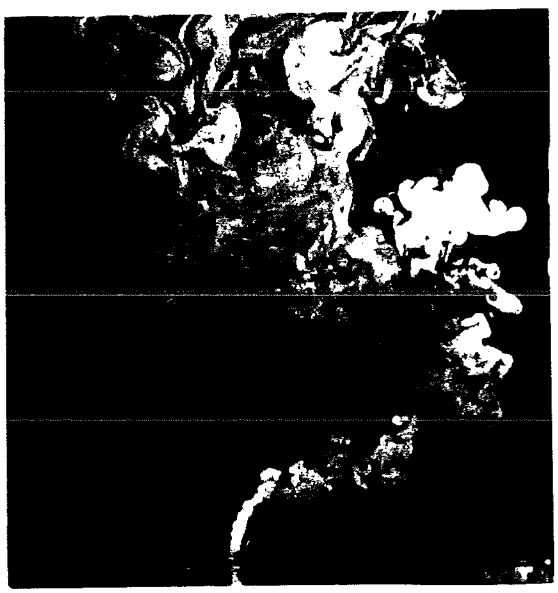

Photo 3.Jet-wave interaction at a phase near wave crest

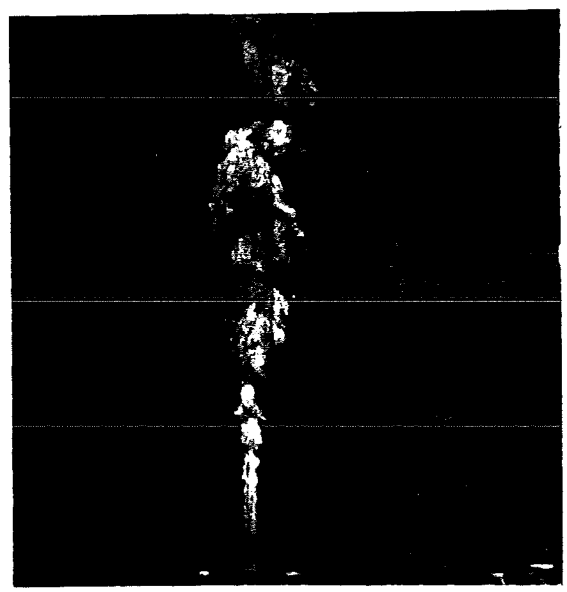

Photo 4.Flow pattern of pure round jet

Fig3 (a),(b) are the dimensionless distribution of velocity and concentration by LDV and LIF ,respectively.It shows that the velocity and concentration distributions under wave action can also be expressed by Gaussian curves. As for the variations of centerline velocity and concentration, the results are plotted in Fig.4 (a),(b). We can see the centerline velocity and concentration of round jet in water wave are smaller than that in pure round jet. Moreover, the corresponding characteristic boundary width which is defined as the

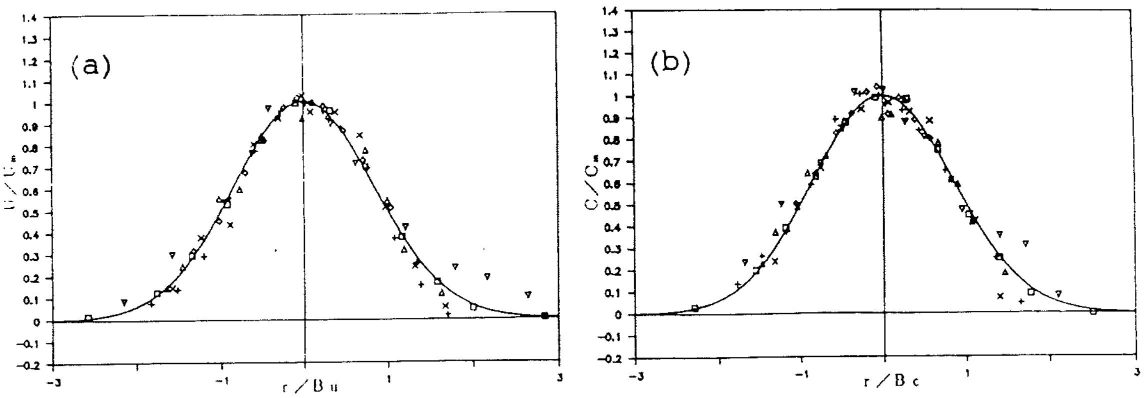

Fig.3 Non-dimensional (a) mean velocity and (b) mean concentration profiles across a jet interacting with wave motion; □ X/D=21.7; + X/D=32.6; ◇ X/D=43.5; △ X/D=54.4; × X/D=65.2; ▽ X/D=87.

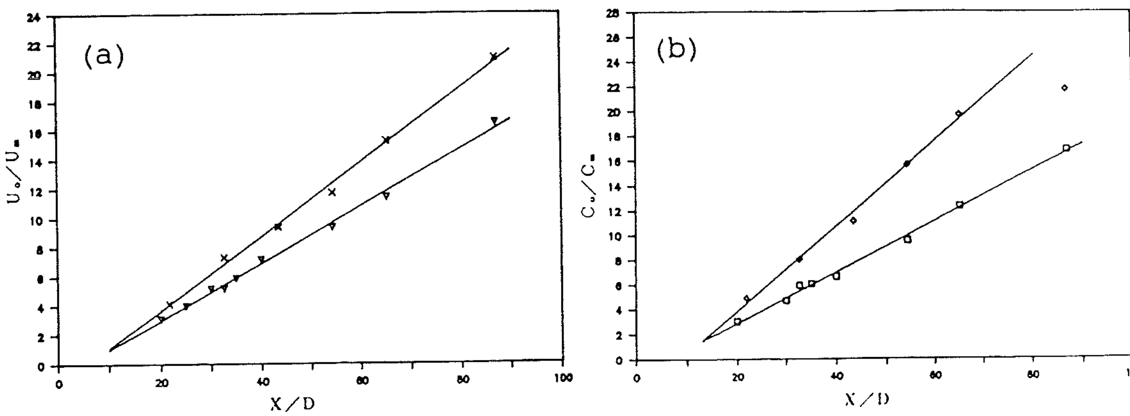

Fig.4 Non-dimensional (a) centerline velocity, ▽ pure jet, × jet-wave interaction (b) centerline concentration, □ pure jet, ◇ jet-wave interaction.

distance from centerline to the position of a half of centerline velocity or concentration, are also obtained in Fig. 5 (a),(b). From the comparison, both of the characteristic boundary width of round jet in wave are larger.

Based on our experiments, the centerline velocity and concentration, and the corresponding characteristic boundary width are established by the following formulas.

$$\frac{U_0}{U_m} = a\left(\frac{X}{D} + b\right), \qquad \frac{C_0}{C_m} = a\left(\frac{X}{D} + b\right)$$

$$\frac{B_u}{D} = a\left(\frac{X}{D} + b\right), \qquad \frac{B_c}{D} = a\left(\frac{X}{D} + b\right)$$

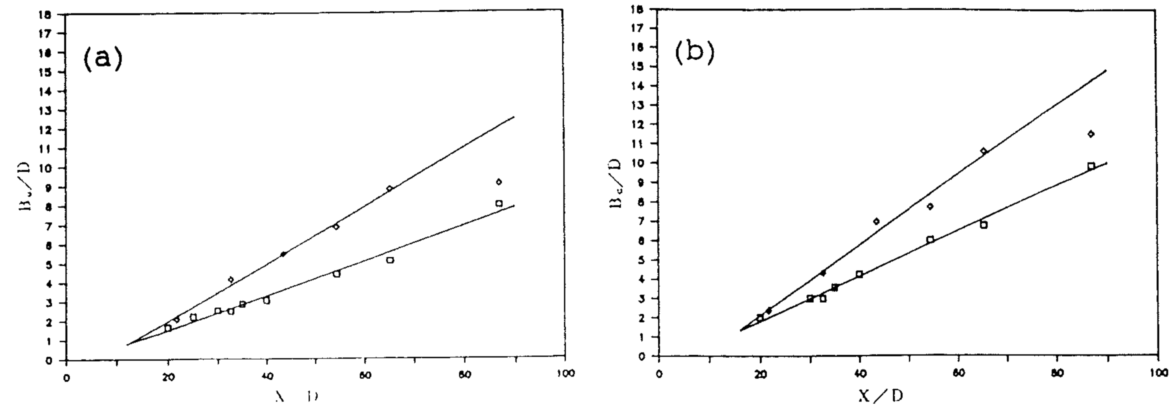

Fig.5 Non-dimensional (a) characteristic velocity width , (b) characteristic concentration width,□ pure jet,◇ jet-wave interaction.

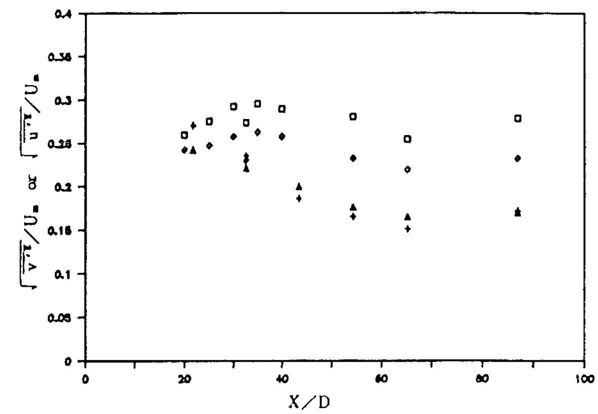

Fig.6 Non dimensional turbulent intensities along the centerline □,◇ axial and radial turbulent intensity of pure jet,+ ,△ axial and radial turbulent intensity of round jet interacting with water waves .

Table 1

	a	a*	b	b*
U_o/U_m	0.196	0.254	-4.8	-5.7
C_o/C_m	0.205	0.340	-5.9	-8.7
B_u/D	0.090	0.149	-3.2	-6.7
B_c/D	0.117	0.182	-4.7	-8.5

The regression constants for the non-dimensionalized formulas of centerline velocity,concentration,and the characterictic width of velocity and concentration, * :wave-jet interaction.

where U_0 , C_0 are the initial velocity and concentration, U_m , C_m are the centerline velocity and concentration, B_u , B_c are the characteristic boundary width. D is the diameter of round jet and X is the longitudinal distance from the orifice. The proportional constants from least square method are listed in table 1. According to the above results we can see that the centerline velocity and concentration in waves are reduced about 23% and 40% compared with the round jet discharged into still water, whilst the characteristic boundary width of velocity and concentration increase about 65% and 56% respectively.

Finally, the dimensionless turbulent intensities along centerline are displayed in Fig.6 . From the results, it shows that the turbulent intensities of pure round jet are higher than those of round jet in water wave. It is also clearly to see that the turbulent intensity of pure jet in longitudinal direction is stronger than those in radial direction, which is similar with the results proposed by Papanicolou (1988), however, the turbulent intensities of round jet in wave are equivalent to both directions.

Conclusions

The characteristics of vertical round jet in water waves are investigated by flow visualization, LDV and LIF measurements in this paper. According to the results, we found that the velocity and concentration distributions can be expressed by Gaussian curves reasonably. In addition, the centerline velocity, concentration and turbulent intensities are smaller than those in pure round jet, however, the characteristic boundary width of velocity and concentration are larger. More detail studied are going to be carried out continously in the future.

Reference :

1. Hwung,H.H.,Frederick,Tang,L.W. and Chen,Y.Y., Theoretical study of turbulent jet interacting with small amplitude wave,J.C.I.E.,Vol.4, No.2,July 1981.
2. Ismail-Awadalla,N.,Wave-current interaction,Technical Report HEL27-7 ,Hydraulic Eng. Lab.,Univ. of California,1980.
3. Papanicolou,P.N., and E.J.List, Investigations of round vertical turbulent jets,J.F.M.,Vol.195,pp.341-391,1988.
4. Andreopoulos,J.,On the structure of jets in crossflow,J.F.M.,Vol.159 ,pp.163-197,1985.

THERMAL PLUME DATA OF CARTER AND REGIER

by

V. H. Chu[1] and M. S. T. Abdelwahed[2]
[1]Department of Civil Engineering and Applied Mechanics
McGill University, Montreal, Quebec H3A 2K6, Canada
[2]Department of Mathematics and Engineering Physics
Cairo University, Cairo, Egypt

Abstract

A remakable degree of consistency have been found between the two sets of thermal-plume data, obtained by Carter and Regier (1974) and Abdelwahed and Chu (1981). The tests of Carter and Regier (1974) were conducted in a 3 meters wide flume which is five time wider than the flume used in the tests of Abdelwahed and Chu (1981). The consistency suggests that both sets of data are relatively free of the scale effect.

Introduction

Experiments were conducted by Carter and Regier (1974) to study surface thermal plumes in crossflows. Warm water was discharged through a nozzle just below the free surface and in a horizontal direction perpendicular to the open-channel crossflow. Temperature measurements were make by a thermistor probe traversing across the plumes. 17 tests were conducted, most of which were conducted to determine the width and the thicknesses of the thermal plumes. Only the results of four tests, which has the maximum temperature determined along the centerline, are analysed here. The results are compared with the results of Abdelwahed and Chu (1981). Table 1 summarizes the test conditions.

The setup of the two series of experiments are the same except that the width of the crossflow is 61 cm in AC compared with the crossflow width of 305 cm in CR. (From now on, the tests of Carter and Regier and the tests of Abdelwahed and Chu will be referred to as CR and AC respectively.) The source densimeteric Froude number of CR and AC are in the same range, varying from 2 to 14. The source Reynolds number are lower in AC with a Reynolds number of 2110 for Test T4. The dimensions of the surface plumes in CR are significantly greater than that in AC. Typical thickness of the surface plumees in CR varies from 7 to 14 cm, while the thickness in AC from 2 to 10 cm. The width of the surface plume in CR is typical four to five time greater than the one found in AC. The source temperature is 5.56 °C above the ambient in CR and varying from 8°C to 17 °C in AC. The conditions of the two series of tests are sufficiently different for the evaluation of the scale effect.

Line-impulse model

The surface plumes in a uniform crossflow are characterized by the volume flux, $Q_o = V_o A_o$, the flow force, $M_o = V_o^2 A_o + g_o' \bar{z}_o A_o$, the buoyancy flux, $F_o = g_o' V_o A_o$, and the crossflow velocity, U; in these expressions, $V_o, g_o', \bar{z}_o$ and A_o are the velocity, the reduced gravity, the depth of the centriod, and the cross-section area at the nozzle exit, respectively; the subscript 'o' denotes the condition at the exit of the nozzle. A simplified description of the surface plume is obtained using a moving reference system which moves with the velocity of the crossflow. In this moving reference system, the ambient fluid is stationary, while the plume moves aways from the source as a line impulse. The momentum per unit length of this line element is M_o/U, and the buoyancy per unit length is F_o/U. The time scale and the length scale of this simplified model are:

$$t_s = \frac{M_o}{F_o}, \tag{1}$$

and

Test no.	d_o cm	b_o cm	U cm/s	d cm	B cm	Q_o cm^3/s	T_a °C	T_o °C	$\Delta\rho_o$ gr/cm^3	Fr_o	Re_o
BV	5.00	1.98	5.61	20.4	305	252.	20*	5.56	0.00103	14.3	8010
AVI1	2.53	5.09	6.01	25.3	305	126.	20*	5.56	0.00153	4.21	3510
GX	3.54	3.44	5.88	25.3	305	252.	20*	5.56	0.00133	9.73	7250
HX	2.68	5.21	5.88	25.3	305	252.	20*	5.56	0.00128	8.38	6790
T1	2.54	2.54	6.19	13.4	61.	158.	23.6	8.15	0.00227	10.3	6230
T2	2.54	2.54	6.23	13.4	61.	110.	23.0	11.0	0.00317	6.10	4340
T3	2.54	2.54	4.99	13.4	61.	78.9	24.1	12.0	0.00361	4.08	3100
T4	2.54	2.54	5.00	13.4	61.	53.6	24.0	17.2	.00553	2.24	2110

* Estimated values; h_o = depth of the nozzle, b_o = width of the nozzle, h = depth of the crossflow, B = width of the crossflow, Q_o = discharge at the source, T_a = temperature of the crossflow, T_o = temperature (above the ambient) at the source, $\Delta\rho_o$ = density difference between the ambient crossflow and the warm water at the source, $Fr_o = V_o/\sqrt{g_o' d_o}$ = densimetric Froude number at the source, $Re_o = V_o d_o/\nu$ = Reynolds number at the source, and $d_o = \sqrt{b_o d_o}$ = characteristic dimension of the nozzle, $g_o' = g\Delta\rho_o$ = reduced gravity.

Table 1: Test conditions.

$$\ell_s = [\frac{M_o^2}{F_o U}]^{\frac{1}{3}}, \tag{2}$$

respectively. The temperature is related to the heat flux at the source, $\Gamma_o = T_o Q_o$. The temperature scale is proportional to the heat flux per unit length of the line element, Γ_o/U, as follows:

$$T_s = \frac{\Gamma_o}{U\ell_s^2} \tag{3}$$

The direct dependency on the volume flux, Q_o, is ignored in the present consideration. Details of the line-impulse model are given in Chu (1985).

Results

The experimental data of CR are compared with the data of AC in Figs. 1, 2 and 3. Fig. 1 shows the maximum half-thickness, δ_m, Fig. 2 the surface width, 2η, and Fig. 3 the temperature, T_m'' and T_m, along the centerline. The plume half-thickness, δ, is the depth where the temperature is one-half of the temperature at the free surface; and δ_m is defined in CR as the half-thickness along the centerline of the plume where the surface temperature is maximum, but δ_m is defined in AC as the cross sectional maximum of δ. Despite this difference in the definitions, the data of both CR and AC are correlated quite well with the time and length scales of the line-impulse model. The plume approaches a maximum thickness of about 0.47 ℓ_s at a longitudinal location $\xi/t_s U \simeq 1$, in which ξ is the distance from the source measured along the centerline of the surface plume.

The half-width, η, is defined at the lateral location where the surface temperature is one-half of the maximum at the centerline; 2η is defined in CR as the width of the

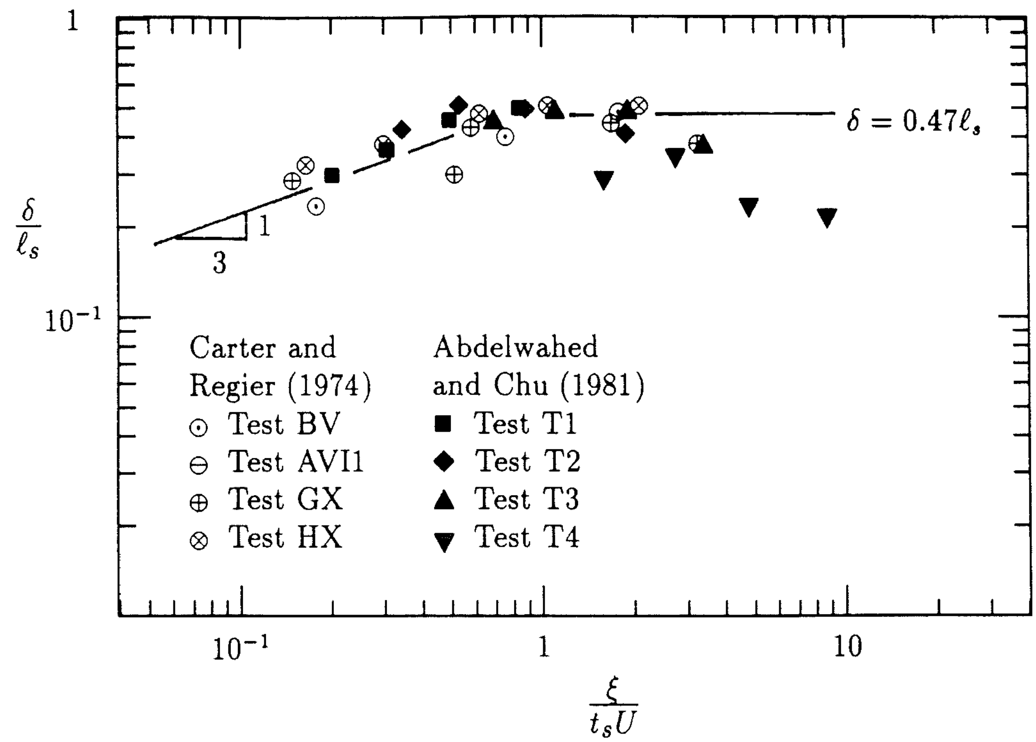

Figure 1: Maximum half-thickness, δ_m.

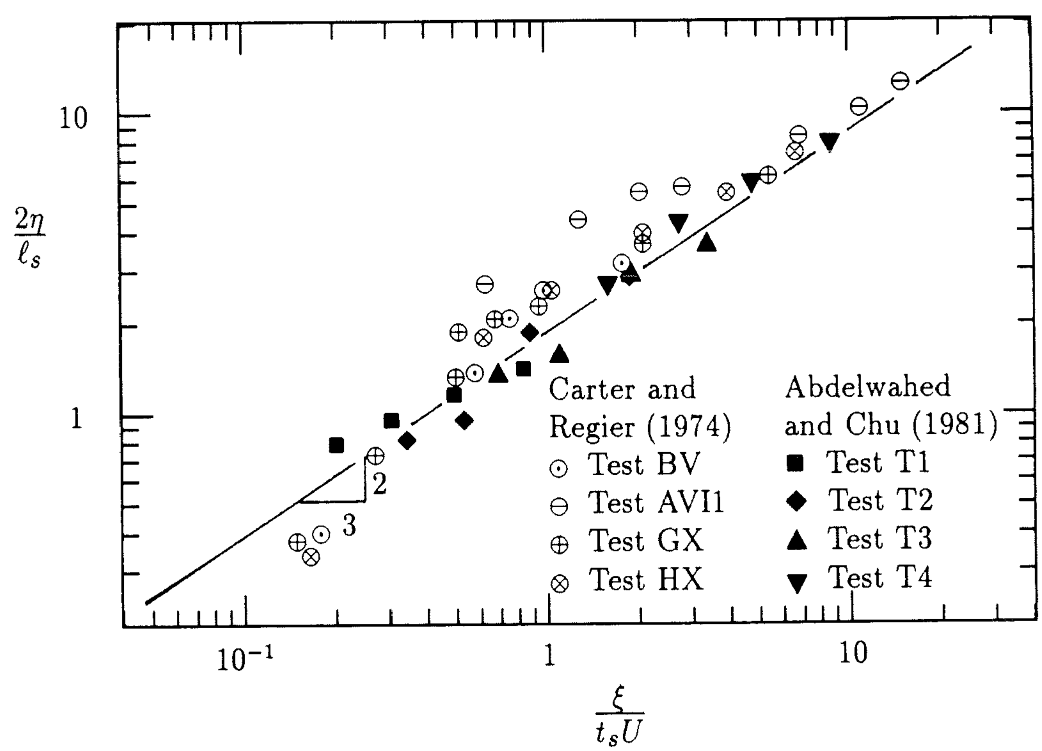

Figure 2: Surface Width, 2η.

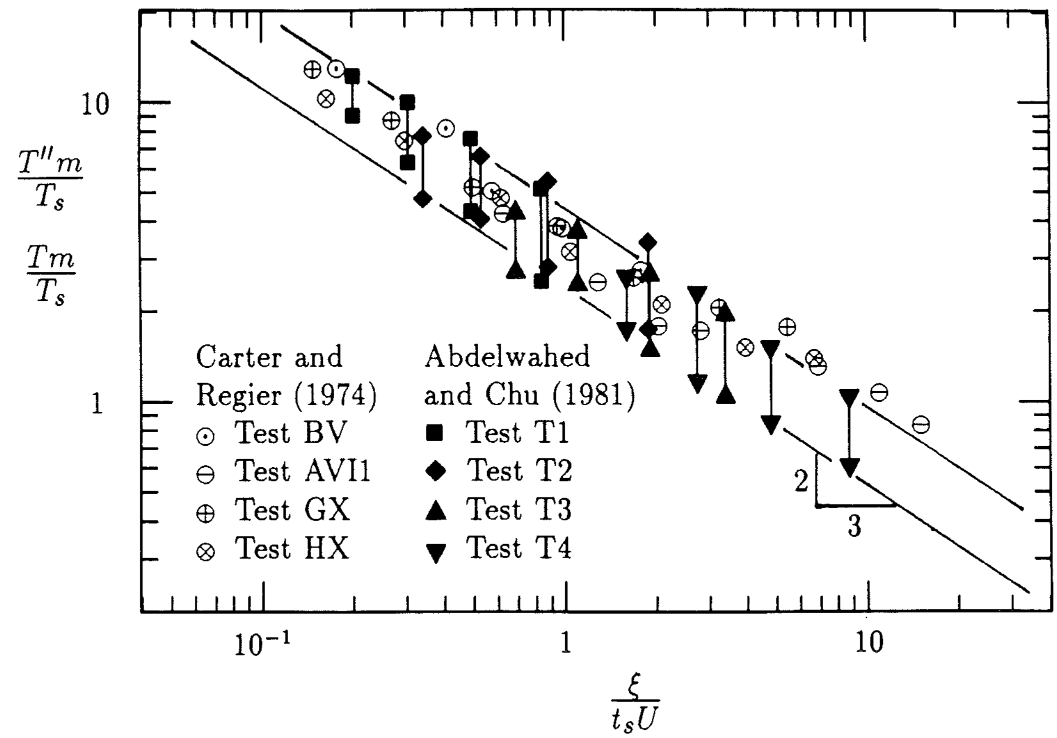

Figure 3: Maximum Temperature, T''_m/T_s or T_m/T_s.

plume cross-section perpendictular to the direction of the centerline, while it is defined in AC as the width of the cross section perpendicular to the direction of the crossflow. The data of AC fits a two-third power law:

$$\frac{2\eta}{\ell_s} = 1.8\,(\frac{\xi}{t_s U})^{\frac{2}{3}} \tag{4}$$

which may be re-written as

$$\eta = 0.9\,(\frac{F_o}{U})^{\frac{1}{3}}(\frac{\xi}{U})^{\frac{2}{3}}. \tag{5}$$

The dependency on the source momentum flux, M_o, cancels out. The lateral spreading relation depends only on the source buoyancy flux. The entrainment of ambient fluid into the surface plumes does not seem to affect the lateral spreading relation. The spreading relation given by Eq. 5 is not significantly different from the following two-third power law obtained by Hoult (1972) for the immicible spreading of oil on flowing waters:

$$r_s = 1.25\,(\frac{F_o}{U})^{\frac{1}{3}}(\frac{\xi}{U})^{\frac{2}{3}} \tag{6}$$

in which r_s is the half-width measured from the leading edge of the oil slick on the water surface. Similar two-third power law relations have been obtained for surface spreading of miscible fluid (see e.g., Abdelwahed, et al., 1983).

The temperature in AC was determined by an array of thermistors which are fixed in space during each of the sampling period of 55 seconds. The samples obtained by the fixed probe determine the temperal maxium temperature, T'', and the mean

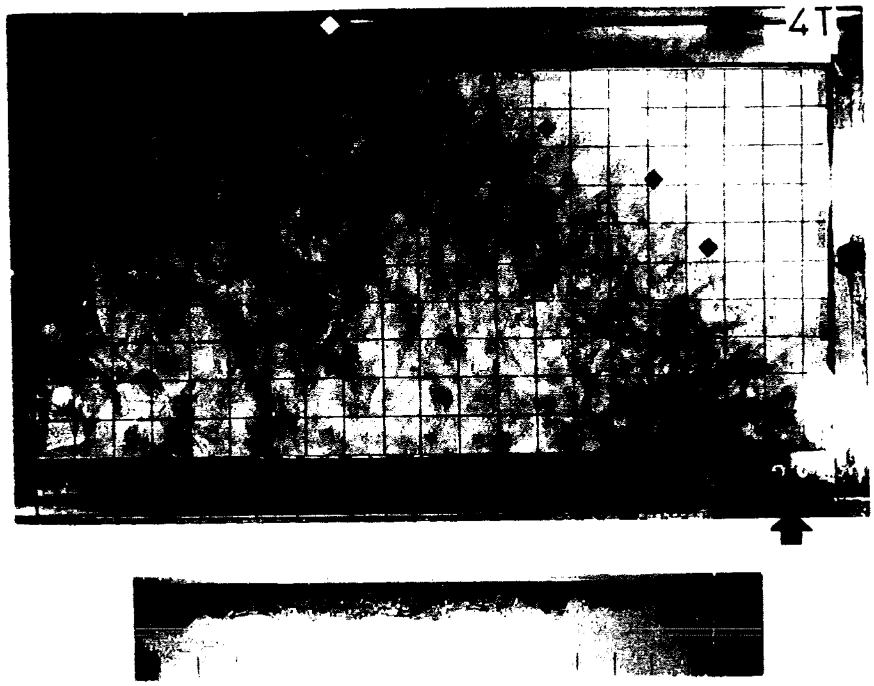

Figure 4: Top-view and side-view photographs of the surface plume of test T4; the direction of the crossflow is from the right to the left.

temperature, T, at each location. The maxima across the plume cross section are T''_m and T_m. The data of AC obtained for T''_m and T_m are plotted on the top and the bottom of the vertical lines as shown in Fig. 3.

The maximum temperature obtained along the centerline by CR is neither T''_m nor T_m, because the probe is not fixed in space during the temperature measurments. The moving thermistor probe in CR traverses across the plume with a speed varying from 1 cm/s to 4 cm/s. Fig. 3 shows the temperature maximum obtained by CR, which lies between the maximum, T''_m, and the mean, T_m, of AC as expected. The data of CR is very close to the temperal maximum, T''_m, in the far field region where the time scale of the turbulence motions is large compared with the traversing time across the surface plume.

Despite the presence of the stable stratification the plume continues to entrain ambient fluid, and the temperature continues to reduce with distance, even in the far field region of the surface plume. The data for T''_m and T_m in Fig. 3 fit quite well the minus two-third power relations:

$$\frac{T''_m}{T_s} = 4.25\,(\frac{\xi}{t_s U})^{-\frac{2}{3}} \tag{7}$$

$$\frac{T_m}{T_s} = 2.25\,(\frac{\xi}{t_s U})^{-\frac{2}{3}} \tag{8}$$

which may be re-written in terms of the momentum length scale, $\ell_m = \sqrt{M_o}/U$, as follows:

$$\frac{T_m U \ell_m^2}{\Gamma_o} = 4.25\,(\frac{\xi}{\ell_m})^{-\frac{2}{3}} \tag{9}$$

$$\frac{T_m U \ell_m^2}{\Gamma_o} = 2.25\,(\frac{\xi}{\ell_m})^{-\frac{2}{3}} \tag{10}$$

These relations are independent of the buoyancy flux. In fact, Eq. 10 is not significantly different from the following relation obtained by Chu (1985) for the maximum concentration (or the maximum temperature) of non-buoyant jets in uniform crossflows:

$$\frac{T_m U \ell_m^2}{\Gamma_o} \simeq 2.63\,(\frac{\xi}{\ell_m})^{-\frac{2}{3}} \tag{11}$$

Fig. 4 shows the surface plume of test T4. The plume is strongly affected by the stable gravity stratification, and is rather spreadout along the free surface ($2\eta = 44$ cm, $\delta_m = 1.2$ cm, at $x = 56$ cm), but the temperature variation along the centerline of the plume is not significantly different from that of the non-buoyant jets in uniform crossflows.

Conclusion

The thermal-plume data of Carter and Regier (1974) are consistent with the data of Abdelwahed and Chu (1981) despite the difference in the sizes of the apparatus. Both sets of data give a lateral spreading relation of the surface plumes which is independent of the mixing events, and a turbulent dilution relation which is independent of the buoyancy effect. These rather surprising results are consistent with the other observations of surface plumes in crossflows and in co-flowing streams (Abdelwahed, Xu and Chu, 1983; Chu and Abdelwahed, 1989).

References

Hoult, D. P. (1972) "Oil spreading on the sea," *Annual Rev. Fluid Mechanics,* Vol. 4, pp. 341-368.

Abdelwahed, M. S. T. and Chu, V. H. (1981) "Surface jets and surface plumes in crossflows," Tech. Rept. no. FML/81-1, Dept. of Civil Engineering and Applied Mechanics, Montreal, 385 pp.

Abdelwahed, M. S. T., Xu, X.-P. and Chu, V. H. (1983) "Surface plumes in co-flowing stream," *Proc. of XXth IAHR Congress,* Moscow, U.S.S.R.

Carter, H. H. and Regier, R. (1974) "The three-dimensional heated surface jets in a cross-flow," Tech. Rept. no. 88, Chespeake Bay Institute, John Hopkins University.

Chu, V. H. (1985) "Oblique turbulent jets in a crossflow," *J. Engrg. Mech. Div., ASCE,* Vol. 111, No. 11, pp. 1343-1360.

Chu, V. H. and Abdelwahed, M. S. T. (1989) "Shore attachment of buoyant effluent in strong crossflow," *J. of Hydr. Engr., ASCE,* Vol. 116, No. 2, pp. 157-175.

Numerical Studies of Buoyant Jets in Crossflows: Sea Outfall Design for Yantai

Gu Guowei ,Wei Heping ,Cai Bute
Tongji University,Shanghai,P.R.C.

Abstract

The main object of this model research is to study the dilution and diffusion of buoyant jets in crossflows.Combining with prototype project of municipal sewerage discharge for Yantai, the model tests were taken.Undistored model has been adopted,and the scale is 1:100.Six integral control equations were deduced,with which can calculate initial dilution, rise height and spreading width of buoyant jet in the near field.

According to model tests and calculating results of integral control equations,we suggest the essential parameter to be used in the diffuser project at Yantai.

I.Introdution

With the Yellow sea to its north, Zhifu Bay to its northeast and Taozi Bay to its northwest, Yantai City has a population of 300,000 and a sewerage discharge of 38m/d. It has been studied and decided that the urban sewage will be amassed at Xishawang, after pretreatment by means of screens and sediment, sewerage is discharged into Yellow sea(see Fig.1). The sea area near the outlet is not stratified, with the average water depth being 20m, the average current velocity 0.16m/s, the density of the urban sewage 0.998g/ml and the average density of the sea water in August 1.002g/ml.

The glass flume tests are preformed mainly for determining the three unknown parameters j, th and Cd to be used in intergral control equations in cross current, and parameters for designing diffuser to be used in Yantai City Sewerage Discharge Project can be provided as well.

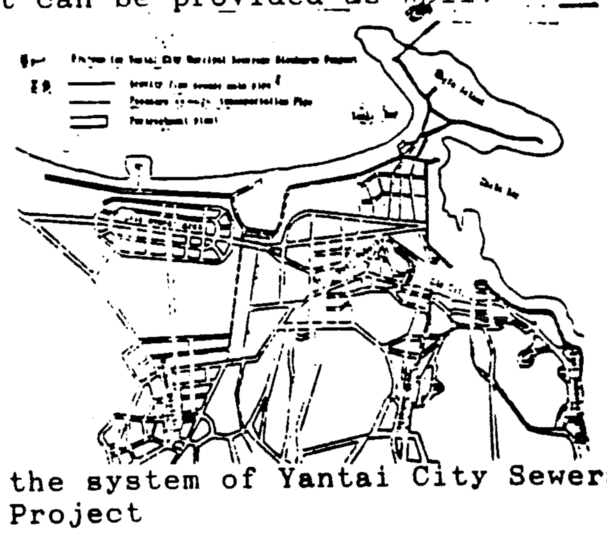

fig.1 sketch of the system of Yantai City Sewerage Discharge Project

II. Integral control Equations for Bbuoyant Jet in Cross Current

After a buoyant jet has been discharged into a flowing environmental water body in the vertical direction, as a result of its own momentum and the buoyant effect, it will rise vertically; on the other hand, influenced by the recycle of the cross current, the jet tends to bend by degrees towards the downstream.Based on the continuity equation,momentum equation and the equation of conservation of mass,a series of integral equations can be derived as follows.

1.The continuity equation:

$$d/ds(\pi b(2Ua\cos\theta+\Delta Um))=2\pi b(\alpha_j\Delta Um+\alpha_{th}Ua\sin\theta\cos\theta) \quad (1)$$

2.Momentum equilibrium equation in the horizontal direction:

$$d/ds(\pi/2\cos\theta b^2(2Ua\cos\theta+\Delta Um)^2)$$

$$=\sqrt{2}Cd b Ua^2\sin^3\theta+2\pi Uab(\alpha_j\Delta Um+\alpha_{th}Ua\sin\theta\cos\theta \quad (2)$$

3.mass conservation of tracer:

$$d/ds(\pi b^2\Delta Cm(2Ua\cos\theta+\Delta Um))=0 \quad (3)$$

4.Momentum equilibrium equation in the vertical direction:

$$d/ds(\pi/2\sin\theta b^2(2Ua\cos\theta+\Delta Um)^2)$$
$$=\pi b^2 g\Delta Cm/\Delta Co-\sqrt{2}Cd b Ua^2\sin\theta\cos\theta \quad (4)$$

5.Path of trajectory:

$$dx/ds=\cos\theta \quad (5)$$

$$dz/ds=\sin\theta \quad (6)$$

The initial condition for solving the above-mentioned equations (1)-(6) are

$\Delta Um(0)=Vj-Ua, \Delta Cm(0)=Co-Ca, b(0)=D/2, x(0)=0, z(0)=0, \theta(0)=\theta_0$.

With the boundary conditions being $Um=Ua, z=(1-\omega)H$

In equation (1)-(6) there exist 6 unknown variables ΔUm, ΔCm, b, θ, x, z and three unknown parameters α_j, α_{th}, Cd.

III. Hydraulic Modelling Tests

The tests are carried out by adopting Froud Law to design model and the model is undistorted,with the glass flume being 8m long,1.6m wide and 0.6m deep (see Fig.2).When length scale is Lr=Yr=100, the speed scale and the discharge scale must be Vr= 10 and Qr=100,000 respectively.

Downstream of the diffuser, at 10cm, 20cm,40cm,60cm,80cm, 100cm,120cm,140cm,we set up sampling cross-sections (fixed), each cross section has 3 or 5 sampling verticals, each vertical establishes 3-5 sampling points,as well as sampling at three characterization points. The test works is as follows.

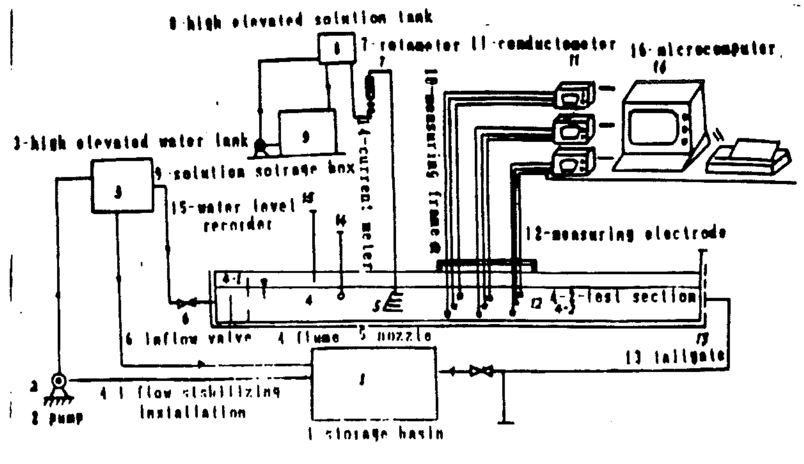

Fig.2 Scheme showing small flume test equipment and installation

1. Dilution

When the sewage has been submeragingly discharged into water body, an upward buoyance and a dynamic entrainment are brought about resulting from the initial momentum of the jet, the density difference , ambient current. Here we perform a combination tests with jet angles being 0°, 15°, 30°, 45°, 90°, the jet speed 2.5m/s, 3.5m/s, 4.2m/s; density difference 0.022, 0.018, effective water deep 18cm. Its results is shown in fig.3-fig.6.

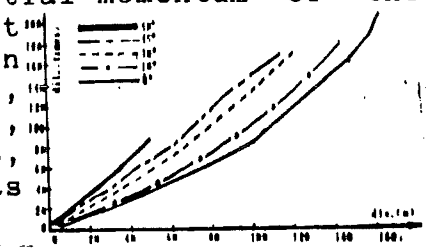

Fig.3 Dilution factors angle comparision

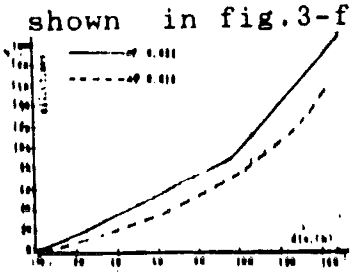

Fig.4 Dilution factors density difference comparision

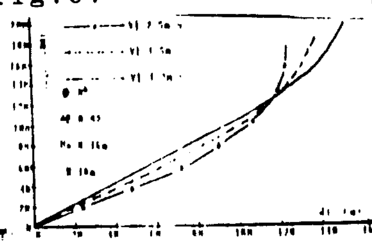

Fig.5 Dilution factors jet velocity comparision

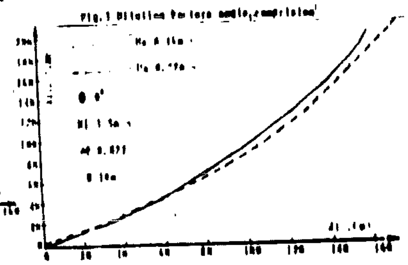

Fig.6 Dilution factors ambient current velocity comparision

2. Width of the jet

It is generally thought that the width of the jet increased as the dilution of the jet becomed higher. Hence, the higher the dilution and the more the entrained ambient water ,the wider the jet spreads. Again we conduct a combination tests on condition that the jet angle is 0°, 10°, 30°, 45° and 90°, the jet velocity is respectively, 2.5m/s, 3.5m/s, and 4.2m/s, the ambient current velocity is 0.16m/s, 0.22m/s and the density difference 0.022, 0.018. Its results can be seen in fig.7-fig.10.

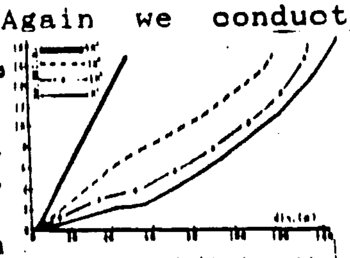

Fig.7 height analysis jet angle comparision

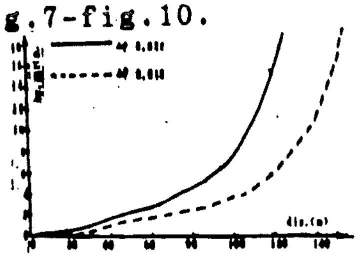

Fig.8 Height Analysis density difference comparision

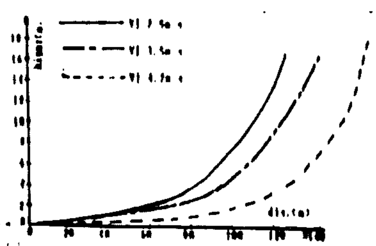

Fig.9 hight analysis jet velocity comparision

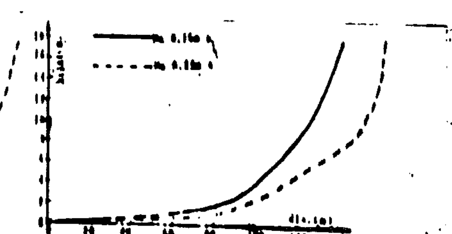

Fig.10 height analysis ambient current velocity comparision

3. Rising Height of the Jet

A combination test is performed on condition that the velocity of ambient current Ua=0.16m/s,0.22m/s,the density difference =0.022g/ml, 0.018g/ml; the jet angles =0 ,10 ,30 ,90 ;and the jet velosity Vj=2.5m/s,3.5m/s,4.2m/s.Its results is shown in Fig.11-Fig.14.

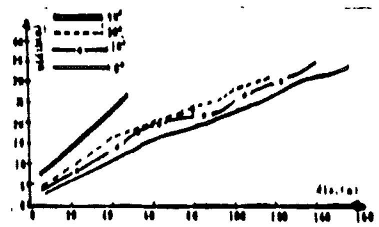

Fig.11 width analysis - jet angle comparision

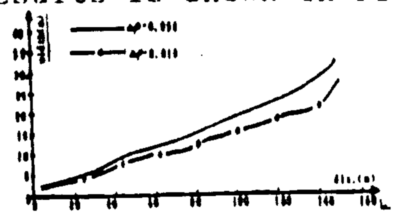

Fig.12 Width Analysis - density difference comparision

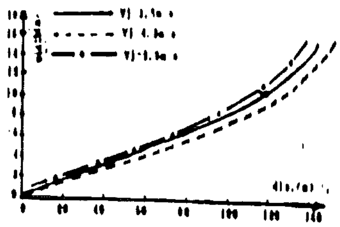

Fig.13 Width Analysis - jet velocity comparision

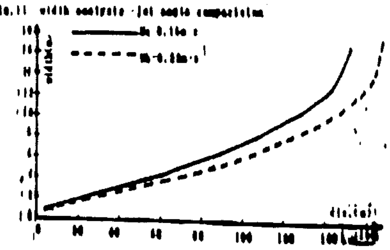

Fig.14 width analysis ambient current velocity comparision

IV. Parameters fitting of the integral equations

In equations (1)-(6) there are six variables, i.e. Um, Cm, b, ,x and z. So they can be solved by means of numerical method, but the parameters j, th and Cd must be determined in accordance with the modelling test data, a group of initial values $\alpha j(o)$, $\alpha th(o)$, $Cd(o)$ can be given. After that they are substituted in equations so that those equations can be solved. Then calculate the squares of the difference between the above calculated values (Shi,Hhi,Whi) and the actually-measured values(Si,Hi,Wi).

$$
\begin{aligned}
\varepsilon_{1ij} &= (Shij - Sij)^2 \\
\varepsilon_{2ij} &= (Hhij - Hij)^2 \\
\varepsilon_{3ij} &= (Whij - Wij)^2
\end{aligned}
\qquad (7)
$$

The sum of the total square difference is

$$(\alpha \varepsilon_{1ij} + \beta \varepsilon_{2ij} + r\varepsilon_{3ij}) \qquad (8)$$

in which $\alpha, \beta, r \geqslant 0$ and $\alpha + \beta + r = 1$

So the leasts-square estimative parameter values are generally translated into the minimal values of functions of many variables. i.e.

$$
\begin{aligned}
\min \varepsilon = \Sigma\,\Sigma\,(\alpha \varepsilon_{1ij} + \beta \varepsilon_{2ij} + r\varepsilon_{3ij}) \\
\text{s.t.}\quad \alpha + \beta + r = 1 \\
0 \leqslant \alpha j \leqslant 1 \\
0 \leqslant \alpha th \leqslant 1 \\
0 \leqslant Cd \leqslant 1 \\
\alpha, \beta, r \geqslant 0
\end{aligned}
\qquad (9)
$$

In solving the nonlinear programming, We can obtain

$\alpha j=0.09$, $\alpha th=0.48$, $Cd=0.29$

V. Engineering Parameters of Diffuser

In consideration of comprehensive analysis of engineering technique and the economical efficiency, the piling and pip-eerecting method is to be used in Yantai Sewerage

Discharge Project, by means of making holes in the pipe wall. The length of the outfall is 1,000m ,of which the diffuser is 300m long,and the diameter of the pipe is 1.6m.(see Fig.15)

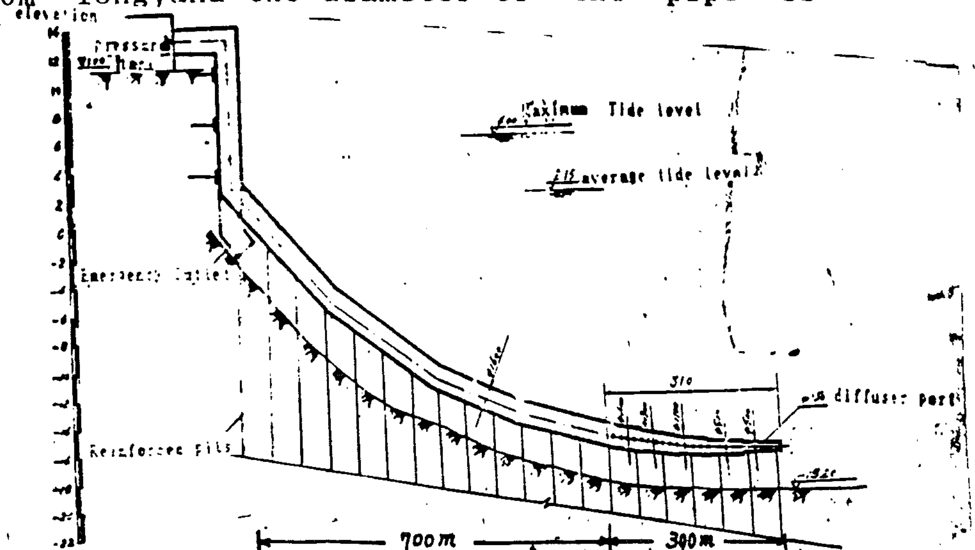

1. Space of Port

As seen in Fig.7,the jet width increases as the jet angle increases.The buoyance resulting from the density difference increases the buoyant inductive entrainment and the transverse shearing entrainment of the jet of,which benefits its widening;on the other hand,the ambient current is harmful to its widening within a certain distance.Bsed on the analysis of the test results and the model calculations, it is found that when the active water is 18m deep,Ua=0.16m/s and Vj=2.5m/s,3.5m/s,8m space between the adjacent ports is preferable.If the ports are to be arranged in two sides of diffuser in staggered way, the actual space between the ports is 4m.

2.Dilution

The initial dilution is the function of F,Fd,Re,Vj/Ua,h/D,θ and x/D,y/D,z/D.

namely $S=Co/C=f(F,Fd,Re,Vj/Ua,\theta,h/D,x/D,y/D,z/D)$ (10)

Derived from the observation of the test, when the distance remains unchanged (less than a certain distance),the more the jet angle,the more the dilution;when the port diameter remains unchanged,the jet velocity,over 3.5m/s,doesn't render any help in increasing in dilution;the ambient current velocity can be influential to the dilution to a considerable degree,mainly in that the jet locus becomes longer,which is benificial to its dilution;however,within a certain scope of the ambient current velocity,the dilution will contrarily decreases when the distance is kept constant (less than a certain distance).Based on the test results and the model calculations, the engineering parameters for the diffuser might be obtained and under hydraulic condition of Ua=0.16m/s,h=18m,Vj=3.5m/s the dilution can be 170 times or so.

The derivation of the above integral equations is directly based on the use of Abraham's entrainment function. The section distribution of buoyant jets in crossflows is supposed to be Gauss-type. All these can be only given an approximate description of the jet process in cross current.However its conclusion basically coincide with the result obtained from our model test.

Acknowledgements

We appreciate the financial support of NEPA (P.R.C.).The part of experimental results of the first series of experiments were taken by the graduated students Xu Liang and Shen Shunyu in the course of their diploma thesis under the supervision of the second writer.

Appendix I References

1. Alberdix et al Diffusion of submerged jets ASCE Vol.115,1950
2. Hun Wei Lee Theory of buoyant jet and its Environmental Application. Hong Kong University 1981.
3. Wei Heping et al Dilution and Diffution Studies on Urban Sewage at Sea Outfall for Yantai. Tong ji University 1987
4. Agg &. Wokeford Field Studies on jet dilution of sewage at Sea Outfall. Inst Pub. Eng. 1972

Appendix II Notation

The following symbols are used in this paper:

- s: axial coordinate of the jet
- r: radial coordinate
- θ: angle of jet center line with horizontal
- Ua: ambient current velocity
- Um: jet velocity of axial
- vj: jet velocity
- Um: velocity difference of the jet in the direction of s
- Co: concentration of the sewage
- Cm: concentration of the jet in the direction of s
- Ca: concentration of the ambient fluid
- b: half-width of the jet
- $\Delta\rho m$: density difference between the density at a certain point of axial and that of ambient fluid
- $\Delta\rho$: difference in density between the ambient fluid and sewage in a jet
- ω: unknow parameter
- H: water depth at point of discharge

Session 10B

Physical Model Studies

Hydraulic Model Test for the Function of Facilities to Create Livable Environments for Fishes at Polluted Urban River

by Takashi Kano
Tokyo University of Fisheries
Minato-ku, Tokyo 108, JAPAN
Mitsuru Satomura
Toda Construction Co. Ltd.
Chuo-ku, Tokyo 104, JAPAN
Shoji Kobayashi
Yaesu Consultant Co. Ltd.
Chuo-ku, Tokyo 104, JAPAN
Hiroyuki Tamaru
Taiyo Kogyo Corporation
Yodogawa-ku, Osaka 532, JAPAN

Abstract

Hydraulic Model Tests were carried out to investigate the effects of bubbling aeration in the enclosed basin of highly polluted urban river in order to create livable environments of fishes and other aquatic living things. Diffusion of aerated water in the enclosed basin by the silt protector sheet is quick and is maintained in the enclosure. Then, this must be effective to improve the environments of polluted river as beginning stage of the project.

Introduction

River Sumida, flowing through the down town of Tokyo Metropolis, is now highly polluted by sewage and industrial waste water. And it is very seldom to be able to see aquatic living things in the river. Recently, they plan the project of river-front development along the river, and Arakawa Play Garden is to be reconstructed at the river bank with recovering livable environments of fishes and other aquatic living things. But river Sumida is a tidal river and maximum flow velocity at flood on ebb of spring tide is estimated as almost 4m/s and river navigation is developed very much, so that it is impossible to improve aquatic environments of the whole river basin at once. Then, they designed the enclosed water basin to improve the concentration of dissolved oxygen mainly. The water quality of river Sumida at the bank of Arakawa Play Garden at present is tabulated as the table 1.

Table 1 . Measured water quality of river Sumida

Date of mesurement(1989)	6 Jun.	26 Jul.	10 Aug.	25 Aug.	1 Sep.
Water temperature(° C)	22.4	23.5	23.5	24.6	23.4
pH	6.9	7.0	7.0	7.2	7.1
Dissolved oxygen(mg/l)	2.0	3.0	4.0	2.3	2.7
Degree of see through(cm)	29	27	8.2	16.5	15
Suspended solid(mg/l)	20	14	70	27	120
BOD(mg/l)	8	6	4	10	4

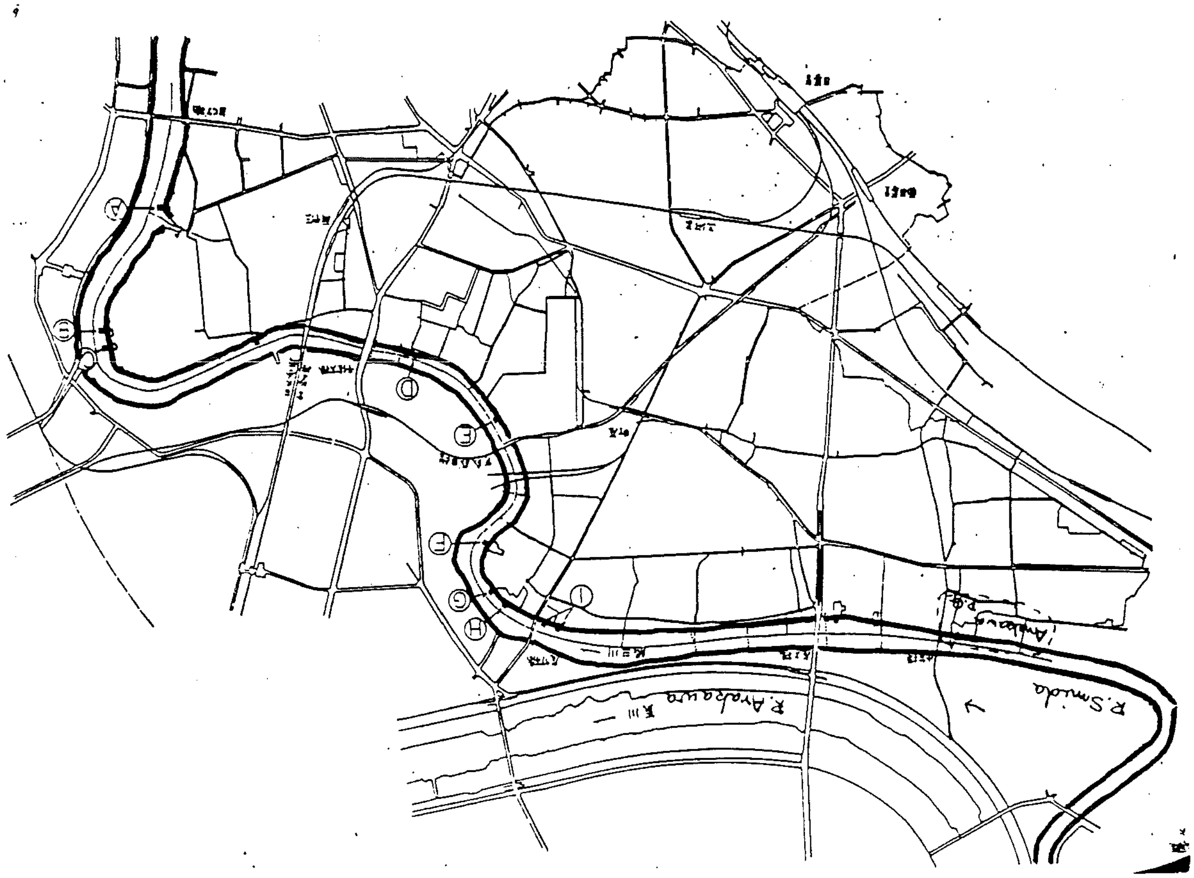

Fig. 1. River Sumida, ArakKawa play garden, and river ArakKawa

As fishes which they expect to keep alive is gibel and carp, most important factor to be improved at present water quality of river Sumida is dissolved oxygen concentration. Aeration by bubbling at the center of enclosed basin is planned, but as the effects of flowing water outside of the enclosing silt silt protector sheet are still unknown, hydraulic model tests were carried out at the flow channel of Tokyo University of Fisheries. The map of river Sumida neighbourhood of Arakawa Play Garden is illustrated in Fig. 1, and model enclosure and the position of bubbling is again illustrated in Fig. 2.

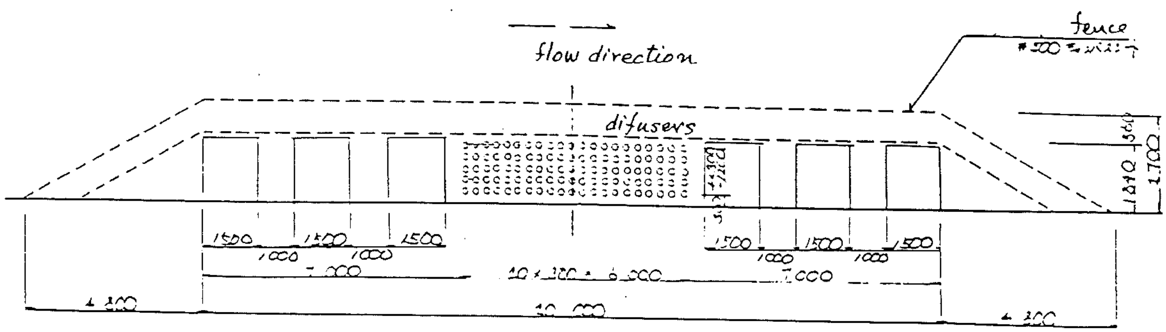

Fig. 2. Enclosing with silt protector sheet in model

Hydraulic model tests

Hydraulic model tests were carried out at the flow channel of Tokyo University of Fisheries in order to know the spread of dissolved oxygen concentration improved water mass in the enclosure by the bubbling, and the effects of flow velocity outside of the enclosure and of blocks which installed in the enclosure for the nest of fishes. Dimensions of the flow channel are 1m in width, 1.5m in height, 25m in length. Enclosure is scaled as shown in Fig. 3. Water depth was kept as 1.0m during the tests and flow velocity was kept as 13.3cm/s. Air quantity of bubbling was set as 22.0l/min. These were the result of 1/6 scaling of actual spot. Blocks for nest of fishes also 1/6 scaled.

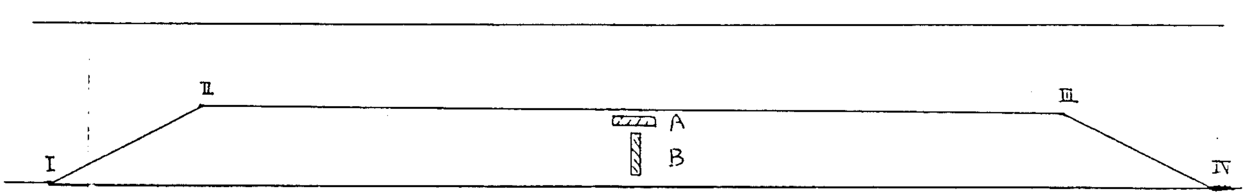

Fig. 3 Enclosing model and bubbling pattern

Velocity measurements were executed with elctro-magnetic current meters, vertical and horizontal 2-dimensional ones, and water blue dye concentration was measured were executed to estimate the distribution of dissolved oxygen concentration. Spreading speed in the enclosure and leakage quantity from the enclosure were observed using under water video camera.

Since river Sumida carries lot of trash usually, upstream and downstream diagonal portions were taken off and bubbling spot removed to upstream end of the enclosing silt protector sheet in order to avoid the broken damage by the striking of flowing trash.

Results of the hydraulic model tests

Measuring points of flow velocities are distributed as shown in Fig. 4, and typical velocity distribution is shown in Fig. 5, the central vertical plane in the enclosure.

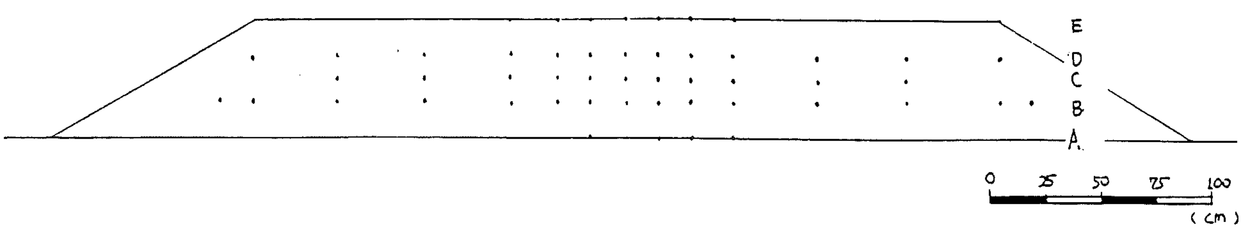

Fig. 4 Horizontal arrangement of measuring points

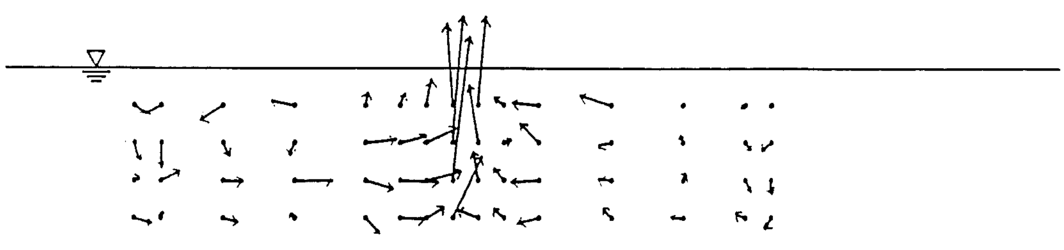

Fig. 5 Velocity vector plot at central vertical plane in the enclosure

Trajectories of water blue dye form circular circulation each direction from the bubbling column, and water blue concentration of enclosed water mass became entirely uniform in several seconds after injection of water blue dye at the center of bubbling. And leakage of water blue dye from the enclosure was quite few. Then, this kind of enclosure can be possible to make another water mass in certain circumstance as it were the pond in the stream. Though the enclosure can hold quality improved water mass to maintain livable environments for aquatic living things, the open silt protector sheet is also investigated, expecting flowing trash to push away and living things to attract from ill environments.

Velocity vector plot for this case is illustrated in Fig. 6. Upward effect of bubbling is again obvious but velocity is not diminished so much and small and vertically longer elliptic circulation was formed at the upstream of bubbling, and comparatively lager and horizontally longer elliptic circulation at the down stream of the bubbling. Injection of

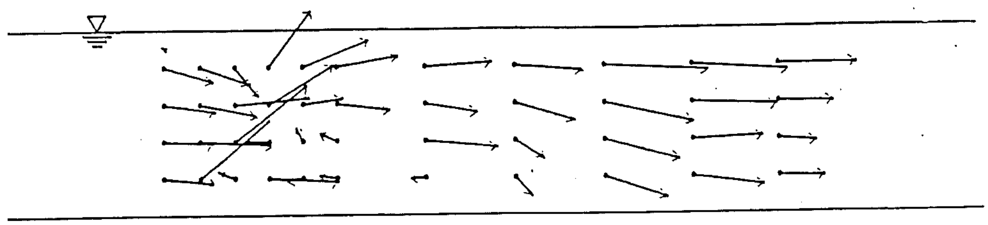

Fig. 6 Velocity vector plot of open silt protector bubbling at upstream end

water blue dye just in front of bubbling passed through the bubbling column with slight rise. This may suggest water from the upstream enters much more than the enclosed case and dissolved oxygen concentration become lower, but living things in ill environments can easily run enter. The contour plot of the water blue concentration is indicated if Fig. 7.

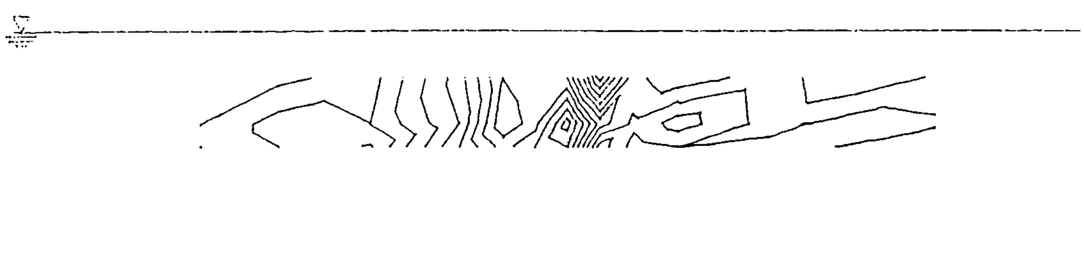

Fig. 7 Contour plot of water blue concentration of open silt protector bubbled at center

Concentration of injected water blue dye was 10g/l for every investigation. Float trajectories were observed for open and upstream end bubbling to recognize the effect to push off the float to the center. This showed the bubbling was effective enough to prevent trash from flowing into and from striking the sheet. The method of sheet installation were tie to fixed frame and rise up by floats. Rise up by float is investigated for the case without diagonal portions. Silt protector sheet, perpendicular to the flow, swelled outward because of the velocity decrease due to the bubbling and the existence of fish nest blocks, but it is not so big disturbances for water quality improvement and safety of silt protector sheet. Wave breaking capacity was investigated for rise up by float, since river Sumida is utilized as a navigation canal. Though it depends upon the dimension and velocity of ships, average wave after sailing ship at river Sumida is 60cm height and angle of incident to the bank is 20°. So that silt protector sheet rose up by floats was installed in wave tank 20° diagonally to wave generator. Many of waves generated changing the period. Wave breaking capacity of silt protector sheet rose up by floats is not so high for every range of wave period. Especially for longer period it is almost same wave height, incident and passed waves. But shorter wave period, that is, 0.65s or shorter, it is possible to expect approximately 25% of wave breaking capacity. The breeding test of gibel and carp at the actual spot of river Sumida, to recognize the effect of bubbling. They put fishes in two cages, and installed one of the cages inside of the enclosure and the the other outside of the enclosure. After a month of breeding, no died in the enclosure, on the contrary 20% were died and survived were not so vigorous compare with those in the enclosure, that is aerated basin.

Conclusions

It is possible to emphasis on dissolved oxygen concentration in case of of water quality improvement in connection with living things recovery. Other factors impossible to neglect but less important than dissolved oxygen concentration. Water mass enclosing with canvas, silt protector sheet quite effective to improve spot and not to mix or leak improved water. If the river flows large amount of trash having possibility to break enclosing canvas, upstream end bubbling may be effective. But canvas enclosing is not so good to break the waves after sailing ships.

MODEL-PROTOTYPE COMPARISON OF THERMAL PLUMES

by
Prahlad Murthy
Johannes Larsen
ALDEN RESEARCH LABORATORY, INC.
and
Dominique N. Brocard
METCALF & EDDY, INC.

ABSTRACT

The N-Reactor (NR) facility on the Columbia River near Richland, Washington, is operated for the Department of Energy by the Westinghouse Hanford Company. Steam generated during the operation of the Nuclear Reactor is partly piped to the Washington Public Power Supply System's (WPPSS) Hanford Generating Station (HGP) to generate electricity. The system works on a once through principle with the waste cooling water discharged back into the Columbia river via separate outfalls for each plant.

In recent years, as part of the regulatory process for both of these outfalls, field and model studies were conducted to investigate the environmental impact of the waste heat discharges. In the course of the model studies new improved outfalls were designed and installed in the field. The new outfalls were shown in the model studies to improve dilution characteristics and also to ensure compliance with regulatory requirements. A field study conducted at the HGP outfall after installation of the recommended structure, confirmed the model predictions. Earlier field surveys at each of the sites were used to validate the operation of the physical model studies.

INTRODUCTION

An overall schematic of the NR/HGP system is shown in Figure 1. The HGP outfall is situated about 700 feet (ft) upstream of the NR outfall. River width is on the order of 1500 ft.

Discharge conditions from NR corresponding to the highest heat rejection to the river constitutes a flow of 730 cubic feet per second (cfs) at a temperature rise of 14 °F. This cooling water discharge is handled by a single outlet structure located about 700 ft offshore. The HGP discharge is handled by a four riser outlet structure with maximum heat rejection being a flow of 1275 cfs at 32.6 °F.

Two of the field studies were conducted by the Pacific Northwest Laboratory (PNL) whereas one other field study and both model studies were conducted by the Alden Research Laboratory, Inc. (ARL).

Except during model validation, the hydraulic models were operated to maximize dilution of the outfall discharge at the highest heat rejection discharge rates. This coupled with low river flows provided the most adverse environmental conditions to test the outfalls under.

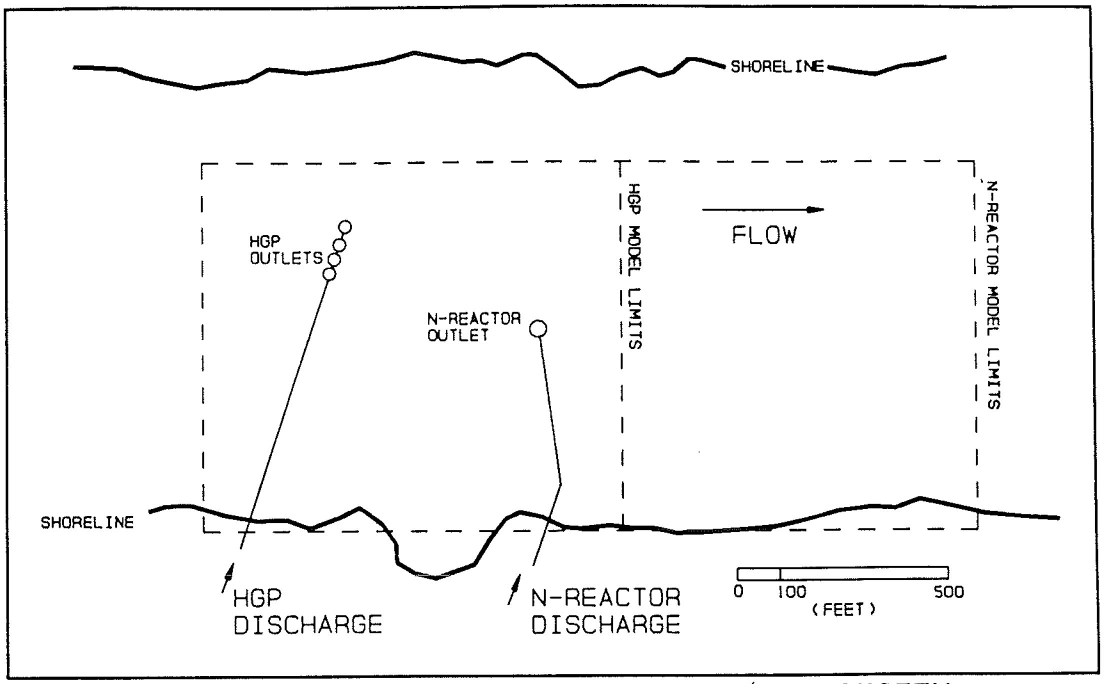

FIGURE 1 ARRANGEMENT OF THE N-REACTOR/HGP SYSTEM

CHRONOLOGY OF PROJECTS

Table I provides a listing of the different studies referred to in this paper.

Data from the field study [1] conducted by PNL was used to calibrate and validate the first model study (HGP outfall) [2]. The objective of the model study was to investigate the performance of the existing outfall structure at HGP and evaluate modifications to it if needed. A field study [3] was performed subsequent to the installation of a modified HGP outfall structure to verify the predicted results from the hydrothermal model.

Another field study [4] was conducted by PNL, at the NR site, to characterize the thermal plume from the NR outfall. Results from this study were used to calibrate and validate the second model study (NR site) [5]. Objectives of the NR model study, conducted by ARL, were varied. The primary objective was to recommend a reconfiguration of the NR outfall structure to improve dilution of the thermal discharge and comply with local thermal criteria. Secondary objectives consisted of an evaluation of past and present performances of the outfall. Interaction between the HGP and NR plumes was also assessed.

MODEL INSTRUMENTATION

Similar arrangements were used to measure temperature rises in both the model studies. This system consisted of a matrix of copper-constantan thermocouples mounted on a movable rack that could be stationed anywhere along the modeled river. The arrangement is shown in Figure 2.

Over a hundred thermocouples were used in the model studies. Temperature

Table I REFERENCED STUDIES OF HGP/NR OUTFALLS

PROJECT	SOURCE	REMARK	REF
Supplemental Information On The Hanford Generating Project In Support Of A 316(a) Demonstration, 1978	WPPSS	FIELD STUDY	1
Hydrothermal Modeling of Cooling Water Diffuser Outfall, Hanford Generating Station, 1982	ARL	MODEL STUDY	2
Hydrothermal Field Study of Cooling Water Diffuser Outfall, Hanford Generating Station, 1985	ARL	FIELD STUDY	3
N-Reactor Thermal Plume Characterization Study During Dual-Purpose Mode of Operation, N-Reactor, 1983	PNL	FIELD STUDY	4
Hydrothermal Modeling of Cooling Water Outfall for N-Reactor, 1988	ARL	MODEL STUDY	5

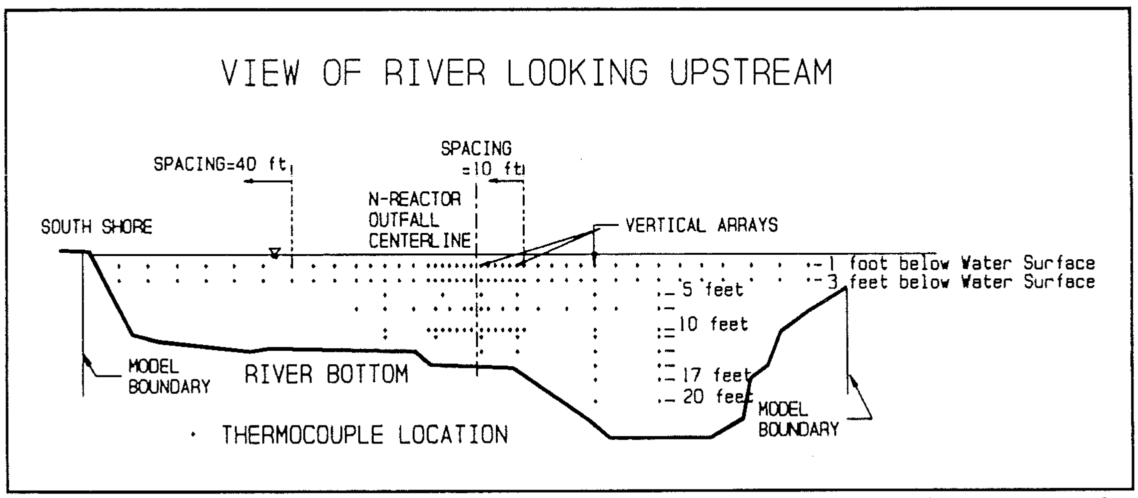

FIGURE 2 DISTRIBUTION OF THERMOCOUPLES ON THE MOVABLE RACK

measurements were automated using a multiplexing circuit and a microcomputer. The accuracy of the temperature rise measurements was ±0.2 °F at a 95% confidence band.

TEST RESULTS

HGP SITE: The model was validated by simulating thermal and hydraulic conditions corresponding to the those in the field study. Thermocouples were located at elevations where temperature measurements were made in the field survey so that direct comparisons could be performed. Typical plots of temperature rise contours (isotherms) at an elevation of 361.3 ft (prototype) are shown in Figures 3 and 4 for the field and model respectively. This elevation is about a foot above the top of the outfall structures. It also represents a 2/3 water depth level which is significant from a thermal criterion point of view.

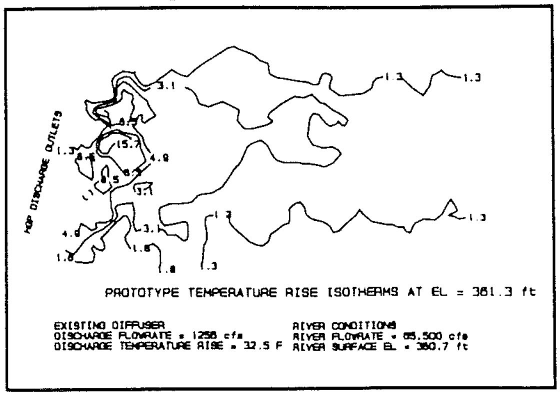

FIGURE 3 ISOTHERMS FROM FIELD SURVEY (REF: 1)

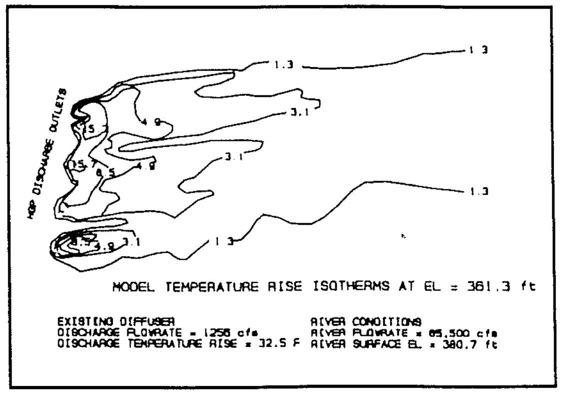

FIGURE 4 ISOTHERMS FROM MODEL STUDY (REF: 2)

While the spatial distribution of the isotherms is slightly different, the extent and magnitudes of the temperature rises are well reproduced. The only significant discrepancy was that the values of the temperature peaks were underpredicted. A reason for this could be that the volume occupied by the probe in the model (in prototype dimensions) was much greater than the probe volume in the prototype. This implies that the model temperatures are averaged values over larger prototype volumes. Three modifications to the existing outfall were tested. All three replaced the single port outlets by multi-nozzle outlets, generating increased discharge velocities. One of the these modifications was recommended and installed in the field.

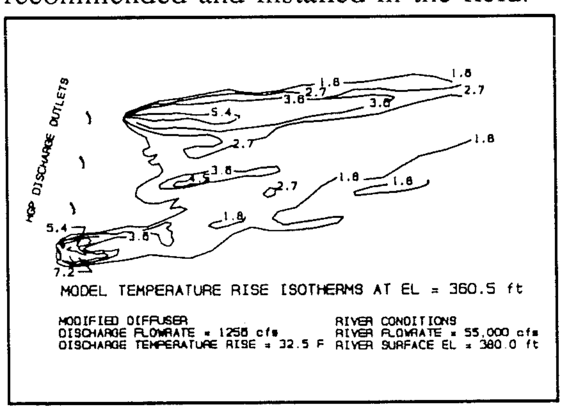

FIGURE 5 ISOTHERMS FROM MODEL STUDY (REF: 2)

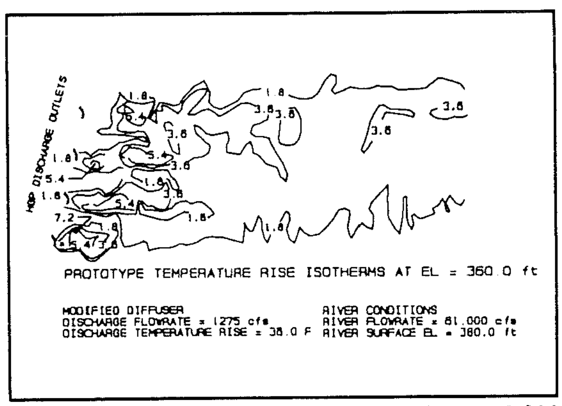

FIGURE 6 ISOTHERMS FROM FIELD STUDY (REF: 3)

A second field study was conducted by ARL to verify the model results. Temperature profiles were obtained in the river by towing a thermistor string in a crisscross pattern with a boat and recording position and temperature at discrete intervals. A microcomputer controlled the data acquisition and storage. Although the river and plant operating conditions varied through the testing, average field conditions were used to compare the field results to model data. Figure 5 and 6 shows respectively two isotherm plots from the model and the field surveys.

The plume is located further downstream of the outfall structure in the model compared to the field. A possible explanation of this displacement is that the air content in the field discharges tended to bring pockets of discharge water to the surface near the structure. The otherwise reasonably close comparison confirmed the predictions of the model.

N-REACTOR SITE: An underwater survey at the NR site in 1987 found the outfall structure partially damaged and upto 85% of the exit area filled in with small rocks. One of the objectives of the model study [5], conducted after the underwater survey, was to determine the condition of the NR structure at the time of the field study [4] conducted in 1983.

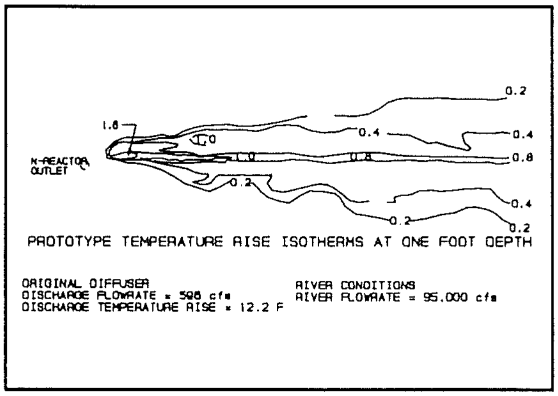

FIGURE 7 ISOTHERMS FROM MODEL STUDY - UNDAMAGED CONDITION (REF: 5)

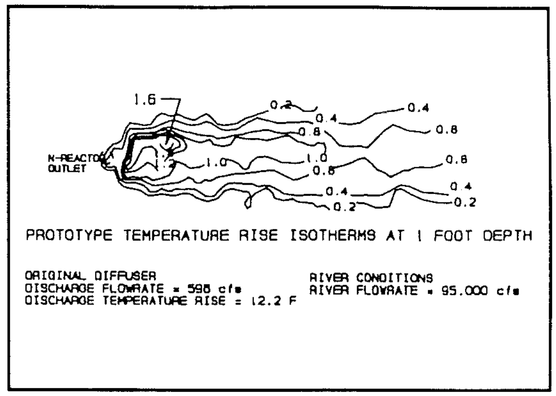

FIGURE 8 ISOTHERMS FOR FIELD SURVEY (REF: 4)

Tests were conducted in the model simulating river and discharge conditions corresponding to field survey conditions. Both an undamaged structure and an "as found" structure were simulated in the model. The "as found" structure was constructed based on the underwater inspection report. Figures 7 and 8 show isotherm plots for the model study (original undamaged structure) and the field survey. Figure 9 shows a comparison of the decay of temperature rise with distance for the two studies.

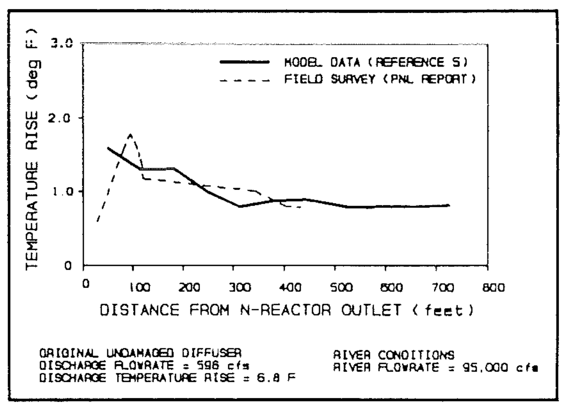

FIGURE 9 DECAY OF CENTERLINE TEMPERATURE RISE (REF: 4 AND 5)

The damaged condition simulation resulted in greater dilution which compared poorly to field data. One reason for the increased dilution rates was the increase in discharge velocities resulting from blockage of the outfall by rocks and stones.

Although the field plume has a greater lateral spread when compared to the model, the decay of centerline temperatures and the spatial extent of the isotherms both bear general agreement. Other tests conducted in the model also showed greater agreement, between model and field results, for an undamaged structure in the model. The inference was therefore that the structure was probably undamaged during the field survey.

CONCLUSIONS AND SUMMARY: There are some significant differences between the model and field results. Field data tends to show higher peak temperatures than model measurements. This may be partly because the spatial resolution of the model measurements is less than in the prototype. Another difference is that the field isotherms have a wiggly structure to them that is not reproduced in the model. This is partly due to the inadequate sensor resolution and also partly due to the possibility that the spectrum of turbulence length scales is truncated in the model.

In spite of these problems the series of model and prototype surveys shows that hydrothermal models can reproduce prototype characteristics reasonably well. The models can therefore be effectively used to design and test new improved outfall structures.

REFERENCES

1. Supplemental Information on the Hanford Generating Project in Support of A 316(a) Demonstration, Washington Public Power Supply System, November, 1978.

2. Hydrothermal Modeling of Cooling Water Diffuser Outfall, Hanford Generating Station, Alden Research Laboratory, December, 1982.

3. Hydrothermal Field Study of Cooling Water Diffuser Outfall, Hanford Generating Station, Alden Research Laboratory, January, 1985.

4. N-Reactor Thermal Plume Characterization Study During Dual-Purpose Mode of Operation, N-Reactor, Pacific Northwest Laboratory Report, September, 1983.

5. Hydrothermal Modeling of Cooling Water Outfall for N-Reactor, Alden Research Laboratory, August, 1988.

EVALUATION OF AUTOMOBILE EXHAUST EMISSION CONCENTRATION IN TUNNELS AND DEPRESSED ROADS

By Yasushi TAKEYAMA
Department of Civil Engineering, Tohoku University
Aoba, Sendai 980, JAPAN

Abstract

In investigating the behaviors of the exhaust emissions in tunnels and depressed roads, experiments using moving traffic, such as model automobile travel apparratus, are generally performed. But, measurements of concentration and wind speed are subjected to restrictions by the existence of moving automobiles. Even if it were possible to make detailed measurements, since the distribution of concentrations and wind speeds in roadway are complex, it is necessary to evaluate items such as ventilation volumes properly by an analysis method which enables to take these influences into consideration.

In this study, the equations express the emission concentrations in a roadway were derived by theoritically modeling the behavior of the air induced by moving traffic. The technique for determining the values of the individual parameters set up were examined applying the measurements obtained to this equation. Some past experiments conducted in Japan were introduced, and the appropriateness of the concentration equations was examined by means of their results.

Introduction

In recent years there has been an increase in cases of underground roads or depressed roads being planned, especially in urban areas, from the viewpoints of giving consideration to the environments of roadside areas and effective utilization of land. It is necessary to study the amount of ventilation needed to secure good visibility in a roadway since dispersion of exhaust emission is restricted in these roads. And from the aspect of environment of roadside areas, it is required to evaluate how much exhaust emissions are discharged to the roadside from the various sections of these roads.

However, concentration characteristics in the roadways cannot be adequately grasped through measurements only at actual roads because still small number of depressed roads are constructed and made available, and because road structures and traffic conditions differ according to individual sites. In surveys by measurements at actual roads, because of factors which cannot be completely controlled such as traffic conditions and meteorological conditions, it is difficult to evaluate the influences of the various factors. Thus, investigations of the phenomena through model experiments are made, but theoretical supplementation is required for evaluating the results.

Theoritical Model of Concentration Distribution in Roadway

(1) Basic Model

The model considered here is an extension of the model used in the past for depressed roads having one-way traffic. Conventionally, the air flow caused by automobile traffic in the roadway, and the exchange of air inside and outside the roadway made through openings are considered in performing analysis.

As seen in visualization experiments, especially in case of reproducing continuous traffic flow using the model automobile travel apparatus, there will be air flow to some degree in the individual traffic lanes in two-way traffic also. From this, by considering independent flows for the individual lanes, and the exchange of air with outside the depressed road through openings, and exchange of air with the opposing lane, it is possible to derive a basic model.

In this case, the amount of air exchanged with outside the depressed road through the openings at the individual lanes is expressed as volume per unit areas of opening per unit length of time, and this is referred to as 'breathing'. As for exchange of air between opposing lanes, this is expressed as volume per unit area of vertical cross section between lanes per unit length of time, and this is referred to as 'mixing'.

By considering the above, the following equations are obtained regarding the air flow in and out per minute length of each lane and the mass balance of pollutants.

$$\begin{array}{llll} & \text{IN} & & \text{OUT} \\ Q_A C_A & + q'HdxC_B + E_A dx & = Q_A(C_A + dC_A) & + qw_A dxC_A + q'HdxC_A \quad (1) \\ Q_B(C_B + dC_B) & + q'HdxC_A + E_B dx & = Q_B C_B & + qw_B dxC_B + q'HdxC_B \quad (2) \end{array}$$

Rearranging the above equations,

$$\frac{dC_A}{dx} = -\frac{q\ w_A + q'H}{Q_A} C_A + \frac{q'H}{Q_A} C_B + \frac{E_A}{Q_A} \tag{3}$$

$$\frac{dC_B}{dx} = -\frac{q'H}{Q_B} C_A + \frac{q\ w_B + q'H}{Q_B} C_B - \frac{E_B}{Q_B} \tag{4}$$

where,
- A, B : Lane A and Lane B
- $Q_{A,B}$: air flow quantity in each lane
- $C_{A,B}$: concentration in each lane
- $E_{A,B}$: emission generation rates of automobile exhaust in individual lanes
- $w_{A,B}$: width of opening of each lane in case of depressed road
- H : height of roadway in tunnel or depressed road
- q : unit breathing
- q' : unit mixing
- $C_{1,2,3,4}$: constants
- x : distance along road

(2) Derivation of Concentration Equation

By considering tunnel/depressed road as the road structure, one-way/two-way as traffic condition, and line source/point source as emission condition, a differential equation (simultaneous equation in case of two-way traffic) is obtained, and the concentration equation is derived as the solution.

By using these concentration equations, even when the structure conditions differ partially, it is possible to express concentration in the roadway by a uniform concept taking into consideration the continuity of air flow inside the roadway.

In order to simplify the explanation of the equation, a to f below were introduced.

$$\frac{q\,w_A}{Q_A} + \frac{q'H}{Q_A} = a \qquad \frac{q'H}{Q_A} = b \qquad \frac{E_A}{Q_A} = e$$

$$\frac{q'H}{Q_B} = c \qquad \frac{q\,w_B}{Q_B} + \frac{q'H}{Q_B} = d \qquad \frac{E_B}{Q_B} = f$$

Examination of Equations by Measured and Experimental Values

(1) Experiments Using Model Automobile Travel Apparatus in Japan

The behavior of exhaust emissions in tunnels and depressed roads differs greatly from the phenomena in normal air ducts or waterways with respect to the points of air flow caused by moving traffic and the transport and dispersion caused through disturbances by automobiles. Therefore, in experiments to grasp these influences, it is not enough to merely reproduce the air flow using equipment such as blowers, and experiments are being conducted reproducing travel of automobiles by model automobiles.

Some experiments using model automobile travel apparatus and field measurement are given in Table 1. With the Reynolds number in actual phenomena as 1, the ratios to Reynolds number in the various experiments are also shown. Here, the traveling speed of a model automobile was taken as the representative value of flow velocity and are shown as ratios of travel Reynolds number. The Reynolds numbers of the experiments compared with actual phenomena were lower by an order of 1 to 3.

Table 1 Experiments (and Measurement) Using Model Automobile Travel Apparatus in Japan

Testing Organization	Testing Facility	Model Scale	Travel Speed Ratio	Fluid	Reynolds Number Ratios
Express Highway Research Foundation [1]	Field	1	1	Air	1
Tokyo Metropolitan Expressway Public Corp. [2]	Water	1/139	0.4	Water	0.04
University of Tokyo [3]	In air	1/90	0.02	Air	0.0002
Ditto	Under water	1/90	1.13	Water	0.2
Public Works Research Institute, Ministry of Construction [4,5]	Wind tunnel	1/100	0.66	Air	0.007

(2) Case of One-way Traffic, Depressed Road

Field measurements were made using sulphur-hexafluoride (SF_6) as the tracer gas in a section of semi-shelter (similar structure to depressed road) of the Chugoku Expressway . An outline of the road structure at the place of measurement and an example of measurement results are shown in Fig. 1.

The equation expressing the concentration in the roadway of the one-way traffic depressed road in case of point source emission is as follow:

$$C_A = C_1 \exp[-(a-b)x] \quad (5)$$

By carrying out application using this concentration equation, 0.15(m/sec) was obtained as breathing value. The theoritical distribution obtained is shown in Fig. 1. By performing similar analyses for other measurement cases, 0.1 to 0.2(m/sec) were obtained as breathing values. Model tests using a water tank were also conducted for the same measurement locations, and breathing values of about the same degrees were obtained from the tests results .[2)]

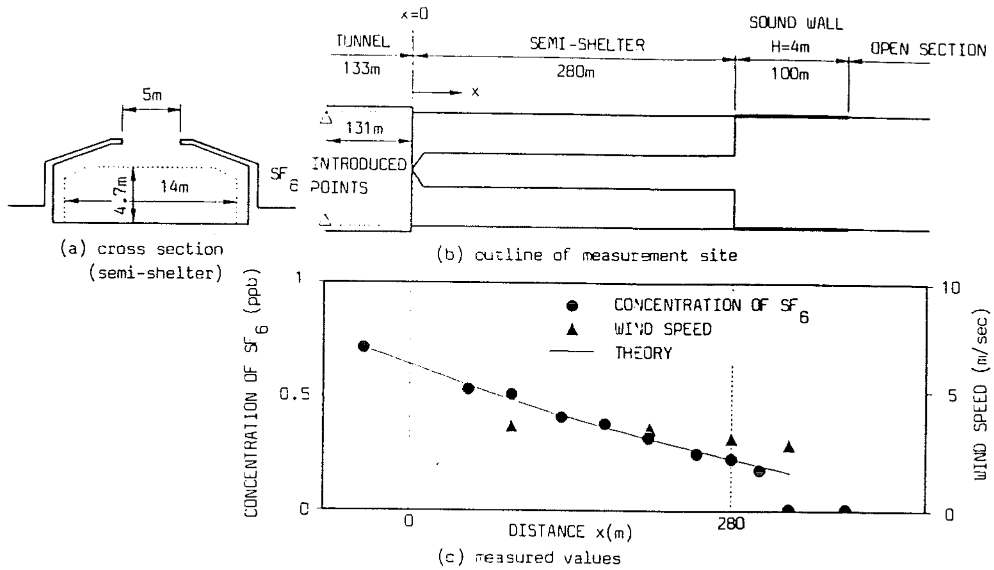

FIG. 1.- Field Measurement at the Chugoku Expressway [1)]

(3) Case of Two-way Traffic, Tunnel

Experiments were conducted using model automobile travel apparatus considering a tunnel of two-way traffic . The concentration equation for point source emission considering these experiments under the condition of ventilation forces equal ($Q_A=Q_B$) of two-way traffic is as follows:

$$C_A = C_1 x + C_2$$
$$C_B = C_1 x + C_3 \quad (6)$$

provided that $C_3 = C_2 - C_1\, b$.

The experimentation apparatus and the longitudinal dispersion coefficient (non dimensional quantity) obtained are shown in Fig. 2. Regarding these experimental results, the concentration and flow volume by automobile lane required for analysis using the model of this study have not been reported.

Analogically inferred from the concentration equation for tunnels based on the longitudinal dispersion coefficient D, the relationship of the following equation will hold between the longitudinal dispersion coefficient and amount of mixing q'.

$$D = \frac{Q_A^{\,2}}{A_T q' H} \quad (7)$$

where, A_T is cross-sectional area of tunnel.

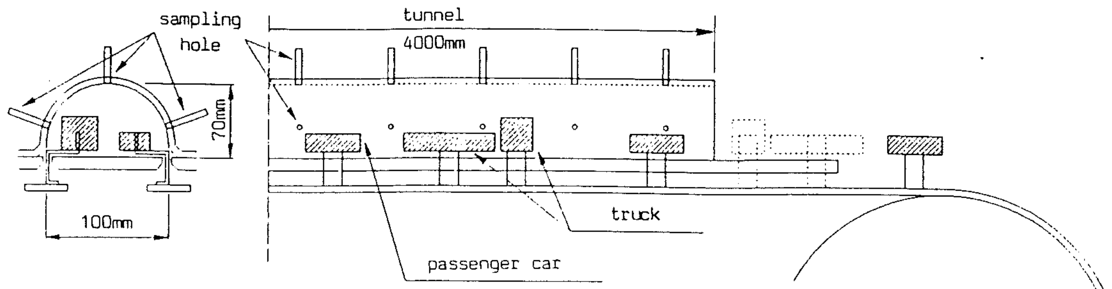

(a) model automobile travel apparatus

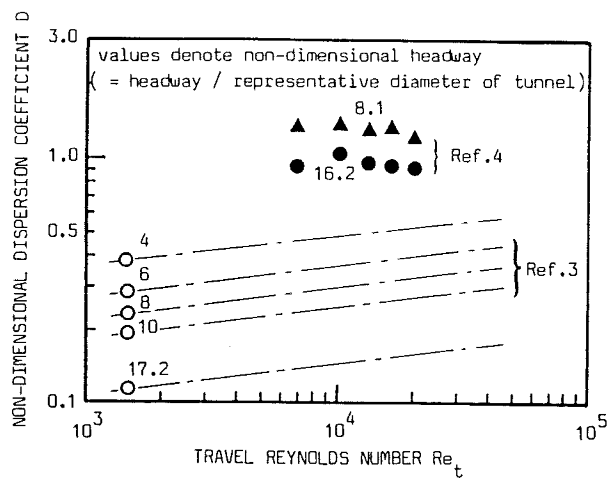

(b) longitudinal dispersion coefficient

FIG. 2.- Experiment on Two-way Traffic, Tunnel [4)]

(4) Case of Two-way Traffic, Depressed Road

The concentration equation for point source emission at two-way traffic depressed road will be as follows:

$$\begin{aligned} C_A &= C_1 \exp(m_1 x) + C_2 \exp(m_2 x) \\ C_B &= C_3 \exp(m_1 x) + C_4 \exp(m_2 x) \end{aligned} \tag{8}$$

provided that

$$m_{1,2} = \frac{1}{2}\left[-(a-d) \pm \sqrt{(a-d)^2 + (ad - bc)} \right]$$

$$C_3 = \frac{m_1 + a}{b} C_1 \qquad C_4 = \frac{m_2 + a}{b} C_2$$

Using the results of model experiments, the amount of ventilation can be calculated by substitution into the above equation. In the case of this study, as a technique to take into consideration scatter in measurements, an algorithm for calculating the volume of ventilation was derived. In this algorithm, first approximations of the amounts of breathing and mixing are suitably given, the various measured values are applied to the concentration equation by the method of least squares, second approximations are calculated from this curve, and by subsequently repeating similar calculations, the volumes of ventilation are derived.

The amount of breathing obtained from experiments varying conditions such as the width of opening are shown in Fig. 3 . The tunnel opening ratio (=opening width/representative diameter of tunnel) is given on the abscissa as the index showing the degree of opening. The amount of breathing shows a tendency to rise slightly as the opening ratio becomes lower, but is roughly in a range of 0.1 to 0.3(m/sec).

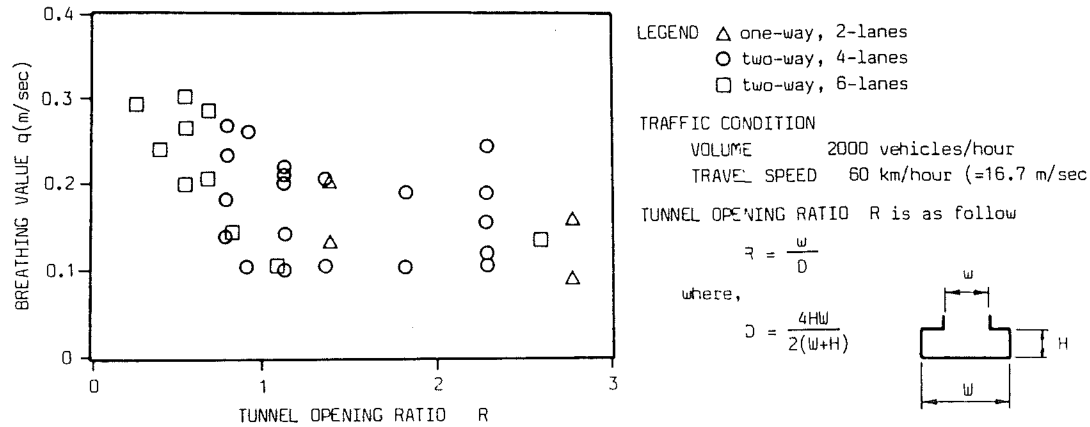

FIG. 3.- Breathing Value at Depressed Roads [5]

Conclusion

The behaviors of exhaust emissions in depressed roads and tunnels have not been adequately understood because of factors such as difficulty of conducting experiments employing model automobile travel apparatus and hindering of measurements due to automobile traffic. Studies on ventilation according to various road structures have not necessarily been carried out based on a unified concept. It is considered that the technique described in this paper will be useful in analyses of the results of model experiments and field measurement, and in studies of ventilation at roads which are combinations of various structural types. In dispersion of exhaust emissions caused by automobile traffic, it is considered that dispersion due to transport is dominant, and it is thought explanations can be provided hereafter regarding the various parameters of ventilation volumes used here through further aerodynamical examinations.

References

1) Express Highway Research Foundation: Report of Survey on Ventilation at Depressed Road, March 1977 (in Japanese).
2) Tokyo Metropolitan Expressway Public Corporation: Report on Survey and Study on Ventilation of Series of Short Tunnels, March 1977 (in Japanese).
3) Ohashi, H., et al.: Dispersion of Exhaust Emission in Automobile Tunnels (Part 1, Longitudinal Dispersion due to Movement of Vehicles), Transactions of the Japan Society of Mechanical Engineers, Vol.48, No.436, pp.2492-2500 (in Japanese).
4) Horiuti, K., and Mizutani, T.: Dispersion of Exhaust Emissions in Highway Tunnels due to Travel of Automobiles, Proceedings of the 41st Annual Conference of the Japan Society of Civil Engineers, 4), pp.417-418, November 1986 (in Japanese).
5) Adachi, Y.: Progress Concerning Road Environments and Landscape of Roads, Technical Report of Public Works Research Institute, Ministry of Construction, No.2614, pp.1-25, March 1988 (in Japanese).

NUMERICAL AND HYDRAULIC MODELING OF CURRENT AND TRANSPORT OF POLLUTANTS IN THE NEVA BAY

by Naum E. Voltzinger

Institute of Oceanology, Leningrad Branch USSR Academy of Sciences 30, Pervaya Liniya 199053 Leningrad USSR,

Konstantin A. Klevanny

State Hydrological Institute 23, Vtoraya Liniya 199053 Leningrad USSR

and Jacov Z. Manevitch

All Union Research Institute of Hydraulic Engineering 21, Gzhatskaya St. 199220 Leningrad USSR

Abstract

The numerical and hydraulic modeling of changes of the hydrodynamical regime and transport of pollutants in the Neva Bay were performed in connection with constraction of the Dam to prevent Leningrad against unundations 30 km far from the city. The results obtained were used to develope recommendations to transfer the sites of wastewater outfalls in the Neva Bay.

Introduction

At present the modeling of the water dynamic and transport of pollutants in the Neva Bay is a very important problem. There are two main tasks which must be solved by modeling: 1) recommendations to transfer the sites of Leningrad urban and industrial wastewater outfalls in the Neva Bay, 2) forecast of changes in the water pollution regime under the influence of the Dam. Location of the outfalls from 3 large treatment plants (with the discharge under 30 cub.m/s) is the most important problem because the Bay is shallow (the depth is less than 5 m) and the effluents after treatment contain large quantity of different pollutants. The choice of the location for these outfalls is strongly restricted by the presence of the resorts along the coasts and by the Kotlin island. The degree of pollution of the Neva and the Bay is unfortunately very high.

The Neva Bay dynamics modeling reveals the problem of its high sensitivity connected with usually small level oscillations and with variable meteorological conditions. The analysis of data of field investigations for more than 20 years has shown that the spectrum of current has many extremes in the wide range of periods (Belishev and Preobrazhensky, 1988).

Numerical Modeling

Two-dimensional shallow-water equations and the equation of depth-averaged transport and dispersion of pollutants are used. A complex shape of the area of computations, especially relatively small (110- 240 m)gates in the Dam makes it necessary to use curvilinear boundary-fitted coordinates and mapping of the domain given onto a canonical one (the system of rectangles). This approach is widely used in aerodynamics (Thompson, 1982)and finds an increasing application in oceanological problems. Details of the domain geometry can have a dramatic influence on the general character of solution. This makes it necessary to use the boundary conditions directly in the nodes of the curvilinear boundary without carring them away in the nodes of the regular grid.

Let us consider the initial boundary-value problem for the shallow-water equations

$$\mathbf{W}_t + \mathbf{A}\mathbf{W}_x + \mathbf{B}\mathbf{W}_y = \mathbf{f}, \quad x,y \in \Omega, \ t \geqslant 0 \qquad (1)$$

$$\mathbf{W} = \begin{vmatrix} u \\ v \\ H \end{vmatrix} \quad \mathbf{A} = \begin{vmatrix} u & 0 & g \\ 0 & u & 0 \\ H & 0 & u \end{vmatrix} \quad \mathbf{B} = \begin{vmatrix} v & 0 & 0 \\ 0 & v & g \\ 0 & H & v \end{vmatrix}$$

$$\mathbf{f} = \begin{vmatrix} lv + \Delta\tau^x/H + a\,\Delta u \\ -lu + \Delta\tau^y/H + a\,\Delta v \\ 0 \end{vmatrix} = \begin{vmatrix} f_1 \\ f_2 \\ 0 \end{vmatrix}$$

where $(u,v)=\mathbf{V}$ -velocity vector, $H=h+\zeta$, h-depth, ζ- level, g -acceleration of gravity, l- Coriolic parameter, $\Delta\tau^x, \Delta\tau^y$ components of shear stress vector, a- coefficient of horisontal eddy viscosity, Ω-the domain with the contour $\partial\Omega$. On the impermeable part of contour $\partial\Omega_1$ we assume $v_n=0$, where v_n-velocity normal to $\partial\Omega_1$.On the permeable part $\partial\Omega_2$ boundary conditions are defined in accordance with the requirements of correctness.Assigment of the initial conditions $\mathbf{W}_{t=0}= \mathbf{W}^0$ completes the formulation of the problem.

We introduce curvilinear coordinates ξ,η concordant with the configuration of Ω : on the segments of $\partial\Omega$ chosen one of the coordinates is fixed, but the other is distributed arbitrary, but monotonically. In the ξ,η- plane the given domain is represented by the rectangle Ω^*.In the new variables , the set of equations (1) written with the respect to vector $\mathfrak{A} = (p,q,\zeta)$, $p=JHU=H(uy_\eta-vx_\eta)$, $q=JHV=H(vx_\xi-uy_\xi)$ is reduced to the form

$$\mathfrak{A}_\tau + \mathcal{A}\,\mathfrak{A}_\xi + \mathcal{B}\,\mathfrak{A}_\eta = \phi, \qquad \xi\ \eta \in \Omega^* \qquad (2)$$

$$\mathcal{A} = \begin{vmatrix} 0 & 0 & \gamma \\ 0 & 0 & -\beta \\ J^{-1} & 0 & 0 \end{vmatrix}, \qquad \mathcal{B} = \begin{vmatrix} 0 & 0 & -\beta \\ 0 & 0 & a \\ 0 & J^{-1} & 0 \end{vmatrix}$$

$$\Phi = \begin{vmatrix} -(U^k p)_{\xi^k} + JHU^j \Gamma^1{}_{kj} U^k + H(f_1 y_\eta - f_2 x_\eta) \\ (U^k q)_{\xi^k} + JHU^j \Gamma^2{}_{kj} U^k + H(f_2 x_\xi - f_1 y_\xi) \\ 0 \end{vmatrix}$$

where $\alpha = gHJ^{-1}g^{22}$, $\gamma = gHJ^{-1}g^{11}$, $\beta = gHJ^{-1}g^{12}$, $g^{11}=x_\eta^2+y_\eta^2$, $g^{22}=x_\xi^2+y_\xi^2$, $g^{12}=x_\xi x_\eta+y_\xi y_\eta$. $\Gamma^i{}_{kj}$-symbols of Cristoffel of the second kind, $i,j,k=1,2$, $U^1=U, U^2=V$. $\xi^1=\xi, \xi^2=\eta$, for summing up with repeating index. U,V -contravariant components of $\mathbf{V}$, $J=x_\xi y_\eta - x_\eta y_\xi > 0$ - Jacobian of transformation.

The equation of transport and dispersion of pollutants

$$C_t + (uC)_x + (vC)_y = (KC_x)_x + (KC_y)_y + \phi \quad (3)$$

in curvilinear coordinates takes the form

$$(JHC)_\tau + (pC)_\xi + (qC)_\eta = (KHJ^{-1}g^{11}C_\xi)_\xi + $$
$$+ (KHJ^{-1}g^{22}C_\eta)_\eta + (KHJ^{-1}g^{12}C_\xi)_\eta + (KHJ^{-1}g^{12}C_\eta)_\xi + JH\psi, \quad (4)$$

where K- coefficient of diffusion, ψ- source function.

Equations (2) were solved by semi-implicit finite-difference method with non- restrictive stability condition ($max(U,V) \leq \sqrt{gH}$). They were approximated by Crank- Nicolson's scheme, which was realised by Peaceman- Rachford's splitting (Voltzinger et.al, 1989).

Equation (4) was approximated by second- order up-stream implicit finite- differences and was realised by Douglas- Gunn's splitting.

Hydraulic Modeling

The hydraulic model is 120 m long and 60 m wide. Its horisontal scale is 1/500, the vertical one 1/50. For steady conditions velocities in the Neva Bay originated by the Neva discharge is about 4- 6 cm/s and $Re_n > Re_{crit}$. In the model if $Fr = idem (Fr = v^2/gH)$ then $Re_m < Re_{crit}$. It is shown (Levy, 1961) that there is an automodel of Fr-number area, if $Fr < 0.05$ In nature $Fr \cong 5.10^{-3}$. so three-fold increase of discharges was used to reach automodelity of Re-number. The big problem usually is the choice of roughness elements height. We have recieved (Manevitch, 1982) that for the conditions of the Neva Bay model at $\lambda > 0.015$ automodelity of $\lambda b/H$ -number is reached (λ- friction coefficient, b-

-width). The height of roughness elements and the distance between them were determined from the nomograms obtained (Manevitch, 1985).

For unsteady conditions the automodelity of Re-number in model is reached even at small intensity of level oscillations (>3cm/h). The conditions of Fr=idem, St=idem is easyly satisfied also if we assume the corresponding scales of velocity and time $\alpha_v = \alpha^{1/2}_h$, $\alpha_t = \alpha_l / \alpha_v = \alpha_l \alpha^{-1/2}_h$. It was necessary to check the influence of increased heights of roughness elements on the long wave propagation. In (Bolotovski and Levina, 1979) it is shown that in the range of $14 > \beta > 3$, $\beta = \lambda / 2l_0$ time history of characteristic nature level oscillations is in a good agreement with numerical ones. As in our case β lies in these limits, so the model and nature current fields must be similar.

Results

Steady and unsteady regimes of the Neva Bay formed by the river discharge, sea level oscillations originated in the Baltic Sea and wind field were investigated using the described numerical and hydraulic models (by wind - only numerically). The model results were tested using current and level field data and sufficient accuracies were achieved. The field data are more variable than numerical model one - it is an expected result because depth averaged quantities calculated numerically are more stable than the measured ones. The deviation between numerical model and natural time averaged directions of cuurent vectors at different stations lies within the limits from 5^0 to 12^0. Only for one of the stations which was situated in the near stagnant south- east region of the Bay it reachs 27^0. The deviation in the amplitudes of the current vectors is within the range from 0.1 to 2.8 cm/s (Voltzinger at al, 1990).

A comparison between numerical and hydraulic model results showed that as the general current patterns at steady state were simillar, the relative vortex intensification was obtained with hydraulic modeling (figure 1).

The different hydrodynamic regimes were investigated with the models for Dam and without Dam conditions. Models results showed that total character of the fluxes did not changed. The main effect of the Dam, according to hydraulic and mathematical models is the increasing of reflection by the Dam with the increasing of wave frequency and amplitude. The most important semidutrnal waves penetrate througt the Dam gates almost without reflection but waves with periods less than 5 hours are reflected significantly.

The results of numerical modeling showed that under the Dam conditions concentrations of pollutants may increase in

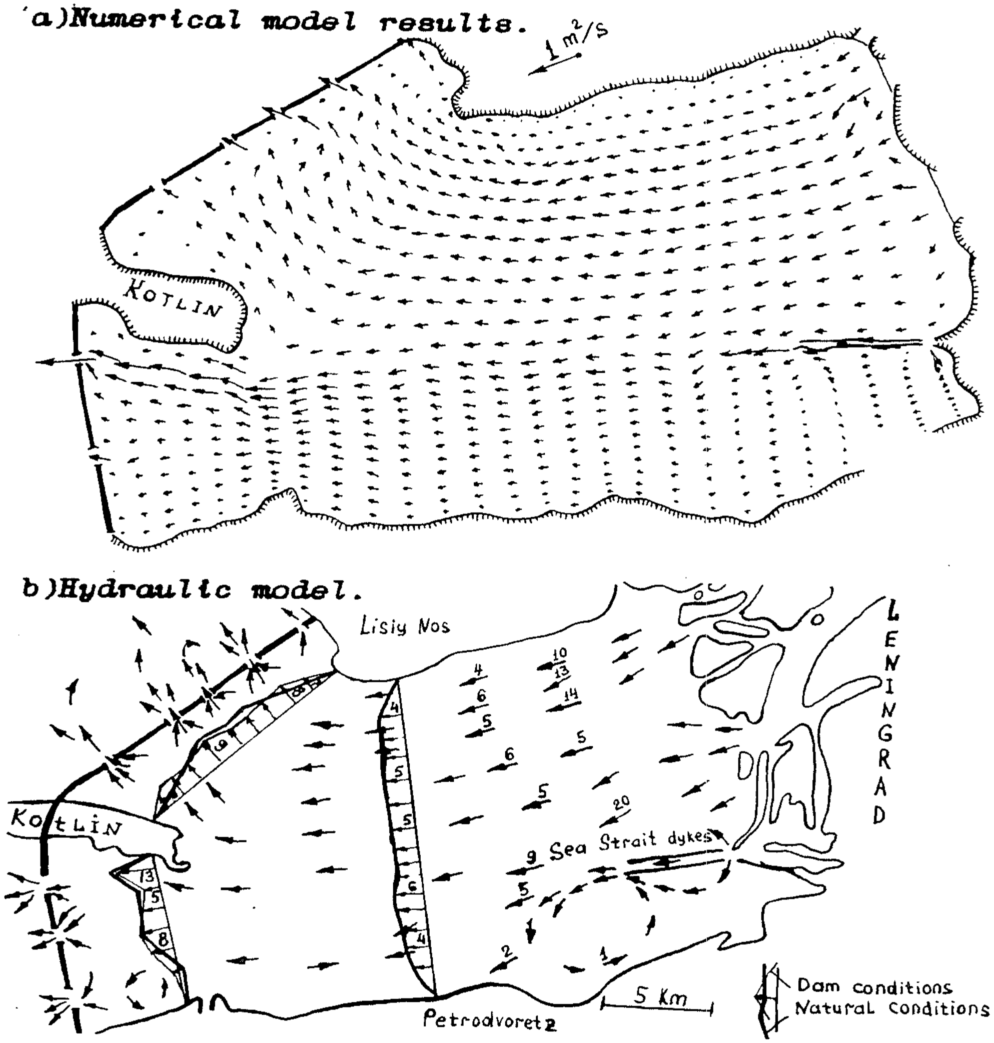

Fig.1 Flow fields in the Neva Bay in Dam conditions at the steady state.

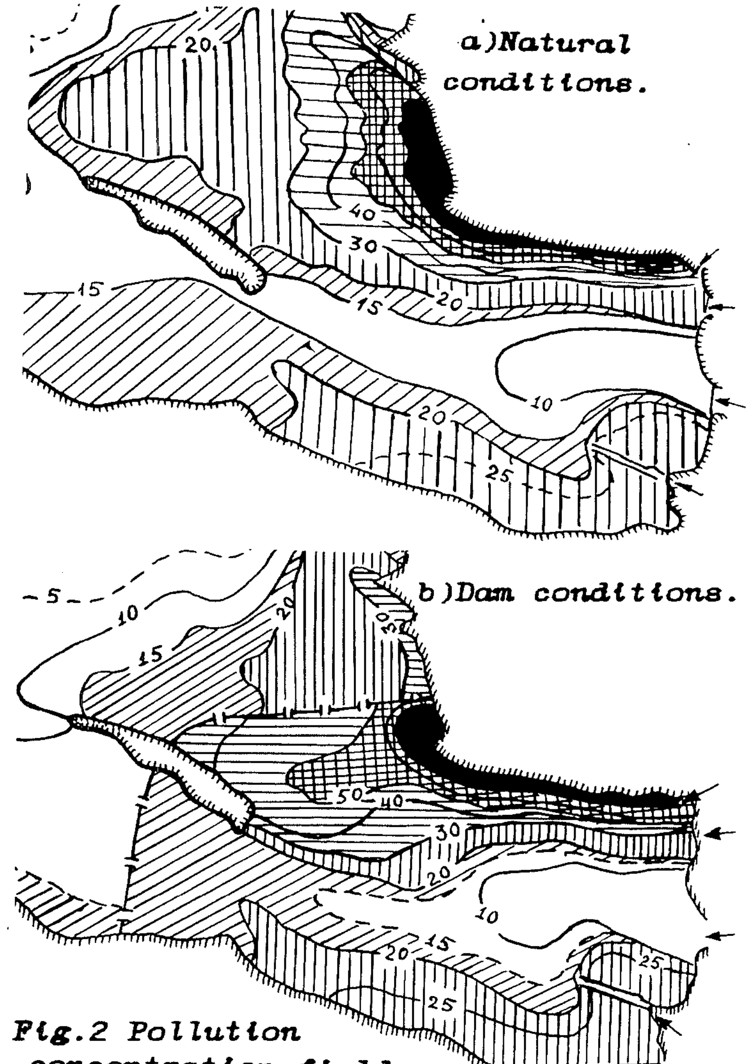

Fig.2 Pollution concentration fields in the Neva Bay at the unsteady state.

Numerical model results.

the north enclosed part of the bay near the Dam (figure 2). Near Kotlin island they will increase in 1.5 - 2 times.Outside of enclosed area concentrations under the Dam conditions will be less. It is explained by the dispersion of wastewater plume by the Dam gates and by the change in current system on this side of the Dam.

Both models revealed that transfer of the North treatment plant outfalls 1 km seaside (2 km from the shore) would result plume movement apart from the shore. The pollution level near the shore would decrease in this case in several times and the corresponding increase of concentrations near Kotlin is insignificant. Transfer of the South-West treatment plant outfalls 2,5 - 3 km to the north from the Sea Strait would result the decreasing of pollution level along the south coast more than 10 times in comparison with their location near the west end of the Sea Strait dykes as it suggested now.

References

Belishev, A.P., and Preobrazhensky, L.Yu. (1988),Current structure in the Neva Bay and the eastern part of the Gulf of Finland,Trans.State Hydrolog.Inst.,v.321:4-16 (in Russian).

Bolotovski, S.W. and Levina,S.M. (1979), Hydraulic investigation of unsteady regimes in the Neva Bay, Trans.All Union Res. Inst. of Hydr. Eng.,v.132: 36-46,(in Russian).

Levi,I.I.(1961), Modeling of Hydraulic Phenomena, Energia Publ.:210 p., (in Russian).

Manevitch, J.Z.(1982), Influence of roughness on current field at distorded hydraulic models, Trans.All Union Res.Inst.of Hydr.Eng.,v.154:65-69, (in Russian).

Manevitch, J. Z. (1985), Friction coefficient investigation for the arranged artificial roughness, Trans. All Union Res.Inst. of Hydr. Eng.,v.179:28-34(in Russian).

Manevitch, J.Z. (1989), The general hydraulic model of the Neva Bay, Trans. All Union Res. Inst. of Hydr.Eng.,v.223 (in Russian).

Thompson, J.F. (1982), Numerical Grid Generation, Appl.Math. Comp.,v.10-11:910 p.

Voltzinger,N.E., Klevanny, K. A. and Pelinovski E. N. (1989), Long- Wave Dynamics of the Coastal Zone,Gidrometeoizdat Publ., Leningrad: 271 p.,(in Russian).

Voltzinger, N.E., Zolnicov A.V., Klevanny K.A. and Preobrazhensky L. Yu. (1990),Calculation of the hydrological regime of the Neva Bay, Meteorology and Hydrology, v.1:70-77.(in Russian).

MODEL STUDY OF WESTERN CAIRO
POWER PLANT COOLING WATER SYSTEM

by
Mohamed Gasser[1] and Ibrahim Eldesouky[2]

1. Abstract

Western Cairo Power Plant (WCPP) was built in the early sixties. It produces 348 MWe at maximum. The decision has been taken to extend its capacity to 1668 MWe. The investigations of the cooling water system of its extension were conducted by the Hydraulics & Sediment Research Institute (HSRI), Delta Barrage, Egypt, on a 1:65 hydraulic scale model. The main purpose of the study was to develop an intake-outfall configuration which results in preventing thermal recirculation as well as fulfilling the regulatory temperature standards.

2. Background

WCPP is located on the left bank of the Nile River, 7 km upstream of the Delta Barrage. The plant has four existing units, producing 87 MWe/unit. It has a once-through cooling water system, its heat rejection load to the river is 492 MWth, its cooling water discharge is 12.4 m^3/s at a temperature rise of 9.5 °C. The plant will be extended by adding four units more, producing 330 MWe/unit. A separate once-through cooling water system will be constructed, its heat rejection load to the river will be 1800 MWth, its cooling water discharge will be 44.4 °C at a temperature rise of 9.7°C.

3. Hydrology

The Nile River at the power plant site is more or less straight, its width varies between 500-600 m, while its mean depth is 6.5 m except during the low discharge period (one-month) when the mean depth is 4.9 m. The river flow at the site is mainly controlled by the Delta Barrage, 7 km downstream. River flow conditions show that:
- Minimum discharge: 630 m^3/s, at a water level of +14.9 m MSL
- Nominal discharge: 1100 m^3/s, at a water level of +16.4 m MSL
- Maximum discharge: 1748 m^3/s, at a water level of +16.5 m MSL

The average water temperature during summer is 28°C and during winter 15°C.

4. Temperature standard

The Egyptian Ministry of Public Works & Water Resources' law no. 48, 1982, specifies that the maximum temperature in the river shall be limited to a rise of 5°C above the natural water temperature, with a maximum absolute value of 35°C.

1. Director of the Hydraulics & Sediment Research Institute, Delta Barrage, Egypt
2. Research Engineer, Hydraulics & Sediment Research Institute, Delta Barrage, Egypt

5. Model Description

5.1 Scale Limitations

Different scale combinations, which meet the model scaling requirements were considered, to match with the dimensions and capacities of the facilities at the Institute. Geometrical scales with a small distortion up to a ratio of horizontal scale/vertical scale = 2 at maximum were considered [3]. Table 1 shows the scale considerations.

5.2 Model Scales

The model study was especially concentrating on the near-field of the cooling water discharge, where the inertia and buoyancy forces are predominant. The model was operated according to densimetric Froude similitude relationships. An undistorted geometrical scale of 1:65 was selected. The scale ratio´s for the other quantities are:

Velocity	1 : 8.06
Time	1 : 8.06
Discharge	1 : 34065

5.3 Model Description

Figure 1 shows the model layout. The model reproduced a 2854 m long stretch of the Nile River and the existing and proposed intake and outfall structures. A data acquisition system including a micro computer was installed to monitor and store all measuring data of flows, water levels and temperatures.

6. Proposed Intake and Outfall Structures

An inland intake of 60 m wide, + 10 m MSL floor level, with a skimmer wall at + 14.0 m MSL, was tested.

A near surface outfall structure with four culverts with a cross section of 2.5 x 2.5 m^2 each, separated by 0.5 m thick dividing walls, was tested. Its ceiling level was + 14.9 m MSL and its bottom level was +12.4 m MSL. It was inclined in the downstream direction at 60 degrees to the river axis.

7. Model Test Program

The intake-outfall configuration has been tested at different river discharges and water levels for 2, 3 or 4 units in operation in addition to the existing 4 units. These tests were repeated after reforming the fixed river bed according to the expected erosion caused by the cooling water jet. Table 2 shows the test program.

Table 1 MODEL SCALE CONSIDERATIONS

scales n_h/n_l parameter	40/80	50/75	65/65	50/100	65/100
distortion ratio	2	1.5	1 (undistorted)	2	1.5
$Re_{river} \geq$ 2000? ($\bar{v}$ = 0.23 m/s , h_s = 10 m a.s.l. in prototype)	4546	3253	2194	3253	2194
$Re_{outlet\ 2}$(future) $\geq$ 750?	5500-15000	3900-10800	2650-17300	3900-10800	2650-7300
$Re_{outlet\ 1}$(existing) $\geq$ 750?	2000	1400-1500	950-1000	1400-1500	950-1000
n_Q	20239	26517	34063	35355	52405
Q_{river} (630 - 1750 m^3/s prototype)	31-87 l/s	24-66 l/s	18-52 l/s	18-50 l/s	12-34 l/s
$Q_{power\ st}$ (56.8 m^3/s prototype)	2.81 l/s	2.14 l/s	1.67 l/s	1.61 l/s	1.08 l/s
reject heat ($\Delta T \leq 12\,^\circ C$ in the model)	142 kW	108 kW	84 kW	81 kW	54 kW
Q_{river} (600 - 1800 m^3/s prototype)	29.6-88.9 l/s	22.6-67.9 l/s	17.6-52.8 l /s	17.0-50.9 l/s	11.4-34.3 l/s
experimental facility	open air hall 1	open air hall 1	open air hall 1	hall 2	hall 2
available model area	12.5 (or14)x70m^2	12.5 (or14) x70m^2	12.5 (or14) x70m^2	max length 24 m	max length 24 m
model dimensions (850 x 2400 m^2) (net area to be modelled)	10.6 x 30 m^2	11.3 x 32 m^2	13.1 x 36.9 m^2	8.5 x 24 m^2	8.5 x 24 m^2

Table 2 Test Program

No.	Q_a	RT	NU	Q_c	$\Delta\rho/\rho$
1	630	P	2	34.6	0.0021
2	630	P	3	45.7	0.0021
3	630	P	4	56.8	0.0021
4	1748	P	2	34.6	0.0034
5	1748	P	3	45.7	0.0034
6	1748	P	4	56.8	0.0034
7	630	F	2	34.6	0.0021
8	630	F	3	45.7	0.0021
9	630	F	4	56.8	0.0021
10	1748	F	2	34.6	0.0034
11	1748	F	3	45.7	0.0034
12	1748	F	4	56.8	0.0034

where:
Q_a = river discharge (m^3/s)
P = present condition
NU = no. of units in operation
ρ = river water density (kg/m^3)
RT = river bed topography
F = future condition
Q_c = cooling water discharge (m^3/s)
$\Delta\rho$ = density difference (kg/m^3)

In each test surface water temperatures, vertical temperature profiles, flow velocity distributions in the plant site vicinity and surface currents have been measured.

8. Scale Effects

The heat exchange with the atmosphere within the cooling water plume in the model was not correctly reproduced because of the undistorted scale. In the model this heat exchange is too large by a factor 8 but this effect can be neglected. For instance, in the prototype the heat exchange over a surface area of about 8000 m^2, enclosed by the 5°C isotherm (mixing zone) at low river discharge and 4 units in operation, will result in a heat loss of 0.07% of the heat disposal:

- surface area of the mixing zone: A = 8000 m^2
- average temperature rise in the mixing zone: ΔT = 7°C
- heat transfer coefficient at the air-water interface [4]: ω = 22 W/m^2 °C
- surface heat loss from the mixing zone: $\omega A \Delta T$ = 1.23 MW
- heat input from the plant(extension): 1800 MW

In the model this heat loss will be 0.5%, which is still negligible in comparison with the temperature reduction in the near-field by mixing and turbulent diffusion.

9. Conclusions

The outfall structure for WCPP extension as proposed by HSRI is satisfactory, as it results in complete prevention of thermal recirculation and fulfilment of the environmental criteria. The maximum mixing zone area is 100 x 80 m^2 (the mean river width is 550 m). Further studies for the optimization of the intake layout and its pumping station are recommended.

10. Acknowledgment

The cooperation and valuable suggestions of Mr. A. Quist of DELFT HYDRAULICS, Netherlands, to conduct the model studies and to prepare the paper are gratefully acknowledged.

11. References

1. HSRI Report "Hydrothermal model study of Western Cairo Power Plant Extension", Dec. 1989.
2. DELFT HYDRAULICS and Massachusetts Institute of Technology "European course on heat disposal from power generation in the water environment", Delft (1975).
3. Hoogendoorn, D. and Quist, A. "Effects of model distortion on the near-field behavior of thermal discharges", Third Waste Heat Management and Utilization Conf. Miami, 1981.
4. H.E. Sweers, "A nomogram to estimate the heat exchange coefficient at the air-water interface as a function of the wind speed and temperature, a critical survey of some literature", Journal of Hydrology 30 (1976) 375 - 401.

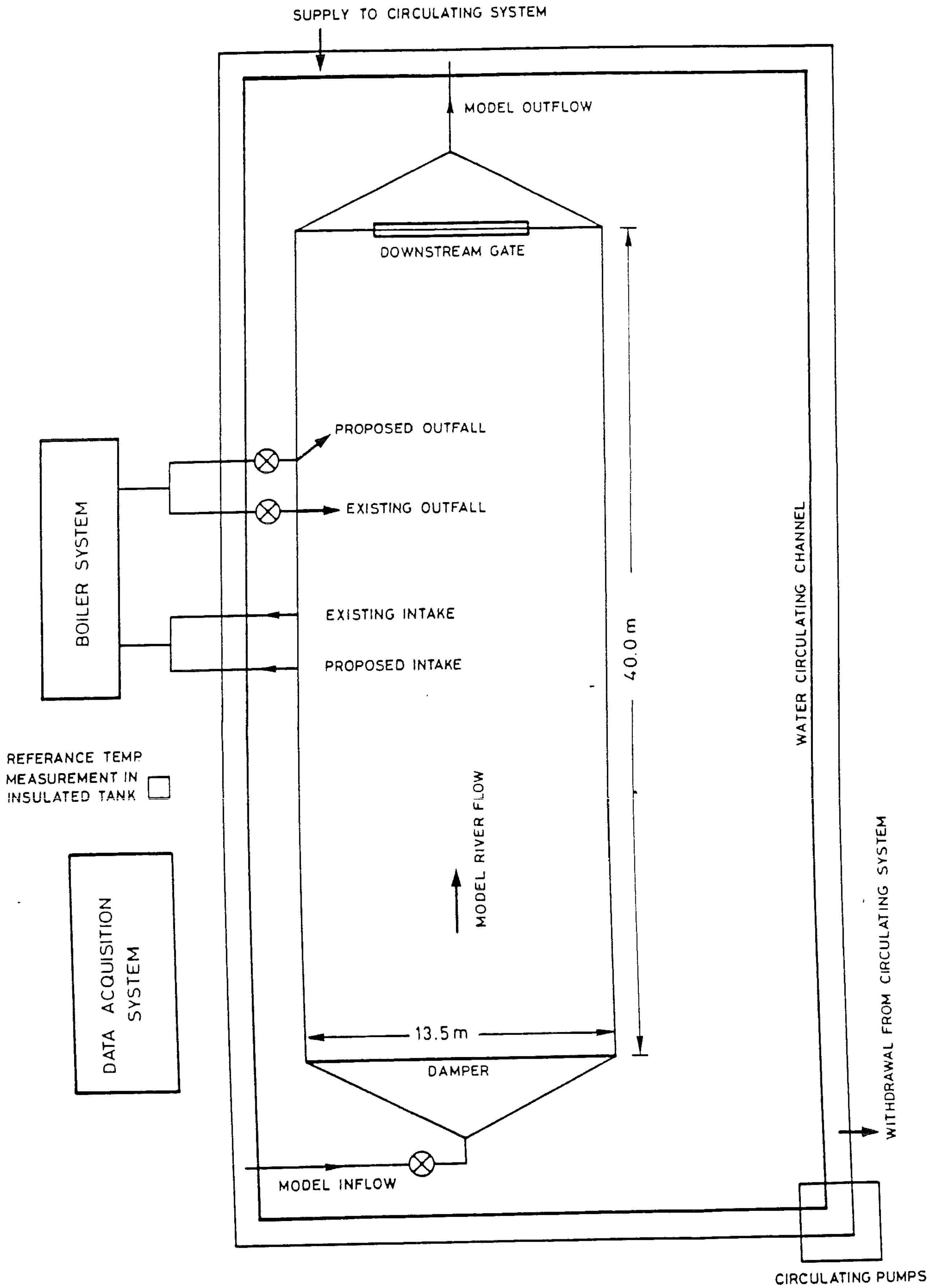

FIG. 1 MODEL LAY-OUT

Prediction Techniques For Salt Water Intrusion in Qiantang Estuary by Physical and Mathematical Models

Han Zengcui[1] Shao Yaqin[2]
Lu Xiangxin[3] Shi Ying[4]

Abstract

The Qiantang Estuary is a famous macrotidal estuary in China and also in the world. Because of the strong mixing, the chlorinity is distributed homogeneously in the cross-section, especially in the spring tide. This paper presents a brief introduction of the numerical and scale models applied jointly to predict the salt water intrusion. Based on the calibration of the two kinds of model, three different schemes of releasing fresh water from upstream reservoir in a certain period have been studied. A superior water release scheme has been put forward. By using this scheme, 30% of fresh water will be saved.

For years of pactice, the predicted chlorinity basically conforms to the observed value. The chlorinity at the water intake site is kept below the permissible limit by releasing sufficient but not too much fresh water from the upstream reservoir since 1979 till 1988 during dry seasons.

Introduction

Hangzhou is a large city with population over one million located along the northern bank of the Qiantang Estuary (Fig.1). Eighty percent of its water supply for domestic and industrial uses and irrigation water of 100,000 ha of farmlands on the southern bank are taken from the Qiantang Estuary. During dry seasons the chlorinity of river water exceeds the limiting standard (250 mg/l for industrial and domestic uses and 1200 mg/l for irrigation use). Owing to salt water intrusion in spring tide. The direct economic loss amounts to 3 million Yuan per day. Therefore, the monitoring and prediction of water chlorinity received great attention from the government and the scientific units. In the recent thirty years, monitoring works and prediction studies have been carried out by means of statistical analysis、numerical simulation and scale model. This paper presents a brief introduction of mathematical and scale models for the prediction of chlorinity in Qiantang Estuary and the counter mesurment to prevent the chlorinity value higher than the permissble.

1. Numerical simulation

The simulation of chlorinity for the strong mixing estuary such as Qiantang Estuary can be made by solving the following differential equations:

$$\frac{\partial z}{\partial t}+\frac{1}{B}\frac{\partial Q}{\partial x}=0 \tag{1}$$

$$\frac{\partial Q}{\partial t}+2u\frac{\partial Q}{\partial x}+Ag\frac{\partial A}{\partial x}=u^2\frac{\partial A}{\partial x}-bg\frac{Q|Q|}{C_z^2R^2}-\frac{AgH}{2\rho}\frac{\partial \rho}{\partial x} \tag{2}$$

$$\frac{\partial S}{\partial t}+u\frac{\partial S}{\partial x}=\frac{1}{A}\frac{\partial}{\partial x}\left(AD\frac{\partial S}{\partial x}\right) \tag{3}$$

$$\rho=1000+1.35S \tag{4}$$

1.2.3 Zhejiang Provincial Institute of Estuarine and Coastal Engineering Research(ZECER), P.R.China
4. Zhejiang University,Hangzhou,P.R.China

in which Z,Q,A,S denote the water stage, discharge, cross-sectional area and chlorinity respectively. Ex is the dispersion coefficient of chlorinity. It is obtained by dimensional analysis using a lots of field data in Qiantang Estuary for different stretches namely[1].

$$\frac{D}{uH} = \left[1 - \exp\left(-\frac{u^2}{gH} \cdot \frac{Q_f t_f}{Q_0 T}\right)\right] \frac{S_1}{S_*} + 10 \qquad (5)$$

in which $u^2/(gh)$ is the froude number, $Q_fT_f/(Q_0T)$ is the ratio of flood tidal volume to fresh water volume in a tidal cycle, $u^2/(gh)\ Q_fT_f/(Q_0T)$ is called the 'number of Estuary'. Eq.(5) demonstrates the effect of fresh water discharge and the tidal flow, especially for the strong tide in the Qiantang Estuary upon the dispersion coefficent. The value of the coefficient of dispersion in Qiantang Estuary is 10-100 times larger than the value in other estuarine. The characteristic oriented finite scheme which can simulate the tidal bore is used and the space step of 4 km, and time step of 180 second are adopted to satisfy the Courant condition. Three runs of different tidal ranges ($\triangle H$=2.7m、1.7m、1.1m) are used for verification of tidal level and chlorinity. Part of the calculated and observed graphs are shown in Fig.2.3. The mean discrepancy of tidal level is about 0.1m with a maxium of 0.3m, that of the chlorinity is less than 30% and that of the duration of exceeding permissible value (250 p.p.m) is within 20%. This shows that the discrepancy is within the range of cross-sectional chlorinity variation of a well-mixed estuary and this model could be used for prediction study of chlorinity.

2. Scale model

A scale model of the Qiantay Estuary was already established years ago in ZECER with a horizontal scale 1:1500 and vertical scale 1:100. The upstream and downstream boundaries of the model lies at Fuyang and Jianshan respectively with a total river length of 180 km. The model is equipped with apparatus of tide generator, fresh water discharge controlling and concentrated recording of tidal levels, velocities and chlorinities. By using eq.(2),(3), the scale of Froude's law ($\lambda_v = \lambda_H^{1/2}$) and other scales (such as $\lambda_E = \lambda_H^{1/2} \cdot \lambda_L, \lambda_s = 1$) can be obtained. The scales of the model are shown in Table 1 and Fig.1.

Table 1 The scales of the physical model

terms	Formula or Signor	Scale
horizontal scale	λ_L	1500
vertical scale	λ_H	100
velocity scale	$\lambda_v = \lambda_H^{1/2}$	10
noughness scale	$\lambda_n = \lambda_H^{2/3} \lambda_L^{1/2}$	0.556
Time scal for flow	$\lambda_t = \lambda_L / \lambda_v$	150
discharge scale	$\lambda_Q = \lambda_L \lambda_H \lambda_v$	1,500,000
chlorinity scale	λ_s	1
dispersional scale	$\lambda_E = \lambda_H^{1/2} \lambda_L$	15,000

strictly speaking, for simulating the chlorinity distribution along the vertical, an undistorted model is neccessary. Owing to the well-mixing and the shallow depth in Qiantang Estuary, the model with a scale distortion of 15 can also be used for the simulation of salt water intrusion. Two periods of in-situ data in 1978 and 1988 are used for verification. The tested and observed graphs are shown in Fig. 2.3.

3. Comparison of the application of two models

First of all, both the physical model and mathematical model, there exist certain discrepancy with the observed chlorinity. The difference between the measured value and modelling values are less than 30%, this shows that the discrepancy is within the range of cross-sectional chlorinity variation of a well-mixed estuary (generally, the chlorinity variation in cross-section is about 30%).

Secondly, physical model can simutaneously measure the values of the chlorinity aside the bank (i.e., at the planned water intake) and in the main stream, but it is impossible to calculate in the one-dimensional mathematical model (Fig.5). It shows the difference between the northern bank and main stream is about 30%. In chosing the place of water intake, this difference is neccessary to be considered. However,the prediction of long period salt water intrusion and scheme studies, the mathematical model is favourable and advantageous for its saving of time and money.

4. Other applications of the models

4.1 Superior water release scheme

For a certain fresh water volume released in a certain period, it can be released uniformly (case 1), with 30% more during spring tide and 30% less during neap tide than the average volume (case 2) and to concentrate 70% of fresh water released near the end of the spring tide (case 3). Table 2 shows the results from numerical and scale models. It indicates that case 2 is the best scheme.

Table 2

	Case 1		Case 2		Case 3	
	numerical model	scale model	numerical model	scale model	numerical model	scale model
chlorinity Zakou p.p.M Shan	2610 1100	1760 1000	1440 700	1040 560	4800 2700	
Days of exceeding at Zakou	6.6	6.0	2.1	2.0	6.2	

4.2 Long period prediction of salt water intrusion

Table 3 shows the monthly fresh water volume required (predicted by mathematical model) and the actual volume released as well as the corresponding days of 'exceeding the chlorinity limit' in 1978 and 1979. When the actual water volume released could not meet the required volume(such as 1978), the number of days 'exceeding the limit' is much more, and the number of days well be less when the actual released water volume approximately equals the predicted volume[2].

4.3 The optimun site selection of water intake[3]

By using this two kinds of model, the chlorinity and the duration hours of 'EXCEEDING THE LIMIT' for different natural discharge, different fresh water release scheme, different tidal range and different river configuration (Qiantang Estuary is an alluvial estuary with frequent and heavy bed deformation) at different sites were predicted and analysed. Based on the analysis, the function of a small-sized regulating reservoir near the water intake is very efficient and is therefore strongly recommended; an optium intake site is finally recommended which can save a lot of construction cost.

Table 3 $10^8\ M^3$

	1978			1979		
	Volume of release		days of exceeding	Volume of release		days of exceeding
	actual	predicted		actual	predicted	
July	7.4	8.5	4	8.6	6.2	0
August	5.8	9.0	5	8.9	6.5	0
September	4.1	9.0	13	9.5	6.5	0
October	2.0	6.5	10	5.2	4.9	0
November	1.5	4.5	30	3.4	3.1	5*
December	1.7	4.5	30	2.4	3.1	0
Total	22.5	42	92	38	30.3	5

* haven't released according to the predicted schedule, notwithstanding the total volume is sufficient.

Reference

[1] Han Zengcui, Cheng Hangpin. The Study of Salinity Prediction in Qiantang Estuary. Journal of Hydraulic Engineering. 1981.6 (in Chinese).

[2] Han Zengcui, Shao Yaqin. Salt water intrusion and its counter measures in some coastal cities in China. Ocean Engineering. Vol 1988

[3] Study on salt water intrusion for new water works of Hangzhou city. ZECHR. Apirl 1989.

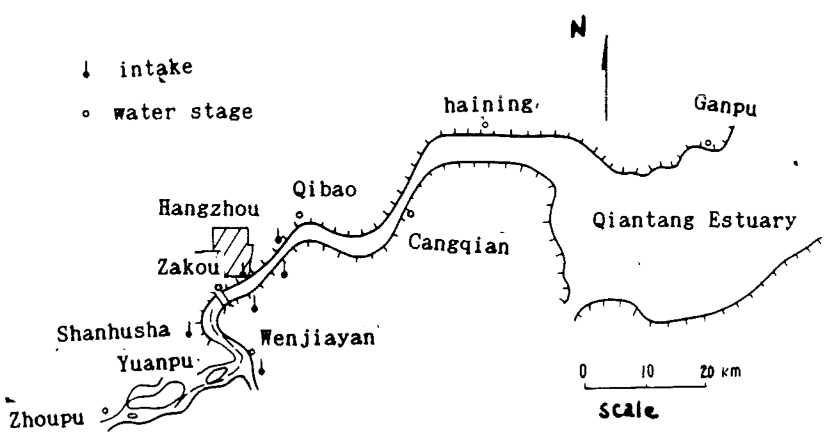

Fig.1 The location for water intake in Qiantang Estuary

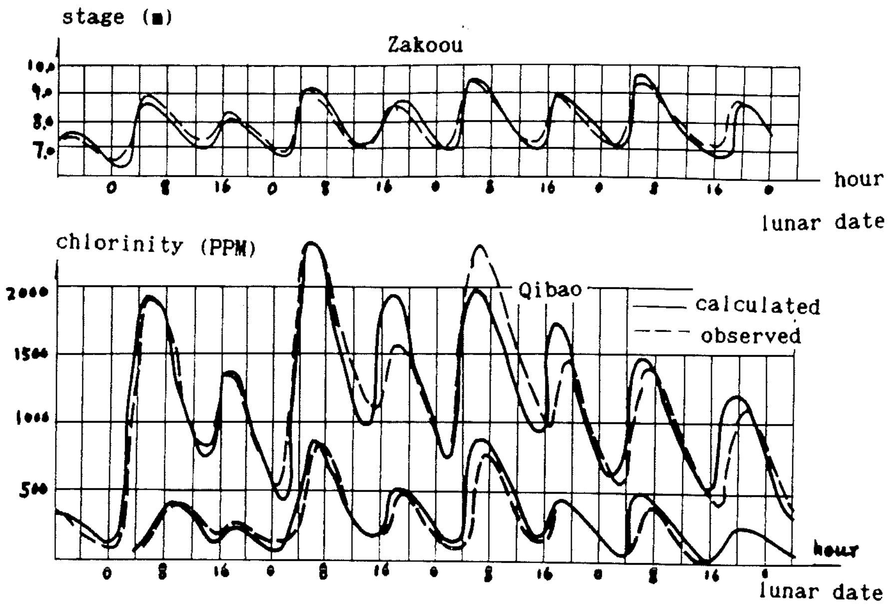

Fig.2 Verification of tide and chlorinity (JULY 29AUG.2,1988)

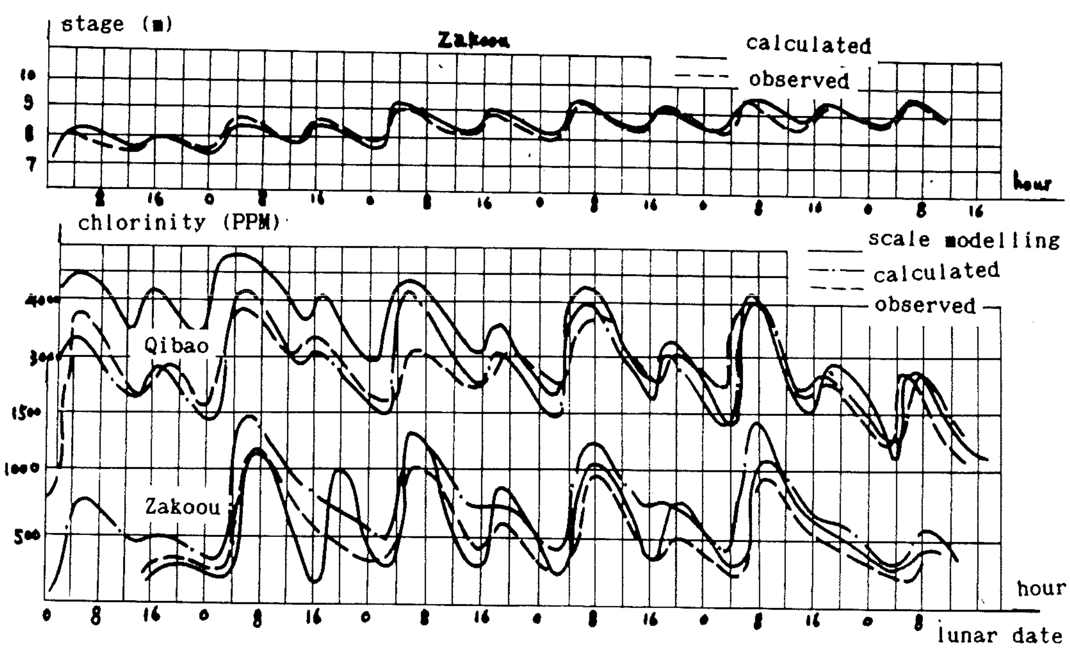

Fig.3 Verification of tide and chlorinity (Sept. 19～21,1978)

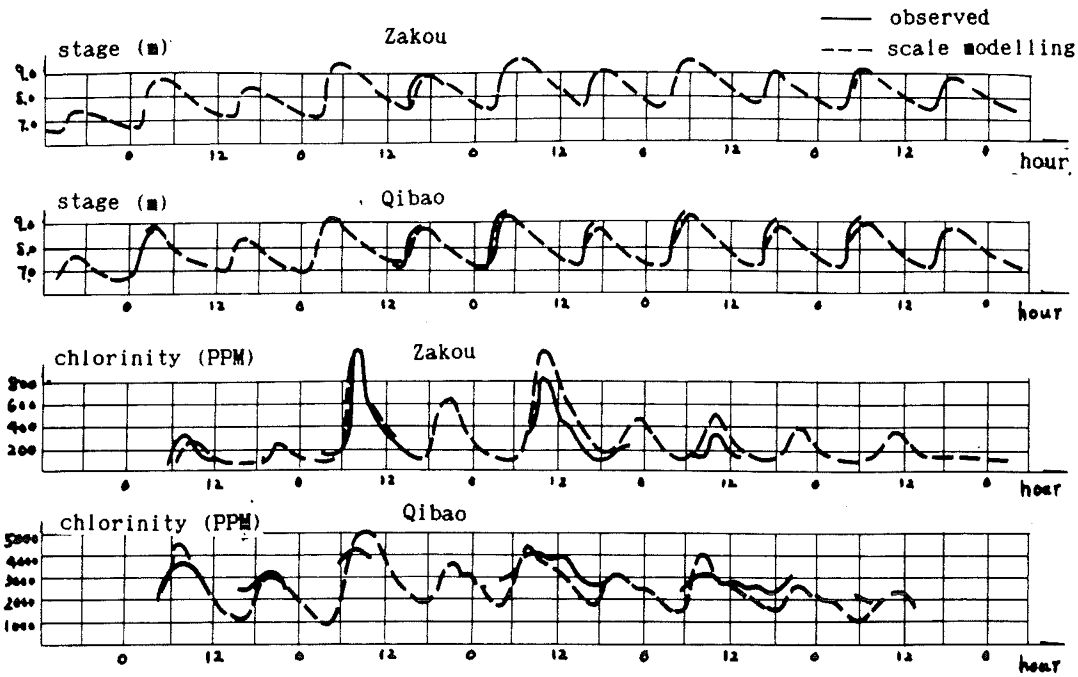

Fig.4 Verification of tide and chlorinity (July 19~24, 1978)

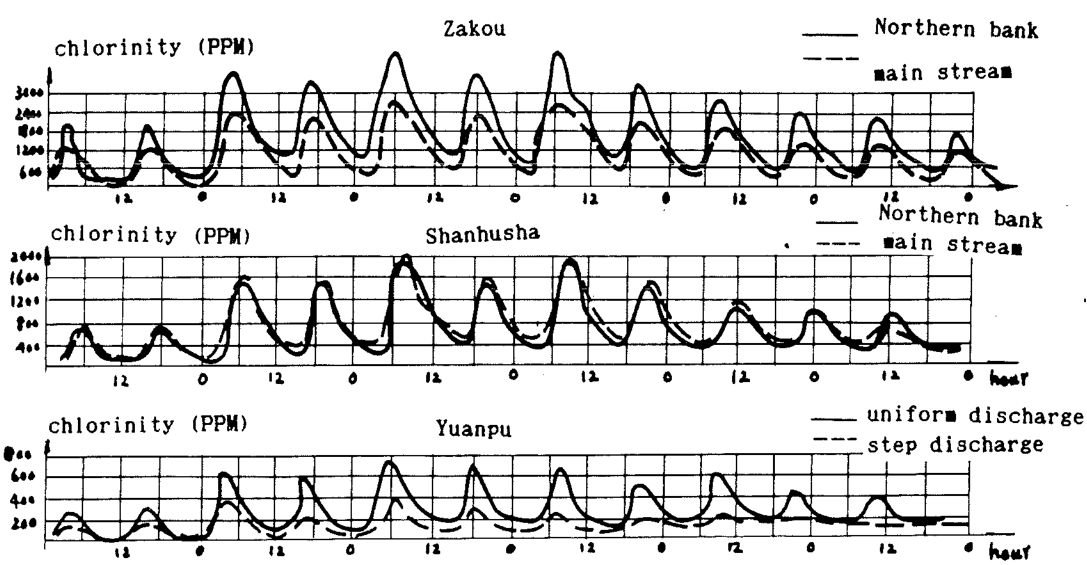

Fig.5 Chlorinity graphs at three sections (scale modelling)

Session 11A

Internal Waves and Jumps

Interaction of an Internal Soliton with a Slope

by Timothy W. Kao and Kamal Saffarinia
The Catholic University of America
Washington, DC 20064

Laboratory experiements were conducted on the interaction of an internal soliton with a sloping bottom. Two classes of experiments were conducted. In the first class the slope extended beyond the free surface. In the second, the slope ended in a submerged shelf. The soliton was generated on the pycnocline of a stratified fluid of total finite depth and propagated from deep water into shallower waters. The depth of the lower layer in the generation region was deeper than the upper layers. In the experiments of the second class the lower layer on the shelf was shallower than the depth of the upper layer. Thus, in both classes a reversal of the polarity of the wave was expected. Such a phenomenon was indeed observed. Viscous dissipation was found to play a crucial role in the dissipation of wave energy in addition to wave breaking.

To model the phenomenon, the full Navier-Stokes and diffusion equations were solved numerically. The effect of viscous dissipation is assessed and comparisons of the numerical and experimental results are made.

MIXING DRIVEN BY THE BREAKING OF INTERNAL WAVES AGAINST SLOPING BOUNDARIES

by G.N. Ivey and R.I. Nokes*
Centre for Water Research,University of Western Australia, Nedlands, Western Australia
* Theoretical and Applied Mechanics,University of Auckland,Auckland, New Zealand.

Abstract

We extend the work of Ivey and Nokes (1989) on mixing due to the breaking of critical internal waves on sloping boundaries by looking at the case of incident wave frequencies differing from the critical. We find the mixing efficiency decreases for both subcritical and supercritical waves compared to the peak mixing efficiencies around the critical frequency. The effect of bottom topography is examined and, while we observe strong mixing around the topography, the mean flow along the slope is disrupted and we see an overall decrease in the mixing efficiency. We show the mixing along the slope may be described by a simple eddy diffusion model.

Introduction

Since internal waves are both ubiquitous in nature and contain a considerable amount of energy they are of interest as a major source of energy for driving mixing in stratified water bodies such as lakes and the oceans. In the oceans, recent work (e.g. Garrett and Gilbert 1988) has drawn attention to the possibility of mixing associated with internal waves reflecting off sloping boundaries. An important aspect of this mixing mechanism is the specification of the efficiency of mixing associated with the interaction and breaking of an internal wave against a sloping boundary. This problem has been studied in a laboratory experiment by Ivey and Nokes (1989) (hereafter denoted by IN) for the case of critical waves ($\omega_c = N\sin\theta$ where ω is the frequency of the incident waves, θ is the angle the sloping bottom makes with the horizontal, and N is the buoyancy frequency) where the slope of the group velocity vector of the wave field was the same as the bottom slope. They found that the mixing efficiency varied from 0 to a maximum value of 0.20 and Ivey and Imberger (1990) argued this was due to variations in the turbulent Reynolds number.

When the frequency of the incident waves is less then the critical frequency (subcritical conditions) the waves are back reflected and, conversely, when the frequency is greater then the critical frequency (supercritical conditions) the waves are forward reflected from the sloping bottom.The results of IN were confined to the critical case, and the mixing efficiency over this full range of incident wave frequencies is addressed in the present work.

Laboratory Experiments

The experiments were conducted in the experimental facility described by IN. The tank consisted of three coupled sections: two 2 m long sections of glass connected by a 22 cm long central section fabricated from acrylic sheet in which a plane paddle wave maker was centrally mounted. At the far end of each of the glass sections acrylic sheets were installed at an angle of $\theta = 30^0$ to the horizontal to form a sloping bottom at one end and a sloping top at the other. The two sloping boundaries were thus installed parallel to one another to create a large parallelogram-shaped working section with the paddle in the middle of the tank (see figure 1) .

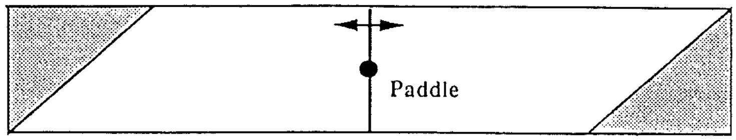

Figure 1 Schematic of laboratory experiment

An eccentric crank and driving arm mechanism was used to drive the paddle in a sinusoidal motion and the paddle amplitude was kept constant during a given run. The paddle was connected to the driving arm via a sensitive ± 0.5 N force transducer mounted so that it measured the applied force perpendicular to the paddle throughout its swing. A displacement transducer was also connected to the paddle and the two transducers logged at 3.5 Hz in a burst mode fashion about every 30 paddle cycles for about 10 cycles. The displacement signal was differentiated to obtain velocity and the work done by the paddle for each cycle W computed as

$$W = \int_0^{2\pi/\omega} Fvdt$$

where ω is the forcing frequency, F the applied force and v the paddle velocity.

As in IN, turbulence was confined to the bottom boundary layers along the slopes and the continual mixing in this region led to the establishment of a slow cavity-scale circulation which weakened the mean density gradient in the tank by differential vertical advection in the laminar interior (see IN for a detailed description) . The amount of mixing was measured by the changes in vertical profiles of density over the course of a run - usually about 100 wave cycles between profiles. For each profile, the potential energy per unit area was then computed as

$$P' = \int_0^H \rho gzdz.$$

and the total increase in potential energy per cycle P computed by dividing the increase in P' between two profiles by the number of cycles and multiplying by A ,the horizontal cross-sectional area of the tank. The accuracy of the measured steady state mixing rate as quantified by the potential energy gain per cycle P from this procedure was estimated as ±2%.

Of the total work or kinetic energy input by the paddle some was lost by viscous effects as the waves propagated from the paddle towards the sloping bottom. This viscous dissipation D was calculated by using the flap wave maker solution of Thorpe (1968) to describe the internal wave field, and then computing the losses due to internal and sidewall viscous effects (see IN).

Waves on Smooth Bottoms

Observations of the flow field

The flow field was visualized using a modified form of the rainbow schlieren technique (see IN for details). For the case of critical waves, a turbulent bottom boundary layer of uniform thickness developed along the sloping bottom and mixing was confined to this region. For subcritical waves, there was some evidence of weak mixing although it does not appear uniform along the slope. In the supercritical case, as the wave rays are inclined closer to the vertical than the bottom slope, forward reflection occurs and they tend to be trapped in the end regions of the tank. Mixing appeared to start preferentially in these corner regions until there was active mixing region along much of the bottom slope The region with active mixing was always adjacent to the bottom slope although, unlike the case for critical waves studied by IN, the turbulent region was not uniform in thickness along the slope but rather appeared to be preferentially distributed towards the end or apex regions of the tank.

Mixing efficiency

The overall mixing efficiency η_0 was defined as $\eta_0 = P/W$, where P was the gain in potential energy per wave cycle and W the work done per cycle by the paddle. With the total laminar viscous dissipation defined by D, the actual mixing efficiency due to turbulent mixing by internal waves breaking on the bottom slope was thus defined by $\eta = P/(W - D)$.

To determine the effects of variable wave frequency, a series of 7 runs was made with a fixed paddle amplitude of A=2.21 cm . The results for the mixing efficiency are shown in figure 2 where the data are plotted against the frequency of the incident wave ω normalized by the critical wave frequency $\omega_c = N\sin\theta = 0.5N$ for the 30^0 bottom slopes used in these experiments.

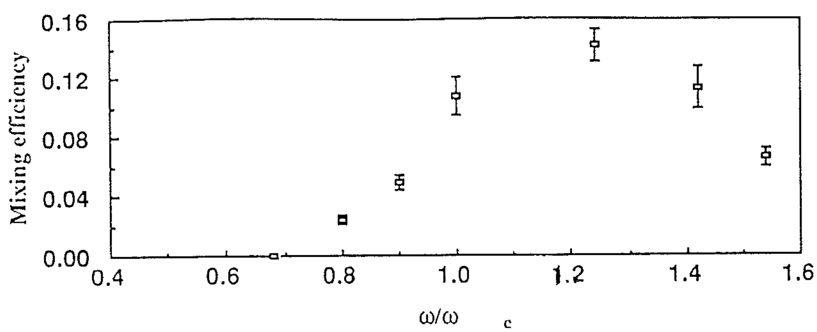

Figure 2. Mixing efficiency as a function of incident wave frequency normalized by the critical wave frequency $\omega_c = 0.5N$

For the sub-critical range where $\omega / \omega_c < 1$, figure 2 indicates a rapid decrease of mixing efficiency as the incident wave frequency decreases. Indeed, for $\omega / \omega_c < 0.7$, there was no measurable mixing in terms of an observable increase in potential energy. In this subcritical range, waves were being reflected backwards from the bottom slope and this rapid decrease in mixing efficiency was consistent with the schlieren flow visualization where there was little visual evidence of overturning structures or mixing in the flow field.

For the supercritical range where $\omega / \omega_c > 1$, figure 2 indicates an initial increase of mixing efficiency followed by a roll-off of the efficiency with further increases in wave frequency. For example, by $\omega / \omega_c = 1.6$, the efficiency had dropped to about one half its value at the critical frequency. It was not possible to extend the data range any higher as it appeared from visual evidence that the required high frequencies were starting to cause some local mixing at the paddle and runs were always aborted in such a case.

It must be remembered that the tank geometry had some influence on the measured mixing efficiencies in this supercritical range. In particular, in this frequency range all waves were forward reflected and thus trapped because of the finite size of the wedge-shaped regions at the ends of the tank. This lead to the preferential overturing and mixing which started in the corners of these wedge-shaped regions and ultimately appeared to 'cascade' down the bottom slope . While this trapping mechanism did operate, figure 2, nevertheless, indicated a decrease in mixing efficiency for increasingly supercritical waves. This decrease appeared to result from the reduction in shear parallel to the sloping bottom as the wave rays become increasingly inclined to the slope. The observed shear-driven mixing then occurred preferentially in the apex of the wedge region and not uniformly along the bottom, as in the critical case for example (see IN). Overall, the mixing became less efficient.

These observations suggest that if the bottom slope were infinite in extent, and thus no trapping of the forward reflected supercritical waves was possible, the mixing efficiency when compared to the critical conditions would tend to decrease for all supercritical waves. Thus, just as for the case of subcritical waves, a cut-off in mixing would occur for increasingly supercritical waves. This suggestion must remain speculative, however, since the configuration of our laboratory experiment does not allow us to test this hypothesis. Our experiment does clearly show, however, that even with the trapping wedge present the mixing efficiency does decrease for increasingly supercritical waves.

Effect of Bottom Topography

In the field one expects to find variations in the bottom topography and certainly field observations (e.g. Imberger 1985, Wolanski 1987) indicate that this can be an important feature of mixing at the boundaries. We chose to look at the simplest possible topographic feature: a single structure whose scale height was of the order of the turbulent boundary layer thickness as measured on a smooth slope. In particular, we installed a semi-cylinder, with radius 5 cm and length 20 cm with the flat face flush with the bottom slope and at mid-height on the sloping bottom boundary. The cylinders were made of wood and turned to produce a smooth surface before mounting with the long axis of the cylinder across the tank and flush with the glass sidewalls.

For these runs, attention was confined to the case of critical waves and observations showed both a complex wave field as the incident wave is reflected off the topographic feature and localized mixing in the vicinity of the cylinder. Indeed mixing was predominantly around the feature with little mixing elsewhere on the slope, even for the critical case, and tended to produce a collapse of mixed fluid into the interior preferentially around the location of the topographic feature.

In figure 3 we show the mixing efficiencies for two runs. For comparison, we also

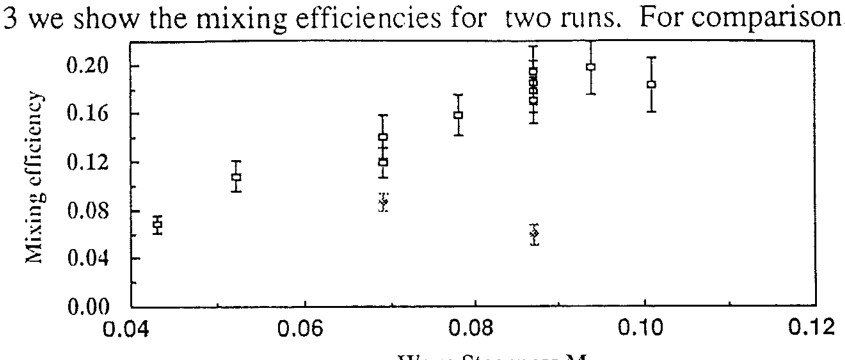

Figure 3. Mixing efficiency for runs with the cylindrical topographic feature ( ) compared with mixing efficiencies measured for smooth bottoms (.

show in figure 3 the measured mixing efficiencies for the case of a smooth slope without any topographic features from IN. It is apparent that the effect of the topographic feature was to reduce the overall mixing efficiency - contrary to intuitive expectation. The likely explanation for this effect, as suggested by the observations , was that while the topographic feature (with a ratio of object height to bottom slope length of 1 to 14.4) locally enhanced the mixing, it did so at the expense of mixing along the remainder of the slope. In particular, it disrupted the strong along-boundary oscillatory flow which drove the mixing . The disruption of mixing due to the weakening of this latter mechanism lead to the overall reduction in the mixing efficiency in the tank.

Eddy Diffusivities

A convenient way of characterizing the mixing is in terms of eddy diffusivities. While the mixing was confined to the sloping boundary regions, from observations of the rate of change of the density profile, one can define an effective eddy diffusivity for the basin or tank K_B (see Ivey 1987a) by:

$$K_B\left(\frac{\rho_o}{g}N^2\right) = \frac{d}{dt}\int_{z_o}^{H}\rho dz$$

where the reference height of z_o is taken as the $z_o = H/2$. Ivey (1987a) argued that the eddy diffusivity in the turbulent boundary layer K in the direction perpendicular to the slope was given by

$$K = K_B\left(\frac{L}{\delta}\right)\frac{\sin\theta}{\cos^2\theta}$$

where L was the container horizontal length, δ the turbulent boundary layer thickness measured perpendicular to the boundary, and θ the bottom slope.

The diffusivity K is a true turbulent diffusivity and is representative of the mixing in turbulent boundary layers for time scales long compared to the wave period. For critical waves incident on a smooth boundary where $\omega = 0.5N$ for all cases, simple dimensional reasoning indicates that, since there are no other scales present, $K = \beta\omega\zeta^2$ where ζ is wave amplitude. This hypothesis is tested in figure 4 where the eddy diffusivity K is computed for the critical runs on the smooth slope listed in Table 1 of IN.

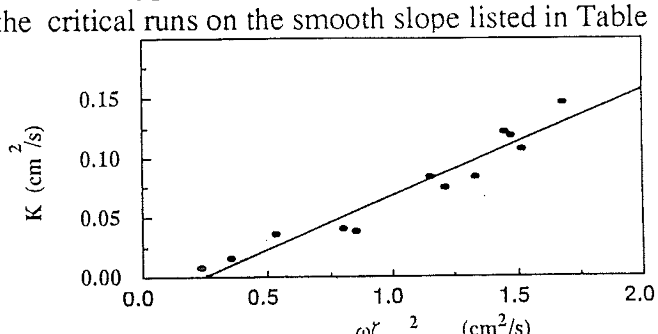

Figure 4.Eddy diffusivities in the bottom boundary layer for critical waves on smooth slopes as a function of $\omega\zeta^2$, where ω and ζ are wave frequency and amplitude, respectively. The best fit straight line shown is $K = -0.021 + 0.089\ \omega\zeta^2$ ($r^2 = 0.96$).

Figure 4 indicates a good fit with $K \approx 0.09\ \omega\zeta^2$ over the range of data. The diffusivity K is actually computed from the differences in the density profiles from the beginning to the end of each run. Additional profiles were taken during each run, and computing K from each consecutive data pair indicates that K in figure 4 is probably accurate to ±30%. It is instructive to compare the prediction derived from figure 4 with deep ocean estimates. For the Garrett-Munk spectrum, the r.m.s. wave displacement is $\zeta = 7.3(N/N_0)^{-1/2}$ m (Munk 1981), where the reference buoyancy frequency $N_0 = 5.2 \times 10^{-3}\ rs^{-1}$. By way of example, let us take $N = 10^{-3}\ rs^{-1}$ and $\omega = f = 7.3 \times 10^{-5} s^{-1}$ at 30° latitude, then the implied diffusivity from the least squares fit in figure 4 is $K = 2 \times 10^{-3}\ m^2 s^{-1}$. While hardly definitive proof that internal waves are driving the mixing at the boundaries, such a range of near-bottom diffusivities is plausible when compared with the field data summarized by Ivey (1987b), for example.

Conclusions

Flow visualization indicated that there was little mixing for subcritical waves. On the other hand, mixing was observed for supercritical waves and this was initiated in the top corners of the laboratory facility. Ultimately this produced a mixing region with a tendency for decreasing thickness with distance from the apex of the wedge-shaped regions.

Measurements of mixing efficiency were consistent with the observations of the flow field. As the incident wave frequency was reduced below the critical frequency, so too the mixing efficiency rapidly decreased. For weakly supercritical waves, the mixing efficiency increased slightly and we argued this resulted from the trapping of waves in the finite size shoaling regions at the end of the laboratory tank. For strongly supercritical waves, however, the mixing efficiency again decreased compared to mixing at critical conditions.

The effect of bottom topography was studied by placing a single semi-circular obstacle along the bottom slope. While this enhanced the mixing in the vicinity of the obstacle, it disrupted the strong shearing motion and the associated mixing along the remainder of the slope. The overall effect was a net reduction in mixing efficiency.

The turbulent eddy diffusivity parameterizing mixing in the bottom boundary layer is given by $K \approx 0.09\ \omega\zeta^2$.

References

Garrett, C. and Gilbert, D. 1988 Proceeds. 19th Int. Colloq. Ocean Hydrodynamics, Nihoul, J.J. (ed), Elsevier, 405-424..

Imberger,J. 1985 *Hydrobiologia.* **125**, 7–29.

Ivey, G.N. 1987a *J. Fluid Mech.* **183**, 25–44.

Ivey, G.N. 1987b *J. Geophys. Res.*, 92, 11873–11878.

Ivey, G.N. and Nokes, R.I. 1989 *J. Fluid Mech.* **204**, 25–44.

Ivey, G.N. and Imberger, J. 1990 *J. Phys. Oceanogr.*, submitted.

Thorpe, S.A. 1968 *Proceeds. Roy. Soc. A* **263**, 563–614.

Wolanski,E. 1987. *Limnol. and Oceanogr.* **32**, 735–739.

Environmental dynamics reference ED 429 GI

Structure of flow in internal hydraulic jumps

by N. Rajaratnam[1] and G.A. Johnston[2]

ABSTRACT

This paper presents the results of an experimental study on the characteristics of mean flow in internal jumps in the lower layer in a two layer stratified flow with the upper layer essentially at rest. The velocity profiles in the jump have been found to be approximately similar with the variation of the velocity and length scales being roughly the same as that of the open channel jumps. Some observations have also been made on the nature of the flow downstream of the internal jump.

Introduction

Let us consider a two-layer stratified flow in a rectangular channel of constant width in which a lower layer with a density of ρ_0 flows under a lighter fluid of density of ρ_a which is essentially at rest. Let U_0 and b_0 be respectively the velocity and depth of the lower stream as it leaves the gate (see Fig. 1(a)). If the densimetric Froude number F_0 of this stream, defined as $F_0 = U_0/\sqrt{g\frac{\Delta\rho_0}{\rho_0}b_0}$ where g is the acceleration due to gravity and $\Delta\rho_0 = (\rho_0 - \rho_a)$, is greater than unity, for a particular depth b_2 of the lower layer further downstream, an internal hydraulic jump would form at the gate. This internal jump has been studied theoretically by Yih and Guha (1955), Hayakawa (1970) and others. Neglecting any entrainment of the ambient fluid and the shear stresses at the interface as well as at the bed of the channel, the sequent depth ratio b_2/b_0 is given by the Belanger-type equation. The recent experiments of Rajaratnam and Powley (1990) have shown that experimental observations agree reasonably well with this equation for F_0 up to about 10. It has also been found (Wilkinson & Wood (1971), Rajaratnam & Subramanyan (1986), and Rajaratnam & Powley (1990)) that in the (intersurface) roller region of the jump, there is hardly any entrainment of the ambient fluid into the jump. However, at the toe of the jump, due to the oscillating nature of the toe, there is some entrappment and eventual entrainment of the ambient fluid into the jump.

Even though several investigators have studied the global characteristics of internal jumps, apart from some preliminary observations by Wilkinson and Wood (1971), very little appears to be known regarding their internal flow characteristics. Hence an experimental study was undertaken in the summer of 1986 and the results are presented in this paper.

Experimental Arrangement and Experiments

The lower layer internal jumps were formed in a rectangular channel of (constant) width of 0.31 m, depth of 0.5 m and length of 5.5 m. A false bottom of thickness of 0.13 m was installed, as shown in Fig. 1(b) inside this flume. Cold water from an overhead tank entered the flume from a reservoir under a gate with a convergent lip and formed the supercritical stream. Hot water from the laboratory

1 Professor, 2. Grad. Student, Dept. of Civil Engrg., Univ. of Alberta, Edmonton, Alberta, Canada

boiler formed the upper layer of the ambient fluid. Hot water and cold water were removed at adjustable rates at the downstream end of the flume. In any given experiment, by proper control of the hot water supply and cold water withdrawal, steady-state conditions could be maintained for several hours.

The gate opening b_0 was set precisely to required values by means of metal bars. The cold water flow rate was measured by means of calibrated rotameters. Time averaged velocities (u) in the longitudinal direction (x) were obtained from the time-lines of hydrogen bubbles generated from eight wires installed in the central part of the flume, immediately downstream of the gate, as shown in Fig. 1(c). For the range of velocities involved in this work, the hydrogen bubble technique was found to be suitable. In the jump region, due to the turbulence, it was sometimes difficult to locate precisely the bubble lines in the photographs whereas in the region downstream of the jumps, it was relatively easy to locate the bubble lines. At each wire, at least two pictures were taken and each velocity u was obtained as an average of four values. Temperature profiles were obtained near each wire with a Fluke digital thermometer. The interface between the two layers was also measured photographically.

Five experiments were performed with the densimetric Froude number at the gate equal to 1.32, 3.26, 4.44, 6.48 and 8.51. The gate opening was given values of 25 mm for the first experiment and 6 mm for the rest. The jumps were formed such that the toe was located just at the gate.

Experimental Results - Jump Region

Let us consider first the velocity profiles u(y) in the jump region where y is the height above the bed, for several values of x, the longitudinal distance from the gate. For each experiment, only a few wires happened to be located in the jump (roller) region with the rest located in the downstream region. The velocity profiles for the jump region, with x less than L_{rj} the length of the surface roller are shown together in a dimensionless form in Fig. 2(a) where u/u_m is plotted against y/b. In Fig. 2(a) u_m is the maximum value of u at any section and b is the length scale, equal to the value of y where $u = 1/2\, u_m$ and $\partial u/\partial y < 0$. It is interesting to see that the several profiles for the different jumps fall together. However, this similarity profile is somewhat different from that of a plane wall jet. For the plane wall jet, at $u/u_m = 1.0$, $y \simeq 0.16$ b; the corresponding value for an open channel jump is about 0.2b whereas for the internal jump, the corresponding $y \simeq 0.6$ b. Further, in the region of reverse flow (or surface roller), the maximum values of u are about 0.2 times u_m.

Considering the behaviour of the length and velocity scales, Fig. 2(b) and 2(c) show the variation of b/b_0 and u_m/U_0 with x/b_0 along with the corresponding curves for the open channel jump (Rajaratnam, 1967). Fig. 2(b) and 2(c) indicate that the results for the internal jump appear to follow the same trend but are somewhat different.

Characteristics of the Downstream Region

In the region downstream of the end of the surface roller of the internal jump, the turbulent flow in the jump degenerates to what appears to be laminar stratified flow. Photographic observations of the interface between the lower and upper layers indicated laminar motion at the interface. Further, the hydrogen bubble lines indicated that for x much larger than L_{rj}, the flow in the lower layer appeared to be laminar.

For the lower layer, Fig. 3(a) shows a typical set of velocity profiles for several values of x larger than L_{rj}, in a dimensionless form. In Fig. 3(a), the velocity scale u_m is the maximum value of u at any x and the length scale d is the value of y where $u = u_m$. It was found that for all the experiments, the velocity profiles at all sections were approximately similar, but were somewhat asymmetrical. The thickness of the lower layer with forward velocity is approximately equal to 2.5d.

The behaviour of the velocity and length scales is shown in Fig. 3(b) and Fig. 3(c). In Fig. 3(b), u_m/U_0 decreases continuously with x/b_0 but each experiment has a separate curve. In Fig. 3(c), the relative length scale d/b_0 increases continuously with x/b_0 with each experiment having a separate end value.

Conclusions

The velocity profiles in the internal jump are approximately similar but are somewhat different from those of the plane turbulent wall jet and the open channel hydraulic jump. The behaviour of the length as well as velocity scales is approximately the same as that of the open channel jump.

In the region downstream of the jump, the stratified lower layer appears to become laminar. In this region, the velocity profiles are similar. Observations have been made on the growth of the length scale and decay of the velocity scale.

References

1. Hayakawa, N. (1970). Internal hydraulic jump in co-current stratified flow, Proc. ASCE, J. of Eng. Mech. Div., Vol. 96, pp. 797-800.
2. Rajaratnam, N. (1967). Hydraulic Jumps in Adv. in HydroScience, Ed. by V.T. Chow, Vol. 4, pp. 197-280.
3. Rajaratnam, N. and Subramanyan (1986). Plane turbulent denser wall jets and jumps, J. of Hydraulic Res., IAHR, Vol. 24, pp. 281-296.
4. Rajaratnam, N. and Powley, R. (1990). Hydraulic jumps in two-layer flows, Proc. Instn. of Civil Engrs., London (in press).
5. Wilkinson, D. and Wood, I.R. (1971). A rapidly varied flow phenomenon in a two-layer flow, J. Fluid. Mech., Vol 47, pp. 241-256.
6. Yih, C.S. and Guha, C.R. (1955). Hydraulic jump in a fluid system of two layers, Tellus, Vol. 7, pp. 358 - 366.

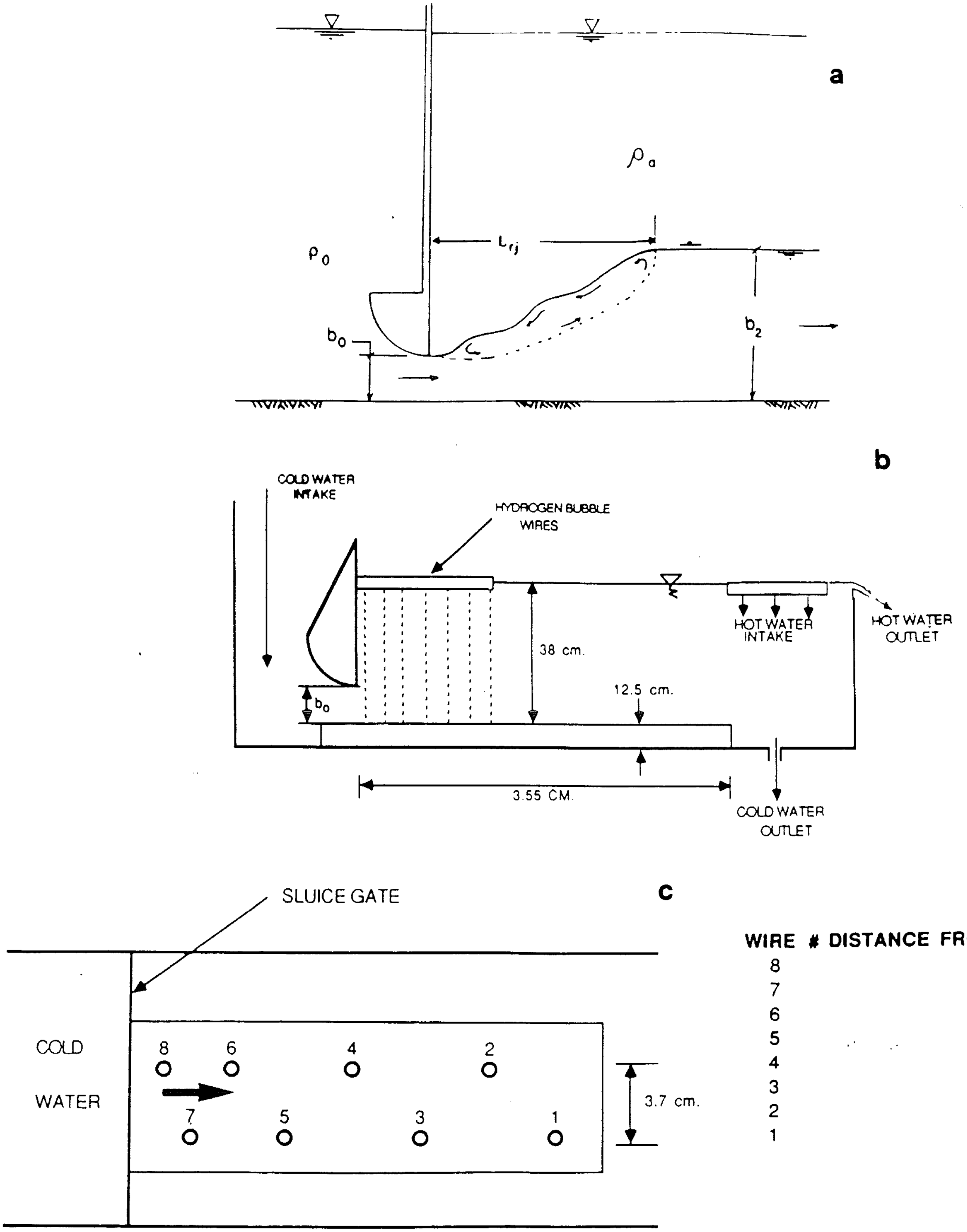

WIRE #	DISTANCE FROM GATE (CM)
8	2.5
7	10
6	20
5	40
4	60
3	80
2	100
1	120

Fig. 1 (a-c) Definition sketch of internal jump and experimental arrangement

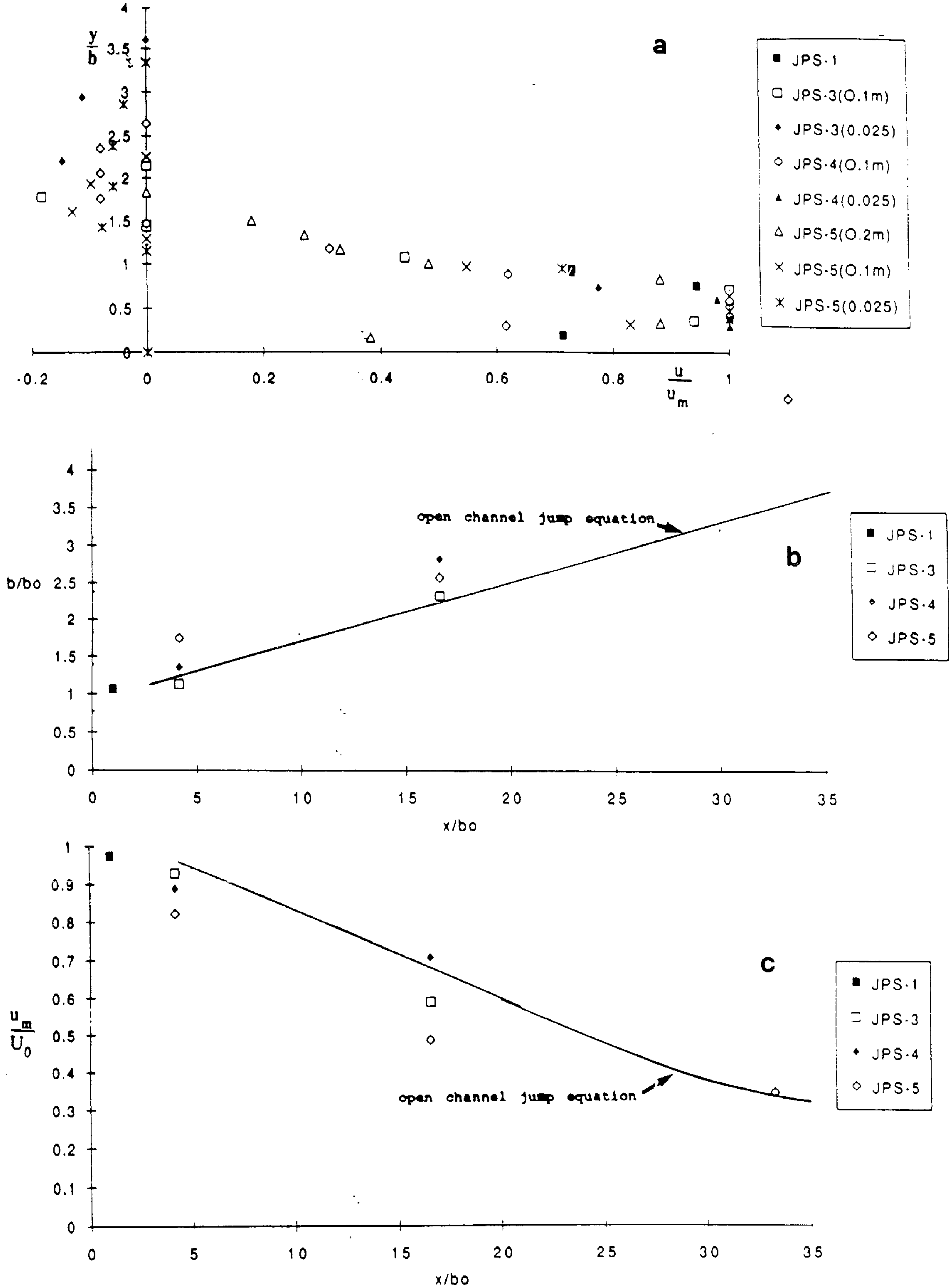

Fig. 2 (a-c) Velocity profile, length and velocity scales for internal jumps.

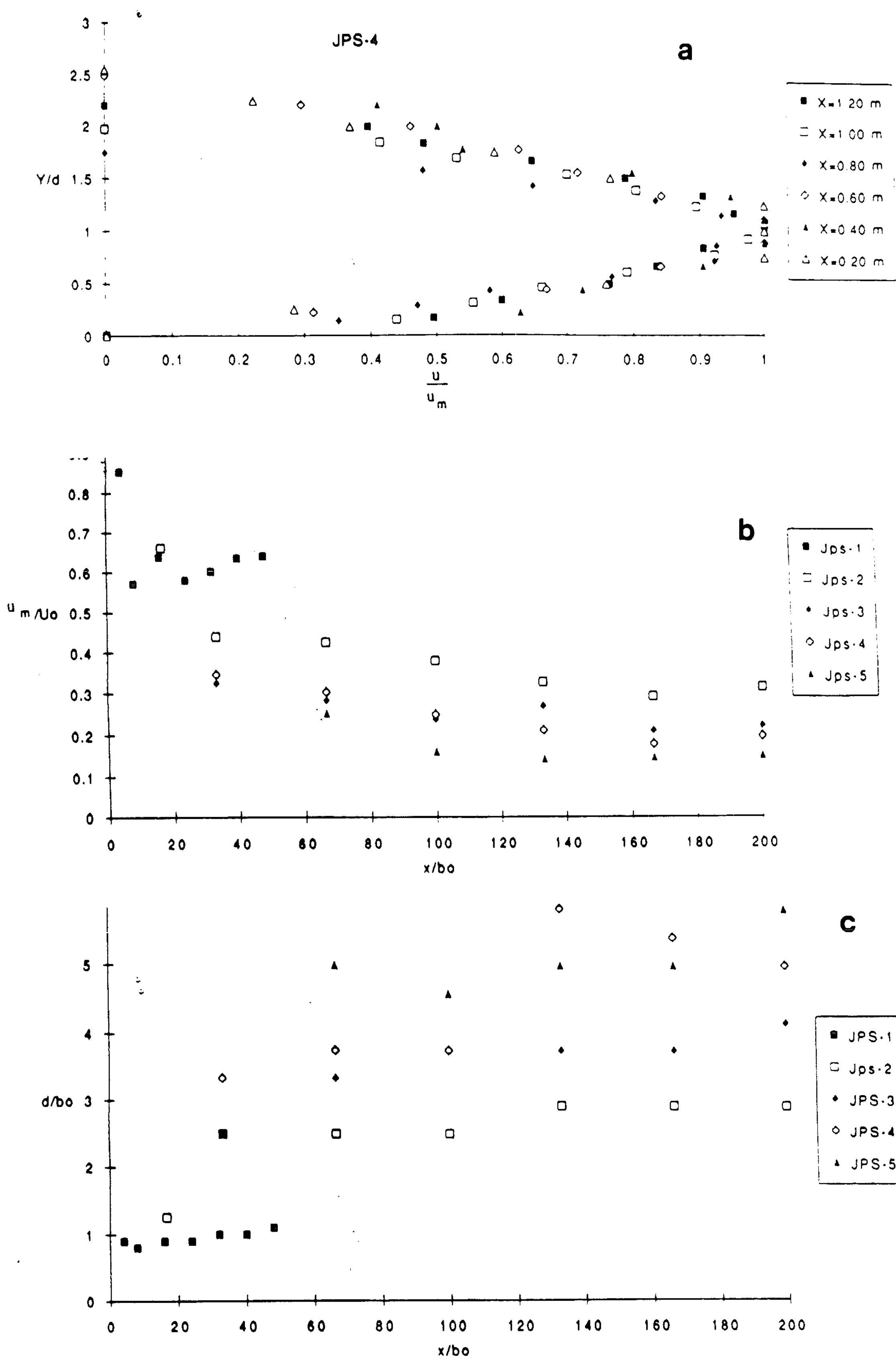

Fig. 3 (a-c) Velocity profile, velocity and length scales for the downstream region

THERMAL HYDRAULIC JUMPS:
Two-Dimensional Experiments

By Raouf E. Baddour and Lu-Li Guo

Department of Civil Engineering
The University of Western Ontario
London, Ontario, Canada

Abstract

Thermally-stratified internal jumps in a fresh water ambient are studied experimentally. The study is based on intensive measurements of temperature fluctuations in summer and winter flows. The results are compared with the thermal jump theory of Baddour (1989).

Introduction

This study differentiates thermal jumps from density jumps. The term density jump introduced by Wilkinson and Wood (1971) is adopted to define a jump when the density field is dependent on the concentration of a dissolved substance (e.g. salt). A thermal jump, on the other hand, is thermally-stratified , and the density field is entirely temperature dependent. Thermal and density jumps are similar but not identical. The difference stems from the nature of the relation between the buoyancy and the physical quantity causing it. In a density jump the buoyancy is a linear function of concentration, and in a thermal jump the buoyancy is a nonlinear function of temperature.

Since temperature differences in most water applications are relatively small (Typically 10-15°C), studies of thermal flows have generally ignored the nonlinearity of the buoyancy-temperature relationship. This assumption has not been scrutinized. And, as will be shown, a linear approximation of the buoyancy function could lead to errors when thermal jumps are modelled numerically or physically as density jumps. One of the objectives of this study is to quantify the error of modelling thermal jumps as density jumps.

Density and thermal jumps

Consider a surface discharge of warm water in a deep channel as illustrated in Fig.1. The inflow rate is q_0, depth y_0 and excess temperature above the ambient temperature T_w is θ_0. The internal jump may be analyzed in a manner similar to a jump in a single layer open channel flow. Accounting for miscible behaviour and entrainment of ambient, the density jump theory gives [Wilkinson and Wood (1971)]:

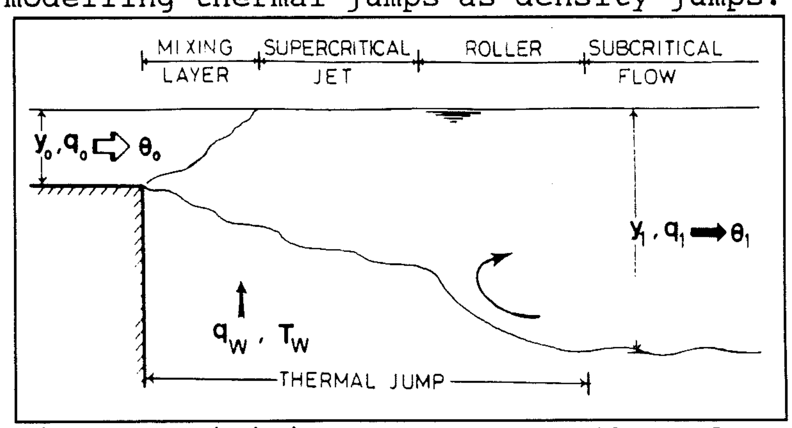

Fig.1 Definition sketch of a thermal jump

$$r_1 = \frac{y_1}{y_0} = f(F_0, S)$$

where r_1 is the conjugate depth ratio, $S = q_1/q_0$ is the dilution, and $\mathbf{F}_0 = [q_0^2 / (g_0' y_0^3)]^{1/2}$ is the inflow densimetric Froude number. The buoyancy $g_0' = g(\rho_w - \rho_0)/\rho_w$, and ρ_w and ρ_0 are, respectively, the density of the ambient and the discharge.

On the other hand, the thermal jump theory gives [Baddour(1989)]:

$$r_1 = \frac{y_1}{y_0} = f(F_0, S, T_w, \theta_0)$$

More specifically a thermal jump was found to be governed by:

$$\frac{1}{2} + F_0^2 = \frac{1}{2} r^2 \left[\frac{\sum_{i=1}^{n} (b_i \theta_0^i / S)}{\sum_{i=1}^{n} (b_i \theta_0^i)} \right] + F_0^2 \frac{S^2}{r}$$

where b_i [i=1,n] are functions of T_w. When the buoyancy function is approximated with a straight line, only the first term is retained in each of the summations on the right hand side of this equation. Hence, the linear approximation gives :

$$\frac{1}{2} + F_0^2 = \frac{1}{2} \frac{r^2}{S} + F_0^2 \frac{S^2}{r}$$

which is the equation governing the miscible behaviour of a density jump in a deep ambient. In the present experiments the dilution was controlled and is hence treated as an independent variable. In practice, the dilution is determined by incorporating the downstream control into the analysis [see Wilkinson and Wood (1971) and Baddour 1987) for more details on the hydraulics of this problem in deep and shallow channels].

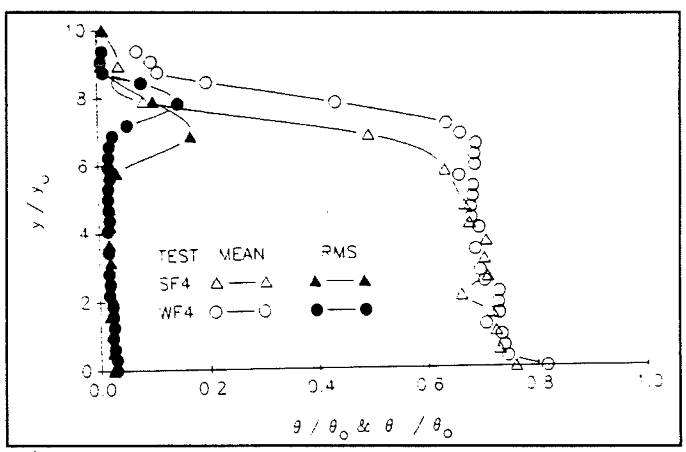

Fig.2 Mean and rms temperature profiles downstream of jump.

The temperature and velocity profiles, downstream of the jump, were assumed to be uniform in shape. Fig. 2 is presented in support of this assumption. In order to compare the experimental results with the theory, the depth y_1 downstream of the jump must be estimated. This depth was considered to be $y_{0.10}$ (i.e. the depth where $\theta = 0.10\ \theta_0$). This depth corresponded well to the average position of the interface as seen through a shadowgraph.

Thermal jump experiments

The experiments were conducted in a channel 2.5m long, 0.15m wide, and 0.5m deep. The channel has double walls to minimize heat exchange with the surrounding. A cooling system controlled the temperature of the ambient water and a mixing valve the temperature of the discharge. The temperature of the ambient could be lowered to a temperature close to the freezing point. The steady supply of warm and cold water to the channel were monitored with flowmeters and adjusted to produce the desired test condition. The temperature was measured with an array of 15 thermocouples. The diameter of the thermocouples was 0.12mm and the frequency response was 100 Hz. The data was collected with a computerized data acquisition system. The system was programmed to scan the output from the 15 probes simultaneously at a frequency of 10Hz per probe over a period of 100s. The test conditions are summarized in the following table.

TEST	T_0 [°C]	T_w [°C]	**S**	F_0	Re_0
SF4	31	16	1.5	5	4,000
SF6	31	16	1.5	5	6,000
SF8	31	16	1.5	5	8,000
SF10	31	16	1.5	5	10,000
WF4	19	4	1.5	5	4,000
S4	31	16	2.0	5	4,000
S6	31	16	2.0	5	6,000
S8	31	16	2.0	5	8,000
S10	31	16	2.0	5	10,000
W4	19	4	2.0	5	4,000

Table 1. Summary of test conditions

Results

The results of tests S4 and W4 are presented in Figs 3 and 4. The iso-mean and iso-intensity contours were obtained from a grid of about 15x15 data points. Tests S4 and W4 have the same Froude number, Reynolds number , dilution , and excess temperature. The remarkable difference between the results of these two tests can be attributed to the nonlinearity of the buoyancy function. Note the ambient temperature of Test S4 is 16°C, while the ambient temperature of test W4 is only 4°C.

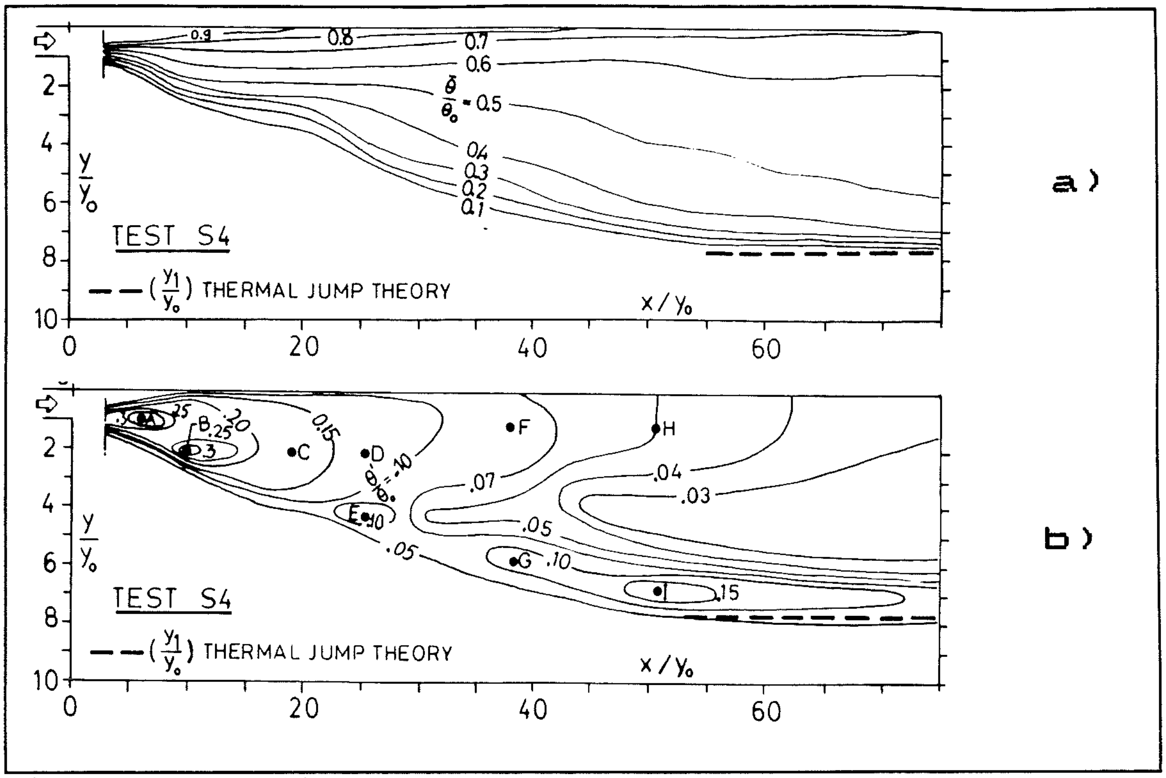

Fig.3 Thermal jump S4 : a) mean b) rms

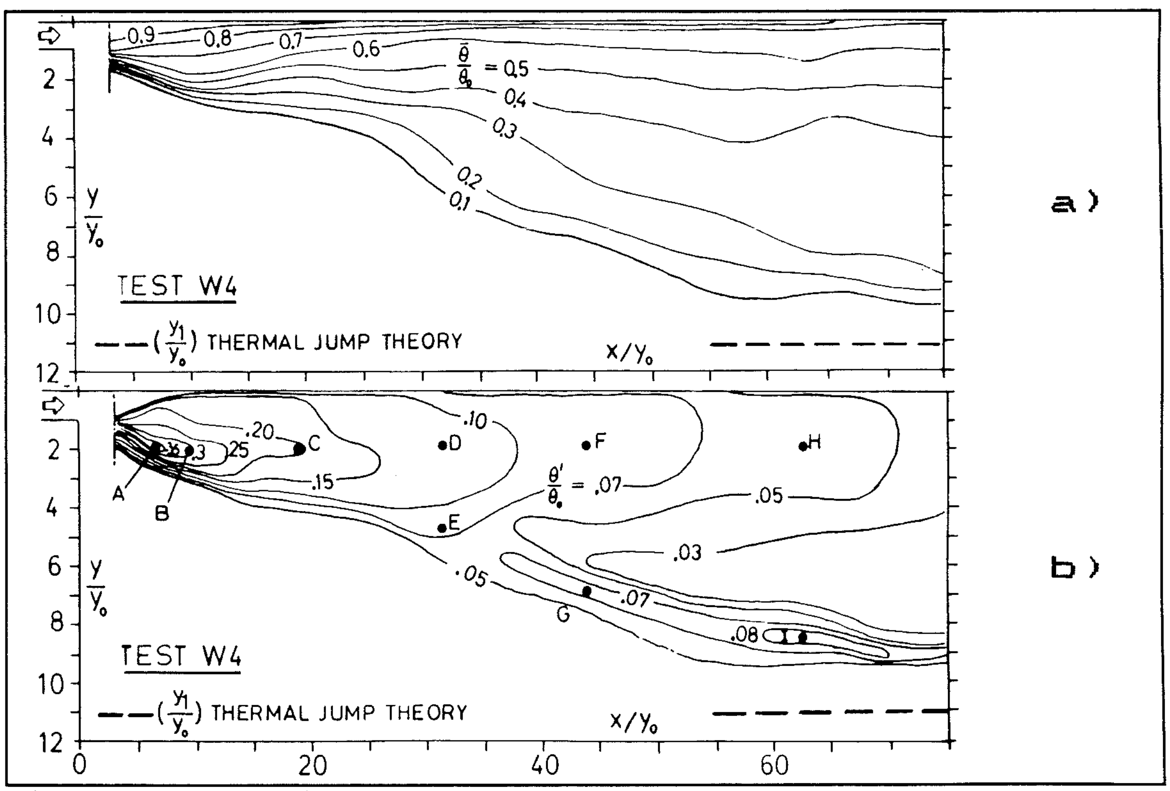

Fig.4 Thermal jump W4 : a) mean b) rms

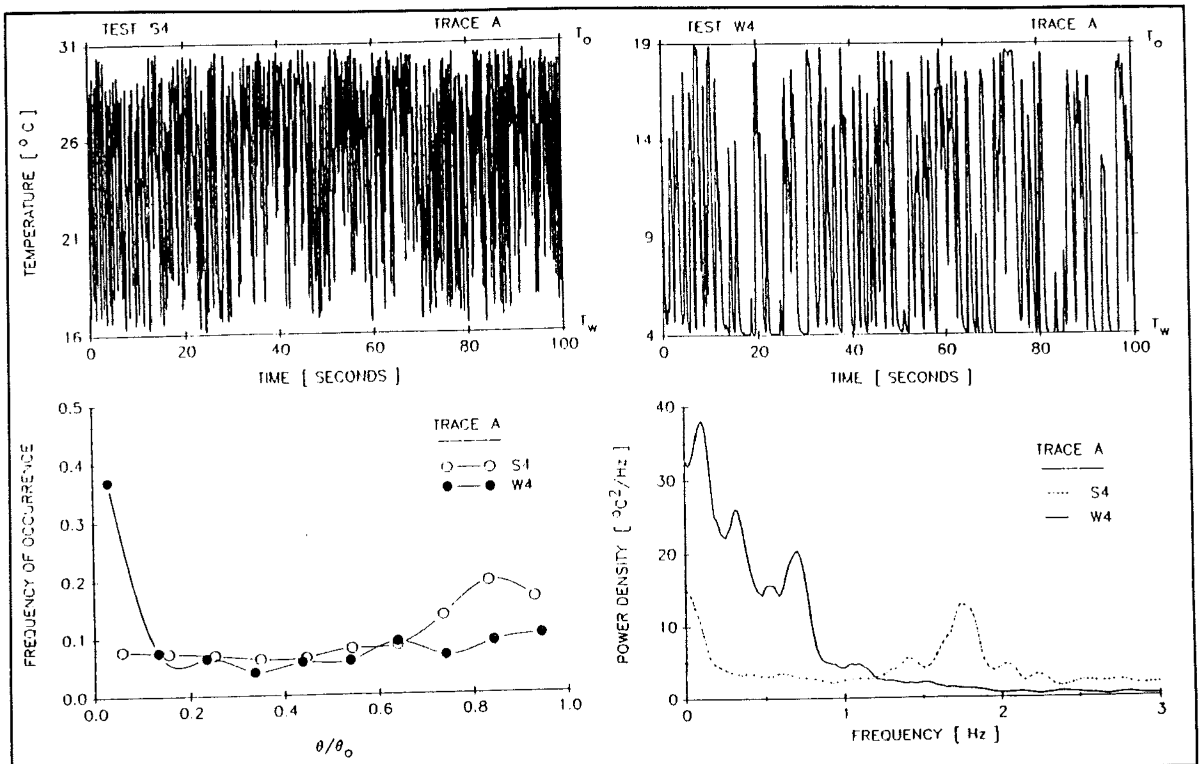

Fig. 5 Analysis of temperature fluctuations at A

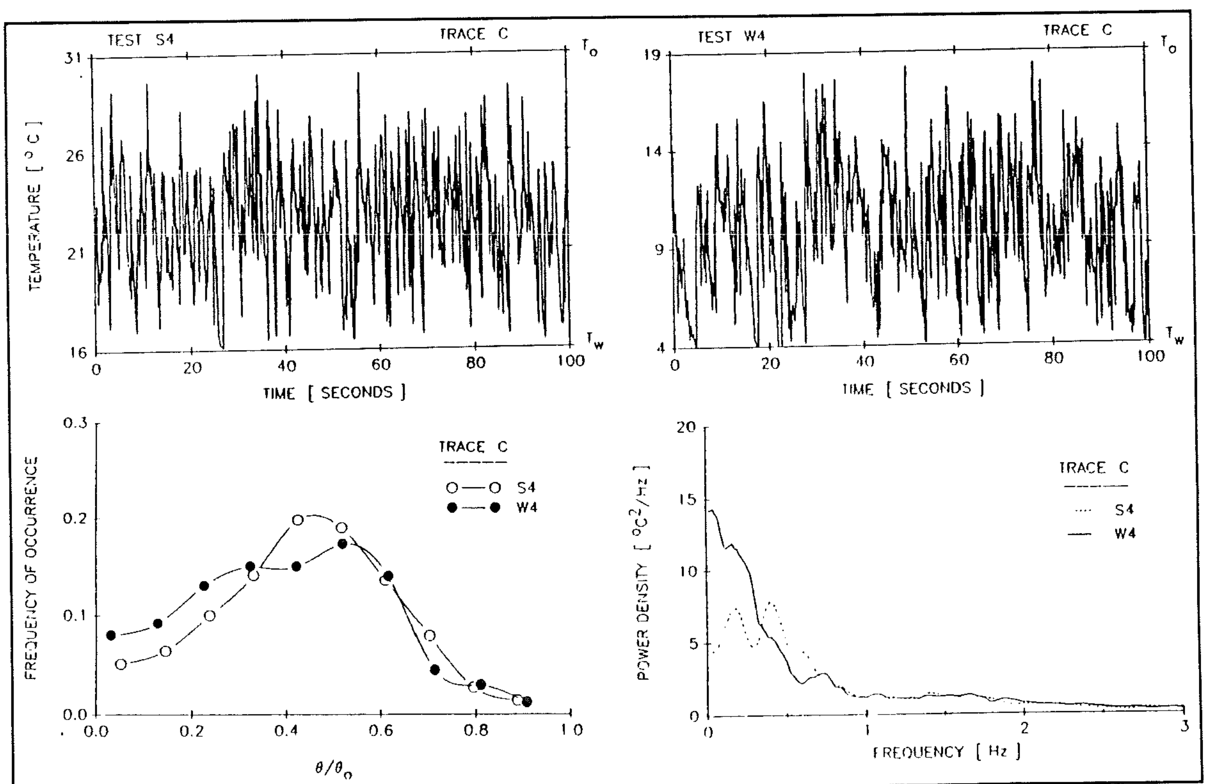

Fig. 6 Analysis of temperature fluctuations at C

The temperature fluctuations at two strategic locations shown in Figs 3 and 4 are analyzed in Figs 5 and 6. This analysis reveals differences in the structure of temperature fluctuation in summer and winter flows. The summer flow is more stable than the winter flow (for the same $\mathbf{F_0}$, $\mathbf{Re_0}$, and θ_0). The summer flow displays initially a dominant frequency at about 2 Hz. At the same location, the winter flow exhibits a number of dominant lower frequencies. It is possible to see that the winter flow is also less effective than the summer flow in mixing the discharge with ambient. This can be noted from temperature traces and histograms. The histogram of signal C of test S4 is essentially Gaussian while signal C of test W4 has a double peak. The double peak distribution is linked to the unmixed nature of the flow, and is caused by a lack of small scale eddies.

The experimental data are compared with the thermal jump theory in Fig. 7. Since the tests shown have the same Froude number , Reynolds number, and excess temperature, the results point to the fact that, as predicted by the theory, the ambient temperature has an important effect on the flow.

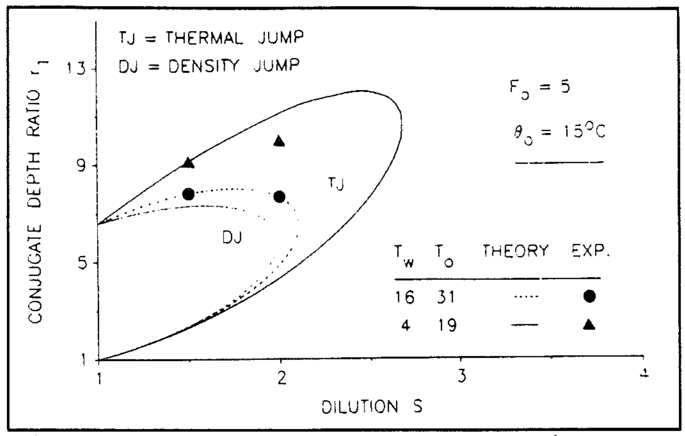

Fig.7 Comparison of theory with experiments

Conclusion

In addition to the Froude number, the modelling of thermal jumps requires some consideration to be given of the ambient temperature and the temperature difference. These two additional parameters are connected to the non-linearity of the buoyancy function. Ignoring their effects may lead to significant modelling error. The error was found to increase with Froude number and temperature difference, and decrease with ambient temperature.

References

-Baddour R.E. (1989). "Thermal hydraulic jumps". Under review, J. of Fluid Mechanics.

-Baddour R.E. (1987). " Hydraulics of shallow and stratified mixing channel". J. of Hydraulic Engineering, ASCE, vol.113, 630-645.

-Wilkinson, D.L. and Wood, I.R. (1971). " A rapidly varied flow phenomenon in a two-layer flow". J. of Fluid mechanics, vol.47, 241-256.

Acknowledgements

The authors are grateful to H. Farghaly for his help with the apparatus and data acquisition system. The study is sponsored by the Natural Sciences and Engineering Research Council of Canada.

MIXING IN DENSITY-STRATIFIED CONJUGATE FLOWS

by

Marco Rasi, E. John List, Greg Sullivan & Regina Dugan
California Institute of Technology
Pasadena, California 91125

ABSTRACT

Conjugate two-layer stratified shear flows have been studied in the laboratory using combined laser-induced fluorescence and laser-Doppler velocimetry. Use of this high-resolution, non-intrusive instrumentation has enabled a new evaluation of the internal hydraulic jump, the entrainment associated with it, and the role of upstream and downstream controls in determining the flow structure.

INTRODUCTION

Internal hydraulic jumps are encountered in many flow systems of interest to engineers and environmental scientists. Such jumps occurring in nature have been observed in Föhn winds, katabatic flows, and fjords (Schweitzer, 1953; Ball, 1959; Lied, 1964; Clarke et al, 1981; Farmer and Denton, 1985). In an engineering context, they can occur in discharge channels where the density of the effluent differs from the ambient fluid density, and it is usually the mixing within the channel that is of primary concern.

We consider a dense fluid discharged at a steady rate at the bottom of the upstream end of a rectangular mixing channel, as in Figure 1 (a). The channel is horizontal and connected to a receiving body containing a finite depth of water with a uniform lower density. The rate of outflow from the channel of this denser lower layer is controlled at the downstream end by either a free overfall or a broad-crested weir. The discharged and ambient fluids are miscible and their relative density difference is small (less than 2%).

The complexity of such internal flows has induced many previous investigators to assume that each layer of the flow has a uniform velocity and density distribution (*e.g.*, Baddour, 1987) and introduce a one-dimensional "hydraulic" theory. The studies reported here evaluate this approach and provide a definitive statement of the role of the upstream and downstream flow controls.

PRELIMINARY OBSERVATIONS

Laboratory observations have shown that there are four substantially different configurations that can occur in a density-stratified channel flow. They are illustrated in Figures 1(a), 1(b), 1(c) and 1(d).

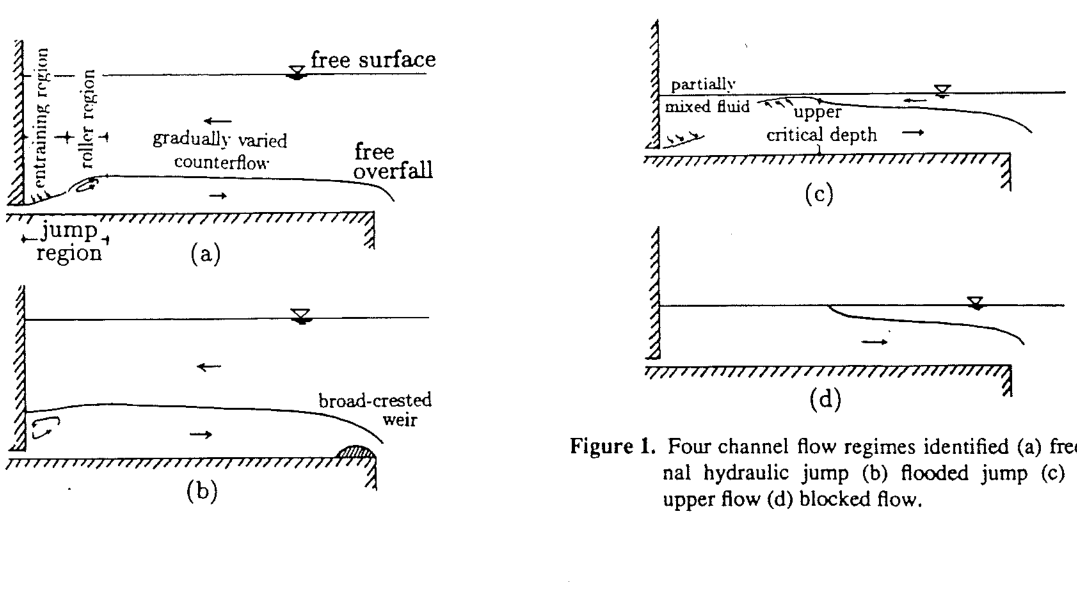

Figure 1. Four channel flow regimes identified (a) free internal hydraulic jump (b) flooded jump (c) critical upper flow (d) blocked flow.

The most obvious and usual flow field is depicted in Figure 1(a), in which the dense lower fluid is supplied at a rate that induces a jet-like flow in the lower layer immediately downstream of the source. A second flow control, provided at a downstream overfall, forces an internal hydraulic jump transition between upstream and downstream flows.

When the downstream control is raised in elevation, the configuration in Figure 1(b) is established in which the jump advances upstream and floods the jet. These two flows are analogous open channel flows, except that here entrainment occurs from the upper fluid layer into the lower.

A third situation, as depicted in Figure 1(c), occurs when the depth of the upper layer is reduced to the point that the jet entrainment creates sufficient flow velocity within the upper layer that a flow control is estabilished in the upper layer. A fourth condition, Figure 1(d), occurs when the lower flow blocks the upper flow and an intrusive wedge is created in the layer of upper fluid, a configuration frequently seen in estuaries.

ANALYSIS AND EQUATIONS OF MOTION

When a layer of dense fluid flows beneath a less dense fluid and both layers are sufficiently shallow for fluid velocities to be approximately uniform over the depth of each layer, it can be shown (Schijf and Schönfeld, 1953; Armi, 1986) that critical flow occurs when

$$F_1^2 + F_2^2 = 1 \tag{1}$$

where $F_1 = u_1/\sqrt{g'h_1}$ and $F_2 = u_2/\sqrt{g'h_2}$ are the densimetric Froude numbers of the two layers. h_1 and h_2 are the depths of the two layers, u_1 and u_2 are their velocities and $g' = g(\rho_1 - \rho_2)/\rho_2$, with ρ_1 and ρ_2 being the respective densities of the lower and upper fluids.

Now consider the flow depicted in Figure 2. By taking due account of the stagnation point rise in surface elevation at section 0, and applying mass and momentum conservation principles at sections 0 and 1, a dimensionless flow force conservation equation is obtained (Rasi, 1989).

$$2SF_0^2\left[\frac{S^2}{r_1} + \left(\frac{S-1}{H-r_1}\right)^2\left(\frac{H}{2} - 1\right) - 1\right] = S - r_1^2 \tag{2}$$

where $r_1 = h_1/h_0$, is the depth ratio after the jump; $S = q_1/q_0$, is the dilution after the jump; $H = d/h_0$, is the dimensionless ambient water depth; $F_0 = q_0/\sqrt{g'_0 h_0^3}$, is the discharge densimetric Froude number.

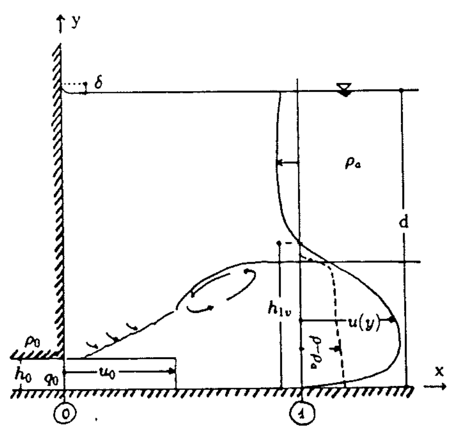

Figure 2. Upstream problem definition sketch.

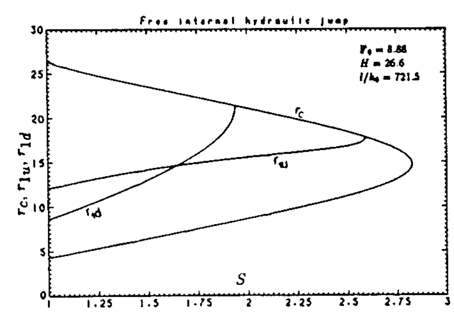

Figure 3. Solving for a free internal jump in the (S,r_1) plane.

Downstream of the jump, a critical flow occurring at a free overfall downstream imposes condition (1) which becomes

$$SF_0^2[\frac{S^2}{r_c^3} + \frac{(S-1)^2}{(H-r_c)^3}] = 1 \tag{3}$$

where $r_c = h_c/h_0$ is the lower layer critical depth ratio.

The gradually varied sub-critical flow between the jump and the critical control section can be shown to satisfy the equation (Rasi,1989)

$$\frac{dr}{d\xi} = \frac{SF_0^2\left[(f_b + \frac{2r}{B}f_{wl})\frac{S^2}{r^3} + f_i(\frac{S}{r} + \frac{S-1}{H-r})^2(\frac{1}{r} + \frac{1}{H-r}) + \frac{2f_{wu}}{B}(\frac{S-1}{H-r})^2\right]}{8\left[1 - SF_0^2(\frac{S^2}{r^3} + \frac{(S-1)^2}{(H-r)^3})\right]} \tag{4}$$

where $r = h(x)/h_0$ is the dimensionless lower layer depth; $\xi = x/h_0$ is the dimensionless distance from the downstream control; $B = b/h_0$ is the dimensionless channel width.

In the derivation of Eq.(4), turbulent boundary friction is represented by a Darcy-Weisbach formulation where f_b, f_i, f_{wl}, and f_{wu}, are the friction factors at the channel bottom, fluid interface, and lower and upper layer channel walls respectively. It is recognized that f_i is simply an empirical representation of the vertical momentum transfer mechanisms and energy dissipation at the interface, including that by both waves and entrainment. The values of S and r_1 must satisfy the obvious physical constraints $0 \le r_1 \le H$ and $S \ge 1$ together with

$$SF_0^2\left[\frac{S^2}{r_1^3} + \frac{(S-1)^2}{(H-r_1)^3}\right] \le 1 \quad \text{and} \quad SF_0^2\left[\frac{S^2}{r_1} + (\frac{S-1}{H-r_1})^2\right] \le 2(1-r_1) + F_0^2 \qquad \text{(5a and 5b)}$$

which state respectively that the flow downstream of the jump must be sub-critical (Harleman, 1960), and that the specific energy cannot increase across the jump (Baddour and Abbink, 1983).

For any specified value of S, Eq.(2) can be solved for r_1 if H and F_0 are fixed. Only one real root satisfies constraint (5b). Note that if S = 1 then Eq.(2) reduces to $r_1 = \frac{1}{2}(\sqrt{1+8F_0^2} - 1)$ the result for immiscible jumps given by Yih and Guha (1955). Baddour and Abbink (1983) show that for $H \rightarrow \infty$ there is a maximum dilution achievable, which is

$$S_m = \frac{2}{3}F_0^{2/3}\left[1 + 1/2F_0^2\right] \tag{6}$$

The gradually varied flow Eq. (4) can be integrated upstream of the downstream control, if values of S and F_0 are assumed along with friction factors. The integration begins at $\xi = 0$ where $r = r_c$, and r_c is determined from Eq.(3). The general solution is then obtained by finding the location where the r_1 value determined from the upstream equation matches that found by integrating the downstream equation upstream. The solution technique is shown in Figure 3 for specified values of the initial jet Froude number F = 8.88, dimensionless overall depth H = 26.6, and a defined location of the downstream control.

The curve labeled r_c is the solution of Eq. (3); that labeled r_{1u} is the solution for r_1 obtained from the conservation of flow force Eq.(2). The curve labeled r_{1d} is the value of r_1 at the jump location determined by integrating Eq.(4) using the prescribed initial condition. The solution values of S and r_1 are defined by the intersection of these two curves.

It is possible that a common intersection point will not always exist for the two r_{1u} and r_{1d} curves. This will occur when either the r_{1u} curve is lowered by reducing F_0, or the r_{1d} curve is raised by either moving the downstream control further downstream, or by raising the sill elevation with a weir. In either case, the internal jump becomes flooded (see Figure 1(b)).

Another possibility occurs if F_0 is increased to produce the opposite effect, in which case the r_{1u} expected from flow force conservation is always higher than the r_{1d} expected from the downstream gradually-varied flow integration. When this occurs another critical point is created immediately downstream of the jump. This corresponds to Figure 1(c).

Finally, when F_0 is so large that the entire depth of the two layer flow d is occupied by source fluid, then the dilution S = 1 and the condition in Figure 1(d) results. r_c is specified and the profile is integrated until it meets the free surface. This can occur if the downstream control is sufficiently far from the source.

EXPERIMENTAL ANALYSIS AND METHODS

A stratified flow was constructed in the laboratory as shown in Figure 4. Horizontal velocities were measured using a laser-Doppler velocimeter system and a density-stratified flow that was optically homogeneous, as described in Hannoun and List (1988). Vertical density profiles were obtained with a laser-induced fluorescence system for concentration measurement that profiles an instantaneous record of dye concentration along the length of a directed laser beam (Papanicolaou and List, 1988; Papantoniou and List, 1989). Typical velocity and density profiles in the flow established with this equipment are shown in Figures 5 and 6 respectively.

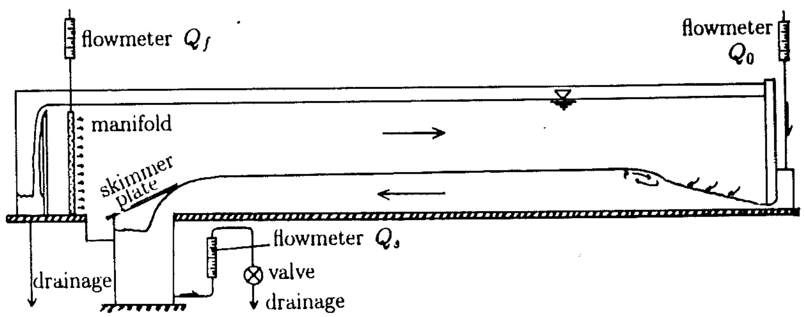

Figure 4. Laboratory set up for internal flow experiments.

A system developed to establish the dilution of the discharged flow involved constructing a flow skimming device at the downstream control as shown in Figure 4. Coloring the bottom layer of fluid with an intense blue dye, made it possible to set the skimmer such that no blue fluid passed over the skimmer or no clear fluid passed below it. The rate of accumulation of flow below the skimmer provided exceptionally reproducible measurements of the dilution S.

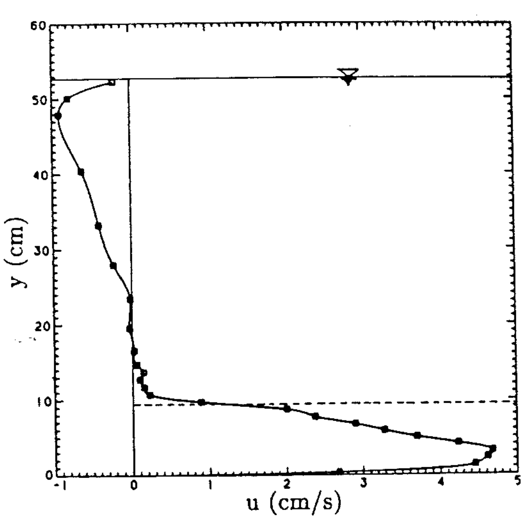

Figure 5. Typical velocity profile in a subcritical flow region

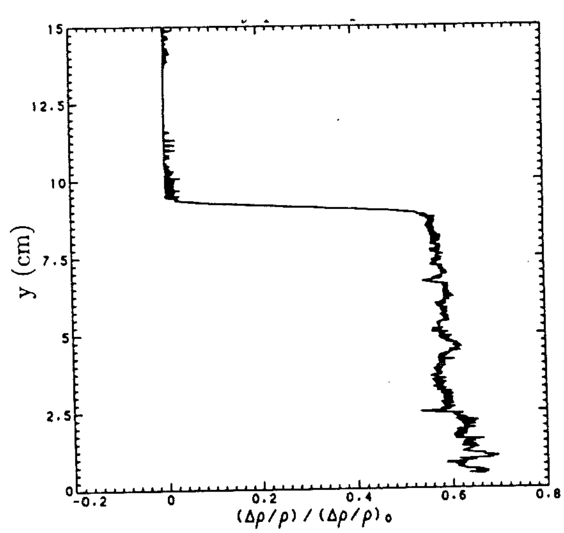

Figure 6. Typical density profile in a subcritical flow region

RESULTS

The experimentally measured dilutions are presented in Figure 7 as functions of the densimetric Froude number. A comparison is also made with the predicted dilution as obtained by the previously discussed theory. It can be seen that the comparison between theory and prediction becomes less agreeable as the water depth and Froude number increase. This is believed to result from the fact that as F_0 and H increase, the intersection point of the r_{1u} and r_{1d} curves is very sensitive to the location of either curve (see Figure 3). Possible sources of error that would result in the movement of either of these curves include the assumption of uniformity in the profiles of density and velocity, and a lack of information about the length of the jump zone.

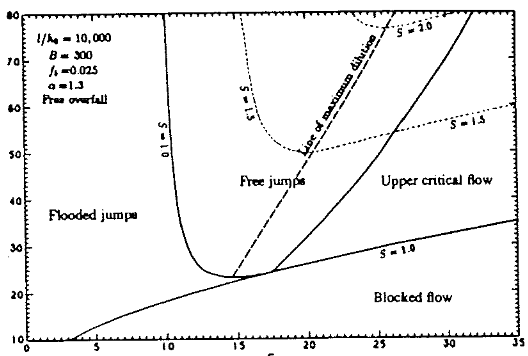

Figure 8. Mixing mode domains for far downstream control.

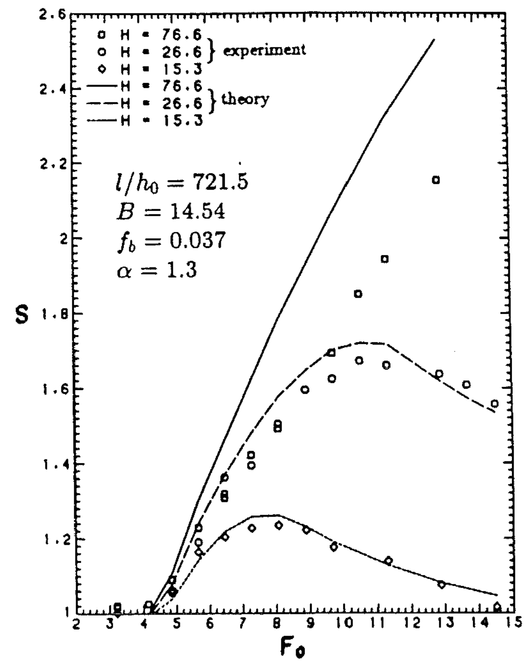

Figure 7. Measured and predicted dilutions.

DISCUSSION AND CONCLUSIONS

An interesting result is that the dilutions predicted on the basis of gross mean flow properties and those measured experimentally are in good agreement (Figure 7). This is somewhat surprising since these dilutions are very dependent on the level of entrainment that occurs, and yet no entrainment assumptions are considered in the analysis. In addition to predicting the dilution over a reasonably wide range of densimetric Froude number, the analysis also indicates a significant dependency of this entrainment on the water depth (see Figure 7).

The prediction that there is a maximum dilution that will occur for any given Froude number and water depth is closely followed. The departure from the prediction surprisingly occurs as the water depth becomes large, which one would imagine would be the simpler flow to predict. These predictions are in no way dependent on a consideration of the turbulence properties of the discharge jet, and yet, clearly, the entrainment and limiting dilution must depend indirectly on the collapse of the turbulence in the jet as the local Richardson number approaches the limiting value. The entrainment actually occurs upstream of the jump and not in the roller region that forms the jump; there is very little entrainment within the jump.

One interpretation of the flow is therefore the following. The initial flow, as it leaves the source, behaves as a two dimensional wall jet that entrains the ambient fluid in the usual way. However, since the entrainment both increases the depth of flow and decreases the local mean velocity, the local densimetric Froude number will decrease with distance downstream. Equivalently, the local bulk Richardson number increases. This reduces the entrainment from that which would occur if the flow were a pure wall jet.

The densimetric Froude number continues to reduce with increasing distance downstream as a consequence of the entrainment until it attains a value that is conjugate to the downstream Froude number that is developed from integrating back from the critical depth at the free overfall. The dilution and maximum depth of the denser flow are therefore determined by the distance downstream to the control. The further downstream this control is located the deeper is the subcritical conjugate flow and the lower the downstream Froude number. This in turn requires that the conjugate upstream Froude number be larger and consequently the jump must move upstream. At the point when the depth downstream of the jump reaches a value specified by $h_1 = (h_0/2)(\sqrt{1 + 8F_0^2} - 1)$ the jump floods the source, since the conjugate upstream depth is deeper than any possible jet flow. Alternatively, should the upstream densimetric Froude number decrease to the point where the conjugate depth is lower than the depth prescribed by the downstream control, then the jump will flood the source. In the situation when the total water depth is limited, two possible different conditions can occur when either the source jet Froude number is increased to the point that the entrainment demand makes the upper flow layer critical, or the water profile integrated from downstream intersects the water surface.

All of these modes of operation can be defined on a dimensionless water depth H versus Froude number F_0 plot for a specific downstream control location, as shown for a "long" channel in Figure 8.

ACKNOWLEDGEMENT

The authors gratefully acknowledge the support of the U. S. Geological Survey and National Science Foundations, who supported this work through Grant Awards 14- 08-0001-G1628 and MSM-881 19584 respectively.

REFERENCES

[1] Armi, L. 1986 The hydraulics of two flowing layers with different densities. *J. Fluid Mechanics*, **163**, 27-58.

[2] Baddour, R.E. 1987 Hydraulics of shallow and stratified mixing channel. *J. Hyd. Eng.*, **113**(5), 630-635.

[3] Baddour, R.E. and Abbink, H. 1983 Turbulent underflow in a short channel of limited depth. *J. Hyd. Eng.*, **109**(5), 722-740.

[4] Ball, F.K. 1959 *Antarctic Meteorology* Pergamon, London.

[5] Clarke, R.H., Smith, R. and Reid, D.G. 1981 The morning glory of the Gulf of Carpinteria. *Mon. Weather Rev.*, **108**, 1726-1750.

[6] Farmer, D.M. and Denton, R.A. 1985 Hydraulic control of flow over the sill in Observatory Inlet. (submitted to *J. Geophys. Res.*)

[7] Hannoun, I.A. and List, E.J. 1988 Turbulent mixing at a shear-free density interface. *J. Fluid Mech.*, **189**,211-234.

[8] Harleman, D.R.F. 1960 Stratified Flow. *Handbook of Fluid Dynamics* V.L. Streeter, ed., Sect. 26, McGraw-Hill, New York.

[9] Lied, N.T. 1964 Stationary hydraulic jumps in a katabatic flow near Davis, Antarctica, 1961. *Aust. Met. Magazine.*, **47**.

[10] Papanicolaou, P.N. and List, E.J. 1988 Investigations of round vertical turbulent buoyant jets. *J. Fluid Mech.*, **195**, 341-391.

[11] Papantoniou, D. and List, E.J. 1989 Large scale structure in the far field of buoyant jets, *J. Fluid Mech.*, (in press).

[12] Schijf, J.B. and Schönfeld, J.C. 1953 Theoretical considerations on the motion of fresh and salt water. *Proc. Minn. Int. Hydr. Conv.*, IAHR & ASCE, 321-333.

[13] Schweitzer, H. 1953 Attempts to explain the Föhn. *Archiv. Meteorologie, Geophisic, Hisclimatologie*, Series A, **5**(3),350.

[14] Yih, C.S. and Guha, C.R. 1955 Hydraulic jump in a fluid system of two layers. *Tellus*, **7**, 358-366.

The Effects of Downstream Conditions on Mixing in Buoyant Surface Jets

Steven J. Wright
The University of Michigan
Ann Arbor, MI 48109

Abstract

A theory of internal hydraulic jumps may be used to estimate the total near field entrainment in a buoyant surface discharge, but requires the specification of a downstream control relation. Most model experiments are performed in a transient mode as the density current front associated with the initiation of the experiment propagates away from the source in a finite tank. After reviewing the relevant theory, the results of an experimental investigation in which various downstream controls were studied, including this transient situation, are presented.

Introduction

Most laboratory investigations of buoyant jets are conducted in a transient mode in which it is assumed that the jet flow is steady once the initial density front has propagated some distance away from the source region and until the effect of the laboratory system boundary is felt. Since the flow is actually unsteady, it is relevant to question this laboratory idealization of a steady discharge in a field application. Jet mixing models generally originate from an application of the boundary layer equations and cannot account for downstream influences, nor do they generally account for the influence of limited depth of receiving fluid. In order to investigate these influences, a theory of internal hydraulic jumps must be applied. Since the distinction between a buoyant surface jet and an internal hydraulic jump is only semantical, both the far field influence and the effect of limited total fluid depth may be assessed.

Analysis

Although there have been a variety of analyses directed towards the description of immiscible internal jumps, the work of Wilkinson and Wood (1971) was apparently the first to consider the possibility of mass exchange between the two layers. The original work was applied to the case of a deep receiving fluid, but has since been extended to consider the effect of limited depth (Baddour and Abbink, 1983 and others). In order to develop the analysis, the case of a dense bottom discharge as indicated in Fig. 1 is considered since that corresponds to the experiments discussed below. Surface buoyant and dense bottom discharges are equivalent if 1.) nonuniformities of velocity and density profiles are ignored and 2.) the Boussinesq approximation of small density differences is made. Both assumptions are employed herein for purposes of clarity in the analysis. Subscript 1 refers to conditions in the lower layer, subscript 2 to the upper layer, ρ_0 is a reference density, in this study the density in the upper layer; $\Delta\rho$ is the density excess above ρ_0 within the dense layer ; and $g' = g\,\Delta\rho/\rho_0$ is a reduced gravity.

The analysis applied by Wilkinson and Wood assumes that the energy in the upper layer remains constant across the jump. This implies a deviation Δ in the free surface elevation which is given by $\Delta = u_2^2/(2g) = q_2^2/(2gh_2^2)$. The momentum balance applied over the total flow is

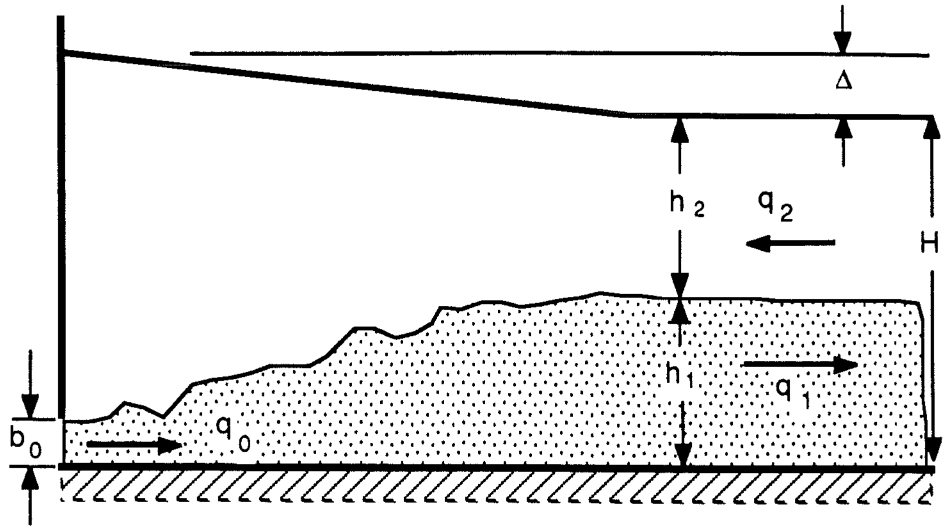

Fig. 1. Definition Sketch for Internal Hydraulic Jump.

$$2\pi r \int_0^H g' u \, dy = B \tag{16}$$

$$\frac{q_0^2}{b_0} - \frac{q_1^2}{h_1} - \frac{q_2^2}{H - h_1} + \frac{g}{2}(H+\Delta)^2 - \frac{g}{2}H^2 + g'_0 b_0^2 - g'_1 h_1^2$$

Additional relations required to complete the specification of the problem include mass and buoyancy flux conservation:

$$q_1 = q_2 + q_0 \qquad \text{and} \qquad g'_0 q_0 = g'_1 q_1$$

Since the jump is assumed to be miscible, there are an infinite number of downstream states that can satisfy the above system of equations. In order to provide closure, a relation describing the state of the flow downstream from the jump, or *downstream control*, is required. Wilkinson and Wood (1971) generally considered applications with a topographic control in the form of a rise in the channel bottom at which the flow was assumed to be internally critical. However, they also showed that the maximum entrainment occurred when the downstream flow is internally critical without a topographic restriction. The internally critical flow condition is most often expressed as

$$F_1^2 + F_2^2 = 1$$

where $F_i^2 = u_i^2/(g'h_i)$. Internally critical flow represents minimum internal energy (defined by Lawrence, 1985 as $E_l = h_1 + u_1^2/2g' - u_2^2/2g'$, as defined by Lawrence (1986) and others) and maximum q_1 for given E_l and $q_1 + q_2$. However, unlike specific energy in single-layer flow, internal energy for given q_1 and q_2 may have both local maxima and minima, each of which represents critical flow. Critical flow with a larger fractional depth h_1/H represents a maximum energy state and is presumed to represent a physically inadmissible flow state. The constraint necessary to be satisfied such that internally critical flow is associated with a local energy minima rather than a maximum, is

$$u_1 h_2 - u_2 h_1 \geq 0$$

Although solutions to internal jumps may be obtained so that this criterion is not satisfied (see Wright, 1986) these flow states are not considered in this paper.

For the case of a starting flow, the density current that is formed as the flow is initiated could serve as a further control on the jet mixing provided that it represents a subcritical flow state. Most analyses of density currents utilize a formulation proposed by Benjamin (1968). However, it was shown by Wright, et al (1987) that such density currents are predicted to be supercritical in many circumstances and inconsistent with the requirements to match the conditions downstream from an internal hydraulic jump and in the density current. Wright, et al (1990) demonstrate that density current propagation may be well described by an analysis which minimizes the total energy flux in the two layer flow subject to maintaining a constant total depth over the density current front. This leads to the following condition for the flow behind the density current head:

$$F_1^2 - q_r F_2^2 = 1$$

where $q_r = -q_2/q_1$ with the convention adopted in Fig. 1. Since q_r will always have a magnitude less than one for the configuration considered, this implies that the density current will be slightly subcritical and will approach the internally critical state in the case of great dilution ($q_1 >> q_0$). Although the experimental results presented below generally only have ratios of q_1/q_0 on the order of 2-4,the differences between the predicted volume flux downstream from the jump with the above expression and that with the internally critical relation are within 1-2 percent of each other. Therefore, it may be considered that the density current does not serve as a significant control on the jet mixing and that the dilution is nearly the maximum possible.

The analysis for density current propagation does not consider the effect of bottom and interfacial shear. If the density current is essentially a critical section propagating away from the source region, the influence of shear will be to increase the lower layer thickness upstream from the density current. The net effect of this will be to develop a more subcritical flow than would exist in the absence of any frictional influences and this would serve to decrease jet mixing. The relative effect would have to analyzed by a gradually varied two layer flow analysis but should be greater in the laboratory because of the lower Reynolds numbers and thus greater viscous effects. The bottom discharge would be more greatly affected because of the shear along the bottom. In a prototype application, the flow field may not be truly two-dimensional so long as the discharge is from a finite length source. This would lead to buoyant spreading in multiple dimensions and a reduction in the far field influence. Thus, so long as the prototype discharge is not confined laterally, it should be anticipated that the internal jump should basically be of the maximum entraining type and comparable to the transient flow in a laboratory model.

Experimental Verification

The experiments are reported in Wright (1986) and were performed by discharging a cold salt water solution at the bottom of a 14 m long and 40 cm wide channel suspended within a larger flume. This allowed for the flow to develop both as the density current propagated down the inner channel, but also after a steady state condition was reached with the more dense fluid spilling into the bottom of the large flume. Fixed racks of thermistor probes measured vertical temperature profiles at four locations along the channel; those reported herein were collected just beyond the end of the active mixing region. Characteristic layer thicknesses and concentrations were computed from the following relations:

$$\frac{\Delta T_a}{T_0} h_1 = \int_0^H \frac{\Delta T}{T_0} dy \qquad \text{and} \qquad \frac{\Delta T_a}{T_0}\frac{h_1^2}{2} = \int_0^H \frac{\Delta T}{T_0} y\, dy$$

where y is the distance from the lower boundary, temperature differences are defined relative to the ambient temperature and ΔT_0 is the source temperature difference. The average dilution q_1/q_0 may thus interpreted as proportional to the inverse of $\Delta T_a/\Delta T_0$. The data of Chu and Baddour (1984) may be used to compare with the present results since they measured both velocity and density profiles. Using the above definitions and their reported profiles, the ratio of this dilution to that predicted from the internal jump model with uniform profiles is about 0.82.

Two sets of experiments were performed; one with the inner channel set on a one percent slope. The purpose of these was to remove the influence of downstream interfacial friction since this slope has been found in previous investigations to result in supercritical flows. The temperature profiles were measured after the starting density current exited from the inner channel and a steady state configuration was obtained. The results of several experiments with relatively small h_1/H obtained with this configuration are presented in Fig. 2 and the observed dilutions are consistent with the observations of Chu and Baddour. The other set of experiments was performed in a horizontal and temperature measurements were made both as the density front propagated down the inner channel and as the steady state configuration was approached. Temperature profiles were recorded continuously throughout the duration of the experiments which often last 20-30 minutes; this was found to be necessary to achieve a steady state condition.

Fig. 3 presents a typical temperature history of measured temperature profiles at a location 1 m downstream from the source (and beyond the visual zone of active mixing) and a second location about 5.6 m downstream. The two temperature records are very similar to each other except for their displacement in time and indicate minimal mixing between the two locations. Fig. 3 also indicates a slow increase in $\Delta T_a/\Delta T_0$ with time and a similar behavior is noted for h_1. This could be interpreted as due to interfacial and bottom shear influences as there was generally a three to four cm decrease in h_1 along the length of the channel after steady state was established. However, the experiments on the sloping bottom also show a similar increase in $\Delta T_a/\Delta T_0$ but not in h_1 and so it is not obvious that friction is the only cause of the behavior. This provides some difficulty in deciding what to compare with the internal jump model and an arbitrary decision was made to use the results as the density current passed the midpoint of the channel, about 2 minutes after the initiation of the flow. These results are presented in Fig. 2 and the results are seen to be very little different than those in the sloping channel and from the observations of surface jets by Chu and Baddour. The somewhat larger mixing implied for the horizontal channel flows would would, of course, be less if the temperature profiles at later times were used in the interpretation of results. In the particular experiment presented in Fig. 2, the reduction in apparent volume flux would be about 30 percent and this would be sufficient to result in a dilution less than observed in the sloping channel experiments. It is apparent therefore that interfacial and bottom shear do play a role in reducing the mixing, but that there are some residual unsteady effects that may more than compensate for this in a transient experiment.

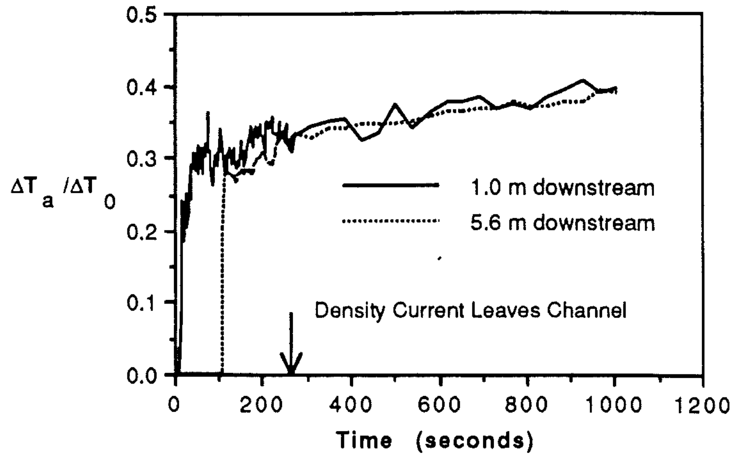

Figure 2. Time Histories for Temperature Difference at Two Locations Downstream from Internal Hydraulic Jump.

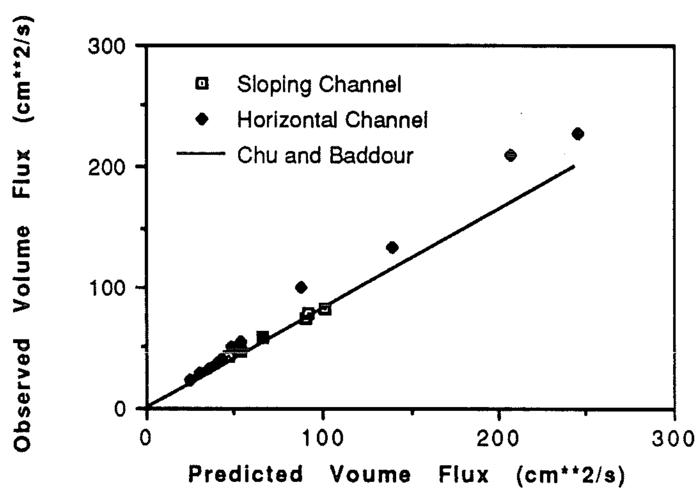

Figure 3. Comparison of Observed and Predicted Volume Fluxes Downstream from Internal Hydraulic Jump.

Conclusions

This study was conducted to determine the influence of far field conditions on mixing within a dense wall jet and to observe any transient behavior when the experiment is conducted as a starting flow. Both of these effects were found to be present, but compensating in the present experiments. The influence of interfacial and bottom friction at the laboratory scale are sufficient to partially drown the internal jump and decrease the jet mixing, at least for the present situation where the channel was 14 m long. At the same time, the mixing was found to decrease slowly with time for reasons that are not entirely clear and experiments would need to be run for nearly 30 minutes in the particular apparatus before a steady state condition was approached. Since the two effects are at least partially compensating, it appears that the differences between a transient laboratory investigation and a steady prototype (without topographic control) are reasonably similar.

It was also found a theory of internal hydraulic jumps may be used to estimate the near source mixing in a wall jet discharge with a reasonable degree of accuracy without specific knowledge of the jet velocity and density profiles. An even more important consideration is that in the absence of a specific topographic control, the attainment of the internally critical state determines the amount of near field mixing. This would be especially relevant to the prediction of dilution from discharges that are not laterally confined since the buoyant spreading in the far field would serve to reduce the combined influences of topography and shear.

Acknowledgements

The research reported in this paper was supported by the National Science Foundations under Grant No. INT-8404553 and by the Swiss National Science Foundation under Grant No. 87.229.0.84 while the author was on sabbatical leave at the ETH in Zürich, Switzerland.

References

Baddour, R.E. and Abbink, H. (1983) Turbulent Underflow in a Short Channel of Limited Depth, *Journal of Hydraulic Engineering*, Vol. 109, No. 5, pp. 722-740.

Benjamin, T.B., (1968), Gravity Currents and Related Phenomena, *Journal of Fluid Mechanics*, Vol. 31, pp. 209-248.

Chu, V.E. and R.A. Baddour (1984) Turbulent Gravity Stratified Shear Flows, *Journal of Fluid Mechanics,* Vol. 138, pp. 353-378.

Lawrence, G. A., (1985), The Hydraulics and Mixing of Two-Layer Flow Over a Obstacle, UCB/HEL-85/02, Hydraulic Engineering Laboratory, University of California, Berkeley, California.

Wilkinson, D.L. and I.R. Wood, (1971) A Rapidly Varied Phenomenon in a Two Layer Flow, *Journal of Fluid Mechanics,* Vol. 47, 2, pp. 241-256.

Wright, S.J., (1986), Aspects of Far-field Control on Buoyant Jet Mixing, *Report 24-86, Institut für Hydromechanik und Wasserwirtschaft, ETH*, Zürich, Switzerland.

Wright, S. J., Kim, Y., and Bühler, J., (1987), Controls on Density Current Propagation, *Third international Symposium on Stratified Flow*, Pasadena, California.

Wright, S. J., Kim, Y., and Bühler, J., (1990), *Density Current Propagation in Flowing Receiving Fluid,* this Proceedings.

Session 11B

Sediment Laden Flows

COMPUTATION OF GRAIN-SIZE DISTRIBUTION OF SUSPENDED LOAD FROM BED MATERIALS

Bijoy S. Mazumder*
Surface Water Section
Illinois State Water Survey
Champaign, IL 61820 USA

Abstract

Experimental results show that the grain-size distribution of suspended material is related to flow parameters and grain-size distribution in the bed. A theoretical model has been developed for suspension grain-size distribution on the basis of diffusion equations, taking into account the effect of hindered settling due to the increased concentration. Fluid velocity closest to the bed is estimated by using the concept of migration velocities of particles moving as bed load. Comparisons of data computed by the proposed method and data from actual observations are shown.

Introduction

Grain-size frequency distributions of sediment populations are believed to be environment sensitive. The sediments transported in hydrodynamic conditions have received much attention in terms of the basic problems related to the phenomenon of grain sorting during transportation. The logarithmic transformation of particle sizes ($\phi = -\log_2 D$, D is in mm) of naturally transported sediments, both ancient and modern, often leads to normal distributions (Krumbein 1934, Blench 1952, Sengupta 1975). However, grain-size distribution other than lognormal have also been reported as log-hyperbolic under certain cases (Bagnold and Barndorff-Nielsen 1980). An investigation in a fluvial river revealed that the suspension deposits on the *point bars* have a tendency to generate lognormal distributions with increasing the distance in the downstream direction (Sengupta 1975). To understand the process of grain sorting during transportation in rivers, grain-size distributions of suspended loads at different flow velocities over six sand beds of different grain sizes were studied in laboratory flumes (Sengupta 1975, 1979; Ghosh et al., 1981). Controlled experiments have shown that grain-size distributions of sediments in suspension bear a definite relationship to bed materials, flow velocity, and height of suspension above the sand bed. These studies have also shown that a sorting process is initiated immediately above the bed and that the grain sizes of the bed layer influence the size distribution of the suspended load above. A theoretical model was developed by Ghosh et al. (1981) to compute the grain-size distribution of bed load and suspended load from bed materials and flow parameters. The conditions of symmetry, unimodality and lognormality of grain sizes in suspension were also studied by Ghosh and Mazumder (1981). They have shown that the suspended load will have a tendency to be log-normally distributed for that size range of the bed material for which the settling velocity is linearly distributed on a logarithmic scale. Several existing methods for computation of bed load and suspended load were discussed in detail in Ghosh et al. (1981).

The purpose of this article is to develop a mathematical model, based on the diffusion equations of sediment and water, for direct computation of suspended grain-size distribution from bed material, taking into account that (1) fluid velocity at the top of the bed layer is assumed to be the same as the migration velocity of representative size moving in the bed layer, and (2) the fall velocity of particles varies with sediment concentration. The efficiency of the present method has been tested against observed data.

---

*Associate Professor, Indian Statistical Institute, Calcutta 700035, India.

Mathematical Model for Computation of Suspended Load

In a steady and uniform turbulent flow, where the concentration C varies only with the vertical coordinate y throughout the depth, and the diffusion coefficients of sediment and water are assumed to be equal (i.e. $\varepsilon_s = \varepsilon_m$), the vertical distribution of the sediment concentration profile can be described (Hunt 1954) as:

$$\varepsilon_s \frac{dC}{dy} + (1 - C)\, CW = 0 \tag{1}$$

where W is the sediment fall velocity in a fluid-sediment mixture. Experiments on fluid-sediment mixtures have shown a substantial reduction of the particle fall velocity due to the presence of neighboring particles. The fall velocity of sediment W varies with concentration C as a result of the hindered effect as defined by Maude and Whitmore (1958):

$$W = w_o (1 - C)^{\alpha} \tag{2}$$

where w_o is the fall velocity in clear water and α is the exponent of reduction of fall velocity, which varies from 0 to 5 depending on particle Reynolds number and the size of noncohesive sediment particles.

For fully developed turbulent flow, the momentum diffusion coefficient for sediment ε_s can be written as

$$\varepsilon_s = \tau_o (1 - y/d) / \rho \frac{du}{dy} \tag{3}$$

where τ_o is the shear stress at the bed and ρ is the density of fluid. The von Karman logarithmic velocity distribution is given by

$$\frac{u - u_m}{u_*} = \frac{1}{\kappa} \left[(1 - y/d)^{1/2} + B \,\mathrm{Ln} \left\{ \frac{B - (1 - y/d)^{1/2}}{B} \right\}\right] \tag{4}$$

which satisfies the maximum velocity (u_m) at the free surface ($y = d$). B is an integrating constant and κ is the von Karman constant (0.4). The constant B was determined by Hunt (1954) experimentally. Ghosh et al. (1981) determined B from the condition that $u = 0$ at $y = k_s$, the roughness of the bed. In this article, the concept of instantaneous migration velocity of particles in the bed layer is used to determine the constant B. The migration velocity (u_s) of a particle in the bed layer is a function of shear velocity (u_*) and critical shear velocity (u_{*c}) corresponding to Shield's grain movement condition for different bed materials. The empirical relation for particle velocity in the bed layer is given by Engelund and Fredsoe (1976):

$$u_s = \beta\, u_* \,(1 - .7 \sqrt{u_{*c} / u_*}) \tag{5}$$

where the value of β is 9 for sand. The velocity of the fine particles (.032 mm – .061 mm) at the top of the bed layer is assumed to be equal to fluid velocity at that layer, that is, $u = u_s$ at $y = y_1$ (y_1 =.25 cm is the height of the bed layer). Hence,using this condition, B is determined from (4). Fig. 1 shows the particle velocity at the bed layer for two maximum velocities (u_m) of fluid over two different sand beds. The velocity distribution (4) with determined B is plotted against y/d in Fig. 2 for two maximum velocities (u_m) above the sand beds. The agreement between the observed and computed velocities is close throughout the depth y.

Since the velocity distribution (4) is valid closest to the bed at a height of about .25 cm, a linear velocity profile is assumed for the bed layer (from k_s to .25cm) as:

$$u = \frac{u_s}{(y_1 - k_s)} (y - k_s), \quad y_1 - k_s \neq 0 \tag{6}$$

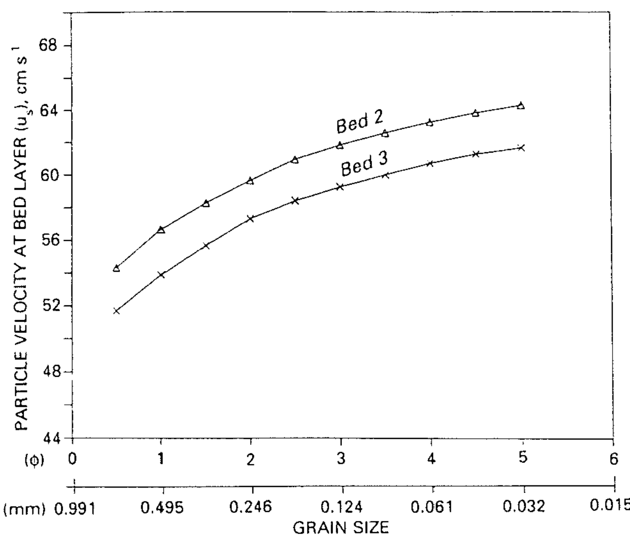

Fig. 1. Average particle velocity at the bed layer
Δ Bed 2 for u_m = 121.3 cm/sec;
X bed 3 for u_m = 97.8 cm/sec

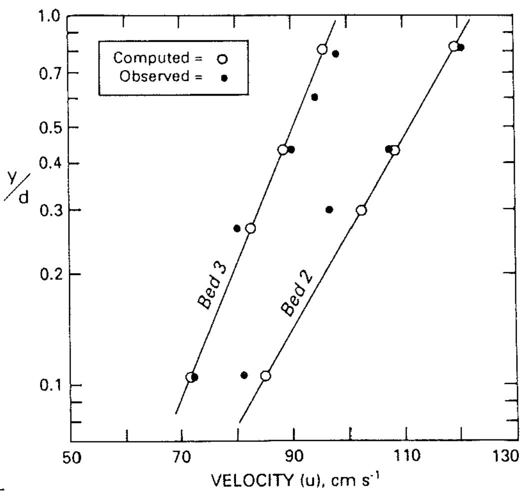

Fig. 2. Logarithmic velocity distribution

The vertical distribution of sediment concentration above the bed is obtained by integrating equation (1) from k_s to y by using equation (2):

$$\int_{k_s}^{y} \frac{dC}{(1 - C)^{\alpha} C} = - \int_{k_s}^{y_1} \frac{w_o}{\varepsilon_s} dy - \int_{y_1}^{y} \frac{w_o}{\varepsilon_s} \tag{7}$$

The expressions of ε_s under the integration sign will be found from equations (3) and (6) for k_s to y_1 and from equations (3) and (4) for y_1 to y. The right side of equation (7) is exactly the same as that of equation (15) of Ghosh et al. (1981), except for the values of u_s and B. Once the concentration function C is known from equation (7), the relative suspension concentration C'_y may be obtained as:

$$C'_y = C_y / \sum_{\phi} C_y \tag{8}$$

Equation (8) is used to calculate the relative suspension concentration of a given grain size having a settling velocity w_o at any height $y > y_1$ above the bed, if the relative bed concentration c_{ks} is known. If $y = y_1$, equation (8) corresponds to equation (7) gives the average concentration of sediment of different grain-sizes in the bed layer.

Experimental Studies

Data used for the verification of the present model are taken from the earlier publications by Sengupta (1975, 1979) and Ghosh et al. (1981). Two closed-circuit laboratory flumes, one designed at Uppsala University and other at the Indian Statistical Institute, Calcutta, were used for conducting the controlled experiments. Bed materials of six different known grain-size distributions were used. Descriptions of equipment setup, techniques of velocity measurement, sample collection, and analysis have been given in the earlier publications. The size distributions of two different sand beds (bed 2, bed 3) are used in this article for computation (Fig. 3a). The flow parameters used for verification of the model are reproduced in Table 1.

Table 1. Flow Parameters Used for Computation

	Bed 2	*Bed 3*
Depth d (cm)	30.0	30.0
Sampling height H (cm)	25.0	20.0
Effective sand bed height h(cm)	~1.7	~2.5
Maximum velocity u_m (cm/sec)	121.3	97.8
Roughness k_s (cm)	.0297	.0450
Vertical height y (cm)	23.3	17.5
Slope J	.0020	.0018
Temperature (°C)	19.0	19.0

Comparison with Observed Values

The computations of equations (7) and (8) have been performed for α = 0, 3, 4. Observed and computed values of suspended grain-size distribution above two sand beds have been plotted in Figs. 3b,c for various values of the exponent α. The relative errors between the observed and computed values are shown in Table 2 for the present method and the methods developed by others. On the whole, it seems that the present method is somewhat better than the others.

Table 2. Errors between Computed and Observed Values

Bed no.	*Height y (cm)*	*Gessler method*	*Ghosh et al. method*	*Present method* $\alpha = 0$	*Present method* $\alpha = 3$	*Present method* $\alpha = 4$
2	23.3	.39	.36	.30	.20	.18
3	17.5	.29	.36	.36	.43	.30

Conclusion

A method of computation of size distribution of suspended sediment from the bed material has been developed with the help of the diffusion approach. The method utilizes the reduction of grain settling velocity with sediment concentration in suspension. The migration velocity of sediment particles moving as a bed load is used to predict the fluid velocity immediately above the sand bed. The results obtained by the present method compare well with the experimental observations.

Acknowledgements

I would like to give my sincere thanks to Dr. Nani Bhowmik, Principal Scientist and Assistant Head of the Surface Water Section, Illinois State Water Survey, for providing the opportunities for doing this work, and to John Brother for graphics work.

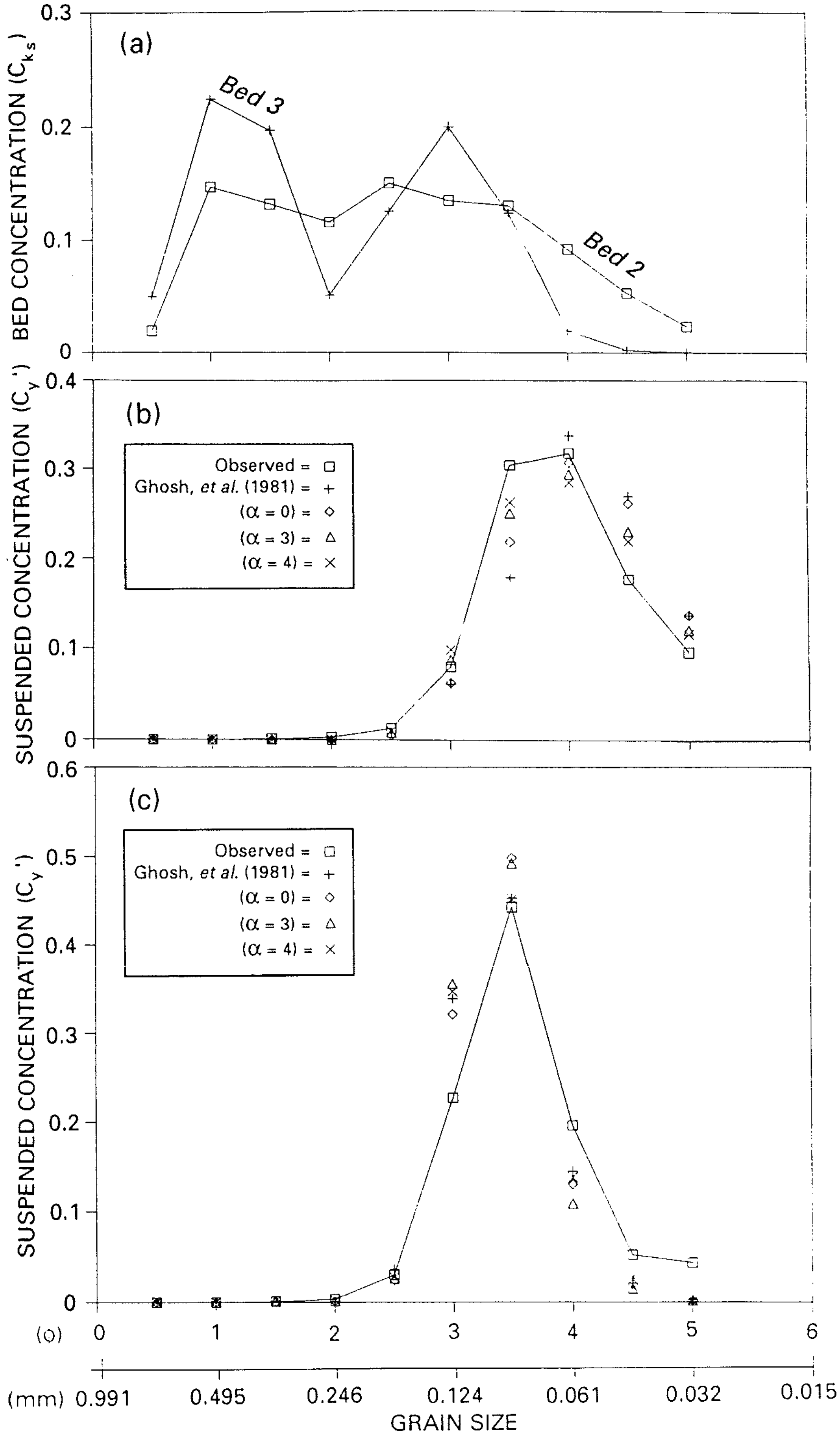

Fig. 3(a). Grain-size distributions of sand beds

(b) Grain-size distribution in suspension (C'_y at y = 23.3 cm) above the sand bed 2

(c) Grain-size distribution in suspension (C'_y at y = 17.5 cm) above the sand bed 3

References

Bagnold, R.A. and Barndorff-Nielsen, O. 1980. The pattern of natural size distributions. Sedimentology, 27,199-207.

Blench, T., 1952. Normal size distribution found in samples of river bed sand. Civil Engineering, 22, 147.

Engelund, F. and Fredsoe, J., 1976. A sediment Transport Model for straight alluvial channels. Nordic Hydrology, 7, 293-306.

Ghosh, J.K. and Mazumder, B.S., 1981. Size distribution of suspended particles - unimodality, symmetry, and lognormality. *In* C. Taillie et al. (eds), Statistical Distribution in Scientific Work, v. 6, D. Reidel Publishing Comp., The Netherlands, p. 21-32.

Ghosh, J.K., Mazumder, B.S. and Sengupta, S., 1981. Methods of computation of suspended load from bed materials and flow parameters. Sedimentology, 28, 781-791.

Hunt, J.N., 1954. The turbulent transport of suspended sediment in open channels. Proceedings, Royal Society of London, A224, 322-335.

Krumbein, W.C., 1934. Size frequency distributions of sediments. Journal of Sedimentary Petrology 4, 65-77.

Maude, A.D. and Whitmore, R.L. 1958. A generalized theory of sedimentation. British Journal of Applied Physics, 9, 477-482.

Sengupta, S., 1975. Sorting processes during transportation of suspended sediments - An experimental and theoretical study. UNGI Report 40, Uppsala University, Department of Physical Geography, 49p.

Sengupta, S., 1979. Grain size distribution of suspended load in relation to bed materials and flow velocity. Sedimentology, 26, 63-82.

COHESIVE SEDIMENT AND PHYSICAL MODELS

by T N Burt BSc CEng MICE
Principal Engineer, Hydraulics Research
Wallingford, England

Abstract

It is not possible to scale the physical properties of fine cohesive sediments in such a way as to make use of a scaled down sediment in a physical model. Cohesive sediments, often termed "mud" have a number of properties which make it impossible. These include flocculation and consolidation. Numerical models, although they have advanced considerably in the last 10 years, have many disadvantages when it comes to resolving detailed flow, siltation and scour near to jetties and other structures. The author has devised a system which combines the use of a physical model and a computational technique "SAP" to study such situations.

SAP takes as input the hydrodynamics from the physical model, sediment properties of settling, consolidation and re-erosion from laboratory and field measurements and suspended sediment concentrations from silt monitoring in the field. The output is time-variation of the bed level over any period from a single tide to a number of spring-neap cycles.

The paper describes the method and how the sediment properties are determined with an example of an interactive study drawn from the author's recent experience.

Introduction

The erosion, transport, deposition and consolidation of cohesive sediment within estuaries can create a wide range of design, maintenance and management problems in ports, harbours and docks. There is a need, for example, to predict the accumulation of cohesive sediment in navigation channels and berths in order to estimate maintenance dredging costs.

The behaviour of cohesive sediment is complex and is governed by many physico-chemical and hydrodynamic parameters (Ref 1). However, for the purposes of modelling its behaviour it is possible to consider that there are four basic processes involved in cohesive sediment transport, namely, erosion, advection, deposition and consolidation.

These processes have been studied in great detail using specialist laboratory facilities at Hydraulics Research and in field experiments over a 20 year period. The research has provided a much better although still incomplete understanding of the dynamic behaviour of mud in tidal estuaries.

While considerable progress has been made in full scale simulating of the processes it is also clear that to simulate them all in a single scaled model would require a material of quite extraordinary properties. The processes are at the present time best described by a series of semi-emperical equations which can be either assumed from published results or experimentally determined specifically for the mud in question.

The following sections describe how the sediment properties have been determined then how they are used in the "zero" dimensional model SAP to evaluate net siltation or erosion during a series of tidal cycles. The technique has been applied to a physical model study of the effects of a tide excluding barrage on the siltation of a dredged navigation channel.

Cohesive sediment properties

Settling:

Deposition of flocculated cohesive sediment from flowing water has been studied using a circular flume called 'The Carousel' (Ref 2). Work using the HR Carousel has shown that settling from suspension only occurs when the near-bed flow velocity is very low. In the case of an estuary in mid-stream this means perhaps only during a half hour period around slack water at high and low water. For the rest of the tidal cycle velocities are able to maintain mud in suspension. This means for example in the Thames that a particle of silt may travel up to about 20 km during a flood or ebb tide. The carousel work has further shown that this deposition threshold is virtually independent of the concentration of silt in suspension up to at least 50,000 mg/litre. In other words if there is a saturation limit, the Thames, with maximum concentrations in the region of 5,000 mg/l, is operating well below it and is therefore capable of carrying a much higher suspended silt load than it does.

When conditions allow settling to occur it happens at a rate dependent on the concentration. This has been studied using a field settling tube method known as the "Owen tube" (Ref 3). This dependence is a result of the process of flocculation by which particles aggregate together to form larger particles which then have a settling velocity higher than the individual particles. High concentration suspensions give more opportunity for particles to collide hence producing larger flocs which then settle faster.

Consolidation:

This was studied by Ginger (Ref 4). Silt having settled on the bed begins to consolidate but there is an intervening period lasting from a few minutes to a few hours, depending on the thickness of the layer, when it is still in a semi-fluid state. If it is left for longer it quickly gains in strength as it reduces in thickness and increases in density, making it more difficult to erode.

Erosion:

Erosion takes place when the flow velocity, or more precisely the bed shear stress , exceeds the threshold value. The threshold value depends on the density of the silt deposit. If it is still in the semi-fluid state it is entrained easily back into suspension in much the same way as would occur at the interface of two fluids of different density.

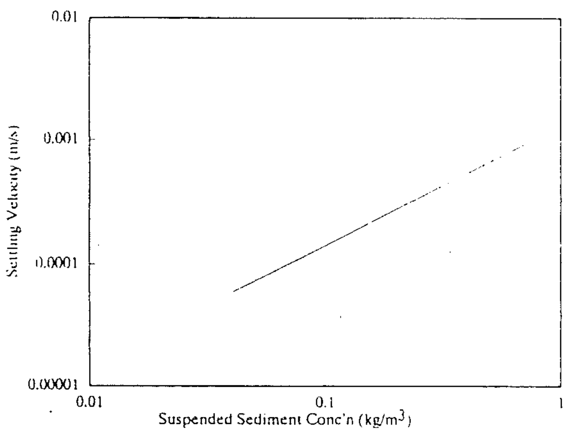

Figure 1 : Median settling velocity against suspended sediment concentration

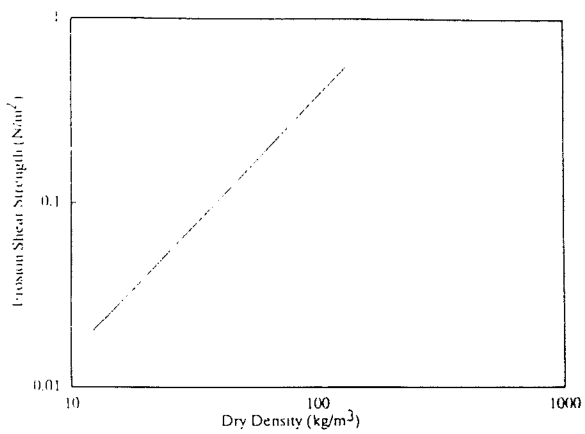

Figure 2 : Erosion shear strength against dry density

The erosion rate is proportional to the excess shear, i.e. the amount by which the applied bed shear stress exceeds the threshold for erosion. In practice the rate of erosion is modified by the fact that the bed itself has a density profile and therefore becomes progressively more difficult to erode as each new surface is exposed by erosion of the one above.

SAP - Prediction of siltation at a point

A full description of the model is given in Ref 5 which includes the relevant equations.

The cohesive sediment bed in the SAP model is represented by ten discrete layers which are each assumed to be homogeneous, with a certain density and thickness. Sediment is subtracted or added to the uppermost layer, according to the processes of erosion and deposition respectively. In addition, the layers are consolidated under their self-weight and the excess pore pressures within the bed are dissipated. At each time step the density and the thickness of each layer is calculated.

At the start of the model the existing bed is described by a density profile. Ideally this should be based on field measurements, obtained using either a density probe or a grab sampler.

When flow velocities are low enough to permit deposition of suspended solids the factor which governs the rate is the concentration thus it is necessary to know how this varies with time by field observation, preferably by monitoring at the site in question over a period of several months to include variations due to tidal range, fresh water flow and other weather factors (Ref 6). In most situations because of the relatively low settling velocity of particles only the near-bed values are relevant.

Because both deposition and erosion are governed by the bed shear stress exerted by the flow it is necessary to input the time variation of this parameter for spring and neap tides. Values for other ranges are determined by interpolation. For an existing situation these can be determined from field observation of the vertical velocity profile. For predictive work they are determined from velocity measurements in a physical model but care is needed to ensure proper calibration of the model because the bed roughness effects will not necessarily scale correctly.

Application

The method described has been applied to a physical model study of a proposed tide excluding barrage (Ref 7). In order to hindcast the present siltation rate in the dredged channel it was necessary to determine the likely range of the near bed suspended sediment concentrations and current induced bed shear stresses during the spring-neap tidal cycle in the channel.

The former were determined from the continuous silt monitoring at two positions in the channel. The pattern during a tide is shown in Figure 3.

The bed shear stresses in the channel were calculated using the depth averaged prototype velocities derived from measurements in the physical model. (Fig 4).

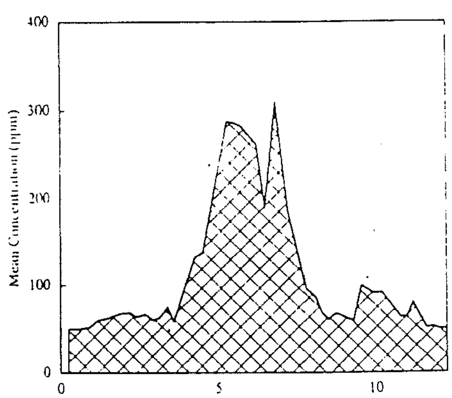

Figure 3 : Suspended solids concentration during a spring tide

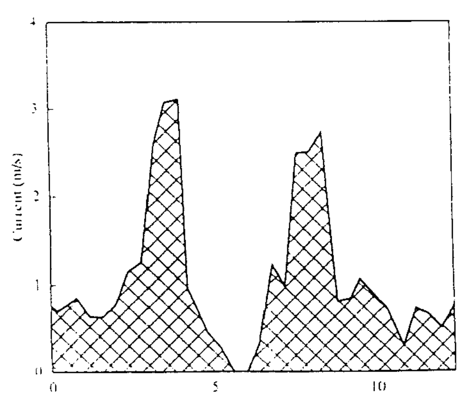

Figure 4 : Typical velocity measurements in the channel

Assuming smooth turbulent flow, the shear velocity u_* in terms of the flow velocity u, at a height above the bed y, is given by:

$$\frac{u}{u_*} = 5.75 \log_{10} \frac{9.04\ y\ u_*}{\gamma} \qquad (1)$$

Where γ = kinematic viscosity (0.84×10^{-6} m^2/s)

The bed shear stress τ, is related to the shear velocity u_* and density of fluid ρ, by:

$$\tau = \rho u*^2 \qquad (2)$$

The settling velocity of the suspended sediment was measured in situ and was found to follow the relationship

$$w_{50} = 0.0003\ c^{1.0} \qquad (3)$$

where w_{50} = median settling velocity (m/s)
c = suspended solids concentration (kg/m^3)

A sample of mud taken from the banks of the River Ely near its entrance to Cardiff Bay was tested in the HR Carousel flume to determine its erosion properties.

The results indicated that the relationship between erosion shear strength τ_c, and dry density ρ_d, of the mud was approximately:

$$\tau_c = 0.00022\ \rho_d^{1.5} \qquad (4)$$

To hindcast the siltation in the whole channel it was necessary to measure the velocity of flow at a number of points along the length of the channel in the physical model and to run SAP for each position.

SAP was run iteratively for a spring-neap sequence of tides to give total net siltation over 14 days which was then multiplied to give the annual rate of 400000 - 550000t. This is near to the lower bound estimation of the present dredging commitment. Making also an allowance for occasionally higher concentrations due to storm effects gave sufficient confidence in the method to use it predictively. The barrage scheme was incorporated in the physical model and the effect on velocities in the channel measured. The input to SAP was thus modified and the model rerun to give the predicted rates.

Conclusions

1. Laboratory simulation of the processes of settling, consolidation and erosion of cohesive sediment, has given rise to semi-empirical equations which can be used with reasonable confidence.

2. Scale modelling of these processes is not a realistic objective.

3. SAP provides an economic and convenient way of using the equations to study the net result of a sequence of tides in terms of erosion or accretion at a point provided it is used sensibly.

4. SAP provides a means of combining state-of-the-art knowledge of sediment properties with the established predictive capability of physical models.

References

1. Delo E A. Estuarine Muds Manual. Hydraulics Research, Wallingford, England, Report SR 164, February 1988.

2. Delo E A. The behaviour of estuarine muds during tidal cycles. Hydraulics Research, Wallingford, England, Report SR 138, February 1988.

3. Burt T N. Field settling velocities of estuary muds. Lecture Notes on Coastal and Estuarine Studies No 14 Estuarine Cohesive Sediment Dynamics. Springer-Verlag 1984.

4. Ginger C M. Simulation and experimental determination of a consolidating mud deposit. Hydraulics Research, Wallingford, England, Report SR 95, July 1987.

5. Delo E A and Ockendon M. Prediction of siltation at a point. Proceedings of National Conference on Hydraulic Engineering, New Orleans, August 1989.

6. Burt T N and Stevenson J R. Monitoring cohesive sediment transport in estuaries, Proc. Int Conf Measuring Techniques of hydraulics phenomena, London, April 1986.

7. Hydraulics Research. Cardiff Bay Barrage Feasibility Study, Tidal Studies Vol II Part 1. Report No EX 1629, February 1988.

HYDRAULIC ANALYSIS OF SEDIMENT INCLUDING FLOWS OVER SMOOTH BED

by Yoshiaki Iwasa and Takashi Hosoda
Dept. of Civil Eng., Kyoto University
Sakyo-ku, Kyoto 606 JAPAN

Abstract

This paper is concerned with the numerical model for open channel flows with suspended sediments over a smooth bed. The basic equations used here are firstly summarized. The five non-dimensional parameters are introduced by transforming the basic equations into the dimensionless form. The numerical simulations are secondly performed for the various values of parameters. The numerical results are compared with the previous experimental ones in order to verify the numerical model. It is also pointed out that the velocity reduction in the vicinity of bed is caused by the stress transmission due to the falling of sediments.

Introduction

The velocity distributions and the resistance law of sediment including flows over both rough and smooth beds have continuously been investigated after initial experimental studies of Vanoni [1]. The previous experimental studies have been summarized as follows [2∼5]:

1. In the case of smooth beds, the resistance coefficient C_f increases (cf. Fig.1) and the velocity in the vicinity of bed becomes smaller than that in the clear water, with the increase of depth avereged concentration of suspended sediments C_m (cf. Fig.2). The velocity increases rapidly toward the free surface compared with the clear water flow.
2. In the case of rough beds, C_f decreases with the increase of C_m (cf. Fig.1). The velocity increases rapidly compared with the clear water flow (cf. Fig.2), which is well-known as the decrease of Kármán constant.

Though the characteristics of flow just mentioned above have been examined from the theoretical and numerical point of view [3,6,7], it seems that the flow characteristics over a smooth bed such as the velocity decrease near the bed have not been well reproduced. In view of this point, the numerical model to describe the velocity distributions of sediment including flows over a smooth bed is investigated and verified.

Basic Equations

The basic equations, in which the following statements are involved, have been derived in view of the analysis of multi-component flows. Further details are described in Ref.[8].

1. The turbulent velocity differences between solid and liquid phase are examined as the interaction term of k (turbulent kinetic energy) equation, which is considered in the previous studies [3,6].
2. In order to reproduce the viscous sublayer, the eddy viscosity is related to the turbulent Reynolds number. This enable us to introduce the effect of Reynolds number.
3. The eddy viscosity is also related to the Richardson number.
4. The stress transmission term due to the falling of sediments is produced in the Reynolds equation. This term is originated from the exact continuity equation of multi-component flows expressed as Eq.(1).

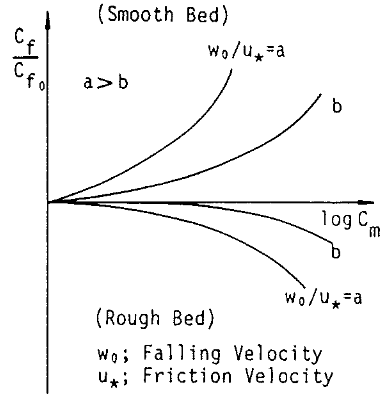

Fig.1 Relation between C_f and C_m

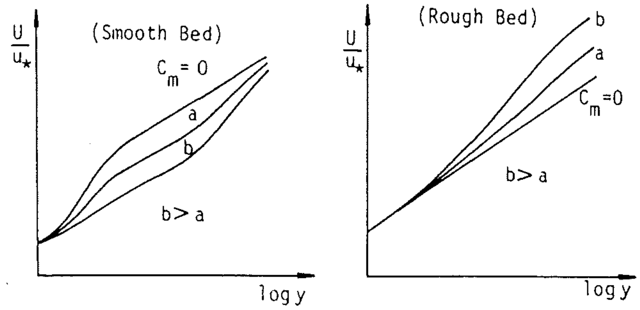

Fig.2 Velocity distributions over rough and smooth beds

$$\frac{\partial}{\partial x_j}\left(U_{fj} - w_0 C \delta_{j2}\right) = 0 \tag{1}$$

in which all notaions are listed in the last. Though the term is usually neglected, it will be made clear theoretically that the velocity decrease in the vicinity of smooth bed is caused by the term.

Referring Fig.3 indicating the coordinate system, the basic equations are expressed as follows [8]:

$$\frac{\partial U_{fx}}{\partial t} + \frac{\partial}{\partial y}\left(\overline{u'_{fx}u'_{fy}}\right) + C w_0 \frac{\partial U_{fx}}{\partial y} = \frac{g sin\theta}{1-C} + \nu \frac{\partial^2 U_{fx}}{\partial y^2} \tag{2}$$

$$\frac{\partial k}{\partial t} = D\left(\frac{\partial U_{fx}}{\partial y}\right)^2 + \frac{\partial}{\partial y}\left(\left(\frac{D}{\sigma_k} + \nu\right)\frac{\partial k}{\partial y}\right) - \epsilon - 2\nu\left(\frac{\partial \sqrt{k}}{\partial y}\right)^2$$
$$-\overline{c'u'_{fy}}\frac{g}{(1-C)}\frac{\rho_p - \rho_f}{\rho_f} - \frac{18\nu}{(1-C)\,d^2}C\left(\overline{u'^2_{fi}} - \overline{u'_{fi}u'_{pi}}\right) \tag{3}$$

$$\frac{\partial \epsilon}{\partial t} = c_{\varepsilon 1}\frac{\epsilon}{k}D\left(\frac{\partial U_{fx}}{\partial y}\right)^2 - c_{\varepsilon 2}\frac{\epsilon^2}{k} + \frac{\partial}{\partial y}\left(\left(\frac{D}{\sigma_\epsilon} + \nu\right)\frac{\partial \epsilon}{\partial y}\right) + 2\nu D\left(\frac{\partial^2 U_{fx}}{\partial y^2}\right)^2$$
$$-c_{\varepsilon 3}\overline{cu'_{fy}}\frac{g}{1-C}\frac{\epsilon}{k}\frac{\rho_p - \rho_f}{\rho_f} \tag{4}$$

$$\frac{\partial C}{\partial t} + \frac{\partial}{\partial y}\left[w_0 C\,(C-1)\right] = \frac{\partial}{\partial y}\left(-\overline{cu'_{fy}}\right) \tag{5}$$

$$-\overline{u'_{fx}u'_{fy}} = D\frac{\partial U_{fx}}{\partial y}\,, \quad -\overline{cu'_{fy}} = D_p\frac{\partial C}{\partial y}\,, \quad D = c_\mu\left(Re_T\right) f\left(R_i\right) f_{DS}\left(y\right)\frac{k^2}{\epsilon}$$

in which the turbulent Reynolds number Re_T and the gradient Richardson number Ri are defined as $Re_T = \frac{k^2}{\nu\epsilon}$, $Ri = -g\frac{\rho_p-\rho_f}{\rho_f}\frac{\partial C}{\partial y}/\left(\frac{\partial U}{\partial y}\right)^2$.

The mathematical expression of interaction term of k-equation has been derived by using the calculated results of the sediment particle motion as Eq.(6).

$$-\frac{18\nu}{(1-C)\,d^2}C\left(\overline{u'^2_{fi}} - \overline{u'_{fi}u'_{pi}}\right) = -c_k\frac{18\nu C k}{(1-C)\,d^2}\frac{1-f}{e c_L R_{eT}\left(\nu/\sqrt{kd}\right)^2 + 1} \tag{6}$$

Numerical value of e,f,c_L and c_k are listed in Table 1.

The ratio of the eddy viscosity to diffusivity β and the relation between the eddy viscosity and the Richardson number Ri have been derived by using Gibson·Launder's study concerning the thermally stratified flows [8].

$$f(R_i) = 1 - \frac{R_i}{R_{ic}} \quad (R_{ic} = 0.4), \qquad D_p = \beta D \quad (\beta = 1.2)$$

The rapid attenuation of depth-wise turbulent velocities near the free surface is also involved by multiplying the function $f_{Ds}(y)$ defined as

$$f_{DS}(y) = 1 - \exp\left[-B\frac{(h-y)\,\epsilon_S}{k_S^{3/2}}\right] \quad , \quad B = 10.$$

in which the subscript $_S$ indicates the value of free surface.

c_μ and $c_{\epsilon 2}$ are related to the turbulent Reynolds number Re_T to introduce the effect of Reynolds number[10].

Introducing the following dimensionless variables

$$U'_{fx} = \frac{U_{fx}}{u_\star},\ k' = \frac{k}{u_\star^2},\ \epsilon' = \frac{\epsilon h}{u_\star^3},\ D' = \frac{D}{hu_\star},\ D'_p = \frac{D_p}{hu_\star},\ t' = \frac{tu_\star}{h},\ y' = \frac{y}{h}$$

can transform the original basic equations into the dimensionless form, in which the following five non-dimensional parameters appear.

$$Fr_\star = \frac{u_\star}{\sqrt{gh}}, \quad Re_\star = \frac{u_\star h}{\nu}, \quad \frac{w_0}{u_\star}, \quad \frac{\rho_p}{\rho_f}, \quad \frac{d}{h}$$

Mechanism of Velocity Decrease in the Vicinity of Bed

As shown in Fig.2, the velocity distribution of sediment including flow over a smooth bed is characterized by the velocity decrease in the vicinity of bed and the increace of velocity gradient with the increace of C_m. One of the reasons of velocity decrease is confirmed by using the simplified equation. In the viscous sublayer, the Reynolds equation (2) is reduced to Eq.(7).

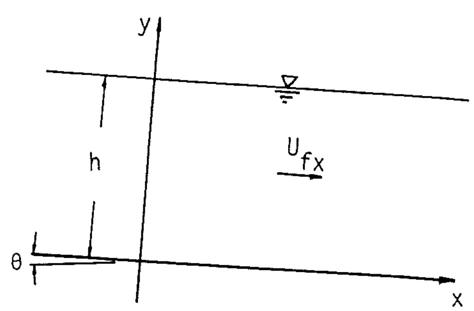

Fig.3 Coordinate system

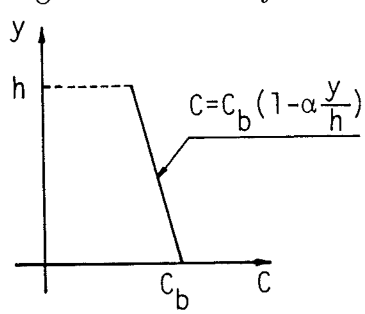

Fig.4 Definition sketch

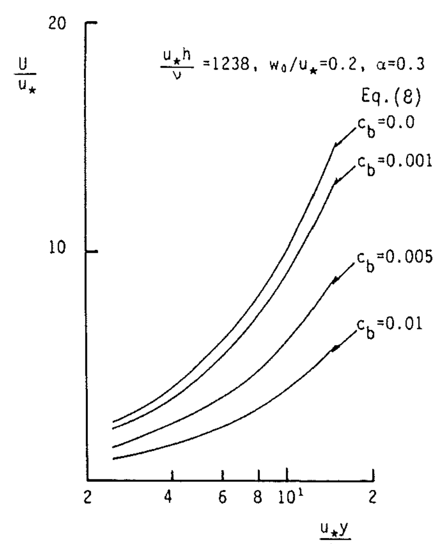

Fig.5 Solution of Eq.(7)

$$\nu \frac{d^2 U_{fx}}{dy^2} - C w_0 \frac{dU_{fx}}{dy} + \frac{g \sin\theta}{1-C} = 0 \tag{7}$$

The second term of Eq.(7) indicates the stress transmission due to the falling of sediments. The term, which is usually neglected , becomes important in the viscous sublayer because of the high concentration of sublayer. Under the conditions illustrated in Fig.4, the solution becomes to Eq.(8) schematically shown in Fig.5.

$$U_{fx} = \int_0^h \frac{g sin\theta}{\nu\, exp\,(Y)\,(1-C)} dy \int_0^y exp\,(Y)\, dy - \int_0^y \frac{g sin\theta}{\nu\, exp\,(Y)\,(1-C)} \int_0^y exp\,(Y)\, dy$$
$$+ \int_0^y \frac{g sin\theta \int_0^y exp\,(Y')\, dy'}{\nu\, exp\,(Y)\,(1-C)} dy\ , \quad Y \equiv \frac{c_b w_0}{\nu}\left(y - \alpha \frac{y^2}{2h}\right) \tag{8}$$

It is shown in Fig.5 that the velocity decreases with the increase of concentration due to the second term of Eq. (7).

Consideration on Numerical Results

In order to examine the flow characteristics with the change of dimensionless parameters, it is necessary to verify the numerical model in view of the comparison between the previous experimental results and the numerical ones.

(1) Boundary Conditions

Numerical simulations have been performed under the boundary conditions described below.

$$(y=0) \qquad U_{fx} = 0, \qquad k = 0, \qquad \epsilon = 0$$

$$(y = \delta \approx 4 \cdot d) \qquad -\overline{cu'_{fy}} = w_0 C\,(C-1)\,, \qquad (y < \delta) \qquad C = C_\delta$$

$$(y = h) \qquad D\frac{\partial U_{fx}}{\partial y} = 0, \qquad D\frac{\partial k}{\partial y} = 0, \qquad D\frac{\partial \epsilon}{\partial y} = 0, \qquad -\overline{cu'_{fy}} = w_0 C\,(C-1)$$

The interaction term of k-equation is applied for $y/h \geq 0.04$. The finite difference method with the spatial variable grid size is used. Under the boundary conditions, the numerical procedure was continued until the flow becomes steady.

(2) Verification of Numerical Results

Hydraulic variables in numerical simulations are listed in Table 1. The condition for Run 1 is coincident with Coleman's experiment ($d = 0.105mm$). The depth of Run 2 is reduced to 1/4 of Run 1 to examine the effect of Reynolds number, which indicates one of the scale effects. Model constants are also listed in Table 2.

Table 1 Hydraulic variables for test runs

	Depth (cm)	$\frac{u_* h}{\nu}$	$\frac{u_*}{\sqrt{gh}}$	$\frac{w_0}{u_*}$	Mean Sediment Diameter (mm)	$\frac{\rho_p}{\rho_f}$	C_m
Run 1*	17.0	6250	0.028	0.27	0.105	2.65	0-0.0041
Run 2	4.25	780	0.028	0.27	0.074	2.65	0-0.0041

*; Exp. of Coleman (Run 1-20), u_* used here is changed so as to fit U/u_* of exp. for the log-law with κ=0.4 and As=5.5.

Table 2 Model constants

$c_{\varepsilon 1}$	$c_{\varepsilon 2\infty}$	$c_{\varepsilon 3}$	$c_{\mu\infty}$	σ_k	σ_ε	c_k	c_L	e	f
1.44	1.92	3.0	0.09	1.0	1.3	2-2.5	0.1	5.0	$\frac{1.5}{\rho_p/\rho_f+0.5}$

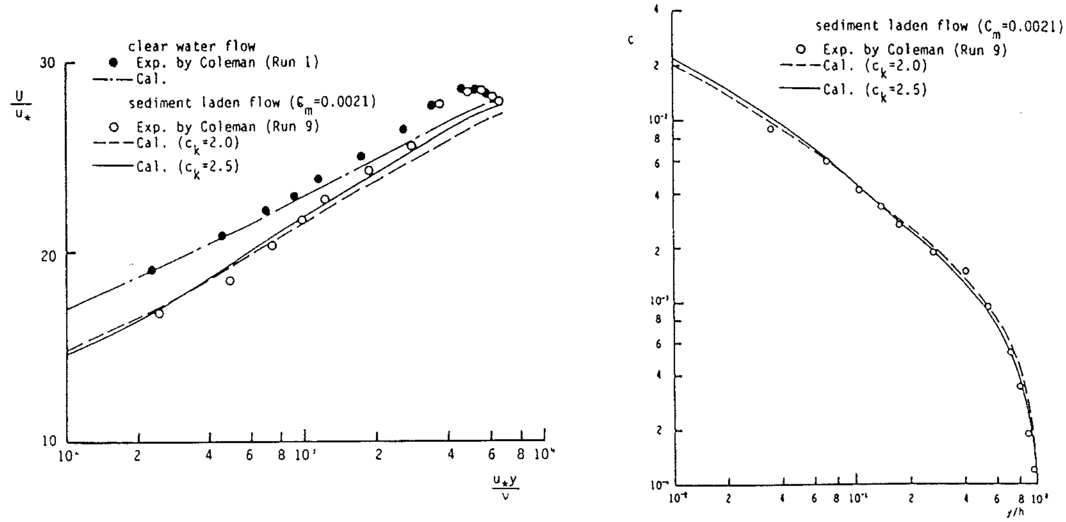

Fig.6 Calculated results of velocity and concentration distributions

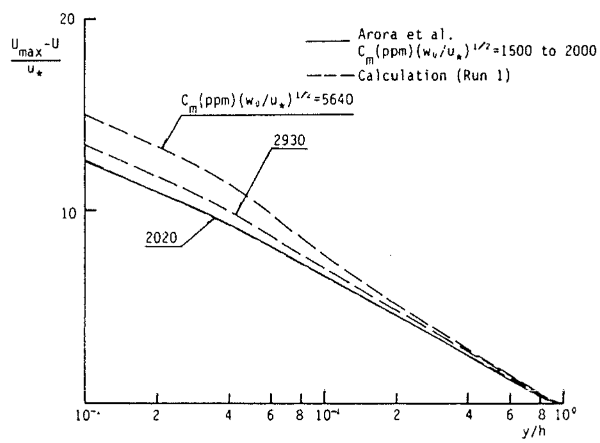

Fig.7 Verification of velocity distribution

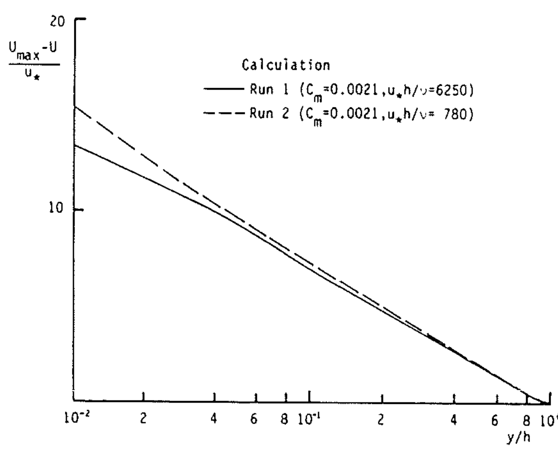

Fig.8 Reynolds number effect for velocity distribution

Numerical results of velocity and concentration distributions are shown in Fig.6 with Coleman's experimental results. The figures indicate that the features of velocity and concentration distributions are fairly good reproduced and it is important to involve the interaction term in k-equation to realize the increase of velocity gradient with the increase of concentration.

The comparison of numerical results with the velocity distribution proposed by Arora·Ranga Raju·Garde [11] for $C_m\,(ppm) \cdot (w_0/u_*)^{1/2} = 1500 \sim 2000$ also verify the usefulness of numerical model as shown in Fig.7.

(3) Reynolds Number Effect

Reynolds number effect for flow characteristics can be examined by using the numerical model. The velocity distributions for the different values of Reynolds number are shown in Fig.8. The feature of distribution is not influenced by the Reynolds number for y/h>0.1. It confirms also the experimental results concerning the resistance coefficient by Imamoto·Ohtoshi [4] in view of the numerical simulation.

Conclusions

The numerical model for sediment including flows over a smooth bed has been developed and verified in view of the comparison of calculated results with previous developed and verified in view of the comparison of calculated results with previous experimental ones. The calculated results indicate that it is important to involve the stress transmission term due to the falling of sediments in the Reynolds equation and the interaction term associated with the turbulent velocity differences between solid and liquid phase in the k-equation in order to reproduce the typical features of velocity distributions. The numerical model may be applicable to the estimation of resistance law of sediment including flows, though further verifications are still required.

References

1. Vanoni,V.A. : Transportation of suspended sediment by water, Tran. ASCE, 111, pp.67-102, 1964.
2. Task Committee : Sediment transportation mechanics, suspension of sediment, progress report, J. Hydraulics Div., ASCE, Vol.89, HY5, pp.45-77, 1963.
3. Itakura,T. and Kishi,T. : Open channel flow with suspended sediment, J. Hydraulics Div., ASCE, Vol.106, HY8, pp.1325-1343, 1980.
4. Imamoto,H. and Ohtoshi,K. : Study on the characteristics of open channel flow with suspended load (1), Annuals Vol.22 B-2, DPRI, Kyoto Univ., pp.453-468, 1979 (in Japanese).
5. Coleman,N.L. : Effects of suspended sediment on the open-channel velocity distribution, Water Resources Research, Vol.22, No.10, pp.1373-1384, 1986.
6. Hino,M. : The change in turbulent structure of flow with suspended solid particles, Trans. JSCE, No.92, pp.11-20, 1963 (in Japanese).
7. Fukushima,Y. : Analysis of non-uniform flow with suspended sediment by using k-ϵ model, Proc. 3rd Int'l Symp. Refined Modelling and Turbulence Measurements, Tokyo, pp.577-584, 1988.
8. Hosoda,T. : Turbulent diffusion mechanism in open channel flows, Ph. D. Thesis, Kyoto University, 1990 (in Japanese).
9. Gibson,M.M. and Launder,B.E. : Ground effects on pressure fluctuations in the atmospheric boundary layer, J. Fluid Mech., Vol.86, pp.491-511, 1978.
10. Launder,B.E. and Sharma,B.I. : Application of the energy dissipation model of turbulence to the calculation of flow near a spinning disc, Letters in Heat and Mass Transfer, Vol. 1, pp.131-138, 1974.
11. Arora,A.K., Ranga Raju,K.G. and Garde,R.J. : Resistance to flow and velocity distribution in rigid boundary channels carrying sediment laden flow, Water Resources Research, Vol.22, No.6, pp.943-951, 1986.

Notations

$c_{\epsilon1}, c_{\epsilon2\infty}, c_{\epsilon3}, c_k, c_L, c_{\mu\infty}$: Model constants
c' : Concentration fluctuations
C : Volumetric time averaged concentration
C_m : Depth averaged concentration
d : Diameter of sediment particle
D, D_p : Eddy viscosity and diffusivity
e, f : Model constants associated with interaction term of k-equation
g : Gravity acceleration
h : Depth
i, j : Indices with respect to spatial direction (1; longitudinal, 2; depth-wise,3; transverse direction)
k : Turbulent kinetic energy
Ri : Gradient Richardson number
Re_T : Turbulent Reynolds number
t : Time
U_{fx} : Longitudinal component of liquid phase
u'_{fi}, u'_{pi} : Velocity fluctuations of liquid and solid phase
u_* : Friction velocity
w_0 : Falling velocity
x, y : Cartesian coordinates
β : D_p/D
ϵ : Turbulent dissipation rate
ν : Kinematic molecular viscosity
ρ_f, ρ_p : Density of water and sediment particle
$\sigma_k, \sigma_\epsilon$: Model cnstant
θ : Inclination angle of bed

FLOW CHARACTERISTICS OF SAND-SILT RIVER BEND

by Hong-Yuan Lee, Wei-Sheng Yu and Kuo-Chien Hsieh
Department of Civil Engineering, National Taiwan University
Taipei, Taiwan, R.O.C.

Abstract

It has been shown by several researchers that the existence of sediment concentration will change the turbulent structure of the straight open channel flow,and hence the vertical distribution of longitudinal velocity. In a sand-silt channel bend, the phenomena are more complicated. The existence of sediment concentration alters the vertical distribution of the longitudinal velocity which in turns affects the strength of the secondary current and the spatial distribution of sediment concentration. An analytical solution is developed in this study to simulate the secondary current distributions in a fully-developed sand-silt channel bend. Series of experiments were conducted to verify the results.

Introduction

Secondary current is one of the most important phenomena in a meandering river. The existence of secondary current significantly changes the vertical distribution of the longitudinal velocity. The location of the maximum velocity shifts downward from the water surface, and the location of the maximum velocity is a function of width-depth ratio and strength of the centrifugal force. A summary of this theory is given by Hussein & Smith (1986).

Secondary current changes the turbulent structure of the flow, which causes the longitudinal velocity profile to deviates significantly from traditional logarithmic law. A detailed literature survey has been performed by Lee and Yu (1990), and they also derived a general velocity profile for the sand-silt straight open channel flow.

The purpose of this study is to incorporate the above mentioned theories to the transverse momentum equation, for the solution of secondary current profiles in the sand-silt channel bend.

Theoretical Analysis

Combining the theories of Hussein & Smith (1986) and Lee and Yu (1990), the depth in a river channel is divided into three regions, inner, middle and outer regions, as shown in Fig. 1. The Karman constant value inside the inner region is a universal constant which equals to 0.41. The velocity profile outside the inner region is a function of both sediment concentration and flow resistance. The velocity profile in the outer region is additionally affected by the strength of the secondary current and it is a function of width-depth ratio and strength of the centrifugal force. The velocity profiles in the three regions can be expressed by:

$$\frac{u-u_s}{u_*} = \frac{1}{\kappa_i}\ln\eta + \left(\frac{1}{\kappa_o} - \frac{1}{\kappa_i}\right)\ln p \qquad 0 \le \eta \le p \tag{1}$$

$$\frac{u-u_s}{u_*} = \frac{1}{\kappa_o}\ln\eta \qquad p \le \eta \le s \tag{2}$$

$$\frac{u-u_s}{u_*} = \frac{1}{\kappa_o}\ln\eta + a(\eta - s)^2 \qquad s \le \eta \le 1 \tag{3}$$

where u_* is shear velocity, p and s are the relative elevations of the interception points between the inner and middle, and middle and outer regions, κ_i is the Karman constant in the inner region, κ_o is the Karman constant outside the inner region, a is a secondary current related coefficient, u_s is the longitudinal velocity at the free surface, and $\eta = z/d$, z is the vertical distance measured from the bed and d is the local flow depth. From Eqs. 1, 2 and 3, u_s can be expressed as:

$$u_s = \bar{u} + u_*[\frac{p}{\kappa_i} + \frac{1-p}{\kappa_o} + a(\frac{1}{3} - s + s^2 - \frac{1}{3}s^3)] \qquad (4)$$

In the above equations, the relative elevation of the interception points between the inner and middle regions is set at η=0.1, as proposed by Lee and Yu (1990), while that for the middle and outer regions is set at η=0.5. This is confirmed by the data taken by Nezu and Rodi (1985).

The Karman constant outside the inner region can be separated into two constants κ_{or} and κ_{os} to represent the cases of clear water and sand-silt water respectively. The regression relation for κ_{or} is (Lee & Yu, 1990):

$$\kappa_{or} = -0.0062\frac{\bar{u}}{u_*} + 0.4914 \qquad 14 < \frac{\bar{u}}{u_*} < 24 \qquad (5)$$

The variation of κ_o due to the effects of suspended sediment is: (Lee & Yu, 1990)

$$\frac{1}{\Delta\kappa} = 0.234(\log R_i)^3 + 1.777(\log R_i)^2 + 4.587(\log R_i) + 4.045 \qquad 5\times10^{-3} < R_i < 5\times10^{-1} \quad (6)$$

where $R_i = [(\rho_s - \rho_w)/\rho_w](C_{0.05}\omega_s/\bar{u}S_f)$ is the Richardson number, ρ_s and ρ_w are the densities of suspended sediment and water separately, S_f is energy slope, ω_s is fall velocity of the suspended sediment, $C_{0.05}$ is sediment concentration at η=0.05 and $1/\Delta\kappa = 1/\kappa_{os} - 1/\kappa_{or}$. The value of $C_{0.05}$ can be calculated by the following formula as proposed by Lee and Yu (1990):

$$\frac{C_{0.05}}{\bar{C}} = 1.9(\frac{\omega_s}{u_*})^{0.19}\kappa_{os}^{-0.844} \qquad (7)$$

where $\bar{C}$ is the depth-averaged sediment concentration. The value of κ_{os} can be calculated by Eqs. 6 and 7.

Assuming hydrostatic pressure distribution, the transverse momentum equation can be simplified as:

$$-\frac{u^2}{r} = -gS_r + \frac{\partial}{\partial z}(\varepsilon\frac{\partial v}{\partial z}) \qquad (8)$$

where r is the radius of curvature, S_r is the transverse water surface slope, g is gravitational acceleration, v is secondary current and ε is eddy viscosity. By the definition of eddy viscosity, $\tau = \rho\varepsilon\frac{du}{dz}$, the corresponding ε distributions in the inner, middle and outer regions are:

$$\varepsilon = \frac{\kappa_i u_* d}{\eta^*}\eta(1-\eta)(\eta^* - \eta) \qquad 0 \le \eta \le p \qquad (9)$$

$$\varepsilon = \frac{\kappa_o u_* d}{\eta^*}\eta(1-\eta)(\eta^* - \eta) \qquad p < \eta \le s \qquad (10)$$

$$\varepsilon = \frac{u_* d}{2a\eta^*}\frac{\eta(1-\eta)}{\eta - b} \qquad s \le \eta \le 1 \qquad (11)$$

where $\eta^* = (s + \sqrt{s^2 + (2/a\kappa_o)})/2$; and $b = (s - \sqrt{s^2 + (2/a\kappa_o)})/2$.
From Eq. 8, assuming v equals to zero at the channel bed, the secondary current profile can be derived as:

$$v(\eta) = d^2 g\int_0^\eta \frac{S_r(\eta - 1) + \int_\eta^1 \frac{u^2}{gr}d\eta}{\varepsilon}d\eta \qquad (12)$$

Letting $S_r = \alpha(\bar{u}^2/rg)$, and substituting Eqs. 1, 2, 3, 9, 10, 11 into Eq. 12, the secondary current profiles for the three different regions are:

$$\frac{vr}{\bar{u}d} = \frac{\eta^*}{\kappa_i}\frac{\bar{u}}{u_*}G_1(\eta) \qquad 0 \le \eta \le p \tag{13}$$

$$\frac{vr}{\bar{u}d} = \frac{v(p)r}{\bar{u}d} + \frac{\eta^*}{\kappa_o}\frac{\bar{u}}{u_*}G_2(\eta) \qquad p \le \eta \le s \tag{14}$$

$$\frac{vr}{\bar{u}d} = \frac{v(s)r}{\bar{u}d} + 2a\eta^*\frac{\bar{u}}{u_*}G_3(\eta) \qquad s \le \eta \le 1 \tag{15}$$

$$G_1(\eta) = \int_0^\eta \frac{I_9(\eta)}{I_7(\eta)}d\eta$$

$$G_2(\eta) = \int_p^\eta \frac{I_5(\eta)}{I_7(\eta)}d\eta$$

$$G_3(\eta) = \int_s^\eta \frac{I_6(\eta)}{I_8(\eta)}d\eta$$

where

$$I_1 = (\frac{1}{\kappa_o} - \frac{1}{\kappa_i})\ln p$$

$$I_2(\eta) = \eta(\ln\eta - 1)$$

$$I_3(\eta) = \eta(\ln^2\eta - 2\ln\eta + 2)$$

$$I_4(s,\eta) = \alpha(s-\eta) - (\frac{u_s}{\bar{u}})^2(s-\eta) - \frac{1}{\kappa_o^2}(\frac{u_*}{\bar{u}})^2[I_3(s) - I_3(\eta)] - \frac{2}{\kappa_o}\frac{u_s}{\bar{u}}\frac{u_*}{\bar{u}}[I_2(s) - I_2(\eta)]$$

$$I_5(\eta) = I_4(1,\eta) + I_{10}(s)$$

$$I_6(\eta) = I_4(1,\eta) + I_{10}(\eta)$$

$$I_7(\eta) = \eta(1-\eta)(\eta^* - \eta)$$

$$I_8(\eta) = \eta(1-\eta)/(\eta - b)$$

$$I_9(\eta) = I_5(p) - (\frac{u_s}{\bar{u}} + I_1\frac{u_*}{\bar{u}})^2(p-\eta) - \frac{2}{\kappa_i}\frac{u_*}{\bar{u}}(\frac{u_s}{\bar{u}} + I_1\frac{u_*}{\bar{u}})[I_2(p) - I_2(\eta)]$$
$$- \frac{1}{\kappa_i^2}(\frac{u_*}{\bar{u}})^2[I_3(p) - I_3(\eta)] + \alpha(p-\eta)$$

$$I_{10}(\eta) = -a^2(\frac{u_*}{\bar{u}})^2(0.2 - s + 2s^2 - s^3 + s^4 - 0.2\eta^5 + \eta^4 s - 2\eta^3 s^2 + 2\eta^2 s^3 - \eta s^4)$$
$$- 2a\frac{u_*}{\bar{u}}\frac{u_s}{\bar{u}}(\frac{1}{3} - s + s^2 - \frac{\eta^3}{3} + \eta^2 s - s^2\eta)$$

$$-\frac{2a}{\kappa_o}\left(\frac{u_*}{\bar{u}}\right)^2\left[-\frac{1}{9}+\frac{s}{2}-s^2-\frac{\eta^3}{3}\left(\ln\eta-\frac{1}{3}\right)+s\eta^2(\ln\eta-0.5)-s^2\eta(\ln\eta-1)\right]$$

The α value in above equations can be calculated by $\int_0^1 v d\eta = 0$. From Eqs. 13, 14 and 15, it can be seen that the factors that affect the strength of dimensionless secondary current, $vr/\bar{u}d$, are a, p, s, κ_i, κ_o and $\bar{u}/u_*$. The $(\bar{u}/u_*)$ can be calculated by the equation suggested by Keulegan (1938)

$$\frac{\bar{u}}{u_*} = 6.25 + 5.75 \log \frac{R}{k_s} \tag{16}$$

where R is the hydraulic radius and k_s is the height of surface roughness. In a meandering channel bend, the hydraulic radius is larger at the outside bend, but due to hydraulic sorting, the mean particle size is also larger there. According to Yen (1967) and Yen & Ho (1990), the friction coefficient at the outside bend is smaller than that of the inside bend. Using Eq. 5, the transverse variation of κ_o value can thus be obtained.

Experiments

Series of experiments were conducted to verify the above theories. The experimental flume is a 180 degree, 1 m wide, 0.8 m deep and 40 m long channel bend. The radius of curvature of the channel center line is 4 m. Three different sediment concentrations, 0%, 1%, and 3% by volume were used for fixed bed conditions. Another three concentrations, 0%, 0.7% and 1.4% by volume, were used for movable bed conditions. The suspended material used was Kaolin with mean grain size equals to 0.004 mm. The average flow conditions at the channel centerline are listed as follows: depth = 0.138 m, average velocity = 0.53 m/sec, bed slope = 0.00085 and Reynolds number = 81,000. The velocity is measured with a two-component electromagnetic meter and suspended samples were taken by a siphon tube.

The results show that the suspended sediment is fairly uniformly distributed in the vertical and lateral directions. This is due to the smallness of the suspension index, ω_s/u_*. The typical secondary current profiles are shown in Fig. 2. The secondary current profile were not strongly influenced by sediment concentrations due to the small ω_s/u_* value and low concentrations. Smaller experimental flumes and coarser suspended materials can produce better experimental data.

Results and Discussions

Sensitivity analyses were performed to investigate the effect of coefficients a, and $\bar{u}/u_*$ on the longitudinal and transverse velocity profiles. The effects of coefficient a are shown in Figures 1 and 3 respectively. The coefficient a can reflect the downward shiftment of the maximum velocity, and if a is large enough, it will generates inward movement of the secondary current near the free surface.

The effects of $\bar{u}/u_*$ are shown in Fig. 4. It shows that the strength of the secondary current increases as $\bar{u}/u_*$ increases.

The effects of concentration on the secondary currents are shown in Fig. 5. The strength of the secondary current increases as the sediment concentration increases. According to the field data taken from the Yellow River (Chien et. al. 1987), the sediment concentration at the inside bend is larger than that of the outside bend. Hence the secondary current is affected more at the inside bend.

Conclusions

1. The coefficient a can reflect the downward shiftment of the maximum velocity and if a is large enough, it will induce the inward movement of the secondary current near the free surface.
2. The strength of the secondary current increases as $\bar{u}/u_*$ increases.

3. The strength of the secondary current increases as the sediment concentration increases.
4. The influence of the suspended sediment can not be reproduced in the experiments with fine suspended material and low concentrations.

References

Chien, N., Zhang, R. and Chow. J.T. (1987). *River Morphology*, Science Press, Beijing, china. (In Chinese)

Hussein, A.S.A. and Smith, K.V.H. (1986). "Flow and Bed Deviation Angle in Curved Open Channels", Journal of Hydraulic Research, Vol.24, pp.93-108.

Keulegan, G.H. (1938). "Laws of Turbulent Flow in Open Channels", J. Res., Nat. Bureau of standards, Vol.21, No.6, PP.707-741.

Lee, H.Y. and Yu, W.S. (1990). "Velocity Profile of Sediment-Laden Flow", Submitted to ASCE Journal of Hydraulic Engineering, for possible publication.

Nezu, I. and Rodi, W. (1985). "Experimental Study on Secondary Currents in Open Channel Flow", Proc. of 21st Congress of IAHR, Melbourne, Australia, PP.114-119.

Yen, C.L. (1967). "Bed Configuration and Characteristics of Subcritical Flow in a Meandering Channel", Thesis presented to University of Iowa in partial fulfillment of the requirements for the degree of Doctor of Philosophy.

Yen, C.L. and Ho, S.Y. (1988). "Variation of Some Flow Characteristics in Channel Bends", Proc. of 6th Congress of APD-IAHR, Kyoto, Japan.

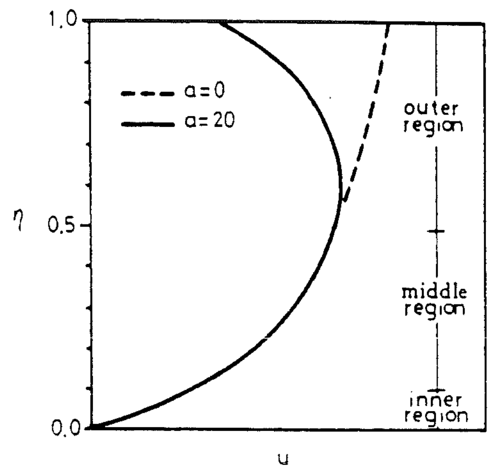

Fig. 1. Vertical Distribution of Longitudinal Velocity

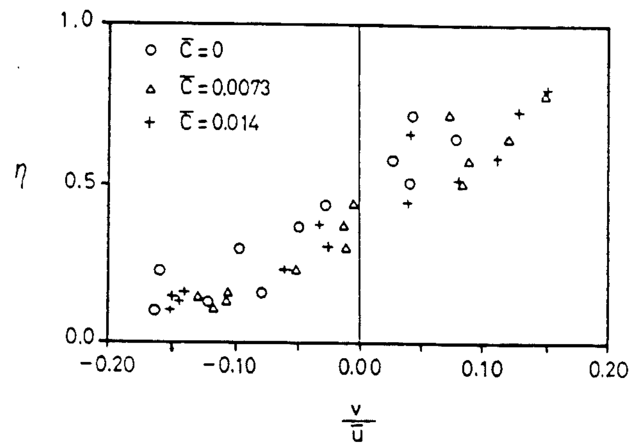

Fig. 2. Influence of Sediment Concentration on Secondary Current (Measured)

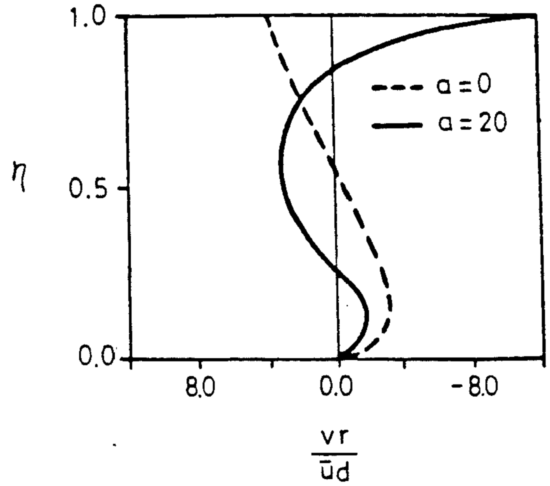

Fig. 3. Influence of Coefficient a on Secondary Current

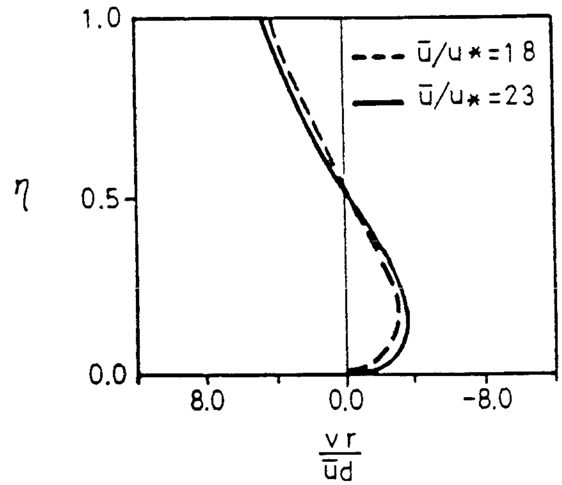

Fig. 4. Influence of $\frac{a}{u_*}$ on Secondary Current

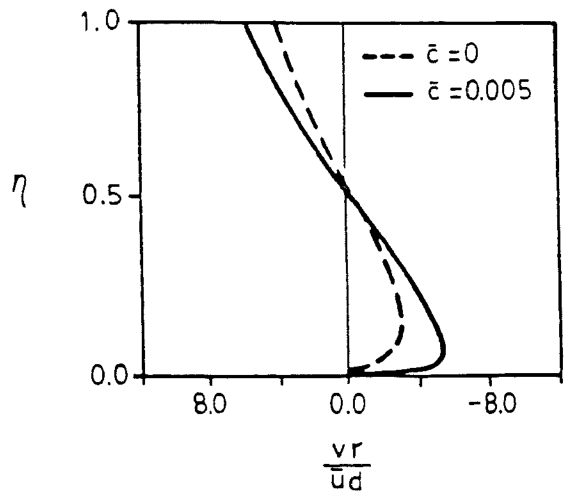

Fig. 5. Influence of Sediment Concentration on Secondary Current

SIMILARITY STUDY OF SEDIMENT TEST IN DATENGXIA RESERVOIR

Yin Hongchang and Yuan Runbao
Scientific reserch institute of Shong-Liao Water Resources committee P.R China

Abstract

To counter the sediment problem of Datengxia reservoir, the test discussed in this paper imitated movement of suspended and bed load in one model. In the design of the model, according to the principle of geometry similarity, current movement similarity and sediment movement similarity, the movement of suspended and bed load was imitated at the same time using the same material. Also the similarity of flocculation of suspended load was imitated. The better result has been obtained in the imitation of movement of current and sediment. The disign way in this test can be consulted for sediment test of other related. project

1 Introduction

In order to study sediment problem of Datengxia project, the sediment model test was developed. The great attention should be paid to the depositing law of sediment in the approach channel, regime of flow when fleet come in or out the gate of approach channel, the influence of bed load transportation to intate of the power station and the distribution law of sediment in the reservoir. Therefore, the simlarity of regime of flow, velocity distribution and sediment movement must be guaranteed in the test.

2 Similarity of regime of flow and velocity distribution

2.1 Main characteristic of the river reach tested

(a) Flow structure is very complex and regime of flow change along the river is very sharp

Datengxia project is situated in the vicinity of the exit of gorge. The topography is very spesific in this reach. The river reach has a 90-degree bend. The deflecting stones of two bank extend into the river. There are some stones and rock beams in the main bed. There is a pool of 71.5 m deep in the bottom of the bed. All of those determine characteristic that main flow moves along the right bank and there are some complex regime of flow which are bubble, whirlpool, current like scissors, reflow and so on. There are some stnes like spur dike on the left bank after the gorge. It not only protect the left bank, but also forces the main flow and the deep current flowing along the right bank. In the exit of the gorge, there is the tributary named Ganwang river. The current suddenly diffuses in the test reach.

(b) The roughness of upstream and downstream of the dam site is very different in the test reach

Because of the resistance influence of partial topography, the roughness of upstream is comparatively large, $n=0.07--0.123$, the downstream of the dam site gradually becomes open, $n=0.04--0.06$, having characteristic of mountain stream.

2.2 Design principle of the model

In order to make regime of flow and velocity distribution similar, the following problem must be considered

(a) To adopt undis tored model in order to guarantee geometry similarity

Because current structure is very complex in this reach, the boundary condition of the river gives a large influence to the circulation and bubble structure. It is very difficult to express this influence element by theoretical formulas. Therefore, guaranteeing geometry similarity and adopting undis tored model is a important condition to guarantee regime of flow and velocity distribution similarity.

(b) To meet the similarity of ratio of initial to gravity and ratio of resistance to gravity.

The plane current movement equations are

$$V_x\frac{\partial V_x}{\partial x} - V_y\frac{\partial V_x}{\partial y} = gJ_x - \frac{V^2x}{c^2h}$$

$$V_x\frac{\partial V_y}{\partial x} + V_y\frac{\partial V_x}{\partial y} = gJ_y - \frac{V^2y}{c^2h}$$

in which

V: velocity

J: slope

c: chezy coefficient

h: depth of water

g: acceleration of gravity

the following can be obtained

$\lambda v = \lambda_l^{1/2}$ ...... (1)

$\lambda n = \lambda_l^{1/6}$ ...... (2)

where

λ: scale

n: roughness

l: lenth

The geometry similarity provides main condition for the similarity of ratio of initial to gravity. To guarantee the similarity of regime of flow and velocity distribtion, the simple multiple roughness similarity is not enough. The similarity of roughness distribution along the river width and the similarity of roughness of bed and bank of the river must be guaranteed. The partial resistance loss caused by the partial topography is important part of resistance loss in the river reach tested, especially in the upstream river reach of the dam site. Therefore, it is a important element to reach the similarity of ratio of resistance to gravity that partial topography is similar to prototype in the disign of the model.

2.3 Contrast test

In order to check the similarity of the regime of flow, the verifying test has been made.

(a) Contrast of the regime of flow between prototype and model

When Q=5800 m^3/s the main flow moves along the deep trough on the right bank after the gorge. Ganwang river do not divide the current. The water depth up the shoal is very shallow. Flow drops and the regime of flow between model and prototype is very similar in the place of deep slope. When Q=24100 m^3/s, because of the influence of two bank in the bend of the river, the current seperates oneself from boundry obviously and from a large flow like scissors. The flow roll and foam very violent in the deep pool region. Large range bubble region occupy 2/3 of the river width. There is a large range reflow downstream the Ganwang river mouth. The main stram concentrate in the right bank. The regime of flow of prototype is similar to model. It can be seen in Fig.1.

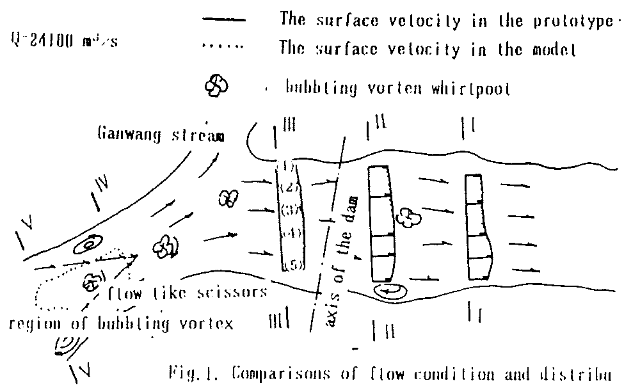

Fig.1. Comparisons of flow condition and distribu and distribution of velocity between the model and the prototype.

section	velocity / measuring poing	①	②	③	④	⑤
I - I	Vp(m/s)	2.8	3.3	3.6	4.2	3.2
	Vm(m/s)	2.6	3.2	3.5	4.2	3.2
II - II	Vp(m/s)	2.3	3.4	3.6	4.3	2.8
	Vm(m/s)	2.1	3.1	3.3	4.4	2.8
III -- III	Vp(m/s)	3.1	3.7	4.5	4.5	4.1
	Vm(m/s)	3.1	3.7	4.0	4.0	3.8
IV -- IV and V -- V	Vp(m/s)	2.2		3.3		
	Vm(m/s)	1.7		3.9		

(b) Contrast of the velocity in the surface between prototype and model

The flow disorders and moves rapidly in the flood period. When Q=24100m³/s, the contrast of velocity in the surface between model and prototype can be seen in Fig.1.
The velocity distribution is similar.

(c) Check of roughness

When Q=5800 m³/s, the roughness of deep trough was checked. When Q=11160 m³/s, 17520 m³/s; the roughness of the river when current overflow was checked. When Q=33600 m³/s, the resistance condition of whole section including shoal was checked . The similarity of water surface is very good through the test releasing water repeated. It can be seen in Fig.2. It meets the demand of resistance similarity.

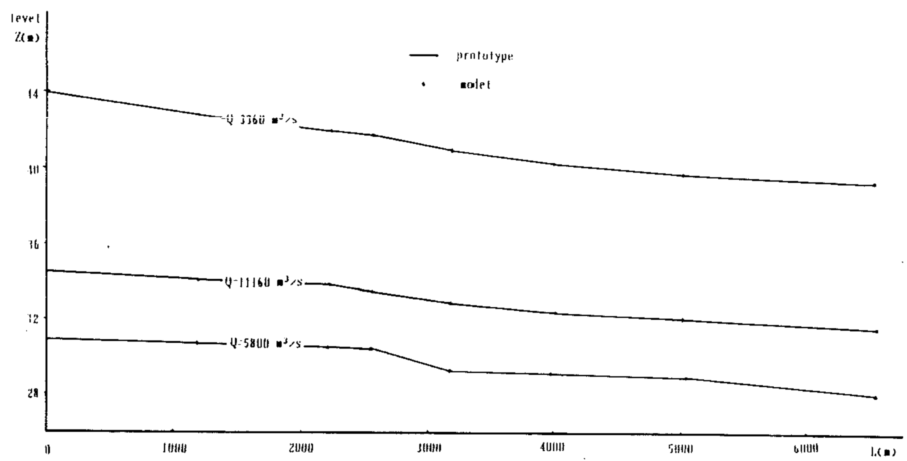

Fig.2. Comparisons of hydraulic grade line between model and prototype

The similarity of velocity distribution and regime of flow establish a foundation for the similarity of the sediment movement. In order to study the sediment problem of the project, the similarity of sediment movement is necessary.

3 Similarity of sediment movement

3.1 Desing principle

Scouring and depositing of each size sediment in the river is entirety of unity. It influences and restricts each other. In order to solve the practical problem of project better, it is necessery to deplicate movement of each size sediment in one model, that is to do synthetical test of suspended and bed load in one model.

The sediment of the river reach tested comes principally in the flood period. The runoff in the flood period occupy 70% of runoff in the whole year. The sediment in the flood period occupy 95% of the sediment in the whole year. The median diameter of suspended load $d_{50}=0.023$ mm. The sand bed load $d_{50}=0.29$ mm, the cobble bed load $d_{50}=31$ mm. Because the diameter of suspended load is too small, flocculation in the river water is very violent. The attention must be paid when imitating.

The common disequilibrium formula of transporting sediment are

$$\frac{ds}{dx} = \frac{\alpha \cdot w}{q}(S - S^*)$$

in which

S : average content of sediment

S^* : transporting sediment ability of the flow

α : coefficient

q : discharge of unit width

w : sinking velocity

It can be obtained that suspended load similarity must meet

(1) suspension similarity condition $\lambda w = \lambda v$ ...... (3)

(2) transporting sediment similarity condition $\lambda s = \lambda s^*$ ......(4)

(3) time scale of scouring and depositing

$$\lambda_{t_1} = \frac{\lambda_l^{1/2}\lambda r'}{\lambda s} \quad \text{......(5)}$$

in which

r' : unit dry weight

t : time

As to bed load, it must meet

(4) critical similarity condition $\lambda_{V_0} = \lambda v$ ......(6)

Equation of varation of the river bed caused by bed load is

$$\frac{\partial q_s}{\partial x} = -r' \frac{\partial z}{\partial t}$$

in which

q_s: sediment discharge of unit width

The time scale of scouring and depositing can be obtained

$$\lambda t_2 = \frac{\lambda_{r'}\lambda_h\lambda_l}{\lambda q_s}$$

The scales of the model can be obtained through the calculation. It can be seen in table 1.

There is a quantitative interchange between bed load and suspended load.

Table 1. number of each scale

Item	scale name	scale symbol	number	Item	scale name	scale symbol	number
geometry	geometry	λl	150	cobble bed load	diameter	λd	4.53
	Velocity	λv	12.25		transport rate per unit width	λg_s	140
	roughness	λn	2.305		time of scouring silt	λt_4	405
suspended load	diameter	λd	0.54	coarse grain bed load	diameter	λd	0.64
	settling	λw	12.25		transport rate per unit width	λg_s	140
	critical velocity	λv_0	12.25		time of scouring silt	λt_s	350
	sediment concentration	λs	0.0765	density flow	velocity	λu	12.25
	time of scouring silt	λt_s	350		time of scouring silt	λt_2	350

In order to meet interchange condition and similarity of shape variation of souring and depositing, the model sand of same material must be ahopted, that is polystyrene plastic ball which specific gravity is 1.05 t/m^3. Form the sinking velocity and critical test, It can be seen that model sand meets the similarity of critical and sinking.

After reservoir is created, suspended load will flocculate and depesit in the upstream approach channel. Therefore, the sand must be added accoding to grade curve after suspended load flocculated when testing (seen in Fig.3). [1].

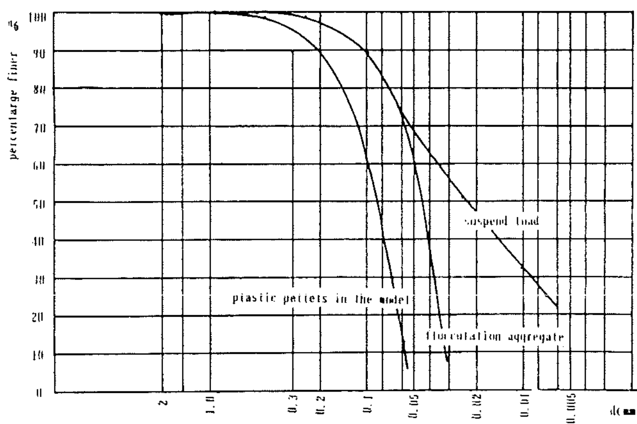

Fig. 3. particle-size distribution curves of suspend load, of flocculation aggregate, of plastic pellets in the model.

3.2 Sediment verification test

In order to check the correction of selecting sand in the model, model test was done according to water and sediment process in the prototype.

(a) Contrast of scope and volume of scouring and depositing between model and prototype

From the test, there are two stable depositing district which are around Ganwang river mouth and from 50# to 64# section, depositing appear when discharge is small, and scouring appear when discharge is large ($Q > 20000\ m^3/s$). From 35# to 49# section, scouring and depositing on the shoal is similar to prototype, depositing volume is small when discharge is small, and scouring volume is large when discharge is large. The phenomenon of scouring and depositing is very obvious. Besides, there are some deposition in the reflow district formed by the influence of river bank. The scope and section varition of scouring and depositing between model and prototype is basically similar (seen in Fig.4). The depositing volume of each district is very close.

Table of deposition ($10^4 m^3$)

zone	Ganwang Zone	35#~55#
prototype	6	52.6
model	7	55.5

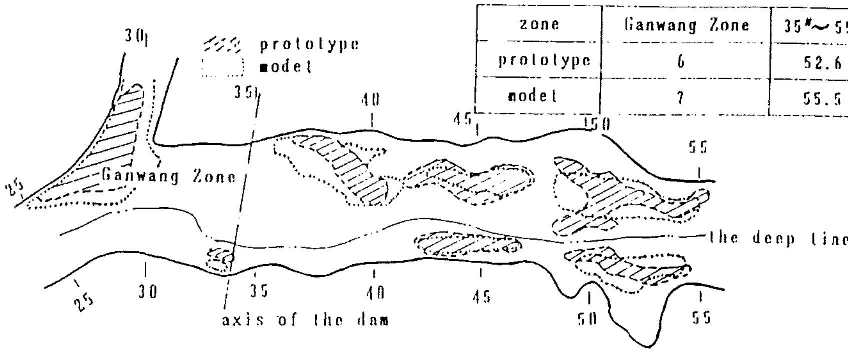

Fig.4 Range comparison between model and prototyqe deposition

(b) Verification of suspended and bed load movement

Because of action that current roll and foam in the bubble region, the distribution of sediment is very even in the exit of the gorge.The lower it is, the larger the sediment charge difference between right and left bank is, which can reach 2 or 3 times.It can be known that bed sediment moves along the deep trough in the right bank.This corresponds to natural situation.

4 Concluding remarks

4.1 Because of the charicristic of the river reach tested,adopting undistored model and paying attention to partial topography provide important condition for guarateeing the similarity of current movement especially similarity of the regime of flow and velocity distribution out of the gate of approach channal. The test has shown that current movement in the model is similar to that in the prototype.

4.2 So long as current, suspended load and bed load all meet the similarity of gravity, resistance, critical Sinking transporting sediment,time scale of suspended and bed load and density current, and the model sand is same material, the scouring and depositing of sediment can be imitated in one model.

4.3 According to characteristic of the project and the river reach tested, the test has shown that design of model and selection of sand are reasonable. It can make flow condition including reflow and bubble similar to prototype. It can repeat movement law of suspended and bed load, the place and volume of securing and depositing are similar to prototype practically.

The correction of model design and selecting sand provide favourable condition for the study of sediment problem of Tatengxia project.

References

[1] Yin Hongchang and Yuan runbao, "Analysis and Simulation on Suspended Load Flocculation in Datengxia Reservoir"
Proceedings of 6th Congress of the APD-IAHR,1988,7.

Session 12A

Density Currents

THE INTERNAL HYDRAULICS OF TUNNELLED OUTFALLS
LESSONS FROM THE MODEL STUDIES OF THE SYDNEY OUTFALLS

by D L Wilkinson
Water Research Laboratory, University of New South Wales
Manly Vale NSW 2093 Australia

Introduction

The ability to successfully purge seawater from an ocean outfall is a basic design requirement. Failure to do so will cause forced circulation of seawater through the diffuser section of the outfall which at the very least will result in substantial hydraulic inefficiency and at the worst lead to partial or complete blockage of sections of the diffuser due to accumulation of sediment and/or marine growth. Purging capability is required at commissioning of the outfall and following any subsequent shut-down of effluent inflow causing seawater to intrude into the risers.

An outfall will purge itself of seawater when the effluent flow reaches a critical value. This flow rate increases as the half power of the length of the risers. Once an outfall has been purged of seawater, the ports themselves become the internal control points for any subsequent intrusion of seawater. Port velocities can typically reduce by an order of magnitude below that required for purging before the outfall will again become flooded with seawater.

The purging capability of outfalls has only become an issue over the past decade following the construction of tunnelled outfalls with risers which are very much longer than those of conventional outfalls.

This paper examines various strategies which were investigated as a means of minimising the effluent discharge required to purge seawater from ocean outfalls. The studies formed a component of the hydraulic model investigations associated with the Sydney Ocean Outfalls. Before proceeding further however, the purging criterion is briefly reviewed.

Purging Criterion

The geometry of a typical tunnelled outfall is shown in Figure 1. The first section of the tunnel is steeply inclined to a point of maximum depth which is determined by geological integrity of the surrounding strata, thereafter the tunnel gently slopes upwards to facilitate dewatering of the tunnel during construction. The tunnel terminates at a riser section through which the effluent is conveyed to seabed diffusers from where it is finally discharged into the ocean.

Purging of the outfall consists of several phases. Firstly there is the displacement of seawater from the incline [Figure 1(a)], on reaching the bottom of the incline the effluent flows along the gently sloping section of the tunnel [Figure 1(b)]. The buoyancy of the effluent will tend to produce a layered flow however behind the front where the layer depth is determined by friction, the effluent may occupy the full depth of the tunnel if the flow exceeds a certain value. On reaching the riser section of the tunnel, effluent will flow into some risers while others remain filled with seawater [Figure 1(c)]. It is at this stage that seawater may commence to circulate through the riser section of the outfall. The presence of relatively buoyant effluent in a riser causes a reduction in the hydrostatic pressure at the bottom of that riser compared with the pressure at the bottom of a riser which still contains seawater. The magnitude of this pressure differential δp is given by

$$\delta p = \left(\rho_o - \rho_e\right) g h$$

in which ρ_o = seawater density
ρ_e = effluent density
g = gravity
h = height of the riser

This pressure differential causes a downward flow in the riser containing the seawater which will then mix with effluent in the tunnel before returning to the ocean through the discharging risers. Only when the dynamically and frictionally induced pressure drop through the discharging riser–diffuser combination is sufficient to offset the densimetric pressure difference will the seawater cease to circulate. The purging criterion can therefore be expressed as

$$\left(\rho_o - \rho_e\right) g h = C_L \frac{\rho_e V^2}{2}$$

in which C_L = combined friction and dynamic loss coefficient for the riser–diffuser combination
V = mean velocity of discharge through the diffuser ports

A relationship of this form was first put forward by Munro (1981) and has been verified in subsequent experimental studies [Wilkinson (1984, 1985)]. For the purposes of the following discussion the purging criterion is most conveniently described in terms of the exit velocity from the diffuser ports when it becomes

$$V = \left(\frac{2 \Delta g h}{C_L}\right)^{1/2} \qquad (1)$$

where

$$\Delta = \left(\rho_o - \rho_e\right) / \rho_e$$

Recent major tunnelled outfalls have risers some 50 m to 60 m in length and with $\Delta = 0.026$ for typical densities of seawater and effluent and C_L of order unity, Eq. 1 indicates that port velocities in excess of 5 m/s are required to purge these outfalls. Port velocities of between 10 m/s and 15 m/s are generally recognised as the maximum for deepwater outfalls where replacement of worn nozzles is a difficult and costly exercise. Consequently purging of the outfalls requires an effluent inflow of between one third and one half of the design maximum and such flows may not be achieved on a regular basis. This is particularly true if there is significant stormwater flow into a sewage system. Consequently means by which purging can be achieved at reduced flow rates are well worth investigation.

Strategies for Facilitating Outfall Purging

Single riser outfalls

Purging of high riser outfalls would be much facilitated if there were only a single riser in which case the work by Jorg and Scorer (1952) and Wilkinson (1989) has shown that seawater would be displaced from the riser when a densimetric Froude number based on the diameter and mean velocity in the riser attained a value of order unity. For a single riser outfall with a diameter of say 2 m, this would amount to purging at a comparatively modest velocity of about 0.7 m/s in the riser. The remainder of the outfall could be of conventional design utilising much lower port velocities than would be employed on a multi-riser outfall. Construction of the diffuser section for such an outfall in deep water does pose problems however.

Premixing of the effluent with seawater

It can be seen from Eq. 1 that a reduction of the buoyancy of the effluent which can be produced by mixing it with seawater before it reaches the risers, will result in a lower purging velocity. This reduction in the buoyancy of the effluent can be produced in a number of ways.

Salt water can be pumped into the outfall with the effluent during initial purging and once this is completed the pumped flow of seawater can be gradually shut down. The disadvantage of this method is the cost associated with the seawater pumping facility which would only be used intermittently. In fully pumped systems premixing may be cost effective in that larger port sizes could be adopted thereby saving in ongoing pumping costs. Additionally the premixing pumps could be used as booster pumps during periods of high effluent inflow.

Mixing devices in the tunnel

Charlton (1985) has advocated the use of a horizontal contraction of the tunnel walls to form a venturi just upstream from the riser section of an outfall tunnel, as shown in Figure 2. The original purpose of the venturi was to inhibit seawater intrusion into the tunnel at extremely low rates of effluent flow once seawater had intruded into the diffusers. Such a device was tested in Sydney Outfall studies and it was found to be of minor assistance with purging at one outfall (Malabar) where because of the relatively large tunnel cross-section, layered flow persisted in the tunnel even after the riser section itself had purged.

The salt water residing in the tunnel after initial purging of the risers was slowly entrained into the upper effluent layer and eventually all of the salt water was removed. It was found that at flow rates which were appreciably less than the purging flow for this outfall, the venturi began to function as an internal control and an internal hydraulic jump formed downstream of the venturi, as shown in Figure 3. Entrainment of seawater into this jump caused a reduction of the buoyancy of effluent and a reduction of between 4% and 10% in the purging flow, depending on the form of the effluent hydrograph. The effect of the venturi was most pronounced when the starting flow was close to the purging flow. Under these conditions a deeper saline layer existed in the tunnel than was the case if the same flow rate was achieved through a hydrograph commencing with a much lower starting flow. In these circumstances considerable seawater had already been removed from the tunnel by interfacial entrainment before critical flow developed in the venturi.

More effective mixing devices than the venturi could have been built into the tunnel, for example a helical screw to fully invert the layers as shown in Figure 4. Some courage would be required to install such a device in an effluent tunnel due to the possibility of grease accumulation, restriction of access and the increased possibility of blockage.

Mixing produced by boundary friction in the tunnel

When the effluent first reached the gently inclined section of the tunnel, its buoyancy caused it to propagate up the incline towards the seaward end of the tunnel. The form of the intrusive layer depended on the rate of effluent inflow. At low rates of inflow a layered flow developed with the effluent forming an intrusive layer above the nearly static seawater still residing in the tunnel. As the effluent inflow increased its layer depth in the tunnel increased until ultimately it occupied the entire tunnel cross-section. The flow in these circumstances was the densimetric equivalent of full pipe flow in a culvert with a simple force balance existing between the along slope component of buoyancy and boundary friction. This flow state is described by

$$Q_f = \left[\frac{\pi^2}{32\,f} \, \Delta g \, D^5 \, S_o \right]^{1/2} \tag{2}$$

where Q_f = flow rate required to first establish full effluent flow in the tunnel
f = tunnel friction coefficient
D = tunnel diameter
S_o = tunnel slope

Figure 5 shows the form of the intrusive layer when the flow rate was less than Q_f [$Q/Q_f = 0.71$ (crosses)] and when the flow rate exceeds Q_f [$Q/Q_f = 1.04$ (circles)] and in both instances layered flow existed at the front of the intrusion where the force balance was dominantly inertia and gravity rather than friction and gravity as exists further behind the front. With $Q/Q_f = 0.71$ the effluent layer ultimately became a uniform flow over a nearly quiescent seawater layer. With $Q/Q_f = 1.04$ the effluent layer ultimately occupied the full tunnel cross-section so that the seawater lying beneath the front was pushed forward with the front. In this case boundary friction both above and below the interface produced turbulence which caused the interface to become increasingly diffuse as it progressed along the tunnel. Ultimately no clear interface was visible and the effluent was diffused across the entire tunnel cross-section. The initial depth of the front when it first formed at the base of the steeply inclined section was very nearly one half the tunnel depth as predicted by Benjamin (1968) in his classic paper on the motion of gravity currents. Thus the mixing of the effluent frontal region with the seawater below, caused by turbulence due to boundary shear, locally reduced the buoyancy of the effluent by a factor of two.

This was confirmed by a reduction in the flow required to purge the outfall by a factor of 0.68 which compared closely with the anticipated reduction of $1/(2)^{1/2} = 0.71$ due to the mixing. To take maximum advantage of this mixing process the tunnel diameter should be designed so that full pipe flow develops when the flow rate is $1/(2)^{1/2}$ that required to satisfy the purging condition expressed in Eq. 1. However, for the mechanism to be effective, it is necessary that the effluent inflow be close to Q_f otherwise the outfall would fail to purge. Advantage can only be taken of this means of reducing the purging flow if the effluent inflow can be regulated.

Conclusions

A number of means by which the flow required to purge a high riser outfall can be reduced were investigated. It was pointed out that if only a single riser is utilised purging would generally not be a problem. In multiple riser outfalls various mechanisms for reducing the buoyancy of the effluent by mixing with seawater were discussed and while all produced some reduction in the purging flow they placed restrictions on how the outfall could be operated. These various options should certainly be investigated by outfall designers but their limitation carefully considered.

Acknowledgement

The author would like to thank the Sydney Water Board ocean outfall project team for their assistance during this study and special thanks are due to Prof Norman Brooks for many fruitful discussions and support.

References

Benjamin, TB (1968), "Gravity currents and related phenomena", *J. Fluid Mechanics*, 31, Part 2, 209-248.

Charlton, JA (1985), "The Venturi as a saline intrusion control for sea outfalls", *Proc. Instn. Civ. Engrs.* Pt. 2, 79, 697-704.

Jorg, O and Scorer, RS (1967), "An experimental study of cold chimneys", *Atmos. Environ.*, 1, 645-654.

Munro, D (1981), "Sea water exclusion from tunnelled outfalls discharging sewage", *Water Resource Centre, Stevenage Laboratory Report* 7-M.

Wilkinson, DL (1984), "Purging of saline wedges from ocean outfalls", *J. Hydraulic Eng., ASCE*, 110 (HY12), 1815-1829.

Wilkinson, DL (1985), "Seawater circulation in sewage outfall tunnels", *J. Hydraulic Eng., ASCE*, 111 (HY3), 846-855.

Wilkinson, DL (1988), "Avoidance of seawater intrusion into ports of ocean outfalls", *J. Hydraulic Eng., ASCE*, 114 (2), 218-230.

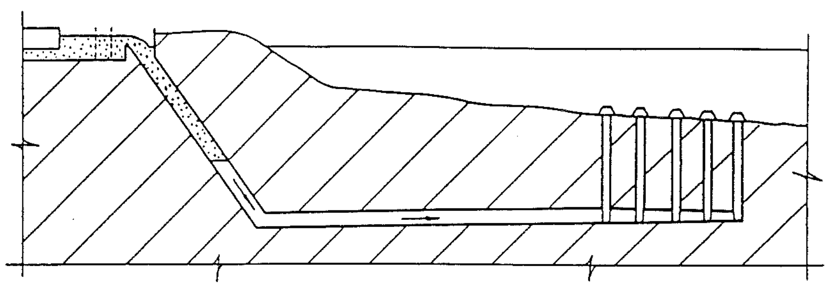

A: DISPLACEMENT OF SEAWATER FROM THE DROPSHAFT

FIGURE 1

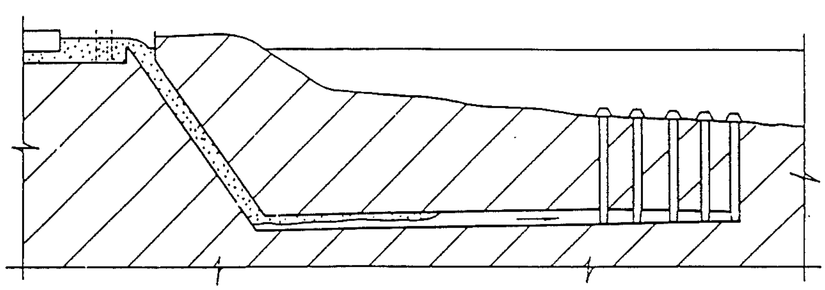

B: INTRUSION OF THE EFFLUENT ALONG THE TUNNEL

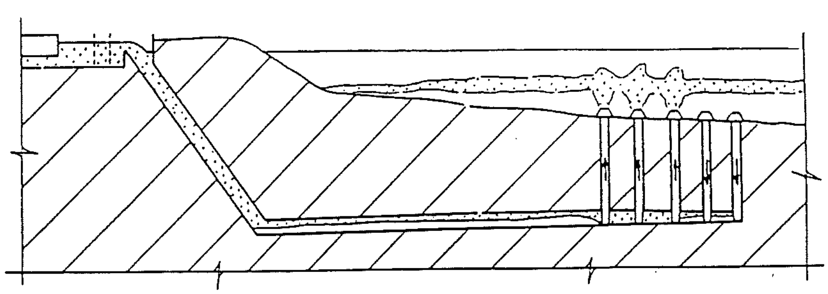

C: SEAWATER CIRCULATION THROUGH UNPURGED RISERS

FIGURE 2
VENTURI GEOMETRY

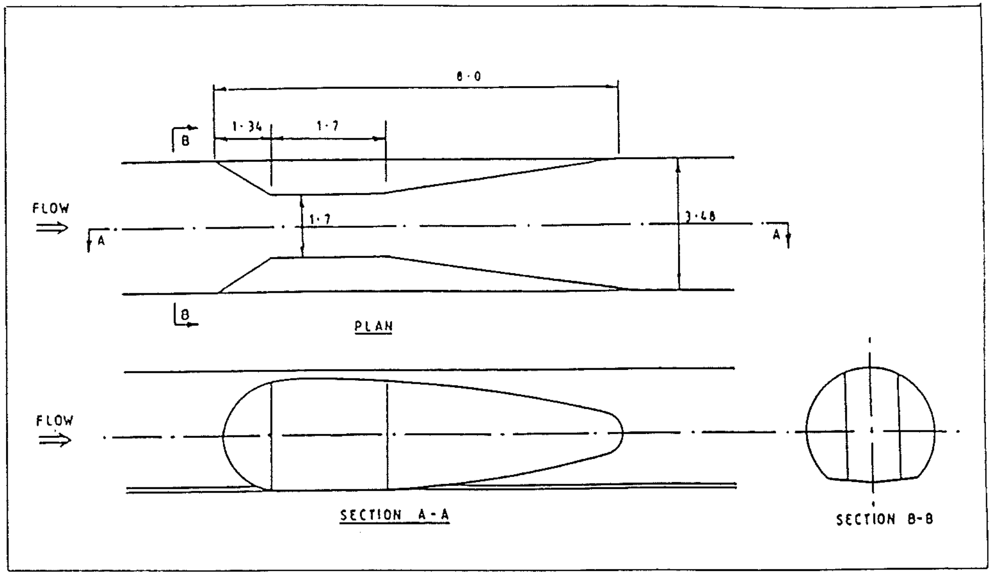

FIGURE 3
INTERNAL HYDRAULIC JUMP
FORMED BY THE VENTURI

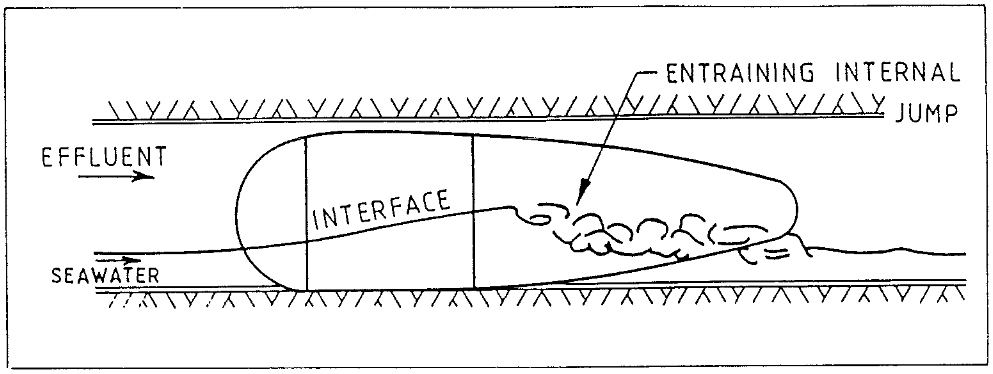

FIGURE 4
PERSPECTIVE VIEW OF
THE INVERTING SCREW

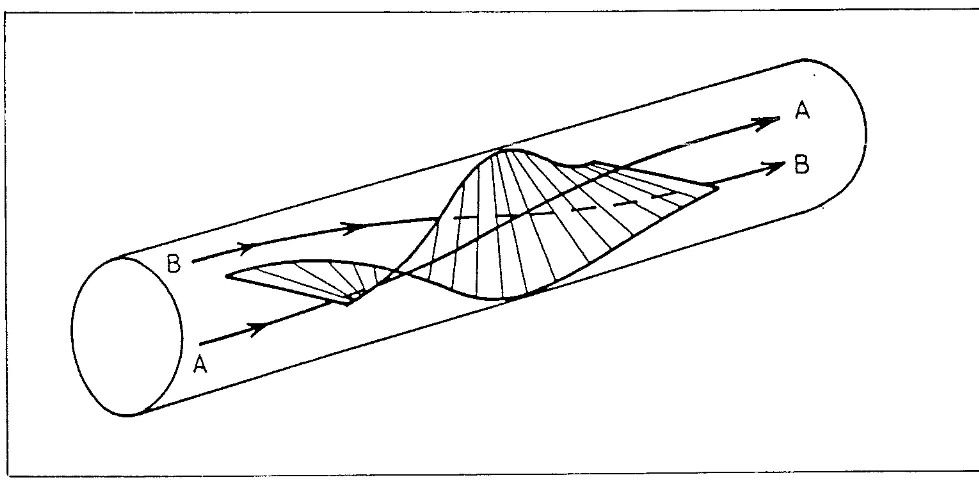

FIGURE 5
INTERFACIAL PROFILES

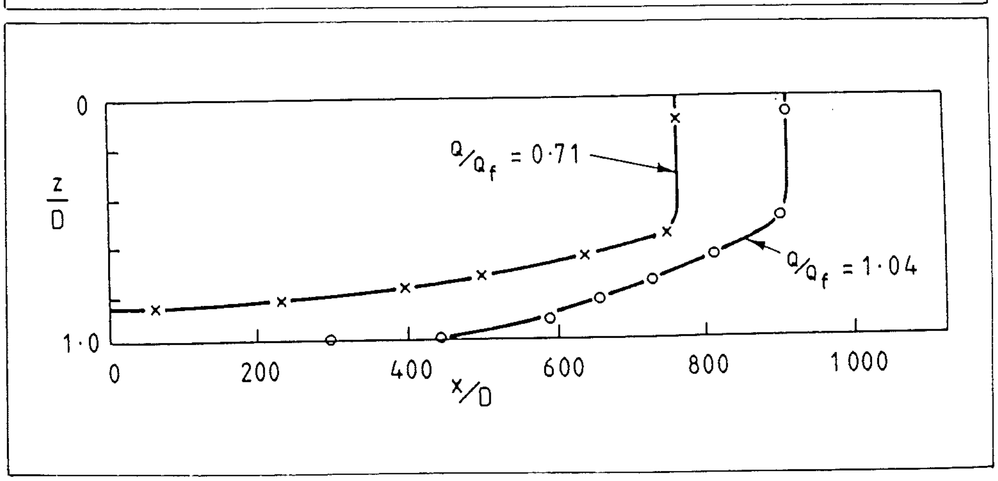

SEAWATER PURGING OF THE BOSTON WASTEWATER OUTFALL

by E. E. Adams, D. Sahoo, and C. R. Liro
Massachusetts Institute of Technology
Cambridge, MA 02139 USA

Abstract

An 83:1 hydraulic scale model was built to study the mechanism of seawater purging in the tunnel outfall designed for Boston's new sewage treatment plant. This paper discusses the model design strategy and summarizes model results. Further details are found in Adams et al. (1990). Under the original outfall design an effluent flow of over 800 mgd would be required to purge the tunnel and a flow of over 900 mgd would be required to purge the risers. These requirements far exceed average flow rates meaning there would be substantial intervals when purging was not possible. However, construction of a tunnel constriction (Venturi section) just upstream from the risers substantially reduced the tunnel purging requirement. In combination with the Venturi section, a short-term increase in effluent flow caused by intermittent dumping of the chlorine-contact tanks significantly reduced the riser purging requirement.

Introduction

Ocean outfalls that extend several miles offshore and include a multi-port diffuser are an economical means of effluent disposal. Such outfalls may be constructed either by tunneling, or by laying a pipeline in a trench cut in the seabed. The former option, which has been chosen for the Boston outfall, allows protection from waves and reduces environmental disruption during construction. There are presently fewer than ten tunneled outfalls throughout the world, with several under construction or in design stage, including three in Sydney, Australia.

Several existing tunneled outfalls have not performed well due to the fact that effluent discharges only from some of the risers. This condition is accompanied by seawater intrusion into the remaining risers and results from incomplete purging of seawater residing in the tunnel prior to start-up. The presence of seawater in an outfall results in hydraulic inefficiencies, causing decreased dilution with ambient receiving water and increased head loss. More importantly, seawater circulation can cause marine biofouling and collection of sediments in the tunnel resulting in partial failure of some tunnels (Bennet 1981, Charlton 1982).

The tunnel for the new Boston Wastewater Treatment Plant will discharge treated effluent into Massachusetts Bay (Figure 1) at daily average flow rates ranging from 320 to 1270 mgd. Instantaneously, however, flowrates as low as 150 mgd may be expected. The tunnel will be about 24.3 ft in diameter and 50,000 ft in length with a 1:2000 upward slope, and will end in a 6600-ft diffuser section with about 55 risers (Figure 2). The riser section will be tapered with decreasing cross section area to allow near-constant tunnel velocities. The decreasing crossection will be obtained by increasing the slope of the tunnel invert while leaving the soffit slope essentially unchanged. Each riser will have a diffuser cap at the top with eight ports per cap. The ports are designed to discharge flow horizontally with a radial distribution. The risers will be connected to the bottom of the tunnel and rise about 250 ft to the sea floor.

Theoretical Purging Criteria

Purging requires that seawater be displaced from both the tunnel and the riser section of the outfall. Purging of seawater from the diffuser tunnel requires, theoretically, that the tunnel "flow full" of effluent which should occur if the flow rate is large enough and the tunnel slope is small enough. Under conditions of uniform pipe diameter, Wilkinson (1988) gives this criterion as

$$Q_{tun} > \left[\frac{2D\ \Delta\rho/\rho\ g\sin\theta}{f}\right]^{\frac{1}{2}} \frac{\pi D^2}{4} \tag{1}$$

where Q_{tun} is the effluent flow, θ is the tunnel slope, and D is the tunnel diameter. This criterion is similar to that governing the inverted situation of having full pipe flow where air is the fluid being expelled by water. Eq. (1) assumes uniform flow and, even if this criterion is satisfied, a saltwater wedge may still persist upstream from the diffuser section (gradually varied flow) depending on downstream boundary conditions (i.e., depth of saltwater at the beginning of the riser section).

Purging of an individual riser requires that, at the riser offtake, the tunnel pressure exceed the hydrostatic pressure associated with the weight of seawater above the offtake (Munro, 1981; Brooks, 1988). Using the elevation of the riser cap as a datum (Figure 3), the tunnel pressure head consists of a hydrostatic term (associated with the effluent density) and an internal head loss due to downstream losses in the tunnel and risers. Hence riser purging requires that the internal head loss (h_L) exceed the *differential* hydrostatic pressure head based on the riser height and the difference in density between seawater and effluent or $\Delta\rho H/\rho$ where H is the riser height. The latter head is referred to as the Munro head and this basic criterion is known as the Munro Criterion. h_L will comprise mainly the exit head loss at the riser discharge port and will be proportional to the square of the discharge flow in each riser, q_i, i.e.,

$$h_L = \alpha q_i^2 \tag{2}$$

If we assume equal flow through all risers, that riser heights are all equal, that there is no downward flow through unpurged risers, and that the number of risers N is large, the Munro criterion becomes

$$Q_M = N\sqrt{\frac{\Delta\rho}{\alpha\rho}H} \tag{3}$$

Q_M is the Munro flow and α is a proportionality constant with dimensions of $\text{time}^2/\text{length}^5$.

It is clear that both the tunnel purging criterion (Eq. (1)) and the riser purging criterion (Eq. (3)) involve some idealizations (e.g., uniform flow, equal flow through all risers, etc.). Hence the theoretical formulae require experimental validation. Such validation was a major purpose of the physical model development.

Hydraulic Model

A hydraulic model was built to study the process of seawater purging, both in the riser section and in the tunnel. From the outset it was recognized that complete geometric similitude could not be achieved. For one thing the number of prototype risers and the exact geometry of their offtakes and caps was still being refined at the time of our study. (See Roberts et al., 1989.) Thus our philosophy was to design the model to *resemble* the expected prototype design; to study the purging phenomena in the model (e.g., by summarizing the observed purging flow as a percentage of a theoretical value); and then to translate this understanding into prototype design.

Model scaling was based on densimetric Froude similarity using a nominal diameter/height ratio of 83:1 (prototype to model). To account for lower model Reynolds number (hence higher friction factor), lengths were distorted by a factor of two. The strategy of basing distortion only on friction and not on considerations of tunnel entrainment differs somewhat from the Sydney models (Wilkinson, 1988). To maximize model Reynolds number, seawater-effluent density differences were exaggerated by a factor of 3. Resulting nominal scale ratios are summarized in the following table.

Froude number	1:1	density differences	1:3	
diameter and heights	83:1	Reynolds numbers	440:1	
friction	1:2	flow rates	36000:1	
slopes	1:2	times	16:1	(risers)
lengths	166:1		32:1	(tunnel)

Model Results, Observations, and Summary

- During start-up with low to moderate flows (up to at least 1000 mgd) observations showed the freshwater wedge advancing downstream along the tunnel soffit. Due to the upward slope of the tunnel invert, the downstream risers (with highest offtake elevation) purged first. Saltwater was observed to intrude *downward* through unpurged risers. In between the purged and unpurged risers several risers exhibited exchange flow and/or mixed upward flow. (See Figure 3.)
- As flow rate increased, additional risers purged, working backwards. Riser 1 (furthest upstream) was consistently the last to purge. Thus for the Boston outfall the theoretical purging criterion (Munro criterion) should be based on Riser 1.
- When flow was increased very slowly (referred to as a static purge test), purging occurred at a flow rate of around 930 mgd or 94% of the Munro flow Q_M. This performance was not sensitive to small changes (± 4 ft) in riser cap elevation due to variation in bathymetry along the diffuser alignment.
- Salt water penetration within the tunnel upstream of the risers depended on flow rate and persisted at rates up to about 830 mgd,

nearly 2.5 times the tunnel purging criterion of Eq. (1) and about 90% of the observed riser purging flow. The reason for the much higher observed tunnel purging flow is the increase in tunnel invert slope which occurs downstream in the riser section

- Rapid purging tests (simulating a temporary flow increase due to discharge from chlorine-contact tanks) were run using generic hydrographs characterized by a constant base flow, followed by increasing flow at a fixed rate of increase, followed by a constant peak flow. The minimum peak flow at which rapid purging occurred ranged from 88-92% of Q_M which is not significantly different from the static tests.
- Because of seawater stored in the tunnel, the time required for rapid purging depended strongly on the base flow rate. The volume of excess flow required for purging became comparable with the active volume of the chlorine-contact tanks at a base flow of around 500 mgd. Because this flow rate is greater than most dry weather flows, there was a strong incentive to explore ways to reduce tunnel intrusion (i.e., through use of a Venturi).
- To limit sea water penetration in the tunnel a "Venturi section" was installed just upstream of the first riser. The Venturi consisted of a lateral constriction with throat width of 10 feet. In general, the Venturi substantially reduced tunnel intrusion. The wedge was eliminated for flows greater than about 340 mgd which corresponds to the original tunnel purging criterion based on full pipe flow.
- Theoretical calculations, based on a condition of densimetric critical flow at the throat and assuming no mixing indicate that the wedge should be expelled at a flow of about 420 mgd. The lesser observed flow is attributed to mixing downstream from the Venturi. In addition to helping decrease the effective tunnel purging flow, this mixing facilitates purging of the upstream risers with the result that "middle risers" (typically numbers 10-30) were the last to purge.
- The flow required for static purging with the Venturi was between 88-93% of Q_M, which is similar to observations without the Venturi. On the other hand rapid purging was greatly improved. Beginning with a base flow of about 400 mgd (no tunnel wedge), purging occurred at peak flows as low as 66% of Q_M. The excess volume of water required was always less than about $6 \times 10^5 ft^3$ or 50% of the active volume within the chlorine-contact tanks. Therefore it is concluded that a tunnel design which includes the Venturi section and provisions to dump the chlorine-contact tanks using a motorized gate will be successful at purging seawater from the outfall, during conditions with no tunnel wedge.

Acknowledgments

This study was sponsored by the Massachusetts Water Resources Authority, Boston, Mass., and by Metcalf & Eddy, Inc., Wakefield, Mass. The authors wish to thank Dr. Dominique Brocard of Metcalf &

Eddy and Dr. Norman Brooks of Cal Tech (serving as consultant to Metcalf & Eddy) for their suggestions throughout the study.

References

Adams, E., D. Sahoo, C. Liro. 1990. Hydraulic model study of seawater purging for the Boston wastewater outfall. Report No. 329, R. M. Parsons Laboratory, Dept. of Civil Engineering, MIT.

Bennet, N. J. 1981. Initial dilution: A practical study on the Hastings Long Sea outfalls. Proceedings, ICE, Vol. 70.

Brooks, N. H. 1988. Seawater intrusion and purging in tunneled outfalls: A case of multiple flow states. *Schweizer Ingenieur und Architekt* 6:156-160.

Charlton, J. A. 1982. Hydraulic modeling of saline intrusion into sea outfalls. Proceedings, International Conference on the Hydraulic Modeling of Civil Engineering Structures, Coventry, England. 349-356.

Munro, D. 1981. Seawater exclusion from tunneled outfall discharge sewage. Report 7-M, Water Research Centre, Stevenage Laboratory.

Roberts, P. J. W. 1989. Dilution hydraulic model study of the Boston wastewater outfall. Report No. SCEGIT 89-101, Georgia Inst. of Techn., School of Civil Engineering, Atlanta, Ga. (Also summarized in this conference.)

Wilkinson, D. L. 1988. Hydraulic modeling of tunneled outfalls. Proc. Int'l Conf. on Marine Disposal of Wastewater, Wellington, New Zealand.

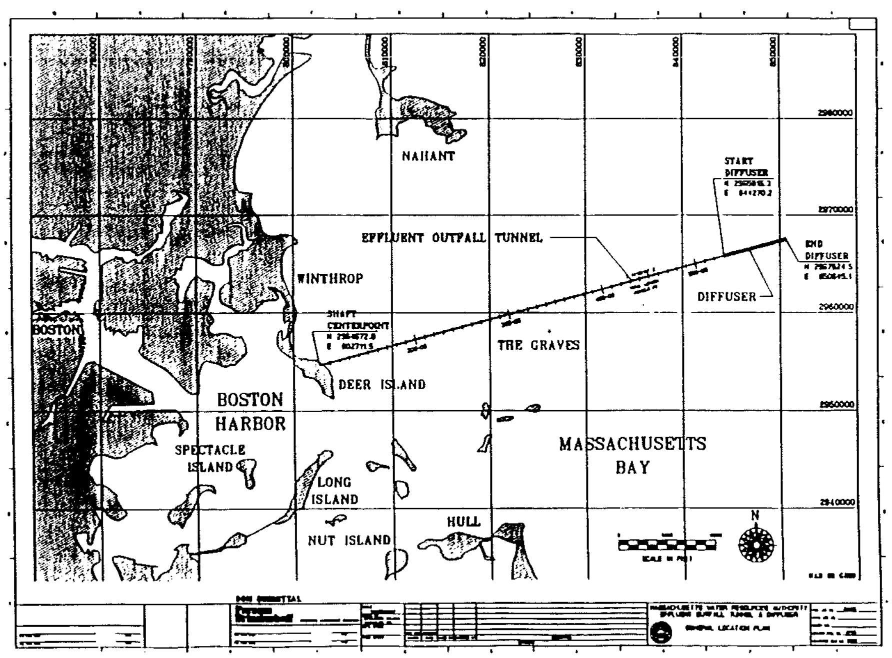

Figure 1 Map of Massachusetts Bay

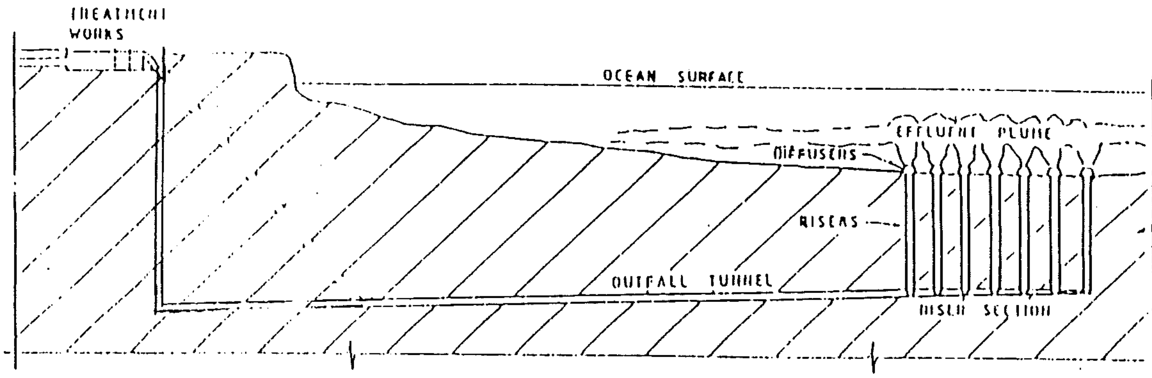

<u>Model dimensions</u>:
tunnel diameter = 3.5 in
riser height = 35.6 in
diffuser section = 40 ft
number of risers = 80
flow rate = 6.2 to 25 gpm

<u>Prototype dimensions</u>:
tunnel length = 50,000 ft (9 miles)
tunnel diameter = 24 ft
tunnel depth (from seabed) = 235 ft
number of risers = 80; later changed to 55
diffuser section = 6600 ft
flow rate = 500 to 2000 cfs

Figure 2 Schematic diagram of the Boston tunnel outfall

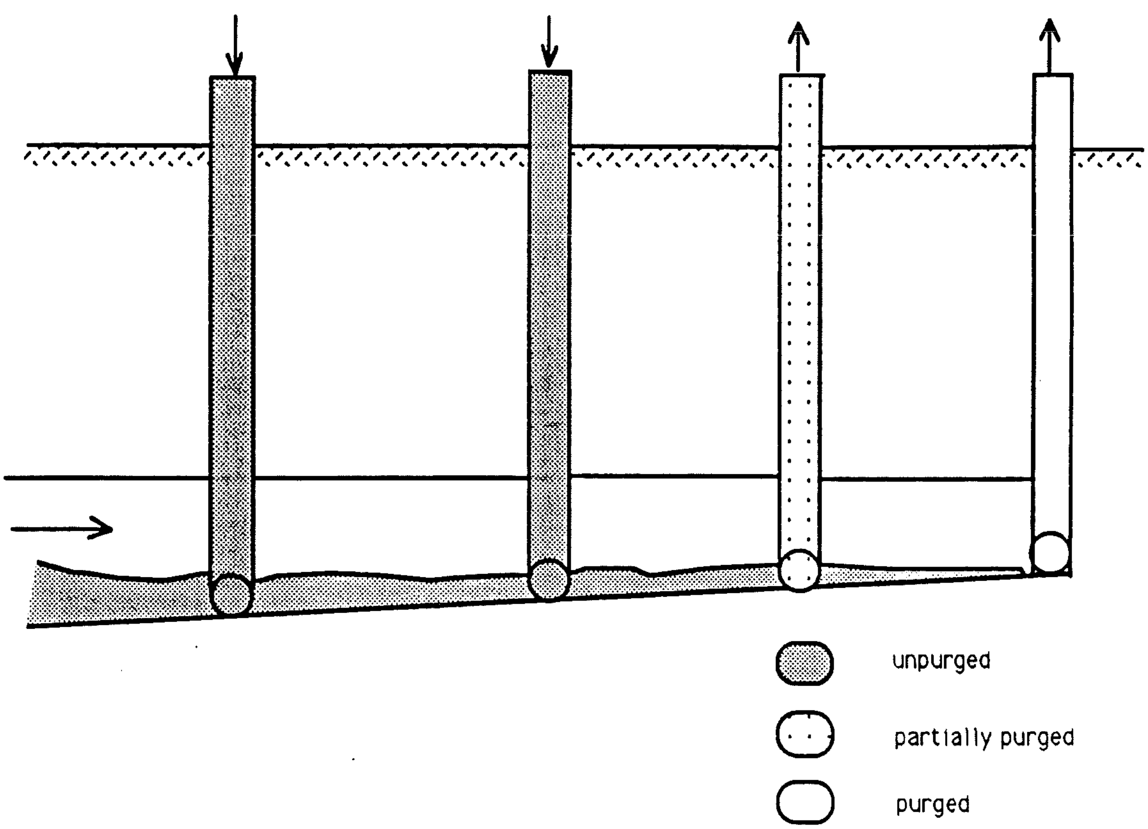

Figure 3 Sketch of partially purged condition in diffuser

Experiments on the motion of buoyant clouds on weakly inclined boundaries

by

Qiang Liu
Daniel Schläpfer
and
Johannes Bühler

Institut für Hydromechanik und Wasserwirtschaft
Eidgenössische Technische Hochschule (ETH)
Zürich CH–8093, Switzerland

Abstract

Depth averaged quantities and flow visualizations of two-dimensional bouyant thermals descending on slopes less than 5^o are presented. The similarity assumption is employed in the analysis. Experimental results were obtained in a 20m long water tank in order to determine the mean shape and temperature field. The internal structure was further examined using flow visualization in a 1m long aquarium. Good agreement is found between the laboratory and analytical results. In particular, the water depth at the source of an inclined thermal has no significant influence on its front velocity.

1. Introduction:

When a volume of dense fluid is released on an incline into a less dense environment, it spreads under the influence of forces produced by its own buoyancy. The resulting flows are often referred to as buoyant clouds or inclined thermals.

There are many situations in the environment where such flows can arise. Powder snow avalanches, airborne debris created by volcanic eruptions, turbidity currents in the ocean set in motion by earthquakes and storm waves, for example, are of considerable practical importance.

Beghin et al (1981) studied inclined thermals by using Morton et al's (1956) similarity solution for free thermals. Their analysis agreed well with the experimental results when the incline was in excess of 5^o. Laval et al (1988) extended this investigation to small slopes. Previous studies on this subject have focused mainly on the global shape and motion of inclined thermals, while less is known on their internal structure and temperature field.

This investigation emphasizes on local depth averaged parameters and the temperature field for inclined thermal on slopes less than 5^o. The concept of self-similarity of the process was used in the analysis. Temperature distributions were measured at four fixed cross-sections through which the thermal was passing. These measurements were made to verify the model. Flow visualization was performed by means of Laser-induced Fluorescence (LIF) to show the essential flow features of an inclined thermal.

2. Assumptions and Analysis:

For the analysis of inclined thermals, as shown in Fig.1, the following assumptions are made which are similar to those adopted for free thermals by Morton et al (1956):

- There is a geometrical and mechanical similarity in the development of a fully turbulent two-dimensional thermal.
- $(\rho - \rho_a)/\rho_a = \Delta\rho/\rho_a \ll 1$, where ρ is the local density within the thermal and ρ_a is the density in its environment, i.e. the Boussinesq approximation is valid.
- Bottom friction is neglected.

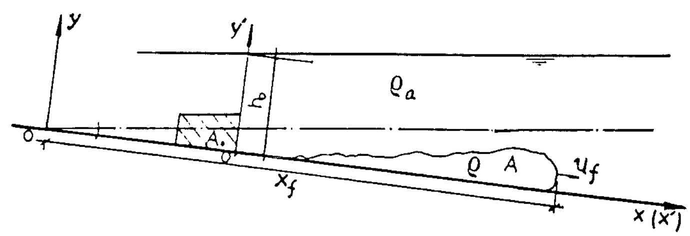

Fig.1 Definition sketch of a thermal moving down an incline

An assumption of constant buoyancy is not required when B is defined as $B = \int_0^\infty \int_0^\infty g' dx' dy' = B_0 = g_0' A_0$, where $g' = (\Delta\rho/\rho_a)g$ and g is the gravitational acceleration, and g_0' and A_0 are the initial reduced gravitational acceleration and initial thermal area.

For a slope of given angle, Θ, the inclined thermal motion and density distribution depend only on thermal source buoyancy B_0, the distance x_f of the front from the virtual origin of the thermal, and possibly on whether the water depth at the virtual origin is zero or can be considered as infinite. Alternatively, the flow can be described in terms of the time t starting at virtual origin. Note that x and t are different from the co-ordinate x' and t' with origins at the lower edge of the inflow box and at the time of release.

From dimensional arguments it is found that the front position x_f, and its velocity u_f are given by the following relations:

$$x_f = C_1 B_0^{1/3} t^{2/3} \tag{1}$$

$$u_f = C_2 B_0^{1/2} x_f^{-1/2} \tag{2}$$

where C_1 and C_2 are proportionality constants for a given slope and configuration, and $C_1 = (\frac{3}{2}C_2)^{2/3}$.

When the flow is self-similar, x_f is the only relevant length scale and the shape of the thermal at different times can be compared, e.g., by means of the transformation $\xi = x/x_f$ and $\eta = y/x_f \tan\Theta$. The local depth averaged velocity u must also correspond to

$$u(x) = \xi u_f \quad . \tag{3}$$

The local densimetric Froude number will be defined as

$$F_r = \frac{u}{\sqrt{g_d' h}} \tag{4}$$

where g_d' is calculated using the depth averaged density ρ_d, which was computed from ΔT_d (Schläpfer, 1990). ΔT_d and h are defined by two intergrations based on the temperature profiles:

$$\Delta T_d h = \int_0^\infty \Delta T dy \tag{5}$$

$$\Delta T_d h^2 = 2 \int_0^\infty \Delta T y dy \tag{6}$$

Furthmore, the local temperature excess ΔT is normalized as:

$$\Pi = \frac{\Delta T x_f^2 \tan \Theta}{2 \Delta T_0 A_0} \tag{7}$$

3. Experiments:

Experiments were performed in a plexiglass channel 0.4m wide, 1.0m high and 16.0m long. The channel was suspended in a 20.0m long water-filled external tank and could be tilted from 0 to 5°. A salt solution with a temperature of about 6^0C, made visible by dye, was introduced into a 0.8x0.4x0.2m box at the upper end of the channel. The water depth at the source, h_0, could be varied. To start an experiment the gate in front of the box was quickly withdrawn by hand, allowing the salt solution to flow downslope from rest. After arriving at the end of the channel the thermal spilled out onto the bottom of the external tank at some distance below. The total depth thus increased along the channel, while Beghin et al (1981) conducted their tests in a prismatic duct. The position x_f' of the thermal front was recorded by taking photographs at constant time intervals. Temperature was measured with a set of 74 thermistors, which were distributed along the bottom of the channel as well as among four vertical racks at distances of x_{s1}'=3.45m, x_{s2}'=7.7m, x_{s3}'=7.8m and x_{s4}'= 12.0m from the source (Schläpfer, 1990).

LIF was used for a more detailed study of the internal structure and the mixing of inclined thermals. Because the size of the illuminated region is limited for this method, we conducted the experiments in an aquarium 0.4m wide, 0.5m high and 1.0m long. The incline could be varied from 0 to 10^0. A $8W$ argon ion laser was used to illuminate a thin vertical plane passing through the long axis of the aqarium. A cylindrical lens was used to obtain a thin sheet of less than 1mm.

4. Results:

4.1 Flow Visualization:

Typical successive luminous profiles of the buoyant thermal spreading down an incline of 4° are shown in Fig.2. The dye was concentrated near the front, which has a length of around 1/5 of the visible length of the thermal. A comparison of the four photographs shows that the frontal structures progress rapidly, while those in the wake stand almost still.

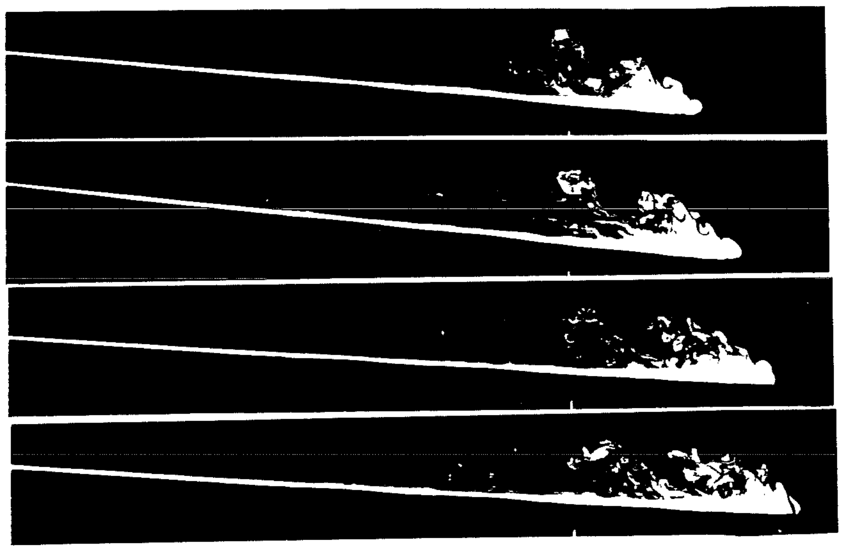

Fig.2 Photographs of an inclined thermal resulting from the release of a small volume of salt solution ($A_0 = 100cm^2$) of density $\rho = 1.017g/cm^3$ in ambient fluid of density $\rho_a = 0.996g/cm^3$; $\Theta = 4^0$, Δt=0.6 sec. Lengths are represented on a scale 1:5. Re=2500, based on the maximum height of the front and the front velocity. The illumination was made by LIF.

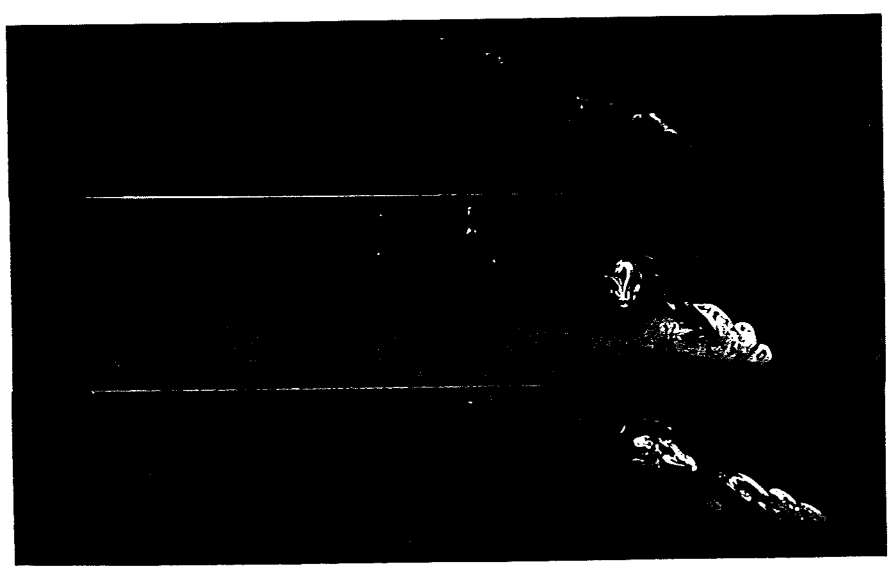

Fig.3 A close-up view of the front and the lateral intrusion of frontal lobes. Length scale is 1:4, Δt =0.4 sec, other experimental conditions are the same as those shown in Fig.2.

4.2 Global Behaviour of an inclined thermal:

The virtual origin x_v' was determined as shown in Fig.4. Similarly, t_v' was found by plotting B_0/u_f^3 vs. t'.

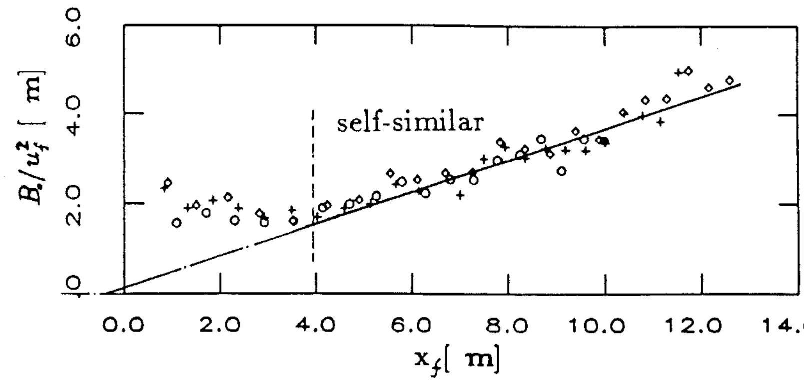

Fig.4. Determinnation of the virtual origin x_v'. x_v'=-0.67m, Θ = 2°; ◇ B_0=0.022 m^3/s^2, h_0=0.19m; + B_0=0.006 m^3/s^2, h_0=0.20m; ○ B_0=0.022 m^3/s^2, h_0=0.38m.

The data show two flow regions, an initial region where the flow accelerates, and a later one where it becomes self-similar. The self-similar state is established after the thermal has travelled a distance of about $5l$, where l is the length of the inflow box. Fig.4 also shows that the data of the three experiments are well represented by a straight line, although each experiment had a different values of B_0 and h_0. This can be expected for a change in B_0. However, the insensitivity to h_0 suggests that the thermal behaves the same as if the depth at the source were infinite.

4.3. Local behaviour of a inclined thermal:

A temperature signal, recorded by the first rack at y'=0.6cm during the time when the thermal was passing is shown in Fig.5a. A strong front can clearly be distinguished from a long wake. Fig.5b presents temperature profiles measured at the same rack at different times.

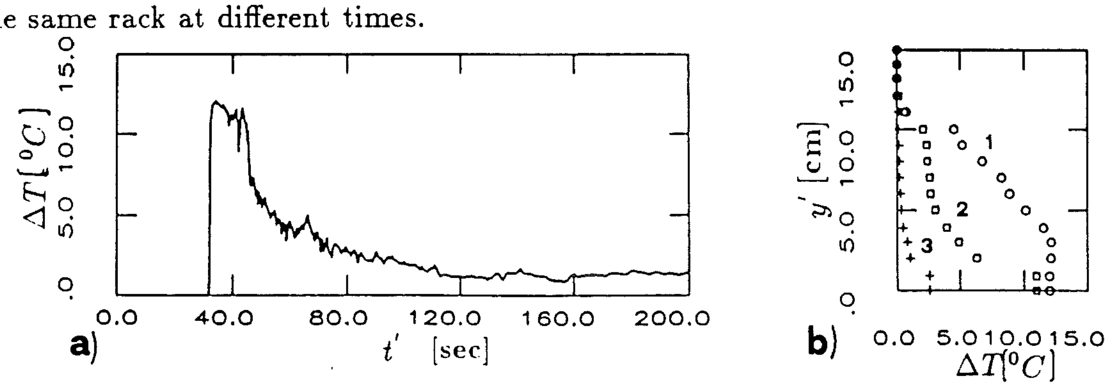

Fig.5 a) Typical temperature pulse as recorded by a single probe during transit of the thermal. b) Vertical profiles measured by 15 probes at the first rack at three times, (1) t_1'=34sec, (2) t_2'=40sec, (3) t_3'=50sec.

The local depth h normalized by $x_f \tan\Theta$ in the ξ and η co-ordinate is shown in Fig.6a.

The variation of the Froude number, which is defined in eq. (4), is shown in Fig.6b.

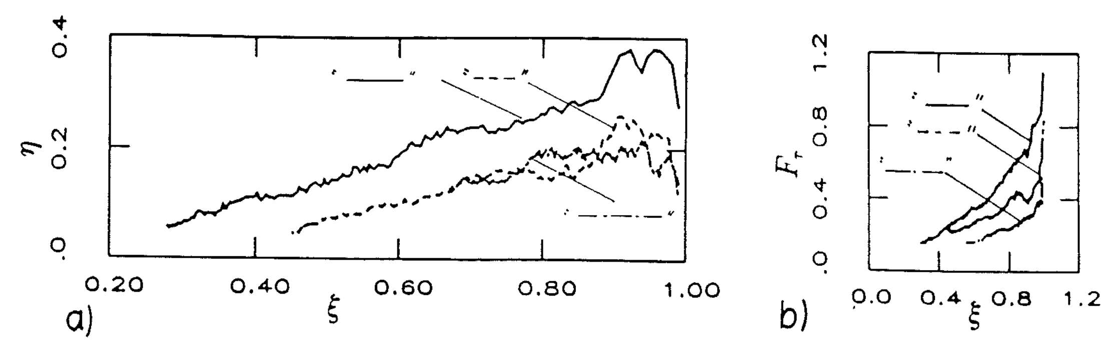

Fig.6a. Reconstruction of thermal shape. — data at x'=3.45m; - - - data at x'=7.7m; —·— data at x'=12.0m; Fig.6b Local Froude number of the thermal. —data at x'=3.45m; - - - x'=7.7m; —·— x'=12.0m, $\Theta=2^{o}$, $B_0=0.022\ m^3/s^2$, h_0=0.19m.

5. Discussions:

The results support the validity of the similarity assumption for buoyant thermals on inclines. Similarity is thus a resonable assumption, which agrees with the conclusion of Beghin et al (1981). An inclined thermal can be well determined by its own source buoyancy and a length scale.

The location of the virtual origin for different water depths at the source suggests that the thermal behaves as if the water was infinitly deep.

Turner (1973) argued that buoyancy flows on small slope may be treated approximately as if they did not mix. Our qualitative observation show that large eddies engulfed the external fluid and mixed it into the deep center within the thermal. The flow pattern of lobes and clefts at the head of a gravity current described by Simpson and Britter (1979) was also detected in our visualization.

Acknowledgement:

We are pleased to acknowledge Mr. K. H. Rümmer for his careful work on digitizing the photographs and Prof. J. Imberger, Prof. Th. Dracos and Dr. D. Papantoniou for very helpful discussions. This research was sponsored in part by the Swiss National Science Foundation, grant no. 2.326-0.86.

Literature cited:

1. Beghin, P., Hopfinger, E.J. and Britter, R.E. J. Fluid Mech. Vol. 107, pp. 407–422, 1981.
2. Laval, A., Cremer, M. Beghin, P and Ravenne, C. Sedimentology. Vol 35, pp.73–84, 1988.
3. Morton, B.R. Taylor, G.I. and Turner, J.S. Proc. Roy. Soci. A234, 1, 1956.
4. Schläpfer, D.B. Diss.(PhD thesis) ETH Nr. 9023 1990.
5. Simpsion, J.E. and Britter, R.E. J. Fluid Mech. Vol. 94, pp. 477–495, 1979.
6. Turner, J.S. Buoyancy effects in fluids. Cambridge University Press, London, 1973.

Density Current Propagation in Flowing Receiving Fluid

Steven J. Wright, Younghan Kim
The University of Michigan
Ann Arbor, MI 48109 USA
Johannes Bühler
Federal Institute of Technology
CH 8093, Zürich, Switzerland

Abstract

Previous theories for density currents using a one-dimensional momentum balance in a frame of reference moving with the density current head are inadequate to predict the propagation characteristics. An alternate theory utilizing energy principles is proposed. An experimental investigation was performed with density currents discharged into both co-flowing and counter-flowing ambient fluids and the experimental results are shown to be consistent with an analysis that minimizes the total energy flux.

Introduction

Density current propagation has been previously analyzed with a variety of one-dimensional analyses, each of which predict the propagation velocity as a function of the layer thickness. Most previous analyses are based upon the work of Benjamin (1968), who formulated a momentum balance in a frame of reference moving with an air cavity intruding into a water filled duct. It was presumed that this would be analogous to the intrusion of a more dense fluid along the bottom of a similar channel. Benjamin showed that energy dissipation must be present at the density current head and assumed that it was confined to the continuous layer above the density current. For flows with energy dissipation, the maximum allowable value of $\eta = h_1/H$ (Figure 1) is 0.347 (Kranenburg, 1978).

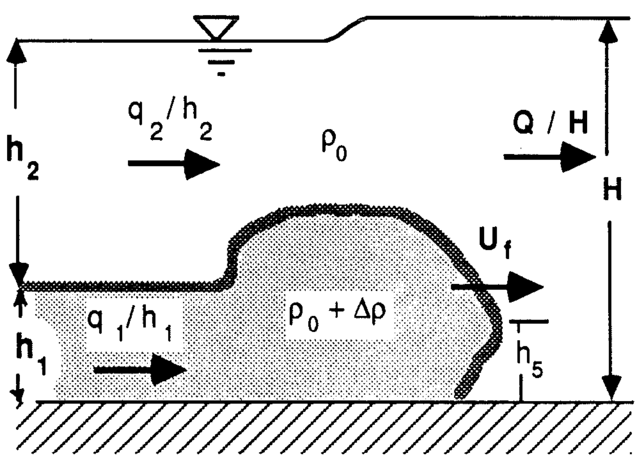

Fig. 1. Density Current Definition Sketch.

Simpson and Britter (1979) performed experiments with density currents arrested on top of a moving boundary which indicate slower propagation speeds than suggested by Benjamin's theory. They account for this difference by considering a super-elevation (h_5 in Fig. 1) of the stagnation point at the density current nose which allows the momentum balance at the front to be satisfied with decreases in density current speed. However, the nose super-elevation was an observed quantity, and leaves open the question of whether the density current head adjusts to a local momentum balance or whether the head adjusts to some other criterion with the required momentum balance satisfied by this mechanism. Kranenburg (1978) accounted for the reduction in the density current speed by considering a localized energy loss at the density current head.

Wright, et al (1987) considered that either of Simpson and Britter's and Kranenburg's mechanisms were simply explanations for the lack of agreement between Benjamin's model and observations and the occurrence of intense energy dissipation near the head of the intrusion voided the assumption of hydrostatic pressure variations through that region. It was suggested that the density currents simply adjusted to a minimum energy state and data was presented to substantiate this notion. This concept is further amplified in this paper and additional experimental findings presented to reinforce the previous findings.

Experiments

In order to differentiate between the various theoretical descriptions, a series of essentially nonmixing (near the source) experiments were performed in a 10 m long flume with a pump to circulate the upper layer. The important feature of this setup is that co-flows or counter-flows could be established. By switching the location of the discharge gate, the density current could be introduced into a flow in the same or opposite direction. Different values of the ratio $q_r = q_2/q_1$ were found to be important in the analysis and this ratio could be easily varied with the experimental configuration. Since the water level in the channel was held constant with an overflow weir at one end, zero pump discharge resulted in the commonly studied cases of *starting flow* ($q_r = 0$, with q_r the ratio of the ambient layer to density current discharge) and *lock exchange flow* ($q_r = -1$) with the two discharge gate locations.

In order to properly formulate a two-layer model, some representation of the actual density and velocity profiles is required, at least in order to interpret experimental results. In the present study, density profiles were measured behind the density current head. The following definitions for the layer properties h_1 and g' are made:

$$g' h_1 = \int_0^H g \frac{\Delta\rho}{\rho} dy \qquad ; \qquad g' \frac{h_1^2}{2} = \int_0^H g \frac{\Delta\rho}{\rho} y \, dy$$

with ρ_0 a reference density, in this study the density in the upper layer; $\Delta\rho$ is the density excess above ρ_0 within the density current, $g' = g\,\Delta\rho/\rho_0$ is a reduced gravity, and y the distance above the channel bed. The profile measurements were obtained at a location 4-5 meters downstream from the discharge gate where the density current was well defined. Density current speeds were taken from visual observations. In general, the propagation speed decreased slightly with distance along the channel due to interfacial friction effects. Only the data from the experiments are presented herein since they provide the most significant results.

Analysis

In order to describe density current propagation characteristics, all limits on physically admissible solutions must be established; these are conceptually similar to the constraint proposed by Benjamin (1968) (with his model assumptions) that the requirement of no energy gain in the direction of flow limits solutions to $\eta \leq 0.5$.

There are additional constraints on density current propagation that may be determined by energy considerations as described below. The analysis is simplified if 1.) nonuniformities of velocity and density profiles are ignored and 2.) the Boussinesq approximation of small density differences is made. Both assumptions are employed herein for purposes of clarity in the analysis. The flow system is indicated schematically in Fig. 1; subscript 1 refers to conditions behind the density current head and subscript 2 to the upper layer.

Velocities relative to the density current head are introduced since all previous theories analyze the problem in a frame of reference moving with the speed U_f of the current head. C_1 is the approach velocity when the current head is brought to rest. From Fig. 1, it is seen that $C_1 = U_f - Q/H$ with $Q = q_1+q_2$ with q_2 positive if in the same direction as the density current. With the modifications of density current head super-elevation introduced by Simpson and Britter (1979) and an energy loss in the head by Kranenburg (1978), Benjamin's theory gives the density current speed as a function of the fractional layer thickness η as

$$\frac{C_1}{\sqrt{g'H}} = \sqrt{\frac{\eta(1-\eta)(2-\eta-2\frac{h_5}{h_1})}{1+\eta+k(1-\eta)}} \tag{1}$$

with k an energy loss coefficient. Simpson and Britter introduced other complications in the analysis that are not included in Eq. (1). It can be seen that positive k and h_5 both serve to reduce C_1 which is consistent with observations. However, at present, these factors are selected to provide agreement with experimental data rather than having a basis in underlying principles. Fig. 2 presents the variation of k as a function of the relative flows in the two layers from the experimental data. The systematic variation raises a question of whether some other principle controls the density current propagation and the so-called momentum balance at the head is altered by internal mechanisms so that it can be satisfied.

Wright, et al (1987) suggested that this must be the case and developed a simple argument to conclude that the flow immediately behind the density current head

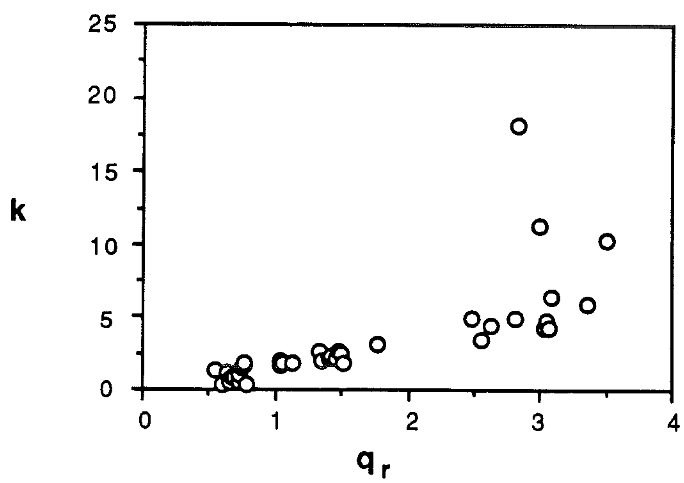

Fig. 2. Variation of Kranenburg's loss coefficient with q_r.

should be internally critical except for cases of strong counterflow. ($q_r < 0$) in which the momentum balance provides a more restrictive constraint on density current propagation. The derivation of critical flow is somewhat analogous to single layer open channel flow. Since two layer flows generally involve different velocities in each layer, energy flux should be used to define the critical flow condition where

$$E_f = (q_1 + q_2)\rho_0 g H + q_1\left(\Delta\rho g h_1 + \frac{\rho_0 u_1^2}{2}\right) + q_2\left(\frac{\rho_0 u_2^2}{2}\right) \tag{2}$$

If the energy in the upper layer is considered to be a constant, setting the derivative of E_f with respect to h_1 equal to zero yields the familiar relation:

$$F_1^2 + F_2^2 = 1 \tag{3}$$

where $F_i^2 = u_i^2/(g'h_i)$. However, the assumption of constant energy in the upper layer is incompatible with the original momentum analysis of Benjamin where all the dissipation was assumed to occur in the upper layer. An alternative assumption is that the total depth H be fixed in which case the differentiation yields

$$F_1^2 - q_r F_2^2 = 1 \tag{4}$$

Note that in the case of starting currents ($q_r = 0$) and lock exchange flows ($q_r = -1$) the two relations are equivalent. In terms of the density current propagation speed C_1, Eq. (3) yields

$$\frac{C_1}{\sqrt{g'H}} = [1-(1+q_r)\eta]\sqrt{\frac{\eta(1-\eta)^3}{(1-\eta)^3 + q_r^2\eta^3}} \tag{5}$$

while Eq. (4) yields the alternate expression

$$\frac{C_1}{\sqrt{g'H}} = [1-(1+q_r)\eta]\sqrt{\frac{\eta(1-\eta)^3}{(1-\eta)^3 - q_r^3\eta^3}} \tag{6}$$

Fig. 3 is a plot similar to that presented by Wright, et al (1987) to demonstrate that Eq. (4) was appropriate. Also provided on the plot are the predictions of Eqs. (1) (with h_5 and $k = 0$), (5) and (6) along with the experimental data for coflows ($q_r > 0$) in which the differences between the various predictions become more obvious. The theory by Benjamin is independent of q_r as presented, while the predictions for either internally critical flow relation is presented as a family of curves with different q_r values. An inspection of Fig. 3 indicates that both critical flow relations fit the data equally well and clearly more satisfactorily than Eq. (1). Although is it possible to conclude that the momentum balance is inappropriate unless the coefficients are introduced to force a fit to the data, it is not possible to distinguish between the two different critical flow relations. In order to investigate the differences an alternate variable q_1 (= $U_f h_1$) is examined. From Eq. (3)

$$\frac{q_1}{\sqrt{g'H^3}} = \sqrt{\frac{\eta^3(1-\eta)^3}{(1-\eta)^3 + q_r^2\eta^3}} \tag{7}$$

while from Eq. (4), the following result is obtained:

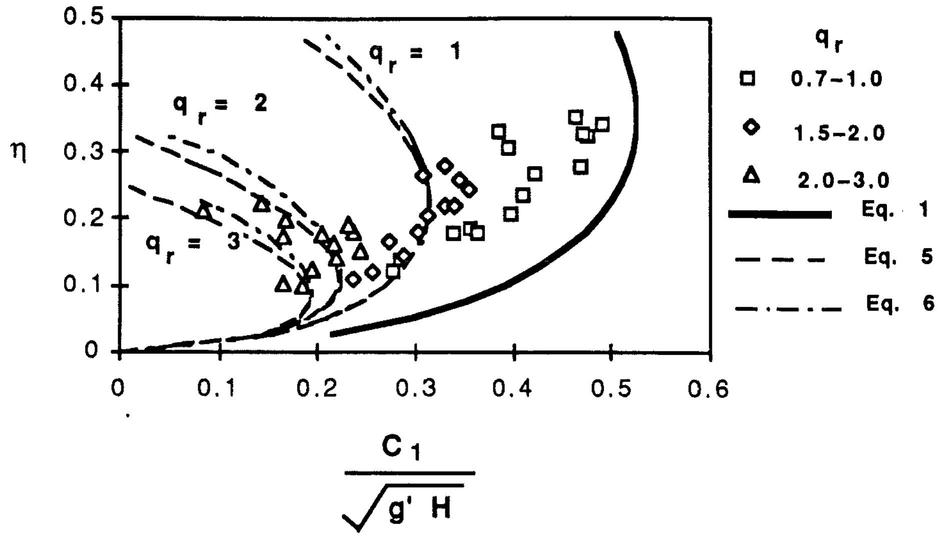

Fig. 3. Predicted and Observed Relative Propagation Speeds.

$$\frac{q_1}{\sqrt{g'H^3}} = \sqrt{\frac{\eta^3(1-\eta)^3}{(1-\eta)^3 - q_r{}^3\eta^3}} \tag{8}$$

These are plotted in Fig. 4 along with the experimental data. Here it is seen that Eq. (7) predicts the wrong trends while Eq. (8) is quite consistent with the observed results. A plot of $F_1{}^2 + F_2{}^2$ in Fig. 5 yields the same conclusion.

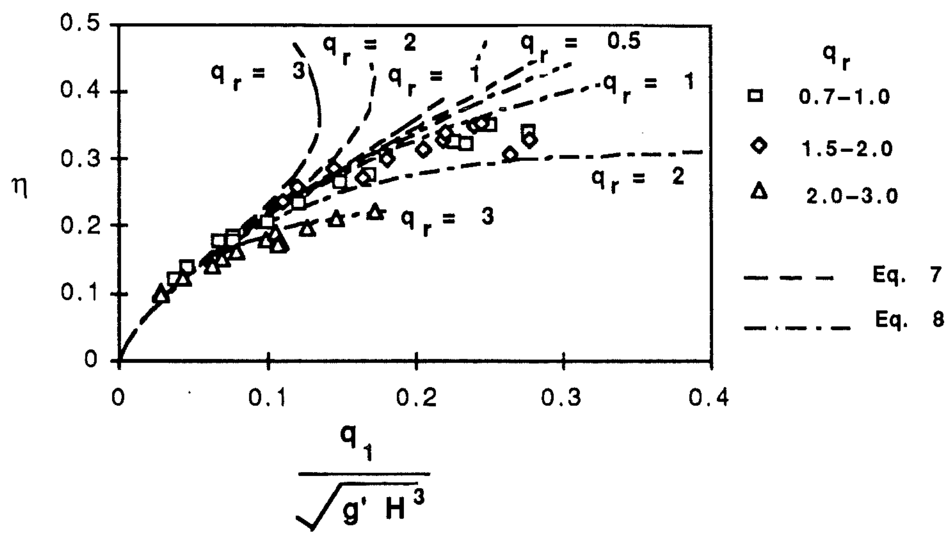

Fig. 4. Predicted and Observed Intrusion Volume Fluxes.

Conclusions

The results of this study have demonstrated previous density current propagation theories to be insufficient to predict experimental observations. The momentum balance at the front of the density current must be discarded as a predictive tool as the conditions at the front adjust to those imposed upon it by other requirements in most situations. For relatively small density current thicknesses, the source discharge condition is found to be the important aspect of the problem as the flow adjusts to a state of minimum energy flux and the density current head dissipates sufficient energy to maintain this flow state. The traditional method for defining internally critical flow requires that the energy in the upper layer be constant. The data do not correspond to this condition and instead require that the energy flux be minimized under the condition of a constant total depth. It is stressed that these arguments do not apply to intruding air cavities in which no energy dissipation is possible within the intrusion.

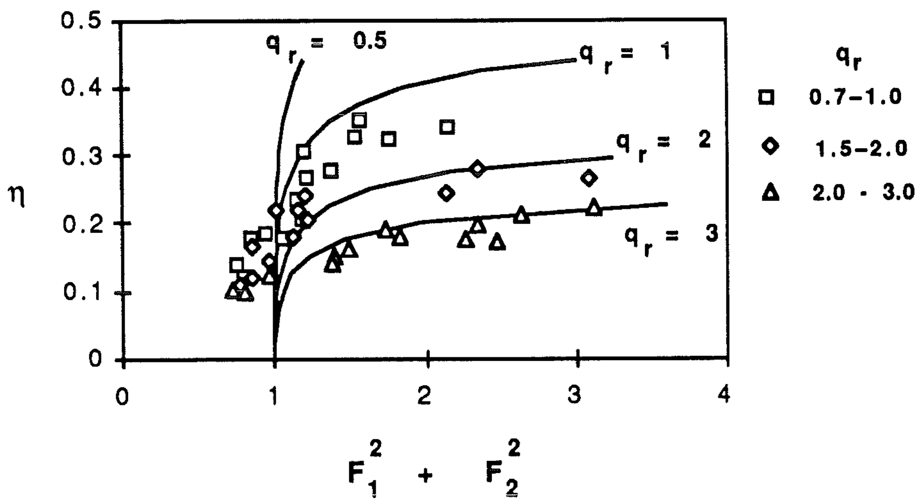

Fig. 5. Predicted and Observed Sum of Layer Froude Numbers.

References

Benjamin, T.B., (1968), Gravity Currents and Related Phenomena, *Journal of Fluid Mechanics*, Vol. 31, pp. 209-248.

Kranenburg, C., (1978), Internal Fronts in Two Layer Flow, *Journal of the Hydraulics Division ASCE*, Vol. 104 (HY10), pp. 1449-1453.

Simpson, J.E. and Britter, R.E., (1979), The Dynamics of the Head of a Gravity Current Advancing Over a Horizontal Surface, *Journal of Fluid Mechanics*, Vol. 74(3), pp. 477-496.

Wright, S. J., Kim, Y., and Bühler, J., (1987), Controls on Density Current Propagation, *Third international Symposium on Stratified Flow*, Pasadena, California.

AIR INTRUSIONS INTO DUCTED FLOWS

by Johannes Bühler,
Eidgenössische Technische Hochschule Zürich,
CH-8093 Zürich, Switzerland, and
Steven J. Wright,
The University of Michigan, Ann Arbor, MI 48109, USA

Abstract

An air intrusion develops when one of the end walls of a long, horizontal and water - filled box is suddenly partly or entirely removed. By arresting the front of the cavity in an opposing ducted flow, instead, it is found that a continuous range of cavity depths smaller than one - half of the duct height is realizable when the duct is tilted to counteract bottom friction. The conditions are also outlined which lead to a parallel flow under a cavity which intrudes into a ducted flow.

Introduction

The flowrate in a nearly horizontal pipe connecting two reservoirs can change considerably when the water level in one of them drops below the roof of the duct, creating an air intrusion. A subsequent rise of this level can also lead to a jump travelling into the duct which either lags behind the front of the cavity or catches up with it. These phenomena are of particular interest for the operation of pipe networks involving free surfaces during variable or transient load conditions.

The analysis of such flows is generally based on work by Benjamin (1968) who examined an air cavity advancing into a long, water-filled box after one of its end wall is suddenly removed. He showed that a loss of mean energy occurs in the flow past slender cavities, which occur when the outflow is party obstructed. His model also includes a singular loss-free solution for which the intrusion into the box occupies one-half of the water depth, and he suggested that cavities in a depth range between about 35% and one - half of the duct height are not possible.

Hydraulic jumps moving within the cavity can be produced by obstructing the outflow after a deep (loss - free) cavity has been established. Benjamin determined the conjugate depth of such a jump for the special case that its velocity is just the same as that of the front. The corresponding cavity depth is then about 22% of the duct height.

Benjamin assumed that the air/water interface in the lee of the front is basically horizontal in the absence of boundary shear. It is then of interest to examine the conditions under which this assumption holds for the entire lengthening part of an air intrusion into a box or a ducted flow.

Predictions based on this model for the velocity of cavities intruding into a water - filled box were experimentally verified by Wilkinson (1982) after making necessary corrections for real fluid effects. He also confirmed the realizability of the loss - free solution but found that even for flows with cavity depths of less than 35% of the duct height the free surface was basically unsteady. However, as Keller and Exley (1985) pointed out, the realizability of flows in a range of cavity depths between about 22 and 35% of the duct height may depend on the way the intrusion is established, i.e. on whether a weir at one end of the box is gradually lowered to its final position or whether it is suddenly lowered completely and then raised again. Wilkinson's boundary conditions did not correspond to either one of these scenarios and it therefore remains uncertain whether cavities in the depth range between 22 and 50% of the duct height are realizable and can have steady interfaces.

Analysis

For the analysis of air intrusions into a horizontal duct, Benjamin (1968) neglected the effect of surface tension as well as any energy dissipation along the boundaries. The flow was considered as being essentially steady in a frame of reference moving with the front, and the downstream interface as being horizontal. The relevant quantities in this frame of reference are defined in Fig. 1. The slope, s, is zero; u_A and u are the approach and downstream velocities, h and H the cavity depth and the duct height. The density of the heavy fluid is denoted by ρ, and the density of air is neglected. The positive direction is to the right in this frame of reference, and only flows in this direction are considered. Additional velocity scales are the phase speed λ of long, interfacial waves (and jumps) of limiting amplitude, and the intrusion velocity u_i, i.e. the velocity of the duct relative to the front.

The flux of volume is conserved through the transition, such that

$$u_A H = u(H-h) \tag{1}$$

The same holds for the flow force, which is the integral over the duct height of the local momentum flux and pressure. By setting the pressure p at the stagnation point B and in the cavity arbitrarily equal to zero, one may write this balance as

$$\rho u_A^2 H + \frac{1}{2}\rho g H^2 + p_A H = \beta \rho u^2 (H-h) + \frac{1}{2}\rho g (H-h)^2 \tag{2}$$

Here it is assumed that any deviations from a uniform velocity distribution in the (slower) approach flow can be neglected, while they are considered in the (faster) flow under the cavity. In analogy to open channel flows the corresponding momentum coefficient β is defined as

$$\beta u^2 (H-h) = \int_0^{H-h} u^{*2} dy$$

where the star denotes a mean local value. With $\eta = h/H$, equations (1) and (2) can be combined to give

$$\beta = \frac{1-\eta}{2}\left(\frac{2p_A}{\rho u_A^2} + \frac{gH}{u_A^2}\eta(2-\eta) + 2\right) \tag{3}$$

Benjamin also conserved energy along the streamline A - B, which leads to

$$p_A = -\frac{1}{2}\rho u_A^2, \tag{4}$$

and by setting $\beta = 1$ his result can be written as

$$U^2 = \frac{\eta(2-\eta)}{1-\eta^2} \tag{5}$$

where $U = u/(gH)^{1/2}$. (Capital letters will be used to denote quantities normalized with appropriate powers of g and H). Von Karman (1940) conserved energy rather than momentum across the front, as it is often done for weak flow discontinuities. By considering eq. (4), energy conservation along the streamline D - E leaves

$$U^2 = 2\eta, \tag{6}$$

which also corresponds to Benjamin's solution for the case of 'great depth' ($\eta \to 0$), and for

$$\eta = 1/2, \qquad U = 1 \tag{7}$$

which represents the loss - free solution. For larger values of U and η energy would be gained through the transition, and Benjamin showed that the corresponding flows are not realizable under the assumptions he made. Eqs. (5) and (6) are shown in Fig. 2 in terms of $U_A = U(1-\eta)$, and the loss-free solution (7) is marked by a solid circle.

Further information can be obtained by considering the propagation of long waves of limiting amplitude on the downstream interface (Fig.1). The nondimensional phase speed, Λ, of such waves is, approximately

$$\Lambda^{\pm} = U \pm \sqrt{1 - \eta - U^2(\beta - 1)} \tag{8}$$

and for $\Lambda^- = 0$, i.e. for $\beta U^2 = 1 - \eta$ the flow is just critical (Chow, 1959). By setting $\beta = 1$ it is found from eq. (5) that the downstream state is supercritical ($\Lambda^- > 0$) for cavities deeper than about 35% of the duct height and subcritical for more slender ones. Benjamin suggested that, except for the loss - free case, no supercritical downstream flows can occur. What one can definitely conclude is that no waves of limiting amplitude can reach the front of intrusions with supercritical downstream flow, i.e. that the frontal speed and depth of the cavity cannot be affected by slightly changing the height of a weir at the outlet of the duct. Any dissipative flows in this region must therefore be controlled by the upstream conditions or a slope of the duct. Depending on the criticality of the downstream state, one may thus distinguish between slender, subcritical intrusions with $\eta < 0.35$, and thicker, supercritical ones with a cavity depth of $H/2$, and possibly less than that. Whether one or the other type of intrusion occurs during an intrusion into a box essentially depends on whether the end wall is entirely or partly removed.

Benjamin considered the flow in a frame of reference moving with the front, and assumed the air/water interface in the lee of the front to be horizontal in the absence of boundary shear. In the general case of an intrusion into a ducted flow, the flow under the cavity is determined both by the conditions at the front, expressed by eq. (5), and those at the source of the intrusion. A mismatch between these boundary conditions may lead to an expansion wave (rarefaction), or to a jump which moves along the interface. In both of these cases the interface level under the intrusion changes in space and time. A rarefaction on the interface appears when a control is established at the source, i.e when the flow in this cross - section becomes critical in the frame of reference of the duct. The condition for a horizontal interface is therefore that the flow is subcritical ($\lambda^+ > u_i$) near the source for slender, subcritical intrusions ($\lambda^- < 0$), where h and u are taken just behind the frontal region. In contrast, the flow must remain supercritical ($\lambda^- > u_i$) for supercritical intrusions ($\lambda^- > 0$). For given values of η and U_i one may then use the first one of eqs. (5) to determine the (positive) flow rate of air and the (positive or negative) one of water into the duct which satisfy the requirements for a horizontal interface. The same considerations apply to flows in circular ducts; which were also analyzed by Bemjamin.

Experiments

A number of experiments were conducted to examine the possibility of cavity depths in the range $0.22 < \eta < 1/2$. They were carried out in a tiltable 8 m long Plexiglass flume of 206 mm width, in which an adjustable, sealed lid was installed to obtain a duct. The front of the cavity was arrested at a backward facing step of 0.7 mm height which was located at the roof of the duct and 6.7 m from its downstream end. Two 4 mm honeycombs of 30 mm thickness were inserted, and centered at 195 and 350 mm upstream of the step, where the flow depth H was 90 mm. The pressure p_A at the upper flow boundary was measured at half - width and 15mm upstream from the step with an accuracy of about $\pm$ 0.5 mm head (out of about 7 mm), while the resolution was considerably better.

For a given flow rate and subcritical intrusions the front was first nudged upstream by increasing the slope, while a free outflow at the end ensured that the flow there remained critical. An obstacle which had the same effect as a weir was then used to obstruct the downstream flow until it became normal, i.e. of constant depth, to obtain a more reliable estimate of the water depth $H - h$. Supercritical intrusions with normal downstream flow could be readily produced, but the discharge did not appear to depend on the cavity depth, which could be varied by changing the slope. A distinct 'nose' of the front, i.e. a depression of the stagnation point below the lid as was noted by Wilkinson (1982) for intrusions into a box, was not discernible. Once the front was at any location in the duct, however, it did tend to remain there even after slight changes in either control parameter. This location also remained unchanged when some detergent was added to the inflow. The frontal adjustment region was exceptionally long (about 1.5 m) in Runs 3 and 7. Stationary waves of about 10 mm height were observed along the entire surface downstream of the frontal region for Run 4.

The results of the experiments are shown in Table 1 and Fig.2. Runs 7 and 8 were undertaken specifically to produce cavities in the range $0.22 < \eta < 0.35$ and close to the loss-free case . For Run 7 we started out with a subcritical flow at the end of the duct and adjusted both the slope and the flow rate to get a uniform flow. The maximum depth of the cavity near the front was particularly large for this run, and corresponded to $\eta_f = 0.42$. Table 1 shows that the nondimensional value of the underpressure $-p_A$ is considerably smaller than 1, as would follow from eq.(4). This is at least partly due to the fact that the stagnation point is within the boundary layer of the lid, and that the local velocity of the approaching fluid is less than u_A. Jirka and Arita (1987) conducted similar experiments for gravity currents. They showed that a steep arrested front in an opposing flow cannot be maintained, and that a slender wedge controlled by interfacial friction is formed instead. The momentum coefficient β is computed from eq. (3). It varies in a range which is typical for open channel flows (Chow, 1959) except for Run 7. The Froude number F is larger than one for the deeper cavities, which shows that supercritical intrusions with steady downstream flow are realizable when the downstream depth is controlled by the slope and bottom friction. It remains to be clarified whether the observed supercritical flows represent some deviation from the loss-free case, which would have $F^2 = 2$, or whether the flow rate corresponds to the maximum at critical flow and a further acceleration to a supercritical state occurs near the lower end of the front.

Conclusions

For intrusions of air into a ducted flow it is shown that the interface under the cavity can be horizontal in the absence of friction until a control at the source of the intrusion is established. It is found that arrested fronts with steady downstream flow are possible in a continuous range of cavity depths smaller than one half of the duct height when bottom friction is offset by a slope of the duct.

Bibliography

Benjamin, T. B., 1968 Gravity currents and related phenomena. J. Fluid Mech. Vol. 88. pp. 223-240.

Chow, V.T., 1959 Open - channel hydraulics. McGraw Hill

Jirka, G.H,, Arita, M. 1987 Density currents or density wedges: boundary layer influence and control methods. J. Fluid Mech., Vol. 177, pp. 187-206.

von Karman, Th. 1940 The engineer grapples with nonlinear problems. Bull. Am. Math. Soc., Vol. 46, pp. 615 - 683.

Keller, J.J., Egli, W., Exley, J. 1985 Force- and loss- free transitions between flow states. ZAMP, Vol. 36 No. 6, pp. 854- 998.

Wilkinson, D.L. 1982 Motion of air cavities in long horizontal ducts. J. Fluid Mech. Vol. 118, pp. 109 - 122.

Table 1 Experimental parameters and results

Run	1	2	3	4	5	6	7	8
$U_A = u_A/(gH)^{1/2}$	0.54	0.55	0.59	0.59	0.60	0.51	0.57	0.58
$\eta = h/H$	0.11	0.13	0.33	0.36	0.43	0.09	0.24	0.43
$s \cdot 10^3$	–	1.8	2.7	4.0	7.2	1.4	2.7	6.0
$-2p_A/(\rho u_A^2)$	0.35	0.35	0.33	0.32	0.30	0.45	0.31	0.31
β	1.05	1.07	1.08	1.09	1.02	1.00	1.14	1.06
$F = U_A\beta^{1/2}/(1-\eta)^{3/2}$	0.66	0.71	1.14	1.19	1.41	0.59	0.92	1.39

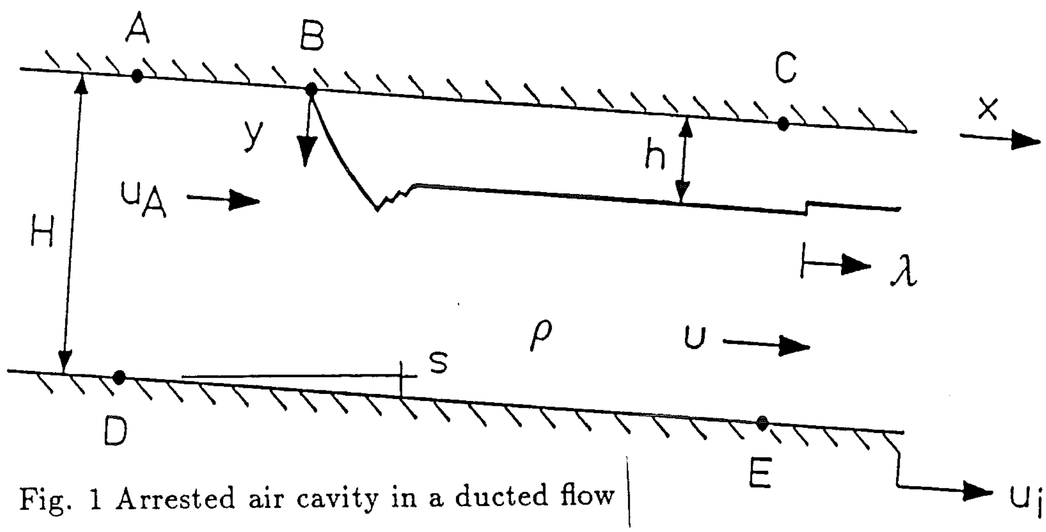

Fig. 1 Arrested air cavity in a ducted flow

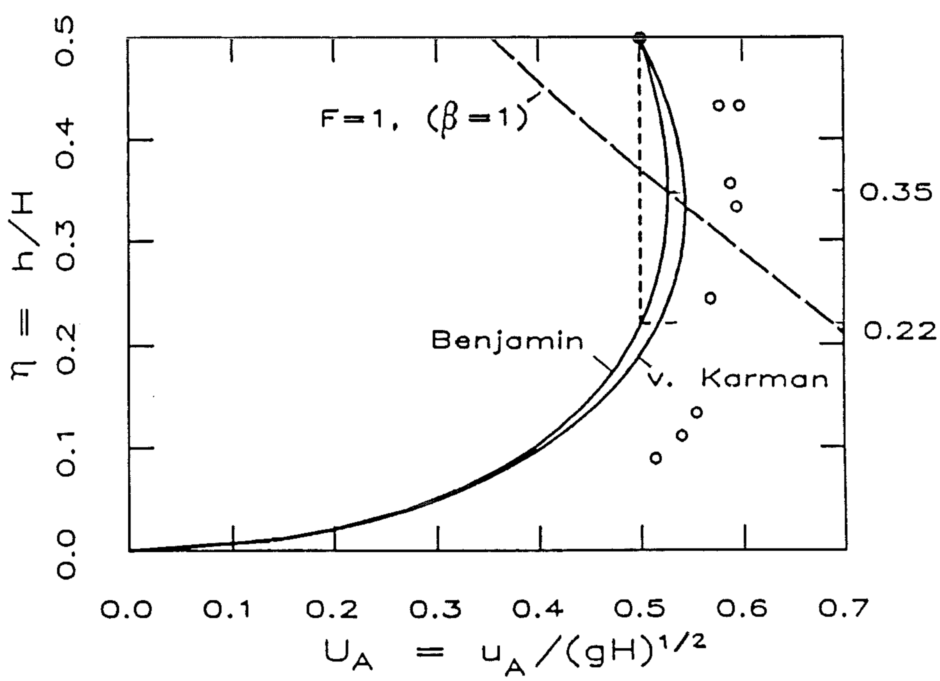

Fig. 2 Data for cavities in an inclined duct

MOTION OF AN AIR CAVITY IN A SLOPING DUCT

by W. Douglas Baines
Department of Mechanical Engineering
University of Toronto, Toronto, ON, Canada, M5S 1A4

Abstract

Experiments on the motion of an air cavity formed in a square duct when a gate at the lower end is opened suddenly are described. If the opening is the full depth of the duct a front is formed which is half the depth and which moves uphill at constant speed. Behind the front a quasi-steady gradually varied flow extends to the outlet. If a weir at the lower end controls the depth of the outflow there are several cases. A low weir produces a jet deflection and no effect on the cavity shape. As the height is increased a level is reached where an hydraulic jump is formed. At larger heights this moves upstream and stops. However, if the weir height exceeds a value dependant on the slope, the free surfaces touches the roof and the cavity is closed. It progresses upstream and a new cavity forms. The result is the generation of a series of closed cavities.

Introduction

The air cavity formed by the opening of a gate at the lower end of a duct containing water is one example of the gravity current first studied by Keulegan(1958). In all cases a smooth front is created which moves at constant speed. The same shape of front is seen in more complex duct flows such as the displacement of fresh by salt water and co-flowing air and water. Other features of the cavity motion such as the profile behind the front depend on the mode of cavity generation but the analysis of the flow is similar in all cases. A steady flow approach can be used because of the constant front speed and the one-dimensional approximation is valid because the curvature of the interface is very small behind the front. This is demonstrated in the simple case considered in this note.

The experiments of Keulegan(1958) were the inspiration for the analysis of the detailed shape of the front presented by Benjamin(1968). This showed that for the two-dimensional case with an ideal fluid in a horizontal duct the cavity height is exactly half the depth of the duct and the velocity of the front is

$$V_f = \frac{1}{2}\sqrt{gH} \tag{1}$$

where the variables are defined in Figure 1. Conservation requirements are sufficient for the development of Eq.(1) but the shape of the front requires the potential flow free-streamline analysis. Wilkinson(1982) measured the shape of an air cavity in a horizontal duct and demonstrated that the front matched Benjamin's profile except near the stagnation point at the wall. Real fluid effects produced a displacement away from the wall of the stagnation point and the deposition of a thin layer of water between the cavity and the wall. This and the surface tension force resulted in a front velocity of up to 10% less than that given by Eq.(1). Measured V_f agreed well with estimates of the real fluid effects.

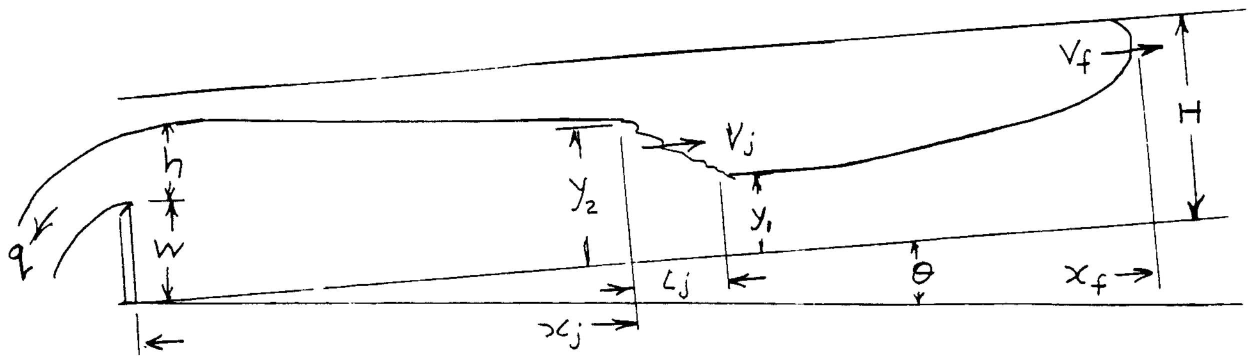

Fig.1. Definition sketch of air cavity.

The effect of duct slope on the air cavity shape and motion were evaluated in this study. A series of experiments was conducted using a square duct 10 cm on a side mounted at slopes from horizontal to 8^0. At the lower end a gate sealed the 4 m long conduit filled with water. When the gate was opened suddenly an air cavity with a smooth front formed and moved along the roof at constant speed. Photographs taken every third of a second showed that the motion was two-dimensional across the width. The profile was readily scaled from enlargements. Another factor in the study was a weir across the outlet. Weir heights of 0.25H, 0.5H and 0.75H were installed for all slopes. A few tests were sufficient to define the flow regimes and indicate the analyses which would define both the shape of the cavity and the water discharge. Duct slope introduces a potential energy variation which does not materially affect the front velocity but changes the one-dimensional flow in the after part of the cavity.

Front velocity

Figure 2 is a typical photo with the flow at the outlet falling free at the open end. The cavity shape is seen to be a front which occupies the upper half of the duct followed by a smooth free surface with continuously decreasing depth. Measurements of the front profile showed it to be the same at all slopes and for all weir heights. The measured V_f was constant for each slope but increased slightly with θ in agreement with the momentum equation.

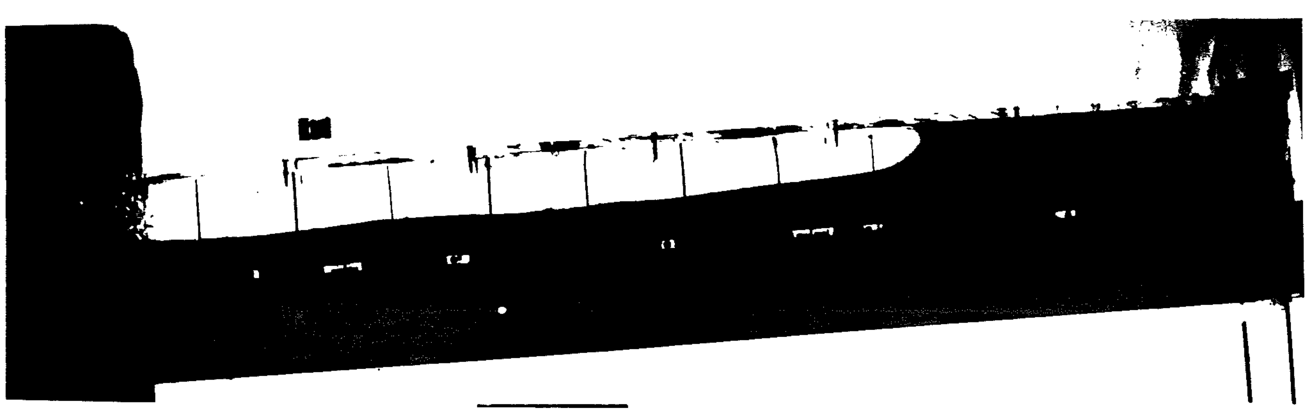

Fig.2. Cavity formed by open discharge on a 4^0 slope.

Open discharge

The flow falls free from the end of the duct if there is no weir. Relative to the front this is a steady super-critical flow. The gradually-varied flow equation can thus be applied to determine the shape of the profile from the end of the front to the overfall. However, the surface friction is due to the velocity relative to the duct and not that relative to the front. The normal depth for all cases is much less than 0.5 H so the free surface follows the S2 curve up to the overfall. A numerical solution of the differential equation for gradually-varied flow agreed exactly with the profile on Fig. 2.

The outflow from the duct is the product of the front velocity relative to the duct and the depth y_0. This is identical to the air inflow

$$q_a = V_f(H-y_0) \tag{2}$$

which increases steadily with time until y_0 reaches steady flow.

Discharge over a weir

Three distinct flow regimes were observed for the range of weir heights.

No upstream influence

A low weir in supercritical flow acts a simple deflector. The sheet of water is deflected upward and inertia is sufficient to carry it over the weir plate. A roller forms upstream of the plate for larger heights but the length and hence the upstream influence is of the order of w which is the weir height. Outflow is exactly the sane as that for open discharge.

Hydraulic jump produced by weir

For a sufficiently high weir a hydraulic jump forms upstream of the plate as sketched on Fig. 1 and as can be seen on Fig. 3.

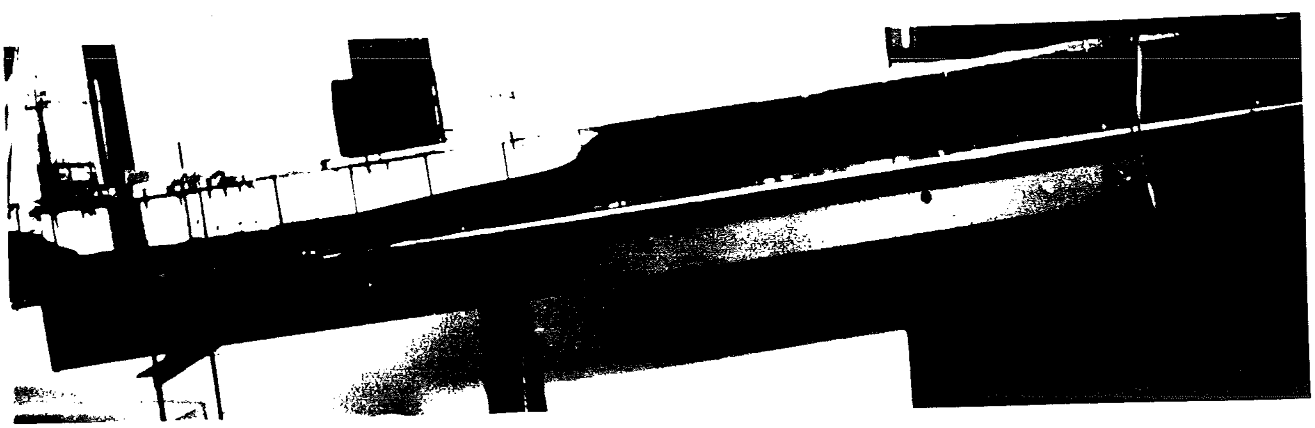

Fig.3. Cavity formed in a duct of slope 4°, weir height = 0.25H.

Flow approaching the weir is sub-critical and consequently the discharge over the weir can be described by the well-known weir formula quoted by Rouse(1946). The jump may move upstream relative to the weir depending on the depths y_1 and y_2 and the speed can be determined from the momentum equation. For a dissipative jump the equations of continuity and momentum relative to the jump are

$$V_1 y_1 = V_2 y_2 \tag{3}$$

$$\frac{g}{2}(y_1^2 - y_2^2)\cos\theta + gkL_j \sin\theta \frac{(y_1 + y_2)}{2} = q(V_2' - V_1') \tag{4}$$

where ' denotes velocity relative to the jump
k describes the profile of the jump
L_j is the length of the jump. Solving for V'_1 and combining with the velocity of the jump in a frame relative to the weir, that is,

$$V_1 = V_1' - \left(\frac{H}{y_1} - 1\right) V_f \tag{5}$$

the velocity of the jump is given by

$$\frac{V_j}{V_f} = 2\left[\frac{y_1}{2H}\cos\theta\left(1 + \frac{y_2}{y_1}\right)\left(1 + kL_j \tan\theta / \left(1 - \frac{y_2}{y_1}\right)\right)\right]^{\frac{1}{2}} - \left(\frac{H}{y_1} - 1\right) \tag{6}$$

It should be noted that this equation does not include real fluid effects on the front. Nevertheless the values do agree with the experimental measurements of jump velocity. The same conclusion was noted by Wilkinson for the horizontal channel. The moving front means that the air and water discharges are

$$q = V_f(H - y_1) - V_j(y_2 - y_1) \tag{7}$$

Between the top of the jump and the weir the velocity is very small and hence the energy equation reduces to the statement that the free surface is horizontal and the elevation of the free surface at the weir is

$$h + w = y_2 + x_j \sin\theta \tag{8}$$

The set of equations (6),(7),(8) and the relations for V_f and weir discharge describe a solution for all of the variables. These can be solved numerically if the initial conditions are specified. The formation of the cavity cannot be described because it is an unsteady free-surface flow and would require the solution of a more complex set of equations. The utility of the equations will be demonstrated by comparing the results to a typical case provided by Experiment 086 which was a 1° slope with a weir 0.5 H. Measurements plotted on Fig.4 show the expected constant velocity of the front, the steady slowing of the jump as y_2 increases and hence the steady increase of h + w. y_1 decreases as the front recedes from the jump.

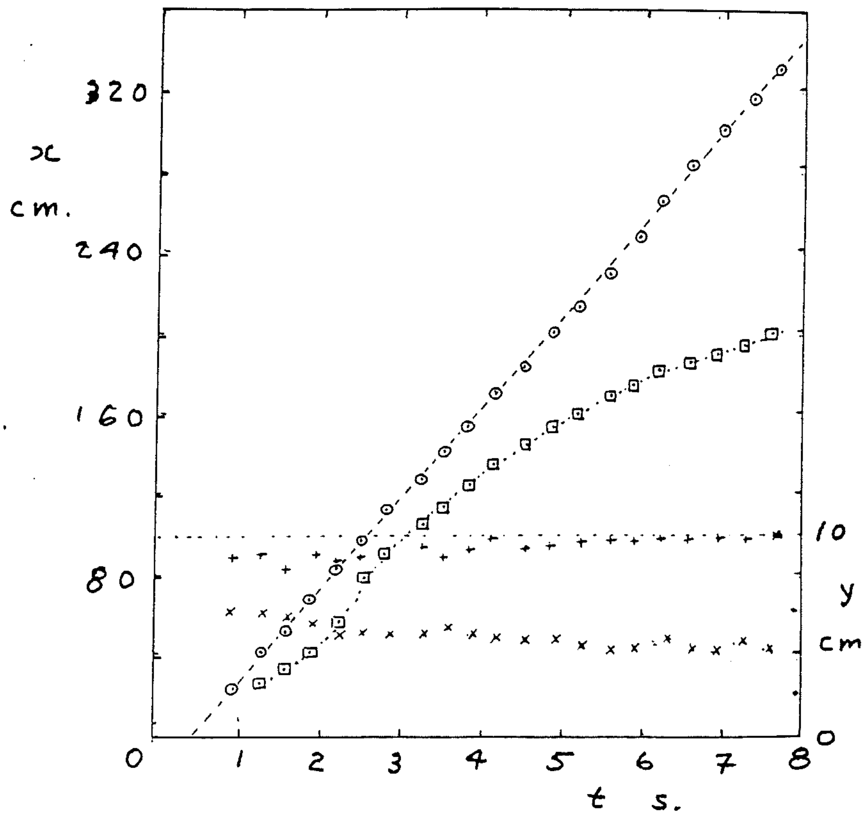

Fig.4. Cavity properties for a 1^0 slope for weir 0.5H. ⊙ x_f front location, ⊡ x_j location of foot of jump, x y_1 depth at foot of jump, + h + w elevation of free surface at weir.

Numerical comparisons of these results with the solutions of the equations are listed in Table 1. The first 5 columns are the measured values. Particular items are used in the equations noted in the next three columns to derive values which should indicate the validity of these equations. The values in the ninth column were found from the numerical solution of the free surface behind the front and the tenth column is the values given by the weir equation. The only values seriously at variance with the measurements is the prediction from the jump velocity equation for t = 7.7s.

Table I
Cavity in a 1^0 slope duct, Experiment 086

Front velocity V_f = 44.8 cm/s

					Eq.(8)	Eq.(7)	Eq.(6)	*	**
time s	V_j cm/s	x_j cm	y_1 cm	y_2 cm	h cm	q cm^2/s	y_1 cm	y_1 cm	q cm^2/s
2.5	36.4	70	5.0	7.4	3.5	140	4.9	5.0	138
5.0	27.8	145	4.5	6.8	4.3	188	4.4	4.6	180
7.7	13.2	186	4.2	6.7	5.0	115	3.9	4.25	224

Cavity Sealing

At t = 7.7s the free surface rose to the roof of the conduit at the weir. This is shown by h = 5.0 in the table. This sealed the cavity and resulted in major changes to the flow. First of all the cavity shortened rapidly because there was no air supply, the jump height increased and in many cases the top sealed on the roof. The jump velocity increased to V_f and the cavity length became constant as in the finite cavities discussed by Baines and Wilkinson(1986). This shape is evident in Fig.5 which is a photo of a cavity on a 2_0 slope. Second a new cavity formed at the weir and accelerated to V_f. This developed exactly as had the original one. Thus as time progressed there was a production of finite cavities at the weir which moved upward at constant velocity.

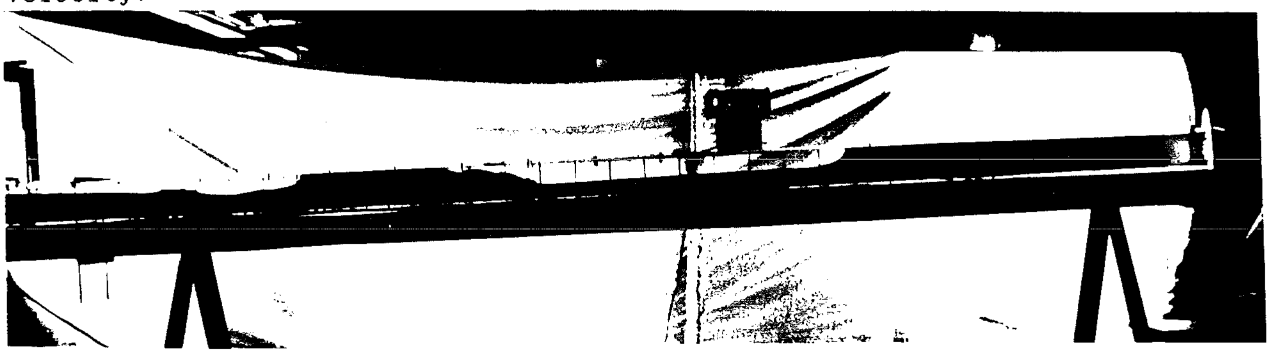

Fig.5. Finite cavities in a conduit on a 2^0 slope, weir height 0.5H. The free surface behind the second cavity is horizontal which indicates that it is not sealed.

This gulping action is seen in many other flows. For example, a bottle of wine gulps when emptied if the neck is steeply tilted. An air cavity is formed at the opening and seals when an hydraulic jump forms in the neck. Another example is the breakup of long air bubbles carried in pipe flow of water. This occurs at changes in slope and is the result of the formation of a jump.

References

Baines, W.D.and Wilkinson, D.L., 1986, The motion of large air bubbles in ducts of moderate slope, J. Hyd. Res.,25, 157-170.

Benjamin, T.B., 1968, Gravity currents and related phenomena, J.Fluid Mech.,31,209-248.

Keulegan,G.H., 1958, The motion of saline fronts in still water,Nat. Bur. Stand. Rep. 5831.

Rouse, H., 1946, Elementary mechanics of fluids, John Wiley and sons, New York.

Wilkinson, D.L., 1982, Motion of air cavities in long horizontal ducts, J.Fluid Mech.,118, 109-122.

Session 12B

Mixing in Channels

TOWARDS RANDOM WALK MODELS IN A LARGE SCALE LABORATORY FACILITY

I. Guymer*, N.J.W. Brockie* & C.M. Allen+.

*Dept. of Civil Engineering, Heriot-Watt University,
Riccarton, Edinburgh, EH14 4AS, U.K.
+Environmental Science Division, Institute of
Environmental and Biological Sciences,
University of Lancaster, Lancaster, LA1 4YQ, UK.

Abstract

Fluorescent tracer experiments and detailed two-dimensional laser anemometry measurements have been performed on a large scale laboratory facility aimed at elucidating the dominant mixing mechanisms in compound channel flows and providing a comprehensive data set with which to assess the suitablity of random walk modelling techniques for describing the measured solute distributions. Preliminary results are presented which illustrate the transverse variability within the concentration plume and variations in the plume concentration from repeated runs of a random walk simulation are also given.

Introduction

An investigation into the applicability of the random walk modelling technique for describing the mixing processes in open channel flows, and in particular within compound channels, requires detailed data describing the spreading of a plume and the flow parameters. Also since the numerical technique predicts one possible variation of the dye concentration at one section at a particular instant and not a time averaged distribution, then a knowledge of the statistical variation of the dye concentration within the plume is required.

Many models of dispersion are based on the standard advection-diffusion equation with a longitudinal dispersion coefficient, which represents the effects of the turbulent fluctuation cross-product term of velocity and concentration. These type of models, based on the work of Taylor (1954) in pipe flows, have often been used in cases where they are not wholly applicable (Chatwin and Allen, 1985), mainly because of the complications in environmental flows.

In practical problems of pollutant dispersion, the usual requirements are to be able to predict the peak concentration likely to occur at a particular location and time in order to assess toxic limits or the build up of hazardous chemicals.

Random Walk Models

In order to overcome these problems, different techniques for numerical simulation have been developed using random walk (particle tracking) models, where a pollutant is simulated by a large number of particles whose paths are tracked by a computer as they move through a fluid.

These Lagrangian models have been used successfully to model dispersion in turbulent shear flows in two-dimensional channels (Allen, 1982). The initial source geometry can be represented by a line source or point source of particles and as an instantaneous or steady release, and the particles move independently of each other in a series of jumps. At each position in the flow, the particle is given mean velocity components and turbulent fluctuations (whose sign is determined by a random number generator).

Random walk models have several advantages: the techniques model the basic principles of dispersion more realistically than standard dispersion equations and the models are versatile and can be easily adapted to take account of many changes, such as source geometry, velocity profiles and cross-sectional shape.

Simulations of dispersion in two-dimensional rectangular channels using random walk models have taken as input, turbulent velocity components derived from laboratory experiments (Sullivan, 1974). For more complex situations such as compound channels and natural rivers, more detailed measurements of turbulent velocity fluctuations are needed to study the variability in the flow which will lead to more complex mixing processes.

The experiments outlined in this paper will obtain information in more detail than is possible in complex natural river geometries (Heslop and Allen, 1989) but on a much larger scale than normal laboratory facilities.

S.E.R.C Flood Channel Facility

A series of experiments wase planned and performed on the SERC Flood Channel Facility at Hydraulics Research Ltd., Wallingford, U.K. to provide the necessary data. The Flood Channel Facility was designed as a large scale central resource enabling a coordinated research programme involving cooperation between several British universities and practising engineers concerned with problems related to flood protection (Knight & Sellin (1987)). The experiments described here formed part of a collaborative project in a series of grants and were designed to investigate the mixing processes in compound channels and to assess the suitability of the random walk modelling technique to describe the measured solute distributions.

The size of the facility is such that the full width of the flood plain and possible sinuosity of the main channel can be studied at a large scale. The outer walls of the flume enclose a tank 56m long by 10m wide with a cement mortar base moulded to the required bed geometry. Flow down the model is provided by six pumps of varying capacity allowing a discharge over the range 0.01 m^3/s to 1.1 m^3/s. The length of the flume allowed a 25m settling length, a 15m test section followed by a lead out length to the tail gate controls.

For these experiments the model geometry consisted of a straight, two-stage, compound channel with a main channel depth of 150mm. The main channel was 1500mm wide at the bed with a 2:1 bank slope horizontal:vertical (Fig. 1). Moveable flood plain banks 300mm high with side slope 1:1 were positioned to give a flood plain width of 2.25m.

Experimental Programme

The experiments were performed at four different flow depths, two in-bank and two over-bank. A fluorescent tracer was continuously injected over a range of source positions and the full vertical, transverse and longitudinal development of the tracer plume was measured. The full range of test configurations is detailed in Fig. 2.

Information on the basic turbulent characteristics of the flow is required as input by the random walk model in order to predict the mixing characteristics. The channel geometry and the flow depths described were selected to correspond with those used for a series of laser anemometry measurements which recorded the turbulent flow velocities throughout the channel cross-section (Shiono & Knight, 1989; Knight & Shiono, 1990).

Experimental Technique

The fluorescent tracer Rhodamine WT was used for these experiments. This was injected into the flow at a constant rate at concentrations of either 100 parts per million (ppm) or 200 ppm for in-bank and over-bank flows respectively. The tracer plume concentration distribution was measured using a vertical array of four Series 10 Turner Designs Fluorometers. Samples from the rake of four inlets spaced at either 10mm for in-bank or 20mm for over-bank flows were continuously pumped through the instruments as the rake was traversed automatically across the flume, stopping at specific sample points for a predetermined period to allow the sample system to flush through and the fluorimeter output to be recorded. The transverse step lengths varied from a minimum of 10mm to a maximum of 40mm. To obtain a full definition of the tracer concentration field at each section repeated sample traverses at different depths were necessary.

As the flume was of recirculating design it was also necessary to monitor the accumulation of the background tracer concentration. This was achieved by placing a single sample inlet at the same downstream section as the sample rake but beyond the transverse limits of the tracer plume. The background concentration was determined by recording the output of a fifth fluorometer.

The fluorometer output signals were sampled at a rate of 40Hz and digitised using a Cambridge Electronics Designs 1401 Intelligent Interface. The data was stored using a microcomputer system with expanded hard disk capacity. In addition to the fluorimeter concentration values, the transverse and vertical position of the sample rake and the sample system flow rates were also recorded.

Preliminary Analysis

To convert the raw data to tracer plume concentration values a 15s block in the record was selected at each of the sample points. For each fluorometer output signal a mean concentration was calculated and the background concentration was then subtracted to give an absolute value. This data, together with the associated standard error for the block length, was then plotted as concentration against transverse distance,y (Fig. 3). At present only a preliminary analysis of the actual results has been performed. However, even at this early stage in the programme some clearly defined trends are evident.

Results

Results available so far show clearly that within the lateral distribution of the plume wherever the larger values of the transverse concentration gradient are present, dc/dy, then an increase in the standard deviation of the sample is recorded. This leads to the twin peak distribution of the standard deviation with transverse distance, evident for the results recorded 6.0m from the source in Fig. 3. As the dye travels further down the channel, the peak concentrations are reduced and the plume spreads transversely, both leading to a reduction in the values of dc/dy, resulting in smaller values of the standard deviation. Although transverse variations of the standard deviation are still evident 16m from the source, Fig. 3, their magnitudes are almost half those at the 6m section and any trends are less evident.

When using this data for numerical model verification it must be noted that the system of pump sampling the concentration leads to a much smoothed record with smaller concentration variations than would actually occur within the flow.

Different runs of a random walk simulation using identical input and boundary conditions illustrate the variability that is apparent in the two or three dimensional structure (Allen, 1990). The repeat runs for a two-dimensional case with a line source release of particles give virtually the same vertically averaged concentration distribution but show significant variability in the two-dimensional picture. Figure 4 illustrates the variability which can be seen in profiles of concentration with depth for similar vertically averaged concentration values.

Conclusions

The preliminary results available from this programme illustrate that it is possible for random walk simulations to describe variations which occur within the concentration distribution of a tracer plume. This should lead to an improved understanding of the mixing mechanisms within compound channel flows and the suitability of random walk models for describing this mixing.

References

Allen, C.M. "Numerical simulation of contaminant dispersion in estuary flows", Proc. Royal Soc. Lond. A, 381, 1982, pp 179-192.

Allen, C.M. "Particle tracking models for pollutant dispersion", Proc. NERC/IMA Conf. on Computer Modelling in the Environmental Sciences, 1990, Oxford Univ. Press. (in press)

Chatwin, P.C. & Allen, C.M. "Mathematical models of dispersion in rivers and estuaries", Ann. Rev. Fluid Mech., 17, 1985, pp 119-149.

Heslop, S.E. & Allen, C.M. "Turbulence and dispersion in larger U.K. rivers", Proc. Int. Assoc. for Hyd. Res. Congress, Ottawa, August, 1989.

Knight, D.W. & Sellin, R.H.J.,"The SERC flood channel test facility", Journal of the Inst. of Water & Environmental Management, IWEM, vol. 1, No. 2,Oct. 1987, pp198-204.

Knight, D.W. & Shiono, K.S.,"Turbulent Measurements in a Shear Layer of a Compound Channel", Journal of Hydraulic Research, IAHR,1990.

Shiono, K.S. & Knight, D.W.,"Vertical and transverse measurements of Reynolds stress in a shear region of a compound channel", Proc. 7th Int. Symp. on Turbulent Shear Flows, Stanford, USA, August, 1989, pp.

Sullivan, P.J. "Instantaneous velocity and length scales in a turbulent shear flow", Advances in Geophysics, 18A, 1974, pp213-223.

Taylor, G.I. "The dispersion of matter in turbulent flow through a pipe", Proc. Royal Soc. Lond. A, 223, 1954, pp 446-468.

Notation

c	concentration
c_d	depth mean concentration
h	depth of flow
x,y,z	longitudinal, lateral and vertical directions in Cartesian co-ordinate system

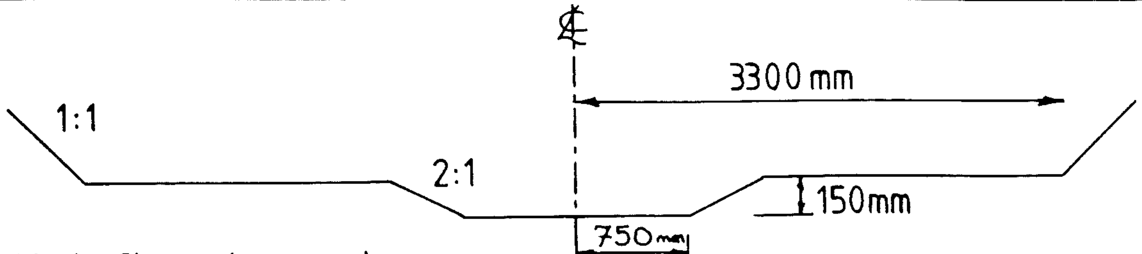

Fig 1 Channel geometry.

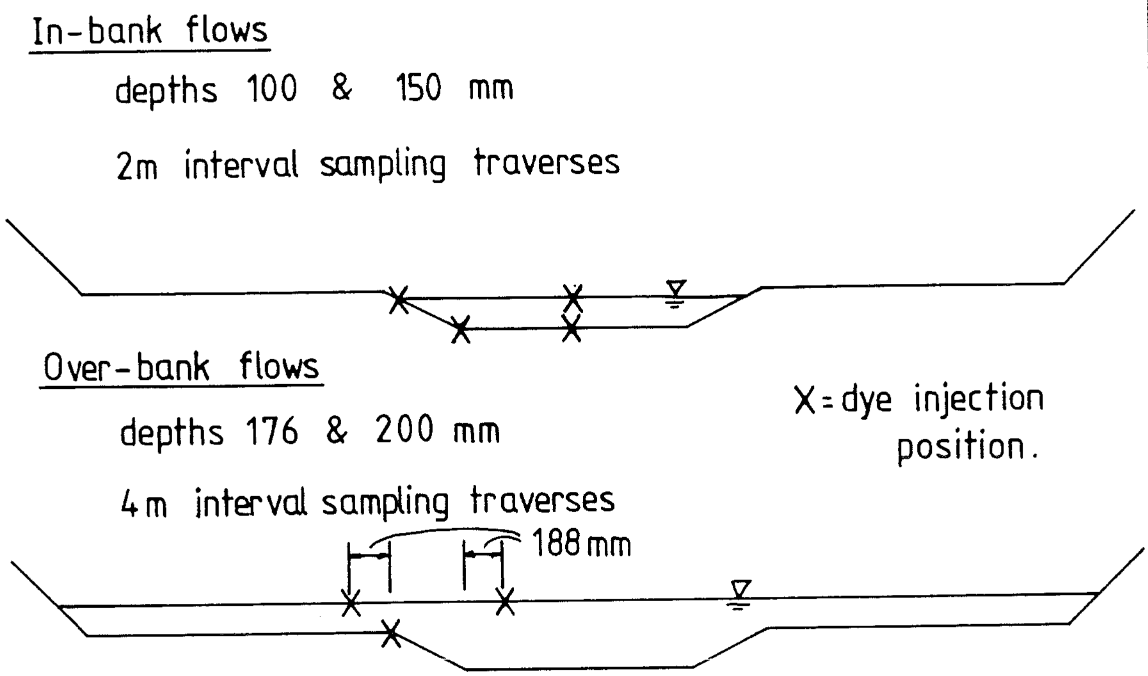

Fig 2 Test Configurations

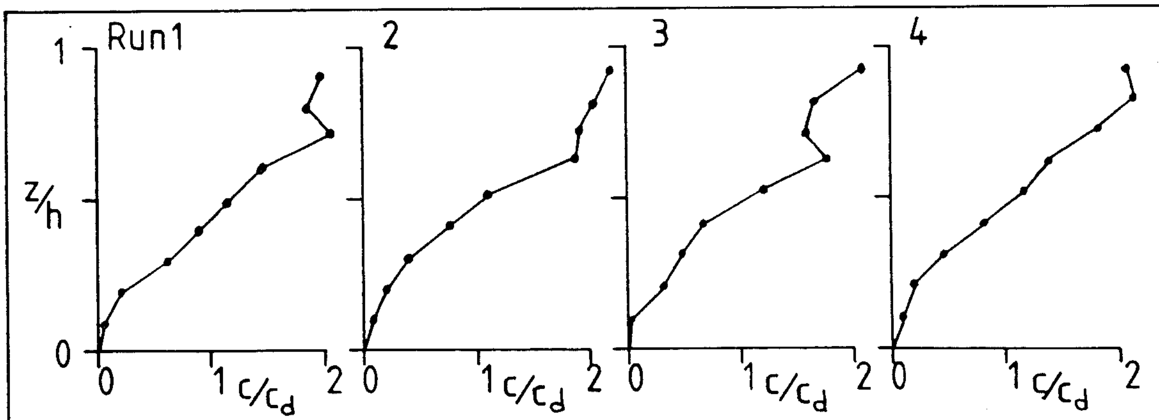

Fig 4 Variation of concentration c/c_d with depth, z for several runs of the same random walk model simulation.

Flow depth, h = 100 mm ; Injection point = channel centre bed ; Inlet height = 9mm above bed.

Section I x = 6 m

Section II x = 16 m

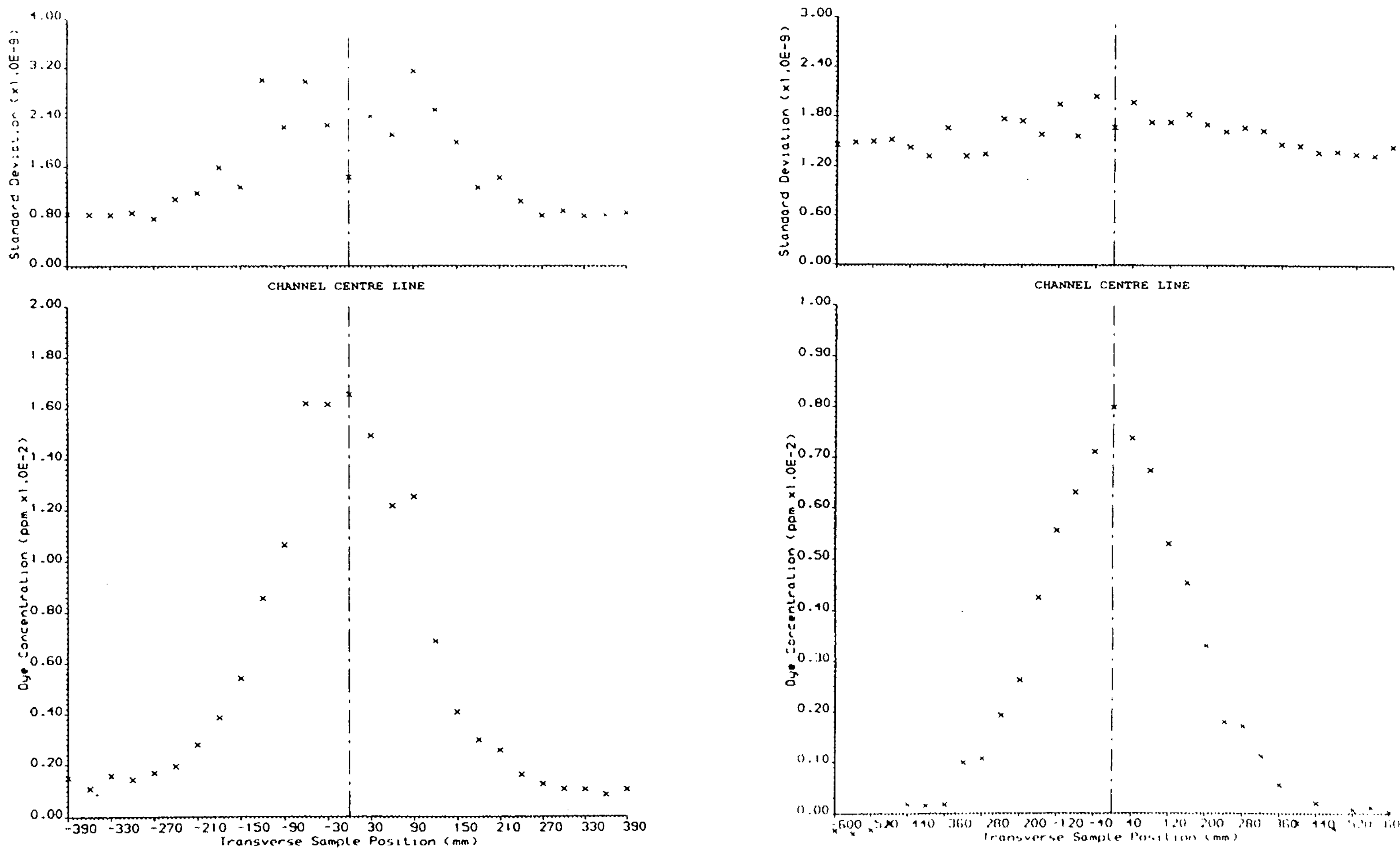

Fig. 3 Comparison of the Transverse Distribution of the Mean Dye Concentration & Standard Deviation.

TRANSVERSE MIXING AT THE CONFLUENCE OF THE THREE RIVERS IN THE YODO RIVER SYSTEM

by Yoshiaki Iwasa, Professor & Shirou Aya, Lecturer
Department of Civil Engineering, Kyoto University
Sakyou-ku, Kyoto 606, Japan
and
Tadashi Takahashi, Senior Civil Engineer
Nikkensekkei Ltd.
Koraibashi Higashi-ku, Osaka 541, Japan

Abstract

This paper deals with the flow behaviors and the transverse mixing at and below the confluence of the three rivers in the the Yodo River system by use of the mathematical and the physical modelings. The numerical experiments are conducted by using the 2-D mathematical models in the generalized curvilinear coordinate system and the characteristics of the flow field and the mixing are obtained. These results are also verified by the simplified physical model study and the mechanism of the mixing is clarified.

Introduction

The Yodo River system is the most important river in Kyoto-Osaka Metropolitan area, Japan. It has three main tributaries, Kizu River, Uji River and Katsura River, with particular flow characteristics and concentration distributions. They merge in Yodo River and the confluence becomes complicated in geometry. The basin-wide sewerage water treatment plants are located in the upper part of the river basin and the intake facilities for the municipal water supply are also located below the confluence. Then, water used in the upstream region flows back into Yodo River and it causes the qualititative problems to water utilization in the downstream region. Therefore, the study on the transverse mixing at and below the confluence in the Yodo River system is highly required for safe civil life, and a lot of research works and field measurements on the mixing have been made since 1950's. Li, Yagi and Sueishi (1987) recently analyized the transverse mixing by using the stream tube model (Yotsukura and Sayre, 1976) and estimated the transverse dispersion coefficient at $0.6 - 2.0hu_*$. However, hydraulic characteristics of the mixing have not yet been clarified.

The transverse dispersion coefficient in open channel flows has been measured in laboratory flumes and natural streams by many investigators and their results are summarized in Fischer (1979). The hydrodynamic transport processes represented by the convective movement is expected to play a more important role in the mixing in a natural river, and therefore the models for flow behaviors and concentrations are required in case the flow field is not simple or unsteady. The velocity field in natural river is mainly influenced by the riverbed topography, then mathematical and/or hydraulic models are usable for investigating the transverse mixing in a river.

Numerical Experiment

Mathematical Models: The basic hydraulic principles applied are the conservation laws of momentum, water and concentration. The length scale and the time scale of mixing in the depth-wise direction are much smaller than those in the transverse and the longitudinal directions of rivers, and the 2-D mathematical models in a horizontal plane will be used. The models are obtained by integrating the basic 3-D mathematical models for turbulent shear flows and concentration with respect to the flow area and written in the generalized curvilinear coordinate system as;

$$\frac{\partial}{\partial t}\left(\frac{1}{J}\right)\begin{pmatrix} M_1 \\ M_2 \\ h \\ N \end{pmatrix} + \frac{\partial}{\partial \xi_i}\left(\frac{1}{J}\right)\begin{pmatrix} U^i M_1 \\ U^i M_2 \\ U^i h \\ U^i N \end{pmatrix} = \frac{\partial}{\partial \xi_i}\left(\frac{1}{J}\right)\begin{pmatrix} h\tau^{1i}/\rho \\ h\tau^{2i}/\rho \\ 0 \\ hS^i \end{pmatrix} + \frac{1}{J}\begin{pmatrix} -gh\cdot\partial\xi_i/\partial x_1\cdot\partial\zeta/\partial\xi_i \\ -gh\cdot\partial\xi_i/\partial x_2\cdot\partial\zeta/\partial\xi_i \\ 0 \\ 0 \end{pmatrix} + \frac{1}{J}\begin{pmatrix} -\tau_{1b}/\rho \\ -\tau_{2b}/\rho \\ 0 \\ 0 \end{pmatrix} \quad (1)$$

and

$$J = |\,\partial\xi_i/\partial x_j\,| \quad (2) \qquad M_i = \int_{z_b}^{\zeta} u_i dx_3 \quad (3)$$

$$U_i = M_i/h \quad (4) \qquad N = \int_{z_b}^{\zeta} c dx_3 \quad (5)$$

$$U^i = \partial\xi_i/\partial x_j \cdot U_j \quad (6) \qquad S^i = \partial\xi_i/\partial x_j \cdot S_j \quad (7)$$

$$\tau^{ij} = \partial\xi_j/\partial x_k \cdot \tau_{ik} \quad (8) \qquad \tau_{ib}/\rho = gn^2 M_i\sqrt{M_1^2+M_2^2}/h^{7/3} \quad (9)$$

where U_i is the x_i component of the depth averaged velocity vector, M_i the x_i component of the momentum flux vector, h the water depth, N the depth-integrated concentration, ζ the water surface elevation, τ_{ij} the x_i directional shear stress acting on the control surface element perpendecular to the x_j direction including the turbulent and dispersion effects, S_i the x_i component of the gradient type mass transport vector including the turbulent diffusion and the dispersion, ρ the density, g the gravitational acceleration, τ_{ib} the frictional shear stress on the bottom, t the time, x_i the Cartesian coordinate in a horizontal plane, $\xi_i(=\xi_i(x_1,x_2))$ the generalized curvilinear coordinate ($i=1,2$) and J the transformation Jacobian. The shear stress τ_{ij} and the gradient type mass transport S^i can be written:

$$\frac{\tau_{ij}}{\rho} = \nu'\left(\frac{\partial\xi_k}{\partial x_j}\frac{\partial U_i}{\partial\xi_k} + \frac{\partial\xi_k}{\partial x_i}\frac{\partial U_j}{\partial\xi_k}\right) \quad (10) \qquad S^i = D^{ij}\frac{\partial C}{\partial\xi_j} \quad (11)$$

$$\left(\, D_{ij} \,\right) = \begin{pmatrix} cos^2\theta D_L + sin^2\theta D_T & sin\theta cos\theta\,(D_L - D_T) \\ sin\theta cos\theta\,(D_L - D_T) & sin^2\theta D_L + cos^2\theta D_T \end{pmatrix} \quad (12) \qquad D^{ij} = \frac{\partial\xi_i}{\partial x_k}\frac{\partial\xi_j}{\partial x_l}D_{kl} \quad (13)$$

where C is the depth-averaged concentration, D_L the longitudinal dispersion coefficient, D_T the transverse dispersion coefficient, θ the angle between Cartesian coordinates and the principal axes of diffusion and dispersion.

The boundary condition at the closed boundary is "non-slip condition" for flows and "no-mass transport" for concentration. The momentum flux or the water surface elevation for flows and the value of concentration for the concentration dispersion are specified at the open boundary.

Followings are notable on the set of Eq. (1); the dependent variables are the same as those in the Cartesian coordinates system and only the independent variables are transformed into the non-orthogonal curvilinear system; the first equation of Eq. (1) is the momentum conservation equation in the x_1 direction, the second one that in the x_2 direction, the third one the continuity equation and the forth one the mass conservation equation for the contaminant.

The system of the partial differential equations (1) can be solved by FDM and the numerical procedures have already been shown in details with the derivations of Eq.

(1) in Iwasa, Aya and Inoue (1989). The verification of the mathematical models was successefully made and it was concluded that the magnitude of transverse dispersion coefficient is less effective on the transverse concentration distribution in the paper of Iwasa, Aya and Baba (1990). The estimated parameters for the Yodo River are; the Manning's roughness coefficient $n = 0.02$; the longitudinal dispersion coefficient $D_L = 5.93hu_*$; the transverse dispersion coefficient $D_T = 0.2hu_*$.

Results of Numerical Experiments: The non-orthogonal curvilinear grid of about 25m in length and 5m in width covers the study area of about 4km in the longitudinal length and about 100m in the transverse width as shown in Fig. 1(a). The general topography of the study area made by use of the interpolation of geographical survey data is illustrated in Fig. 1 (b) and the non-unifrom distributions of riverbed elevation and the existence of depression areas are seen.

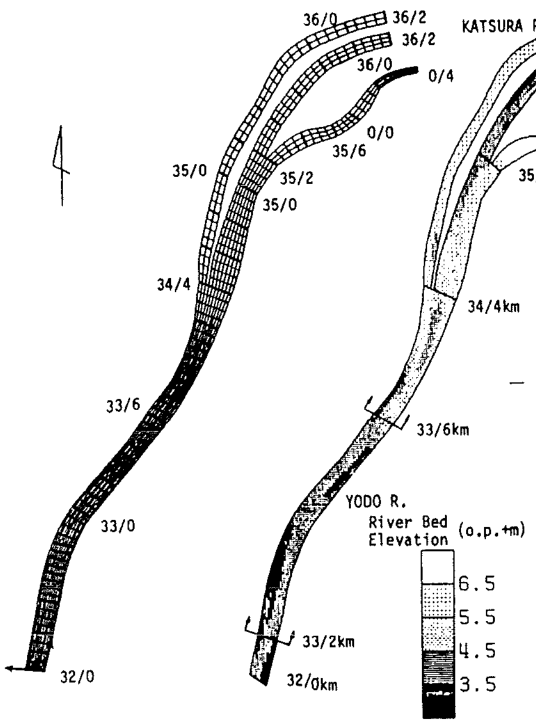

(a) Generated grid (b) Topography of the study area

Fig. 1 Curvilinear grid and topography.

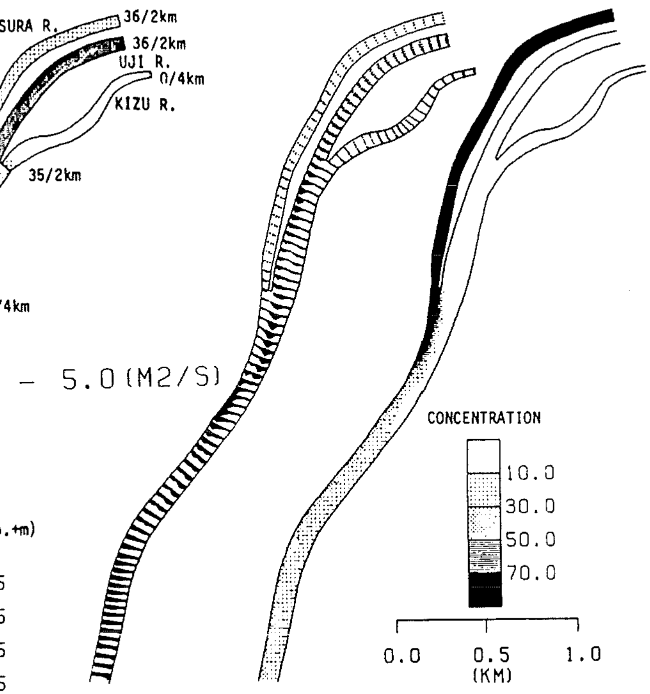

(a) Momentum flux vector distributions (b) Spreading of tracer

Fig. 2 Results under Regime 355.

Table 1 Summary of hydraulic conditions in numerical experiments.

Regime	Discharge Q(m^3/s)			
	Katsura River	Uji River	Kizu River	Total
Average	62.0	203.0	56.0	321.0
185: Ordinary Water Discharge	50.0	160.0	38.0	248.0
275: Low Water Discharge	35.0	108.0	27.0	170.0
355: Drought Discharge	30.0	75.0	18.0	123.0
6294	19.0	120.4	11.2	150.6

A series of numerical experiment was conducted under the flow regimes listed in Table 1 and another series was also done with different cross-section channels under the same boundary conditions of Regime 6294. The simulation models can disclose the unsteady behaviors of flow and the spreading of tracer cloud, but only the results under the steady conditions will be shown. The momentum flux vector distributions and the spreadings of tracer cloud from Katsura River under Regimes 355 are shown in Figs. 2 (a) and (b). The momentum flux distributions and the bathymetry at the confluence under Regimes Average and 355 are also shown in details in Figs. 3 (a) and (b).

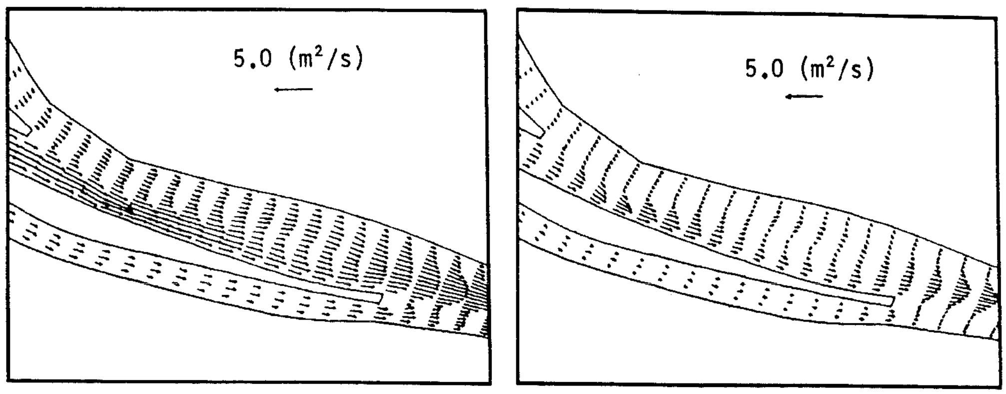

(a) Regime Average (b) Regime 355

Fig. 3 Momentum flux vector distributions at the confluence.

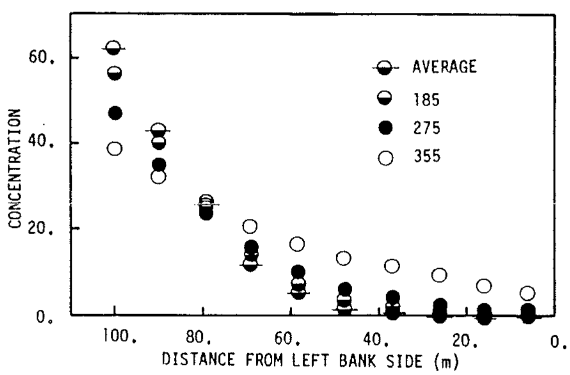

Fig. 4 Concentration distributions under some flow regimes.

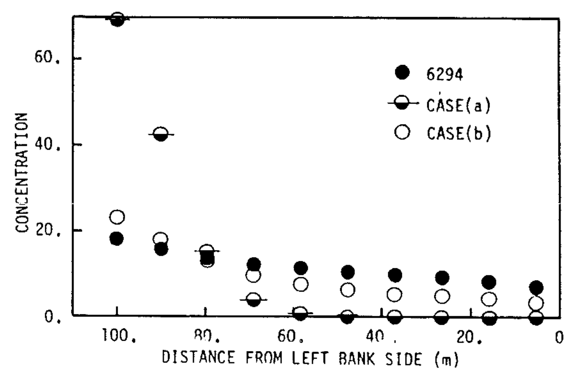

Fig. 5 Concentration distributions under different cross-section conditions.

The riverbed in Kizu river is the highest and that in Uji river is the lowest in the elevation, and the waters in Kizu River and Katsura River merge into the water in Uji River at the confluence. Below the confluence, the river water mainly flows down in the lower part of the riverbed and the main stream changes its route from one side to the opposite side of channel according to the non-uniform riverbed topography.

Tracer cloud from Katsura River mainly flows down along the right bank of Yodo River as shown in Fig. 2 (b). The spreading width of the tracer cloud changes in the longitudinal direction because of the divergence and the convergence of flows caused by the non-uniform riverbed topography as stated earlier. The tracer cloud spreads more widely as total discharge is smaller as shown in Fig. 4 which illustrates the transverse distributions of the concentration at the 33.6km section under different flow regimes. Fig. 5 also shows the three transverse distributions of concentration obtained at the 33.6km section under Regime 6294 in the actual river channel, the model river of rectangular cross-section and another model river dredged along the right-side bank. Spreading width of tracer cloud in the rectangular cross section channel is much smaller and its peak concentration is the highest among the three curves. The dilution by the waters from Uji River and Kizu River makes the peak concentrarion in other two ones lower and the transverse mixing is accelerated.

Simplified Hydraulic Model Experiment

Outlines of Experiment: A series of hydraulic experiment by use of the laboratory flume was conducted in order to verify the characteristics of the mixing obtained in the numerical experiment. The straight flume of 25cm in width has the series of rectangular-shaped depressions on the bottom alternately located beside a right or left channel-side. Its dimensions are 75.0cm long, 5.0 cm wide and 1.0cm deep. This flume was used as a simplified hydraulic model for the Yodo River System below the confluence, and its scale is about 1/400 in the horizontal plane and 1/200 in the vertical direction. A rectangular cross-section channel was also used. The hydraulic conditions in the experiments are summarized in Table 2 and the discharge in Run 1 is equivalent to the annual average discharge in the prototype.

Table 2 Summary of hydraulic conditions.

Run No.	Depth h(cm)	Discharge Q(l/s)	Velocity V(cm/s)	Flume
1	0.610	0.239	15.7	rectangular
2	0.696	0.263	15.1	simplified model
3	1.040	0.536	20.6	simplified model

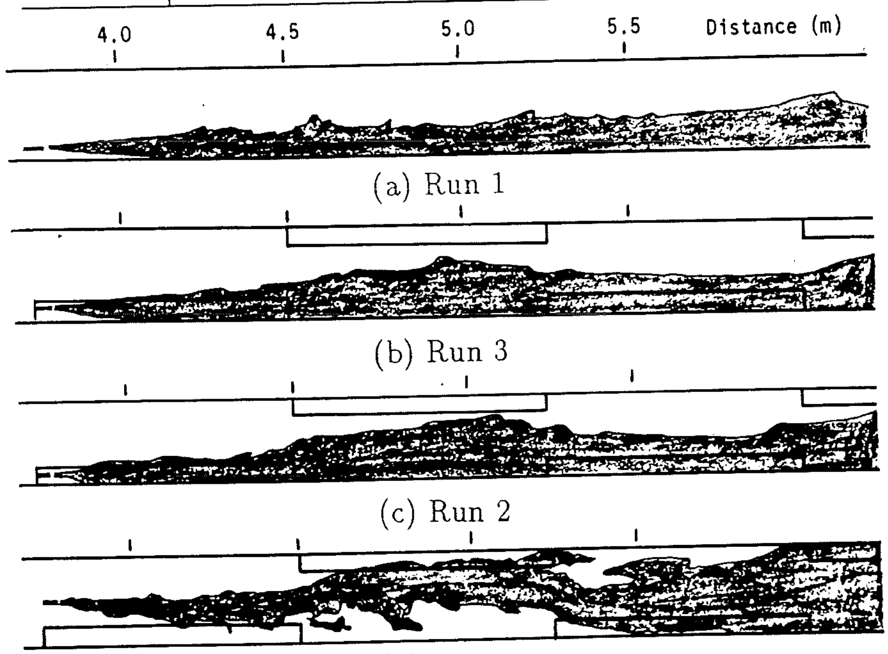

(a) Run 1

(b) Run 3

(c) Run 2

(d) Run 2

Fig. 6 Spreadings of continuously injected dye solution.

The dye-solution used as the tracer was continuously injected as a point source at the upstream section of the flume. The injected tracer spread in the transverse and the longitudinal directions and its dispersion cloud was observed and recorded by a photo-camera, but quantitative measurements were not made.

Results of Hydraulic Experiment: The spreading of the tracer cloud observed in a rectangular cross-section flume test is illustrated in Fgi. 6 (a) and Figs. 6 (b), (c) and (d) were obtained in tests with a flume with depressions. The tracer injected near the channel-side spreads in the transverse direction in flowing down, but the width of tracer cloud is smaller on depressions and larger below the ends of depressions. The transverse mixing is the largest in Run 2, the second one in Run 3 and the third one in Run 1 and these results are equivalent to the results obtained in numerical experiments. Fig. 6 (d) shows the spreading of the tracer cloud injected at the half-width. The meandering of the cloud suggests the flow also meanders and it is caused by the existence of the depressions; the flow concentrating on depressions spreads in the transverse direction below the downstream end of them, because the flow depth becomes shallower; at the upstream end of depressions, the flow again converges and concentrates on them. Thus, the speading and convergence of flow caused by depressions make the transverse mixing accelerated. This effect is stronger as discharge and/or average depth is smaller as shown in Figs. 6 (b) and (c).

Discussions

The results obtained by numerical and hydraulic experiments are summarized that the flow behaviors are influenced by the riverbed topography and flow regimes and that the spreading of tracer cloud in the transverse direction is wider as discharge is lower. It is also much wider in a non-uniform riverbed channel than in a rectangular cross-section channel.

The mechanism of the transverse mixing in the Yodo River system below the confluence can be explained as; the riverbed is not uniform and the river water mainly flows down in the lower part of the riverbed, therefore, the main stream meanders within the channel; this meandering causes spreading and convergence of tracer cloud and makes concentration distributions more uniform as clearly shown in the hydraulic experiments. Therefore the convective transport is more dominant than the turbulent and dispersion transport. In case the total discharge is larger or the cross-section of channel is rectangular, the variation of the transverse distribution of the momentum flux vectors in the longitudinal direction is smaller and the transverse mixing is also smaller.

Conclusions

The hydraulc characteristics of the flow behavior and the associated mixing at and below the confluence in the Yodo River system were investigated by the mathematical and the hydraulic modelings. The mechanism of the transverse mixing is clarified as the non-uniform distributions of the momentum flux vector varied in the longitudinal direction makes the transverse mixing accerelated. The convective transport plays a more important role in the mixing than the diffusive and dispersive tranport.

References

Fischer, H. B. et al (1979) Mixing in Inland and Coastal Waters, Academic Press.

Iwasa, Y., Aya, S and Baba, H. (1990) Proc. 7th Congress of APD-IAHR, Beijin-China. (in printing)

Iwasa, Y., Aya, S. and Inoue, T. (1989) Annuals, DPRI, Kyoto University, No. 32 B-2, pp. 669-687. (in Japanese)

Li, S., Yagi, S. and Sueishi, T. (1987) Proc. 31st Japanese Conference on Hydraulics, pp. 311-316. (in Japanese)

Yotsukura, N. and Sayre, W. W. (1976) Water Resources Research, Vol. 12, No. 4, pp. 695-704.

EFFECT OF CENTRAL ANGLE ON LONGITUDINAL DISPERSION IN MEANDERING CHANNELS

by Houshang Afshari & S.K. Pathak
Department of Civil Engineering
University of Roorkee
Roorkee 247 667 INDIA

Abstract

Due to existance of bends, longitudinal dispersion in meandering channel is quite different from that in a straight channel, so the results obtained in straight channels could not be used as such for meandering channels. Not much work has been done regarding dispersion in meandering channels. In the present study several meandering channels with 4 to 6 bends having different central angle ranging from 90^{o} to 270^{o} have been fabricated. In each flume several dispersion runs with flow depth ranging from 4 cm to 15 cm have been taken. This study showed that as the central angle of the bend is increased the dispersion is also increased. The effect of central angle and flow parameters on dispersion coefficient have been analyzed and are being presented in this paper.

Introduction

Regulation of the release of pollution into the river system is one of the most important and effective measures of water pollution control. This regulation requires knowledge of the rate at which the stream system is capable of dispersing the pollutant.

Longitudinal dispersion is a bulk one-dimensional equation written in the direction of the flow to describe the process by which a flowing stream spreads and dilutes a pollutant.

Taylor [5] proposed a simplified one dimensional longitudinal dispersion model as :

$$\frac{d\bar{c}}{dt} = DL \frac{d^2\bar{c}}{dx^2} - U \frac{d\bar{c}}{dx} \qquad (1)$$

in which t = time ; x = distance in the direction of the flow ; $\bar{c}$ = average cross-sectional concentration ; U = average velocity of flow ; and DL is known as longitudinal dispersion coefficient.

Bends are always present in meandering rivers and these play an important role in dispersion process, so the knowledge obtained from tests in straight channels is not always adequate to understand the basic mechanism of dispersion in natural stream, while most of the laboratory experiments on longitudinal dispersion have been performed in straight channels. Literature review indicates that only a few investigations on dispersion in either laboratory or natural meandering channels have been carried out [2,3]. In the present study the effect of central angle (θ), width to depth ratio (B/D) and friction factor (f) on longitudinal dispersion coefficient (DL) has been investigated by conducting experiments on laboratory meandering channels.

Methods of Calculating Dispersion Coefficient

The two widely used methods for calculating the dispersion coefficient from the observed concentration versus time curves are the change of moment method and the routing method. These methods have been described by Fischer [1] for straight channels and by Fukoka [3] for meandering channels. In the present study the value of DL is first obtained by the method of moments and then this value is further improved by the routing procedure.

Description of Experiments

It was planned to fabricate seven meandering channels on a sloping wooden floor (slope = 0.024) with prefabricated 45 cm high G.I. sheet walls. These channels were having central radius (r_c) 180 cm, central angle (θ) ranging from 90° to 270° and with width from 18 cm to 60 cm. A neutrally buoyant salt solution (mixture of sodium chloride, water and denatured spirit) was used as tracer. A concentration measuring system, consisting of a set of conductivity probes, conductometer, universal amplifier and strip chart recorder, was used for getting the concentration (c) - time (t) records. In all, 24 runs were conducted in these meandering channels and the experimental data was processed on DEC 2050 Computer system at Roorkee University.

Discussion of Results

Fukoka [3] has concluded from the experimental data of Fischer [1] that the dimensionless dispersion coefficient in a straight channel does not depend on width to depth ratio (B/D). Figure 1 shows the plot of DL/RU Vs. B/D for present study. From this figure, it is seen that in smooth meandering channel: (i) for a given B/D, DL/RU increases as the value of friction factor (f) increases (ii) for a given f, the value of DL/RU increases as B/D is increasing (iii) the effect of central radius to width ratio r_c/B on DL/RU, in smooth meandering channel is insignificant and therefore it could be neglected for further analysis.

Figure 2 shows the plot of DL/RU Vs. θ. It is seen that the value of DL/RU is increasing with increase of central angle, however, rate of increase in DL/RU is low upto θ = 180°, relatively high for θ more than 180°. In view of the above qualitative trends namely, DL/RU is indirectly proportional to $U/U_*(=\sqrt{8/f})$ and directly proportional to the value of B/D and θ, an empirical predictive model for DL/RU may assume the following form :

$$DL/RU = c_1[1 + (B/D)^{c_3}\,\theta^{c_4}] / (U/U_*)^{c_2} \quad , \tag{2}$$

where U_* is shear velocity and θ is in radian.

The optimal value of c_1, c_2, c_3 and c_4 which minimize the cumulative absolute error between observed DL/RU and predicted DL/RU (using Eq. 2) were obtained using grid search method. Equation (2) is valid for smooth straight channel by assigning value of θ as zero. A grid search optimization computer program was developed and used for the analysis of the present laboratory data along with data of Fukoka [3] and Magazine [4]. It was found that the model for longitudinal dispersion coefficient comes out as :

$$\frac{DL}{RU} = 56.79\,[1 + (\frac{B}{D})^{0.48}\,\theta^{1.42}] / (U/U_*)^{1.52} \tag{3}$$

Figure 3 shows the plot of observed DL/RU Vs. predicted values using equation 3, and it can be seen that the performance of the empirical predictive model is satisfactory.

References

1. Fischer, H.B., "Longitudinal Dispersion in Laboratory & Natural Streams", Report No. KH-R-12, California Inst. of Tech., 1966.

2. Fischer, H.B., "The Effect of Bends on Dispersion in Stream", Water Reso. Res., Vol.5, No.9, 1969, pp. 496-506.

3. Fukoka, S., "Longitudinal Dispersion in Sinous Channels", Ph.D. Thesis, The University of Iowa, Iowa City, Iowa, 1971.

4. Magazine, M.K., "Effect of Bed and Side Roughness on Dispersion and Diffusion in Open Channels", Ph.D. Thesis, University of Roorkee, Roorkee, 1983.

5. Taylor, G.I., "The Dispersion of Matter in Turbulent Flow Through A Pipe", Proceeding, Royal Society of London, England, Series A, Vol.223, May 1954, pp. 446-468.

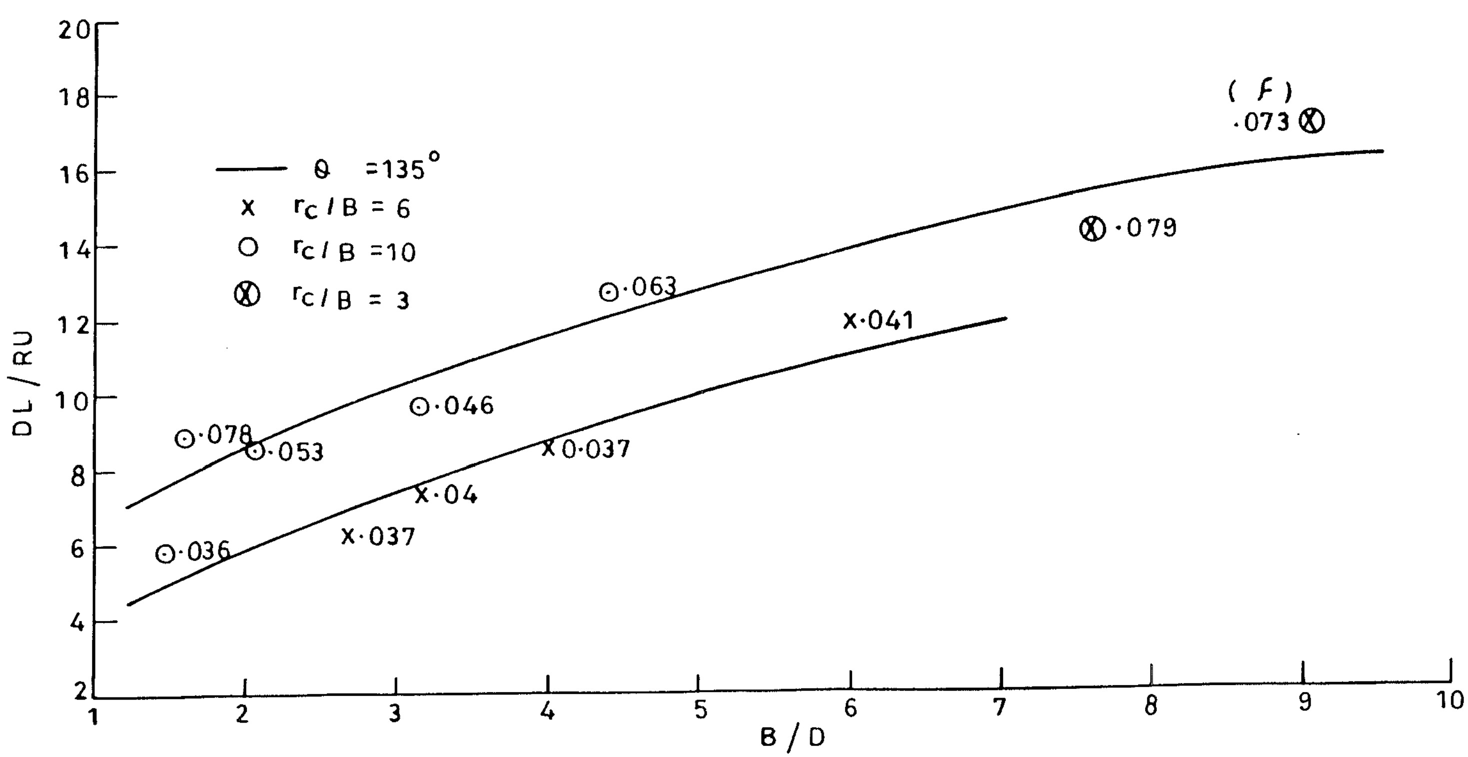

FIG. 1 —DL / RU Vs WIDTH DEPTH RATIO B / D

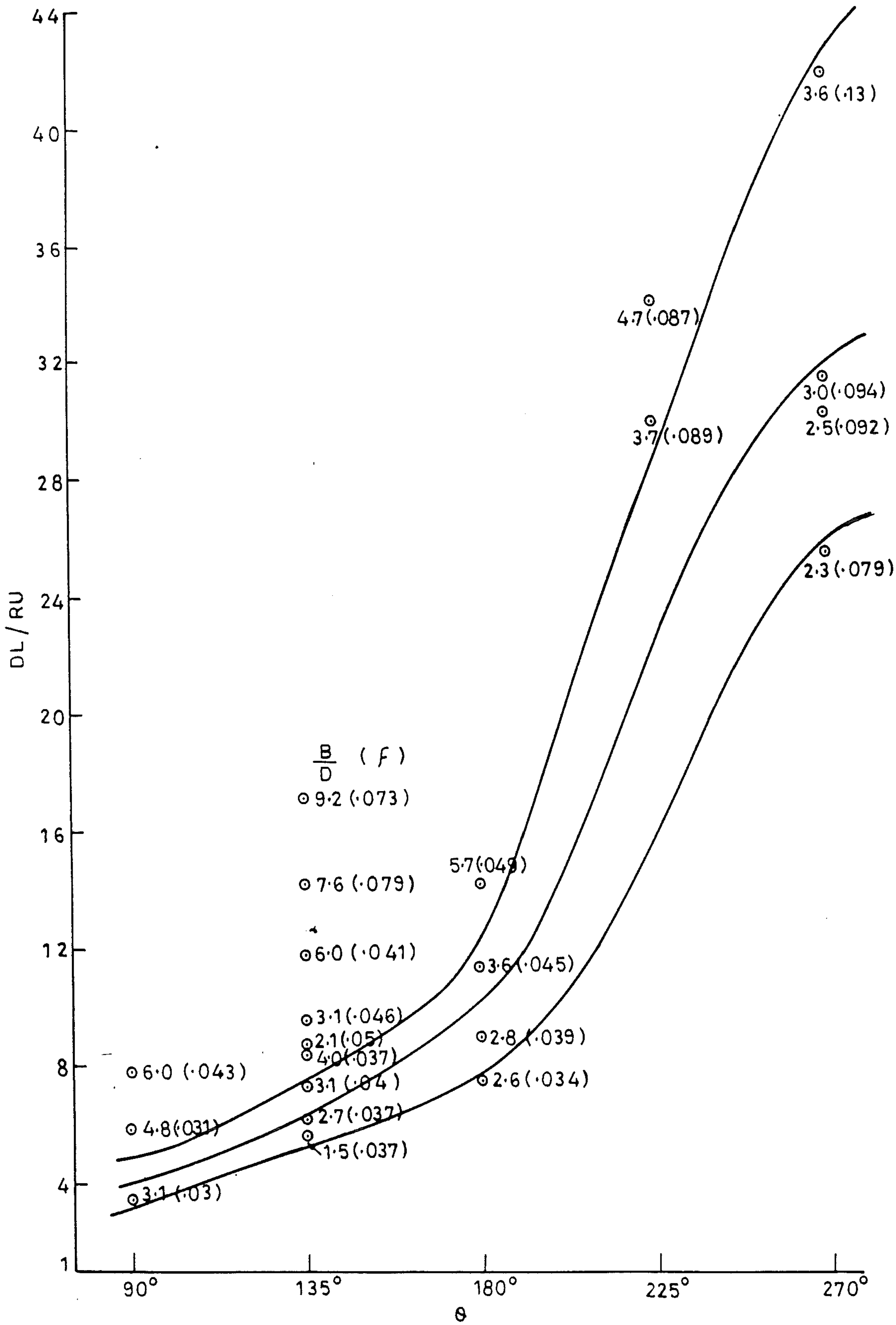

FIG. 2 — DL/RU Vs CENTRAL ANGLE θ

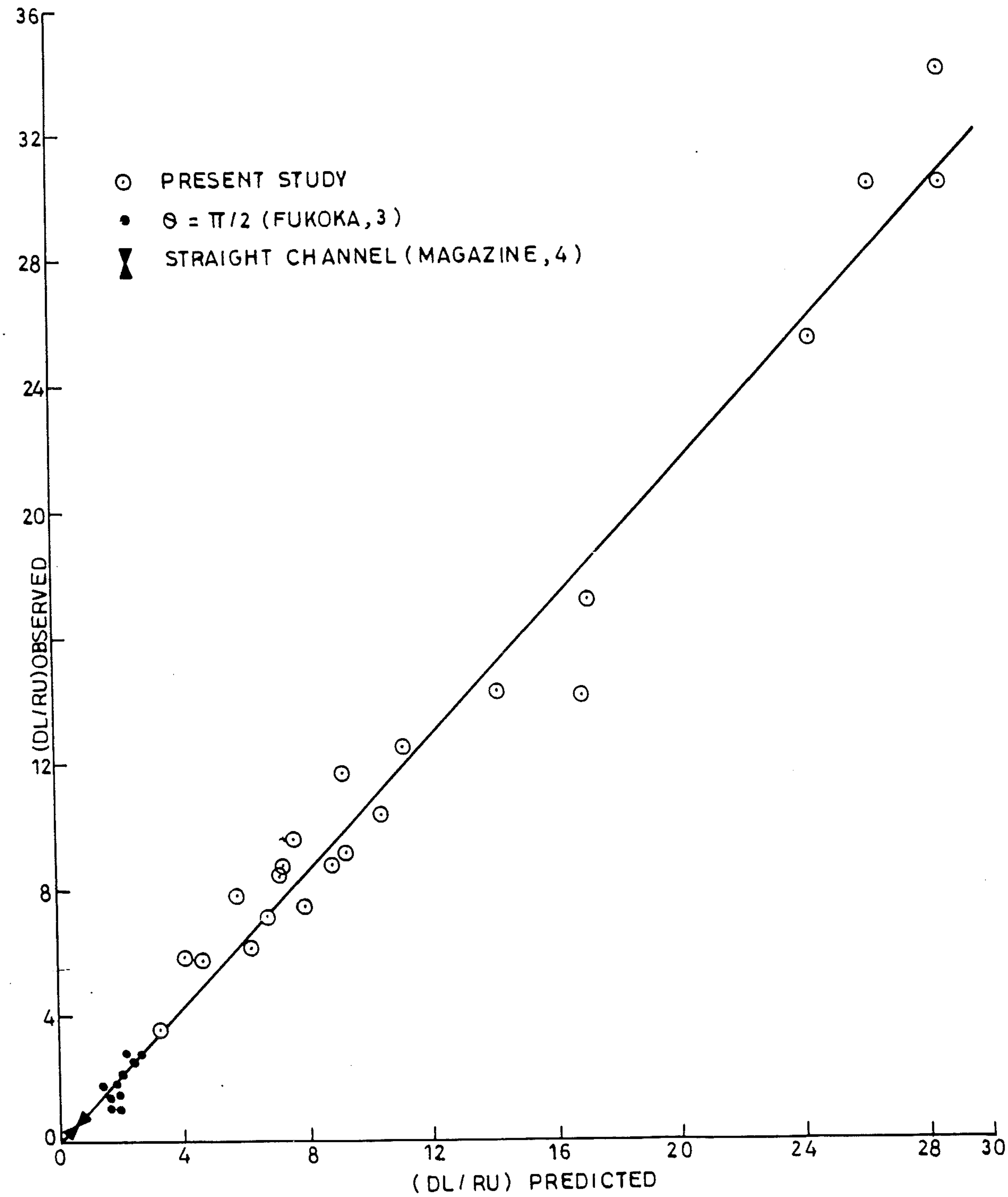

FIG. 3– COMPARISON OF OBSERVED AND PREDICTED (DL/RU)

TURBULENCE CONTROL OF COHERENT VORTEX IN MIXING LAYER OF OPEN-CHANNEL PARALLEL COFLOWS

Iehisa Nezu and Hiroji Nakagawa
Department of Civil Engineering,
Kyoto University, Kyoto 606, Japan.

Abstract: This study verified experimentally that coherent vortex or turbulence in mixing layer of coflows was enhanced by lower-frequency oscillations, while it was depressed by high-frequency ones.

1. Introduction

The significance of the mixing layer in confluence of rivers is well recognized in river engineering. A mixing layer with different velocities and water qualities is formed downstream of the confluence point. Many previous studies with probe-measurements such as hot-wires and hot-films revealed that turbulent structure of mixing layer indicated a self-preserving property. Of the most essential significance, however, is that an existence of large-scale coherent vortices in a plane turbulent mixing layer was first discovered by Brown & Roshko(1974) and Winant & Browand(1974) on the basis of flow visualization. They observed that adjacent vortices tended to roll around each other before coalescence and formation of a large-scale vortex. These vortex pairing and coalescence are responsible for the growth of the mixing layer. This process plays an essential role in the turbulent mixing and diffusion of momentum, heat and mass, like different water qualities. Some attentions have been paid on artificial control techniques of coherent vortex in mixing layer in order to control the generation of turbulence and jet noise. Oster & Wygnanski(1982) investigated a sensitivity of turbulent shear layer to small-amplitude, controlled oscillations which were introduced at the initiation of air mixing layer. Nezu et al.(1988) have recently conducted some probe and visual measurements of coherent vortices in water mixing layers with and without forced oscillations. It is a very important topic in hydraulic engineering to investigate coherent structures in mixing layer of confluent rivers and then to develop control techniques of the turbulent mixing and diffusion mechanisms by introducing artificially forced oscillations in order to enhance or depress the mixing phenomena of different water qualities.

In the present study, effects of periodic two-dimensional excitation on the development of a turbulent mixing region in open-channel parallel coflows are investigated using both visual study and hot-film anemometers. The mechanism of a birth-development-coalescence-decay of coherent vortices is revealed, and a possibility of turbulence control is examined experimentally.

2. Experimental Equipment and Procedures

An iron partition plate with 1mm thick and 7.7m long was set up along the center line of the tilting flume with 15m long and 50 cm wide. Water discharges in two flumes were determined separately by using flow meters and each water flow through honeycomb joined each other 7.7m downstream of the channel entrance. In order to prevent the wake effect of the partition plate on the mixing layer as largely as possible, the channel width was contracted as 5 : 3. The oscillation plate was set-up at the initiation of mixing layer, as shown in Fig.1. The frequency of the sinusoidal oscillations was changed from 0.1Hz to 6Hz, and its amplitude was kept to be 3mm.

x and y are the longitudinal and spanwise directions, respectively. $x=y=0$ corresponds to the confluence point of water flow. The water depth h was set to be 5cm, 10cm and 15cm. Denoting that the bulk mean velocities on the high velocity side ($y>0$) and on the low velocity side ($y<0$) as U_1 and U_2, respectively, the velocity ratio U_2/U_1 was changed from 0.2 to 1.0, in which U_1 was set to be 5cm/s, 10cm/s and 15cm/s.

The dye was injected at the confluence point and coherent vortices were visualized using video-camera. The video picture of coherent vortices was then analyzed frame by frame by using position analyzer. The velocity measurements were conducted by using X-type hot-film anemometers. The measuring points were traversed in the y direction of the horizontal section at $z/h=0.8$, in which x was changed from 0.2cm to 80cm. The total number of the measuring points was 150 for each case.

3. Two Patterns of Coherent Vortices in Mixing Layers

Fig.2(a) shows a typical photograph of coherent vortices without forced oscillations in the case of $U_2/U_1=0.6$. The positions of dye injections are $y=-2$, 0 and 2cm. The size of grid in the photograph is equal to 2cm. Immediately downstream of the confluence, an instability wave is generated due to a high shear layer, i.e. Kelvin-Helmholtz (K-H) instability, and it is rolled up to become coherent vortex. These vortices are convected downstream during a lifetime that is terminated when they interact and coalesce with neighboring vortices to form larger ones. Finally, the larger vortices collapse to be chaotic turbulence. These behaviors of coherent vortices coincide well with

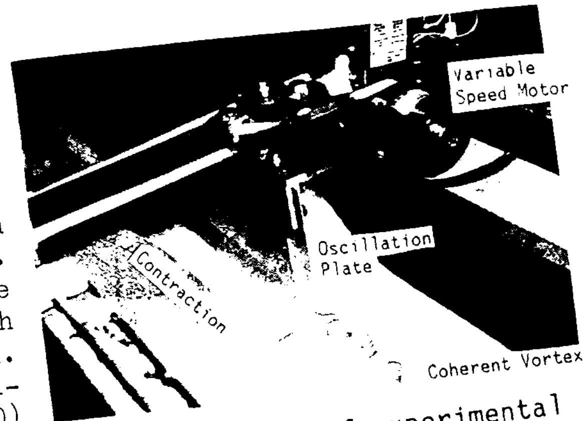

Fig.1 Photograph of experimental flume and oscillation equipment.

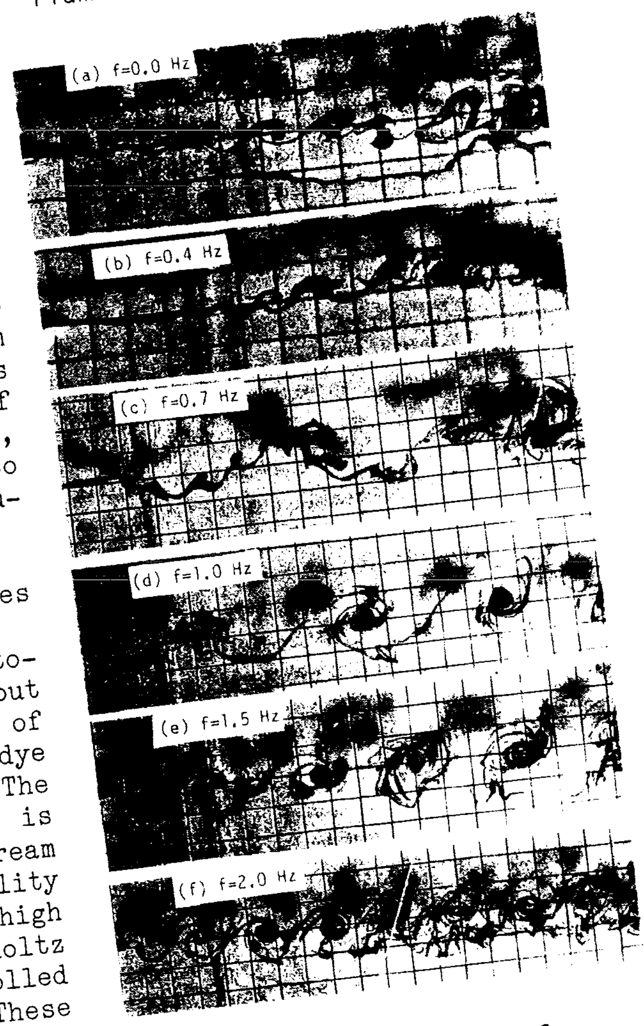

Fig.2 Visual photographs of coherent vortices by varying the frequency of forced oscillations.

previous observations in mixing layer (e.g. Winant & Browand (1974)) and also in water jet (e.g. Nakagawa et al.(1982)).

Of particular significance in the present study is that, when artificial oscillations are introduced at the initiation of the mixing layer, the patterns of coherent vortices depend strongly on the forced frequency f. For f=0.4Hz, the generation frequency of coherent vortex is nearly equal to the frequency f_n of "naturally" generated vortex due to K-H instability with no forced oscillation. As a vortex is convected, an undulated vortex on the high-speed side catches up with the forward undulated vortex on the low-speed side and they coalesce with each other to become larger vortex. This larger-scale vortex tends to be governed by the forced oscillation f. For f=0.7Hz, a larger-scale coalescence occurs more upstream than that for f=0.4Hz. However, the pattern of coherent vortices for the forced oscillations of f=1.0Hz is different from that for f=0.4 and 0.7Hz. Although the frequency of vortex generation is nearly equal to the "natural" frequency f_n immediately downstream of the partition plate, the frequency of convected vortices coincides well with that of the forced oscillation. When higher frequency oscillations of f=1.5 and 2.0Hz are introduced, well-controlled vortices are generated at the initiation of mixing layer, and this generation frequency coincides with the forced frequency. As seen in Fig.2(f), a vortex rotates several times and it is convected downstream. It should be noted that these well-controlled vortices never coalesce with each other and thus the spacing between vortices keeps constant.

When any forced oscillation is introduced in the mixing layer of confluence, the effect of oscillation on coherent vortex can be classified into two categories. There are two patterns of coherent vortices; one is naturally generated vortex due to K-H instability, and the other is resonant vortex due to forced oscillation. In the case of forced oscillation with a frequency lower than a transitional frequency f_t, naturally generated vortices are convected with receiving a large undulation, and consequently the coalescence of some vortices occurs to become a large-scale vortex. The spreading rate of flow is increased by enhancing the coalescence of neighboring vortices. On the other hand, for higher-frequency oscillation, i.e. $f>f_t$, well-controlled vortices are generated and convected in a single array of large vortices, which never coalesce with each other. Consequently, the development of vortices is depressed and the decay of vortices is also faster than that for low-frequency oscillation. In this sense, f_t is called here "transitional frequency", at which all of natural vortices are just controlled by forced oscillation, as seen in Fig.2(d). The following results were obtained from visual analysis. As U_2/U_1 becomes larger, the size of coherent vortex becomes smaller and the positions of the roll-up and vortex pairing occur more downstream. As the forced frequency f becomes larger, the position of vortex generation occurs closer to the confluence point. When f is greater than the transitional frequency f_t, the vortex coalescence doesn't occur and a well-controlled vortex array is formed.

Fig.3 shows the variation of the transverse scale L of vortex against the streamwise direction, x. The values of L in unforced mixing layer increase linearly with x. It should be noted that a forced coherent vortex with lower frequency $f<f_t$ is quite different from that with higher frequency $f>f_t$. For $f<f_t$, the size of natural vortex decreases with an increase of the forced frequency f. The size of the resonant vortex is much larger than that of this natural vortex, as seen in Fig.3. Because

the natural vortex coalesces with resonant vortex, the size of the resonant vortex increases rapidly and then attains constant. On the other hand, for $f>f_t$, only the well-resonant vortex is generated downstream of the confluence. This high-frequency forced vortex is evidently larger than the lower-frequency one near the confluence, i.e. x<10 cm. However, the former develops much less than the latter, and furthermore it disappears faster than the latter.

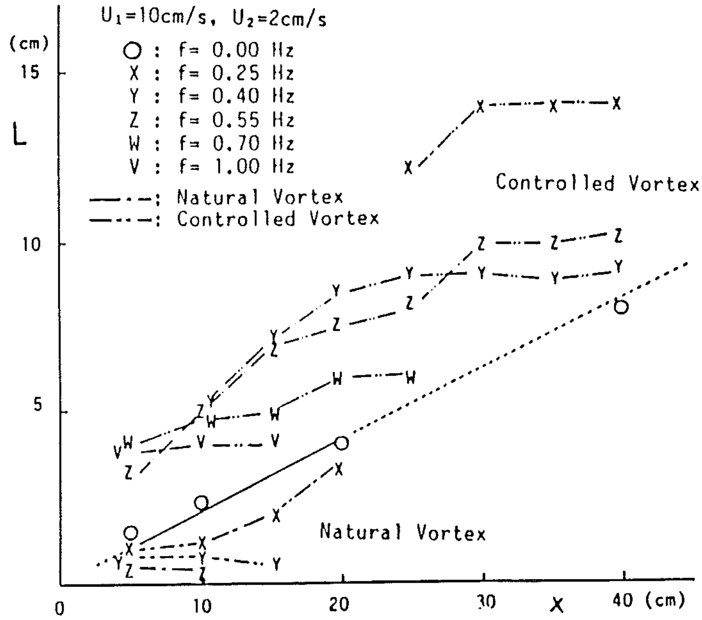

Fig.3 Variation of vortex scale L of natural and controlled vortices against the streamwise direction, x.

4. Turbulent Structure of Forced Mixing Layer

The mean velocity profiles and the distributions of turbulence intensities u' and v' and the Reynolds stress $-\overline{uv}$ were obtained for unforced and forced mixing layers. Although the present equipment had a 5:3 contraction unit of 50 cm length, the effect of wakes appeared near the confluence (x<5cm) in the unforced mixing layers, i.e. f=0 Hz, and the mixing-layer type profiles were established downstream of this section. On the other hand, in the case of forced mixing layers, the effect of wakes became weaker in all of experiments. This implies that the turbulent mixing is enhanced when the forced oscillation is introduced at the confluence. Of particular significance is that the negative Reynolds stress was generated near the confluence in the case of $f>f_t$. This suggests that the suppression of vortex interaction results in the generation of negative Reynolds stress and hence an extraction of energy from turbulence to mean motion occurs, as pointed out by Oster et al.(1982) and Nezu et al.(1988). More detailed information is given in Nezu et al.(1988).

5. Spectral Distribution of Coherent Vortex

Fig.4 shows some examples of spectral distributions of u and v along the center line in unforced mixing layer. In the region of x=5 to 10 cm in which an unstable wave rolls up and becomes coherent vortex, the predominant part of f=3Hz is seen clearly. Such a first predominant frequency f, or Strouhal number $St=f\theta_1/U_1$ (θ_1=initial momentum thickness), was evaluated from the spectral distributions in all experimental cases. The value of St increases gradually with x/θ_1 and then attains a maximum, i.e. St=0.02-0.04 at about x/θ_1=50. This implies the generation of coherent vortex from the non-linear wave of K-H instability. On the other hand, the value of St decreases with x/θ_1, which implies the occurrence of vortex coalescence. At x>30 cm, i.e. x/θ_1>100, only the peak value of 1Hz becomes large, which corresponds to the transitional frequency f_t. At x=80cm, the spectral distribution obeys -5/3 power law in fully developed turbulence. Fig.5 shows the

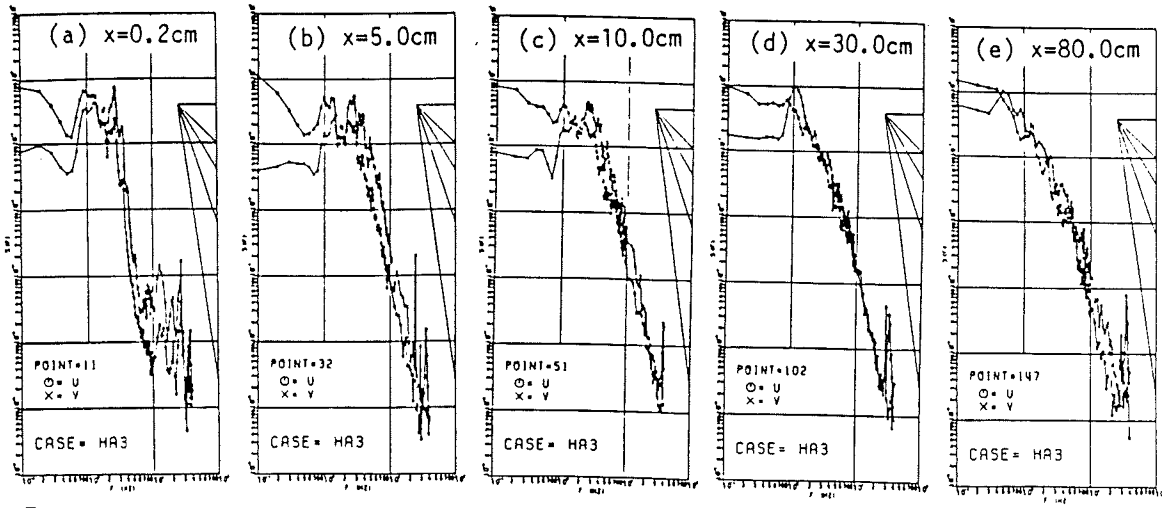

Fig.4 Spectral distributions of u and v along the center line, i.e. y=0, in the unforced mixing layer of f=0 Hz.

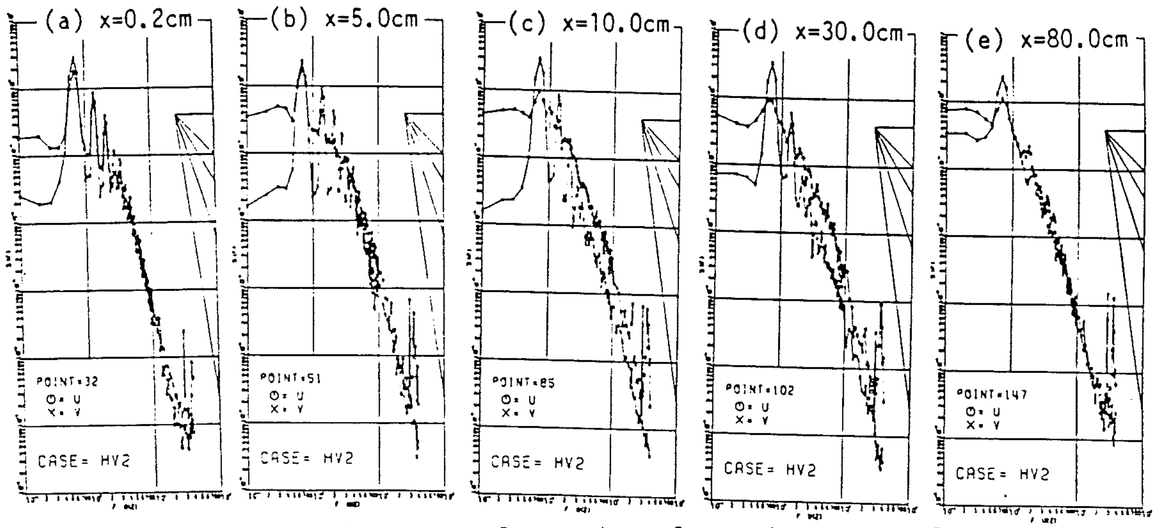

Fig.5 Spectral distributions of u and v along the center line, i.e. y=0, in the forced mixing layer of f=0.7Hz, i.e. $f<f_t$.

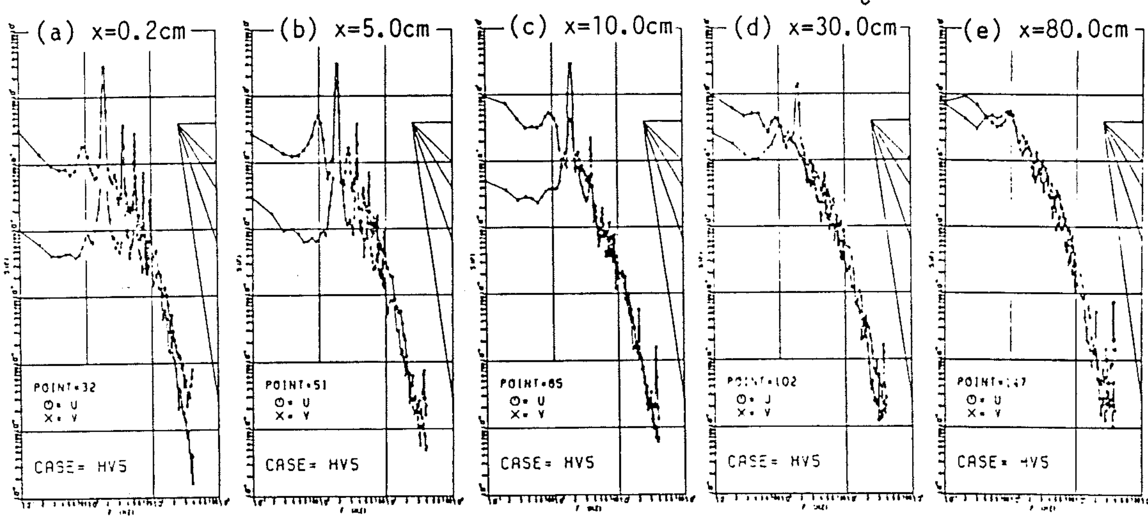

Fig.6 Spectral distributions of u and v along the center line, i.e. y=0, in the forced mixing layer of f=2.0 Hz, i.e. $f>f_t$.

spectral distributions in the forced mixing layer of f=0.7Hz, i.e. $f<f_t$. Although a small peak of 3Hz corresponding to natural vortex generation is seen, the spectral peaks are very large at harmonic parts, i.e. f, 2f 3f etc., by the forced oscillation f. At sufficiently downstream, the turbulent energy is concentrated on the forced oscillation part of f=0.7Hz due to a large-scale vortex coalescence.

Fig.6 shows the spectral distributions in the case of f=2Hz. Because the transitional frequency of this mixing layer is 1Hz, a kind of resonance occurs for the forced oscillation of f=2Hz. The forced mixing layer of 2Hz is controlled more strongly than that of f=0.7Hz. The decay of the former is, however, faster than that of the latter. These features coincide well with the visual observation which was described previously.

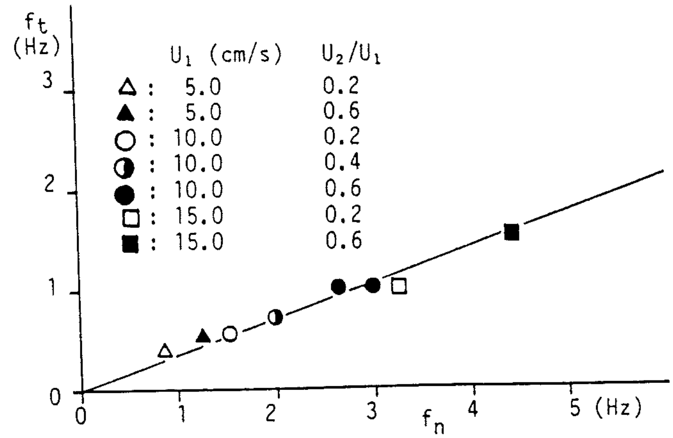

Fig.7 Relation between natural frequency f_n and transitional frequency f_t.

6. Relation between Natural and Transitional Frequencies

When one tries to control various turbulent transports in which coherent vortices play an essential role, one must know the transitional frequency f_t in the mixing layers. Fig.7 shows the variation of f_t against the frequency f_n of naturally generated vortex in all cases. The value of f_t was determined as a forced frequency at which no natural vortex was just generated. These visual data coincided well with the spectral data. Fig.7 indicates that f_t is nearly equal to $f_n/3$ in the present experiments. Any physical model isn't yet available to explain such a relation of $f_t=f_n/3$. It is further necessary to investigate a physical model of controlled coherent vortex by forced oscillations.

7. Conclusions

In the present study, the effect of periodic two-dimensional excitation on the development of a turbulent mixing region in open-channel parallel coflows was investigated by making use of visual study and hot-film anemometers. When the frequency of forced oscillations was lower than the transitional frequency which might describe the interaction of vortices, i.e. vortex pairing, the spreading rate of flow was increased by enhancing the coalescence of neighboring vortices. On the other hand, at frequency higher than the transitional one, the controlled and resonant vortices were generated in a single array of large vortices, which did not interact nor coalesce with each other. Consequently, the spreading rate of flow was depressed, and also the Reynolds stress became negative in this region.

References

1) Brown, G.L. and Roshko, A.(1974), J. Fluid Mech., vol.64, pp.775-816.
2) Nakagawa, H., Nezu, I., et al.(1982), J. of Flow Visualization Soc. of Japan, vol.2, pp.629-634.
3) Nezu, I. et al.(1988), 3rd Symp. on Refined Flow Modelling, pp.927-936.
4) Oster, D. and Wygnanski, I.(1982) , J. Fluid Mech., vol.123, pp.91-130.
5) Winant, C.D. and Browand, F.K.(1974), J. Fluid Mech., vol.63, pp.237-255.

FLOW RESISTANCE DUE TO LATERAL MOMENTUM TRANSPORT ACROSS VEGETATION IN THE RIVER COURSE

by Shoji Fukuoka,
Tokyo Institute of Technology, Tokyo, Japan
and
Koh-ichi Fujita
National Institute for Research Advancement, Tokyo, Japan

Abstract

A great lateral velocity difference is created in a flood flow where there is vegetation growth in the river course. This velocity difference causes a lateral momentum transfer and sometimes greatly affects the flow resistance. This paper quantitatively clarifies the influence of the lateral velocity difference for the purpose of establishing the methods of predicting the flow resistance in a river course having vegetation.

Method of the Study

The experiments were performed by using a straight water channel (length of 48m) with uniform width and uniform bed slope of 1/1000 which had a large width 3m and was capable of creating a two-dimensional plane flow having a large width to water depth as same as the case of real river course.

In the experiments, vegetation model having the height greater than water depth and a very high porosity as shown in Table. 1 were installed in part of the channel, water was so applied to create the uniform flow, and then the discharge, water level and velocity distribution were measured.

As shown in Fig.1, two kinds of experiments were conducted : the vegetation was placed in contact with the side wall at the one side of channel(arrangement I), and the vegetation was placed at the center of channel(arrangement II), and the influence of various factors upon lateral momentum transfer was checked.

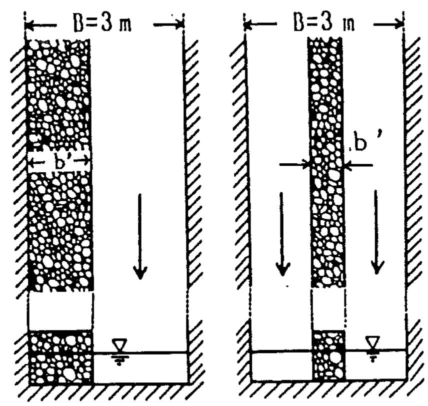

Fig.1 Method of arranging vegetation model

Table. 1 Characteristics of vegetation model used

	Porosity	Resistance law	Coefficient of permeability K
b	97%	$V_w=K\ I_e^{1/2}$	0.96 m/s
c	91%	$V_w=K\ I_e^{1/2}$	0.38 m/s

・V_w : Apparent mean velocitry,
I_e : Energy gradient.
・All the vegetations are plastic strings intertwinted each other

Interference of Flows between the Inside and Outside the Vegetation

Fig.2 shows typical lateral velocity distributions of arrangement II. From this Figure, it can be known that a significant velocity defect is created in the region close to but outside the vegetation (hereafter called main flow portion). Photos 1 and 2 express the flow regimes respectively corresponding to arrangement I and II by means of successive photographing. In the case of arrangement I it can be known that a slow current in the vegetation (white dye portion) flows to the main flow portion and is mixed with the current in the main flow portion. In the case of arrangement II, the dye placed in the vegetation flows out alternately to the right and left periodically. At the same time, inflow from the main flow portion to the vegetation is made alternately so as to compensate the outflow and this periodic pattern of fluid movement as a whole in the lateral direction appears as the flow regime having the progress of fluid downstream at a constant velocity. A fluid having a very small velocity in the downstream direction compared to the mean velocity in the main flow portion flows out from the vegetation to right and left main flow portions, thereby increasing flow resistance of the overall channel.

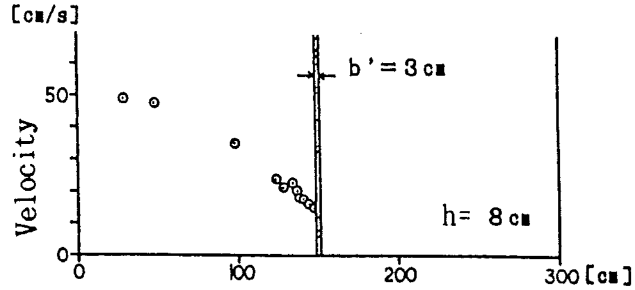

Fig. 2 Lateral velocity distribution (arrangementII, b' =3cm)

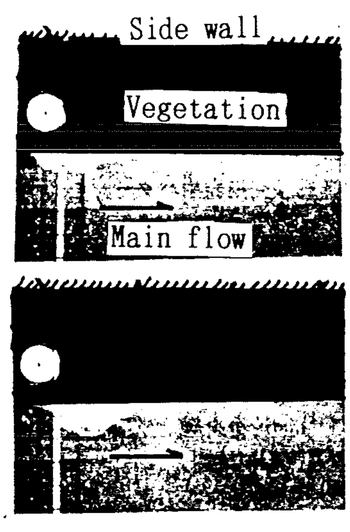

Photo. 1

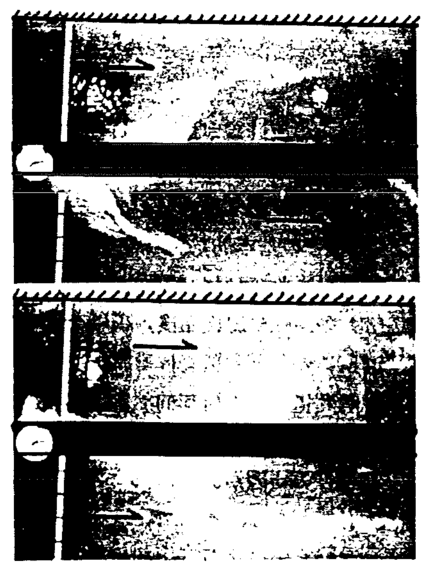

photo. 2

Photo. 1 Typical flow pattern of arrangement I (h=8cm, b' =123cm, photographing intervals of 1 sec.)

Photo. 2 Typical flow pattern of arrangement II (h=8cm, b' = 30cm, photographing intervals of 3 sec.)

The interference effect is the phenomenon of mixing of a slow fluid and a fast fluid at the boundary between them. From a macro viewpoint, the acting of shearing force at the boundary between the inside and outside of vegetation can be considered as same as the apparent shear stress[1),2)] acting to the boundary between flood channel and main channel as shown in Fig. 3. Shear force acting between two parallel currents is generally related with the velocity difference in the following form[3]:

$$\tau = \rho f (\Delta u)^2 \qquad (1)$$

Where, ρ : density of water, Δu : velocity difference between the inside and outside of vegetation, f : boundary mixing coefficient. The value of f was determined by using the results of the present experiment. In calculating the value of f, it was assumed[4] that the Manning's resistance formula stands good at each lateral position ; bed shear force at each position of the main flow portion was obtained from mean vertical velocity distribution in the lateral direction ; and then τ was determined by considering that the difference between the sum of the bed shear force obtained and the component in the downstream direction of the gravity acting to the current in the main flow portion is equivalent to the shear force $\tau \times h$ at the boundary. Then f was determined from τ obtained by using equation (1). At that time, Δu was determined from the following equation:

$$\Delta u = \overline{u} - K I_b^{1/2} \qquad (2)$$

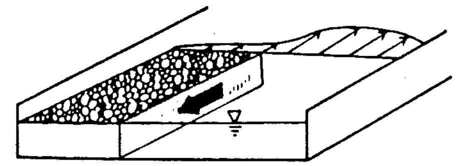

Fig. 3 Shear force acting to the boundary between the inside and outside of vegetation

Vegetation		b	c
K(m/s)		0.96	0.38
Arrange-ment	I	●	⊙
	II	▲	△

(water depth 4~8cm)

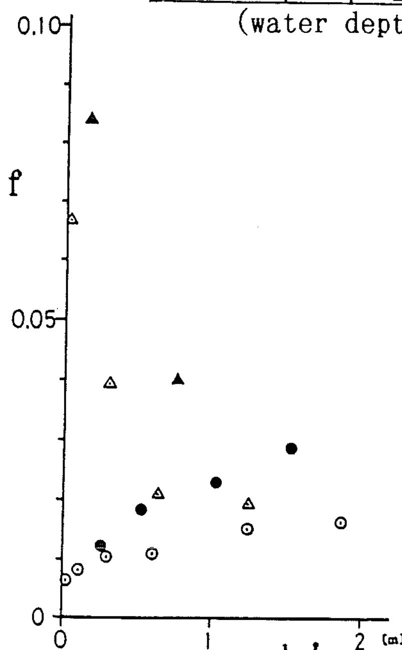

Fig. 4 Relation between f and b'

where, $\overline{u}$ is the mean velocity in the main flow portion. $KI_b^{1/2}$ means the velocity inside the vegetation in the region where no interference is created.

Relations between the value of f and the width b' of vegetation for the arrangements I and II are shown all together in Fig. 4. From this Figure, the following can be known : In the case of arrangement I, f-value suddenly increases as b' increases from 0, and the rate of increase of f-value soon decreases and an almost constant f-value occurs. The f-value increases as the coefficient of permeability K of vegetation becomes larger. On the other hand, in the case of arrangement II, as b' becomes smaller, f-value suddenly increases and is much greater compared to the case where the vegetation is located at the one side. When b' increases, f-value tends to gradually approaches to a constant value. As same as the case of arrangement I, f-value increases when the coefficient of permeability K is larger. From the above, it has been clarified that the boundary mixing coefficient f is not constant and greatly varies depending on the arranging method and the values of b' and K: and the resistance characteristics are completely different from each other between the arrangements I and II, and general expressing method of f-value must be reviewed based on different concepts.

General Expression of the Boundary Mixing Coefficient f

Arrangement I

Both b' and K, which govern f-value, are the quantities related to the restriction of fluid mixing in the lateral direction; If b' is sufficiently large, then mixing region in vegetation accelerated by the current in the main flow portion will be present as shown in Fig.5. Now let's consider L_w as the characteristic length expressing the width of this region. The importance of the mix-restricting effect by the side wall depends on whether b' is larger or smaller than L_w, It is considered that the decrease in f due to the presence of side wall at the vegetation side can be expressed by the relations between two non-dimensional quantities $(f-f_{b'=0})/(f_{b'=\infty}-f_{b'=0})$ and b'/L_w, where, $f_{b'=\infty}$ is the f-value at $b'=\infty$ and actually indicates the f-value when b' is sufficiently large and the change in f-value due to b' has disappeared.

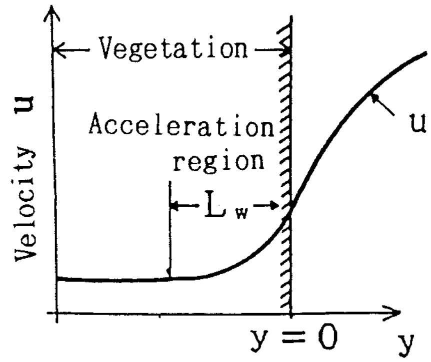

Fig.5 Characteristics of lateral velocity distribution in vegetation

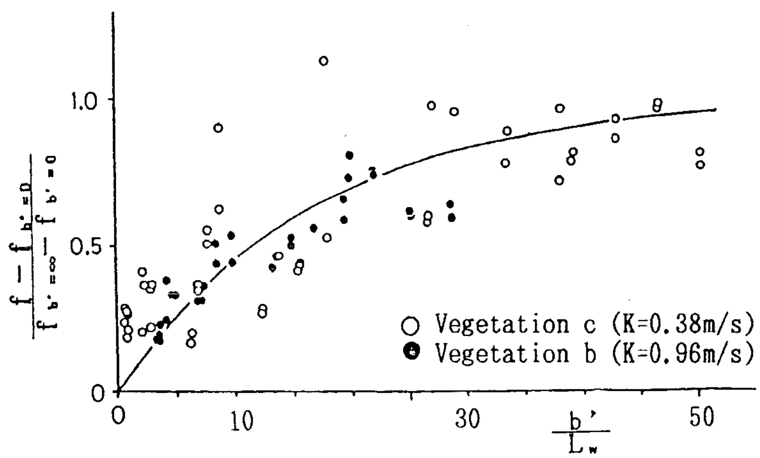

Fig.6 Relation between $\frac{f-f_{b'=0}}{f_{b'=\infty}-f_{b'=0}}$ and $\frac{b'}{L_w}$

Length L_w representing the width of mixing region in vegetation can be given by the following expression [4]:

$$L_w=\sqrt{hK/2g}\times f_{b'=\infty}\times\{\sqrt{2gh/F_m}-K\}\times\{(2F_m gh)^{-1/4}+\sqrt{K/2gh}\} \quad (3)$$

where, h : Water depth, F_m : Frictional loss coefficient of the main flow portion. In order to check whether the thought described above is appropriate, the relation of $(f-f_{b'=0})/(f_{b'=\infty}-f_{b'=0})$ and b'/L_w was checked based on the experiment data previously described. The results are shown in Fig.6. From this Figure, it can be known that the $(f-f_{b'=0})/(f_{b'=\infty}-f_{b'=0})\sim b'/L_w$ almost has an universal relation. The influence of b' and K upon the f-value seems to be generally expressed by

$$(f-f_{b'=0})/(f_{b'=\infty}-f_{b'=0})=1-\exp(-0.06b'/L_w) \quad (4)$$

Arrangement II

Fig. 7 shows the water level fluctuations Δh_0 near the boundaries as well as the velocity fluctuations (Vx, Vy) near one of the boundaries. From this Figure, the following can be known. Water levels at the right and left of the vegetation fluctuate with time with the same wave profile and the phase being different by π approximately. Because of this, a slope of water surface appears periodically in the lateral direction at the right and left of the vegetation. This periodic fluctuation in water level causes a periodic current across the vegetation. The fluid flowing out of the vegetation has a very small velocity in downstream direction ; and on the other hand, a current flowing into the vegetation has a velocity in downstream direction almost the same as the mean velocity of the main flow portion.

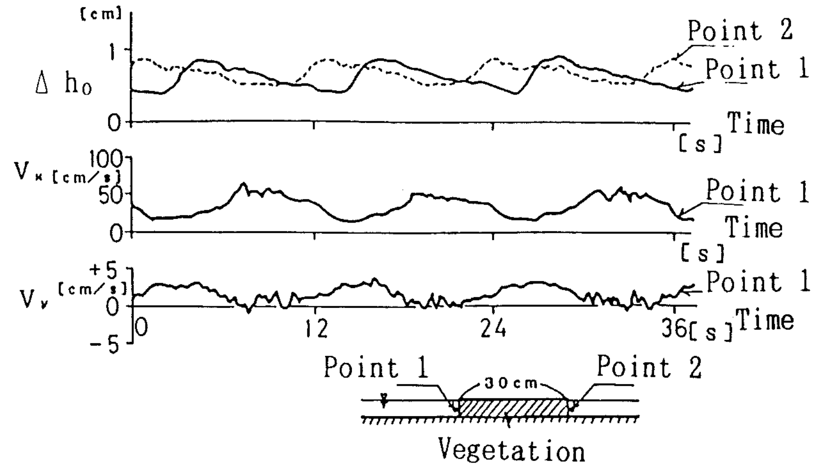

Fig. 7 Fluctuations in water level and velocity near the vegetation (Arrangement II, h=8cm, b'=30cm)

Where the vegetation is located at the center of channel, fluid movement in the lateral direction becomes more active compared to the case where the vegetation is located at one side only.

Now let Δh be the amplitude of water level fluctuation of the main flow portion, and let v_0 be the amplitude of lateral inflow velocity. It is expected that there will be a relation as shown below between Δh and v_0 for each Froude number F_r in the case where lateral momentum transfer is stably present.

$$\Delta h / h = F\,(F_r,\ v_o/\overline{u}) \tag{5}$$

where, F: Function expressing the relation of Δh and v_0.

The following relation is considered to exist between Δh and v_0 ;

$$v_o = K\sqrt{I_T} = K\frac{\sqrt{\Delta h}}{\sqrt{b'}} \tag{6}$$

By using (5) and (6), the following equation can be obtained:

$$\left(\frac{v_o}{u}\right)^2 \cdot \frac{b' u^2}{h K^2} = F\,\left(F_r,\ \frac{v_o}{u}\right) \tag{7}$$

The boundary mixing coefficient f is considered to be proportional to v_o/u because of its physical meaning, and thus the above expression means that the mixing coefficient f is goverened by the non-dimentional quantities such as Froude number and $K\sqrt{h}/(u\sqrt{b'})$.

In orther to clarify the validity of the results of review started above, the relation of $f \sim K\sqrt{h}/(u\sqrt{b'})$ was checked based on the results of experiment. The results are shown in Fig. 8.

Though the data are slightly dispersed, there is an apparent overall relation that f increases as $K\sqrt{h}/(u\sqrt{b'})$ becomes larger; It is rational to consider that f is governed by the non-dimentional quantities $K\sqrt{h}/(u\sqrt{b'})$ as long as Fr is the same.

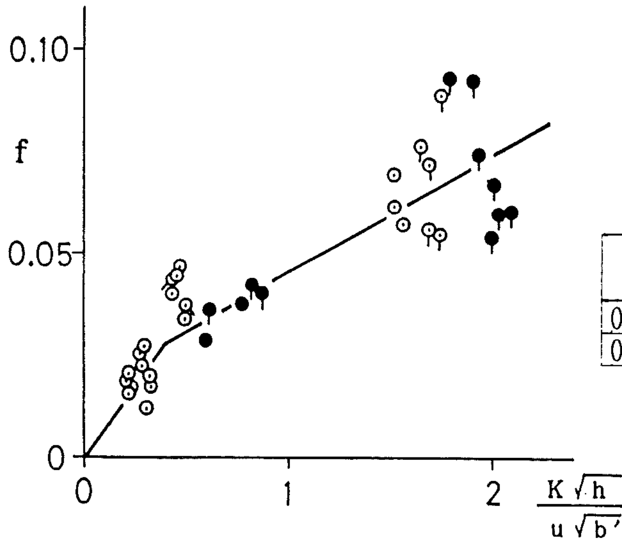

F_r	b K=0.96	c K=0.38
0.45～0.54	●	⊙
0.38～0.45	●	⚲

Fig.8 Relation between f and $K\sqrt{h}/(u\sqrt{b'})$

Conclusions

(1) The currents between the inside and outside of the vegetation interfere with each other, resulting in the active transfer of momentum, and causing the increase in flow resistance.
(2) Amount of the transfer of momentum increases as the width b' of the vegetation becomes larger in the case where the vegetation is placed in adjacent to the side wall of channel; and it increases as b' becomes smaller in the case where the vegetation is placed at the center of channel. The degree of transfer of momentum in the latter case is larger than the former case. Also, the transfer of momentum becomes active as the permeability of the vegetation increases.
(3) Momentum transfer can be quantitatively expressed by the boundary mixing coefficient f which indicates the degree of mixing between the inside and outside flow of vegetation. A non-dimensional hydraulic quantity governing the boundary mixing coefficient f has been obtained, and also a quantitative relation between f-value and the non-dimensional hydraulic quantity has been obtained.

References

1) Myers,W.R.C : Momentum Transfer in a Compound Channel, J Hydraulic Research, vol.16,No2,1978.
2) Fukuoka,S.and Fujita,K : Prediction of Flow Resistance in Compound Channels and Its Application to Design of River courses, Proc. JSCE, 411/II-12,1989 (in Japanese).
3) Ishikawa,T and Tanaka,M : Studies on the Resistance Characteristics of the Bushes in the Open Channel Flow, Proc.31st Japanese Conference on Hydraulics,1987 (in Japanese).
4) Fukuoka,S and Fujita,K : Hydrailic Effect of Luxuriant Vegetations on Flood Flow, Report of Public Works Research Institute, Ministry of Construction,vol.180,1990(in Japanese).

A THEORETICAL MODEL FOR VELOCITY
DISTRIBUTION IN SMOOTH RECTANGULAR OPEN CHANNEL

by Ni Jinren
The Institute of Remote Sensing, Beijing University, China

and
Wang Guangqian
Department of Hydraulic Engineering, Tsinghua University, China

Abstract

On the basis of systematic analyses of relations among the width-depth ratios, the positions of maximum velocity and the boundary shear stress distributions, a simple model for the velocity distribution in the smooth rectangular open channels is presented in this paper. This makes it possible to reasonably predict the velocity value at every point of the rectangular section. The theoretical model agree well with the experimental data.

1. Introduction

For two-dimensional flows, the effects of both walls on the fluid characteristics can be neglected and the shear stress along the width is distributed uniformly. In such a circumstance, the vertical distributions of velocities are also considered to be the same with each other along the width and a semi-logarithmic formula tested by Keulegan (1938) is suggested

$$\frac{U_{max} - U}{U_*} = \frac{1}{K} \mathrm{Ln} \frac{H}{y}, \quad K \doteq 0.4$$

in which, U_{max} is the maximum velocity at a vertical line; U, velocity at any given point; U_*, shear velocity; H, the depth; and K, the karman coefficient. For three-dimensional flow, the factors, such as the effects of boundaries etc., become so important that it must be fairly considered if we want to get a reasonable model for the velocity distribution.

So far, a lot of available work has been made by Keulegan (1938), Goncharov (1970), Shen (1981), Knight etal (1981, 1984), Sarma etal (1983), Hu (1985) and Ni (1985) and many experiments have been made, but none of the previous models can be used to calculate the velocity distribution in the whole section of a smooth rectangular open channel with various width-depth ratio B/H. To do so, the following basic understandings must be fully noted when a theoretical model is developed.

(i) The studies on the isovels for varying B/H in a rectangular open channel show that the locations of the maximum velocity will drop gradually from the water surface with the decrease of the width-depth ratios. The maximum velocity of the whole section is certainly in the central vertical line, and the maximum locations $y/H|_{U_{max}} = \alpha$ (from the bottom) always meet the condition of $\alpha > 0.5$ for any given B/H.

(ii) For three-dimensional flows, the shear stress along the boundaries distributed nonuniformly, see Fig. 4.

(iii) The locations of the maximum velocities in different verticals of the same cross section are different. In general, the maximum locations in the verticals near the wall are more far from the water

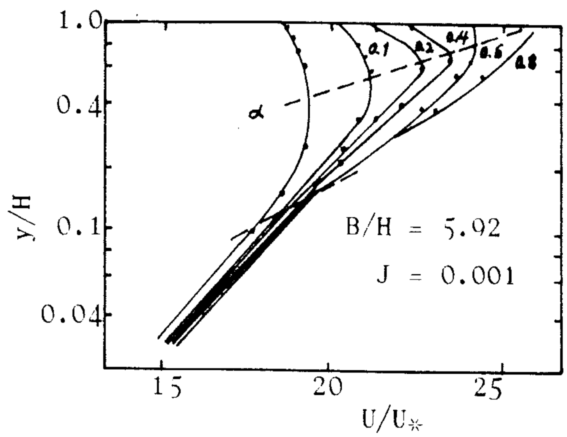

Fig. 1 Varying of maximum velocity locations in verticals along the width

surface than those near the central line. Noting the symmetry of the velocity distributions in the cross section, the examples of the varying maximum locations in different verticals for half a section is Fig. 1. In which, J is the channel slope and 2Z/B is the relative width from the wall.

(iv) If the roughness of the boundary is changed, both the maximum velocity locations and the shear stress distributions along the wall and bed will be changed correspondingly.

2. The relation between B/H and α for the central vertical

From the above mentioned, a lot of measured data has been collected by the writer and a very good relation between B/H and α for the central vertical has been found. The relation obtained from the data of smooth rectangular open channel with $B/H \geqslant 1$ is shown in Fig. 2 and from the Fig., a trend of α =1 is clear when $B/H > 1.0$. The curve in Fig. 2 is well described by the equation

$$\alpha = \begin{cases} 1-0.002\ (10-B/H)^{2.5} & 1 \leqslant B/H \leqslant 10 \\ 1 & B/H > 10 \end{cases} \qquad (1)$$

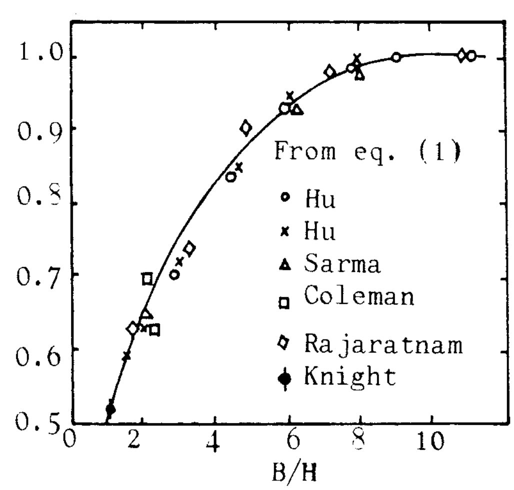

Fig. 2 Relation between α and B/H for the central vertical

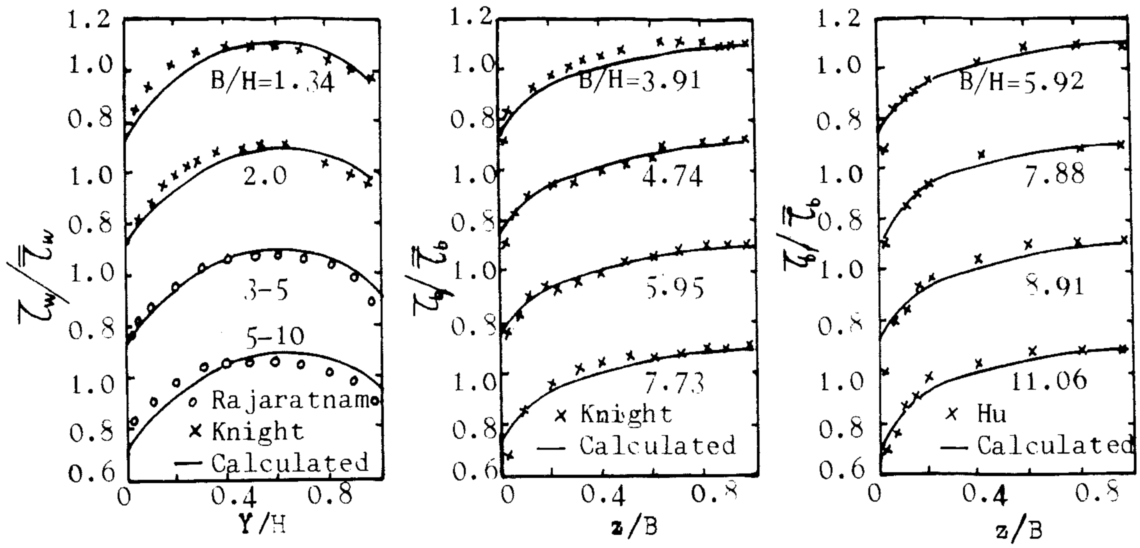

Fig. 3 Comparisons between measured $\tau_w/\bar{\tau}_w$ or $\tau_b/\bar{\tau}_b$ distribution and eq. (3)

For rough boundaries, eq. (1) is not available and new relations should be developed in connection with the corresponding measured data.

3. Shear stress distributions in smooth boundaries

According to Knight (1984), Ghosh & Roy (1970), Rajaratnam et al (1969) and Hu (1985), the maximum shear stress along the bed should be appear at the central part and those along the wall appear below the water surface as shown in Fig. 4. For flows in smooth rectangular open channels, noting that

$$\frac{2}{B}\int_0^{\frac{B}{2}} \frac{\tau_b}{\bar{\tau}_b}\,dz = 1, \quad \frac{1}{H}\int_0^{H} \frac{\tau_w}{\bar{\tau}_w}\,dy = 1 \tag{2}$$

the following empirical formula is given by the writer

$$\frac{\tau_w}{\bar{\tau}_w} = 0.6+1.67\,\frac{y}{H} - 1.32\,\left(\frac{y}{H}\right)^2, \quad \frac{\tau_b}{\bar{\tau}_b} = 0.6+0.5\,\left(\frac{z}{B}\right)^{0.25} \tag{3}$$

in which, $\bar{\tau}_w$ and $\bar{\tau}_b$ is defined by Knight (1984)

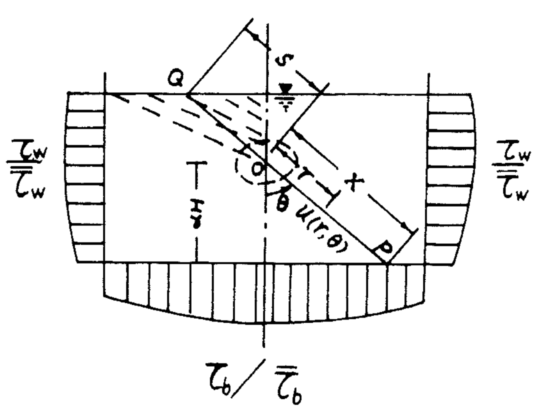

Fig. 4 Sketch for section velocity distribution analysis

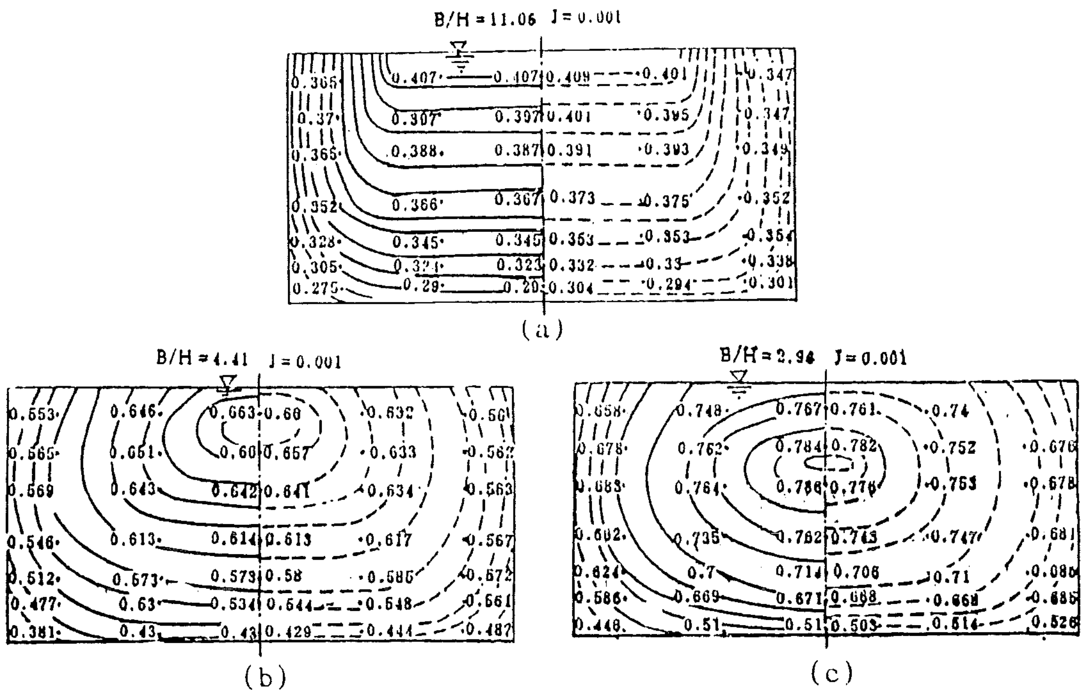

Fig. 5 Comparisons of the present model with measured data
——— measured - -·- - calculated

$$\overline{\tau}_w = 0.01\gamma\ H\ J\ A\ \left(\frac{B}{2H}\right) \tag{4}$$

where
$$A=\exp\left\{-3.23\ \log\ \left(3+\frac{B}{H}\right) + 6.146\right\} \tag{5}$$

$$\overline{\tau}_b = \gamma\ H\ J\ (1-0.01\ A) \tag{6}$$

Comparisons have been made, which is shown in Fig. 3.

4. The theoretical model for vertical velocity distribution

In consideration of the zero shear stress at the location (point 0 in Fig. 4) of maximum velocity in the cross soction, the following assumptions are made by the writer: (a) The shear stress at any point of the straight lines, which link 0 (in Fig. 4) and any point of the wall or bed at an angle of θ with the central vertical, accord with the linear relation

$$\tau_r = \tau \frac{r}{X} \tag{7}$$

In which, τ is boundary shear stress (τ_w or τ_b) and the meaning of X or r in shown clearly in Fig. 4. (b) the prandtl mixing length hypothesis is still available for τ_r along any given straight line from point 0 to the boundary, or

$$\tau_r = \rho l^2\left(\frac{\partial u(r,\theta)}{\partial r}\right)^2,\quad l=K\ (X-r)\sqrt{\frac{r}{\alpha X}} \tag{8}$$

then, from eq. (7) and eq. (8), we obtain

$$\frac{U_{max} - U(r)}{\sqrt{\frac{\tau}{\rho}}} = \frac{1}{K} \ln \frac{r}{X-r}, \quad K=0.4 \tag{9}$$

Here U_{max} is the maximum velocity in the central vertical. If $0 \leq \theta \leq \arctg(B/2\alpha H)$, then $\tau = \tau_b$, $X = \alpha H/\cos\theta$ and if $\arctg(B/2\alpha H) < \theta < 90^\circ + \arctg 2(1-\alpha) H/B$, we have $\tau = \tau_w$, $X = B/2 \sin\theta$. When the straight line OP is reversely stretched to the water surface, or point Q, the water surface velocity at Q can be determined by the relation

$$U(r)\big|_{\text{water surface}} = U_{max} - \frac{1}{K}\sqrt{\frac{\tau}{\rho}} \ln \frac{X}{X-S} \tag{10}$$

Here τ, K and X are the same as the original values in eq. (9) for the line OP. In such a way, not only the difficulties in the determination of shear stress at water surface are overcome, but also a general model for the velocity distribution of whole cross section is developed. The eq. (1) is only a special case of the present model when B/H is large. In general, S is the maximum value of r in the reversely streched line OQ and $S < X$ is always true for the open channel, so the velocity at water surface is nonzero for three dimensional flows. The comprisons with data are shown in Fig. 5

5. Conclusion

Details on the differences between the two and three dimensional flows in consideration of variations of the locations of maximum velocity and shear stress distributions along the boundary are fully discussed with the observations, as a result, a theoretical model for the velocity distribution in smooth rectangular open channels is developed. The good agreement of the present model with measured data is shown in the paper.

References

Ghosh, S.N. and N. Roy, (1970) Boundary shear distribution in open channel flow, J. Hydr. Div. Proc., ASCE, Vol. 96, Hy4.

Goncharov, V.N., (1970) Dynamics of channel flow, 2nd ed, Israel Program for Scientific Translations, Jerusalem (Translated from Russian).

Hu, C.H., (1985) The effects of width-depth ratio and wall roughness on the velocity distribution and friction factor in rectangular open channel, master dissertation, Tsinghua University (in Chinese).

Keulegan, G.H., (1938) Law of turbulent flow in open channels, Research paper RP 1151, National Bureau of Standards, U.S. Department of Commerce, Washington, D.C. Vol. 21.

Knight, D.W., (1981) Boundary shear in smooth and rough channels, ASCE, Vol. 107, Hy7.

Knight, D.W. etal, (1984) Boundary shear in smooth rectangular channels, ASCE, Vol. 110, Hy4.

Ni, J.R., (1985) An investigation on the law of turbid flow velocity and the vertical distribution of suspended sediment concentration, master dissertation, Tsinghua University (in Chinese).

Rajaratam, N. and D. Muralidhar, (1969) Boundary shear distribution in rectangular open channels, La Houille Blanche, Vol. 24, No. 6.

Sarma, K.V.N., D. ladshminarayana and N.S. Lakshmana Ras, (1983) velocity distribution in smooth rectangular open channels, Proc. of the ASCE, Vol. 109, No. 2.

Shen, Y.J., (1981) Velocity distributions on the upstream reach in Chang Jiang River (in Chinese), The Institute of Chang Jiang Hydraulic and Electric Engineering.

Session 12C

Sediment Laden Flows

INNOVATIVE TECHNOLOGIES FOR DREDGING CONTAMINATED SEDIMENTS

by Paul A. Zappi and Donald F. Hayes
US Army Engineer, Waterways Experiment Station
Vicksburg, MS 39180 USA

Abstract

Contaminated marine sediments exist in many U.S. rivers and harbors. Dredging is a convenient, economical method of safely removing these contaminated sediments. However, significant concern exists over the potential environmental effects resulting from localized sediment resuspension and contaminant release which may result during the removal operation. This paper describes various innovative dredging technologies developed to control sediment resuspension at the point of dredging. Hydraulic, mechanical, and pneumatic dredging innovations and their application to dredging contaminated sediments are presented.

Introduction

While only a small portion of the sediment dredged by the U.S. Army Corps of Engineers for navigation projects is considered contaminated, safe removal of these sediments is important. The U.S. Army Engineer Waterways Experiment Station, Environmental Laboratory is conducting research to provide guidance for dredging contaminated sediment (Hayes 1986, 1988; Havis 1988; Hayes, et al. 1988; McLellan, et al. 1989; Zappi and Hayes, In prep). This paper focuses on the research effort associated with innovative hydraulic, mechanical, and pneumatic technologies for dredging contaminated sediments.

Water quality impairment due to suspended sediment and resulting turbidity can have significant short and long term effects upon the aquatic habitat and aquatic species (Lunz 1987). It may also be an aesthetic concern in some areas. Sediment contamination often results from river commerce, industrial activities, wide spread use of agricultural pesticides, and intentional or unintentional dumping of pollutants. The presence of contaminants, however, adds an additional dimension of concern. The energy induced by the dredging process may strip contaminants previously bound to sediment particles and cause them to be released into the water column. The potential for such releases depends upon many factors such as sediment characteristics, contaminants present, and local environmental conditions. Also, contaminants typically adhere more tightly to fine grained sediments which have characteristically slow settling velocities. Thus, they may be transported well away from the dredging area. For these reasons, minimizing sediment resuspension is an important aspect of dredging contaminated sediments and is a primary consideration in comparing dredging methods and equipment.

Hydraulic Dredging Equipment

Conventional hydraulic dredge types include the cutterhead, dustpan, bucketwheel, and hopper dredges. These dredge types routinely operate in almost every harbor and move millions of cubic yards of sediment each year. Cutterhead dredges are the most common hydraulic dredge in the United States and are efficient movers of sediment. Cutterhead dredges use a rotating cutter to dislodge sediment and guide it into a suction inlet. Once the material enters into the suction inlet it is pumped through a pipeline to its point of discharge or disposal. The magnitude of sediment resuspension by cutterhead dredges is dependent upon dredge movement, cutter penetration, and cutter rotation speed. The dynamics of the cutter rotation have led to a general perception that cutterhead dredges resuspend large quantities of sediment due to this violent mixing action. However, recent research has proven this perception to be largely unfounded. With proper operational controls, sediment resuspension associated with cutterhead dredges may be quite low (Hayes, et al. 1988; McLellan, et al. 1989; Otis, et al. in preparation). McLellan et al. (1989) reported sediment resuspension concentrations range from 10 to 300 mg/l near the cutterhead to a few mg/l beyond one thousand feet from the dredge.

When dealing with contaminated sediments, however, just being low is not sufficient. Every reasonable effort to minimize the impacts of the removal process must be made. For this reason, significant interest in hydraulic dredging innovations exists and most efforts have revolved around improvements to cutterhead dredges or dredge plants. Tested and published innovations include the cleanup, matchbox, refresher, waterless, and cutter-suction dredges. The cleanup dredge, developed in Japan, uses an auger type cutterhead rotating along the suction pipe axis to cut the sediment and guides it toward the suction intake. A shield over the cutter contains resuspended sediment and a gas collection system removes sediment laden gas. Sonar devices monitor the elevation in the front and back of the dredge and an underwater camera monitors sediment resuspension (Barnard 1978). Herbich and Brahme (In prep) reported that the cleanup dredge effectively reduced sediment resuspension.

The matchbox dredge, developed in The Netherlands, covers the suction intake with a matchbox-like shield. Material is guided into the suction intake through an opening which moves horizontally along the bottom as the dredge swings from side-to-side. The suction pipe opening on the trailing side of the matchbox closes to increase the available suction pressure. The matchbox dredge was brought to the U.S. in 1985 by Bean Dredging Co. and tested in Calumet Harbor, Illinois (Hayes, et al. 1988) along with a conventional cutterhead. Sediment resuspension around the matchbox dredge was low, but the cutterhead also performed well. A similar comparison was performed in 1989 on contaminated sediment in New Bedford Harbor, Massachusetts. The matchbox dredge experienced problems with clogging during these tests, but was generally less effective than the cutterhead dredge (Otis et al. 1989).

Less information is available on other innovative equipment modifications. The Japanese-developed refresher dredge uses a helical-shaped cutterhead to cut and guide material into the suction intake. The cutter is shielded to contain sediment resuspended by the cutter. Kaneko et al. (1984) reported that several tests showed the refresher dredge is capable of removing sediment with a minimum amount of resuspension. The waterless dredge, developed in the United States, consists of paddlewheel-like cutters and a submerged centrifugal pump enclosed in a half-cylindrical shield. The shield contains the sediment resuspended by the cutters. The waterless system is reported to remove sediments at a high concentration with a minimum amount of sediment resuspension (Mitre Corporation 1983).

The cutter-suction combination uses the suction pipe as both the suction and drive shaft of the cutter. Standard cutterhead designs include one shaft to turn the cutterhead and one to provide suction at the cutterhead. The standard design requires that the cutterhead be large enough to fit the suction intake pipe at the bottom of the cutter. The combination of the suction pipe and cutter drive shaft enables the suction intake to extend farther into the cutter with the suction intake located in the center of the cutter. Extending the suction intake into the cutterhead decreases the distance between the channel bottom and the intake and increases the amount of material picked up. With the suction intake in the center of the cutterhead, the cutter can be reduced to half its original size, the suction intake can be designed with a more hydraulically efficient bell-shaped mouth, and the suction intake can draw in sediment from all directions instead of just the bottom of the cutter. The reduced cutter size requires less torque to yield same force on the cutter blades and should result in lower sediment resuspension (Barnard 1978).

Mechanical Dredging Equipment

Mechanical dredges are often used for low volume dredging, dredging in tight areas such as around piers, docks, and areas where waterborne traffic should not be interrupted. The clamshell dredge, probably the most common mechanical dredge, will be the focus here. A clamshell dredge may simply be a crane mounted on a barge. The crane lowers a clamshell bucket rapidly, grabs a bucket of sediment, lifts it through the water column, and either dumps the sediment into an adjacent hopper barge or casts the material to the side (only in clean, sandy sediments). Sediment resuspension results from the bucket striking the channel bottom, leakage while being raised through the water column, and washing during the lowering process. Significant resuspension occurs when the hopper barge overflows. Overflow may account for much of the total sediment resuspension. Barnard (1978) reported the plume downstream of a clamshell dredge may extend 300 m at the water surface and 450 m near bottom. He also reported resuspended sediment concentrations of up to 500 mg/l with water column averages normally below 100 mg/l.

An enclosed clamshell bucket has been developed which reduces the sediment resuspension associated with leakage. The enclosed bucket is a standard clamshell bucket with the top portion of the bucket covered and either gasketed or tongue-in-groove jaws. The use of an enclosed bucket can reportedly reduce the amount of sediment in the water column by thirty to seventy percent (Barnard 1978). Tests conducted in Florida's St. Johns river showed that the enclosed bucket attributes appear to be a trade off between decreasing the upper water column sediment concentration and increasing the lower water column sediment concentration (McLellan et al. 1989).

Pneumatic Dredging Technology

Pneumatic dredges utilize the differential between atmospheric and hydrostatic pressures in deep water. The dredge maintains atmospheric pressure inside an empty submerged cylinder via an open duct above the water surface. Hydrostatic pressure exists outside the submerged cylinder and forces sediment into the cylinder when the cylinder's inlet valve opens. Once the cylinder is full, the inlet valve closes and compressed air is directed into the cylinder. When the outlet valve opens, sediment flows out of the cylinder and through a pipeline that leads to the disposal site or hopper barge. Once the cylinder is empty, the process repeats. This process can occur automatically, but must be in deep water to create the pressure differential necessary to remove most sediments (Barnard 1978). The pneuma and oozer dredges are the most common type of pneumatic dredges.

The pneuma dredge consists of three cylinders, an air compressor, various shovel attachments, and a distributor system. It can be mounted on a crane or dredge ladder and pulled through the sediment. As the pneuma dredge pulls through the sediment, material enters the cylinders through shovel attachments mounted on the inlet valves. The shovels can be changed to suit the dredging conditions. A distributor system insures that there is always one cylinder discharging material (Barnard 1978). A variation of the standard pneuma dredge, the Amtec pneuma dredge, uses a vacuum system to reduce the amount of hydrostatic pressure required. This allows the dredge to operate in depths as shallow as 12 feet and reduces the chance of choking the intake with sediment (Herbich and Brahme In prep).

The pneuma dredge was used to remove contaminated sediment from the Duwamish Waterway, Washington. Results showed three distinct advantages of the pneuma dredge over conventional dredges: the ability to prevent overdredging by controlling the cut depth and rate of travel, the ability to follow the contours of the waterway bottom, and the ability to dredge fluid or low viscosity materials at high concentrations. Pneuma dredge disadvantages include: its inability to remove sand at in situ density, its inability to sustain a significant discharge density, and its much lower pump efficiency than that of conventional centrifugal pumps. Tests also indicated that the pneuma dredge was effective at maintaining resuspension levels slightly above background concentrations (Herbich and Brahme In prep).

The oozer dredge was developed in Japan to dredge highly contaminated sediments. The design and operation of the oozer dredge is similar to a cutterhead dredge with the oozer pump being mounted on the end of a ladder. The oozer dredge consists of two cylinders and a vacuum system for use when the hydrostatic pressure is insufficient. A metal hood placed over the suction helps recover released oils and gases and contain sediment resuspension. The oozer dredge also includes a rotating blade parallel to the channel bottom to guide the material into the intake, an underwater camera and sensors to monitor the thickness of cut, the channel bottom elevation after dredging, and the amount of sediment resuspension, and a recorder that prints out a final record of the actual amount of material dredged. Reports of Japanese tests indicate that suspended solids levels associated with the oozer dredge were within background concentrations (Barnard 1978; Mitre Corporation 1983).

Another pneumatic dredge which is a modification of the oozer dredge uses compressed air to drive a piston that pumps the sediment; a cutter system can be added to the dredge if necessary (Barnard 1978). Field tests of this dredge were conducted in Osaka Bay, Japan. Almost all measured resuspension values were just slightly above background concentrations. This dredge used three sonar devices positioned on the upper side of the suction mouth to allow the dredge to follow the contours of the water bottom (Koba and Shiba 1981).

Comparisons

A comprehensive comparison of the performance of various dredge types is difficult. Even if such a comparison was possible, the results would be largely inconsequential since site characteristics usually dictate the dredge type which must be used. Efforts should therefore focus on improving the capabilities of each dredge type and possibly customization for certain conditions. In any case, variability in sediment characteristics and testing conditions make quantitative comparisons of the resuspension characteristics difficult; qualitative comparisons are best accomplished under as near identical circumstances as possible. In the two studies which have pitted various dredges operating under near identical conditions, conventional dredges have proven to be surprisingly successful (Hayes, et al. 1988; Otis, et al. 1989). This does not, however, negate the need for pursuing equipment innovations to improve current operations. Also, evaluating the effectiveness of any cleanup alternative must also consider other existing sources of sediment spread such storm surges and boat traffic.

Summary

It seems clear that other countries are more advanced in developing and testing innovative dredging technologies than the U.S. The innovations discussed in this paper certainly show promise for future applications. Unfortunately, details of data collection efforts and the raw data is not easily accessible to independently evaluate the effectiveness of these innovations. Valuable information could be gained from their experiences, however, through the exchange of test results, observing their equipment in operation, and testing their equipment in the U.S. Research and development on equipment innovations in the U.S. must continue.

Acknowledgements

The U.S. Army Corps of Engineers Improvement of Operations and Maintenance Techniques (IOMT) Research Program funded the research described in this paper. The research was accomplished at the Environmental Laboratory of the U.S. Army Engineer Waterways Experiment Station. Mr. Daniel E. Averett and Dr. Michael R. Palermo reviewed the original manuscript. The Chief of Engineers granted permission to publish this information.

References

Barnard, William D. 1978. "Prediction and Control of Dredged Material Dispersion Around Dredging and Open-Water Pipeline Disposal Operations," Contract Report DS-78-13, U.S. Army Engineer Waterways Experiment Station, CE, Vicksburg, MS.

Havis, Robert N. 1988. "Sediment Resuspension by Selected Dredges," Technical Note EEDP-09-2, U.S. Army Engineer Waterways Experiment Station, Vicksburg, MS.

Hayes, Donald F. 1986. "Guide to Selecting a Dredge for Minimizing Resuspension of Sediment," Technical Note EEDP-09-1, U.S. Army Engineer Waterways Experiment Station, Vicksburg, MS.

Hayes, Donald F. 1988. "Sediment Resuspension by Selected Dredges," Technical Note EEDP-09-2, U.S. Army Engineer Waterways Experiment Station, Vicksburg, MS.

Hayes, D.F., T.N. McLellan, and C.L. Truitt 1988. "Demonstrations of Innovative and Conventional Dredging Equipment at Calumet Harbor, Illinois," Miscellaneous Paper EL-88-1, U.S. Army Engineer Waterways Experiment Station, Vicksburg, MS.

Herbich, John B. and Brahme, Shashikant B. In prep. "Literature Review and Technical Evaluation of Sediment Resuspension During Dredging," Contract Report HL-90-xx (In Preparation), prepared by Texas A&M University, College Station, TX, for the U.S. Army Engineer Waterways Experiment Station, Vicksburg, MS.

Lunz, John D. 1987. "Environmental Considerations During Dredging Operations," Sedimentation Control To Reduce Maintenance Dredging of Navigational Facilities in Estuaries: Report and Symposium Proceedings, National Academy Press, Washington, DC.

Kaneko, A., Watari, Y., and Aritomi, N. 1982. "Specialized Dredges Designed for the Bottom Sediment Dredging," Proceedings of the 8th US/Japan Experts Conference on Toxic Bottom Sediments, Tokyo, Japan, November 1982.

Koba, Hiromi and Shiba, Toyoaki 1981. "Test Dredging of Bottom Sediments in Osaka Bay," November 1981, Proceedings of the 7th US/Japan Experts Meeting on Management of Bottom Sediments Containing Toxic Substances, New York, New York.

McLellan, T.N., Havis, R.N., Hayes, Donald F., and Raymond, Gene L. 1989. "Field Studies of Sediment Resuspension Characteristics of Selected Dredges," Technical Report HL-89-9, U.S. Army Engineer Waterways Experiment Station, Vicksburg, MS.

Mitre Corporation (Mclean, VA) 1983. "Implementation of Innovative Dredging Techniques in the Chesapeake Bay Region," Prepared for the United States Environmental Protection Agency, Annapolis, MD.

Otis, Mark J., Andon, Steve, and Bellmer, Russell 1989. "New Bedford Harbor Superfund Pilot Study: Evaluation of Dredging and Dredged Materials Disposal," June 1989, In preparation, US Army Engineer Division, New England, Waltham, Mass.

Zappi, P.A. and Hayes, D.F. 19xx. "Innovative Technologies for Dredging Contaminated Sediments," Miscellaneous Paper EL-90-xx, in preparation, US Army Engineer Waterways Experiment Station, Vicksburg, MS.

Sediment Model Study on The Sluice Tunnel at the Outfall of the Taohe River in Liujiaxia Reservoir

Jiang Ruqin
Institute of Water Conservancy and Hydroelectric
Power Research, 1990, 4 Beijing

Abstract

In order to avoid rapid siltatioin in the upstream of the Liujiaxia dam, it is suggested to construct a sluice tunnel along the left bank of the Yellow River to interrupt the density current coming from the outfall of the Taohe River and the sediment eroded from the upper reaches of the Taohe River. Comparison between the experiment of the condition of formation and the characteristics of the density current with the field measurement give a fairly good results. Results of the model test show the density current from the outfall of the Taohe River obviously passes through the bed of the Yellow River and is sluiced out stablely from the tunnel.

1. Introduction

Lijiaxia dam located at the downsteam of the confluence of the Taohe River and the Yellow River, was constructed in 1969. The dam is 147 m high. A Reservoir with a total storage capacity of 5.74 X $10^9 m^3$, serving a total installed capacity of 1.225 X 10^6kW, is formed.

After twnety years of operation, the main trouble arises from the swift silting in the upstream of the dam, since the outfall of the Taohe River is only 1.5 km upstream from the dam (Fig. 1). The Taohe River brings an average suspended load of 2.86 X 10^7 t annually, which constitutes about 1/3 of the total sediment. It is comparatively large to the capacity of the Taohe River reaches.

The inflow of the Taohe River during flood season always forms density currents, reaching the confluence of the Taohe River and the Yellow River, and moving in the upstream direction of the Yellow River. It results in a sand bar across the river, as shown in Fig. 2. The existing sand bar would prevent the diversion of water for power generation at low water levels.

The Taohe River delta resached the confluence in 1978. The sediment carried by density current from the Taohe River reaches the damsite. It causes the swift silting in front of the dam and brings about a series of disadvantages:

(1) The turbine is abrased due to a great amount of sediment, particularly coarse grains, passing through the turbine.

(2) Because the elevation of the sediment deposition is higher than that of the soll of the sluice gates, the function of sluicing would be menaced during flood season.

Since 1981, experiments have been conducted on drawing down the water level in the Liujiaxia Reservoir before the flood season to erode deposits from the reservoir. Observations indicats that the

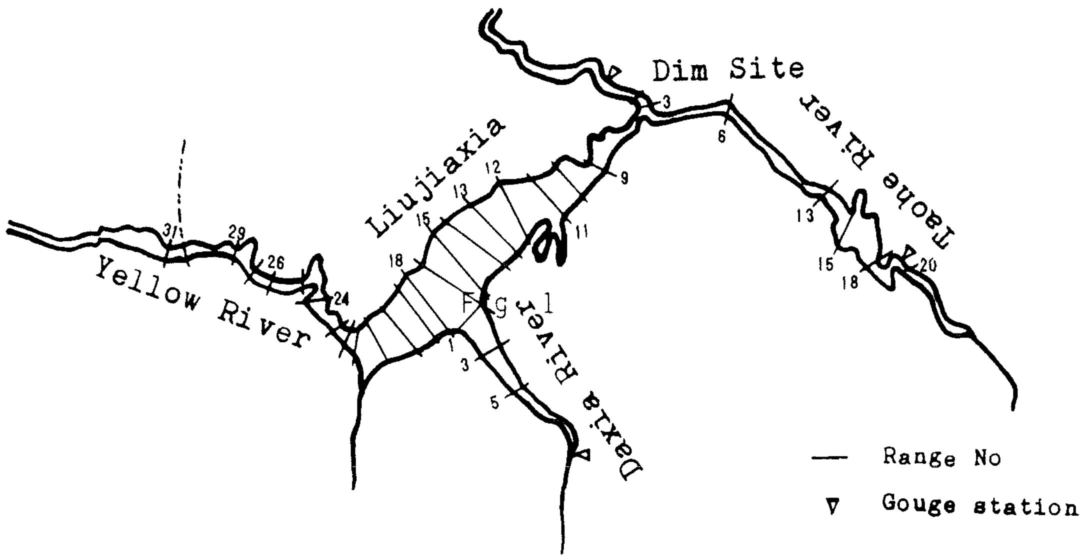

Fig.1 Plan of Liujiaxia Reservoir

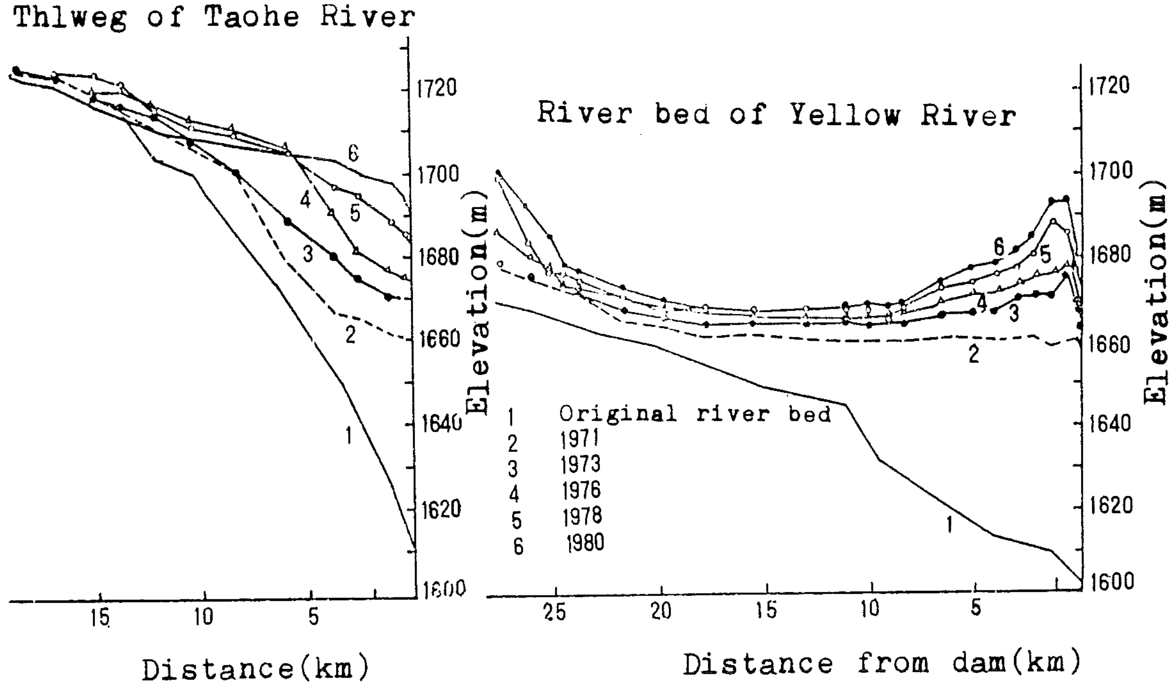

Fig.2 Sand bar formed by deposition of density current from Taohe River in Liujiaxia Reservoir

flushing efficiency is quite higher. The problem is that a great amount of the silt deposition at the upper reaches of the Taohe River is eroded and transported to the front of the dam and dpeosited there to raise rapidly the elevation of deposition.

2. Model design

The sluice tunnel is suggested to be constructed along the left bank of the Yellow River to interrupt the density current and the sediment eroded from the upper reaches of the Taohe River. The key problem is whether the density current passes through the bed of the Yellow River, reaches the left bank and enters stablely the tunnel with high sluicing efficiency.

During 1986-1988, experiments on three undistored models with fixed bed were carried out.

According the condition of laboratory, the length scale is chosen as 120, i.e. $\lambda_h = \lambda_l = 120$. The model study is conducted for quanlitatively checking the presence of the density current from the Taohe River. In order to satisfy the similarity of the gravity and the formation of density current, the scale of volume weight of density current must equal to 1. When the clay at the Zhu-Wo Reservor located downstream of the Guanting Reservoir was selected as the model sand, the concentration in the model test would be the same as that in the prototype. Grain composition curves both of the prototype and of the model are shown in Fig. 3.

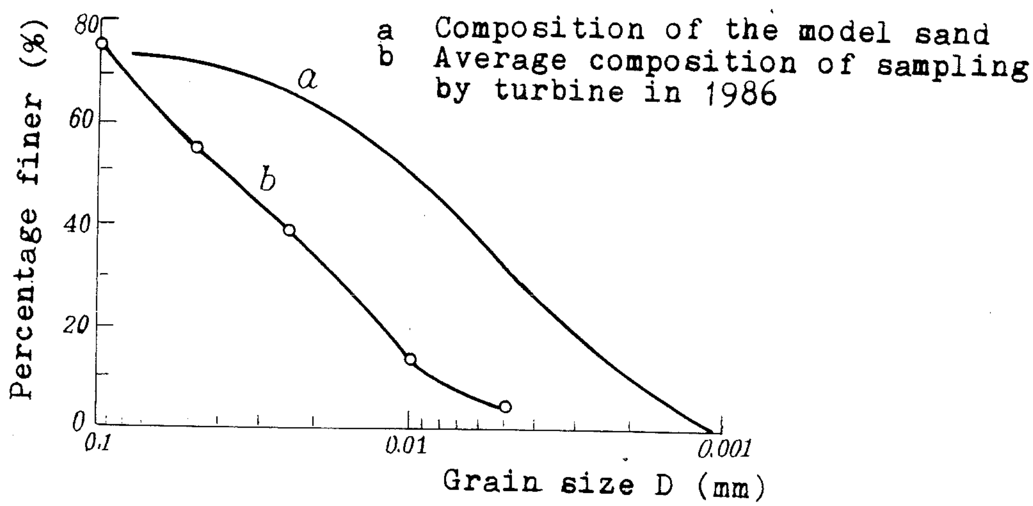

Fig.3 Mechanical composition of the model and the prototype

3. The verification tests

(1) The critical condition of the formation of the density current for different discharge of the Taohe River was investigated. In order to investigate the critical condition of the formation of the density current, velocity, depth and silt concentration of the flow at the plaunging point were observed.

A plot of the relationship between u and $\sqrt{\frac{\Delta\rho}{\rho} gh}$, is given in Fig. 4. It is shown that the critical Froude Number $u^2/\frac{\Delta\rho}{\rho} gh$ of density current formation equals to 0.6.

(2) The characteristics of the density current. The sites of

measuring were taken along the Taohe River. The vertical distribution of the velocity u and the silt concentration c in longitudinal direction are plotted in Fig. 5. The data measured in Liujiaxia Reservoir are given in Fig.6. The following characteristics of the density current in the Liujiaxia Reservoir may be noted:

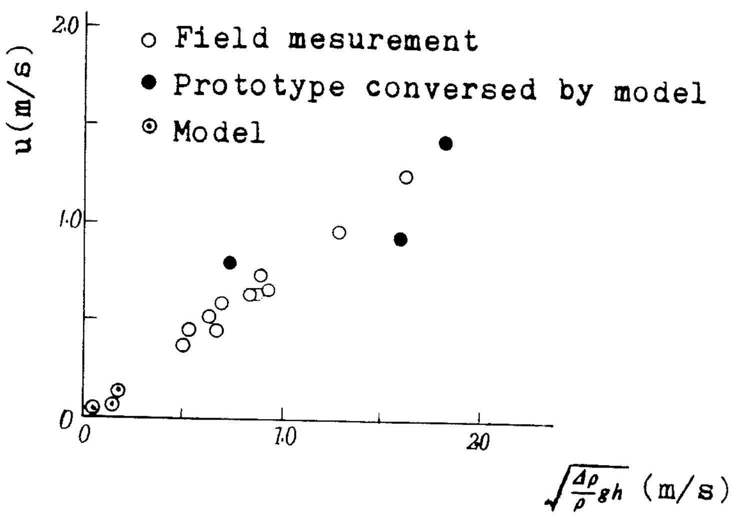

Fig.4 Relationship between u and $\sqrt{\frac{\Delta\rho}{\rho}gh}$

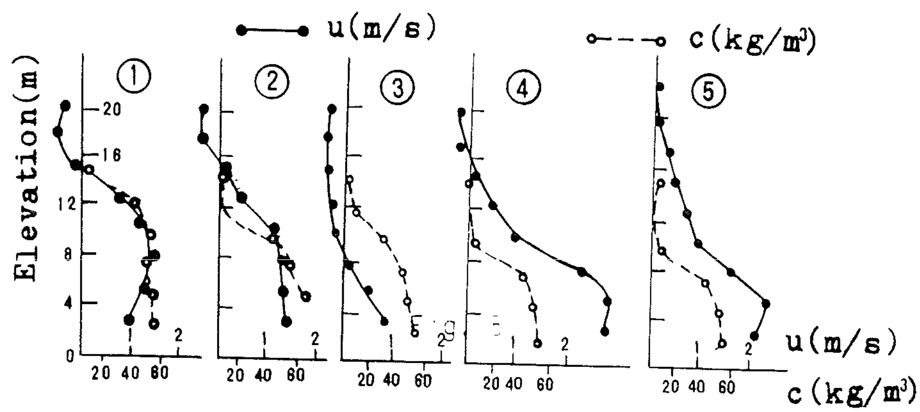

Fig.5 Distribution of velocity and silt concentration in model

① 4.2km upstream from the outfall of the Taohe River
② 3.2km upstream from the outfall of the Taohe River
③ 1.7km upstream from the outfall of the Taohe River
④ 1.0km upstream from the outfall of the Taohe River
⑤ 0.4km upstream from the outfall of the Taohe River

i) The acceleration of the desity current in the Taohe River is caused by the topographic profile features of the reservoir deposit (See Fig. 2).

ii) The settling of coarse and fine particles in turbid density current and the diffusion at the interface result in the decrease of the thickness of the density current.

iii) As the Taohe River reaches are narrow in width (about 100-200m), the transverse diffusion of the density current is comparatively small, the thinkness of the density current and the inflow concentration maintain as unchanged.

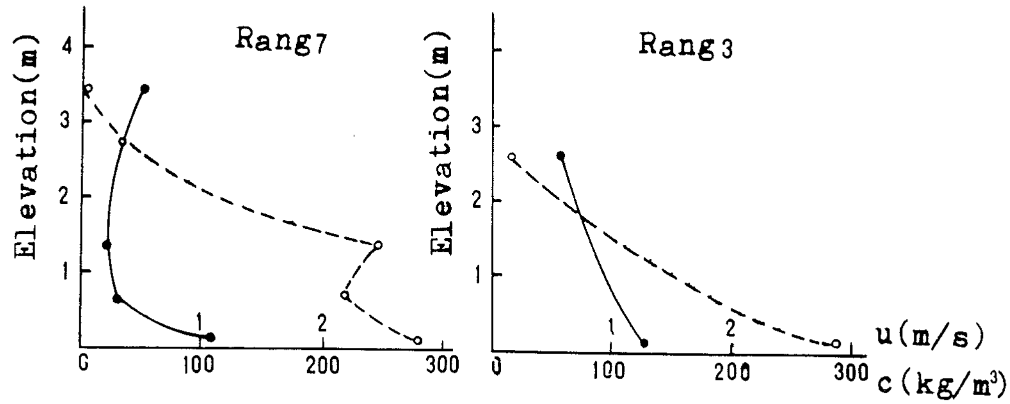

Fig.6 Distribution of velocity and silt concentration in field mesurement

4. The phenomenom of passing through "The Yellow River" of the density current from the outfall of the Taohe River

Data of model tests shown by the lantern slides revealed that the density current from the outfall of the Taohe River obviously passes through the bed of the Yellow River to the left bank and is backed up so that a weak adverse current moves toward the upstream of the Yellow River. Most part of the density current is interrupted and evented out stabley from the sluice tunnel. A small part of the density current moves toward the dam along main channel.

5. Results of the model test

(1) Series of systemic tests dealing with the influence of the inflow discharge and soil concentration of the Taohe River, the discharge for power generation, water level at the damsite, the discharge of sluicing tunnel, the shape of the funnel in front of sluicing tunnel and the elevation of the sill of the sluice tunnel have been carried out. The sluicing eficiency is quite high, about 53.3-80.5% of the amount of inflow sediment from the Taohe River is sluiced, the average is 67%, which depends on discharge capacity of the tunnel and the water level in the reservoir during the period of sluicing.

(2) With the tunnel opening the amount of the sediment passing through turbine can be roduced 3/4 compared with the case without the tunnel. The amount of sediment deposited in front of the dam is reduced by 2/3.

Reference

1. Pu Naida, Su Fengyu and Zhang Ruitong, Some problems of sedimentation in Liujiaxia and Yanguoxia Reservoirs, Proceedings of the international symposium on river sedimentation, p. 737, (1980).

MODELLING OF FINE-GRAINED SEDIMENT TRANSPORT IN A COASTAL AREA

by A.B.Veksler (Engr) , Ye.A.Zavediy (Engr)
The B.E.Vedeneev All-Union Research Institute of Hydraulic Engineering (VNIIG) , Leningrad, USSR

Abstract

The paper describes one of the methods for simulating the studies of sand gravel sediment transport in hydraulic modelling. The introduction of scale coefficients is substantiated based on the similitude conditions of transport initiation and flow induced sediment movement. The ratios relating the grain size and density to the model scale are obtained. The examples are given of applying this technique to the studies on a number of structures located in the coastal area.

When studying scour, sediment transport and sedimentation phenomena on hydraulic models one of the most difficult problems is the recalculation of a grain size of sediments composing the channel according to the model scale, since the grain size of model soil particles proves to be below 1.0 mm. As well known, the scour and transport processes are strongly affected not only by gravity forces but by viscosity which cannot be simulated when applying Froude's similitude technique usually adopted in hydraulic engineering practice. To avoid this difficulty is sometimes possible by the use of distorted scale modelling /1, 2/ which according to /3/ might produce approximate similitude. However, in case the model must display both the structure and the basin area adjacent to it, the distorted scale modelling might prove to be impermissible. So, one of the most efficient methods in modelling river bed scouring is to employ soil substitutes whose density is lower than that of prototype soils.

A conventional method to choose the substitute material is to meet the calculating conditions of Froude's ultimate nonscouring velocity. Because of this, when studying bed deformations, the use is often made of plastic powders, calcined sawdust, etc., i.e. the materials lighter than sediments, with the obtained results showing a good agreement with the prototype data. One of the most detailed substantiations of scale coefficients defining the characteristics of model soils is given in /4/ as applied to the solution of different problems which may arise in hydraulic studies of erodible channels and suspended flows. Further developments of these problems are described in /5/. The considerations given in this work confirm a unified approach to introduction of scale coefficients which define the model soil parameters when making studies of scour, sediment transport and deposition, i.e. in most cases inseparable phenomena arising simultaneously as different components of river bed evolution.

The similitude conditions of transport initiation and flow induced sediment movement can be achieved by meeting the necessary criteria determining the process both in the model and in-situ conditions:

$$d = \frac{v_{nb}}{\sqrt{\rho' g d}} = idem \qquad (1)$$

$$Re_d = \frac{d}{\nu}\sqrt{\rho' g d} = idem \qquad (2)$$

where v_{nb} is the bottom nonscouring velocity for soils with the grain size d ; $\rho' = \rho_s - \rho_w / \rho_w$, where ρ_s and ρ_w is the density of soil particles and water, respectively; ν is the kinematic coefficient of water viscosity and g is the free fall acceleration.

The similitude conditions of sediment transport and deposition by the channel flow can be attained by meeting both on the model and prototype the necessary criteria determining the flow induced particle resistance, i.e. the criterion Re_d according to 2) and the following coefficient of resistance:

$$C_s = \frac{4}{3} \frac{\rho' g d}{w^2} = idem \qquad (3)$$

where w is the relative velocity of sediment and water transport.

The criteria a and C_s are self-similar according to Re_d with $Re_d > Re_{dcr}$. Therefore, meeting the conditions of (2) is necessary only with $Re_d < Re_{dcr}$. As evident from the experimental results in Fig.1 based on the studies of channel flow nonscouring velocities /6, 7/, wave flows /8/ and particle grain size /9, 10/, the value Re_{dcr} is taken as 500. However, with the error below 5% it is permissible to expand somewhat the self-similitude area assuming $Re_{dcr} \approx 100$.

To attain on the model the similitude conditions of sediment transport and bed scouring by the flow, the soil hydraulic characteristics w and v_{nb} should be presented in conformity with the velocity scale coefficient equal to $\alpha_v = \alpha_L^{1/2}$ in Froude's modelling, where α_L is the scale line of the model, $\alpha_L = L_m / L_p$; $\alpha_v = v_m / v_p$; the indices „m" and „p" refer to the model and prototype values, respectively. Proceeding from this, one can assume $w \sim v_{nb} \sim v$ showing (1) and (3) as $v_m^2 / \rho'_m g d_m = v_p^2 / \rho'_p g d_p$. Hence,

$$\alpha_{\rho'} \alpha_d = \alpha_v^2 = \alpha_L \qquad (4)$$

Taking account of the fact that in the self-similitude area C_s and d are independent of the Reynolds number Re_d, allowance can be made for a decrease in Re_d when modelling. From (2) it follows:

$$\alpha_d = \alpha_{\rho}^{-\frac{1}{3}} \cdot \alpha_{Re_d}^{\frac{2}{3}} \qquad (5)$$

Solving (4) and (5) simultaneously we obtain the ratio of the α_d scale coefficients and the relative density to the model geometric scale α_L :

$$\alpha_d = \alpha^{-\frac{1}{2}} \cdot \alpha_{Re_d} , \quad \alpha_{\rho'} = \alpha_L^{\frac{3}{2}} \alpha_{Re_d}^{-1} \qquad (6)$$

Apparently, if the model soil with the grain size d_m can relate in accordance with Re_d to the self-similitude area we obtain when modelling in Froude's conditions: $Re_{dm} = \alpha_L^{\frac{3}{2}} Re_{dp}$ or $\alpha_{Re_d} = \alpha_L^{\frac{3}{2}}$

Then with $Re_{dm} > Re_{dcr}$ we derive from (6) as follows:

$$\alpha_{\rho'} = \alpha_L^{\frac{3}{2}} (\alpha_L^{\frac{3}{2}})^{-1} = 1, \quad \alpha_d = \alpha_L^{-\frac{1}{2}} \alpha_L^{\frac{3}{2}} = \alpha_L \qquad (7)$$

i.e. natural soils can be used as the model ground whose grain size is defined by direct geometric calculations of the prototype grain size.

When employing the substitutes whose density is different from that of the prototype $\alpha_{\rho'} \neq 1$ we obtain from (6) $\alpha_d = \alpha_L \alpha_{\rho'}^{-1}$. However, this case is hardly to be referred to as practically advisable.

With $Re_{d_m} < Re_{dcr} < Re_{d_p}$, where $Re_{d_m} = \alpha_L^{-\frac{3}{2}} Re_{d_p}$, the shift beyond the self-similitude area on the model will result in breaking the conditions of (1) and (3). Therefore, it should be assumed $Re_{d_m} = Re_{dcr}$ i.e. $\alpha_{Re_d} = Re_{dcr}/Re_{d_p}$. Hence,

$$\alpha_{\rho'} = \alpha_L^{\frac{3}{2}} \frac{Re_{d_p}}{Re_{dcr}}, \quad \alpha_d = \alpha_L^{-\frac{1}{2}} \frac{Re_{dcr}}{Re_{d_p}} \tag{8}$$

With $Re_{d_p} \leq Re_{dcr}$ the condition (1) is to be met accurately, i.e. $\alpha_{Re_d} = 1$; the scale coefficients in this case will be:

$$\alpha_{\rho'} = \alpha_L^{\frac{3}{2}} \quad \text{and} \quad \alpha_d = \alpha_L^{-\frac{1}{2}} \tag{9}$$

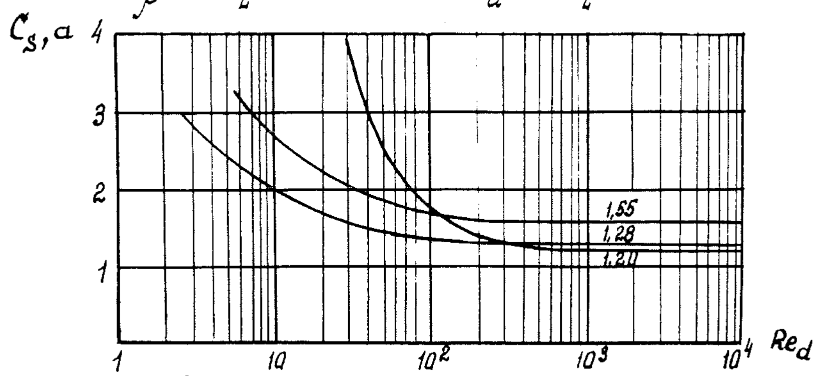

Fig. 1. Relationships between the soil particle mobility criteria in a channel flow (a_p) and in a wave flow (a_B) or the coefficient of flow induced particle resistance C_s and the Reynolds number Re_d.

Apparently, when using the substitutes the volume of scoured or deposited soils cannot be transferred from the model to the prototype conditions by mere geometric calculations. Bearing in mind that the concentration of sediments S on the model will differ from the prototype due to grain size changes, i.e. $\alpha_s = \alpha_d^3 \alpha_L^{-3}$, and assuming the volume of the sediment transport $W = SV\omega t$ (where V is the mean velocity; ω is the free area and t is the time) we have $\alpha_W = \alpha_d^3$. Similar to this, for the discharge of deposits it will be $\alpha_{Q_s} = \alpha_L^{\frac{1}{2}} \alpha_d^3$. In case of exact adherence to (6) as a result of good selection of substitutes we have $\alpha_W = \alpha_L^{-\frac{3}{2}}$ and $\alpha_{Q_s} = \alpha_L^{-2} \alpha_{Re_d}^3$.

This approach to the introduction of scale coefficients defining the size and density of scoured soils on the model and the quantitative characteristics of their transfer and bed evolution is based on the assumption that there are similitude conditions of transport initiation and flow induced sediment movement in kinematic and dynamic similar flows. Proceeding from this, to meet the similitude conditions the observance of the criteria a, C_s and Re_d was assumed to be quite enough from the relationships (1)-(3) rather than by equations for sediment transport, nonscouring velocity or grain size versus flow hydrodynamic parameters and physical-mechanical properties of soils /4, 5, 11/. However, the selection of soils to be scoured according to the above-mentioned technique results in breaking the similitude conditions of bed surface roughness, which in its turn causes a break in kinematic similitude /4/.

In the majority of cases the effect of the mentioned factors may be negligible due to a small concentration of sediments and the resulting distortion will be within a tolerable error inherent in experimental studies.

The above-mentioned technique was used in the studies of a number of structures located in a coastal area. A sea water intake with an open canal whose underwater area is protected by rockfill groins has the maximum discharge of 120 m^3/s /12/. This area is characterized by a considerable wave impact (wave height up to 10 m). The underwater slope is gentle (1:60) composed of sand deposits with the grain size d_p = 0.3-0.4 mm and the density ρ_{sp} = 2700 kg/m^3. The purpose of these studies was to define the optimum version for arrangement of protective structures providing for a reliable operation of the water intake at rough seas and sediment transport. The model with a scale of 1:75 was manufactured from concrete. The protective structures were made of crushed rock material and concrete blocks. With the given scale the modelled soils must have the density ρ_{sm} = = 1003 kg/m^3 according to (9). To study the bed sediment transport rate and sediment entrance into the water intake based on the obtained results polystyrene grains were taken as the model soils, their grain size and density being d_m = 3.9 mm and ρ_{sm} = 1030 kg/m^3, respectively. An increase in the assumed soil density (by 2.7 %) causes some distortion in the obtained results but simplifies the experimental procedure since the soil particles seem to be less subjected to floating in case of air bubbles developed on their surface. The schemes of the model and alternative versions of protective structure arrangement are given in Fig. 2.

In the course of these investigations the transport capacity of the flow entering the water intake was studied with various water discharges and sea wave height values. The flow transport capacity curves along the water intake canal length for the simplest arrangement are given in Fig. 3. As stated, the rough sea with wave heights of 3.5 m is the most unfavourable factor from the sedimentation point of view. With an increase in wave heights the sediment transport discharge decreases. With waves higher than 5 m the scour in sediments and their washing away at sea was observed at the canal site 100-120 m long.

As the results of the studies show the Schemes 1 and 2 (Fig. 2) are the most effective of all the versions considered from the canal protection point of view as the structures fully protecting the water intake.

A protective structure designed for coast protection at the river mouth is a man-made sand beach with a protective groin (Fig. 4). The beach is 2 km long and 0.2 km wide. The groin is arranged at an angle of 115^o to the beach line, its length being 280 m. The mean diameter of grains is 0.2 mm. In the course of the studies the curve of beach scouring intensity was obtained for a 10-year period (Fig. 4).

The sedimentation of the ship canal in the lake with 0.9 mm bed sediments was studied on a fragment model of the canal cross-section

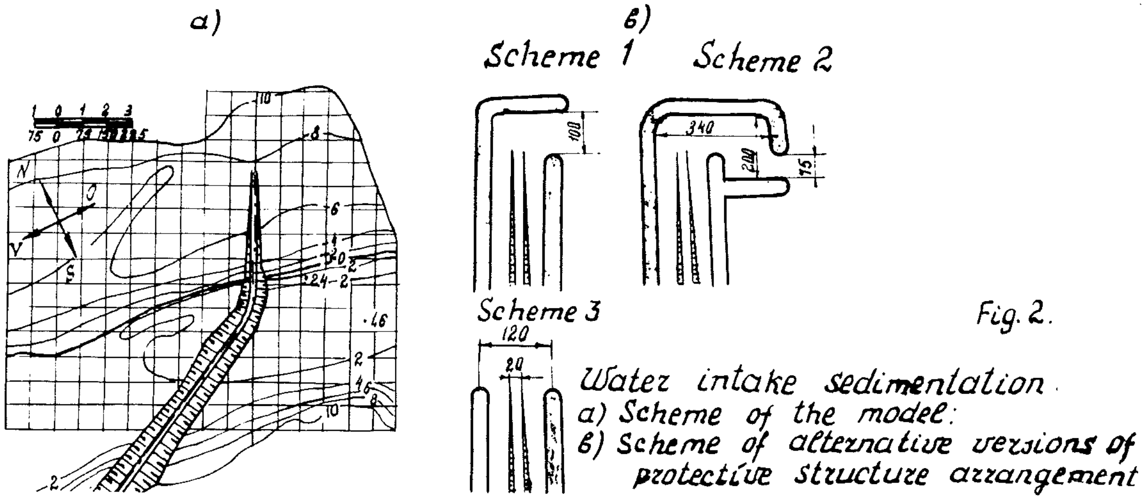

Fig. 2.

Water intake sedimentation.
a) Scheme of the model;
б) Scheme of alternative versions of protective structure arrangement

Fig. 3. Curves of flow transport capacity in water intake canal (Scheme 3) with d = 8m.
1, 2 - 120 and 60 m³/s, respectively;
ℓ = distance along the canal length;
q_s = specific discharge of sediments.

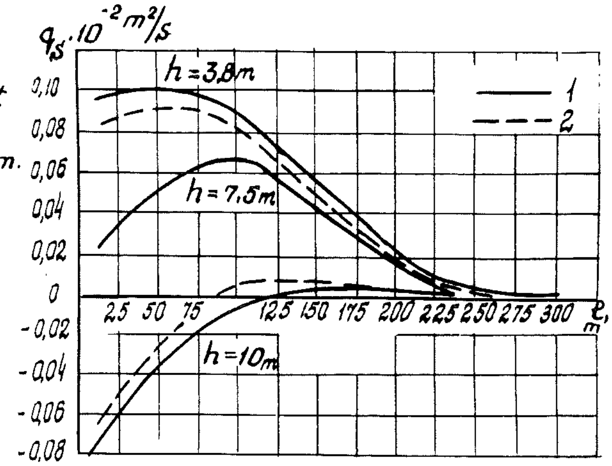

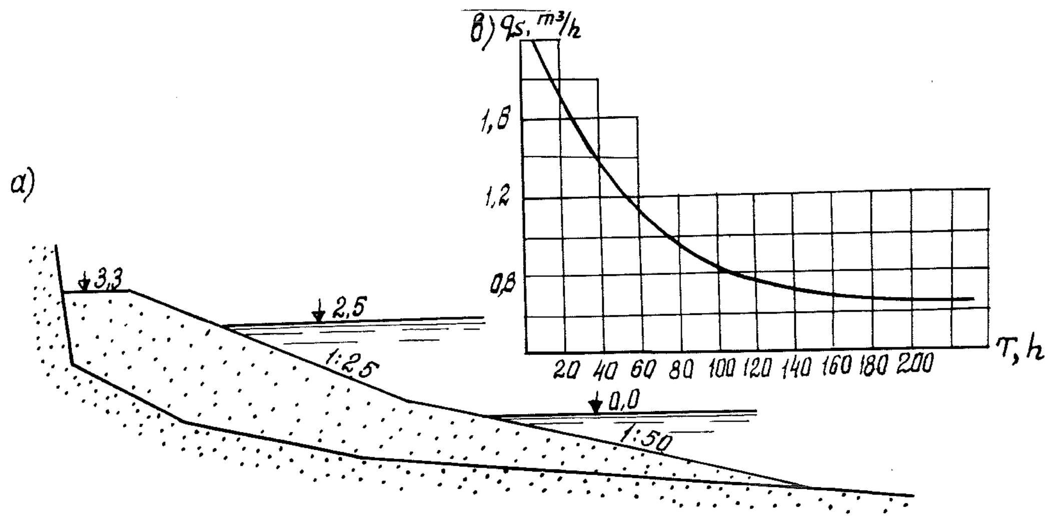

Fig. 4. Scour of coast protective structure.
a) initial beach profile;
б) curve of beach scouring intensity;
q_s = discharge of sediments washed away per 1m of beach lenght;
T = wave impact time.

average in length. The scale of modelling is 1:15. The depth and wave heights are given in Fig. 5. There are also shown the sedimentation volumes for waves various in height.

The experience gained in application of man-made grain materials (polystyrene, PVC, ect.) points to a possibility of simulating flow induced sediment transport with the use of them. At the same time it should be noted as an addition to the above-mentioned disadvantages that because of their non-wettability the long-term preliminary wetting is required in experimental studies which, nevertheless, cannot be a garantee against air bubbles apt to distort strongly the particle behaviour in water.

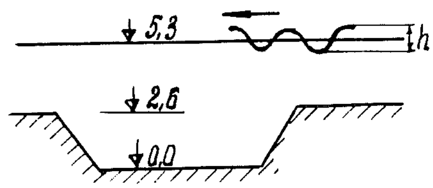

h, m	1,40	0,95	0,66
q_s, m^3/s	$36\cdot10^{-7}$	$16\cdot10^{-7}$	$36\cdot10^{-8}$

Fig. 5. Ship canal sedimentation.
q_s = specific discharge of sediments entering the ship canal;
h = wave height.

References

1. Znamenskaya, N.S. Bed sediments and channel processes. Leningrad, Gidrometeoizdat, 1976, 192 p.
2. Lapshenkov, V.S. Prediction of channel evolution at river power plants. Leningrad, Gidrometeoizdat, 1979, 239 p.
3. Lyatkher, V.M., Prudovsky, A.M. Hydraulic modelling. Moscow, Energoatomizdat, 1984, 392 p.
4. Levi, I.I. Modelling of hydraulic phenomena. Leningrad, Energia, 1967, 236 p.
5. Mikhalev, M.A. General principles of hydraulic modelling in an erodible channel. Izvestia VNIIG imeni B.E.Vedeneeva, 1983, v.168, p.9-15.
6. Knoroz, V.S. Nonscouring velocity for noncohesive soils and its determining factors. Izvestia VNIIG imeni B.E.Vedeneeva, 1958, v.59, p.62-81.
7. Mirtskhulava, Ts.Ye. Channel scour and method of estimating channel stability. Moscow, Kolos, 1967, 18? p.
8. Popov, I.Ya., Gorshukova, N.M. Nonscouring velocity for noncohesive soils and distribution of maximum bed velocity under wave impact on hydraulic structures. Izvestia VNIIG imeni B.E.Vedeneeva, 1978, v.123, p.88-96.
9. Veksler, A.B. About a grain size and coefficient of sediment resistance. Izvestia VNIIG imeni B.E.Vedeneeva, 1971, v. 96, p.74-88.
10. Veksler, A.B. Effect of sediment particle shape on hydraulic characteristics of particles. Izvestia VNIIG imeni B.E.Vedeneeva, 1982, v.154, p.52-58.
11. Ackers, P. Modelling sediment in rivers. Adv. Water Eng. Proc. Int. Symp., Birmingham, July, 1985, London; New York, 1985, p.289-301.
12. Veksler, A.B., Ivoilov, A.A., Popov, I.Ya. Hydraulic studies of wave impact and effect of long-shore currents on the water intake with an open canal. Izvestia VNIIG imeni B.E.Vedeneeva, 1984, v.70, p.83-89.

VELOCITY AND SHEAR STRESS DISTRIBUTION IN SCOUR HOLES CAUSED BY SUBMERGED WALL JET

by Siow-Yong Lim
Department of Civil & Structural Engineering
Universiti Kebangsaan Malaysia
43600 UKMBANGI, Malaysia.

Abstract

Experimental results of the velocity and boundary shear stress distribution in localized scour holes caused by turbulent wall jets with finite tailwater depths are reported. The main focus has been the flow field near the bed of the scour holes and in particular the associated characteristics of the fluctuating boundary shear stresses. It is shown that the local velocity measured at 0.8 cm from the bed using a propeller current meter can be used to compute the bed shear stress. A qualitative description has been given on the scouring process based on the mean flow characteristics.

Introduction

An essential part of research into sediment transport is the measurement of local shear stress close to the bed. A knowledge of this information is pertinent in order to explain the mechanism by which sediment particles are entrained from the bed and their subsequent transportation by the main flow. In fact, most of the sediment transport formulas currently available incorporate either explicitly or implicitly the effect of shear stress as a function of the local hydraulic conditions. The present paper deals primarily with the measurements of mean flow characteristics and their associated shear stresses in scour holes under clear water scour condition caused by two and three dimensional turbulent wall jets with finite tailwater submergence.

The objectives are twofold. Firstly, a method is sought on the computation of boundary shear stress involving local scour and a brief review on related works has been conducted. A method described herein has been proven to be useful and supported the approach used by many researchers using the local velocity near the bed to calculate shear stress. Secondly, this approach has been applied to study the distribution of boundary shear stresses in scour holes produced by a plane jet and a square jet. A qualitative description is given on the time development of scour and to account for the fact that some of the bed shear stresses computed have values smaller than the Shields critical criterion for the initiation of sediment motion.

Experimental set-up and velocity measurements

Two series of flow patterns experiments have been conducted for this study. A recirculating channel 5.0m long, 0.61m wide and 0.5m deep was used for the experiments involving a plane turbulent wall jet. The jet opening was 5.1 cm and was issued under a well designed sluice gate. The working section was 2 m from the downstream end of the channel with a sand bed filled to a depth of 0.3m. The invert of the jet was positioned at the same height as the levelled sand bed. A square jet of 5.1 cm x 5.1cm was used in the three dimensional scour tests. The set-up consisted of a header tank connected by a 0.6m long square pipe to a downstream working section made of galvanised steel 1.83 m long, 0.61 m wide and 0.46 m deep. The sand was filled to a depth of 0.25m in the downstream tank.

Only one type sand was used in this study. The sand had a uniform grading curve with d_{50} = 0.82 mm, angle of repose = 33^o, a specific gravity of 2.66, a porosity of 0.403 and a mean fall velocity corresponding to d_{50} of 11.0 cm/s. The experiments were confined to the clear water scour condition. The tailwater depths in all the experiments were adjusted so that the jet outlet was just submerged. For both series, the streamwise mean flow characteristics were measured for the time development of scour holes at various stages of the erosion process.

Because of the continuously changing flow boundary as scour progresses with time, the transient, non-uniform flow has to be first transformed into a steady-state fixed bed model. The method used simply involved covering and moulding the scour hole in situ with aluminium tin foil, which forms an impermeable layer between the sand and the water. The flexibility and toughness of the foil enables the complicated scour geometry to be moulded easily. The experimental section was covered completely so that no water leaked into the soil. The surface of the foil was then coated with the sand grains used in the experiment, to simulate the original roughness of the bed.

Velocities were measured using a Nixon stream flow miniature current meter of diameter 16 mm. Velocity measurements were taken over a grid of locations in both the horizontal and the vertical planes. In this study, particular attention was given to the measurements of the streamwise bed velocity, u_b at a distance 0.8cm above the bed of the scour hole.

Flow characteristics in scour holes

The time development of scour represents a very complicated shear flow phenomenon involving the movement of sediment-water mixture along the bed of the scour hole. A typical sequence of the centerline velocity profiles illustrating the development of a scour hole from the initial flat bed stage through to the approximate equilibrium scour condition produced by a 5.1cm x 60.7cm plane jet is shown in Fig. 1. It can be seen that the flow distribution resembles that of a diverging-converging flow situation. As the diffused jet starts to flow over the erodible bed, a scour hole is formed immediately, creating a region of intense mixing and shearing. From the measured velocity profiles, the displacement thickness δ_*, the momentum thickness, θ and the corresponding shape factor $H_{12} = \delta_*/\theta$ were also evaluated. Some typical values of H_{12} are also listed in Fig. 1.

For boundary layer flow on a smooth flat bed, it has been found that H_{12} grows larger with an increase in x and in pressure gradient, dp/dx [1]. For the present case, the increasing value of H_{12} shown in Fig. 1 corresponds to the expansion and diffusion of the jet into the scour hole which causes a deceleration to the mean flow and an increase in dp/dx, in this case adverse since $H_{12} > 1.4$ and $dp/dx > 0$ [2]. Beyond the section of maximum scour, the flow accelerates with the decrease in H_{12} and the pressure gradient is favourable ($dp/dx < 0$ and $H_{12} < 1.4$). Clearly, it can be seen that the flow in localized scour is strongly influenced by the presence of pressure gradient, particularly in the section of maximum erosion. It will be seen in the following section that this factor needs to be considered in the determination of boundary shear stress.

Computation of boundary shear stress

For a plane surface, the simplest technique for measuring the boundary shear stress is perhaps the Preston tube. Measurement of boundary shear stress in a scour hole presented great problem in that the curvature of the scour zone precludes the use of the Preston tube. It should be mentioned that short of direct measurements at the boundary, there is as yet no reliable method of determining the actual shear stress in a scour hole. For local scour around bridge piers, Melville and Raudkivi [3] were two of the few who studied the flow characteristics in the scour holes. The velocities were measured using the DISA anemometer and the boundary shear stress was estimated from the mean bed velocity measurements, u_b at a level of $y_b = 2$ mm from the boundary using the equation

$$\tau_b = K \cdot u_b / y_b \qquad (1)$$

where K = 2, which is the calibration constant obtained by comparing τ_b from Eq. (1) with those obtained from the slope of the logarithmic velocity profiles of the approach flow and with Preston-tube measurements.

A method similar to that of Melville and Raudkivi is used for the present investigation. This method has the principal advantage of easy mobility. The mean local bed velocity at $y_b = 0.8$ cm which is half the diameter of the propeller current meter will be used as the characteristic velocity in the equation

$$\tau_b = \rho f u_b^2 / 8 \qquad (2)$$

where f is the friction factor, assumed to be given by the Colebrook-White equation, written for the present purpose as

$$1 / f^{1/2} = -2 \log_{10} [d_{50} / 14.83 h + 2.52 / f^{1/2} (Re)_h] \qquad (3)$$

where h = the local flow depth above the scoured bed and $(Re)_h = u_b h/\nu$.

In an attempt to check the applicability of Eq.(2), the rough law equation and the characteristics of the velocity profiles have also been employed to determine the boundary shear stress. For the present purpose, the commonly accepted rough law equation for fully developed turbulent layer on a flat plate can be written as

$$u_b / u_* = 2.5 \ln [30.1 y_b / d_{50}] \qquad (4)$$

where $u_* = (\tau_b / \rho)^{1/2}$. Initial comparison of τ_b calculated from Eq.(2) and Eq.(4) indicated that the latter values are larger by as much as 25% (see Fig. 3). An analysis of the flow characteristics in the turbulent boundary shear layer of the scoured zone is then carried out to check the reason for this discrepancy.

For turbulent boundary layer over a flat plate, Ludwieg and Tillmann [1] found that in spite of the presence of a pressure gradient, a narrow inner region existed in which the law of the wall still holds. It follows that with the reduction of velocity near the boundary when $dp/dx > 0$, τ_b should also be reduced accordingly [2]. In other words, any flow problems in the presence of strong pressure gradients should made allowance for the variation of the shape factor H_{12}, particularly under conditions of imminent separation. Following the method of Ludwieg and Tillmann, the velocity, u_θ at a distance of y_b = momentum thickness, θ was read off or extrapolated if necessary for those velocity profiles under the influence of a pressure gradient. As shown in Fig. 2, the velocity u_θ is plotted in a non-dimensional form as u_θ/u_m against H_{12}, where u_m = maximum velocity at a section. The agreement of the present data with the curves of Ludwieg and Tillmann and that of Spence [1] is excellent. In view of the agreement and the fact that u_0 is usually very near to the bed, it is postulated that the skin friction formula suggested by Ludwieg and Tillmann may be used to calculate the bed shear stresses and to compare with that from Eq.(2). The equation has the form

$$\tau_b = 0.123\,\rho\,(Re)_\theta^{-0.268} \cdot 10^{-0.678H_{12}} \cdot u_m^2 \qquad (5)$$

where $10^3 < (Re)_\theta = u_m\theta/\nu < 4 \times 10^4$. The results of the above comparison is shown in Fig. 3 and it can be seen that reasonable agreement is obtained. Therefore, it can be concluded that reasonable estimates of τ_b could be obtained using Eq.(2) from measurements of the velocity near the bed.

Results of boundary shear stress distributions

Fig. 4 shows the boundary shear stress distribution along the centerline bed profile for the plane jet. For the square jet, the calculated shear stresses for three stages of the erosion process have been plotted in contour form as presented in Fig. 5. In general, it can be seen that the values of τ_b decrease as the scouring time and size of the hole increases and that negative shear stresses were obtained for those sections where reversed flow was observed (Fig.1). The negative sign indicates that the boundary shear stress is in the direction of flow. Figs. 4 and 5 also show that the boundary shear stress is lowest around the region of maximum scour and is highest near the crest of the scour hole. In both cases, the region of the highest value of boundary shear stress also coresponded to the region where the bed velocities were large and vice versa. It should be mentioned that the friction factors f computed from Eq. (3) for all data points remain quite constant with an average value of 0.032 for the flat bed data and a maximum of 0.039 for the maximum scour section.

Using the Shield's criterion for the initiation of sediment motion [5], the critical shear stress, τ_c obtained for the bed material (d_{50} = 0.82 mm) used herein is $\tau_c = 0.42$ N/m^2. Referring to Figs. 4 and 5, it can be seen that all the boundary shear stresses, except for the flat bed condition, have values less than the critical value. Similar trend has also been observed by Raudkivi [6]. This observation contradicts the accepted fact that the boundary shear stress would gradually reduce to the critical value when the scour hole approaches the equilibrium condition [4,5]. It must be pointed out that in the calculations of τ_b, no consideration has been given to the effect of turbulent intensity near the bed. From observations during the measurement, it was noted that there were occasional turbulent bursts near the bed which brought sand particles from the upstream slope of the hole to the section of maximum erosion and vice versa.

This clearly indicates that the turbulent agitation near the bed plays an important role in the entrainment of particles although the observed mean τ_b did not show a higher value than τ_c to indicate this trend. Fluctuations of up to 50% in the mean velocity of turbulent flows near the bed has been observed and because shear stress is proportional to u_b squared, instantaneous shear stresses acting on the bed having more than twice the average intensity are to be expected [4]. It follows that any attempt to explain the detailed behaviour of τ_b in the scour zone must take into account the effects of these fluctuations on local entrainment and sediment transportation. This aspect has not been dealt with in this study mainly due to the limitation of the instrumentation used.

However, works by researchers such as Breusers [7] and Schoppmann [8] have proven experimentally that scouring is indeed more severe when the turbulent intensity in the scour zone increases. It was found that the turbulence itself does not erode the bed material but only agitates and loosen the particles on the bed so that they are more easily entrained by the flow. Therefore, base on these works, it appears reasonable to conclude that turbulent agitation near the bed is an important mechanism for the entrainment of particles and that although the local time-averaged boundary shear stress is smaller than the Shields critical value, relatively large instantaneous value due to the strong turbulent velocity fluctuations near the bed can occur frequently enough to cause an enhanced rate of entrainment and transport of sediment particles from the scour hole.

Conclusions

The following conclusions can be drawn from the study:

1. The flow characteristics in a scour hole was found to be greatly influenced by strong presure gradient and that this factor needs to be considered in the determination of boundary shear stress.
2. It has been demonstrated that Eq.(2) can be used to calculate the mean boundary shear stress in a scour hole from a velocity measurement made at a distance of 0.8 cm above the eroded bed.
3. The study shows that the criteria of critical shear stress alone could not account for the enhanced rate of entrainment and transport of sediment particles in the scoured zone and that measured mean boundary shear stresses have been found to be lower than the Shields critical value.
4. A qualitative description revealed that turbulent agitation near the bed is an important mechanism and that the rates of entrainment and transport of sediment are not unique functions of the boundary shear stress but depend also on the turbulent intensity near the bed.

References

1. Duncan, W.J., Thom, A.S., and Young, A.D.(1970). Mechanics of fluids. 2nd. edition, Edward Arnold, London.
2. Daily, J.W. and Harleman, D.R.F. (1966). Fluid Dynamics. Addison-Wesley Publishing Co. Inc., New York.
3. Melville, B.W. and Raudkivi, A.J. (1977). Flow characteristics in local scour at bridge piers. J. of Hyd. Research, 15, No. 4, pp. 373-380.
4. Vanoni, V.A. (1977). Editor, Sedimentation Engineering. ASCE-Manuals and reports on Engineering Practice, No. 54.
5. Ali, K.H.M and Lim S.Y. (1986). Local scour caused by submerged wall jets. Proc. Inst. of Civil Engineers, U.K., Part 2, Dec.,pp. 607-645.
6. Raudkivi, A.J. (1963). Study of sediment ripple formation. J. of Hyd. Div., Proc. ASCE., Vol. 89, No. HY6, Nov., pp. 15-33.
7. Breusers, H.N.C. (1967). Time scale of two dimensional local scour. Proc. 12th Congress, IAHR, Fort Collins, Vol. 3, pp. C32-1-8.
8. Schoppmann, B. (1975). The mechanics of flow and transport of a progressive scour. 16th Congress, IAHR, Sao Paulo, Vol. 2, pp. 189-195.

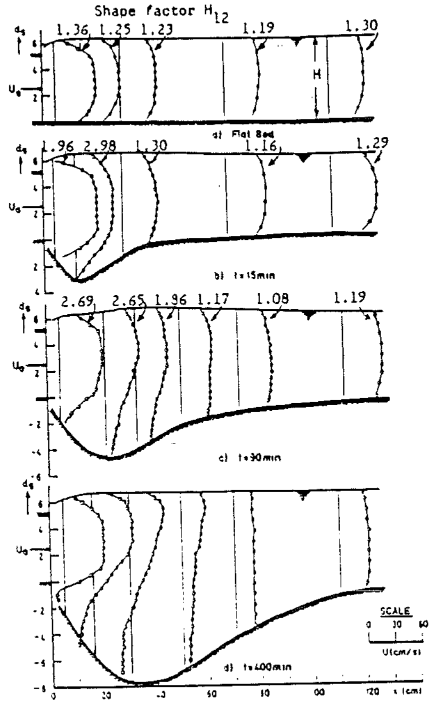

Fig.1. Typical velocity profiles at various stages of the erosion process. (5.1cm x 60.7cm jet, U_o=55.0cm/s, H=6.7cm)

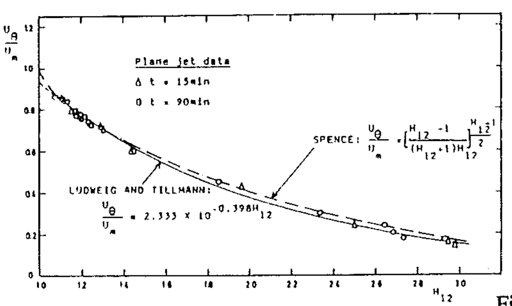

Fig.2. Variation of u_0/u_m against H_{12}.[5]

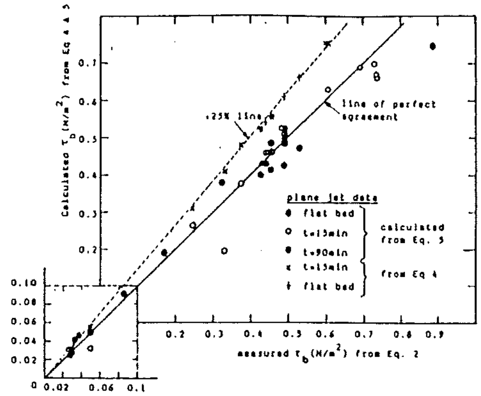

Fig.3. Comparison of boundary shear stress from Eqs.(2),(4) & (5)

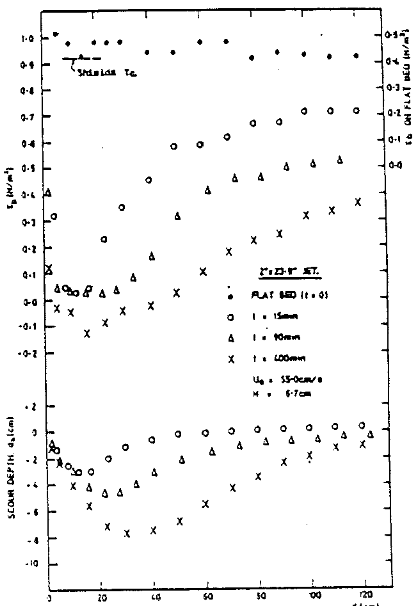

Fig.4. Boundary shear stress distributions in scour holes along the centerline bed profile. (5.1cm x 60.7cm jet, U_o=55.0cm/s, H=6.7cm)

Fig.5. Boundary shear stress distributions in scour holes caused by the 5.1cm x 5.1cm jet. (U_o=60.31cm/s, H=5.5cm)

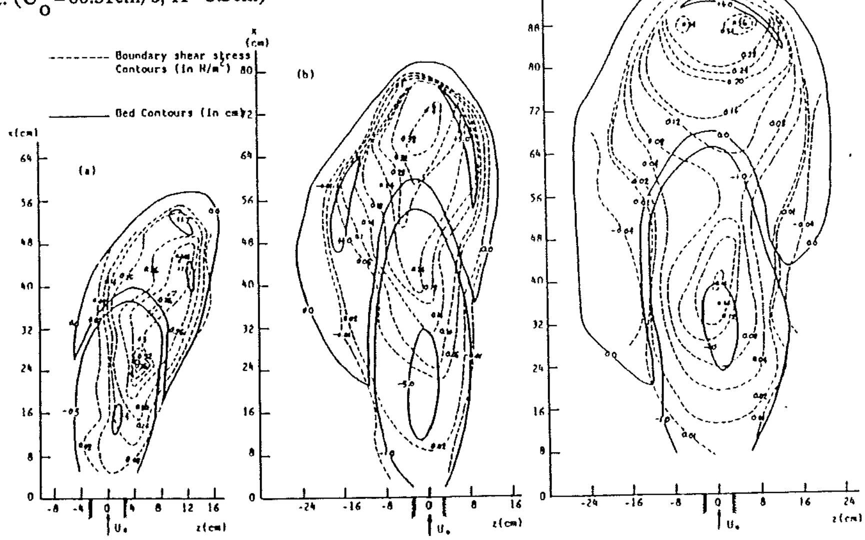

Session 13A

Mixing in Ponds, Lakes, and Reservoirs

NUMERICAL AND EXPERIMENTAL STUDY OF THE ADVANCED SOLAR POND (ASP) PERFORMANCE

by Hillel Rubin, Yehuda Keren
and Giorgio A. Bempord*
CAMERI-Coastal and Marine Engineering Research Insitute
Department of Civil Engineering
Technion-Israel Institute of Technology
Haifa 32000, Israel

Abstract

The conceptual structure and operation of the advanced solar pond (ASP) was presented by the authers in several previous articles. The present study concerns the theoretical and experimental evaluation of the ASP performance. The theoretical calculations were carried out by applying some simplified flow, heat transfer and mass transfer models. The experimental part of the study included simulations of transport processes in the conventional solar pond (CSP) as well as such processes taking part in the ASP.

The thoeretical calculations as well as the experiments indicated that the ASP may operate at higher efficiency and higher bottom temperature than those typical to the CSP.

Introduction

In several previous publications [1,2,3] the authors introduced the concept of the advanced solar Pond (ASP). Fig. 1 provides a schematical description of the ASP. This structure of the ASP was suggested by Osdor [4]. Osdor suggested to modify the conventional solar pond (CSP) by adding a stratified thermal layer on account of the homopeneous thermal layer, which is also termed LCZ (lower convective zone), and the barring layer layer, which is also lermed GZ (gradient zone). Osdor also suggested to increase the salinity in all layers of the solar pond and thereby to reduce the rate of evaporation from the CSP surface and enable a certain increase of the temperature of the homogeneous thermal layer.

Osdor's idea can be materialized provided that it is possible to create the stratified thermal layer and control its flow conditions.

* Present address: Mathematical Models Div., ISMES Spa, Viale Giulio Cesare 29, 24100 Bergamo, Italy

The mathematical modelling

In order to evaluate the possible use and advantages of the ASP we developed a simplified mathematical model able to simulate basic momentium, heat and mass transfer phenomena. Complete details concerning this model are given in our previous studies [1,2].

The model incorparated an analytical solution of the flow equations, considering only horizontal flow in the various major fluid layers, with numerical solution of the heat and mass transfer processes, considering dominant convection in the horizontal direction and dominant diffusion in the vertical direction.

We also performed some analyses of the flow field stability which provided information concerning differences in stability criteria between the ASP subject to field conditions and a possible simulator of the ASP operating in the laboratory [5]. The analyses indicated that in most practical cases the flow in the laboratory simulator of the ASP is more stable, and convection currents may develop in planes different from those typical to instability of the flow carried out in the ASP subject to field conditions. However if carefully planned experiments, carried out even in a comparatively narrow flume, can provide the important information concerning the feasibility of the ASP.

The experimental set-up

Fig. 2 provides the schematic of the experimental set-up utilized to simulate the performance of the ASP. It consists of a flume whose length, width and depth are 915cm, 60cm, 162cm, respectively. It is made of concrete, and its inner walls are covered with an insulating material which has a high chamical resistivity.

At the upstream side of the flume a special entrance unit was used in order to create the stratification of the stratified thermal layer as required. At the downstream end of the flume a special exit unit was installed in order to enable adequate conditions for the multiselective withdrawal. Parts of the homogeneous thermal layer and the stratified thermal layer were diverted into a series of small containers employed as a mixing unit which provided the various discharges, salinities and temperatures as needed for the stratified thermal layer. The mixing unit and a special pumping system controlled the flow conditions in the homogeneous thermal layer and the sublayers comprising the stratified thermal layer.

The solar radiation was simulated by metal halide lamps and G.E. Duralight reflectors which provided radiation energy of 225 W/m^2 at the surface of the water body.

The experiments and experimental results

The experimental set-up described in the previous section may simulate transport phenomena taking place in a sector of the CSP or ASP whose length is about 9m. However such a short sector includes the region affected by the selective injection as well as the region affected by the selective withdrawal.

In order to consider differences in transport phenomena between different sectors of the ASP we had to create in the experimental set-up the adequate salinity and temperature profiles by injecting for the simulation of transport phenomena in a downstream sector the resulted profiles obtained in the withdrawal of the upstream sector. Meanwhile we only completed a very limited set of experiments concerning transport phenomena taking place in the first sector of the CSP and the first sector of the ASP.

Operating the experimental set-up as a CSP simulator, the energy losses were about 80 pecent of the radiation energy existing at the water surface. The brines were injected into the homogeneous thermal layer at a temperature of 70 centigrade, as shown in Fig. 3a. The withdrawal temperature was 75.5 centingrade.

Operating the experimental set-up as an ASP simulator, the energy losses were about 70 percent of the radiation energy existing at the water surface. About 23 percent of the 30 percent useful energy were obtained from the homogeneous thermal energy, and 7 percent were obtained from the stratified thermal layer. As shown in Fig. 3b the temperature of the brine injected into the homogeneous thermal layer was 70 centigrade. The withdrawal temperature of that layer was 76.3 centigrade. The average entrance temperature of the various sublayers comprising the stratified thermal layer was 63 centigrade. The average exit temperature of those sublayers was 64.9 centigrade.

Summary and conclusions

In the framework of this study we theoretically evaluated the possible advantages of the ASP. However it was needed to follow the feasibility of the ASP by performing a set of experiments that were also carried out in the framework of the present research. These experiments were carefully planned and performed in a flume comprising a simulator ofthe CSP or ASP. The experimental part of the present study showed that it is possible to create and control the ASP. It is possible to create two thermal layers in a solar pond. The homogeneous thermal layer is located at the bottom of the ASP, and the stratified thermal layer is located on top of the homogeneous thermal layer.

However adequate entrance, exit, pumpage and mixing units should be utilized in order to control the appropriate flow conditions in the ASP.

The study indicates that the ASP can be more efficient that the CSP. The bottom temperature of the ASP can also be hgiher than that of the CSP.

References

1. H. Rubin and G.A. Bemporad, The advanced solar pond (ASP) basic theoretical aspects, Solar Energy, vol. 43, No. 1, pp. 35-44, (1989).

2. H. Rubin and G.A. Bemporad, Analysis of turbulent flow in thermal layers of the advanced solar pond (ASP), vol. 43, No. 1, pp. 25-33, (1989).

3. Y. Keren, G.A. Bemporad, and H. Rubin, Basic experiments related to the advanced solar pond (ASP) performance, accepted for publication to Trans. of ASMe J. of Fluids Engrg.

4. A. Osdor, Method of trapping and utilizing solar heat, U.S. Ptent No. 4,462,389, (1984).

5. G.A. Bemporad and H. Rubin, The onset of thermal and thermohaline convection in a rectangular duct flow, in press.

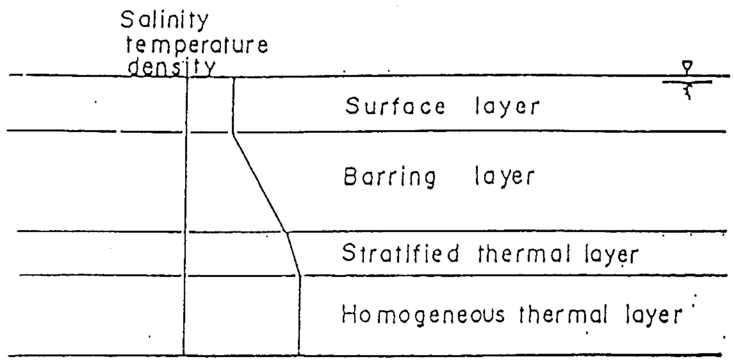

Fig. 1 : The major fuild layers characterizing the ASP.

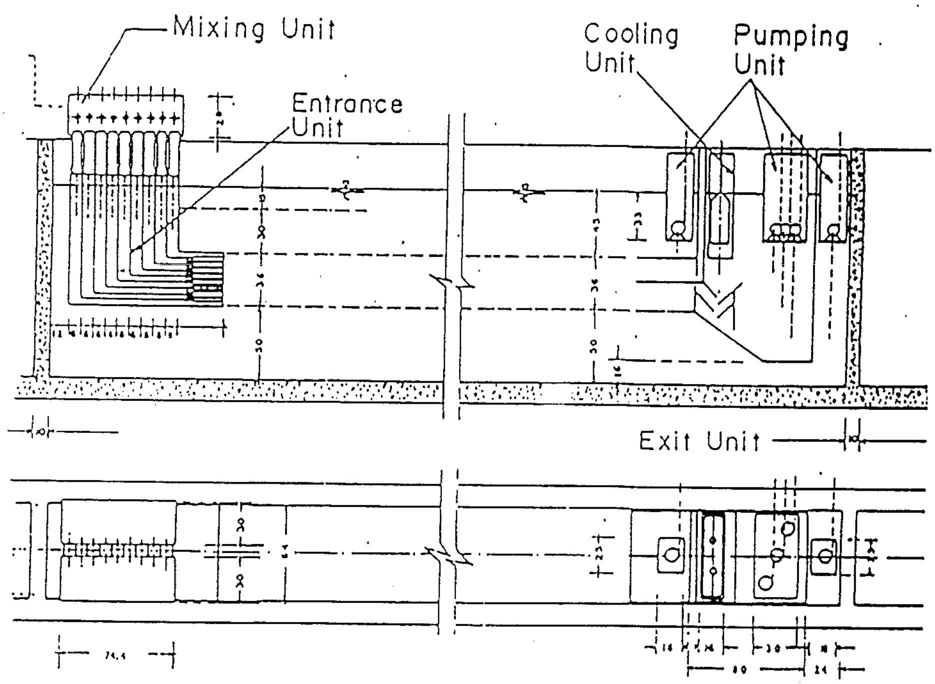

Fig. 2 : The experimental set-up

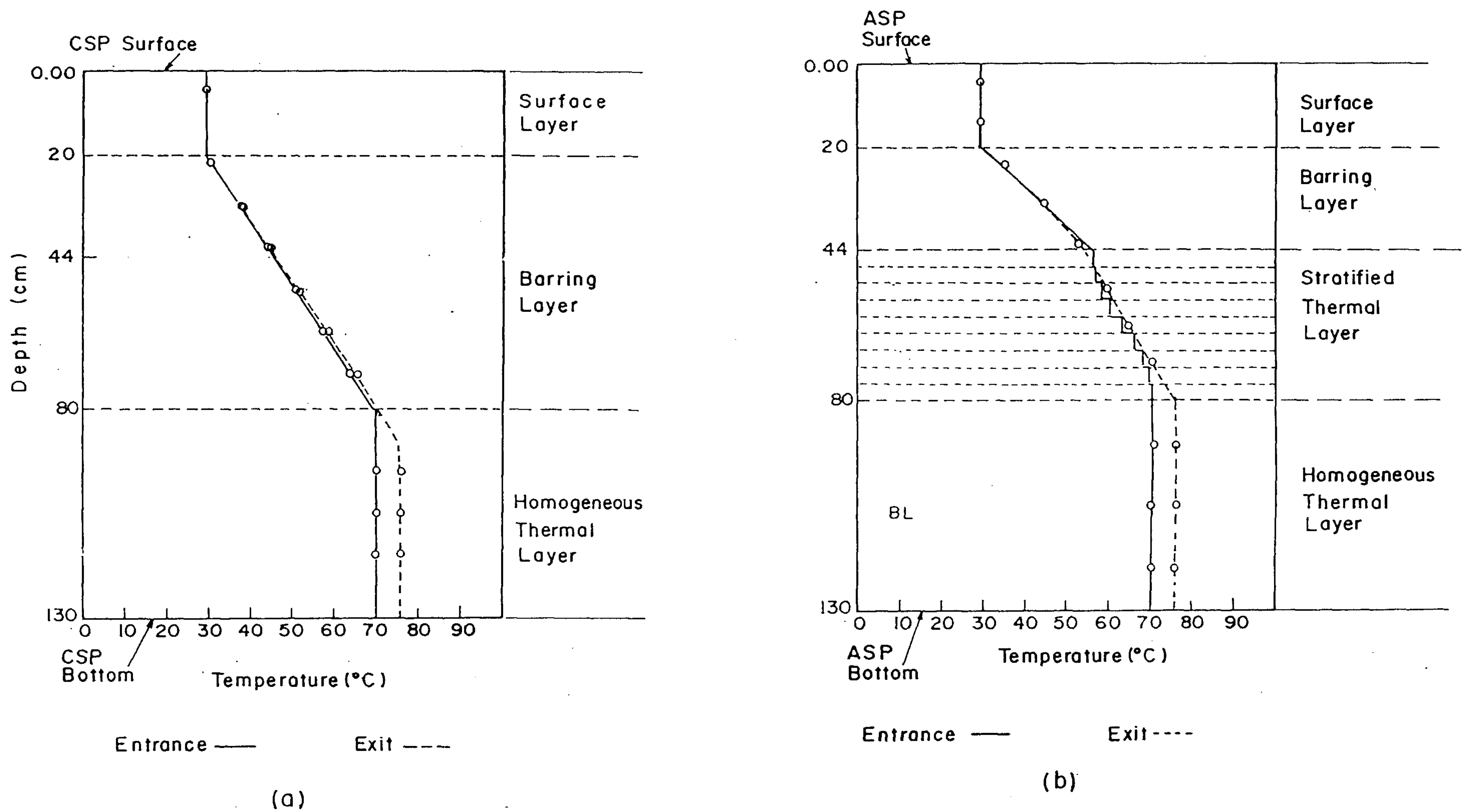

Fig. 3 : Temperature profiles at the entrance and exit of the solar pond simulator (a) CSP (b) ASP

THE MODEL STUDY OF A SHALLOW COOLING POND

By Yu Changzhao   Li Yuzhu
Zhou Xueyi   Zhou Bingliang
Department of Hydraulic Engineering, Tsinghua Univ.
Beijing, 100084, China

Abstract

This paper presents the model study for the cooling pond of a thermal plant for its enlargement project. The cooling water of the plant discharges into a shallow region of a natural lake. There are some prototype data of temperature in the pond for the original plant disposal. It provides a good chance for model verification. The model study conducted includes the physical model and the numerical model.

Introduction

In the enlargement project of a thermal plant in Yunnan Province, the cooling water of the plant is discharged directly into a shallow region of the Kunming Lake. A dike was built to separate the outlet and the intake as shown in figure 1. In order to verify the validity of the disposal design proposed and to improve it if necessary, a physical model test was conducted and a numerical model computation was carried out to investigate the heat dissipating effect of the cooling pond and to predict the temperature at the intake for the given project. The prototype data of temperature distribution in the pond obtained for the original plant disposal were used for models' verification.

Design of physical model and measuring apparatus

The physical model was designed according to the Richardson's criterion and to fulfill the requirments of geometric similarity, of kinematical similarity of flow and of the similarity of heat balance. Hot water with temperature automatic controlled was used as testing medium. Since the prototype depth of water in the pond is shallow (average 1.5 m), the model is distorted to enlarge the vertical scale to ensure enough depth of water in the model. The model discharge is kept greater than the critical discharge to ensure the flow in model to be turbulent regime. The horizontal scale of the distorted model is $L_r=260$, and the vertical scale is $Z_r=20$ so that the distortion ratio is $L_r/Z_r=13$. A set of multipoint thermoprobes was used to measure the temperature. The data were put into a computer for processing to get the instantaneous value and the mean value of temperature. Temperatures measured in the model were converted to prototype by the rule $[(T-T_\infty)/(T_1-T_2)]_r=1$ [1], where T_∞ - natural temperature; T_1- temperature at the outlet; T_2-temperature at the intake. The flow pattern and the range of diffusion of hot water were obtained by floating scraps of paper and dye visualization.

Physical model verification

Basing on the prototype data of temperature in the pond for cooling water disposal for the original plant, the physical model verification test was carried out. The comparison of the model results with the prototype was shown in Table 1 and Figure 1 which show that they are consistant with each other for the temperature at the intake though there are somewhat difference in the pond field.

Results of prediction test in physical model

Experiments were conducted in the hydraulic laboratory without climatic control but in July to August in which the climatic condition is similar to that in the prototype field. The experiment consists of three sets, the plant outputs are 10 x 10^4 kw, 12.4 x 10^4 kw and 20 x 10^4 kw and the corresponding discharges of circulation are 5.1 m^3/s, 7.1 m^3/s and 10.2 m^3/s respectively. The main purpose of the test is to predict the temperature at the intake under given temperature of the outlet and given water level in the lake. Table 2 shows the experimental results for two sets. The flow pattern and the temperature distribution in the pond for the set with output 20 x 10^4 kw are shown in figure 2 and figure 3 respeclively.

Table 1 Physical model verification result

Phant output (10^4kw)	Discharge (m^3/s)	Water level in pond (m)	Outlet temperature (°C)		Intake temperature (°C)	
			Prototype	Model converted	Prototype	Model converted
2.4	1.50	1890.4	29-30.2	30.2	23.7	23.6
Natural temperature in pond=23°C						

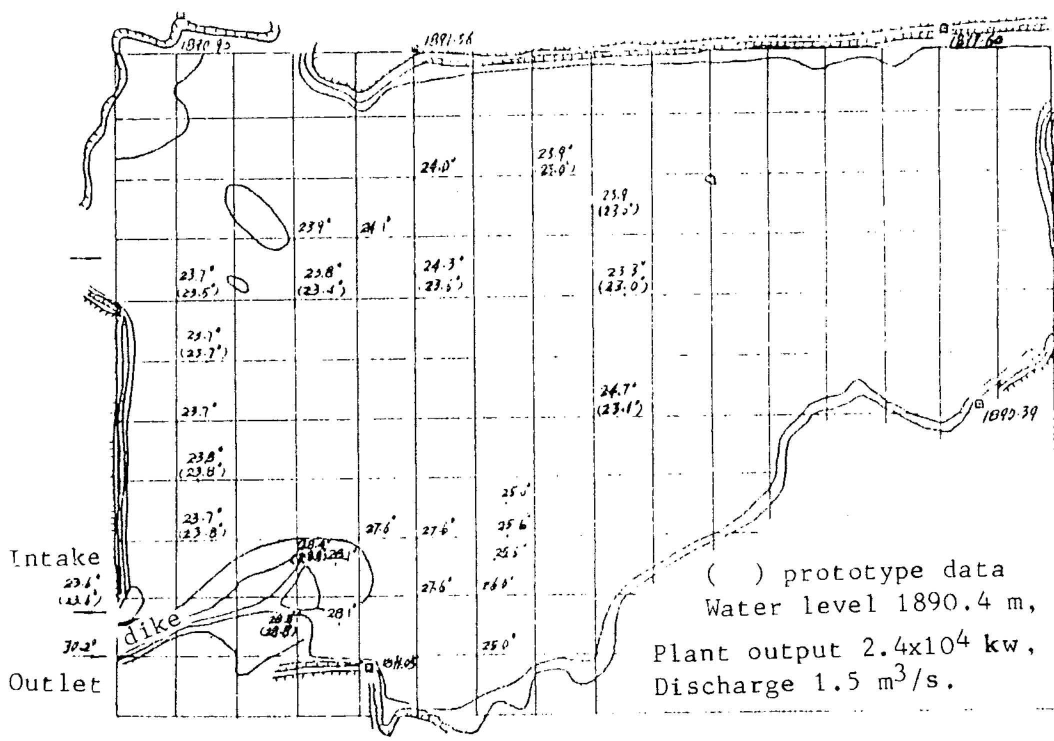

Figure 1 Verification test result for physical model

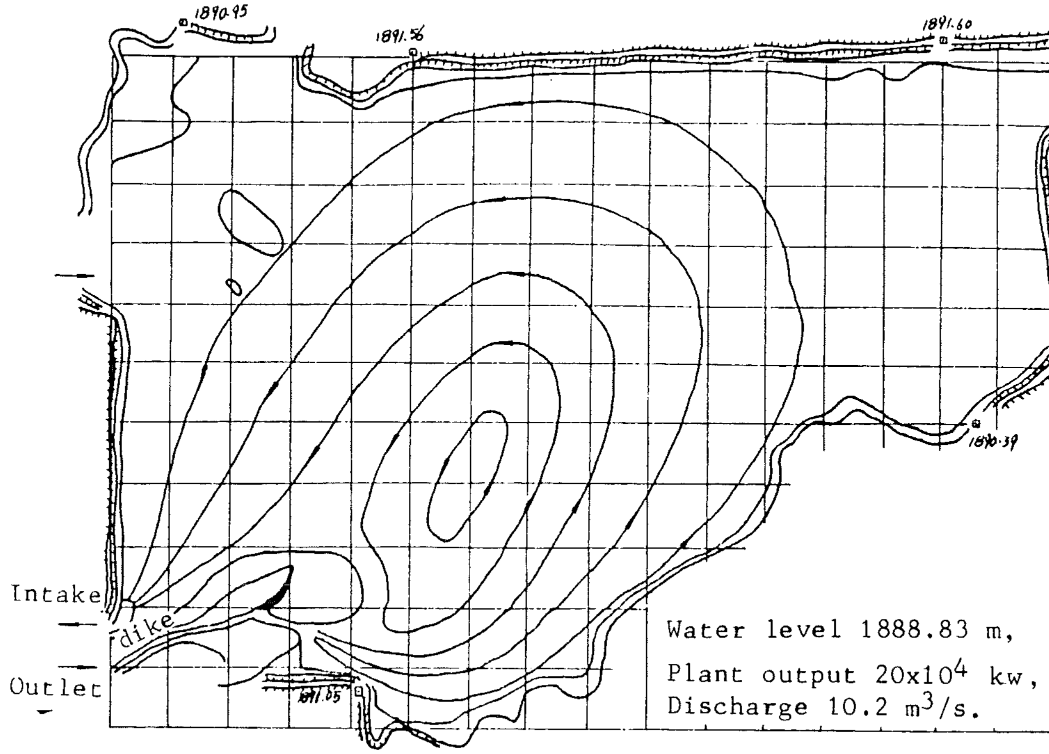

Figure 2 Flow pattern in a cooling pond

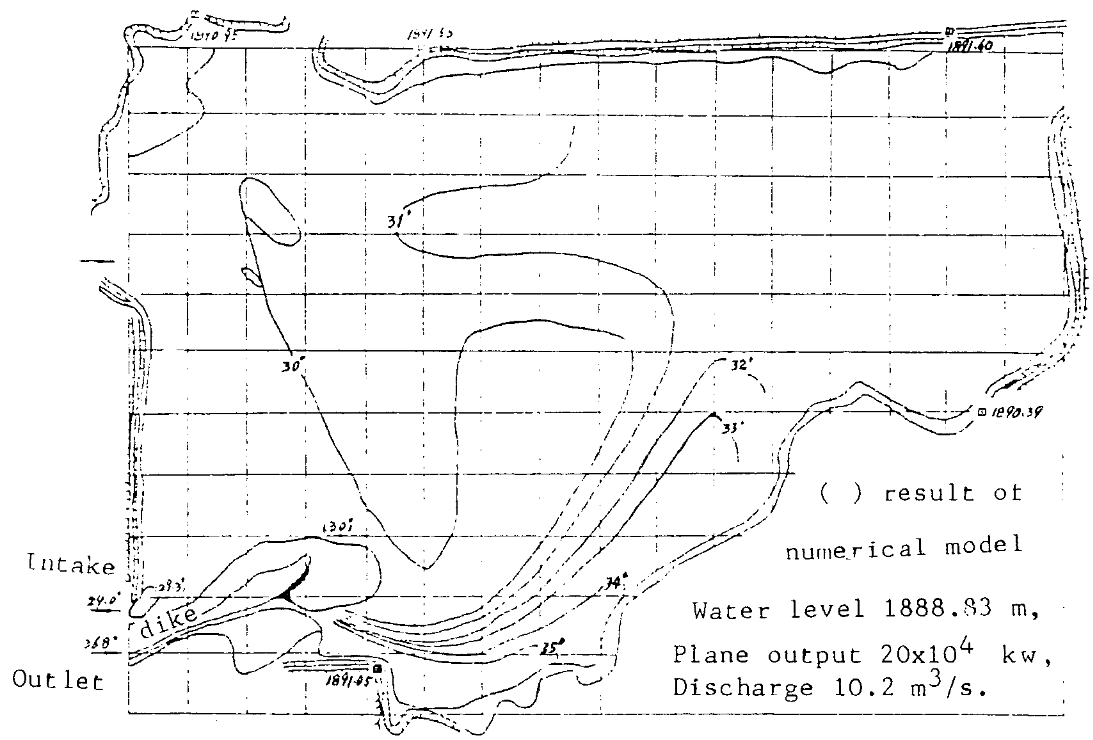

Figure 3 Temperature distribution in the pond

Table 2 Results of physical model prediction test

Output of the plant (10^4 kw)	12.4	20
Water level in the pond (m)	1888.83	1888.83
Circulating discharge (m^3/s)	7.1	10.2
Outlet temperature, T_1 (^oC)	36.8	36.8
Intake temperature, T_2 (^oC)	27.1	29.0
Natural temperature in pond, T_∞ (^oC)	22.5	22.5
Temperature difference between outlet and intake, T_1-T_2 (^oC)	9.7	7.8
Relative temperature rise at intake, T_2-T_∞ (^oC)	4.6	6.5

The numerical computation model and its verification and prediction result

The near-field and the far-field are modelled separately in computation. The result of the fore is used as the boundary condition of the later. The near-field is considered as a plane jet and computed by Albertson's fomula with the range of the field determined empirically. The numerical computation of the far-field is based on the conservation equations of mass, momentum and heat for steady incompressible flow. Considering the shallow water condition without occurance of density current, it is simplified as a plane motion. The convective term and the horizontal viscous term are neglected by order magnitude analysis. Assumptions of hydrostatic pressure distribution in vertical direction, adiabatic solid boundaries, constant overall water surface heat transfer coefficient and negligible energy loss by internal friction are then taken. Coverting the three-dimensional equations into a two-dimensional equation system and introducing the stream function ψ we get the governing equations for solving the flow field (ψ) and the temperature field (T) as follows:

$$\frac{\partial}{\partial x}\left(h\frac{\partial\psi}{\partial x}\right)+\frac{\partial}{\partial y}\left(h\frac{\partial\psi}{\partial y}\right)=4\left(\frac{\partial h}{\partial x}\frac{\partial\psi}{\partial x}+\frac{\partial h}{\partial y}\frac{\partial\psi}{\partial y}\right)+\frac{fh^2}{a}\left(\frac{\partial h}{\partial y}\frac{\partial\psi}{\partial x}-\frac{\partial h}{\partial x}\frac{\partial\psi}{\partial y}\right)$$
$$+\frac{h^2}{\rho a}\left(\tau_y\frac{\partial h}{\partial x}-\tau_x\frac{\partial h}{\partial y}\right)+\frac{h^3}{\rho a}\left(\frac{\partial\tau_x}{\partial y}-\frac{\partial\tau_y}{\partial x}\right) \qquad (1)$$

$$\frac{\partial}{\partial x}\left(h\alpha\frac{\partial T}{\partial x}\right)+\frac{\partial}{\partial y}\left(h\alpha\frac{\partial T}{\partial y}\right)-\left(\frac{\partial\psi}{\partial y}\frac{\partial T}{\partial x}-\frac{\partial\psi}{\partial x}\frac{\partial T}{\partial y}\right)-\frac{K_sT}{\rho C_p}=0 \qquad (2)$$

where ρ -density of fluid; f-Coriolis coefficient; a-bottom frictional resistance coefficient; τ_x, τ_y -surface wind shear stresses; α-thermal diffusivity; K_s - overall water surface heat transfer coefficient; h - depth of water. The boundary conditions for flow field computation are shown as figure 4 in which

$$S_1: \quad \psi_A=-\frac{q}{2}, \quad \psi_B=Q_o+\frac{q}{2}$$

where Q_o - discharge at outlet; q - increment of discharge by entrainment determined from near-field calculation.

$$S_2: \quad \psi=0; \qquad S_3: \quad \psi=Q_o; \qquad S_4: \quad \frac{\partial\psi}{\partial n}=0.$$

The boundary conditions for temperature field computation are $T=T_1$ at outlet; $\partial T/\partial n = 0$ for other boundaries.

The governing equations (1) and (2) are solved by the method of finite elements. Using four-point curvilinear tetragonal isoparametric finite element scheme, by Galerkin approach the equations of finite element are established as:

$$[A_{\alpha\beta}]\{\psi_\beta\} = \{F_\alpha\} \tag{3}$$

$$[AA_{\alpha\beta}]\{T_\beta\} = 0 \tag{4}$$

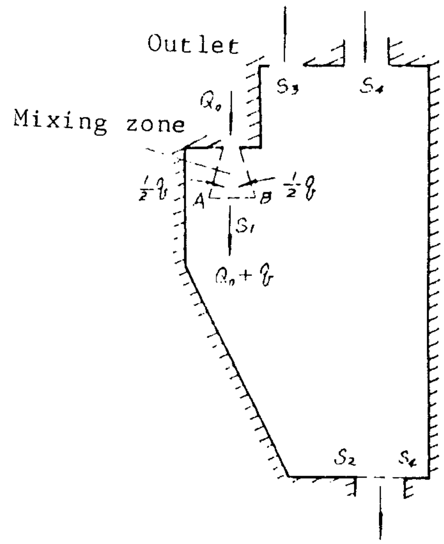

Figure 4

where $[A_{\alpha\beta}]$ $[AA_{\alpha\beta}]$ are coefficient matrices; $\{\psi_\beta\}$ $\{T_\beta\}$ are unknown vectors and vector $\{F_\alpha\}$ contains known information on boundary conditions. The equations (3) and (4) are solved independently. At first solve equation (3) to get the stream function ψ and then substitute into equation (4) to find the distribution of temperature T.

Parameters a, K_s, α are evaluated preliminary by some empirical formulas and the numerical model established are then verified basing on the prototype data, measured in 1982 and 1984 until getting a satisfactory result and the suitabl values of these basic parameters are finally determined. One of the modal verification results is given in table 3 and figure 5. It shows that the temperature at the intake for model and for prototype are consistant with each other though some what difference exist in the pond field.

Table 3 Verification and prediction results of numerical model

Items	Verification		Prediction
	prototype	model	
Out put of the plant (10^4 kw)	2.4		2.0
Water level in the pond (m)	1890.4		1888.83
Circulating discharge (m^3/s)	1.5		10.2
Natural temperature in pone (°C)	23		22.5
Bottom resistance factor, a	0.00026		0.001
Thermal diffusivity, α	0.8		0.8
Wind speed (m/s)	no wind		0.92
Overall surface heat transfer coefficient K_s	0.89		0.90
Temperature at outlet T_1 (°C)	29–30.2	29	36.8
Temperature at intake T_2 (°C)	23.7	23.8	29.0
Temperature difference between outlet and intake, T_1-T_2 (°C)	5.3–6.5	5.2	7.8
Relative temperature rise at intake (°C)	0.7	0.8	6.5

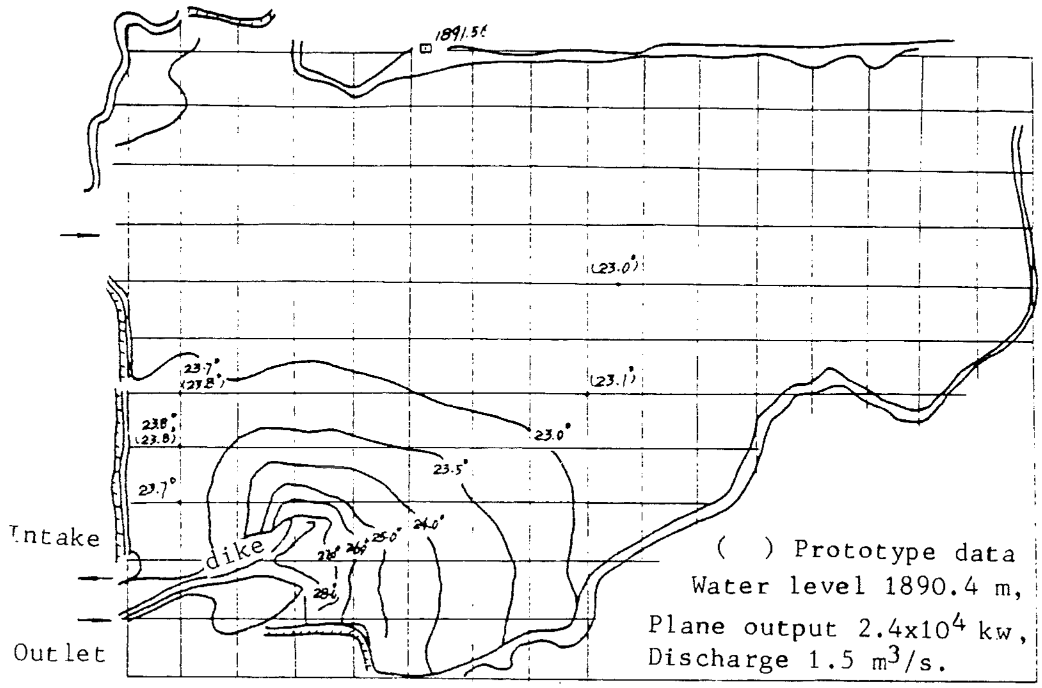

Figure 5 Verification of numerical model

Prediction computations for various given conditions were worked out with the verified numerical model. One of the computation results is given in table 3 too, the distribution of temperature is shown in figure 3 for comparing with the result of the physical model test.

Concluding remarks

1. The model test and numerical computation were carried out for various conditions and for some improved plans. Only the typical results are given in this paper. The enlargement project of the plant has been put in construction.

2. The consistancy for model verification and of the overall results between the physical model and the numerical model shows that the modelling work is fairly successful. Some difference in the distribution of temperature in the pond would be caused by the large distortion ratio of the physical model and owe to some assumptions in the numerical model. Further investigation is still required for clarifacation of these effects.

References

[1] Chen Hui-quan, "The Law of Similarity of Flow in Cooling Reservoirs", Journal of Hydraulic Engineering No.4, 1964, Peking (in Chinese).

AN EXPERIMENTAL STUDY OF THE INITIAL RESPONSE OF A STRATIFIED LAKE TO A SURFACE SHEAR STRESS

Craig Stevens and Jörg Imberger
Department of Civil and Environmental Engineering
and
Centre for Water Research
University of Western Australia
Nedlands, WESTERN AUSTRALIA, 6009.

Abstract

An experimental study is described of the transient response of a stratified body of water to a surface shear stress. Data from two experiments is discussed, the experiments were initially stratified with three layers. The strength of the stratifications were chosen such that in the first experiment the stress was insufficient to force the intermediate fluid to the surface at the upwind end, however it initiates internal seiching in the lower layers of the fluid. In the second experiment the stress was strong enough to force the intermediate zone to the surface.

§1 Introduction

Most lakes and reservoirs are temperature stratified for some period during the year, at which time warm water overlies cold fluid with some intermediate transition region (the thermocline). The dynamics of the stratification and the entrainment and mixing processes within the fluid govern the ecology of the lake to a large extent. The wind stress has far reaching effects on the dynamics and entrainment at scales ranging from the full dimensions of the basin down to the Kolmogorov scales (Imberger and Patterson; 1990).

The development of the flow is described here in the context of a wind stress on a two layered fluid with an infinitely thin interface and coriolis force is ignored. When a wind starts up the shear at the air-water interface generates a boundary layer in the fluid at the surface, and consequently a turbulent front propagates downward through the warm surface layer. The steady-state surface tilt that responds to the stress is twice that required to balance it. Consequently, to balance forces applied to the upper layer, a second applied force is required for equilibrium (Hellström; 1941). This force is supplied by horizontal gradients in the stratification, so the interface tilts such that the thermocline rises at the upwind end of the fluid and is depressed downwind. The magnitude of the tilt is dependent on the strength of the stratification relative to the surface shear stress.

The startup phase of the problem is a wave response from the initial horizontal stratification to the tilted steady condition. The wave response is usually a damped seiche where the tilt increases past the steady state condition and then oscillates around, and decays to, the steady state condition. The shear generated by the seiche response is described in Spigel and Imberger (1980) along with a discussion of the timescales associated with the entrainment mechanisms. For a given wind stress, if the stratification is weak enough, the tilt will bring heavier fluid to the surface, and into the wind-driven shear zone, this is termed upwelling (*figure 1*). This fluid is then dispersed downwind via a Taylor shear dispersion mechanism (Monismith; 1986, Imberger and Monismith; 1986).

Upwelling must generate two-dimensional entrainment and mixing, but initial experimental studies modelled the entire entrainment process with a one-dimensional entrainment velocity law linked to some kind of bulk Richardson number (Keulegan and Brame; 1960, Wu; 1973, Kranenburg; 1985), regardless of whether the fluid had upwelled or not. The two-dimensional nature of the problem was considered by Monismith (1986); an appendix to that paper (Imberger and Monismith; 1986) shows how a two-dimensional model of the entrainment also gives a bulk Richardson number law. Most of the experiments mentioned examined only initially two-layered fluids and most had significantly diffuse interfacial regions (Monismith; 1986 includes some initially linearly stratified experiments). The effect of a finite interface is important as it allows more than one baroclinic mode to

Environmental Dynamics reference ED-424-CS

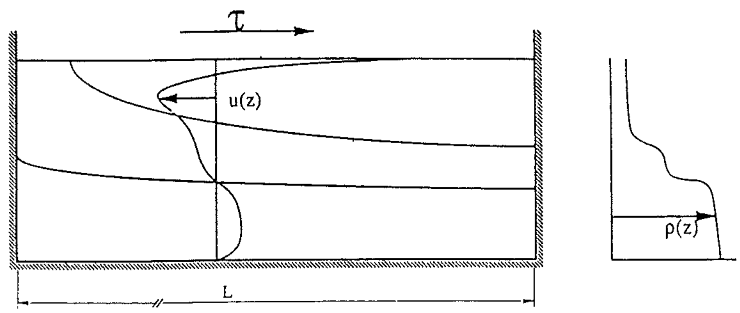

figure 1; wind driven upwelling; a schematic

exist (Monismith; 1985, Stevens; 1989). Consequently the two experiments discussed here describe the startup of the response of a three layered fluid. The middle layer is an approximation to the continuously stratified thermocline region.

There is an obvious need to describe the likely response of a lake or reservoir under different wind and stratification combinations. Two parameters quantify the balance described above, where the surface stress is balanced by horizontal gradients in the stratification. Spigel and Imberger (1980) introduced the Wedderburn number (W) to describe the dynamics of the upper interface. However it is apparent that the effects of the stress are not confined to the upper interface. Imberger and Patterson (1990) introduced the Lake number (L_N) to described the response of the entire fluid. Qualitatively, if $W \gg 1$ and $L_N \gg 1$, the stress is not strong enough to cause any large scale interfacial tilt, and conversly, if $W \ll 1$ and $L_N \ll 1$ the lower layers will upwell.

The force/moment ratios described by W and L_N are comparable in the field and laboratory, however the aspect ratio (L/H) will usually be smaller in the laboratory. A typical aspect ratio for a lake is $L/H \approx 10000/100 = 100$, this would require a laboratory experiment with a typical vertical scale of 100 mm to be 10 m long, an unobtainable scale given the nature of the apparatus. Consequently, the circulation in the surface mixing layer reaches quasi-steady state sooner than might occur in a field experiment. Nevertheless the stress transfer at the base of the surface layer is still present, and when comparing modal models (internal wave modes such as that of *figure 2(c)* have no horizontal velocity zero crossings in homogeneous portion of the water column), the circulation, as described by Baines and Knapp (1965) must be integrated over the upper layer before comparing with baroclinic modes.

§2 The experiments

Two experiments are described to elucidate the initial response of the fluid. Rather than describing experiments at opposite ends of the L_N and W parameter scheme the experiments chosen are just either side of $L_N = 1$ and $W = 1$ where the stress just balances the baroclinic restoring force. The first experiment $E6$ has $W = 1.7$ and $L_N = 1.8$ while the second experiment $E5$ has $W = 0.4$ and $L_N = 0.5$.

The laboratory experiments were performed in a glass tank (2.0 x 0.4 x 0.4 m) with a horizontal moving belt in contact with the fluid surface to introduce the shear stress, and the stratification was achieved using saline fluid. Conductivity probes periodically recorded the density profiles at several locations along the main axis of the fluid. The belt was made from light-weight mylar coated with small (1 mm diameter) balls acting as rougness elements, and was suspended from pivots above the tank. A force transducer (LVDT) held the belt in place and was used to measure the stress imparted to the fluid, allowing the first direct measurements of the actual work input in this kind of experiment.

For a variety of reasons velocity measurements of the flow field are difficult to obtain in this type of experiment, however, in this study successful measurements of the flow field were taken by applying a correlation technique to digitised images of aluminium flakes suspended in the flow (Stevens and Coates; 1990). This allows a quantitative description of the *mean* flow field. It must be noted that

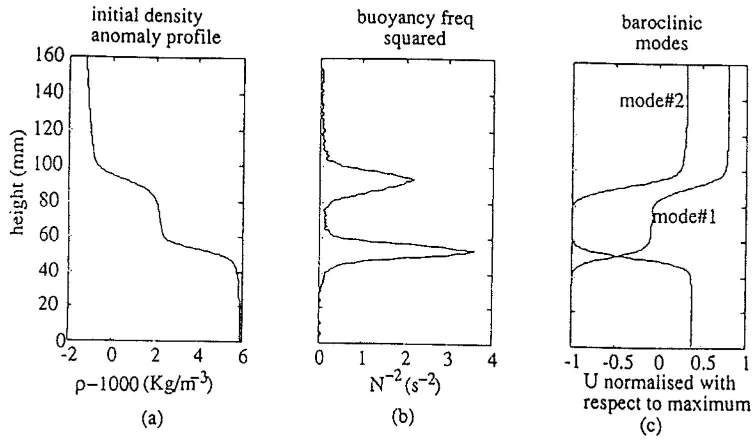

figure 2; Experiment E6 (a) density profile, (b) buoyancy frequency squared profile and (c) the first two horizontal baroclinic wave modes normalised with respect to their own maximum

the technique employs a search radius, and the flow near the belt (i.e the top 10 mm) was such that it was unrecordable. However, this region can be estimated with reasonable confidence using boundary layer models and conservation of volume. The horizontal velocity measurements (profiles in the vertical), shown in *figures 3(a), (b) and (d)*, were taken at approximately $x/L = 0.33$ and were averaged over a 120 mm longitudinal section of the flow. The density profiles of *figures 3(c) and (e)* were taken at x/L=0.4. The fluid depth was 160 mm in both experiments.

Experiment $E6$; $L_N = 1.8$ **and** $W = 1.7$: Given the periods for the first two baroclinic modes (86 seconds and 167 seconds) and assuming the tilting caused by each mode occurs over a timescale comparable with the quarter-period, the first 50 seconds are clearly of interest. The initial density profile and buoyancy frequency squared profiles for $E6$ are shown in *figures 2(a) and 2(b)* respectively. The first two baroclinic modes are shown in *figure 2(c)*. The parameterisation for this experiment gave $W = 1.7$ and $L_N = 1.8$. This qualitatively implies that the fluid should not upwell and that the tilting should be comparable for the two interfaces. The stress was introduced over a period of 30 seconds, just under a third of the fundamental period (86 seconds), to reduce the oscillations in the tilting of the internal interfaces about the quasi-steady state tilt.

Considering *figure 3(a)* the initial profile ($t = 9$ seconds) shows the downwind near-belt flow and the barotropic upwind return flow; there is no vertical shear below $z = 140$ mm. The near-belt region appears to have thinned at $t = 19$ seconds (the boundary layer is still laminar at this time and location). By $t = 29$ the boundary layer is turbulent over almost the entire belt-water contact area, and the turbulent front has penetrated to half the upper layer depth. Scaling for the propagation speed of this front suggests a timescale for the entrainment of the entire upper layer as $t_e = h_1/u_*$, where h_1 is the upper layer thickness and u_* is the friction velocity within the fluid (Spigel and Imberger; 1980). The return flow in the lower half of the surface layer at $t = 29$ seconds (before the turbulent front has reached the base of the surface layer) implies a barotropic circulation within the upper layer. The middle layer has accelerated upwind slightly at $t = 29$ and appears fully developed by $t = 39$ seconds. This strong flow in the middle layer must be associated with the second baroclinic mode shown in *figure 2(c)*. Also the lower layer has stopped, there is considerable shear at both interfaces at $t = 39$. If the fast flowing near-belt region is incorporated into an integrated mean average velocity for the upper layer it results in a *down-wind* flow of approximately 8 mms^{-1}. The stagnation in the lower layer at $t = 39$ seconds can be attributed to a reduction in the effect of the first mode ($T_1/2 = 43$ seconds).

The velocity profile remains unchanged for the next twenty seconds, however by $t = 64$ seconds the lower layer has started moving downwind reaching a peak at $t = 74$ seconds. This is attributed to a reversal in the first mode from that shown in *figure 2(c)*. Similarly the flow at $t = 104$ seconds is linked to a reduction and subsequent reversal of the second mode. The duration of the experiment was not long enough to make any conclusions about the decay of the second mode, the lower interface

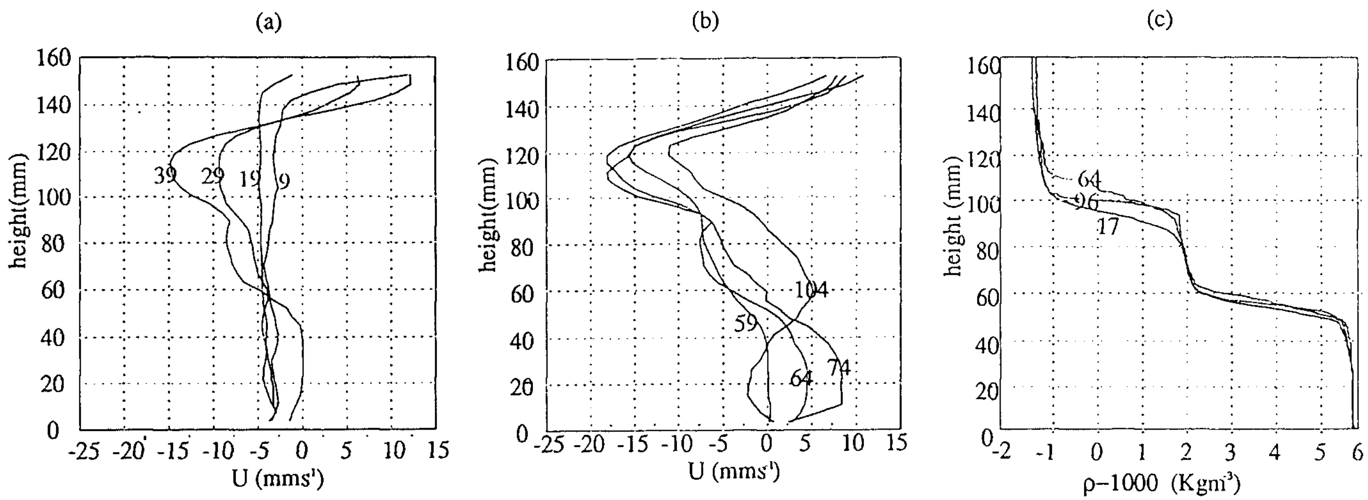

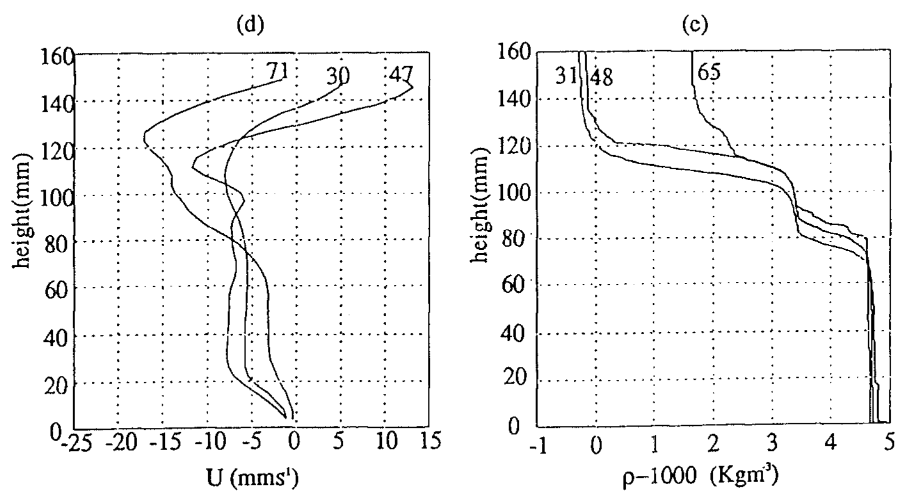

Figure 3(a-e)

3(a) E6; U profiles at t=9,19,29 and 39 s

3(b) E6; U profiles at t=59, 64 74 and 104 s

3(c) E6; density profiles at t=17, 64 and 96 s

3(d) E5; velocity at t=30,47 and 71 s

3(c) E5; density profile at t=31,48 and 65 s tilt shown in *figure 4(b)* was still present, but with a smaller amplitude, at $t = 230$ seconds, when the belt was switched off.

Experiment $E5$; $L_N = 0.5$ **and** $W = 0.4$: The stratification for this experiment was weaker than that of experiment $E6$ and the interfacial regions were higher in the water column. The u_* was only slightly larger than that for $E6$ and the resultant parameters were $W = 0.4$ and $L_N = 0.5$. The baroclinic periods were longer (100 and 241 seconds), reflecting the weaker density differences. A major difference between this experiment and $E6$ described above is, in this experiment, the upper interface reaches the surface at the upwind end (i.e. upwells) at $t \approx 40$ seconds. From *figure 3(e)* the middle layer is identifiable at least for the period examined here, although it is partially entrained into the upper layer later in the experiment. The effect of the upwelling on the density profile is obvious at $t = 65$ seconds; the density difference between the upper and middle layers has been halved.

Integrating the velocity in the upper layer (after incorporatng the near-belt flow) gave upper layer velocities of approximately $8 - 10$ mms^{-1} downwind. The velocity fluctuations do not appear nearly as complicated as those of experiment $E6$. The initial first mode response grows till at least $t = 42$ seconds, this is apparent in the upwind velocity in the lower layer. By $t = 71$ seconds the first mode has relaxed, the lower layer flow is only slightly upwind and the integrated velocity in the upper layer has dropped to nearly zero. The second mode is still present generating the strong flow in the middle layer at $t = 71$ seconds. At later times the velocities vary little from this last profile, indicating the upwelling must be removing the fluid advected upwind in the middle layer via the mode two response. The complete reflection of both modes seen in experiment $E6$ is not apparent here.

§3 Discussion

The experiments described in section §2 illustrate an initial barotropic flow, then as the boundary layer at the belt grows and entrains the surface mixing layer the baroclinic modes become apparent. The behaviour of the modes, after the initial startup, depends on whether the fluid upwells. The circulation in the upper layer appears to grow quickly in the initial phase of the experiment, there is no circulation in the lower two layers.

The modal dynamics are apparent from the velocity information, however, the upwelling mechanism appears to dampen the wave response. *Figures 4(a) and 4(b)* show density contours for $E6$ at a transient time and quasi-steady state. *Figure 4(c)* shows contours for $E5$ during the startup (the $\Delta\rho = 4$ Kgm^{-3} contour defines the lower interface), there was no quasi-steady state in this experiment; the upper layer continued to entrain the two lower layers until the belt was stopped. The small amount of entrainment of the middle layer into the surface layer in $E6$ is not suprising as *figure 4(b)* shows that the $\Delta\rho = 0$ Kgm^{-3} contour never reaches the surface shear zone. The flow reversal in the lower layer during experiment $E6$ is reflected by the change in sign of the slope of the lower interface.

Predicting exactly what conditions upwelling occurs is important for two reasons. Firstly, if upwelling occurs it dominates the entrainment processes in the surface layer, whether the entrained fluid is from the deeper fluid and/or the intermediate layer. Secondly, the tilting mechanism drives basin scale motions deep in the fluid, which generates velocity shear entrainment processes far from the original energy input. The experiments discussed here show that if the fluid does not upwell then the wave response is less-damped than if the fluid had upwelled.

The authors would like to thank John Taylor and Greg Ivey for their support and John Bagrie for building the apparatus. This work was supported by a Commonwealth Postgraduate Award and the Australian Research Council.

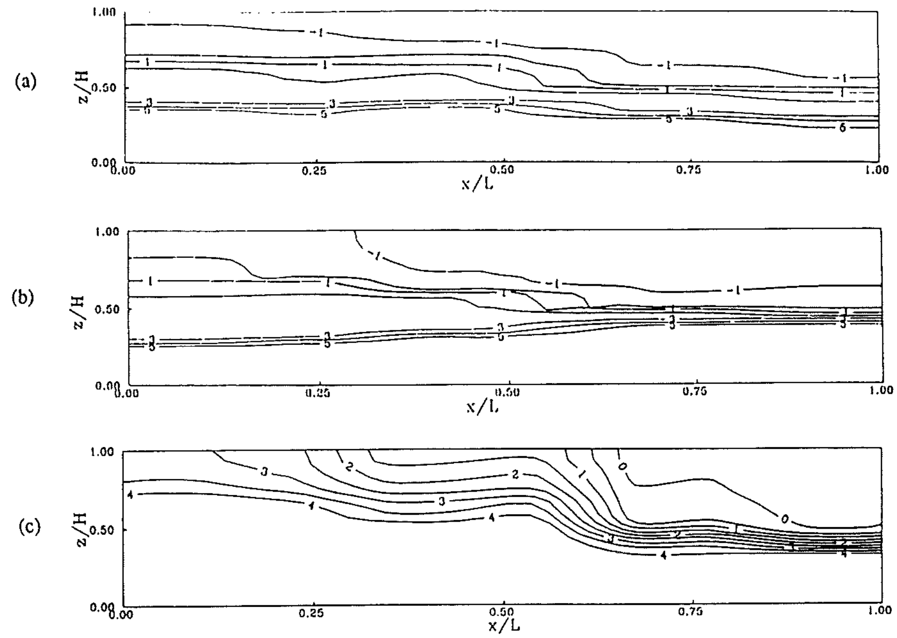

figure 4; spatial density contours of $\Delta\rho = \rho - 1000$, (a) experiment $E6$ at $t = 48$ seconds (1 Kgm^{-3} contour intervals), (b) experiment $E6$ at $t = 96$ seconds (1 Kgm^{-3} contour intervals) and (c) experiment $E5$ at $t = 47$ seconds (0.5 Kgm^{-3} contour intervals).

References

Baines, W.D. and D.J. Knapp, (1965): Wind driven water currents. *J. Hyd. Div., ASCE,* **91(HY2)**, 205-221.

Hellström, B., (1941): Wind effect on lakes and rivers. *Ing. Vetensk. Akad. Hadlingar* , **NR158**, pp183.

Imberger, J. and S.G. Monismith, (1986): A model for deepening due to upwelling when $W > 1$. *appendix to Monismith (1986).*

Imberger, J. and J.C. Patterson, (1990): Physical Limnology. *Advances in Applied Mechanics,* **Vol.27**, 303-473.

Keulegan, G. and V. Brame, (1960): Fourteenth progress report on model laws for density currents: Mixing effects of wind induced waves. *National Bureau of Standards Report,* **NBS-6638**, 35pp.

Kranenburg, C., (1985): Mixed-layer deepening in lakes after wind set-up. *J.Hyd. Div., ASCE,* **111(HY9)**, 1279-1297.

Monismith, S.G., (1986): An experimental study of the upwelling response of stratified reservoirs to surface shear stress. *J. Fluid Mech.*, **171**, 407-439.

Monismith, S.G., (1985): Wind-forced motions in stratified lakes and their effect on mixed layer shear. *Limnol. Oceanogr.*, **30(4)**, 771-783.

Spigel, R.H. and J. Imberger, (1980): The classification of mixed-layer dynamics in lakes of small to medium size. *J. Phys. Oceanogr.*, **vol 10**, 1104-1121.

Stevens, C., (1989): The response of a stratifed lake to a surface shear stress. *Proceedings of the 10th Australasian Fluid Mechanics Conference,* **10AFMC**.

Stevens, C. and M.J. Coates, (1990): An automated velocity field measurement technique for laboratory experiments. *Enviromental Dynamics report,* **ED-425-CS**

Wu, J., (1973): Wind induced entrainment across a stable density interface. *J. Fluid Mech.*, **61**, 257-287.

MEASUREMENTS OF STRATIFIED FLOW IN RESERVOIR AND CONSIDERATIONS OF EFFECT OF INTAKE CONDITION ON ITS DOWNSTREAM WATER ENVIRONMENT

by Sotoaki Onishi
Science University of Tokyo
Noda city,Chiba ,Japan,278

Abstract

Distributions of water temperature and turbidity were observed directly in a reservoir and its downstream river and sea, simultabaneously with the Landsat remote sensing, and adaptability of the remote sensing to observe the relation between turbidities in the reservoir and its downstream water environment are shown. And the depth of the stratified flow toward the intake were discussed by comparing both results obtained with the in-field measurements and model tests.

Introduction

The water in relatively small reservoirs will be flushed through by occasional flood. However, the turbidity of water in large reservoirs will be increased by floods and can remain at a high level for a considerable period after the flood. Such prolonged turbid conditions will also prolong the turbidity of the river downstream. This downstream turbidity will effect activities associated with water use from and in the river downstream. The effect of temperature changes , downstream from the reservoir, will have environmental implications as well. To quantify the above effects , we should monitor turbidities and temperatures at various depths in the reservoir and at various selected points downstream.

Systems to drain water from the reservoir must be designed to maximize the quality of water drawn off. Selective withdrawal intakes are an engineering solution to maximizing water quality in regard to turbidity and temperature. Criteria to be considered in such intake are (1) depth at which water is withdrawn,(2)location within the reservoir,(3)Froude number of flow toward the intake and (4) its effect on water quality downstream.

Present study observes and documents hydraulic phenomena at a chosen man-made reservoir with selective withdrawal intake. The study also aims to investigate the use of satellite monitoring of the reservoir and downstream to establish the inter-relationship of water quality in these two areas.

Measurements of water turbidity and temperature at reservoir and downstream

Hydraulic behavior of flow toward the selective withdrawal intake should depend on various physical parameters such as rates of inflow and outflow, inflow density, densimetric stratification in the reservoir and the intake location and opening height. From the end of September through to the beginning of October 1988,in-field studies were done at the Kumano river,which flows in the Kii peninsula and opens into the Pacific Ocean. In the upstream region of this river, eight man-made reservoirs (three of which are at the Totsu tributary and five at the Kitayama tributary) are operated for hydro-electric power generation, flood control and irrigation (figure 1). Only the K-reservoir out of the eight has the selective withdrawal intake(figure 2). This has been operated since June 1976. In the present study, vertical distrib-utions of

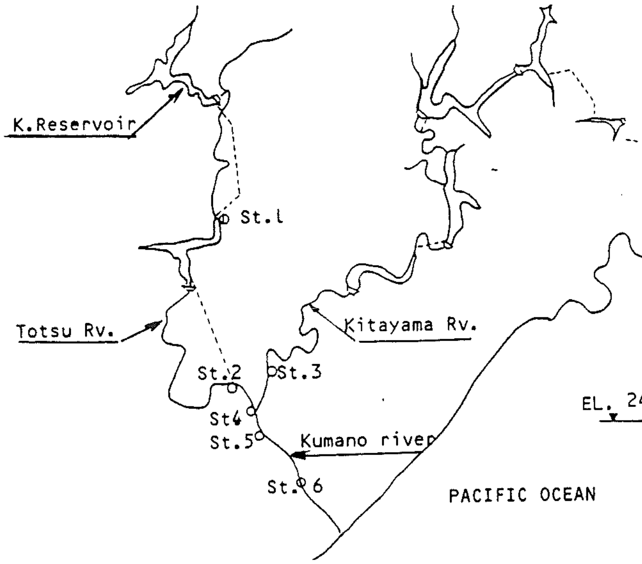

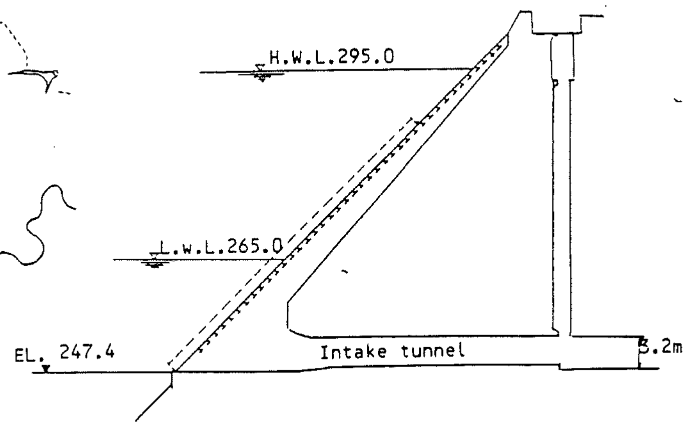

Figure2 Intake in K-reservoir

Figure 1 Studied river and measurement stations

water temperature and turbidity were measured at eight stations within the K-reservoir and at another six stations in its downstream river for two weeks following September 20 ,during which the Landsat passed over the site on September 26. The rates of inflow and outflow were measured as well. The results are presented in table 1. In the table the intake locations are indicated as "upper" and "lower".The "upper" range allows intake from the water surface down to depth 8 meters, the "lower" range being from the water surface to EL.252.6 m(that is, the level 5.2m above the intake tunnel ceiling).

Table 1 Daily averaged rates of inflow and outflow (m3/sec)

	September 1988							
	21	22	23	24	25	26	27	28
Inflow	23.9	20.6	43.5	42.1	532.6	173.8	91.2	61.0
Outflow	19.9	20.9	20.9	41.7	485.8	281.0	80.6	51.9
Intake	upper	upper	upper	lower	lower	lower	lower	lower

	September 1988		October 1988				
	29	30	1	2	3	4	
Inflow	47.2	45.2	39.3	30.9	23.7	22.3	
Outflow	59.5	59.6	59.3	59.4	60.6	60.8	
Intake	lower	lower	lower	lower	lower	lower	

Figure 3 to 5 indicate the measurement results of the water turbidity and temperature in the reservoir obtained on September 21, September 26 and October 4,respectively. And figure 6 present those readings before and after lowering the intake level to EL. 252.6m from EL.281.3m to discharge the flood flow on September 25.

In the figure 3 (September 21), both the inflow and outflow are small and the reservoir water is thermally stratified. Thus only the water at its surface layer with turbidity less than 5ppm is discharged through the intake. These results indicate that the intake could fulfill the purpose required. Other readings to note in figure 3 show that the water with the highest turbidity exists around the EL.247.40m level corresponding to the level at the intake tunnel bottom. The results in figure 6 show that the temperature distribution was not affected significantly by the flood of the magnitude studied here. Results all suggest that the densimetric stratification in this particular reservoir is due to the water temperature difference mainly, and not due to the turbidity difference. Heavy rain fell in this district on September 25 and the inflow and outflow rates at the reservoir increased rapidly by 532.6 m3/s and 485.8 m3/s respectively. The intake opening was lowered by EL.252.6m and remained there until October 17, 1988 to flush out the turbid water body in the middle layer. Figure 4 represents the results observed in a day after the rainfall had passed. It is seen that the water turbidity increased throughout the whole reservoir,reaching the maximum value of 1000 ppm in the middle layer between EL.250 m and EL.270 m. Water turbidities above and below the middle layer decreased. However, the water temperatures after the rainfall were maintained in vertical distribution, as they were before the rainfall. Stratification in the reservoir has remained stable. In the figure 4 , are seen a couple of clear stable interfaces , at several meters below the water surface and at the level of intake tunnel bottom,(namely EL.247.40m). The reason the interface is formed at EL.247.40m, is thought to be due to some water may leak leaking through the gap between the movable intake gate and its supporting structure because it is not a tight fit. Another interesting item seen in figure 4 is that the water approximately 20m below the intake opening bottom can be drawn up into the intake. Figure 5 shows results measured nine days after the heavy rainfall on September 25. The intake opening bottom had been kept at EL.252.6 m since September 24. The figure shows that the bodies of water with a depth of about 30 m, and with turbidities less than 300 ppm, flow toward the intake.Other turbid water bodies with turbidities much less than those in figure4 stagnate around the level of the intake bottom.

As shown above,flood flow, which bring solid particles in and stirs up sedimentary particles from the bottom,increases reservoir turbidity which takes a long time to settle. In this study the intake opening was maintained at EL.252.6m) until October 17,1988 to flush out remaining turbidity from the flood of September 25, 1988.

Effects of intake opening height upon the withdrawal depth

The turbidity in the river water downstream from the reservoir can be tolerably controlled by the withdrawal intake. With assumptions of invisid fluid and linear vertical distribution of water density, Yih (1958) analyzed the stratified flow toward a line sink and suggested that the withdraw depth(D) shall be depend

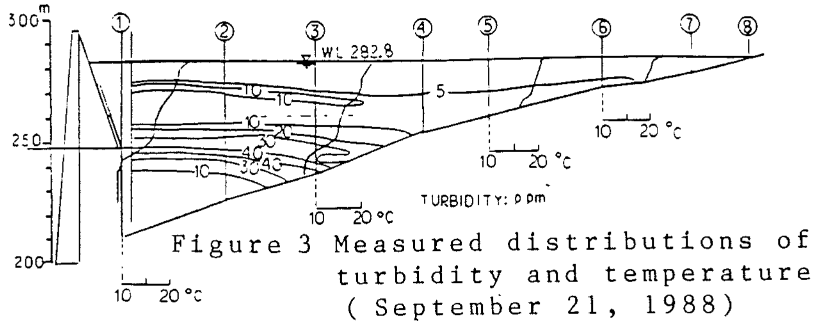

Figure 3 Measured distributions of turbidity and temperature (September 21, 1988)

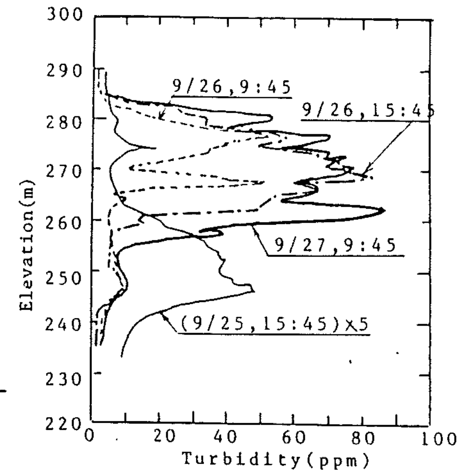

(a) Turbidity changes

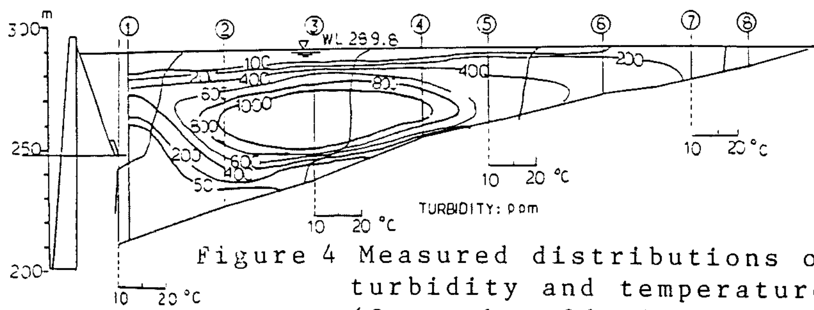

Figure 4 Measured distributions of turbidity and temperature (September 26, 1988)

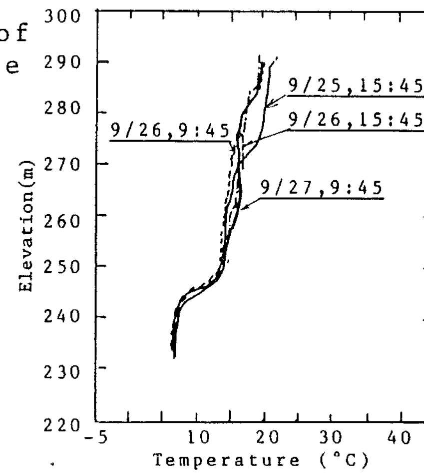

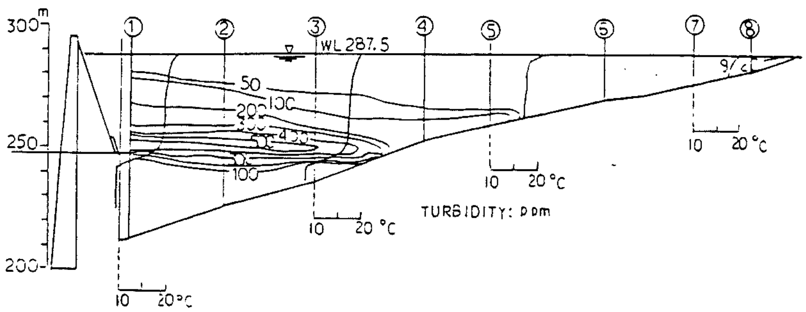

Figure 5 Measured distributions of turbidity and temperature (October 4, 1988)

(b) Temperature changes

Figure 6 Changes in vertical distributions of turbidity and temperature with lowering intake gate

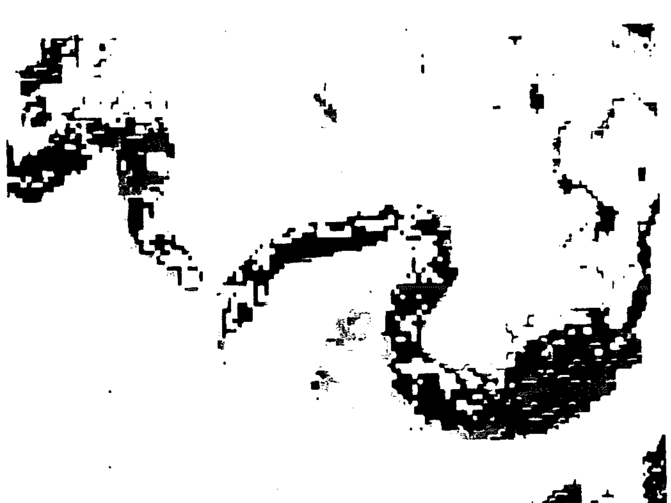

Plate 1 TM 2band image of water surface of K-reservoir (Sept.26) (Sept.26,1988)

Plate 2 TM 2band image of water surface of the sea off the Kumano river (Sept.26,1988)

upon densimetric Froude numbers defined as following;

$$(D/h)^2 = \pi Fr \ : \quad Fr = (Q/Bh2)\sqrt{(1/g\beta)} \ : \quad \beta=(\rho_b-\rho_s)/\rho_b h \qquad (1)$$

where, Q=rate of intake flow, B=intake width, h=reservoir depth, g=gravity acceleration, Fr=densimetric Froude number and ρb and ρs= densities at water surface and reservoir bottom respectively. In practical intakes, the opening heights are usually finite, even larger than the dividing depths estimated with equations (1). Thus a series of model tests were done in the present study to investigate the effect of such finite opening height on the withdrawn depth.The tests were done in a channel with 0.12m width, 0.6m depth and 5m length. Eight linear distributions of water density were assumed by referring to those observed in the K-reservoir. The intakes were opened at the water surface and its opening heights were varied over the range between 2cm and 10cm.Vertical distributions of density and velocity were measured at each section fixed at 1.5m, 2m, 2.5m and 3m upstream from the intake. The water density was adjusted by changing the salt concentration. Vertical distribution of velocities were measured by taking photograph of vertical visible dye lines added in the observation section at every 10 seconds interval. Total discharge at the intake was measured. Also the flow rate at each section, where the velocities were measured, was calculated by integrating the measured velocity distribution.

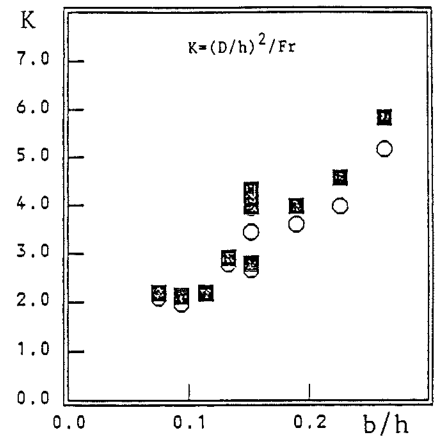

Figure7 Effect of intake opening height on withdrawn layer depth

The results indicate that D/h can be presented by the following formula, as showing in figure 7.

$$(D/h)^2 = K\ Fr\ , \quad K=17.93(b/h)+0.614, (b=\text{intake opening height}) \qquad (2)$$

Observation of turbidity at downstream water region from satellite

The turbid water discharged from the reservoir into the river downstream will be mixed with its environment and decrease its turbidity gradually, with flowing downstream. To study effect of the turbid water discharged from the reservoir on its downstream water environment, I analyzed the Landsat TM data obtained over the K-reservoir and its downstream region including coastal sea area on September 26,1988. Plate 1 indicates the TM-2 band image of its water surface. The water turbidities at six stations shown in the figure 1 were measured on the ground simultaneously. It has been known by the previous study (Onishi, S.(1988)) that both the brightness in the TM2 band image (CCT value) and the turbidity correlate well. For this particular case, the correlation can be expressed by the following equation.

$$Y = (2.96 \times 10^{-[illegible]})X^{[illegible]} \qquad (3)$$

where, Y=turbidity(ppm) and X≒CCT value.

With equation (3) and the plate 2, contour maps showing horizontal distributions of water turbidity at both the reservoir and the coastal water zone around river mouth can be drawn, as shown in figures 8 and 9. With comparing both figures, and referring to the plate 1 , one can see that the turbidity in water discharged downstream from the intake decreases its level in rather short distance. And one can also see that the high turbidity at the coastal sea off the river mouth results from rolling up the sedimentation around the river mouth,sand drift at the coastal water zone, but not from the turbidity at the reservoir upstream.

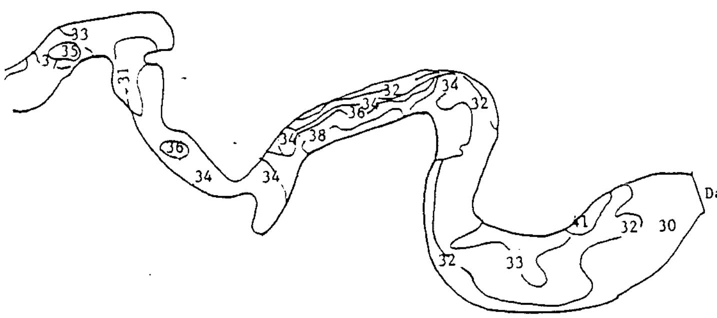

Figure 8 Turbidity distribution in K-reservoir (Sept.26,88)

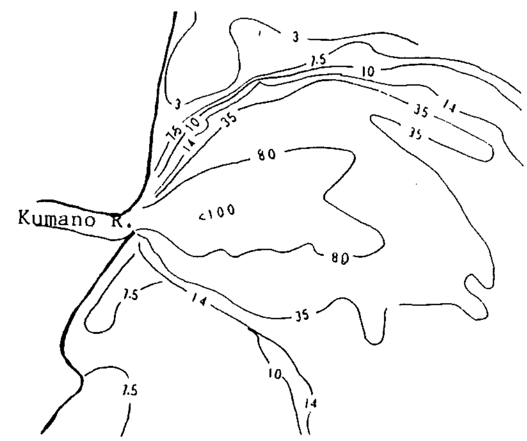

Figure 9 Turbidity distribution off river mouth (Sept.26,88)

Concluding remarks

It has been well known that selective withdrawal intake is an effective engineering solution to reduce environmental effect of man-made reservoir on its downstream water region. Turbidity and temperature of the water discharged from the reservoir depend on the density distribution in the reservoir and the intake conditions such as the opening height, location and Froude number of the current in the reservoir. For the case studied here , the water density in the reservoir is mostly determined by the temperature, and contribution of solid particles floating in the water is minor.The thermal stratification can remain stable even at the time of considerable heavy flood, then one can operate the intake with taking into consideration only of the distribution of water temperature. The model tests were done for the temperature distributions observed in this particular reservoir, and the experimental formula (2), representing the relationship between the withdrawn layer depth, the intake opening height and Froude number, was obtained. From a view point of water quality conservation, continuous monitoring of the water quality in reservoir and its downstream is also important. The present study could indicate the satellite remote sensing is useful to monitor those.

References

Yih,C.S.;On the flow of a stratified fluid,Prod.3rd.U.S.Nat.cong. of Appl.Mach.(1958).

Onishi,S.;Hydraulic engineering and remote sensing,Jour.of J.A.C.E. Vol.393,No.2-9 (1988),(in Japanese).

DIURNAL STRATIFICATION AND ITS EFFETS ON WIND-INDUCED CURRENT

by Tadaharu Ishikawa
Department of Civil Engineering, Tohoku University, Aoba, Aramaki, Sendai 980, Japan
and Masahiro Tanaka
Department of Civil Engineering, Tokyo Institute of Technology, O-okayama, Meguroku, Tokyo 152, Japan

ABSTRACT

Field data obtained in Lake Kasumigaura(36°N,140°E,Japan) show that a diurnally developed weak stratification distorts the wind-induced currents and dispersion process in a shallow lake. Theoretical consideration on the deepening of the diurnal mixed layer leads to a result that the Wedderburn number is a parameter governing the similarity in a physical model with such a weak stratification.

INTRODUCTION

If a lake is shallower than usual depth of seasonal thermocline, which is 5-15m, the seasonal stratification is not developed. Such a lake is called "a shallow lake" herein. It has been assumed that the process of transport and dispersion in a shallow lake is not much affected by thermal structure of water body. Accordingly, a physical model with non-stratified water has been adopted to investigate the hydraulic processes in such a lake.

Even in a shallow lake, however, a weak stratification caused by daily cycle of solar radiation is often observed in daytimes, and it sometimes remains even at midnight. There is a possibility that this weak stratification modifies the pattern of wind-induced currents and dispersion process in a shallow lake.

The effects of diurnal thermal stratification on wind-induced current has not been much investigated because of difficulty of fine scale measurements of velocity and turbulence in the field. Recent progress of facilities, however, enables us to measure this faint phenomenon.

The objects of the present study are followings ;
(1)to investigate the diurnal stratification and its effect on wind-induced currents through field observation and
(2)to find a similarity law for dispersion in a shallow lake for a physical model with weakly stratified water.

FIELD OBSERVATION

Study Site

Lake Kasumigaura is located 70km east from Tokyo. The lake has a surface area of 170km^2, a mean depth of 3.9m and a maximum depth of 7.3m. The residence time of the lake is about 6 months so that the lake can be assumed to be a closed system in the research of the diurnal stratification. The

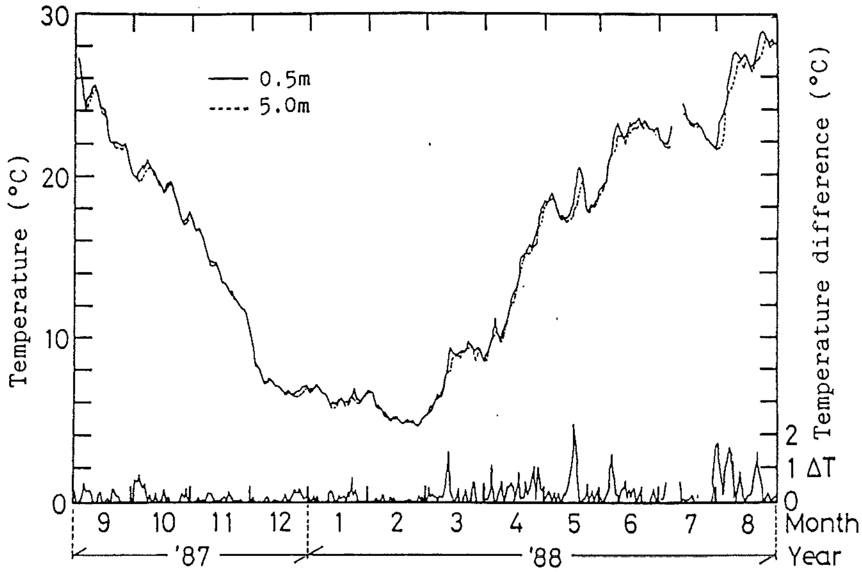

Figure 1. Water temperature in a year(September 1987 to August 1988).

measurement station is located at the center of the lake where the depth is 5.8m.

Fig.1 shows water temperature records at the depths of 0.5m and 5m in a year. Both records almost coincide to each other, that is, the seasonal stratification is not developed. The difference of two records is shown along the axis of abscissa. There are a lot of pulse like fluctuations whose magnitudes are 1-2°C and durations are 1 to 3 days. These fluctuations are caused by diurnal stratification. The diurnal stratification seems to be intensified from March to May and in August when the averaged water temperature goes up.(It is a rainy season from June to July in Japan. The rainy season ended July 31 in 1988.)

Equipments

Two electro-magnetic current meters were used to measure three components of velocity. Their sensors are so small that they hardly disturbed the flow. The response frequency is 20Hz which is higher than the representative frequency of wind-induced turbulence. Temperature was measured using a thermometer with accuracy of 0.1°C.

All sensors were mounted on an elevator which was guided by a fixed vertical pile. The vertical profiles of temperature and velocity were taken at 0.25m or 0.5m intervals with the sampling time of 30sec for each point. The total time required to complete the profiles was 15 min. All analog outputs were transformed into digital time series by an A/D convertor with sampling interval of 0.02 sec. and stored in micro-computer.

<u>Observation results</u>

Two layered flow was observed whenever a thermocline existed, although the temperature difference across the thermocline was sometimes less than 1°C. Fig.2 shows the data obtained on August 24 in 1987 when the water was well stratified and almost stationary before the wind started blowing. Wind tractive force accelerated only the water of the mixed layer. This fact means that the thermocline with the temperature difference of even 1°C prevents the vertical transport of momentum completely. Fig.3 shows the data obtained on August 26 in 1987 when the wind direction suddenly changed in the evening. The response of the flow keeps to show the pattern of the two layered flow.

Fig.4 shows a velocity profile observed when the whole water column was well mixed. The velocity is almost uniform in vertical. It is clear that the dispersion capability of the two layered flow shown in figs.2 and 3 are much larger than that of the well mixed flow. Therefore, the horizontal transportation and mixing of suspended and dissolved materials in the lake must be highly affected by the diurnal stratification.

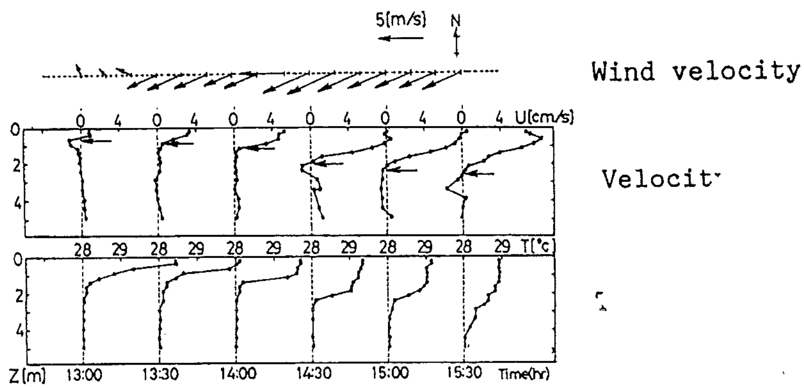

Fig.2. Vertical profiles of velocity and temperature (24 August 1987).

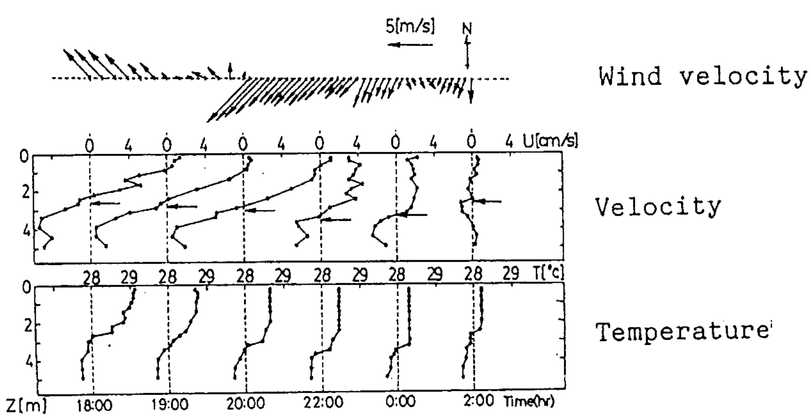

Fig.3. Vertical profiles of velocity and temperature. (26 August 1987).

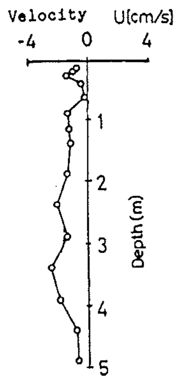

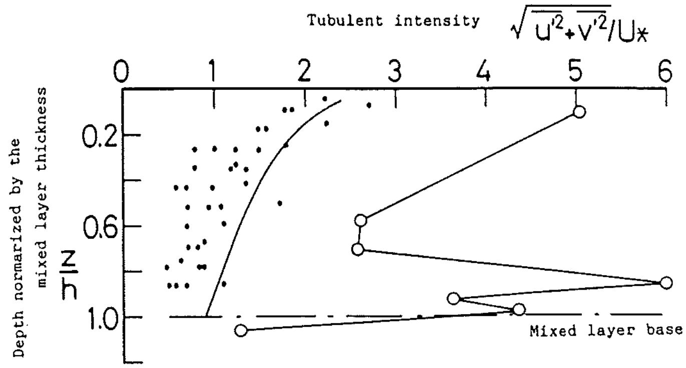

Fig.5 Vertical profile of turbulent intensity.

Fig.4 Velocity Profile without a thermocline(28 August 1987).

Circles in fig.4 show nondimensional turbulent intensity, which is obtained by removing the surface wave motion from the observed velocity records, against the depth normalized by the thickness of the mixed layer. Turbulent intensity has a peak at the bottom of the mixed layer. Small dots in the figure are the turbulent intensity observed when whole water column was well mixed. The solid line is a corresponding curve for wall turbulence (The depth is normalized by the total depth.) It should be noted that the turbulence intensity in a mixed layer over the thermocline is much larger than that without the thermocline. This fact implies that the shear near the bottom of the mixed layer rather than the stirring at the water surface is the major source of turbulence in the mixed layer.

DISCUSSION

Entrainment Rate

The entrainment rate is a basic factor for describing the behavior of the stratified water. Price et al.(1978) suggested two basic models of wind-induced entrainment reference to the parameterized turbulent energy equation presented by Niiler & Kraus(1977). One is the dynamic instability model (DIM) which assumes that the energy for mixing is produced by the shear instability at the mixed layer base. The other is the turbulent erosion model (TEM) which assumes that turbulence for mixing is diffused from the upper surface thin layer.

As data described above imply that DIM might be suitable for describing the deepening of the diurnal mixed layer. In this section, a new formulation of DIM is presented in order to discuss the dispersion in a shallow lake.

Turbulent energy produced by the shear deformation (*Es*) is estimated as follows.

$$E_S = \int \tau \frac{du}{dz} \propto U_*^2 \Delta U \qquad (1)$$

where U_*;the surface friction velocity and ΔU;the velocity difference between the mixed layer and underneath calm layer.

The increase of the potential energy accompanied with the mixed layer deepening is written as follows.

$$E_p \sim \frac{1}{2} W_e \varepsilon g h = \frac{1}{2} W_e B_u \qquad (2)$$

where $\varepsilon=\Delta\rho/\rho_0$, $\Delta\rho$;the density difference between the two layers, ρ_0;the reference density, g;the gravitational acceleration, h;the mixed layer thickness and B_u;the total buoyancy of the mixed layer. Assuming that E_p is a certain fraction of E_s, we obtain the following relation for the entrainment rate.

$$W_e = A \cdot U_*^2 \Delta U/Bu \quad \text{or} \quad E[\Delta U] = A \cdot Ri[U_*]^{-1} \qquad (3)$$

where W_e;the entrainment rate, A;some constant, $E[\Delta U]=We/\Delta U$ and $Ri[U_*]=B_u/U_*^2$.

Fig.6 shows the relation between $E[\Delta U]$ and $Ri[U_*]$ obtained from the field observation. The field data shows the relation described by eq.(3) and the value of A is almost constant and about 1.

Eq.(3) is consistent with formulation in existing studies, when the internal setup is negligible. Under such a condition, the horizontal movement of the mixed layer is described by the following equation.

$$\frac{d}{dt}(h\Delta U) = U_*^2 \qquad (4)$$

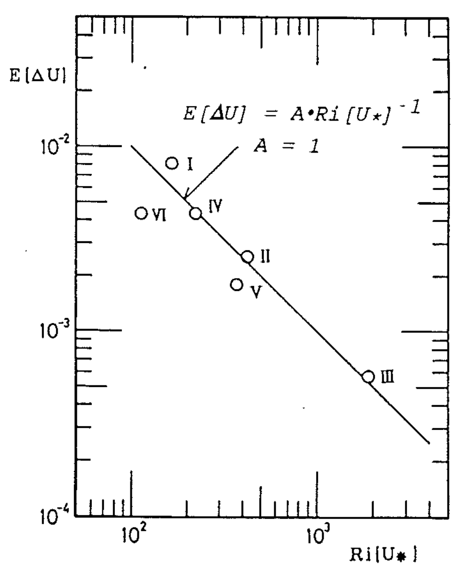

Fig.6 Dimensionless entrainment rates $E[\Delta U]$ versus $Ri[U_*]$.

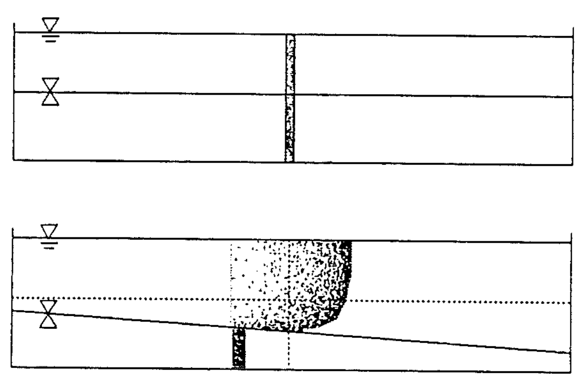

Fig.7.Schematic diagram of dispersion process in diurnally stratified lake.

From Eqs.(3) and (4), we obtain

$$E[U*] = Ri[U*]^{-1/2} \quad (5) \quad \text{or} \quad Ri[\Delta U] = const. \quad (6)$$

Similarity Condition

Similarity condition for physical model are studied considering a water tank with a length L and the depth of H and assuming that the wind blows for a duration of T. Water particles initially set on a vertical line are dispersed as shown in fig.7. The following two conditions are required so that kinematic similarity is established for dispersion in two tanks of different size.

Firstly, the ratio of horizontal travel distance to the tank length must be common.

$$(\Delta U \cdot T/L)_r = 1 \quad (7)$$

where the subscript r means the ratio of values for each tank. Secondly, the ratio of mixed layer deepening to the tank depth must be common.

$$(W_e \cdot T/H)_r = 1 \quad (8)$$

Substituting eqs.(3) and (7) into eq.(8), we obtain,

$$[W_d]_r = \left(\frac{Bu}{U*^2}\,\frac{H}{L}\right)_r = 1 \quad (9)$$

where W_d is a dimensionless parameter known as Wedderburn number which Spigel and Imberger(1980) used to classify the mixing in lakes.

CONCLUSION

A weak stratification, which is made by daily cycle of solar radiation, distorts the modifies wind-induced currents and affects dispersion process in a shallow lake. The deepening process of the thermocline is described well by the dynamic instability model (DIM). This model suggested that the Wedderburn number is the parameter which governs the similarity of dispersion in a physical model with a weak stratification.

Reference

Niiler, P.P. and Kraus, E.B. 1977 : One-dimensional models. Modelling and prediction of Upper Layers of the Ocean. E.B.Kraus, Ed., Pergamon press, 285 pp.

Price,J.F.,Moors,C.N.K. and Leer,J.C.V.1978: Observation and simulation of storm-induced mixed layer deepening, J.Phys. Oceanogr., Vol.8, pp.582-599.

Spigel,R.H. and Imberger,J.1980: The classification of mixed-layer dynamics in lakes of small to medium size, J.Phys. Oceanogr.,Vol.10, pp.1104-1121.

OBSERVATIONS OF MIXING AND MASS TRANSPORT PROCESSES IN GLENMORE RESERVOIR, CALGARY, ALBERTA

by Steve Graham
Nolan, Davis and Associates (1986) Ltd,
St John's, Newfoundland A1L1C4

Introduction

Glenmore Reservoir (22,800 acre-feet) is the principal drinking water supply for the City of Calgary, Alberta. The City commissioned a study (1,2) of mixing processes in Glenmore as a preventative measure to ensure public health and safety.

Initially, consideration was given to performing analytic-numeric, physical modeling, and/or field studies. However, each had limitations to address the problem at hand--*id est* to predict the transport characteristics of an introduced miscible contaminant until it reaches the water supply intake at the dam. Characteristic flow-thru speed ,V_c, defined as:

$$V_c = L/T_R \qquad [1]$$

where T_R is the characteristic retention time (= Vol/Q), and L is the reservoir length (18,500'), had mean monthly values of 0.9 to 7.1 mm/s (see Table 1), which would have afforded very comfortable response times in the event of a spill. However initial drogue experiments showed that drogues could be blown to any point in the reservoir overnite. The surficial advective transport processes clearly were wind-dominated. The effect of this upon dispersive processes in the reservoir was not known.

To investigate these further, tracer experiments using both salt and fluorescein were conducted. (Use of rhodamine and similar conservative tracers was forbidden by the Dept of Health on the basis of evidence that they are mutagens and/or carcinogens). Typical results are shown in Figures 1 and 2. Transport of the dye cloud was almost completely determined by local wind direction, and exhibited vertical shear. Local wind direction, in turn, was strongly influenced by local topography, paticularly in the lower portion of the reservoir which lies in a semi-canyon. Appropriate physical modeling would thus have to correctly simulate the local wind field in a wind-tunnel. Detailed combined wind tunnel and hydraulic model testing is quite rare, and neither suitable facilities nor adequate budget was available for this type of approach

For initial interpretation of field data, none of the many analytic formulations offered a significant improvement (until the dye cloud reached the boundaries) over the general heat equation:

$$\frac{dc}{dt} = E_h \frac{\partial^2 c}{\partial x_i^2} + E_z \frac{\partial^2 c}{\partial z^2} - kt \qquad [2]$$

For an instantaneous surface release, the expected maximum concentration, c_m, is:

$$C_m = \frac{2c_0}{(4\pi t)^{3/2}\,(E_h^2\,E_z)^{1/2}}\,\exp(-kt) \qquad [3]$$

As shown in Figure 3, the mixing was fairly "well-behaved". The peak concentrations (adjusted for photochemical decay) of the clouds were:

$$c/c_m = (4.07E-02) * t^{-0.87} \qquad [4]$$

The difference in the coefficient of t (-0.87 vs. -1.5 in eqns [4] and [3]) is unexplained, but not uncharacteristic for uncontrolled field experiments. Typical values of horizontal turbulent diffusivity/dispersion, E_h, (0.15 m^2/s), increased 2 to 3 times this value for periods of high wind-induced advection. Typical values of vertical diffusivity, E_z, varied an order of magnitude with stratification, but evidently traded off with E_h as well in order for eqn (4) to be so well-behaved. It is also not self-evident that these processes could be reproduced in a physical model, particularly a distorted one.

Finally, a point about local processes is made. These are seldom investigated in the course of large-scale field studies. A limited sampling of short time and length phenomena was done for the Glenmore study, and the results were most interesting. Overall temperature profiles in the reservoir had typical gradients of 1 deg C/15m vertically and 1 deg C/2.1 km horizontally. Yet, as shown on Figure 4, temperature profiles taken **at the same spot** midway along the reservoir over a period of 5 hours had a range of 1 deg C at the surface. Similarly, profiles **taken within 5 to 10 meters of each other** at about the same time had about the same temperature range at the surface (see Figure 5). In both cases local variations decreased rapidly to about the 5 meter depth level. This would appear to indicate that turbulent activity is confined to this depth. As it corresponds to the lengthscale of surface variation, it is surmised that the surface layer is comprised of 5 m convective cells (at most). These data obviously have implications about timescales and lengthscales of mixing, as well as appropriate sampling procedures. Given that measured local variations were significant relative to macroscopic ones, correct reproduction in a physical model would be difficult.

<u>Summary</u>

The results may be specific to small western impoundments, and not generic. Nevertheless the methods of analysis must be appropriate to both the problem at hand and to the physical conditions at the site. Wind-driven mixing in shallow partially-stratified impoundments may not be a suitable case for simulation with for physical modeling.

<u>References</u>

As it is difficult to distil a 200+pp report into 6 pages; the reader is referred to the original study report and a 20 pp summary, which are listed below.

1. Envirocon Ltd., Vancouver BC, "Elbow River Watershed Study, Appendix 1, A Study of Mixing Characteristics in Glenmore Reservoir, Calgary, Alberta", prepared by S. Graham, 200+ pp., Nov 1983.

2. Graham, D.S., "Fluorescein Tracer Mixing Experiments in Glenmore Reservoir, Calgary", Proceedings of the CSCE 1984 Annual Conference, held May 23-25, 1984, at Halifax, NS, pp. 989-1010.

Acknowledgements

I wish to acknowledge the assistance of Mr Jack Parkinson PEng of Envirocon and EPS, Dr Reid Seidner of the City of Calgary, Envirocon and Marshall-Macklin-Monoghan Ltd. in preparing this study. I also acknowledge the assistance and support of Nolan Davis and Assoc. Finally, I wish to thank Wayne Huber of UF for his excellent instruction of dispersion theory.

Disclaimer

The comments in this article are for information and discussion purposes only and are not to be relied upon in any particular situation without the express written consent of the author.

Table 1 Monthly and Annual Retention Times of Glenmore Reservoir

Month	Average Discharge (cfs)	EOM WSL (ft)	Volume (acre-ft)	T_R (days)	V_c (mm/s)
Jan	106	87.5	13500	64	1.02
Feb	109	85.5	11900	55	1.10
Mar	132	85.5	11900	45	1.45
Apr	255	89.5	15180	30	2.18
May	569	90.0	15630	14	4.67
Jun	943	91.5	16980	9.1	7.17
Jul	586	94.5	19820	17	3.84
Aug	350	94.0	19320	28	2.33
Sep	297	94.0	19320	33	1.99
Oct	239	94.0	19320	41	1.59
Nov	172	93.5	18820	55	1.19
Dec	121	90.5	16980	71	0.92
Year	325	91.0	16530	26	2.51

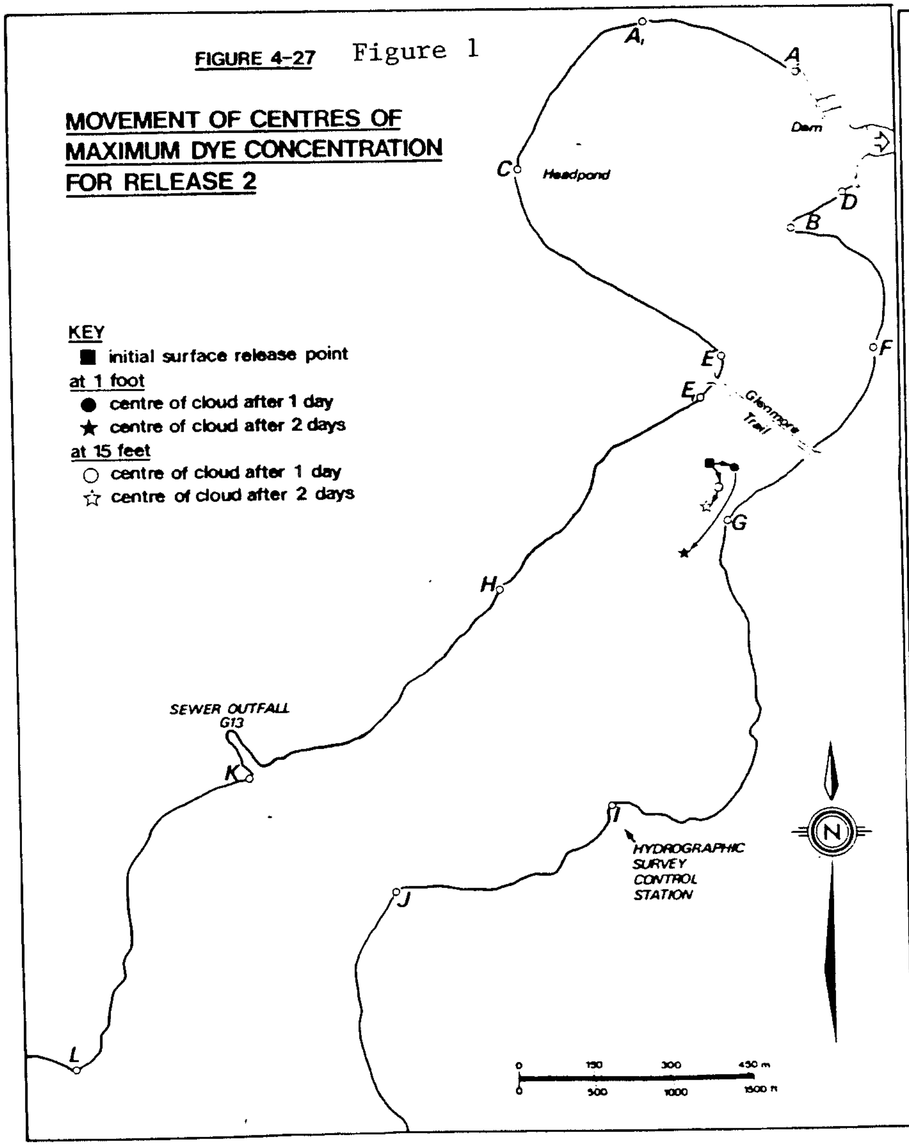

FIGURE 4-27 Figure 1

MOVEMENT OF CENTRES OF MAXIMUM DYE CONCENTRATION FOR RELEASE 2

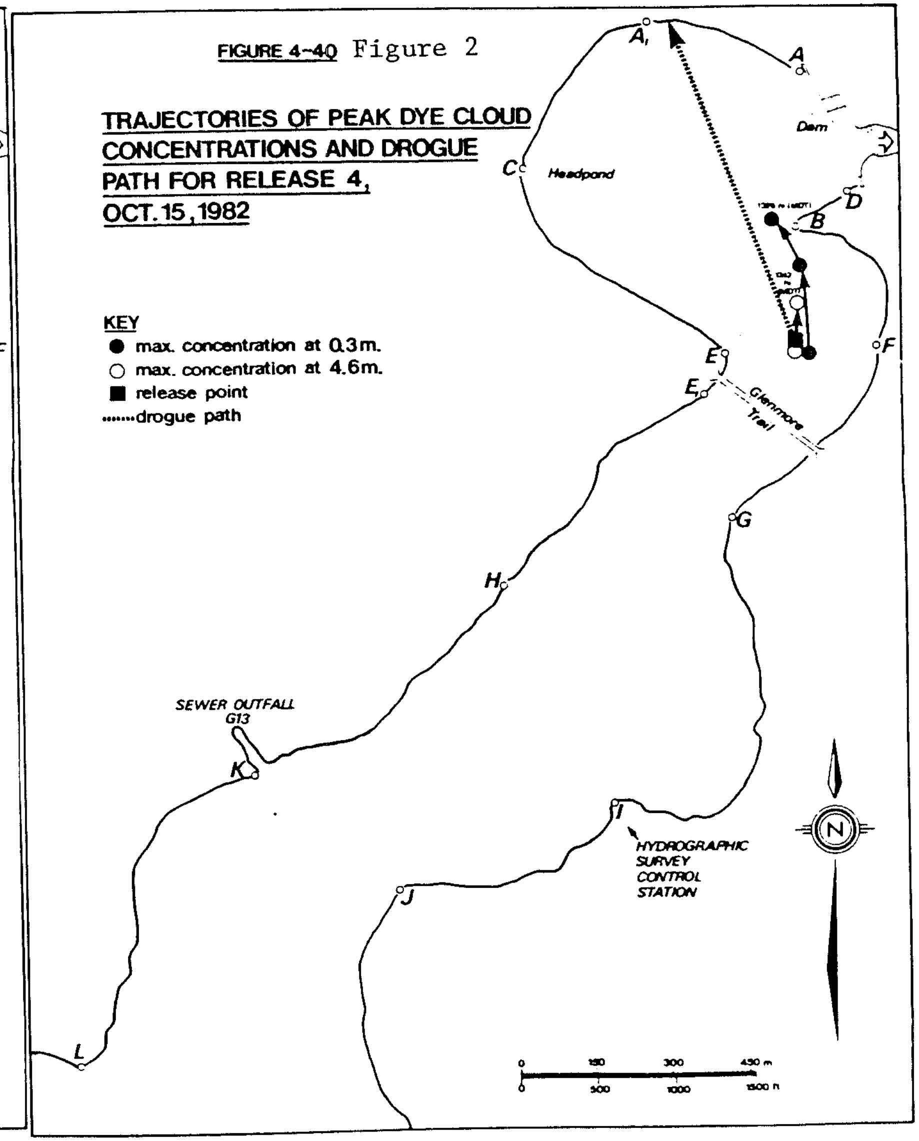

FIGURE 4-40 Figure 2

TRAJECTORIES OF PEAK DYE CLOUD CONCENTRATIONS AND DROGUE PATH FOR RELEASE 4, OCT. 15, 1982

Figure 3

RELATION BETWEEN MAXIMUM CONCENTRATION AT 0.3m. DEPTH AND INITIAL CONCENTRATION (after momentum mixing) FOR SEVERAL EXPERIMENTS

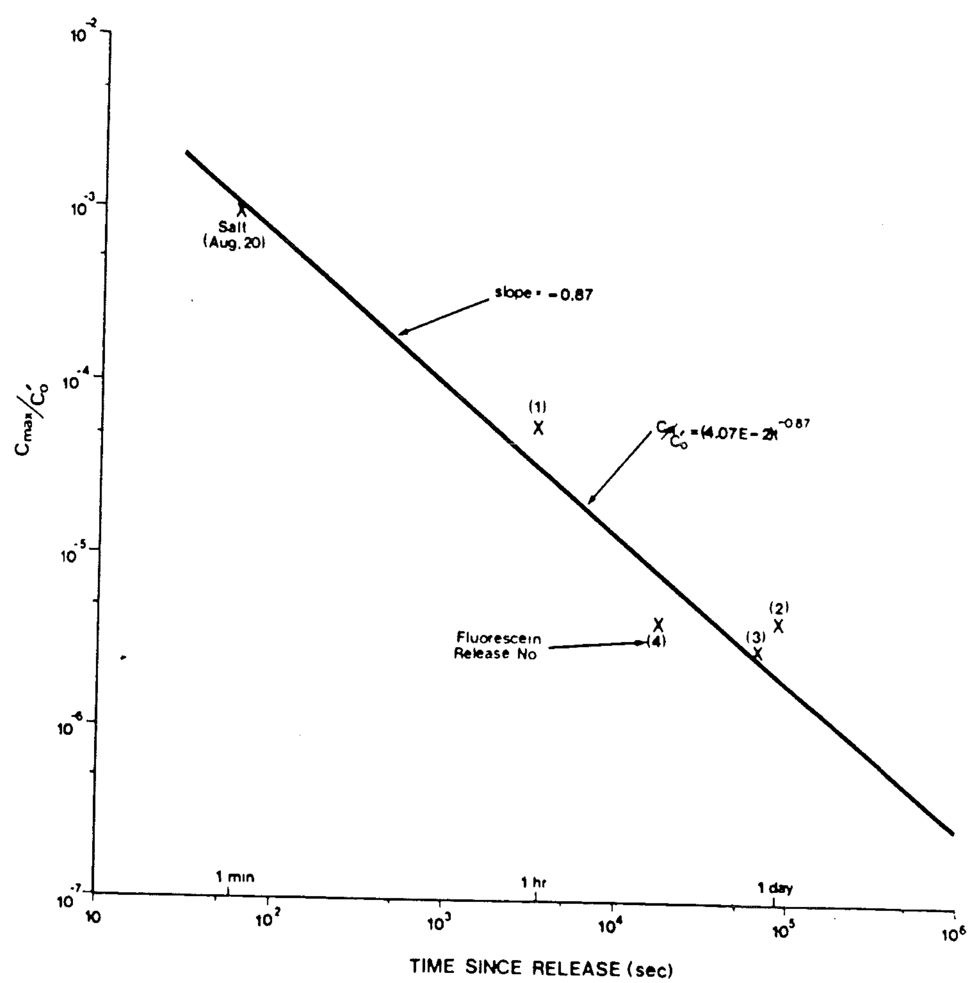

Figure 4

TEMPERATURE PROFILES IN GLENMORE RESERVOIR AT STATION (3,3)* ON SEPT. 1, 1982

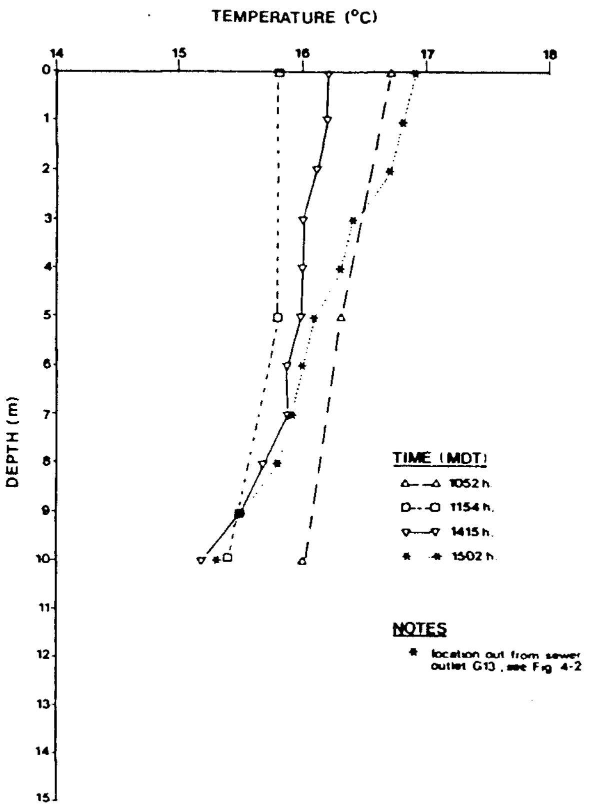

Figure 5

TEMPERATURE PROFILES IN GLENMORE RESERVOIR AT SEVERAL PROXIMATE LOCATIONS ON SEPT. 1, 1982

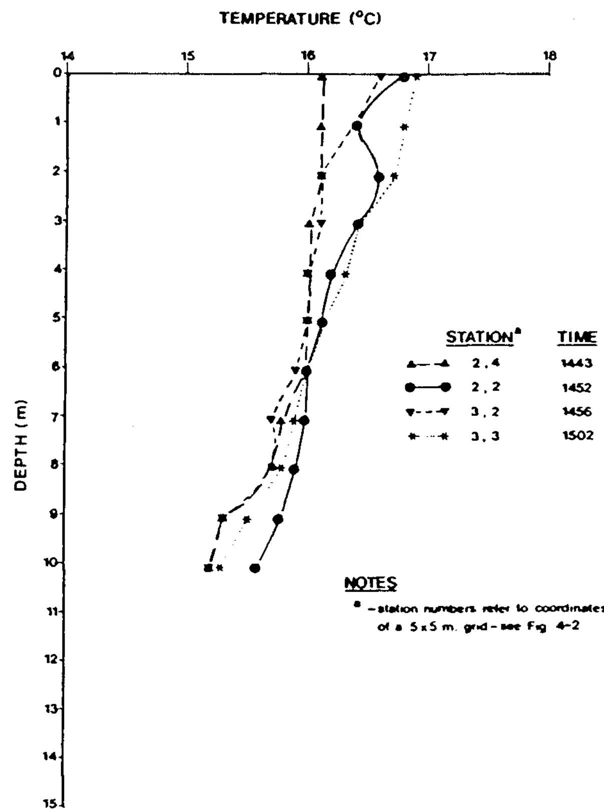

Session 13B

Coastal and Ocean Mixing

EVALUATION OF TIDAL EFFECTS ON THERMAL PLUMES USING A PHYSICAL MODEL

By
M. Padmanabhan
Alden Research Laboratory, Inc.
Holden, Massachusetts USA

Abstract

A 1:150 scale hydraulic model study of thermal plumes from a surface discharge and a submerged diffuser, each tested separately under identical conditions, was conducted to evaluate the unsteady temperature rise patterns during a typical tidal cycle. The unsteady offshore temperature distributions for the surface discharge and the diffuser during a tidal cycle were compared to determine the relative effects of re-entrainment of previously discharged heated water. In general, no noticeable differences in re-entrainment due to tide reversals between the tested surface discharge and diffuser were apparent. The model also indicated some site bathymetry effects on the re-entrainment as shown by the variation of areas for given temperature rise isotherms.

Introduction

Cooling water discharge structures of steam-electric power plants are designed to function so that the water temperature rise due to the discharge is within the limits imposed by regulatory agencies, and so that any thermal recirculation from the discharge to the intake is insignificant. Tidal effects cause time dependant entrainment and re-entrainment of water into the plume, and hydraulic model studies are often used to study this important unsteady phenomenon.

A comprehensive hydraulic model study involving both a surface discharge and a diffuser with approximately the same total offshore momentum was conducted for a power station discharging warm water to the ocean. Unsteady tidal currents were simulated in the model over a 1.25 tidal cycle starting at the maximum ebb current by imposing reverse flows at the two extremities of the model basin. Appropriate amplitude and phase differences based on sinusoidal variations were generated. Each of the two discharge structures was tested separately and changes in areas within given temperature rise isotherms during the tidal reversal were evaluated for each case to quantify the effect of re-entrainment of previously discharged water.

This paper provides a comparison of the effects of tide reversal on the thermal plumes for the tested surface discharge and diffuser designs. Since analytical or numerical simulation of plumes in unsteady currents is very complex, the results provided may be useful in calibrating or evaluating the reliability of such models. Also, by comparing results to a previous study, [1], site bathymetry effects were evaluated.

Description of Physical Model

A 1:150 scale model of the cooling water system of a power plant was built in a 50 m x 25 m model basin. The bathymetry was scaled, based on the map of Figure 1, down to the 30 m contour, the plume being relatively thin and hence unaffected by deeper contours.

The model was designed and operated based on Froude similitude, that is, keeping the model Froude number and densimetric Froude number the same as in the prototype. The thermal discharge temperature was adjusted to give a nondimensional density difference, $\Delta\rho/\rho_o$, of 0.0037, equal to that in the prototype at an ambient water temperature of about 23°C, a salinity of 30 ppt and a temperature rise in the discharged water of about 11°C.

Typical tide currents, with a net to maximum tidal current ratio of 0.23, were simulated assuming a sinusoidal variation over a period of 1.25 cycle, the first 0.25 cycle being designed to establish initial conditions. The tidal sequence was started at maximum ebb current. Water surface variations were also simulated with an amplitude of 40 cm and a lag of 1.35 hr with respect to the current, all prototype values. Such a variation was achieved by imposing computer controlled reversing flows at the two extremities of the basin.

The intake structure was modeled at the location shown on Figure 1. The selected surface discharge and diffuser locations and orientations are also marked in Figure 1, and the details of the designs are included in Figure 2. The diffuser discharge was about 240 to 420 m away from the shore. The total offshore momentum produced by the surface discharge was approximately the same as that of the diffuser.

Temperatures throughout the test basin were measured by a total of 705 thermocouples close to the water surface. A few vertical arrays were also installed to measure temperature profiles at selected locations. A multiplexer activated by an on-site mini computer scanned all 705 probes in 200 seconds. A total of 23 scans constituted the 1.25 tide cycle with a total model time of about 73 minutes. The thermocouple outputs were digitized and sent to a VAX 750 computer for data analysis.

Test Results

Near surface temperature rise isotherms at maximum flood, slack after flood, maximum ebb and slack after ebb using the test data from a typical test are shown in Figure 3 for the diffuser. Similar general plume features were observed for the surface discharge, designed to meet the same thermal criteria. From Figure 3 considerable variations of the area under given isotherms and change in plume directions are evident, underlining the importance of including any tidal effects in a thermal model.

Using data from a typical test, the variation of area within the temperature rise isotherm equal to 13% of the initial temperature rise at the discharge is plotted in Figure 4 for one tide cycle. During flood tide, temperature rise and, therefore, the area within the stated isotherms decreases with increasing current, as expected, since there is little re-entrainment at that time. The area increases as flood current decreases, and at slack after flood, essentially the same area is obtained as at the first slack after the one quarter ebb cycle used to start the test. Without any re-entrainment and with symmetrical topography, one would expect the area to again decrease with ebb currents. However, temperatures and areas increase due to a combination of both factors.

The previously heated water discharged during flood current, see Figure 3, returns with ebb currents to be re-entrained into the plume. In addition, ebb currents are not as strong due to the topography effects, leading to the indicated net current on Figure 4, and thus do not increase local dilution as much as flood currents. An earlier study by Brocard [1], which had no topographical effects, showed lesser area variations during ebb. The cumulative effect of re-entrainment and topography is that areas during ebb current are even greater than those at either slack.

The increases in areas under temperature rise isotherms during a tidal cycle are indicative of the re-entrainment back into the plume of the hot water previously discharged. Examining the results of Figure 4, allowing for some experimental scatter, the isotherm area increases for the tested surface discharge and diffuser are more or less the same. Hence, in terms of re-entrainment effects due to tidal current reversals, no noticeable differences between a diffuser and a surface discharge of the same total offshore momentum were apparent.

Conclusions

- Model test results show a considerable variation of the thermal plume area and direction during a tidal cycle, confirming the importance of simulating tidal effects in a thermal model.

- Comparing the variations of areas under corresponding temperature rise isotherms for the tested diffuser and surface discharge under identical ambient and discharge conditions and same total offshore momentum, the extent of re-entrainment due to tidal effects was found to be more or less the same for both the surface discharge and the diffuser.

- Site bathymetry may influence the re-entrainment due to tide reversal, and should be carefully modeled.

References

1. Brocard, D.N., "Surface Buoyant Jets in Reversing and Steady Cross Flows," Alden Research Laboratory Report No. 18-84/M424F, February 1984.

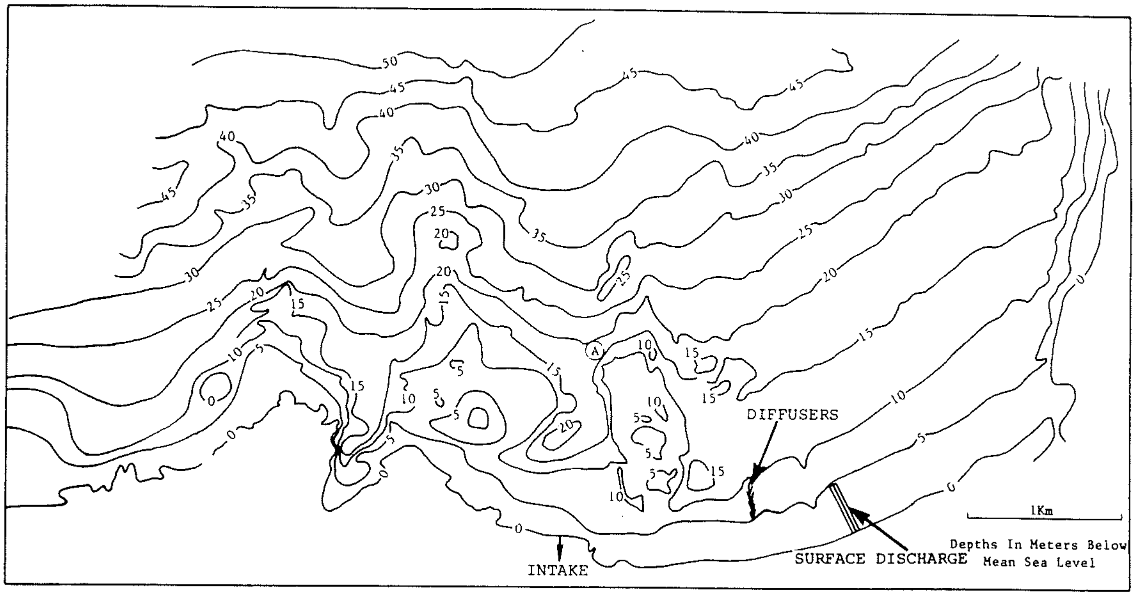

FIGURE 1 BATHYMETRY OF SITE AND INTAKE OF DISCHARGE LOCATIONS (SURFACE DISCHARGE OR DIFFUSER AT ONE TIME)

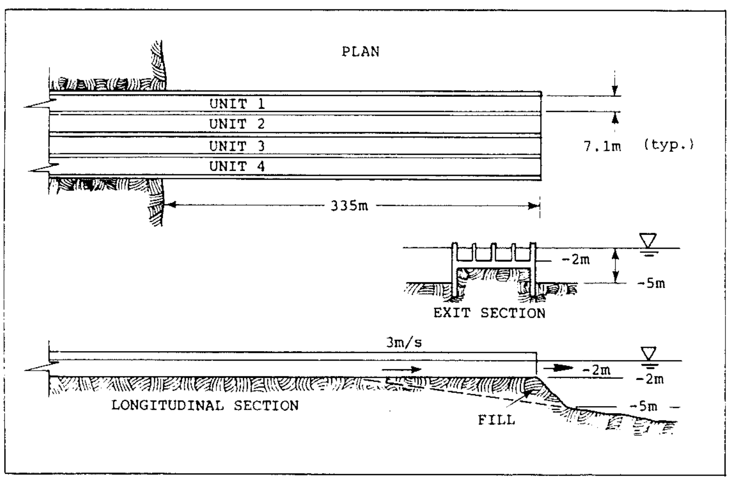

A. SURFACE DISCHARGE

NOTE: PROTOTYPE DIMENSIONS SHOWN

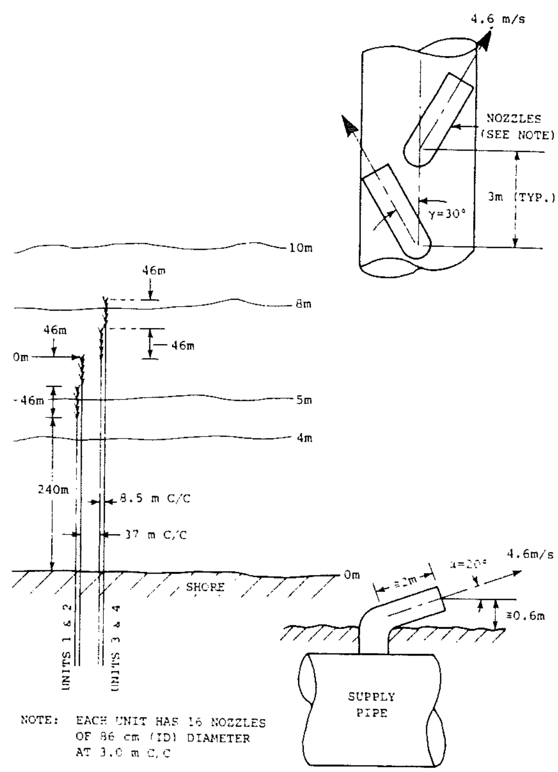

B. DIFFUSERS

FIGURE 2 SURFACE DISCHARGE AND DIFFUSER DESIGNS TESTED IN THE MODEL

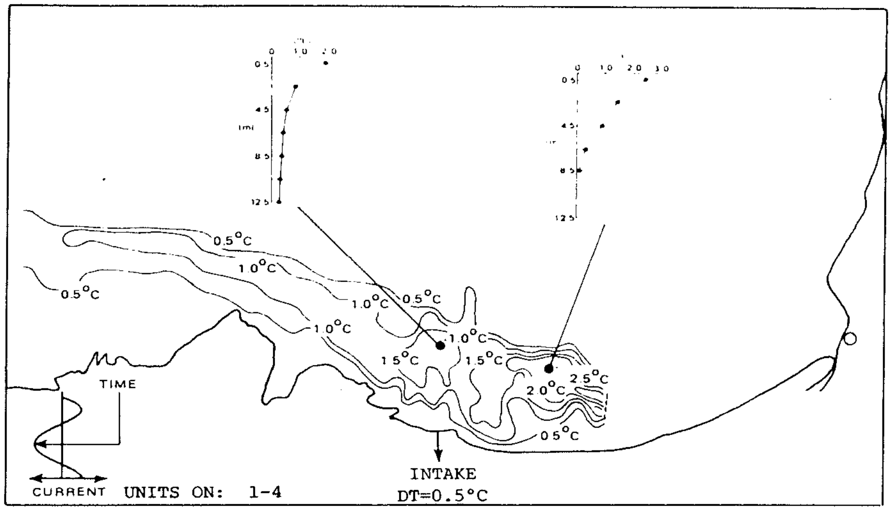

A. AT MAXIMUM FLOOD CURRENT

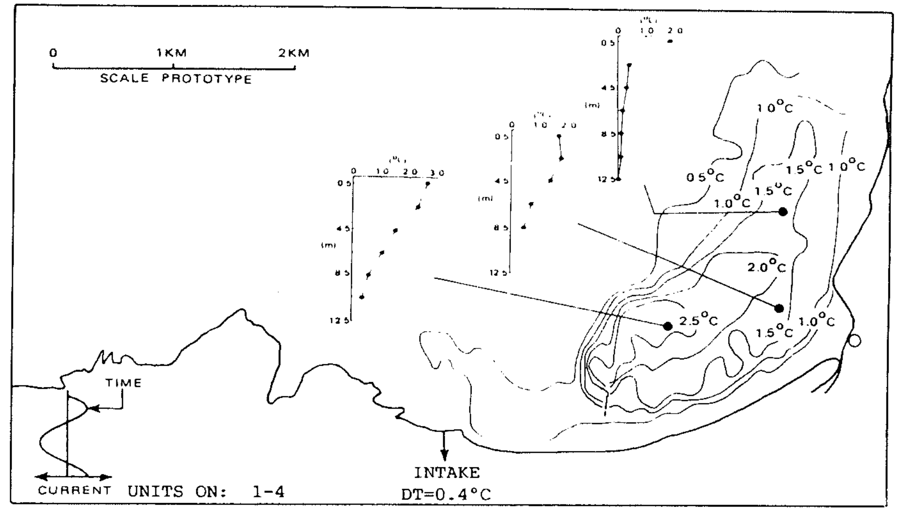

C. AT MAXIMUM EBB CURRENT

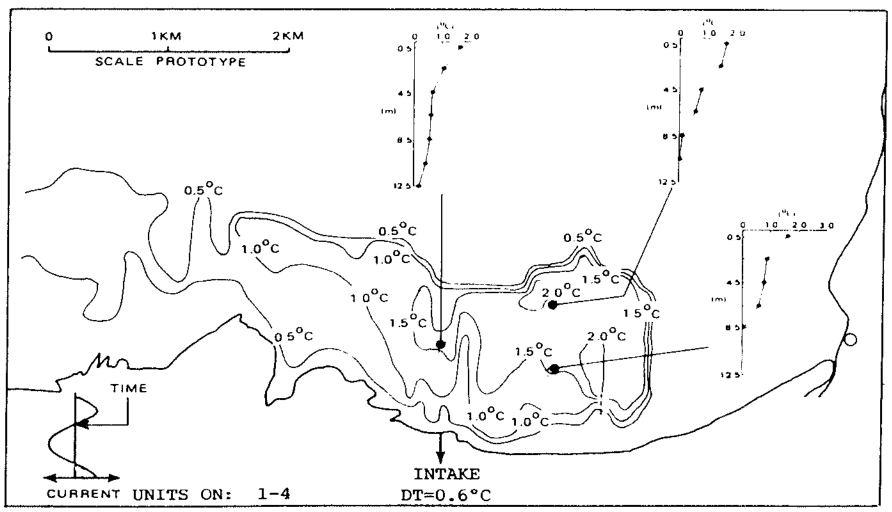

B. AT SLACK AFTER FLOOD

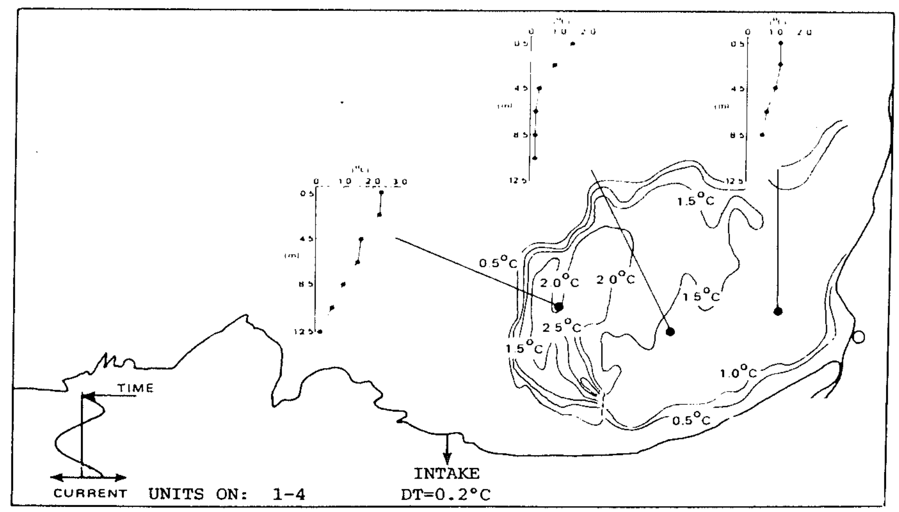

D. AT SLACK AFTER EBB

NOTE: VERTICAL TEMPERATURE PROFILES AT FEW LOCATIONS ARE INDICATED IN THE TOP OF EACH PLOT

FIGURE 3 SURFACE TEMPERATURE RISES; DIFFUSER WITH $\Delta T_o = 11°C$

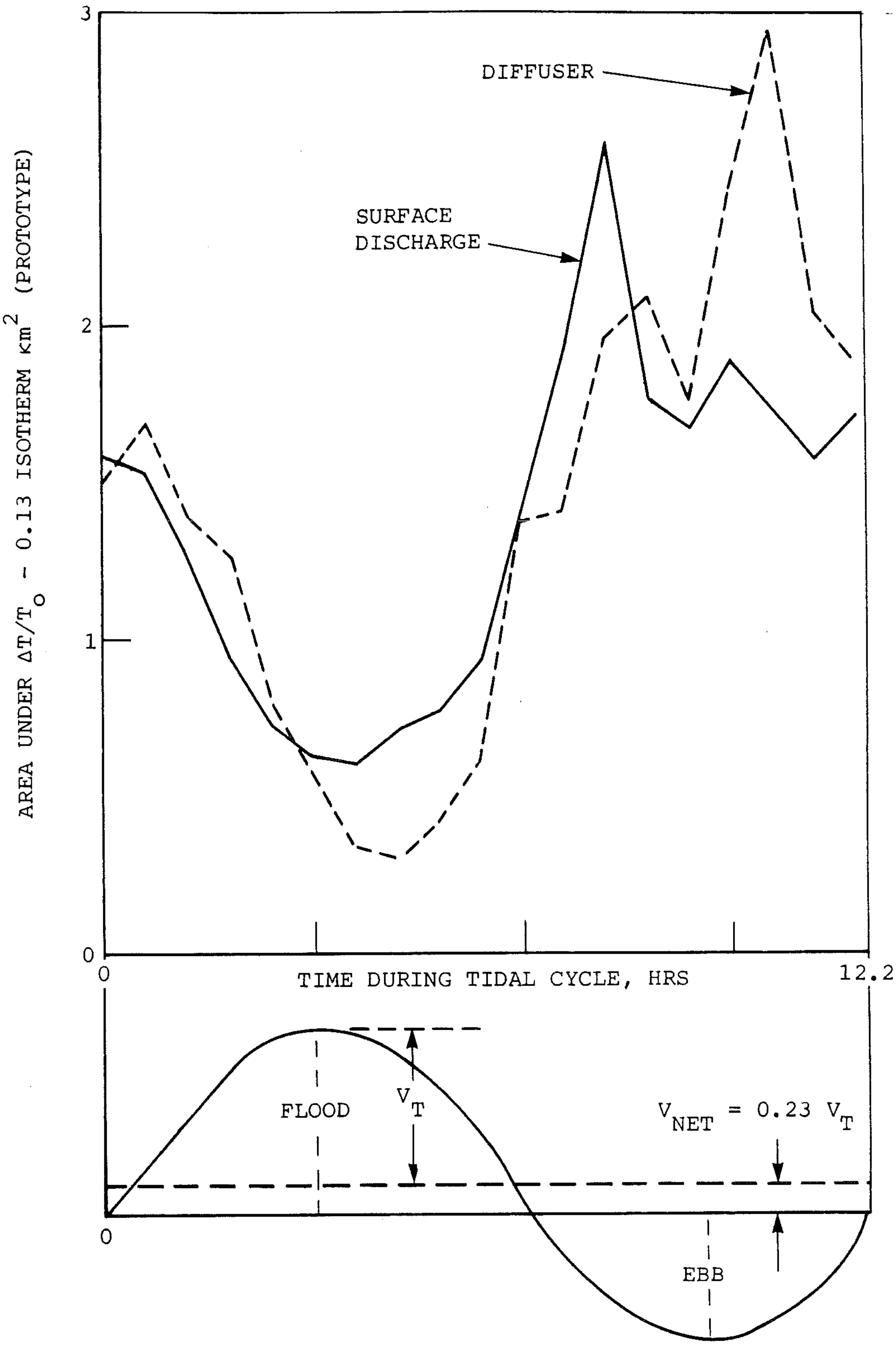

FIGURE 4 AREA UNDER $\Delta T/T_o = 0.13$ ISOTHERMS DURING A TIDE CYCLE

THERMAL PLUME STUDY IN THE DELAWARE RIVER: PROTOTYPE MEASUREMENTS AND NUMERICAL SIMULATIONS

by Bryan R. Pearce[1], Vijay G. Panchang[1], Diane Foster[1], Liaqat Ali Khan[2], Peter Sucsy[1], Howard McIlvaine[3], Robert F. Daugherty[3], Charles C. Miller[4], and Victor J. Schuler[4]

Abstract

To examine a variety of possible configurations for heated water discharge at the Atlantic Electric Company's Deepwater Power Plant on the Delaware River, a pair of numerical models and a field measurement program were established. The hydraulic information necessary as input to the heat transport equation is obtained from a hydrodynamic model, applied to a 12 Km portion of the Delaware River, between New Castle, Delaware and Penns Grove, New Jersey. The model is calibrated by comparing the computed results with measured water surface elevations and velocities. A Lagrangian tracer technique has been used for simulating the transport and mixing of the hot water into the river. The far-field heat transport model was calibrated by adjusting the diffusion coefficient and comparing to field measurements.

Introduction

Figure 1 shows a section of the Delaware River between New Castle, DE and Penns Grove, NJ, the location of the heated water discharge, and the location of the current meter stations, S, and transects, T. This study has been undertaken to examine the effects of the heated water discharge into the river, especially the propagation of the thermal plume and the boundaries of the 1.0 °F and 1.5 °F isotherms. To simulate the thermal plume, two models were developed. The first model, TIDE, is a two-dimensional water flow model. The depth integrated momentum and continuity equations are solved by an explicit finite-difference method. This model provides the hydraulic information necessary for the solution of the heat transport equation. The second model, PLUME, simulates the transport of heat, and computes the temperature increase due to the hot water discharge. Plume is a "Far-Field" model, that is, the physical processes in the river govern the mixing. The PLUME model simulates the transport and mixing process using a Lagrangian method or "tracer technique" (Fisher, et al., 1979; Bugliarello and Jackson, 1964).

Heat Transport Model

The transport of heat is governed by the advection-diffusion equation. For the two-dimensional case this equation (Fisher et al., 1979) can be written as follows:

$$\frac{\partial T}{\partial t} + U\frac{\partial T}{\partial x} + V\frac{\partial T}{\partial y} = D\left[\frac{\partial^2 T}{\partial x^2} + \frac{\partial^2 T}{\partial y^2}\right] + \lambda\,(T - T_e) + Q_s$$

where: T is the water temperature, T_e is the equilibrium water temperature, U is the depth mean velocity in x-direction, V is the depth mean velocity in y-direction, D is the diffusion coefficient, λ is a heat decay coefficient, and Q_s is the rate of heat added to the system. Instead of solving the heat transport equation numerically, these processes are simulated in the PLUME model by "tracers" (imaginary particles) that are injected into the channel and their movements are traced in time.

[1] Department of Civil Engineering,University of Maine, Orono, ME, 04469.
[2] School of Civil and Environmental Engineering, Cornell University, Ithaca, NY 14853.
[3] Atlantic Electric Co. ,P.O. Box 1500-MLC, Pleasantville, NJ, 08232.
[4] Environmental Consulting Services, Inc.100 South Cass St, Middletown, DE, 19709

With respect to mixing in estuaries and coastal water bodies, there are several reasons (Dimou and Adams, 1989) one might use a particle-tracking model instead of the more common concentration (Eulerian) models: 1) Dispersion coefficients in estuaries are not constant, but vary as a function of tidal velocity; this variation is more easily modeled by a random walk process. 2) Sources are more easily represented in a particle-tracking model (i.e., by introduction of particles), whereas concentration models have difficulty resolving concentration fields whose spatial extent is small compared to that of the discretization. 3) In particle-tracking models the computational effort is concentrated in regions where most particles are located, i.e. regions with highest concentrations, whereas in concentration models all regions of the domain are treated equally in terms of computational effort. 4) Particle tracking is well suited to the capabilities of new supercomputers, particularly parallel processors. 5) Particle tracking models have zero numerical diffusion which is a very important consideration in modeling plumes with large lateral extent.

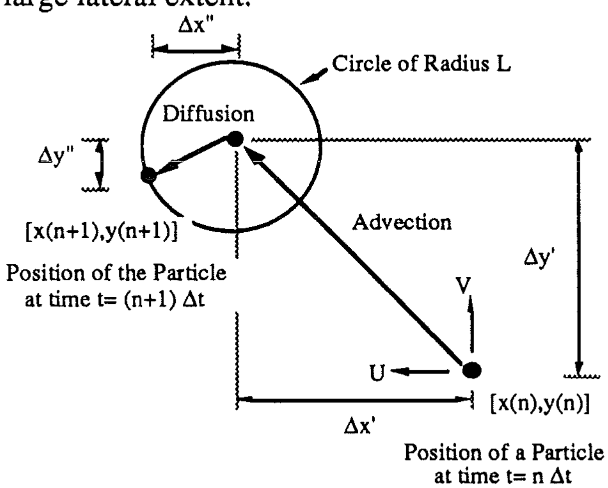

Figure 2. Schematic of Tracer Technique

The process consists, essentially, of having all tracer particles move or jump at each time step. The jump consists of two parts (see Figure 2): the advection part due to the motions of the water body and a random part which represents the diffusion process. In the limit of small jumps and time steps, it can be shown that this process represents the above heat transfer equation. The particles each carry an amount of heat determined by the number of particles input and by the heat discharge. The temperature at a certain location is computed from the number of particles in a computational cell fixed in space. Thermal decay can be simulated by adjusting the probability that a particle will be removed from the simulation. The theoretical details of this method, based on "random walk", are described by Fisher et al.(1979), Bugliarello and Jackson (1964), and others.

Water Flow Model

To determine the flow velocities for the PLUME model a circulation model was constructed and applied with the help of extensive current measurements. The two-dimensional equations of motion (eg. Abbott, 1979) describing the fluid flow are:

$$\frac{\partial \eta}{\partial t} + \frac{\partial (HU)}{\partial x} + \frac{\partial (HV)}{\partial y} = 0 , \qquad \frac{\partial U}{\partial t} - fV = -g\frac{\partial \eta}{\partial x} - \frac{kU\sqrt{U^2+V^2}}{H} ,$$

$$\frac{\partial V}{\partial t} + fU = -g\frac{\partial \eta}{\partial y} - \frac{kV\sqrt{U^2+V^2}}{H}$$

where: g = gravity, f = the Coriolis parameter, η = the deviation of the free surface from mean sea level, and k = the bottom friction coefficient. Both the flow data and the fact that the plume remains largely in shallow water suggest that the vertically averaged equations are suitable for this simulation. The added complexity of a three-dimensional model is not necessary.

Model Applications

Figure 1 shows the schematic representation of the model domain with $\Delta x = \Delta y = 96$ m. The total number of computational cells is 112 x 44 or 4928. The open boundaries of the model are located at New Castle and Penns Grove. The locations of these boundaries have been selected such that the 1°F isotherm is far inside the model domain, and the boundary conditions do not affect the computed results in the region of interest. Figure 3 shows the bed topography of the river (in meters) below the chart datum. These data were extracted from the 1: 40000 scale hydrographic chart of the Delaware River, "Smyrna River to Wilmington" (NOAA Chart No. 12311).

In order to simulate the actual field conditions for tuning the model, the amplitude and phase for the major tidal constituents were obtained from NOAA and then used to resconstruct the tide at the model boundaries. The tide is then:

$$\eta \text{ (tidal elevation)} = \sum_{i}^{n} f_i(t)\, a_i \cos(\omega_i t + V_{oi}(t) - \kappa_i)$$

where: f is a slowly varying factor, a is the constituent amplitude, t is time, $V_{oi}(t)$ is the phase referenced to Greenwich, and κ_i is the phase of the constituent (Shureman, 1958). Figure 4 shows the plot of the water level boundary conditions used in this model application, in particular August 22, 1989, the day of the field campaign. Note the phase differences which are primarily responsible for driving the flows. For the boundary conditions shown in Figure 4, the flow model was calibrated by adjusting the bed friction coefficient, k. The model is run for several tidal cycles to eliminate undesirable transients. Figure 5a,b,c compares the computed velocities to measurements at several stations. (Reference Figure 1 for locations.) In order to achieve a reasonable calibration it was necessary to use a friction factor that varied with depth. In this case the shallow regions required a much larger damping factor than the relatively deep water of the channels. This may be caused by the fact that in some areas the water is so shallow that there is a significant boundary layer development due to the wind wave activity which results in consequently high bottom friction. Considering the approximations involved and the uncertainty in many parameters, the results of the model calibration appear satisfactory. The flow model was run with a time step of 5 seconds.

To simulate the plume, it is assumed that hot water is discharged continuously at one or more locations (See Figure 1 for the discharge location used for this study). The model is started with $\Delta T = 0°C$ throughout the model domain. The time-step used in these computations is 5 minutes. To avoid excessive storage requirements, the output from the TIDE model is stored at 15-minute intervals. The intermediate values necessary for the computations are obtained by linear interpolation.

A step length comparable to a value of $D = 2.5\ m^2/s$ was used to obtain the plumes shown in Fig. 6a,b for ebb and flood tide respectively. There are two isotherms in the figures, 1.5°F and 1.0°F. These plots represent the conservative case of zero decay. Numerical experiments indicate that the computations reach quasi-steady state in about three tidal cycles. Thereafter, there are no significant changes in the boundaries of the isotherm at low water slack and excess heat is leaving through the model boundaries. The situation with zero decay is especially realistic on a hot and calm summer day. Figure 7, by comparison, shows the measured thermal field (ebb tide) with the same heat input that was used in the simulation represented by Figure 6a,b (ACEC,1973).

Summary

The above paragraphs describe initial modelling efforts to simulate the thermal regime in the Delaware River between New Castle, DE and Penns Grove, NJ. The simulations are made using two coupled computer models, TIDE and PLUME. The hydrodynamic model, TIDE, was calibrated by adjusting the friction coefficient and forced with the predicted tide as boundary conditions. The computed water surface elevations and velocities match the observed values reasonably well. The computed thermal plume boundaries are consistent with the limited field data obtained by the US Army Corps of Engineers in 1972 (ACEC, 1973). Since the PLUME model results are not highly dependent on the coefficient of diffusion, we may surmise that advection is the dominant mode of heat transport in this reach of the river. Diffusion becomes important at high and low water slack, when the velocity of flow approaches zero.

Our present efforts are now directed towards obtaining improved model tuning and refinement that will allow the models to make accurate predictions of various scenarios (e.g. with other diffuser locations or heat discharges).

References

Abbott, M.B., 1979, Computational Hydraulics: Elements of the Theory of Free *Surface Flows*, Pitman, London, U.K.

Atlantic City Electric Company (ACEC), 1973, Thermal Hydrology Study, Deep Water Station, Delaware River Pennsville, New Jersey.

Bugliarello, G., and Jackson, E.D., 1964, Random Walk Study of Convective Diffusion, Journal of the Engineering Mechanics Division, ASCE, EM4, August, pp.4877

Dimou, K.N., and E.E. Adams, "2-D Particle Tracking Model for Estuary Mixing", *Proceedings, Estuarine and Coastal Modeling*, Nov 1989, Newport, RI.

Fisher, H.B. et al.,1979, *Mixing in Inland and Coastal Waters*, Academic Press, N.Y.

Pearce, B.R., L.A. Khan, V.G. Panchang, D. Foster, *Numerical Thermal Plume Simulation for the Delaware River between New Castle and Penns Grove*, Interim Report, Department of Civil Engineering, University of Maine, Orono, ME and Environmental Consulting Services Inc, Middletown, DE.

Shureman, P., 1958, *Manual of Harmonic Analysis and Prediction of Tides,* Government Printing Office, Washington D. C.

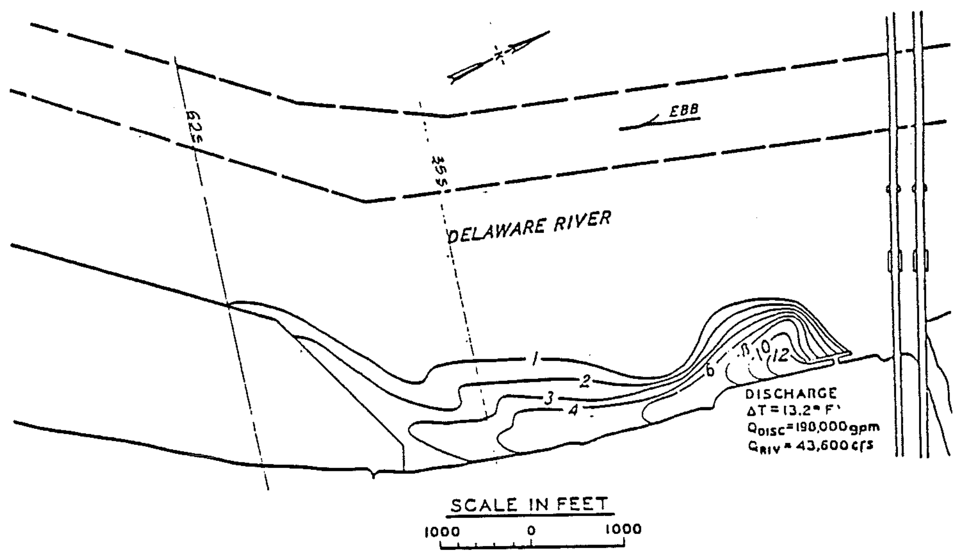

Figure 7 - Prototype Thermal Plume Data - °F

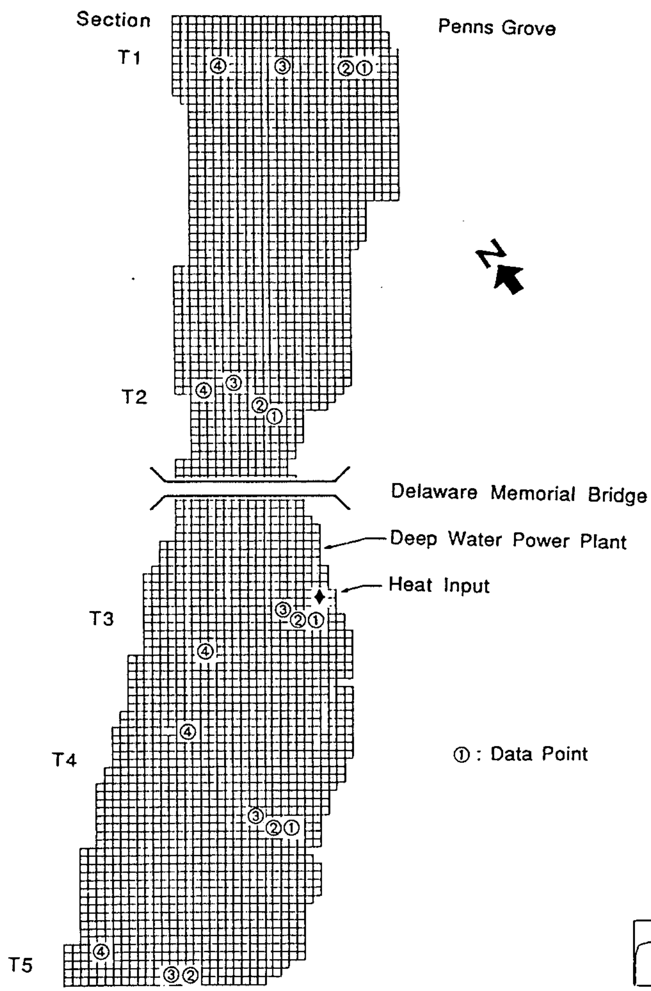

Figure 1- Grid Showing Current Meters Transects and Stations.

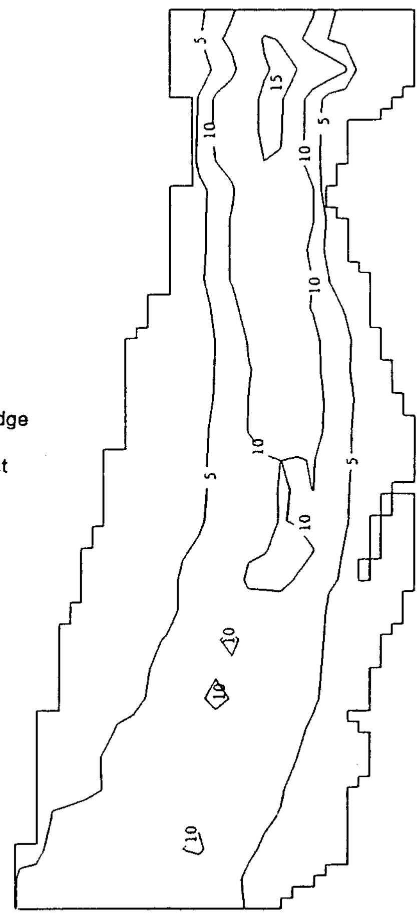

Figure 2 - Riverbed Topography (Meters)

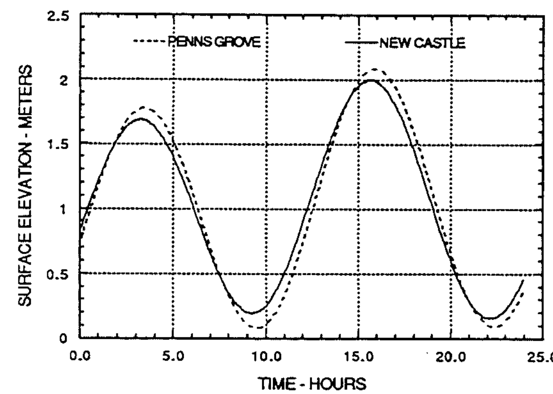

Figure 4 - Boundary Conditions for Water Flow Model

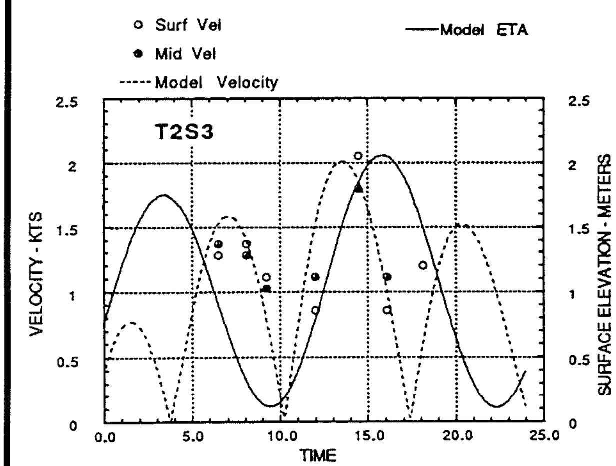

Figure 5a - Prototype and Model Velocity Comparisons (T2S3)

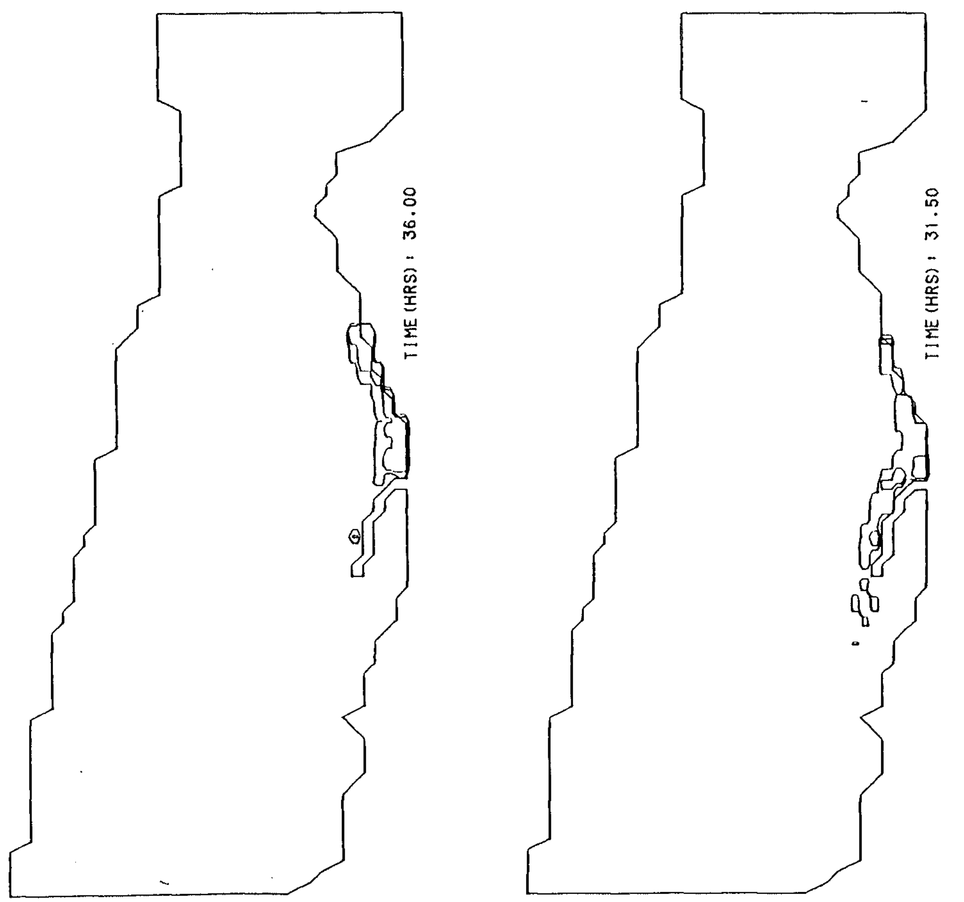

Figures 6a,b - Calculated Isotherms for Flood and Ebb Tide (1 F and 1.5 F)

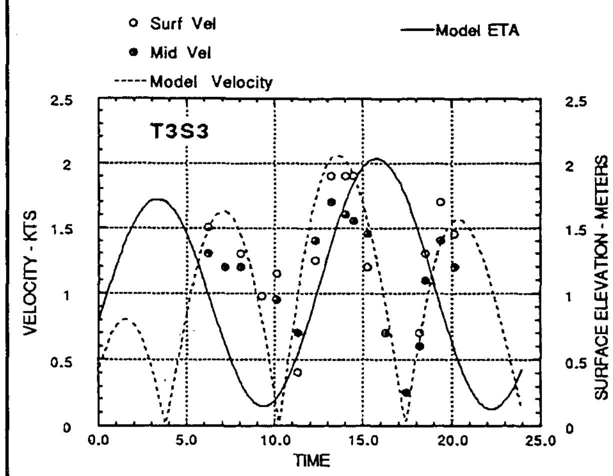

Figure 5b - Prototype and Model Velocity Comparisons (T3S3)

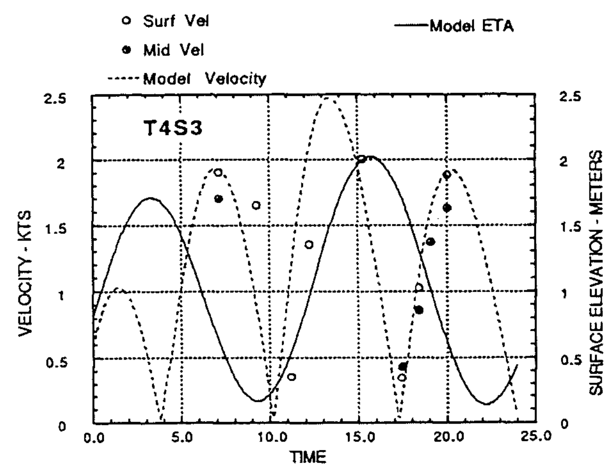

Figure 5c - Prototype and Model Velocity Comparisons (T4S3)

NUMERICAL AND EXPERIMENTAL STUDIES OF WAVE FORCES IN DIFFRACTION REGIME ON MULTIPLE CYLINDLRICAL PIERS

Dr.H.RAMAN & T.V.GOPALAKRISHNAN, IIT, MADRAS, INDIA.

Introduction

The phenomenon of diffraction of water waves by natural boundaries or man-made structures is of considerable significance in wave structure interaction. This phenomenon becomes extremely important in the determination of wave forces, particularly when the size of the structure increases, because the incident wave field gets deformed by the presence of the structure. However, the problem of determining the wave loading on structures is quite complex. The fluid-structure interaction manifests in the complex hydrodynamic pressure distribution on the structure as well as the resultant forces and moments. The work presented herein addresses the approaches of model testing in the laboratory and numerical analysis using finite element models for the study of wave forces on groups of cylinders.

Numerical Model

The scattering of regular plane waves by a group of rigid, bottom-fixed, surface-piercing vertical cylinders in water of uniform depth was considered in this study. This three dimensional problem could be reduced to two dimensions by introducing the depth transfer function involving the vertical coordinate, both for constant depth and mildly sloping cases. By solving the Laplace equation in three dimensions with appropriate boundary conditions we get,

$$\Phi(x,y,z) = Z(z).\phi(x,y) \quad \ldots \ldots (1)$$

where ϕ and Φ are the complex 2D and 3D potentials respectively and $Z(z)$ is the depth transfer function. Berkhoff (1975) showed that under the assumption of mildly sloping seabed, employing the same depth transfer function, a consistent approximation called the mild-slope equation governing the diffraction-refraction of linear waves could be obtained.

The problem of water wave diffraction by large bodies essentially involves unbounded domain in plan . To solve the problem using a versatile finite element based numerical technique, it is expedient to divide the problem domain into inner and outer domains. The inner domain would consist of the solid obstructions to flow extending to about 100 times the linear dimension (here diameter) of the obstruction whereas the outer domain would extend from the boundary of the inner domain to infinity.

In this study, the problem of diffraction around groups of cylinders was treated numerically by employing a two dimensional finite element model. The inner domain was modelled using conventional finite elements. Two types of finite elements were used in the inner region. These were the isoparametric forms of the 6 noded triangular and 8 noded rectangular elements. The infinite element approach proposed by Bettess and Zienkiewicz (1977) was used for modelling the outer domain. As the outer domain extends to infinity in one of the co-ordinates, exponential shape functions were used. The parent shape of the infinite elements used in this study is the strip shown in Fig.1. It is a rectangle extending to infinity in the ξ direction, ξ and η being the reference coordinates. The element has three reference points, in each of the directions, giving a total of 9 nodes. The above techniques essentially attempt to enforce the Sommerfeld radiation condition in the far-field. The variational formulation could be readily used in conjunction with the Rayleigh-Ritz method to derive the numerical approximation to the diffraction problem. Standard numerical integration procedures using Gauss-Legendre numerical integration were employed for the finite elements, whereas a special integration scheme was used for the infinite elements. The assembly and solution of the finite element equations were based on the frontal scheme due to Ivons (1970). The integrals associated with forces in any given direction and moments due to these on cylinders were evaluated using numerical quadrature (Simpson`s Rule) both circumferentially and vertically.

Experimental Investigations

The aim of the experimental investigation was to study the pressure distribution around a vertical circular cylinder at different elevations and to measure the inline forces due to linear plane incident wave field. Three cases were considered: single cylinder, two cylinder and three cylinder cases. The experiments were conducted in a 0.9m wide and a 2m wide flume at Indian Institute of Technology, Madras, India.

For groups of cylinders with spacing parameter S/a the force function could be expressed as

$$F/(\rho g H D^2) = f(ka, \frac{S}{a}) \qquad \ldots\ldots (2)$$

where F is the force, ρ is the density of water, g is the acceleration due to gravity, H is the wave height, D is the diameter of the cylinder, k is the wave number and a is the radius of the cylinder. This relation could be used in conjunction with the numerical results on model cylinders in order to predict the forces on prototype structures.

For measuring forces a single component drag balance working on the principle of strain gauge bridge was used. The model was connected to a drag balance leaving a clearance of approximately 5mm. Pressure fluctuations were sensed by flush type inductive pressure transducers with a range of + 1kgf/sq.cm. For measuring incident wave heights, resistance type wave gauges were used. These were located about 3m. away from the model on the upstream side. The experiments were conducted in two different wave flumes as given below:

1. Various geometric and wave parameters used in 0.9m wide wave flume: Model cylinder: 20cm diameter rigid PVC pipes, 90 cm long; Still water depth : 50cm; Location of pressure transducers: 15cm, 35cm and 45 cm vertically below still water level at $\theta = 0°, 90°$ and $180°$ with respect to the direction of wave propagation; Parameters measured: Total inline force, pressures at four elevations and incident wave field; Spacing parameter: S/a = 3,4,5 and 6 for two cylinder case; Wave period : 0.5s to 1.8s in steps of 0.1s; Wave direction: $\theta = 0°$ for single cylinder and two cylinder cases. The experiment was run for 12 different wave heights for the single cylinder case and three different wave heights for the two cylinder case.

2. Various geometric and wave prameters used in 2m wave flume: Model cylinder: 20cm. diameter rigid PVC pipes 150cm long; Still water depth : 100 cm; Parameters measured : Total inline force and incident wave field; Spacing parameter : S/a = 3,4,5 and 6 for two cylinder case and S/a = 4 and 5 for three cylinder case; Wave period : 0.5s to 1.8s in steps of .1s; Wave direction : $\theta = 0°, 45°$ and $90°$ for two cylinder case and $\theta = 0°, 90°$ and $180°$ for three cylinder case. The experiment was run for 8 different wave heights for single, two cylinder and three cylinder cases.

Discussion of Results

Two Cylinder Case: The numerical and experimental results of the study showed that the leading cylinder experiences the most severe force for $\theta = 0°$. The force ratio R (ratio of the force on the leading cylinder of the two-cylinder case to the corresponding force on the single cylinder case obtained from experimental work in the 0.9m wide flume) was compared with numerical results for $\theta = 0°$ and S/a = 4. Issacson`s (1978) numerical results based on Green`s Function Approach was also used for comparision. Good correlation was observed for the peak and trough values of the force ratio which exhibits an oscillatory trend with respect to ka. Similar results were obtained for the trailing cylinder also. It was found that the leading cylinder experiences about 25% to 30% higher force than the trailing cylinder.

The force ratio R on the leading and trailing cylinders of the two cylinder case based on the present work was compared with the results of other investigators for $\theta = 0°, 45°$ and $90°$ and for S/a = 3,4,5 and 6 . The case with $\theta = 0°$ gave the largest increase in force ratio and exhibited marked fluctuations of R with ka. The leading cylinder is exposed to the partial standing waves due to the interference of the trailing cylinder and hence experiences considerable increase in force. Interference effect was found to be severe on the leading cylinder for $\theta = 0°$ and S/a = 3. The increase in force on the leading cylinder was about 51% higher compared to an isolated cylinder at ka = 0.75.

To illustrate the importance of interference effects in large diameter cylinder groups numerical results for an array of two cylinders of equal radius was considered. The numerically evaluated maximum inline and lateral wave forces and moments for the large diameter two cylinder group (in non-dimensional form) were compared with the corresponding quantities for a 20m diameter isolated cylinder. For a pair of cylinders aligned perpendicular to the direction of wave advance ($\theta = 90^\circ$) the peak inline force on either of the cylinders was found to be only 4 to 5% more than the force experienced by an isolated cylinder. This demonstrated the insignificance of interference effect. For a pair of cylinders aligned in the direction of wave advance, it was observed that the leading cylinder experiences about 33% larger inline peak force in comparison to the isolated cylinder peak force. Also, the forces on the leading and trailing cylinders show an oscillating trend with ka and the peak forces occur at slightly different ka values. In the case of the trailing cylinder, the peak force was only slightly larger than the isolated cylinder value.

Three Cylinder Case: The FEM and experimental results pertaining to the variation of force ratio R with scattering parameter ka was compared with the approximate analytical solution due to Spring and Monkmeyer (1974) and also with the results of McIver and Evans (1984). The correlation obtained among the methods was generally found to be good. As observed in the two cylinder group, the largest increase in force ratio occured when $\theta = 0^\circ$. Also, in this case there was marked fluctuation between the maximum and minimum values of R with ka. Agreement between the numerical predictions and experimental results could be considered satisfactory in all cases. Out of the three wave angular approaches ($\theta = 0^\circ$,90° and 180°) and two spacing parameters (S/a = 4 and 5) considered, the interference effect was found to be severe on the leading cylinder for $\theta = 0^\circ$ and S/a = 4. ($\theta = 0^\circ$ means one cylinder is directly in front of the remaining two cylinders). For this case there was a 52% increase in the force on the leading cylinder compared to an isolated cylinder at ka = 0.65. The increase in peak force on the leading cylinder when compared to the peak force on an isolated cylinder is 42% for this case. This clearly brings out the predominant interference effect in the three cylinder case even for a larger spacing compared to the two cylinder case. The two trailing cylinders were found to experience only about 6% increase of force over the corresponding isolated cylinder values. Considering possible errors due to side effects of the flume, partial reflection from the beach and nonlinear effects of waves, the agreement between the numerical and experimental results might be considered good for the single and two cylinder cases and satisfactory for the three cylinder case.

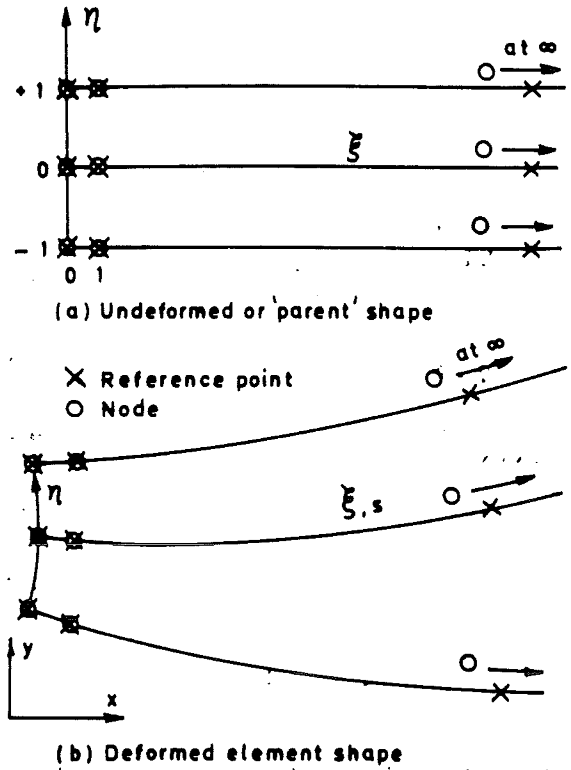

FIG. 1 – INFINITE ELEMENT GEOMETRY

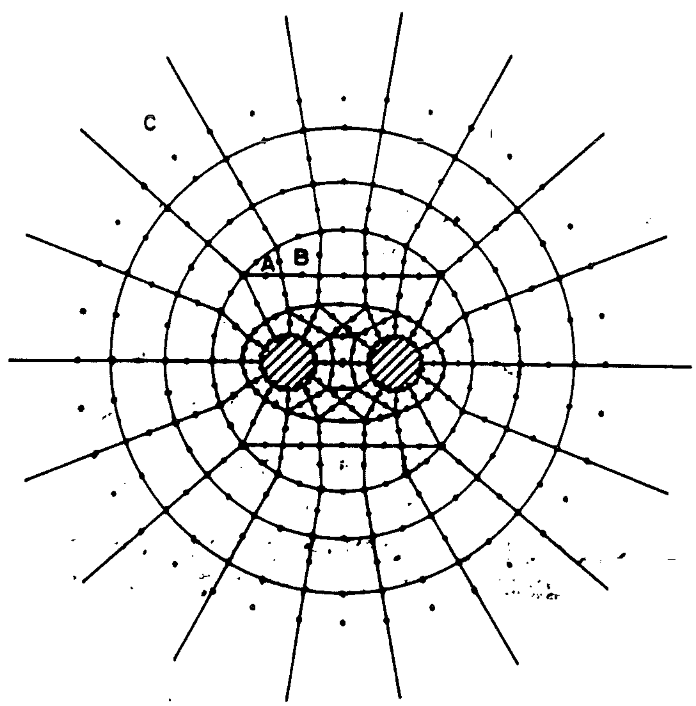

NUMBER OF NODES = 407
NUMBER OF FINITE ELEMENTS = 102
NUMBER OF INFINITE ELEMENTS = 18

FIG. 2 – TWO-CYLINDER DISCRETIZATION

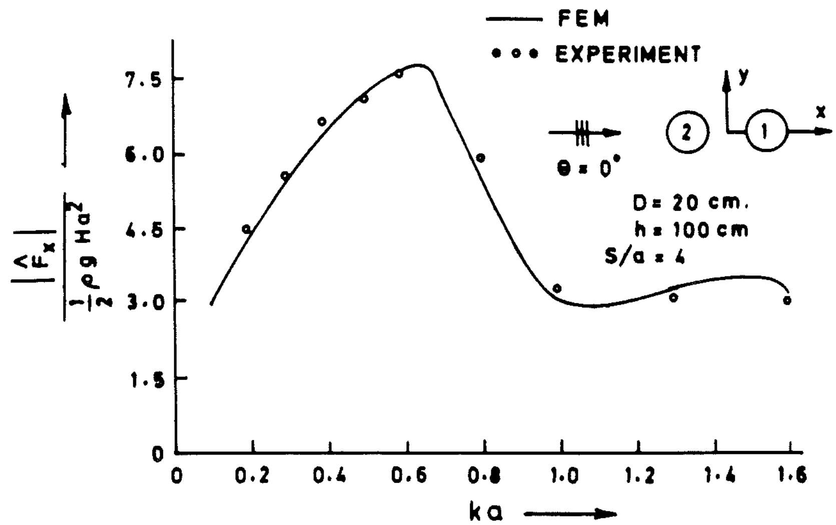

FIG. 3-MEASURED AND COMPUTED FORCES ON CYL-2 OF TWO-CYLINDER CASE.

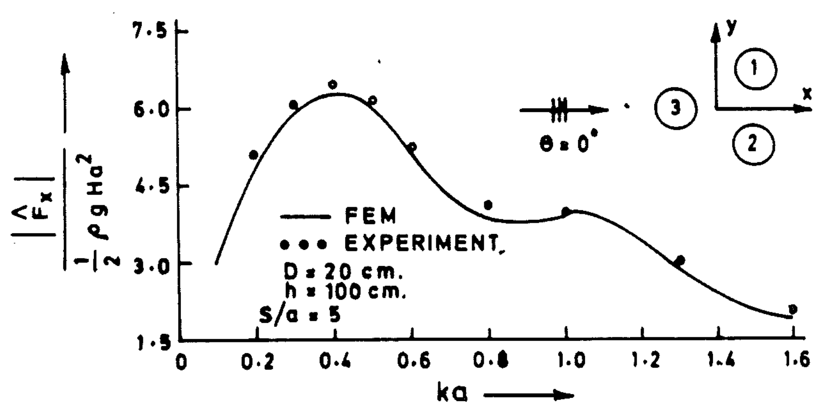

FIG. 4-MEASURED AND COMPUTED FORCES CYL-1 OR CYL-2 OF THREE CYLINDER CASE.

Session 14A

Mixing in Tanks and Channels

MIXING IN WASTEWATER DECHLORINATION BASINS: PHYSICAL MODELING CRITERIA AND APPLICATIONS

by Heinz G. Stefan, Thomas R. Johnson, John R. Thene,
Frederick N. Luck and Craig A. Silver
St. Anthony Falls Hydraulic Laboratory
University of Minnesota, Minneapolis, Minnesota 55414 USA

Abstract

The injection, transport and mixing of an SO_2–solution in chlorinated wastewater was studied in physical models of five treatment plants. The criteria and considerations which were applied to the modeling are presented. In the operation of the models non–reactive tracers, high–speed concentration measurements and statistical data analysis were used. Model scales ranged from 1:4.8 to 1:12. Field data were collected in one case study, and a model/prototype comparison for this case will be given. Prototype flow rates ranged from 180 ℓ/s to 28,500 ℓ/s.

Introduction

Removal of residual chlorine from wastewater after disinfection is required by the U.S. Environmental Protection Agency because chlorine is toxic and harmful to organisms in the receiving water. One method of dechlorination is to inject a solution of SO_2 into the chlorinated effluent. The SO_2 solution must become thoroughly mixed with the effluent for the reaction with the residual chlorine to be complete. The reaction is nearly instantaneous.

Existing and projected wastewater treatment plants (WWTPs) are therefore modified or built with "dechlorination basins" as the last stage of the treatment process. Five such basins were recently studied in physical models (see Stefan and Johnson, 1987; Stefan et al., 1988; Silver et al., 1989; Luck and Stefan, 1989; Thene and Stefan, 1989a; Thene et al., 1989b) with three main objectives: (a) to determine if the SO_2 solution was well distributed and mixed in the wastewater, (b) to recommend design modification if objective (a) was not met, and (c) to make recommendations for sampling locations and procedures at the outlet from the basin.

Figure 1 gives an example of a typical flow pattern (streamlines) through the largest of the dechlorination basins studied. The proposed designs, although different in sizes and basin geometries, had the following common features:

(1) The flow was a free surface (open channel) flow.
(2) The SO_2–solution was injected through one or several multiport diffusers with jet port diameters typically on the order of 5 to 8 mm spaced 75 to 290 mm.
(3) Multiport diffusers were perpendicular to the flow, horizontal and usually near the bottom of the approach channel.
(4) Jet discharge velocities of the SO_2–solution were typically from 3.1 to 6.2 m/s and typically 5 to 20 times the wastewater mean flow velocities.
(5) A skimmer (baffle) wall or a lateral channel contraction downstream from

(5) A skimmer (baffle) wall or a lateral channel contraction downstream from the manifold system forced either a vertical or horizontal flow contraction and hence acceleration of the flow.
(6) A weir usually at the downstream end of the basin controlled stages and water depths in the basin.
(7) Downstream from the weir a hydraulic jump would form at low enough tailwater stages.

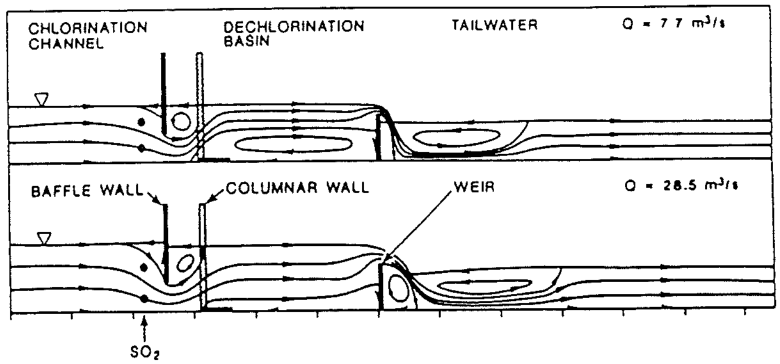

Fig. 1. Streamlines at normal tailwater and two–flow rates. Manifolds for injection of SO_2 solution are upstream from baffle wall.

Modeling Criteria and Constraints

An ideal physical (or mathematical) model of a dechlorination basin would allow the exact reproduction of SO_2–concentration time series at all locations in the model. To achieve this, the distributions of flow velocities and turbulence and the reaction kinetics would have to be duplicated at a specified geometrical and time–scale. The actual model had to fall short of some of these requirements and was developed based on the following reasoning:

(1) The dominant flow patterns are driven by gravity and inertial forces and hence Froude similarity was used to scale flow rates, velocities and time.
(2) A conservative tracer (dye or NaCl) instead of a reactive one was used in the model. This was done to avoid the addition of a reagent to the water in the model study. The effect of a loss of material by a reaction is to delay complete mixing. Use of a conservative tracer therefore is less rigorous. This was accepted to save on study costs.
(3) Full Reynolds similarity would have been desirable but was not achievable simultaneously with Froude scaling. To maintain sufficient turbulence levels geometrical scales were chosen from 1:4.8 to 1:12. As a result, Reynolds numbers scaled from 1:14 to 1:40. A more detailed discussion of Reynolds effects in this study will be given below.
(4) Mass transfer in fluids is scaled by use of a Peclet number. In a dechlorination basin, molecular diffusion is so small compared to turbulent diffusion that it can be ignored. Hydraulic residence times in the basin are on the order of minutes. Turbulent Peclet numbers match in model and prototype if the turbulent eddy diffusion coefficient is linearly related to mean flow velocities and length scales as is usually the case. The coefficient of proportionality is, however, a function of Reynolds numbers.

The main source of turbulence which produces the mixing in the basin is shear. Referring to the flow regions shown in Fig. 1, one can see that different free shear and/or wall shear producing flow mechanisms are present. The SO_2–multiport diffusers and the jets discharged from them produce small–scale turbulence. The separated flow regions shown in Fig. 1 typically produce large–scale turbulence. Columnar walls and steps in the bottom can be added to produce intermediate–scale turbulence. Length and velocity scales of different elements shown in Fig. 1 are summarized in Table 1. Reynolds numbers (calculated with a temperature of 20°C) were all in the turbulent range, except those based on the smallest geometrical scale (jets and manifolds). The jets and manifolds are not significant sources of turbulence, however, because of their small momentum input relative to the total flow (ratio is 1:1000 or less). Jet mixing has, however, significance for the initial dilution of the injected SO_2 (tracer) and is a Reynolds number dependent process (Kuhlman, 1985).

Table 1. Length Scales, Velocities and Reynolds Numbers in the Basin Flow Field

		Prototype	Model
(1) Tracer jets			
diameter	D_0 (m)	0.0044	0.00037
velocity	V_0 (m/s)	3.45	1.00
Reynolds No.	Re	15,000	370
(2) Manifold			
diameter	D (m)	0.076	0.006
velocity	V (m/s)	0.35–1.31	0.1–0.37
Reynolds No.	Re	27,000–99,000	600–2200
(3) Port inlet to basin			
depth	h (m)	0.37	1.14
velocity	V (m/s)	0.35–1.31	0.1–0.37
Reynolds No.	Re	480,000–1,800,000	1,000–42,000
(4) Approach channel			
depth	h (m)	2.7–3.7	0.23–0.31
velocity	V (m/s)	0.073–0.35	0.021–0.10
Reynolds No.	Re	270,000–960,000	6500–23,000
(5) Column wall			
width	d (m)	0.3	0.025
velocity	V (m/s)	0.15–0.70	0.042–0.20
Reynolds No.	Re	45,000–210,000	1,100–5,000

Local measurements of concentrations give the cumulative effect of mixing, integrated along a pathline and over travel time. The measured concentrations, therefore, do not indicate a local behavior of the flow.

Model Validations

Several tracer studies were conducted in a prototype to examine the validity of the model. The field measurements were made in the largest of all basins studied which was also the one that required the largest geometrical scale reduction (1:12) for laboratory model studies. The procedures for field and laboratory measurements are described in detail elsewhere (Stefan et al., 1990 or 1988). Prototype and model measurements of mean dye concentration at 15 points in the original basin are compared in Fig. 2. The values given are expressed as the ratios of measured concentrations to the concentration at the weir. Isopleths were drawn from each set of measurements. The general shape of the dye plume inside the basin was similar except in regions of strong concentration gradients where a slight error in scaling or location would change concentration drastically. The slightly greater width of the plume in the prototype probably indicated greater turbulent spreading in the prototype than in the model. The air plume shown in Fig. 2 was scaled according to buoyancy flux, but air bubble size could not be scaled. (It was eventually removed in both prototype and model for lack of well–defined mixing effectiveness.) The SO_2 (tracer) plume rose somewhat faster in the prototype than in the model basin. There was a separated flow region extending from the bottom of the weir upstream into the basin. In the model, that region was smaller than in the prototype as can be inferred from the isopleths. It is shown as a dotted line in Fig. 2. Standard error between model and prototype mean concentrations measured in the basin was 0.39 and at the six most downstream data points, 0.25.

The results shown in Fig. 2 were those of a diagnostic study indicating a poorly functioning basin. The injected SO_2 solution (dye) was carried along the basin bottom and did not get in contact with half of the water flow. Concentration fluctuations measured on top of the weir were high. The coefficient of variation was from 0.18 to 0.34 in the model for flow rates from 10.5 m^3/s to 28.5 m^3/s and approximately 0.25 in a prototype measurement. It was decided that the laboratory and field data matched well enough so that the model could be used to find modifications of the basin which would give better mixing than that shown in Fig. 2. A second multiport diffuser and a columnar wall shown in Fig. 1 were eventually added to the prototype.

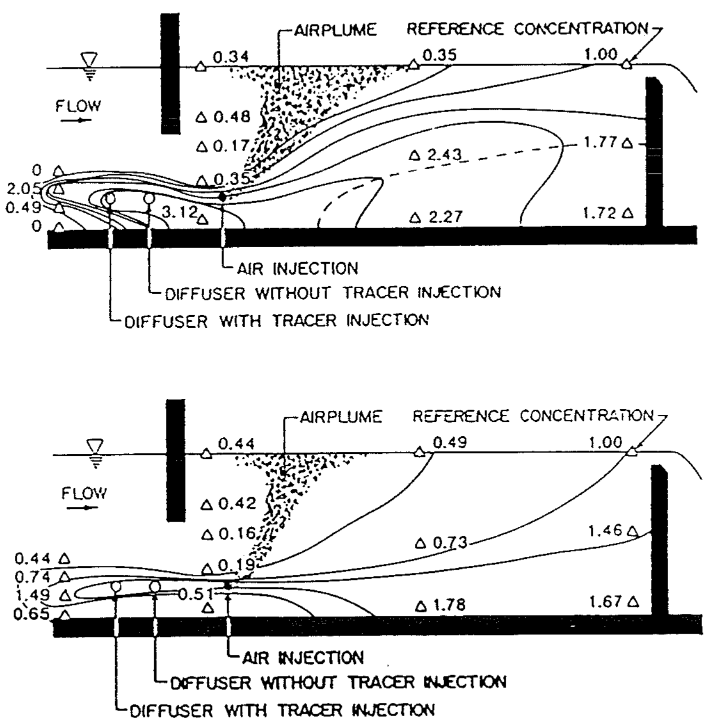

Fig. 2. Mean dye concentrations measured in the field (top) and mean conductivity distribution measured in model experiments (bottom). The means are relative to the values of the overflow.

Measurements made in the prototype after basin modification provided a source of post–audit model validation. Coefficients of variation $S/\bar{X}$ and normalized means $\bar{X}/\bar{X}_{ave}$ of concentration measurements near the end of the basin are given in Table 2. The $S/\bar{X}$ values indicate that the same level of mixing has been achieved in both model and prototype. $S/\bar{X}$ can range from zero for fully mixed conditions to larger than 1.0 for very incompletely mixed conditions. The $\bar{X}/\bar{X}_{ave}$ values in model and prototype are also within a few percent of each other and within a few percent of 100 percent, indicating that the average concentrations $\bar{X}$ measured in the model and field are in reasonable agreement.

Table 2. Range of Statistical Parameters of Concentrations Measured in Field Tests and Model Experiments After Structural Modifications in Basin

Tests	q m^2/s	Tracer	Location of Samples	$\bar{X}/X_{ave}$	$S/\bar{X}$
9 Field Tests[1]	0.30–0.41	Rhodamine WT dye	pier	0.88–1.14	0.02–0.07
2 Model Tests[2]	0.27–0.39	Salt	mid–weir	—	0.05–0.07
2 Model Tests[3]	0.27–0.47	Blue dye	pier	1.00–1.05	0.05–0.07
2 Model Tests[3]	0.27–0.47	Blue dye	mid–weir	0.94	0.03–0.08

All sampling points located 2 m above bottom and 0.5 m upstream of weir.
[1]Metropolitan Waste Control Commission (1987)
[2]Stefan and Johnson (1986)
[3]Stefan and Johnson (1987)

Model Applications

Physical models were also used to study four new dechlorination basins which are now under construction. Two of these were of the type shown schematically in Fig. 3. Geometrical and flow features are described in the reports listed in the references. Because the flow rates were smaller than in the above described case, geometrical scale ratios could be kept within 1:4.8 to 1:9.1 and Reynolds numbers ratios from 1:14 to 1:27.

A recurring question in these designs was for the optimum angle for the multiport diffuser jets relative to the water flow direction. Figure 3 shows some of the options. In all cases the main objective for the orientation of the multiport diffuser was not the jet mixing but the uniform distribution of the injected SO_2 solution over the depth and width of the flow. Without this initial good distribution of the chemical the effluent from the basin was never uniformly mixed. Secondary flows and separated flow regions were two of the causes for non–uniform initial distribution. Another objective in the orientation of the multiport diffuser in the cross flow was to aim for a jet trajectory which would reach about mid–depth, i.e. the flow region where high turbulent diffusivities would complete the vertical mixing. The horizontal jet spacing was from 16 to 46 jet diameters.

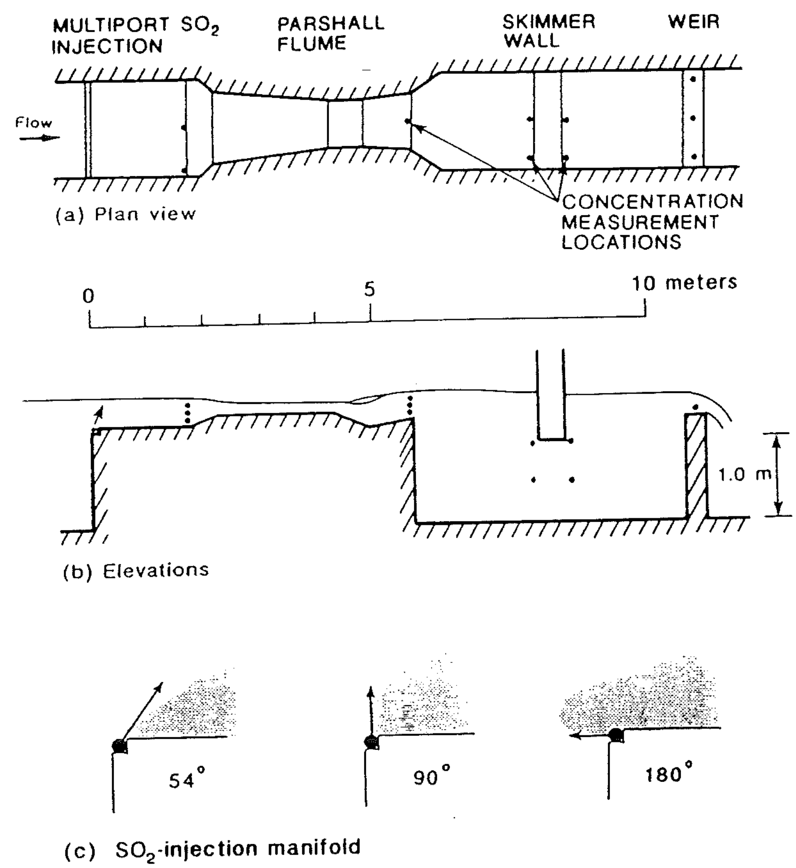

Fig. 3. Geometry of new dechlorination basin. Sampling locations are shown by small circles.

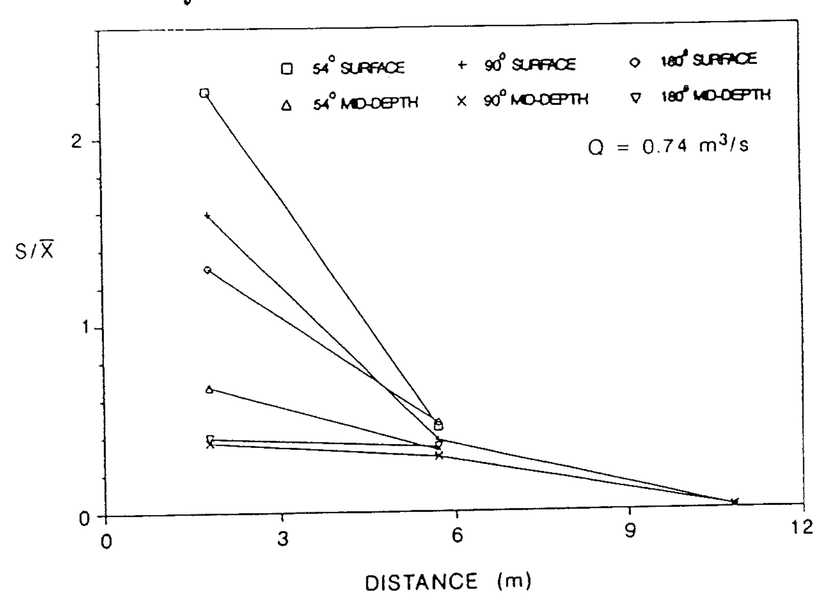

Fig. 4. Normalized concentration fluctuations $S/\bar{X}$.

Of the different flow mechanisms which contributed to mixing (e.g. jets, open channel flow), those that produced large scale and high velocity eddies were the most effective (hydraulic jumps, separated flow regions). The least contributions to mixing occurred in flow contractions and accelerating flows where turbulent eddies were strained. Design engineers sometimes have the notion that high velocity regions have the most mixing when in effect the opposite may be true.

An example of the progressive mixing with distance from the injection is shown in Fig. 4. Time–series records of concentrations were analyzed to obtain standard deviations S and means of the concentrations $\bar{X}$. $S/\bar{X} = 0$ indicates fully mixed conditions.

Conclusions

Physical model studies of mixing in free surface flow reactor basins have been conducted, validated and found very useful. Despite some limitations in turbulence modeling imposed by geometrical scales, physical models reproduce the key flow and mixing phenomena. When reactor basins of complex three–dimensional geometry are to be investigated, model studies are particularly useful.

References

Kuhlman J.M. (1985). Survey of nearfield Reynolds number effects and initial condition effects on nonbuoyant jets. ASME, *Proceedings, Int'l. Symposium on Modeling Environmental Flows*, Albuquerque, NM.

Luck F. and H.G. Stefan (1989). Model Study of Mixing in the proposed Dechlorination Facility of the Seneca Wastewater Treatment Plant in Eagan, Minnesota, Project Report No. 293, St. Anthony Falls Hydraulic Laboratory, University of Minnesota, Minneapolis, MN., 110 pp.

MWCC (1986). Operational and Monitoring Report on the Dechlorination Facilities—Metropolitan Wastewater Treatment Plant. Metropolitan Waste Control Commission, St. Paul, MN, Quality Control Dept. QC–87–128.

Silver, C.A., F.N. Luck and H.G. Stefan (1989). Model Study of Mixing in the proposed Dechlorination Facility of Blue Lake Wastewater Treatment Plant near Skakopee, Minnesota, Project Report No. 286, St. Anthony Falls Hydraulic Laboratory, University of Minnesota, Minneapolis, MN, 264 pp.

Stefan, H.G. and T.R. Johnson (1986). Dechlorination Basin Hydraulics, Project Report No. 250, ibid, 114 pp.

Stefan H.G. and T.R. Johnson (1987). Effluent Sampling Locations and Duration Study for the Metropolitan Wastewater Treatment Plant, St. Paul, Minnesota, Project Report No. 259, ibid., 66 pp.

Stefan, H.G. and T.R. Johnson, H. McConnell, and C. Anderson (1988). "Model–Prototype Correlation of Mixing in a Wastewater Dechlorination Basin," P. Burgi (ed.), *Proceedings, Int'l. Symposium on Model–Prototype Correlations of Hydraulic Structures*, ASCE, 1988, pp. 158–169.

Stefan, H.G., T.R. Johnson, H.L. McConnell, C.T. Anderson, and D.R. Martenson (1990). Hydraulic Modeling of Mixing in a Wastewater Dechlorination Basin, *Journal of Environmental Engineering*, ASCE, Vol. 116, No. 3, pp. 524–541.

Thene, J.R. and H.G. Stefan (1989a). Flow Visualization Study of the Dechlorination Basins at the Empire Wastewater Treatment Facility, Ext. Memorandum No. M–217, St. Anthony Falls Hydraulic Laboratory, University of Minneapolis, Minneapolis, MN., 17 pp.

Thene, J.R. and F.N. Luck and H.G. Stefan (1989b). Model Study of Mixing in the Proposed Dechlorination Facility of the Stillwater Wastewater Treatment Plant in Oak Park Heights, Minnesota, Project Report No. 300, ibid, 134 pp.

SIMILARITY AND SCALE EFFECTS IN MODELLING FREE–SURFACE MIXING VESSELS

Martín Vide, J.P. Loscertales, C. Cisneros, A. Dolz, J.
Civil Engineering School.
Jordi Girona Salgado, 31. 08034 Barcelona. Spain.

ABSTRACT – Experimental research in a free–surface mixing vessel proves the existence of a domain of self–similarity. Two lower limits to this domain caused by the scale effect of viscous and densimetric forces are found. However, no upper limit due to the free surface disturbances is found.

1. Introduction

This paper presents some results from experimental research carried out in order to ascertain the similarity laws and scale effects in one particular hydraulic structure: a free–surface circulation vessel containing a constant volume of fluid which is continuously renewed by the discharge of a jet and the extraction of the same flow rate through an orifice. Water supply tanks are an example of hydraulic structures that respond to this pattern. Due to the highly three–dimensional nature of the flow, the scope of the research is the physical models used to determine the mean flow characteristics such as the mean residence time, for design or operation purposes. This is a performance parameter which provides an overall efficiency of the mixing flow induced by the jet.

2. Experimental set–up and measuring technique

Figure 1 shows the experimental set–up. It is a rectangular vessel 1.075 m long, 0.528 m wide, built of perspex, with a water depth of 0.541 m. Water discharge enters the vessel through a 22 mm diameter pipe attached vertically to one of the walls. The outlet is a 28 mm diameter orifice located on the same wall. Fig.1 also shows two different discharge pipes used for different aspects of the research [1], [2]. The reason for this experimental set–up was a 13.8 scale model of a protoype in which the risk of short–circuiting between inlet and outlet was of concern. Short–circuiting means in this context that one part of the jet discharge leaves the vessel rapidly due to the short distance between inlet and outlet. This flow behaviour would reduce the efficiency of the mixing scheme.

The tool for the overall flow analysis in the vessel is the residence time distributions, which are obtained by using an ionic tracer technique. An injection device providing a known mass of NaCl solution over 2 seconds was installed at the inlet pipe. Two in–flow conductivity probes at the inlet and outlet pipes recorded electrical signals caused by the traced water entering the vessel and the traced water extracted from it. The experimental results are conductivity vs. time curves, which are transformed into curves in terms of tracer concentration vs. time. The response of the system to a quasi–instantaneous tracing input exhibits some typical features. The first phase showing several peaks and troughs is the immediate response in which the existence of some short–circuiting could be discussed. The long–term phase is a regular decreasing curve fitting an exponential exhaustion equation, which proves that a complete mixing has already been achieved in the vessel. During this long–term phase most of the tracer mass ($\simeq$ 80 %) is extracted. However, only the short–term phase is used in the similarity research.

3. Similarity analysis

The experimental set–up in Fig.1 is well suited to basic research concerning the role of the different hydrodynamic forces. Firstly, the Froudian scaling criterion was considered appropriate since a free–surface exists and the degree of turbulence in the model was regarded as sufficient for the development of a fully turbulent flow regime. The Reynolds number of the jet in the model operated according to the Froudian discharge scale (flow rate of 2000 l/h in the model) was 32200. The flow patterns in the vessel are mostly governed by the momentum of the jet. The jet has no different densimetric properties from the receiving water, so it does not appear necessary to take into account any other similarity condition.

On the other hand, the nearly stagnant free–surface during the model tests with pipe I (fig.1) suggested that the adherence to the Froudian criterion could be relaxed. If the free–surface does not play any relevant role in the flow, self–similarity could exist for the flow in the vessel. This particular kind of similarity is known in close–conduit flow with a sufficient degree of turbulence, in which neither viscous forces nor gravitational forces play a role. The similarity theory states for this case that the kinematic scales (velocity, flow rate) and the dynamic scales (pressure, head loss) are not fixed by the geometric scale. Thus mechanical similarity between a prototype and a geometrically similar model enables us to freely choose the kinematic scale for model testing (e.g. flow rate scale) and the following statements can be made:

a. The model can be operated at any flow rate within certain limits of what will be called the self–similarity domain. Clearly, it should not be operated at such a low discharge that viscous forces start to play a role (flow not fully turbulent). This would be a lower limit for the self–similarity domain. Another self–similarity limit may exist when the flow boundaries are not rigid but flexible, as a free–surface is. The latter would be an upper limit to the free choice of the flow rate scale in the model, since the flow may not be self–similar if the model is operated at such a high discharge that gravitational or surface tension waves or any disturbance at the free–surface appear.

b. One set of different tests (i.e. different flow rates in the same model) could be used to determine the limits of the self–similarity domain. Such a study would fulfil the same task as a set of geometrically similar models built to different sizes and tested following a particular scaling criterion, in order to ascertain scale effects.

As a summary, the flow in circulation vessels like the one in Fig.1 might prove to be self–similar, like the close–conduit flow. This self–similarity can be verified with a Q–set of tests (Q: discharge) instead of a λ–set of models (λ: geometric scale). This self–similarity would extend over a certain domain, limited in the lower range of flow rates by the effect of viscous forces and probably also in the upper range of flow rates by the disturbances at the free–surface. If these limits were exceeded, scale effects would start to act. These scale effects are properly "kinematic scale effects", for they are not produced by a model too small, but by a model of any scale operated at a flow rate too low (and probably also at a flow rate too high).

In addition to these scale effects, attention must be paid to the effect of the measuring technique on the flow behaviour. The traced water with a certain amount of salt has a density ρ' that is slightly greater than the receiving water density ρ. It produces a negative buoyancy in the traced water. This is, firstly, a purely experimental drawback which might disturb the self–similarity. A limit on the self–similarity domain by the effect of this densimetric force arises by physical reasoning in the same sense (lower limit) as the effect of viscous forces. This limit will deserve further attention, not only with respect to the measuring technique assessment, but also as a general scale effect of densimetric forces.

4. Experimental strategy

If self–similarity takes place in the flow, enabling us to operate it with different flow rates, this self–similarity would mean that the flow is similar to itself. In the model testing with two different flow rates Q_1, Q_2, one of them (say Q_1) can be taken as a reference flow rate. Then, between the two tests there is an intrinsic kinematic scale $\lambda_Q = Q_2/Q_1$. The scales of other magnitudes relevant to the residence time distributions can be derived from this kinematic scale. For the flow in any circulation vessel there is a characteristic parameter called the circulation time T, defined as $T = V/Q$, where V: volume of water in the vessel and Q: water flow rate. Therefore, the intrinsic scale of this temporal magnitude between the two tests is $\lambda_T = (\lambda_Q)^{-1}$, since the volume remains constant for any test. Another important parameter related to the tracing technique is C_0, tracer concentration in case of instantaneous perfect mixing in the vessel, $C_0 = M/V$, where M: total mass of tracer injected. The intrinsic scale of C_0 is $\lambda_{C_0} = \lambda_M$, i.e. the ratio between the total mass of tracer injected in the two tests (M_2/M_1).

The experimental curves are obtained in terms of concentration C vs. time t, where t is the elapsed time from the instant of tracer injection and C is the tracer concentration at any instant t at the outlet pipe. If self–similarity holds, C and t will follow the same intrinsic scales between the two tests as the parameters C_0 and T. Then, the non–dimensional quotients C/C_0 and t/T will prove to have scale unity, whatever the intrinsic scales λ_Q, λ_M are. In other words, the average plots C/C_0 vs. t/T should be equal in the self–similarity domain.

C_0 and T are common parameters used to obtain non–dimensional plots from experimental concentration curves in many studies dealing with residence time distributions. The variables C/C_0 and t/T are suitable since the equation of tracer mass conservation can be written: $\int_0^\infty \frac{C}{C_0} d(\frac{t}{T}) = 1$, irrespective of flow rate Q and tracer mass M. This continuity equation also shows that the area of this curve is unity, which is the mathematical condition for the non–dimensional plot to be the actual residence time distribution.

Therefore, the experimental work to investigate the similarity in the flow under consideration consists of testing the model with different flow rates (10 runs each test), measuring the conductivity at the outlet pipe and comparing the average residence time distributions. If self–similarity holds, these distributions will show agreement. The experimental program was planned to verify self–similarity for the flow in the vessel as well as to find out the lower and upper limits of the self–similarity domain. The experimental program was divided into two parts. In the first part, discharge pipe I was used (fig.1). This inlet arrangement does not produce any perceptible disturbance at the free–surface (the maximum water discharge tested is 4000 l/h). The aim of the tests with pipe I is to verify self–similarity and find out its lower limits. The relevant non–dimensional parameters for this program are the jet Reynolds number $Re = \frac{vD}{\nu}$, where v–mean jet velocity, D–inlet pipe diameter, ν–kinematic viscosity and the jet Densimetric Froude number $Fr_d = \frac{v}{\sqrt{g'D}}$, where $g' = g\frac{\rho'-\rho}{\rho}$, ρ–density of receiving water (1.00 gr/cm^3) and ρ'–density of traced water, which can be controlled by the density of the tracer solution ($\rho_t \leq 1.15 gr/cm^3$)

In the second part of the experimental program, discharge pipe II was used (fig.1). The free–surface now shows some degree of perturbation. The surface agitation increases as the flow rate increases. The horizontal jet direction, far from the opposite wall, is thought to be responsible for this agitation, whereas the vertical direction of pipe I causes the jet to impinge and spread out over the bottom. The aim of the tests with pipe II is to check if self–similarity continues holding and if an upper limit of the self–similarity domain can be found due to the effect of the free–surface disturbances. For pipe II two kinds of tests were performed: the first one as described and the second one after putting a floating cover on the free surface. This floating cover keeps the atmospheric pressure unchanged but suppresses the surface perturbation completely.

5. Results and discussion

Pipe I tests.- By decreasing Q and keeping the remaining parameters constant, a set of tests with Re and Fr_d both decreasing was planned. If the residence time distributions C/C_0 vs. t/T show agreement, self–similarity domain would be proven over the corresponding range of Re and Fr_d. Furthermore, additional tests were planned for decreasing Re with constant Fr_d and decreasing Fr_d with constant Re in order to recognize the two different scale effects. This can be achieved by varying Q and ρ_t, keeping the remaining parameters constant. Table 1 displays the complete set of tests. They are plotted in a $Fr_d - Re$ plane in Fig.2.

Figures 3.1–3.9 are the C/C_0 vs. t/T curves obtained as the average of 10 runs of tests 1-9. Tests 1,2 and 3 show a very good coincidence, although number 3 exhibits a little damping. This slight tendency becomes an abrupt change of form in tests 4 and 5, demonstrating that the self–similarity domain fails. Whether viscous or densimetric forces are responsible for this abrupt change is elucidated in test 6 in which Fr_d has the same value as in test 3 and Re has the same value as in test 5. Since the curve in no.6 recovers the form of no.3, this makes clear that at $Fr_d \simeq 17.0$ the self–similarity fails due to the effect of densimetric forces. The following tests are designed to find the starting point of viscous forces scale effect. Tests 7,8 and 9 keep Fr_d constant whereas Re decreases. Tests 7,8 show a very good agreement with tests 3 and 6. Finally, the expected change of form is found in test 9.

Therefore, the limiting value of Re is found to be about 11000. Self-similarity holds for values of Re larger than 11000 and for values of Fr_d larger than 17. It must be emphasized that these limiting values of Re and Fr_d are specific for the geometry illustrated in Fig.1 (pipe I). The scale effects produced by exceeding these self–similarity limits are clear in figs.3.1, 3.5 and 3.9. As a consequence of the change of form, the mean residence times t_m (centre of gravity of the area, table 1) in the case of an incorrect model operation (a flow rate so low that $Fr_d < 17$ or $Re < 11000$ or both) are slightly greater ($\simeq 5$ %) than within the self–similarity domain for correct model operation.

Pipe II tests.- The test results are presented in fig.3. The residence time distributions for different inlet arrangements (pipes I and II) are different, since the change in depth or direction of the jet changes the flow pattern. However, residence time distributions also feature a remarkable coincidence in pipe II tests, in spite of the disturbances at the free–surface. Nevertheless, if some scale effect related to the free–surface perturbation was hidden in figs.3.10–3.13, the tests with the floating cover would reveal a difference in the residence time distributions. But this is not the case, as can be seen by comparing figs.3.10–3.13 with figs.3.14–3.17. Table 1 displays the complete set of tests with pipe II.

These results prove that the self–similarity domain for the specific geometry in Fig.1 (pipe II) still holds when the free surface is not stagnant but showing disturbances of up to $\simeq 10$ mm. Some related results can be found in references [3], [4]. The following physical interpretation may be proposed. The surface perturbation is not produced by an external force, but is due to the velocity fields induced by the jet, which can be assumed to be self–similar. Thus, the magnitude of point mean velocities will increase at the same rate as the discharge increases, so that the velocities close to the free surface will end up as able to deform this flexible boundary. However, the flow field remains essentially unchanged in this situation. The resisting force against the free surface deformation is the surface tension force. Therefore, the scale effect of surface tension forces would be negligible.

6. Conclusions

The existence of self–similarity for the three–dimensional flow in the vessel, (Fig.1) in the presence of rigid boundaries as well as a free surface, has been proven. The self–similarity properties enable us to operate the model at any discharge scale within the so–called self–similarity domain.

There are two lower limits to this domain, corresponding to the effect of viscous and densimetric forces. If these limits for the model's operation are exceeded, scale effects will arise, resulting in greater mean residence times than for a correct model operation.

Within the self–similarity domain the mixing process in the vessel is driven by the momentum flux of the jet, which is dominant with respect to the densimetric and viscous forces. As the discharge increases, the velocity fields induced by the jet are more intense, until they manage to overcome the resistance to the free surface deformation. In spite of this upper limit being exceeded (the free surface experiences perceptible disturbances), the self–similarity continues holding, at least as regards the residence time distributions. This fact is interpreted in the sense that no relevant scale effect is attributable to the surface tension when a free surface is present.

References

[1] - Martín Vide, J.P.; Dolz, J.; Berga,L. "Hydraulic model study of the residence time of water flowing through circulation vessels" (in Spanish).*Revista de Obras Publicas.* Nov.1988, pp.1035-1042

[2] - Martín Vide, J.P.; Cisneros, A.; Dolz, J. "Similarity for turbulent mixing vessels. Reynolds number effect". *Proceedings of the XXIII Congress I.A.H.R.* Ottawa, Aug.1989, vol.A, pp.231-238

[3] - Dat, J; Fonade, Ch. "Sur la similitude des écoulements provoqués par des jets". *La Houille Blanche.* 6, 1978, pp.435-442

[4] - Kobus, H. *Hydraulic Modelling.* Verlag Paul Parey. Hamburg, 1980. Case study in Chapter 5, pp.101-104

Figures

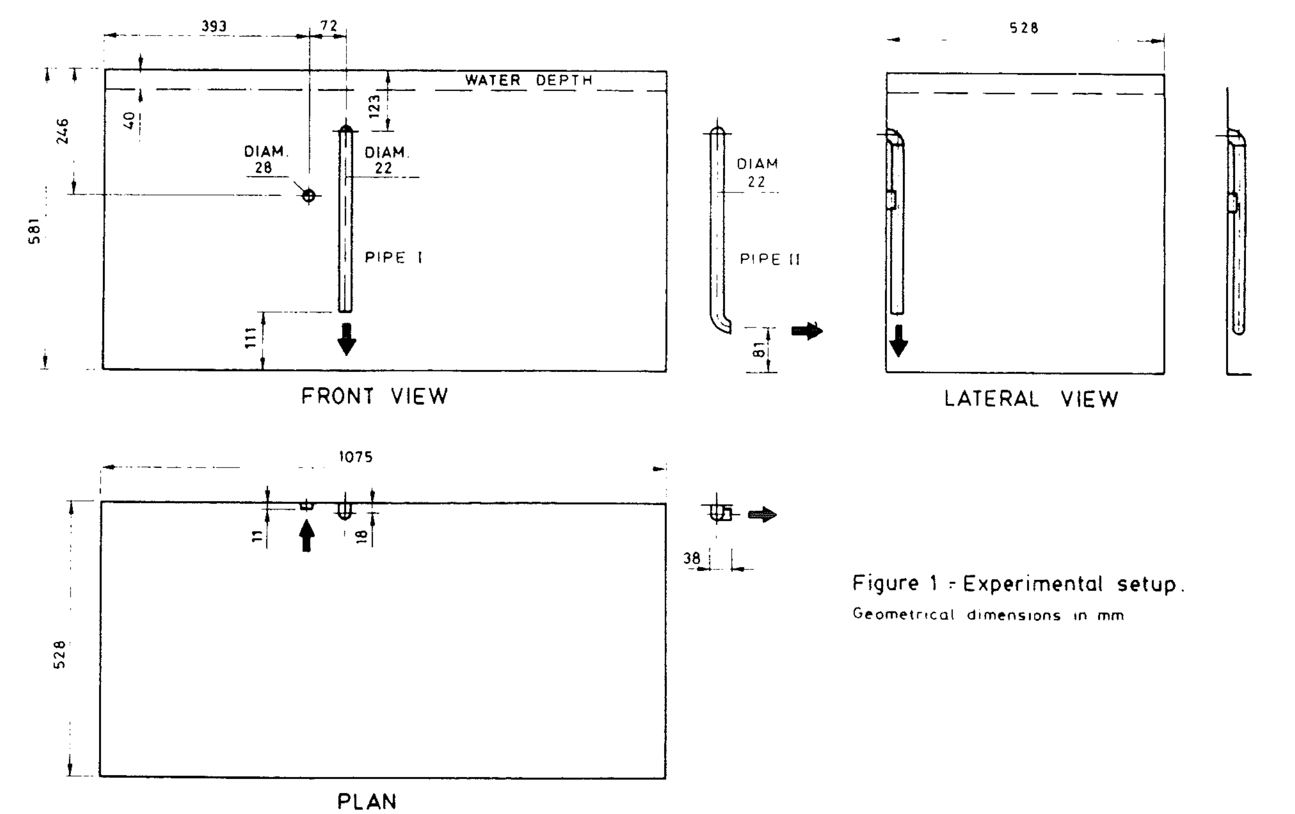

Figure 1 - Experimental setup.
Geometrical dimensions in mm

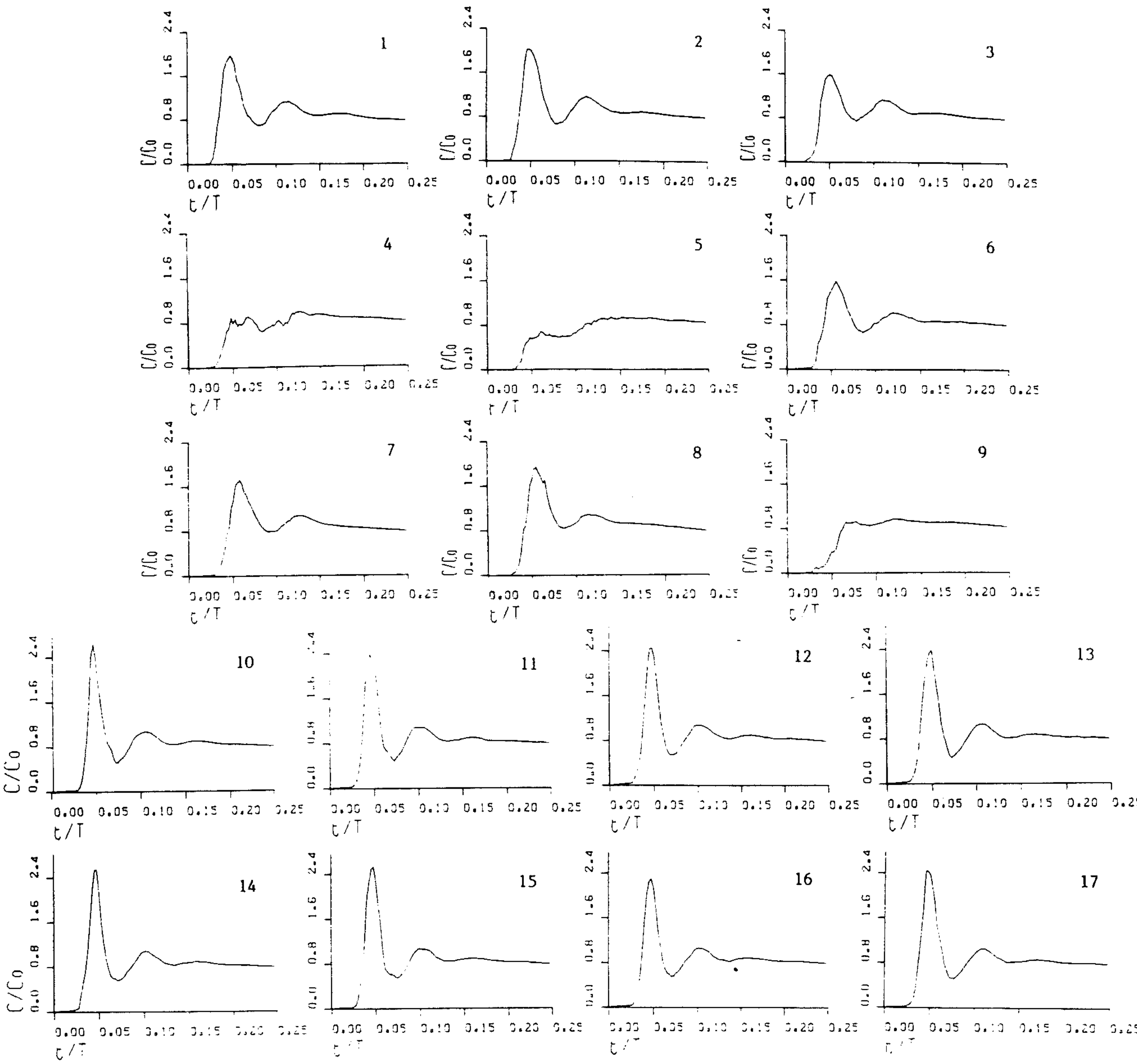

Figure 3 .- Non-dimensional residence time distributions for tests 1-17.
Average plots of 10 runs.

nr	pipe	surface	Q (l/h)	ρ_t (g/cm^3)	$\frac{\rho'-\rho}{\rho}\cdot 10^2$	Re	Fr_d	T (min.)	t_m/T
1	I	stagnant	3000	1.15	1.03	48200	46.6	6.1	1.012
2	I	stagnant	2000	1.15	1.49	32200	25.8	9.2	1.012
3	I	stagnant	1500	1.15	1.93	24100	17.0	12.3	1.020
4	I	stagnant	1400	1.15	2.07	22500	15.3	13.2	1.051
5	I	stagnant	1200	1.15	2.36	19300	12.3	15.3	1.066
6	I	stagnant	1200	1.08	1.25	19300	16.9	15.3	1.017
7	I	stagnant	1000	1.045	0.80	16100	17.6	18.4	1.030
8	I	stagnant	700	1.017	0.41	11300	17.2	26.3	1.022
9	I	stagnant	500	1.007	0.21	8000	17.0	36.8	1.054
10	II	disturbed 2.7 mm	2500	1.10	0.82	40200	38.9	7.4	1.021
11	II	disturbed 3.8 mm	3000	1.10	0.68	48200	51.3	6.1	1.019
12	II	disturbed 5.6 mm	3500	1.10	0.58	56300	64.9	5.3	1.019
13	II	disturbed 9.5 mm	4094	1.10	0.48	65800	82.8	4.5	1.021
14	II	covered	2500	1.10	0.82	40200	38.9	7.4	1.021
15	II	covered	3000	1.10	0.68	48200	51.3	6.1	1.018
16	II	covered	3500	1.10	0.58	56300	64.9	5.3	1.022
17	II	covered	4094	1.10	0.48	65800	82.8	4.5	1.022

Table 1.- Experimental program and results.

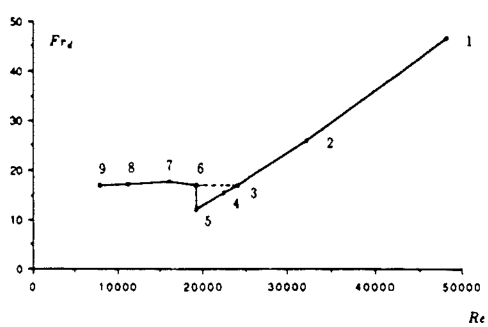

Figure 2 .- Pipe I experimental program plotted in a Fr_d-Re plane

Longitudinal Dispersion in Overland Flow of Wastewater

Donald Dean Adrian, PhD, PE
Professor of Civil Engineering
Louisiana State University
Baton Rouge, LA 70803-6405
504-388-8636

C. James Martel, PhD, PE
Research Environmental Engineer
US Army Cold Regions Research and Engineering Laboratory
Hanover, NH 03755
603-646-4100

Abstract

A series of experiments were conducted to measure dispersion in an overland flow system. The overland flow system consisted of three parallel grass covered areas 30.5 m long, and 2.9 m wide, and sloping at 5 percent. Primary wastewater was applied at the upper end of the slopes and was collected at the lower end of the slope. Steady hydraulic flow was established prior to a line source of chloride tracer being applied to the upstream end of the slope. The chloride tracer concentration was measured at the outlet of the overland flow system. Data were collected during three consecutive years so that the effects of grass growth and slope maturation on dispersion could be studied.

Twenty four, twenty five, and eight dispersion measurements were made in years one, two, and three, respectively. The average velocities during the dispersion measurements varied from 3×10^{-3} m/s to 2.5×10^{-2} m/s. Longitudiual dispersion coefficients varied from a low of 2×10^{-2} m^2/s to a high of 3×10^{-1} m^2/s. Phenomena which lead to difficulties in relating the dispersion measurements to velocity include the continual changing growth patterns of the grass, grass harvesting patterns, and the development of erosion channels on the slope.

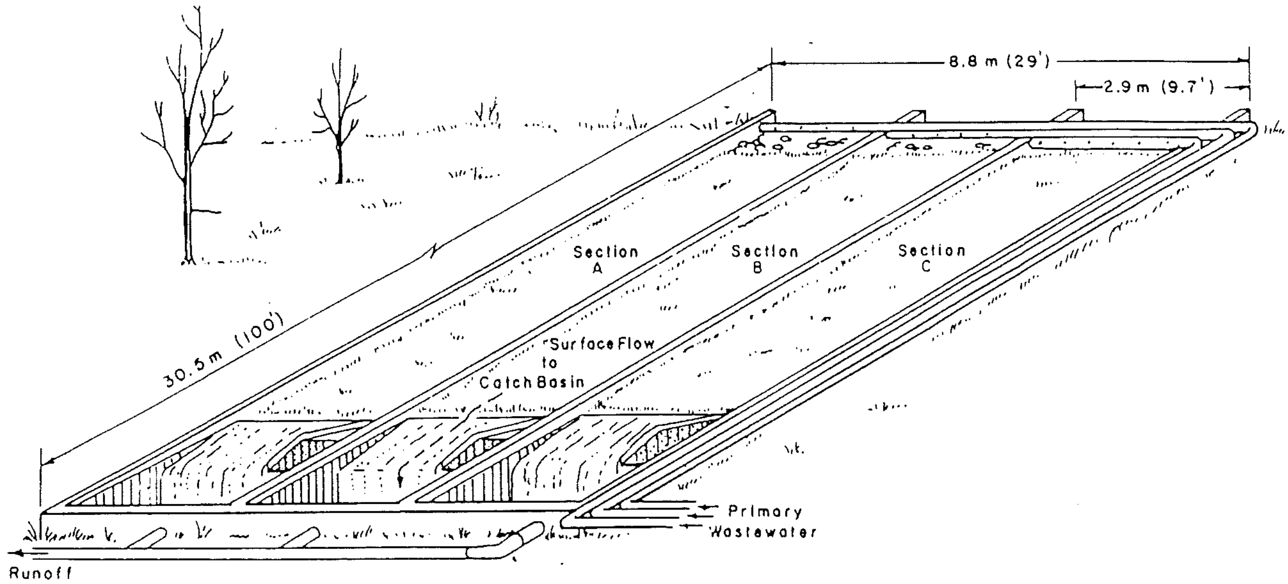

Figure ~~2~~ 1. Schematic of CRREL overland flow test site.

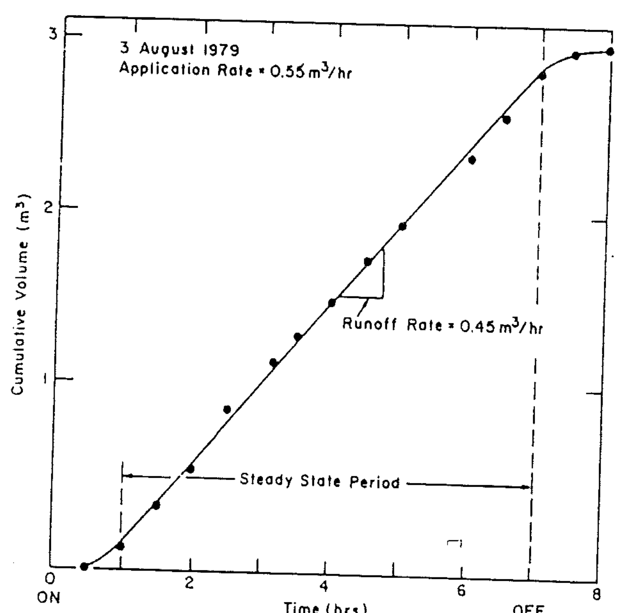

Figure ~~3~~ 2. Typical runoff hydrograph.

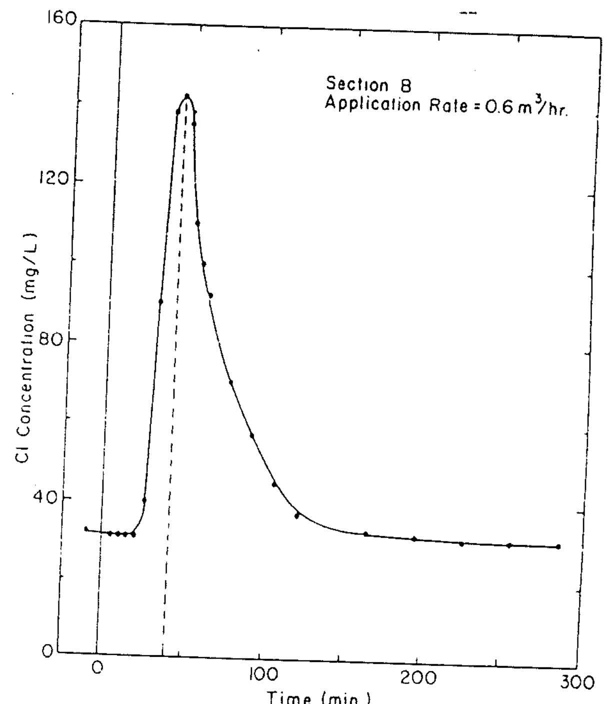

Figure ~~4~~ 3. Typical chloride response curve for measuring detention time.

THE MODEL LAW FOR TRANSVERSE MIXING PROCESSES

by

Vincent H. Chu
Department of Civil Engineering and Applied Mechanics
McGill University, Montreal, Quebec H3A 2K6, Canada

Abstract

Flows in natural waterways are affected by wide variation of bed material and channel topography. The large-scale turbulence, generated by the transverse shear, controls the mixing processes. The small-scale bed-generated turbulence may be ignored. Hence, it is possible to achieve dynamic similitude of the mean flow field and, at the same time, the transverse mixing processes, using distorted-scale physical models. The bed-friction coefficient in the model should be selected according to the model law originally derived for the mean flow; that is, the model-to-prototype ratio of the friction coefficients, $(c_f)_r$ should be chosen to be equal to the vertical-to-horizontal distortion ratio, Z_r/X_r.

Introduction

Most natural waterways have wide variation of roughness, depth, and velocity of the flow across the width and longitudinal section. The horizontal length scale of these lateral and logitudinal variations is usually very large compared with the water depth. The flows around the islands as shown in the aerial photographs of Figs. 1(a) and 1(b) are examples. The cross-stream diameters of the islands (D in the figures) are 280 m and 560 m, while the water depths in the region around the islands are only two to three meters. Turbulence in the wakes of these islands is characterized by two distinct length scales. The large-scale turbulence, generated by transverse shear, has a horizontal length scale comparable to the diameter of the island. The small-scale turbulence, generated by the vertical shear and limited by the water depth, are not visible because their length scale is small compared with the resolution of the photographs.

Physical models may be constructed to simulate these transport processes in natural waterways. However, it is not possible to obtained the model-and-prototype similarity of the mean flow and, at the same time, the similitude of the bed-generated turbulence.

Figure 1: Aerial Photographs of Flows around Islands in Rupert Bay, Quebec; (a) D = 280 m, h = 3 m, c_f = 0.0056, L = 290 m, $c_f D/4h$ = 0.13; (b) D = 560 m, h = 2 m, c_f = 0.0062, L = 270 m, $c_f D/4h$ = 0.43. From Babarutsi, Ganoulis and Chu (1989).

It is the aim of in this note to show that the large-scale turbulence is the one controlling the transverse mixing processes in natural waterways and, hence, the similitude requirement for the bed-generated turbulence may be ignored.

The Wake of a Circular Island

The significance the transverse-shear generated turbulence, may be demonstrated by considering the disturbance generated by a circular island of diameter, D, in an open-channel flow of velocity, U_1 and depth, h. Turbulence is generated in the wake of this circular island by the transverse shear which is related to the velocity defect of the wake. As the wake increase in width, the velocity deflect in the wake reduced, but the eddy diffusivity associated with the turbulent motion stay constant.

The eddy diffusivity of this transverse-shear generated turbulence in the wake of the circular cylinder is $\nu_t = 0.035 D U_1$ (Townsend, 1956). The eddy diffusivity of the bed-generated turbulence in a wide open-channel of uniform depth is $\nu_b = 0.13\sqrt{c_f/2}\, U_1 h$ (Noke and Wood, 1988). in which c_f is the bed-friction coefficient. The ratio of the two eddy diffusivites is

$$\frac{\nu_t}{\nu_b} = 0.26\sqrt{\frac{2}{c_f}}\frac{D}{h} \tag{1}$$

Thus, $\nu_t/\nu_b = 5.8\ D/h$ for a typical value of $c_f = 0.004$. According to this relation, if the diameter of the circular island is twice as large as the water depth, the eddy diffusivity associated with the transverse-shear generated turbulence would be more than ten times greater than the diffusivity due to the bed-generated turbulence. Thus the contribution due to transverse shear generated turbulence is quite substantial. If the wake disturbance is allowed to grow in width, the horizontal length scale of the wake eventually will become very large compared with the water depth.

The Effect of the Bed-friction Inluence

But the bed friction effect becomes important as the horizontal length scale of the transverse motion becomes large compared with the water depth. The bed-friction effect on the transverse-shear generated turbulence has been the subject of a series of recent investigations. The large-scale transverse motions created by various transverse shear flows, such as the recirculating flows (Babarutsi, Ganoulis and Chu, 1989), jets (Chu and Baines, 1989), mixing layers (Chu and Babarutsi, 1988), and wakes (Ingram and Chu, 1987), were all found to be affected by the stabilizing influence of the bed-friction. Under this stabilizing influence, the transverse disturbance in a uniform flow will diminish over a distance of about one friction length scale, h/c_f. The horizontal length scale of the transverse motion is limited to about $0.1\,h/c_f$, that is, one tenth of the bed-friction length scale.

The island wake bubbles as shown in Fig. 1 are examples of this bed-friction influence. The wakes of the islands do not increase in width without bound, but are limited in length scale under the bed friction influence. The lengths of the wake bubbles as marked in figure are $L = 290$ m and 270 m, which are large compared with the water depth, but comparable to the friction length scales of $h/c_f = 535$ m and 323 m for the flows in Figs. 1(a) and 1(b), respectively.

In natural waterways, the bed-topography are quite irregular with wide variation of bed-material, depth and flow velocity. Large-scale transverse motion are created from time to time as the local transverse shear exeeds the critical condition defined by Chu, Wu and Khayat (1983). These transverse motion generated by the irregular topography of the waterways is the dominant mechnanism affecting the mixing processes. It is important that the bed topography is reproduced faithfully in the physical model. Features of the topography which are small compared with the water depth may be treated as bed roughnesses. However, for model-to-prototype similarity of the mean flow, the bed roughness is not to be scale down according to the vertical scale.

Simlarity Requirements for the Depth-averaged Flow Field

The similitude requirment is deduced from an inspection of the equations of motions:

$$\frac{\partial \tilde{u}h}{\partial x} + \frac{\partial \tilde{v}h}{\partial y} = 0 \tag{2}$$

$$\begin{aligned}\frac{1}{St}\frac{\partial \tilde{u}}{\partial t} + \tilde{u}\frac{\partial \tilde{u}}{\partial x} + \tilde{v}\frac{\partial \tilde{u}}{\partial y} &= -\frac{1}{Fr^2}\frac{\partial \tilde{\zeta}}{\partial x} - Be\frac{\tilde{u}\sqrt{\tilde{u}^2+\tilde{v}^2}}{2h} \\ &+\frac{1}{h}\frac{\partial}{\partial x}[\nu_s(\frac{\partial \tilde{u}}{\partial x} - \frac{\partial \tilde{v}}{\partial y})] + \frac{1}{h}\frac{\partial}{\partial y}[\nu_s(\frac{\partial \tilde{u}}{\partial y} + \frac{\partial \tilde{v}}{\partial x})]\end{aligned} \tag{3}$$

$$\begin{aligned}\frac{1}{St}\frac{\partial \tilde{v}}{\partial t} + \tilde{u}\frac{\partial \tilde{v}}{\partial x} + \tilde{v}\frac{\partial \tilde{v}}{\partial y} &= -\frac{1}{Fr^2}\frac{\partial \tilde{\zeta}}{\partial y} - B_e\frac{\tilde{v}\sqrt{\tilde{u}^2+\tilde{v}^2}}{2h} \\ &+\frac{1}{h}\frac{\partial}{\partial x}[\nu_s(\frac{\partial \tilde{v}}{\partial x} + \frac{\partial \tilde{u}}{\partial y})] + \frac{1}{h}\frac{\partial}{\partial y}[\nu_s(\frac{\partial \tilde{v}}{\partial y} - \frac{\partial \tilde{u}}{\partial x})]\end{aligned} \tag{4}$$

in which $(\tilde{u}, \tilde{v})$ in the horizontal component of the depth-independent velocity vector, $\tilde{\zeta}$ the free surface elevation, (x, y) the cartesian co-ordinates on the horizontal plane, and

$$\nu_s = c_\nu h\sqrt{\frac{c_f}{2}}\,(\tilde{u}^2+\tilde{v}^2)^{\frac{1}{2}}, \tag{5}$$

the eddy viscosity associated with the bed-generated turbulence. The variables in the above relations are dimensionless, and are normalized by the horizontal length scale, X, the vertical length scale, Z, the velocity scale, V, and the time scale, T, as follows:

$$x = \frac{x^*}{X}, \quad y = \frac{y^*}{X}, \quad \tilde{u} = \frac{\tilde{u}^*}{V}, \quad \tilde{v} = \frac{\tilde{v}^*}{V}, \quad \tilde{\zeta} = \frac{\tilde{\zeta}^*}{Z}, \quad h = \frac{h^*}{Z}. \tag{6}$$

The variables with dimension are denoted by the superscript '$*$'.

To determine the similitude requirements for the transverse-shear generated turbulence, the depth-independent part of the velocity is further separated into parts; i.e.,

$$\tilde{u}(x,y,t) = U(x,y,t) + u'(x,y,t) \tag{7}$$

in which U represents the mean flow and u', the velocity fluctuation of the large-scale transverse-shear generated turbulence. The Reynolds stress equations for the transverse-shear generated turbulence can be derived, but it does not lead to new dimensionless parameters. (see, e.g., Babarutsi and Chu, 1989).

The relevant dimensionless parameters, which appears in the governing equations, are:

$$Fr = \frac{V}{\sqrt{gZ}} = \text{Froude number}$$

$$St = \frac{VT}{X} = \text{Strouhal number}$$

$$Be = \frac{c_f X}{Z} = \text{Bed friction number}$$

$$c_f = \frac{\tau_b}{\rho V^2} = \text{Bed friction coefficient}$$

The model and the prototype will be dynamic similar if the numerical values of these dimensionless parameters are the same for the model and the prototype. Equality of these dimensionless parameters between the model and the prototype leads to the following requirments:

$$V_r = g_r^{\frac{1}{2}} Z_r^{\frac{1}{2}}, \tag{8}$$

$$T_r = X_r / V_r = X_r\, g_r^{-\frac{1}{2}} Z_r^{-\frac{1}{2}}, \tag{9}$$

$$(c_f)_r = Z_r / X_r, \tag{10}$$

$$(c_f)_r = 1 \tag{11}$$

in which $V_r = V_m/V_p, T_r = T_m/T_p, X_r = X_m/X_p, Z_r = Z_m/Z_p, g_r = g_m/g_p, (c_f)_r = (c_f)_m/(c_f)_p$; the subscripts 'p', 'm' and 'r', denote the prototype, the model, and the model-to-prototype ratio, respectively.

Eq. 10 and Eq. 11 can not be satisfied simultaneously in a distorted scale model, since $Z_r > X_r$. Since the bed-generated turbulence is of minor importance in natural waterways the dependent on the eddy viscosity ν_s may be ignored and the requirement of Eq. 11 removed. The result is the similarity requirements given by Eqs. 8, 9, and 10, which are the requirements originally derived for the mean flow (see, e.g., Steven et al., 1942).

The aerial photographs in Fig. 1 may be used as an exmple to demonstrated *the lack of* dynamic similariy between a distorted scale model and its prototype. Dynamic similitude is not achieved in this example because the friction coefficients around the two islands are approximately the same. The clear-water wake of the large island (the prototype) has a rather lower level of sediment suspension. The turbid wake of the small islands (the model) is marked by high level of turbulent mixing events.

For these two islands, the horizontal length scale ratio is X_r = 280:560; the vertical length scale ratio is Z_r = 3:2; this gives a distortion ratio of $Z_r/X_r \simeq$ 3:1. Hence, the bed-friction coefficient around the small island should be about 3 times greater than the friction coefficient around the large island, according to the model law given by Eq. 10.

Manning-Strickler Empirical Relation

The grain-size of the roughness element, k_s, may be determined using the Manning-Strickler empirical relation:

$$c_f = 0.030\,(\frac{k_s}{h})^{\frac{1}{3}} \tag{12}$$

According to this relation, $(c_f)_r = (k_s)_r^{\frac{1}{3}}/Z_r^{\frac{1}{3}}$; this requirement and Eq. 10 lead to the following relation for the grain-size ratio:

$$\frac{(k_s)_r}{Z_r} = (\frac{Z_r}{X_r})^3 \tag{13}$$

For a vertical-to-horizontal distortion ratio, $Z_r/X_r = 3$, the relative grain-size in the model will be 27 time greater than the prototype. The island-model may be used as example: a 2 cm pebble in the 2 m depth of water in the prototype will have a model grain-size of 81 cm in the 3 m water depth of the model. The model-grain size is 27% of the water depth in the model! The relative grain size in the model is so large that the Manning-Strickler relation may not be applicable at all. It is this kind of difficulty that make model calibration a requirement in practice.

Modelling of Sediment Transport

The modelling of sediment transport follows the conventional approach (see e.g., Steven et al., 1942). The specific weight, γ, of the movable bed material is selected by the requirement that the value of the entrainment function,

$$F_s = \frac{u_*^2}{\gamma k_s} = \frac{c_f}{2}\frac{(\tilde{u}^2 + \tilde{v}^2)}{\gamma k_s}, \tag{14}$$

in the model be the same as in the prototype; that is $(c_f)_r V_r^2/\gamma_r(k_s)_r = 1$. This requirement and the Manning-Strickler requirement lead to the following relation between the distortion ratio and the specific ratio of the bed material:

$$\frac{X_r}{Z_r} = \sqrt{\frac{\gamma_r}{g_r}} \tag{15}$$

The vertical-to-horizontal distortion ratio, Z_r/X_r, will be 4.06, for a model-bed material with a solid-fluid density ratio of 1.1 (i.e., $\gamma_r = 1 : 16.5$), and $g_r = 1$. It, further more, the grain Reynolds number,

$$Re_* = \frac{u_* k_s}{\nu} = \sqrt{\frac{c_f}{2}}\frac{\sqrt{(\tilde{u}^2 + \tilde{v}^2)}k_s}{\nu} \tag{16}$$

in the model is required to be the same as in the prototype, $(c_f)_r^{\frac{1}{2}} V_r (k_s)_r/\nu_r = 1$. Eliminating of $(c_f)_r$ and V_r, and making use of the Manning-Strickler relation, leads to the more restrictive requirments as follows:

$$Z_r = (\frac{\gamma_r}{g_r})^{\frac{7}{6}}\frac{\nu_r^2}{g_r} \tag{17}$$

$$X_r = (\frac{\gamma_r}{g_r})^{\frac{5}{3}}(\frac{\nu_r^2}{g_r})^{\frac{9}{7}} \tag{18}$$

Using a model-bed material with a solid-fluid density ratio of 1.1, the vertical length scale ratio, Z_r, will be 1:26.3, and a horizontal length scale ratio, X_r, 1: 107, if the gravity ratio, $g_r = 1$, and viscosity ratio, $\nu_r = 1$. These requirements are inflexible. More flexible solution may be obtained if the condition for the grain Reynolds number is relaxed. But, this and other details pertaining to the art of sediment-transport modelling will not be considered here.

Modelling of Stratified Flows

The governing equations for one-layer stratified flow is the same as Eqs. 2 to 5, except that gravity g is replaced by the reduced gravity $g' = g(\Delta\rho)/\rho$ and the bed-friction coefficient is replaced by interfacial friction coefficient, c_{fi}. Thus the model law:

$V_r = g'^{\frac{1}{2}}_r Z_r^{\frac{1}{2}}, T_r = X_r/V_r = X_r g'^{-\frac{1}{2}}_r Z_r^{-\frac{1}{2}}, (c_{fi})_r = Z_r/X_r$. These requirements have been used by Harleman and Stolzenbach (1967) in modelling cooling water discharge from power plants. The model law is applicable for two-layer stratified flows, if the interfacial friction coefficient is assumed to depend on the relative roughness and the Reynolds number in the same way as the bed-friction coefficient.

Conclusion

A model law for transverse mixing processes in natural waterways are derived based on a depth-averaged formulation. The effect of the bed-generated turbulence and the effect of secondary current are ignored because these effects are small in natural waterways, compared with the effect of the transverse-shear generated turbulence. The mixing associated with the bed-generated turbulence and the secondary current is exaggerated in a distorted scale model; and it may have an undesirable effect at the outfall where mixing is three-dimensional. This, and other difficulties pertaining to the art of physical modelling, has to be corrected by judgements which may depend on circumstance.

References

Babarutsi, S., Ganoulis, J. and Chu, V. H. (1989) "Experimental investigation of shallow recirculating flows," *J. Hydraulic Engineering,* Vol. 115, No. 7, pp. 906-924.

Chu, V. H. and Babarutsi, S. (1988) "Confinement and bed-friction effects in shallow turbulent mixing layers," *J. Hydraulic Engineering,* Vol. 114, No. 10, pp. 1257-1274.

Chu, V. H. and Babarutsi, S. (1989) "A k-ϵ model for depth-averaged flow calculation," *Proceedings of the 3rd National Conference on Hydraulic Engineering,* pp.999-1004.

Chu, V. H. and Baines, W. D. (1989) "Entrainment by a buoyant jet between confined walls," *J. Hydraulic Engineering,* Vol. 115, No. 4, pp. 475-492.

Chu, V. H., Wu, J.-H. and Khayat, R. E. (1983) "Stability of turbulent shear flows in shallow channel," *Proc. 20th Congress of IAHR,* Moscow, U,S.S.R., Vol. 3, pp. 128-133.

Harleman, D. F. R. and Stolzenbach, K. (1967) "A model study of thermal stratification produced by condenser water discharge," M. I. T. Hydrodynamic Laboratory, Tech. Rept. No. 107.

Steven, J. C. et. al. (1942) *Hydraulic Models,* ASCE Manuals of Engineering practice, No. 25, prepared by the Committee of the Hydraulic Division on Hydraulic Research.

Townsend, A. A. (1956) *The Structure of Turbulent Shear Flows,* Cambridge University Press, New York.

OBSERVATION OF THE RIVER CLOSURE AT THE BAISHAN HYDROELECTRIC PROJECT AND VERIFICATION BY MODEL

Xu Bingheng[1] and Li Xinzhou[2]

ABSTRACT

Discussions of the paper presented are focused on the design observation and model test verification of the construction closure of Baishan hydropower plant, which is a large-scale hydroelectric project with total installed capacity of 1500 MW, built on the Second Songhua river, the river closure of which was achieved at the dam site in October, 1976.

1. INTRODUCTION

The river closure at Baishan hydropower plant was executed in October, 1976. When the actual discharge was 118 m^3/s and the max. flow velocity was 4.81 m/s with the max. water level difference in the gap being 1.28 m. The two-direction vertically closing method with double closing dikes at upstream and downstream respectively was adopted. Approximately a total quantity of 20 000 m^3 ripraps were consumed for the closure with max. weight of single rock block being about 2.5 t. In the following presented are the brief account of the closure design, prototype observation and verification by model test.

2. CLOSURE DESIGN

The dam of Baishan hydropower plant is a concrete gravity arch one, 149.5 m high, 676.5 m arc length at its top, consisting of 40 monoliths. Multi-phase cofferdams and open channels connected with bottom outlets were adopted in construction diversion.

The first-stage diversion works were to the right of No.13 monolith including a longitudinal concrete cofferdam and two diversion bottom outlets with an invert elevation of 285.0 m, 9m×21m entrance and 9m×14.2m exit (width by height), and an open channel with 20m bottom width at upstream and downstream.

The second-stage diversion structures were at the left bank composing of two earth-rockfill cofferdams, one at the upstream and the other downstream, designed to protect against once-in-ten-year frequence flood with a discharge being 2910 m^3/s. Each one of the cofferdams was accompanied with a closing dike, 8 m wide at the top, 220 m axis spacing between the dikes. The layout of the axes of the open diversion channels, bottom outlets as well as the upstream and downstream earth-rockfill cofferdams are illustrated in Fig 1.

---

1. Senior Expert, Institute of Research, Songliao conservancy comm. P.R.China.

2. Senior Engineer, Institute of Research, Songliao conservancy comm. P.R.China.

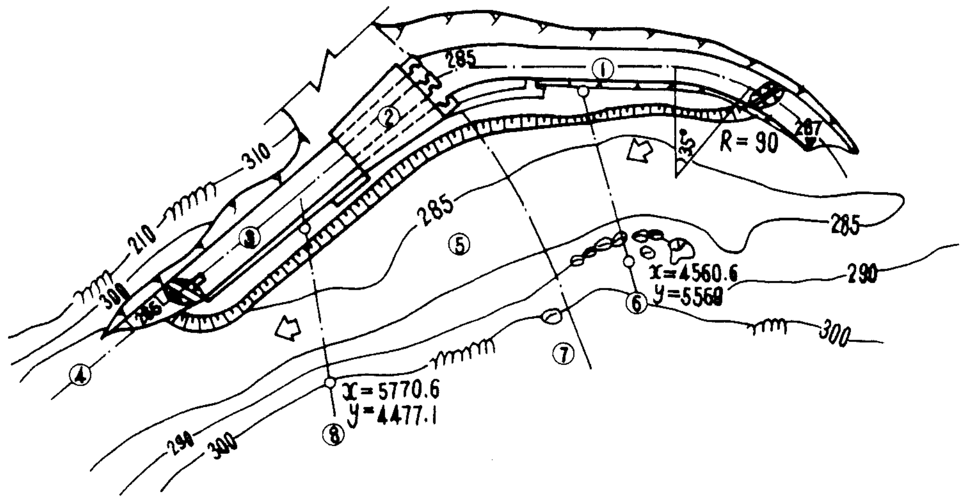

Fig.1 Layout of diversion Cofferdams of Baishan Hydropower Plant ①upstream open channel ②bottom diversion outlets ③downstream open channel ④central line of the open channel ⑤the Second Songhua river ⑥axis of the upstream rockfill closure dike ⑦axis of the arch dam ⑧axis of the downstream rockfill closure dike.

3. RIVER CLOSURE OBSERVATION

The river closure process started on Oct.15.1976. When the river discharge was 135 m^3/s. The construction was conducted with vertically closing method from the right and left banks simultaneously, both for the upstream and the downstream cofferdams. The actual approaching elevations for upstream and downstream rockfill closing dikes were 293.5 m and 292.0 m respectively. The parts of cofferdams at the entrance and exit of the open channels and water-resisting rock barriers were brocken off by blasting at 12 noon of Oct.17. and the river closure succeeded at 9 a.m. on Oct.21 when the inflow was 118 m^3/s. The discharges measured at the open channel and gaps were 90.2 m^3/s and 27.8 m^3/s respectively when the water surface widths of upstream and downstream gaps were 6.7 m and 11.1 m, the max. water head difference were 1.28 m and 0.2 m, and the max. velocities were 4.81 m/s and 2.41 m/s respectively before the river closure. Twenty 20t self-dumping trucks for each shift were employed for rockfill material conveyance, a total of 53 trucks were employed on the very day of river closure. The borrow areas were about 1 and 2 km downstream from the dam site for the right and left banks respectively. Three electric shovel of 3,4 and 6m^3 capacity separately were adopted for loading while D_{80} type dozers were for material leveling and closing progress was with the max. dumping intensity being 2400 m^3/shift. Show in Table 1 is the graduation of the ripraps used.

The diameters of rock pieces dumped in the course of river closure were greater than usual, the graduation was estimated as follows; about 30 percents of smaller than 200mm particles, 40 percents 200 to 400mm and about 30 percents of larger than 400 mm.

In the course of diversion, closing progress and hydraulic parameters were observed, see Table 2 for the observed results. The schematic closing progress along the axis of upstream and downstream rockfill closing dikes was illustrated in Fig. 2.

Table 1 Graduation of Ripraps

Diameter of rock particle (cm)	< 5	5 ~ 20	20 ~ 40	> 40
Right bank (%)	60	20	15	5
Left bank (%)	20	20	30	30

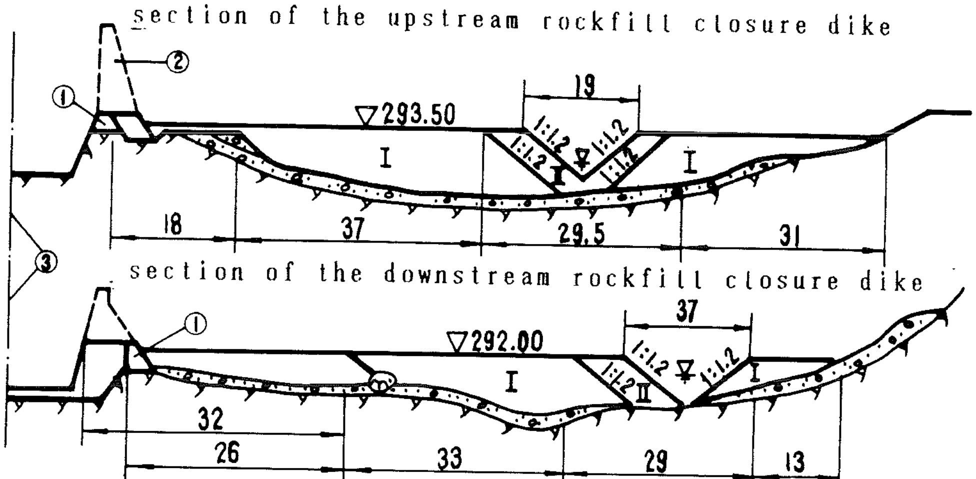

Fig. 2 The Closing Progress Sections of Upstream and Downstream Rockfill Closure Dikes
① first-stage cofferdam ② longitudinal concrete cofferdam
③ central line of open diversion channel
I— finished from 15 to 17 of Oct. 1976.
II— finished from 17 to 18 of Oct. 1976.

4. MODEL TEST VERIFICATION

The closure progress was in-lab. verified with an integral model, geometric scale $\lambda_L = 40$, simulated range of which was 350 m from dam axis both for upstream and downstream , including the whole open diversion channel. In addition, the rectification test was conducted on the similarity of river roughness. The situations verified by the model are: (1) both the discharge of river course and that at the closure mouth are 126 m^3/s, and the water surface widths at the closure mouths of upstream and downstream cofferdams are 18.1 m and 20.2 m respectively, before the entrance and exit of open channel were brocken off by blasting. (2) The actual river discharge is 118 m^3/s whereas that of the open channel and that at the closure mouth are 98.6 m^3/s and 19.4 m^3/s respectively, the water surface widths at upstream and downstream closure mouths are 7.7 m and 11.1 m respectively. The results of model verification in comparison to the prototype observation are listed in Table 3, from which it can be seen that as long as the river inflow, the locations

Table 2. Measured Results in Progress of River Closure at Baishan Hydropower Station

Time			10							
	month		10							
	day		15	16	17	18	19	20	21	22
	hour		8,00	8,00	8,00	8,00	8,00	8,00	8,00	8,00
Discharge (m^3/s)	river inflow		135	129	126	118	115	112	110	110
	closure mouth		135	129		19.4				
	open channel		0	0		98.6				
Water level (m)	U.C.	upstream	288.12	288.18	288.67	289.38	289.38	289.34	289.40	289.55
		downstream	288.10	288.05	288.12		288.10			
	D.C.	upstream	288.08	288.06	288.18		288.10			
		downstream	288.06	288.04	287.98	287.92	287.91	287.87	287.89	287.98
Accumulative length of closing progress (m)	U.C.	right bank		55.0	57.5	61.5				
		left bank		31.0	31.0	35.0				
	D.C.	right bank			65.0	73.5				
		left bank			13.0	13.0				
Width of closure mouth (m)	U.C		43.7	21.2	18.1	19.6/ 7.7			19.0/ 6.7	
	D.C		41.5	34.3	20.2	21.0/ 11.1			21.0/ 11.1	
Velocity at closure mouth (m/s)	U.C		1.57	1.85	2.87/ 2.92/ 2.79	1.69	1.91/ 3.29/ 4.81			
	D.C		1.35	1.33	1.37/ 1.95/ 2.41	0.99				
Accumulative volume of ripraps (m^3)	U.P			3080	6260	8820	9793	9793	9799	11450
	D.C			2190	4210	6330	6330	6450	6450	7820

Notes,
1. The upstream cofferdam and the downstream cofferdam was abbreviated to U.C and D.C respectively.
2. The entrance and exit of the open channel were broken off at a.m. of Oct.17,1976, closure was achieved from 8,15 to 9,10 a.m. of Oct.21.
3. The water level observation points upstream and downstream the closure mouth were both approximately 20 m away from the axis of cofferdam. Width of closure mouth, top width / water surface width.
4. The flow velocities at closure mouth are listed in a sequence of left, middle and right ; the max. water head difference and max. flow velocity at the mouth of upstream cofferdam prior to river closure were 1.28 m and 4.81 m/s respectively.
5. The calculating bases of the accumulated length of the closing progress were the closing elevation for the toll bank and on base of the left bank top elevation of the open channel for the right bank.

Table 3. Results of Model Verification of Upstream and Downstream Water Levels and Flow Velocities at the Closure Mouths of Upstream and Downstream cofferdams in Comparison Prototype Observation

Time			8,00 a.m. Oct.17.		8,00 a.m. Oct.18.	
			Prototype	Model	Prototype	Model
discharge (m^3/s)	open channel		0	0	98.6	92.0
	closure mouth		126.0	126.0	19.4	26.0
	total		126.0	126.0	118.0	118.0
Upstream Rockfill Cofferdam	closing length (m)	right	57.5	57.5	61.5	61.5
		left	31.0	31.0	35.0	35.0
	water surface width of closure mouth (m)		18.1	18.1	7.7	7.7
	surface flow velocity at the axis of closure mouth (m/s)		2.87/2.92/ 2.79	2.20/2.60/ 2.80	1.91/3.29/ 4.81	1.60/3.20/ 4.40
	upstream water level (m)		288.67	288.68	289.38	289.40
	downsteram water level (m)		288.12	288.12		288.10
Downstream Rockfill Cofferdam	closing length (m)	rigth	65.0	65.0	73.5	73.5
		left	13.0	13.0	13.0	13.0
	water surface width of closure mouth (m)		20.2	20.2	11.1	11.1
	surface flow velocity at the axis of closure mouth (m/s)		1.37/1.95/ 2.41	2.30/2.30/ 2.30	0.99	1.10/1.30/ 1.40
	upstream water level (m)		288.18	288.20		288.00
	downstream water level (m)		287.98	287.88	287.92	287.92

and the widths of water surface of the closure mouth for both the upstream and the downstream cofferdam are equal, the water levels upstream and downstream of the closure mouth and the velocities at the closure mouth measured in the model tests are very close to those of prototype observation and the water surface elevations of corresponding observation points were in very close accordance. In addition, the model flow regimes at the entrance of open channel and at the clsure mouths of upstream and downstream cofferdams are quite similar.

When the river inflow measured 118 m^3/s and the water surface widths at the closure mouths of upstream and downstream cofferdams were 7.7 m and 11.1 m respectively, the entrance water level of the model open channel reached 289.4 m with the discharges through the open channel and closaure mouth of the model being 92 and 26 m^3/s which present 6% difference comparing with the corresponding prototype results of 98.6 m^3/s and 19.4 m^3/s respectively.

5. CONCLUTION

5.1. River Closure Scheme: It is proved to be successful by construction practice that the river closure was accomplished by way of two directional vertically closing method simultaneously from the left and right banks, along double closing dikes of earth-rockfill cofferdams at baishan dam site. the vertically closing method demands simple and easy construction work. In closing process, the sound effects that the lower water head difference, velocities at the closure mouths, the less amount of large rock blocks and lost rockfill materials were can be achieved due to the interaction of the double closing lines of rockfill cofferdams, In addition, the above closing method is relatively reliable, favorable to mechanization of construction making use of local materials, less or not affected by geological and geographical conditions.

5.2. Location of Closure Mouth: The model tests showed that the water level at the entrance of open channel rose to its highest value when the closure mouth of the upstream cofferdam was near the left bank consequently, the open channel inflow was increased by about 30% in comparison to the case wherein the closure mouth was close to the right bank, which then indicates the closure mouth of the upstream cofferdam should be set near the left bank, while the location of the downstream closure mouth had little influence on the discharge of open channel, In execution of river closure, the upstream closure mouth was so located that the distances from banks right and left to the mouth were 61.5m and 35m respectively with satisfactory results. Moreover, it is suggested that the amount of dumped materials and closing length for the downstream cofferdam be greater than that of the upstream one with the closure mouth at downstream being formed earlier than upstream.

5.3. Open Diversion Channel: The hydraulic parameters in river closure are very close related to the discharge capacity of diversion structures and the flood storage capacity of the river course. A favorable flow diversion condition should be created for the purpose of lowering the closing water head and the discharge per.unit width at the closure mouth. The entrance of diversion channel for Baishan project was set on the concave bank of river course with stones protuding out on the opposite bank, functioning as a spur dike, the diversion condition of which was to be fine by prototype observation, the main flow was directed toward to the entrance of the open channel. since the underwater excavation of the entrance and exit of open channel was difficult to execute, especially the stone barriers at the downstream exit were rather hard to treat after blasting, which may result in the increase of discharge at the closure mouth, therefore, the lower protruding heights of stone barriers at the entrance and exit of diversion channel and at the unlining places the better effects achieved.

5.4. Dumping Technique: In execution of river closure, close attention should be paid to the upstream angle development of the closing dike and the flow condition. Whenever the closing progress with ordinary-graded material met with difficulty (e.g. the ordinary-graded rock particles started to be washed away by water flow with 4.5 m/s velocity), it is advisable to dump large block materials with an 45° angle to upstream so as to form an arc protruding upstream, called upstream diversion angle while the ordinary-graded material was placed in the back-draft zone with low velocity. No sooner the too closing dikes began to contact each other at their bottom parts than large amount of dumping materials began to run off, some was conveyed downstream to form a tongue-shapped cushion. In the course of tongue-shapped cushion formation, the upstream angle area should be successively filled with large blocks of rock at high speed to achieve a wide, thick and short tongue cushion instead of a narrow, thin and long one, i.e. to force the front part of closure mouth to shrink rapidly and to increase the disperse area of water flow at the back flow regime in order to reduce the water depth and velocity so that ordinary-graded material could be placed instead of large-sized rock blocks and to control the volume of material lose to be minimum.

5.5. Relation Between Model Test and Prototype Observation: It is shown that the hydraulic factors at different locations, flow regime, the hydraulic parameters of flow division and river closure as well as the characteristics of dumped material and dumping approach in the model tests have good similarity in comparison to the prototype observation when a normal integral model with a linear scale of 1 to 40 was adopted and its boundary condition and the river roughness had good similarity to those of the prototype, which indicates that model tests are reliable for conducting the design and execution of river closure.

Session 14B

Sediment Laden Flows

RELIABILITY OF EXPERIMENTAL AND NUMERICAL METHODS OF HYPER-CONCENTRATED, SEDIMENT-LADEN, AND CLEAR-WATER FLOOD FLOW ROUTING

by M. Nouh

Department of Civil Engineering, Sultan Qaboos University,
P. O. Box 32483 Al-khod, Muscat, Sultanate of Oman.

Abstract

Hyperconcentrated, sediment-laden, and clear-water flood flows were routed using three numerical finite difference methods and measured in a physical model with mobile bed and 18 ephemeral channels. The numerical methods are the explicit Leap-Frog finite difference formulation, the implicit four-point finite difference formulation, and the fixed mesh characteristic method. For mean concentration of suspended sediment equal to or less than 16 gpl in hyperconcentrated flood flows, or 10 gpl in sediment-laden flood flows, the accuracy of the numerical methods in producing results similar to the observations from the ephemeral channels is almost the same as that of the physical model. For higher concentrations of suspended sediments, the accuracy of the numerical methods, while varies from one method to another, is less than that of the physical model. The difference in the accuracy between the physical model and any of the numerical method increases as the mean concentration of suspended sediment increases. The results of the physical model are generally sensitive to distortion ratio more than to model scale of typical grain size and model scale of specific grain weight in fluid.

Introduction

The characteristics of water flows with large amounts of suspended sediment are different from those of clear-water flows. At large concentrations of suspended sediment, the fluid viscosity and density are increased; and turbulence intensity, velocity and sediment concentration distributions, flow resistance and sediment transport capacities are changed. Due to the effect of suspended sediment concentration on flow resistance and on sediment transport capacities, previous investigations (Nouh, 1988) have indicated that the accuracy of commonly used flood routing methods; namely, the constant and variable parameter Muskingum-Cunge methods, and the constant and variable parameter diffusion methods, varies with the characteristics of both flood and suspended sediment flows as well as with the boundary conditions of problem. Another recent study (Nouh, 1990) has shown that the accuracy and efficiency of some second-order accuracy numerical methods; including the Leap-Frog explicit finite difference formulation, the four-point implicit finite difference method, and the fixed mesh characteristics method of routing flood flow with large amounts of suspended sediment are normally less than that of routing clear-water flood flow. The present study is an extension to the above previous on the subject of accuracy of flood routing methods. Its main objectives have been to : (1) investigate the reliability of the above numerical finite difference methods by comparing computed hydrographs with hydrographs measured in 18 ephemeral channels; (2) investigate the reliability of a physical model by comparing hydrographs measured in the physical model with hydrographs measured in the ephemeral channels; (3) study the variation of the physical model reliability with various scale parameters; (4) compare the reliability of the numerical methods with that of the physical model; (5) relate the difference between the reliability of the numerical methods and that of the physical model to various hydrograph and suspended sediment characteristics; and (6) recommend conditions under which experimental and numerical methods can be best utilised.

Characteristics of Data Utilised for the Study

Data collected from 18 ephemeral channels and from a physical model were used to achieve the objectives of the study. The channels are located in the southwest region of Saudi Arabia. In these channels, measurements of discharge and sediment concentration were made during 237 flood hydrographs. The channels are almost straight, and the distance between the upstream (inflow) and downstream (outflow) measuring sections varied from 41.20 km to 89.75 km. The range of the measured peak flowrate was between 1.10 to 5.20 hours, that of peak flowrate was between 138 to 1220 m^3/s, that of hydrograph duration was between 6.50 to 68.0 hours, and that of suspended sediment concentration was between 2.35 to 78.5 gpl. Details of the measurements techniques are reported elsewhere (Nouh, 1986, 1988).

The physical model is a straight plexiglass tilting flume having 18.4 m length, 0.80 m depth, and width adjustable to be in the range between 0.40 to 0.80 m. Bed material was sand composed of desired logarithmic-normal size distribution to suit the model-prototype similarity. Discharge of water was supplied to the flume by a centrifugal pump. An automatically operated valve located in the supply line provided a means of obtaining flowrates which varied with time. Micropropellers and limnimeters located at approximately 4.0 m intervals along the flume centreline provided a means to measure the velocity and the corresponding depth of flow at a certain time. Suspended sediment samples were collected during the rising and falling branches of hydrographs, and at the points of velocity measurements using a system of pumps and regulating valves. Flow discharge, varying from 20 lps to 250 lps during a time interval of 300 seconds, was measured by an electromagnetic flow meter, located 2.0 m from the flume entrance. Details of the measurements techniques can be found elsewhere (Nouh, 1989, 1990).

Different experimental set-ups were performed. Each set-up was designed to provide similarity to observed hydrographs in the ephemeral channels. The model similarity is determined by the vertical and horizontal model scales, denoted as s_y and s_x respectively, by the scale of specific grain weight in fluid "s_w", and by the scale of typical median grain size "s_D". These scales are computed using the available data and a procedure proposed by Yalin and MacDonald (1987). In such a procedure, the scales of gravity acceleration, fluid density, kinematic viscosity, and Froude number are equal to unity. The scale of a quantity is taken as the ratio of the prototype value to the model value of the quantity. The model distortion "s_r" is computed as $s_r = s_x/s_y$.

For each set-up of experiment, clear-water was admitted to the flume. After reaching the bed stability condition, measurements of flow velocities and depths as well as concentrations of suspended sediment were made. Then, an increment of sediment at a predetermined size distribution was injected very slowly to the flow, and the same measurements were made. Table 1 shows the range of data collected during the experiments (more information about data collection and model scales computation in oral presentation).

TABLE 1. Range of Data Collected During the Experiments.

Type of flow	Number of experiments	Average rate of discharge (lps)	Suspended sediment: Mean concentration (gpl)	Suspended sediment: Median diameter (mm)	s_r	s_w	s_D
Hyper-concentrated	68	120-360	3.2-68	0.01-less than 0.1	2.1-63	1.5-67	2.0-65
Sediment-laden	78	100-400	3.1-67	0.10-less than 0.5	2.3-66	1.5-68	2.0-67
Clear-water	22	120-200	less than 1.5		2.0-63	1.5-67	2.0-65

Results and Discussions

The presence of suspended sediment in an open channel fluid flow changes the viscosity of the fluid and the friction slope of the channel. In this study, the friction slope and both dynamic viscosity and mean concentration of suspended sediment were evaluated experimentally under the effect of steady flow conditions. It has been found that the increase in suspended sediment concentration increases the dynamic viscosity of fluid, but decreases the friction slope of channel. Such decrease in the friction slope is believed to be due to the decrease in turbulence (which reduces flow resistance) with the increase of suspended sediment in a fluid flow. The relative dynamic viscosity (defined as the ratio between the measured dynamic viscosity of water with sediment to the dynamic viscosity of clear-water at the same temperature) and the percentage decrease in friction slope (computed as [friction slope in case of clear-water - friction slope in case of water with suspended sediment][100/friction slope in case of clear-water flow]) were plotted against mean concentration of suspended sediment "C", and are shown in Fig. 1. The friction slope was evaluated using Manning formula, with a calibrated Manning coefficient equal to 0.015.

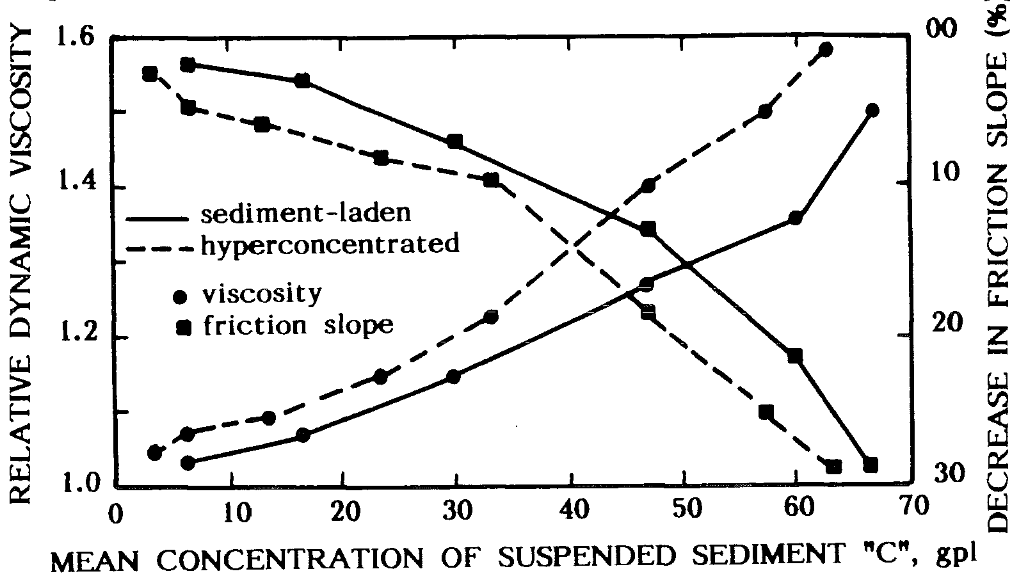

Fig. 1. Variation of viscosity and friction slope with suspended sediment concentration.

Inspection of the above figure indicates that there is a substantial increase in dynamic viscosity and decrease in friction slope due to the increase in suspended sediment in the flow. It is also apparent that the grain size of suspended sediment affects the amount of change of viscosity and friction slope; the finer the grain size (i.e. case of hyperconcentrated flow) the more increase in dynamic viscosity, and the more decrease in friction slope. Such changes of viscosity and friction slope may influence the accuracy of flood routing methods.

In evaluating the accuracy, it has been assumed that the observed data from the ephemeral channels and the measured data from the physical model are correct. For a certain mean concentration of suspended sediment in an observed hydrograph in an ephemeral channel, the out-flow hydrograph was computed by the numerical methods, and was determined using the physical model data and an interpolation technique. In the numerical methods, the space step and time step of 5.0 m and 360 seconds, respectively, and modification in the friction slope due to characteristics of suspended sediment (as in Fig. 1) were considered. The ratios of a hydrograph component predicted by the numerical methods and the physical model to the hydrograph component observed in the ephemeral channel were evaluated, then averaged and plotted against mean concentration of suspended sediment (Fig. 2).

Inspection of Fig. 2 indicates that: (1) the accuracy of the numerical methods, while varies from one method to another, decreases as mean concentration of suspended sediment increases; (2) the accuracy of the numerical methods is generally less than that of the physical model, and the difference in accuracy between the physical model and any of the numerical methods increases as the mean concentration of suspended sediment increases; (3) both the numerical methods and the physical model over-estimate hydrograph peak discharge and under-estimate hydrograph volume, and such over- and under-estimation of hydrograph component increase as mean concentration of suspended sediment increases; (4) the numerical methods displayed accuracy approaching that of the physical model in case of C is less than or equal to 16 gpl in hyperconcentrated flood flows, or in case of C less than or equal to 10 gpl in sediment-laden flood flows.

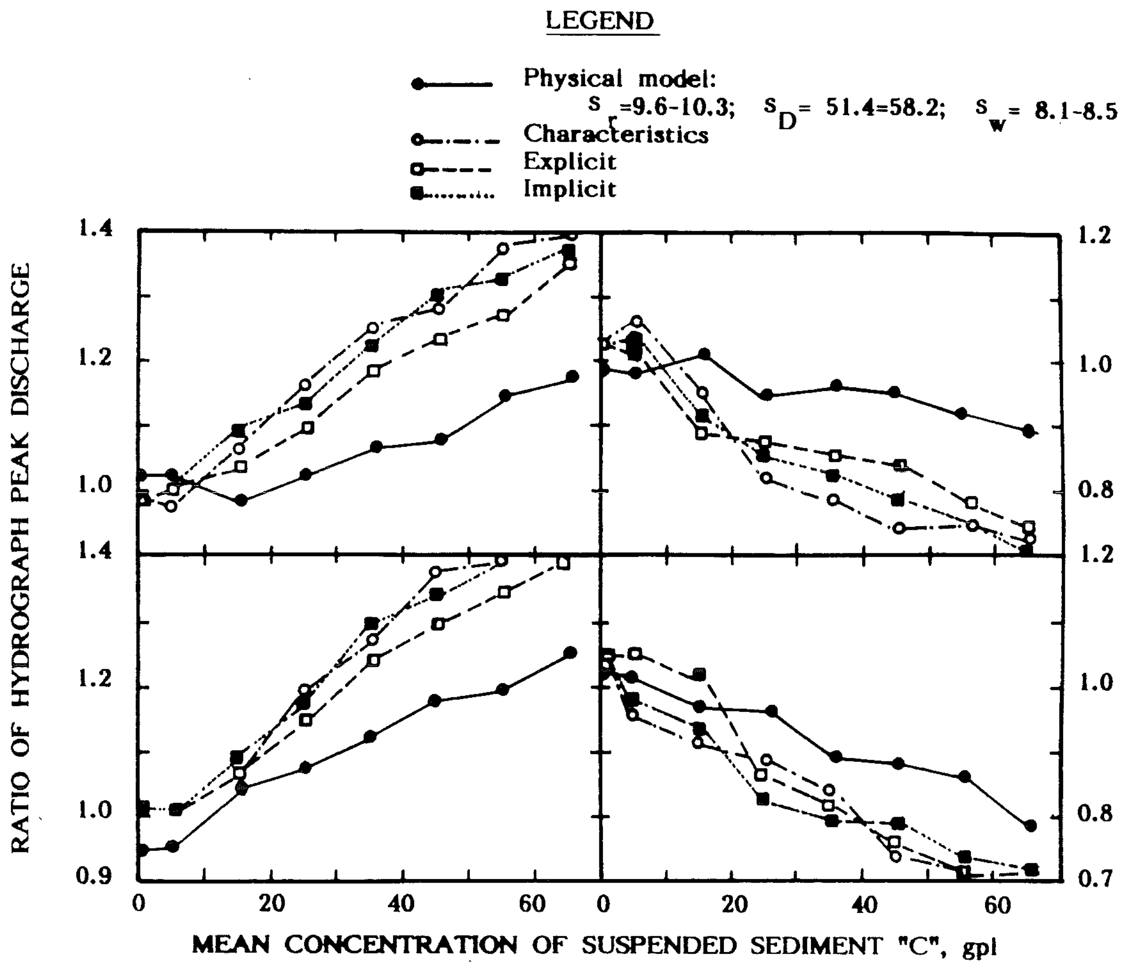

Fig. 2. Average variation of ratios of hydrograph peak discharge and volume with mean concentration of suspended sediment for sediment-laden (top) and hyperconcentrated (bottom) flood flows.

The decrease in accuracy of both the numerical methods and the physical model with the increase of C may be due to the change of friction slope "S_f" with that of C, and due to the effect of lateral flows which have not realistically considered by either the numerical methods or the physical model. More discussions on the accuracy of the numerical methods can be found elsewhere (Nouh, 1990).

The lateral flow, which varies with time and along any of the ephemeral channels, is ignored by the physical model. Because there is generally considerable lateral outflow from an ephemeral channel during the rising branch of hydrograph (i.e. beginning of storm) and lateral inflow to the channel during the falling branch of hydrograph, the peak discharge measured in the model is larger than that observed in the channel, and the hydrograph volume measured in the model is smaller than that observed in the channel. The presence of suspended sediment magnifies this phenomena due to its effect on S_f. Fig. 3 shows the ratio of hydrograph peak discharge and that of hydrograph volume under different conditions of model scales, and compares these ratios with the same predicted by the explicit Leap-Frog finite difference formulation. In the figure, QPN(H) and QPN(S) are the peak discharge ratios for hyperconcentrated and sediment-laden flows, respectively, and QVN(H) and QVN(S) are the hydrograph volume ratio for hyperconcentrated and sediment-laden flows, respectively.

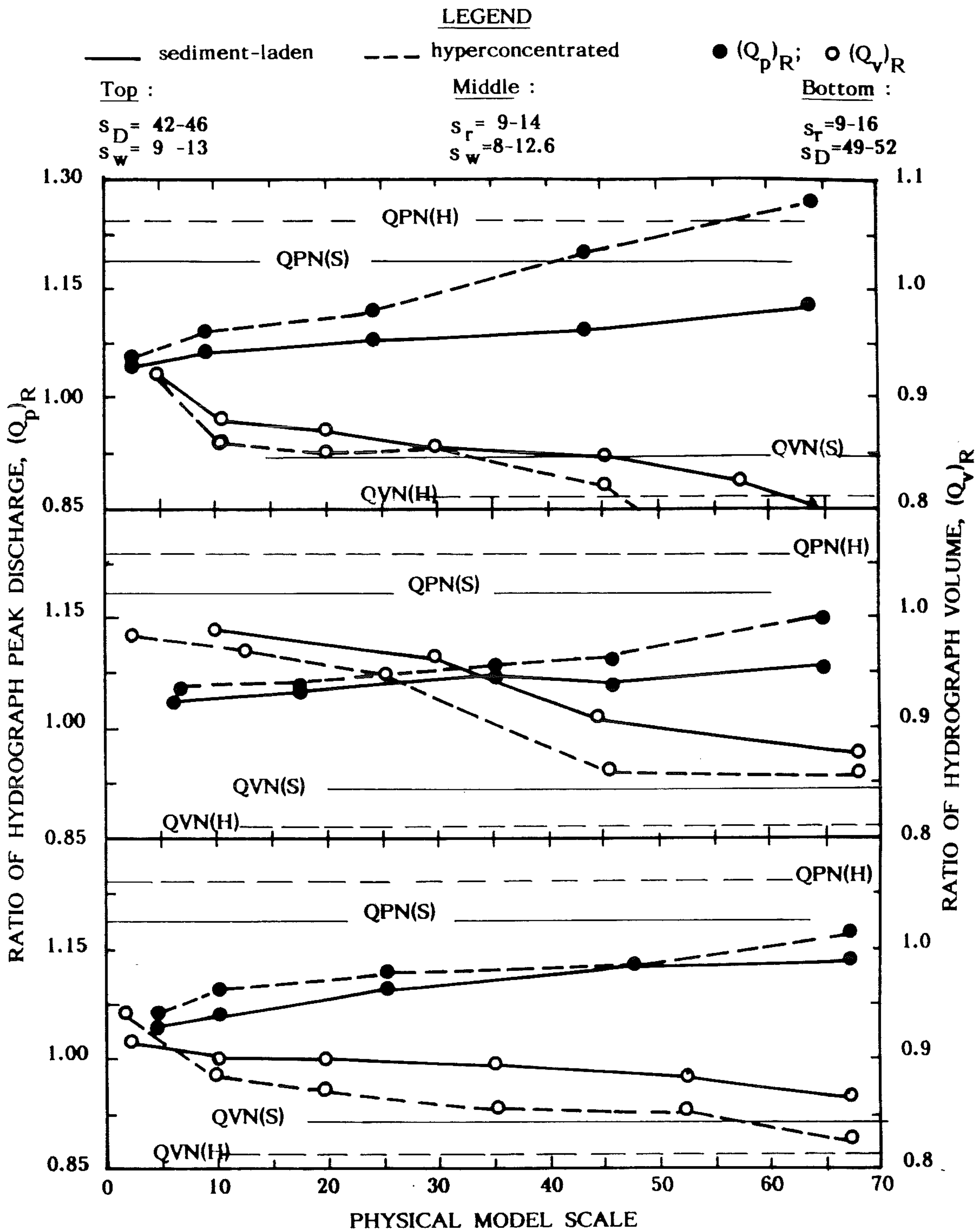

Fig. 3. Average variation of $(Q_p)_R$ and $(Q_v)_R$ with model distortion (top), with model scale of typical grain size (middle), and with model scale of specific grain weight in fluid (bottom) [C = 38.6 - 42.3 gpl].

Fig. 3 indicates that the accuracy of the physical model for hyperconcentrated flow is less than that for sediment laden flow. This may be due to the internal structure of suspended sediment which has not been taken into consideration in the similarity. It is apparent also that the model over-estimation of peak discharge, or under-estimation of hydrograph volume, increases as any of the model scales increases. The accuracy is sensitive to s_r more than to s_W and s_D, meaning that the external geometric similarity is more important in flood routing than the internal structure similarity of bed material. It can also be seen that the prediction accuracy of peak discharge is generally higher than that of hydrograph volume. This, as mentioned before, due to the lateral flow which has not been considered by the model. As Fig. 3 shows, the explicit Leap-Frog finite difference numerical method may become more accurate than a physical model of large scales.

Conclusions

[1] The accuracy of the Leap-Frog explicit finite difference formulation, the four-point implicit finite difference formulation, and the fixed mesh characteristic method of flow routing as well as that of the mobile bed physical model decrease as mean concentration of suspended sediment increases, and as the grain sizes of the suspended sediment decrease. Thus, the numerical methods are not recommended for routing flow with large concentration (C more than 15 gpl) and/or fine sizes (i.e. hyperconcentrated) of suspended sediment. In such cases, the physical model may be preferred up to C less than 40 gpl. For larger concentrations, the accuracy of the physical model was not satisfactory, and thus the model should not be used.

[2] The accuracy of the physical model is sensitive to distortion ratio (i.e external geometric similarity parameters) more than to scales of internal similarity parameters of bed layer (i.e. model scale of typical grain size and model scale of specific grain weight in fluid), and it decreases as any of such scales increases. Thus, for results of reasonable accuracy, distortion ratio less than 20, scale of typical grain size less than 45, and scale of specific grain weight in fluid less than 30 are recommended.

[3] The accuracy of the physical model for predicting peak discharge was higher than that for predicting hydrograph volume. Thus, the model may be used for estimating peak discharges, needed for flood control projects, rather than for estimating hydrograph volumes, needed for water management projects.

[4] The physical model accuracy for routing hyperconcentrated flows (especially at large concentrations) was generally unsatisfactory. Thus, improvement of the model to consider the internal structure of suspended sediment is recommended as a research topic of engineering importance.

[5] For small values of C (less than about 15 gpl), the numerical methods displayed accuracy approaching that of the physical model. Thus, in these cases, the numerical methods are recommended.

Acknowledgements: This study was partially supported by the Saudi Arabian National Water Research Project Number AR-05-62.

References

Nouh, M. (1986) Construction damages due to floods in Wadi Ad-dilah. Report Prepared on the Saudi Arabian National Water Research Project Number AR-5-62 for the King Abdulaziz City for Science and Technology, Riyadh, Saudi Arabia.

Nouh, M. (1988) Routing of floods with large amount of sediment. Proceedings of the 3rd International Symposium on Refined Flow Modelling and Turbulence Measurements, IAHR, Tokyo, Japan, July, Publisher: Universal Academy Press Inc.

Nouh, M. (1989) The Von-Kármán coefficient in sediment laden flow. Journal of Hydraulic Research, IAHR, Vol. 27, No. 4, pp. 477-499.

Nouh, M. (1990) Hyperconcentrated, sediment-laden, and clear-water flow routing using numerical methods. International Conference on River Flood Hydraulics, Wallingford Hydraulic Research, Wallingford, England, September, Publisher: John Wiley & Sons Ltd.

Yalin, S. and MacDonald, N. J. (1987) Determination of a physical river model with mobile bed. Proceedings of the XXII Congress of IAHR - Topics in Hydraulic Modelling, Lausanne, Switzerland, August, pp. 221-226.

CRITICAL VELOCITY OF INITIAL MOTION IN NON-UNIFORM FLOW

by Haizhou TU*
Laboratoire de Recherches Hyrauliques
Ecole Polytechnique Fédérale, Lausanne, Switzerland

ABSTRACT

Three schematic models, being similar to a large sand bar in a natural river (Fig.1(2)), have been constructed to study the initial motion in non-uniform flow. The obtained data are used to establish an empirical relation (Fig.4) for the coefficients of the deduced critical velocity formula (Eq.5), which is shown to be valid in non-uniform as well uniform flow.

INTRODUCTION

In natural rivers, there exist many large sand bars and shoals, as shown in Fig.1. The flows over them are usually non-uniform ones, which, in turn, could initiate sediment movements in ways different from those in uniform flow. These kind of large sand bars pose usually serious problems due to their insistent movement. A shoal, for example, might develop in such a way that it disables the navigation, and a large sand bar near a busy port may block it partly or even completely. Thus researches on the flow structure and the sedimentation processes, the two closely related aspects of the problem, are badly needed. The present paper intends to study the sediment initial motion on a large bar, based on three schematic models of the sand bar shown in Fig.1(2).

EXPERIMENTS

The experiments were carried out in a 86m long, 1.2m wide glass sided flume, which has cemented bottom and a constant slope of 0.1%. The maximum water depth is 60cm, and the maximum flow discharge is 200 l/s. Uniform flow can be developed in a working section as long as 40m.

From the modified longitudinal profile in Fig.1(2) (the broken line), three schematic models were built in the flume. The first one, being 1/40 of the natural size, is shown in Fig.2, where the flow is divided into five zone, designated as A, B, C, D, E, respectively. The second and the third models, while having the same dimension with the first one in the vertical direction, are reduced by a factor of two and four, respectively, in the longitudinal direction. The angles (α and β) in the three models are in the following range (in degrees): α from 2 to 8, β from 1.3 to 5.2.

In the experiments, the point velocities were measured by micro-propellers with a diameter of 1cm, and point gauges were employed to measure the water depth.

For each of the three models, eighteen holes (each has a volume of 10 x 3 x 1 cm^3) were made on the surface (Fig.2), such that, if given by x coordinates in Fig.1(2), there are:

three holes in zone A, located separately at: x=-60m, -40m, -20m
four holes in zone B, located separately at: x=20m, 40m, 60m, 80m
four holes in zone C, located separately at: x=250m, 400m, 550m, 700m
four holes in zone D, located separately at: x=880m, 910m, 940m, 970m
three holes in zone E, located separately at: x=1020m, 1040m, 1060m

---

*On leave from the Wuhan University of Hydraulic and Electric Engineering, China

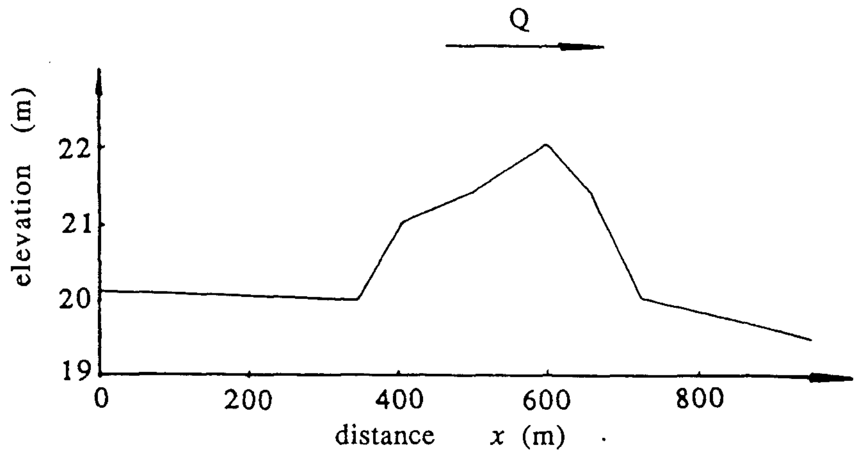

Fig.1(1) the Longitudinal Profile of A Shoal in the Yantze River

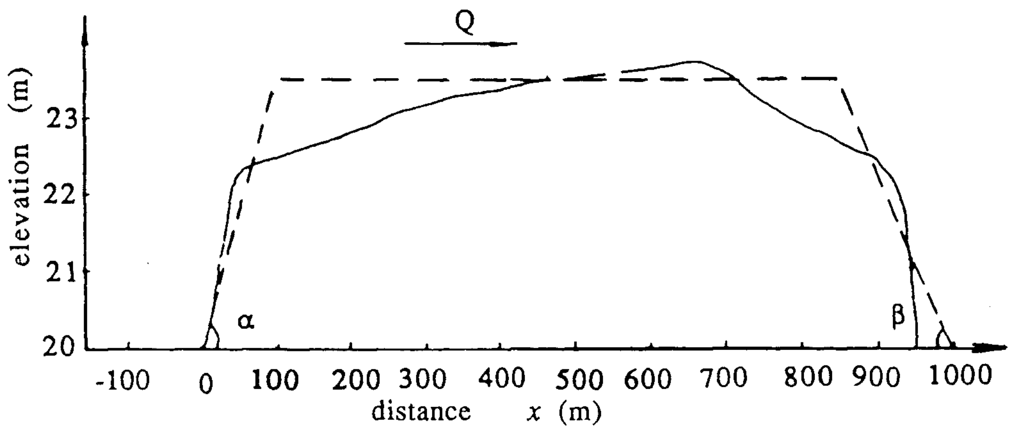

Fig.1(1) the Longitudinal Profile of A Sand Bar in the Han River (the Solid Line)

According to the possible range of the velocity over the models, two types of natural sands, with d_{50} being 0.35mm and 0.67mm respectively, were used. The sands were sieved to be as uniform as possible, having $\phi(=\sqrt{d_{75}/d_{25}}=1.14$ for the first group (d_{50} =0.35mm) and ϕ=1.20 for the second group (d_{50} =0.67mm). The specific weight of the sands (γ_s) is 2650kg/m^3.

When the flow discharge Q increases to a certain value, there will be some sands somewhere (in one, or several, of the 18 holes) engaged in initial motion. Since the sands in all the 18 holes do not begin to move in the meantime, the experiments were carried out in each zone separately. For example, while the tests being done in D zone where the four holes were filled with sands, all the other holes were filled with pre-made wooden blocks of the same size (10 x 3 x 1 cm^3). The processes are as in the follows:

1) close the tailgate in the downstream;

2) fill water in the downstream reach of D zone;

3) begin to run a flow of small discharge in the flume and increase gradually the discharge. In the meantime open the tailgate slowly till its

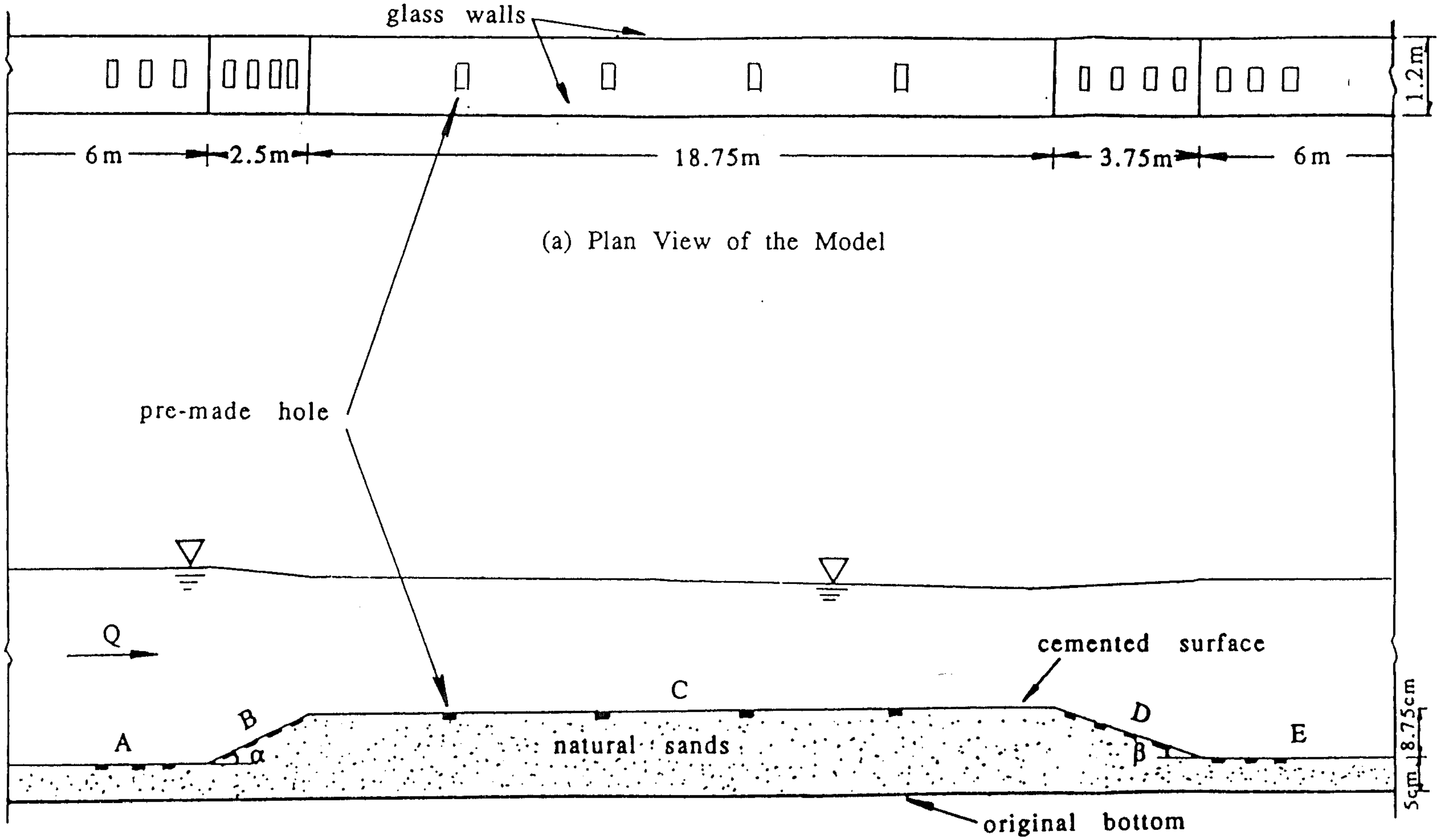

(b) Side View of the Model

Fig.2 the First Model (not to scale)

~~maximum~~;

4) if there appears sediment movement in one of the holes in the zone under observation, then measure the corresponding discharge and keep it a constant, and measure the water depth and the velocity distribution over the hole where the initial motion has appeared. The integrated vertical mean velocity is the corresponding critical velocity for the initial movement.

DATA ANALYSES

The data will be analyzed together with a formula for the critical velocity developed in the following way.

In non-uniform flows considered in the present case, a single grain could rest on the bottom in one of the five zones (A, B, C, D, E). Here the two cases shown in Fig.3 (corresponding to B zone and D zone, separately) are to be studied, bearing in mind that the other three zones (A, C, E) are of special cases with $\alpha=0$.

As shown in Fig.3, the forces acting on a single particle in a state of initial motion are the following:

$$F= C_f a_1 d^3 \gamma \frac{u_b^2}{2g}$$

$$W= a_2 (\gamma_s-\gamma) d^3 \qquad (1)$$

$$N=W \cos\alpha$$

$$M_f= K_2 d N = K_2 d W \cos\alpha$$

where: a_1, a_2, C_f and K_2 are coefficients; d, the grain diameter, here assumed to be equal to d_{50}; g, the gravity acceleration; u_b, a representative velocity acting on the grain; and γ_s, γ are the specific weight of the natural sands and the water.

For a particle in a state of initial movement, the resultant moment is equal to zero, i.e.

$$\Sigma M_{oi}=0$$

Considering that in Fig.3(2) α is negative, one has

$$K_1 d F- M_f -K_3 d W \sin\alpha=0 \qquad (2)$$

from Eq.1

$$u_b=\sqrt{[\frac{2a_2(K_2\cos\alpha+K_3\sin\alpha)}{a_1K_1C_f}]}.\sqrt{(\frac{\gamma_s-\gamma}{\gamma}.gd)} = A \sqrt{(\frac{\gamma_s-\gamma}{\gamma}.gd)} \qquad (3)$$

with

$$A= \sqrt{[\frac{2a_2(K_2\cos\alpha+K_3\sin\alpha)}{a_1K_1C_f}]}$$

An investigation on the velocity distribution was undertaken before

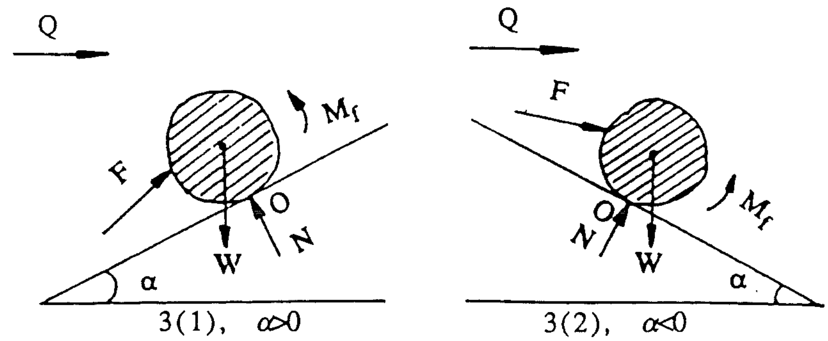

Fig.3 the Forces Acting on A Particle in the State of Initial Motion

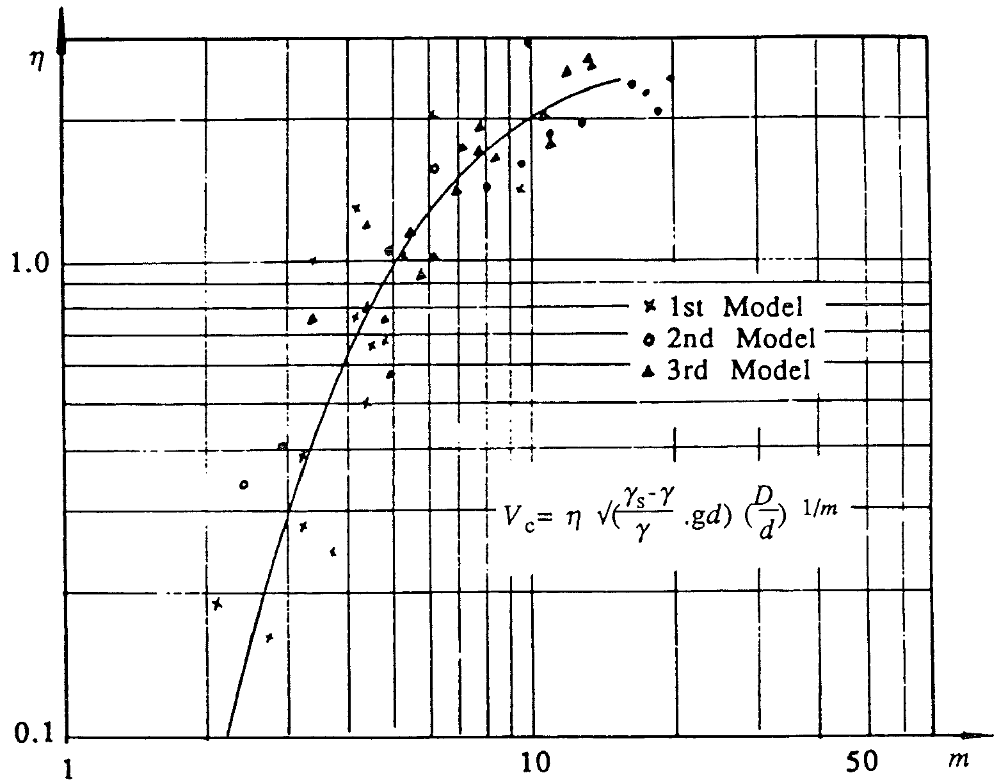

Fig.4 the Plot of η against m

the initial-motion experiments by the author (TU, 1985), by using the same models described above, and it was shown that a power law

$$u = (1 + \frac{1}{m})\ V\ (\frac{y}{D})^{1/m} \tag{4}$$

could be used to describe the velocity distribution in non-uniform flow, where: D is the water depth, u and V are the point velocity and the vertically averaged velocity, respectively; m depends on the flow resistance and the flow uniformity (the author proposed (TU, 1985) using the longitudinal variation of the kinetic energy, $\frac{\partial}{\partial x}(\frac{V^2}{2g})$, as an index for the flow uniformity in non-uniform flows). While in uniform flow m is about 6 to 8 (Li et al., 1983), it varies in our non-uniform experiments from 2 to 20.

It--follows from Eqs.2, 3 and 4 that, by assuming that for $y=\xi d$, $u=u_b$,

$$V_c = \eta \sqrt{\left(\frac{\gamma_s-\gamma}{\gamma}.gd\right)} \left(\frac{D}{d}\right)^{1/m} \tag{5}$$

where V_c is the critical average velocity for the initial motion, and

$$\eta = \frac{1}{\left(1+\frac{1}{m}\right)\xi^{1/m}} \sqrt{\left[\frac{2a_2(K_2\cos\alpha+K_3\sin\alpha)}{a_1K_1C_f}\right]}$$

From the present initial motion experiments, an empirical relation between η and m is obtained (Fig.4). It is seen from Fig.4 that:

1) in non-uniform flow, m in Eq.4 varies from 2 to 20, and the corresponding η changes from 0.1 to 3.0;

2) assuming η=1.14 and m=6 in Eq.5, one would have the formula of Shamof (Chien, 1983, p.238) for initial motion in uniform flow,

$$V_c = 1.14 \sqrt{\left(\frac{\gamma_s-\gamma}{\gamma}.gd\right)} \left(\frac{D}{d}\right)^{1/6} \tag{6}$$

3) for m=6, as in the formula of Shamof and also widely used for the velocity distribution in natural flow (Li et al., 1983), one has, from Fig.4, η=1.24. Seeing that in the formula of Shamof, η=1.14 leads to underestimated critical velocities (Xie, 1981, p.42), η=1.24 seems justified. In other words, Eq.4, together with Fig.4, is also valid for the initial motion in uniform flow.

SUMMARY

Experiments of sediment initial movement in non-uniform flows have been carried out. A relation (Eq.5) representing the critical condition is developed, from which the critical velocity for the initial motion in both uniform and non-uniform flow can be estimated, by using the empirical relation from the present experimental data (Fig.4).

Acknowledgment This paper is part of the author's Thesis for Master Degree of Science in Civil Engineering, supervised by Professor Xie Janheng, to whom he is deeply indebted.

REFERENCES

Li Zhenru, Chen Yuaner and Zhao Yun (1983), "Laboratory Investigation on Drag and Lift Forces Acting on Bed Spheres", Proceedings of the Second International Symposium on River Sedimentation, Nanjing, China, p.330-343.

Ning Chien (1983), Mechanics of Sediment Transport, Science Press, Beijing, 656pp.

TU Haizhou (1985), A Preliminary of Several Problems in 2-D Non-Uniform Flow, Thesis presented to the Wuhan University of Hydraulic and Electric Engineering, in partial fulfillment for Master Degree of Science in Civil Engineering.

Xie Janheng (1981), River Sedimentation, Water Resourcese Press, Beijing, Vol.1, 372pp.

DESIGN OF PHYSICAL MODEL WITH HIGH CONCENTRATED FLOW AND ITS APPLICATION TO STUDY A LATERAL DIVERSIONAL POWER STATION ON THE YELLOW RIVER

by Zhou Wenhao & Zeng Qinghua
Institute of Water Conservancy and Hydro-electric Power Research (IHWR), Beijing, 100044, China

Abstruct

In flume , the flow with high Concentration is a Binghan fluid and has the characteristics of Non-Newtonian fluid, but the high concentrated flow in the Yellow River still has the behaviors of turbulent flow. Similarities for the ordinary sediment-laden flow can also be applied to the high concentrated flow of the Yellow River. A model with high concentrated flow has been designed and conducted to study a lateral diversional power station on the Yellow River. A series of phenomena of flow and sediment transport which are quite different from that of the frontal diversion was acquired.

Introduction

In China, just as the analyses of field data and numerical calculation, the physical model is also one of the important tools to study and solve the sedimentation problems in hydraulic engineerings. Especially for the complicated major engineering,the physical model has to be used to get a thorough solution of engineering sedimentation. Up to now, more experience for modeling the ordinary sediment-laden flow has been gained. The Yellow River is a famous river in the world with its high sediment concentration. The maximum concentration of the river was 911 kg/m^3 (at Sanmenxia Station). How to simulate the high concentrated flow is much more significance in the design of the physical model related to the flow of the Yellow River. The key problem is whether the similarity principles for the ordinary sediment laden flow can be used to that of high concentrated flow. After ananlyzing the field data from the Yellow River, the problem has been solved.

Characteristics of High Concentrated Flow

1) Results of flume experiments

The results of laboratory experiments indicate that the low concentrated flow is a Newtonian fluid, but when the concentration inereases to a certain value, the flow behaves a Non-Newtonian fluid, Bingham fluid. The critical concentration is 400-500 kg/m. The velocity distribution for the high concentrated flow is nearly uniform in vertical direction and the velocity qradient is almost equal to zero when $Z/H < 0.2$ (Z is the height from the bottom, H is the depth) Fig.1. As the ordinary sediment-laden flow, the high concentrated flow also has two flow regime: the laminar flow and the turbulent flow. The critical effective Reynolds' number is 2000-4500.

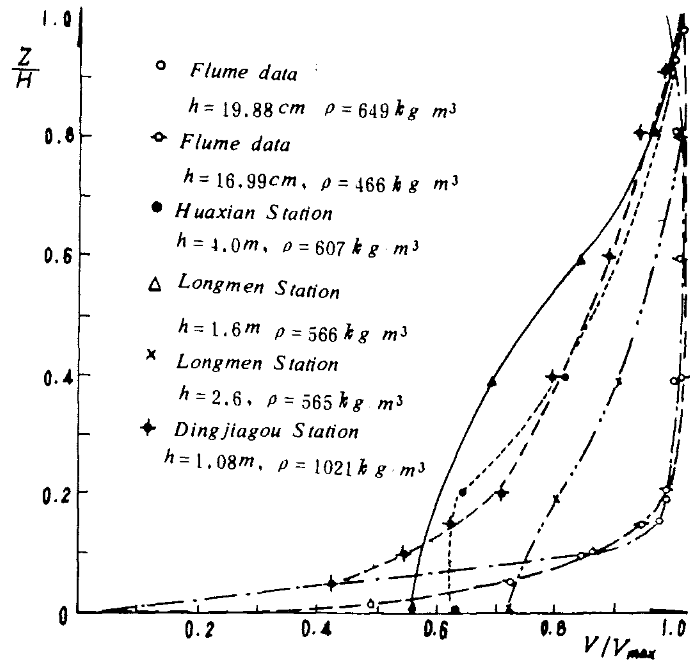

Fig. 1 Comparison of velocity distributions in the Yellow River and flume

2. Features of high concentrated flow in the Yellow River

The high concentrated flood occurred every year in the Yellow River and its tributaries. Analyses reveal that when the average concentrations for the vertical line are in the range of 360-1270 kg/m^3, or in the range of 528-933 kg/m^3 for cross-section, the flows both for the vertical line and cross-section are turbulent flow with the effective Reynolds'number more than 8000-2000. Therefore, the conclusion can be drawn that the high concentrated flows both in the Yellow River and its tributaries are qenerally the turbulent flow. The vertical distribution of velocity is not unifome.

The data from the Yellow River and its tributaries further indicate that: (1) the vertical distribution of velocity in high concentrated flow follows the law of Logarithmic distribution with the Karmen Coefficient of 0.4; (2) the vertical distribution of sediment concentration follows the Law of ordinary sediment Laden flow and (3) the sediment carrying capacity of bed material load also follows the same law of the ordinary sediment laden flow. Therefore , the laws of ordinary sediment laden flow can be used to the high concentrated flow, even the concentration reaches 911 kg/m . This implies that the criteria of similarities for the ordinary sediment laden flow can be used for the high concentrated flow in the Yellow River.

In addition, because the sediment in the Yellow River is very fine (d_{50} = 0.03mm), the suspended load is the predominant part in the flow and bed load can be neglected. This further makes the model design simplified.

Criteria of similarities (undistorted model)

1. Similarity of flow

$$\lambda_V = \lambda_H^{1/2} \; ; \quad \lambda_n = \lambda_H^{1/6} = \lambda_L^{1/6} \; ; \; (\lambda_L = \lambda_H)$$

2. Similarity of flow pattern

$$\lambda_{Rem} > 1000 - 2000$$

3. Similarity of continuity

$$\lambda_Q = \lambda_L^{5/2}$$

4. Similarity of suspended load transport

a) Similarity of deposition

$$\lambda_\omega = \lambda_V \frac{\lambda_H}{\lambda_L} = \lambda_V \; ;$$

$$\lambda_d = \sqrt{\frac{\lambda_V \lambda_\omega}{\lambda_{r_s - r}}} = \lambda_L^{1/4} \Big/ \lambda_{r_s - r}^{1/2}$$

b) Similarity of sediment carrying capacity

$$\lambda_S = \lambda_{S*} = \lambda_{r_s} \Big/ \lambda_{r_s - r}$$

c) Time scale

$$\lambda_t = \frac{\lambda_{r_0} \lambda_L}{\lambda_V \lambda_S}$$

d) Similarity of vertical distribution of concentration

$$\lambda_\omega = \lambda_{V*} = \lambda_V$$

5. Similarity of density current

$$\lambda_S = \frac{\lambda_{r_s}}{\lambda_{r_s - r}}$$

In which, λ is the scale; V is velocity; H is depth; L is length; Rem is Reynolds' number for flow in model; Q is dischange; ω is settling velocity; d is grain size; r_s is specific weight of sediment, r is specific weight of water; r_0 is volume weight of deposition; S_* , S is sediment concentration.

A Case Study on a Lateral Diversional Power Station

1. Description of the model

The project will be constructed on the Middle Yellow River. Because of the poor qeological conditions, all the intakes for the tunnels of power station, flood release, and sediment sluice have to be laid in a gully beside the main valley. All the intakes are set on six towers. The main valley is blocked by an earth-rock dam.

The purposes of the model of the project are to study the flow pattern, the silted topography, the flow and sedment transport in front of the intakes, and the measures to prevent the block of the intakes.

This is an undistorted model with the scale $\lambda_L = \lambda_H = 100$. The fly-ashes were used as the sediment in the model. The calibration showed that the charateristics of the sedimentation in the model was similar to that in the Sanmenxia, Yanguoxia and other reservoirs in China.

2. Results of the model testing

Because the intakes are located in the gully beside the main channel, the incoming main current sharply turns to the intakes with an angle of 90°, thus a bend is formed, which causes the behaviors of lateral diversion and a series of features of flow and sediment transport.

(1) Flow pattern

The flow pattern in front of the intakes is determined by the layout of intakes. Because of the effects of circulating flow, the flow structure and sediment transport in front of these intakes are quite complicated and have a great effect on the flow pattern. Under the worst layout condition, i.e., the six towers are not in a straight line, and the bend will develop further because of erosion on concave bank. The main current is spured by tower No.1. Therefore, three circulating flows with vertical axis and different directions, sizes and intensities occur in front of these intakes (Fig. 2) the optimum alternatives plan was found that all the intakes are in a straight line and a quiding wall is set up beside the tower No.1.(Fig.3). The flow pattern is obviously improved, and only one small circulating occurs. If a floating-delivering sluice is set up on the left side of tower No. 6, all the floatings coming from the upstream can be delivered away.

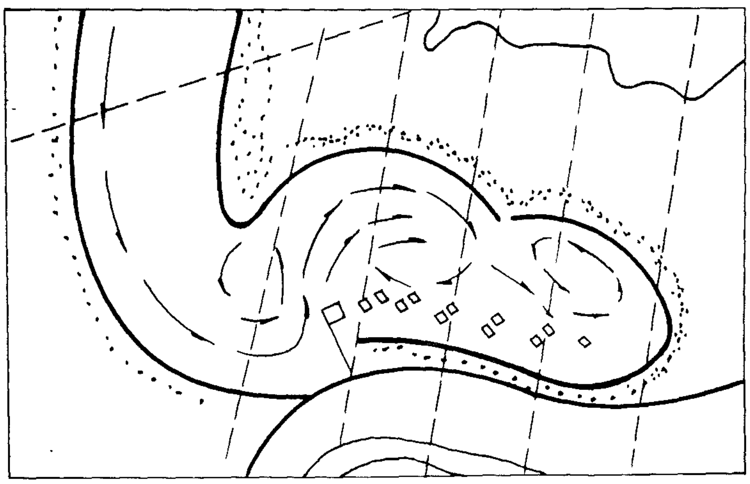

Fig. 2 Flow pattern in front of intakes

(2) Distributions of velocity and sediment concentration

In accordance with the natural bend flow, the maximum velocity in plan always approaches to concave side, i.e., near the front of intakes. The farther the distance from the intakes, the lower the ve-

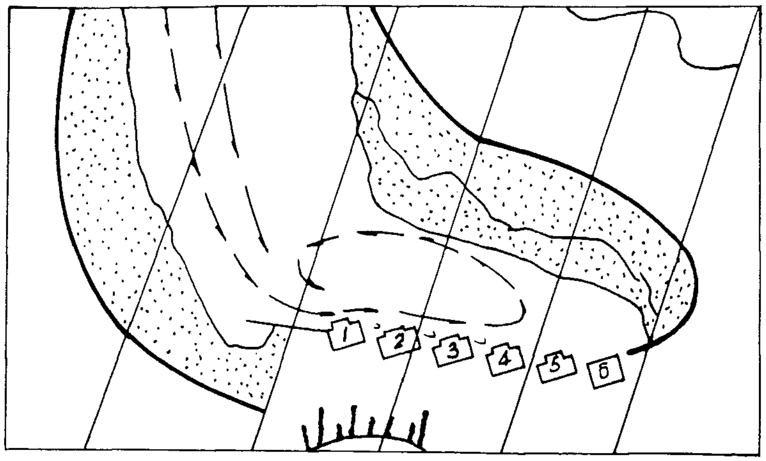

Fig. 3 Flow pattern in front of intakes

locity. But the velocity decreases gradually from tower No. 1 to NO.6 due to the decrease of discharge correspondingly. In vertical direction, owing to the strong influences of circulating flow and turbulence, the velocity distribution is comparatively uniform and the law of logarithmic distribution of velocity in open chanel is no longer followed (Fig.4). The vertical ditribution of concentration is also uniform and the general law of vertical distribution of concentration is not folloed either (Fig.5). Of course, the operation of outlet facilities also plays a certain role in the concentration distribution.

The density current occurs only in the initial stage of reservoir operation. It would disappear when the reservoir deposition reaches in equilibrium.

(3) Funnel pattern

Under the lateral diversional condition, a funnel-shape toporaphy always occurs in front of the intakes. The funnel is provided with

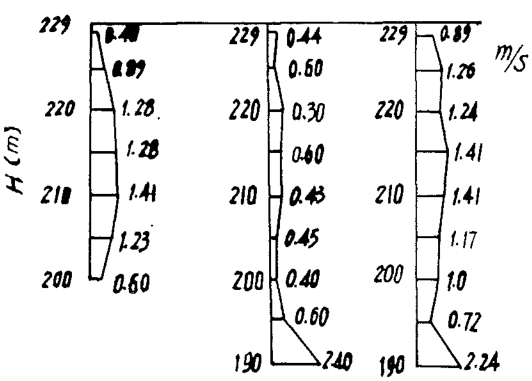

Fig. 4 Vertical distribution of velocity

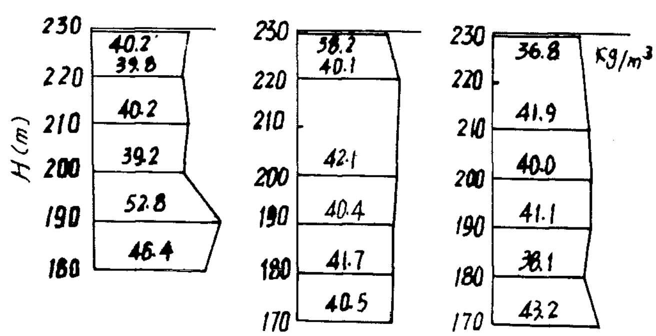

Fig. 5 Vertical distribution of Sediment Concentration

the following features: (1) The plan-form is determined by the flow in front of these intakes. In worst flow condition, two extending sand-spit on the opposite side of the intakes can be formed (Fig.3). A smooth-going funnel with wider outside and narrow inside is formed when the flow is smooth; (2) The depth of the funnel depends on the operation of those intakes. For example, when the inside intakes No. 4 - 6 are put into operation, a deep thalweg would occur in front of all intakes, but when the outside intakes NO.1-No.3. are in operation, the deposition would happen in front of intakes No. 4 - No.6; (3) The side slope of the funnel is 0.3-0.4 that is similar to the under water respose angle of the material used in the model; and (4) The longitudinal profile along main current is not in continuity. The bed elevation gradually drops from the entrance of the bend with a slope of 0.015 - 0.03. The bed in front of intakes is in undulation with the lowest elevation for those operating intakes.

4. Conditions of normal operation of intakes

In the funnel, there is a small funnel closed to the lower intakes. When the intakes are in operation, whether the small funnels can be maintained is the bey point for the normal operation of the intakes. As mentioned above, the submerged sand bar or sandspit may occur and threaten the operation of the intakes. So, under the condition of lateral diversion, it is most important to maintain a better flood condition with a single circulating flow and a high velocity area closed to the intakes.

Conclosions

The high concentrated flow in the Yellow River is a turbulent flow. The similarities of ordinary sediment laden flow can be used to the high concentrated flow. The similarities have been applied to the model of a lateral diversional power station on the Yellow River and a lot of phenomena that are quite different from the frontal diversion has been found: The flow pattern in front of the intakes depends on the layout of the intakes; A funnel can be formed and its topography is determined by flow condition. The vertical distributions of both the velocity and sediment concentration are uniform and do not follow the general laws of velocity and sediment concentration distributions; To keep a good flow condition in front of the intakes is most significant for the normal operation of the intakes:

References

1. Qian yiying et. al. "Basic characteristics of flow with hyperconcentration of sediment". Proceedings of the First International Syposium on River Sedimentation, March 24-29, 1980, Beijing, China.
2. Zhou Wenhao, Zeng Qinghua et al. "Characteristics of Fluvial Process for the Flow with hyperconcentration in the Yellow River", Proceedings of the Second International Syposium on River Sedimentation, Oct. 11-16, 1983, Nanjing, China, pp. 618-626.
3. Zeng Qinghua, Zhou Wenhao, "A study on Silting-prevention and Float-delivering for Lateral Diversion Hydro-power Station", Proceedings of the Fourth International Syposium on River Seidmentation, June 5-9, 1989, Beijing, China, pp. 1174-1180.

SLURRY FLOW THROUGH BENDS

Baljeet S. Kapoor
Assistant Professor
Deptt. of Civil Engineering
Punjab Engineering College
Chandigarh, India

Somesh K. Kansal
Assistant Executive Engineer
Military Engineer Services
CE, Chandigarh Zone
Chandigarh, India

The effect of flow direction on bends metering slurry flows has been considered. The existing models [2,5,6,7] based on analytical considerations and dimensional homogeneity related to vertically upward and horizontal sediment laden flows through bends have been validated for vertically downward flow. Analysis of the experimental data related to slurry flows through bends has been carried out and the bend meter discharge coefficient predictors proposed for the different flow directions (horizontal, vertically upward and vertically downward).

Metering of Slurry Flow by Bends

Modern electronic equipment like ultrasonic flow meters, Laser doppler velocity meters, nuclear density gauges, magnetic flow meters etc. have been considered for measuring sediment laden flows but often this equipment is expensive and is still in the development stage [2].

Off the conventional flow rate meters like venturimeters and orificemeters, the bend meter not only being the simplest; has the advantage of offering least obstruction to slurry flow being metered by it. Metering of slurry flows by bends thence assumes significance and a problem worth investigation.

Metering of flows

For clear water flow the discharge equation of a bendmeter may be written in the standard form as

$$Q = C_O A \sqrt{2gh_L} \tag{1}$$

where, Q is the discharge, $A(\pi D^2/4)$ being the cross sectional area of the pipe, D the dia of the pipe and h_L the pressure difference across the bendmeter.

For two phase flows, studies related to metering by bendmeters are limited [1,2,5,6,8].

Previous Studies

Brook [1] in 1962 performed experiments using a recirculatory flow system, on a 90° bend. To eliminate any pressure difference due to mixture relative density, the pressure taps at the same height were used. The flow direction was vertically upward. The solids used were bakelite(0.635-0.9525cm,0.9525-1.27cm) and basalt(0.635-0.9525cm) of relative density 1.35 and 2.82 respectively. The carrier medium was water.

Brook observed that the bend coefficient was not affected by the specific gravity of the mixture. The value of the meter coefficient was more or less constant and close to the clear water values; the manometer readings being expressed in metres of water. The study not specifying the flow regime, limits its practical application.

Kapoor [2] in 1980 performed experiments on a 90°bend using a recirculatory flow system. The pressure taps were fixed at the same height and the flow direction was vertically upwards. Sand (120-150μm, 150-180μm, 180-212μm) and coal (300-355μm) of relative density 2.65 and 2.046 respectively, constituted the sediment and the carrier medium was water. Considering the flow to be irrotational, a theoretical model was proposed as follows

$$C/C_o = 1/\sqrt{(\rho_* - 1)X + 1} \tag{2}$$

with C and C_o as bendmeter discharge coefficients for two phase flow and clear water flow respectively, ρ_* as the ratio of the mass density of solids to the mass density of the carrier medium, and X the absolute volumetric concentration of sediment.

This model was found to be in poor agreement with the experimental data of his study. As an alternative to predict bendmeter discharge coefficient for sediment laden flows Kapoor [2] proposed the following relationship based on dimensional homogeneity:

$$C/C_o = f(\omega d/\nu, X) \tag{3}$$

where ω is the fall velocity of sediment in clear fluid, ν is the kinematic viscosity of fluid and d is the mean particle diameter. The model was well supported by his experimental data and enables the bend discharge coefficient to be predicted with an accuracy of $\pm 0.5\%$

Considering the flow to be rotational, the model

$$C/C_o = \frac{\sqrt{1/r_1^2 - 1/r_2^2}}{\sqrt{(1/n)(1/r_1^{2n} - 1/r_2^{2n})[(\rho_* - 1)X + 1]}} \tag{4}$$

where r_1 and r_2 are the two radii of the bend and n a constant greater than 1, was proposed by Sharma [4].

Kansal [5] extended the work of Kapoor over a wider range of pertinent variables. The experimental data of his study related to vertically upward sediment laden flow through bends; (surkhi (75-150μm) of relative density 2.54 being the sediment and water the carrer medium) ably supported Kapoor's model based on dimensional homogeneity; however Kapoor's analytical model was in poor agreement herein also.

Analysis of the experimental data related to horizontal sediment laden flows through bends [The sediment being Surkhi (75-150μm) of relative density 2.54 and water the carrier medium] enabled Garg [6] to conclude that Kapoor's model based on dimensional homogeneity was suitable towards prediction of the meter coefficient for horizontal slurry flows also. He modified Sharma's model defined above by Eqn.4 and proposed 'n' values as a function of X and $\omega d/\nu$; however this model did not show significant improvement and promise of application. A predictor of the form [7]:

$$C/C_o = \log[(\omega d/\nu)^A . X^B] \qquad (5)$$

was proposed by him. This predictor was found to be in fair agreement with data related to various studies pertaining to horizontal and vertically upward flows. Values of A and B were found to be a function of the flow direction (Table 1)

TABLE -1

Flow Direction	Coefficient A	Coefficient B
Horizontal	1	2.0
Vertically upward	1	0.5

Present Study

Objective: It was proposed to study the effect of vertically downward slurry flows on bends. The aim being to study the effect of flow direction in totality on bends metering slurry flows. The existing models finding favour towards predicion of the meter coefficient for horizontal and vertically upward flows need to be verified for vertically downward flows. It would be an utopia achieved if a universal model could be proposed towards prediction of the discharge coefficient for bends metering slurry flows for any flow direction in any plane over a wide range of pertinent variables.

Experimental Study [5,7,8]

The experimental study was carried out in a recirculatory flow system, the details of the system and the experimentation can be picked up at Fig.1.

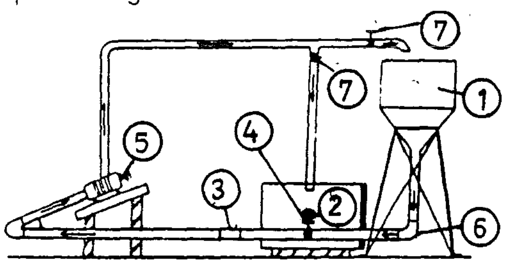

Experimental set up features
1. Recirculating tank
2. Discharge measuring tank
3. Transparent Section
4. Regulating valve
5. Centrifugal pump
6. Bend meter
7. Diversion valves

Fig.1

Experimental Details: (i) Surkhi (75-90µm, 90-125µm, 125-150µm) of relative density 2.54 constituted the sediment. (ii) Carrier medium was water. (iii) Tappings were at the same height [1]. (iv) Volumetric measurement of sediment using a visual sand accumulator [2,5,6]. (v) Maximum error in the discharge measurement was 1%.

Verification of Kapoor's Model based on Dimensional Homogeneity

Equation 3 given by $C/C_o = f(\omega d/\nu, X)$
represents Kapoor's model based on dimensional homogeneity. Taking the value of C_o as 0.826, Fig. 2 illustrates the variation of C/C_o with $\omega d/\nu$ & X. It can be seen herein that C/C_o increases with increase in X for a

given $\omega d/\nu$. Also C/C_0 increases with increase in $\omega d/\nu$ for a given X. By introducing an empirical coefficient Ψ, it has been possible to bring all the data on a plot of $\Psi C/C_0$ Vs X (Fig.4). Ψ decreases with increase in $\omega d/\nu$ as shown in Fig.3. The overall scatter of the data from the mean curve drawn in Fig.4 is indeed very small the coefficient of correlation being 0.9998.

Figs. 2,3,4 illustrates that Kapoor's model based on dimensional homogeneity [2] for sediment laden flows through bends for horizontal and vertically upward flows holds good for vertically downward flows too.

Kapoor's model based on analytical considerations [2] Sharma's model [4] and Sharma's modified model [4] were found to be in poor agreement with the experimental data related to vertically downward sediment laden flows also.

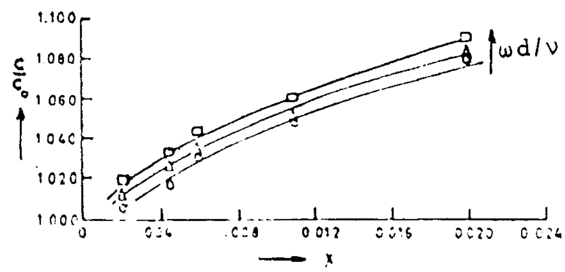

Fig.2 Variation of C/C_0 with X and $\omega d/\nu$

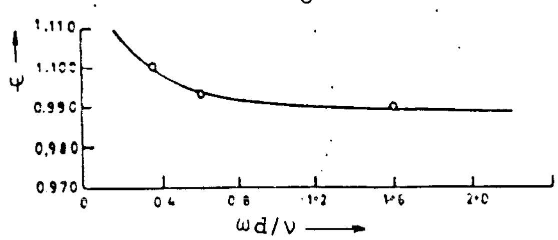

Fig.3 Correction Ψ as a function of $\omega d/\nu$

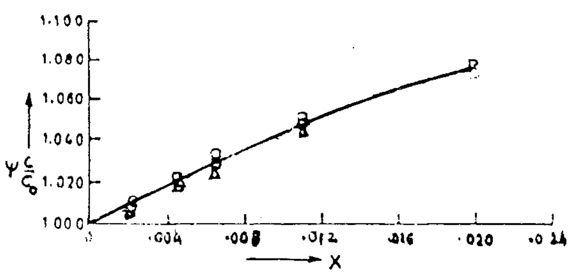

Fig.4 Relation for $\Psi C/C_0$ for vertically downward flows

SURKHI SIZE	NOTATION
75 – 90 µm	△
90 – 125 µm	○
125 – 150 µm	□

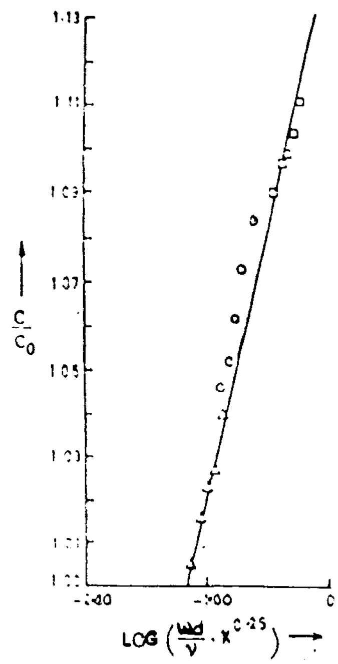

Fig.5 Variation of C/C_0 with $\log(\omega d/\nu . X^{0.25})$ for vertically downward flows

Model $C/C_0 = \log[(\omega d/\nu)^A (X)^B]$

On examination it was observed that the model $C/C_0 = \log[(\omega d/\nu)^A (X)^B]$ ably supported the data related to this study; Fig.5 illustrates the same. Values of A and B were found to be 1 and 0.25 respectively.

Generalised Models

To take into consideration the effect of flow direction in totality on bends metering slurry flows, the placement of bends has been considred in: (i) horizontal plane (ii) vertical plane.

For the horizontal plane no change is envisaged for want of gravity effect over the range of experimentation performed. The analysis of the concerned available data indicates that model

$$C/C_0 = \log[(\omega d/\nu)^A.(X)^B] \quad \text{with } A=\sin^2\theta,\ B = 2\sin^2\theta$$

where θ is the angle of the bend in horizontal plane,holds good (Fig.6).

The data related to bends metering vertical slurry flows was examined and a generalised model was envisaged for $A = \sin^2\theta$ and $B=0.375\sin^2\theta+0.125\sin\theta$, where θ is the angle of the bend in a vertical plane; as can be seen at Fig.7 & 8; however, it needs to be validated experimentally for various flow angles in horizontal and vertical planes and for a larger range of data.

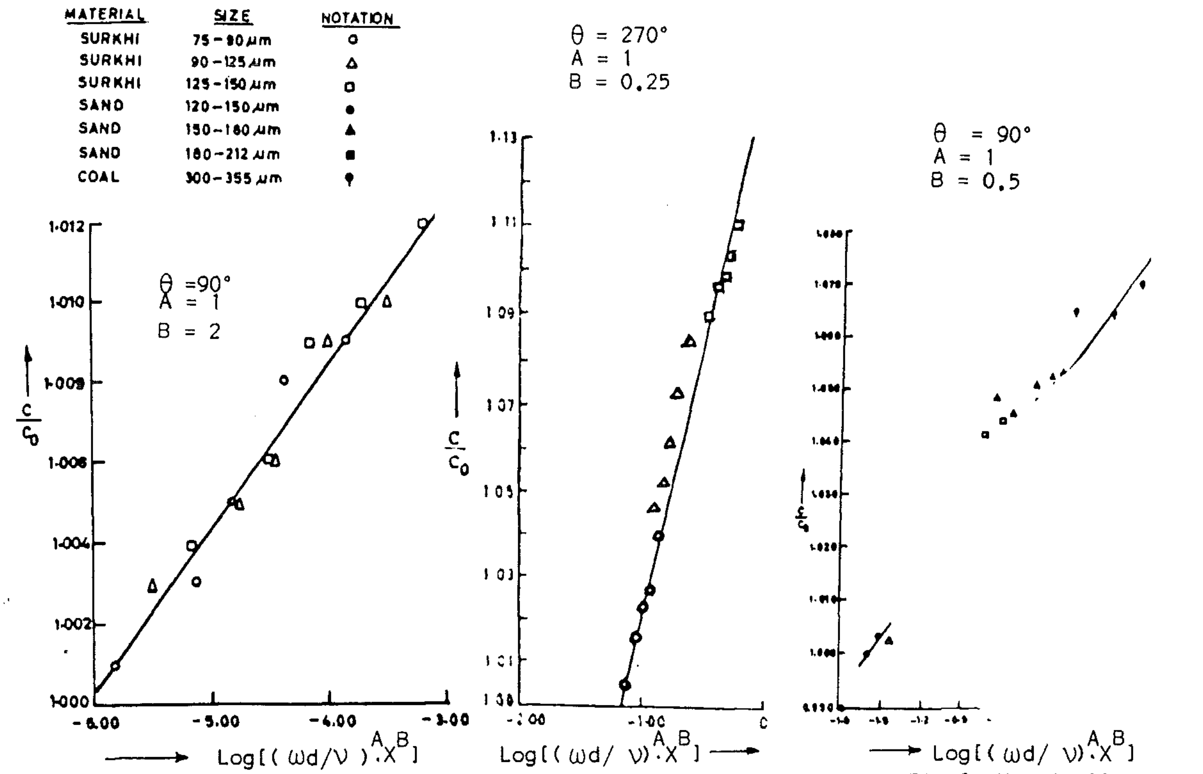

Fig.6 Horizontal flow

Fig. 7 Vertically downward flow

Fig.8 Vertically upward flow

$A=\sin^2\theta$, $B=2\sin^2\theta$

$A=\sin^2\theta$, $B=0.375\sin^2\theta + 0.125\sin\theta$

Verification of model $C/C_o = \log[(\omega d/\nu)^A.X^B]$

The effect of flow direction on bends has been examined and can be surmised as:

C/C_0 (vertical downward flows) >

C/C_0 (vertical upward flows) > C/C_0 (Horizontal flow)

being valid over the range of the pertinent variables studied.

Statistical Analysis of the models

This exercise was carried out to establish the suitability of the various models towards the prediction of the discharge coefficient for vertically downward sediment laden flow through bends.

TABLE 2

Model	Statistical correlation
Kapoor's Model based on dimensional homogeneity[2]	0.9726
Predictor Model for Vertically downward flow [8]	0.9998

Conclusions

1. Kapoor's theoretical model [2], Sharma's model [4] and Sharma's modified model [4] have not been ably supported by the experimental data related to the sediment laden flows through bends in various directions.
2. Kapoor's model based on dimensional homogeneity [2] along with the model $C/C_0 = \log[(\omega d/\nu)^A (X)^B]$ shows high statistical correlation and can predict the bend coefficient fairly accurately within the range of experimentation performed.
3. C/C_0 values for horizontal sediment laden flows have been found to be less than C/C_0 values for vertically upward flows through bends; which in turn were highest in case of vertically downward flows.

References

1. Brook, N., Flow Measurement of solid-liquid mixture using venturi and other meters, Proc.Inst. of Mech.Engrs., Vol.176, No.6, 1962, pp.127-140.
2. Kapoor, B.S., Measurement of Sediment Laden Flows, Ph.D. thesis, 1983, Deptt. of Civil Engineering, University of Roorkee, Roorkee, India.
3. Ranga Raju, K.G., Garde, R.J. & Kapoor, B.S., Discharge Characteristics of Bendmeters & Venturimeters in sediment laden flows, Irrigation & Power, 1987.
4. Sharma, J.P., 'Sediment Laden Flow through a Bendmeter-Theoretical considertations', M.E. Thesis, 1985, P.G.Deptt. of Irrigation & Hydraulics, Punjab Engineering College, Chandigarh, India.
5. Kansal, S.K., Experimental and Theoretical Studies related to vertical sediment laden flow through Bendmeters, M.E. thesis 1988, P.G. Deptt. of Irrigation & Hydraulics, Punjab Engineering College, Chandigarh, India.
6. Garg, C.R., Effect of flow direction on Bendmeters for Sediment Laden flows, M.E. Thesis, 1989, P.G. Deptt. of Irrigation and Hydraulics, Punjab Engineering College, Chandigarh, India.
7. Kapoor, B.S. & Garg, C.R., Horizontal Sediment Laden Flows through Bends, Third International Workshop on Alluvial River Problems, University of Roorkee, Roorkee, India, 1989, pp. 311-320.
8. Goel, R.K., Experimental Studies related to vertically downward sediment laden flows through Bendmeter, M.E. Thesis, 1989, P.G. Deptt. of Irrigation & Hydraulics, Punjab Engineering College, Chandigarh, India.

LABORATORY MODELING OF RESERVOIR SEDIMENTATION AND SLUICING: SCALE CONSIDERATIONS

Rollin H. Hotchkiss
Department of Civil Engineering
W348 Nebraska Hall
University of Nebraska-Lincoln
Lincoln, NE 68588-0531

Gary Parker
Department of Civil and Mineral Engineering
St. Anthony Falls Hydraulic Laboratory
University of Minnesota
Minneapolis, MN 55414

Abstract

Experiments of reservoir sedimentation and sluicing were performed in a laboratory flume. Upon creation of a reservoir backwater in the flume, a depositional delta formed at the upstream entrance to the flume and progressed in the downstream direction. The topset slope during delta migration was observed to be very nearly equal to the original channel slope. When the delta had progressed to its equilibrium position near the simulated dam, the simulated reservoir was drained using sluice gates, which produced upstream progressing degradation until the original equilibrium conditions were recovered. Mathematical modeling and scaling considerations show that the flume was much shorter than the actual length required to fully accomodate the backwater profile; this accounted for the steeper than expected topset slope during delta migration and the faster than expected delta migration rate. Informational feedback between physical and mathematical models in this case produced a rational representation of reservoir sedimentation and sluicing.

Introduction

Sedimentation in reservoirs decreases storage capacity and reduces the useful life of constructed projects. Because the number of new reservoir sites is decreasing, it is important to preserve existing reservoir capacity. The purpose of the research project reported herein was to investigate the basic nature of sedimentation in reservoirs and to examine sediment sluicing as one possible means of restoring reservoir capacity. The research was conducted using a laboratory flume and a mathematical computer model. The purposes of this paper are to discuss what was learned by observing the experiments of sedimentation and sluicing and to discuss the limitations of modeling reservoir sedimentation and sluicing in a laboratory environment as revealed by mathematical modeling and scale considerations.

Experimental Program

Reservoir sedimentation and sluicing were simulated in two stages in a laboratory flume at St. Anthony Falls Hydraulic Laboratory at the University of Minnesota. The flume in the first stage was 12.2 meters long, 38 centimeters high, and 15 centimeters wide. The flume was fitted with a single sluice gate about nine meters from the entrance that extended the full width of the flume. The flume was modified for the second stage by adding a two-meter long diverging section at the end of the original flume. The single sluice gate was replaced by three 15 centimeter-wide sluice gates at a location about one meter into the diverging portion of the addition (Figure 1). Each of the three sluice gates was operated independently and manually.

Quasi-uniform, non-cohesive crushed walnut shells (median diameter 0.67 millimeters, gradation coefficient 1.3, specific gravity 1.35) were used as the model sediment. Crushed walnut shells have been used successfully elsewhere in mobile-bed models (Parker, Martinez, and Hills, 1982, and Vries, Hartman, and Amorocho, 1980).

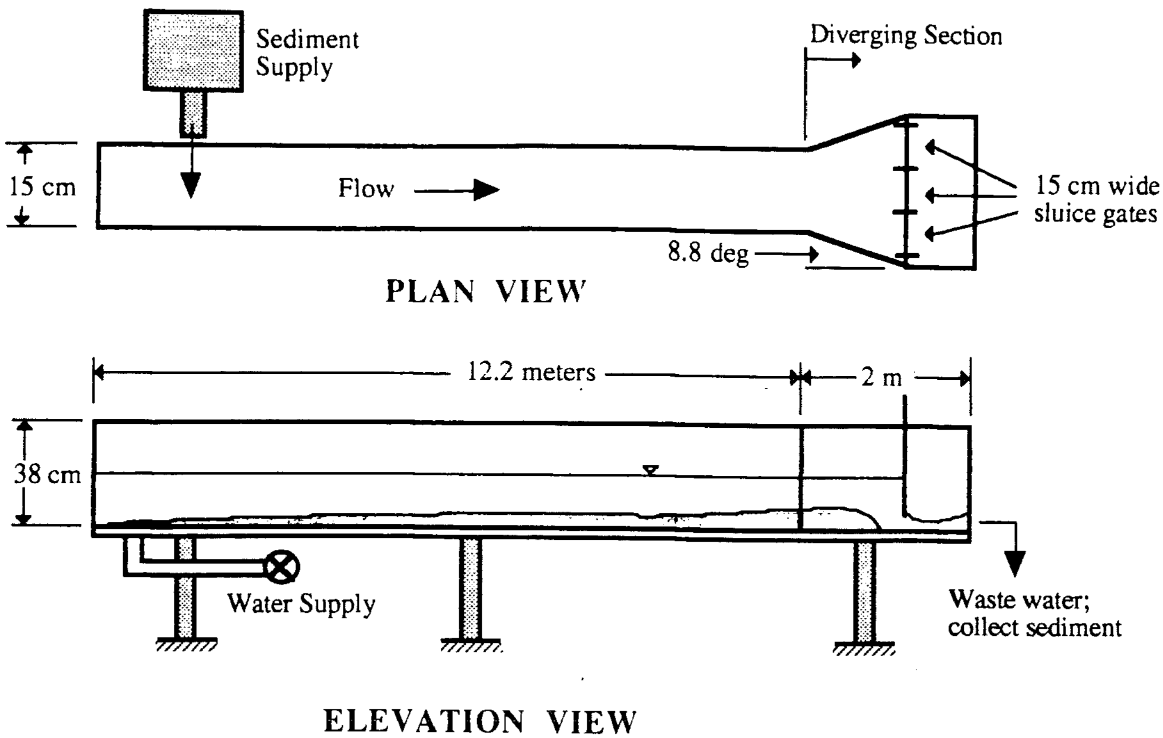

Figure 1. Experimental facility (not to scale)

Water and sediment enters the flume at predetermined and set rates. The ranges of flow rate and sediment feed rates varied from 1.5 to 4.25 liters per second and from 50 to 570 grams per minute, respectively. Sediment transport similarity based on Shields stress was satisfied for the experiments (Parker, Martinez, and Hills, 1982). Each experiment was initially run with the sluice gate(s) open until open channel equilibrium conditions were achieved. Then the sluice gate(s) were lowered a predetermined amount to simulate a dam. Measurements were taken to describe the ensuing hydraulic and sediment characteristics of flow. Once equilibrium was once again established, the sluice gate(s) were either raised to simulate sluicing or lowered again to increase sedimentation.

In order to limit the investigation to the basic process of reservoir sedimentation, only bedload-dominated transport was simulated. The use of the quasi-uniform, non-cohesive sediment eliminated longitudinal sorting, armoring and consolidation effects. A narrow facility reduced three-dimensional effects of bedforms and non-uniform sediment deposition and erosion. Steady input of water and sediment eliminated the unsteady effects of daily or seasonal hydrographs.

Understanding of Processes

Aggradation. Upon lowering the sluice gate a significant amount, the water surface in front of the dam quickly rose to a new equilibrium elevation sufficient to pass the flow through the more restricted sluice gate opening. The backwater influence quickly extended to the flume entrance. Any further adjustment in water level was in response to changes in bed levels. Sediment transport ceased throughout the flume as bedforms were "frozen" in place and sediment in suspension dropped out. Sediment accumulated at the upstream end of the flume. Due to the increased depth and decreased velocity, the sediment deposited until the flow depth decreased sufficiently to produce adequate velocity for transport. A delta thus formed at the flume entrance and moved downstream. The sediment was transported across the lip of the advancing delta and fell onto the foreset slope under the influence of gravity. The foreset slope attained the submerged angle of repose, and the delta moved downstream into the flume as the sediment continued to be transported across the lip to the foreset slope (Figure 2). The channel slope upstream of the delta appeared to be equal to the slope before the sluice gate setting was changed, even in the diverging region of the flume upstream from the dam.

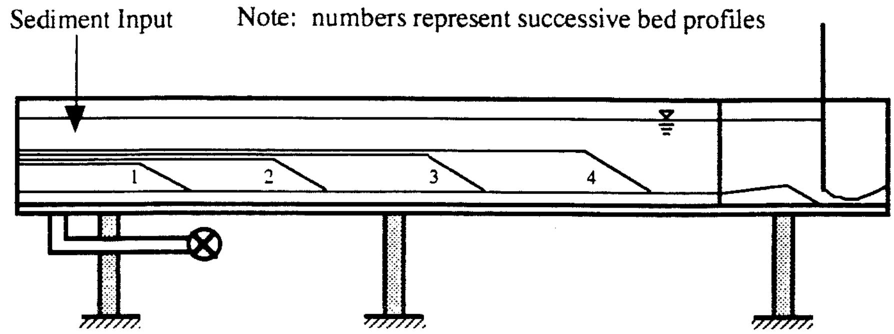

Figure 2. Successive delta locations after lowering sluice gate

In the experiments with an expanding region upstream from the dam, the delta entered the flared region, and the sediment spilling down the foreset slope spread laterally to fill the width of the flume. The delta then continued downstream. The delta eventually stopped progressing downstream as it approached the sluice gates, and the incoming sediment was transported down the foreset slope and passed under the sluice gates.

This description agrees with Garde and Ranga Raju's 1985 thought experiment of reservoir sedimentation in that the bed rose as much as the water surface and all sediment passed under the sluice gate (over the dam in their case). The process also agrees with experimental observations of Chee and Sweetman (1971), especially as they describe a mound of sediment forming at the inlet to the reservoir. The observed formation of two distinct reaches, one upstream and the other downstream of the delta, agree exactly with the experimental observations of Bhamidipaty and Shen (1971), including their description of the foreset slope attaining the submerged angle of repose. Observations seem to confirm Sugio's experimental results in that the aggrading profile can be considered to be almost in equilibrium as the sediment front advances (1972). That the equilibrium bed slope after lowering the sluice gate is the same as before agrees with the observations of the scale model of Chitale, Galgali, and Appukuttan (1975).

The basic sedimentation process shows 1) a delta formation at the entrance of the flume that moves downstream with time and 2) very little sediment transport downstream of the delta toe. The delta thus represents a shock in that sediment transport is reduced to zero over the very short horizontal distance from the delta lip to the delta toe. The observation that the topset slope upstream from the delta lip is about at the original channel slope as the delta progresses downstream is in disagreement with field observations. Borland (1971) collected data which shows the topset slope is usually from between one-half to two-thirds the original channel slope.

Degradation. Upon raising the sluice gate after a delta had reached equilibrium, the headwater surface elevation dropped rapidly in response to the increase in flow area beneath the sluice gate. A negative surface wave proceeded upstream and was followed more slowly by upstream progressing degradation of the channel bed. Sediment transport rate increased throughout the flume, and plane-bed conditions prevailed for some time. Eventually bedforms appeared at the upstream end of the flume and proceeded downstream, and a new equilibrium profile was established. The bed recovered the same slope as before, and the height of the delta was decreased and was located nearer to the sluice gate than before. Uniform scour was observed across the flume width, even in the expanding region. While there is little field data with which to compare the experiments, the expected process of upstream progressing degradation was observed in all runs.

Limitations Based on Scale Considerations

A one-dimensional, uncoupled steady flow sediment transport model was developed to simulate the sedimentation and sluicing process (Hotchkiss, 1989). A special shock-fitting procedure was included to track the evolution and development of the delta. The use of the mathematical model revealed how the laboratory scale influenced the aggradation and sluicing process.

Aggradation. The computed lengths of the backwater profiles resulting from lowering the experimental sluice gate(s) the prescribed amounts were ten times longer than the experimental flume. This means that the upstream boundary in the laboratory experiments was located relatively close to the simulated dam. This explains why a delta formed immediately in the flume entrance and why the topset slope upstream of the moving delta was very close to the slope of the original channel. Had the laboratory simulations been done in a flume ten times longer, topset slopes would have been flatter. Figures 3 and 4 show the differences in sediment transport rate

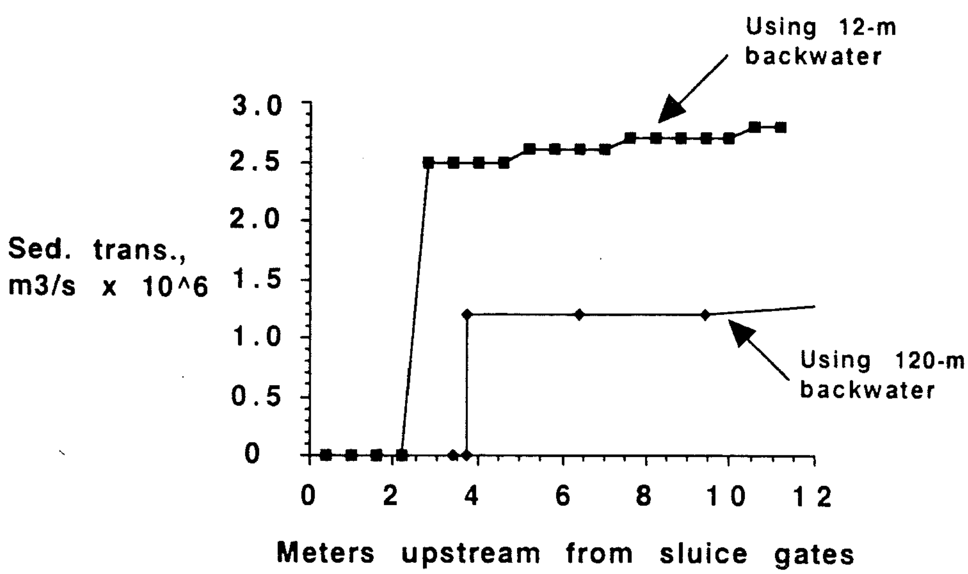

Figure 3. Computed sediment transport rates for 12-meter-long and 120-meter-long backwater reaches

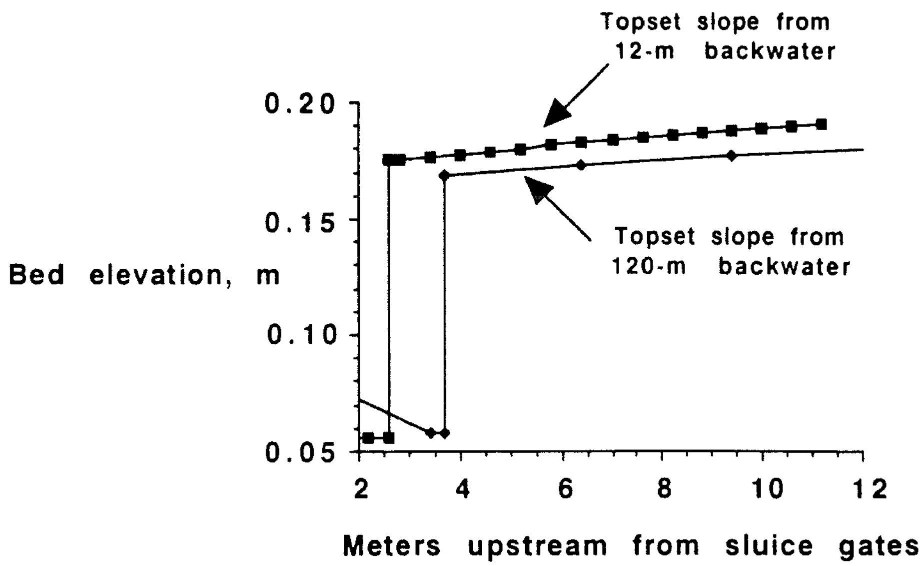

Figure 4. Computed bed profiles when the delta is about three meters upstream of the sluice gates for the 12-meter-long and 120-meter-long backwater reaches

and topset slope as influenced by the short experimental facility. Each figure shows the difference in the independent variable as a function of backwater length. The topset slope of the computer simulation in Figure 4 using the full backwater profile is about 76 percent, much closer the field observations than the near 100 percent in the experiments. Not shown is the computed result that delta propagation speed in the flume was much faster than prototype expectations, again influenced by the closeness of the sediment source to the simulated dam.

Degradation. The sluice gate(s) for most of the experimental runs were opened completely and suddenly, resulting in unsteady transients and reflected water waves upstream and downstream in the flume. Scale considerations produce a more reasonable gate opening rate, which was subsequently used in the computer program and in the experiments. Computed and observed results then agreed well. Assuming Froude number similarity and an undistorted scale of 1:100, the time scale for simulation is 1:10. Assuming a relatively fast prototype drawdown of one month, the model drawdown should be about three days. Sluicing experiments were repeated using a model drawdown rate of three millimeters every 20 minutes, which restored the original open channel conditions in about 12 hours. Subcritical flow was maintained throughout the flume for the entire sluicing simulation.

Summary

Laboratory simulations of reservoir sedimentation and sluicing showed the essential features of each process. Sedimentation produced deltas, which essentially constitute a shock front that grows downstream. Sluicing with the proper time scale produced orderly upstream progressing degradation. Because the experimental facility was too short, deltas move downstream too rapidly with topset slopes that are too steep. Sluicing in the laboratory model must be done very carefully to avoid extremely unsteady features not observed in the field. Even with these limitations, laboratory modeling, coupled with mathematical modeling of the same processes, reveals important facts that can be used when designing new projects or rehabilitating existing ones.

REFERENCES

Bhamidipaty, Suryanarayana, and Hsieh W. Shen. 1971. Laboratory Study of Degradation and Aggradation. American Society of Civil Engineers Harbors and Coastal Engineering Division, vol. 97, No. WW4, November, p. 615-630.

Borland, Whitney M.. 1971. Reservoir Sedimentation. In River Mechanics, Vol. II. H.W. Shen, editor. Fort Collins, Colorado: Water Resources Publications.

Chee, S.P., and A.P. Sweetman. 1971. An Experimental Investigation of Reservoir Sedimentation. Proceedings of 14th Congress of the International Association of Hydraulic Research, vol. 1, p. 21-24, Paris, France.

Chitale, S.V., V.G. Galgali, and K.N. Appukuttan. 1975. Simulation of Delta Building Process. Proceedings of Symposium on Modeling Techniques, vol. 2, 2nd Annual Symposium of the American Society of Civil Engineers Waterways, Harbors and Coastal Engineering Division, San Francisco, September 3-5.

Garde, R.J., and K.G. Ranga Raju. 1985. Mechanics of Sediment Transportation and Alluvial Stream Problems. New Delhi, India: Wiley Eastern Limited.

Hotchkiss, Rollin H. 1989. Reservoir Sedimentation and Sediment Sluicing: Experimental and Numerical Analysis. Ph.D. thesis, University of Minnesota Department of Civil and Mineral Engineering.

Parker, Gary, Ismael Martinez, and Randall Hills, 1982. Model Study of the Minnesota River near Trunk Highway No. 169 Bridge, Minnesota. Project Report No. 213. University of Minnesota: St. Anthony Falls Hydraulic Laboratory. September.

Sugio, Sutesaburo. 1972. Discussion of "Laboratory Study of Degradation and Aggradation." American Society of Civil Engineers Journal of the Waterways Division, WW4, November, p. 588-591.

Vries, J.J. de, W. Hartman, and F. Amorocho. 1980. Sediment Modeling for the Sacramento River Diversion to the Peripheral Canal. In Proceedings of the American Society of Civil Engineers Specialty Conference on Computer and Physical Modeling in Hydraulic Engineering. Chicago, Illinois: August 6 - 8.

VARIED DIAMETER SCALE METHOD IN MOVABLE BED MODEL DESIGN

Lo Fuan* Xu Yongnian**

ABSTRACT

The movement behavior of coarse and fine sand in the flow is different from each other. In model design, it would be very difficult to satisfy the similarity of movement of every grain size if only one grain diameter scale were to be adopted. The irrational discontinuity or fault of the grain composition curve would be appeared when the grain diameter scale were to be chosen according to flow region. As a trial of practice, the varied diameter scale method was used to avoid the above mentioned defect.

BASIC PRINCIPLE

In the movable bed model with bed load the threshold similarity of sediment should be considered principally besides the similarity of flow. As the exist of the local complex spiral and turbulent flow in the channal of some cases, the chance of suspension of the sediment near the bed would still be frequent, many designers considered that the similarity of settling velocity should be taken into account where the local flow pattern is complex, so as to ensure the achievement of the similarity of scouring and deposition of the river bed for gravel, coarse and fine sand simultaneously.

By the theorem of the threshold of sediment, it is known that the movement behavior of the coarse and fine sand is different from each other, the movement of the gravel and coarse sand is mainly governed by gravity, while the movement of the fine sand is affected by laminar boundary layer of the flow besides the gravity. Since 1950s, the mechanism of the movement of the fine sand has been further revealed by Chinese scholares, they considered that the cohesion among the particles of fine sand is the governing cause of the threshold movement of the fine sand.

By the research of Shields and others, the threshold drag force can be expressed by the following formula and Figure. 1.

$$\frac{\tau_c}{(\gamma_s-\gamma)d} = f\left(\frac{V_* d}{\nu}\right) = \Psi$$

in which, $\tau_c = \rho V_*^2$ — the threshold drag force of sediment, u_* — the threshold friction velocity, ρ — density of water, d — diameter of sediment, γ_s, γ — unit weight of sediment and water, Ψ — comprehensive coefficient of threshold of the sediment. From the figure, it is shown:

As $\frac{V_* d}{\nu} > 500$, or $d > 6.4$ mm, in coarse region Ψ approaches to a constant, 0.06, or 0.04 according to M.C. Miller, the threshold of

---

* Senior Engineer, ** Engineer, Institute of Water conservancy and Hydroelectric Power Research, Beijing, China

sediment is independent with the grain Reynolds number, but in relations with the flow condition (V, h) and sediment properties (γ_s, d).

As $\frac{V_* d}{\nu}$<500, or d<6.4 mm, in the transition region and smooth region, ψ is the function of grain Reynolds number, $\psi = f\left(\frac{V_* d}{\nu}\right)$,

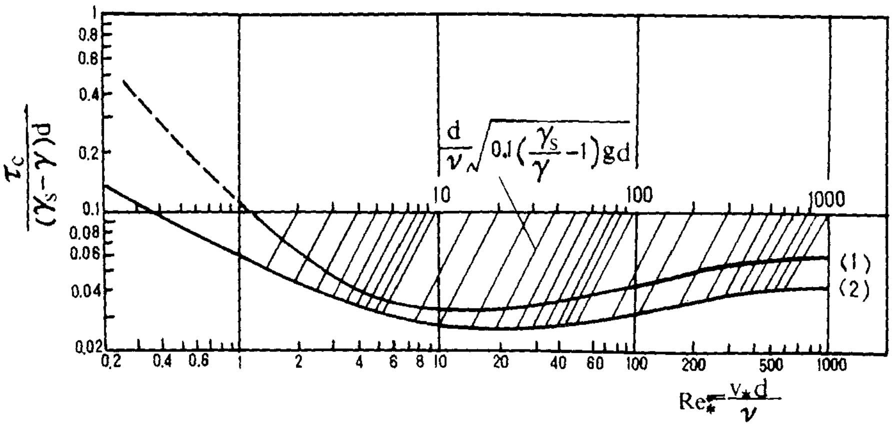

Figure 1 $\qquad \frac{\tau_c}{(\gamma_s-\gamma)d} \sim \frac{V_* d}{\nu}$ relation

(1) Shields, (2) M. C. Miller

the threshold of sediment would be affected by the laminar boundary layer of the flow, and varies with the variation of the grian Reynolds' number.

The above expression can be transformed into the form of threshold velocity,

$$V_c = \psi \frac{A}{\sqrt{g}} \sqrt{\frac{\gamma_s-\gamma}{\gamma} g d}\left(\frac{h}{d}\right)^{1/6},$$

in which, V_c — threshold velocity, A — a constant related with Chezys' coefficient, h — water depth.

By the researches of Zhang Reijin, Dou Guoren and others, the threshold velocity of coarse and fine sand can be unified into one formula, which includes the effects of both the gravity and cohesion. The achievements of this kind of research can be seen as in Figure 2. For example, the Zhang Reijin formula is

$$V_c = 1.34\left(\frac{h}{d}\right)^{0.14}\left[\frac{\gamma_s-\gamma}{\gamma} g d + 0.000004 96\left(\frac{d_1}{d}\right)^{0.72} g\,(h_a+h)\right]^{1/2},$$

in which, d_1 — reference grain diamter, taken to be 1 mm, ha — the height of water column of the atmospheric pressure, about 10 m. In the square bracket, the former term denotes the gravity effect and the later denotes the effect of cohesion. For water depth is 0.15 m, and coarse sand d>2mm, gravity is the principal force and cohesion may be neglected; for extreme fine sand d<0.02 mm, the cohesion is the principal force, and gravity may be neglected; and for d=2 - 0.02 mm in transition region, both forces play in the action.

The sand chosen in the model design should be adapted in accordance with the above conditions, it is neccessary to choose different grain diameter scales according to different flow region, and then the grain diameter scale of coarse and fine sand to be different. For example, from the above Shields' threshold velocity formula, we have

$$\lambda_{V_c}=\lambda_{\psi}\lambda_{\gamma_s-\gamma}^{1/2}\lambda_d^{1/3}\lambda_h^{1/6} ,$$

in which, $\lambda_{V_c}, \lambda_{\psi}, \lambda_{\gamma_s-\gamma}, \lambda_d, \lambda_h$ are similarity scales of V_c, Ψ, $\gamma_s-\gamma$ d and h respectively. For the coarse sand, λ_{ψ} =const., after the geometric scale and the kind of sand in the model test has been chosen,

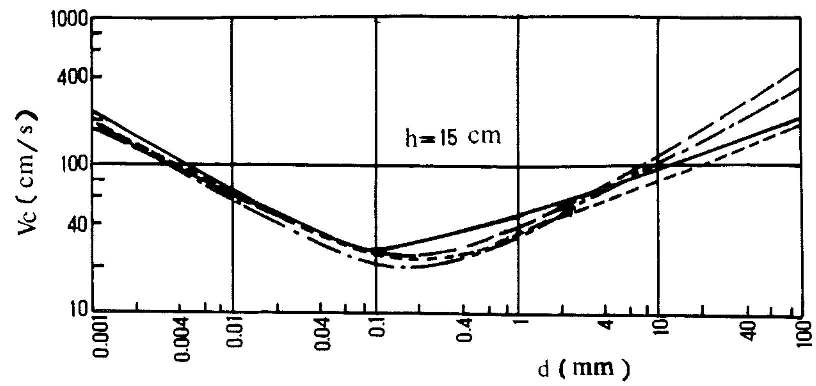

Figure 2. Unified threshold velocity formula of coarse and fine sand

the grain diameter scale can be determined. For the fine sand, the grain diameter scale have to be varied with the variation of the grain diameter in accordance with $\lambda_{\psi}=\lambda_{f(\frac{v_* d}{\nu})}$.

In the past for fulfil the requirement of different grain diameter, the grain diameter scale was determined according to different flow region only , the composition curve of model sand would be discontineous or faulted as shown in Figure 3. It is irrational that one size of grain with two percentages at the point of demarcation grain diameter of flow region.

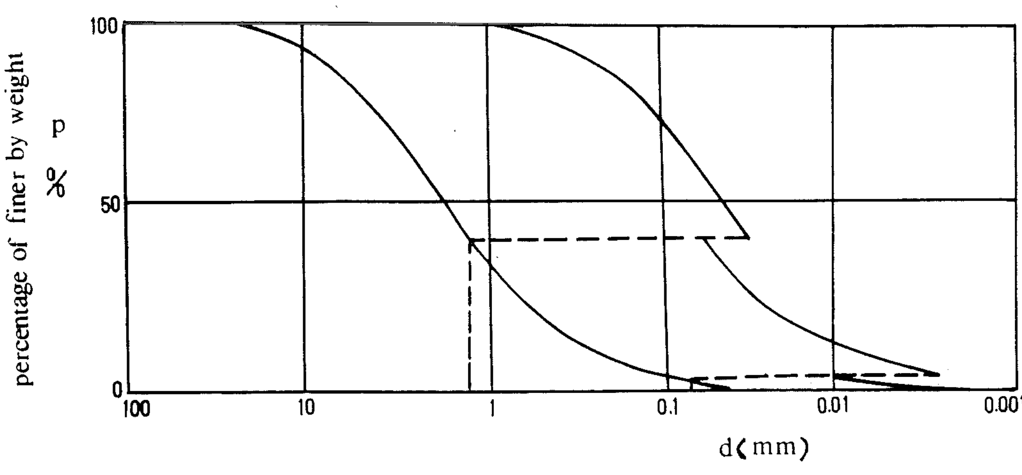

Figure 3 The sketch of composition curve of the model sand according to different flow region with different diameter scale

The general formula of settling velocity of particles is

$$\omega=\sqrt{\frac{4}{3C_d}}\sqrt{\frac{\gamma_s-\gamma}{\gamma}gd} ,$$

in which C_d —— settling resistance coefficient, a function of the grain Reynolds' number. by the researches of scholares, in the laminar flow region, Red < 0.5, d < 0.1 mm, $C_d = N/\frac{\omega d}{\nu}$; in the turbulent flow region, Red > 1000, d > 2 mm, C_d=const., in the transition region, Red = 1000 - 0.5, d = 2 - 0.1 mm, $C_d = f(\frac{\omega d}{\nu})$.

The corresponding similarity scales of settling velocity of the three flow regions can be written as follows:

for the laminar flow region, d<0.1 mm, $\lambda_\omega = \lambda_{\gamma_s-\gamma}\lambda_d^2$,

for the turbulent flow region, d>2 mm, $\lambda_\omega = \lambda_{\gamma_s-\gamma}^{1/2}\lambda_d^{1/2}$,

for the transition region, d=2 - 0.1 mm, $\lambda_\omega = \lambda_{f(\frac{\omega d}{\nu})}\lambda_{\gamma_s-\gamma}^{1/2}\lambda_d^{1/2}$,

in which, $\lambda_\omega, \lambda_{\gamma_s-\gamma}, \lambda_d, \lambda_{f(\frac{\omega d}{\nu})}$ —the scales of similarity of the $\omega, \gamma_s-\gamma$, d, $f(\frac{\omega d}{\nu})$ respectively. We had designed the grain scale in accordance with various flow regions, the discontinuity or fault of the model sand composition curve still exists, it is much more prominent expecially in the transition region, because the continuous variation was often replaced by average condition.

Moreover, in natural river, the threshold of gravel is in the turbulent flow region, the threshold of sand is in the transition region and the threshold of suspended load is in the laminar flow region or hydraulic smooth region, but the flow region of the model sand reduced according to the scale are not certainly in the same flow region of the prototype, even sometimes the light material was used. Therefore, to compute the prototype and model sand with one formula in one region sometimes is not reasonable.

For keeping the continuity of the composition curve of the model sand, to overcome the above mentioned defect, the varied diameter scale method will be presented in this paper. The principle of this method is very simple. Due to the settling resistant coefficient Cd and the threshold comprehensive coefficient ψ of the prototype (every region) and model (every region) sand are different for each grain size, the scale of resistant coefficient λ_{C_d} and the scale of threshold coeffient λ_ψ are also different from each grain size, so the grain diameter scale of the model sand becomes to be a variable and varies with the variation of grain diameters.

DESIGN METHOD OF VARIED DIAMETER SCALE

This model design method is very simple. On the basis of the model geometric scale, kind of model sand and hydraulic scale have preliminarily been chosen, the design can be proceeded, firstly, to compute the threshold velocities Vcp and settling velocities ωp of various grains of the prototype respectively by the formulas of threshold velocity and settling velocity, secondly, to compute the threshold velocity Vcm and settling velocity ωm of corresponding model sand by the threshold velocity scale $\lambda_{V_c} = \lambda_V$ and settling velocity scale $\lambda_\omega = \frac{\lambda_V \lambda_h}{\lambda_L}$, and finally to compute the grain diameter of model sand dmvc and dmw corresponding to the Vcm and ωm by threshold velocity formula and settling velocity formula. Thus two sets of grain diameter scales are obtained , i.e. the threshold grain diameter scale $\lambda_{dV_c} = d_p/d_{mV_c}$ and the settling grain diameter scale $\lambda_\omega = d_p/d_{m\omega}$. It is shown here: 1. due to the prototype and model sand are in different flow region, the obtained grain diameter scale is different for the two regions, 2. since there is no close relation between the threshold velocity formula and settling velocity formula, so the two sets of grain diameter scales obtained are different.

However, only one set of the grain diameter scale can be used finally, so that the grain diameter scale should be further modified. There are two principles of modification: 1. to take account the similarities of the threshold and settling velocities simultaneously, and to satisty the two similarities approximately; 2. for the gravel and coarse sand, the similarity of the threshold velocity should be emphasized and some deviation of similarity of settling velocity would be allowed, and for the fine sand, the consideration of the similarity of settling velocity should be emphasized and some deviation of threshold similarity would be allowed. the readjustment includes revising the grain diameter scale, geometric scale, and changing the model sand. The final model design for sand is to make $\lambda'_{V_c} \approx \lambda_V$ and $\lambda'_\omega \approx \lambda_V \lambda_h / \lambda_L$.

EXAMPLE

A hydropower station intended to research the sediment prevention installations, and to carry out model experiments. by the way of model study, the problem of preventing the gravel and coarse sand from entering the intake of hydropower station should be solved. The bed material of the river is $d_{90} = 100$ mm, $d_{50} = 18$ mm, $d_{10} = 1$ mm.

Due to the complexity of the local river features, on the respect of the flow movement, it is required the model to satisfy the similarities of

gravity $\qquad \lambda_V = \lambda_h^{1/2}$,

resistance $\qquad \lambda_V = \lambda_n^{-1} \lambda_h^{2/3} \lambda_J^{1/2}$,

simultaneously. On the respects of sediment movement, the following similarities should be taken into account,

threshold velocity, $\qquad \lambda_{V_c} = \lambda_V$, $\quad \lambda_{V_c} = \lambda_\psi \lambda_{\gamma_s-\gamma}^{1/2} \lambda_d^{1/3} \lambda_h^{1/6}$,

settling velocity, $\qquad \lambda_\omega = \lambda_V \lambda_h / \lambda_L$, $\quad \lambda_\omega = \lambda_{C_d}^{-1} \lambda_{\gamma_s-\gamma}^{1/2} \lambda_d^{1/2}$,

sediment discharge, $\qquad \lambda_{g_s} = \dfrac{\lambda_{\gamma_s}}{\lambda_{\gamma_s-\gamma}} \cdot \dfrac{\lambda_\psi^4}{\lambda_{C_0}^2} \lambda_\omega$,

time scale of river bed deformation, $\lambda_{t_1} = \lambda_{\gamma_0} \lambda_h \lambda_L / \lambda_{g_s}$,

in which $\lambda_n, \lambda_J, \lambda_{g_s}, \lambda_{C_0}, \lambda_{\gamma_0}$ —— scale of roughness, slop, sediment discharge, nondimensional Chezys' coefficient and volume weight of deposit, respectively.

According to the river, construction, and laboratory condition, an undistorted movable bed model with $\lambda_L = \lambda_h = 100$ was selected, and the ground peach-stone grains with unit weight $\gamma_s \doteq 1.25$ T/m was selected as the model sand. On the basis of preparatory experiments, checking computations of every scale had been carried out. After revision and adjustment of the grain diameter scale λ_d, threshold velocity scale λ_{V_c}, and settling velocity scale λ_ω, the scale of model sand was determined as shown in Figure 4. From the figure, it is shown that the grain diameter scale is varied, $\lambda'_{V_c} \approx \lambda_V$, $\lambda'_\omega \approx \frac{\lambda_V \lambda_h}{\lambda_L}$, the deviation of the threshold velocity scale and settling velocity scale to the exact velocity scale $\lambda_V = 10$ is only about 10%, so that the achievement of the similarity of scouring and silting of the gravel and coarse and fine sand could be ensured. By the conditions stated above, the sediment discharge scale can be computed as $\lambda_{g_s} = 321$, and the time scale of river bed deformation can be computed as $\lambda_{t_1} = 85$.

By the model experiments and analysis, sediment prevention installations of the project was suggested as shown in figure 5. The prevention efficiency of the installation are more than 99%, so the problem of sediment prevention of this hydropower station has been solved successfully.

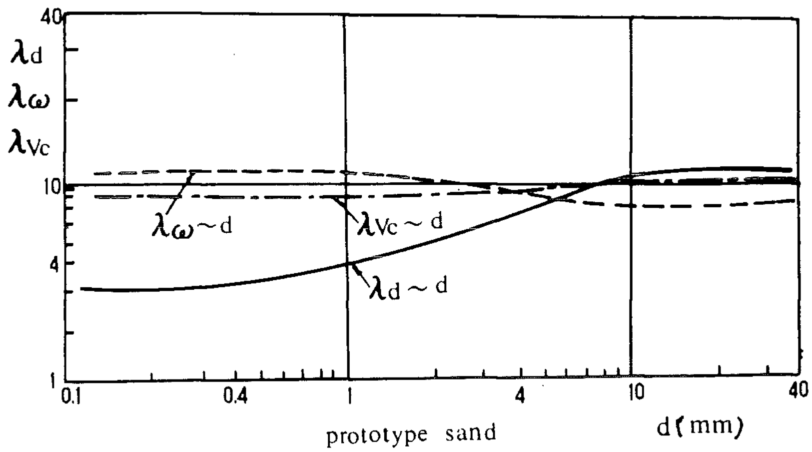

Figure 4 Model sand scale curves

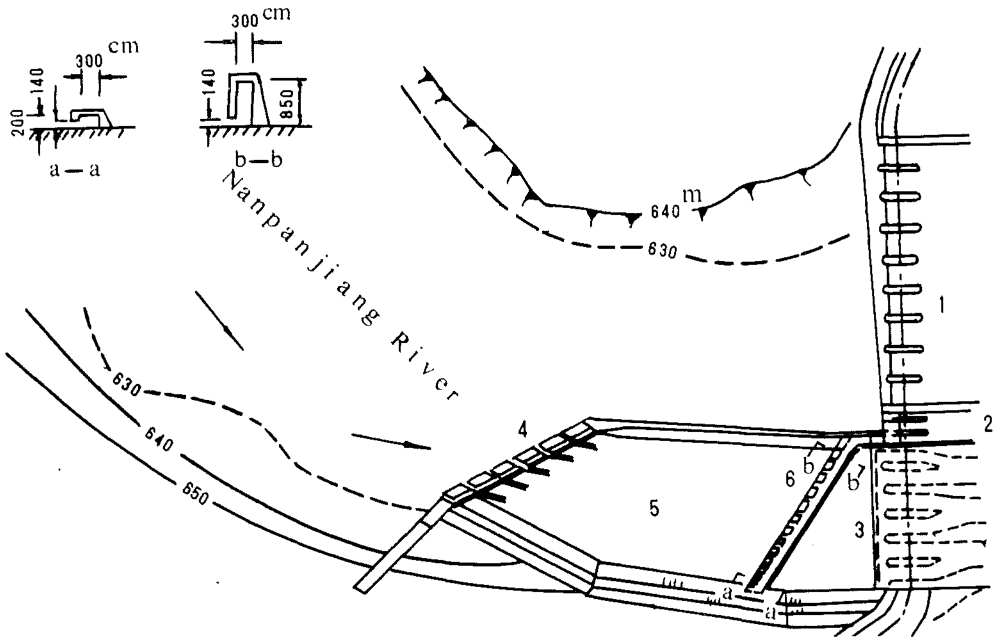

Figure 5. The layout of the sediment prevention installations of the intake of a hydropower station

1. overflow dam, 2. sluicing gate, 3. intake gate,
4. sand guiding weir, 5. settling tank, 6. sluicing gallery